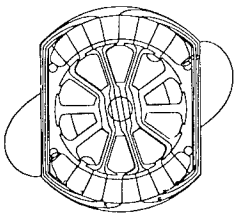

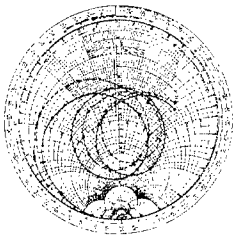

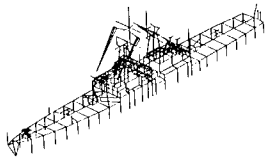

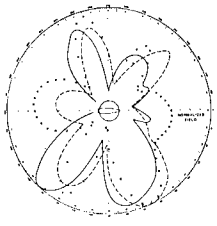

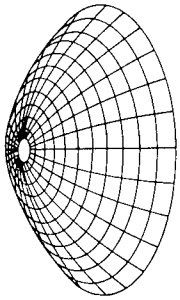

12th Annual Review of Progress in

APPLIED COMPUTATIONAL ELECTROMAGNETICS

at the

Naval Postgraduate School

Monterey, CA

March 18-22, 1996

CONFERENCE PROCEEDINGS

DISTRIBUTION STATEMENT A
Approved for public release;
Distribution Unlimited

CONFERENCE PROCEEDINGS

VOLUME II

12th Annual Review of Progress in APPLIED COMPUTATIONAL ELECTROMAGNETICS

at the

Naval Postgraduate School

Monterey, CA

March 18-22, 1996

TECHNICAL PROGRAM CHAIRMAN

Richard K. Gordon

19970910 101

Sponsored by

The Applied Computational Electromagnetics Society,

NPS, DOE/LLNL, University of Mississippi, University of Illinois

USAF, DOD AND DOE IN COOPERATION WITH IEEE, URSI, ASEE, SIAM AND AMTA

THE NAVAL POSTGRADUATE SCHOOL

Table of Contents i

1997 Call for Papers xii

1996 Symposium Program Committee xiv

Technical Program Chairman's Statement xv

ACES President's Statement xvi

ACES 96 Short Courses xvii

Agenda xviii

VOLUME 1

SESSION 0: AMATEUR RADIO SESSION
Chair: W.P. Wheless, Jr.

"Ground-Plane Antennas with Elevated Radial Systems" by J.S. Belrose 2

"Review of Characteristics for HF Dipole Antennas Including the Cases Where the Dipoles are Above and Parallel to the Surface of Real-World Grounds" by G.M. Royer 12

"HF Multi-Frequency Antennas Using Coupled Resonators" by G.A. Breed 26

"The Optimized Wideband Antenna (OWA) and its Application" by J.K. Breakall 33

"The Quad-Rhomb Antenna - A New All Band Antenna for Amateur Radio Applications" by R. Anders 40

"SKY-WAVES-95" by R. Anders 46

"Using Ham Radio CEM Codes to Gain Insight to VHF Ground Plane Antennas and to Mitigate 75 Meter Mars RFI at a Naval Receiving Site" by A. Hoffman and R.W. Adler 52

"Development of Practical Landstorfer Antennas for Amateur Use" by M.C. Tarplee 60

"Two-Port Network Specification of Baluns for NEC Analysis and Other Applications" by W.P. Wheless, Jr. and C.S. Wheless 68

SESSION 1: HIGH FREQUENCY METHODS
Chair: R.J. Burkholder

"Physical Theory of Diffraction Analysis of Impedance Structures" by H.H. Syed and J.L. Volakis 76

"Hybrid SBR/GTD Radio Propagation Model for Site-Specific Predictions in an Urban Environment" by J. Schuster and R. Luebbers 84

"Analysis of Dielectric Structures Using the NEC-BSC" by R. Marhefka and L. Henderson 93

"Hybrid MM-PO-Fock Analysis of Monopole Antennas Mounted on Curved Convex Bodies" by U. Jakobus and F.M. Landstorfer 101

SESSION 1: continued

"Numerical Diffraction Coefficient for an Impedance Wedge with a Material Body Attached to its Edge" by M.F. Otero and R.G. Rojas 109

"Reflection and Diffraction of Well-Focussed General Astigmatic EM Gaussian Beams" by G. Zogbi, H.T. Chou, P.H. Pathak, and R.J. Burkholder 117

"Polarized Scattered Light by a Semicylindrical Boss on a Conducting Flat Plane" by H.A. Yousif 125

"Divergence of Rays in Modulated Atmospheric Ducts" by I.P. Zolotarev 131

"Diffraction by a Weak Dielectric Wedge" by A.V. Popov 138

"Far-field Diffraction Effects of EUV Fresnel Zone Plates" by Y.V. Kopylov, V.A.Baranov, A V.Popov, and A Vinogradov 142

SESSION 2: INVERSE SCATTERING
Chairs: P.M. Goggans and L. Riggs

"Radar Time and Frequency-Domain Received Signals for Realistic Antennas and Scatterers" by P.M. Goggans and J.D. Pursel 152

"The Extraction of Scattering Mechanisms from Measured Data" by H.M. Chizever and K.M. Pasala 153

"Using the E-pulse Technique and Hypothesis Testing to Perform Radar Target Identification" by L. Riggs, J. Mooney, and C. Smith 163

"A Boundary-Integral Code for Electromagnetic Nondestructive Evaluation" by K. Murphy and H.A. Sabbagh 171

"The Numerical Analysis of Planar Antennas Buried in Layered Media" by J. van Tonder, J. Cloete, and D. Davidson 179

SESSION 3: RCS ANALYSIS
Chair: M. El-Shenawee

"A Response Surface Methodology Study of Electromagnetic Data Compression and Reconstruction" by V.M. Floyd, Jr., A. Terzuoli, Jr., G.C. Gerace and P.F. Auclair 188

"Curvilinear, Isoparametric Modelling for RCS Prediction, Using Time Domain Integral Equations" by S.P. Walker, M.J. Bluck, M.D. Pocock, C.Y. Leung, and S.J. Dodson 196

"Double Scatter Radar Cross Sections for Two Dimensional Random Rough Surfaces that Exhibit Backscatter Enhancement" by M. El-Shenawee and E. Bahar 205

SESSION 4: APPLICATIONS OF PARALLEL COMPUTING
Chairs: L. Epp and K. Naishadham

"Solution of Electromagnetic Eigenproblems on Multiprocessor Superscalar Computers" by M.P. Debicki, P. Jedrzejewski, J. Mielewski, P. Przybyszewski, and M. Mrozowski 214

"Implementation of Hybrid FDTD/FVTD Conformal Algorithm on a Massively Parallel Computer" by J.S. Chen and A.A. Seidl 221

SESSION 4: continued

"Parallel CARLOS-3D Code Development" by J.M. Putnam and J.D. Kotulski 228

SESSION 5: NEW DEVELOPMENTS IN TLM MODELING
Chair: W.J.R. Hoefer

"On the Advantages of ATLM Over Conventional TLM" by M. Krumpholz and P. Russer 238

"Advanced Node Formulations in TLM - The Matched Symmetrical Condensed Node (MSCN)" by V. Trenkic, C. Christopoulos, and T.M. Benson 246

"A General and Complete Two-Dimensional TLM Hybrid Node Formulation Based on Maxwell's Integral Equations" by N. Pena and M.M. Ney 254

"A General Formulation of a Three-dimensional TLM Condensed Node with the Modeling of Electric and Magnetic Losses and Current Sources" by N. Pena, and M.M. Ney 262

"A Numerical Comparison of Dispersion in Irregularly Graded TLM and FDTD Meshes" by F.J. German, J.A. Svigelj, and R. Mittra 270

"Accuracy Considerations of a Class of Frequency-Domain TLM Nodes" by S. Chen and R. Vahldieck 279

"Distributed Simulation of Planar Circuits by TLM Method in a Parallel Computing Environment" by B. Isele, J. Schmöller, and P. Russer 287

"Modeling Gyromagnetic Media in Symmetrical Condensed Node TLM" by L. de Menezes and W.J.R. Hoefer 294

"A Comparative Performance Study of Absorbing Boundary Conditions in TLM and FDTD" by C. Eswarappa and W.J.R. Hoefer 302

"Modelling of Coplanar Waveguide Discontinuities Using the Alternating Transmission Line Matrix (ATLM) Method" by B. Bader and P. Russer 310

"Quasi-Static Correction of a Knife Edge Corner in 2D TLM Algorithm" by L. Cascio, G. Tardioli, T. Rozzi, and W.J.R. Hoefer 317

SESSION 6:INTERACTIVE TECHNICAL SESSION

"Electromagnetic Visualization Using Commercial Software" by H.A. Nott 326

"Performance of Multiple, Thin Layers of Lossy Dielectrics as Broadband Attenuators" by G.W. Jarriel, Jr., M.E. Baginski, and L.S. Riggs 334

"Research & Engineering Framework (REF) Data Dictionary Specification for Computational Electromagnetics" by J.A. Evans 340

"Development of an Electromagnetic and Mechanical Simulation Tool for the Computer Modeling of the TACAMO LF/VLF Communication System" by M.C. Longtin, R.W. Sutton, K.J. Laskey and P.J. Morrison 347

"A New Look at Antenna Traps" by P.W. Leonard 354

SESSION 6: continued

~~"Block Wavelet Transforms for Fast MOM Computations: An Application to Pocklington's Equation" by W.L. Golik~~ *PAPER WITHDRAWN* 359

"Imaging of Conductive and Ferromagnetic Materials Using a Magnetic Induction Technique" by J. Ferreira, F. Linhares, J. Velez, J. de Ribomar S. Oliveira, and A.R. Borges 367

"Investigation of the Properties of Wavelet-Like Basis Functions in the Finite Element Analysis of Elliptic Problems" by L.A. Harrison and R.K. Gordon 375

"Continuing Development of the Research and Engineering Framework (REF) for Computational Electromagnetics" by L.W. Woo, B. Hantman, K. Siarkiewicz, J. LaBelle, and R. Abrams 383

"Numerical and Experimental Modelling of Liquid Dielectrics Using a Coaxial Cavity" by M. Bingle, D.B. Davidson, and J.H. Cloete 391

"Hardware/Software Codesign Model for XPATCHF Optimization" by B.A. Kadrovach, T.S. Wailes, A.J. Terzuoli, Jr., and D.S. Gelosh 398

"3D FDTD Simulation of EM Detection of Buried Waste" by D. Sullivan, B. Hansen and N. Skousen 406

"Application of Digital Filters to the Construction of Wideband Dispersive Boundary Conditions" by M. Mrozowski, M. Niedźwiecki, and P. Suchomski 413

"Note on Large Crane Coupling to Nearby AM Radio Stations" by P.W. Leonard and J.B. Hatfield 421

"XPATCHF Software System Analysis and Profiling" by B.A. Kadrovach, T.S. Wailes, A.J. Terzuoli, Jr., and D.S. Gelosh 429

"Theoretical Studies of Photonic Band Gap Materials" by M. Sigalas, R. Biswas, C. Chan, K. Ho, and C. Soukoulis 436

"On the Use of Richardson Extrapolation in the Finite Element Analysis of Two-Dimensional Electrostatics Problems" by W.E. Hutchcraft and R.K. Gordon 443

"Scattering from Chirally Coated Bodies" by R. Sharma and N. Balakrishnan 448

"A Mixed Formulation to Compute the Source Current Density in Inductors of Any Shape" by F. Robert, P. Dular, J.F. Remacle, M. Umé, and W. Legros 456

"High Power Microwave Amplification for High-Intensity Relativistic Electron-Beam Storage-Rings" by R.A. Speciale 464

"Real-Time Digital Signal Processor in Ionosphere Measurements" by A.L. Karpenko and V.V. Koltsov 469

"High Frequency Electromagnetic Safety Analysis by Numerical and Empirical Methods on Mobile Platforms" by M.J. Packer and R.C. Ferguson 473

"Computational Modeling of Wave Plasma Interaction" by V.A. Eremennko and Y.Cherkashin 481

SESSION 6: continued

"Attenuation of HF Radio Waves in a Forest: Results from Experiment"
by I.P. Zolotarev. V.A.Popov, and V.P. Romanuk 486

"Statistical Reflection Properties of Electromagnetic Monopulse by Buried Object in Subsurface Random Ground Using FDTD" by Y. Miyazaki and Y. Jyonori 492

SESSION 7:FDTD APPLICATIONS AND ENHANCEMENTS
Chair: J.H. Beggs

"UHF/VHF Propagation Model Characterization Over Irregular Terrain Using MOM/FDTD"
by K.A. Lysiak, J.K. Breakall, and J. Zmyslo 502

"Validation of FDTD Modeling of Ground-Penetrating Radar Antennas" by B.J. Zook 508

"FDTD Analysis of Radiation from a Lens Terminated Conical TEM Antenna"
by S.A. Blocher, E.A. Baca, and T.S. Bowen 516

"FDTD Analysis of a Dipole Antenna Driven from Various Excitation Sources"
by M.R. Zunoubi, N.H. Younan, C.D. Taylor, and J.H. Beggs, ... 523

"An Efficient Hybrid PEE-FDTD Field Modeling Technique in Cylindrical Coordinates"
by M. Mrozowski, M. Okoniewski, and M.A. Stuchly 529

"Absorbing Boundary Conditions for Optical Pulses in Dispersive, Nonlinear Materials"
by P.M. Goorjian 533

SESSION 8:FINITE ELEMENT AND FINITE VOLUME METHODS FOR ELECTROMAGNETIC FIELD SIMULATION
Chairs: R. D-Edlinger and R. Lee

"Local Tetrahedron Modeling of Microelectronics Using the Finite-Volume Hybrid-Grid Technique"
by D.J. Riley and C.D. Turner 536

"Full Wave Vector Maxwell Equation Modeling of Self-Limiting Effects and Optical Nonlinear Vortices" by S.V. Polstyanko and J-F. Lee 555

"A Hybrid FEM-FMM Technique for Electromagnetic Scattering"
by S. Bindiganavale and J.L. Volakis 563

"Finite Element Method Analysis of the Celestron-8 Telescope"
by R.R. DeLyser and H. Pohle 571

SESSION 9:NUMERICAL ERROR ANALYSIS AND CONTROL I
Chair: J.L. Volakis

"Error Analysis in the Adaptive Integral Method (AIM)"
by E. Bleszynski, M. Bleszynski, and T. Jaroszewicz 580

"Using Model-Based Parameter Estimation to Estimate the Accuracy of Numerical Models"
by E.K. Miller 588

"Guidelines for Using the Fast Multipole Method to Calculate the RCS of Large Objects"
by S.S. Bindiganavale and J.L. Volakis 596

SESSION 9: continued

"Developments in Error Estimation for Covolume and Staggered Mesh Approximations to Maxwell's Equations" by R.A. Nicolaides and D-Q. Wang 604

"Adaptive Methods for the Numerical Solution of Reaction-Diffusion Problems" by D.J. Estep, M.G. Larsson, and R.D. Williams 611

"Error Estimates for Subgridded FDTD Schemes" by P. Monk 619

SESSION 10:NUMERICAL LINEAR ALGEBRA IN COMPUTATIONAL ELECTROMAGNETICS
Chair: A.S. Hodel

"Applications of Numerical Linear Algebra in Electromagnetics" by G.K. Gothard, J.H. Henderson, and A.S. Hodel 622

"Multilevel Preconditioning for the Time-Harmonic Maxwell Equations" by G. Starke 630

"Iterative Solution Methods for ill-Posed Problems" by D. Calvetti, L. Reichel, and Q. Zhang 638

"Methods for Large Sparse Eigenvalue Problems from Waveguide Analysis" by C. Peng and D. Boley 645

"Iterative Solution of Field Problems in Space-Decoupled Configurations" by G. Bürger, and H. Singer 653

AUTHOR INDEX 661

VOLUME II

SESSION 11:NEC APPLICATIONS
Chairs: M. Ney and C. Christopoulos

"Numerical Investigation of Antennas for Hand-Held Radiotelephones Using NEC Code" by A.A. Efanov, M.S. Leong, and P.S. Kooi 664

"Evaluation of the Discrete Complex-Image Method for a NEC-Like Moment-Method Solution" by G.J. Burke 671

"The Improvement of NEC-2's Out-of-Core Operation and the Analysis of UHF Monopole Antenna Mounted on a Car Model" by K. Natsuhara, T. Suda, Y. Kazama, and K. Madono 679

"MatNEC: A MATLAB Based Graphical Interface to SuperNEC" by R.M. Cooper 687

SESSION 12:VALIDATION
Chair: D.R. Pflug

"First and Second Generation Transformable Scale Aircraft-Like Models for Code Validation: Present Results and Future Plans" by D.R. Pflug, T.W. Blocher, D.E. Warren, and D.O. Ross 696

"Software for Modeling Helix Antennas with NEC and Validation by Measurement" by C.W. Trueman, N. Sultan, S.J. Kubina, and T. Pellerin 703

"Evaluation of the Sensitivity of Scattering Predictions to Uncertainties in Material Characteristics" by G.A. Barnhart, A.J. Terzuoli, Jr., and G.C. Gerace 712

SESSION 12: continued

"Validation of the PO-based RCS Code SIGMA by Using IEM and Experiments"
by E. Kemptner, D. Klement, and V. Stein 719

SESSION 13:OPTIMIZATION
Chair: E. Michielssen

"Optimization of Broad-Band Loaded Wire Antennas in Real Environments Using Genetic Algorithms" by D.S. Weile, E. Michielssen, and A. Boag 726

"Genetic Algorithms Based Pattern Synthesis Approach for Arbitrary Array Designs"
by Y. Lu and K.K. Yan 734

"Speeding Convergence of Genetic Algorithms for Optimizing Antennas Arrays"
by R.L. Haupt 742

"Order Recursive Method of Moments for Iterative Design Application"
by K. Naishadham and P. Misra 750

SESSION 14:MULTIPOLE TECHNIQUES
Chair: P. Leuchtmann

"Discrete Sources Method for the Silicon Wafers Defect Discrimination"
by Y. Eremin and N.V. Orlov 758

"Iterative Scheme of Discrete Sources Amplitudes Determination Based on D-matrix Approach"
by Y. Eremin 763

"An Improving Technique for MMP Solutions Based on Ficticious Surface Sources"
by M. Gnos and P. Leuchtmann 769

SESSION 15:ANTENNA ANALYSIS
Chairs: A.W. Glisson and A.A. Kishk

"Accurate Design of Shaped Beam Doubly Curved Reflector Antennas for Airborne Applications"
by B.S. Shridhar and N. Balakrishnan 776

"Rapid Parametric Study of Antennas Using Moment Method Codes"
by G.P. Junker, A.A. Kishk, and A.W. Glisson 784

"A Numerical and Experimental Investigation of a Shipboard DF Antenna Array"
by J.B. Knorr 792

"Radiation Patterns of Antennas Mounted on an Attack Helicopter"
by O. Givati, A. Fourie, and J. Dresel 802

"Modelling of a Discone Antenna Mounted on a Communication Van" by J.S. Seregelyi 818

"Dielectric Resonator Antenna Analysis and Design Using the FDTD Method" by K.P. Esselle 826

"A Numerical and Experimental Investigation of a Semi-Loop Antenna on a Metal Box"
by J.B. Knorr and D.C. Jenn 832

SESSION 16:EMI/EMC
Chairs: T.H Hubing and J.L. Drewniak

"On the Suitability of Simple Voltage Source Models for the Study of Mutual Coupling Effects" by G.P. Junker & A.W. Glisson, and A.A. Kishk 842

"Susceptibility Modeling for PCBs with Long Wires Attached" by B. Archambeault and H.S. Berger 850

"Computer Modeling Tools for EMC" by T.H. Hubing and J.L. Drewniak 857

"Electromagnetic Induced Timing Defects in CMOS Chips" by R. Perez 861

"Finite-Difference Time-Domain Analysis of Common Mode Cable Currents" by C-W. Lam 870

"Statistical Coupling of EM Fields to Cables in an Overmoded Cavity" by R. Holland and R. St. John 877

"Power and Ground Plane Modeling and Decoupling in High Speed Printed Circuit Board and Multichip Modules" by F. Yuan, C-W. Lam, and L. Rubin 888

SESSION 17:ARRAYS
Chair: L. Epp

"Synthesis of Phased Arrays Aperture Distributions" by R.A. Speciale 898

"New Results in the Synthesis of Aperture-Field Distributions for Ultra-High-Gain Phased Arrays" by R.A. Speciale 914

"Advanced Design of Phased Array Beam-Forming Networks" by R.A. Speciale 918

SESSION 18:FINITE ELEMENTS II
Chair: J.M. Jin

"Adaptive Mesh Refinement Concepts for Electromagnetics" by Z. Chen and R. Lee 932

"Analysis of Complete Basis Sets of DivergencelessVector Expansion Functions for Finite Element Problems" by M.J. Walker 939

"Multi-Mode S-Parameter Computation Using Finite Elements and Perfectly Matched Absorbers" by G.C. Lizalek, J.J. Ruehl, and J.R. Brauer 946

"Characterization of MIMICs Packages Using a Parallelized 3D FEM Code" by J-G. Yook and L.P.B. Katehi 954

"Combined PML and ABC for Finite Element Analysis of Scattering Problems" by J.M. Jin and W.C. Chew 962

"Modeling Microstrip Patches Using the Finite Element Method" by D.B. Davidson, D.H. Malan, and C.B. Wilsen 972

"H_1(curl) Tangential Vector Finite Element Method with Additional Constraint Equation" by P. Bretchko, S.V. Polstyanko, and J-F. Lee 980

SESSION 18: continued

"Extension of Higher-Order 3-D Vector Finite Elements to Curved Cells and Open-Region Problems" by J.S. Savage and A.F. Peterson 988

"The Hybrid FEM/BEM Solution for EM Scattering from Arbitrary Cavity with Lossy and Anisotropic Material" by J. Xu, Y. Lu, and J.S. Fu 995

SESSION 19: FUTURE FIELDS FOR FDTD ANALYSIS
Chairs: D. Katz and M. Piket-May

"FDTD Analysis of a Dielectric Leaky-Wave Antenna Using PML" by M. Chen, B. Houshmand, and T. Itoh 1004

"FDTD Analysis in Cylindrical Coordinates of a TEM Pyramidal Horn Antenna" by D. Menditto, P. Tognolatti, and F. Bardati 1010

"A Modified FDTD (2,4) Scheme for Modeling Electrically Large Structures with High Phase Accuracy" by M.F. Hadi, M. Piket-May, and E.T. Thiele 1023

"Application of the FDTD Method to Three-Dimensional Propagation in a Magnetized Ferrite" by J.W. Schuster, and R.J. Luebbers 1031

"Symmetry-Aided FDTD Analysis of Finite Phased Arrays" by D. Crouch 1041

"Conformal FVTD with a Rectangular Grid for PEC Scattering Objects" by K.S. Yee and J.S. Chen 1049

"Application of Recent Advances in FDTD Modeling to the Problem of Acoustic Propagation in Shallow Water" by J.B. Schneider, F.D. Hastings, and C.J. Railton 1057

"FDTD Analysis of Small Loop Antennas for Partial Exposure of Rat Head at 837 MHz" by K.W. Chan, J.A. McDougall, and C.K. Chou 1065

"Scattering from Complex Geometries Using a Parallel FVTD Algorithm" by V. Ahuja and L.N. Long 1072

"FDTD Simulation of High Frequency Devices by Using Locally Refined Meshes" by P. Thoma and T. Weiland 1083

SESSION 20: NUMERICAL ERROR ANALYSIS AND CONTROL II
Chair: J.L. Volakis

"A WWW-Based Data Base for Code Validation" by C.W. Trueman and S.R. Mishra 1092

"Code Scaling" by M.J. Schuh and A.C. Woo 1100

"An Overview of Numerical Dispersion Error in PDE Methods for Electromagnetics" by R. Lee 1108

"Non-rigorous CEM Error Estimates and Their Limitations" by A.F. Peterson 1116

"Comparisons of Staggered and Non-Staggered Schemes for Maxwell's Equations" by D. Gottlieb and B. Yang 1122

"Minimizing the Number of Frequency Samples Needed to Represent a Transfer Function Using Adaptive Sampling" by E.K. Miller 1132

SESSION 21:MODELING TOOLS FOR VISUALIZATION: PRE- AND POST-PROCESSING
Chair: J. Karty

"MATLAB NEC Toolbox: The Cross Platform GUI Pre-and Post-processing Tool for NEC Applications"
by Y. Lu 1142

"Computation and Graphic Visualization of Plane-Wave K-Space Spectra and Far-Field Patterns with MATLAB 4.0" by R.A. Speciale 1150

"The Intelligent Computational Electromagnetics Expert System (ICEMES)"
by A.L. Drozd, T.W. Blocher, V.K. Choo, and K.R. Siarkiewicz 1158

"NECSHELL - A New Graphical User Interface for the NEC Code"
by M.Y. Mikhailov, V.O. Lomtev, and A.A. Efanov 1166

SESSION 22:FINITE ELEMENT ANALYSIS
Chair: J.R. Brauer

"Finite Element Scattering and Radiation Analysis Using Prismatic Meshes and Artificial Absorbers for Conformal Domain Truncation"
by M. Casciato, M. Nurnberger, T. Özdemir, and J.L. Volakis 1174

"Application of Fast Multipole Method to Finite Element-Boundary Integral Solution of Scattering Problems" by N. Lu and J-M. Jin 1182

"Use of Perfectly-Matched Absorber Boundaries in Finite Element Analysis of Patch Antennas"
by J.F. DeFord and G.C. Lizalek 1190

"A New Permanent-Magnet Synchronous Motor Design Configuration and Finite Element Analysis"
by Q.K. Zhang, N. Ida, Y. Qiu, and Z.R. Jiang 1196

"Investigation of ABC Behavior in Axisymmetric Electrostatic Finite Element Analysis"
by A. Konrad and L. Han 1202

"An Efficient Scheme for Finite Element Analysis in the Frequency Domain"
by M. Kuzuoglu, R. Mittra, J.R. Brauer, and G.C. Lizalek 1212

"Finite-Element Modelling of Head Coils for High-Frequency Magnetic Resonance Imaging Applications" J.G. Harrison and J.T. Vaughan 1220

"H_1(curl) TVFEM in Conjunction with PML for Modeling 3D Waveguide Discontinuities"
by S.G. Perepelitsa, R. Dyczij-Edlinger, and J-F. Lee 1227

SESSION 23:METHOD OF MOMENTS APPLICATIONS
Chair: A.F. Peterson

"Global Fourier-Series Basis Functions for EM Scattering" by M.H. Smith and A.F. Peterson 1230

"A Numerically Stable Method of Moments Time Domain Model"
by L.B. Gravelle and J-P. Estienne 1238

"Method of Moments Analysis of the Celestron-8 Telescope"
by R.R. DeLyser, P. Ensaf, and P. McDaniel 1248

SESSION 24:FDTD ANALYSIS AND APPLICATIONS
Chair: A. Elsherbeni

"Dynamic Analysis of V Transmission Lines"
by O.M. Ramahi, A.Z. Elsherbeni, and C.E. Smith 1260

"An Absorbing Boundary Condition for the FDTD Method Using Digital Filters Design Technique"
by C-N. Kuo and T. Itoh 1267

"Application of the FDTD Method to the Electromagnetic Modeling of Patch Antenna Arrays"
by M.F. Pasik, G. Aguirre, and A.C. Cangellaris 1273

SESSION 25:MICROWAVE COMPONENTS
Chairs: M.E. Baginski and M.M. Ney

"Parallel Coupled Microstrip Patch Resonators on a Ferrimagnetic Layer"
by J.de Ribamar S. Oliveira and A. Gomes d' Assunção 1280

"Fullwave Analysis of Circular Cylindrical Backed Slotlines"
by L. Martins de Mendonça and A. Gomes d' Assunção 1286

"Properties of Tapered Microstrip Lines on Dielectric and Magnetized Ferrimagnetic Layers"
by A. Gomes d' Assunção, F. de Lima, and M.R.M. Lins de Albuquerque 1290

"Frequency and Time Domain Computations of S-Parameters Using the Finite Integration Technique" by R. Schumann, M. Clemens, P. Thoma, and T. Weiland 1295

"Time Domain Analysis of Microwave Structures by MRTD"
by M. Krumpholz, E. Tentzeris, R. Robertson, and L.P.B. Katehi 1303

"A Parasite-Free Non-Orthogonal Finite-Difference Frequency-Domain Method for the Analysis of Inhomogeneous Lossy Waveguides" by L. Zhao and A.C. Cangellaris 1311

SESSION 26:BIOMEDICAL ELECTROMAGNETICS
Chairs: A.M. Morega and R.K. Gordon

"A Spectral Approach to the Cardiography" by A.M. Morega, D. Mocanu, and M. Morega 1320

"Optimal Transcutaneous Pacing" by A.M. Morega, B. Ciocârlan, and M. Morega 1326

AUTHOR INDEX 1333

THE APPLIED COMPUTATIONAL ELECTROMAGNETIC SOCIETY

1997 CALL FOR PAPERS 1997

The 13th Annual Review of Progress
in Applied Computational Electromagnetics

March 17-21, 1997

Naval Postgraduate School, Monterey, California

Share your knowledge and expertise with your colleagues

The Annual ACES Symposium is an ideal opportunity to participate in a large gathering of EM analysis enthusiasts. The purpose of the Symposium is to bring analysts together to share information and experience about the practical application of EM analysis using computational methods. The symposium offerings include technical presentations, demonstrations, vendor booths and short courses. All aspects of electromagnetic computational analysis are represented. Contact Richard Gordon for details.

Technical Program Chairman
Eric Michielssen
ECE Department
University of Illinois
1406 West Green Street
Urbana, IL 61801-2991
Phone: (217) 333-3803
FAX: (217) 333-5962
Email:michiels@decwa.ece.uiuc.edu

Symposium Administrator
Richard W. Adler
ECE Dept./Code ECAB
Naval Postgraduate School
833 Dyer Rd. Room 437
Monterey, CA 93943-5121
Phone: (408) 649-1111
FAX: (408) 649-0300
Email: rwa@mcimail.com

Symposium Co-Chairman
Jiaming Jin
ECE Department
University of Illinois
1406 West Green Street
Urbana, IL 61801-2991
Phone: (217) 244-0756
FAX: (217) 333-5962
Email:jjin@uvh.cso.uiuc.edu

Symposium Co-Chairman
Keith Whites
ECE Department
University of Kentucky
453 Anderson Hall
Lexington, KY 40506-0046
Phone: (606)-257-1768
FAX: (606)-257-3092
Email:whites@engr.uky.edu

1997 ACES Symposium
Sponsored by: ACES, NCCOSC, NPS, DOE/LLNL
In cooperation with: The IEEE Antennas and Propagation Society, the IEEE Electromagnetic Compatibility Society and USNC/URSI

THE APPLIED COMPUTATIONAL ELECTROMAGNETIC SOCIETY

CALL FOR PAPERS

The 13th Annual Review of Progress
in Applied Computational Electromagnetics

Papers may address general issues in applied computational electromagnetics, or may focus on specific applications, techniques, codes, or computational issues of potential interest to the Applied Computational Electromagnetics Society membership. Areas and topics include:

- Code validation
- Code performance analysis
- Computational studies of basic physics
- Examples of practical code application
- New codes, algorithms, code enhancements, and code fixes
- Computer hardware issues
- Partial list of applications:

antennas	wave propagation
radar imaging	radar cross section
shielding	bioelectromagnetics
EMP, EMI/EMC	visualization
dielectric & magnetic materials	inverse scattering
microwave components	**MIMIC** technology
fiberoptics	remote sensing & geophysics
communications systems	propagation through plasmas
eddy currents	non-destructive evaluation

- Partial list of techniques:

frequency-domain & time-domain techniques	
integral equation & differential equation techniques	
finite differences & finite element techniques	
diffraction theories	physical optics
modal expansions	perturbation methods
hybrid methods	moment methods

INSTRUCTIONS FOR AUTHORS AND TIMETABLE

For both summary and final paper, please supply the following data for the principal author: name, address, Email address, FAX, and phone numbers for both work and home.

October 6, 1996:	Submission deadline. Submit four copies of a 300-500 word summary to the Technical Program Chairman.
November 24, 1996:	Authors notified of acceptance.
December 22, 1996:	Submission deadline for camera-ready copy. The papers should not be more than 8 pages long including figures.

Registration fee per person for the Symposium will be approximately $245. The exact fee will be announced later.

SHORT COURSE

Short courses will be offered in conjunction with Symposium covering numerical techniques, computational methods, surveys of EM analysis and code usage instruction. It is anticipated that short courses will be conducted principally on Monday March 25 and Friday March 29. Fee for a short course is expected to be approximately $90 per person for a half-day course and $140 for a full-day course, if booked before March 3, 1997. Full details of 1997 Symposium will be available by November 1996. **Short Course Attendance is not covered by the Symposium Registration Fee!**

EXHIBITS

Vendor booths and demonstrations will feature commercial products, computer hardware and software demonstrations, and small company capabilities.

1996 Symposium Program Committee

for the

12th Annual Review of Progress in

APPLIED COMPUTATIONAL ELECTROMAGNETICS

at the
Naval Postgraduate School
Monterey, CA

Technical ProgramChairman: Richard K. Gordon
EE Department
Univ. of Mississippi
Anderson Hall, Box 41
University, MS 38677
Phone: (601) 232-5388
FAX: (601) 232-7231
Email:eegordon@vm.cc.olemiss.edu

Co-Chair: Eric Michielssen
ECE Department
University of Illinois
1406 West Green Street
Urbana, IL 61801-2991
Phone: (217) 333-3801
FAX: (217) 333-8986
Email:michiels@decwa.ece,edu

Co-Chair: Jin-Fa Lee
ECE Department
Worcester Polytechnic Institute
100 Institute Road
Worcester, MA 01609
Phone: (508)831-5778
Fax: (508) 831-5491
Email:jinlee@ece.wpi.edu

Technical Asst. Winn E. Hutchcraft
Univ of Mississippi, Dept.
EE Department
42 Midland Cove
Oxford, MS 38655
(601) 234-4912
Email:eeweh@cypress.mcsr.
olemiss.edu

Symposium Administrator Richard W. Adler
ECE Department, Code EC/AB
Naval Postgraduate School
833 Dyer Road, Room 437
Monterey, CA 93943-5121
Phone: (408) 646-1111
FAX: (408) 649-0300
Email:rwa@mcimail.com

Short Course Chairman: Robert Lee
Ohio State University, EE Department
2015 Neil Avenue
Columbus, OH 43210-1272
Phone: (614) 292-1433
FAX: (614) 292-7596
Email:lee@ee.eng.ohio.state.edu

Conference Secretary: Mrs. Pat Adler

Advisory Committee:

Richard W. Adler, Naval Postgraduate School
Duncan C. Baker, University of Pretoria
Robert Bevensee, Consultant
Pat Foster, Microwave & Antenna Systems
Todd Hubing, University of Missouri-Rolla
Adalbert Konrad, University of Toronto
Ray Luebbers, Penn State University
Edmund K. Miller
Andrew Peterson, Georgia Institute of Tech.
Harold Sabbagh, Sabbagh Assoc. Inc.
W. Perry Wheless, Jr., University of Alabama

ACES

1996

March 18-22, 1996
Monterey, CA

For more information, please contact:

Technical Program Chairman
Richard Gordon
EE. Dept., University of Mississippi
Anderson Hall, Box 41
University, MS 38677
Phone: (601) 232-5388
FAX: (601) 232-7231
Email: eegordon@cypress.mcsr.olemiss.edu

Short Course Chairman
Robert Lee
Dept. Of Electrical Engineering
ElectroScience Laboratory
The Ohio State University
1320 Kinnear Road
Columbus, OH 43212
Phone: (614) 292-1433
FAX: 614-292-7596
Email: lee@ee.eng.ohio-stat.edu

Symposium Administrator
Richard W. Adler
ECE Department/Code ECAB
Naval Postgraduate School
833 Dyer Road, Room 437
Monterey, CA 93943-5121
Phone: (408) 646-1111
FAX: (408) 649-0300
Email: 5541304@mcimail.com

Conference Co-Chair
Eric Michielssen
Department of Electrical and Computer Eng.
Everitt Laboratory
1406 West Green Street
University of Illinois at Urbana-Champaign
Urbana, Illinois 61801-2991
Phone: (217) 333-3803
FAX: (217) 333-8986
Email: michiels@decwa.ece.uiuc.edu

Conference Co-Chair
Jin-Fa Lee
Department of Electrical and Computer Eng.
Worcester Polytechnic Institute
100 Institute Road
Worcester, MA 01609-2280
Phone: (508) 831-5778
Email: jinlee@ee.wpi.edu

APPLIED COMPUTATIONAL ELECTROMAGNETICS SOCIETY

The Twelfth Annual Review of Progress in Applied Computational Electromagnetics

Welcome to the 12th Annual Review of Progress in Applied Computational Electromagnetics. I want to especially thank several individuals who contributed significantly to the conference. Jin-Fa Lee arranged the advertising for the conference. Robert Lee once again did an excellent job of organizing the Short Courses. Eric Michielssen and Shirley Dipert received all the papers and put them together to produce these Proceedings. Robert Bevensee assisted in the preparation of the preliminary agenda. Elliott Hutchcraft helped me in the construction of the author database and in the preparation of an electronic mail database. And, of course, Richard and Pat Adler must be recognized for arranging for the printing of the Proceedings, for providing access to the NPGS Facilities, and for all their other contributions to the conference.

Please enjoy your time in Monterey as much as possible, whether listening to a paper being presented, catching up on the latest "gossip" in the hallways, or enjoying the sights of Monterey.

Richard K. Gordon
Technical Program Chairman
1996 ACES Conference

ACES PRESIDENT'S STATEMENT

Were it not for the ACES Annual Reviews, it would be difficult to justify being in Monterey in March. (This coming from one who spent the Winter of '95-'96 in the Midwest!) But it is time for ACES'96, so here we are in Monterey, once again. And we think that this will be the best review yet.

In addition to our regular staple of high-quality technical papers, and our world-renowned short-courses, we are adding a new feature this year --- an amateur radio session. Judging from the number of interesting questions and applications described in the NEC-LIST, amateur radio operators are a natural part, or should be, of the ACES community. Perry Wheless is to be commended for assembling this session, which appears to be well populated.

Our congratulations go to Dick Gordon, who is the Technical Program Chairman, and his colleagues, Eric Michielssen, Jin-Fa Lee, Robert Lee, W. Elliott Hutchcraft, Bob Bevensee, and Dick Adler for organizing and managing the 12th Annual Review. Their hardwork is another manifestation of the can-do spirit of dedicated volunteers in a voluntary society.

There must be more of you out there who are ready to step forward and offer your time and services to ACES. Call me! The Society, the Profession, and you will benefit enormously.

Enjoy the 12th Annual Review.

Harold A. Sabbagh
Sabbagh Associates, Inc.
4635 Morningside Drive
Bloomington, IN 47408
(812) 339-8273
(812) 339-8292 FAX
email:has@sabbagh.com

ACES 1996 SHORT COURSES

MONDAY MARCH 18 **FULL-DAY COURSES**

0830-1630 "Wavelets: Theory, Algorithms, and Applications"
by Andrew K. Chan, Texas A&M.

0830-1630 "Using Mathematical Software for Computational Electromagnetics"
by Jovan Lebaric, Naval Postgraduate School.

0830-1630 "Practical EMI/EMC Design and Modeling"
by Todd Hubing, University of Missouri-Rolla.

MONDAY MARCH 18 **HALF-DAY COURSES**

0830-1200 "An Application Oriented Introduction to the NEC-BSC Workbench"
by Ron J. Marhefka and Lee W. Henderson, The Ohio State University.

1300-1630 "Application of Modern Analytical and Hybrid Tools for Antenna Modeling and Synthesis",
by Roberto Rojas and Prabhakar Pathak, The Ohio State University.

FRIDAY MARCH 22 **FULL-DAY COURSES**

0830-1630 "Finite Element Methods for Electromagnetics"
by John Volakis, University of Michigan and
John Brauer, Mac-Neal-Schwendler Corporation.

0830-1630 "Conformal Time Domain Numerical Electromagnetics"
by Kane Yee, Lockheed.

FRIDAY MARCH 22 **HALF-DAY COURSES**

0830-1200 "Using Model-Based Parameter Estimation to Increase the Efficiency and Effectiveness of Computational Electromagnetics"
by Ed Miller.

1300-1630 "Antenna Properties in Linear and Nonlinear Environments"
by Robert Bevensee, BOMA Enterprises.

FINAL AGENDA

The Twelfth Annual Review of Progress in Applied Computational Electromagnetics

NAVAL POSTGRADUATE SCHOOL
18-22 MARCH 1996

Richard Gordon, Technical Program Chairman

Eric Michielssen, Conference Co-Chair

Jin-Fa Lee, Conference Co-Chair

Robert Lee, Short Course Chairman

W. Elliott Hutchcraft, Technical Assistant

Robert Bevensee, Assistant Conference Co-Chair

Richard W. Adler, Conference Facilitator

MONDAY MORNING 18 MARCH 1996

0745-0830	**SHORT COURSE REGISTRATION**	**103 Glasgow Hall**
0830-1200	**SHORT COURSE (HALF-DAY)** "An Application Oriented Introduction to the NEC-BSC Workbench" R.J. Marhefka & L.W. Henderson, The Ohio State University	**102 Glasgow Hall**
0830-1630	**SHORT COURSE (FULL-DAY)** "Wavelets: Theory, Algorithms, and Applications" A.K. Chan, Texas A&M	**122 Ingersoll Hall**
0830-1630	**SHORT COURSE (FULL-DAY)** "Using Mathematical Software for Computational Electromagnetics" J. Lebaric, Naval Postgraduate School	**419 Spanagel Hall**
0830-1600	**SHORT COURSE (FULL-DAY** "Practical EMI/EMC Design and Modeling" T. Hubing, University of Missouri-Rolla	**119 Ingersoll Hall**
0900-1200	**REGISTRATION**	**103 Glasgow Hall**

MONDAY AFTERNOON

1300-1630	**SHORT COURSE (HALF-DAY)** "Application of Modern Analytical and Hybrid Tools for Antenna Modeling and Synthesis" R. Rojas & P. Pathak, Ohio State University	**102 Glasgow Hall**
1630-1900	**REGISTRATION**	**103 Glasgow Hall**
1700-1915	**AMATEUR RADIO DINNER**	
SESSION 0:	**AMATEUR RADIO SESSION** Chair: W.P. Wheless, Jr.	**122 Ingersoll Hall**
1930	"Ground-Plane Antennas with Elevated Radial Systems"	J.S. Belrose
1950	"Review of Characteristics for HF Dipole Antennas Including the Cases Where the Dipoles are Above and Parallel to the Surface of Real-World Grounds"	G.M. Royer
2010	"HF Multi-Frequency Antennas Using Coupled Resonators"	G.A. Breed
2030	"The Optimized Wideband Antenna (OWA) and its Application"	J.K. Breakall
2050	"The Quad-Rhomb Antenna - A New All Band Antenna for Amateur Radio Applications"	R. Anders
2110	**BREAK**	
2130	"SKY-WAVES-95"	R. Anders
2150	"Using Ham Radio CEM Codes to Gain Insight to VHF Ground Plane Antennas and to Mitigate 75 Meter Mars RFI at a Naval Receiving Site"	A. Hoffman & R.W. Adler
2210	"Development of Practical Landstorfer Antennas for Amateur Use"	M.C. Tarplee
2230	"Two-Port Network Specification of Baluns for NEC Analysis and Other Applications"	W.P. Wheless, Jr., & C.S. Wheless

TUESDAY MORNING 19 MARCH 1996

0700-0800	**REGISTRATION**		**103 Glasgow Hall**
0700-0745	**CONTINENTAL BREAKFAST**		**Glasgow Hallway**
0730	**ACES BUSINESS MEETING**	President Hal Sabbagh	**102 Glasgow Hall**
0745	**WELCOME**	Richard Gordon	**102 Glasgow Hall**
SESSION 1:	**HIGH FREQUENCY METHODS (Parallel with Sessions 2, 3, 4, & 5)** Chair: R.J. Burkholder		**102 Glasgow Hall**
0800	"Physical Theory of Diffraction Analysis of Impedance Structures"		H.H. Syed & J.L. Volakis
0820	"Hybrid SBR/GTD Radio Propagation Model for Site-Specific Predictions in an Urban Environment"		J. Schuster & R. Luebbers
0840	"Analysis of Dielectric Structures Using the NEC-BSC"		R. Marhefka & L. Henderson
0900	"Hybrid MM-PO-Fock Analysis of Monopole Antennas Mounted on Curved Convex Bodies"		U. Jakobus & F.M. Landstorfer
0920	"Numerical Diffraction Coefficient for an Impedance Wedge with a Material Body Attached to its Edge"		M.F. Otero & R.G. Rojas
0940	"Reflection and Diffraction of Well-Focussed General Astigmatic EM Gaussian Beams"		G. Zogbi, H.T. Chou, P.H. Pathak, & R.J. Burkholder
1000	**BREAK**		
1020	"Polarized Scattered Light by a Semicylindrical Boss on a Conducting Flat Plane"		H.A. Yousif
1040	"Divergence of Rays in Modulated Atmospheric Ducts"		I.P. Zolotarev
1100	"Diffraction by a Weak Dielectric Wedge"		A.V. Popov
1120	"Far-field Diffraction Effects of EUV Fresnel Zone Plates"		Y.V. Kopylov, V.A.Baranov, A V.Popov, & A Vinogradov
1200	**LUNCH**		
SESSION 2:	**INVERSE SCATTERING (Parallel with Sessions 1, 3, 4, & 5)** Chairs: P.M. Goggans and L. Riggs		**Engr Auditorium**
0800	"Radar Time and Frequency-Domain Received Signals for Realistic Antennas and Scatterers"		P.M. Goggans & J.D. Pursel
0820	"The Extraction of Scattering Mechanisms from Measured Data"		H.M. Chizever & K.M. Pasala
0840	"Using the E-pulse Technique and Hypothesis Testing to Perform Radar Target Identification"		L. Riggs, J. Mooney, & C. Smith
0900	"A Boundary-Integral Code for Electromagnetic Nondestructive Evaluation"		K. Murphy & H.A. Sabbagh
0920	"The Numerical Analysis of Planar Antennas Buried in Layered Media"		J. van Tonder, J. Cloete, & D. Davidson
SESSION 3:	**RCS ANALYSIS (Parallel with Sessions 1, 2, 4, & 5)** Chair: M. El-Shenawee		**Engr Auditorium**
0940	"A Response Surface Methodology Study of Electromagnetic Data Compression and Reconstruction"		V.M. Floyd, Jr., A. Terzuoli, Jr., G.C. Gerace & P.F. Auclair
1000	**BREAK**		
1020	"Curvilinear, Isoparametric Modelling for RCS Prediction, Using Time Domain Integral Equations"		S.P. Walker, M.J. Bluck, M.D. Pocock, C.Y. Leung, & S.J. Dodson
1040	"Double Scatter Radar Cross Sections for Two Dimensional Random Rough Surfaces that Exhibit Backscatter Enhancement"		M. El-Shenawee & E. Bahar
SESSION 4:	**APPLICATIONS OF PARALLEL COMPUTING (Parallel with Sessions 1, 2, 3 & 5)** Chairs: L. Epp and K. Naishadham		**Engr. Auditorium**
1100	"Solution of Electromagnetic Eigenproblems on Multiprocessor Superscalar Computers"		M.P. Debicki, P. Jedrzejewski, J. Mielewski, P. Przybyszewski, & M. Mrozowski
1120	"Implementation of Hybrid FDTD/FVTD Conformal Algorithm on a Massively Parallel Computer"		J.S. Chen & A.A. Seidl
1140	"Parallel CARLOS-3D Code Development"		J.M. Putnam & J.D. Kotulski
SESSION 5:	**NEW DEVELOPMENTS IN TLM MODELING (Parallel with Sessions 1, 2, 3, & 4)** Chair: W.J.R. Hoefer		**122 Ingersoll Hall**
0800	"On the Advantages of ATLM Over Conventional TLM"		M. Krumpholz & P. Russer
0820	"Advanced Node Formulations in TLM - The Matched Symmetrical Condensed Node (MSCN)"		V. Trenkic, C. Christopoulos, & T.M. Benson
0840	"A General and Complete Two-Dimensional TLM Hybrid Node Formulation Based on Maxwell's Integral Equations"		N. Pena & M.M. Ney

TUESDAY MORNING 19 MARCH 1996

SESSION 5:	**NEW DEVELOPMENTS IN TLM MODELING (Parallel with Sessions 1, 2, 3, & 4) (cont)**	**122 Ingersoll Hall**
0900	"A General Formulation of a Three-dimensional TLM Condensed Node with the Modeling of Electric and Magnetic Losses and Current Sources"	N. Pena, & M.M. Ney
0920	"A Numerical Comparison of Dispersion in Irregularly Graded TLM and FDTD Meshes"	F.J. German, J.A. Svigelj, & R. Mittra
0940	"Accuracy Considerations of a Class of Frequency-Domain TLM Nodes"	S. Chen & R. Vahldieck
	BREAK	
1020	"Distributed Simulation of Planar Circuits by TLM Method in a Parallel Computing" Environment"	B. Isele, J. Schmöller, & P. Russer
1040	"Modeling Gyromagnetic Media in Symmetrical Condensed Node TLM"	L. de Menezes & W.J.R. Hoefer
1100	"A Comparative Performance Study of Absorbing Boundary Conditions in TLM and FDTD"	C. Eswarappa & W.J.R. Hoefer
1120	"Modelling of Coplanar Waveguide Discontinuities Using the Alternating Transmission Line Matrix (ATLM) Method"	B. Bader & P. Russer
1140	"Quasi-Static Correction of a Knife Edge Corner in 2D TLM Algorithm"	L. Cascio, G. Tardioli, T. Rozzi, & W.J.R. Hoefer
1200	**LUNCH**	
1200	**BOARD OF DIRECTORS MEETING/LUNCHEON**	**DelMonte Room, , Herrmann Hall**

TUESDAY AFTERNOON

1400-1800	**VENDOR EXHIBITS AND STARTING AT 1600 -1800, WINE AND CHEESE BUFFET**	**Ballroom, Herrmann Hall**
SESSION 6:	**INTERACTIVE TECHNICAL SESSION,**	**Ballroom, Herrmann Hall**
1400-1800	"Electromagnetic Visualization Using Commercial Software"	H.A. Nott
	"Performance of Multiple, Thin Layers of Lossy Dielectrics as Broadband Attenuators"	G.W. Jarriel, Jr., M.E. Baginski, & L.S. Riggs
	"Research & Engineering Framework (REF) Data Dictionary Specification for Computational Electromagnetics"	J.A. Evans
	"Development of an Electromagnetic and Mechanical Simulation Tool for the Computer Modeling of the TACAMO LF/VLF Communication System"	M.C. Longtin, R.W. Sutton, K.J. Laskey, & P.J. Morrison
	"A New Look at Antenna Traps"	P.W. Leonard
	"Imaging of Conductive and Ferromagnetic Materials Using a Magnetic Induction Technique"	J. Ferreira, F. Linhares, J. Velez, J. de Ribomar S. Oliveira, & A.R. Borges
	"Investigation of the Properties of Wavelet-Like Basis Functions in the Finite Element Analysis of Elliptic Problems"	L.A. Harrison & R.K. Gordon
	"Continuing Development of the Research and Engineering Framework (REF) for Computational Electromagnetics"	L.W. Woo, B. Hantman, K. Siarkiewicz, J. LaBelle, & R. Abrams
	"Numerical and Experimental Modelling of Liquid Dielectrics Using a Coaxial Cavity"	M. Bingle, D.B. Davidson, & J.H. Cloete
	"Hardware/Software Codesign Model for XPATCHF Optimization"	B.A. Kadrovach, T.S. Wailes, A.J. Terzuoli, Jr., & D.S. Gelosh
	"3D FDTD Simulation of EM Detection of Buried Waste"	D. Sullivan, B. Hansen & N. Skousen
	"Application of Digital Filters to the Construction of Wideband Dispersive Boundary Conditions"	M. Mrozowski, M. Niedźwiecki, & P. Suchomski
	"Note on Large Crane Coupling to Nearby AM Radio Stations"	P.W. Leonard & J.B. Hatfield
	"XPATCHF Software System Analysis and Profiling"	B.A. Kadrovach, T.S. Wailes, A.J. Terzuoli, Jr., & D.S. Gelosh
	"Theoretical Studies of Photonic Band Gap Materials"	M. Sigalas, R. Biswas, C. Chan, K. Ho, & C. Soukoulis
	"On the Use of Richardson Extrapolation in the Finite Element Analysis of Two-Dimensional Electrostatics Problems"	W.E. Hutchcraft & R.K. Gordon
	"Scattering from Chirally Coated Bodies"	R. Sharma & N. Balakrishnan

TUESDAY AFTERNOON 19 MARCH 1996

1400-1800	**VENDOR EXHIBITS AND STARTING AT 1600 -1800, WINE AND CHEESE BUFFET**	**Ballroom, Herrmann Hall**
SESSION 6:	**INTERACTIVE TECHNICAL SESSION, (cont)**	**Ballroom, Herrmann Hall**
	"A Mixed Formulation to Compute the Source Current Density in Inductors of Any Shape"	F. Robert, P. Dular, J.F. Remacle, M. Umé, & W. Legros
	"High Power Microwave Amplification for High-Intensity Relativistic Electron-Beam Storage-Rings"	R.A. Speciale
	"Real-Time Digital Signal Processor in Ionosphere Measurements"	A.L. Karpenko & V.V. Koltsov
	"High Frequency Electromagnetic Safety Analysis by Numerical and Empirical Methods on Mobile Platforms"	M.J. Packer, & R.C. Ferguson
	"Computational Modeling of Wave Plasma Interaction"	V.A. Eremenko & Y.Cherkashin
	"Attenuation of HF Radio Waves in a Forest: Results from Experiment"	I.P. Zolotarev. V.A.Popov & V.P. Romanuk
	"Statistical Reflection Properties of Electromagnetic Monopulse by Buried Object in Subsurface Random Ground Using FDTD"	Y. Miyazaki & Y. Jyonori
	"Running NEC4 on the Cray at NPS"	B. Neta
1730	**NO HOST BAR**	**Terrace Room**
1830	**AWARDS BANQUET**	**Ballroom, Herrmann Hall**

WEDNESDAY MORNING 20 MARCH 1996

0715	**CONTINENTAL BREAKFAST**	
SESSION 7:	**FDTD APPLICATIONS AND ENHANCEMENTS (Parallel with Sessions 8, 9, 10, 11 & 12)** Chair: J.H. Beggs	**102 Glasgow Hall**
0800	"UHF/VHF Propagation Model Characterization Over Irregular Terrain Using MOM/FDTD"	K.A. Lysiak, J.K. Breakall, & J. Zmyslo
0820	"Validation of FDTD Modeling of Ground-Penetrating Radar Antennas"	B.J. Zook
0840	"FDTD Analysis of Radiation from a Lens Terminated Conical TEM Antenna"	S.A. Blocher, E.A. Baca, & T.S. Bowen
0900	"FDTD Analysis of a Dipole Antenna Driven from Various Excitation Sources"	M.R. Zunoubi, N.H. Younan C.D. Taylor, & J.H. Beggs,
0920	"An Efficient Hybrid PEE-FDTD Field Modeling Technique in Cylindrical Coordinates"	M. Mrozowski, M. Okoniewski, & M.A. Stuchly
1000	**BREAK**	
SESSION 8:	**FINITE ELEMENT AND FINITE VOLUME METHODS FOR ELECTROMAGNETIC FIELD SIMULATION** Chairs: R. D-Edlinger and R. Lee **(Parallel with Sessions 9, 10, 11 & 12,**	**102 Glasgow Hall**
1020	"Local Tetrahedron Modeling of Microelectronics Using the Finite-Volume Hybrid-Grid Technique"	D.J. Riley & C.D. Turner
1040	"Full Wave Vector Maxwell Equation Modeling of Self-Limiting Effects and Optical Nonlinear Vortices"	S.V. Polstyanko & J-F. Lee
1100	"A Hybrid FEM-FMM Technique for Electromagnetic Scattering"	S. Bindiganavale & J.L. Volakis
1120	"Finite Element Method Analysis of the Celestron-8 Telescope"	R.R. DeLyser & H. Pohle
1200	**LUNCH**	
SESSION 9:	**NUMERICAL ERROR ANALYSIS AND CONTROL I (Parallel with Sessions 7 8, 10, 11, & 12)** Chair: J.L. Volakis	**122 Engersoll Hall**
0800	"Error Analysis in the Adaptive Integral Method (AIM)"	E. Bleszynski, M. Bleszynski, & T. Jaroszewicz
0820	"Using Model-Based Parameter Estimation to Estimate the Accuracy of Numerical Models"	E.K. Miller
0840	"Guidelines for Using the Fast Multipole Method to Calculate the RCS of Large Objects"	S.S. Bindiganavale & J.L. Volakis
0900	"Developments in Error Estimation for Covolume and Staggered Mesh Approximations to Maxwell's Equations"	R.A. Nicolaides & D-Q. Wang
0920	"Adaptive Methods for the Numerical Solution of Reaction-Diffusion Problems"	D.J. Estep, M.G. Larsson & R.D. Williams
0940	"Error Estimates for Subgridded FDTD Schemes"	P. Monk
1000	**BREAK**	

WEDNESDAY MORNING 20 MARCH 1996

SESSION 10:	**NUMERICAL LINEAR ALGEBRA IN COMPUTATIONAL ELECTROMAGNETICS** Chair: A.S. Hodel **(Parallel with Sessions 7, 8, 9, 11, & 12)**	**122 Ingersoll Hall**
1020	"Applications of Numerical Linear Algebra in Electromagnetics"	G.K. Gothard, J.H. Henderson, & A.S. Hodel
1040	"Multilevel Preconditioning for the Time-Harmonic Maxwell Equations"	G. Starke
1100	"Iterative Solution Methods for ill-Posed Problems"	D. Calvetti, L. Reichel, & Q. Zhang
1120	"Methods for Large Sparse Eigenvalue Problems from Waveguide Analysis"	C. Peng & D. Boley
1140	"Iterative Solution of Field Problems in Space-Decoupled Configurations"	G. Bürger, & H. Singer
1200	**LUNCH**	
SESSION 11:	**NEC APPLICATIONS (Parallel with Sessions 7, 8, 9, 10, & 12)** Chairs: M. Ney and C. Christopoulos	**Engr. Auditorium**
0800	"Numerical Investigation of Antennas for Hand-Held Radiotelephones Using NEC Code"	A.A. Efanov, M.S. Leong, & P.S. Kooi
0820	"Evaluation of the Discrete Complex-Image Method for a NEC-Like Moment-Method Solution"	G.J. Burke
0840	"The Improvement of NEC-2's Out-of-Core Operation and the Analysis of UHF Monopole Antenna Mounted on a Car Model"	K. Natsuhara, T. Suda Y. Kazama, & K. Madono
0900	"MatNEC: A MATLAB Based Graphical Interface to SuperNEC"	R.M. Cooper
1000	**BREAK**	
SESSION 12:	**VALIDATION (Parallel with Sessions 7, 8, 9, 10, & 11)** Chair: D.R. Pflug	**Engr. Auditorium**
1020	"First and Second Generation Transformable Scale Aircraft-Like Models for Code Validation: Present Results and Future Plans"	D.R. Pflug, T.W. Blocher D.E. Warren, & D.O. Ross
1040	"Software for Modeling Helix Antennas with NEC and Validation by Measurement"	C.W. Trueman, N. Sultan, S.J. Kubina, & T. Pellerin
1100	"Evaluation of the Sensitivity of Scattering Predictions to Uncertainties in Material Characteristics"	G.A. Barnhart, A.J. Terzuoli, Jr., & G.C. Gerace
1120	"Validation of the PO-based RCS Code SIGMA by Using IEM and Experiments"	E. Kemptner, D. Klement, & V. Stein
1200	**LUNCH**	

WEDNESDAY AFTERNOON

SESSION 13:	**OPTIMIZATION (Parallel with Session 15 & 16),** Chair: E. Michielssen	**Engr. Auditorium**
1320	"Optimization of Broad-Band Loaded Wire Antennas in Real Environments Using Genetic Algorithms"	D.S. Weile, E. Michielssen, & A. Boag
1340	"Genetic Algorithms Based Pattern Synthesis Approach for Arbitrary Array Designs"	Y. Lu & K.K. Yan
1400	"Speeding Convergence of Genetic Algorithms for Optimizing Antennas Arrays"	R.L. Haupt
1420	"Order Recursive Method of Moments for Iterative Design Application"	K. Naishadham & P. Misra
1500	**BREAK**	
SESSION 14:	**MULTIPOLE TECHNIQUES** Chair: P. Leuchtmann	**Engr. Auditorium**
1520	"Discrete Sources Method for the Silicon Wafers Defect Discrimination"	Y. Eremin & N.V. Orlov
1540	"Iterative Scheme of Discrete Sources Amplitudes Determination Based on D-matrix Approach"	Y. Eremin
1600	"An Improving Technique for MMP Solutions Based on Ficticious Surface Sources"	M. Gnos & P. Leuchtmann
SESSION 15:	**ANTENNA ANALYSIS (Parallel with Sessions 13 & 16)** Chairs: A.W. Glisson and A.A. Kishk	**122 Ingersoll Hall**
1320	"Accurate Design of Shaped Beam Doubly Curved Reflector Antennas for Airborne Applications"	B.S. Shridhar & N. Balakrishnan
1340	"Rapid Parametric Study of Antennas Using Moment Method Codes"	G.P. Junker, A.A. Kishk, & A.W. Glisson
1400	"A Numerical and Experimental Investigation of a Shipboard DF Antenna Array"	J.B. Knorr
1420	"Radiation Patterns of Antennas Mounted on an Attack Helicopter"	O. Givati, A. Fourie, & J. Dresel
1440	"Modelling of a Discone Antenna Mounted on a Communication Van"	J.S. Seregelyi

WEDNESDAY AFTERNOON 20 MARCH 1996

SESSION 15:	**ANTENNA ANALYSIS (Parallel with Sessions 13 & 16) (cont)**	**122 Ingersoll Hall**
1500	**BREAK**	
1520	"Dielectric Resonator Antenna Analysis and Design Using the FDTD Method"	K.P. Esselle
1540	"A Numerical and Experimental Investigation of a Semi-Loop Antenna on a Metal Box"	J.B. Knorr & D.C. Jenn
SESSION 16:	**EMI/EMC (Parallel with Sessions 13 & 15)** Chairs: T.H Hubing and J.L. Drewniak	**102 Glasgow Hall**
1320	"On the Suitability of Simple Voltage Source Models for the Study of Mutual Coupling Effects"	G.P. Junker & A.W. Glisson, & A.A. Kishk
1340	"Susceptibility Modeling for PCBs with Long Wires Attached"	B. Archambeault & H.S. Berger
1400	"Computer Modeling Tools for EMC"	T.H. Hubing & J.L. Drewniak
1420	"Electromagnetic Induced Timing Defects in CMOS Chips"	R. Perez
1440	"Finite-Difference Time-Domain Analysis of Common Mode Cable Currents"	C-W. Lam
1500	**BREAK**	
1520	"Statistical Coupling of EM Fields to Cables in an Overmoded Cavity"	R. Holland & R. St. John
1540	"Power and Ground Plane Modeling and Decoupling in High Speed Printed Circuit Board and Multichip Modules"	F. Yuan, C-W. Lam, & L. Rubin
SESSION 17:	**ARRAYS** Chair: L. Epp	**122 Ingersoll Hall**
1600	"Synthesis of Phased Arrays Aperture Distributions"	R.A. Speciale
1620	"New Results in the Synthesis of Aperture-Field Distributions for Ultra-High-Gain Phased Arrays"	R.A. Speciale
1640	"Advanced Design of Phased Array Beam-Forming Networks"	R.A. Speciale
1730	**BOARD OF DIRECTORS DINNER**	

THURSDAY MORNING 21 MARCH 1996

0715	**CONTINENTAL BREAKFAST**	
SESSION 18:	**FINITE ELEMENTS II (Parallel with Sessions 19, 20, & 21)** Chair: J.M. Jin	**102 Glasgow Hall**
0800	"Adaptive Mesh Refinement Concepts for Electromagnetics"	Z. Chen & R. Lee
0820	"Analysis of Complete Basis Sets of DIvergencelessVector Expansion Functions for Finite Element Problems"	M.J. Walker
0840	"Multi-Mode S-Parameter Computation Using Finite Elements and Perfectly Matched Absorbers"	G.C. Lizalek, J.J. Ruehl, & J.R. Brauer
0900	"Characterization of MIMICs Packages Using a Parallelized 3D FEM Code"	J-G. Yook & L.P.B. Katehi
0920	"Combined PML and ABC for Finite Element Analysis of Scattering Problems"	J.M. Jin & W.C. Chew
0940	"Modeling Microstrip Patches Using the Finite Element Method"	D.B. Davidson, D.H. Malan, & C.B. Wilsen
1000	**BREAK**	
1020	"H_1(curl) Tangential Vector Finite Element Method with Additional Constraint Equation"	P. Bretchko, S.V. Polstyanko, & J-F. Lee
1040	"Extension of Higher-Order 3-D Vector Finite Elements to Curved Cells and Open-Region Problems"	J.S. Savage & A.F. Peterson
1100	"The Hybrid FEM/BEM Solution for EM Scattering from Arbitrary Cavity with Lossy and Anisotropic Material"	J. Xu, Y. Lu, & J.S. Fu
1200	**LUNCH**	
SESSION 19:	**FUTURE FIELDS FOR FDTD ANALYSIS (Parallel with Sessions 18, 20 & 21)** Chairs: D. Katz and M. Piket-May	**122 Ingersoll Hall**
0800	"FDTD Analysis of a Dielectric Leaky-Wave Antenna Using PML"	M. Chen, B. Houshmand, & T. Itoh
0820	"FDTD Analysis in Cylindrical Coordinates of a TEM Pyramidal Horn Antenna"	D. Menditto, P. Tognolatti, & F. Bardati
0840	"A Modified FDTD (2,4) Scheme for Modeling Electrically Large Structures with High Phase Accuracy"	M.F. Hadi & M. Piket-May, & E.T. Thiele
0900	"Application of the FDTD Method to Three-Dimensional Propagation in a Magnetized Ferrite"	J.W. Schuster, & R.J. Luebbers

THURSDAY MORNING 21 MARCH

SESSION 19:	**FUTURE FIELDS FOR FDTD ANALYSIS (Parallel with Sessions 18, 20 & 21) (cont)**	**122 Ingersoll Hall**
0920	"Symmetry-Aided FDTD Analysis of Finite Phased Arrays"	D. Crouch
0940	"Conformal FVTD with a Rectangular Grid for PEC Scattering Objects"	K.S. Yee & J.S. Chen
1000	**BREAK**	
1020	"Application of Recent Advances in FDTD Modeling to the Problem of Acoustic Propagation in Shallow Water"	J.B. Schneider, F.D. Hastings. & C.J. Railton
1040	"FDTD Analysis of Small Loop Antennas for Partial Exposure of Rat Head at 837 MHz"	K.W. Chan, J.A. McDougall, & C.K. Chou
1100	"Scattering from Complex Geometries Using a Parallel FVTD Algorithm"	V. Ahuja & L.N. Long
1120	"FDTD Simulation of High Frequency Devices by Using Locally Refined Meshes"	P. Thoma & T. Weiland
1200	**LUNCH**	
SESSION 20:	**NUMERICAL ERROR ANALYSIS AND CONTROL II (Parallel with Sessions 18, 19, & 21)** Chair: J.L. Volakis	**Engr. Auditorium**
0800	"A WWW-Based Data Base for Code Validation"	C.W. Trueman & S.R. Mishra
0820	"Code Scaling"	M.J. Schuh & A.C. Woo
0840	"An Overview of Numerical Dispersion Error in PDE Methods for Electromagnetics"	R. Lee
0900	"Non-rigorous CEM Error Estimates and Their Limitations"	A.F. Peterson
0920	"Comparisons of Staggered and Non-Staggered Schemes for Maxwell's Equations"	D. Gottlieb & B. Yang
0940	"Minimizing the Number of Frequency Samples Needed to Represent a Transfer Function Using Adaptive Sampling"	E.K. Miller
1000	**BREAK**	
SESSION 21:	**MODELING TOOLS FOR VISUALIZATION: PRE- AND POST-PROCESSING** Chair: J. Karty **(Parallel with Session 18, 19, & 20)**	**Engr. Auditorium**
1020	"MATLAB NEC Toolbox: The Cross Platform GUI Pre-and Post-processing Tool for NEC Applications"	Y. Lu
1040	"Computation and Graphic Visualization of Plane-Wave K-Space Spectra and Far-Field Patterns with MATLAB 4.0"	R.A. Speciale
1100	"The Intelligent Computational Electromagnetics Expert System (ICEMES)"	A.L. Drozd, T.W. Blocher, V.K. Choo, & K.R. Siarkiewicz
1120	"NECSHELL - A New Graphical User Interface for the NEC Code"	M.Y. Mikhailov, V.O. Lomtev, & A.A. Efanov
1200	**LUNCH**	

THURSDAY AFTERNOON

SESSION 22:	**FINITE ELEMENT ANALYSIS (Parallel with Session 23 & 25)** Chair: J.R. Brauer	**102 Glasgow Hall**
1320	"Finite Element Scattering and Radiation Analysis Using Prismatic Meshes and Artificial Absorbers for Conformal Domain Truncation"	M. Casciato, M. Nurnberger T. Özdemir, & J.L. Volakis
1340	"Application of Fast Multipole Method to Finite Element-Boundary Integral Solution of Scattering Problems"	N. Lu & J-M. Jin
1400	"Use of Perfectly-Matched Absorber Boundaries in Finite Element Analysis of Patch Antennas"	J.F. DeFord & G.C. Lizalek
1420	"A New Permanent-Magnet Synchronous Motor Design Configuration and Finite Element Analysis"	Q.K. Zhang, N. Ida, Y. Qiu, & Z.R. Jiang
1440	"Investigation of ABC Behavior in Axisymmetric Electrostatic Finite Element Analysis"	A. Konrad & L. Han
1500	**BREAK**	
1520	"An Efficient Scheme for Finite Element Analysis in the Frequency Domain"	M. Kuzuoglu, R. Mittra, J.R. Brauer, & G.C. Lizalek
1540	"Finite-Element Modelling of Head Coils for High-Frequency Magnetic Resonance Imaging Applications"	J.G. Harrison & J.T. Vaughan
1600	"H_1(curl) TVFEM in Conjunction with PML for Modeling 3D Waveguide Discontinuities"	S.G. Perepelitsa, R. Dyczij-Edlinger, & J-F. Lee

THURSDAY AFTERNOON 21 MARCH 1996

SESSION 23:	**METHOD OF MOMENTS APPLICATIONS (Parallel with Sessions 22 & 25** Chair: A.F. Peterson	**Engr. Auditorium**
1320	"Global Fourier-Series Basis Functions for EM Scattering"	M.H. Smith & A.F. Peterson
1340	"A Numerically Stable Method of Moments Time Domain Model"	L.B. Gravelle & J-P. Estienne
1400	"Method of Moments Analysis of the Celestron-8 Telescope"	R.R. DeLyser, P. Ensaf, & P. McDaniel
1500	**BREAK**	
SESSION 24:	**FDTD ANALYSIS AND APPLICATIONS (Parallel with Session 26)** Chair: A. Elsherbeni	**102 Glasgow Hall**
1520	"Dynamic Analysis of V Transmission Lines"	O.M. Ramahi, A.Z. Elsherbeni, & C.E. Smith
1540	"An Absorbing Boundary Condition for the FDTD Method Using Digital Filters Design Technique"	C-N. Kuo & T. Itoh
1600	"Application of the FDTD Method to the Electromagnetic Modeling of Patch Antenna Arrays"	M.F. Pasik, G. Aguirre, & A.C. Cangellaris
SESSION 25:	**MICROWAVE COMPONENTS (Parallel with Sessions 22 & 23)** Chairs: M.E. Baginski and M.M. Ney	**122 Ingersoll Hall**
1320	"Parallel Coupled Microstrip Patch Resonators on a Ferrimagnetic Layer"	J. de Ribamar S. Oliveira & A. Gomes d'Assunção
1340	"Fullwave Analysis of Circular Cylindrical Backed Slotlines"	L. Martins de Mendonça & A. Gomes d' Assunção
1400	"Properties of Tapered Microstrip Lines on Dielectric and Magnetized Ferrimagnetic Layers"	A. Gomes d' Assunção, F. de Lima, & M.R.M. Lins de Albuquerque
1420	"Frequency and Time Domain Computations of S-Parameters Using the Finite Integration Technique"	R. Schumann, M. Clemens, P. Thoma, & T. Weiland
1440	"Time Domain Analysis of Microwave Structures by MRTD"	M. Krumpholz, E. Tentzeris, R. Robertson, & L.P.B. Katehi
1500	**BREAK**	
1520	"A Parasite-Free Non-Orthogonal Finite-Difference Frequency-Domain Method for the Analysis of Inhomogeneous Lossy Waveguides"	L. Zhao & A.C. Cangellaris
SESSION 26:	**BIOMEDICAL ELECTROMAGNETICS (Parallel with Sessions 24)** Chairs: A.M. Morega and R.K. Gordon	**122 Ingersoll Hall**
1540	"A Spectral Approach to the Cardiography"	A.M. Morega, D. Mocanu, & M. Morega
1600	"Optimal Transcutaneous Pacing"	A.M. Morega, B. Ciocârlan, & M. Morega
	CLOSE	

FRIDAY MORNING 22 MARCH

0830-1200	**SHORT COURSE (HALF-DAY)** "Using Model-Based Parameter Estimation to Increase the Efficiency and Effectiveness of Computational Electromagnetics" E.K. Miller	**122 Ingersoll Hall**
0830-1600	**SHORT COURSE (FULL-DAY)** "Conformal Time Domain Numerical Electromagnetics" K. Yee, Lockheed	**102 Glasgow Hall**
0830-1630	**SHORT COURSE (FULL-DAY)** "Finite Element Methods for Electromagnetics" J.L. Volakis, University of Michigan, and J. Brauer, Mac-Neal Schwendler Corporation.	**109 Glasgow Hall**

FRIDAY AFTERNOON

1300-1630	**SHORT COURSE (HALF-DAY)** "Antenna Properties in Linear and Nonlinear Environments" R. Bevensee, BOMA Enterprises	**122 Ingersoll Hall**

SESSION 11:

NEC APPLICATIONS

Chairs: M. Ney and C. Christopoulos

Numerical Investigation of Antennas for Hand-Held Radiotelephones Using NEC Code.

A. A. Efanov, M. S. Leong and P. S. Kooi

Department of Electrical Engineering
National University of Singapore
10 Kent Ridge Crescent, Singapore 0511
FAX: (+65) 777-3117

ABSTRACT - The classic quarter- and half-wavelength monopole antennas, the quarter-wavelength helical antenna, the bottom-loaded monopole antenna and the modified sleeve dipole have been modelled using the NEC-2 code. The last two antenna configurations are new, they have a good performance and relatively small sizes. These antennas could be used for hand-held radiotelephones as well as for other applications.

1. INTRODUCTION

Development of the modern personal communication systems stimulates an improvement of portable radiotelephone antennas. A design of such antennas must satisfy several quite contradictory requirements such as good performance, small size, cost factor, etc. Numerous papers were devoted to this problem [1].

This report presents the results of the numerical investigation and the mutual comparison of several types of antennas for hand-held radiotelephones. The following antennas are considered here: the classic quarter- and half-wavelength monopoles, the quarter-wavelength helix, the bottom-loaded monopole and the modified sleeve dipole. The last two antenna configurations are new, and they could be used for portable radiotelephones as well as for other applications.

All the antennas have been modelled for the GSM band (890-960 MHz, European standard), but the obtained results could be used for the PCS/PCN applications (1.8/1.9 GHz) as well.

The characteristics of the portable antennas are dependent on the radiotelephone box sizes and on the actual antenna position. It is assumed that the antennas are placed at the center of the top side of a conducting box with the following dimensions: 40 x 50 x 180 mm (0.123 x 0.154 x 0.555 λ). A wire-grid model (Fig.1) has been used for the modelling of the box. The NEC-2 code [2] has been used for the numerical simulations.

2. MONOPOLE AND HELICAL ANTENNAS

The quarter- and half-wavelength monopoles and the quarter-wavelength helix are the well known antennas widely used for mobile communications [1]. There are several papers devoted to an investigation of the characteristics of a monopole antenna mounted on a conducting box [3-5]. Mobile applications of various helical antennas have been considered in [6-7].

The quarter-wavelength monopole (Fig.1) has the 84 mm length. Its calculated radiation pattern (ZOX vertical plane) is shown in Figure 3. There is a deep null in the vicinity of the Θ = 90 degrees, since the resonant $\lambda/4$-monopole antenna excites strong RF currents (Fig. 8) on the portable radio case, which is an integral part of the radiating system. This is the most negative feature of this antenna, because the standard operating Θ angular range for the hand-held radiotelephone systems (in an

elevation plane) is from 40 to 140 degrees [1]. The quarter-wavelength resonant monopole antenna has very good input impedance characteristics (Fig. 4a).

The half-wavelength monopole (the end-fed dipole) has the 155 mm length. Its radiation pattern has much better performance (Fig.3). However, it is necessary to match its high radiation resistance (Fig.4b) to the standard 50-Ohms output impedance of a radiotelephone.

A typical helical monopole antenna used for mobile communications has a physical length of about 1/12 wavelength and an electrical length of about a quarter wavelength [1]. The helical antenna is shown in Figure 2. It has 4 and 7/8 turns of the 10 mm diameter with the whole height of 30 mm. The antenna electrical length has been chosen a little bit longer than at resonance to obtain an input resistance of about 50 Ohms. For this case it is necessary to use a matching capacitor to compensate an inductive component (+j316 Ohms) of the input impedance. The input characteristics (with the 0.5 pF capacitor) are shown in Figure 4c. The antenna radiation pattern (Fig. 3) suffers from the same shortcomings as for the quarter-wavelength monopole case. The resonant helical antenna also strongly excites the RF currents on the radiotelephone box (Fig. 8).

4. BOTTOM-LOADED MONOPOLE

The bottom-loaded monopole (Fig.5) consists of a horizontal rectangular conducting plate placed near to the top side of the radiotelephone box and a monopole rod connected to the plate from above. The antenna feeding point is between the plate and the top side of the box. The plate is placed at the 15 mm (0.046 λ) height above the box, and the whole antenna height is 113 mm (0.35 λ).

This configuration, which has a radiation pattern (Fig.6) similar to the half-wavelength monopole, however, leads to a whole antenna height that is sufficiently smaller for practical implementation. The calculated input characteristics are shown in Figure 7. A good impedance matching could be made by a proper choice of the feeding point position. This antenna excites much smaller RF currents on the radiotelephone box (Fig.8) than the quarter-wavelength monopole and the helix.

5. MODIFIED SLEEVE DIPOLE

The classic sleeve dipole antenna [8] is widely used for various applications. It contains a quarter-wavelength coaxial resonant choke which isolates the dipole from the feeding coaxial line. However, a resonant nature of the choke leeds to the rapid radiation pattern deteriorations for even a small frequency detuning [1]. The whole antenna length is about half-wavelength.

We have improved a construction of the sleeve dipole to increase its operating band and to reduce the antenna height. The modified sleeve dipole (Fig.9) consists of a quarter-wavelength helical monopole fed by a coaxial line and a quarter-wavelength sleeve formed by four wire arms placed parallel to the coaxial line. The diameter of the helix is 10 mm (0.03 λ), the whole antenna length is 100 mm (0.31 λ). The distance between the opposite sleeve arms is 10 mm (0.03 λ). The calculated radiation patterns are shown in Figure 10. The calculated input characteristics are shown in Figure 11. The antenna has a good performance and a relatively small sizes what makes it possible to use it for a hand-held radiotelephones as well as for various other mobile applications.

6. CONCLUSIONS

The several antennas suitable for the hand-held radiotelephone applications have been modelled using the NEC-2 code. The gain of the considered antennas is compared in Figure 12, where the radiation patterns are shown in dBi for the 925 MHz central operating frequency. The bottom-loaded monopole and the modified sleeve dipole antenna have a good performance and relatively small sizes. They could be used for hand-held radiotelephones at GSM and PCS/PCN bands as well as for several other portable mobile applications.

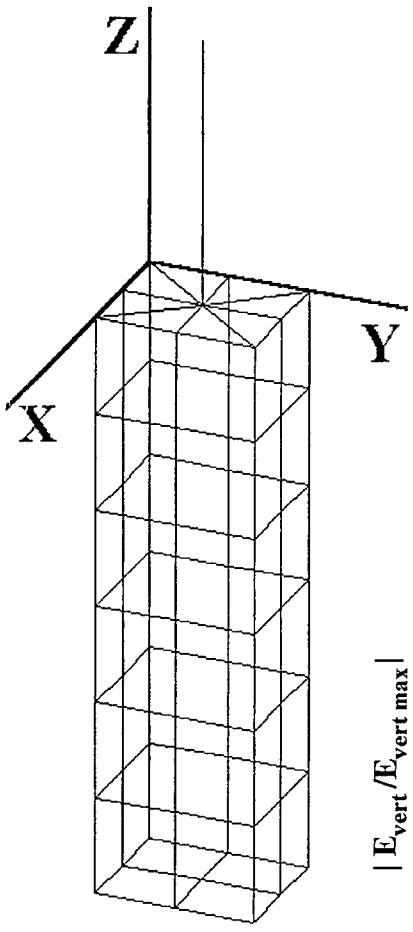

Figure 1. Wire-grid model of the radiotelephone box with the quarter-wavelength monopole antenna.

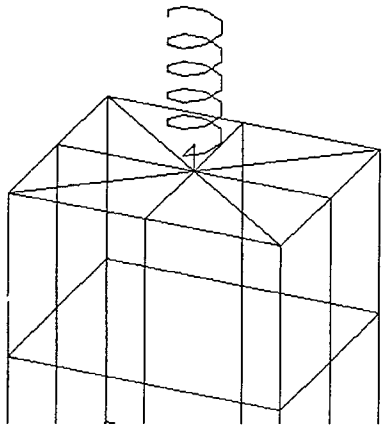

Figure 2. Wire-model of the quarter-wavelength helical antenna.

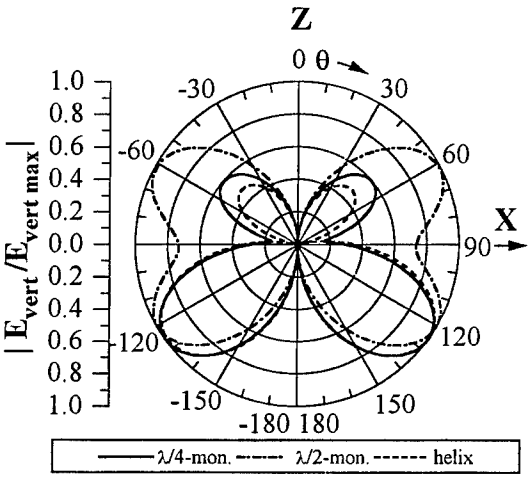

Figure 3. Calculated radiation patterns of the monopoles and the helix at 925 MHz.

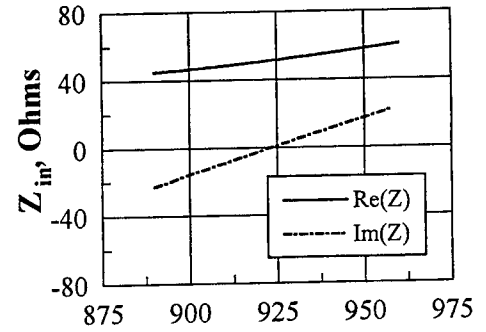

a) λ/4-monopole

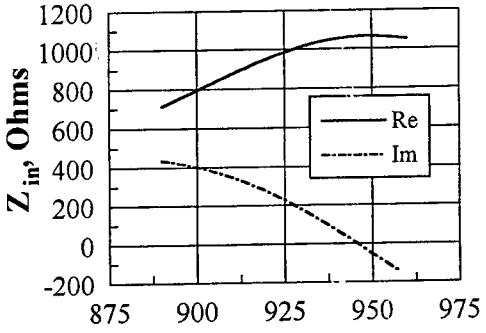

b) λ/2-monopole

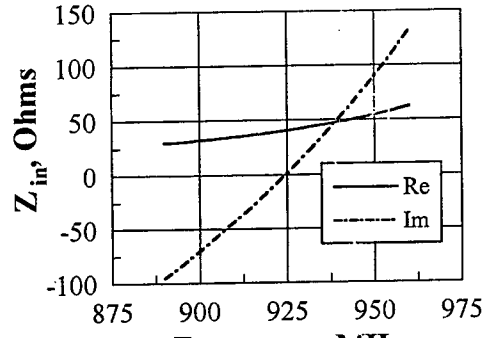

c) λ/4-helix with the matching capacitor

Figure 4. Calculated input impedance of the monopoles and the helix.

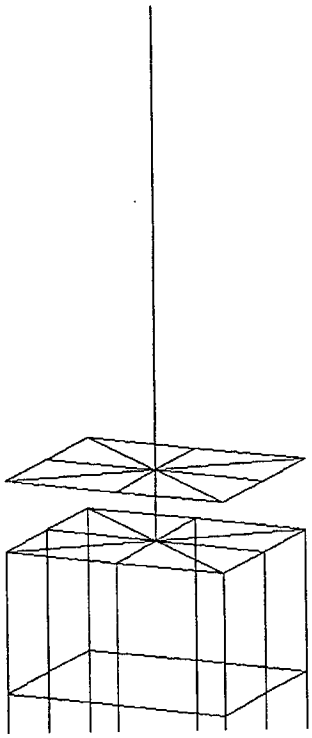

Figure 5. Wire-grid model of the bottom-loaded monopole antenna.

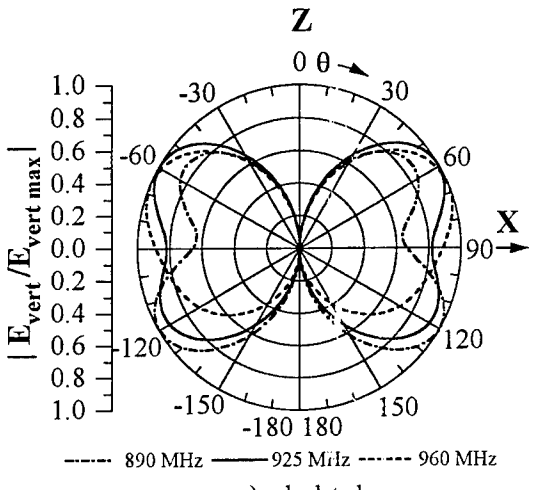

a) calculated

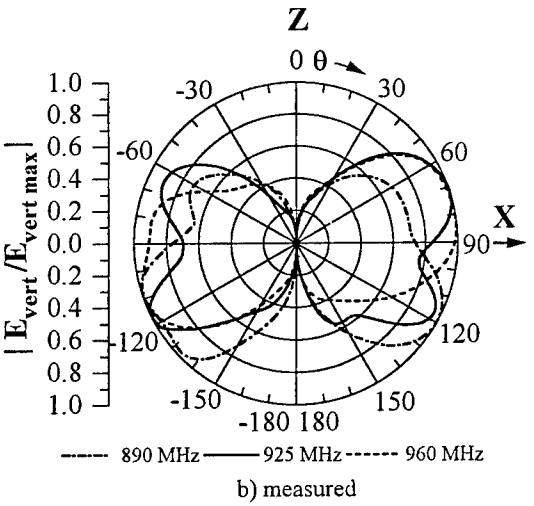

b) measured

Figure 6. Radiation patterns of the bottom-loaded monopole antenna.

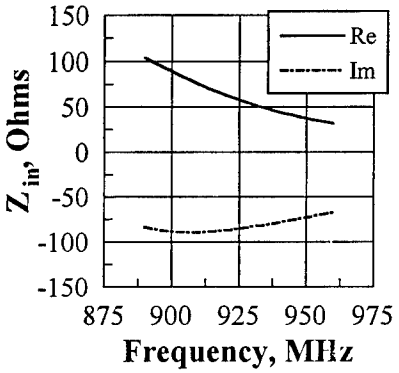

Figure 7. Calculated input impedance of the bottom-loaded monopole antenna.

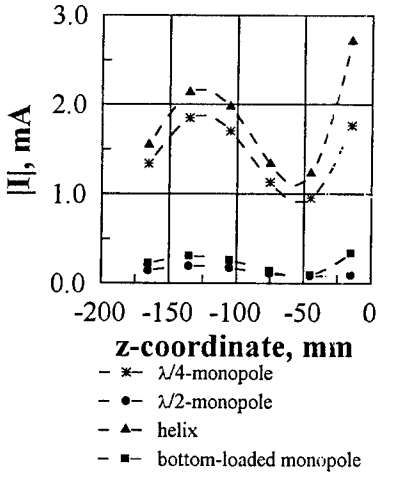

Figure 8. Calculated current distributions along the edge of the radiotelephone box.

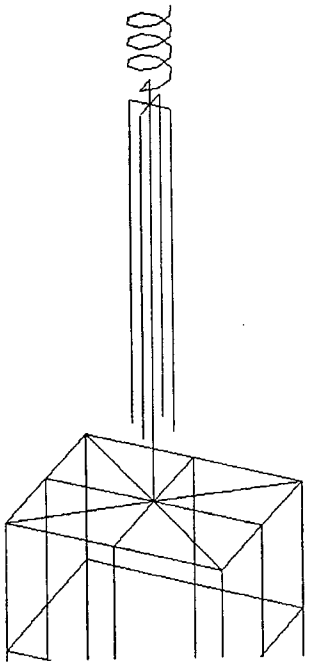

Figure 9. Wire-model of the modified sleeve dipole antenna.

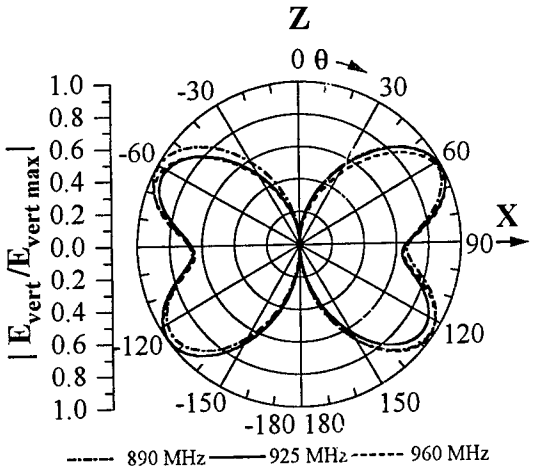

Figure 10. Calculated radiation patterns of the modified sleeve dipole antenna.

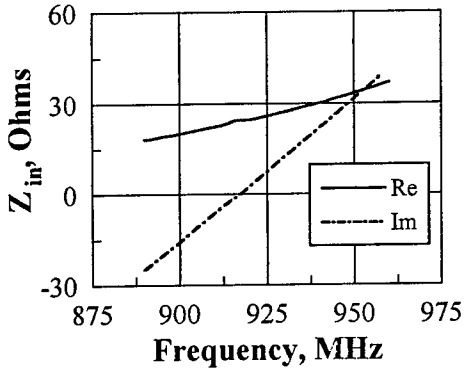

Figure 11. Calculated input impedance of the modified sleeve dipole antenna.

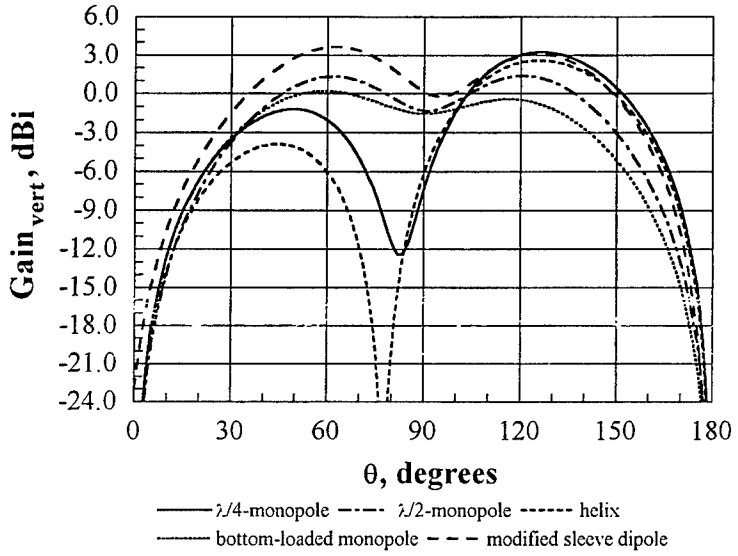

Figure 12. Calculated antenna gain (vertical polarization) at 925 MHz.

REFERENCES

[1] *Mobile Antenna Systems Handbook* / edited by K. Fujimoto, J. R. James, Boston, London, Artech House, 1994.

[2] G. J. Burke and A. J. Poggio, "Numerical Electromagnetics Code (NEC-2)", Naval Ocean Systems Center, San Diego, Calif., Tech. Doc. 116, January 1981.

[3] A.W.C. Chu, S.A. Long and D.R. Wilton, "The Radiation Pattern of a Monopole Antenna Attached to a Conducting Box", *IEEE Transactions on Antennas and Propagation*, Vol. AP-38, pp. 1907-1911, December 1990.

[4] R. Luebbers, L. Chen, T. Uno and S. Adachi, "FDTD Calculation of Radiation Patterns, Impedance and Gain for a Monopole Antenna on a Conducting Box", *IEEE Transactions on Antennas and Propagation*, Vol. AP-40, pp. 1577-1583, December 1992.

[5] M. A. Jensen and Y. Rahmat-Samii, "Performance Analysis of Antennas for Hand-Held Transceivers Using FDTD", *IEEE Transactions on Antennas and Propagation*, Vol. AP-42, pp. 1106-1113, August 1994.

[6] Q. Balsano, *et al.*, "The Near Field of Omnidirectional Helical Antennas", *IEEE Transactions on Vehicular Technology*, Vol. VT-31, pp. 173-185, November 1982.

[7] K. Fujimoto, A. Henderson, K. Hirasawa and J. R. James, *Small Antennas*, Letchworth, England, Research Study Press, 1987.

[8] H. Jasik, Antenna Engineering Handbook, New York, McGraw-Hill, 1961.

EVALUATION OF THE DISCRETE COMPLEX-IMAGE METHOD FOR A NEC-LIKE MOMENT-METHOD SOLUTION *

G. J. Burke
Lawrence Livermore National Laboratory
P.O. Box 5504, L-156, Livermore, CA 94550

Abstract

The discrete image approximation for the field of a half-space is tested in the NEC antenna modeling program as an alternative to the interpolation method presently used. The accuracy and speed of the discrete image approximation are examined for varying number of images and approximation contour, and the solution for current is obtained on a horizontal wire approaching the interface.

1. INTRODUCTION

A common extension to frequency domain moment-method codes is to model structures in a stratified medium or at least near a homogeneous ground. The solution then requires the Green's function for the stratified medium or half-space, which in its exact form involves an integral over an infinite spectrum of waves [1, 2]. The moment-method solution generally requires many evaluations of the Green's function for numerical integration over sources, so evaluation time and accuracy become critical. A number of methods have been used in this evaluation, including integration over the real radial wavenumber or on a contour deformed to the steepest descent path [3]. Linear filters have been very effective for lossy media [4]. Lindell [5] has converted the spectral integrals of Sommerfeld into integrals over an image distributed in complex space. While this solution remains exact, it still requires numerical integration over the distributed images, although the integrals may be more easily evaluated than the spectral form. The code NEC [6] uses an interpolation method for a half-space [7]. The Sommerfeld integrals are evaluated numerically on contours deformed to accelerate convergence [8]. The values are then transformed using the approximate quasistatic or asymptotic behavior of the fields to remove rapid variations, and are stored in tables from which the required values are obtained by interpolation. Alternatively, a "model" containing functions from the asymptotic solution and variable parameters is fit to the computed values in a technique known as model-based parameter estimation [9]. These interpolation methods are fast, accurate and reasonably simple when source and evaluation points are in the same medium, but can get complicated for interactions across interfaces.

More recently a simple approximation of the Green's function for a stratified medium or half-space has been developed in terms of a sum of discrete images in complex space [10]. This method has been applied to the solution of microstrip problems [11, 12] and to antennas over a homogeneous ground [13] using the mixed-potential form of the integral equation. In this paper results of using the discrete image method in a solution with continuous current expansion and

* Work performed under the auspices of the U. S. Department of Energy by the Lawrence Livermore National Laboratory under Contract W-7405-Eng-48.

point matching of the field are reported. The accuracy of the discrete image approximation is investigated, and the speed is compared with the interpolation method in NEC.

2. THE DISCRETE IMAGE APPROXIMATION FOR A HALF-SPACE

The discrete image approximation is obtained by numerical processing of the Sommerfeld integrals for the potentials due to a half-space, after first extracting a quasistatic term to improve convergence. The method is outlined here to obtain the field components needed in NEC. The solution for the field of a source in the presence of a half-space can be found in many references, for example [1, 2]. The geometry of the problem is shown in figure 1, using the convention that the lower medium is medium 1 and the upper is medium 2. The wavenumbers are $k_1 = k_0(\epsilon_1 - j\sigma_1/\omega\epsilon_0)^{1/2}$ and $k_2 = k_0(\epsilon_2 - j\sigma_2/\omega\epsilon_0)^{1/2}$ with $k_0 = \omega\sqrt{\mu_0\epsilon_0}$ and $e^{j\omega t}$ time variation assumed. The form of the solution used here is from [2] in terms of the potentials U_{22} and V_{22} which, together with the free-space Green's functions for the source and its image, yield all of the components of electric field in the upper medium due to vertical and horizontal electric dipoles in the upper medium. The potentials involve infinite integrals over the radial component of wavenumber k_ρ which can be written in terms of either Bessel or Hankel functions in k_ρ as

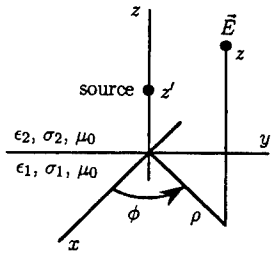

Fig. 1. Geometry for source and evaluation points above a half-space

$$V_{22} = 2\int_0^\infty R_V(k_{z2})\frac{e^{-jk_{z2}(z+z')}}{k_{z2}}J_0(k_\rho\rho)k_\rho\,dk_\rho \tag{1a}$$

$$= \int_{-\infty}^\infty R_V(k_{z2})\frac{e^{-jk_{z2}(z+z')}}{k_{z2}}H_0^{(2)}(k_\rho\rho)k_\rho\,dk_\rho \tag{1b}$$

$$U_{22} = 2\int_0^\infty R_U(k_{z2})\frac{e^{-jk_{z2}(z+z')}}{k_{z2}}J_0(k_\rho\rho)k_\rho\,dk_\rho \tag{1c}$$

$$= \int_{-\infty}^\infty R_U(k_{z2})\frac{e^{-jk_{z2}(z+z')}}{k_{z2}}H_0^{(2)}(k_\rho\rho)k_\rho\,dk_\rho \tag{1d}$$

where

$$R_V(k_{z2}) = \frac{k_{z2}}{k_2^2k_{z1} + k_1^2k_{z2}}, \qquad R_U(k_{z2}) = \frac{k_{z2}}{k_{z1} + k_{z2}}$$

and $k_{z1} = (k_1^2 - k_\rho^2)^{1/2}$ and $k_{z2} = (k_2^2 - k_\rho^2)^{1/2}$ with $\mathrm{Im}(k_{z1},\, k_{z2}) \le 0$. The basic contours for evaluating these integrals on the real axis are shown in figure 2 as C_0 for the Bessel function form and C_1 for the Hankel function form.

As $R_1 = [\rho^2 + (z + z')^2]^{1/2}$ becomes small the integrals in (1) converge more slowly, leading to a R_1^{-1} singularity in the integrals. The quasistatic term containing this singularity can be extracted by subtracting the constant limits that R_V and R_U approach as k_ρ or k_{z2} become large.

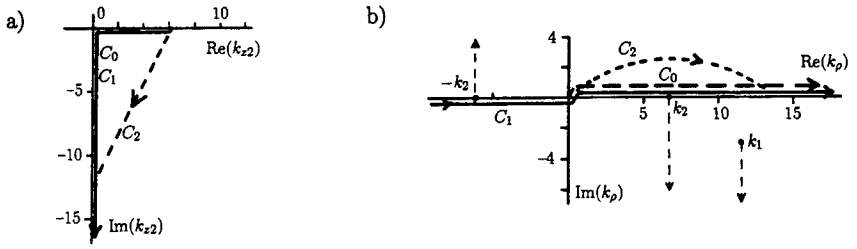

Fig. 2. Contours for evaluation of the Sommerfeld integrals: a) contours in the k_{z2} plane, b) contours in the k_ρ plane, with branch cuts from k_1 and k_2.

The remainders of the potentials after subtracting the quasistatic terms are

$$v_{22} = 2\int_0^\infty R_v(k_{z2})\frac{e^{-jk_{z2}(z+z')}}{k_{z2}} J_0(k_\rho\rho)k_\rho\, dk_\rho \tag{2a}$$

$$u_{22} = 2\int_0^\infty R_u(k_{z2})\frac{e^{-jk_{z2}(z+z')}}{k_{z2}} J_0(k_\rho\rho)k_\rho\, dk_\rho \tag{2b}$$

where

$$R_v(k_{z2}) = \frac{k_{z2}}{k_2^2 k_{z1} + k_1^2 k_{z2}} - \frac{1}{k_1^2 + k_2^2}, \qquad R_u(k_{z2}) = \frac{k_{z2}}{k_{z1} + k_{z2}} - \frac{1}{2}. \tag{3}$$

The extracted quasistatic terms can be combined with the free space Green's function for the image by applying the Sommerfeld identity,

$$\int_0^\infty \frac{e^{-jk_{z2}(z+z')}}{k_{z2}} J_0(k_\rho)k_\rho\, dk_\rho = \frac{e^{-jk_2R_1}}{R_1}. \tag{4}$$

The equations for the electric field components are then

$$E_\rho^V = \frac{-j\omega I\ell\mu_0}{4\pi k_2^2}\frac{\partial^2}{\partial\rho\partial z}\left(G_{22} + \frac{k_1^2 - k_2^2}{k_1^2 + k_2^2}G_{21}\right) + S_\rho^V \tag{5a}$$

$$E_z^V = \frac{-j\omega I\ell\mu_0}{4\pi k_2^2}\left(\frac{\partial^2}{\partial z^2} + k_2^2\right)\left(G_{22} + \frac{k_1^2 - k_2^2}{k_1^2 + k_2^2}G_{21}\right) + S_z^V \tag{5b}$$

$$E_\rho^H = \frac{-j\omega I\ell\mu_0}{4\pi k_2^2}\left(\frac{\partial^2}{\partial\rho^2} + k_2^2\right)\left(G_{22} - \frac{k_1^2 - k_2^2}{k_1^2 + k_2^2}G_{21}\right)\cos\phi + S_\rho^H \tag{5c}$$

$$E_\phi^H = \frac{j\omega I\ell\mu_0}{4\pi k_2^2}\left(\frac{1}{\rho}\frac{\partial}{\partial\rho} + k_2^2\right)\left(G_{22} - \frac{k_1^2 - k_2^2}{k_1^2 + k_2^2}G_{21}\right)\sin\phi + S_\phi^H \tag{5d}$$

$$E_z^H = \frac{-j\omega I\ell\mu_0}{4\pi k_2^2}\frac{\partial^2}{\partial\rho\partial z}\left(G_{22} - \frac{k_1^2 - k_2^2}{k_1^2 + k_2^2}G_{21}\right)\cos\phi - S_\rho^V\cos\phi \tag{5e}$$

where the subscripts on E or S indicate the cylindrical component of the field and the superscript indicates a vertical electric dipole (V) or horizontal dipole on along the x axis (H). G_{22} and G_{21}

are the free space Green's functions for the source and its image, $G_{22} = \exp(-jk_2R_2)/R_2$ and $G_{21} = \exp(-jk_2R_1)/R_1$ with $R_{\frac{1}{2}} = \left[\rho^2 + (z \pm z')^2\right]^{1/2}$. The final terms, containing the remaining Sommerfeld integrals, are

$$S_\rho^V = \frac{-j\omega I\ell\mu_0}{4\pi k_2^2}\frac{\partial^2}{\partial\rho\partial z}k_1^2 v_{22} \tag{6a}$$

$$S_z^V = \frac{-j\omega I\ell\mu_0}{4\pi k_2^2}\left(\frac{\partial^2}{\partial z^2} + k_2^2\right)k_1^2 v_{22} \tag{6b}$$

$$S_\rho^H = \frac{-j\omega I\ell\mu_0}{4\pi}\cos\phi\left(\frac{\partial^2 v_{22}}{\partial\rho^2} + u_{22} + G_{21} - \frac{2k_2^2}{k_1^2+k_2^2}G_{21}\right) \tag{6c}$$

$$S_\phi^H = \frac{j\omega I\ell\mu_0}{4\pi}\sin\phi\left(\frac{1}{\rho}\frac{\partial v_{22}}{\partial\rho} + u_{22} + G_{21} - \frac{2k_2^2}{k_1^2+k_2^2}G_{21}\right). \tag{6d}$$

The final G_{21} terms are included in (6c) and (6d) to complete the field of the quasistatic image in (5) as the field of a source in free space. After subtracting the quasistatic terms, the remaining integrals u_{22} and v_{22} remain finite as R_1 goes to zero, while the field components in equations (6) have $1/R_1$ singularities from the derivatives of v_{22}. The advantage of extracting the quasistatic components for the discrete image approximation is that the functions $R_u(k_{z2})$ and $R_v(k_{z2})$ in equation (3) decay as k_{z2}^{-2} for large k_{z2}, and these decaying functions are better suited to approximation by a sum of exponentials than are R_U and R_V which become constant. The quasistatic terms are also subtracted in the interpolation method used in NEC, where the singular remainders in equation (6) are multiplied by R_1 so that they can easily be approximated with linear or quadratic interpolation. Alternatively, the singularities in equations (6) can be approximated [6] and also the next constant terms can be obtained. For example, in S_ρ^H

$$\frac{\partial^2 v_{22}}{\partial\rho^2} \approx \frac{k_2^2(k_2^2-k_1^2)}{(k_1^2+k_2^2)^2}\left(\frac{\sin\alpha}{1+\sin\alpha}\right)\frac{1}{R_1} + \frac{jk_2^2\left(k_1^4+k_1^3k_2-k_1^2k_2^2-2k_1k_2^3-2k_2^4\right)}{3(k_1+k_2)(k_1^2+k_2^2)^2} + \frac{jk_1^4k_2^4C_k}{2(k_1^2-k_2^2)(k_1^2+k_2^2)^{5/2}} \tag{7}$$

for small R_1, where

$$C_k = \tan^{-1}\left(\frac{2(k_1-k_2)(k_1^2-k_1k_2+k_2^2)\sqrt{k_1^2+k_2^2}}{2k_1^4-4k_1^3k_2+5k_1^2k_2^2-4k_1k_2^3+2k_2^4}\right)$$

with $\mathrm{Im}(C_k) \le 0$ and $\sin\alpha = (z+z')/R_1$.

For the discrete image approximation $R_u(k_{z2})$ and $R_v(k_{z2})$ are approximated with a sum of exponential functions in k_{z2} by means of the Prony [14] or Matrix Pencil [15] methods. Since these methods require equally spaced samples in a real variable, the substitution $k_{z2} = k_2[t_a + t(t_b - t_a)]$ is made. Applying the Matrix Pencil method with equally spaced samples over $0 \le t \le 1$ yields the exponential approximation over the range $k_{z2} \in (k_2t_a,\ k_2t_b)$ as

$$R_v(t) \approx \sum_{i=1}^{N_t} A_i e^{B_i t}, \qquad R_v(k_{z2}) \approx \sum_{i=1}^{N_t} a_i e^{b_i k_{z2}}$$

with $a_i = A_i e^{-B_i t_a/(t_b - t_a)}$ and $b_i = B_i/[k_2(t_b - t_a)]$. When the exponential approximation of $R_v(k_{z2})$ is substituted into (2) the integral for each term can be evaluated using the Sommerfeld identity (4) to get a sum of discrete images

$$v_{22} \approx \sum_{i=1}^{N_t} a_i \frac{e^{-jk_2 R_i}}{R_i} \tag{8}$$

with $R_i = [\rho^2 + (z + z' + jb_i)^2]^{1/2}$. Thus v_{22}, and similarly u_{22} are approximated by a sum of free-space Green's functions for images in complex space.

In applying the discrete image method a contour similar to C_2 in figure 2 is usually chosen for the approximation [10]. Hence, $t_a = 1$ and t_b is a negative imaginary value. This deformation from C_0 yields a linear path in the k_{z2} plane and also avoids surface-wave poles that would occur for a stratified medium. It also moves the path further from the Zenneck pole in R_V, making the approximation easier.

3. NUMERICAL RESULTS

The accuracy of the discrete image approximation was tested against the numerical evaluation routines in SOMNEC [6] after reducing the error limits in the Romberg adaptive integration by two orders of magnitude and increasing the accuracy of the Bessel and Hankel functions. With these changes the relative error in the integration seems to be around 10^{-6} to 10^{-7}.

The error from the discrete image approximation for v_{22} is shown in figure 3a for a lossy ground with the number of images N_t varied. The matrix pencil method was used with $N_s = 300$ samples and $t_b = -j10$. $N_t = 12$ was the maximum number of terms that could be obtained from the matrix pencil method with the tolerance in the singular-value decomposition set to 10^{-10}. The approximation is seen to converge rapidly in the region of $0.1 < R_1/\lambda_0 < 1$. The error with varying t_b is shown in figure 3b, where N_t was always the maximum returned by matrix pencil. The increased error for small R_1 is due to the truncation of the approximation contour at $k_2 t_b$ as the integrand converges more slowly, so a larger t_b reduces the error. The use of the Sommerfeld identity for equation (8) implies an integration contour to infinity, but the error is uncontrolled beyond $k_2 t_b$ and increases as the integrand decays. The increased error in figure 3b for large R_1 and large t_b is due to insufficient sampling, and would be reduced with a larger N_s at the cost of increased time for determining the image parameters. Figure 3c shows the error with varying t_b for grazing incidence along the ground. The error due to truncation at t_b occurs sooner as R_1 is decreased than for points off the interface, since the integrand decays more slowly without the $e^{-jk_{z2}(z+z')}$ term. In numerical integration the Hankel function form of equation (1) could be used in this case, with the integration contour deformed downward to a steepest descent path. The contour C_2 used in the discrete image approximation is more nearly optimum for large $(z + z')/\rho$. For large R_1 the error increases rapidly, apparently from difficulty in approximating R_v near the Zenneck pole near $k_{z2} = k_2$. A small t_b reduces the error for large R_1 with increased error for small R_1. Figure 3d shows the same result as 3c but for dielectric ground. In this case the error increases more rapidly for large R_1, perhaps due to the difficulty in approximating the lateral wave. Although the lateral wave, with wavenumber k_1, must be synthesized from exponentials in k_2 the approximation is successful for a number of cycles determined by the number of discrete image terms. For example, the lateral wave was approximated to about $R_1/\lambda = 0.7$ with 5

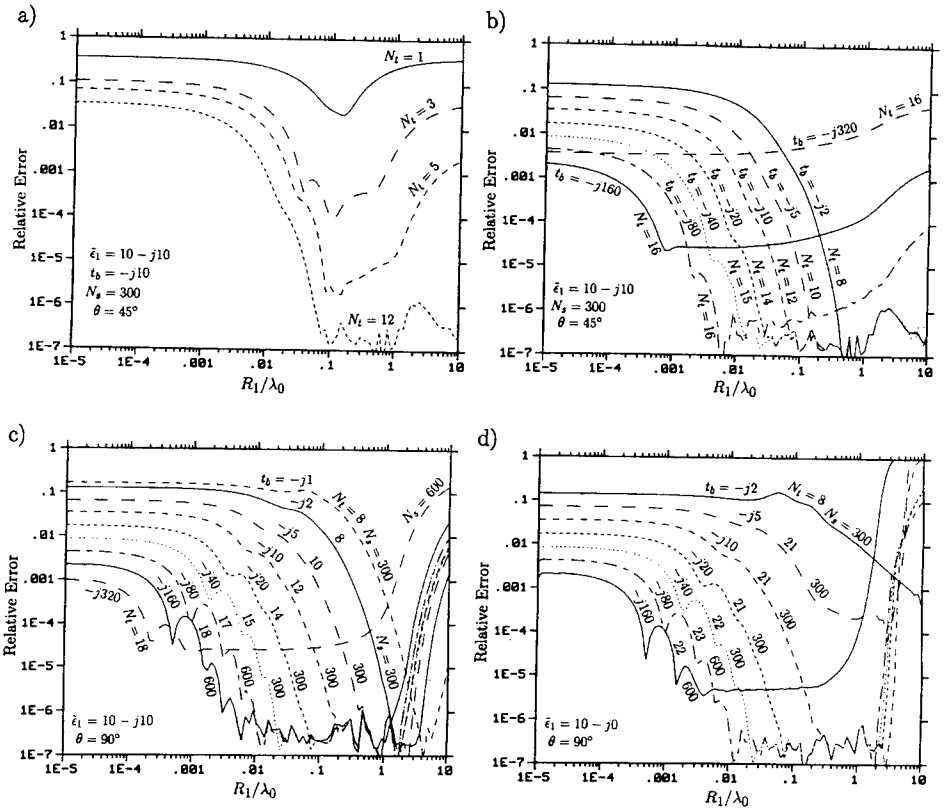

Fig. 3. Error in the discrete image approximation of v_{22} with N_t images and N_s samples. The ground permittivity is $\tilde{\epsilon} = \epsilon_1 - j\sigma/\omega\epsilon_0$ and $\theta = \tan^{-1}[\rho/(z + z')]$.

images, to $R_1/\lambda = 1.3$ with 10 images and to $R_1/\lambda = 3$ with 22 images. Beyond these distances the approximation diverged rapidly.

Figure 4 shows the relative error in approximating $\partial^2 v_{22}/\partial\rho^2$ for the E_ρ^H field component needed to model a horizontal wire over ground. The increased error over the approximation for v_{22} shows that the $1/R_1$ singularity in this second derivative is not contained in the discrete image approximation. When integrated over a filament of current, this $1/R_1$ term contributes to the log singularity in the field parallel to the filament, although the importance of it relative to the integral of the quasistatic image terms depends on the coefficients multiplying the terms. If necessary the approximations from equation (7), shown as curves A_1 and A_2 in figure 4, can be used to reduce the error.

A version of NEC-2 has been set up to use the discrete image approximation instead of interpolation for arbitrary wire structures above ground. As an initial test, a horizontal $\lambda/2$

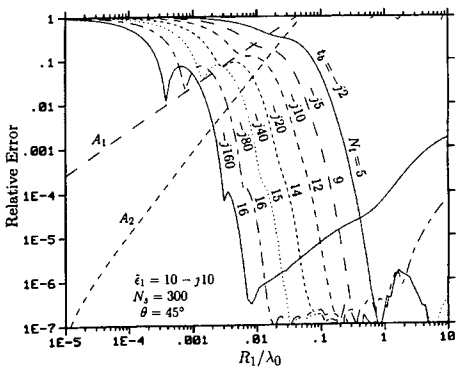

Fig. 4. Error in approximating $\partial^2 v_{22}/\partial\rho^2$ for varying contour limit t_b. Curves A_1 and A_2 are quasistatic approximations from equation (7) with the first term $(1/R_1)$ and all terms, respectively.

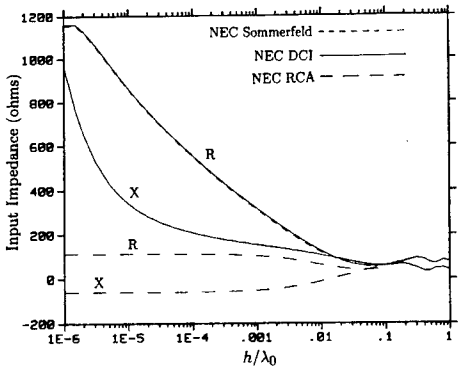

Fig. 5. Input impedance of a $\lambda_0/2$ dipole with radius $10^{-7}\lambda_0$ at height h above the ground, comparing results of NEC Sommerfeld/interpolation, discrete image (DCI) and Fresnel reflection coefficient (RCA).

dipole over ground was modeled, since it was expected to be a more difficult test than a vertical wire. Results with varying numbers of images, with and without the quasistatic approximation in equation (7), were in excellent agreement with the standard NEC-2. Figure 5 shows the result with one discrete image for u_{22} and zero discrete images for v_{22}, and the agreement is very good. With three images for each potential the noticeable difference between the curves essentially disappears. If the single discrete image for u_{22} is dropped, using only quasistatic terms, the error in impedance for small h/λ_0 is about twenty percent, and the wiggles between 0.1 and 1 in h/λ_0 are not tracked well. Hence it appears that for the horizontal $\lambda/2$ dipole close to the ground, the quasistatic images are most important, and a relatively crude approximation of the remainder is sufficient. Other structures, such as a long horizontal wire or top loaded monopole may put more demand on accuracy of the discrete image approximation and will be investigated in the future. The result of using the Fresnel plane-wave reflection coefficient is also shown in figure 5 and, as expected, is accurate for h/λ greater than about 0.1.

The CPU time for evaluating all field components in equation (6) by the discrete image method on a DEC 3000/400 computer was 89 μs with 3 images for each potential and 283 μs with 10 images. For comparison, the time for a single evaluation by the NEC–2 interpolation is 7.2 μs. The difference is mainly due to the number of complex exponentials that must be evaluated. The time to compute the parameters of the discrete image approximation is proportional to N_s^3, and ranged from 0.04 s with 50 samples to 58 s with 600 samples, while the time to generate the NEC–2 interpolation table was 1.3 s.

4. CONCLUSION

The discrete image approximation can provide a simple and accurate approximation for the field over ground for separations of image and evaluation points in the range of about 0.01 to several wavelengths. The limit for large distance is most restrictive along the interface where surface and lateral waves are significant, but asymptotic approximations can fill the gap to infinity.

Accuracy decreases for very small distances due to truncation of the approximation contour, but the errors become less significant relative to the quasistatic terms. The approximation contour and number of images can be adjusted to optimize the approximation for a given range of distances and accuracy. The discrete images provide a simple and highly compact representation for the field. The code to obtain the image parameters using the matrix pencil method was about 24,000 lines using the LAPAC routines, but simpler routines should be available.

The discrete image approximation can also be used when source and evaluation points are on opposite sides of the interface, but its usefulness seems much more limited since the image parameters must be recomputed for each new source location, or for each new evaluation point [10]. It still might be usable in a moment-method with efficient "bookkeeping" in filling the matrix.

References

[1] A.Sommerfeld, "Über die Ausbreitung der Wellen in der drahtlosen Telegraphie," *Ann. Physik*, Vol. 28, p. 665, 1909.

[2] A. Baños, *Dipole Radiation in the Presence of a Conducting Half-Space*, Pergamon Press, New York, 1966.

[3] K. A. Michalski, "On the efficient evaluation of integrals arising in the Sommerfeld halfspace problem," *IEE Proc.*, Vol. 132, Pt. H, No. 5, Aug. 1985.

[4] O. Koefoed, D. P. Gosh and G. J. Polman, "Computation of type curves for electromagnetic depth sounding with a horizontal transmitting coil by means of a digital linear filter," *Geophysical Prospecting*, Vol. 20, pp. 406-420, 1972.

[5] I. V. Lindell and E. Alanen, "Exact image theory for the Sommerfeld half-space problem — Pt. 1: Vertical magnetic dipole," *IEEE Trans.*, AP-32, pp. 126-132, 1984.

[6] G. J. Burke and A. J. Poggio, "Numerical Electromagnetics Code (NEC) – Method of Moments,", Lawrence Livermore National Laboratory Rept. UCID-18834, January 1981.

[7] J. N. Brittingham, E. K. Miller and J. T. Okada, *SOMINT: An Improved Model for Studying Conducting Objects Near Lossy Half-Spaces*, UCRL-52423, Lawrence Livermore National Laboratory, CA, February 24, 1978.

[8] R. J. Lytle and D. L. Lager, *Numerical Evaluation of Sommerfeld Integrals*, UCRL-51688, Lawrence Livermore National Laboratory, CA, October 23, 1974.

[9] G. J. Burke, *Numerical Electromagnetics Code – NEC-4*, UCRL-MA-109338, Lawrence Livermore National Laboratory, CA, January 1992.

[10] D. G. Fang, J. J. Yang and G. Y. Delisle, "Discrete image theory for horizontal electric dipoles in a multilayered medium," *IEE Proc.*, Vol. 135, Pt. H, No. 5, Oct. 1988.

[11] Y. L. Chow, J. J. Yang, D. G. Fang and G. E. Howard, "A Closed-Form Spatial Green's Function for the Thick Microstrip Substrate," *IEEE Trans. MTT*, Vol. 39, No. 3, March 1991.

[12] M. I. Aksun and R. Mitra, "Derivation of Closed-Form Green's Functions for a General Microstrip Geometry," *IEEE Trans. MTT*, Vol. 40, No. 11, Nov. 1992.

[13] R. M. Shubair and Y. L. Chow, "A Simple and Accurate Complex Image Interpretation of Vertical Antennas Present in Contiguous Dielectric Half-Spaces," *IEEE Trans. Ant. and Propag.*, Vol. 41, No. 6, June 1993.

[14] F. B. Hildebrand, *Introduction to Numerical Analysis*, McGraw Hill Co., New York, pp. 378-382, 1956.

[15] T. K. Sarkar and O. Pereira, "Using the Matrix Pencil Method to Estimate the Parameters of a Sum of Complex Exponentials," *IEEE Antennas and Propagation Magazine*, Vol. 37, No. 1, February 1995.

The Improvement of NEC-2's Out-of-Core Operation and the Analysis of UHF Monopole Antenna Mounted on a Car Model

Keiichi Natsuhara, Tamotsu Suda, Yasuhiro Kazama, Kazuhito Madono

Japan Radio Co.,Ltd.
5-1-1 Shimorenjaku, Mitaka-shi
Tokyo, Japan 181

1. Introduction

NEC-2 is the well known FORTRAN program for electromagnetic analysis based on the method of moment. Because the method is a low frequency method, as the electrical size of objects increases, the required computer's memory increases drastically, and the upper limit is set by the computer's memory size. NEC-2 has adopted an out-of-core technique in order to be applicable beyond the upper limit[1]. That is, the large impedance matrix can be stored to the hard disk instead of memory. However, the out-of-core operation is not efficient because it uses the several sequential-access files of which each size is equal to the matrix size as working space. It is known that this problem can be overcome by using single direct-access file[2], and the techniques has already been adopted in NEC-4[3]. Unfortunately, NEC-4 is still under the export control[4].

In this paper, we modified the out-of-core operation of NEC-2 to use a direct-access file based on the reference[2], and expanded their method into the symmetrical case and the Numerical Green's Function(NGF) option[1]. Using the modified NEC-2, the radiation patterns of the UHF band's monopole antenna mounted on a car model were computed. We have investigated the performance of the modified NEC-2 by comparing with the original NEC-2 and checked the accuracy by comparing with the radiation patterns using Uniform Geometrical Theory of Diffraction(UTD).

2. Modification

In order to expand the upper limit of NEC-2, we modified the out-of-core operation. Although NEC-2 becomes more efficient by the following modifications, the results by the modified NEC-2 are identical with those by the original NEC-2.

2-1 Out-of-core operation

(Original NEC-2)[1]

If the required storage volume of the impedance matrix [Z] is greater than what a computer's memory(core) can provide, NEC-2 stores [Z] to the sequential-access file 11 block by block in subroutine CMSET. The block size is such that two blocks will fit into the provided memory for Gauss elimination.

In subroutine FACIO, [Z] is factored to a lower and a upper triangular matrices by

using four sequential–access files(files 11 ,12 , 13, and 14), of which each size is equal to the given matrix size. This is because the sequential–access files only allow appending data blocks to the end of the file. File 11 is used to keep the original matrix, and file 12 is to store the final factorized matrix. Files 13 and 14 are used for intermediate process. If the matrix is divided into Nb blocks, the matrix is factored as follows. Firstly, two of the blocks(blocks 1 and m) are read from file 11 into the core memory. If the two blocks are adjacent, they are completely factored and stored to files 12 and 13. If not, the two blocks are partially factored and stored to file 13. These processes are repeated for m=2 ~ Nb. Secondly, for m=3 ~ Nb, two of the blocks (blocks 2 and m) are read from file 13, and according as the blocks are adjacent or not, they are completely or partially factored and stored to file 12 or 14. In later process, files 13 and 14 are swapped each other for each process and it is repeated until file 12 is filled with the completely factored matrix [Z].

Then, in subroutine LUNSCR, file 12 is unscrambled, and is written block by block in file 13 in ascending order and in file 14 in descending order for the forward and backward substitution in subroutine LTSOLV.

(Modified NEC–2)

In the out–of–core operation, the modified NEC–2 firstly opens the direct–access file 31 and stores [Z] to the file block by block in subroutine CMSET.

In subroutine FACIO, [Z] is factored block by block using only file 31 of which size is equal to the matrix size. The factored blocks are put back to the same file 31 to replace the original blocks, because the direct–access file can be read and written to the arbitrary blocks, directly. The factorization process is almost the same as the original NEC–2, except that the single direct–access file 31 is used in place of the four sequential–access files. The matrix is factored as follows. Two of the blocks (blocks n and m (n<m)) are read from file 31, and according as the blocks are adjacent or not, they are completely or partially factored using subroutine LFACTR and stored to the same file 31 to replace the original blocks. The same procedure is repeated for all combinations of n and m, and file 31 is filled with the completely factored [Z].

After the factorization, in LUNSCR subroutine, file 31 is unscrambled, but the rearrangement for the forward and backward substitution is not performed because the direct–access file 31 is also used in subroutine LTSOLV.

After all, only single direct–access file of which size is the same volume as the matrix size is required as working space, and the required disk volume is only a quarter of that of the original NEC–2[2].

2–2 Symmetrical Case

(Original NEC–2)[1]

If the number of symmetrical section of the object is K, the impedance matrix [Z] is replaced by the set of K submatrices which have been Fourier–transformed.

$$\overset{Np}{\longrightarrow}\quad Np\downarrow [Z_1][Z_2][Z_3]\cdots[Z_K] \tag{1}$$

For the out-of-core operation, subroutine CMSET stores the submatrices to file 11 block by block in the sequence as shown in left below, and then in subroutine FACTRS, the order is changed as shown in right below and stored to file 12.

column 1 of submatrix 1		column 1 of submatrix 1
column 1 of submatrix 2		column 2 of submatrix 1
:		:
column 1 of submatrix K	change →	column Np of submatrix 1
column 2 of submatrix 1		column 1 of submatrix 2
:		:
column 2 of submatrix K		column Np of submatrix 2
column 3 of submatrix 1		column 1 of submatrix 3
:		:
column Np of submatrix K		column Np of submatrix K

This change of the order requires reading through file 11, K times.
If the size of each submatrix is also greater than the provided core volume, file 12 is copied to file 11 without change, and then file 11 is factored using files 13 and 14 by the same way as section 2-1 for each submatrix and store to file 12.

The total process requires four sequential access files(11,12,13 and 14) of which each has the same volume as the sum of submatrices $[Z_1],[Z_2],[Z_3],\cdots,[Z_K]$, as well as the non-symmetrical case(section 2-1).

(Modified NEC-2)
In the out-of-core operation, subroutine CMSET stores the submatrices to the direct-access file 31 block by block in the same sequence as the original NEC-2. In subroutine FACTRS, the sequence in file 31 is changed into the following order.

block 1	column 1 of submatrix 1
	:
	column L of submatrix 1
	column 1 of submatrix 2
	:
	column L of submatrix 2
	:
	column L of submatrix K
block 2	column L+1 of submatrix 1
	:
	column 2L of submatrix 1
	column L+1 of submatrix 2
	:
	column 2L of submatrix K
	column 2L+1 of submatrix 1
	:

(L is the number of columns per submatrix per block)
The rearrangement of the columns are performed only in the block in order not to use another scratch files.

If the size of each submatrix is also greater than the provided core volume, the submatrices are factored one by one using modified subroutine FACIO and then solved using modified subroutine LTSOLV.

The hard disk volume required by the total process is the same size as the sum

of the submatrices and it is only a quarter of that of the original NEC−2.

2−3 NGF option[1]

The NGF option is the method to prevent the unnecessary repetition of matrix calculations, and is frequently used for such large structures that the out−of−core operation is needed.
In the case of the NGF option, the impedance matrix [Z] is divided into four matrices.

$$[Z]=\begin{bmatrix}[A] & [B]\\ [C] & [D]\end{bmatrix} \tag{2}$$

[A] is the impedance matrix for NGF object, [D] is that for NEW object, and [B],[C] are those for the mutual interaction between the two objects. At the first run, the matrix [A] is computed and factored, and then stored to the NGF file. At the subsequent run, [A] is read from the NGF file and [B],[C] and [D] are computed.

(original NEC−2)

At the first run, if the size of matrix [A] is greater than a half of the provided core volume, [A] is factored by using four sequential access files 11,12,13 and 14, and then stored block by block to file 13 in normal order and to file 14 in reverse order, as well as section 2−1. If the WG card is entered, the contents of the two files are copied to the NGF file 20 as shown below.

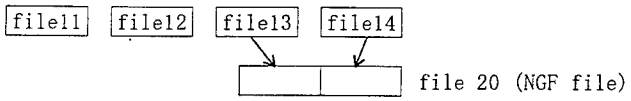

So the required hard disk volume is the 6 times as much as the size of [A].
At the subsequent run, file 20 is copied to file 13, and then [B],[C] and [D] are computed.

(modified NEC−2)

At the first run, if the size of matrix [A] is greater than a half of the provided core volume, [A] is factored and stored block by block to the direct−access file 31, as well as section 2−1. File 31 is not copied to NGF file regardless of entering of the WG card.
At the subsequent run, file 31 is used as the alternative file of file 13 in the original NEC−2. If [B],[C] and [D] can be factored in core memory, the total required hard disk volume is the same size as the matrix [A]. This volume is a 1/6 of that required for the original NEC−2 and a half of the core memory required for the in−core operation.

3. Performance Test of Modified NEC-2

3-1 Car Model and Computer

The radiation patterns of a quarter wave monopole antenna mounted on the center of the roof of a car model in Fig.1 were computed in order to verify the performance of the modified NEC-2.

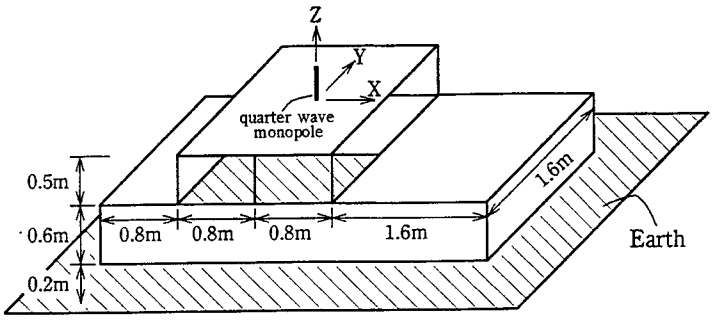

Fig.1 Monopole antenna mounted on a car model above earth

The effects of the earth were included using the Fresnel Reflection Coefficients[1]. The relative complex dielectric constant of the earth was set to $\varepsilon g = 10 - j0.1$. The windshields, the obstacles in the car, and the bottom plate of the car body were neglected.
The car was modeled by Wire-grid as shown in Fig.2.

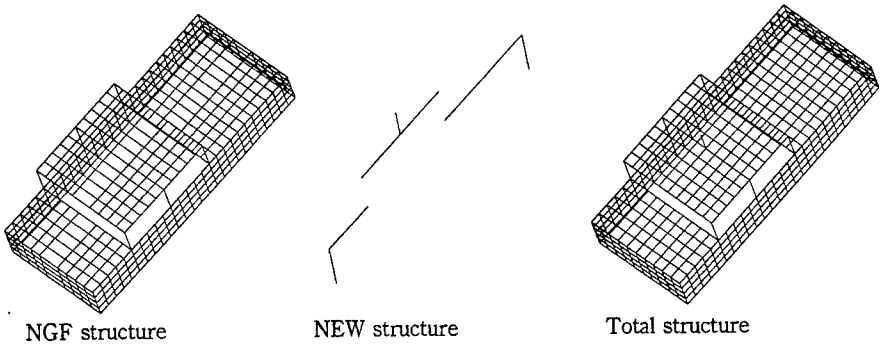

NGF structure NEW structure Total structure

Fig.2 The Wire-grid models for the car model in Fig.1

In order to make use of the symmetry of the car body about XZ-plane and the NGF option, the car model was composed of two structures(NGF structure and NEW structure) . At the first run, the matrix [A] for NGF structure is computed, factored, and stored to the direct-access file 31.

At the subsequent run, the matrices [B],[C] and [D] are computed, factored, and then the total matrix is solved. The all segments were set to about 0.1 wavelength in length and about 0.01 wavelength in radius to assure the numerical accuracy. We computed these structures using the following computer resources.

CPU: DEC−3000/900 (21064A/275MHz)
OS: openVMS/AXP Ver.6.1
Compiler: DEC−Fortran Ver.6.2
Physical Memory Quota: 25MByte
Virtual Memory Quota: 25MByte
} Total Memory Quota: 50MByte
Hard Disk Quota: 600MByte (SCSI drive)

The single precision version of NEC−2 was used. In PARAMETER statements in the NEC−2's source code, the maximum number of segments(MAXSEG) was set to 14,000, and the maximum matrix size which can be in core(MAXMAT) was set to 1,000. In the OPEN statement for the direct−access file 31, the record length was set to the maximum(8,190 long words) to minimize the number of file−access.

3−2 Examination of run−time and storage volume

The run−time and the storage volume for the Wire−grid model in Fig.2 were compared between the original and the modified NEC−2 as shown in Fig.3. Only the first run in the NGF option was computed for various frequencies(number of segments). The symmetry about XZ−plane and the out−of−core operation were used for both the original and the modified NEC−2. The run−time in Fig.3 was defined as the total clock time(elapsed time) to run a input file. To avoid the influence of the another user's situation in the computer, PRIORITY was set to be higher than the another users'.

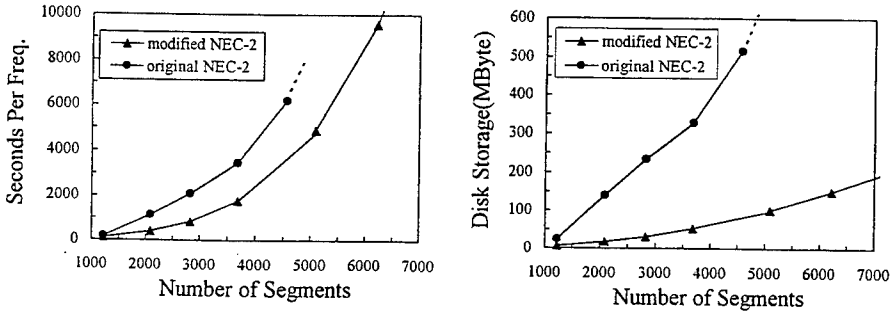

Fig.3 Comparison run−time and storage volume between original and modified NEC−2

The run−time of the modified NEC−2 was shorter than that of the original NEC−2 because the number of I/O operation is much less than that of the original NEC−2. The required disk

storage volume was about a 1/6 as written in section 2−3. In the case that the disk quota is 600MByte, the original NEC−2 could not compute over 4,700 segments, while the modified NEC−2 could compute until about 12,000 segments.

3−3 Comparison the radiation patterns with UTD results

The radiation patterns of the car model in Fig.1 were computed by the modified NEC−2 for various frequencies and compared with the calculated results by Uniform Geometrical Theory of Diffraction(UTD) as shown in Fig.4. In the UTD computation, the monopole antenna was divided into five small dipoles of which each current amplitude was determined assuming the cosine distribution. The car in Fig.1 was modeled by seven rectangular plates, and the window−pillars were neglected. The included rays were direct rays, reflected rays, diffracted rays, diffracted−reflected rays, diffracted−diffracted rays, and diffracted−diffracted−reflected rays. The effects of the earth were included by using the Fresnel Reflection Coefficients.

In Fig.4, the computed patterns by the modified NEC−2 appear in good agreement with the results by UTD. Although the discrepancy between two results is conspicuous in the YZ−plane pattern, this is assumed to be due to the neglect of the window−pillar's effect in UTD.

4. Conclusion

In this paper, NEC−2's out−of−core operation was modified in order to make use of the single direct−access file as working space. The required disk volume of the modified NEC−2 was about a 1/4 for non−NGF option and about a 1/6 for NGF option as much as the original NEC−2's. The run−time was also shorter than the original NEC−2's. Using the modified NEC−2, the radiation patterns of UHF band's monopole antenna mounted on a car model were computed and compared with UTD results. Both results showed good agreements in spite of over 10,000 segments.

References

[1] G.J.Burke and A.J.Poggio, "Numerical Electromagnetics Code(NEC)−methods of moments part 1,2, and 3," Naval Ocean Systems Center, San Diego, CA, NOSC TD 116, Jan. 1980.

[2] J.Peng, J.Choi, and C.A.Balanis,"Improvement of the NEC Code's Upper Limit and Pattern Prediction of a Helicopter Structure," IEEE AP−S Symposium Digest, vol.1, pp.56−59, June 28−July 2, 1993

[3]G.J.Burke, "NEC−MoM Update," ACES Newsletter, vol.7, no.2, pp.31−37, July 1992

[4]G.J.Burke, "MODELER'S NOTES," ACES Newsletter, vol.10, no.1, pp.15−20,March 1995

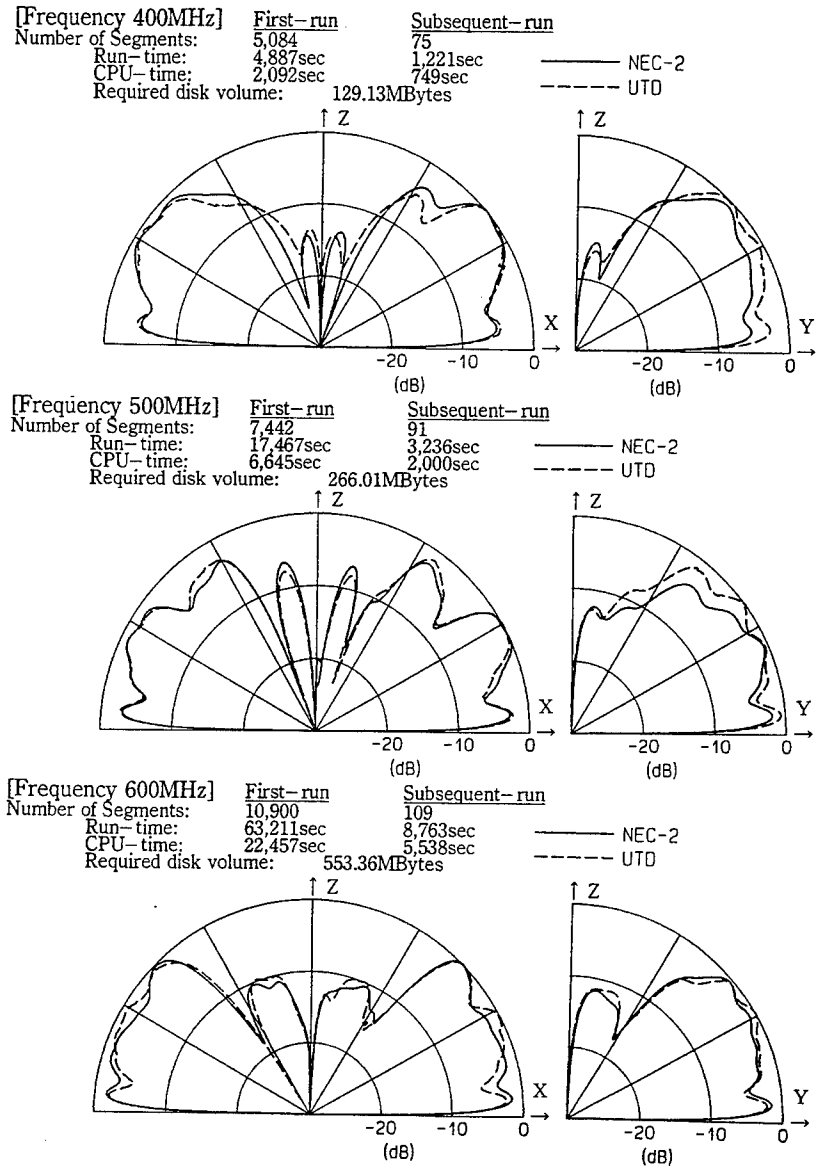

Fig.4 Radiation patterns of monopole antenna mounted on a car model

MatNEC: A Matlab Based Graphical Interface to SuperNEC

Richard M. Cooper
rcooper@bobcat.ent.ohiou.edu
Department of Electrical Engineering
University of The Witwatersrand, Johannesburg, South Africa

Abstract

This paper introduces a tool for creating a standard ascii text based NEC input file. MatNEC is a menu driven graphical program built from the popular graphical analysis package of Matlab. MatNEC uses the powerful graphical capabilities of the Matlab package to allow for a real time on screen development of a valid electromagnetic model for subsequent analysis by a NEC computational engine. To achieve complete independence from any computational engine, MatNEC creates a standard text file that can subsequently be used as an input file to a NEC program. SuperNEC is an enhanced version of NEC-2 based on an object orientated design which is being developed in conjunction with MatNEC at Wits University. SuperNEC maintains backward compatibility with NEC2.

1. Background

There are currently many programs available that serve as development tools for a NEC simulation. An extensive collection of these programs can be obtained via ftp transfer from the internet site ftp.netcom.com under the /pub/ra/rander/NEC directory. Functionally, these programs offer such features as model generation tools and output display tools. Examples of the appearance of some of these tools are shown below in figures 1 and 2. In general, these programs are all strong in their specific bailiwick and prove very useful. However, the limitation of these programs is in their

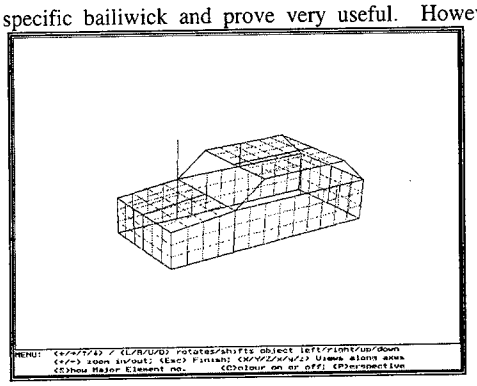

Figure 1: a model from the WIREGRID program

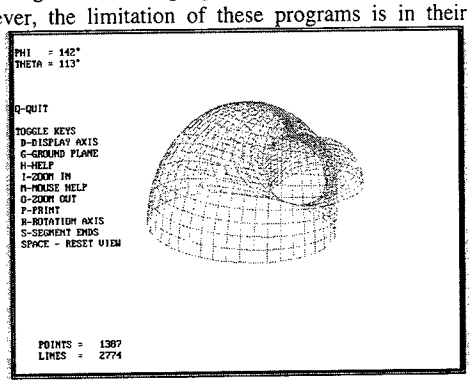

Figure 2: pattern from the NEC-WIN program

versatility and flexibility. These programs are available as executables and the user has few options if they want to add another feature to the program. If source code is available, it must first be understood, modified and recompiled to effect any changes. The advantage of building a tool from the matlab environment is that any user with a moderate amount of experience with matlab may either

modify the source script m-files or create a new script m-file to operate on the variables in the workspace to create a new feature or function of MatNEC. The interactive interpreter nature of matlab eliminates extensive recompiling and debugging and affords an open flexible workspace environment for future data analysis and interface growth. Once a variable is defined in the matlab workspace, it may be manipulated and/or displayed via any of the many built in matlab functions, a MatNEC function or a user defined function.

2. Design of MatNEC

The entire implementation of MatNEC uses version 4.2c.1 of matlab and has been both developed and tested on unix, windows3.1 and win95 operating systems. MatNEC is comprised of two main units: a preprocessor and a postprocessor. The preprocessor is used to build the actual electromagnetic model and define all the appropriate variables such as operating frequency, ground parameters and excitation. The postprocessor is designed to accept a standard ascii text NEC output file and extract all the data into the matlab workspace for subsequent display and processing. Presently, the postprocessor is not yet completed. Once fully implemented, the postprocessor will offer such features as radiation pattern display in 2 or 3 dimensions and graphing of the various model parameters such as impedance and efficiency.

2.1. Model Construction with the Preprocessor

The initial appearance of the preprocessor is shown in figure 3. As can be seen, the preprocessor is comprised of and controlled by a series of matlab windows and control widgets such as pull down menus, slider bars and pushbuttons. The main window is labeled as the modeling workspace and is where the actual electromagnetic model is developed and displayed in real time. As the model is defined, the electromagnetic structure is shown in the modeling workspace. A smaller matlab window shown in the lower left of figure 3 contains a preview tool for controlling the viewpoint and perspective of the modeling workspace. It is noted here that a portion of the source script for the preview tool has been scavenged from the public domain archives of the mathworks ftp repository. The small matlab window in the lower right of figure 3 contains pushbuttons and popups to control several special functions and miscellaneous variables. Across the top of the modeling workspace is a series of pulldown menus which are used to launch most of the functions that generate and define the model. The matlab

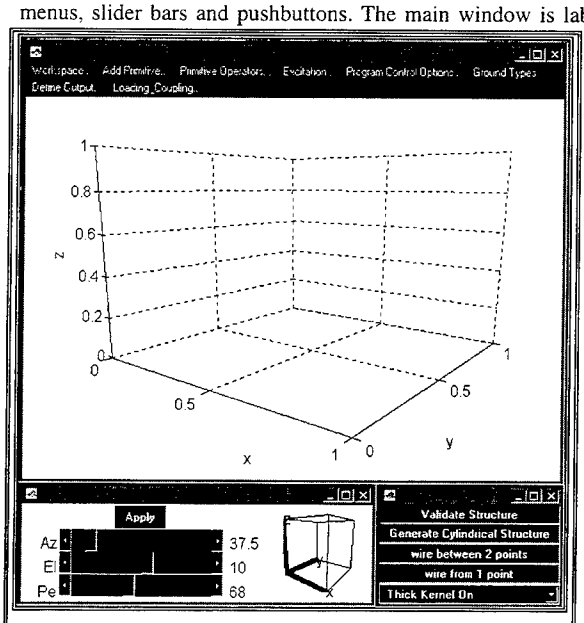

Figure 3 : the initial apearance of the preprocessor

command window is not shown in figure 3 but is used in the preprocessor. A combination of mouse clicking on the model and command line prompting is used to gather data for the model.

2.1.1. Electromagnetic Primitives

The construction of an electromagnetic model with the MatNEC preprocessor centers around the concept of an electromagnetic primitive. All models are composed of one or more electromagnetic primitives. By far, the most common electromagnetic primitive is the straight wire segment. NEC2 introduced 2 additional modeling primitives: the arc and the helix. MatNEC generalizes this concept by using the low level line features of the matlab graphics engine to allow any structure that can be defined in a specific script m-file to be an electromagnetic modeling primitive. Any structure whose features can be exhaustively defined in a single m-file in a specific location will automatically be incorporated into the MatNEC preprocessor and offered as a choice as one of the building blocks that can be used in the construction of the electromagnetic model. Aside from the primitives previously mentioned, MatNEC currently offers a finite wire mesh of variable density as a modeling primitive. The source m-files that govern the various electromagnetic primitives are designed to a adhere to a standard format. If a MatNEC user can follow the primitive format when designing a new modeling primitive, they can then add that function to their preprocessor for future use. This open ended design will hopefully encourage the formation of a public domain library of primitive functions as more and more users create and share their custom made primitives.

2.1.2. Menu Options in the Modeling Workspace

Figure 4 shows a collage of the various menus and sub-menus that can be accessed in the Modeling Workspace window of the preprocessor.

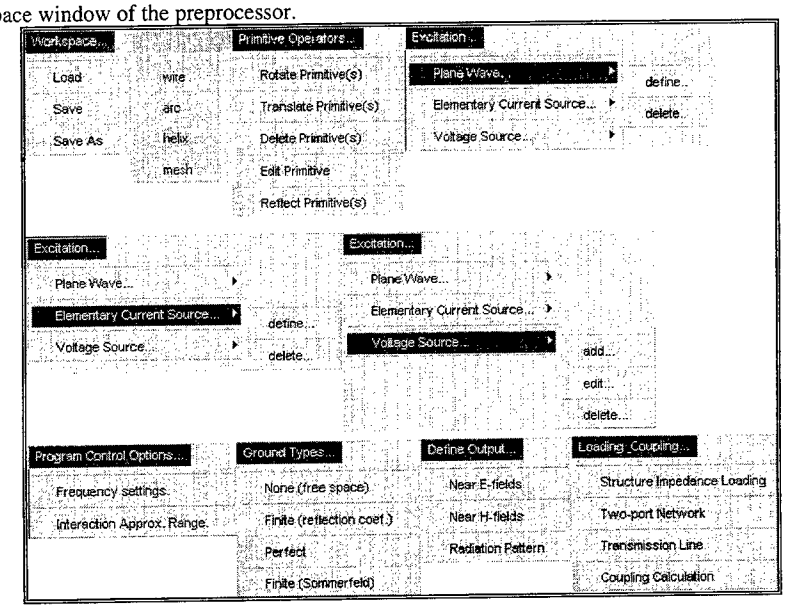

Figure 4 : a collage of all menu options of the modeling workspace

- The **Workspace** menu enables the user to construct a model over multiple sessions by allowing them to save a present model or load a previous model.
- The **Add Primitive** menu is the initial starting point for all new models. This menu is used to spawn a new primitive of the desired type. As can be seen, there are four primitives currently available: the wire, arc, helix and mesh.
- The **Primitive Operators** menu is used to launch a function that will perform some type of operation on a selection of primitives such as rotation or translation/duplication.
- The **Excitation** submenus allow the selection and definition of any of the three primary source types.
- The **Program Control Options** menu controls frequency and interaction approximation settings.
- The **Ground Types** menu sets the type of ground that is used in the model.
- The **Define Output** menu allows the user to set the parameters of the desired output.
- The **Loading and Coupling** menu allows the user to load the model or create two port networks on the model.

2.1.3. An Example Model

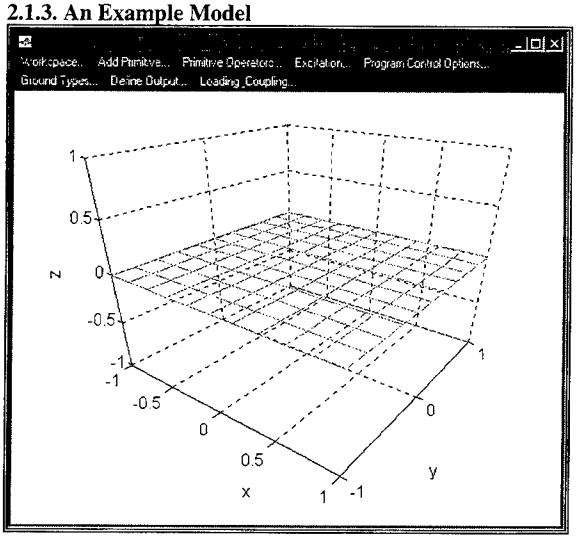

Figure 5 : an new model with a single mesh primitive

A simple model will be constructed to illustrate some of the features and overall feel of the preprocessor. Figure 5 shows a new modeling workspace into which a mesh primitive has been spawned. The mesh is defined with a 10 by 10 density. These density features can be modified at any time with the edit primitive option of the primitive operators menu. Now, a wire primitive will be added by using one of the special functions options. Since the wire segment is essentially the elmers glue of all NEC models and is used more frequently than other primitives, a few special routines have been created to speed model construction. The wire from one point function lets one end point of a wire primitive be defined by attaching it to a junction point of an existing primitive. Figure 6 shows the nature of this function. The existing primitive is first selected by mouse clicking. In this case, the mesh primitive was selected. The function then highlights all the junction points of the selected primitive. The desired junction point which will be one of the endpoints of the wire primitive is then selected by mouse clicking on it. Figure 7 shows the model with the new wire after the other end has been defined by text prompting in the command window. The special function of wire between 2 points is similar to the wire from one point function except both ends of the wire primitive are attached to the junction points of existing primitives. This new wire primitive will now be translated and duplicated. The translate primitives option of the Primitive Operators menu

prompts the user to select one or more primitives to translate and/or duplicate. Figure 8 shows the model once the wire primitive has been selected and duplicated along the y axis of the mesh primitive.

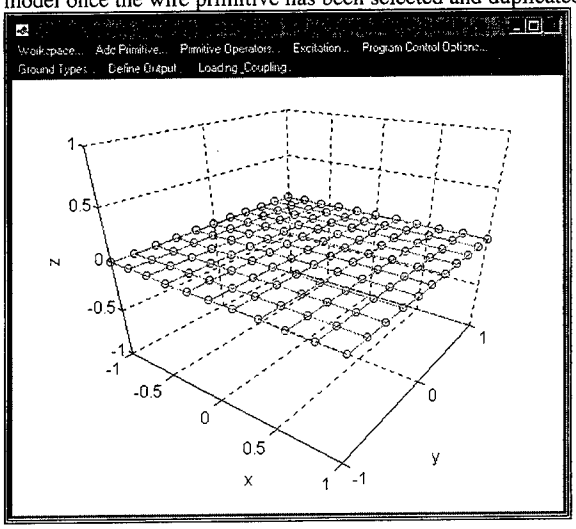

Figure 6 : mesh primitive with junction points shown as per the wire from 1 point special function

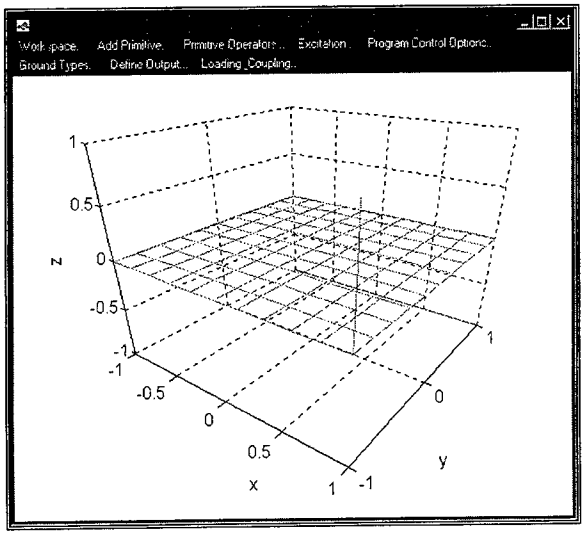

Figure 7 : model with wire primitive added

This new array of wire primitives is then selected for duplication on the other y axis of the mesh primitive as shown in figure 9. The GW cards generated by the preprocessor for the model shown in figure 9 are listed in figure 10. Approximately 5 minutes were needed to create this simple example model.

3. Limitations

The price paid for a memory intensive package such as matlab is speed of operation. Since MatNEC is layered on top of matlab, it also suffers from this lag as the model size grows and the complexity of the operations increases. Every attempt has been made to vectorize the source scripts to boost the performance speed as much as possible. The very nature of the problem makes this difficult though since the size of the model is not known beforehand. The inexorable advance of computer hardware and speed will alleviate this problem to a certain degree but will probably never allow for the speed of an executable type of tool.

Another obvious limitation is the need to either own or have access of a proper version of matlab in which to run MatNEC. As personal experience shows, matlab enjoys a fairly widespread distribution and popularity so this is not likely to be a severely limiting problem for most users.

4. Availability

The source script for MatNEC will be posted to the matlab public domain repository at the mathworks internet site once the remaining design is

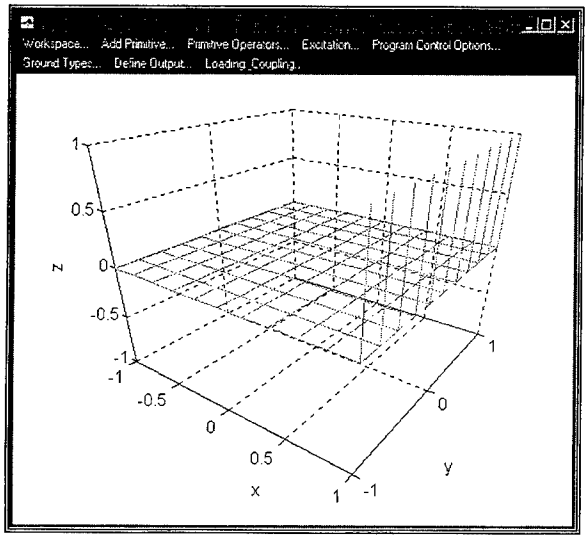

Figure 8 : model with initial wire primitive duplicated along the y-axis of the mesh primitive

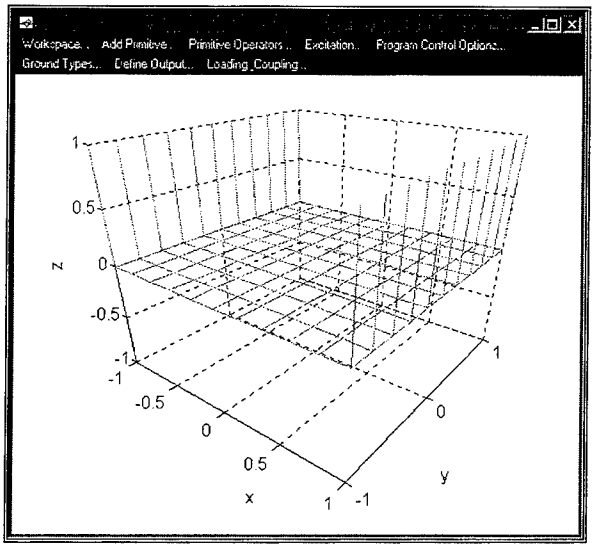

Figure 9 : model with verticle wire array duplicated to the oposite side of the mesh primitive

fully implemented.

5: Future Work

The postprocessor is not yet fully designed so that it can extract all possible data from a NEC output file. Also, some of the more computationally intensive sections of MatNEC may be rewritten as an executable mex interface file to matlab. This would greatly increase the operational speed of the interface.

Plans are also laid to include canonical GTD scattering objects so the interface can be used with the BSC member of the NEC family.

```
GW 0  10  -1.000  -1.000  0.000  1.000  -1.000  0.000  0.001
GW 0  10  -1.000  -0.800  0.000  1.000  -0.800  0.000  0.001
GW 0  10  -1.000  -0.600  0.000  1.000  -0.600  0.000  0.001
GW 0  10  -1.000  -0.400  0.000  1.000  -0.400  0.000  0.001
GW 0  10  -1.000  -0.200  0.000  1.000  -0.200  0.000  0.001
GW 0  10  -1.000   0.000  0.000  1.000   0.000  0.000  0.001
GW 0  10  -1.000   0.200  0.000  1.000   0.200  0.000  0.001
GW 0  10  -1.000   0.400  0.000  1.000   0.400  0.000  0.001
GW 0  10  -1.000   0.600  0.000  1.000   0.600  0.000  0.001
GW 0  10  -1.000   0.800  0.000  1.000   0.800  0.000  0.001
GW 0  10  -1.000   1.000  0.000  1.000   1.000  0.000  0.001
GW 1  10   1.000  -1.000  0.000  1.000   1.000  0.000  0.001
GW 0  10   0.800  -1.000  0.000  0.800   1.000  0.000  0.001
GW 0  10   0.600  -1.000  0.000  0.600   1.000  0.000  0.001
GW 0  10   0.400  -1.000  0.000  0.400   1.000  0.000  0.001
GW 0  10   0.200  -1.000  0.000  0.200   1.000  0.000  0.001
GW 0  10   0.000  -1.000  0.000  0.000   1.000  0.000  0.001
GW 0  10  -0.200  -1.000  0.000 -0.200   1.000  0.000  0.001
GW 0  10  -0.400  -1.000  0.000 -0.400   1.000  0.000  0.001
GW 0  10  -0.600  -1.000  0.000 -0.600   1.000  0.000  0.001
GW 0  10  -0.800  -1.000  0.000 -0.800   1.000  0.000  0.001
GW 0  10  -1.000  -1.000  0.000 -1.000   1.000  0.000  0.001
GW 0   1   1.000  -1.000  0.000  1.000  -1.000  1.000  0.001
GW 0   1   1.000  -0.800  0.000  1.000  -0.800  1.000  0.001
GW 0   1   1.000  -0.600  0.000  1.000  -0.600  1.000  0.001
GW 0   1   1.000  -0.400  0.000  1.000  -0.400  1.000  0.001
GW 0   1   1.000  -0.200  0.000  1.000  -0.200  1.000  0.001
GW 0   1   1.000   0.000  0.000  1.000   0.000  1.000  0.001
GW 0   1   1.000   0.200  0.000  1.000   0.200  1.000  0.001
GW 0   1   1.000   0.400  0.000  1.000   0.400  1.000  0.001
GW 0   1   1.000   0.600  0.000  1.000   0.600  1.000  0.001
GW 0   1   1.000   1.000  0.000  1.000   1.000  1.000  0.001
GW 0   1   1.000   0.800  0.000  1.000   0.800  1.000  0.001
GW 0   1  -1.000  -1.000  0.000 -1.000  -1.000  1.000  0.001
GW 0   1  -1.000  -0.800  0.000 -1.000  -0.800  1.000  0.001
GW 0   1  -1.000  -0.600  0.000 -1.000  -0.600  1.000  0.001
GW 0   1  -1.000  -0.400  0.000 -1.000  -0.400  1.000  0.001
GW 0   1  -1.000  -0.200  0.000 -1.000  -0.200  1.000  0.001
GW 0   1  -1.000   0.000  0.000 -1.000   0.000  1.000  0.001
GW 0   1  -1.000   0.200  0.000 -1.000   0.200  1.000  0.001
GW 0   1  -1.000   0.400  0.000 -1.000   0.400  1.000  0.001
GW 0   1  -1.000   0.600  0.000 -1.000   0.600  1.000  0.001
GW 0   1  -1.000   0.800  0.000 -1.000   0.800  1.000  0.001
GW 0   1  -1.000   1.000  0.000 -1.000   1.000  1.000  0.001
```

Figure 10: The GW cards for the sample model shown in figure 9

SESSION 12:

VALIDATION

Chair: D. Pflug

First and Second Generation Transformable Scale Aircraft-Like Models for Code Validation: Present Results and Future Plans

Donald R. Pflug, Timothy W. Blocher, Daniel E. Warren and David O. Ross
Rome Laboratory/ERST
525 Brooks Road
Rome, NY 13441-4505
e-mail: pflugd@ers.rl.af.mil

INTRODUCTION

Validation is a continuous ongoing problem for any computational electromagnetics (CEM) simulation code and is particularly difficult for large scale simulations consisting of numerous code modules, program paths and options. Differences between computed and measured results are very difficult to relate quantitatively, or even qualitatively, to specific shortcomings or limitations within the code. It is essential that the range of validity of a simulation be known as accurately as possible in order for the code to be useful for the analysis and design of systems.

For the past two years as part of an in-house CEM research program Rome Laboratory (Rome, NY) constructed and performed measurements on a novel test article, the Transformable Scale Aircraft-Like Model (TSAM), to serve as a CEM code validation tool for the antenna radiation problem.[1,2]. This **first generation** TSAM consists of an all-metal aircraft-like platform resembling a wide-bodied aircraft on which are mounted a set of six simple monopole antennas. The antennas were located on the fuselage structure, three on top and three on the bottom. The primary objective of TSAM is to study the effects of an aircraft-like platform on the patterns and the isolation of the mounted antennas. TSAM was designed to be modular with all components (including antennas) removable and replaceable at will (transformable). As a result measurements can be made on a variety of intermediate structural and antenna configurations instead of having to rely on just one static configuration. Initially, TSAM has been designed to accurately reflect the geometry modeling capabilities of a number of CEM codes and, as a result, it holds great promise for allowing algorithm and modeling limitations embedded within a CEM code to be estimated using measurements on the TSAM as a guide. The code then can be adjusted as necessary to achieve a given level of code simulation accuracy. TSAM was designed primarily to study platform effects on the radiation pattern of a co-located antenna (radiation problem) but also can be used to study antenna and platform radar cross sections.

A large number of antenna measurements have been performed on a number of first generation TSAM configurations ranging from a fuselage-only structure to the full-up test article that includes wings, horizontal and vertical stabilizers, and four engine nacelles with pylons. Principal plane pattern cuts were

measured for all six antennas at 4.5, 6 and 8 GHz. Antenna isolation data has been measured for frequencies in the interval 4-8 GHz. A representative set of TSAM antenna isolation measured results can be found in [2].

In this paper, an overview of the first generation TSAM is given and a representative set of antenna pattern results are reported. These results are compared to computations using the General Electromagnetic Model for the Analysis of Complex Systems (GEMACS) computer code. To illustrate the effects of platform complexity, measured principal plane patterns at a fixed frequency are compared to corresponding patterns computed using the GEMACS code for a fuselage-only TSAM configuration. A corresponding set of measured and computed TSAM patterns at the same frequency then are compared for the fuselage-plus-wings configuration. Finally, current plans at Rome Laboratory are described and discussed for designing and building a **second generation** TSAM. These plans represent a combination of current thinking at Rome Laboratory plus suggestions received from a limited number of members of the CEM community.

THE FIRST GENERATION TSAM

The first generation TSAM design conforms roughly to a 1/20 scale model of a wide-bodied aircraft. and consists of modular aluminum components fabricated into canonic shapes to represent wings, fuselage, stabilizers, engines and pylons. This design is shown in Figure 1. The fuselage is a hollow elliptical cylinder approximately 93 inches long with diameters 8.5 and 7.5 inches respectively. The cylinder is capped at both ends forming a blunt nose and tapered end. Two thin flat plates serve as wings with rectangular aluminum supporting plates underneath to maintain wings rigidity. The wingspread is 76 inches. Three thin flat plates form the horizonal and vertical stabilizers. Four capped circular cylinder structures represent the engines and are attached to the wing structures by four thin plates acting as pylons. All components are hinged and individually removable. Each component geometry can be modeled accurately and the metallic structure is assumed perfectly conducting. The thin plates serving as wings are hinged in order to vary the wing cant. Fuselage rigidity is maintained by an I-beam positioned inside the cylinder.

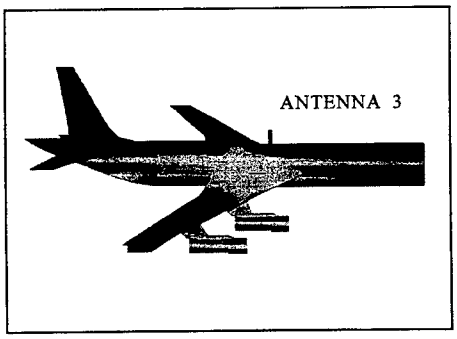

Figure 1. First Generation TSAM Configuration

Six thin wire monopole antennas are mounted on the TSAM cylindrical fuselage structure, three located on top and three on the bottom. Antenna #3 is shown in Figure 1. Because each antenna is 15 mm long, antenna #3 is not shown to scale.

The novelty of the first generation TSAM concept lies in making measurements on a scale aircraft-like model that is a duplicate, in both form and substance, of the model in the code. Differences between measured and computed results then are attributable to algorithm error since measured and computed geometry models coincide. These differences now can point to specific modules within a given CEM code where the overall CEM algorithm validity limits now are known from measurements. Currently TSAM is composed of components and antennas having a canonic shape and structure that were chosen for modeling convenience. Detail and complexity in shape and materials are to be added incrementally to allow an assessment to be made of the impact of each change on antenna performance

FIRST GENERATION TSAM ANTENNA PATTERN MEASUREMENTS

All antenna pattern measurements were performed in the large anechoic chamber located in the Rome Laboratory Electromagnetic Environmental Effects Research Center. These facilities have been described in detail elsewhere [2]. TSAM principal plane (roll, pitch and azimuth) patterns have been measured for all six antennas at 4.5, 6 and 8 GHz. for a large number of TSAM configurations. Electromagnetic and geometry models for a selected number of TSAM configurations have been constructed using the GEMACS code and the computed results compared to the corresponding measured data. GEMACS models for other TSAM configurations are currently being developed. Consequently, the patterns reported here will be just for antenna #3 at 6 GHz. (see Figure 1) located first on the fuselage-only configuration and then on the fuselage-with-wings configuration.

The principal plane roll, pitch and azimuth pattern cuts for antenna #3 on the fuselage-only configuration are shown below in Figures 2-4. A TSAM profile also is included within each figure to better define each pattern cut. The thick solid line shows the measured pattern while the thin solid line is the GEMACS computed pattern. Note that a complete GEMACS pattern is shown while measured patterns that are shown here extend to just below the wings.

The measured roll pattern is very smooth although is slightly asymmetrical in keeping with the small asymmetries that are present on TSAM. The pitch and azimuth measured patterns have a well defined global structure but considerable scalloping is present, especially on the pitch pattern. These effects represent diffraction at the cylinder end caps. The GEMACS computed patterns follow the overall shape of the measured patterns but can deviate considerably in selected regions. The roll pattern main lobes contain spikes, which are probably numerical in origin, and is more symmetric which probably indicates modeling limitations. The scalloping in the measured pitch pattern is reproduced only slightly by GEMACS while the GEMACS azimuth pattern contains numerous spikes. The GEMACS roll and pitch cuts also deviate significantly from the measured patterns under the fuselage.

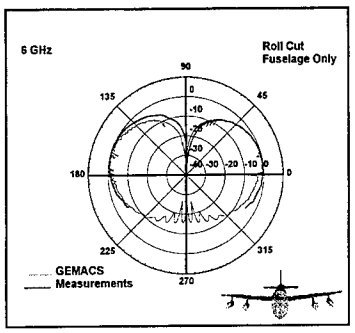

Figure 2. Roll Cut for Antenna #3
Fuselage Only

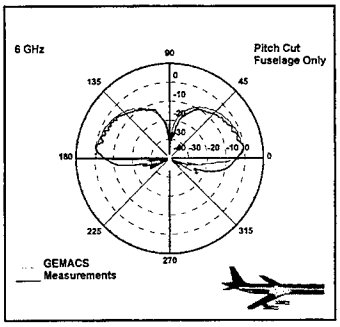

Figure 3. Pitch Cut for Antenna #3
Fuselage Only

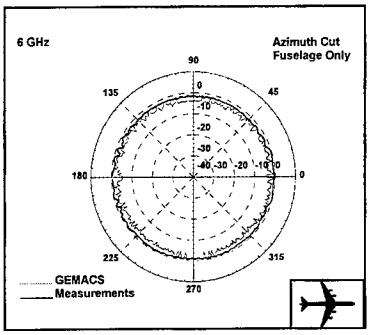

Figure 4. Azimuth Cut for Antenna #3
Fuselage Only

The measured roll pattern is very smooth although is slightly asymmetrical in keeping with the small asymmetries that are present on TSAM. The pitch and azimuth measured patterns have a well defined global structure but considerable scalloping is present, especially on the pitch pattern. These effects represent diffraction at the cylinder end caps. The GEMACS computed patterns follow the overall shape of the measured patterns but can deviate considerably in selected regions. The roll pattern main lobes contain spikes, which are probably numerical in origin, and is more symmetric which probably indicates modeling limitations. The scalloping in the measured pitch pattern is reproduced only slightly by GEMACS while the GEMACS azimuth pattern contains numerous spikes. The GEMACS roll and pitch

cuts also deviate significantly from the measured patterns under the fuselage.

The changes that occur in the antenna patterns when wings are added to the TSAM configuration are shown in Figures 5-7. The wings are flat and parallel to the azimuth plane. The most significant changes are in the measured roll pattern in Figure 5 where a complex lobbing structure exists. This was expected since antenna #3 is located over the wings.

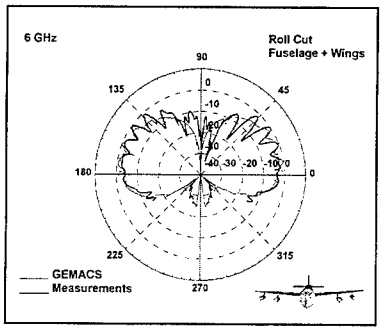

Figure 5. Roll Cut for Antenna #3 Fuselage with Wings

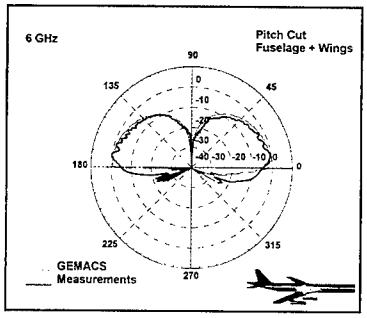

Figure 6. Pitch Cut for Antenna #3 Fuselage with Wings

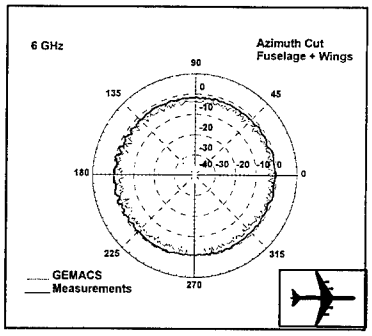

Figure 7. Azimuth Cut for Antenna #3 Fuselage with Wings

The lobbing is far less pronounced in the GEMACS roll pattern where only the overall pattern structure

is followed. This difference in measured and computed results appears to indicate a problem in the GEMACS electromagnetic model. Validation studies currently are underway to explain and resolve these results. The pitch and azimuth patterns in Figures 5 and 6 are very similar to the corresponding patterns for the fuselage-only configuration for both measurements and simulation.

THE SECOND GENERATION TSAM

A second generation TSAM design currently is being carried out by Rome Laboratory. Such a design, in its present form, represents experience and lessons learned by Rome Laboratory from the original TSAM as well as commentary from selected members of the CEM community. It is felt that wide community input is essential if TSAM is to serve its purpose well as an antenna/platform benchmark. The next TSAM will have more realistically shaped components and retain the transformability property that is essential to understanding the complex antenna platform electromagnetic environment. A wider range of frequency measurements are contemplated to encompass low as well as high frequency methods. Also many different antenna types will be mounted on TSAM and other antenna properties besides the pattern and isolation will be measured. The current thinking on the new TSAM design is summarized in the following paragraphs.

Fuselage: A new fuselage will be constructed for the next TSAM whose design will be determined by a combination of realism, additional structural stability and the need to maximize internal space. Two modular antenna panels will be provided along the side, one being forward of the left wing and the other aft near the tail structure. The antenna panels will be designed with interfaces that will permit easy integration onto the fuselage surface and easy removal and replacement with other antenna panels or with just a fuselage panel. Provision also will be made to attach antennas on top and on the bottom of the fuselage. The antennas will consist of both individual elements (such as the thin-wire monopoles from the first generation TSAM or microstrip or cavity-backed patches) or arrays of elements in a conformal or billboard design. The wing attachment slots will be integrated into the structure and will permit the attachment of a variety of wing shapes. Wing dihedral angle motion will be restricted to a few angles only. A set of nose and tail bulkheads of varying shape and apertures will be provided for a variety of experiments. Internal bulkheads will be equipped with fixed RF feedthroughs and the body will contain RF cabling. All apertures (holes, panels, wing slots) will be tightly sealed against RF. Current overall shapes under consideration range from cylindrical shapes to a real fuselage with a doubly curved surface.

Wings and Tail Structure: Several sets of wing shapes are under consideration. A very thin wing shape will be included similar to the flat plate design of the original TSAM but possibly with curvature. Thin structures with near singularities along the edges will stress CEM codes. Other wing designs include various 3D structures, including a wing with a triangular taper and one with a smooth taper. Provision will be made for mounting antenna structures on the top and bottom of the wings near the forward and trailing edges. These antenna panels will have the same ease of placement and removal as the panels on the fuselage. Such antenna placement will demonstrate near field edge diffraction effects. Also under consideration is the use of nonmetallic panels on the wings in place of the antennas. The tail structure will be designed along the same lines as the wings.

Engine Nacelles and Pylons: Engine pylons will be designed similarly to the wings. The nacelles will

be either cylindrical structures or possibly real nacelle shapes. The nacelles will have removable caps front and back. Consideration also is being given to designing a nacelle with significant internal engine structure for the future.

Materials: The most probable material to be used will be highly conducting metal for the fuselage and possibly a substrate coated with metal for the non loadbearing structures. As noted above nonmetallic panels which can replace metal panels are under consideration as are dielectric metals coated metals.

Antennas and Sources: It is planned that the new TSAM will accomodate a variety of antenna structures. The antenna panels proposed for the wings and fuselage will be designed to interface simply to the TSAM structure thus permitting easy manufacture of antenna panels. Both individual antenna elements and arrays are planned. Individual elements include simple monopoles, rectangular and circular patches and cavities and tapered slots. Arrays will have both a conformal and billboard design and will be constructed on the standard antenna panels. Antenna properties of interest include the pattern, input impedance and the active scan impedance for arrays. In addition, the use of arrays can demonstrate scanning technology and experiment with beamforming algorithms to cancel platform scattering. To determine antenna properties accurately, especially the imaginary part of the antenna input impedance, the feed structure must be designed in such a way as to allow accurate feed modeling.

CONCLUSIONS:

A unique test article, TSAM, that appears to hold great promise for the validation of complex computational electromagnetics (CEM) codes has been described. A set of measured principal plane radiation patterns has been reported at 6 GHz for one of the three antennas mounted on the TSAM upper fuselage for two configurations; fuselage-only and fuselage with wings. These results were compared to computed results from the GEMACS code. Computations followed measurements overall but differed in detail by as much as 4 dB in isolated regions of the pattern. The most significant difference was in the roll pattern results with and without wings. Measurements showed a considerable difference in these two cases but computations showed a much smaller difference. The reasons for this unexpected result currently are under investigation. These findings illustrate the critical role that carefully controlled measurements can play in validating complex simulation software.

The next generation TSAM being planned by Rome Laboratory was described in some detail and represents a significant advance over the original TSAM, especially in surface geometry and the antennas to be mounted. The new TSAM design is still in its formative stages and suggestions from the CEM community on how such a test article should be designed to be of maximum benefit are eagerly sought.

REFERENCES:

1. Pflug, D.R. and Warren, D.E. 1994. "Transformable Scale Aircraft Model for the Validation of Computational Electromagnetics Models and Algorithms" in *10th Annual Review of Progress in Applied Computational Electromagnetics, (*Monterey, CA, March 21-26). ACES, 352-359.

2. Pflug, D.R. and Warren, D.E. 1995. "Transformable Scale Aircraft Model for the Validation of Computational Electromagnetics Models and Algorithms: Initial Configuration and Results" in *11th Annual Review of Progress of Applied Computational Electromagnetics* (Monterey, CA, March 20-25). ACES, 268-275.

Software for Modeling Helix Antennas with NEC and Validation by Measurement

C.W. Trueman* N. Sultan† S.J. Kubina* T. Pellerin†

* Electromagnetic Compatibility Laboratory
Concordia University
Montreal, Quebec, Canada

† Space Systems Directorate
Canadian Space Agency
St-Hubert, Quebec, Canada

Abstract

This paper presents a package of software for creating a wire-grid model of a helix antenna and its ground cup for analysis using the "Numerical Electromagnetics Code"(NEC). The package consist of rogram HELIX which provides the user with menus for entering the design of a helix antenna of up to 30 sections, each with its own length, pitch and taper, permitting a very general class of helix antennas to be studied. HELIX automatically generates a wire-grid model of the ground cup. Program CHECK is used to verify that the resulting model conforms to NEC's requirements. MKSWEEP aids in the preparation of input files for NEC at multiple frequencies. GETPARAS computes the helix performance parameters such as gain and axial ratio from NEC's output data. This system offers the possibility of rapidly investigating the performance of a variety of helix designs to find the optimum design. The accuracy of the computations is assessed in comparison with the measured gain and axial ratio for two cylindrical helices and for a broadband helix using sections of two different diameters. The good agreement demonstrates the usefulness of the software modeling system.

1.0 Introduction

A helix antenna operating against a ground cup, such as that of Fig. 1(a), is commonly used for spacecraft applications[1-3]. Kraus[4] provides a discussion of how helix antennas work and some design information. Much more extensive design data was derived from measurements by King and Wong[5] for a limited range of pitch angles. Sultan et al.[2] investigated further the effect of varying pitch angles and variable pitch on helical antennas. However, comprehensive design data permitting the length and weight of a helix antenna to be minimized for a given performance are not available. NEC[6] computes the currents flowing on an interconnection of thin wires, and has been used by Wood[3] to model a helix antenna, representing the solid surface of the ground cup with a wire grid. This paper presents software for generating such a computational model of a helix antenna and ground cup rapidly, for a very general class of helix designs. The NEC code can then be used to study a variety of designs to minimize the size and weight of the helix for a given application.

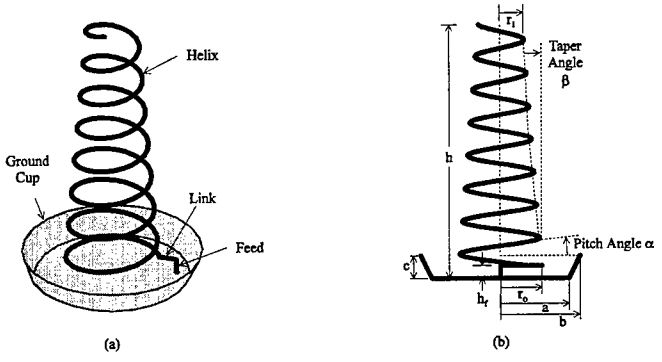

Fig. 1 (a) A tapered helix antenna against a ground cup. (b) Geometric parameters of the tapered helix and ground cup.

2.0 Helix Antenna Geometry

Figure 1(a) shows a tapered helix antenna with a "cup" configuration for its ground plane. The helix is fed with a coaxial bulkhead connector at a radial distance r_f from the cup center that is often greater than the radius of the base of the helix. A link wire is used to connect the top of the feed to the helix. Fig. 1(b) defines the basic geometric parameters of the helix and cup. The helix has an overall length h and tapers from a radius of r_o at the base to r_1 at the top. The taper angle β is given by

$$\tan\beta = \frac{(r_0 - r_1)}{h}$$

The helix rises at pitch angle α. If the feed is located on the x axis and the centerline of the helix is on the z-axis, then points on the helix (r, ϕ, z) in cylindrical coordinates are given by

$$z = (r_0 \tan\alpha)\phi \qquad \text{and} \qquad r = r_0 - z\tan\beta$$

The ground cup has a circular base of radius a, and a sidewall of top radius b and height c. By making height c equal to zero, the helix can be operated against a disc ground plane with no sidewall.

Figure 1(b) shows a helix with one "section". Fig. 2(a) extends the geometry to a helix made up of four sections and the software described below can generate GW cards for a helix with up to 30 sections. Fig. 2(a) represents a broadband helix having a large-diameter bottom half and a smaller-diameter top half. Section 1 is the bottom half, which tapers from radius r_o at the base to r_1 at the top, and has length h_1. Then a short sharply tapered section is used to reduce the radius rapidly from r_1 to r_2 in a short distance h_2. The top half is section 3 and has length h_3 and tapers from radius r_2 to radius r_3. The fourth section tapers sharply from radius r_3 to radius r_4 in a short distance h_4 and is a "matching section" which terminates the helix in an approximate matched load, so that the current flow on the helix will be principally a traveling wave.

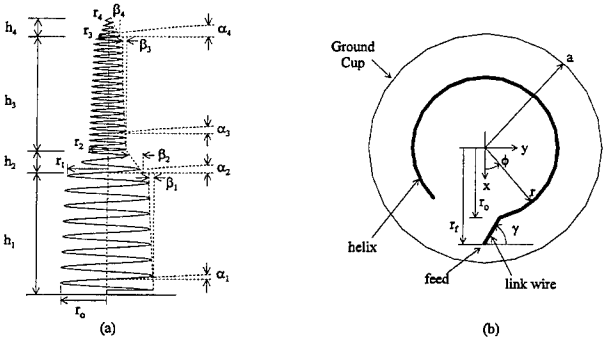

Fig. 2 (a) A four-section tapered helix and its parameters. (b) The geometric parameters of the feed.

Figure 2(b) shows some details of the feed geometry. The feed connector at radius r_f is often farther from the center of the ground cup than the base radius r_o of the helix. A link wire is used to connect the feed to the helix. The user must specify the angle γ that the link wire makes to the y-axis. If a helix antenna is constructed for measurement, then of course this angle must be the same in the measurement model and the computer model. If the feed radius is equal to the helix base radius then no link wire is required.

Measurement models of helices are often wound on a Styrofoam core. The Styrofoam slightly slows down the wave on the helix. This can be modeled by introducing additional capacitance between the turns of the helix[3]. However, the helices flown on spacecraft do not usually have such a core and so the additional capacitance has not been included in the present model.

3.0 Program HELIX

Since this project is intended to validate the performance of a great many helix designs, a quick convenient method was needed to generate GW cards for input to NEC for each. Program HELIX was developed for this purpose. HELIX uses a system of menus to let the user specify: a wire or tape helix; the lengths and radii of up to 30 helix sections; the feed radius r_f and height h_f; and the ground cup geometry. Helices for spacecraft applications often have a metal rod along the axis of the helix, which is used to deploy the helix. Program HELIX includes such a rod as an option.

As the user enters the helix design, program HELIX finds various gross errors, such as a feed radius smaller than the base radius of the helix or larger than the ground cup base radius. More subtle errors are also found, such as a feed angle γ which is so shallow that the link wire misses the first turn of the helix altogether. Error messages are given and the user must modify the input geometry to remove the error. When the user has completely specified the geometry, the user instructs program HELIX to generate a set of GW cards modeling the helix and the ground cup. In the flow chart of Fig. 3, program HELIX generates GW card file "helix.gw". Also, the program writes a "setup file" called "helix.set" which saves the helix geometry, so that next time the user runs HELIX, the program comes up with the geometry previously entered. Then the user only needs to change those parameters that are different from their previous values. File "helix.set" is self-explanatory and contains a full description of the helix geometric parameters. For documentation, program HELIX includes a copy of the "helix.set" file in the comments section of the GW card file.

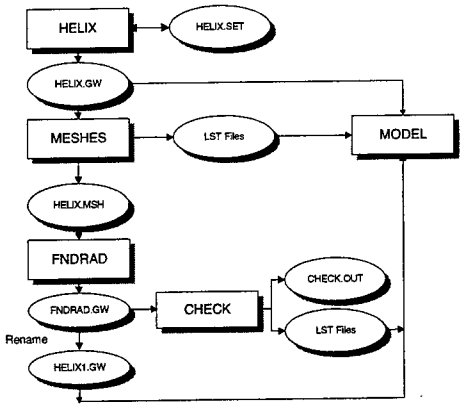

Fig. 3 Flowchart describing the process used to create GW cards for a helix antenna and its ground cup.

Program HELIX generates a representation of the helix itself in terms of straight wire segments. The helix radii are adjusted slightly so that the path length along the helix model is approximately equal to the actual length of the real helix.

Program HELIX automatically generates a wire-grid model of the ground cup, as illustrated in Fig. 4. The program is based on the "wire-grid modeling" guidelines of Ref. [7]. The first step is illustrated in Fig. 4(a). A circle of wire segments is generated directly underneath the segments of the first turn of the helix, with the segment boundaries aligning with those of the helix. Then a "feed region" is generated, which has a segment directly underneath the link wire between the top of the feed and the helix, and has other radial wires from nearby points to the feed point. Then the adjacent circles of wires are generated, as in Fig. 4(b), including radial wires joining the three circles. Part (c) shows the center of

the ground disc filled with wires, in such a way that the segment length is approximately uniform everywhere. Finally the sidewall of the cup is added, as in part (d). When HELIX has completed the model in file "helix.gw", program MODEL can be used to display the helix geometry in the format shown in Fig. 5.

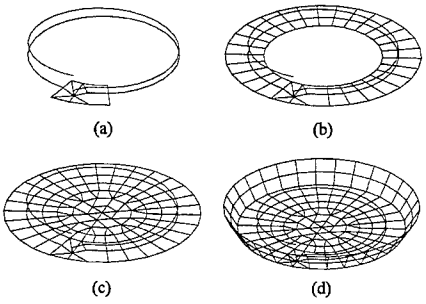

Fig. 4 Building a wire-grid to represent the ground cup.

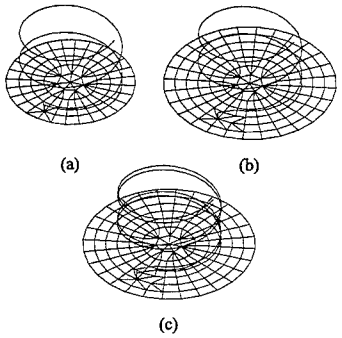

Fig. 5 Three helix and ground disc designs.

Figure 5 shows three feed and helix configurations that program HELIX can handle. In part (a), the radius at which the feed is located is the same as the base radius of the helix, and HELIX generates a set of eight radial wires surrounding the feed point. No link wire is used. In part (b), the ground disc is larger and the radius at which the feed is located is greater than the base radius of the helix. Program HELIX uses a link wire to join the feed to the helix. One of the eight radials surrounding the feed point lies directly underneath the link wire. Some additional wire segments are included in the ground to avoid creating large-area meshes. In part (c), the user has specified a tape helix to be modeled with two parallel wires.

Program HELIX uses a thin radius for the wires of the ground-cup grid. These wires must have their radius chosen according to the "equal-area" rule[8]. Equal-area radii are supplied by running programs MESHES and FNDRAD[9]. MESHES searches the ground-cup grid for mesh paths, which are written to file helix.msh. Program MESHES generates some "LST" files for display with MODEL, which help the user to identify and understand certain errors that sometimes occur in wire-grid models. Then program FNDRAD uses the areas of the meshes and the distances around the mesh peripheries to compute the "equal-area" wire radius for each of the grid wires, and writes the revised wires to file "fndrad.gw". The user usually renames this file. Here it has been called "helix1.gw", to denote the first helix model in a series, to be followed by "helix2.gw", "helix3.gw", and so forth as changes are made in the helix geometry and the resulting performance is computed.

To ensure reliable results when NEC is executed to determine the currents and far fields of the helix model, the model must conform to NEC's "modeling guidelines". This is verified by running program CHECK[10]. CHECK systematically compares all the individual wires, all the wires making up wire junctions, and all the pairs of wires in the model to the requirements of the "modeling guidelines" and writes files giving the tag numbers of wires which are in violation. These can be examined with MODEL and the helix geometry revised to clear the errors. The feed geometry is quite critical for these helices. Often small changes in the feed are required to satisfy the NEC modeling guidelines fully.

4.0 Computing the Performance Parameters

The performance of a given helix design must be evaluated over a certain bandwidth, and usually it is desired that the helix be solved at 50 or more frequencies to generate smooth curves of the gain, the axial ratio, the 3 dB beamwidth, and so forth. Rather than run NEC for one enormous run of 50 frequencies, the computation is usually subdivided into, say,

10 runs of 5 frequencies each. The required input files are prepared with program MKSWEEP or "make a frequency sweep", shown in the flowchart of Fig. 6. MKSWEEP accepts the geometry file "helix1.gw" as input, asks the user for the frequencies for each individual run, and generates a set of input files for NEC for specific frequencies, "helix1.1i", "helix1.2i",..., "helix1.10i". MKSWEEP prepares a list of the input file names and the corresponding output file names in file "helix1.run". This is used by a batch file or script file called NECRUN which runs the NEC program for each input file named in "helix1.run". Not shown in Fig. 6 is program STRIP, which reads the output file from NEC, and copies the currents on the wire segments and the radiation patterns to compact disc files "helix1.1", "helix1.2", ..., "helix1.10", which are saved on tape as a permanent record of the runs.

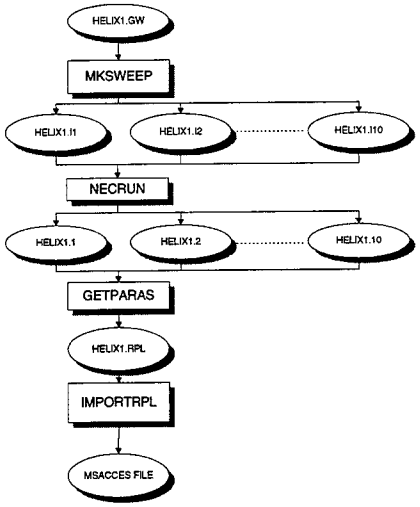

Fig. 6 Flowchart describing the process used to compute the performance of one helix design as a function of frequency.

To graph the gain, axial ratio, beamwidth, and so forth as a function of frequency, we must extract the values of these parameters from the radiation patterns computed by NEC. Program GETPARAS ("get parameters") reads each output file, and at each frequency find the gain, axial ratio, beamwidths, and other parameters, and write these to an "rplot" data file "helix1.rpl". If addition frequency points are desired, MKSWEEP is used to prepare a new set of input files, "helix1.11i", ..., then NEC is again run, and GETPARAS appends the new data to the "helix1.rpl" file. So that the rpl file will be a complete "stand-alone" record of a helix design and its performance, GETPARAS includes a copy of the "helix.set" geometry file in the header of the "rpl" file. Then program IMPORTRPL imports these parameters as a function of frequency in MSAccess™. Since MSAccess™ for Windows™ is a relational database software, the analysis of the results is made easy.

5.0 Studying Many Helix Designs

In trying to optimize the design for a given application, the geometry of a variety of different helices is typically studied. For example, fifteen different combinations of radius, taper angle, pitch angle and so forth might be examined. For each of the 15 cases, program HELIX is run, followed by MESHES and FNDRAD, then CHECK to verify compliance to the modeling guidelines. The result is 15 helix models that have slightly different geometry: "helix1.gw", "helix2.gw", ..., "helix15.gw". Each of the 15 models must be analyzed at, say, 50 different frequencies. Hence GETPARAS is used to obtain 15 files of performance parameters: "helix1.rpl", "helix2.rpl", ..., "helix15.rpl". To compare the 15 designs, it was found convenient to import the data from all the "rpl" files into a single spreadsheet. The spreadsheet software can then graph and compare parameters as a function of frequency quickly and conveniently. Further, the database software package

MSAcces™ can read the same spreadsheet and prepare parametric design graphs such as the gain as a function of the pitch angle of the helix.

It is intended that this software system be used to develop optimum designs for various applications. To be sure that the antennas are being modeled correctly and to assess the accuracy of the results being obtained, an extensive set of comparisons with measured data are being prepared. The following presents some initial results.

6.0 Experimental Results to Validate the Software

In order to validate the modeling software described above, several helix antennas were built and tested at a range of frequencies between 600 and 1400 MHz, for a variety of different configurations and parameters:

- Uniform / tapered and combinations of both.
- Single / multiple pitch angles.
- A range of diameters.
- A range of pitch angles.
- A range of helix lengths.
- A range of ground plane configurations.
- Wire / tape radiating elements.

As an illustration, Fig. 7 shows the results of a uniform helix using a 1/4" diameter copper wire radiating element. This was wound with a constant pitch angle α of 10.4°, using a mean helix diameter of 4.694", above a ground plane, in the form of an aluminum cup, tapering from 5.5" lower diameter to a 8.48" upper diameter, over a vertical height of 3.44".

The Boresight Gain (Go) and Axial Ratio (AR) are plotted over a frequency range over which the axial ratio did not exceed 2 dB. This is a practical range of axial ratios to consider for useful elliptically polarized antennas. Fig. 7 demonstrates that the curve predicting the theoretical results of Go vs. frequency, using the modeling software, is validated by the experimental results. Fig. 8 validates the modeling software when the helix antenna pitch angle is changed from 10.4° to 11.8°, with the same antenna as in Fig. 7, with a relatively good fit between theoretical and experimental results.

Using the same ground cup, a four section helix antenna was tested. As shown in Fig. 2(a), the dimensions were as follows:

$r_0 = 2.36"$	Wire Diameter = 3/16"	Total Height = 25.5"
$r_1 = 2.36"$	$\alpha_1 = 10.04°$	$h_1 = 10.0"$
$r_2 = 1.59"$	$\alpha_2 = 10.10°$	$h_2 = 3.1"$
$r_3 = 1.59"$	$\alpha_3 = 15.20°$	$h_3 = 9.3"$
$r_4 = 0.35"$	$\alpha_4 = 14.30°$	$h_4 = 3.1"$

Figure 9 demonstrates an even better fit between the predicted and measured boresight gain, within a fraction of a dB. Although both sets of results show an axial ratio below 1 dB throughout the frequency range, there is less agreement between the modeling and the measured AR. This is less important than the accurate fit for the antenna gain values.

Finally, Fig. 10 compares the modeled gain results for the two pitch angles used: 10.4° and 11.8°. The gain response curve shifts up in frequency and slides slowly up in gain, as the pitch angle increases from 10.4° to 11.8°, confirming what has already been established experimentally[5].

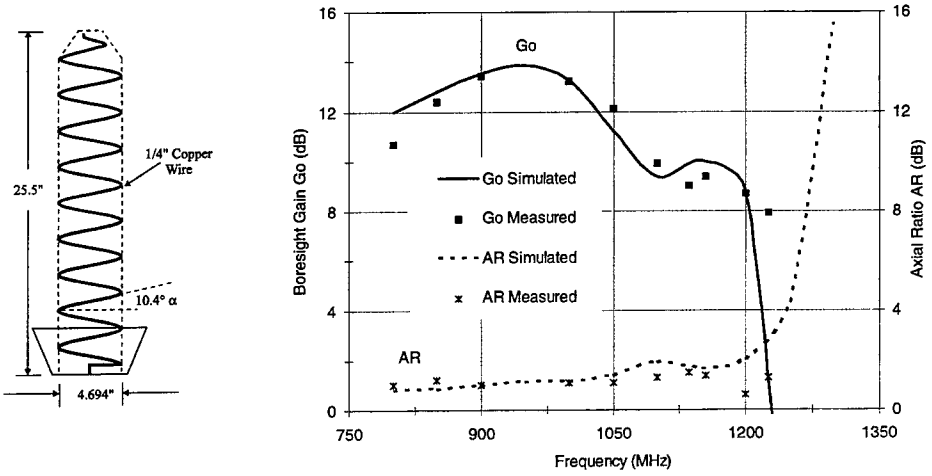

Fig. 7 Boresight Gain (Go), and Axial Ratio (AR), vs. Frequency of a uniform helix using 1/4" diameter copper wire & 10.4° pitch angle.

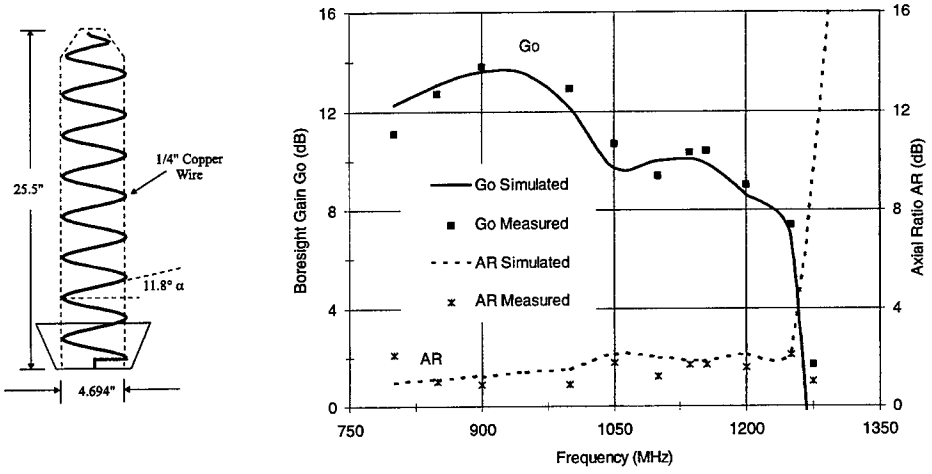

Fig. 8 Boresight Gain (Go), and Axial Ratio (AR), vs. Frequency of a uniform helix using 1/4" diameter copper wire & 11.8° pitch angle.

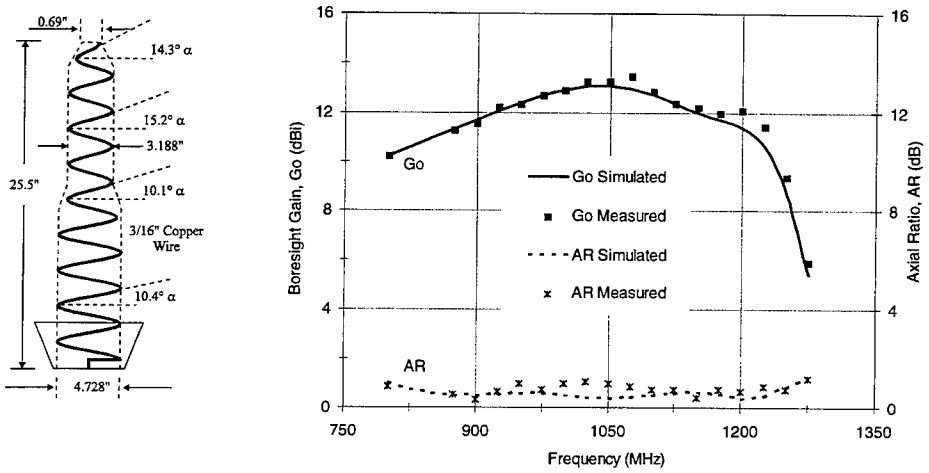

Fig. 9 Boresight Gain (Go), and Axial Ratio (AR), vs. Frequency of a four section helix antenna.

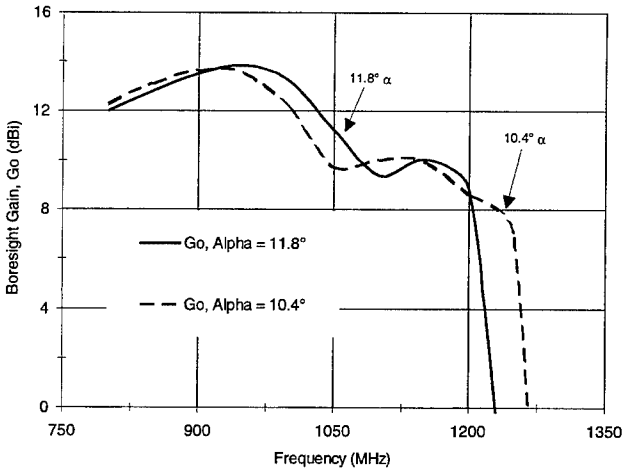

Fig. 10 Comparison of Boresight Gain (Go) vs. Frequency of uniform helix using 1/4" diameter copper wire of 10.4° and 11.8° pitch angle.

Conclusion

This paper has described a software system for modeling helix antennas of complex design. The software rapidly generates a computer model for a given helix design, and rapidly supports solving the model with NEC at many frequencies, collecting the gain, axial ratio and other parameters into an input file for a database program. The system makes easy the comparison of the performance of helices of various designs, to optimize the design for a given application.

The comparison of computed gain and axial ratio with measured values for three cases was presented. Cylindrical helices of two different pitches were examined, with good agreement of the gain and axial ratio with measured data. For a more complex design, using a helix with two sections of two different diameters to broaden the bandwidth, the predicted gain is in excellent agreement with the measurement, although the agreement of the axial ratio is less good. The computer model accurately predicts the changes in the gain as a function of frequency when the pitch is changed for the uniform cases. Any improved prediction of antenna gain values, and hence optimization, is of paramount importance. This is particularly true for satellite antenna, where there are several constraints of power, mass, size etc.. The modeling software described here provides the means for such optimization.

References

1. Sultan, N., "A Novel Broadband Double Pitch Cylindrical Helical Antenna for Satellite and Ground Applications", *1984 International Symposium Digest, Antennas and Propagation*, Vol. 1, 1984.
2. Sultan, N., "Design of Broadband Tapered Helical Antennas", *4th International Conf. on Antennas and Propagation*, 1985.
3. Wood, P.J., "Electromagnetic Wire Segment Modeling Applied to the Skynet Deployable UHF Antenna", *ANTEM*, Ottawa, 1994.
4. Kraus, J.D., *Antennas*, 2nd edition, McGraw-Hill, 1988.
5. King, H.E., and Wong, J.L., "Characteristics of 1 to 8 Wavelength Uniform Helical Antennas", *IEEE Trans. on Antennas and Propagation*, Vol. AP-28, No. 2, pp. 291-296, March, 1980.
6. Burke, G.J., Poggio, A.J., Logan, J.C., and Rockway, J.W., "NEC - Numerical Electromagnetics Code for Antennas and Scattering", *1979 IEEE International Symposium on Antennas and Propagation Digest*, IEEE Publication No. 79CH1456-3AP, Seattle, Washington, June, 1979.
7. Trueman, C.W., and Kubina, S.J., "Fields of Complex Surfaces using Wire-Grid Modelling", *IEEE Trans. on Magnetics*, Vol. 27, No. 5, pp. 4262-4267, Sept. 1991.
8. Ludwig, A.C., "Wire-Grid Modeling of Surfaces", *IEEE Trans. on Antennas and Propagation*, Vol. AP-35, No. 9, pp. 1045-1057, Sept. 1987.
9. Trueman, C.W., "Automated Radius Calculation for Wire-Grid Models", *7th ACES Symposium*, Monterey, California, March 18-22, 1991.
10. Trueman, C.W., and Kubina, S.J., "Verifying Wire-Grid Model Integrity with Program CHECK", *Applied Computational Electromagnetics Society Journal*, Vol. 5, No. 2, pp. 17-42, Winter 1990.

EVALUATION OF THE SENSITIVITY OF SCATTERING PREDICTIONS TO UNCERTAINTIES IN MATERIAL CHARACTERISTICS[1]

G. A. Barnhart, A. J. Terzuoli, Jr., G. C. Gerace
Air Force Institute of Technology • Dayton, Ohio 45433

ABSTRACT

The material characteristics of a dielectric were measured by two separate X-band waveguide set-ups. Scattering measurements were then made at normal incidence of the same material backed with and without a metal square plate. Scattering predictions were calculated with: (1) reflection coefficients and physical optics; and (2) Xpatch, a high frequency scattering prediction code. It was found that variations in scattering predictions were proportional to variations of the imaginary part of the permittivity. Furthermore, the magnitude of the variations in scattering corresponded to the relative magnitude of the reflection coefficient.

INTRODUCTION

An important factor in evaluating the accuracy of a scattering prediction is understanding the accuracy of the model for the scatterer. If the object's size or shape is erroneous, the resulting scattering prediction is faulty, but these can typically be measured quite accurately. This is not true, however, when evaluating the accuracy of the object's material composition. Both measurement uncertainties and manufacturing tolerances contribute to the variations of the characteristics. At best, a material's specifications may provide an estimate of these characteristics under certain frequency and temperature conditions. The actual values, however, may vary greatly from these specifications.

The primary objective of this study was to evaluate the sensitivity of scattering predictions to uncertainties in material characteristics. Also, as part of a continuing effort to validate and improve Xpatch as an scattering prediction tool [1-4], this study evaluated Xpatch's material coated object prediction capabilities by comparing simulation results to scattering measurements. This work was limited to commercially available dielectric materials, but provides the fundamentals of scattering materials error analysis which can be applied to any material.

METHODOLOGY

For this research, the commercially available material evaluated was ECCOSORB VF-60 by Emerson & Cuming Incorporated. The VF-60 material is a non-magnetic dispersive, homogeneous, conductive plastic dielectric film. To create a semi-Salisbury Screen configuration a 1.5 cm thick Styrofoam layer was used for a spacer behind a 0.15 cm thick VF-60 layer. To assess the degree of material measurement error, the material characteristics of these materials were measured using rectangular waveguides. Two different X-band waveguide set-ups were used limiting measurements to 8-12 GHz, with data was taken every 0.25 GHz.

The first rectangular waveguide set-up is designated RQ, with data from this set-up labeled as such. This set-up was a reflectometer consisting of a network analyzer containing the material sample in port #2 backed by a short. This reflectometer can only measure the S_{11} parameter. The second rectangular waveguide set-up is designated IQ, with data from this set-up labeled as such. The IQ set-up was a full two-port configuration which measured both S_{11} and S_{21}. The material sample was placed in a sample holder which is a section of waveguide (of the same thickness as the sample).

Using the IQ setup, a six inch square slab of VF-60 material, was measured alone (called *air backed*) and then was measured in front of a highly conducting square plate (called PEC backed). Scattering predictions were made using two methods. The first method calculated the reflection coefficients of the materials and then applied physical optics (PO) theory to predict the scattering. A major restriction on PO theory is that it is only accurate for electrically large objects. Since all

[1]This work was supported by the U. S. Air Force Wright Laboratories.

measurements were done in X-band and the object was six inches square, the use of PO theory was valid. The second scattering prediction method utilized was Xpatch, performing object simulations at normal incidence.

Since there was no identifiable true value associated with the material characteristics, the sample mean of the measured material data was adopted as the best estimate of the true value, and the sample standard deviation of the replication error provided a measure of the root mean square deviation from the sample mean. These two statistical values were used to analyze the scattering measurements, theoretical predictions, and Xpatch simulations.

RESULTS

The VF-60 material characteristics were measured twenty times with both the RQ and IQ X-band waveguide set-ups. The permittivity sample means over 8-12 GHz are shown in Figure 1. The VF-60 manufacturer specification for the relative dielectric constant was 37.0 at 8.6 GHz. The RQ measurements averaged about 30 and the IQ measurements averaged about 27 at this frequency. Not only were there large discrepancies between the material measurements and the specification at 8.6 GHz, but also between the two measurement techniques themselves. The IQ set-up measured the permeability as well as the permittivity. Figure 2 shows that the real part of the relative permeability was measured to be about 1.0, and the imaginary part to be about 0.0 which is consistent with the expected values for a dielectric. The RMS error of the VF-60 permittivity measurements was computed; the average correlation of the permittivity curves with the sample mean curve was calculated. In general, the RMS deviation was 10-20% of the materials' permittivities (both real and imaginary parts), and the repeated measurements were highly correlated with the sample means.

The statistics of the scattering predictions and Xpatch simulations based on measured material characteristics were compared to scattering measurements performed in the IQ range. Despite differences in the permittivity sample means measured by these two set-ups, the RQ and IQ scattering predictions were quite similar for both the air backed and PEC backed VF-60. The agreement between the predicted and measured scattering for the air backed VF-60 and the low scattering RMS deviations indicate that the measured material characteristics were accurate. Figure 3 shows sample means of the scattering measurements, predictions, and Xpatch simulations for this case. From PEC plate measurements, it was found that a slight vertical plate tilt of 1.05 degrees was inherent in the scattering measurements, causing the observed small bias error. For the PEC backed VF-60, a higher average RMS deviation and a lower correlation was noticed. In this semi-Salisbury Screen configuration, a quarter wavelength null was experienced at about 9.25 GHz. This degradation was associated with the inability of the scattering measurements to characterize the deep null. Figure 4 shows the sample means of the scattering measurements, scattering predictions, and Xpatch simulations for this situation.

The evaluation of how the material characteristics variations affected the scattering predictions was independent of the accuracy comparisons to scattering measurements. The material characteristics measurements, scattering predictions, and Xpatch simulations were statistically evaluated using RMS deviation and correlation indicators. It was determined that variations in the *imaginary part* of the permittivity and the *magnitude* of the reflection coefficient had the largest influences on the scattering variations. In general, for both the air backed and PEC backed configurations using both the RQ and the IQ material characteristics measurements, there was a fairly high negative correlation between the scattering variations and the magnitude of the reflection coefficient. Figures 5 and 6 demonstrate this relationship for the PEC backed case using the RQ material characteristics. Clearly, an inversely proportional relationship exists. Although not as obvious, there is also a relationship with the imaginary part of the relative permittivity. This is more visible in Figures 7 and 8 which show the high correlation for the air backed case using the IQ material characteristics.

CONCLUSIONS

Examination of all the acquired data indicated two trends. First, the variations in scattering predictions were directly proportional to variations in the material's relative permittivity. Second, the magnitude of the scattering variations was inversely proportional to the magnitude of the reflection coefficient which magnified the effect of the material characteristic variations. As the reflection

coefficient increased, the scattering was less influenced by material variations and vice versa. The primary reason for this relationship was that higher reflection coefficients were the result of lower electromagnetic absorption of the material. Since the material had a lower effect on the total scattering, slight uncertainties in its characteristics caused only slight variations. On the other hand, for a highly absorbing material in which the reflection coefficient was low, the material properties dominated the electromagnetic scattering mechanisms. In this situation, slight material characteristic variations were magnified in the scattering variations.

The primary objective of this study was to evaluate the sensitivity of scattering predictions to uncertainties in measured material characteristics. In general, it was found that the scattering variations were most influenced by the relative magnitude of the reflection coefficient. A lower reflection coefficient resulted in a larger scattering variation. Also, for a relatively constant reflection coefficient across the frequency band, the RMS error of the scattering predictions were seen to be directly proportional to the replication error in the imaginary part of the dielectric permittivity.

ACKNOWLEDGMENTS

The authors are grateful for the essential assistance with the measurements and the suggestions of: Paul Skinner, Joe Sacchini, Mike Proudfoot, Stan Bayshore, Fred Jones, Rob Layden, Andy MacFarland, and Bill Kent.

REFERENCES

[1] E. M. Miller, D. J. Andersh, A. J. Terzuoli, Jr., "Facetization Level and the Effect on XPATCH Predictions," *Proceedings of the Ninth Annual Review of Progress in Applied Computational Electromagnetics*, Monterey, CA, March 22-26, 1993, pp. 610-617.

[2] R. O. Jernejcic, A. J. Terzuoli, Jr., R. Schindel, "Evaluation of Full Radar Signature Predictions Using XPATCH," *Proceedings of the Tenth Annual Review of Progress in Applied Computational Electromagnetics*, Monterey, CA, March 21-25, 1994, pp. 343-351.

[3] R. G. Layden, A. B. MacFarland, and W. J. Kent, "A Comparison Between Physical Optics Codes XPATCH and NoseScat Versus Measured Data on the MRC Nose Radome Test Body," Mission Research Corporation, Dayton, OH, Nov. 1994.

[4] M. C. Christensen, S. W. Lee, and D. J. Andersh, "Scattering from Dielectric Loaded Cavities Using Shooting and Bouncing Rays," *Proceedings of the Eleventh Annual Review of Progress in Applied Computational Electromagnetics,* Monterey, CA, March 20-25, 1995, pp. 1111-1117.

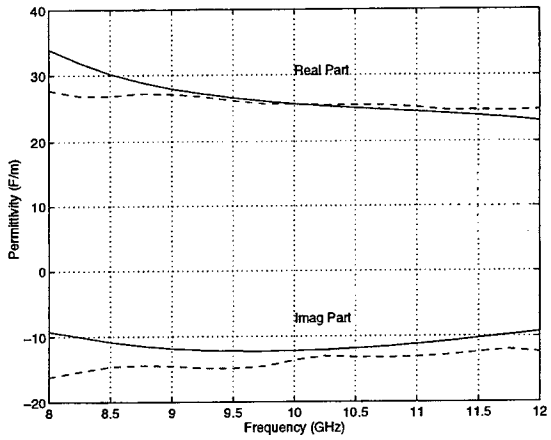

Figure 1. Relative VF-60 Permittivity Sample Means from RQ (solid line) and IQ (dashed line) Waveguide Material Characteristics Measurements.

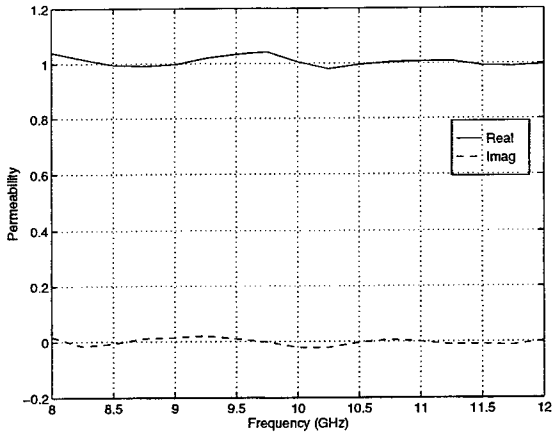

Figure 2. Relative VF-60 Permeability Sample Mean for IQ Waveguide Measurements.

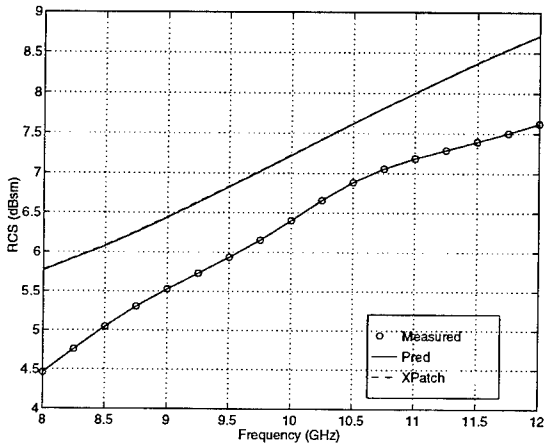

Figure 3. Scattering Prediction and Measured Sample Means for Air Backed VF-60 Using RQ Measured Material Characteristics.

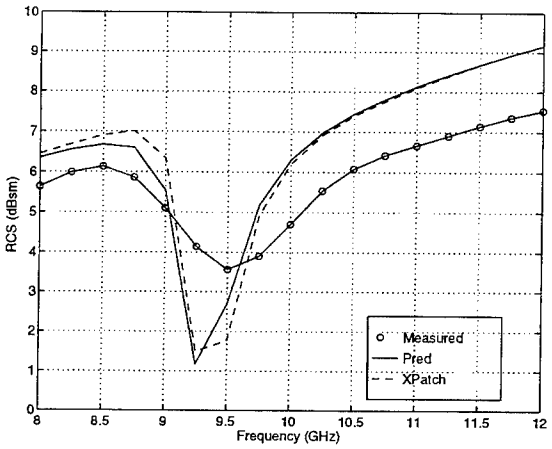

Figure 4. Scattering Prediction and Measured Sample Means for PEC Backed VF-60 Using RQ Measured Material Characteristics.

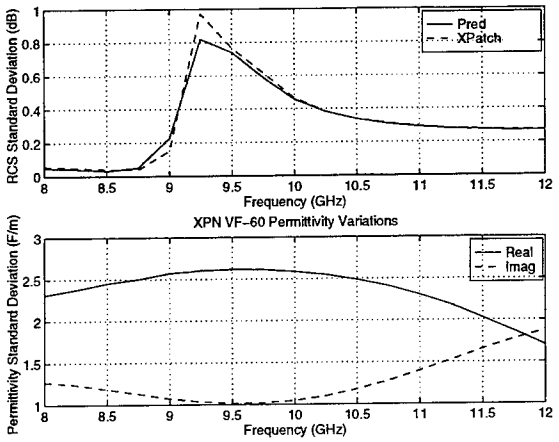

Figure 5. Permittivity Measurement and Scattering Prediction Variations for PEC Backed VF-60 Using RQ Measured Material Characteristics.

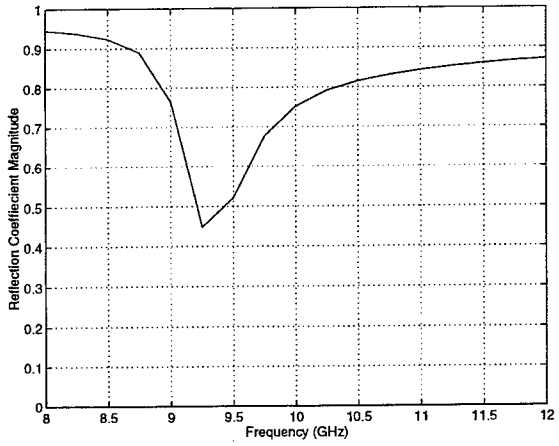

Figure 6. Average Reflection Coefficient for PEC Backed VF-60 Using RQ Measured Material Characteristics.

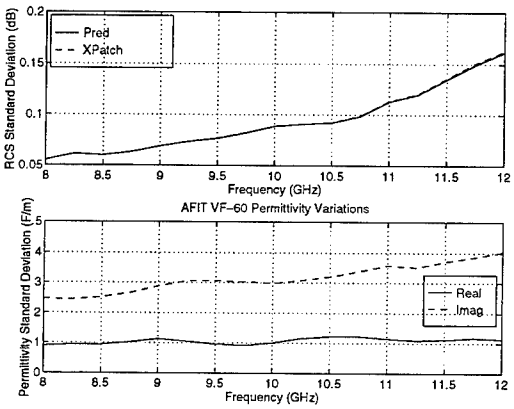

Figure 7. Permittivity Measurement and Scattering Prediction Variations for Air Backed VF-60 Using IQ Measured Material Characteristics.

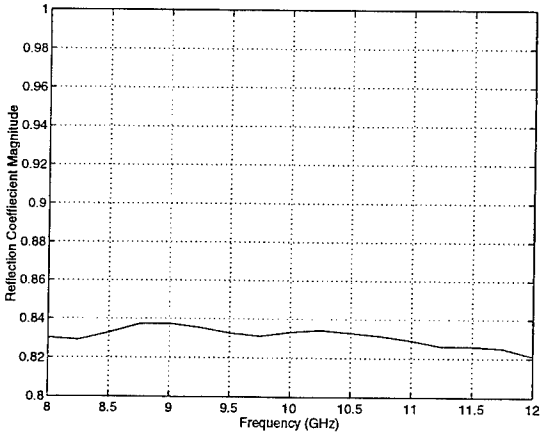

Figure 8. Average Reflection Coefficient for Air Backed VF-60 Using IQ Measured Material Characteristics.

Validation of the PO-based RCS Code SIGMA by Using IEM and Experiments

E. Kemptner, D. Klement, V. Stein

Institute of Radio Frequency Technology
German Aerospace Research Establishment (DLR)
D-82230 Wessling, Germany

ABSTRACT

The RCS computer code SIGMA was developed and validated at DLR to predict the monostatic radar cross section of complicated objects which are large compared to the wavelength. It is based on high frequency methods.

Recently work has started to investigate the range of application of SIGMA toward lower ratios of object dimensions to wavelength. For this purpose a canonical object like an ogival cylinder with dimensions $4\lambda x2\lambda x4\lambda$ is well suited. In this paper the results of SIGMA are compared with those of the computer code NEC-2 and of precise experiments carried out at DLR.

1. INTRODUCTION

The computer code SIGMA was developed at DLR in order to calculate the monostatic RCS of complex structures. SIGMA is based on the Physical Optics (PO) theory [1] and extended to the Physical Theory of Diffraction (PTD) by incorporating the Method of Equivalent Currents (MEC) [2]. PO as a high frequency approximation is usually applied for objects which are large compared to the wavelength. In the past SIGMA was successfully applied for e.g. a periscope like structure [3] or a stealth design [4]. Presently the application of SIGMA for objects with dimensions of only a few wavelengths is under investigation. Some different types of cylinders (elliptical, ogival, airfoil-like) are chosen for that purpose. In this paper the results of ogival cylinders, which include two vertical edges, are presented. In order to validate the results of SIGMA the well-known code NEC-2 [5], based on the Integral Equation Method (IEM), and experiments at 94 GHz are used and presented.

2. BASIC THEORIES OF SIGMA AND NEC-2

In order to apply PO to complicated objects several modules have to be combined to a powerful computer code. In the past a hidden surface algorithm, a double reflection tool including its ray tracing, the already mentioned application of MEC in order to consider edge effects and a module to apply Fresnel's reflection coefficients for nonmetallic surfaces have been incorporated into SIGMA. In the present work the results of SIGMA for metallic ogival cylinders with and without the application of the optional MEC module are shown.

PO as a high frequency method is only applicable down to a minimum ratio of object dimensions to wavelength. This minimum was thought to be several wavelengths. Detailed investigations in the last years have shown that for much lower ratios very good results can be achieved. This extension

to higher values of the wavelength for a given object is of great importance because the area of application of the IEM now joins this of PO and PTD. Therefore the development of a special hybrid method for this transition area seems to be unnecessary.

To achieve reference results by the IEM the well-known computer code NEC-2 was used. In order to compare the PO, PTD and IEM results the objects are modeled by flat panels for SIGMA as well as for NEC-2. The panel model was chosen for NEC because of the lower CPU time compared to that of the wire-grid model and of the possibility to make use of three planes of symmetry for the ogival cylinder. The size of the objects compared to the wavelength is already large for the IEM (6960 panels, corresponding to a maximal panel size of 0.1λ) and quite small for PO and PTD. The panel model for SIGMA consists of only 288 panels. Here the panel size is not limited by a fraction of the wavelength but only by the curvature of the surface, because the contribution of each panel is evaluated analytically.

3. MEASUREMENT FACILITY

The equipment for the measurements of RCS diagrams works at the frequency of 94 GHz and is established in an anechoic chamber. Full polarimetric coherent measurements are possible. The setup can also be changed to perform bistatic measurements. The distance between antenna and object is 3.2 m and the objects may have a maximum diameter of 64 mm. Absolute calibration (trihedral corner reflector) and vacant-room calibration can be carried out for every diagram. The lowest RCS which can be measured is -45 dBsm and the dynamic range is 50 dB with an accuracy of ±1 dB.

4. RESULTS

Calculations and measurements have been carried out on a cylinder with an ogival cross section. This basic object (fig 1) is enlarged in 4 steps by 2.5% each in both horizontal dimensions.

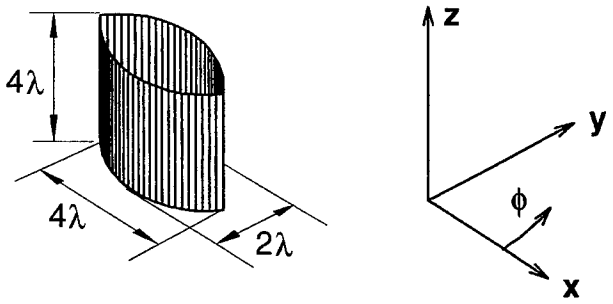

Fig. 1 Sketch of one of the ogival cylinders

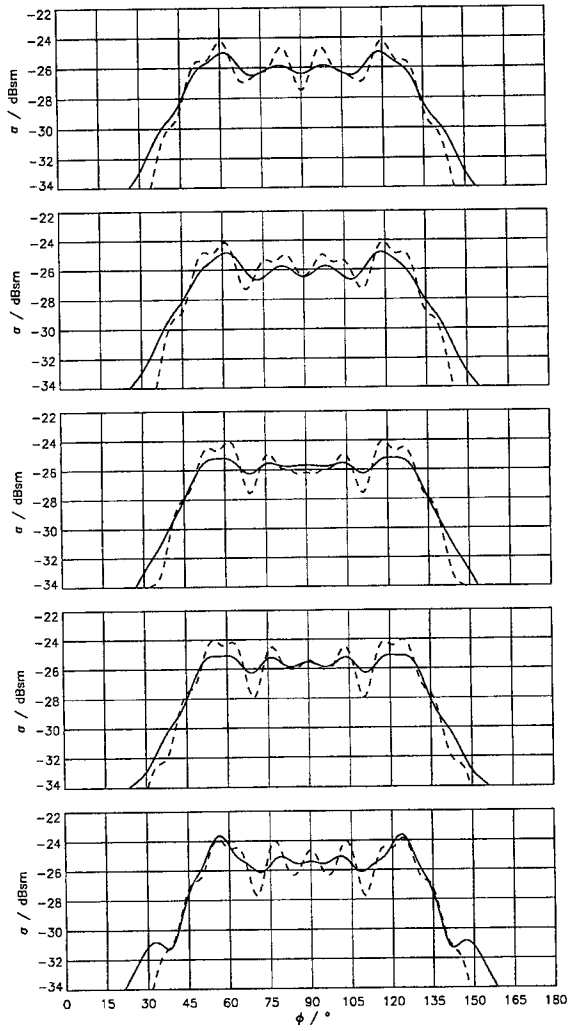

Fig. 2 Monostatic RCS-results by NEC-2 for five ogival cylinders;
solid line: vv- , dashed line: hh-polarization.
first (top) diagram: 4λx2λx4λ-object,
second obj.: 4.1λx2.05λx4λ; third obj.: 4.2λx2.1λx4λ,
fourth obj.: 4.3λx2.15λx4λ, fifth obj.: 4.4λx2.2λx4λ.

The backscattered signal of an ogival cylinder is caused by the following centers of cross section:

- specular reflection of the surface,
- 2 vertical edges,
- 2 visible horizontal edges,
- 2 horizontal rear edges at the top surfaces,
- creeping waves.

The calculated result of the IEM contains all these contributions. The edge contributions and the creeping waves are different for the two polarizations and the relative phases of all contributions depend on the object dimensions. The RCS of the ogive is a superposition of all contributions. In fig. 2 the results of the IEM calculations are shown for a variation of the horizontal dimensions of only 10%, which causes significant changes of the diagram. The CPU time on a CRAY-J916 required by NEC-2 is 32 minutes for each object.

The calculated results of the high frequency solutions PO and PTD are shown in fig. 3. PO only takes into account the specular reflection and the edge diffraction effect in the high frequency limit. The result of PO is independent of the polarization. PTD enhances the result of PO by the MEC for the visible edges. The contributions of invisible edges and creeping waves are neglected. The validation of the results by IEM and experiments can indicate whether the employed approximations are sufficient or which further modules are necessary to improve SIGMA. The CPU time on a IBM-3090 is 9 seconds for the PO option and 16 seconds for the PTD option of SIGMA for each object.

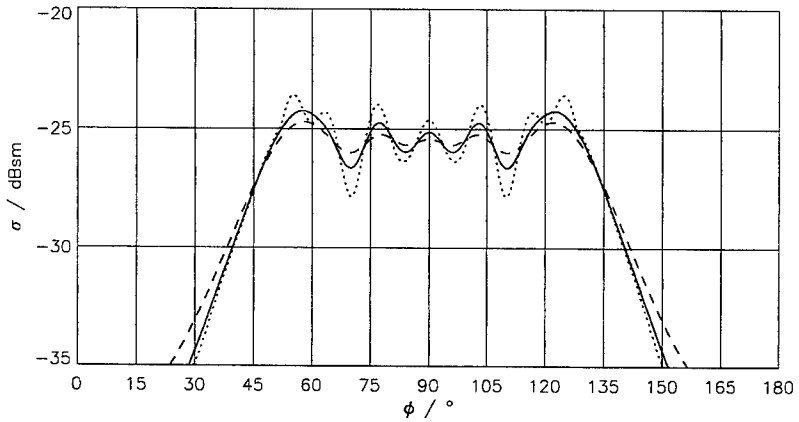

Fig. 3 Monostatic RCS-results by SIGMA for the fifth object of fig. 2;
solid line: PO result; dashed line: PTD result (vv-pol.); dotted line: PTD result (hh-pol.).

In fig. 4 the results of IEM, PTD, and measurement are compared. For the horizontal polarization very good agreement between the measurements and both calculations can be observed. However for the vertical polarization differences of 1 dB occur. At 55° and 125° measurement and IEM agree well while the PTD fails. It is supposed that a creeping wave at the top and bottom surface of the

ogive, which is reflected at the horizontal back edge, is responsible for these maxima of the diagram. Up to now this effect is not handled by SIGMA.

In the region around 90° difficulties in the experiments become obvious. The test objects have been mounted on a styrene cylinder on a turntable and an interaction between the horizontal styrene surface and the side wall of the ogival cylinder occurred at that aspect. The influence of the styrene alone is eliminated by vacant-room calibration, but this does not work for interactions between object and room or turntable.

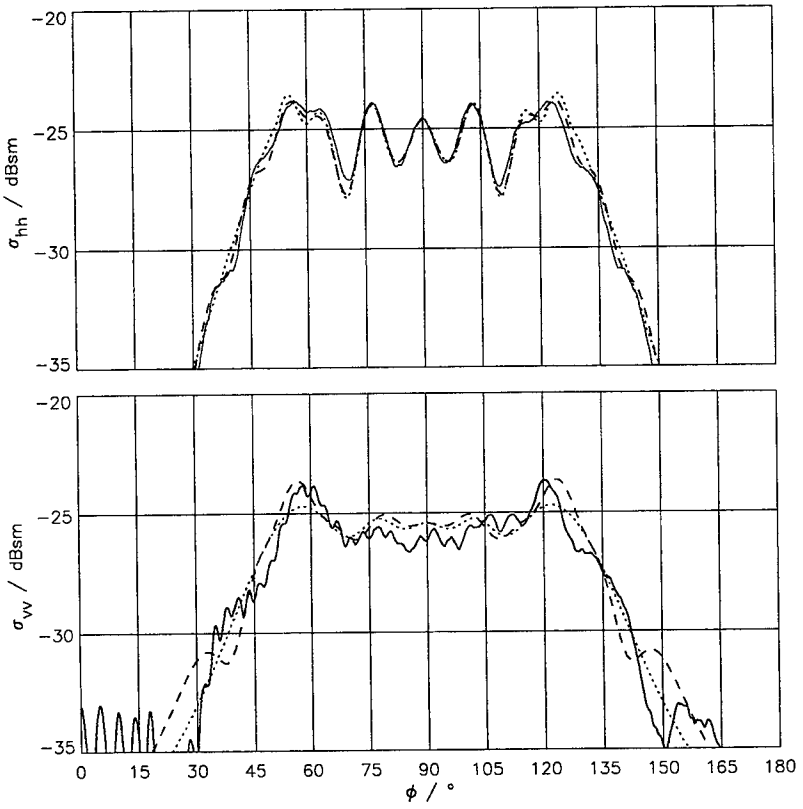

Fig. 4 Monostatic RCS-results for the fifth object of fig. 2; top: hh-pol., bottom: vv-pol.; solid line: measurements, dotted line: PTD (SIGMA), dashed line: IEM (NEC-2).

5. CONCLUSION AND FUTURE WORK

For five ogival cylinders the RCS results of the computer code SIGMA have been validated by results of NEC-2 and measurements at 94 GHz. Although the five objects vary just about 10% in their horizontal dimensions the diagrams are distinctly different. This has been confirmed by all three methods. The extension of SIGMA using the equivalent edge currents leads to very good results for the test objects. The very short computer times of SIGMA in contrast to NEC-2 have to be emphasized.

One option implemented in SIGMA is the capacity to treat nonmetallic structures. At this time however there are no reliable validations. For this purpose not only the theory but also the experimental setups to evaluate material parameters have to be completed. As the influence of creeping waves is very important for a lot of objects this tool has to be implemented in SIGMA as well as multiple reflections in the future.

ACKNOWLEDGMENT

The authors would like to thank Karl-Heinz Dreher who has carried out the RCS measurements with great care and Stefanie van der Piepen who was engaged in the design of the numerical object models for SIGMA and NEC and in the graphical representation of the results.

REFERENCES

[1] D. Klement, J. Preissner, V. Stein
Special Problems in Applying the Physical Optics Method
for Backscatter Computations of Complicated Objects
IEEE-A&P, Vol. 36, No. 2, 1988, p. 228-237

[2] V. Stein
Application of Equivalent Edge Currents to Correct the Backscattered
Physical Optics Field of Flat Plates
ACES-Journal, Vol. 7, No. 1, 1992, p. 24-47

[3] D. Klement, J. Preissner, M. Ruppel, V. Stein
State of Development, Validations and Application
of the Radar Signature Models SIGMA and BISTRO at DLR
Proceedings of 'Ground Target Modeling & Validation Conference',
Houghton, Michigan, August 23-25, 1994

[4] W. Friess, E. Kemptner, D. Klement, J. Preissner, V. Stein
Mono- and Bistatic RCS-Analysis of a Generic Airplane Design
with Stealth Characteristics Using Low and High Frequency Computational Methods
Proceedings of 'Ground Target Modeling & Validation Conference',
Houghton, Michigan, August 22-24, 1995.

[5] G.J. Burke, A.J. Poggio
Numerical Electromagnetics Code (NEC-2) - Method of Moments
Technical Document 116, Naval Ocean System Center, San Diego, Calif., Jan. 1981

SESSION 13:

OPTIMIZATION

Chair: E. Michielssen

Optimization of Broad-Band Loaded Wire Antennas in Real Environments Using Genetic Algorithms[1]

*D. S. Weile and E. Michielssen**
Center for Computational Electromagnetics
University of Illinois at Urbana-Champaign
Urbana, IL 61801

A. Boag
Israel Aircraft Industries
Department 4464
Ben-Gurion Airport 70100, Israel

Abstract

The design of a loaded wire antenna situated on an arbitrary platform is considered. A genetic algorithm-based technique is developed for optimizing the design. The analysis of the behavior of the loaded antenna on the platform is performed with numerical Green's functions constructed using the Method of Moments. Without requiring any preliminary design, the genetic algorithm selects the locations and impedances of the antenna loads, as well as the topology and design parameters of the matching network. The design of a whip antenna residing on a tank demonstrates the method. To evaluate the method, these results are compared with those obtained using simulated annealing optimization.

1. Introduction

Though wire antennas have been in use since the inception of electromagnetic theory and the experiments of Heinrich Hertz, they continue to be used in a myriad of applications. The radiation from these antennas was understood fairly well even in 1897 by Pocklington [1]; today they may be analyzed easily with a plethora of computer codes implementing any one of various numerical solution techniques, such as the Method of Moments (MoM) [2]. Unfortunately, even though the analysis of radiating wire structures is quite well understood, the synthesis of such structures still presents some difficulty, and fully automated methods for the design of wire antennas are rare. The optimization of antenna characteristics is intrinsically complicated, as necessary goals such as high gain, broad bandwidth and low Voltage Standing Wave Ratio (VSWR) often conflict. To further complicate matters, any objective function used to compare different antenna designs is likely to be highly multimodal. Thus, as Popovic [3] notes, "Although the CAD design of wire antennas is of course desirable, for various reasons it can not be implemented in all cases."

An additional problem in antenna synthesis that is rarely considered in the design procedure is the environment in which the antenna radiates. Antennas are usually designed in vacuum or some other idealized environment; that is, the realistic platform on which they reside is ignored in their design, so they are rarely truly optimized to radiate in the environment in which they will be used. Also, antennas are usually designed separately from their matching networks, which inhibits creation of truly integrated designs. Thus, in contrast to a previous paper on the design of wire antennas [4], this paper designs the antenna for radiating in its intended environment, and is able to fully design the matching network and its topology.

In this study, we design broad-band, loaded wire antennas which are optimized for use on their platforms. To overcome the problems of the multimodality and general complexity inherent in any wire antenna design, we use Genetic Algorithms (GAs) for optimization. These algorithms are stochastic

[1]This study is an abridged version of a study submitted to the *IEEE Transactions on Antennas and Propagation.*

antenna design, we use Genetic Algorithms (GAs) for optimization. These algorithms are stochastic search procedures based on the theory of evolution and survival of the fittest [5]. Unlike gradient-based searches and other deterministic techniques, GAs do not tend to settle into the first local optimum they discover, but instead consider large populations of designs at a time and combine their traits until a more global optimum is found.

Specifically, the problem we treat with GAs can be stated as follows. We consider a wire antenna, typically (but not necessarily) fed at or near its base, attached to an arbitrarily shaped Perfect Electric Conductor (PEC) which may or may not reside on an infinite PEC ground plane (Fig. 1). We use the GA to optimize the locations and impedances of parallel RLC loads along the wire, as well as the topology and component values for a matching network, so that the resulting antenna has high gain and low VSWR across a broad frequency band when radiating in the presence of the platform for which it was designed. We do not optimize the shape of the antenna, nor any aspects of the platform. Thus, if the antenna is to be used on an automobile, the GA designs the antenna loads and matching network to optimize the characteristics of the antenna in the presence of that automobile without moving the antenna relative to the automobile or changing the length of the antenna. GAs are perfectly suited to this task because of the complexity of the problem and the massive multimodality of the search space.

2. Formulation

In this section, we outline a procedure for applying GAs to the design of loaded wire antennas residing on an arbitrary PEC platform. Although the action of the GA itself is quite simple, optimizing the design of a complicated physical system using GAs can be rather involved. In Section 2.2, we develop a fast MoM-based analysis to efficiently cope with the computational burden inherent in GAs. Finally, in Section 2.3, we discuss the problem of crafting the objective function for the GA optimization to achieve optimal results.

2.1. Genetic Algorithms

Genetic algorithms are a class of parallel, nonlinear stochastic optimization techniques that attempt to locate global optima of a function over a given domain. Based on Charles Darwin's theory of natural selection, GAs have been applied to very broad sets of problems ranging from antenna array design and optical filter design to classifier systems and neural nets [5].

GAs operate with just three basic operators: *reproduction*, *crossover* and *mutation*. In contrast to the operators governing more classical optimization procedures, these operators are stochastic in nature and are applied simultaneously to an entire population of candidate designs rather than deterministically optimizing just one design at a time. Application of these three operators to a population of design candidates results in a new population (called the next *generation*), which will on the average consist of better designs due to the evolutionary action of the operators. The GA applies these operators iteratively to each new generation until the population contains members that satisfy the design specifications or until no further genetic improvement of the members appears feasible.

To use the three basic operators, the GA requires all design candidates to be specified by a binary string, called a *chromosome*, which describes all of the salient features of a design. For example, our chromosomes will contain information which describes the values of the components in the antenna loads and their location. The GA starts by generating a randomly selected initial population containing N of these chromosomes of length N_l. The designs in the initial population are then evaluated by a *fitness* or *objective function* which allows the GA to compare the performance of the initial designs and reproduce the best ones for the next generation. This study employs a scheme known as random tournament selection. In random tournament selection, two members of the population are selected under a uniform random distribution, and the better one is placed into the next generation. The process is continued until the entire next generation population is filled [5].

After selection, the designs exchange traits through the action of the crossover operator. During crossover, the selected designs are paired randomly, and crossover is applied to these pairs with some predetermined probability p_c usually between 0.8 and 1. For each pair that is crossed over, a random crossover site is picked between the k^{th} and $k{+}1^{\text{th}}$ bits of each chromosome in the pair. The bits between the $k{+}1^{\text{th}}$ bit and the l^{th} bit are then exchanged yielding child chromosomes that are hybrids of their parents. Crossover enables the GA to search for better designs by mixing traits of good designs [5].

The mutation operator is applied to maintain the genetic variety in the population and to ensure against the loss of beneficial traits which may have been contained in poor designs in early generations, but which could later prove beneficial. The mutation operator simply changes the value of a bit in any given population member with a predetermined probability p_m usually between 0.001 and 0.01 [5].

In our GA implementation, the chromosomes describe the wire antenna loading and its matching network. The first part of each chromosome describes the positions and component values of the antenna loads. Assuming that the antenna carries a fixed number of N_A loads, this part of the chromosome consists of N_A concatenated strings, each describing a single load. The first portion of each string describes the position of a load on the antenna. If a load is permitted to reside on $N_T^A = 2^{N_P^A}$ distinct locations along the wire antenna, its position is described by N_P^A bits. N_P^A will naturally depend on the MoM discretization used in the evaluation of the antenna's gain and VSWR characteristics—see Section 2.2. The remaining part of each string describes the values of the components that compose the load. For each of the three component types—R, L, and C—the maximum and minimum values that the component can assume are fixed between two values $Q_{\max}$ and $Q_{\min}$, and the number of bits used for modeling the component is fixed at N_Q^A, where Q is either R, L, or C. Then, for each load, component values are calculated from their binary representations as using a geometric mapping.

The second part of the chromosome describes the topology and component values of the matching network. We assume that the matching network consists solely of reactive components. Though several schemes can be conceived for encoding a topology, a good scheme must ensure that similar designs are characterized by similar strings to prevent premature convergence. In this vein we assume the matching network consists of an integral number of four component sections as shown in Figure 2. The total number of components in the matching network, N_M, equals four times the number of sections. We then allow the L and C matching network components to take on values in the same way as the antenna loads do, i.e., by modeling them in terms of N_L^M and N_C^M bits. However, the matching network components described by these bits are also permitted to take on values of infinity or zero in addition to the finite values in between. Infinity and zero are coded in the GA, respectively, as the largest or smallest few binary numbers in the binary representation of the component value, and the finite values are decoded with a geometric spacing similar to the antenna components. Since capacitors with infinite capacitance act like shorts, and capacitors of zero capacitance act like opens (and vice versa for inductors), this coding scheme permits the matching network topology to evolve slowly, with similar "genotypes" producing similar "phenotypes". The sole disadvantage of this coding scheme is that typically the SGA will tend to use all available matching network components. To avoid the use of an excessive number of components, and to force the topology to evolve and be optimized, it is necessary to add a penalty term into the objective function that avoids the use of too many components. This will force the GA to select among all available components and find an optimal topology with a given number of elements—see Section 2.3.

2.2. Analysis of Candidate Antenna Designs

The above described GA optimization process typically requires a significant number of objective function evaluations. For the purpose of synthesizing loaded wire antennas that reside on an arbitrary platform, the objective function incorporates knowledge of the gain and VSWR of the antenna over the frequency band of interest—see Section 2.3. Given the antenna and platform geometry, this information

can be obtained by standard integral equation based techniques. However, because modeling the antenna and platform typically calls for hundreds or even thousands of unknowns, analyzing the antenna/platform over the entire frequency band for each design candidate often requires a prohibitive amount of computer time. To make the proposed synthesis method practical, the GA must evaluate the objective function efficiently.

A fast algorithm for rapidly computing the gain and VSWR of a design candidate can be devised because it is assumed that the shape of the antenna and platform always remain unchanged. For the purpose of analyzing the antenna using the MoM, the wire and its platform are approximated by straight segments of constant radius and planar triangular facets, respectively. The wire typically is attached to the surface at a vertex of a triangle, and is assumed to be excited by N_S voltage sources (we will typically assume $N_S = 1$) located at the nodes connecting two wire sections. Loads can be placed at any node except for those nodes occupied by a source or by another load.

Given this discretization of the wire and its platform, the antenna's electromagnetic response to any excitation can be computed using standard MoM techniques, e.g., the RWG method [6], which expands the wire and surface current into linear basis functions and models the current near a surface-wire junction using a special singular junction basis function. To facilitate the fast analysis of an arbitrarily loaded wire, the system's response caused by unit delta gap voltage excitations at every of the $N_S + N_T^A$ wire nodes is precomputed. Two different types of vector system response functions are of interest. The first set of such functions is $\mathbf{I}_k$, which contains the current at each of the $N_S + N_T^A$ nodes on the antenna due to a delta gap excitation in the k^{th} node. The second set of vector functions are labeled $\mathbf{E}_k$, and give the electric field at any far-field location requested for the gain computation due to unit voltage excitation in the k^{th} node. Computing $\mathbf{I}_k$ and $\mathbf{E}_k$, $k = 1,..., N_S + N_T^A$ requires the solution of the MoM equations for the unloaded system for multiple excitations.

Given $\mathbf{I}_k$ and $\mathbf{E}_k$, the GA solves for the currents on an arbitrarily loaded antenna and computes its far fields as follows. Assume that the N_S sources and N_A loads are located in nodes $s(i)$, $i = 1,..., N_S$, and $l(i)$ $i = 1,..., N_A$, respectively. The vector $\mathbf{I}_{tot}$ containing the total current at each wire node containing a load is given by

$$\mathbf{I}_{\text{tot}} = \sum_{i=1}^{N_s} V_{s(i)} \mathbf{I}_{s(i)} + \sum_{i=1}^{N_l} V_{l(i)} \mathbf{I}_{l(i)} \tag{1}$$

where V_k signifies the voltage excitation on segment k. Noting that

$$V_{l(i)} = -Z_{l(i)} I_{tot,l(i)} \tag{2}$$

where Z_k is the load impedance on segment k and $I_{tot,k}$ is the total current on segment k, the $l(j)^{\text{th}}$ row of (1) becomes

$$I_{\text{tot}_{l(j)}} = \sum_{i=1}^{N_s} V_{s(i)} I_{l(j),s(i)} - \sum_{i=1}^{N_l} Z_{l(j)} I_{tot_{l(j)}} I_{l(j),l(i)} \tag{3}$$

Collecting all rows $l(j)$ into a matrix equation and then moving all terms involving $\mathbf{I_{tot}}$ to the left-hand side yields

$$(\bar{\bar{\mathbf{I}}} + \mathbf{Z_{eff}})\tilde{\mathbf{I}}_{\text{tot}} = \mathbf{V_s} \tag{4}$$

where $\bar{\bar{\mathbf{I}}}$ is the $N_A \times N_A$ identity matrix, $\tilde{I}_{tot_i} = I_{tot_{l(i)}}$,

$$Z_{eff_{i,j}} = Z_{l(j)} I_{l(i),l(j)} \tag{5}$$

and the components of $\mathrm{V_s}$ are given by

$$V_{s,j} = \sum_{i=1}^{N_s} V_{s(i)} I_{l(j),s(i)} \tag{6}$$

Solving Equation (4) for $\tilde{\mathbf{I}}_{tot}$ gives the current through each of the loads. Now using superposition, we may calculate the far fields due to the source excitation in combination with the voltages at the loads,

$$\mathbf{E}_{\text{tot}} = \sum_{i=1}^{N_s} V_{s(i)}\mathbf{E}_{s(i)} - \sum_{i=1}^{N_l} Z_{l(i)}\tilde{I}_{tot_{l(i)}}\mathbf{E}_{l(i)} \tag{7}$$

We can also determine the current (and hence impedance) at the input. Thus, using this technique, we circumvent inverting the entire MoM matrix for each design, replacing the problem with the inversion of a matrix with dimension $N_A \times N_A$. Given the input impedance of the antenna over the band, the VSWR is calculated assuming that the transmitter feed is connected to a transformer which steps up the impedance to the average impedance of the antenna-matching network combination over the band. Since this may always be done, this makes the matching network design completely independent of the value of the impedance of the transmitter (except for the turns ratio in the transformer). The VSWR at each frequency can thus be calculated assuming the presence of this transformer.

2.3 Design of Objective Functions

Perhaps the most important element in the successful implementation of a GA is the careful design of the objective function which can enhance or hinder the algorithms performance. For all of our designs, the objective function, F_{tot}, is composed as a sum of two parts: a basic part (F_{bas}) and a penalty part (F_{pen}). F_{bas} single-mindedly attempts to improve the gain and the VSWR at every test frequency in the band, while F_{pen} is incorporated to speed convergence, flatten frequency response, and strike a judicious balance between the often competing goals of high gain and low VSWR. F_{bas} is a monotonic function of the overall antenna system gain in a desired direction, and thus really represents the whole of our concern. F_{pen} consist of four parts: Designs are punished separately for (i) very low gains, (ii) very high VSWRs, for (iii) uneven frequency response, and (iv) for using an excessive number of elements in the matching network. The first two penalties aid F_{bas} directly by ensuring that VSWR is not sacrificed for gain or vice-versa. The third penalty helps the code find designs with low VSWRs and the last penalty encourages evolution of the network topology.

3. Numerical Results

In this section, several results will be presented that illustrate the application of the above described algorithm to the design of whip antennas mounted on a tank.

Finally, to test the GA method on a more realistic problem, we design a monopole antenna for the tank of Figure 3 over the 15-60 MHz band. In this example, capacitances were allowed to vary from 10 to 1110 pF, while inductors varied from 30 to 5000 nH. The upper frequency limit was dictated by the dimensions of the MoM matrix describing the tank and the monopole. Also, because we do not expect the radiation from the tank monopole to be the same in all directions, we optimized its pattern simultaneously in three directions: in front of the gun, behind the gun, and perpendicular to the gun. Incorporating more than one angle into the design is trivial; we simply took the average value over the set of angles of interest. The resulting matching network is pictured in Figure 4; all load values are given in Figure 3. The gain and VSWR of the optimal design are shown in Figure 5. These are compared to a result obtained on the same problem using Simulated Annealing (SA) [7]. Though SA was allowed more function evaluations than the GA, the design it evolves is inferior.

4. Conclusions

This study presented a systematic approach to the design of loaded wire antenna/matching network systems residing in a realistic environment. The process was made possible via a technique involving a precalculation of the response of an unloaded antenna system to excitation at different points along the wire and included a method to incorporate the matching network topology into the design process. The procedure was then successfully applied to a series of realistic problems with very little tuning of the

objective function. In all of these problems, even those radiating on complex structures or with very large bandwidths, an acceptable design was arrived at efficiently making this procedure a robust and reliable method for the design of wire antennas radiating on a given platform.

5. Acknowledgments

The authors would like to thank the University of Illinois Research Board and the National Science Foundation for funding this project and J.Veihl for allowing the authors to use his tank model.

References

[1] H. E. Pocklington, "Electrical oscillations in wires, " *Cambridge Phil. Soc. Proc.*, vol. 9, pp.324-32, 1897.

[2] K. Hirwasa and M. Haneishi, *Analysis, Design and Measurement of Small and Low Profile Antennas*. Artech House, 1992.

[3] B. C. Popovic, *CAD of Wire Antennas and Related Radiating Structures*. Somerset, England: Research Studies Press, 1991.

[4] A. Boag, A. Boag, E. Michielssen and R. Mittra, "Design of Electrically Loaded Wire Antennas Using Genetic Algorithms," *IEEE Trans. Ant. Propag.*, submitted.

[5] David E. Goldberg, *Genetic Algorithms in Search, Optimization and Machine Learning*. Reading, Massachusetts: Addison-Wesley Publishing Company, Inc., 1989.

[6] S. M. Rao, "Electromagnetic radiation and scattering from a system of conducting bodies interconnected by wires," Ph.D. dissertation, University of Mississippi, 1980.

[7] S. Kirkpatrick, J. C. D. Gelatt, and M. P. Vechi, "Optimization by simulated annealing," *Science*, vol. 220, pp.671-80, 1983.

Figures

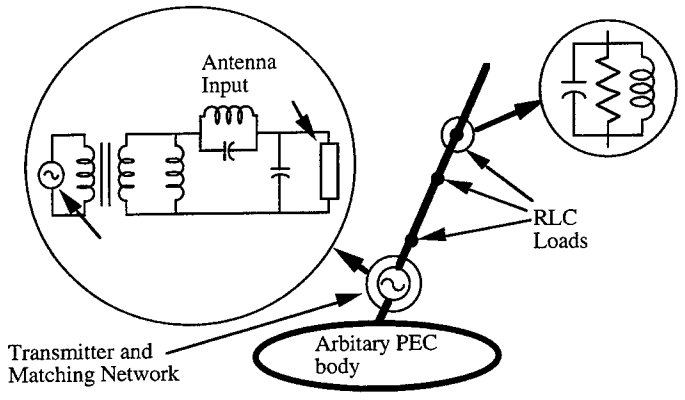

Figure 1. The design problem at hand.

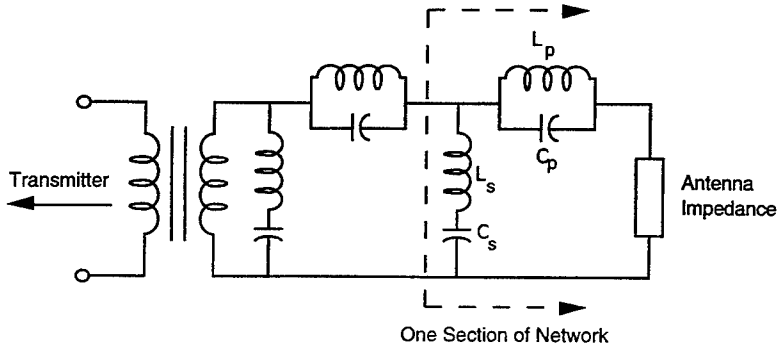

Figure 2. Generalized topology for matching network design.

Simulated Annealing Design				
Load No.	Location (cm)	Resistance (Ω)	Capacitance (pF)	Inductance (nH)
1	84.6	31.6	173.	783.
2	107.7	474.	119.	4430
3	161.5	16.8	362.	1680
4	392.3	423.	10.8	1080
5	446.1	5.01	37.9	199.

Genetic Algorithm Design				
Load No.	Location (cm)	Resistance (Ω)	Capacitance (pF)	Inductance (nH)
1	226.6	1500	706.	36.7
2	257.8	1500	76.6	244.
3	273.4	238.	59.1	3930
4	289.1	1500	76.6	753.
5	320.3	1500	107.	2420

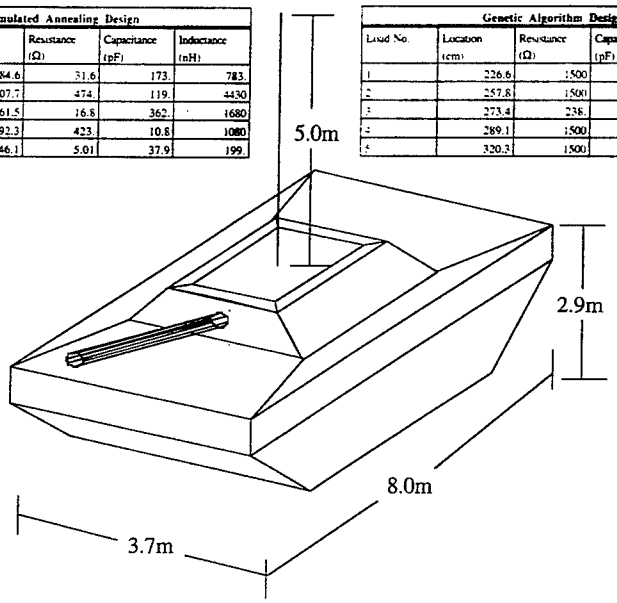

Figure 3. Tank geometry with designs optimized by GA and SA.

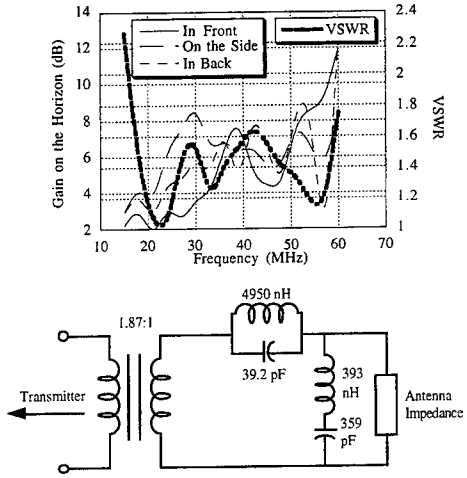

Figure 4. Matching network and response of GA design.

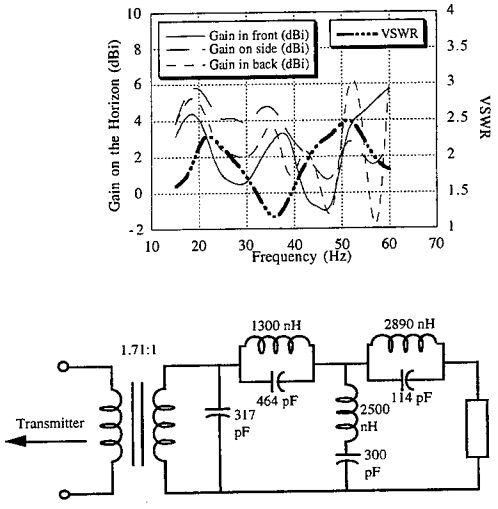

Figure 5. Matching network and response of simulated annealing design.

Genetic Algorithms Based Pattern Synthesis Approach for Arbitrary Array Design

Yilong Lu and Keen Keong Yan

School of Electrical and Electronic Engineering
Nanyang Technological University
Singapore 639798

I. Introduction

In array pattern synthesis, the main concern is to determine the complex excitation coefficients (weights) of radiators to have desired pattern characteristics, such as maximum radiation direction, specified beamwidth and sidelobe level. Most of the traditional analytical and numerical techniques are not flexible and limited to simple linear or planar arrays; moreover the resulting phase and magnitudes of complex excitation coefficients are usually irregular so that costly customized components are needed. In this paper, we present a flexible pattern synthesis approach based on the genetic algorithm for array pattern synthesis of arbitrary array.

Genetic Algorithm (GA) [1],[2] is a stochastic search and optimization technique modeled on the mechanics of natural evolution and genetics rather than a simulated reasoning processing. GAs are randomized but not random, they can efficiently exploit historical information to speculate on new search points with expected improved performance. Most of the traditional optimization methods are prone to local minima [2], GAs are able to test for solutions outside the current minimum due to their random components and large sampling population. Although GAs may converge slowly and not suitable for real-time application, they can still be very useful and flexible for the design of non-adaptive antennas.

GAs were introduced to array applications just two or three years ago. Haupt [3] applied GA to determine which element should be on in the large thinned linear and planner array in order to obtain low sidelobes. Tennant [4] used GA to steer the array nulls precisely to the required interference directions and to achieve prescribed null depths by element position perturbations. Shimizu [5] used GA to determine the required values for the digital phase shifters so as to control the phases of the excitation coefficient. However, these applications [3]-[5] share the same approach, in which only binary parameters are used. For examples, Haupt used "1" and "0" to switch on and off a radiator respectively, and Shimizu used the binary combination in activating the digital phase shifter.

The approach that we propose treat directly real or complex numbers. This approach can be applied not only to pattern synthesis of array factors or simplified total radiation pattern but also to optimization for complicated model taking into account the mutual coupling among radiators and the effects of environment when used together with a realistic simulator. In addition, the phase and/or magnitude values can be restricted to certain discretized (digital) values for easy implementation by commercially available digital phase shifters and digital attenuators so as to reduce greatly the complexity and cost of array antennas. Examples of linear and curved arrays will be shown to demonstrate the effectiveness of this approach.

II. The Genetic Algorithm

Genetic Algorithms are search and optimization techniques modeled on the mechanics of natural evolution of living beings. Evolution takes place on *chromosomes* - organic devices for encoding the structure of living beings. A living being is created partly through a processing of *decoding* chromosomes. A standard GA can be briefly described using the flow chart in Fig. 1.

A. Construction of Chromosomes and Initial Population

In this approach for array pattern synthesis, radiation patterns correspond to living being and a set of excitation coefficients corresponds to a chromosome.

GA was invented to manipulate string of binary coding. Most of the published GA applications encode the parameters in binary strings (*chromosomes*) and perform binary genetic operations. In our GA for array pattern synthesis, parameters are encoded in terms of real or complex numbers directly, that is, a chromosome $\boldsymbol{c}$ is directly represented by a vector of complex numbers (including integers and real numbers)

$$\boldsymbol{c} = [c_1 \; c_2 \ldots c_n \ldots c_N], \quad c_n \in C_n \tag{1}$$

where c_n known as a genetic material in GA here represents the excitation of the n-th radiator and C_n is the set or a subset of all complex numbers, in other words, C_n can be a set of some integers or real numbers or complex numbers or their mixed combination. The length of the vector is equal to the number of array radiators. This simple encoding explicitly shows the relations between chromosomes and array excitations and therefore it is simple, flexible, and easy to implement.

Before starting the GA cycles, the initial population can be prepared by simply selecting random and/or approximate (by other simple techniques) and/or any guess (based on experience) excitations.

B. Decimal Genetic Operations

A simple genetic algorithm is composed of three basic genetic operations: *reproduction*, *crossover*, and *mutation.*

Reproduction is a process in which individual chromosomes are selected for copying according to their objective function values. Hence the more highly fit chromosomes have higher chances of being selected for producing the child for the succeeding generation. In reproduction, two *parent* chromosomes are selected to produce two new or *child* chromosomes. From the current population, pairs of chromosomes are selected as parents for the next reproduction. Ranking Selection is applied to choose the couple according to their ranking, i.e., getting the first and the last ones, the second and second last, and so on.

Crossover is another process that involves partial exchange of information between two chromosomes. Crossover recombines parts of the genetic materials in two parent chromosomes to make two child chromosomes. Taking one point crossover for example, each parent chromosome is split at a crossover point into two portions, a fragment and a remainder. As shown in Fig. 2, the fragment or remainder of one parent chromosome is swapped with the fragment or remainder of the other parent chromosome to produce two child chromosomes. By

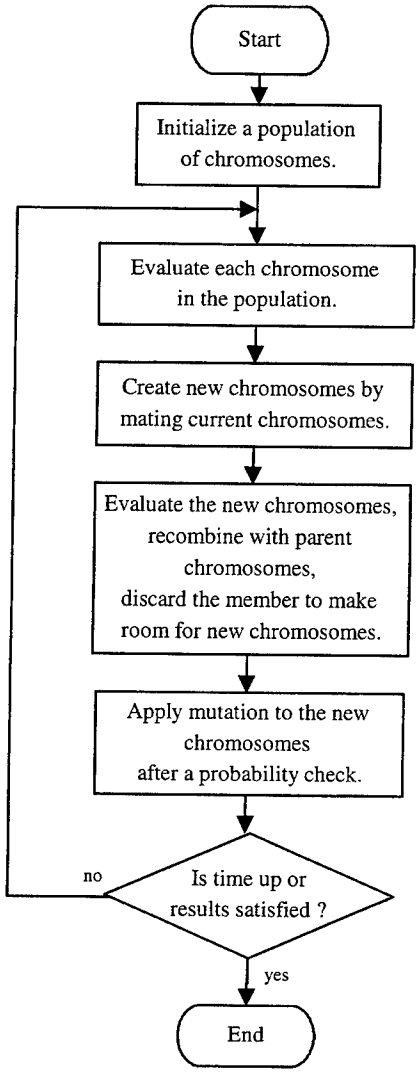

Fig. 1. Steps of a Genetic Algorithm.

just swapping the fragments of the parents is not good enough for real/complex number coding, hence the concept of *linear crossover* is adopted to provide a more logical approach. For example, from two points (genetic materials), p_1 and p_2, three new points can be generated from crossover I: $(p_1+p_2)/2$, crossover II: $(p_1+3p_2)/4$, and crossover III: $(3p_1+p_2)/4$. Crossover I gives the (average) midpoint of p_1 and p_2, and the other two give points shifting $\pm|p_1-p_2|/4$ from the midpoint. If both points, p_1 and p_2 are identical, the new points will be the same as p_1 or p_2, and no new move is tested for this couple. Fig. 3 shows how the six child chromosomes are produced after the linear crossover. In the example shown in Fig. 3, six children are produced by two parents, but only two best children will be selected to compete for survival to next generation.

Parent X :	**0.83**	**1.00**	0.94	0.97	0.96	Child X :	**0.79**	**0.97**	0.94	0.97	0.96
	Fragment		Remainder								
Parent Y :	**0.79**	**0.97**	0.91	0.97	0.93	Child Y :	**0.83**	**1.00**	0.91	0.97	0.93

Fig. 2. Example of one point cross over.

Parent P1 :	**0.45**	**0.70**	**0.82**	**0.92**	1.00	1.00	0.95	0.82	0.70	0.45	
Parent P2 :	**0.50**	**0.50**	**0.50**	**0.92**	1.00	1.00	0.50	0.50	0.50	0.50	
Child A :	**0.48**	**0.60**	**0.66**	**0.92**	1.00	1.00	0.95	0.82	0.70	0.45	crossover I
Child B :	**0.48**	**0.60**	**0.66**	**0.92**	1.00	1.00	0.50	0.50	0.50	0.50	
Child C :	**0.49**	**0.55**	**0.58**	**0.92**	1.00	1.00	0.95	0.82	0.70	0.45	crossover II
Child D :	**0.49**	**0.55**	**0.58**	**0.92**	1.00	1.00	0.50	0.50	0.50	0.50	
Child F :	**0.46**	**0.65**	**0.74**	**0.92**	1.00	1.00	0.95	0.82	0.70	0.45	crossover III
Child F :	**0.46**	**0.65**	**0.74**	**0.92**	1.00	1.00	0.50	0.50	0.50	0.50	

Fig. 3. Example of one point linear cross over.

Once the children population is formed and their fitness is evaluated for selection of suitable chromosomes for the next new generation. There are a few selection techniques available. In our approach, both the children and parent population are ranked together in the ascending order (for example, from the lowest sidelobe level to the highest sidelobe level). Then based on the principle of survival of the fittest, those producing superior output survive, while those producing weak output die off. Please note that the competitors of survival selection include both parents and their children so that the members of next generation may include members of the previous generation. This guarantee that the newer generation performs better than old ones. It also means no oscillation in the optimization convergence curves.

Mutation plays a secondary role in GA. Reproduction and crossover effectively search and recombine extant useful genetic materials and occasionally they may become overzealous and lose some of these potential materials. So mutation is needed to protect against such an

irrecoverable loss. Mutation is carried out by intentionally altering one or more genetic materials in a chromosome. In optimization, it corresponds to prevention of the algorithm of being stuck in a local minimum. Mutation is only carried out when a chromosome passes a probability check. When it does, one or a few randomly selected genetic materials of the chromosome are replaced with other randomly generated genetic materials. Generally, mutation does not improve the solution, but it is essential. It should be noted that mutation can be done before or after the selection of the next population.

C. Two Stage GA Optimization for Accurate and Efficient Solution

For accurate and efficient solution, two-stage GA optimization can be adopted. In stage 1, the GA works with a fast approximate pattern evaluation formula based on a simple array antenna model. Then, the preliminary results from stage 1 are used as the initial population for stage 2.

If satisfactory result is not achieved after a certain number of iterations, it is suggested to start the optimization again for more effective and efficient solution. In our experience, 100 generations (iterations) is sufficient for each trial and more iteration will not help much to converge. The re-start helps the algorithm to begin with another search direction. Because of the randomness, the result will not be identical for each re-start. Thus several trials of a fixed number of iterations each may be necessary.

In stage 2, the GA works with an accurate pattern simulator, based on a more realistic model, to fine tune the excitation coefficients. For example, mutual coupling among radiators and reflector can be taken into account if NEC [6] is used. Moreover, the initial population for stage 1 can be a combination from different fast approximations including simple optimization techniques and guesses based on experience. Better initial population will considerably speed up an optimization.

III. Examples

The GA described above has been successfully applied to various arrays, including uniform/nonuniform spaced linear/curved arrays. Two examples are shown here to demonstrate the usefulness and flexibility of the approach for array pattern synthesis.

1. Linear array with main beam at 100°

A linear array of 30 isotropic elements equally spaced at half wavelength is considered. A pattern with the main beam aiming at the angle of 100° from the array axis and with the half power beamwidth of 5° and the lowest possible sidelobe level is desired. The initial population consists of six sets of complex excitation coefficients generated by the Minimization Mean Square Error (MMSE) method. The fitness (sidelobe level) of the initial population is ranging from –13.19 dB to –25.32 dB. 10 trials of 100 iterations each are carried out for the example.

After 10 trials, the overall results show that the genetic algorithm works well for this example and sidelobe level of about –38 dB can be achieved. The best radiation pattern in the initial population and obtained after 10 trials of the GA are shown in Fig. 4 and Fig. 5, respectively.

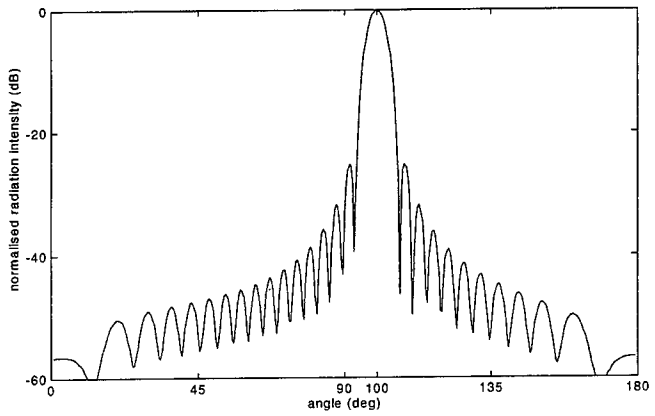

Fig. 4. Best radiation pattern in the initial population.

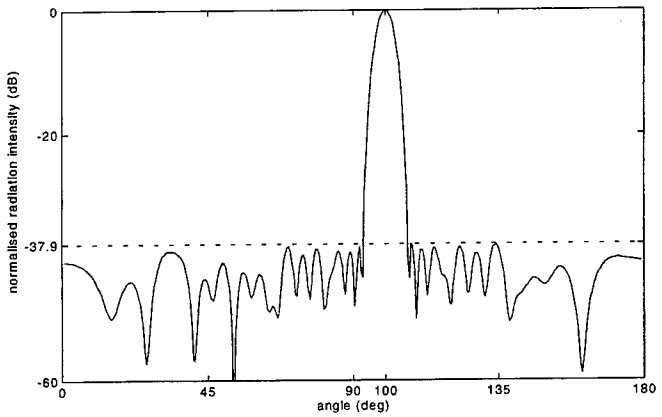

Fig. 5. Best radiation pattern from 10 trials of the GA.

2. Cylindrical Arc Array with Digital Phases

In the second example, we consider a curved phased array consisting of 32 half-wavelength dipoles around an electrical conducting cylinder of radius 5 wavelength. At any one time, only 16 dipoles are activated to form the desired beam. The geometry of the array is shown in Fig. 6. The desired pattern should have half power beamwidth less than 15° and sidelobe level less than −25 dB. Furthermore, the phases of the excitations are required to be equal to values suitable for 6-bit digital phase shifters, that is, multiples of 11.25°.

The optimization using the GA is done in two stages. In stage 1, GA works with the simple approximated pattern evaluation formula (2)

$$E(\theta,\phi)=\sum_{n=1}^{16} c_n e^{jka\sin\theta\cos(\phi-(n-\frac{1}{2})\Delta\phi)} A(\phi-(n-\tfrac{1}{2})\Delta\phi) \quad , \qquad (2)$$

where $A(\phi)=0.5(1+\cos\phi)$ is the approximated element pattern, c_n the excitation coefficient of the n-th dipole, k wave number, a radius of the circle, and $\Delta\phi=\pi/32$ angular difference between adjacent elements.

The results from stage 1 are then used as the initial population of stage 2 for fine tuning. In stage 2, the GA works with the realistic and accurate moment method based EM field simulator NEC-2 [6] taking in account of the mutual interaction among dipoles as well as the reflective surface of the cylinder.

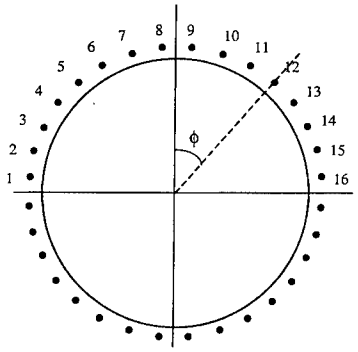

Fig. 6. Geometry of a cylindrical arc array with 32 dipoles but only dipoles 1 to 16 are activated.

The GA helps to determine a set of excitation coefficients for the cylindrical arc array to design the desired pattern. Fig. 7 shows the pattern produced from the GA/NEC-2 approach. The solutions obtained through the use of GA work well even when the mutual interaction effects are taken into account. Again from Table 3, it can be observed that the phases of the coefficients are restricted to only in multiples of 11.25°.

Table 3: Normalized excitation coefficients with "digital" phases.

Element	Excitation coefficients
1 & 16	0.05 ∠–90.00°
2 & 15	0.12 ∠ 33.75°
3 & 14	0.18 ∠–157.50°
4 & 13	0.19 ∠45.00°
5 & 12	0.29 ∠–45.00°
6 & 11	0.65 ∠–146.25°
7 & 10	0.89 ∠135.00°
8 & 9	1.00 ∠101.25°

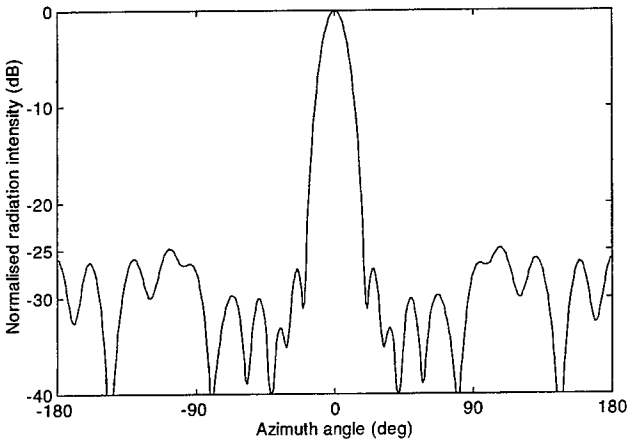

Fig. 7. Radiation pattern of the final GA/NEC-2 results.

IV. Conclusion

The GA has been successfully applied in pattern syntheses of linear and curved arrays. The algorithm can also be applied to pattern synthesis of arbitrary arrays which are difficult to be treated by other analytical or numerical methods. The algorithm is capable of directly treating both real and complex data.

The phase or magnitude values can be confined to certain discretized (digital) values for easier and more cost effective implementation by commercially available digital phase shifters and digital attenuators. This would greatly reduce the complexity and cost of (phased) array antennas.

References

[1] G.J.E. Rawlins, (Ed), *Foundations of Genetic Algorithm*, San Mateo, CA: Morgan Kaufmann Publishers, 1991, pp 211-213.

[2] L. Davis, (Ed), *Handbook of Genetic Algorithms*, Van Nostrand Reinhold, New York, 1991.

[3] R.L. Haupt, "Thinned Arrays Using Genetic Algorithms," *IEEE Trans. Antennas Propagat.*, Vol. 42, Jul. 1994, pp. 993-999.

[4] A. Tennant, M.M. Dawoud, A.P. Anderson, "Array Pattern Nulling by Element Position Perturbations using a Genetic Algorithm," *Electronics Letters,* Vol. 30, No. 3, Feb. 1994, pp. 174-176.

[5] M. Shimizu, "Determining the Excitation Coefficients of an Array using Genetic Algorithms," *Proc. 1994 IEEE AP Int. Symposium*, pp. 530-533.

[6] J. Burke and A. J. Poggio, *Numerical Electromagnetics Code (NEC) - Method of Moment*, Lawrence Livermore Labroratory, Jan. 1981.

SPEEDING CONVERGENCE OF GENETIC ALGORITHMS FOR OPTIMIZING ANTENNA ARRAYS

Randy L. Haupt
Department of Electrical Engineering
HQ USAFA/DFEE
2354 Fairchild Dr, Suite 2F6
USAF Academy, CO 80840-6236
email: haupt@shelter.usafa.af.mil
719/472-3190 (work)
fax: 719/472-3756

Abstract.

Numerically optimizing antenna array performance can be time consuming. Genetic algorithms have shown great success in finding amplitude and phase tapers for low sidelobe antennas. One way to speed convergence of the algorithms is to encode the parameters with a gray code. A gray code representation has a hamming distance of one and is less likely to be disturbed during crossover operations of the genetic algorithm. This paper explains when the gray code is appropriate to use for antenna array optimization, while demonstrating a simple derivation of optimum low sidelobe amplitude tapers.

Introduction.

The goal of this paper is to optimize the amplitude taper of a linear array in order to minimize the maximum sidelobe level. Many analytical methods exist to accomplish this goal, so why use a numerical method? There are two reasons. First, the analytical methods do not optimize subject to practical constraints, such as scan angles and bandwidth. Second, errors and array alignment problems make theory difficult to implement in practice.

The approach taken in this paper is to use a genetic algorithm to find the optimum amplitude weights. A genetic algorithm is a computer program that optimizes the output of a function by simulating evolution in nature [1]. Most traditional optimization methods rely on derivative information and easily get stuck in local minima. Genetic algorithms efficiently search the very large but finite output space to arrive at a "global" minimum.

Genetic algorithms are beginning to be used for many different applications in electromagnetics. In particular, absorber [2],[3] and antenna array designs [3],[4] have been fertile grounds for this approach. Their attraction stems from several advantages: They

1. optimize with discrete parameter,
2. optimize well with a large number of parameters,
3. explore a vast portion of the cost surface,
4. do not require derivative information, and
5. are ideal for parallel processing.

This paper examines the use of a gray code representation of the parameters in a genetic algorithm [4]. First, the motivation for the use of gray codes is provided. Then, various examples are presented to show when gray codes can enhance genetic algorithm performance.

Problem Formulation.

The linear array is modeled by

$$ff(\phi) = \underbrace{\frac{1}{2N}\sum_{n=1}^{N} a_n \cos[(n-.5)\Psi]}_{\text{array factor}} \underbrace{\sin\phi}_{\text{element pattern}}$$

where

a_n = amplitude weight at element n
$2N$ = number of elements in the array
$\Psi = kd(u-u_0)$
$k = 2\pi/\text{wavelength}$
d = spacing between elements
$u - u_0 = \cos\phi - \cos\phi_0$
ϕ = angle from x-axis or from the array face
ϕ_0 = steering angle

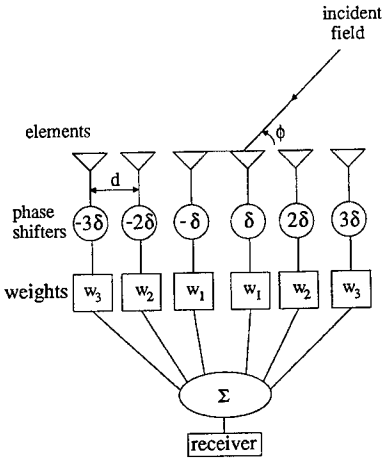

Figure 1. Diagram of a linear array.

A diagram of the array is shown if Figure 1. The elements have a sinϕ element pattern and a symmetric amplitude taper.

The Genetic Algorithm.

The genetic algorithm encodes the array weights in a binary sequence called a gene and places the genes in an array known as a chromosome. The algorithm generates a random matrix of ones and

zeros where each row of the matrix is a chromosome. Next, the cost function for each chromosome is calculated. Cost is a function of far field pattern features, such as maximum sidelobe level, and is a quantity to be minimized. The chromosomes are ranked from the least to the most cost. Mating takes place between chromosomes that have small enough costs to be part of the mating pool. Offspring or new chromosomes produced from mating contain parts of the two parents. The crossover function randomly picks a point in the chromosome. Mating takes place by keeping the binary strings to the left of the crossover point for each parent and swapping the binary strings to the right of the crossover point. Consider two parent chromosomes (Only one gene in each chromosome and its corresponding parameter value is shown.) given by

chromosome parameter value

parent #1 = [...10000000...] = [...128...]
parent #2 = [...01111111...] = [...127...]

One gene in the chromosome is split by the crossover operation. The offspring resulting from a crossover point between bits three and four are given by

offspring #1 = [...10011111...] = [...159...]
offspring #1 = [...01100000...] = [...96...]

The fitness of the new offspring are computed. Mutations change a small percentage of the bits from "1" to "0" or visa versa. The new list is ranked from best to worst and the process repeated. The algorithm stops when an acceptable solution is found or a set number of iterations has lapsed.

The parameters of the genes that are split by the crossover operation in the above examples have decimal representations of 128 and 127. Note that the parameter representations and, most likely, the costs are very close, but the binary representations are exactly opposite. Consequently, the offspring that result from the parents are quite different. In this case, the parameter values change to 159 and 96. The parameter values should be converging, but they are not. This example is an extreme, but not unlikely example. Increasing the number of bits in the parameter representation magnifies the problem.

One way to avoid this problem is to encode the parameters using a gray code. Consider the previous example using a gray code. A binary representation of 10000000 has a gray code of 11000000 and mates with a binary representation of 01111111 having a gray code of 01000000. The children are given by 01000000 and 01100000, which are the same as the parents! By definition, the parents are good solutions. Thus, we would expect the offspring to be good solutions too - which occurs when a gray code is used.

The above argument indicates that gray codes speed convergence time. Speeding convergence of antenna optimization problems is very important, because the numerical calculations take a long time. The next section compares optimization using a genetic algorithm with and without gray codes.

Results.

As an example, consider optimizing the amplitude taper of a 40 element linear array with elements spaced .5 wavelengths apart in order to reduce the relative sidelobe levels between u = .6 and u = 1. The genetic algorithm started with an initial population of 500. Only 200 chromosomes were kept

each iteration and 25% of these were placed in the mating pool. The algorithm stopped after 100 iterations.

The first example uses a ten bit encoding of the amplitude weights. Figure 2 is the convergence graph for the genetic algorithm without gray coding, and Figure 3 is the convergence graph for the genetic algorithm with gray coding. The solid line represents the cost of the best chromosome and the dashed line is the average cost of all the chromosomes. Iteration 0 is the cost of a uniform array. In general, using the gray code does not work as well as not using a gray code. Figure 4 shows the optimized amplitude weights, and Figure 5 shows the resulting far field pattern.

Increasing the number of bits representing the amplitude parameters significantly changes the situation. For instance, using a 20 bit representation of the amplitude weights results in the convergence graphs in Figures 6 and 7. In general, gray codes improve genetic algorithm performance when many bits are used to represent a parameter.

The amplitude taper is not smooth in Figure 4. Changing the cost function from the maximum sidelobe level to

$$\text{cost} = \max \text{ sll in dB} - \Sigma a_n/(2N) + 10\Sigma(a_n - a_{n+1})^2 + 10\sigma_a$$

where σ_a is the standard deviation of the weights, improves the smoothness of the amplitude taper. Figure 8 shows the optimized amplitude weights, and Figure 9 shows the resulting far field pattern. The new cost function lowers the sidelobe level over the specified angles while keeping the amplitude taper smooth.

Conclusions.

Using a gray code for antenna array optimization is only important when more than ten bits represent the parameters. Since many antenna optimization problems do not require this accuracy, the gray code can be skipped.

Genetic algorithms do not always produce desirable results at first, because the cost function is not carefully considered. Adding additional smoothing costs produces a more desirable amplitude taper.

References.

[1] J. H. Holland, "Genetic algorithms," Sci. Amer., pp. 66-72, Jul 92.

[2] E. Michielssen, et.al, "Design of lightweight, broad-band microwave absorbers using genetic algorithms," IEEE MTT Trans., Vol. 41, No. 6/7, pp. 1268-1271, Jun/Jul 93.

[3] R. L. Haupt, "An introduction to genetic algorithms for electromagnetics," IEEE Antennas and Propagation Magazine, Vol. 37, No. 2, pp. 7-15, Apr 95.

[4] R. L. Haupt, "Optimum quantized low sidelobe phase tapers for arrays," IEE Electronics Letters, Vol. 31, No. 14, pp. 1117-1118, 6 Jul 95.

[5] J. Meitkoetter and D. Beasley, eds. "The Hitchhiker's Guide to Evolutionary Computation: A List of Frequently Asked Questions (FAQ),", USENET: comp.ai.genetic.

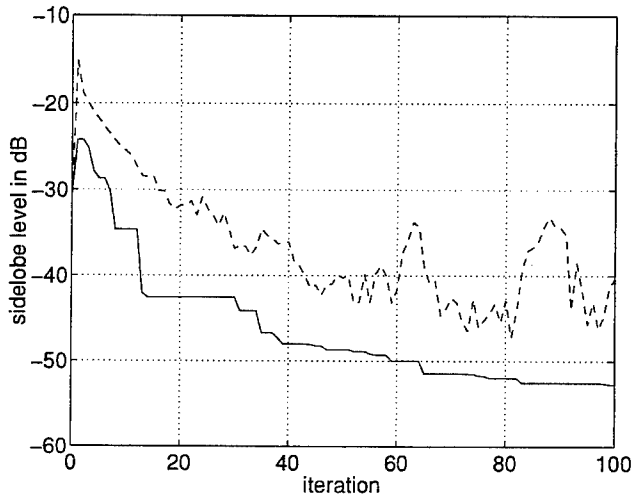

Figure 2. Convergence of the genetic algorithm without a gray code for a 10 bit representation of the amplitude weights.

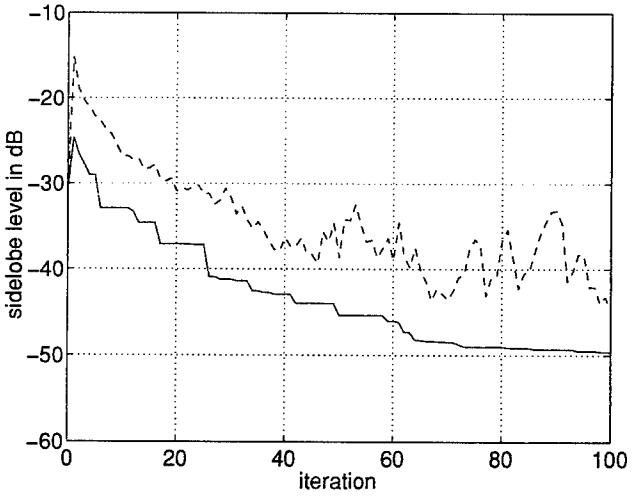

Figure 3. Convergence of the genetic algorithm with a gray code for a 10 bit representation of the amplitude weights.

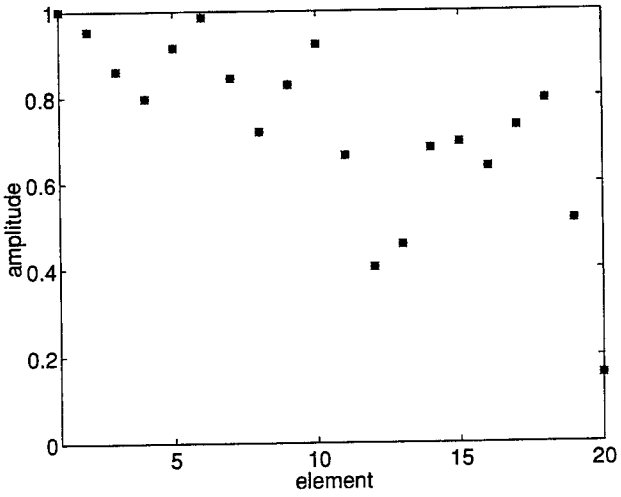

Figure 4. Optimized amplitude taper from genetic algorithm without a gray code.

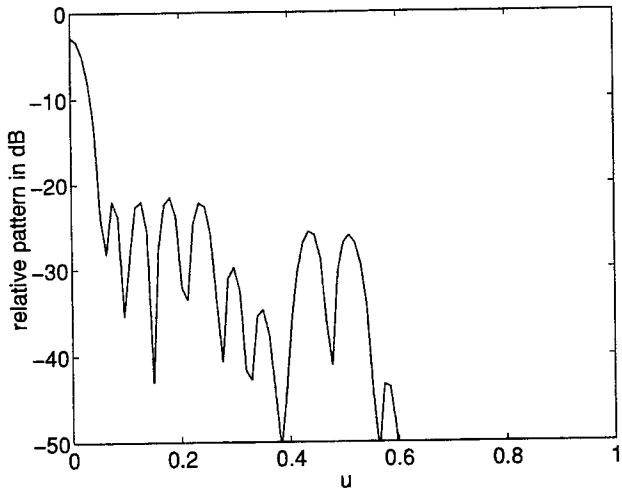

Figure 5. Optimized far field pattern from genetic algorithm without a gray code.

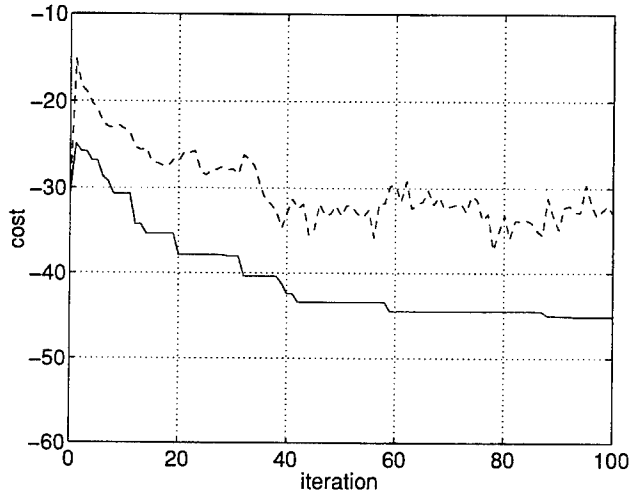

Figure 6. Convergence of genetic algorithm without a gray code for a 20 bit representation of the amplitude weights.

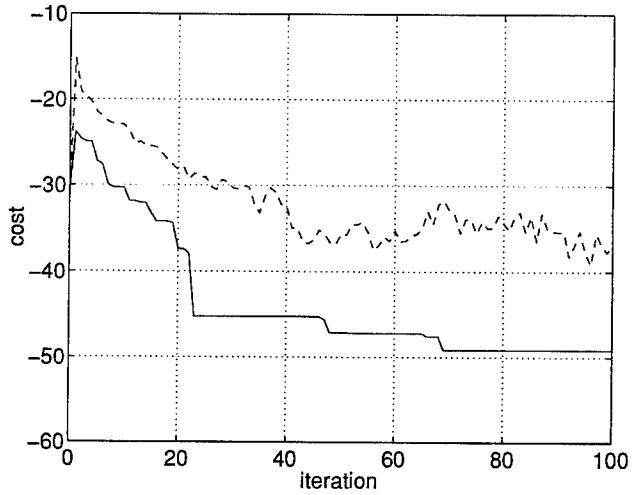

Figure 7. Convergence of genetic algorithm with a gray code for a 20 bit representation of the amplitude weights.

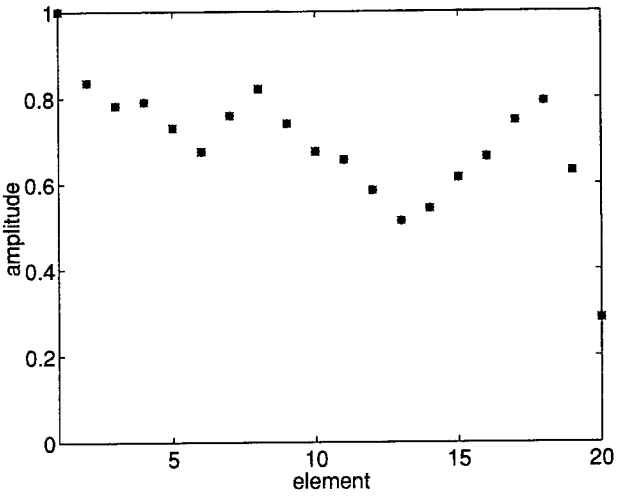

Figure 8. Amplitude taper resulting from a modified cost function.

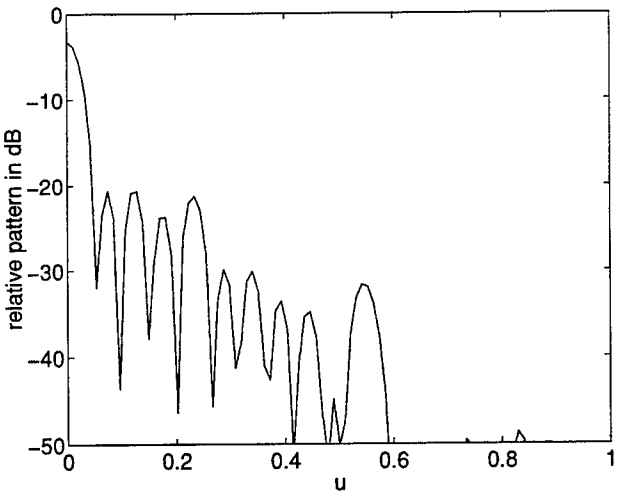

Figure 9. Far field pattern resulting from the amplitude taper in Figure 8.

Order Recursive Method of Moments for Iterative Design Application

Krishna Naishadham and Pradeep Misra
Department of Electrical Engineering
Wright State University
Dayton, OH 45435

email: knaish@gamma.cs.wright.edu
tel.: (513)873-5057
fax: (513)873-5009

Abstract

An order-recursive variant of standard LU decomposition has been presented for the efficient solution of linear systems arising in the application of method of moments to iterative design problems. The method is applied to the iterative design (or tuning) of dual band patch antennas, which are of potential interest in mobile communications systems.

1 Introduction

Multi-band conformal patch antennas find application in mobile communications systems because of their light weight, low profile and ease of fabrication. It is well-known that rectangular microstrip patch antennas with reactive stubs placed along the radiating edges exhibit dual frequency operation [1], [2]. Electromagnetic (EM) simulation methods such as the method of moments (MoM) and the multiport network model facilitate the design and tuning of such elements in a rapid prototyping environment.

In MoM, the boundary value problem for the unknown current distribution over the surface of the conductors is typically formulated as an electrical field integral equation (EFIE). The EFIE is then converted into a system of linear algebraic equations (for the current) by the application of suitable basis and testing functions. Parameters of interest, such as S-parameters, radiation and metallization losses, can be derived from the computed current distribution.

The system (or moment) matrix that represents the interactions between the basis and the test elements is typically dense. For moderately high-order models ($\mathcal{O}(200 - 300)$), the current distribution may be obtained as the solution of a system of linear algebraic equations using LU decomposition and subsequent solution of two triangular systems of equations. The computational complexity of the solution of system

of equations of order N is N^3. For several applications, where N is fixed, the use of conventional LU decomposition provides an efficient means for solving the linear systems.

However, in design applications, the order of the linear system to be solved may change from N to $N + M$, where the original $(N \times N)$ data matrix becomes a submatrix of the higher-order $(N + M) \times (N + M)$ matrix as a result of augmenting the model. This is frequently encountered, for example, in the tuning of patch antennas, where the data matrix is recursively augmented with new row and column vectors that correspond to shorting pins, stubs, etc. In a CAD environment, the order M of augmentation is usually not known *a priori*. At present, each augmented matrix is treated as a new data matrix and the solution of the augmented system of equations is recomputed from scratch. The resulting solution procedure becomes computationally inefficient, and, as shown elsewhere [3], the computational complexity can become $\mathcal{O}((N + M)^4)$. The objective of this paper is to apply an order-recursive variant of LU decomposition to develop a solution procedure of computational complexity $\mathcal{O}((N + M)^3)$. This order of magnitude reduction in computations is clearly very attractive for interactive design tasks.

There are also situations encountered in design where one iteratively decreases the size or spacing of certain elements in a circuit or antenna geometry in order to meet the design specifications. Consider, for example, the reduction in stub length in the optimization of a monolithically loaded tunable patch antenna, or the reduction in width of a section of a microstrip quarter-wave transformer to compensate for dispersion. In these situations, the moment matrix is affected by removal of (or, is decremented by) certain row or column vectors associated with the changes in the circuit. As in augmented systems, the order of decrementation is not known *a priori*. At present, the solution of each decremented system of equations is recomputed from scratch. We propose an order-recursive solver for decremented MoM systems as well, wherein the solution (specifically, the LU-decomposition) at the prior iteration is used to efficiently solve the reduced system of equations at the present iteration. The application of efficient solvers for augmented and decremented systems to MoM results in a powerful technique, termed as the *order recursive method of moments* (ORMoM), with potential improvement in iterative design of complex structures using full-wave simulation.

The resulting computational efficiency of ORMoM is illustrated by applying the proposed method to the iterative design of stub-loaded dual-band patch antennas [2].

2 Order Recursive LU Decomposition

The proposed algorithm assumes that *all* the leading principal submatrices of the system (or moment) matrix $\mathbf{A}$ are nonsingular. Therefore, the solution (albeit suboptimal) can always be computed without the need of pivoting. Note that in the sequel, when computing LU decomposition, we refer to Crout reduction (1's along the diagonal of upper triangular matrix U). Identical results may be stated for Doolittle reduction, (1's along the diagonal of lower triangular matrix L).

2.1 Augmented Systems

Assume that the LU decomposition of A (=LU) has been computed. Denote an augmented matrix and its LU decomposition as:

$$A := \left[\begin{array}{c|c} A_{11} & \mathbf{a}_{12} \\ \hline \mathbf{a}_{21} & a_{22} \end{array}\right] = \left[\begin{array}{c|c} L_{11} & \mathbf{o} \\ \hline \mathbf{l}_{21} & l_{22} \end{array}\right] \left[\begin{array}{c|c} U_{11} & \mathbf{u}_{12} \\ \hline \mathbf{o} & 1 \end{array}\right]. \tag{1}$$

Then, it is readily seen that the unknowns may be computed as:

$$\begin{array}{rcl} \mathbf{u}_{12} & = & L_{11}^{-1}\mathbf{a}_{12} \\ \mathbf{l}_{21} & = & \mathbf{a}_{21}U_{22}^{-1} \\ l_{22} & = & a_{22} - \mathbf{l}_{21}\mathbf{u}_{12}. \end{array} \tag{2}$$

Of course one *must not* compute the inverses of matrices as shown in (2). Instead, the unknowns are obtained by solution of the triangular system of equations, which is known to be numerically stable. The above result is easily extended to the case when the matrix is bordered by several rows and columns. Specifically, if

$$A := \left[\begin{array}{c|c} A_{11} & A_{12} \\ \hline A_{21} & A_{22} \end{array}\right] = \left[\begin{array}{c|c} L_{11} & O \\ \hline L_{21} & L_{22} \end{array}\right] \left[\begin{array}{c|c} U_{11} & U_{12} \\ \hline O & U_{22} \end{array}\right], \tag{3}$$

then, the unknowns may be computed as:

$$\begin{array}{rcl} U_{12} & = & L_{11}^{-1}A_{12} \\ L_{21} & = & A_{21}U_{11}^{-1} \\ L_{22}U_{22} & := & A_{22} - L_{21}U_{12} \end{array} \tag{4}$$

where, the last equation in (4) represents an LU decomposition of the matrix on its right-hand side.

2.2 Decremented Systems

Next, we consider the update of LU decomposition of a matrix some of whose rows and columns are removed. It is, of course, assumed that the LU decomposition of the original *higher* order matrix is available. Consider the following (3 × 3) block matrix:

$$A = \begin{bmatrix} A_{11} & A_{12} & A_{13} \\ A_{21} & A_{22} & A_{23} \\ A_{31} & A_{32} & A_{33} \end{bmatrix} = \begin{bmatrix} L_{11} & O & O \\ L_{21} & L_{22} & O \\ L_{31} & L_{32} & A_{33} \end{bmatrix} \begin{bmatrix} U_{11} & U_{12} & U_{13} \\ O & U_{22} & U_{23} \\ O & O & U_{33} \end{bmatrix} \tag{5}$$

To see the effect of decrementing the matrix order by removing some rows and columns, it is instructional to consider the (block) LU decomposition of the matrix. Assuming that $A_{11} = L_{11}U_{11}$ is known, the remaining entries of the decomposition may be computed as follows.

$$\begin{aligned} U_{12} &= L_{11}^{-1}A_{12} \\ L_{21} &= A_{21}U_{11}^{-1} \\ L_{22}U_{22} &:= A_{22} - L_{21}U_{12} \end{aligned} \tag{6}$$

$$\begin{aligned} U_{13} &= L_{11}^{-1}A_{13} \\ L_{31} &= A_{31}U_{11}^{-1} \\ U_{23} &= L_{22}^{-1}(A_{23} - L_{21}U_{13}) \\ L_{32} &= (A_{32} - L_{31}U_{12})U_{22}^{-1} \\ L_{33}U_{33} &:= A_{33} - L_{31}U_{13} - L_{32}U_{23} \end{aligned} \tag{7}$$

where equations (6) and (7) represent LU decomposition of the matrix on the right-hand side.

The following three possibilities for deletion of block rows and columns exist:

Case 1: *Delete* $(1, 1)$ *block row and column.* In this case, the entire LU decomposition of the decremented matrix

$$A := \left[\begin{array}{c|cc} A_{11} & A_{12} & A_{13} \\ \hline A_{21} & A_{22} & A_{23} \\ A_{31} & A_{32} & A_{33} \end{array}\right] \longrightarrow \begin{bmatrix} A_{22} & A_{23} \\ A_{32} & A_{33} \end{bmatrix}$$

must be recomputed. This is evident from the dependence of the entire decomposition on the LU decomposition of A_{11}.

Case 2: *Delete* $(2, 2)$ *block row and column.*

$$A := \left[\begin{array}{c|c|c} A_{11} & A_{12} & A_{13} \\ \hline A_{21} & A_{22} & A_{23} \\ \hline A_{31} & A_{32} & A_{33} \end{array}\right] \longrightarrow \begin{bmatrix} A_{11} & A_{13} \\ A_{31} & A_{33} \end{bmatrix}$$

Following the operations described in recursive LU decomposition above, it is seen that if

$$\begin{bmatrix} A_{11} & A_{13} \\ A_{31} & A_{33} \end{bmatrix} = \begin{bmatrix} L_{11}^{\text{new}} & O \\ L_{21}^{\text{new}} & L_{22}^{\text{new}} \end{bmatrix} \begin{bmatrix} U_{11}^{\text{new}} & U_{12}^{\text{new}} \\ O & U_{22}^{\text{new}} \end{bmatrix},$$

then, the matrices L_{11}^{new}, L_{21}^{new}, U_{11}^{new} and U_{12}^{new} are the same as the matrices L_{11}, L_{31}, U_{11} and U_{13}, respectively. Hence they need not be recomputed. However, L_{22}^{new} and U_{22}^{new} are obtained from the LU decomposition of the original matrices $A_{33} - L_{31}U_{13}$ and need to be recomputed.

Case 3: *Delete* $(3,3)$ *block row and column.*

$$A := \left[\begin{array}{cc|c} A_{11} & A_{12} & A_{13} \\ A_{21} & A_{22} & A_{23} \\ \hline A_{31} & A_{32} & A_{33} \end{array}\right] \longrightarrow \begin{bmatrix} A_{11} & A_{12} \\ A_{21} & A_{22} \end{bmatrix}$$

Again referring to the relations in recursive decomposition, it is easily seen that for this case, no new computations are required since the LU decomposition of the first (2×2) block submatrix is independent of the third (block) row and column.

3 Design Example

The solution procedure described in Section 2 is applied to the iterative design of a coax-fed tunable dual-band patch antenna, whose geometry is shown in Fig. 1. The substrate is 0.79 mm thick duroid (ϵ_r =2.17). The current distribution on the structure is computed using an efficient PC-based MoM simulator described in [4]. The patch and the stub are gridded into a rectangular mesh which supports rooftop basis functions. The resulting moment matrix for the patch alone is of the order 216. The return loss of the untuned patch is shown in Fig. 2 and a fundamental resonance is observed at 2.5 GHz. In order to provide dual-band operation, an open-circuited $\lambda/4$ monolithic stub is connected perpendicular to a radiating edge (Fig. 1) and its position along the edge or length is varied iteratively. At each iteration, instead of solving the linear system of moment equations from scratch, the LU decomposition of the patch is efficiently utilized in solving the augmented system created by the addition of the stub. Two positions of the 20 mm long stub are simulated: (a) center of the radiating edge, (b) 4 mm above the center. In either case, the 216×216 system matrix of the patch is augmented by 8 rows and columns. Location (a) produces two resonances at 2.31 and 2.635 GHz (Fig. 2) in contrast to the experimentally observed values, 2.275 and 2.666 GHz, respectively [2]. The separation of the resonances can be varied by moving the stub along the radiating edge. Location (b) produces the resonances at 2.35 and 2.65 GHz (Fig. 2), clearly demonstrating the tuning nature of the stub. Because of symmetry, a similar band separation has been observed when the stub is located 4 mm below the center of the radiating edge. The resonances were also varied by changing the length of the stub with its position fixed.

As an indication of computational efficiency of ORMoM, the conventional MoM implementation of solving the currents from scratch at each iteration for the antenna shown in Fig. 1 would have required $216^3+224^3 = 21,317,120$ operations, whereas ORMoM requires only $216^3+2\times8\times216^2 = 10,824,192$ operations (savings of about 50%). It is evident that the computational savings would be larger for higher-order problems, and for those problems involving many iterations of dimensional changes (*e.g.*, within an optimization framework). In general, order-recursive solution of augmented systems is of computational complexity $\mathcal{O}((N+M)^3)$, an order of magnitude lower than the complexity for solving the currents at

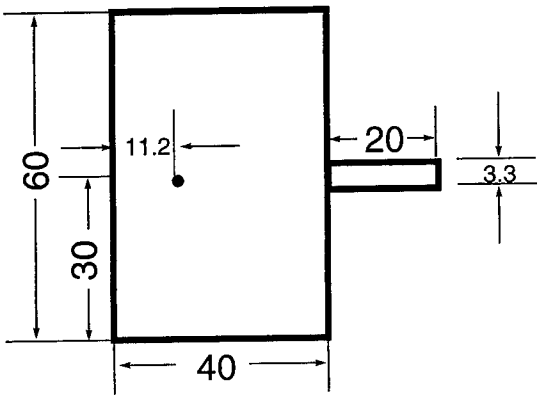

Figure 1: Patch antenna geometry.

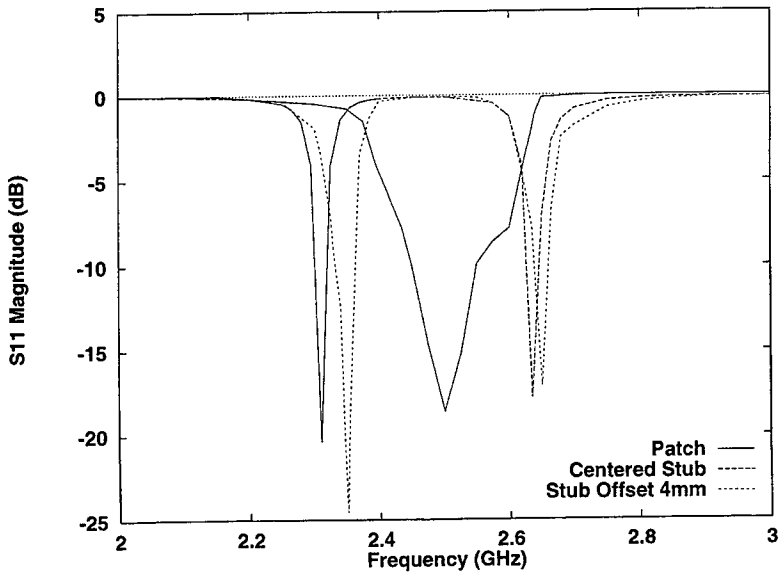

Figure 2: Return loss of the tuned patch antenna.

each iteration from scratch. It is recalled that N is the order of the original matrix and M is the order of augmentation.

4 Conclusions

An order-recursive variant of conventional LU decomposition has been presented for the efficient solution of linear systems arising in an iterative moment method simulation. The method is illustrated by application to the interactive design of a tunable dual-band microstrip patch antenna with a monolithic stub connected to the radiating edge. The proposed iterative solution method has also been applied to the efficient CAD of microwave circuits [3], and is expected to be a valuable CAD tool in EM simulation and optimization. For example, a cost-effective simulation technique is to initially employ a coarse grid to assess regions of marked parametric variation, and then to re-solve the problem employing a finer grid where higher resolution of the field is desired. In the conventional MoM approach, the latter solution is recomputed from scratch. With the iterative solvers employed in ORMoM, a significant portion of information from the former solution, namely, the LU decomposition of the former system matrix, is used in the latter solution to achieve considerable computational savings for large-order problems. Thus, besides iterative design tasks necessitated by changes in the geometry, ORMoM is anticipated to be useful in improving the solution accuracy and numerical resolution of the simulation. This aspect of ORMoM is currently being investigated, and results will be forthcoming.

References

[1] J.R. James and P.H. Hall, *Handbook of Microstrip Antennas*, vol. I, Peter Peregrinus, London, 1989.

[2] S.E. Davidson, S.A. Long, and W.F. Richards, "Dual band microstrip antenna with monolithic reactive loading," *Electron. Lett.*, vol. 26, pp. 936-937, 1985.

[3] K. Naishadham and P. Misra, "Order recursive Gaussian elimination and efficient CAD of microwave circuits," *IEEE Microwave Symp. Dig.*, pp. 1435-1438, May 1995.

[4] K. Naishadham and T.W. Nuteson, "Efficient analysis of passive microstrip elements in MMICs", *Int. J. Microwave and Millimeter-Wave Comp. Aided Eng.*, vol. 4, no. 3, pp. 219–229, 1994.

SESSION 14:

MULTIPOLE TECHNIQUES

Chair: P. Leuchtmann

Discrete Sources Method for the Silicon Wafers Defect Discrimination

Yu. Eremin and N. Orlov

Applied Math & Computer Science Faculty of Moscow Lomonosov State University
Vorobyov Hills, Moscow 119899, Russia
E-Mail: EREMIN@cs.msu.su

Abstract. The demonstration of the discrete sources method is carried out for the problem of light scattering from the silicon wafers' defects. There are demonstrated the algorithm principles. The examples of numerical calculations are regarded. Results of the light scattering analysis are shown as compared with an experimental data from the real world scanning detection systems

1. Introduction

At present the numerical analysis of scattering from the obstacle on the boundary of layered half-space is a very actual problem due to various practical applications. Control of a contamination of silicon wafer surface is of the great significance in semiconductor manufacturing. Advance inspection technologies should have a reliable detectors of micro-contamination sizes down to 0.06 mkm. It is impossible to establish the morphology of micro-contamination without of the analysis of a mathematical model and computer simulation. The subject of the main interest of the wafer manufacturers are such a defects as "pit" and "bumps", and especially contamination from micro-particles. The present inspection systems use the laser beam for scanning the wafer surface. So, the calculation of the light scattering from a such defects on wafer surfaces is of great interest in simulation, development and calibration of inspecting systems.

The problem of interest can be formulated as a light scattering problem, where the size of an obstacle is about wavelength of laser light source. The stringent mathematical model leads to Boundary Value Problem (BVP), including Maxwell equations, transmission conditions at the boundaries of permittivity discontinuities, and radiation/attenuation conditions at the infinity.

When constructing our model we assume some positions.

- The wafer is simulated as a homogeneous dielectric half-space having a certain complex characteristics.
- The obstacle regarded has an axial symmetry (axis is to be normal to interface surface).
- We shall suppose the exciting field to be a linear polarized plane wave, propagating with certain angle to the wafer surface.

2. Formalism

The main idea of The Discrete Source Method (DSM) is to construct solution of BVP as a finite linear combination of EM fields produced by the dipole and multipole auxiliary sources [1]. The location of those sources is to be chosen at the symmetry axis for the sake of simplicity of the construction. When investigating the scattering problems we developed a special construction for used sources to satisfy the boundary conditions at the half-space surface. So, being an exact semi-analytical approach, DSM enables to remove the usual disadvantages of other techniques.

The main features of our approach are [1]:

1) AS analytically satisfies the all BVP conditions, including conditions on the half-space boundary, except conditions on the obstacle surface that have to be fitted numerically;
2) orientation of the multipoles used was chosen taking into consideration the polarization of exciting plane wave;
3) there was chosen the special combination for azimuth dependence, due to that it was be able to build the numerical scheme separately for the each azimuth harmonics.

Algorithmization of the problem means to transform the original BVP to the linear algebraic system with respect to the complex vector of unknown amplitudes of discrete sources. This procedure has been developed as including the following steps:

1) replacement of the continual boundary conditions at the obstacle surface to the discrete ones (set of collocation points);
2) transition to the Fourier harmonics (with respect to azimuth variable ϕ) for the components of an exciting field (the representation for the scattered field is itself the trigonometric polynomial on azimuth variable);
3) matching the azimuth harmonics of the scattered field and exciting one at the set of collocation points with accordance of point-matching approach.

The feature of the present BVP is the existence of the half-space (i.e. substrate). Here we express the fundamental solution need via Fourier-Hankel transform [2]. The realization of algorithm allows to calculate the all need integrals in real time. Algorithm allows to calculate the all incident angles of the plane wave and the both polarizations in parallel. It has an internal criterion of the posterior evaluation of the results obtained. This evaluation is the mean square norm residual of fields at the obstacle surface.

3. Numerical examples

Let us consider an example of numerical analysis of the scattering problem for the case when scatterer on the wafer surface is spherical particle. In Fig. 1 the scattered intensities (mkm^2) versa scattering angle are demonstrated. Here wavelength is 0.488 mkm, incidence is 45° from the normal (S polarization). The particle refractive index n = 1.59 (corresponds to the polisterine latex calibration spherical particle), for silicon substrate n = 4.5 – 0.4i. Curves 1, 2, 3 mean the particle diameter as 0.15 mkm, 0.22 mkm and 0.496 mkm. The markers correspond to the experimental data [3].

The integral cross-section (response) $R = \int_{\Omega} I \, d\sigma$ is the important characteristics of the surface scanner. Here Ω is the collector surface of the real unit. The response from polisterine calibration spheres is shown in Fig. 2 as function of particle diameter. Markers corresponds to the data from WIS-8500 set-up of ADE Optical Systems [3]. The beam incidence is 15°, the wavelength and polarizations are the same as in previous Fig.

In Fig. 3 the scattered intensity from 0.4 mkm aluminium spheres (n = 0.4 – 4.6i) are demonstrated as compared with the model of perfect conducting particle. Here the incident angle is 65° from the normal. Graphs 1, 3 correspond to the aluminium particle (P and S cases, respectively), and 2, 4 are the perfect conductor model (P, S).

We can also compare the scattering from the different kinds of inhomoginities. In Fig. 4 the two kinds of obstacles are presented: polisterine spherical particle and pit in the wafer. The pit is the hole of finite depth in the substrate (actually it has a form of semi-sphere). The P-polarized beam incidence is 45°. The both scatterers pit and particle are rather small ones, and their sizes are so, that particle and pit surfaces are equal. So, diameter of the particle is 0.07 mkm (curve 1), corresponding pit is of 0.1 mkm (curve 2). The next pair is particle of 0.14 mkm (curve 3) and pit 0.2 mkm (curve 4).

4. Conclusions

The approach used seems to be very attractive for investigation of similar problems.

- First, this approach is easy. The algorithms used generate the compact codes, moderate of computer resources. These codes are fast and available for PCs.
- This approach is universal. It can be used for various types of particles (both metallic and dielectric) and for various types of wafers' defects as well.
- This approach is reliable. The results predicted via DSM were compared with experimental data from real world scanning detection systems and demonstrate a good agreement. Besides, the algorithm has an internal criterion of obtained result accuracy.

References

1. Yu. Eremin, N. Orlov, and A. Sveshnikov. "Electromagnetic scattering analysis based on Discrete Sources Method". ***Appl. Comput. Electrom. Soc. J.***, 1994. V. 9. No. 3. Pp. 46-56
2. Yu. Eremin and N. Orlov. "Simulation of light scattering from particle upon wafer surface". ***Appl. Optics*** (to be published)
3. L. Clementy, M. Fossey, and A. Rakhmanov. "The Experimental Study of the Angular Scattering Distribution of the PSL Particle Placed on Silicone Substrate". ***Report of ADE & ADE Optical System res. lab.*** from November 1994.

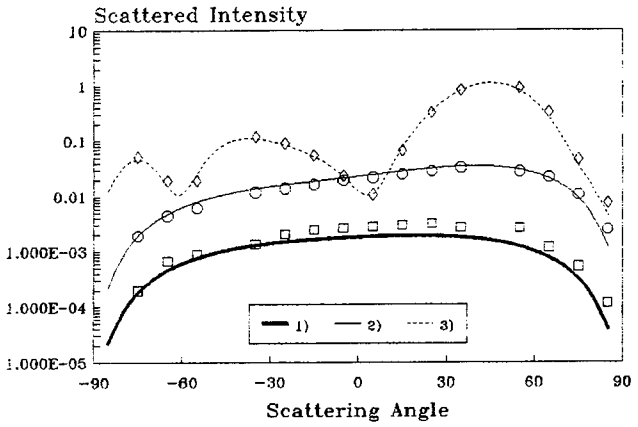

Figure 1.

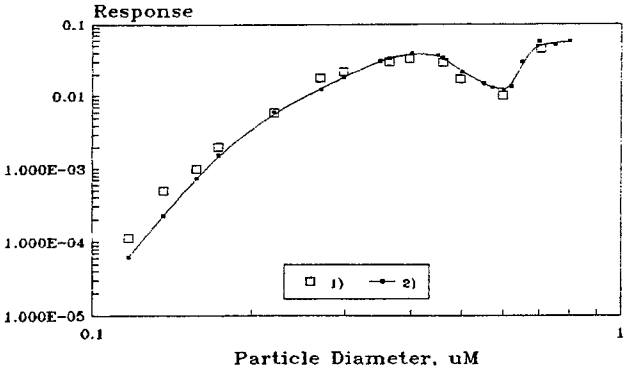

Figure 2.

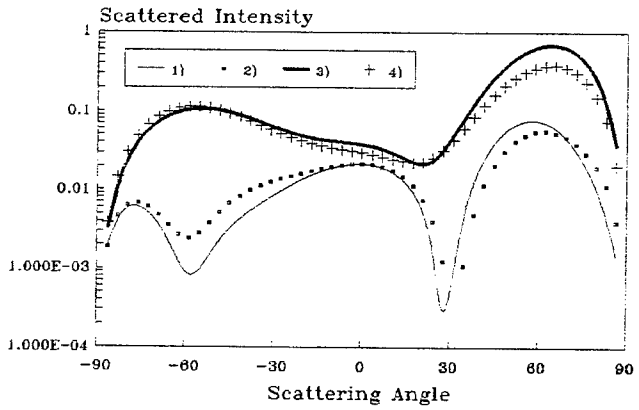

Figure 3.

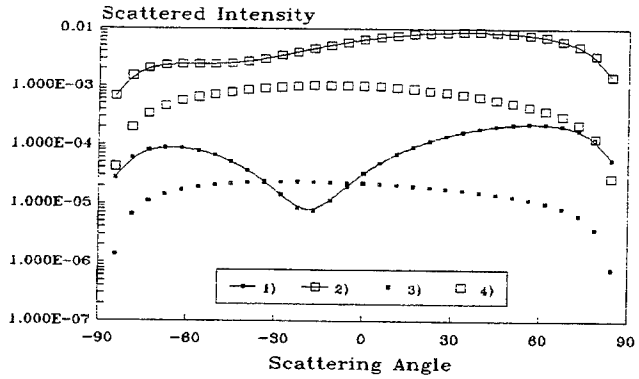

Figure 4.

Iterative Scheme of Discrete Sources Amplitudes Determination Based on D-matrix Approach

Yu. Eremin

Applied Mathematics and Computer Science Faculty
Moscow Lomonosov State University
Vorobyev'Hills, 119899 Moscow
Russia
FAX: +7-(095)939-1776, E-mail: EREMIN@cs.msu.su

Introduction

The General Multipole Technique is a relatively new approach to investigate electromagnetic Boundary-Value Scattering Problem (BVSP). It may be realized in different forms: Multiple Multipole Technique [1], Discrete Sources Method (DSM) [2] or Auxiliary Current Technique. The main idea of DSM is to represent a solution of BVSP as a finite linear combination of elementary field sources. It satisfies Maxwell equations anywhere outside the medium discontinuities and radiation conditions at the infinity. So, BVPS solution is reduced to approximation problem of an exciting field by discrete sources (DS) fields at the obstacle surface. Point or distributed dipoles and multipoles are usually used as the DS. Unknown DS amplitudes are to be determined from a boundary condition enforced at the obstacle surface.

Point-matching approach is preferably employed for DS amplitudes determination. It means that it ought to fulfil a boundary condition at a discrete set of the points distributed at the obstacle surface. Therefore the resulting equation is automatically a matrix equation. It was established that overdetermined linear systems are more proper to provide fast and stable numerical scheme. It allows to decrease the number of DS required for the field approximation.

The most appropriate algorithm to get a pseudosolution of overdetermined linear system is the Given's algorithm. However if matrix is drastically increase the single way is to implement an iterative scheme to get its pseudosoluion. Unfortunately there is no way to prove a convergence of any iterative scheme for DSM point-matching matrix. First of all it is a consequence that matrix operator transforms $\Re^N$ into $\Re^M$ ($N<M$). Lately it was proposed to employ GMRES [3] for the solution of some BVSP on the basis of boundary integral equation approach. The convergence GMRES was ensured by a dissipativity of the boundary operator. It allows to investigate the scattering problems on conductive screens or resistive shells [4].

In this report we are going to extend above approach for DS amplitudes determination. We intend to propose to use a dissipative matrix in the frame of DSM and apply GMRES to get its pseudosolution. We have justified the convergence of GMRES based on the dissipativity of the matrix [5].

1. Acoustic waves scattering

We will consider the scattering of time-harmonic acoustic waves by local obstacle D in R^3 with impedance boundary condition at the obstacle surface ∂D. So, the following BVSP for the acoustic velocity potential U holds

$$(1)\qquad \begin{aligned} &\Delta U + k^2 U = 0 \quad D_e = \Re^3 / \overline{D} \\ &\partial U + \zeta U = U^0 \quad \partial D \\ &\partial U / \partial r - ikU = o\left(r^{-1}\right) \quad r \to \infty \end{aligned}$$

where k - wavenumber, k>0, Im ζ>0, $\zeta \in C(\partial D)$, $\partial = \partial/\partial\nu$, ν- unit outward normal to ∂D, $\partial D \in C^{(1,\alpha)}$. U^0 - functional depends from external excitation. There exists a single solution of BVSP (1).

Based on DSM we will seek approximate solution of (1) in the following form

$$(2)\qquad U_N(M) = \sum_{n=1}^{N} T_n^N \Psi_n(M)$$

here $\Psi_n(M) = \exp\left\{ikR_{MM_n}\right\} / 4\pi R_{MM_n}$ - fundamental solution of Helmholtz equation, $\{M_n\}_{n=1}^{N} \subset D$. Therefore representation (2) satisfies to Helmholtz equation in D_e and radiation conditions at the infinity. Let us determine the unknown amplitudes of DS T_n^N from the following relations

$$(3)\qquad \int_{\partial D} \left\{\partial U_N + \zeta U_N - U^0\right\} \Psi_m^* d\sigma = 0, \quad m = \overline{1, N}$$

where asterisk implies a conjugate value. According to (2) and (3) we obtain a linear system for DS amplitudes determination

$$(4)\qquad \sum_{n=1}^{N} D_{mn} T_n^N = \int_{\partial D} U^0 \Psi_m^* d\sigma; \quad m = \overline{1, N}$$

where matrix elements are $$D_{mn} = \int_{\partial D} \left\{\partial \Psi_n \Psi_m^* + \zeta \Psi_n \Psi_m^*\right\} d\sigma$$

Theorem 1. For any N there exists a single solution of the linear system (4).

Proof. We shall show the dissipativity of D-matrix. That is for any $\vec{T}^N = \left\{T_n^N\right\}_{n=1}^{N}$ holds

$$(5)\qquad \mathrm{Im}\left\langle \mathbf{D}\vec{T}^N, \vec{T}^N \right\rangle > 0, \quad \forall \vec{T}^N \neq 0$$

and besides

$$\left\langle \mathbf{D}\vec{T}^N, \vec{T}^N \right\rangle = 0, \quad \Rightarrow \left\| \vec{T}^N \right\| = 0$$

Let us choose arbitrary $\vec{T}^N$ and construct a function

$$V_N(M) = \sum_{n=1}^{N} T_n^N \Psi_n(M)$$

It can be directly checked that

$$(6) \qquad \mathrm{Im}\left\langle \mathbf{D}\vec{T}^N, \vec{T}^N \right\rangle = \mathrm{Im} \int_{\partial D} \partial V_N V_N^* d\sigma + \mathrm{Im} \int_{\partial D} \zeta |V_N|^2 d\sigma$$

Applying the second Green's theorem to V_N and conjugate value V_N^* yields

$$(7) \qquad \mathrm{Im} \int_{\partial D} \partial V_N V_N^* d\sigma = k \int_{\Omega} |F^N|^2 d\omega$$

where F^N - far field pattern of V_N field and Ω - unite sphere. Since k>0 and Imζ>0, then from (6)-(7) follows (5). Let now $\left\langle \mathbf{D}\vec{T}^N, \vec{T}^N \right\rangle = 0$ is valid, then from (6)-(7) we obtain $F^N = 0$. From the analytic property of V_N follows that $V_N = 0$. Therefore accounting that all points M_n are different and by virtue of Ψ_n singularities in M_n we can conclude that $\left\| \vec{T}^N \right\| = 0$.

Now we proceed to the proof of a convergence of the approximate solution (2) to the exact solution of BVSP (1). From the completeness of the system $\chi_n(P) = \left(\partial_p + \zeta\right)\Psi_n(P)$ at the obstacle surface ∂D in $L_2(\partial D)$ we find that there exists a function $V_N(M) = \sum_{n=1}^{N} t_n^N \Psi_n(M)$ such that

$$(8) \qquad V_N = U + \varepsilon^N \text{ and } (\partial + \zeta)\varepsilon^N = \delta^N : \left\| \delta^N \right\|_{L_2(\partial D)} \to 0, \text{ under } \mathrm{N} \to \infty$$

Then the following result is valid

Theorem 2. Let approximate solution of BVSP (1) be (2) and DS amplitudes are determined from the linear system (3), then U_N converges to the exact one

$$\lim_{N \to \infty} \left\| U_N - U \right\|_{L_2(\partial D)} = 0.$$

Proof. Let us show that U_N be uniformly confine for all N. Multiplying (3) by T_m^* and summing yields

$$\int_{\partial D} \partial U_N U_N^* d\sigma + \int_{\partial D} \zeta |U_N|^2 d\sigma - \int_{\partial D} \partial U^0 U_N^* d\sigma = 0$$

accounting (7) we can conclude that

$$(9) \qquad k\int_{\Omega} |F_N|^2 d\omega + \int_{\partial D} \left| \sqrt{\operatorname{Im}\zeta} U_N - U^0 / 2i\sqrt{\operatorname{Im}\zeta} \right|^2 d\sigma = \int_{\partial D} \left| U^0 \right|^2 / 4\operatorname{Im}\zeta d\sigma$$

Hence, we have got a uniform boundedness of U_N in $L_2(\partial D)$ sense. Now we can prove the convergence. From (8) it follows

$$(10) \qquad \int_{\partial D} \left\{ \partial V_N + \zeta V_N - U^0 \right\} \Psi_m^* d\sigma = \int_{\partial D} \delta^N \Psi_m^* d\sigma, \qquad m = \overline{1, N}$$

Creating a discrepancy $W^N = V_N - U_N$ then (3) and (10) yield

$$\int_{\partial D} \left\{ \partial W^N + \zeta W^N \right\} \left(W^N \right)^* d\sigma = \int_{\partial D} \delta^N \left(W^N \right)^* d\sigma,$$

or finally

$$k\int_{\Omega} \left| F_w^N \right|^2 d\omega + \int_{\partial D} \operatorname{Im}\zeta \left| W^N \right|^2 d\sigma = \operatorname{Im} \int_{\partial D} \delta^N (W^N)^* d\sigma \le \left\| \delta^N \right\|_{L_2(\partial D)} \left\| W^N \right\|_{L_2(\partial D)}$$

From the last relation and uniform boundedness of W^N we get the convergence of the approximate solution to the exact one.

Theorem 3. Linear system (3) is correctly solvable for any N.

Proof. Let us introduce the following notations:

$$B_{mn} := \int_{\partial D} \partial \Psi_n \Psi_m^* d\sigma \qquad\qquad G_{mn} := \int_{\partial D} \zeta \Psi_n \Psi_m^* d\sigma$$

Then $D_{mn} = B_{mn} + G_{mn}$. Let us examine **B** matrix first. Applying the second Green's theorem to Ψ_n and Ψ_m^* yields

$$\int_{\partial D} \left\{ \partial \Psi_n \Psi_m^* - \partial \Psi_m^* \Psi_n \right\} d\sigma = i / 2\pi \; S_{mn}$$

here $S_{mn} = \sin\left(kR_{M_nM_m}\right) / R_{M_nM_m}$ is real valued symmetric matrix. Rewriting relation obtained we find that

$$B_{mn} = B^*_{nm} + i / 2\pi \; S_{mn} \tag{11}$$

Therefore, matrix $\mathbf{C} = \mathbf{B} - i / 4\pi \; \mathbf{S}$ is Hermitian matrix. It implies that $\mathrm{Im}\left\langle \mathbf{C}\vec{T}^N, \vec{T}^N \right\rangle = 0$ for $\forall \vec{T}^N$. So, the following holds

$$\mathrm{Im}\left\langle \mathbf{B}\vec{T}^N, \vec{T}^N \right\rangle = 1/4\pi \;\; \mathrm{Re}\left\langle \mathbf{S}\vec{T}^N, \vec{T}^N \right\rangle = \; s_1^N / 4\pi \left\| \vec{T}^N \right\|^2$$

here s_1^N is minimal eigen value of positive determined matrix **S**. Let us do the same transformation with **G** matrix. It can be easy seen that

$G_{mn} - G^*_{nm} = 2iE_{mn}$ where $E_{mn} = \int\limits_{\partial D} \mathrm{Im}\,\zeta \Psi_n \Psi^*_m d\sigma$. So **E** is Hermitian positive determined matrix. Introducing into consideration Hermitian matrix **H**: $H_{mn} = G_{mn} - iE_{mn}$ and following the same way as before we obtain

$$\mathrm{Im}\left\langle \mathbf{G}\vec{T}^N, \vec{T}^N \right\rangle = \mathrm{Re}\left\langle \mathbf{E}\vec{T}^N, \vec{T}^N \right\rangle = \; \mathrm{e}_1^N \left\| \vec{T}^N \right\|^2$$

where e_1^N is minimal eigen value of Hermitiam positively determined matrix **E**. Hence, the following relation is valid

$$\left| \left\langle \mathbf{D}\vec{T}^N, \vec{T}^N \right\rangle \right| \geq \mathrm{Im}\left\langle \mathbf{D}\vec{T}^N, T^N \right\rangle > \left(s_1^N / 4\pi + e_1^N \right) \left\| \vec{T}^N \right\|^2$$

where from correct solvability follows

$$\left\| \mathbf{D}\vec{T}^N \right\| \geq (s_1^N / 4\pi + e_1^N) \left\| \vec{T}^N \right\|$$

Corollary 1. From the theorem 2 follows that it is possible to employ GMRES for the solution of the system (3) for any N.

Corollary 2. For the cases ζ=0 (sound-hard) or ζ=∞ (sound-soft) it is easy to prove the same results. To do this it is necessary to find $\zeta \neq 0$ such that corresponding BVSP gives the solution close to original one.

2. Computer simulation results

Let us consider computer simulation results relevant to plane wave scattering at sound-soft 3-axis ellipsoid. Axis relation is 2:1:8. Table 1 contains results comparison received by D-matrix approach and normal system using. Matrix columns mean

- discretes number per wavelength
- total DS number - N
- M/N ratio, where M - matching points number
- number of GMRES iterations completed
- residual value corresponds to D-matrix
- residual value corresponds to normal system

L	N	M/N	niter	resD(%)	resN(%)
8	40	3.2	7	11.3	24.1
9	50	3.1	7	8.0	16.7
10	50	3.7	7	5.2	15.4
11	63	3.4	8	4.6	12.5
12	78	3.6	8	2.1	11.2

Table 1.

Computation has been carried out in the following manner:

1. Scattering problem was solved by D-matrix approach with the boundary residual in matching points less then 5%.
2. We done the same number of iterations GMRES for the normal system.

It can be seen that in all cases boundary residual for D-matrix approach less then for the normal system.

Summary

D-matrix approach has been proposed to use iterative scheme for discrete sources amplitudes determination in the frame Discrete Sources Method. Computer simulation results showed that D-matrix approach seems to be promising tool. It can be extended on penetrable acoustic obstacle or even electromagnetic wave scattering investigation.

References

1. Hafner Ch. The Generalized Multipole Technique for Computational Electromagnetics. Artech, Norwood, MA, 1990.
2. Eremin Yu.A., Sveshnikov A.G. *Electromagnetics*. - 1993, Vol.13, no.2, pp.203-216.
3. Saad Y., Shultz M.N. *SIAM J. Sci. Stat. Comput.* - 1986. Vol.7, no.3, pp.856-869.
4. Eremin Yu.A., Sveshnikov A.G. *Comput. Maths Math. Phys.*- 1991, Vol.31, no. 10, pp. 81-86.
5. Eremin Yu. *Differential equations*. - 1995. Vol.31, no. 9.

An Improving Technique for MMP Solutions Based on Ficticious Surface Sources

M. Gnos and P. Leuchtmann
Lab. of El.-mag. fields and Microwave Electronics, ETH Zurich
CH-8092 Zurich, Switzerland

Abstract: *The MMP technique delivers an approximate field solution which satisfies Maxwell's equations exactly inside of homogeneous subdomains, but does not satisfy the boundary conditions between subdomains. This so-called mismatching is equivalent to non physical field sources on the boundary. The paper describes some numerical experiments using a technique for compensating the non physical sources with additional sources on the boundary. This technique works satisfactorily for both electrostatic and magnetostatic problems in 2D and in 3D. In the time harmonic case as well as in true 3D-situations of electrostatics the violation of the charge conservation principle of the ficticious sources may causes difficulties.*

1. Introduction

The MMP-program package [1] is a tool for computational electromagnetics in frequency domain for situations smaller than, say five to ten, wave lengths and piecewice homogeneous, linear and isotropic materials. More over, a static version of the program is available. Solutions of this code may be used in the dynamic program for calculating quasistatic situations [2].

As it is well known, MMP expands the unknown electromagnetic field

$$\begin{pmatrix}\vec{E}\\ \vec{H}\end{pmatrix} = \begin{pmatrix}\vec{E}_0\\ \vec{H}_0\end{pmatrix} + \sum_{k=1}^{N} a_k \begin{pmatrix}\vec{E}_k\\ \vec{H}_k\end{pmatrix} \qquad (1)$$

in a series which is different for each homogeneous subdomain. Each $\begin{pmatrix}\vec{E}_k\\ \vec{H}_k\end{pmatrix}$ is an analytical solution of Maxwell's equations, i.e., the electric field $\vec{E}_k$ and the magnetic field $\vec{H}_k$ are exactly coupled through Maxwell's equations. However, on the boundaries between the subdomains the continuity conditions for the fields are satisfied only approximatively, i.e., the boundary conditions are fulfilled in a least squares sense. This results in a certain error — the so-called 'mismatching' on the boundaries. Though the mismatching is not equal to the true error (the fields on both sides of the boundary may be wrong but still fit in a particular boundary point) it is still closely related to the real error: With a vanishing mismatching on all the boundaries the true error becomes also zero. To be correct, one must state that this is only true for well posed problems, i.e., problems with a unique solution.

2. The Mismatching and its Sources

In the general case the mismatching has six components in each boundary point and is expressed with the difference of the respective field components:

$$\begin{aligned}
&\Delta E_{t1} = \Delta\vec{E}\cdot\vec{u}_{tang1}, \quad \Delta E_{t2} = \Delta\vec{E}\cdot\vec{u}_{tang2}\\
&\Delta H_{t2} = \Delta\vec{H}\cdot\vec{u}_{tang1}, \quad \Delta H_{t2} = \Delta\vec{H}\cdot\vec{u}_{tang2},\\
&\Delta D_n = \Delta\vec{D}\cdot\vec{u}_{norm}, \quad \Delta B_n = \Delta\vec{B}\cdot\vec{u}_{norm}.
\end{aligned} \qquad (2)$$

Thereby, $\vec{u}_{tang1,2}$ are unit vectors tangential to the boundary and $\vec{u}_{norm}$ is a normal unit vector, while $\Delta\vec{X}$ stands for the vectorial difference of the vector $\vec{X}$ at both sides of the boundary, e.g.,

$$\Delta\vec{E} := \vec{E}_{left} - \vec{E}_{right} \qquad (3)$$

or for the electric displacement density

$$\Delta\vec{D} := \varepsilon_{left}\vec{E}_{left} - \varepsilon_{right}\vec{E}_{right}. \qquad (4)$$

Similar formulae with the magnetic field $\vec{H}$ and the magnetic induction $\vec{B} = \mu\vec{H}$ are used. ε and μ are the possibly complex electric permittivity and magnetic permeability respectively.

On ideal conductor surfaces the quantities $\Delta H_{t1,2}$ and ΔD_n are not restricted while on other boundaries all components listed in (2) must vanish. In the practical applications they are "small" instead. Nonzero parts are equivalent to (or may be considered as) certain non physical electric and/or magnetic sources:

$$\begin{aligned}
\Delta D_n &\mathrel{\hat{=}} \text{el. surface charge } \varsigma_e\\
\Delta B_n &\mathrel{\hat{=}} \text{mag. surface charge } \varsigma_m\\
\Delta H_{t1,2} &\mathrel{\hat{=}} \text{el. surface current } \vec{\alpha}_e\\
\Delta E_{t1,2} &\mathrel{\hat{=}} \text{mag. surface current } \vec{\alpha}_m
\end{aligned}$$

Note that the vectorial surface current densities are rotated by 90° in the tangential plane compared to the tangential components of the related mismatching quantity. If we define the vectorial tangential mismatching

$$\vec{\Delta}E_{\mathrm{t}} := (\Delta E_{\mathrm{t}1})\vec{u}_{\mathrm{tang}1} + (\Delta E_{\mathrm{t}2})\vec{u}_{\mathrm{tang}2} \qquad (5)$$

(similar for $\vec{\Delta}H_{\mathrm{t}}$) and suppose $\vec{u}_{\mathrm{tang}1}$, $\vec{u}_{\mathrm{tang}2}$ and $\vec{u}_{\mathrm{norm}}$ forming a right handed system in this order ($\vec{u}_{\mathrm{norm}}$ points from the 'right' to the 'left' side of the boundary) then we have the equations

$$\begin{aligned} \Delta D_{\mathrm{n}} &= \varsigma_{\mathrm{e}} \\ \Delta B_{\mathrm{n}} &= \varsigma_{\mathrm{m}} \\ \vec{\Delta}H_{\mathrm{t}} &= \vec{\alpha}_{\mathrm{e}} \times \vec{u}_{\mathrm{norm}} \\ \vec{\Delta}E_{\mathrm{t}} &= \vec{\alpha}_{\mathrm{m}} \times \vec{u}_{\mathrm{norm}} \end{aligned} \qquad (6)$$

After performing the MMP calculation the situation is as follows: In each subdomain D_i we have an (approximation of an) electromagnetic field $\begin{pmatrix}\vec{E}_i\\ \vec{H}_i\end{pmatrix}$ satisfying Maxwell's equations of this particular domain. But the fields do not properly match at the boundaries. We seem having a solution of a slightly modified problem, namely a problem with additional impressed sources on the boundaries. However, this is only part of the truth. As it is well known sources (currents and charges) may not be given arbitrarily but they must satisfy the continuity equation (the charge conservation principle). Since our ficticious sources are located exclusively on the boundaries these relations are ($e^{-i\omega t}$-time dependency is assumed)

$$\mathrm{div_S}\,\vec{\alpha}_{\mathrm{e}} = i\omega\varsigma_{\mathrm{e}}, \quad \mathrm{div_S}\,\vec{\alpha}_{\mathrm{m}} = i\omega\varsigma_{\mathrm{m}} \qquad (7)$$

where $\mathrm{div_S}$ is the surface divergence operator. Note that in statics the angular frequency ω is zero and thus the surface charges are not restricted in this case. On the other hand, in the stationary case (i.e. time harmonic fields with single angular frequency ω) the surface charge density may be obtained straightforwardly from the surface current density.

3. The Ficticious Fields

Suppose B is the boundary of a particular field subdomain filled with a material being described with ε and μ, then the electromagnetic field related to the current density $\vec{\alpha}_{\mathrm{e}}$ is given by [3]

$$\begin{aligned} \vec{H}_{\mathrm{e}}(\vec{r}) &= \frac{-1}{4\pi}\iint_{\mathrm{B}}(\vec{\alpha}_{eT}(\vec{r}\,')\times\vec{u}_R)\left(ik-\frac{1}{R}\right)\frac{e^{ikR}}{R}dS', \\ \vec{E}_{\mathrm{e}}(\vec{r}) &= \frac{-1}{4\pi i\omega\varepsilon}\iint_{\mathrm{B}}\left[\vec{\alpha}_{eT}(\vec{r}\,')\left(k^2+\frac{ik}{R}-\frac{1}{R^2}\right)\right. \\ &\quad \left. -2\vec{\alpha}_{eR}(\vec{r}\,')\left(\frac{ik}{R}-\frac{1}{R^2}\right)\right]\frac{e^{ikR}}{R}dS', \end{aligned} \qquad (8)$$

where $\vec{r}$ and $\vec{r}\,'$ are the position vectors of field point and source point respectively, $\vec{R} := \vec{r}-\vec{r}\,'$, $R = |\vec{R}|$, $\vec{u}_R := \vec{R}/R$, $k = \omega\sqrt{\mu\varepsilon}$ is the wavenumber of the medium and the current density has been split with respect to $\vec{u}_R$:

$$\vec{\alpha}_{eR} := (\vec{\alpha}_{\mathrm{e}}\cdot\vec{u}_R)\vec{u}_R, \qquad \vec{\alpha}_{eT} := \vec{\alpha}_{e} - \vec{\alpha}_{eR}. \qquad (9)$$

Similarly the magnetic current density has the field

$$\begin{aligned} \vec{E}_{\mathrm{m}}(\vec{r}) &= \frac{1}{4\pi}\iint_{\mathrm{B}}(\vec{\alpha}_{\mathrm{m}T}(\vec{r}\,')\times\vec{u}_R)\left(ik-\frac{1}{R}\right)\frac{e^{ikR}}{R}dS', \\ \vec{H}_{\mathrm{m}}(\vec{r}) &= \frac{-1}{4\pi i\omega\mu}\iint_{\mathrm{B}}\left[\vec{\alpha}_{\mathrm{m}T}(\vec{r}\,')\left(k^2+\frac{ik}{R}-\frac{1}{R^2}\right)\right. \\ &\quad \left. -2\vec{\alpha}_{\mathrm{m}R}(\vec{r}\,')\left(\frac{ik}{R}-\frac{1}{R^2}\right)\right]\frac{e^{ikR}}{R}dS'. \end{aligned} \qquad (10)$$

We call these fields "ficticious fields" and use for the i-th subdomain the symbols $\begin{pmatrix}\vec{E}_{\mathrm{e}i}\\ \vec{H}_{\mathrm{e}i}\end{pmatrix}$ and $\begin{pmatrix}\vec{E}_{\mathrm{m}i}\\ \vec{H}_{\mathrm{m}i}\end{pmatrix}$ respectively. The ficticious fields may be subtracted from the original (approximative) fields leading to a new and — hopefully — more accurate solution.

4. The Time Harmonic Case

By construction we have at any point in the i-th subdomain

$$\begin{pmatrix}\vec{E}_i^{\mathrm{new}}\\ \vec{H}_i^{\mathrm{new}}\end{pmatrix} = \begin{pmatrix}\vec{E}_i^{\mathrm{old}}\\ \vec{H}_i^{\mathrm{old}}\end{pmatrix} - \begin{pmatrix}\vec{E}_{\mathrm{e}i}\\ \vec{H}_{\mathrm{e}i}\end{pmatrix} - \begin{pmatrix}\vec{E}_{\mathrm{m}i}\\ \vec{H}_{\mathrm{m}i}\end{pmatrix}. \qquad (11)$$

Let us examine the mismatching of the new field $\begin{pmatrix}\vec{E}_i^{\mathrm{new}}\\ \vec{H}_i^{\mathrm{new}}\end{pmatrix}$ in a particular boundary point at position $\vec{r}_0$. For this purpose a further splitting of the ficticious fields is performed by separating a small portion B^0 around $\vec{r}_0$ from the boundary. We may write $\mathrm{B} = \mathrm{B}^0\cup\mathrm{B}'$ and decompose the integrals accordingly, e.g.

$$\vec{E}_{\mathrm{e}i} = \vec{E}^0_{\mathrm{e}i} + \vec{E}'_{\mathrm{e}i} \qquad (12)$$

(analogous for $\vec{H}_{\mathrm{e}i}$, $\vec{E}_{\mathrm{m}i}$, $\vec{H}_{\mathrm{m}i}$ as well as $\vec{B}$ and $\vec{D}$). The primed parts are obtained by integrals only over B'. The remaining integrals over B^0 (a flat circular piece of boundary with a supposed constant source density on it) may be obtained analytically and yield (at $\vec{r}_0 = \lim_{h\to 0}\vec{r}_0 + h\vec{u}_{\mathrm{norm}}$)

$$\begin{aligned} \vec{H}^0_{\mathrm{e}} &= \frac{1}{2}\vec{\alpha}_{\mathrm{e}}\times\vec{u}_{\mathrm{norm}} \\ \vec{E}^0_{\mathrm{e}} &= \frac{\vec{\alpha}_{\mathrm{e}}}{4i\omega\varepsilon} \\ \vec{E}^0_{\mathrm{m}} &= -\frac{1}{2}\vec{\alpha}_{\mathrm{m}}\times\vec{u}_{\mathrm{norm}} \\ \vec{H}^0_{\mathrm{m}} &= \frac{\vec{\alpha}_{\mathrm{m}}}{4i\omega\mu} \end{aligned} \qquad (13)$$

Thereby, $\vec{u}_{\text{norm}}$ points into the field domain. Note that the normal components become zero which is due to the fact that we assumed a constant $\vec{\alpha}$ on B_0.

The new tangential mismatchings become

$$\begin{aligned}\vec{\Delta}E_{\text{t}}^{\text{new}} = &\underbrace{\vec{E}_{\text{t,left}}^{\text{old}} - \vec{E}_{\text{t,right}}^{\text{old}}}_{=\vec{\Delta}E_{\text{t}}^{\text{old}}} \\ &- \vec{E}'_{\text{et,left}} + \vec{E}'_{\text{et,right}} \underbrace{-\vec{E}^0_{\text{et,left}} + \vec{E}^0_{\text{et,right}}}_{=\frac{\vec{\alpha}_{\text{e}}}{4i\omega}\left(\frac{1}{\varepsilon_{\text{left}}} - \frac{1}{\varepsilon_{\text{right}}}\right)} \\ &- \vec{E}'_{\text{mt,left}} + \vec{E}'_{\text{mt,right}} \underbrace{-\vec{E}^0_{\text{mt,left}} + \vec{E}^0_{\text{mt,right}}}_{=-\vec{\alpha}_{\text{m}}\times\vec{u}_{\text{norm}}}\end{aligned} \tag{14}$$

$$\begin{aligned}\vec{\Delta}H_{\text{t}}^{\text{new}} = &\underbrace{\vec{H}_{\text{t,left}}^{\text{old}} - \vec{H}_{\text{t,right}}^{\text{old}}}_{=\vec{\Delta}H_{\text{t}}^{\text{old}}} \\ &- \vec{H}'_{\text{et,left}} + \vec{H}'_{\text{et,right}} \underbrace{-\vec{H}^0_{\text{et,left}} + \vec{H}^0_{\text{et,right}}}_{=\frac{\vec{\alpha}_{\text{m}}}{4i\omega}\left(\frac{1}{\mu_{\text{left}}} - \frac{1}{\mu_{\text{right}}}\right)} \\ &- \vec{H}'_{\text{mt,left}} + \vec{H}'_{\text{mt,right}} \underbrace{-\vec{H}^0_{\text{mt,left}} + \vec{H}^0_{\text{mt,right}}}_{=\vec{\alpha}_{\text{e}}\times\vec{u}_{\text{norm}}}\end{aligned} \tag{15}$$

and the normal mismatchings are

$$\begin{aligned}\Delta D_{\text{n}}^{\text{new}} = &\underbrace{\varepsilon_{\text{left}} E_{\text{n,left}}^{\text{old}} - \varepsilon_{\text{right}} E_{\text{n,right}}^{\text{old}}}_{=\Delta D_{\text{n}}^{\text{old}}} \\ &- \varepsilon_{\text{left}} E'_{\text{en,left}} + \varepsilon_{\text{right}} E'_{\text{en,right}} \\ &- \varepsilon_{\text{left}} E'_{\text{mn,left}} + \varepsilon_{\text{right}} E'_{\text{mn,right}}\end{aligned} \tag{16}$$

$$\begin{aligned}\Delta B_{\text{n}}^{\text{new}} = &\underbrace{\mu_{\text{left}} H_{\text{n,left}}^{\text{old}} - \mu_{\text{right}} H_{\text{n,right}}^{\text{old}}}_{=\Delta D_{\text{n}}^{\text{old}}} \\ &- \mu_{\text{left}} H'_{\text{en,left}} + \mu_{\text{right}} H'_{\text{en,right}} \\ &- \mu_{\text{left}} H'_{\text{mn,left}} + \mu_{\text{right}} H'_{\text{mn,right}}\end{aligned} \tag{17}$$

Thus we can see that the normal mismatching is changed not by the local sources on B_0 but by the sources on B′ only. Now we suppose for the moment large fields $\vec{X}^0$ and try to compensate the old mismatching with only those fields. In formulae:

$$\begin{aligned}\vec{\Delta}E_{\text{t}}^{\text{old}} &= \frac{\vec{\alpha}_{\text{e}}}{4i\omega}\left(\frac{1}{\varepsilon_{\text{right}}} - \frac{1}{\varepsilon_{\text{left}}}\right) + \vec{\alpha}_{\text{m}} \times \vec{u}_{\text{norm}} \\ \vec{\Delta}H_{\text{t}}^{\text{old}} &= \frac{\vec{\alpha}_{\text{m}}}{4i\omega}\left(\frac{1}{\mu_{\text{right}}} - \frac{1}{\mu_{\text{left}}}\right) - \vec{\alpha}_{\text{e}} \times \vec{u}_{\text{norm}}\end{aligned} \tag{18}$$

This system may be solved[1] with respect to the surface currents $\vec{\alpha}_{\text{e}}$ and $\vec{\alpha}_{\text{m}}$:

$$\begin{aligned}\vec{\alpha}_{\text{e}} &= \frac{\vec{\Delta}E_{\text{t}}^{\text{old}} C_{\text{m}} - \vec{\Delta}H_{\text{t}}^{\text{old}} \times \vec{u}_{\text{norm}}}{C_{\text{e}}C_{\text{m}} - 1} \\ \vec{\alpha}_{\text{m}} &= \frac{\vec{\Delta}H_{\text{t}}^{\text{old}} C_{\text{e}} + \vec{\Delta}E_{\text{t}}^{\text{old}} \times \vec{u}_{\text{norm}}}{C_{\text{e}}C_{\text{m}} - 1}\end{aligned} \tag{19}$$

[1] Cross-multiply the equations with $\times\vec{u}_{\text{norm}}$ and exploit the fact $\vec{\alpha}_{\text{m}} \times \vec{u}_{\text{norm}} \times \vec{u}_{\text{norm}} = -\vec{\alpha}_{\text{m}}$, then eliminate the vectors $\vec{\alpha}_{\text{e,m}} \times \vec{u}_{\text{norm}}$.

with the constants

$$\begin{aligned}C_{\text{e}} &= \frac{1}{4i\omega}\left(\frac{1}{\varepsilon_{\text{right}}} - \frac{1}{\varepsilon_{\text{left}}}\right) \\ C_{\text{m}} &= \frac{1}{4i\omega}\left(\frac{1}{\mu_{\text{right}}} - \frac{1}{\mu_{\text{left}}}\right)\end{aligned} \tag{20}$$

Using the sources (19), the new mismatching is optimised in a certain (local) sense but only with respect to its tangential components. Note that these sources are not 'negative equal' to the sources given in (6).

Since no complete correction is possible in a single step the given procedure is applied iteratively. Convergence is not guaranteed in all cases. However, experience shows that there are converging situations (see examples in sect. 6!).

5. Special Cases (Statics)

Let us discuss now some special situations. If either the electric or the magnetic properties are the same on both sides of a boundary, the respective constant C_{e} or C_{m} becomes zero and the surface current densities will reduce to the negative of that given in (6).

A second case worth to be discussed is the static situation. According to (7), the current sources of true static fields must be free of divergence while the charges are decoupled from the currents. The integrals (8) and (10) take the charge conservation into account: This means that all charges coupled by (7) to the currents are taken into account but true static charges are not. They can not exist in the time harmonic case. For very low frequencies the second integrals of (8) and (10) are still true: Either $\vec{\alpha}$ is free of divergence — in this case the total integral tends faster to zero than ω and the associated field vanishes — or $\text{div}_{\text{S}}\,\vec{\alpha} \neq 0$ — and the related charges increase with decreasing ω resulting in an increasing field. However, the decomposition (12) should not be used in this case since the local and non physical fields $\vec{E}_{\text{e}}^0$ and $\vec{H}_{\text{m}}^0$ tend to large values with decreasing ω, in spite of the fact that the sum $\vec{E}_{\text{e}}^0 + \vec{E}'_{\text{e}}$ becomes zero. In summary we state that in static cases we may take into account charges and currents separately using the integrals

$$\begin{aligned}\vec{H}_{\text{e}}(\vec{r}) &= \frac{1}{4\pi}\iint_{\text{B}} \frac{\vec{\alpha}_{eT}(\vec{r}') \times \vec{u}_R}{R^2} dS', \\ \vec{E}_{\text{m}}(\vec{r}) &= \frac{-1}{4\pi}\iint_{\text{B}} \frac{\vec{\alpha}_{\text{m}T}(\vec{r}') \times \vec{u}_R}{R^2} dS',\end{aligned} \tag{21}$$

known as Biot-Savart integral in the magnetic case

and the well known Coulomb integrals

$$\vec{E}_e(\vec{r}) = \frac{1}{4\pi\varepsilon} \iint_B \frac{\varsigma_e(\vec{r}')\vec{u}_R}{R^2} dS',$$
$$\vec{H}_m(\vec{r}) = \frac{1}{4\pi\mu} \iint_B \frac{\varsigma_m(\vec{r}')\vec{u}_R}{R^2} dS'. \quad (22)$$

The local fields (with upper index 0) resulting form (21) are equal to those given in (13) while the local fields resulting from (22) are simply

$$\vec{D}_e^0 = \frac{\varsigma_e}{2}\vec{u}_{\text{norm}},$$
$$\vec{B}_m^0 = \frac{\varsigma_m}{2}\vec{u}_{\text{norm}}, \quad (23)$$

where the normal vector $\vec{u}_{\text{norm}}$ points to the side of the field point.

Using a similar technique discribed in the general section 4 with compensating sources according to (6):

$$\varsigma_e = \Delta D_n^{\text{old}}$$
$$\varsigma_m = \Delta B_n^{\text{old}}$$
$$\vec{\alpha}_e = -\vec{\Delta} H_t^{\text{old}} \times \vec{u}_{\text{norm}} \quad (24)$$
$$\vec{\alpha}_m = -\vec{\Delta} E_t^{\text{old}} \times \vec{u}_{\text{norm}}$$

we may locally compensate both the tangential and the normal mismatching. Note that in common static applications only one field (either the magnetic fields ($\vec{B}$ and $\vec{H}$) or the electric fields ($\vec{E}$ and $\vec{D}$) are used but hardly ever both of them simultaneously. Nevertheless, both types of compensating sources are used — either the pair $(\vec{\alpha}_e, \varsigma_m)$ or the pair $(\vec{\alpha}_m, \varsigma_e)$.

6. Examples

We discuss two examples, one in 2D and one in 3D. For both examples, both the electric and the magnetic field is calculated. Figure 1 gives the cross section of a two wire line and in fig. 4 a straight wire above a non flat ground is shown. Materials are either ideal conductors or ideal dielectrics and the overall dimensions of the relevant parts are supposed to be small compared to the wavelength. This allows a quasistatic calculation of both the electric and the magnetic field separately. The boundary conditions on all the surfaces are: $\vec{E}_{\text{tang}} = \vec{0}$ in the electric case and $B_{\text{norm}} = 0$ in the magnetic case. In both cases the boundary conditions at the infinity must be respected which is done by choosing the starting condition and the 'excitation' in a correct way.

Let us discuss the 2D-example first (see fig. 1). For the *electrostatic calculation* the charge neutrality (with given charge on one wire) is a sufficient condition. It is given by the starting condition — the field of two oppositely equally charged thin wires placed inside the wires — and may not be altered by introducing correcting longitudinal magnetic currents since a single magnetic current does not contribute any charge. Furthermore, the total magnetic current in each wire must vanish. This results in the condition $\oint \vec{E} \cdot \vec{dl} = 0$ (integral around one wire) which is satisfied in our case only in a weak sense: The integral vanishes for the final (correct) solution. For the *magnetostatic calculation* the electric current neutrality (with currents of equal amount but different sign in both conductors) is necessary. This is obtained through the starting condition — the field of two thin straight wires leading opposite equal currents. The correcting sources are magnetic charges which must be of zero amount in total on each conductor. Again, this is guaranteed in a weak sense only: The $\vec{B}$-flux integral over the whole surface vanishes for the final (correct) solution.

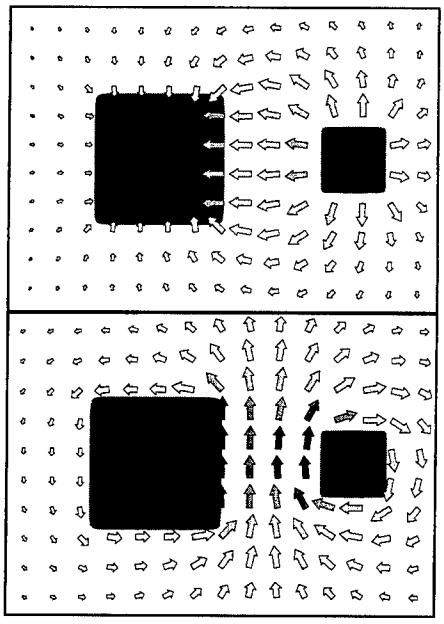

Figure 1: In the cross section of a two wire line with almost square shaped ideally conducting wires the electric field (top) and the magnetic field (bottom) are computed by means of statics. Two thin wires placed in the center of the 'squares' are used to produce the starting condition. In the electric case they carry opposite equal charge (per unit length) and in the magnetic case they lead opposite equal currents. See figs 2 and 3 for details of the field.

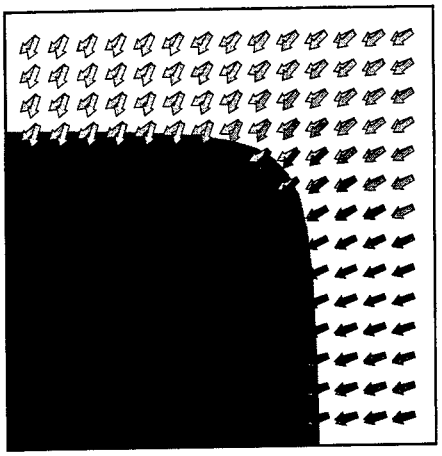

Figure 2: The (wrong) electrostatic field of only two thin wires is corrected using magnetic surface currents. The picture shows both the starting field and (in front of it) the corrected field (6 iterations) which stands perpendicular on the surface of the wire.

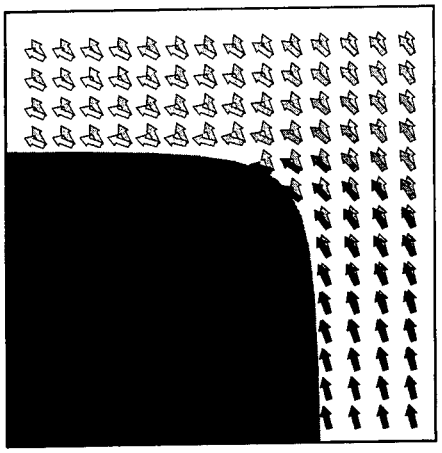

Figure 3: The (wrong) magnetostatic field of only two thin wires is corrected using magnetic surface charges. The picture shows both the starting field and (in front of it) the corrected (6 iterations) field which is tangential to the surface of the wire.

The 3D-example (see fig. 4) is somehow more sophisticated. The most important difference is that in the 2D-case the surface divergence of the currents vanishes automatically while in the 3D-case this is no longer true. It is important to note that the Biot-Savart integrals (21) deliver non Maxwellian fields in cases where the current density is not free of divergence. A second difficulty consists of the starting condition. Our particular example may be considered as a disturbed 2D-situation where the undisturbed problem consists of a thin wire over a flat conducting plane. This were a problem to be solved using the image principle. The solution of the undisturbed problem is (at least part of) a good starting field for the full problem. First of all it satisfies the 'boundary condition at infinity' and it covers all possible problems arrising from the infinite elongation of the wire and the ground plane, such as charge neutrality and opposite equal currents respectively. Since the field domain is essentially a half space (and not a full one as we had it in the 2D-example) in principal the correcting magnetic current may simulate a net electric charge on the hump (electrostatic calculation) and the correcting magnetic charge may simulate the field of local electric currents. The only remaining difficulty is the surface divergence of the correcting magnetic currents in the electrostatic subproblem. Work is in progress to solve this particular 3D-problem.

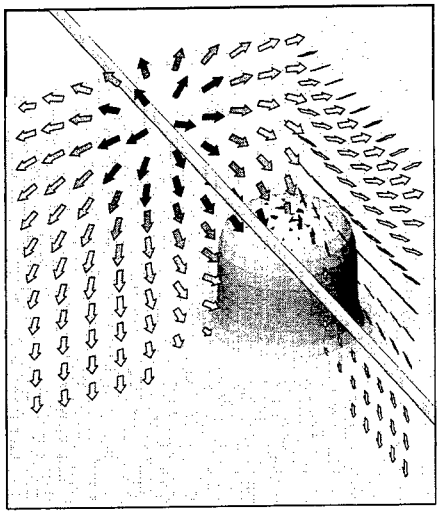

Figure 4: The electrostatic field of a long thin wire atop ground. The ground is almost flat — with a hump close to the wire. The correction is done using electric surface currents only. The picture shows the corrected electric field on two rectangles one perpendicular to the wire and the other parallel to it. Its locations are adjusted to the hump.

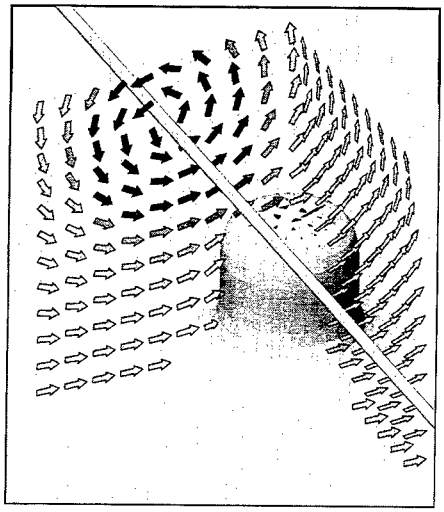

Figure 5: The corrected magnetostatic field of the situation shown in fig. 4. Here, only the field in a plane perpendicular to the wire is given. See fig. 6 for more informations of the field in other places.

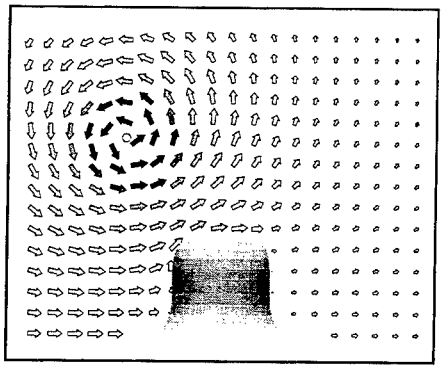

Figure 6: The magnetostatic field has been corrected using magnetic surface charges. Note that the field is tangetial to all the surfaces.

7. Summary

The mismatching on the boundaries may be reduced by adding ficticious sources compensating the local mismatching. This works perfectly in the 2D-case. The major difficulties in applying this technique in 3D is the fact that the ficticious sources do not necessarily fulfil the charge conservation principle.

Further problems may arise through the non local effect of the correction field: The ficticious sources do not only influence the field at their own location (though the strongest effect occurs exactly there) but also more fare away from them. Experience shows that this problem is not essential in the treated examples.

It has been shown that for particular cases the approach is very useful and leads to remarkably improved approximations.

8. References

[1] Ch. Hafner and Lars H. Bomholt. *The 3D Electrodynamic Wave Simulator*. John Wiley & Sons, 1993.

[2] Marcel Gnos and Pascal Leuchtmann. A new MMP-code for static field computation. In *11th Annual Review of Progress in Applied Computational Electromagnetics, Conference Proceedings*, Monterey, CA, March 1995.

[3] Ch. Hafner. *The Generalized Multipole Technique for Computational Electromagnetics*. Artech House Books, 1990.

SESSION 15:

ANTENNA ANALYSIS

Chairs: A. Glisson and A. Kishk

Accurate Design of Shaped Beam Doubly Curved Reflector Antennas for Airborne Applications

B S Shridhar [1] and N Balakrishnan [2]
Department of Aerospace Engineering
Indian Institute of Science
Bangalore 560 012.
India

Abstract

Doubly Curved Reflector Antennas which produce a directional pattern having a shaped beam in one plane find wide applications in search radars. The radiation pattern of the reflector gets affected by rim diffraction, scattering from supporting struts and due to feed blockage. In this paper, a numerical design procedure is presented for predicting the radiation pattern of the doubly curved reflector antenna. The procedure is similar to that developed for parabolic reflectors, but extended to doubly curved surfaces. Illustrative examples have been presented and compared with measured patterns.

1 Introduction

Several radar applications need beam shaping. For applications such as surface search by airborne antennas, the coverage pattern has a *cosecant-squared* shape in the elevation plane and a pencil beam in the azimuth plane. This type of a shaped beam can be obtained from a *Doubly Curved Reflector Antenna.* The conventional procedures for synthesising such antennas rely on Geometrical Optics (GO) fields to obtain the shaped vertical sections [1, 2, 3]. The radiation pattern of the shaped reflector can be calculated using Physical Optics (PO) techniques [4]. However, for an accurate analysis of the complete radiation pattern, it is necessary to take into account the

[1]Research Scholar
[2]Professor, also affiliated to Jawaharlal Nehru Centre for Advanced Scientific Research

diffraction from the rim of the reflector, aperture blockage due to feed and also the scattering from the struts supporting the feed [5].
Recent trends in the reflector antenna design have shown the need to combine the advantages of Aperture Integration (AI), Geometrical Theory of Diffraction (GTD), PO and the Method of Characterstic Moments. This approach which is well documented in the literature has been successful in the accurate prediction of the radiation pattern of parabolic reflectors [6]. Lee and Ruddock [7] describe AI techniques for computing the main beam and near sidelobes, and Uniform GTD [8] techniques for computing the wide–angle sidelobes and backlobes, of parabolic reflectors. Aperture blockage by feed is modeled by Physical Optics (PO) model of a rectangular or a circular plate [9]. Strut Scattering is modeled by considering that each strut segment scatters in the same way as an infinite circular cylinder [10]. The scattering from each segment is calculated using the method of characterstic moments and then summed up to obtain the total strut scattering.
In this paper, a technique that combines the advantages of the above methods is presented for an accurate design of a *shaped beam doubly curved reflector antenna.* Appropriate modifications necessary to extend the parabolic reflector analysis to the doubly curved reflector are described. With this technique both the co–polarised and cross-polarised fields can be calculated. The design procedure has been verified by comparing these theoretical predictions with experimental measurements at S-band. The effects of strut scattering and the feed blockage on the radiation pattern of the doubly curved reflector are also demonstrated.
The paper first reviews the reflector synthesis procedure described by Carberry [4].

2 Reflector Synthesis

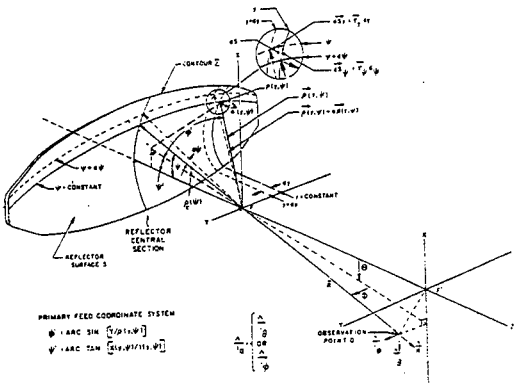

Figure 1: Geometry of a Doubly Curved Reflector and far-field coordinate system

The synthesis procedure described by Carberry [4] is based on Geometrical Optics theory. The first consideration is that the central vertical section of the reflector shown in Fig.1 must be designed to produce the desired far-field elevation plane pattern. The second consideration requires that the reflector be properly focused in the transverse planes. This requires that the rays emanating from the point source feed reflect from the conducting surface and emerge parallel to the central vertical plane. This focusing action requires that the transverse planes of the reflector be parabolic with a focal length of

$$F(\psi) = \rho_c(\psi)\cos^2\left(\frac{\beta}{2}\right) \tag{1}$$

where, $\beta = \psi + \theta(\psi)$
ψ = angle of ray incident on the reflector central section w.r.t z–axis
$\theta(\psi)$ = angle of reflected ray w.r.t z–axis
$\rho_c(\psi)$ = distance from origin to reflector central section

Using the synthesis procedure described in [4], for a given $G(\psi)$ (feed illumination function) and $P(\theta)$ (far-field function), $\rho_c(\psi)$ and the reflector co–ordinates can be computed.

3 Reflector Analysis

The radiation characterstics of the doubly curved reflector antenna can be analysed by Aperture Integration Method [11]. In this method, the fields reflected by the surface of the antenna is first found out over a plane, which is adjacent to and in front of the reflector and is normal to the axis of the reflector. Geometrical Optics (ray tracing) techniques are usually employed to accomplish this. The aperture plane is divided into a rectangular grid and equivalent sources are then formed over the grid. Fig.2 shows the central vertical section of the reflector with feed at $F(0, y_s, z_s)$. A ray starting from F at an angle ψ w.r.t the z-axis gets reflected from point $P(0, y_r, z_r)$ on the reflector surface. The reflected ray passes through the equiphase surface S at $P'(0, y', z')$ making an angle $\theta(\psi)$ w.r.t the horizontal at P. With $FP = \rho$ and $PP' = \rho'$, the equiphase surface S will be completely in front of the reflector if $\rho + \rho' \geq \rho_{max}$. The electric field at each point on the equiphase surface is given by

$$\vec{E}_{p'} = \frac{\sqrt{\eta G(\psi, \phi)}}{\rho + \rho'} e^{-jk(\rho+\rho')} \tag{2}$$

where $G(\psi, \theta)$ is the feed illumination function. The coordinates of P' are given by

$y' = \rho\sin\psi + \rho'\sin\theta$
$z' = \rho_0 - \rho\cos\psi + \rho'\cos\theta$

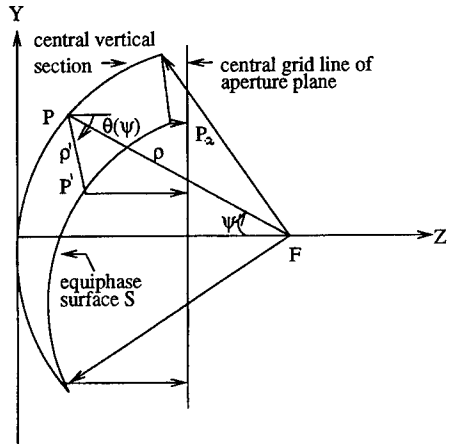

Figure 2: Ray tracing to find the aperture fields

The electric field at a point $P_a(0, y_a, z_a)$ on the central grid line is given by

$$E^a = E_{p'} e^{(-jkd)}, \text{ where, } d = |z' - z_a| \tag{3}$$

The x and y components of the aperture field E^a are given by

$$E_x^a = E^a \cos(\tau)$$
$$E_y^a = E^a \sin(\tau)$$

where, τ, is the feed polarization angle.
Since the transverse sections of the reflector are parabolic in shape, the electric field at each point on the aperture plane can be obtained by multiplying the central vertical section fields with a phase factor.

3.1 Far-field calculation using Aperture Integration

The far–field of the reflector antenna with its axis coincident with the z-axis and its aperture defined in the x–y plane, can be determined by the field distribution on the aperture using the relation [7]

$$E = \frac{jk}{2\pi} \int\int (\vec{F}_x E_x^a + (\vec{F}_y E_y^a) \frac{e^{-jkr}}{r} dxdy \tag{4}$$

E_x^a and E_y^a are the x and y components of the aperture electric field and r is the distance from the aperture point to the observation point. $\vec{F}_x$ and $\vec{F}_y$ are the modified vector element patterns associated with two Huygen's sources (crossed electric and magnetic dipoles) each having its electric field vector parallel to the x-axis and y-axis respectively. Efficient techniques for carrying out the aperture integration have been described in [7].

3.2 GTD Analysis

Uniform GTD is used to compute the wide-angle sidelobes and backlobes [7]. The use of empirical corner diffraction solution proposed by Burnside *et.al.*[12] permits the reflector rim to be modeled by piecewise linear segments. Consequently, the GTD analysis of the reflector is similar to that of diffraction by flat plate, in that, each rim segment is treated as an edge of a flat plate which is tangent to the reflector surface. A suitable criterion for each segment of the reflector rim is that it be small enough so that the focus of the reflector lies in the far-field of the rim segment. The total diffracted field is obtained by superimposing the edge diffracted field, the slope diffracted field and the corner diffracted field from each rim segment.

3.3 Feed Blockage Calculation

The blockage effects caused by the feed blocking the aperture fields of the main reflector, reduce gain and raise the sidelobe level of the antenna. The effect of the feed blockage is estimated by computing the scattered field of a conducting flat plate (rectangular or circular) whose area is equal to the maximum cross section of the feed horn structure [9]. The scattered fields caused by the feed horn blockage is found by physical optics approach. These forward scattered fields from the blockage aperture are then subtracted from the main reflector patterns.

3.4 Strut Scattering Calculation

For strut scattering calculation only perfectly conducting strut sections are considered. The strut axes are specified as linear with arbitrary locations of strut end-points. The strut scattered fields are determined by multiplying the incident field on the strut with diffraction coefficient. The incident field on the strut is obtained from the reflected field of the main reflector (aperture fields). The diffraction coefficients are determined from eigen function solutions of the scattering from a circular conducting cylinder [10]. Due to the aperture taper of the reflector, the incident fields along a long strut in a reflector system are typically not uniform. Consequently, the long strut has to be divided into many small segments and the incident field on each segment is determined. The method of equivalent currents is then used to obtain the total scattered field from the long strut by integrating the scattered field from each strut segment.

4 Computer Results

The formulations developed in the previous sections were evaluated using numerical techniques. Firstly, a doubly curved reflector was synthesised for obtaining a far–field pattern of $\csc^2(\theta)$. The assumed illumination was a cosine–squared function with a 12–dB taper along the contour (ϕ–plane). The maximum reflector dimension was 46 wavelengths. Figures 3 to 5 illustrate the central vertical section parameters.

Using the analysis theory described in sec.3, the radiation pattern of the synthesised reflector was computed. Fig.6 shows the far-field principal polarised elevation pattern ($\Phi = 0$ degrees) computed with only rim diffracted fields included. No feed blockage or strut scattering is considered. These calculations are compared with previously measured pattern [4]. Fig.7 shows the computed principal polarised pattern for $\Phi = -8$ degrees and the measured pattern. The compued and the measured patterns are in excellent agreement.

To study the effects of feed blockage and strut scattering a rectangular plate of dimensions $0.5\lambda \times 0.5\lambda$ was modeled as feed. The diameter of strut was increased from 0.5λ to 2λ. Fig.8 shows the effect of strut scattering and feed blockage on the elevation pattern. It can be seen that the main lobe and near sidelobes are not affected but the far sidelobe levels increase with increase in strut size. This increase is of the order of 1.5dB for the 0.5λ strut considered.

5 Conclusion

An analysis theory for computing the radiation pattern of a shaped beam doubly curved reflector antenna including the effects of rim diffraction, feed blockage and strut scattering has been presented. The results obtained by using the analysis theory have been compared with available measured patterns.

References

[1] A.S.Dunbar, "Calculation of doubly curved reflectors for shaped beams," *Proc. of the IRE*, vol. 36, pp. 1289–1296, October 1948.

[2] S.Silver, *Microwave Antenna Theory and Design.* McGraw-Hill, New York, 1949.

[3] A. Brunner, "Possibilities of dimensioning doubly curved reflectors for azimuth-search radar antenna," *IEEE. Transactions on Antennas and Propogation*, vol. AP-19, pp. 52–57, January 1971.

[4] T. Carberry, "Far-field analysis theory for a shaped beam doubly reflector antenna," *IEEE. Transactions on Antennas and Propogation*, vol. AP-17, pp. 131–138, March 1969.

[5] R. Elliot, *Antenna Theory and Design.* Prentice-Hall Inc, New Jersy, 1981.

[6] R. R. W.D. Burnside and R. Marhefka, "Summary of GTD computer codes developed at the ohio state university," *IEEE. Transactions on Electromagn. Compat.,*, vol. EMC-22, pp. 238–243, November 1980.

[7] S.H.Lee and R.C.Ruddock, "Aperture integration and GTD techniques used in the NEC reflector antenna code," *IEEE. Transactions on Antennas and Propogation*, vol. AP-33, February 1985.

[8] R.G.Kouyoumijan and P.Pathak, "A uniform geometrical theory of diffraction for an edge of a perfectly conducting surface," *IEEE. Transactions on Antennas and Propogation*, vol. 62, pp. 1448–1461, November 1974.

[9] T.H.Lee, R.C.Ruddock, and K.M.Lambert, "Pattern measurements of reflector antennas in the compact range and validation with computer code simulation," *IEEE. Transactions on Antennas and Propogation*, June 1990.

[10] R.F.Harrignton, *Time Varying Electromagnetic Fields.* McGraw-Hill, New York, 1961.

[11] C. A. Balanis, *Antenna Theory - Analysis and Design.* Harper & Row, Publishers, New York, 1982.

[12] W.D.Burnside, N.Wang, and E.L.Pelton, "Near field pattern analysis of aircraft antennas," *IEEE. Transactions on Antennas and Propogation*, vol. AP-28, pp. 318–327, May 1980.

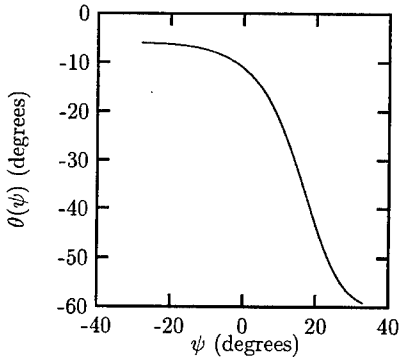

Figure 3:

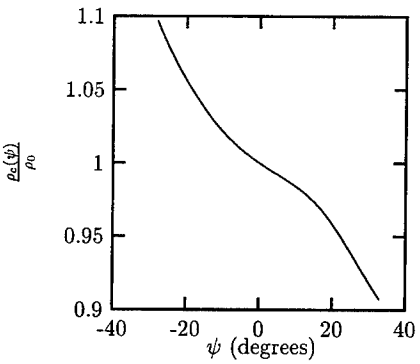

Figure 4:

Reflector central section parameters

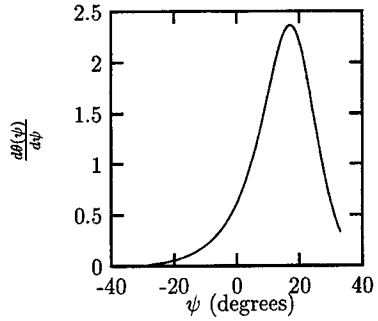

Figure 5: Reflector central section parameter

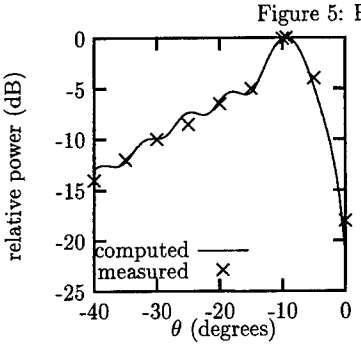

Figure 6: Pattern for $\Phi = 0^o$

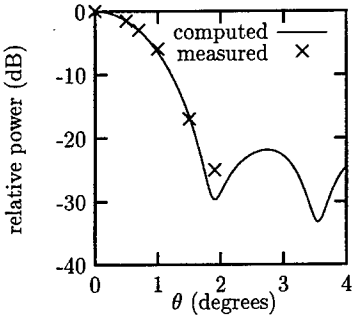

Figure 7: Pattern for $\Phi = -8^o$

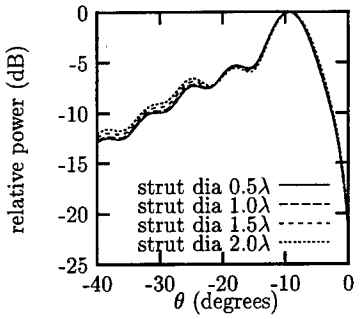

Figure 8: Effect of feed blockage and strut scattering

Rapid Parametric Study of Antennas Using Moment Method Codes

G.P. Junker, A.A. Kishk*, A.W. Glisson
Department of Electrical Engineering
University of Mississippi, University, MS 38677

Abstract: A procedure technique to accelerate moment method (MM) or any reaction based codes (RBCs) in such a way as to permit rapid parametric studies of a specific class of antennas is presented. The class of antennas under consideration in this study are dielectric resonator antennas (DRAs) situated on a conducting ground plane and fed by a coaxial probe through the back of the ground plane. The specific MM code to which this acceleration technique is applied is based upon a surface integral equation formulation for the coupling of a body of revolution (BOR) to a non-BOR geometry. For some simple antenna geometries, parametric studies are performed in the traditional way, i.e., the computer code is executed for each new set of parameters. The CPU time for these studies have compared to the CPU times for the same parametric study using the proposed accelerated coding techniques. Significant savings in CPU time can be realized by using the acceleration techniques presented in this paper.

Introduction: The nature and character of antenna design is, in essence, trial and error. That is to say, the design process is based upon previous experience and available data. Then comes the hard part: design optimization. Typically, in the course of the design procedure, a computer code must be repetitively executed, each time with a new set of parameters. This process can be very expensive in terms of CPU time. Because of this, a procedure technique to accelerate MM or any RBCs in such a way as to permit rapid parametric studies of a specific class of antennas is presented. From a computational point of view, the most expensive part of MM techniques is building the moment matrix. In the design procedure, rarely is there a need to change every component or "parameter" of the antenna during the design cycle. Indeed, for most of the time, a small part of the antenna needs to be modified while the major bulk of the antenna remains the same. Therefore by holding this part of the antenna constant, i.e., storing the corresponding part of the moment matrix, modifications can be made to another part without having to completely refill the moment matrix for each additional change. This can result in a significant savings in terms of computational effort. What is to be presented in this paper are simple coding techniques for the modification of an existing MM code which is capable of analyzing DRAs in such a way as to enable rapid parametric studies of the antenna [1].

Solution Procedure: The antenna of Fig. 1a is the specific DRA to be considered in this work. It consists of a half-split cylindrical DRA (CDRA) of relative permittivity ϵ_1 loaded with another half-split CDRA of relative permittivity ϵ_2. To model the half-split CDRAs as axisymmetric requires application of image theory to remove the conducting ground plane. Doing so results in an equivalent problem consisting of a dielectric body of revolution (DBOR) excited by a dipole antenna as illustrated in Fig.1b. Fig.1c illustrates a section cut through the y-z plane of the equivalent problem of Fig.1b

together with its relevant parameters. The DBOR is represented as the cross section of a surface of revolution, S_{de}. The surface S_{de} has, in essence, been created by the rotation of a simple curve or a generating arc about the Z-axis in a right-handed cylindrical coordinate system (the generating arc may be thought of as the intersection of a surface of revolution and a plane defined by a constant angle ϕ in a cylindrical coordinate system). The region exterior to a particular dielectric region d is composed of a homogeneous medium of constituent parameters ϵ_e and μ_0. The dipoles, which must adhere to the constraints of thin wire theory, are represented by S_{wd} and S_{we} where the subscripts "wd" and "we" refer to wire elements interior and exterior to the dielectric region d, respectively. The electric and magnetic field vectors are represented by the symbols $\underline{E}$ and $\underline{H}$, respectively. Superscripts "dt" and "et" refer to the total field interior and exterior to the region d, respectively. The field vectors $\underline{E}$ and $\underline{H}$ with superscripts "d" and "e" refer to the fields which arise from the equivalent currents which reside on the surfaces in the interior and exterior regions, respectively. The superscript "i" refers to the known field, that is, the source field which excites the dipole. The equivalent electric and magnetic surface currents which arise from application of the field equivalence principle are represented by the symbols $\underline{J}$ and $\underline{M}$, respectively.

Application of the field equivalence principle [2], together with enforcement of the electromagnetic field boundary conditions, results in a system of integro-differential equations from which the unknowns $\underline{I}_{wd}$, $\underline{I}_{we}$ (dipole currents), $\underline{M}_{de}$, and $\underline{J}_{de}$ (DBOR surface equivalent currents) can be determined. This system of equations can be written in operator form as the following:

$$\underline{E}^e_{tan}(\underline{J}_{de}+\underline{J}_{we}, \underline{M}_{de}) + \underline{E}^d_{tan}(\underline{J}_{de}+\underline{J}_{wd}, \underline{M}_{de}) = \underline{E}^{id}_{tan} - \underline{E}^{ie}_{tan} \quad \text{on} \quad S_{de} \tag{1}$$

$$\underline{H}^e_{tan}(\underline{J}_{de}+\underline{J}_{we}, \underline{M}_{de}) + \underline{H}^d_{tan}(\underline{J}_{de}+\underline{J}_{wd}, \underline{M}_{de}) = \underline{H}^{id}_{tan} - \underline{H}^{ie}_{tan} \quad \text{on} \quad S_{de} \tag{2}$$

$$\underline{E}^e_{tan}(\underline{J}_{de}+\underline{J}_{we}, \underline{M}_{de}) = -\underline{E}^{ie}_{tan} \quad \text{on} \quad S_{we} \tag{3}$$

$$\underline{E}^d_{tan}(\underline{J}_{de}+\underline{J}_{wd}, \underline{M}_{de}) = \underline{E}^{id}_{tan} \quad \text{on} \quad S_{wd} \tag{4}$$

The above system of equations consists of the electric field integral equation (EFIE) on the conductor surface, and both the EFIE and the magnetic field integral equation (MFIE) on the DBOR surface. The system of surface integral equations (1-4) are solved using Galerkin's MM procedure [3]. The unknown equivalent electric and magnetic currents on the DBOR are modeled as harmonic ($e^{jn\phi}$) entire domain basis functions for the circumferential variation, where n is the n^{th} Fourier azimuthal mode, and as piecewise liner subdomain basis functions for the dependence on axial curvature [4]. The unknown equivalent electric current on the dipoles are modeled as piecewise linear basis functions [3]. Modelling of the source fields with the extended delta source [5] results in the right hand side of equations (3) and (4) being set to zero.

Upon application of the Galerkin MM procedure, the above system of equations may be

expressed in matrix form as

$$\begin{bmatrix} [BB]_{-n} & . & \cdots & . & \cdots & . & . & [BW]_{-n} \\ . & [BB]_{-n+1} & \cdots & . & \cdots & . & 0 & [BW]_{-n+1} \\ . & . & \cdots & \cdots & \cdots & \cdots & \cdots & \cdots \\ . & . & \cdots & [BB]_0 & \cdots & . & . & [BW]_0 \\ . & 0 & \cdots & . & \cdots & \cdots & . & \cdots \\ . & . & \cdots & . & \cdots & [BB]_{n-1} & . & [BW]_{n-1} \\ . & . & \cdots & \cdots & . & . & [BB]_n & [BW]_n \\ [WB]_{-n} & [WB]_{-n+1} & \cdots & [WB]_0 & \cdots & [WB]_{n-1} & [WB]_n & [WW] \end{bmatrix} \begin{bmatrix} |JM>_{-n} \\ |JM>_{-n+1} \\ \cdots \\ |JM>_0 \\ \cdots \\ |JM>_{n-1} \\ |JM>_n \\ |J_w> \end{bmatrix} = \begin{bmatrix} |0> \\ |0> \\ \cdots \\ |0> \\ \cdots \\ |0> \\ |0> \\ |V_w> \end{bmatrix} \quad (5)$$

The submatrix [BB] represents the interactions of the DBOR equivalent surface currents with themselves, and the submatrices [BW] and [WB] represent the interactions between the DBOR equivalent surface currents and the wire currents, and vice versa, respectively. The vector $|JM>_n$ represent the electric and magnetic current coefficients for the n^{th} Fourier mode of the basis functions which reside on S_{de} and are given by

$$\begin{bmatrix} |J_{de}> \\ |M_{de}> \end{bmatrix}_n \quad (6)$$

The vector $|J_w>$ represents the current expansion coefficients for the currents that reside on the surface S_{wq}, q=d or e, and is given by

$$\begin{bmatrix} |J_{wd}> \\ |J_{we}> \end{bmatrix} \quad (7)$$

The vector $|V_w>$ represents the impressed electric field at the driven dipole surface. Since the final goal is to match the antenna a 50Ω line, computation of input impedance and subsequently the input reflection coefficient S_{11} is required. Therefore, the following steps, which are in essence a "mode by mode" elimination procedure, can be performed to obtain the solution for the current coefficients, J_{wq}, from which the input impedance can be calculated.

$$|JM>_n = -[BB]_n^{-1}[BW]_n|J_w>, \; n=-N,\ldots,N \quad (8)$$

These results can be substituted into the last equation system (last row) of (5) to obtain

$$\left[[WB]_{-n}\cdot[BB]_{-n}^{-1}\cdot[BW]_{-n} + \ldots + [WB]_0\cdot[BB]_0^{-1}\cdot[BW]_0 + \ldots + [WB]_n\cdot[BB]_n^{-1}\cdot[BW]_n - [WW]\right]|J_w> = -|V_w> . \quad (9)$$

Representing the bracketed term containing the matrix products on the left hand side of (9) as Z_w results in a matrix equation of the form

$$[Z_w]|J_w> = -|V_w> . \tag{10}$$

where $[Z_w]$ is an $N_w \times N_w$ matrix generated by applying the method of moment on an EFIE on the wire surface due to the "numerical" Green's function of the cylindrical dielectric resonator [6]. The wire current is easily obtained by inverting $[Z_w]$ and multiplying the result by $-|V_w>$.

Acceleration Procedure and Results: For ease of discussion, equation (5), shall be rewritten as

$$\begin{bmatrix} [BB] & [BW] \\ [WB] & [WW] \end{bmatrix} \begin{bmatrix} |JM> \\ |J_w> \end{bmatrix} = \begin{bmatrix} |0> \\ -|V_w> \end{bmatrix} \tag{11}$$

The main part of the antenna is that consisting of the dielectric resonator which is numerically represented as the matrix [BB] in (11) since it is this part of the antenna which has the desirable radiation characteristics. In order to obtain the best 50Ω match, as well as to excite the desired radiating mode, the feed probe position and length must be properly selected. It is not necessary to recompute the elements of the matrix [BB] for each new feed probe position in the design procedure since this part of the matrix is independent of the feed probe. Hence, the matrix [BB], $[BB]_n$, or $[BB]_n^{-1}$ can be stored. For the present application, it is more efficient to store $[BB]_n^{-1}$. Also, by taking the probe length to be the maximum possible length for a given dielectric region, it is possible to analyze the antenna for many different probe lengths. This can be accomplished by first storing the matrix [WW] since its elements are independent of the matrix [BB]. Therefore, after initial set up, only the matrices [BW] and [WB] require filling for each new probe position. Decreasing the length of the feed probe i.e., "cutting" the probe "bit by bit" by eliminating the basis functions on the dipole, one from the top and its image basis function on the bottom, is equivalent to decreasing the order of the matrix $[Z_w]$ by two for each "cut." This will require changing the matrix order for each cut. However, rather than changing the matrix order, its elements can be manipulated by placing zeros everywhere along the matrix rows and columns corresponding to the indices of the eliminated basis functions excluding the diagonal elements. The elements of the excitation vector corresponding to the index of the basis functions spanning the portion of the dipole which was cut away must be set equal to zero. An efficient procedure technique has been described which allows a given feed probe to be moved throughout the dielectric part of the antenna, as well as have its length changed, with only having to fill the matrices [BW] and [WB].

For this study, the following three antennas were analyzed on a CRAY J916 computer.

Antenna #1 h_1=39.5mm, a_1=24.5mm, ϵ_1=12.0, unloaded with a maximum probe length 22.5mm.

Antenna #2 h_1=39.5mm, a_1=24.5mm, ϵ_1=12.0, h_2=22.8mm, a_2=14.15mm, ϵ_2=36.0, d=9.95mm, probe in region with relative permittivity ϵ_1, with a maximum length of 22.5mm.

Antenna #3 h_1=39.5mm, a_1=24.5mm, ϵ_1=12.0, h_2=22.8mm, a_2=14.15mm, ϵ_2=36.0, d=9.95mm, probe in region with relative permittivity ϵ_2, with a maximum length of 11.0mm.

Attention is now called to Fig. 2 which gives actual CPU times for the three antennas for one probe position and eight different lengths analyzed in the traditional way, i.e., the program was executed for each different probe length. Rather than labeling the horizontal axis as "feed probe length," it was labeled as N_w, where N_w is the number of basis functions on the wire, since in the rapid study procedure, the length of the feed probe was changed by "cutting" away elements of $[Z_w]$. The DBOR surfaces were modelled with 76 basis functions and Fourier modes -3 to +3 were used in all cases. The difference in CPU times for the analysis of antennas #1 and #3 is due solely to the fact that antenna #3 is loaded; and as such, the DBOR surfaces are modeled with a total of 152 basis functions. Furthermore, since the dipole basis functions interact only with 76 DBOR basis functions, the increase in CPU time is due mainly to the additional DBOR basis function self interactions. Note that the time required to analyze antenna #2, and the rate at which the CPU time increases with respect to increasing N_w, is greater than that of either #1 or #3. This is because the dipole basis functions interact with all 152 DBOR basis functions since it is located between the free space exterior region and the region with relative permittivity $\epsilon_2=36.0$. Fig. 3 is a histogram which shows the total amount of CPU time required to analyze each antenna in the traditional way together with that of the rapid study procedure. The traditional time represents the sum of the individual times shown in Fig. 2 for each antenna. The rapid study time is for the same antennas except that the dipole was modeled at full length, and then cut away two basis functions at a time. As can be seen from the histogram, a significant savings in CPU time can be achieved.

Fig. 4 is a histogram which presents the actual CPU time required for the complete rapid study analysis which was performed. The projected CPU times for the traditional method of analysis were taken from the data of Fig. 2 and multiplied by the appropriate factors. Antenna #1 was analyzed with 4 different feed probe positions, 8 probe lengths, and 29 different frequencies. Antenna #2 was analyzed with 1 probe position, 8 probe lengths, and at 26 different frequencies. Antenna #3 was analyzed using 3 probe positions, 8 probe lengths, and at 26 different frequencies. Again, it is obvious that the rapid study procedure technique is quite effective. Finally, attention is called to Fig. 5 which gives the return loss, $|S_{11}|$ vs. frequency for antenna #1 for the feed probe position of z=7.9mm for 7 different feed probe lengths.

Conclusions: A procedure technique to accelerate moment method or any reaction based codes in such a way as to permit rapid parametric studies of a specific class of antennas has been presented. The specific MM code to which this acceleration technique is applied is based upon a surface integral equation formulation for the coupling of a BOR to a non-BOR geometry. The CPU time for these studies has been compared to the CPU times for the same parametric study using the proposed accelerated coding techniques. Significant savings in CPU time can be realized by using the acceleration techniques presented in this paper. In an industrial, or consulting environment, generalization of these techniques would definitely give one a competitive edge in the marketplace.

REFERENCES

[1] G.P. Junker, A.A. Kishk, and A.W. Glisson, "Input impedance of dielectric resonator antennas excited by a coaxial probe," *IEEE Trans Antennas Propagat.*, vol. 42, pp. 960-966, July 1994.

[2] R.F. Harrington, *Time Harmonic Electromagnetic Fields*, New York, McGraw Hill, 1961.

[3] R.F. Harrington, *Field Computation by Moment Methods*, Malabar, Fla., Robert E. Kreiger Publishing, 1968.

[4] A.A. Kishk, and L. Shafai, "Different formulations for numerical solution of single and multibodies of revolution with mixed boundary conditions," *IEEE Trans. and Propagat.*, vol. AP-34, No. 5, pp.666-673, 1986.

[5] G.P. Junker, A.A. Kishk, and A.W. Glisson, "A novel delta gap source model for center fed cylindrical dipoles," *IEEE Trans. Antennas Propagat.*, vol. AP-43, pp. 537-540, May 1995.

[6] A.W. Glisson and C.M. Butler, "Analysis of a wire antenna in the presence of a body of revolution," *IEEE Trans. Antennas Propagat.*, vol. AP-28, No. 5, pp. 604-609, 1980.

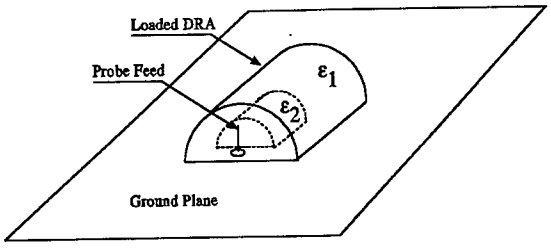

(a)

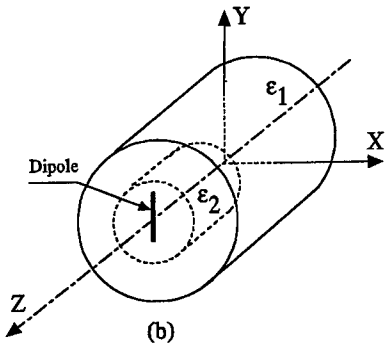

(b)

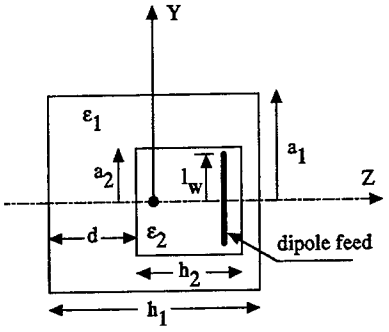

(c)

Fig. 1 Antenna Geometry. (a) Original problem, (b) Equivalent imaged problem, (c) Y-Z plane section cut.

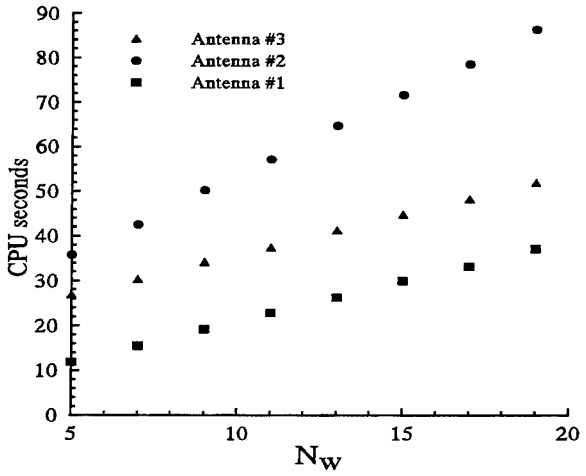

Fig. 2 CPU time vs. number of dipole basis functions for traditional study.

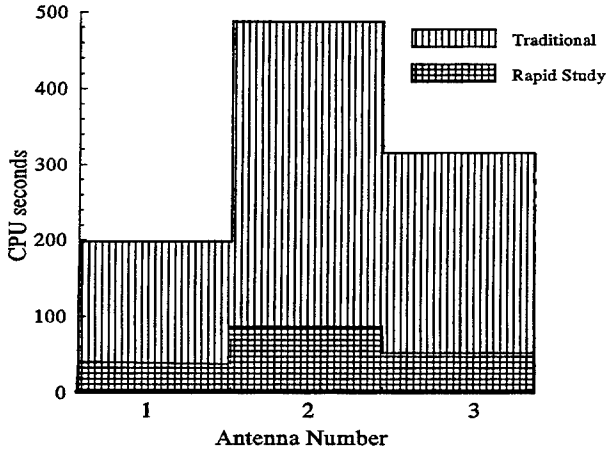

Fig. 3 Comparison of actual CPU times for traditional vs. rapid study procedure for the cases of Fig. 2.

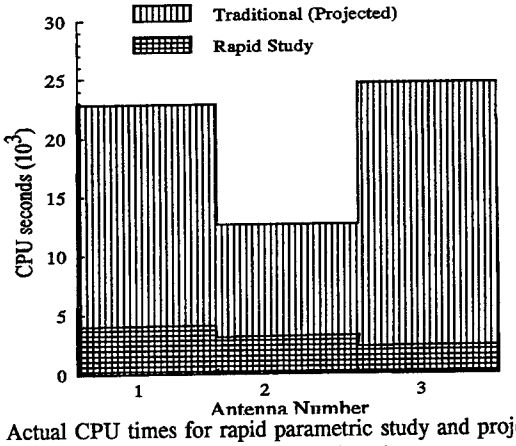

Fig.4 Actual CPU times for rapid parametric study and projected CPU times for traditional study.

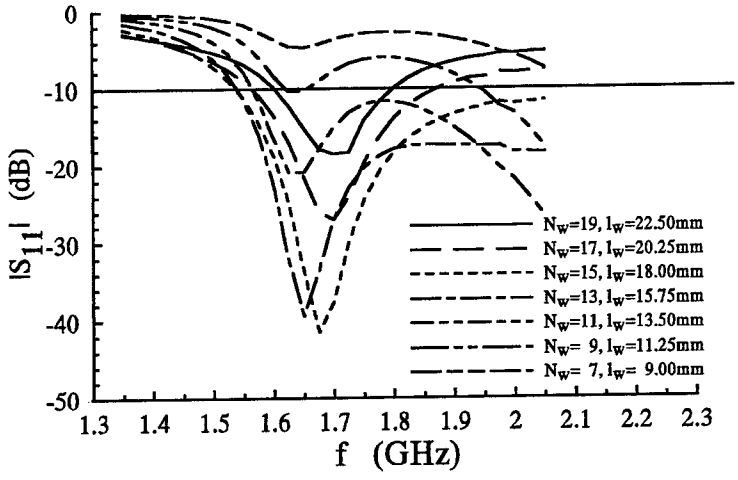

Fig. 5 Return losses for antenna#1 for different probe lengths for the feed position at z=11.85mm.

A NUMERICAL AND EXPERIMENTAL INVESTIGATION OF A SHIPBOARD DF ANTENNA ARRAY

Jeffrey B. Knorr
Department of Electrical and Computer Engineering
Naval Postgraduate School
Monterey, CA 93943-5121

Abstract

This paper describes a computer simulation of a shipboard high frequency direction finding (DF) system. The DF system utilizes a correlation interferometry direction finding (CIDF) algorithm. The algorithm requires a database which is obtained by calibrating the ship to obtain the complex voltages for an array of DF antennas at selected azimuth angles at any frequency of interest. The direction of arrival (DOA) of an incoming signal is then estimated by correlating the measured antenna voltages for the incoming signal with the previously stored calibration voltages.

To implement a computer simulation of a CIDF system, one must compute the response of each of the DF system antennas to an incoming plane wave which is incremented over 360 degrees in azimuth. The primary purpose of this paper is to describe the results obtained using NEC 4.1 and a wire grid model of the ship and its DF antenna array to compute these responses. The paper also describes the results obtained using a brass model of the ship and its DF antenna array to obtain measured antenna responses. Numerical and experimental results are presented and compared for two different ship configurations at several frequencies.

I. Introduction

Direction finding from a ship at HF is a challenging problem because in this frequency range, an HF antenna may interact strongly with the ship's superstructure. As a result, the response of an HF antenna aboard a ship may change considerably relative to its free space response. Thus, DF techniques which can be used at higher frequencies do not work well aboard ship at HF. The problem is not insurmountable, however. Saucier and Struckman [1] have described a correlation technique which will permit accurate bearings to be obtained if a sufficiently robst array is used. The correlation technique utilizes a CIDF algorithm which computes the correlation between the complex antenna voltages for an incoming signal, and complex antenna voltages stored in a data base for discrete azimuth angles at the same frequency. The angle of

maximum correlation is used as the bearing estimate.

Implementation of a CIDF system aboard ship requires that the ship be calibrated to create a database of complex voltages. Ships are often reconfigured, however, as new equipment is added and old equipment is removed or upgraded. Modifications may perturb the complex voltages because of the interaction of the array elements and the superstructure. If the voltages are perturbed, then bearing estimates will likely be in error unless the ship is recalibrated. The problem, of course, is that it is difficult to predict exactly what effect a particular change in ship configuration might have on the accuracy of a CIDF system.

This paper describes a computer simulation of a shipboard correlation interferometry direction finding system operating at HF. The simulation was built to determine the feasibility of using this approach to predict the effect of topside changes on DF system accuracy. The most difficult part of such a simulation is modeling the ship and its DF array, and subsequently, computing the response of each element of the DF array to an incoming plane wave which is incremented over 360 degrees in azimuth. In the following sections, wire grid ship models will be described, and computed antenna responses will be presented and compared with experimental data.

II. CIDF System Simulation

Computer simulation of a CIDF system is straightforward in principle. Three basic modules are required. The first module performs the computation of array antenna element responses. NEC 4.1 was used for this purpose. Computations were carried out using wire grid ship models which are described in more detail below. The second module implements the correlation algorithm. This module is used to investigate the effect of topside changes by cross-correlating the DF array voltages for one ship configuration with those for another configuration. The last module displays results. The correlation and bearing error processes generate vast amounts of data and this module is necessary to enable the user to interpret results. It generates three dimensional correlation and bearing error surface displays as well as two dimensional displays obtained by taking cuts through the three dimensional surfaces.

III. Wire Grid Ship Models

Computer simulation of a CIDF system has been investigated using two ship models. The first model is a destroyer with an anti-submarine rocket (ASROC) launcher located just forward of the deckhouse as shown in Figure 1. The second model is the same destroyer with the ASROC launcher removed and replaced with a vertical launch system (VLS). The VLS is also located just forward of the deckhouse but it is nearly flush with the deck and is a much less prominent structure than the ASROC launcher. These computer

models were developed to replicate, as accurately as possible, a 1/48th scale brass ship model which was used to obtain experimental data for validation of the simulation.

The ship models have identical, 24 element DF arrays. The elements are located around the periphery of the ship. Some are mounted on the edge of the deck and some are mounted on bulkheads. There are 12 starboard antennas and 12 port antennas in approximately mirror image locations. The brass model was built with coaxial semi-loop antenna elements, which effectively respond to the current flowing on the surface beneath the loop [2]. As a simplification, the semi-loop antennas used on the brass model were each represented by a single wire in the wire grid computer models.

The ship wire grid computer models contained approximately 4000 wires and 7000 segments. In those areas near the DF array elements, the grid size was on the order of 1 meter on a side, or 0.1 wavelengths at 30 MHz. In areas considered less critical, fewer wires were used. This approach was used successfully by Peng, et al., to compute helicopter antenna patterns [3], and also by Givati and Fourie to compute antenna patterns for a fighter aircraft [4]. Overall, the fidelity of the models permits their use at frequencies up to approximately 30 MHz.

IV. Computational Considerations

Determination of the response of each DF array element to an incoming plane wave, incremented over 360 degrees, is the most computationally intensive task which must be carried out to build a computer simulation of a CIDF system. It is this aspect of the simulation which is the focus of this paper.

Numerical computations of antenna responses were carried out with NEC 4.1, using the wire grid ship models described above. The approach used was to first compute the numerical Green's function; then compute antenna responses. The computations reported here were carried out using a CRAY EL98, located at the Naval Postgraduate School. This is an 8 processor machine with 256 MW (2 GB) of core memory. On this machine the ship computations were carried out in core, using one processor (NEC 4.1 is not configured for multiprocessing), and required 108 MW (860 MB) of memory. Approximately 8 hours of CPU time was required to compute the Green's function, and 1 hour to compute the 24 antenna responses at a selected frequency.

V. Measurement Program

Experimental data for validation of the DF system simulation was collected in a measurement program conducted at the RDT&E Division of the Naval Command Control and Ocean Surveillance Center (NRaD) in San Diego, CA. The 1/48th scale ship models were placed on an outdoor groundplane turntable and were illuminated at scaled

HF frequencies. The amplitude and phase of the signal received by each of the 24 DF antennas were recorded in 1 degree azimuth increments as the ship models were rotated. The center of rotation was a point halfway between the bow and the stern as measured at the waterline. The illuminating signal was theta polarized and at an elevation angle of 5 degrees. A sample of the output from the signal generator (transmitter) was routed to the receiver and used as a phase reference.

Data were collected for two different ship configurations (ASROC and VLS) at 20 different frequencies in the (scaled) HF band. For each of these combinations, amplitude and phase data were recorded for the 24 DF antennas.

VI. Numerical and Experimental Results

At the time of this writing, computations have been carried out for the two ship configurations (ASROC and VLS) at frequencies of 1.85 MHz, 6.34 MHz, and 9.25 MHz. The ship is approximately one wavelength long at 1.85 MHz and five wavelengths long at 9.25 MHz. Experimental data have been gathered for the two ship configurations at 20 frequencies, including the three above.

Figure 2a shows the computed, normalized patterns for port antenna P-3 and starboard antenna S-3 at a frequency of 1.85 MHz. These antennas are mounted on the deckhouse immediately behind the ASROC launcher and "look" about 20 degrees to port and starboard of the bow, respectively. It can be anticipated that these antennas will be most affected by the removal of the ASROC launcher. The antenna response for the ASROC configuration is shown by a solid line and the response for for the VLS configuration is shown by a dashed line. Figure 2b shows the experimental patterns. These results show that the numerical patterns agree well with the experimental patterns and that there is little difference between the patterns for the two configurations at this frequency.

Figures 3a and 3b show the numerical and experimental phase response for antennas S-3 and P-3 at 1.85 Mhz. The phase references for the measurements and computations were arbitrary and different so the values of phase on the two figures cannot be compared directly. Both figures, however, show about the same phase change as the source azimuth varies through 360 degrees. The phase change at this frequency is almost entirely due to the physical displacement of these antennas from the center of the ship. Again, there is little difference in the phase responses for the two configurations.

Figures 4a and 4b show the numerical and experimental patterns for antennas S-3 and P-3 at a frequency of 9.25 MHz. The agreement between the numerical and experimental patterns for these antennas is less precise at this higher frequency, but in both cases, it can be seen that the removal of the ASROC launcher perturbs the

patterns of the antennas.

As a final example, Figures 5a and 5b show the patterns of stern mounted antennas S-12 and P-12 at 6.34 MHz. Numerical and experimental results both show these antennas exhibit maximum response in the sector around 180 degrees relative bearing and that the removal of the ASROC launcher has little effect on the patterns of these two antennas.

VII. Conclusions

The objective of this work has been to investigate the feasibility of using computer simulation to predict the effect of topside changes on the performance of a shipboard direction finding system. The most challenging problem is computation of the responses of the DF array elements. Results obtained thus far are very encouraging.

Acknowledgements

The work presented here represents a significant effort. It could not have been accomplished without the support and participation of a number of individuals. First and foremost, the author wishes to acknowledge the role of CAPT Charles Ristorcelli, Space and Naval Warfare Systems Command, who had the foresight to recognize the potential of this research, and to support it. The wire grid models were created for the author through subcontract with NRaD by Lance Koyama. At NPS, Prof. Beny Neta assisted with the installation of NEC. Helpful discussions on the use of NEC in this application were held with Gerald Burke at Lawerence Livermore Laboratory and Dr. Jay Rockway at NRaD. The measurement program was carried out at NRaD by Carl Firman. Visualization software for a Silicon Graphics workstation was developed and installed under subcontract by Linda Russell at NRaD. Without this visualization capability, a structure as complex as a ship becomes extremely difficult to work with. Lastly, Dr. Ashok Das played an integral role at NPS. He assisted with computer runs and developed the software used to display the numerical and experimental DF antenna responses.

References

[1] N. Saucier and K. Struckman, "Direction finding using correlation techniques," Proc. IEEE International Symposium on Antennas and Propagation, pp. 260-263, June 1975.

[2] J. B. Knorr and D. C. Jenn, "A Numerical and experimental investigation of a loop antenna on a metal box", to be published, "Proc. ACES 12th Annual Review of Progress in Applied Computational Electromagnetics", Monterey, CA, March 18-22, 1996.

[3] J. Peng, et al., "Improvement of the NEC code's upper limit and pattern prediction of a helicopter structure", Proc. IEEE Int. Symposium on Antennas and Prop., pp. 56-59, June 1993.

[4] O. Givati and APC. Fourie, "The NEC2 radiation patterns of under-segmented wire grid models of a fighter aircraft compared to measurements", ACES Journal, Vol. 10, No. 1, pp. 5-14, March 1995.

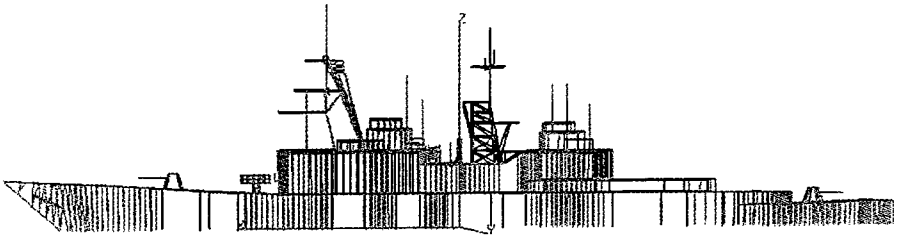

Figure 1a. Wire grid model of Spruance Class destroyer with ASROC launcher.

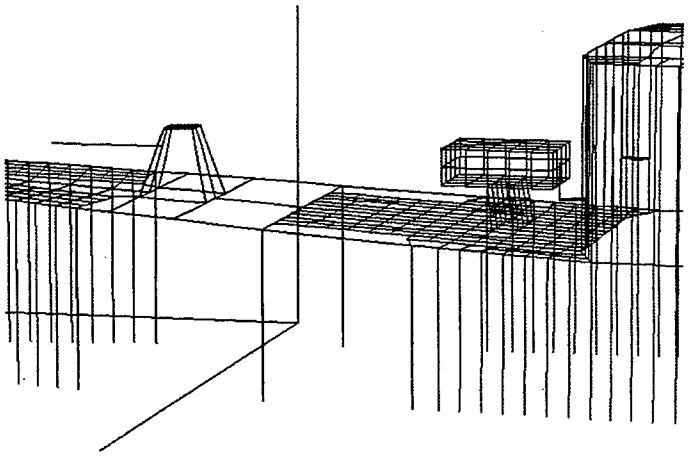

Figure 1b. Detail of area surrounding ASROC launcher.

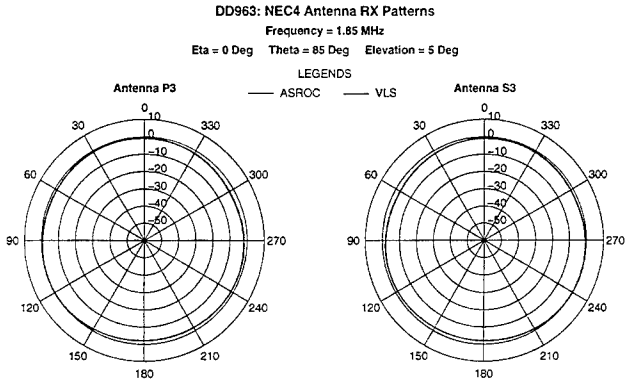

Figure 2a. Receiving patterns for DF antennas S-3 and P-3 computed using NEC 4.1. Frequency is 1.85 MHz.

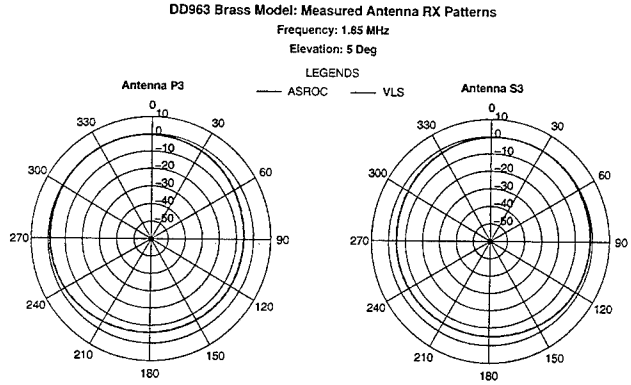

Figure 2b. Receiving patterns for DF antennas S-3 and P-3 measured using a 1/48th scale brass model of the ship. Unscaled frequency is 1.85 MHz.

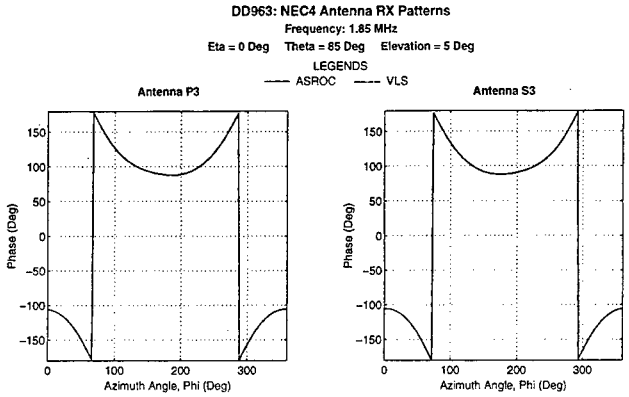

Figure 3a. Received signal relative phase for DF antennas S-3 and P-3 computed using NEC 4.1. Frequency is 1.85 MHz.

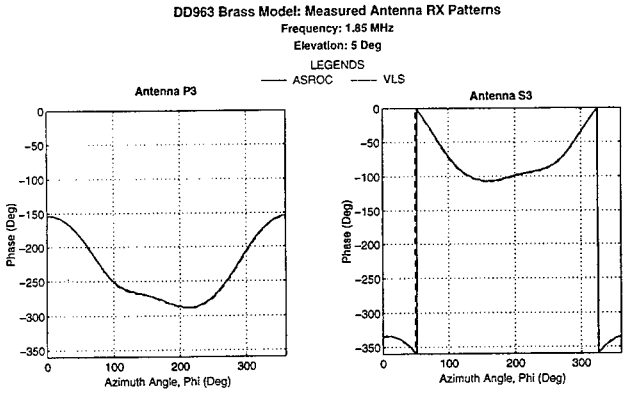

Figure 3b. Received signal relative phase for DF antennas S-3 and P-3 measured using a 1/48th scale brass model of the ship. Unscaled frequency is 1.85 MHz.

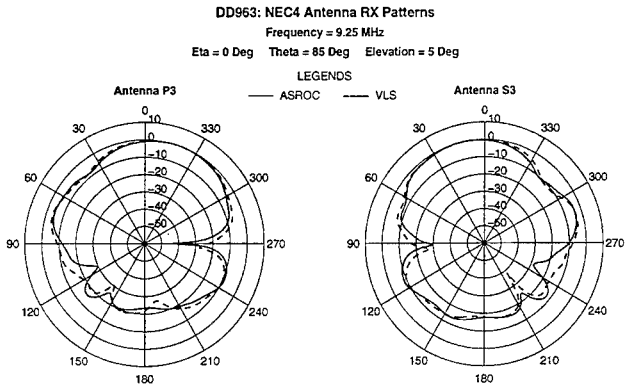

Figure 4a. Receiving patterns of DF antennas S-3 and P-3 computed using NEC 4.1. Frequency is 9.25 MHz.

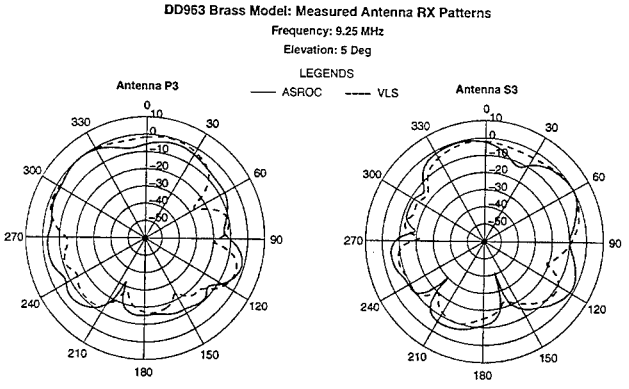

Figure 4b. Receiving patterns of DF antennas S-3 and P-3 measured using a 1/48th scale brass model of the ship. Unscaled frequency is 9.25 MHz.

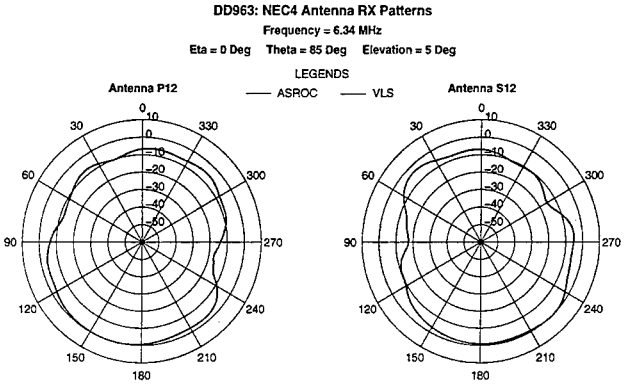

Figure 5a. Receiving patterns of stern mounted DF antennas S-12 and P-12 computed using NEC 4.1. Frequency is 6.34 MHz.

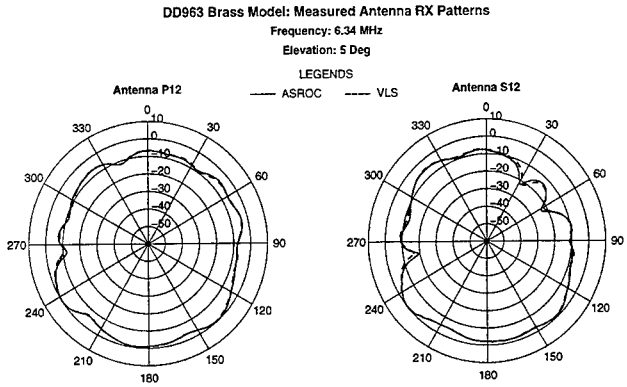

Figure 5b. Receiving patterns of stern mounted DF antennas S-12 and P-12 measured using a 1/48th scale brass model of the ship. Unscaled frequency is 6.34 MHz.

RADIATION PATTERNS OF ANTENNAS MOUNTED ON AN ATTACK HELICOPTER

O. Givati, APC. Fourie and J. Dresel
University of the Witwatersrand, Johannesburg
Private Bag 3, P O WITS 2050, South Africa
E-Mail: Givati@odie.ee.wits.ac.za

ABSTRACT

This paper presents results of a NEC2 method of moments evaluation of VHF/UHF antennas on a wire grid model of an attack helicopter. The study shows that practically useful radiation patterns results can be obtained when the grid model is considerably under-segmented in aircraft regions which are electrically far removed from the antennas. Normal modelling guide-lines requires approximately 37500 segments for the helicopter grid model at 420 MHz; judicious under-segmentation gave useful results using a model comprising about 4500 segments. This reduction in segments reduced computer time by a factor of 579 and memory requirements is reduced by a factor of 69. NEC2 radiation patterns are compared to measurements on a 1/20th scale model which was performed in an anechoic chamber compact range.

1 INTRODUCTION

The paper consider a study of radiation patterns from antennas mounted on an attack helicopter. NEC2 [1] computed radiation patterns are used for subsequent statistical assessment of link performance for the helicopter during typical mission profiles. Wire grids and segments much longer than the recommended [1] 0.1λ were used in areas far removed from the antennas to reduce execution time and memory requirements. Measured results, as well as comparison to more densely segmented numerical models, were used to ensure that these violations of modelling rules still produced useful values. It may be argued that numerical modelling is superfluous when measured results are available, but this is not the case when considering that:

- measurements in only three principle planes were performed and compared to a subset of the computed values; the statistical link analysis requires full three dimensional pattern information which is difficult and time consuming to obtain by measurement.
- traditional engineering normally argues that measurements constitute the more definitive characterization of a system when compared with calculation. This is definitely not always the case with radiation pattern measurements, especially on scale models, and many electromagnetics engineers can attest to cases where more confidence can be placed on values obtained from calculation or simulation.

The engineer is hence in a difficult position. He has two methods giving two sets of results - both associated with some potentially large errors. On the positive side is the fact that the two sets of results were obtained using two entirely different methods, with appropriate techniques used in both cases to minimize errors. Qualitative agreement will definitely demonstrate the absence of major blunders in both methods, and engineering judgement and cost will dictate which set of results is likely to be more appropriate.

Valid numerical models, for the purpose of subsequent statistical link analysis, are hence those which show qualitative agreement with measured results. Quantitative comparison between the measured and computed radiation patterns is difficult and often misleading, because:

- errors may be large when comparing measured and computed values at specific angles, but such errors may only be due to a slight offset in the position of a radiation pattern null, for instance. Such small angular offsets are not of any concern when performing statistical analysis of communication link performance.
- the existence of significant measurement errors also frustrate efforts to call the deviation from measured values "simulation errors".

It is hence evident that some of the more traditional quantitative measures of agreement between measured and computed results will be less useful and often meaningless. It is indeed left to the reader to assess the presented comparisons between measured and computed results and decide on their worth for a specific application. The most difficult aspect of the comparison, in fact, is the inaccuracies with the measurements themselves; the extent of such inaccuracies can easily be gouged by the deviations from symmetry in certain planes, as well as comparing corresponding points where different planes intersect.

2 SCALE MODEL MEASUREMENTS

A 1/20th scale model of the attack helicopter was constructed from UREAL foam which was covered with polymer sheets. The model was then copper-plated to ensure adequate conductivity. The antennas were incorporated into the model by internally guiding coaxial cable to the antenna positions and protruding the inner conductors by the appropriate scale measures to form the monopoles corresponding to the top-fin and bottom-fin antennas respectively.

Radiation pattern measurements in the principle planes (azimuth, side and pitch roll) were then performed on the scale model using a compact range suitable for the frequency range 2GHz-18GHz. The compact range consists of a 25 m x 10 m x 10 m anechoic chamber, calibrated feed antenna, offset parabolic reflector and positioner with three axes of freedom. The range was calibrated using a vertically polarized, standard gain horn in the frequency range 2 GHz-4 GHz. The standard gain antenna was then replaced with the scale model with the mounting bar in the same horizontal position as the standard gain antenna and the middle of the model at the same height as the standard gain antenna. The measurement system hence measured absolute gain in dB relative to an isotropic source (dBi). The only adjustment to the measured dBi values was to compute the losses in the cable leading from the calibrated connector to the antenna and to subtract these losses from the measurements in order to obtain the actual gain as measured at the antenna port.

The following movements were executed with the positioner to measure the pattern in the three principle aircraft planes (only the position and movements for the top-fin antenna are given below; the bottom-fin was measured using exact inverse positions and positioner movements):

- Azimuth (yaw) plane: The model was mounted horizontally (on its bottom for the Top-Fin antenna and on its top for the Bottom-Fin antenna) with its nose pointing towards the receiving antenna. The model was then rotated through 360°.
- Roll plane: The model was mounted vertically with its nose pointing downwards, and the top of the rotor pointing towards the receiving antenna. The model was then rotated through 360°.
- Pitch plane: The model was mounted horizontally on its side (ie at a 90° bank angle) and the top of the rotor pointing towards the receiving antenna. The model was then rotated through 360°.

It should be noted that only vertically polarized gain was measured, since this is the dominant polarization from both antennas and was also the only polarization of interest when performing link assessments. The signal source for measurements was also linked to the scale model via a cable which was always routed along the body of the scaled model to ensure that the cable enters the model at the opposite side of the model in relation to the antenna position (model mounting upright and upside down was possible using the mounting arrangement to facilitate this aim). When HF measurements on scale models were performed, a stand alone source was constructed and housed inside the scale model fuselage, because at lower frequencies the aircraft electrical dimensions are small in terms of wavelengths, and the cable shield carries substantial currents which affect the measurements. At higher frequencies, however, the interaction between an antenna mounted on one side of the aircraft with the measurement cable on the opposite side is minimal. A stand alone signal source would have been a disadvantage, in the VHF/UHF case where one is interested in absolute gain values, because it would need to be custom designed with suitable calibrated characteristics.

No measurements are error-free, and measurement uncertainty is particularly difficult to ascertain when radiation patterns are measured. Using the described measurement set-up the following factors may have been the cause of some of the errors (these are more or less listed in order of their severity):

- Inaccuracies in the scale model finish and dimensions. Some of the results presented shows some signs of asymmetry which is most likely due to slight errors in curvature on either side of the antenna
- Rotation "wobbles" because the mount in the fuselage is not absolutely perpendicular to the fuselage horizontal datum line.
- Angular errors due to certain amount of bending in the perspex mounting bar.
- Errors due to the fact that the protruding monopoles were not always exactly straight. This manifests itself most commonly in terms of errors in the position of the natural monopole pattern nulls.

No significant errors were caused by source amplitude instability, reflections from the chamber walls and other systematic errors associated with the range. The compact range used is professionally constructed and designed for measurements in the frequency range of interest. The calibration procedure ensures that equipment error levels are accounted for, and the quiet zone associated with the measurements is larger than the maximum movement and model dimensions during the course of the measurement manoeuvres.

3 GENERATION OF THE NUMERICAL MODELS

In this section, representations of the aircraft grid models, used for the evaluation of the top and bottom fin antennas' performance, are shown in Figures 2 through to 8. Different grid models were constructed in order to evaluate the antennas' performances at different frequencies. The numerical models used at the higher frequencies, apart from being under-segmented at regions which are sufficiently removed from the antenna of interest, were also substantially truncated. The numerical models of the aircraft were constructed using the Structure Interpolation and Gridding software package, SIG [2], developed by EM-Simulations (Pty) Ltd. The SIG package generates a three-dimensional grid model from a set of user defined cross-sectional cuts at points of abrupt change along the three dimensional structure - as indicated in Figure 1. The user-defined cross-sections shown in Figure 1 form the basis for the grid models, shown in Figures 2 through to 8. Wings and other features attached to the main fuselage are accommodated, using the SIG package, by tagging curves which represents features in a user defined cross section and using corresponding tag numbers in later user defined cross sections. In this way, for instance, cross-section 3 in Figure 1 consists of 4 curves with four tag numbers: The first curve represents the main fuselage, the second the top extension of the cockpit, the third curve represents the cannon support and the last curve in that cross section will just be a single point representing the start of the cannon itself. In the next cross section (4 in Figure 1) these four curves are re-defined with the dimensions at that cross sectional point and additional curves defining the canopy structure are defined; interpolation between the curves in cross-sections 3 and 4 which have identical tag numbers is then performed. The ability of SIG to accommodate appendages to a fuselage in this fashion is exceedingly useful, because the gridding routine ensures that the attached features are connected at all points of the grid.

The grid models shown in Figures. 2 through to 8 are generated by interpolating the cross-sectional cuts between the user defined cross-sections (in Figure 1), at intervals which are not greater than the specified target segment lengths of the user-defined cross-sections. The segmentations produced by SIG are mainly quadrilaterals, with the side lengths approximately equal to the target segment lengths requested. Some triangular grid elements are also formed when curves expand or contract from one cross-section to the next. These triangular grid elements also have edge lengths approximately equal to the required segment length. The segment radii are calculated by the SIG package to ensure that the surface area of the segments comprising the grid is approximately twice the surface area of the structure which is modelled. When structure's symmetry exist SIG automatically generates segments abutting the symmetry plane which are only half the grid length to ensure grid size continuity across the symmetry plane.

The SIG program allows the user to define cutting planes in order to remove parts of the structure. In a similar fashion the SIG program also allows the user to specify a specific target segment length for every user defined cross section. This target segment length is then used until a new target length is specified in a subsequent user defined cross section. In this fashion the structure can be formed using variable grid sizes at different parts of the structure. These features of the SIG software were used during this study.

The use of segment lengths larger than 0.1λ significantly reduces the number of segments used in the numerical model. Generally, such a violation of the numerical modelling rules can result in an invalid numerical model. In this paper, it is shown that the effect of under-segmentation and structure truncation, in regions which are sufficiently removed from the antennas, is negligible on electrically large structures. In return, the reduction in computation time is significantly large.

Target segment length	Section No. Top-Fin (220MHz)	Section No. Bottom-Fin (220MHz)	Section No. Top-Fin (320MHz)	Section No. Bottom-Fin (320MHz)	Section No. Top-Fin (420MHz)	Section No. Bottom-Fin (420MHz)
0.10λ	12-15	19-21	13-15	19-21	13-15	19-21
0.13λ	-	18, 22	12, 16	18, 22	12, 16	18, 22
0.15λ	11,16	17, 23	11, 17	17, 23	11, 17	17, 23
0.18λ	17	16, 24	10, 18	16, 24	10, 18	16, 24
0.2λ	10	15, 25	9, 19	15, 25	9, 19	15, 25
0.23λ	18	14, 26	8, 20	14, 26	8, 20	14, 26
0.25λ	8,9,19	13, 27	7, 21	13, 27	7, 21	13, 27
0.28λ	7	12, 28	6, 22	12, 28	6, 22	12, 28
0.30λ	1-6 & 20-28	1-11	1-5 & 23-28	1-11	1-5 & 23-28	1-11
Total No. of Segments	4481	4012	2729	2339	4501	4037

Table 1: The segmentation schemes used to generate the grid models of the helicopter at 220MHz, 320MHz and 420MHz.

The numerical model of the helicopter generated at 118MHz comprised of 0.1λ segments throughout and resulted in 4146 segments. The segmentation schemes used to generate the numerical models of the aircraft at 220MHz, 320MHz, and 420MHz, and for which theoretical results are also presented in this paper, are indicated in Table 1. The total number of segments used to numerically model the aircraft in its entirety (as indicated in Table 1) are much reduced compared to that which would be required if target segments length of 0.1λ and the entire aircraft structure were used. Specifying a target segment length of 0.1λ would result in approximately 13100 segments for the complete 220MHz grid model, 22700 segments for the complete 320MHz grid model and 37500 segments for the complete 420MHz grid model.

4 CONCLUSION

The main conclusions and recommendations of this study are listed below:

- Under-segmentation of the aircraft geometry in areas removed from the antennas made the evaluation of antennas at UHF frequencies possible; without this technique most available computer resources will be inadequate for such an evaluation.
- Limited measurements (with some significant errors in some cases) proved useful in qualitatively assessing the merit of the computed results.
- The SIG program [2] proved to be useful for automatic grid generation of the aircraft. Particularly due to the ability to vary grid size, omit parts of the structure and generate grid models for different frequencies.

Appreciating the electrical size and geometrical complexity of the aircraft model, the numerically predicted radiation patterns are showing good agreement with the measured radiation patterns in Figures 9 to 32. A close examination of the results reveals, however, that some disagreement between measured and simulated results do exist; the discussion in Sections 2 and 3 gave possible reasons for these disagreements. Although comparison of patterns in terms of normalized values, as presented in [3, 4 and 5], are based on pattern integration on a complete volumetric data set, including both polarizations for both measured and computed patterns, the comparison between measured and theoretical results in this paper is shown in terms of absolute gains which are associated with the dominant polarization.

REFERENCES

[1] Burke, G.J. and Poggio, A.J. (1981) *"Numerical Electromagnetics Code (NEC) - Method of Moments"*, Naval Oceans Systems Centre, San Diego, C.A., 92152. Technical Document 116, Vol. 1.

[2] Structure Interpolation and Gridding (SIG) software package developed by EM-Simulations (Pty) Ltd, P O Box 1380, Pinegowrie, 2123, South Africa.

[3] Kubina, S.J. (1983) *"Numerical Modelling Methods for Predicting Antenna Performance on Aircraft"*, AGARD Lecture Series No. 131, Sept. 1983, pp 9-1 to 9-38.

[4] Peng, J., Balanis, C.A. and Britcher, C.R. (1993) *"Improvement of the NEC Code's Upper Limit and Pattern Prediction of a Helicopter Structure"*, IEEE Antennas and Propagation Society International Symposium, University of Michgan, Ann Arbor, Michigan, USA.,June 28 - July 2, 1993, Vol. 1., pp 56-59.

[5] Peng, J., Choi, J, and Balanis, C.A. (1991) *"Progress: Development of an interactive graphics program for EM codes"* 7th Annual Review of Progress in Applied Computational Electromagnetics at Naval Postgraduate School Monterey, CA., March 1991, pp 10-19.

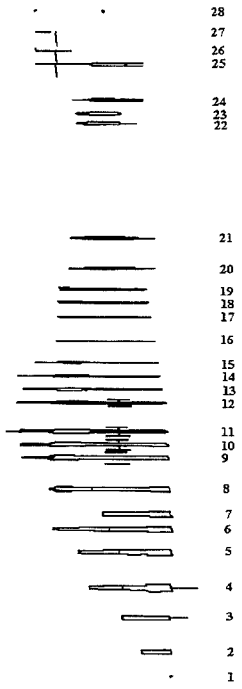

Figure 1: The user defined cross-sections used to generate the grid models of the helicopter.

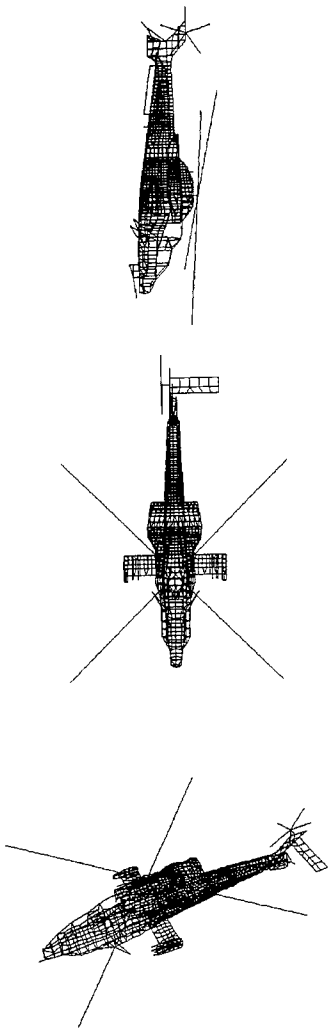

Figure 2: Side, top and perspective views of the helicopter grid model at 118MHz. This model was used for the comparison of theoretical to measured radiation patterns of the Top-Fin and the Bottom-Fin antennas.

Figure 3: Side view of the helicopter grid model at 220MHz. This model was used for the comparison of theoretical to measured radiation patterns of the Top-Fin antenna.

Figure 4: Side view of the helicopter grid model at 220MHz. This model was used for the comparison of theoretical to measured radiation patterns of the Bottom-Fin antenna.

Figure 5: Side view of the helicopter grid model at 320MHz. This model was used for the comparison of theoretical to measured radiation patterns of the Top-Fin antenna.

Figure 6: Side view of the helicopter grid model at 320MHz. This model was used for the comparison of theoretical to measured radiation patterns of the Bottom-Fin antenna.

Figure 7: Side view of the helicopter grid model at 420MHz. This model was used for the comparison of theoretical to measured radiation patterns of the Top-Fin antenna.

Figure 8: Side view of the helicopter grid model at 420MHz. This model was used for the comparison of theoretical to measured radiation patterns of the Bottom-Fin antenna.

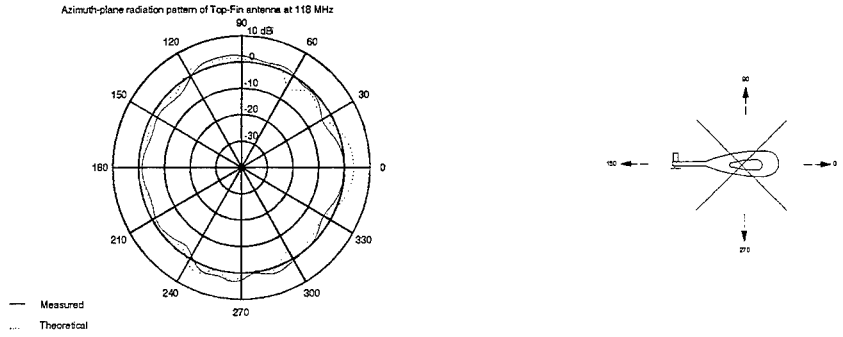

Figure 9: Theoretical and measured azimuth radiation patterns of the Top-Fin V/UHF antenna at 118MHz.

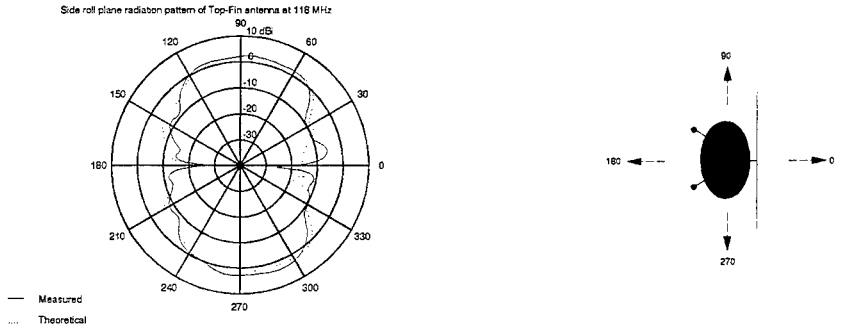

Figure 10: Theoretical and measured side roll elevation-plane radiation patterns of the Top-Fin V/UHF antenna at 118MHz.

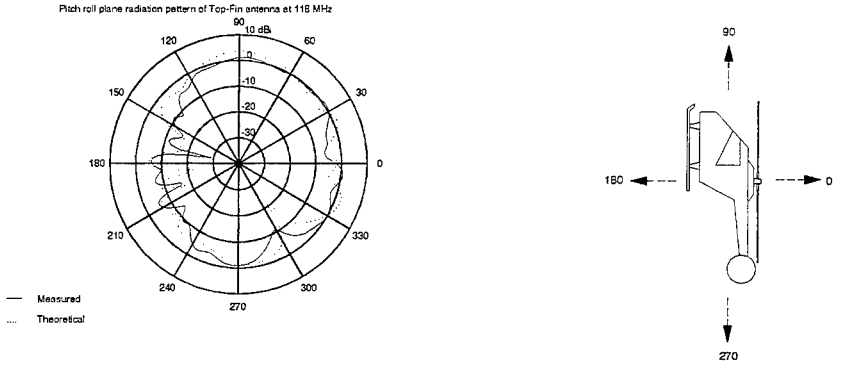

Figure 11: Theoretical and measured pitch roll elevation-plane radiation patterns of the Top-Fin V/UHF antenna at 118MHz.

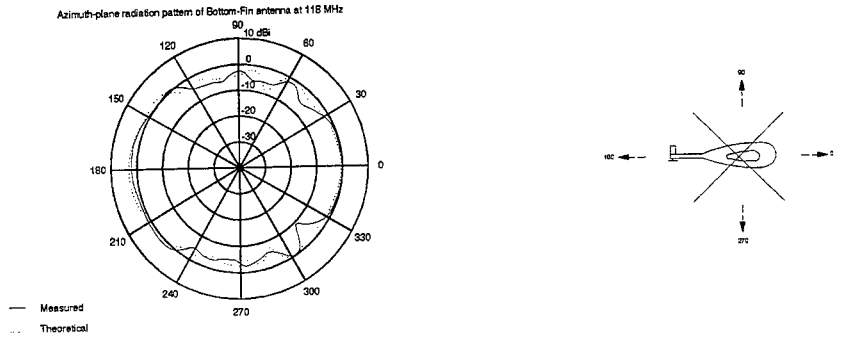

Figure 12: Theoretical and measured azimuth radiation patterns of the Bottom-Fin V/UHF antenna at 118MHz.

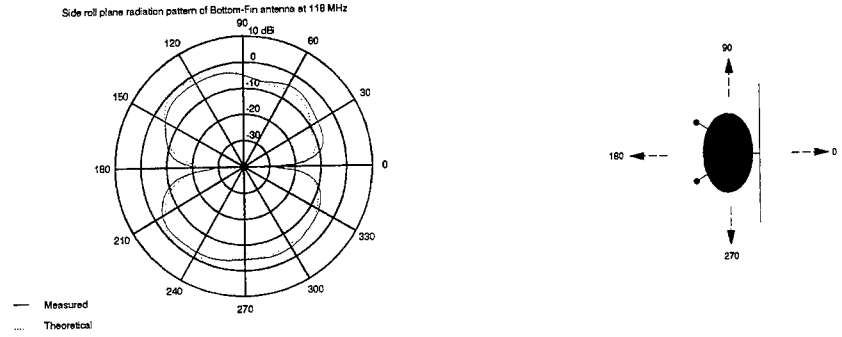

Figure 13: Theoretical and measured side roll elevation-plane radiation patterns of the Bottom-Fin V/UHF antenna at 118MHz.

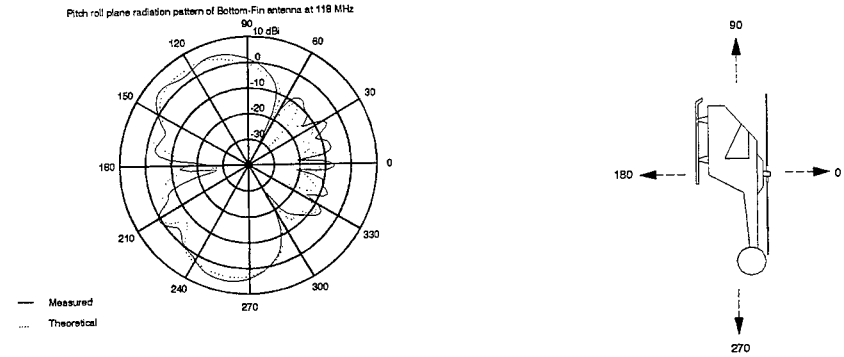

Figure 14: Theoretical and measured pitch roll elevation-plane radiation patterns of the Bottom-Fin V/UHF antenna at 118MHz.

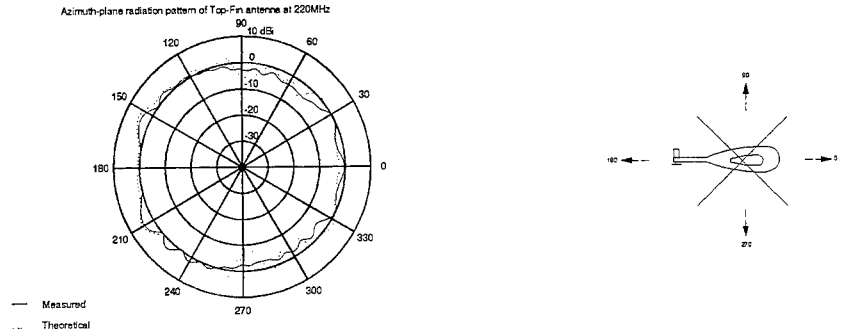

Figure 15: Theoretical and measured azimuth radiation patterns of the Top-Fin V/UHF antenna at 220MHz.

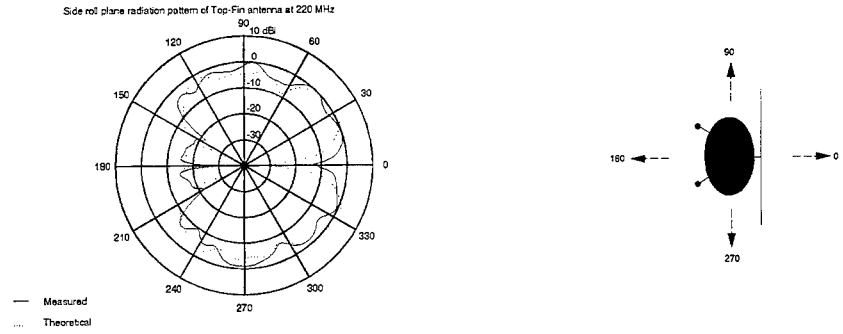

Figure 16: Theoretical and measured side roll elevation-plane radiation patterns of the Top-Fin V/UHF antenna at 220MHz.

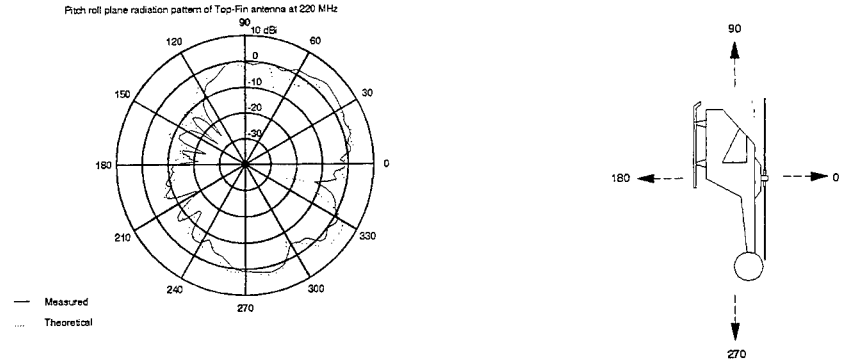

Figure 17: Theoretical and measured pitch roll elevation-plane radiation patterns of the Top-Fin V/UHF antenna at 220MHz.

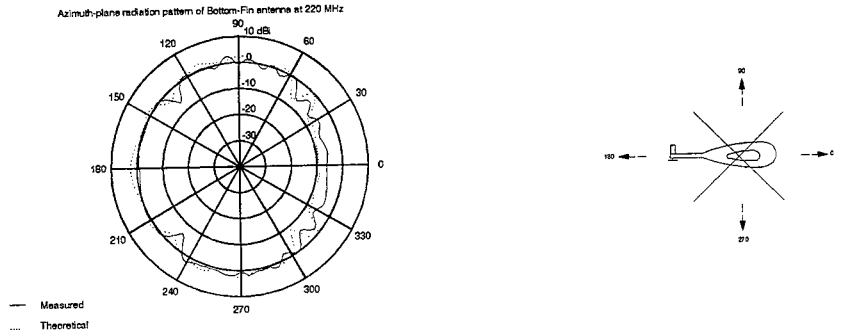

Figure 18: Theoretical and measured azimuth radiation patterns of the Bottom-Fin V/UHF antenna at 220MHz.

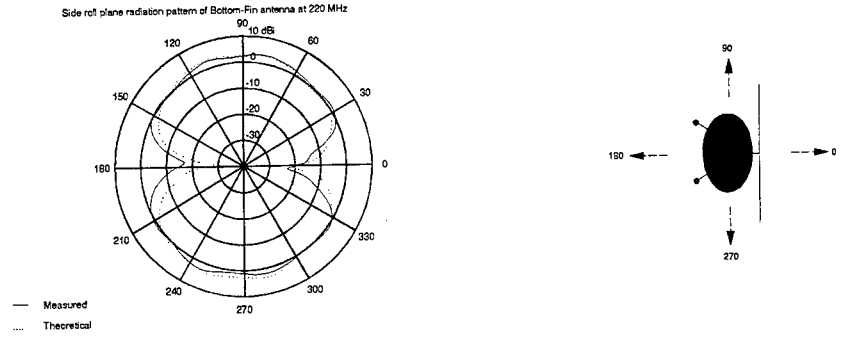

Figure 19: Theoretical and measured side roll elevation-plane radiation patterns of the Bottom-Fin V/UHF antenna at 220MHz.

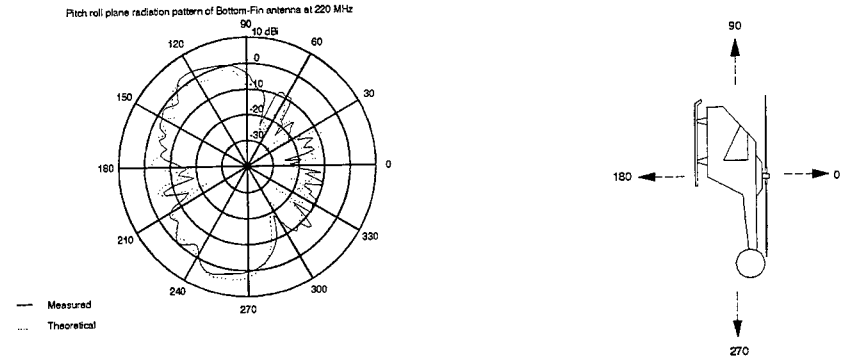

Figure 20: Theoretical and measured pitch roll elevation-plane radiation patterns of the Bottom-Fin V/UHF antenna at 220MHz.

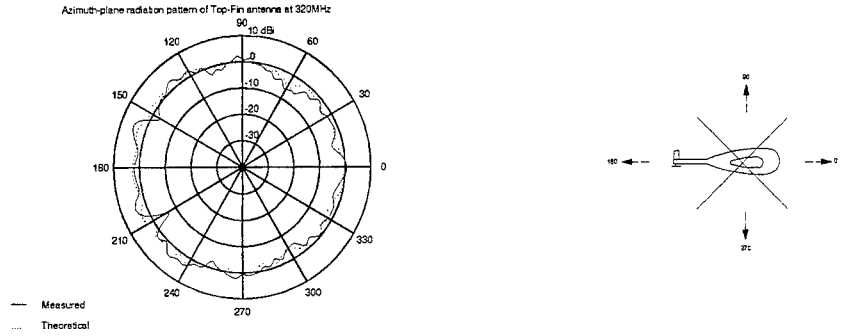

Figure 21: Theoretical and measured azimuth radiation patterns of the Top-Fin V/UHF antenna at 320MHz.

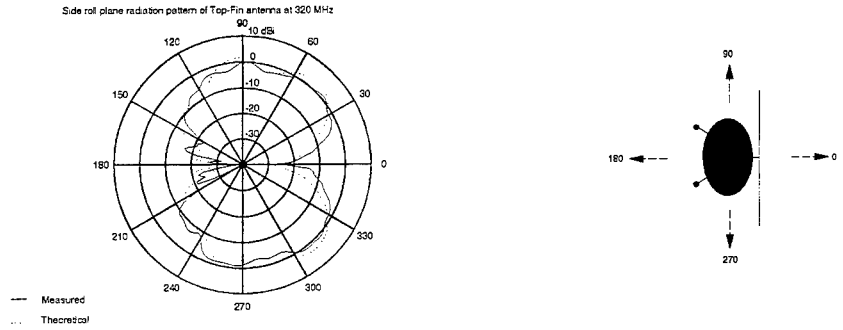

Figure 22: Theoretical and measured side roll elevation-plane radiation patterns of the Top-Fin V/UHF antenna at 320MHz.

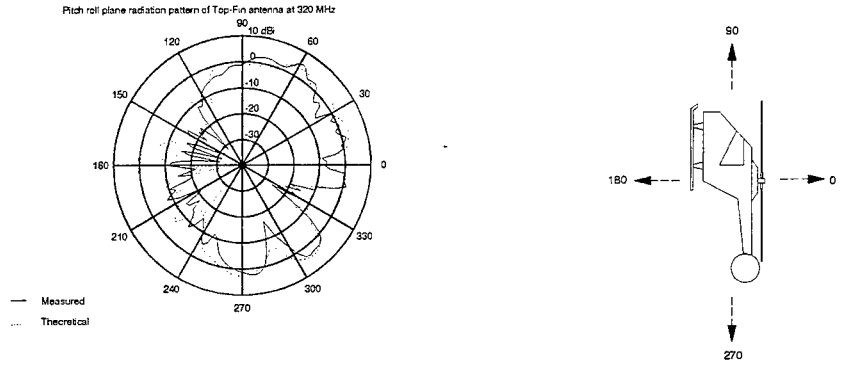

Figure 23: Theoretical and measured pitch roll elevation-plane radiation patterns of the Top-Fin V/UHF antenna at 320MHz.

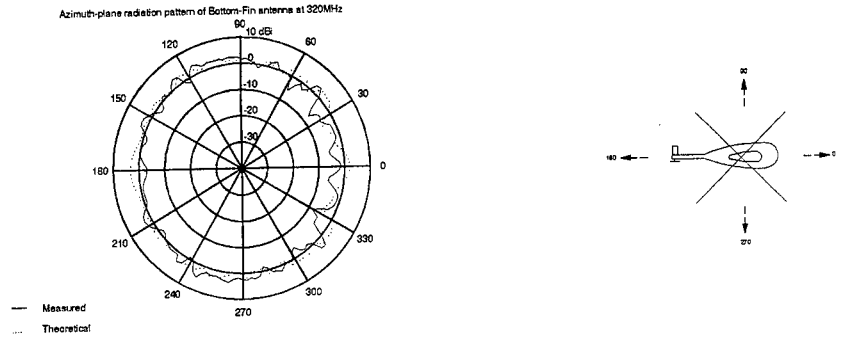

Figure 24: Theoretical and measured azimuth radiation patterns of the Bottom-Fin V/UHF antenna at 320MHz.

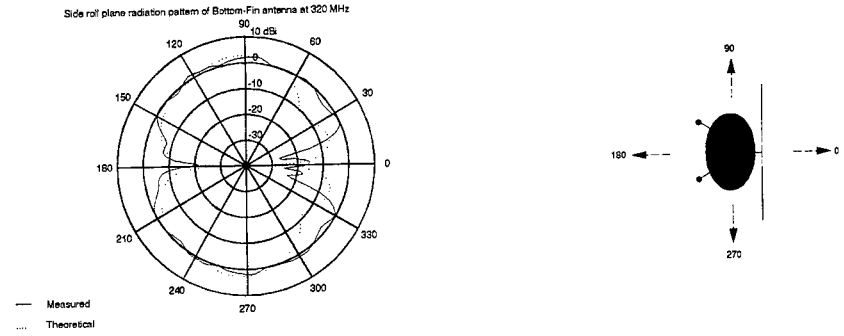

Figure 25: Theoretical and measured side roll elevation-plane radiation patterns of the Bottom-Fin V/UHF antenna at 320MHz.

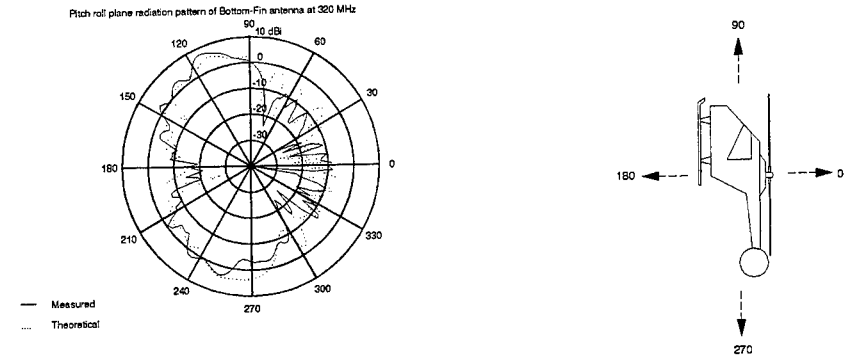

Figure 26: Theoretical and measured pitch roll elevation-plane radiation patterns of the Bottom-Fin V/UHF antenna at 320MHz.

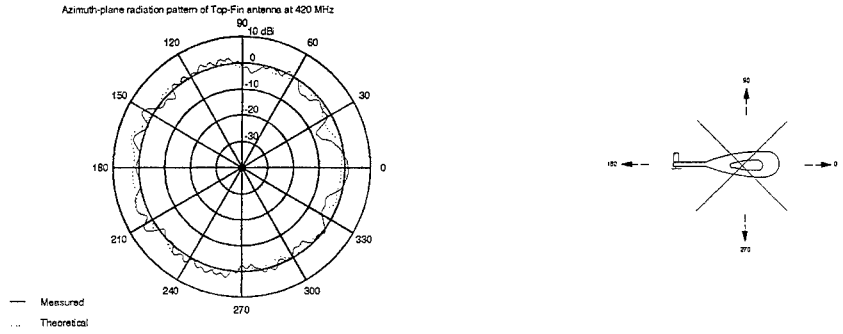

Figure 27: Theoretical and measured azimuth radiation patterns of the Top-Fin V/UHF antenna at 420MHz.

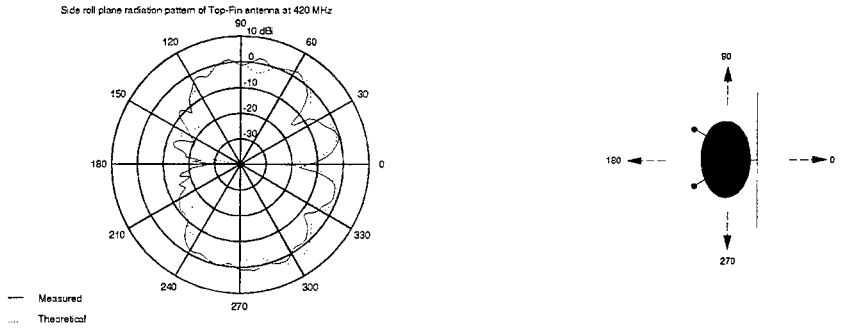

Figure 28: Theoretical and measured side roll elevation-plane radiation patterns of the Top-Fin V/UHF antenna at 420MHz.

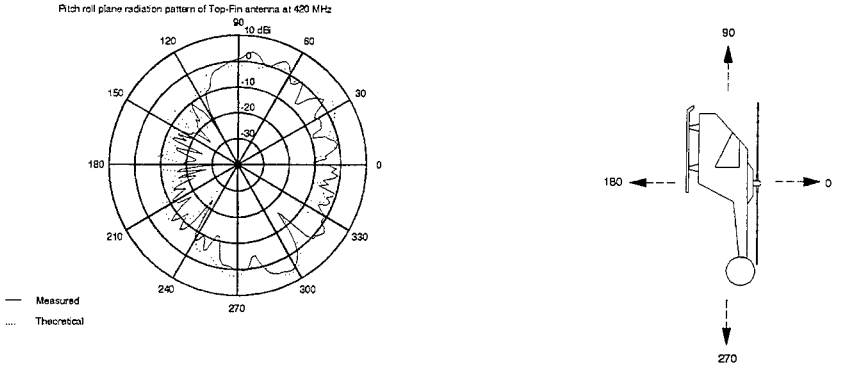

Figure 29: Theoretical and measured pitch roll elevation-plane radiation patterns of the Top-Fin V/UHF antenna at 420MHz.

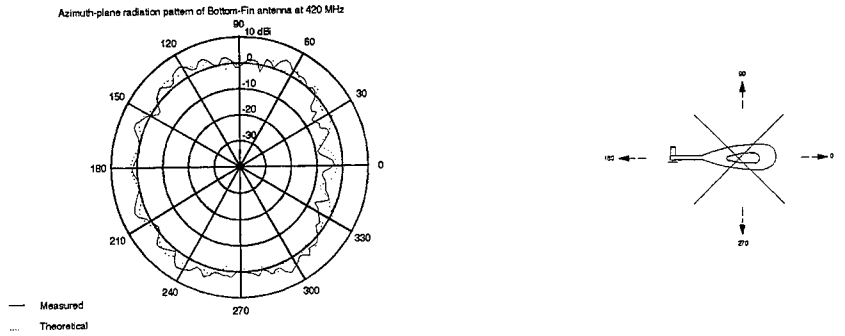

Figure 30: Theoretical and measured azimuth radiation patterns of the Bottom-Fin V/UHF antenna at 420MHz.

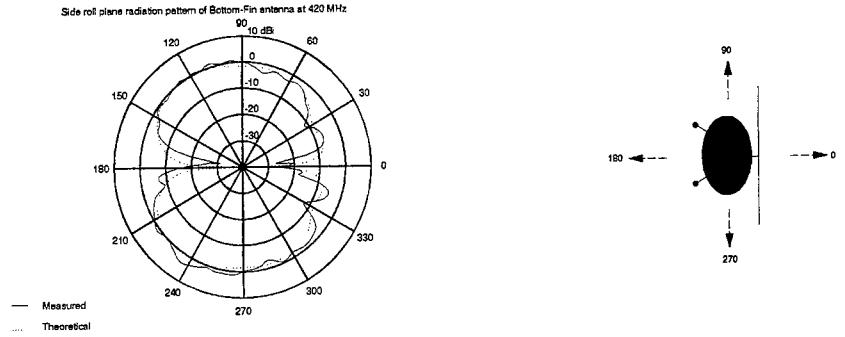

Figure 31: Theoretical and measured side roll elevation-plane radiation patterns of the Bottom-Fin V/UHF antenna at 420MHz.

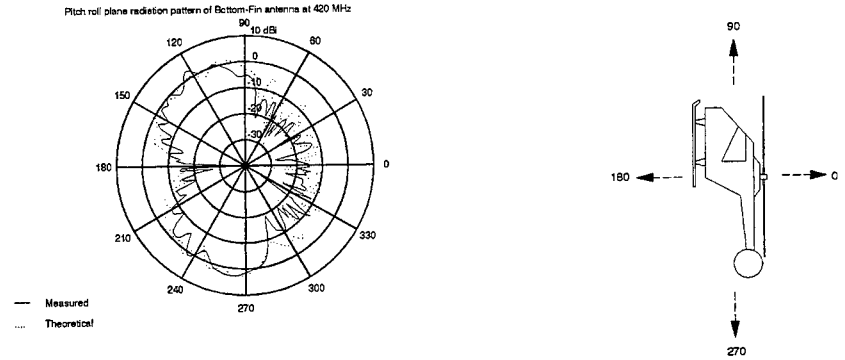

Figure 32: Theoretical and measured pitch roll elevation-plane radiation patterns of the Bottom-Fin V/UHF antenna at 420MHz.

Modelling of a Discone Antenna Mounted on a Communication Van

Joseph S. Seregelyi
Communications Research Centre
P.O. Box 11490, Station "H"
Ottawa, Ontario, Canada. K2H 8S2.
E-mail: joe.seregelyi@dreo.dnd.ca

Abstract:

Information about an antenna's performance is often given for free-field conditions; however, in most practical situations the antenna is mounted on a mast, tower or vehicle of some type. In many cases, a knowledge of how the support structure effects the antenna performance is critical in evaluating the obtained measurements.

In this paper the Numerical Electromagnetic Code (NEC-3) [1] is used to numerically model the electrical characteristics of a discone antenna which is suspended at a given height above a ground plane in three configurations; 1) antenna alone, 2) with a mast attached, and 3) mounted to a communication van. The model is optimized by correlating the calculated input impedance of the antenna (mounted on the van) to measured values. A comparison of the input impedance and far-field antenna patterns for these configurations determines how the mast and van effect the antenna performance. From this albeit limited example, a few general guidelines for evaluating how a support structure can effect an antenna are proposed.

Antenna Structure:

The physical characteristics of the discone antenna [2] are given in Fig. 1. The eight symmetric ground plane wires are 109 cm in length from hub to tip and form a cone at approximately 30° with respect to the antenna mast. The horizontal wires, which form the upper disc, are 34 cm long. The antenna may be physically located on a cube van in order to allow measurements to be made at a variety of remote locations. The dimensions of the van, the antenna location and details of the ladder network on the back of the van are also included in Fig. 1.

Measured Results:

The input impedance of the discone antenna was measured (50 to 250 MHz) when it was mounted on a communication van, see Fig. 4. This was done using a Hewlett Packard HP8753 Network Analyzer located inside the van. The antenna was mounted on a mast attached to a ladder network on the back of the van. The response of the co-axial cable used to connect the antenna to the network analyzer was incorporated into the instrument's calibration and ferrite beads were used to suppress cable coupling. A delay factor has been incorporated into the measurements to compensate for the discrepancy between the input connector of the antenna and the feed point in the NEC model.

NEC Model:

NEC inherently represents a structure as a series of wires and, therefore, is ideal for modelling a wire discone antenna. The model was originally generated using commercial CAD software (AutoCAD). This drawing was then exported as a *.DXF (Drawing Exchange Format) file which was converted to a NEC file using DIDEC.DREO [3], Fig. 2.

The overall lengths and diameters of the radial arms in the model are similar to those of the antenna. However, each arm in the model is composed of several segments, as depicted in Fig. 3. This is done for two reasons; the first is because the frequency range over which the model is valid is determined by the length of the individual segments. The second is because current on the structure is only calculated at the center of each segment. Hence, if a complex oscillation is to be represented or resolved along a wire length, the wire must be subdivided into many parts.

The segment lengths, wire spacing and diameters etc. have been carefully chosen according to the rules for model construction [1, 4 and 5]. In general, the frequency response of a model is established by the segment length with the upper and lower frequency corresponding to $\lambda/5$ and $\lambda/1000$, respectively. The source segment is the most critical element in the model.

In general it should be $\lambda/10$ which, for the frequency range of interest, would be about 20 cm. However, the separation between the ground and excitation wires on the antenna is approximately 4 cm. This length should be subdivided 3 or more times in order to have identical segments on both sides of the excited segment [1, Part 1, p. 67]. Therefore, the source segment (and those in its vicinity) will have to be 1.33 cm or about $\lambda/150$ in length. Unfortunately, this value exceeds the requirements of the model and the segments are too short be efficient radiators particularly at the lower frequencies. This is the most likely reason that the model and measured results of Fig. 4 deviate progressively below ~75 MHz. To partially compensate for this problem, each segment of a radial wire is scaled by 1.25 with respect to its predecessor as the end of the radial is approached [6], see Fig. 3. This produces a final length of about 6 cm and allows for more efficient radiation at the frequencies of interest. The antenna mast is established using a similar procedure.

An additional problem exists at the feed point of the antenna. The antenna hub is composed of metal plates and the determination of appropriate wire diameters to emulate a solid surface (particularly a small one) is not trivial. In addition, the effective separation of the disc and cone section is, unfortunately, critical in determining the antenna impedance [7] . A rule of thumb dictates that the circumference of the wire should be the same as the spacing of the wire grid elements used to simulate the surface [8]. However, in this problem this rule is difficult to implement since it is not possible to overlap wire segments or to join wires with large variations in diameter [1]. As a compromise, the radials are connected at the hub by wires with the same diameter as the rest of the model. In general, these diameters should be fixed by their counterparts on the antenna, however, this criteria led to difficulties with overlapping. As a result, the diameters were uniformly set to 0.5 cm, half of that on the real antenna. Some attempts were made to vary the diameters throughout the model, but this generally did not improve the response. It is anticipated that changing from NEC-3 to NEC-4 (which can model wire diameter transitions accurately) may assist with this problem, but results are not presently available.

An additional advantage in increasing the segment size is that the number of segments in the model, n, is inherently reduced. Since the CPU time required for the analysis varies as approximately n^3, even a small reduction can have a profound effect on the run time. The antenna model used in this analysis is composed of approximately 350 segments and each frequency requires about 16 seconds of CPU time to execute on a DEC 3000, Model 400 computer. If the antenna is modelled exclusively with segments which are 1.33 cm in length (like the source), then there would be about 900 segments and the execution time would increase by a factor of about 17 to 4.5 minutes. If the van model is also included (which is represented by a cube composed of about 800 patches) then the CPU time changes from 10.6 minutes to $[(900 + 800)/(350 + 800)]^3 \times 10.6 = 34.2$ min. per frequency.

The patches which are used to represent the van in NEC are interpreted differently by the software and the user. Although a patch may physically cover a certain area on the model, NEC only considers an average radius and position [1, p. 9]. As a result, the individual patch geometry used must be square to minimize "gaps" in the structure. A rectangular patch geometry produces superfluous spikes in the antenna response. In this model the front and back of the van were composed of a 10 by 10 grid while the sides, bottom and top were 10 by 15.

In order to simulate the impedance of the 50Ω cable attached at the input of the antenna, the segments connecting the ground plane wires to the source segments have each been impedance loaded (see Fig. 3). Although the arms of the discone should be capacitively coupled and in parallel (hence the resistors should be as well), a comparison (not shown) of the model and experimental results indicates that this is not true. As a result, the resistors are treated as though they are in series and a 50Ω value, rather than 400Ω, is used. This is an empirical observation and the truth is probably somewhere between the two extremes.

Model Verification:

A means of checking the modelling results is necessary in order to establish confidence in the results. This is accomplished by two means; the first is a numerical check on the average power gain of the antenna model and the latter is to compare the calculated and measured antenna input impedance.

i) Numerical

A means of correcting the antenna input impedance as calculated by NEC is available [1, p. 96]. This is done by computing the average power gain of the antenna. If there are no ohmic losses in the structure and it is situated over a perfect ground, the result should be equal to 2.0 with any discrepancy indicating an inaccuracy in the input impedance. Fortunately, a compensation factor, and therefore a more accurate input value, can be established as

$$P_R = \frac{1}{2} G_{AVG} \times P_I \quad , \tag{1}$$

$$R_{RAD} = 2 \frac{P_R}{|I_S|^2} \quad , \tag{2}$$

where P_R is the radiated power, G_{AVG} is the average gain (in the far-field), P_I is the computed input power, R_{RAD} is the radiation resistance and I_S is the source current. The need to correct the data is primarily because of inherent limitations in the model of the antenna (for example, excessively small segment lengths, etc.) and secondarily due to minor problems with the way that NEC solves the electromagnetic system (for example, NEC-3 cannot numerically tolerate abrupt changes in wire diameter).

Equations 1 and 2 are only valid when there are no ohmic losses in the antenna, however, there is a 50 ohm cable attached to the real antenna which the model must accurately simulate. This difficulty is overcome by using NEC to calculate the response of an antenna model which is physically identical to the antenna of interest but is perfectly conducting. By dividing the resistance of the antenna established via the NEC output by that determined with Eqn. 2, a compensation factor can be established for each frequency of interest in the antenna response. Since this compensation factor is a result of the physical aspects of the model, then it should also apply to an impedance loaded structure. By multiplying the antenna impedance obtained from the NEC analysis of the impedance loaded structure by the compensation factor, a compensated antenna impedance is established. This result should be a reasonable approximation of the result which would be obtained if the calculation could be done directly. For the model used, the above compensation factor rarely changes a directly calculated impedance value by more than a few percent.

ii) Comparison to Measurements

During the course of the model development several variations of segment length, diameter and interconnecting geometry were attempted before an optimal result was achieved. The quality of the results were judged based on the model's ability to emulate the measured input impedance of the van-mounted antenna. This type of "fine tuning" emphasizes the need for a pre-established response (an analytically determined or measured field pattern, impedance etc.) which can be used as a reference to establish the model's validity. The resulting representation can then be used to study circumstances which cannot be easily determined by other means.

A delay factor of 600-700 ps has been incorporated into the measurements to compensate for the discrepancy between the feed point of the antenna and the feed point in the NEC model (center of the antenna hub). The difference physically corresponds to the length of an N-type connector and half the distance of the antenna hub. The variation in the measured input impedance is only significant at the higher frequencies. The antenna feed point often requires some manipulation when comparing experimental and modeled results [6].

One discrepancy that exists is the fact that the modelled results are over a perfect ground plane while the measured values are over real ground. This was done since NEC-3 cannot accurately model patch/ground interaction when the patches are too close (~λ) to a non-perfect ground [1, p 11.]. The antenna (with no mast or van) was modelled over both ground types and the differences were found to be small.

Results:

The first step in the analysis is to establish the validity of the NEC model by comparing the calculated input impedance to the measured values, Fig. 4. Although the magnitude of the impedance at specific values may deviate, the overall match between the two curves is very good. The primary problem is in establishing the correct magnitudes at the high (>230 MHz) and low (<75 MHz) frequencies, where the accuracy of the NEC model diminishes, and at strong resonance values (~150 MHz for example). However, the overall shape and magnitude of the curves correlate well and the model accurately predicts the resonance frequencies in the response.

Since the model is reasonably accurate in predicting the input impedance (one of the more sensitive parameters to both

measure and model), it is reasonable to use it to explore the interaction of the antenna with its support structure. This can be done by removing the mast and/or the van from the NEC model, as is done in Fig. 5. From these curves it is determined that the response of the antenna alone is relatively smooth. The addition of the 2.65 m mast creates a series of resonances at ~55 MHz spacing which are superimposed on the original response. These values correspond to the resonance frequencies of the mast.

Placing the van in the calculation adds an additional resonance to the basic antenna response. The value approximately corresponds to the sum of the height and length of the van (i.e. 2 x (2.2 + 3.7 m) = 11.8 m [~25 MHz]). It appears that the van can be interpreted as a "fat" dipole end driven by the antenna and mast. As a test of this idea, the mast and van were replaced by an L-shaped wire running from the antenna hub down to the same height as the bottom of the van, then horizontally for the length of the van. The NEC simulation (not shown) of this structure produced a reasonable approximation of the resonances in the antenna input impedance as calculated above. The advantage of the latter wire simulation is the significant reduction in computation time.

Once the validity of the NEC model has been established, it can be used to compute a variety of antenna properties, especially those which are difficult or costly to measure. One parameter that is of particular interest to the author is the azimuthal variation in the far-field radiation pattern. Figure 6 depicts the magnitude of the electric field around the van (at ground level and 160 MHz) for the three configurations described earlier, and is typical of the response at most frequencies. The pattern for the antenna alone is very symmetric and uniform, which is not surprising due to the symmetric nature of the antenna. The addition of the mast does not alter this condition but does slightly increase the E-field magnitude (input powers were held constant). Finally, the van changes both the magnitude and the uniformity of the E-field with variations of typically 1-2 dB.

The implication of the above results is that, for example, if the antenna were to be used as a receiver, then the addition of the mast would change the pick-up slightly. In addition, if the antenna were mounted on a van, then the orientation of the vehicle with respect to the source will also alter the signal strength slightly.

Finally, the L-shaped wire (which was previously used to emulate the antenna/van structure and which produced a reasonable approximation of the input impedance) was also used to calculate the far-field pattern (not shown) of the antenna. The additional wire failed to produce the variations seen in Fig. 6. It is believed that this is due to the fact that the antenna/van and van/ground coupling are drastically underestimated by the wire. Hence, this model simplification is not justified under all circumstances.

In addition, the elevation profile for the model can be calculated, see Fig. 7. The dashed curve depicts the antenna with no mast or van while the solid curve corresponds to the van-mounted antenna. The number of nodes in the response correspond to the height of the antenna (relative to λ) above the ground and can be varied by changing the height or frequency. The lack of a null in the vertical (i.e. 90°) orientation is of interest and it is speculated that this is due to currents flowing in the van structure.

Conclusions:

NEC-3 can be used to model a discone antenna but care must be taken when representing the excitation region, which is critical in determining the antenna characteristics. A comparison of the predicted and measured input impedance of the antenna were necessary to "fine tune" the model. This emphasises the need to have some type of experimental or analytical model validation. Once this has been established, then the model can be used to compute a variety of antenna properties, especially those which are difficult or costly to measure.

The calculations were performed for three configurations; 1) antenna alone, 2) with a mast attached, and 3) mounted to a communication van. By removing the van and the mast it is possible to investigate how different support structures effect the input impedance and far-field $|E|$. It is concluded that the antenna mast adds a series of resonances to the basic antenna response which are equivalent to treating the mast as an end driven dipole. Likewise, the van adds an additional series of resonances which, again, are equivalent to treating the van as a "fat" end driven dipole. Operation of the antenna near these resonances will effect the input impedance and slightly alter the antenna response.

It was found to be necessary to include the entire structure in the simulation to accurately predict all the antenna parameters. Replacing the van with a wire produced a reasonable approximation of the input impedance but failed to reproduce the far-field E-field pattern. It is believed that this is due to the fact that the antenna/van and van/ground coupling are drastically underestimated by the wire.

The azimuthal variation in the far-field E-field pattern varies typically by 1-2 dB. The implication of the above results is that, for example, if the antenna were to be used as a receiver, then the addition of the mast would change the pick-up slightly. In addition, if the antenna were mounted on a van, then the orientation of the vehicle with respect to the source will also alter the signal strength slightly.

Acknowledgements:

The author wishes to thank J.M. Bertrand for assisting with the measurements of the discone impedance and the Defence Research Establishment (DREO) for loan of the computer facilities.

References:

1) G.J. Burke and A.J. Poggio, Numerical Electromagnetic Code (NEC) - Method of Moments, Naval Ocean Systems Center, Technical Document 116, Part III (User's Guide), 1980.
2) DC-100 UHF Discone Antenna Instruction Booklet, Antenna Products, 101 S.E. 25th Ave, Mineral Wells, TX, 76067
3) M. Dion, S. Kashyap and A. Louie, "A Sophisticated CAD Tool for the Creation of Complex Models for Electromagnetic Interaction Analysis", Defence Research Establishment Ottawa, Report 91-16, 1991.
4) C.W. Trueman and S.J. Kubina, "Verifying Wire-Grid Model Integrity with Program 'Check' ", ACES Journal, Volume 6, No. 2, 1991, p. 38-52.
5) J. Peng, C.A. Balanis and G.C. Barber, "NEC and ESP Codes: Guidelines, Limitations and EMC Applications", IEEE Trans. on EMC, Vol. 35, No. 2, May 1993.
6) S.M. Mann and A.C. Marvin, "Characteristics of the Skeletal Biconical Antenna as Used for EMC Applications", IEEE EMC, Vol. 36, No. 4, p. 322-330, Nov. 94.
7) J.J. Nail, "Designing Discone Antennas", Electronics, pp 167-69, August, 1953.
8) S. Kashyap and A. Louie, "Surface Modelling for EM Interaction Analysis", ACES Journal, Vol. 6, No. 2, 1991, p. 38-52.

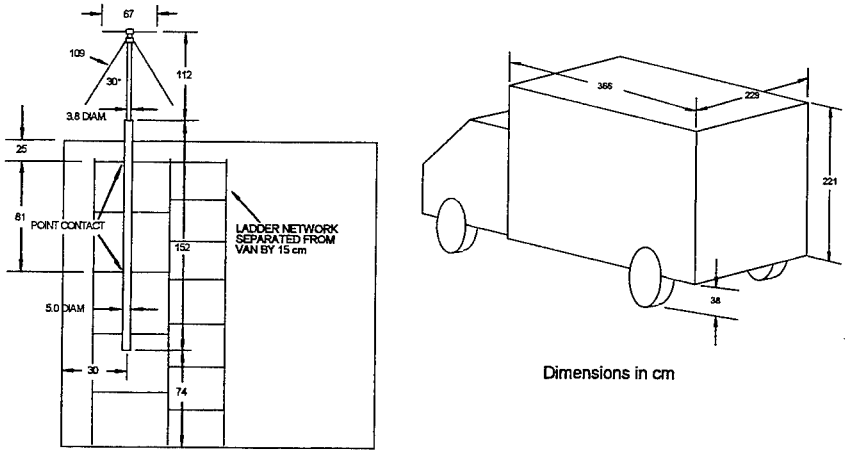

Figure 1: Details of the cube van used to transport the discone antenna to remote locations. The ladder network is slightly simplified in the schematic and NEC-3 model.

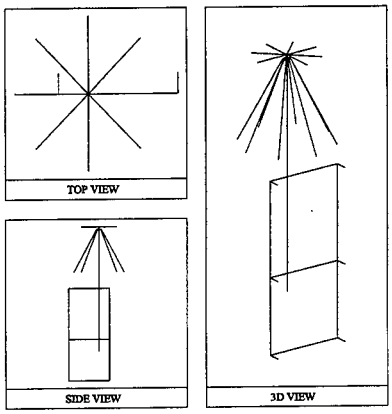

Figure 2: An overview of the NEC-3 model of the discone antenna. The model was created using AutoCAD and then converted to a NEC wire grid structure using DIDEC.DREO. The jumpers on the ladder network are used to attach the wire grid to the patch model of the van. Various portions of the structure can be removed to investigate the effect on the antenna response.

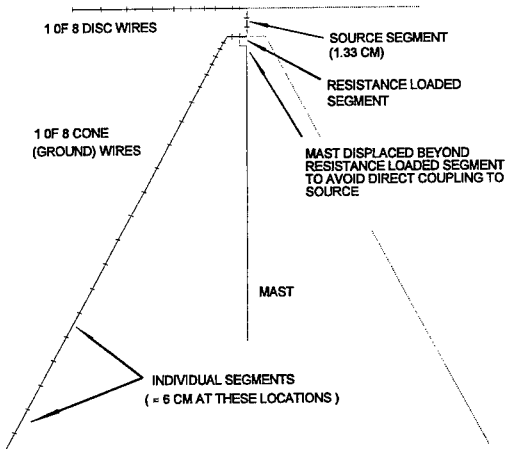

Figure 3: A schematic representation of the segment distribution on the discone antenna. The wire element joining the disc and cone has been divided into 3 segments so that the source element is surrounded by segments of the same length. This practice is also extended into the hub area. However, as the far ends of the wires are approached, the segment lengths are gradually increased to be more compatible with the radiation wavelengths of interest.

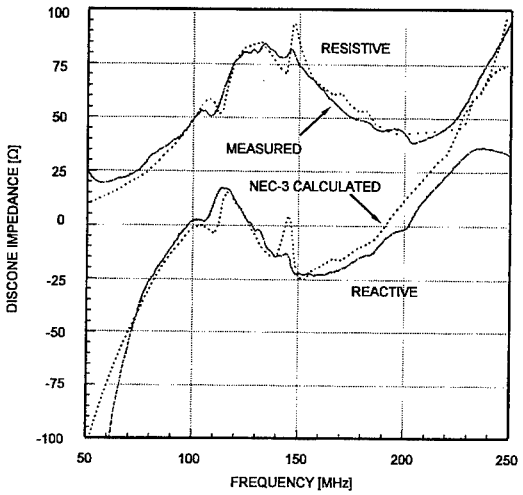

Figure 4: A comparison of the NEC-3 calculated input impedance and measured values for the van-mounted discone antenna. The correlation is generally very good with the overall shape and resonance frequencies accurately predicted. Difficulties exist in calculating the magnitude of the impedance at the high and low frequencies and at strong resonance values.

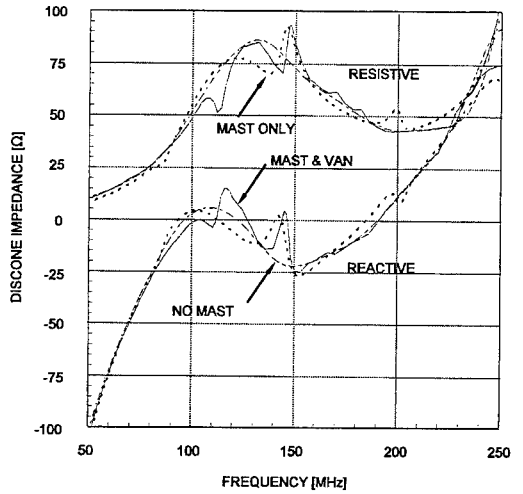

Figure 5: Variation in the input impedance with changes in the antenna support structure. The addition of the mast to the antenna creates a resonance corresponding to an equivalent length, end-driven dipole. Likewise, the van adds a resonance which is equivalent to superimposing an end-driven "fat" dipole.

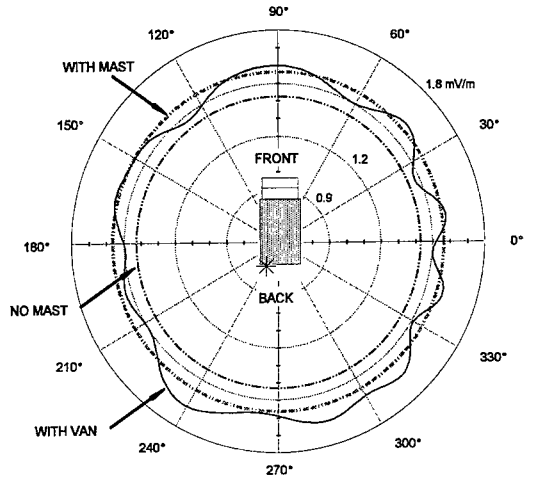

Figure 6: Relative values of the far-field E-field magnitude (azimuthal) at ground level as predicted by NEC-3 for various configurations of antenna support. The values correspond to a constant input power and are calculated at f = 160 MHz. The addition of a mast to the antenna alters the magnitude of the response but not the symmetry, however, further addition of the van to the model creates an angular variation in the response. This causes the antenna characteristics to vary with respect to the source/receiver location.

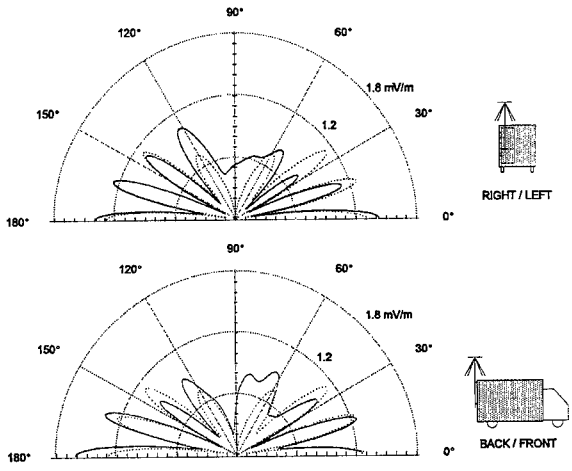

Figure 7: Relative values of the far-field E-field magnitude (elevation) in the elevation profile. The values correspond to a constant input power and are calculated at f = 160 MHz. The lack of a null in the vertical (i.e. 90°) orientation is of interest and it is speculated that this is due to currents flowing in the van structure.

DIELECTRIC RESONATOR ANTENNA ANALYSIS AND DESIGN USING THE FD-TD METHOD

Karu P. Esselle
Electronics Department, E6A
Macquarie University
Sydney NSW 2109
Australia
esselle@mpce.mq.edu.au

ABSTRACT

A technique, based on the Finite-Difference Time-Domain (FD-TD) method, is used for the analysis and design of aperture-coupled dielectric-resonator (DR) antennas. Computed far-field patterns are presented for a linearly polarised antenna, a circularly polarised antenna and a linearly polarised array. They compare well with measured patterns.

INTRODUCTION

DR antenna is basically a piece of dielectric that resonates at or close to the operating frequency. It is not shielded, and hence, radiates electromagnetic waves. DR antennas can be designed to have low-profile geometry and, like microstrip antennas, they can be integrated with microwave and millimetre-wave circuits. DR antennas usually have wider bandwidth than microstrip antennas. In aperture-coupled case, they need less dielectric material than microstrip antennas, and therefore cost and weigh less. The lack of metal in the radiating element is an additional advantage at millimetre-wave frequencies where conductor loss is significant.

We have implemented a software package for the analysis of aperture-coupled DR and similar antennas. Taking advantage of the flexibility of the FD-TD method, and using the Macquarie University Cray supercomputer, we have analysed many configurations of DR antennas including linearly polarised (LP) rectangular antennas, LP cylindrical antennas, circularly polarised (CP) "cross" antennas [1], CP rectangular antennas and two-element arrays. Several LP and CP antennas have also been designed through iterative analysis.

METHOD

Our FD-TD software employs a unique combination of first- and second-order Mur absorbing boundary conditions (ABCs), to simulate accurately the substrate that extends beyond the FD-TD computational volume (see Figure 1) [2]. Second-order Mur ABC was used for most regions of the boundary [3]. However, the normal electric-field component is discontinuous at the air-substrate interfaces (due to the normal electric-field interface condition, or due to the ground plane), and the lateral extrapolation in second-order Mur ABC is not appropriate. Therefore first-order Mur ABC was applied around the air-substrate interfaces. It was also used along the edges of the grid

boundary, but in this case the preferred direction of propagation of the wave was assumed to be diagonal to the edge.

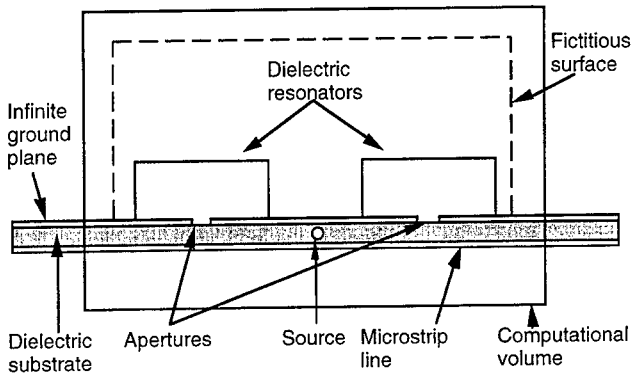

Figure 1. FD-TD Computational volume and fictitious surface

The far field of the antenna or array is calculated by applying the Field Equivalence Principle directly in the time domain, over a fictitious surface enclosing all radiating elements (i.e. DRs and apertures), as shown in Figure 1. For these calculations, an *infinite* ground plane is assumed on the top side of the substrate. At a generic point (x',y',z') on the fictitious surface, equivalent electric and magnetic currents are given by

$$\vec{j} = \hat{n} \times \vec{h} \tag{1}$$

$$\vec{m} = -\hat{n} \times \vec{e} \tag{2}$$

where $\hat{n}$ is the unit vector normal to the surface in outward direction. The magnetic and electric vector potentials generated by the above equivalent currents, at a point (x,y,z) outside the surface, are given by

$$\vec{a}(x,y,z,t) = \frac{\mu_0}{4\pi} \iint \vec{j}(x',y',z',t-\frac{R}{c_0}) \frac{ds'}{R} \tag{3}$$

$$\vec{f}(x,y,z,t) = \frac{\varepsilon_0}{4\pi} \iint \vec{m}(x',y',z',t-\frac{R}{c_0}) \frac{ds'}{R} \tag{4}$$

where R is the distance between (x,y,z) and (x',y',z'); ε_0, μ_0 and c_0 are free-space permittivity, permeability and speed of light; and the surface integration is over the fictitious surface. The vector potentials generated by the images of the equivalent currents (due to the infinite ground plane) are then added to $\vec{a}$ and $\vec{f}$. Finally, the two

spherical-coordinate components of the radiated electric field at a distant point, where far-field conditions can be assumed, are given by

$$e_\theta(x,y,z,t) = -\frac{\partial a_\theta(x,y,z,t)}{\partial t} - \eta_0 \frac{\partial f_\phi(x,y,z,t)}{\partial t} \tag{5}$$

$$e_\phi(x,y,z,t) = -\frac{\partial a_\phi(x,y,z,t)}{\partial t} + \eta_0 \frac{\partial f_\theta(x,y,z,t)}{\partial t} \tag{6}$$

where η_0 is the intrinsic impedance of free space.

Frequency-domain far fields and other characteristics (eg. radiated power density, axial ratio or ellipticity of CP radiation) are obtained using conventional FFT techniques.

RESULTS

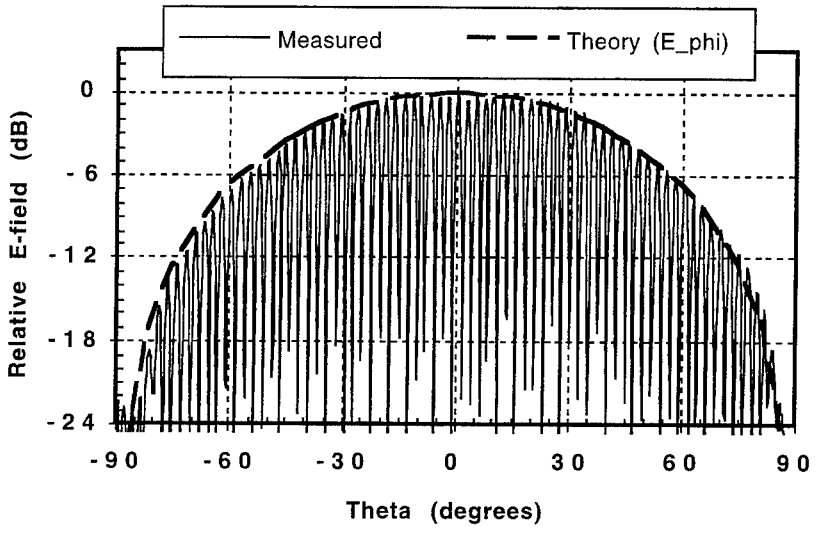

Figure 2. H-plane patterns of a low-profile rectangular LP DR antenna

Rectangular LP DR Antenna

The rectangular dielectric resonator has dimensions of 15.2 (L) × 7.0 (W) × 2.6 (H) mm, and a dielectric constant of 10.8. It is fed by a 50Ω microstrip line through a 3.4 × 1.2 mm aperture in the ground plane. The substrate is approximately 0.64 mm thick and has a dielectric constant of 10.5. Figure 2 shows the theoretical and measured far-field patterns of this antenna in the H-plane at 11.6 GHz. It should be noted that the antenna

is almost perfectly matched to the 50Ω input at this frequency, giving an input reflection coefficient of 0.013 (-38 dB). The pattern was measured using a spinning linearly polarised horn antenna in order to simultaneously obtain the cross-polarisation level. Not only does the measured pattern compare extremely well with the theoretical one, but also it reveals that the cross-polarisation is at least -15 dB below the co-polarisation within the 3dB beamwidth.

Two-element Array

This E-plane array consists of two rectangular DR elements, each having dimensions of 15(L) × 3(W) × 7.5(H) mm and a dielectric constant of 10.8. They are fed, in equal magnitude and phase, by a 50Ω microstrip line through two apertures (6.1 × 1.2 mm each) in the ground plane. For comparison, the radiation pattern of the array is also computed using Array Theory, neglecting mutual coupling between the two elements. The theoretical E-plane pattern of a single DR element, resonating in the 'magnetic-dipole' mode, is a half circle [2]. Hence the pattern of the array in the E-plane is directly given by the array factor, which for two elements excited in equal magnitude and phase is cos ($k_o s \sin\theta$ /2), where s is the element spacing (centre to centre) and $k_o = 2\pi/\lambda_o$.

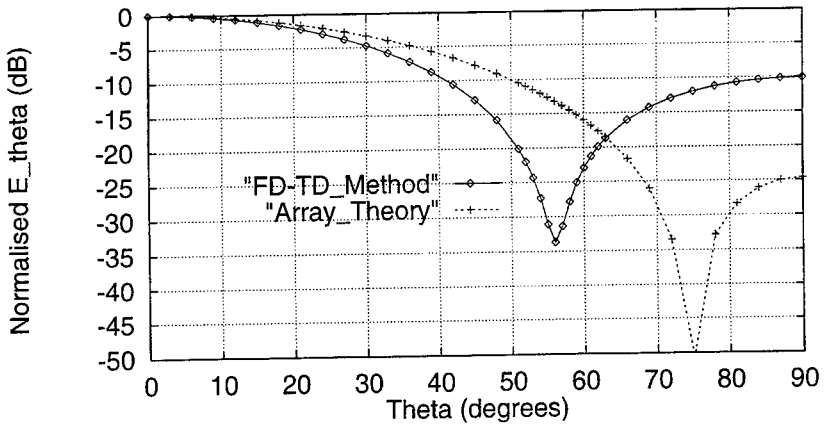

Figure 3. Radiation patterns of the array computed using FD-TD and Array Theory

Figure 3 shows the computed radiation patterns of the array using the FD-TD method and Array Theory, for s=2.14 cm (≈ $\lambda_o/2$) at 7.27 GHz. The two patterns are significantly different; notably the two pattern nulls are at θ=56° and 75°. In previous measurements of this array, pattern nulls were observed at about -52° and +56° angles at 7.2 GHz [4], hence the FD-TD results should be accurate as expected. On the other hand, the array-theory results are in error because of the neglect of mutual coupling that seems to be significant for this spacing. For a wider spacing of s=3.22 cm (≈ $3\lambda_o/4$), both computed patterns are similar and compare well with the measurements.

CP Rectangular Antenna

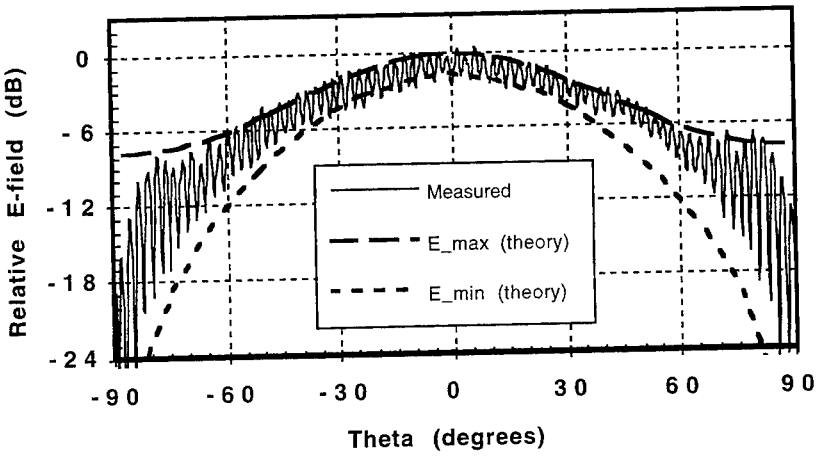

Figure 4. Theoretical and measured patterns of a CP rectangular DR antenna

This circularly polarised antenna consists of a rectangular 14(L) × 3.7(W) × 2.6(H) mm dielectric resonator (ε_r=10.8), placed on the ground-plane side of a dielectric substrate (ε_r=10.5), and fed by a 50Ω microstrip line through an aperture. The aperture dimensions are 1.2 mm × 2.8 mm; the substrate thickness is approximately 0.64 mm; the matching stub length is 0.4 mm from the centre of the aperture. The resonator is rotated by 45° with respect to the aperture [5].

The theoretical and measured patterns at 14.75 GHz, in the elevation plane along the aperture, are shown in Fig. 4. The measured pattern was obtained by spinning a linear-polarised horn antenna. The axial ratio can be obtained from this pattern as the difference between an adjacent maximum and minimum. The two theoretical curves are the relative lengths of the major and minor axes of the polarisation ellipse; the gap between the two gives the theoretical axial ratio. The theoretical and measured results compare very well for directions within ±30° from the boresight. Discrepancies between them at higher $|\theta|$ values are attributed to the finite size of the ground plane in the test antenna and to fabrication tolerances. In general, the axial ratio remains close to 3 dB over a wide range of angles in this elevation plane.

CONCLUSIONS

The FD-TD method is successfully used for the analysis and design of several aperture-coupled dielectric-resonator antennas. Computed radiation patterns of a linearly polarised rectangular antenna, a linearly polarised two-element array and a circularly polarised rectangular antenna compare well with measurements. The only limitation of this approach seems to be the high demand for computer resources. All theoretical results presented here were computed using a Cray Y/MP four-processor supercomputer with 512 Mbytes of memory, in 64-bit words.

ACKNOWLEDGMENTS

Assistance from Dr Trevor Bird and others at the CSIRO Radiophysics Division, during antenna testing in their laboratory, is greatly appreciated. The author wishes to thank Dr Y.M.M. Antar and Capt. G.D. Loos, both at the Royal Military College, Kingston, Canada, for providing measurement results of the array. This research was sponsored in part by the Australian Telecommunications and Electronics Research Board and the Australian Research Council.

REFERENCES

[1] Esselle, K.P., "Circular polarised dielectric resonator antenna: analysis of near and far fields using the FD-TD method," IEEE Antennas and Propagation Society International Symposium and URSI Meeting, Newport Beach, CA, p. URSI:28, 1995.

[2] Esselle, K.P., "Finite-difference time-domain analysis of a rectangular dielectric resonator antenna," *Journal of Electrical and Electronics Engineering, Australia*, Vol. 15, No. 1, pp. 63-70, March 1995.

[3] Mur, G., "Absorbing boundary conditions for the finite-difference approximation of the time-domain electromagnetic-field equations," *IEEE Trans. Electromagn. Compat.*, Vol. 23, No. 4, pp. 377-382, Nov. 1981.

[4] Loos, G.D., *Investigation of a novel aperture coupled dielectric resonator antenna array*, M.Eng. Thesis, Royal Military College, Kingston, Canada, May 1994.

[5] Oliver, M.B., Antar, Y.M.M., Mongia, R.K. and Ittipiboon, A., "Circularly polarised rectangular dielectric resonator antenna," *Electronics Letters*, Vol. 31, No. 6, pp. 418-419, 1995.

A NUMERICAL AND EXPERIMENTAL INVESTIGATION OF A SEMI-LOOP ANTENNA ON A METAL BOX

Jeffrey B. Knorr and David C. Jenn

Department of Electrical and Computer Engineering
Naval Postgraduate School
Monterey, CA 93943-5121

Abstract - This paper presents the results of a numerical and experimental investigation of a coaxial semi-loop antenna mounted on one face of a 1 foot metal cube which sits on a ground plane. The numerically computed far-field amplitude and phase are compared with measurements for the frequency range 96 to 1440 MHz.

I. Introduction

The loop antenna is a structure which has many practical applications, one of which is in signal direction finding (DF). The investigation reported here was motivated by related work to develop a computer simulation of a shipboard correlation interferometry direction finding (CIDF) system [1] operating in the high frequency (HF) band. An existing, 1/48th scale, physical model of the ship and its DF system utilized the coaxial semi-loop antenna which is the subject of this paper.

At HF there is strong coupling between a shipboard antenna and the surrounding ship superstructure. This interaction must be accurately accounted for in a computer simulation. Prior to modeling the behavior of an antenna in an environment as complex as that of a ship, it seemed judicious to show that it could be accurately modeled in a simpler environment. Thus, an investigation of a semi-loop antenna mounted on a metal box, as described here, was carried out in the scaled frequency range of 96 to 1440 MHz. Numerical results were obtained by applying the method of moments to wire grid and triangular patch models, and these were compared with experimental data.

II. Physical Model

The semi-loop antenna is constructed from 0.085 inch diameter, semi-rigid coaxial cable. The semi-loop radius is 0.230 inches and the feed is a 0.015 inch slit cut in the outer conductor of the coax at the center of the semi-loop (highest point above the mounting plate). At one end of the semi-loop, the coax is shorted by the mounting plate, and at the other end, the coax passes through the mounting plate to provide an output to the feed line. The box is one foot on a side, and the antenna is located 4 inches below the top of the box, half-way between the sides.

The semi-loop antenna is electrically small. The loop senses the vertical surface current produced by a field incident on the

box. The loop will respond to both θ- and ϕ- polarized incident fields. The primary response is to a θ-polarized field, however, and only results for this case will be reported here.

III. Wire Grid Model

A wire grid model of the loop and metal box, shown in Figure 1, was developed for use with the EM code NEC 4.1. The bottom edges of the box are attached to a perfectly conducting ground plane. Since the box is 12 inches on a side, a 1 inch grid spacing was chosen to give a vertical wire at the center of each side, which was necessary to attach the semi-loop. At the highest frequency, 1440 MHz, the grid was 0.12λ on a side, so each wire consisted of only one segment. A wire radius of 0.159 inches was chosen to provide a 1 inch wire circumference thereby satisfying the equal area guideline [2].

To provide for attachment of the semi-loop to the box, additional nodes were created at a height of 7.77 inches and 8.23 inches above the ground plane. The coaxial semi-loop was modeled as a 5 segment arc with a radius of 0.23 inches. It was centered on one face of the box and the ends of the arc were attached at the nodes defined above. The third segment of the 5 segment arc was used as the semi-loop antenna feed point. The box consisted of 1512 wires, each having one segment, and therefore the complete model contained a total of 1517 segments.

Calculations were also performed for a simplified feed model consisting of a single vertical wire segment replacing the semi-loop. The far-field patterns were found to be essentially unchanged from the detailed model, which is expected given the small electrical size of the loop.

IV. Patch Model

The radiation patterns were also computed using PATCH, a method of moments code employing triangular subdomains [3]. The faceted box is shown in Figure 2. The triangular facet model is built in ACAD [4] and a translator is used to generate an input file recognized by PATCH. The box is located on a perfectly conducting infinite ground plane.

Several mesh configurations were generated. The box in Figure 2 was obtained using the ACAD "Shell Mesh" command. Other models were generated in which triangles were aligned in rows and columns, but their pattern data exhibited some asymmetry at low levels. Both conductively attached and isolated plates were investigated. Isolated plates were simulated by introducing duplicate edges; that is, triangles that lie along the box edges are each given their own edge, they do not share an edge with their neighbors on the adjacent face. Thus the number of unknowns (edges) is greater for the isolated face model than for the conductively attached face model (2738 vs 2815). For all the PATCH data shown here, the box faces are assumed to be insulated from each other. This model gave the best agreement with NEC and measured data.

For the patch model, the semi-loop is simply represented by a

thin short slot. This was deemed acceptable because the calculation of antenna impedance was not of interest and, NEC results demonstrated that variations in the fine detail of the feed did not affect the far-field patterns.

V. Measurement Facility

Experimental data were obtained from measurements taken at NRaD, the RDT&E Division of the Naval Command Control and Ocean Surveillance Center, located in San Diego, CA. The antenna and box was placed on an outdoor turntable and illuminated with a plane wave using both vertical and horizontal polarizations. Data were recorded every 1 degree in azimuth over a full 360 degrees. This was done for elevation angles of 5, 10, 20, 30, 45, and 60 degrees.

The signal received by the semi-loop antenna was routed to a control room where the amplitude and phase were recorded. The phase reference was established by sampling the output from the signal source and providing it as an input to the vector receiver. As the metal box was rotated in azimuth, the phase of the signal received by the semi-loop antenna was compared to this reference signal. Thus, the phase reference was arbitrary. Amplitude measurements were referenced to the signal level from a quarter wave monopole which was recorded prior to taking data using the semi-loop antenna.

VI. Computational Platforms

Computations for the wire grid model were carried out using NEC 4.1 running on a Silicon Graphics (SGI) Indigo Extreme workstation with 64MB of RAM. The time to compute the Numerical Green's Function at 4 frequencies was about 5 hours. The time to compute the amplitude and phase of the feed point current at the same 4 frequencies using 10 degree azimuth steps was about 30 minutes.

For PATCH, the execution time for a set of 5 frequencies, 1 degree increments in pattern angle, took 3 hours and 50 minutes on the SGI for the largest number of edges.

VII. Comparison of Numerical and Experimental Results

The numerical and experimental patterns for a θ-polarized incident plane wave at 96, 480, and 1440 MHz for 10 degrees elevation are shown in Figures 3 through 5. The side of the box with the semi-loop antenna is 0 degrees azimuth. To simplify comparison, all patterns were normalized. It can be seen that the wire grid and patch models yield essentially identical results. Both agree well with the experimental data in the forward hemisphere, but have some differences in the rear hemisphere.

At the higher frequencies asymmetries appear in the experimental patterns, which should ideally be symmetric for a θ-polarized incident field. The asymmetries are believed to be due to radio frequency interference from the urban San Diego environment adjacent to the outdoor measurement facility and scattering from support arches that are used to move the transmit antenna in elevation.

Figures 6 through 8 show the pattern phase as the metal box is rotated in azimuth. Each curve is normalized to its value at 180 degrees azimuth. This allows comparison of the shape of the phase curves. At the higher frequencies the plots show phase moving in the negative direction as the face of the box on which the loop is mounted moves away from the signal source, as expected. The wire grid and patch models indicate phase changes of about 410 and 460 degrees, respectively, as the box rotates through 360 degrees in azimuth. The measured data indicates 335 degrees of change. The difference could be a result of inaccurate positioning of the metal box on the turntable, but there was no way to check if this might possibly have occurred.

It is interesting to note that the actual physical displacement of the semi-loop feed point over 360 degrees of azimuth rotation is about 0.5λ at 480 MHz. Thus, physical displacement accounts for only about 180 degrees of the total phase shift which occurs when the box is rotated. At the low frequency the phase vs azimuth does not behave as just described for the higher frequencies. At this frequency the entire box is acting as a radiating structure, and thus its phase center does not necessarily correspond to the location of the loop [5].

VIII. Conclusions

Computed and measured far-field patterns for a small semi-loop antenna mounted on a box on a ground plane have been presented. The pattern magnitudes are within a couple of dB except in the vicinity of pattern nulls, and there the difference is attributed to extraneous error signals. The agreement in pattern phase is generally not as good as that in magnitude. This may be caused by a combination of experimental and computational inaccuracies. Some error is inherent in the wire grid representation of the solid box walls. In the case of the patch model, error may be due to the fact that some of the frequencies considered are near the internal resonances for a cubic cavity.

Acknowledgments

The authors wish to acknowledge the contributions of Mr. Carl Firman and Dr. Ashok Das. Carl Firman carried out the measurement program at NRaD, and supplied the authors with the experimental data. Ashok Das wrote the software to plot the numerical and experimental results.

References

[1] N. Saucier and K. Struckman, "Direction finding using correlation techniques," Proc. IEEE Symposium on Antennas and Propagation, pp. 260-263, Urbana, IL, June 2-4, 1975.
[2] G. J. Burke, "Numerical Electromagnetics Code - NEC-4, Method of Moments, Part I: User's Manual," Lawrence Livermore National Laboratory, UCRL-MA-109338, January 1992.
[3] W. A. Johnson, D. R. Wilton and R. M. Sharpe, "PATCH Code Users'

Manual," Sandia National Laboratories, SAND87-2991, May 1988.
[4] "The ACAD User's Manual," Lockheed Martin Corp., (Lockheed Fort Worth Co.), April 1995.
[5] D. Carter, "Phase Centers of Microwave Antennas," IRE Trans. on Antennas and Prop., vol. AP-4, p. 597, Oct. 1956.

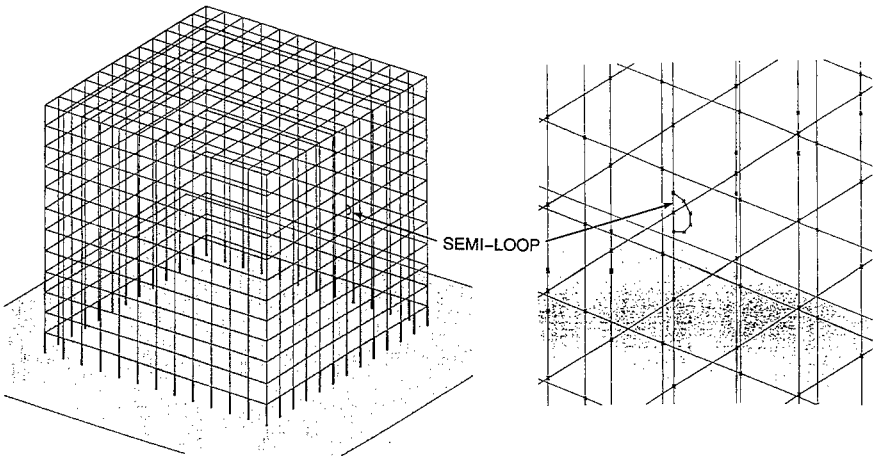

Figure 1. NEC model of the semi-loop antenna on a metal box.

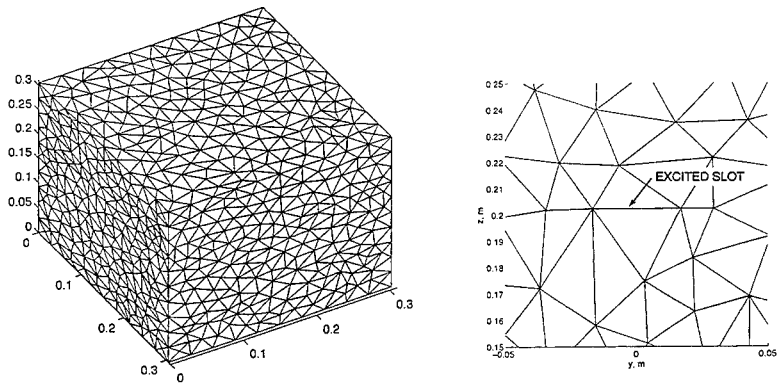

Figure 2. PATCH model of the box.

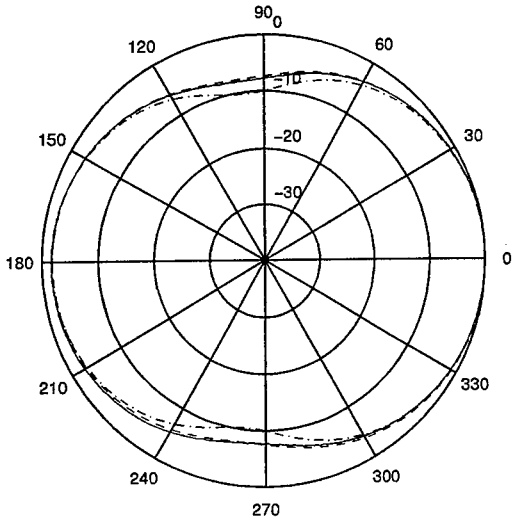

Figure 3. Computed and measured pattern magnitude for 96 MHz.
(___ =measured,_ _ =PATCH,_.._.=NEC)

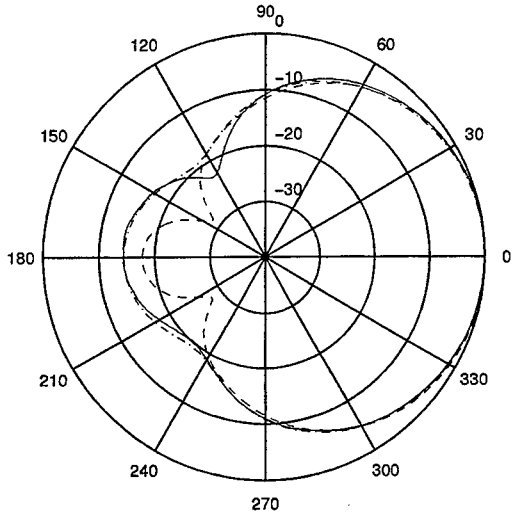

Figure 4. Computed and measured pattern magnitude for 480 MHz.
(___ =measured,_ _ =PATCH,_.._.=NEC)

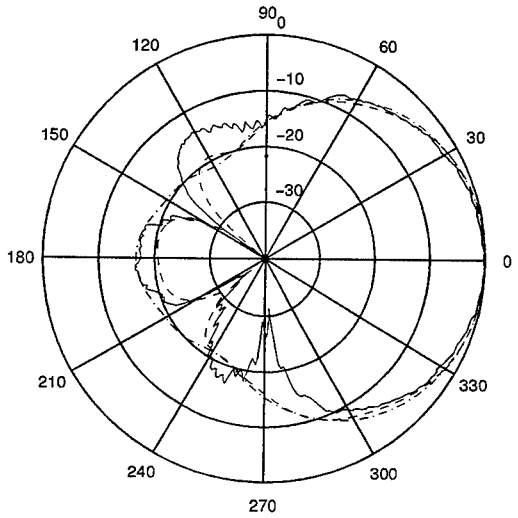

Figure 5. Computed and measured pattern magnitude for 1440 MHz.
(___ =measured,_ _ =PATCH,_._.=NEC)

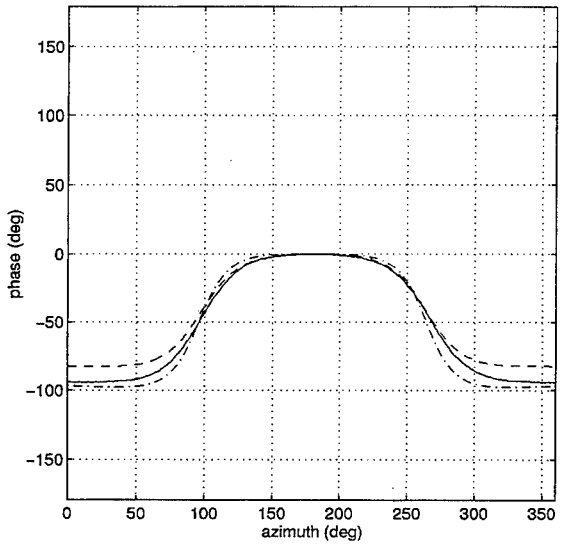

Figure 6. Computed and measured phase for 96 MHz.
(___ =measured,_ _ =PATCH,_._.=NEC)

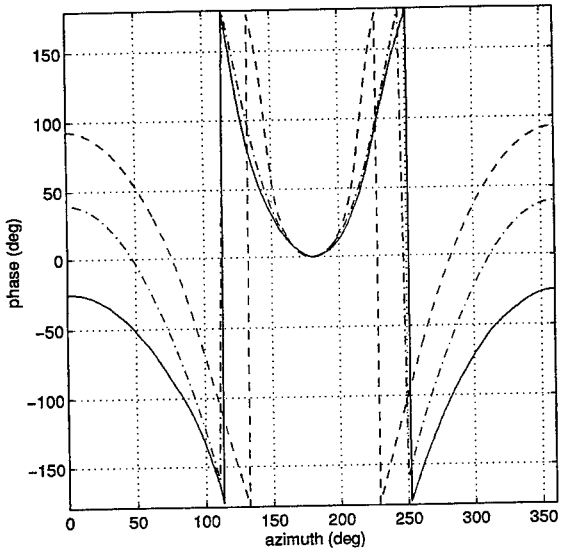

Figure 7. Computed and measured phase for 480 MHz.
(___ =measured,_ _ =PATCH,_._.=NEC)

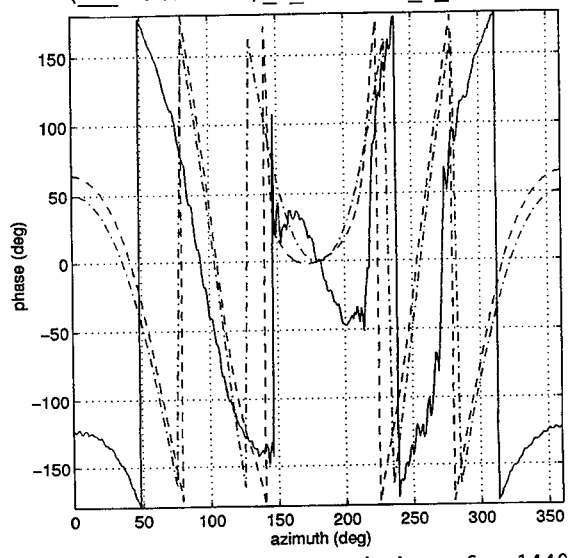

Figure 8. Computed and measured phase for 1440 MHz.
(___ =measured,_ _ =PATCH,_._.=NEC)

SESSION 16:

EMI/EMC

Chairs: T. Hubing and J. Drewniak

On the Suitability of Simple Voltage Source Models for the Study of Mutual Coupling Effects

G.P. Junker, A.W. Glisson*, and A.A. Kishk
Department of Electrical Engineering
University of Mississippi
University, MS 38677

Abstract: This paper addresses the suitability of simple voltage source models as forcing functions for the electric field integral equation (EFIE) of thin wire theory. It has been found that under certain conditions, delta-gap source models may fail to produce an accurate solution to the EFIE in regions far removed from their point of application. This failure is contrary to the common view that accurate results are obtained for the current distribution on thin wire antennas with the possible exception of the current near the source location. Causes of these solution inaccuracies, and suggested remedies are presented together with numerical studies of arrays of cylindrical monopole antennas.

Introduction: The problem of mutual coupling between elements of an array of thin cylindrical dipole antennas has been investigated by numerous researchers [1,2,3,4]. These early theoretical studies placed restrictions upon the dipole lengths in addition to the restrictions imposed by thin wire theory. To study mutual coupling effects between thin cylindrical dipoles subject only to the constraints imposed by thin wire theory, one must turn to modern numerical methods, such as the method of moments (MoM), to solve the integral equations associated with thin wire theory. This is necessary because the EMF method does not, in general yield results of sufficient accuracy to determine the self and mutual impedances [2], since it is in fact merely an integral identity and is not directly related to the currents at the driving points of the antenna [1].

In an attempt to accelerate the solution convergence, much research has been devoted to developing efficient techniques for the accurate evaluation of the elements of the impedance matrix associated with MoM as applied to the electric field integral equation (EFIE) of thin wire theory [5,6,7]. By comparison, relatively little work has been directed toward the improvement of simple voltage source models, such as the recently introduced *extended delta* source model [8], so the *traditional delta-gap* model is still widely used as a thin wire source. This paper addresses the suitability of simple voltage source models as forcing functions for the EFIE of thin wire theory under a MoM Galerkin solution procedure. The form of the EFIE to be considered in this work is the so called "mixed potential" integral equation [9]. It has been found that under certain conditions, both the *extended delta* and *traditional delta-gap* source models can cause solution inaccuracies in regions far removed from their point of application. Since the delta gap source model is often used as a forcing function for antenna arrays composed of parts other than thin wires, the exposure and explanation of this problem sheds light upon apparent discrepancies between computed and measured multiport network parameters. Another simple source model to be considered, as well as one which is suggested as a potential alternative to the existing delta source models, is a *modified* extended delta source model. The *modified* extended delta source model differs from that of [8] in that it takes into consideration the characteristic impedance of the coaxial lines which feed the monopole antennas. It

has been found that even the extended delta source model of [8], despite the fact that it offers great solution stability when compared to the *traditional* delta-gap source, may yield input susceptances that are unacceptable when monopole antennas are fed by coaxial lines whose characteristic impedances Z_c are greater than approximately 25Ω. This finding should come as no great surprise since upon increasing the characteristic impedance of the coaxial feed line, the area of the coaxial aperture also increases thereby resulting in a decrease in electric field strength tangent to the surface of the driven element. To date, all existing delta source models are insensitive to the characteristic impedance of the feed line since they do not allow for the modelling of the monopole/feed line junction. The consequences of not accurately modelling the coaxial apertures which feed the antenna array elements represents the thrust of this paper and will be discussed throughout its body. The fourth model under consideration, and by far the most accurate *approximate* source model to date for the field at the open end of a coaxial line operating in the TEM mode is the magnetic frill model [10,11]. This model is used as a benchmark for this work. In its most general form, the magnetic frill model may pose certain difficulties in implementation since its evaluation relies on techniques based upon numerical differentiation and Taylor series expansions.

Model Description: To analyze a monopole antenna, image theory is commonly invoked to remove the ground plane. The monopole is then treated as a dipole in free space, of half length h and radius a_w, as illustrated in Fig. 1a. In accordance with the MoM procedure, the unknown z-directed current J_z has been expanded as a series of subdomain basis functions, J_i, as

$$J_z = \sum_{i=1}^{N_w} c_i J_i \tag{1}$$

where

$$J_i = \frac{T_i}{2\pi a_{wi}} . \tag{2}$$

The c_i's in (1) are the unknown current coefficients, T_i in (2) is the "triangle function," N_w is the total number of basis functions employed, and T_{pn} (as indicated in Fig. 1a) is the basis function which spans the point of source application. Under a Galerkin MoM procedure, the testing functions are triangles whose apexes are located by the coordinate z_j. The usual procedure is then to form the inner product

$$< J_j, L (\sum_{i=1}^{N_w} c_i J_i) > = < J_j, f(g) >, \quad j=1,2,..,N_w \tag{3}$$

where J_j is the testing function, $j=1,2,\ldots,N_w\text{-}1,N_w$, L(⊗) represents the mixed potential operator [12, p.82, eq.(5-1)] with the unknown current expanded as per (1), and $f(g)$ represents the forcing function. Evaluation of (3) results in a matrix equation of the form

$$[Z_M]\,|\,c\,> = |\,V\,> \qquad (4)$$

where $[Z_M]$ is the $N_w \times N_w$ moment matrix, and $|V>$ is the generalized voltage matrix [12], i.e., in this case, the "tested" impressed electric field along the dipole surface. The elements of matrix $|c>$, which are the unknown current coefficients, can be easily obtained by forming the matrix product

$$[Y_M]\,|\,V\,> = |\,c\,> \qquad (5)$$

where $[Y_M]$ is the moment admittance matrix $[Z_M]^{-1}$. Given that the matrix $[Z_M]$ has been evaluated in accordance with the constraints of thin wire theory, it should now become obvious from (5) that the solution c_i is a function of the matrix $[V] = [<J_j, f(g)>]$ because $[Y_M]$ is completely determined. Furthermore, assuming that we have employed a sufficient number of basis functions to adequately represent the current variation, we should note that the quality of our model at this point depends only upon our ability to simulate the *"natural"* or *"physical"* forces which provide the stimulus for the antenna.

Admittance Calculations: After imaging, the antenna arrays under consideration here consist of dipoles that are oriented perpendicular to the x-y plane and equally spaced by a distance d. Fig. 1b illustrates the i^{th} and j^{th} elements of such an array with the coaxial apertures replaced by the equivalent *"magnetic frills"* of radii b_i and b_j, respectively. The most direct way to obtain the multiport network description of the antenna array from the MoM model is to determine the short-circuit multiport admittance matrix $[Y]$. The elements of the admittance matrix can be determined by driving the q^{th} port with the appropriate voltage source while the remaining elements are treated as scatterers, i.e., their input terminals are short circuited. Thus, $Y_{pq} = c_p/V_q|_{Vr=0}$, for $r=1,2,\ldots,N$, and $r \neq q$, where N is the number of feed ports, and p, q, and r are port indices (as distinguished from subdomain indices).

Source Models: Four source models have been implemented for this study. The first is the *"traditional"* or *"true"* delta source model $\delta(z)$ [9,12]. Forming the inner product $<J_j,\delta(z)>$ for each dipole in the usual manner evaluates to a 1 in the generalized voltage matrix of equations (4-5) at the position corresponding to T_{pn} and zero elsewhere. Hence, the solution for the currents on the dipoles is numerically identical to the column of the matrix $[Y_M]$ whose index corresponds to the basis function number at the driven port, which in this case would be pn. Forming the inner product $<J_j,E_g^{\,G}>$, where $E_g^{\,G}$ is the extended delta source whose form is given in [8], results in a generalized voltage matrix with non-zero elements corresponding to the indices of the basis functions on the driven dipole, and zero elsewhere, since it involves evaluating a "Gaussian pulse" which depends upon the wire radius [8] and which never decays to zero (although it may be negligible a few subdomains away from the excited port). The matrix $|\,c\,>$ obviously cannot be the same as for the case $<J_j,\delta(z)>$, since it now involves the sum of the products of row elements of $[Y_M]$ neighboring the driven port with the elements of the matrix $[<J_j,E_g^{\,G}>]$. Since part of the magnetic frill source model is needed in the implementation of the *modified* extended delta source model, $E_g^{\,M}$, it shall be discussed presently. Forming the inner product $<J_j,E_z^{\,F}>$ results in a completely filled generalized voltage matrix. The form implemented in this work is based upon the formulation of Tsai and is given as

$$\langle J_j, E_z^F \rangle = \frac{1}{2\pi \ln \frac{b_i}{a_{wi}}} \int_{z_j-\Delta}^{z_j+\Delta} T(z)\left[\int_0^{\pi} \left\{\frac{e^{-jkR_a}-1}{R_a} - \frac{e^{-jkR_b}}{R_b}\right\} d\phi' + \frac{2}{R_{a1}} K\left(\frac{\pi}{2}, p^2\right)\right] dz \tag{6}$$

$$R_a = [z^2 + \rho^2 + a_{wi}^2 - \rho a_{wi} \cos\phi']^{1/2} \tag{7}$$

$$R_b = [z^2 + \rho^2 + b_i^2 - \rho b_i \cos\phi']^{1/2} \tag{8}$$

$$R_{a1} = [z^2 + (\rho + a_{wi})^2]^{1/2} \tag{9}$$

$$p^2 = \frac{4\rho a_{wi}}{z^2 + (\rho + a_{wi})^2} \tag{10}$$

and $K(\pi/2, p^2)$ is the complete elliptic integral of the first kind, ρ and z are the cylindrical coordinate variables which locate the testing function (observation points) and Δ is the length of each segment which supports the triangular testing function $T(z)$ whose apex is located by z_j. For observation points not on the driven dipole, the terms $1/R_a$ and $K(\pi/2, p^2)$ dealing with the singular part of (6) may be omitted. For regions far from the source location, the magnitude of $\langle J_j, E_z^F \rangle$ may be numerically insignificant, depending upon the frequency of operation and the characteristic impedance of the feed line.

Finally, formation of the inner product $[\langle J_j, E_g^M \rangle]$ also results in a completely filled generalized voltage matrix, since it utilizes (6) for observation points not on the driven dipole. Its form is given as

$$\langle J_j, E_g^M \rangle = \frac{1}{\sqrt{2\pi}\delta_M} \int_{z_j-\Delta}^{z_j+\Delta} T(z) e^{-\frac{z^2}{2\delta_M^2} - j\theta} dz + F(z) \tag{11}$$

where θ is a phase factor and δ_M is the artificial gap length both of which were obtained from a linear curve fit using magnetic frill data for $0 < Z_c \leq 125\Omega$ (although other possibilities exist for determining these parameters) and are respectively given as,

$$\theta \approx z\pi\left[\frac{b_i}{a_{wi}}\left(\frac{b_i}{a_{wi}} - 1\right)\right]/28 \tag{12}$$

$$(a)\quad \delta_M \approx \frac{2b_i+5a_{wi}}{14}, \quad (b)\quad \delta_M \approx \frac{5b_i+2a_{wi}}{14} \tag{13}$$

Typically, (13a) is used for feed lines with larger coaxial apertures. For thin monopoles, the phase factor (12) may be omitted. The function *F(z)* accounts for the electric field on the distant scatterers and is the part of (6) for the electric field away from the driven monopole. Note that in the limit as $b_i \to a_{wi}$, $E_g^M \to E_g^G$ since $\delta_M \to \delta_G \to a_{wi}/2$, and $\theta \to 0$.

Results: A vast wealth of measured dipole admittances exits for isolated monopole antennas with a large range of radii and fed by a coaxial feed lines with a variety of characteristic impedances. To verify the new source models presented in this work for the case of an isolated monopole, data collected by Holly [13] and Hartig [14], some of which is also available in [15], was used as a base of comparison. Attention is now called to Fig. 2 which plots computed and measured input admittances for a monopole of radius $a_w=0.0423\lambda$ fed by a coaxial line of characteristic impedance $Z_c=10.27\Omega$ versus monopole length h/λ. As expected, the source model $\delta(z)$ does not predict good values for the input susceptances, B_{in}, and as such it is unacceptable. However, as expected, the other three source models predict values of B_{in} which are indeed acceptable when compared to each other and to the experimental data. For this case, (13b) was used for E_g^M. Note too that E_g^M, E_g^G, and E_z^F all yield reasonable values for B_{in} for monopole length to radius ratios as small as 2.36 in accordance with the discussion presented in [8]. Fig. 3 plots computed and measured input admittances for monopoles with hemispherical caps of radii $a_w=0.0159\lambda$ fed by a coaxial line of characteristic impedance $Z_c=93.0\Omega$ versus monopole length $(h+a_w)/\lambda$ (where the monopole length is taken to be $h+a_w$ for consistency with Fig. 1b). Note that both source models E_g^G and $\delta(z)$ do not predict good values for B_{in}, whereas E_g^M and E_z^F do. For this analysis, (13b) was used.

Finally, attention is called to Figs. 4a and 4b. These figures plot self and mutual admittances for a two element array of quarter-wave monopoles fed by coaxial lines with $Z_c=125.4\Omega$, versus separation distance d/λ. The driven monopole is of radius $a_{w1}=0.04\lambda$ and the passive monopole is of radius $a_{w2}=0.01\lambda$. For this analysis, (13a) was used in (11). It should be mentioned that for this antenna array, the phase factor of (12) could not be neglected in implementing E_g^M, and that (13b) did not produce acceptable values for the multiport admittances. As can be seen from these figures, both E_g^G and $\delta(z)$ will yield a multiport admittance matrix which is of little value since both the self and mutual admittances exhibit large deviation from those admittances computed using E_g^M and E_z^F. Also note that E_g^G and $\delta(z)$ yield results for the mutual admittance at locations far from their point of application which are less accurate than those obtained from E_g^M when compared to E_z^F. No experimental data was available to us at this time for the self and mutual admittance of antenna arrays fed by coaxial lines with large characteristic impedances; however, judging from the results of Fig. 4, the source model E_g^M should yield multiport admittance matrices comparable to those obtained by measurement since it tracks the admittances obtained from E_z^F quite well.

Conclusions: This work introduces a *modified* extended delta source model which yields results for monopole input admittances comparable to those obtained from the magnetic frill source model since it takes into consideration the characteristic impedance of the feed line. Furthermore, the *modified* extended delta source model and the magnetic frill source model when used as a forcing function for

the EFIE yield comparable results for the multiport-network description of thin cylindrical dipole arrays, but the *modified* extended delta source is much simpler to implement. This work represents a preliminary investigation into improvements to, and generalizations of, existing simple voltage source models for use as forcing functions.

References:

[1] R.W.P. King, R.B.Mack, and S.S. Sandler, *Arrays of Cylindrical Dipoles,* Cambridge, MA, 1968.

[2] V.W.H. Chang and R.W.P King, "On two arbitrarily located identical parallel antennas," *IEEE Trans. Antennas Propagat.*, vol. AP-16, pp. 309-317, May, 1968.

[3] J.D. Tillman, Jr., *The Theory and Design of Circular Antenna Arrays*: Knoxville, TN, The University of Tennessee Experiment Station, 1966.

[4] R.W.P. King, "The linear antenna-Eighty years of progress," *Proc. IEEE,* vol. 55, pp. 2-26, Jan. 1987.

[5] C. M. Butler, "Evaluation of potential integral at singularity of exact kernel in thin wire calculations," *IEEE Trans. Antennas Propagat.*, pp. 293-295, Mar. 1975.

[6] D. H. Werner, "An exact formulation for the vector potential of a cylindrical antenna with uniformly distributed current and arbitrary radius," *IEEE Trans. Antennas Propagat.*, vol. 41, pp. 1009-1018, Aug. 1993.

[7] S. O. Park and C. A. Balanis, "Efficient kernel calculation of cylindrical antennas," *IEEE Trans. Antennas Propagat.*, vol. 43, pp. 1328-1331, Nov. 1995.

[8] G.P. Junker, A.A. Kishk, and A.W. Glisson, "A novel delta gap source model for center fed cylindrical dipoles," *IEEE Trans. Antennas Propagat.*, vol. AP-43, pp. 537-540, May 1995.

[9] T.K. Sarkar, "A study of the various methods for computing electromagnetic field utilizing thin wire integral equations," *Radio Sci.*, vol. 18, pp. 29-38, 1983.

[10] L.L. Tsai, "A numerical solution for the near and far fields of an annular ring of magnetic current," *IEEE Trans. Antennas Propagat.*, vol. AP-20, pp. 569-576, Sept. 1972.

[11] C.M. Butler and L.L. Tsai, "An alternate frill field formulation," *IEEE Trans. Antennas Propagat.*, vol. AP-21, pp. 115-116, Jan. 1973.

[12] R.F. Harrington, *Field Computation by Moment Methods*: Malabar, FL, R.E. Krieger, 1968.

[13] S. Holly, *Experimental Study of Electrically Thick Monopole Antennas,*Doctoral Dissertation, Harvard University, Cambridge, MA, June 1969.

[14] E. O. Hartig, *Circular Apertures and Their Effects on Half-Dipole Impedances,* Doctoral Dissertation, Harvard University, Cambridge, MA, June 1950.

[15] R.W.P. King, *Tables of Antenna Characteristics,*IFI/Plenum Data Corp., NY, NY, 1971.

SUSCEPTIBILITY MODELING
for
PCBs with LONG WIRES ATTACHED

Bruce Archambeault
SETH Corporation
Johnstown, PA

H. Stephen Berger
Siemens ROLM Communications Company
Austin, Texas

INTRODUCTION

Numerical modeling of EMI/EMC problems has become more popular over the past few years, due to the commercial availability of modeling software and drive to reduce product development cycle times. These market forces combined with an increase of the data and clock speeds (and associated pulse rise/fall times) and ever increasing pressure on product costs have fueled a widespread use of numerical modeling among EMI/EMC engineers in order to remain competitive.

Most of the focus on EMI modeling has been on radiated emissions. Historically the emissions problem has had priority over immunity for various reasons. However, immunity issues are becoming increasingly important due to the new European EMI requirements, and the increased density of electronic devices. This paper presents some techniques for adopting the modeling techniques developed for radiated emissions to immunity problems.

This paper describes both modeling and experimental validation of these techniques on a simple, unshielded circuit board with long wires attached. A number of different models were developed to determine which components and circuitry were primarily involved in a known immunity problem. The model was then altered to study the effectiveness of various solutions such as the use of filtering components, power decoupling and signal trace position.

MEASUREMENT APPROACH

The technique reported in this study was developed on a set of digital telephone products. The analog circuitry in telephones has historically been sensitive to modulated RF fields. The nature of these circuits makes them natural demodulators of RF fields. The resulting demodulated noise is then transmitted with the intended signal resulting in unwanted interference. The telephone which was the subject of this study was demonstrated to have a sensitivity to RF fields in the 500 MHz region. The designers of this product were experienced engineers who had applied sound layout and design techniques to the product. Probing with small probes suggested that the analog circuitry associated with the CODEC analog inputs was the most likely point of demodulation. It was necessary to determine how the RF was being coupled into this circuitry and which solutions would prove effective in resolving the problem. The circuitry in question had been carefully contained within a small area to reduce the possibility of RF coupling into this area of known sensitivity. Further, the circuit board, which was two sided, had a good ground reference grid on one side. However, it was noted that the digital bus coming into the CODEC chip made a "U" around the analog circuitry in order to reach the required pins on the chip. The analog circuitry, this digital bus and the ground grid became the primary subjects of the investigation.

Ultimately it was determined that the digital bus was the coupling path used to the sensitive circuit area. A minor amount of capacitance placed at the middle of this bus proved effective in bring the product into compliance with its specification. The numeric modeling techniques used proved very useful in gaining both an in-depth insight into the mechanism of this problem and quickly evaluating the likely success of a number of possible solutions.

MODELING APPROACH

The simulation was performed using the Method of Moments (MoM) modeling tool within the SETH Corporation's EMIT^{tm} (EMI Toolbox for Modeling). Reciprocity was used to make the modeling more straightforward. That is, a source was modeled at the point where the circuit sensitivity was known to exist. The calculated radiated field provided a transfer function (across the frequency range) for the voltage at the component to the field strength. Furthermore, all impinging field angles and polarizations were examined to determine the point of maximum sensitivity. By this application of reciprocity all angles of incidents could be investigated simultaneously greatly reducing the number of models required.

The model for this problem contained four major components. These were: the ground grid of the PWB, the CODEC analog circuitry, the digital bus and the telephone line coming to the product. The addition of the telephone line was important in that its long length made it highly likely to be a part of the structure which was receiving the RF field. The model for the PCB etches is shown in Figures 1 through 3. Note that the traces that connected to the sensitive component, traces connected to the long external wires, and any traces that could act as significant fortuitous conductors between the previous two classes of traces were all included in the model. All other traces were eliminated from the model to simplify the overall model and to achieve faster solution times.

Several passes were required on the baseline model before the critical elements of the problem were identified. It became apparent that it the design of the source needed enhancement. In order to provide an accurate model, the source must be designed such that it reciprocates the frequency response of the CODEC circuitry. If a generalized source, such as that illustrated, is used it will predict susceptibility at higher frequencies than may exist in reality. This is because the circuitry may not respond at these frequencies, even though energy is conducted into the circuit area. Accordingly, the output impedance of the source is designed to replicate the target circuit's frequency response.

Another issue which must be addressed is that of multiple mechanisms contributing to a given immunity issue. The primary peak in this problem was at 500 MHz. However, there is a secondary peak in the measured data near 390 MHz. This peak is due to a different mechanism, which was verified both experimentally and by modeling. It should be noted that the amplitude of this peak did not respond to the solution developed for the primary peak. The models developed for the primary peak also did not adequately anticipate this peak. This issue was noted but disregarded since this peak was within the product's performance specification limit.

The simulation was performed with the circuit traces as originally designed, that is, with the immunity problem intact. Note that in Figure 4 the measured data clearly shows the susceptibility response at 500 MHz, and although the modeled response (Figure 5) is more broadbanded, the increase in susceptibility around 500 Mhz is clear also. The model's broadband response was expected since all the capacitance and inductance in the circuit (which

are likely to cause sharper resonances) has not been modeled (to simplify the model). The model was considered accurate, and the search for the proper design change to implement to correct the immunity problem was undertaken.

Once the problem was adequately modeled three lines of investigation were followed. The first was to improve the filtering present at the input connector of the telephone line. The second was to introduce capacitance onto the bus lines. The third alternative investigated was alternate routing for the digital bus lines.

The input filtering was investigated by bounding the problem at the extremes. A model was run with no filtering. Then a model with perfect filtering was run. Perfect filtering was designed as a 1 cm gap between the telephone line approaching the board and its connector. One of the tremendous strengths of modeling is that this kind of physically impossible structure can be investigated in order to gain insight into the problem. It was discovered that while filtering at the input was helpful, this problem could not be adequately resolved by filtering alone. In all cases frequency regions exist where there is little or no flow of RF current through the filter. As a result the filtering components are totally useless at these frequencies. As a result of this bounding of the problem this area of investigation was quickly set aside.

The introduction of capacitance onto the digital lines looked promising as a way of defeating this resonant structure. This approach was effective both in the model and experimentally. The modeled response predicted an improvement of 12 dB at 500 MHz. The experimental data found also found a significant improvement of 12 dB (as can be seen in Figure 4) at 500 MHz. Then alternate implementations of this solution were evaluated. Figure 6 shows a number of locations where a capacitor was simulated in the model to determine the effect on the immunity response. Only one capacitor was installed in the model at a time, so as to determine the effect of each potential component location. As can be seen in Figure 5, the location of the capacitor made a significant difference in the susceptibility response at 500 Mhz. Note that position #1 was selected as the optimum location, and the capacitor physically installed on the PCB.

Before a final solution was selected alternate routing of the digital lines was investigated. The addition of capacitance onto these lines would require a change in the board layout to allow for these components. That being the case, if alternate routing was a possibility, that would be the optimal solution from a cost standpoint. The strength of this approach to an immunity problem is that it allows for quick evaluation of many different solutions. A solution may be bounded at the extremes, such as was done with the input filtering. Even though some implementations are not physically possible their models have value in that they show at the extreme limit what is possible with a given approach. If the absolute limit, such as an open in an input line, is not sufficiently effective then a given line of investigation may be quickly abandoned. Alternately, solutions which are difficult or time consuming to test experimentally, such as alternate routing on very dense, surface mount boards, may be quickly modeled. Thus a high degree of confidence may be gained before the expense of implementation is incurred.

TECHNIQUE SUMMARY

The technique described here may be reduced to the following steps.

1. An immunity problem is selected and measured over a frequency band of interest.
2. Using small probes or engineering analysis the critical circuit is identified.
3. The frequency response of the critical circuit is measured.
4. A baseline model is developed which replicates the product's response
5. General solution approaches are suggested and bounded by modeling at the extremes to investigate feasibility.
6. Once a promising and practical approach is determined, alternate implementations are investigated in order to determine the optimum implementation within a given product's cost constraints.
7. The solution selected in experimentally verified and implemented.

SUMMARY

This paper introduces a technique for using applying numeric modeling to immunity problems. Modeling can be used to simulate the effects of radiated immunity as well as radiated emissions. Second, models eliminate the 'brute force approach' to immunity problems of guessing at the source of an immunity mechanism and experimentally trying many possible solutions until an effective remedy is found. With modeling, solutions are not considered until the central mechanism of the problem is adequately understood. Once an adequate model is developed inspection of the RF current flows at the frequencies of primary interest is particularly instructive in this regard. Then using well known electromagnetic effects (such as reciprocity), modeling can be made much simpler, and effectively extend the usefulness of existing modeling tools.

Figure 1
Typical Telephone Station

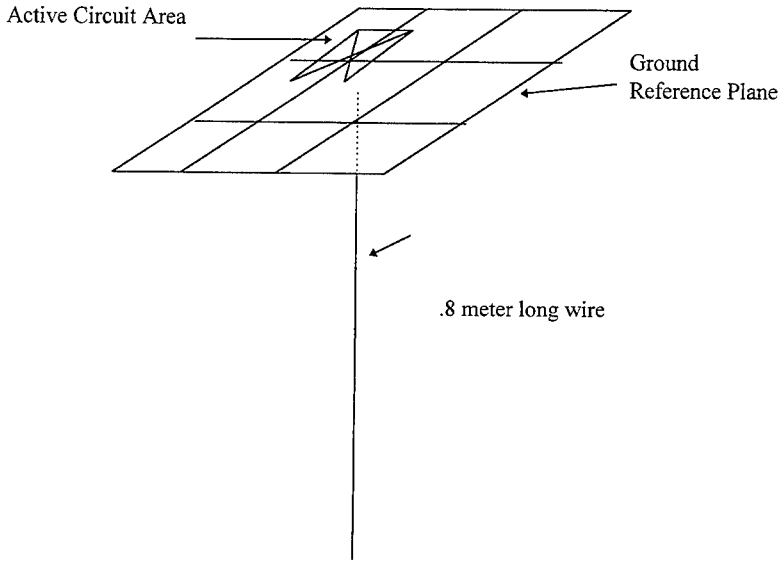

Figure 2
Simplified Model

Figure 3 Partial MoM Model for Phone susceptibility

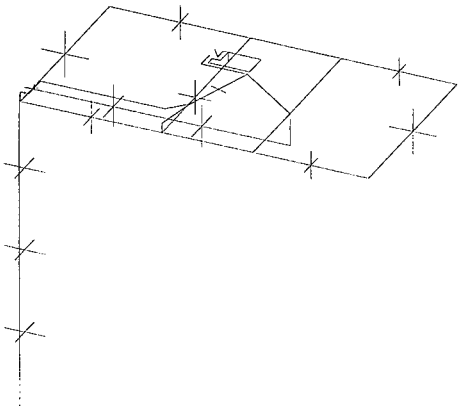

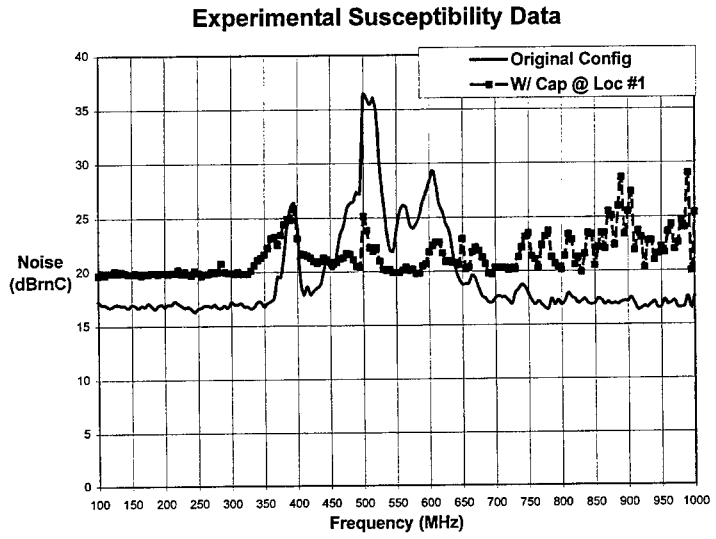

Figure 4

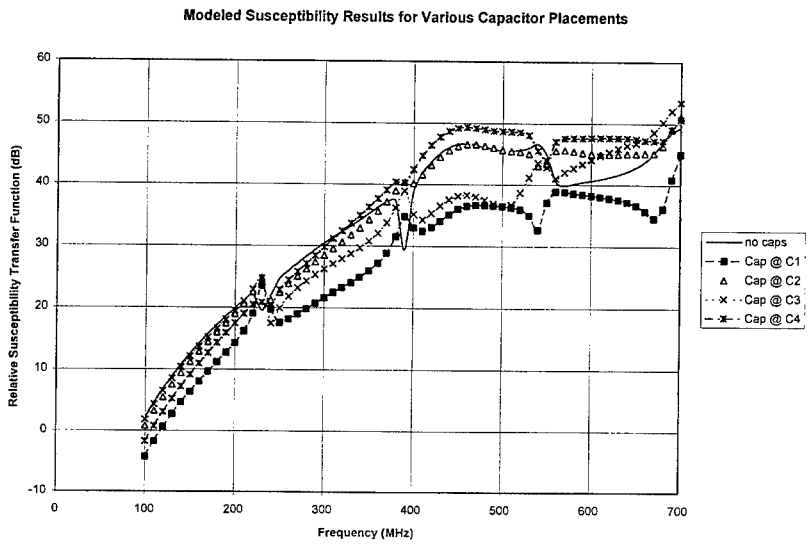

Figure 5

Figure 6
Location of Capacitors in Models

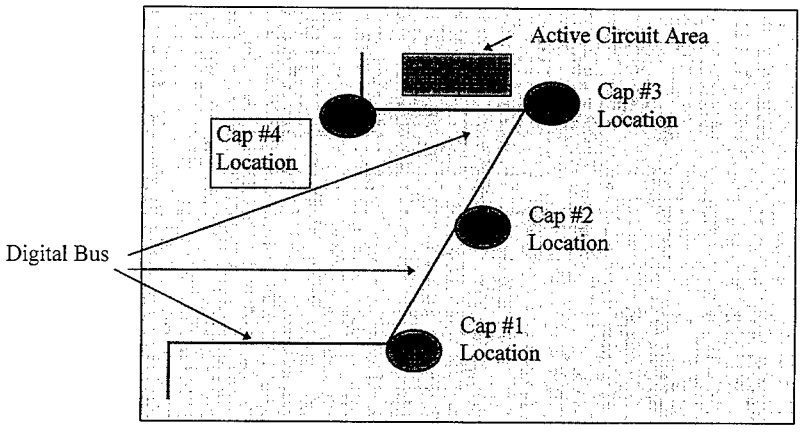

Computer Modeling Tools for EMC

T. H. Hubing and J. L. Drewniak
Electromagnetic Compatibility Laboratory
University of Missouri-Rolla

Abstract

Computer modeling tools for EMC analysis generally fall into one of three categories: numerical modeling codes, analytical modeling codes, or design rule checkers. Although these tools can be very helpful to the experienced EMC engineer, computer modeling tools are rarely used to analyze or prevent EMC problems during the development phase of new products. This paper discusses computer tools that are currently available and introduces a new class of EMC modeling software based on an expert system approach.

Introduction

There are a number of computer modeling codes available to EMC engineers and circuit designers today. Computer modeling tools can be used to provide information about a particular design that is not readily obtained in any other manner. For example, computer modeling tools can calculate values of parasitic inductances and capacitances in a circuit, model the behavior of the radiated fields, determine current distributions, calculate crosstalk, evaluate the effectiveness of a shielded enclosure, or locate simple design mistakes.

Generally, software tools for EMC analysis fall into one of three categories: numerical modeling codes, analytical modeling codes, or design rule checkers. Numerical modeling codes analyze problems by numerically solving Maxwell's equations subject to particular boundary conditions. Analytical modeling codes use closed-form equations and/or pre-calculated solutions to analyze EMC problems. Design rule checkers scan a printed circuit board or system design for errors or violations of EMC design guidelines without attempting to calculate fields or currents.

Numerical Modeling Codes

Numerical electromagnetic modeling software is widely viewed as a promising new tool to help EMC engineers and circuit designers anticipate electromagnetic compatibility problems. Numerical EM modeling codes solve field equations subject to appropriate boundary conditions in order to determine the electromagnetic behavior of different source configurations.

The ability of a numerical modeling code to model a particular geometry is largely dependent on the numerical technique employed by the code. Finite element modeling codes (e.g. MSC/EMAS or AnSoft's MAXWELL codes) excel at modeling relatively complex geometries with lossy or even nonlinear materials. Codes that employ surface integral techniques (e.g. NEC, COMORAN, HFSS, EM, IE3D, COMPLIANCE, MAXSIM-F) are very well suited for modeling relatively large, resonant structures; particularly structures with long wires or cables. Finite difference time domain (FDTD) codes (e.g. XFDTD, EMA3D, EMIT) are usually the best choice for time domain or broadband modeling.

Ansoft, Cadence, Hewlett-Packard, Quad Design, and Quantic Laboratories have packaged numerical modeling software with software that automatically extracts printed circuit board geometry data from automated board layout tools. These tools make it easier for EMC or signal integrity engineers to take advantage of numerical modeling software. INCASES (EMC Workbench) and Seth Corporation (EMIT) have developed software environments that bring together a variety of numerical modeling tools with a common interface designed specifically for EMC engineers.

Despite the availability of software that models geometries of interest to EMC engineers with a high degree of accuracy, numerical codes have not been widely utilized for EMI modeling. Only a small percentage of EMC engineers use numerical modeling codes on a regular basis. One reason for this is that numerical codes require well defined sources. Defining the source of an EMC problem is often the most difficult step in the solution process. When an EMC engineer can identify the parameters necessary to do a numerical analysis (i.e. source location, source amplitude, and antenna geometry), then often the problem can be corrected without doing a numerical analysis. Numerical electromagnetic modeling codes are sometimes used to analyze specific circuits or structures, but typical printed circuit board configurations are much too complex to be analyzed in their entirety using strictly numerical methods.

There is an additional problem with existing numerical EM modeling codes that often prevents them from being used, even in cases where relatively simple well-defined model geometries can be identified. Existing modeling codes have a fairly steep learning curve. The user must be reasonably well versed in the procedures for applying the code as well as the techniques used by the code and their limitations. Few EMC engineers can afford to be an expert user of several EM modeling codes that may or may not be occasionally helpful. Numerical EM modeling codes are potentially a very valuable tool for EMC problem analysis, but in their present form they require too much expertise on the part of the user to be widely used as an EMI modeling tool.

Analytical Modeling Codes

Analytical modeling software, which uses relatively simple closed-form expressions to calculate parameters such as field strengths or currents tends to be much faster and a little easier to use. Analytical methods fit problems to pre-defined geometries with known solutions. IEMCAP is one relatively well known example of a code based primarily on analytical techniques. Analytical modeling codes for EMC engineers are also marketed by Interference Control Technologies, Kimmel Gerke Associates, CKC Laboratories and Atkinson Engineering. Each of these codes is much faster and easier to use than a general purpose numerical modeling code, however each code has a limited set of functions that it performs.

Although analytical modeling codes tend to be easier to use than numerical modeling codes, the user must still be aware of assumptions that the code is using and limitations imposed by these assumptions. Learning to use the code is not the same as learning how and when to apply the code.

Like numerical modeling software, analytical modeling codes rely on the user to define sources and other critical parameters. Identifying these parameters requires a certain amount of EMC knowledge. There is little value in performing a highly accurate analysis of an incorrect model.

Rule Checking Codes

EMC rule checking software reads board layout information from automated board layout tools and looks for violations of basic EMC design rules. This type of software does not usually attempt to predict the electromagnetic behavior of the system, but instead is intended to help designers avoid costly mistakes

early in the design stage. Cadence markets an EMC design rule checker under the name DF/EM Control. Zuken-Redac has a design rule checker called EMC Adviser. These tools can help board designers to locate potential problems with their designs and they can also help experienced EMC engineers to quickly identify problems that would otherwise be hard to spot.

Unlike numerical and analytical modeling software, rule checkers do not require the user to understand basic principles of electromagnetic modeling. However, the available rule checking codes do require the user to identify critical nets and supply information about the signal parameters. This requires a certain amount of expertise on the part of the user, but it is a different kind of expertise. Another difficulty with rule checkers is that design rules and their impact on EMC can vary significantly from one design to another. Design rule violations that are a major problem for one design may be of little consequence in another design.

Expert System Codes

Although each of the techniques above can be a very powerful tool in the hands of a knowledgeable user, software employing these techniques is not widely used by EMC engineers or circuit designers. The learning curve associated with available tools is often too steep. Few engineers have the knowledge and experience required to use these tools effectively.

To circumvent this problem, a new class of EMC software is currently being developed at a number of laboratories around the world. This new class of software attempts to emulate the thinking process of experienced experts in EMC. EMC engineers rely on design rules, but when a rule is violated, they perform a quick analysis of the overall design to evaluate the impact of that rule violation. EMC engineers may take advantage of numerical and analytical modeling tools, but only after the critical parameters of the problem have been identified. Software that works like this is appropriately classified as expert system software rather than numerical, analytical, or rule-checking software.

EMC expert system software seeks information from a variety of sources. By definition, expert system software does not assume a high level of expertise on the part of the user. Like an EMC expert, the more information the software has about a particular problem, the more effective its analysis will be. Nevertheless, even with incomplete information, expert system software attempts to provide a helpful and accurate EMC evaluation of a design.

Conclusion

There are a number of software tools that can help product developers to meet their EMC requirements. Modeling codes that employ numerical, analytical or rule checking techniques can analyze a wide range of EMC problem geometries and are readily available. To the experienced user, these codes can be valuable EMC design tools.

EMC expert system codes won't eliminate the need for other types of EM modeling codes, but they will play a significant role in the future of EMC engineering. By emulating the thought processes and techniques used by EMC engineers, EMC expert system codes will zero in on the most significant features of a design from an EMC standpoint. EMC expert system software promises to identify and evaluate EMC problems faster and more accurately than existing modeling codes. Also, because expert system software does not require any expertise on the part of the user, circuit designers, board layout personnel, EMC engineers, technicians and others can use the software to evaluate a product at different stages in the design process.

Companies with Software Products Mentioned in this Paper

Ansoft Corporation (Maxwell)
Phone: 412-261-3200
WEB: http://www.ansoft.com

Bay Technology (IE3D)
Phone: (408) 688-8919
WEB: http://www.bay-technology.com/

ElectroMagnetic Applications, Inc. (EMA3D)
Phone: (303) 980-0070

HP EEsof (HFSS)
Phone: (415) 964-2456
WEB: http://www.tmo.hp.com:80/tmo/hpeesof

INCASES North America Inc. (EMC-Workbench)
Phone: 214 373 7344
Fax: 214 373 7784

MacNeal-Schwendler Corporation (MSC/EMAS)
Phone: (414) 357-8723
WEB: http://www.macsch.com

MATRA-MARCONI (MAXSIM-F)
Phone: (+33) 61.39.65.12
Fax: (+33) 62.24.77.90
email: estienne@maxwell.matra-espace.fr

Quad Design Technology (QUIET)
Phone: (805) 988-8250

Quantic Laboratories (Compliance)
Phone: (800) 665-0235

Remcom Inc. (XFDTD)
Phone: (814)-353-2986
WEB: http://www.remcominc.com

SETH Corporation (EMIT)
Web: http://www.sethcorp.com

Sonnet Software Inc. (EM)
Phone: (315) 453-3096
Web: http://www.sonnetusa.com

ELECTROMAGNETIC INDUCED TIMING DEFECTS IN CMOS CHIPS

Reinaldo Perez
Jet Propulsion Laboratory
California Institute of Technology
Pasadena, California 91109

Abstract

The Magellan spacecraft synthetic aperture radar experienced a failure when the receiver protect circuitry in the PRF/Timing subsystem failed. The receiver protect circuitry failed due to electromagnetic coupling from the ultra stable oscillator/clock generator circuit located on an adjacent board. Some ICs in this ultra stable oscillator/clock generator circuit had previously become detached from their traces when a thermal test caused the conformal coating to expand. The ICs were re-attached to the PCB traces using "small wire loops" which apparently radiated significantly to cause the failure of the receiver protect circuits. The analysis which discovered the above failure mechanism is discussed. The analysis also includes the use of the method of moments to model the radiation from a portion of the noisy board and coupling into the susceptible circuits of another board. Only one of such models is discussed herein for brevity. The simple solution to the electromagnetic coupling problems is discussed in the conclusion of this work.

1.0 Introduction of Problem: A Failed Synthetic Aperture Radar

During final functional checkout of the Magellan spacecraft synthetic aperture radar (SAR) at the Kennedy Space Center, and two weeks before launch to the planet Venus for mapping its surface, the radar experienced a failure in which its PRF/Timing Unit-A was not working. Failure of such unit would mean that range, and transmitter signals to the SAR and altimeter (ALT) antennas would be corrupted, in essence rendering one half of the redundant (side A and side B)radar totally useless. Figure 1 shows a functional block diagram of the sensor subsystem of the SAR. Notice the redundancy of all functional blocks. The figure shows the PRF Timing Module being fed by the ultra stable oscillator (STALO). The STALO/PRF Timing unit generates all the timing and clock signals needed by the radar's subsystems such as the range dispersion units, transmitters, receivers, baseband processors, and data formatters. Figure 2 shows a detailed block diagram of the STALO and PRF Timing unit. The PRF timing unit consists of a clock generator which feeds its clocks (1.13 MHZ, 2.26MHz, and 141.2 KHz) into the SAR, ALT, and Radiometer pulse generators. The receiver-protect-circuitry serves as the interface between the transmitter and receivers subsystems of the radar and a series of pulses are generated to toggle the control between transmitting and receiving bursts. Figure 3 shows a timeline illustration of the different bursts in the mapping process.

2.0 Finding the Problem

Approximately six weeks before launch during thermal testing at the system level it was discovered that some IC mounted on two PCB within STALO have become detached (or displaced from their position) resulting in a loss of contact with PCB traces. The accidental positional displacement was attributed to a chemical expansion of the conformal coating in the IC during cycles of thermal testing ranging from -20C to 85C. The design and building of new boards was not feasible in the scheduled time remaining before launch (a "window" of opportunity for a launch to Venus exists only every 18 months and last only a few days), hence, it was decided to fix the problem by connecting "wire loops" between the leads of the chips and the PCB traces. The wire loops were made of copper, wire gauge 32 (0.0201 cm), and were about 0.4 inches long. This procedure was used to attach a total of 8 chips to their respective PCB traces in two different boards within STALO. Functional check out of these boards proved the solution to have been adequate. Figure 4 shows an illustration of the above fix.

3.0 Fixing the Problem Created New Ones; this Time of EM Nature

In the final system level functional check out of the radar, telemetry reading showed a systematic failure of the radar in its PRF/Timing Unit-A (in Figure 1). A series of troubleshooting steps were performed which isolated the problem to the "receiver-protect-circuitry" located within the PRF/Timing module (see Figure 2). When the receiver-protect-circuitry board was removed and individually tested for its functionality, no anomalies were observed. However, when installed back into the unit, the failure re-occurred (this was done three times). These anomalies consisted in the corruption and eventual loss of the "Pre/post PRF" and "pulse-complete" signals from/to the receiver-protect-circuitry (see Figure 2). After checking for noise/compatibility problems between the different conductive (i.e through cables/connectors) interfaces and observing no problems, it became evident quickly that an external "radiated" interference source was at the root of the problem and that the main cause of such anomalies was radiated coupling. Next to the receiver-protect-circuitry board and separated by only 7 cm were the two STALO boards which were previously fixed using wire loops for the attachment of displaced chips. Near field probe measurements were made and the results indicated the presence of strong electromagnetic fields near the receiver-protect-circuitry board. The use of wire loops in the STALO boards became an immediate suspect in the rationale for the strong presence of electromagnetic fields at the receiver-protect-circuitry board. The wire loops, specially those attached to the clock outputs of chips, can become "complex radiating structures" as shown in Figure 5. This paper deals with the displaced chip (and then re-attached using wire loops) containing the 72 MHz clock output. The top half of Figure 5 shows a "radiating structure" consisting of: a) a voltage source Vs (frequency dependent) located at the clock output (5 volts peak-to-peak, trapezoidal waveform, 50% duty cycle, 72 MHz, rise time=fall time of 1.0 nSec) of a chip, b) the wire element structure which is composed of a wire loop plus the PCB trace, c) loading effects as represented by the input capacitance of chips which receive the clock, and d) a return path through the ground plane of the PCB. The bottom half of Figure 5 shows a portion of a "susceptible" circuit located in the

receiver-protect-circuitry board. A transmission line representation of such susceptible circuit is also shown.

4.0 The Use of Computational Electromagnetics in this Application

It was necessary to verify the above model because: a) it was important to determine the source of the emissions so that the appropriate corrective actions could be taken, and b) the analysis would reveal insights into the failure mechanisms inside the CMOS chips. The Method of Moments (MOM) for thin wires [1] was used in the above analysis. Figure 6 illustrate some of the details corresponding to the use of the method of moments for modeling the radiating structure in Figure 5. Notice that: a) the rectangular shape of PCB microstrip traces were converted to equivalent round wires [2] for simplicity, b) the dielectric effects of the PCB were not included in the modeling since we had a low loss scenario [3]. Neglecting dielectric effects give reasonable results at lower frequencies [4]. Since we were not in pursue of accurate models but rather in the positive "identification" of a radiating source the neglect of dielectric was appropriate, and c) the ground plane was not modeled (again for simplicity) but instead an "image return" trace (converted to its equivalent round wire) was used. Figure 6 also shows details about modeling the susceptible circuit using a transmission line approach known as the field-to-wire coupling [5,6]. The field-to-wire coupling approach is more simple (though less accurate) than numerically calculating the near field wire-to-wire coupling with the help of the method of moments. The field-to-wire coupling approach is good for plane waves. However, in this work we developed an approximation for near fields. For the sake of simplicity our near field calculations were modified in the following matter in order to use the field-to-wire coupling model of Figure 6: 1) the (x,y,z) components of the near electric fields were calculated at points P1, P2, and P3 as shown in Figure 5. These points expand the length of the susceptible circuit (more points can be used if desired). Tables 1a through 1c shows the results of near field calculations for the different harmonics of the 72 MHz clock, 2) an average (of the three points) is obtained for the x, y, and z components so that only one set of values for Ex, Ey, and Ez is obtained, and 3) simple equations for field-to-wire coupling will be used. For example, equation (1) represents the expression from field-to-wire coupling for calculating the induced current on a transmission line for a no-loss, homogeneous medium. The wire sits in the x-y plane over a ground plane (similar equations for the x-z and y-z plane will be stated in the paper).

$$I(s,\omega) = \frac{2}{D}\int_0^{s'} (2j\ Sin\ (\beta h))\ E_y^t\ [Z_o\ (Cos\ \beta y + jZ_1\ Sin\ (\beta y)]dy$$

$$+\frac{2Z_o}{D}\int_0^h E_x^t\ (x,0,\omega)\ dx - \frac{2}{D}[Z_o\ Cos(\beta s) + jZ_1\ Sin\ (\beta s)]\int_0^h E_x^t(x,s,\omega)\ dx \qquad (1)$$

$$where \quad D = (Z_0Z_1 + Z_oZ_1)Cos\ (\beta s) + j(Z_o^2 + Z_1Z_2)Sin\ (\beta s)$$

In equation 1 Z_1 and Z_2 are the capacitive loads in the susceptible circuit of Figure 5 or 6b (in CMOS chips input capacitance is the primary impedance, hence Ra=Rb=0 in Figure 5). Zo is the characteristic impedance of the trace (35 ohms in Figure 6b) and Ey and Ex are the average field

values (numerical constants) along the length of the circuit which were already calculated from the method of moments. Transmission line equations for current distribution are evaluated for each of the 5 sections (see Figure 6) in which the susceptible circuit is divided. The total induced current can then be obtained. Transmission line equations of the type shown by equation 1 become very simple to evaluate leading to simple analytical expressions. Notice that this approach is only an approximation but it is feasible and fast for simple susceptible circuits. A more complex approach for near field wire-to-wire coupling, based on the method of moments, which is an extension of the original work of A.T.Adams [7].

The more simple of the above procedures was used to calculate the induced current in the susceptible circuits and eventually the calculation of the induced voltages in the capacitive loads corresponding to the IC. The susceptible circuit shown in Figures 5 and 6b is the major portion of the most prominent susceptible circuit within the receiver-protect-circuitry PCB in the PRF/Timing block (three chips and small portions of traces are missing from Figure 6b). When the analysis was performed, it was found that the induced load voltages were on the order of 1.43V for the 10.0 pF load and 1.28V for the 3.5 pF load. These induced voltages are much higher than the noise margins. Usually noise margins range from 0.2 to 0.5 volts for most CMOS chips. The results are that such chips will "latch up" on a give state. A latch up chip will prevent all subsequent digital functions from being performed. This scenario is illustrated in Figures 7 and 8. Figure 7 shows the timing diagram of some inputs and output signals from the receiver-protect-circuitry in Figure 2. In Figure 8 the receiver-protect-command has been interrupted. The receiver-protect-command is generated from a circuit within the receiver-protect-circuitry. It is in this receiver-protect-command circuit where the coupled noise current was found. A portion of the receiver-protect-command circuit is shown in Figure 6b. Once the receiver-protect-command is interrupted the Pre/post PRF signal is also interrupted (see Figure 8). The pulse-complete command (a feedback from the receiver-protec- circuitry) also goes bad (see Figure 8). The end result is that no toggle between the transmitters and receivers ever occurs--the radar is dead.

Once the problem was identified and corroborated with the analyses a simple, cheap, and fast solution was arrived to: shielding the noise sources. The IC with their "wire loops" were shielded and the small shields grounded. To prevent heating problems the IC shields were also connected to heat sinks. After the fix the noise coupling problem disappeared. The spacecraft was launched on time and it successfully completed its mission almost three years later in October 1994 with the radar mapping of Venus entire surface (Venus' surface can not be photographed because if its dense CO2 atmosphere).

References

[1] Harrington,R.F. Field Computation by Moment Method, Macmillan Co., N.Y., 1968.

[2] Springfield, W.K., "Multilayer printed circuitry in computer applications," Fall Meeting of Printed Circuits, Chicago, 1964.

[3] Perez, R. "Simple radiation models in lieu of EMC radiated emissions testing," 11th Annual

Review of Progress in Applied Computational Electromagnetic Society, Monterey, CA. March 20-25, 1995.

[4] Hoffman, T.R. Handbook of Microwaves Integrated Circuits, chapter 3, Artech House, 1987

[5] Smith, A.A. Coupling of External Fields to Transmission Lines, Interference Control technologies, 1987.

[6] Paul, Clayton, Analysis of Multiconductor Transmission Lines, Wiley Interscience, 1994.

[7] Adams, T.A and Strait, B.J. "Modern analysis methods for EMC," IEEE Symposium in Electromagnetic Compatibility, San Diego, CA. 1974.

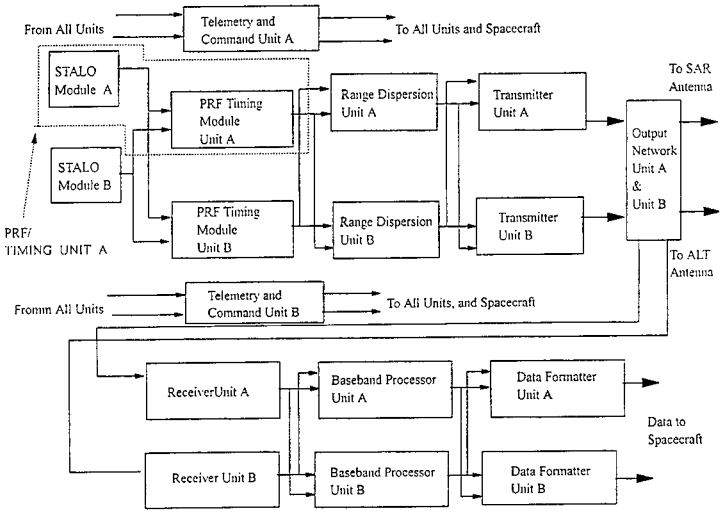

Figure 1. SENSOR SUBSYSTEM FUNCTIONAL BLOCK DIAGRAM

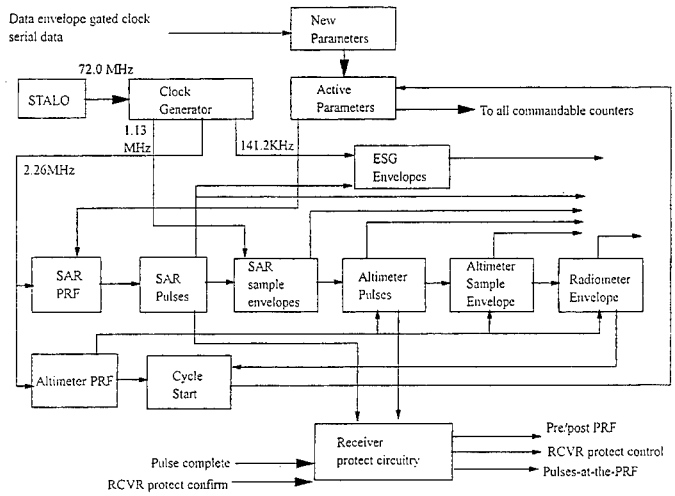

Figure 2 PRF/TIMING BLOCK DIAGRAM

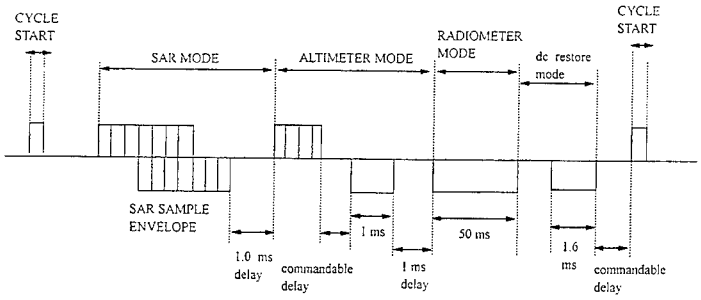

FIGURE 3. BURST CYCLE TIMELINE

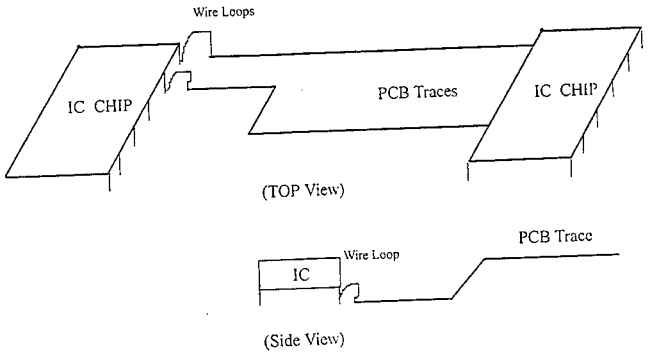

FIGURE 4. WIRE LOOP CONNECTING LEADS IN IC CHIPS TO PCB.

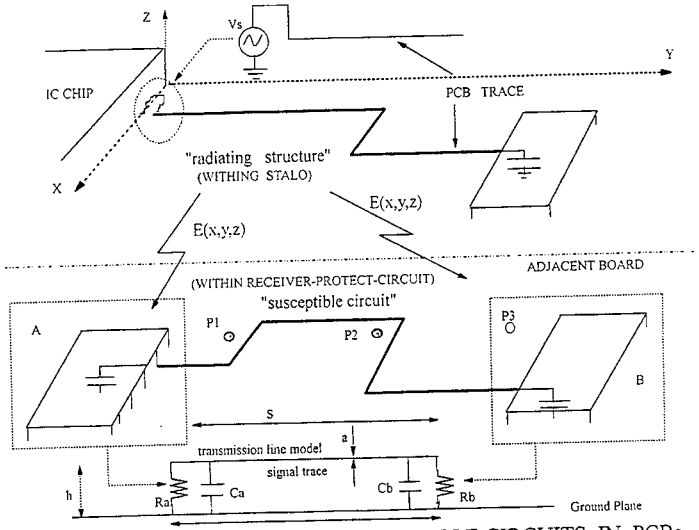

Figure 5: RADIATING AND SUSCEPTIBLE CIRCUITS IN PCBs

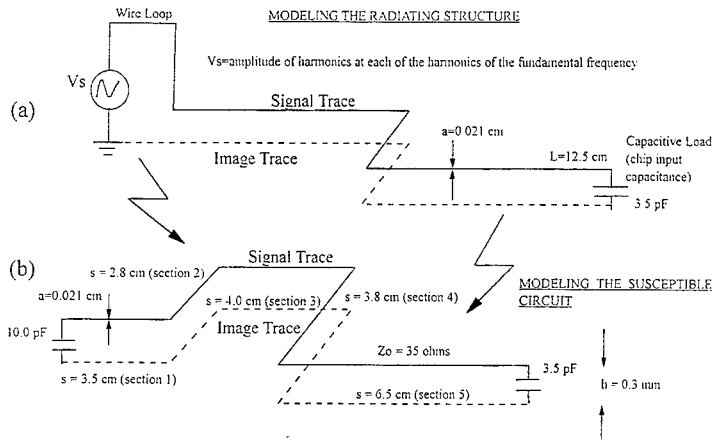

FIGURE 6. (a) METHOD OF MOMENTS MODELING OF RADIATING STRUCTURE.
(b) FIELD-TO-LINE COUPLING ON SUSCEPTIBLE CIRCUIT .

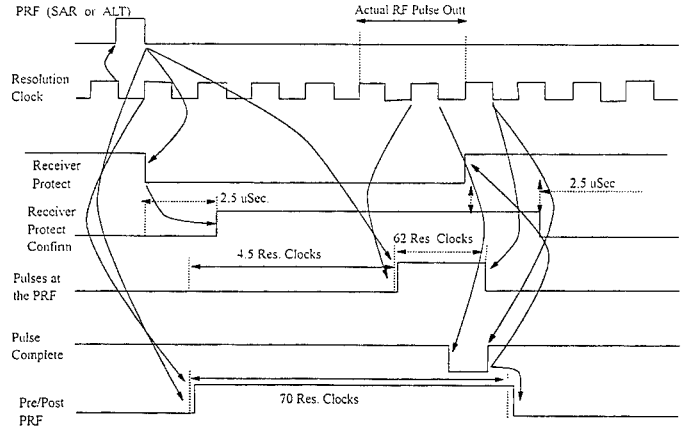

FIGURE 7. PULSE TRANSMISSION TIMELINE WHEN RECEIVER PROTECT CIRCUIT IS WORKING PROPERLY.

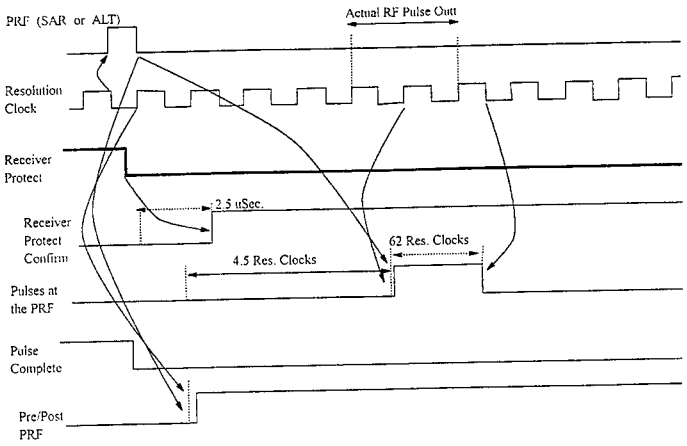

FIGURE 8. PULSE TRANSMISSION TIMELINE WHEN RECEIVER PROTECT CIRCUIT IS NOT WORKING PROPERLY DUE TO INTERFERENCE. THE **RECEIVER PROTECT** SIGNAL ABOVE IS SET AT THE WRONG TIME .

Finite-Difference Time-Domain Analysis of Common Mode Cable Currents

Cheung-Wei Lam
Quad Design Technology, Inc.
1385 Del Norte Road
Camarillo, California 93010
Phone: (805) 988-8250
Fax: (805) 988-8259
E-mail: lam@qdt.com

I. ABSTRACT

In this paper, the Finite-Difference Time-Domain (FDTD) method is used to calculate common mode cable currents in simplified system structures. The FDTD results correlate very well with measurements on a canonical structure. The effects of using ferrites to reduce cable currents are investigated.

II. INTRODUCTION

Electromagnetic interference (EMI) from electronic equipments has become an issue of greater concern as clock speeds and edge rates continue to go up in today's digital designs. Numerical modeling and simulation of EMI not only help us better understand the problem itself and the effects of different configuration parameters, but also allow early prediction and prevention of potential EMI problems. Common mode cable currents have been shown experimentally in many recent publications to be the major contributor to system EMI [1,2]. Calculation of radiation from common mode cable currents is quite straightforward and will not be discussed here. The challenges in modeling system EMI include the identification of the common mode coupling mechanism and the prediction of the induced cable currents. This paper is focused on the latter issue. The Finite-Difference Time-Domain (FDTD) method [3-5] is used in the analysis of typical system structures with attached cables.

Full-wave analysis is necessary in modeling common mode cable currents in such structures. Other than the FDTD method, the Finite Element method (FE) and the Method of Moment (MoM) have also been widely used in numerical studies of radiation problems. We believe the FDTD method is more efficient than the other two methods in modeling system EMI problems, in which a broad spectrum is of interest. Being a time domain approach, the pulse based FDTD method can generate results over a wide frequency range from one single simulation. The availability of FDTD models for thin wires [6,7], small holes and slots, thin dielectric sheets, and etc. alleviates the need of meshing down to the dimensions of small structures as required by the FE method.

Section III discusses the application the FDTD method in analyzing simplified system structures with attached cables. In Section IV, a canonical structure [8] proposed for modeling small table-top products is analyzed. The FDTD results are compared with measurements and other published simulation results [9]. In Section V, the effects of ferrites in reducing common mode currents on cables are investigated. Section VI concludes this paper.

III. THE FDTD METHOD

In the FDTD method [3-5], the problem space is discretized over a finite 3-D computational domain with both space and time derivatives in Maxwell's equations approximated by a second-order accurate centered difference scheme. E and H are calculated at alternate half time steps and at different positions according to Yee's grid model [3]. The FDTD equations in free space are:

$$H^{n+\frac{1}{2}} = H^{n-\frac{1}{2}} - \frac{\Delta t}{\mu_0}\nabla\times E^n \tag{1}$$

$$E^{n+1} = E^n + \frac{\Delta t}{\varepsilon_0}\nabla\times H^{n+\frac{1}{2}} \tag{2}$$

In the application of the FDTD method the size of a unit cell is first chosen to be smaller than the smallest dimension of the structure and a fraction of the shortest wavelength of interest. Then the time step is chosen to satisfy Courant stability criterion:

$$\Delta t < \frac{1}{c\sqrt{\left(\frac{1}{\Delta x}\right)^2 + \left(\frac{1}{\Delta y}\right)^2 + \left(\frac{1}{\Delta z}\right)^2}} \tag{3}$$

The second order Mur's absorbing boundary conditions [10] are used to truncate the computation domain. The domain size is chosen such that the open boundary is at least 2 times the longest dimension of the structure away from it. This is to make sure that the near field region corresponding to the first resonance is contained within the computation domain.

To avoid meshing down to the typically small cable cross section, the thin wire model discussed in [6,7] is used to model cables. The backward Euler formulation is adopted in modeling lump source and load in an FDTD cell. A modulated Gaussian pulse which cover the frequency range of interest is used as the source.

IV. Analysis of a Canonical Structure

The two structures with attached cables shown in Fig. 1 were proposed in [8] to model radiation from small table-top products. Figs. 1(a) & 1(b) show the straight wire and the bent wire configurations, respectively. Other than the thin wire above the thin plate, the two configurations share the same dimensions as labeled in Fig. 1(b). The wires above and below the thin plate have diameters of 0.2 cm and 0.4 cm, respectively. The thickness of the thin plate, 0.3 cm, is small enough to be neglected. In the original configuration [8], the bottom wire is the shield of a 50 Ω coaxial cable, which is driven by a 50 Ω matched voltage source at the base. In our FDTD modeling, since the phase relationship between the cable current and the voltage source is not of interest, we can model the excitation by an equivalent 50 Ω voltage source between the top wire and the thin plate as indicated in Fig. 1(a). The FDTD cell sizes for (a) and (b) are 42 x 49 x 40 mm and 45 x 49 x 23 mm, respectively. The computational domain for (a) and (b) are 132 x 108 x 92 cells and 100 x 88 x 131 cells, respectively. In all our FDTD simulations, the time step is chosen to be 0.99 of the Courant stability limit.

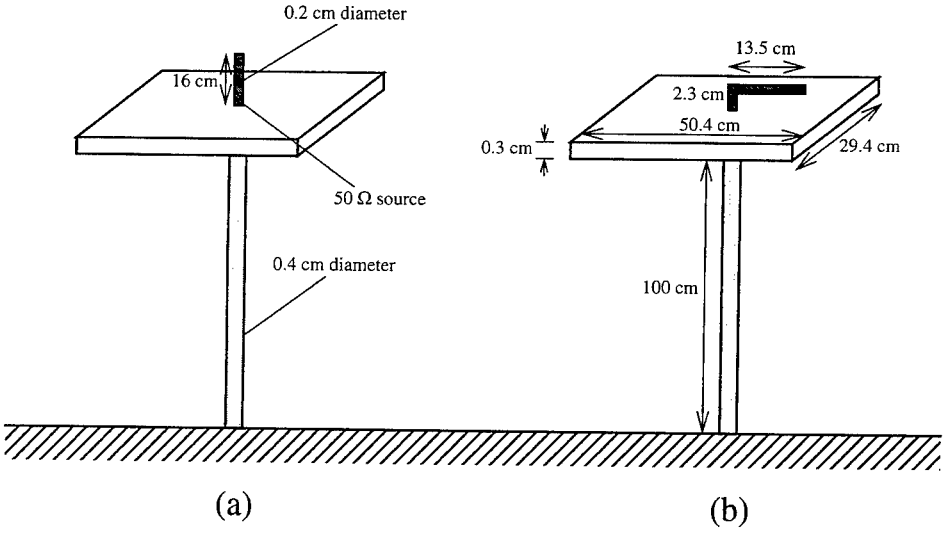

FIGURE 1. (a) The straight wire structure. (b) The bent wire structure.

In Figs. 2(a) & 2(b), the FDTD simulated cable currents at the base are compared with measured results [8] and the Method of Moment (MoM) results [9]. It is interesting to see that FDTD and MoM predict the same resonant frequencies in both cases, while the measured resonances occur at slightly higher frequencies. As explained in [9], the difference is probably due to some proximity effect associated with the measurement or the surrounding environment of the physical structure. In both cases, the FDTD simulated resonance magnitudes are very close to the measured values, while the MoM results are about 5 dB lower.

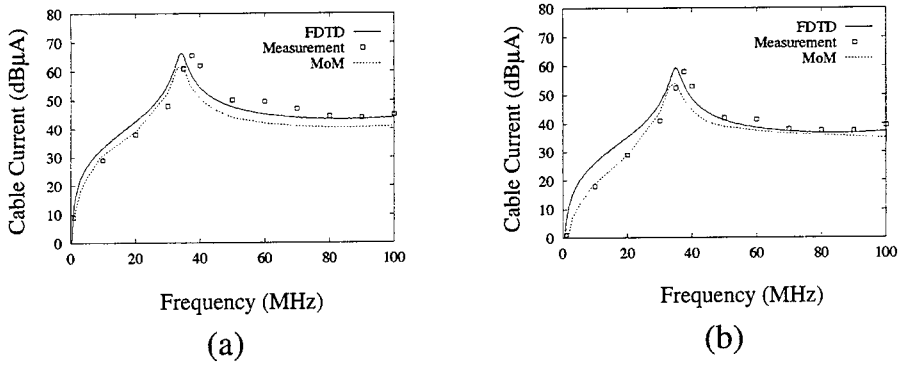

FIGURE 2. Simulated and measured results of the cable current normalized with the source voltage: (a) the straight wire structure, (b) the bent wire structure.

V. USE OF FERRITES

In this section, a similar structure with the cable attached to the edge of the thin plate as shown in Fig. 3 is analyzed. The thin plate represents the ground plane of a printed circuit board. The common mode cable current is driven by a noise voltage at the connection which may correspond to the connector ground drop due to its partial inductance. The FDTD cell size is 40 x 40 x 40 mm, and the computational domain is 112 x 108 x 75 cells.

Fig. 4 shows the input impedance of the cable structure from DC to 1 GHz. This plot reveals the resonant frequencies around which common mode radiation from the cable may cause problems and shows the input impedance values at those resonances. This information can help designers in choosing the right ferrite to suppress the common mode current.

Figs. 5(a) & 5(b) show the normalized cable currents from DC to 200 MHz covering the first two resonances. Fig. 5(a) shows the effect with Ferrite 1 added, while Fig. 5(b) shows the effect with Ferrite 2 added. Ferrite 1 and 2 correspond to Ferrite A and B in Fig. 5 of [11], respectively. As discussed in

[11], typical ferrites can be modeled well by an equivalent RLC circuit. In the equivalent circuit of Ferrite 1, R = 90 Ω, L = 4.6 μH, and C = 22 pF. In the equivalent circuit of Ferrite 2, R = 129Ω, L = 0.82 μH, and C = 0.86 pF. It is observed that both Ferrite 1 and 2 reduce the current at the first resonance by about 12 dB. At the second resonance, Ferrite 2 is shown to be much more effective than Ferrite 1. The difference between their performance can be easily predicted by simply looking at the input impedance of the structure and the ferrite impedance shown in Fig. 6. The ferrite basically increase the input impedance of the structure, which results in reduction of common mode currents. For structures with high input impedance at resonance, the use of ferrite may not be effective at all. It is interesting to see that Ferrite 1 and Ferrite 2 cause a shift in the second and the first resonance, respectively. This is due to the large variation of the ferrite impedance $Z'(f)$ at those resonance frequencies. This effect is sometimes desirable if it shifts the resonance away from major clock harmonics.

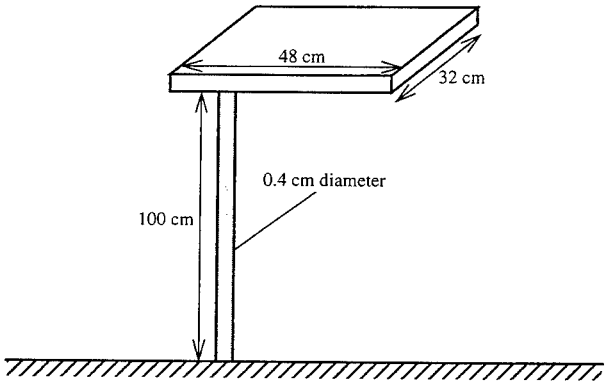

FIGURE 3. A thin plate with a cable attached to its edge.

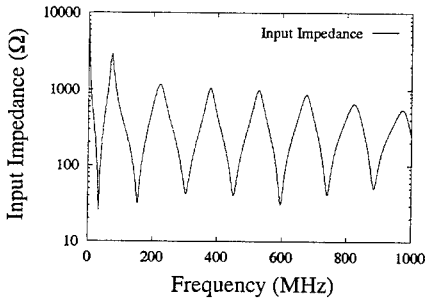

FIGURE 4. Input impedance of the structure.

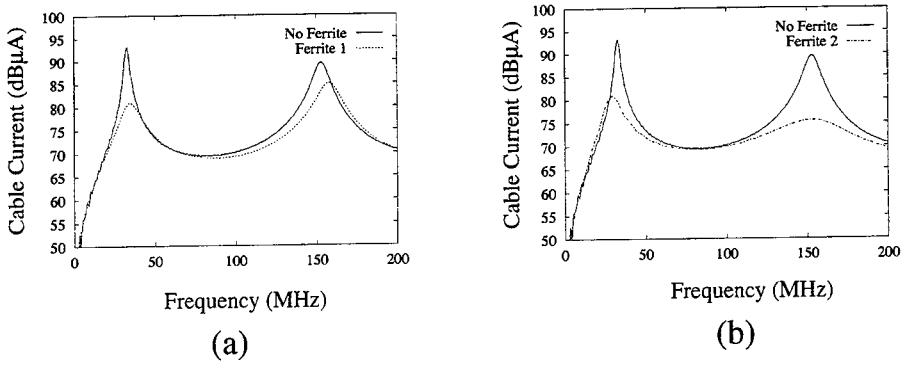

FIGURE 5. Normalized cable current with and without ferrite: (a) Ferrite 1, (b) Ferrite 2.

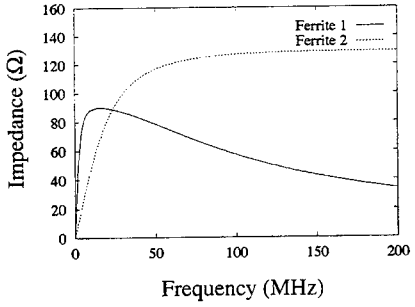

FIGURE 6. Impedance magnitude of Ferrite 1 and 2.

VI. CONCLUSIONS

In this paper, the FDTD method is used to analyze common mode cable currents in simplified system structures. The FDTD results correlate very well with measured results for a canonical structure. The effect of using ferrites on a similar cable structure is investigated. The input impedance obtained from the FDTD results can help designers in choosing the right ferrite to suppress common mode currents. It is shown that the addition of ferrite not only reduces the cable current at resonance, but may also cause a resonance shift due to large ferrite impedance variation around the resonant frequency.

REFERENCES

[1] J. L. Drewniak, F. Sha, T. P. Van Doren, and T. H. Hubing, "Diagnosing and modeling common-mode radiation from printed circuit boards with attached cables," *1995 IEEE Electromagnetic Compatibility Symposium Proceedings*, Atlanta, GA, pp. 465-470, 1995.

[2] J. L. Drewniak, T. H. Hubing, and T. P. Van Doren, "Investigation of fundamental mechanisms of common-mode radiation from printed circuit boards with attached cables," *1994 IEEE Electromagnetic Compatibility Symposium Proceedings*, Chicago, IL, pp. 110-115, 1994.

[3] K. S. Yee, "Numerical solution of initial boundary value problems involving Maxwell's equations in isotropic media," *IEEE Trans. Antennas Propagat.*, vol. AP-14, pp. 302-307, May 1966.

[4] A. Taflove, *Computational Electrodynamics: The Finite-Difference Time-Domain Method.* Norwood: Artech House, 1995.

[5] K. S. Kunz and R. J. Luebbers, *The Finite Difference Time Domain Method for Electromagnetics.* Boca Raton: CRC Press, 1993.

[6] D. M. Hockanson, J. L. Drewniak, T. H. Hubing, and T. P. Van Doren, "FDTD modeling of thin wires for simulating common-mode radiation from structures with attached cables," *1995 IEEE Electromagnetic Compatibility Symposium Proceedings*, Atlanta, GA, pp. 168-173, 1995.

[7] A. Taflove and K. Umashankar, "The finite-difference time-domain method fro numerical modeling of electromagnetic wave interactions," *Electromagnetics*, vol. 10, pp. 105-126, 1990.

[8] T. H. Hubing, "Calculating the currents induced on wires attached to opposite sides of a thin plate," *The ACES Collection of Canonical Problems*, Set 1, pp. 9-13, Applied Computational Electromagnetic Society, Spring 1990.

[9] S. Daijavad and B. J. Rubin, "Detailed analysis of a canonical structure in electromagnetic radiation problems," *IEEE Trans. Electromagn. Compat.*, vol. EMC-35, pp. 231-234, May 1993.

[10] G. Mur, "Absorbing boundary conditions for the finite difference approximation of the time domain electromagnetic field equations," *IEEE Trans. Electromagn. Compat.*, vol. EMC-23, pp. 377-382, Nov. 1981.

[11] B. Rall, "New methods in modeling EMC ferrites," *ITEM Update*, pp. 35-39, 1995.

STATISTICAL COUPLING OF EM FIELDS TO CABLES IN AN OVERMODED CAVITY

Richard Holland, Shield Rite, Inc., Box 8250, Albuquerque, NM 87198, 505-842-6018
Richard St. John, Mission Research Corp., 1720 Randolph Rd., Albuquerque, NM 87106, 505-768-7655

ABSTRACT

This paper describes the statistics of EM fields and power fluxes inside a highly overmoded cavity. It explores various combinations of normal, log normal, and chi square (with two and six degrees of freedom) distributions. Logarithmic convolution of the two chi square models provides the best match with observation. Field models are input as drivers to cable codes representing wiring in an aircraft shell. Resulting cable current distributions match observed results within a factor of two, which is commensurate with the experimental uncertainty.

INTRODUCTION

The current response of cables in a complicated, highly overmoded chamber is not a problem which is tractable by deterministic solution of Maxwell's equations.

Our approach, which is probably the only feasible one, is first to characterize the statistical distribution of electromagnetic fields or power flux in the chamber.[1-4] This distribution, in general, may have frequency or position as the independent variable. Depending on the nature of the enclosure (frequency-dependent Q, degree of homogeneity, etc.) the electromagnetic fields have a zero-bias normal distribution, a bipolar log-normal distribution, some mix of the two, or some, as yet unevaluated, distribution with the property that the associated power-flux distribution $f(z)$ looks like a modified Bessel function of the second kind

$$f(z) = \Lambda^2 z\, K_2(2\sqrt{\Lambda z}) \qquad \Lambda = 3/\text{mean}[z] = 3/\mu \tag{1}$$

A normal field distribution leads to a chi square (with two degrees of freedom) power-flux distribution. A bipolar log-normal field distribution leads, at least approximately, to a monopolar log-normal power-flux distribution. (This is a novel and unpublished statement.) Formulas relating the field distribution parameters to the power flux distribution parameters prove to be quite simple for the normal, log-normal, and mixed distributions (see below). This may also prove to be true for the modified Bessel distribution, although we have not yet been clever enough to work through the requisite modified Bessel function algebra.

Our goal, then, becomes one of modeling the cavity field or power flux distribution from measured samples. These fields are then applied as drivers to a model of the chamber cables. Lastly, the resulting cable currents on the model are compared in statistical distribution to measured cable currents. When the driven cable model yields currents with a distribution in good agreement with the measured cable current distribution, we consider the simulation to be performing well.

This work was supported by the Air Force Phillips Laboratory under contract F29601-95-C-0045.

COMPARISON OF THEORY AND EMPTAC-BASED DATA

A typical case to which we have applied this technique is the Air Force Phillips Laboratory EMPTAC 720 shell externally illuminated by the ellipticus antenna and swept from 10^8 Hz to 10^9 Hz. The magnetic field squared observed axially in this configuration (Run B050MBHZ) essentially has a monopolar log-normal distribution with a mean μ of 7.86e-8 $(A/m)^2$ and a standard deviation σ of 1.28e-7 $(A/m)^2$. These values correspond to a field whose amplitude has a standard deviation of 1.7e-4 (A/m). This last value was used to generate a chi-square-model driving field ensemble which, after appropriate manipulations to restore bipolarity, has a square with a mean μ of 5.02e-8 $(A/m)^2$ and a standard deviation σ of 1.08e-7 $(A/m)^2$. Applying fields thusly characterized to the model of the cable network resulted (Run B0oc2002.3, Fig. 1) in cable currents squared with a mean of 3.27e-8 A^2 and standard deviation of 10.62e-8 A^2. On the other hand, measured EMPTAC cable currents (Run B032211Y, Fig. 2), when squared, had a mean of 2.65e-8 A^2, and a standard deviation of 5.91e-8 A^2. This result is typical of 20 or so tests we have made, and indicates model fidelity well within a factor of 2. (This factor, in turn, is probably a fair guess at the repeatability or uncertainty in the measurements--both of cavity fields and of cavity cable currents; see Fig. 3.)

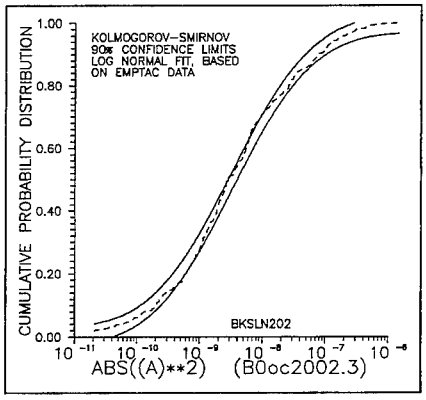

Fig. 1. Model-based cumulative distribution of the squared currents on the EMPTAC cables (with 90% Kolmogorov-Smirnov confidence limits for being log normal).

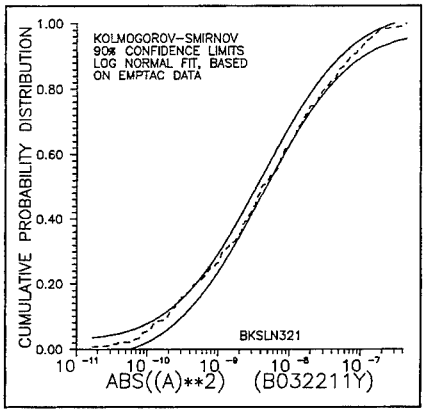

Fig. 2. Measured cumulative distribution of the squared currents on the EMPTAC cables (with 90% Kolmogorov-Smirnov confidence limits for being log normal).

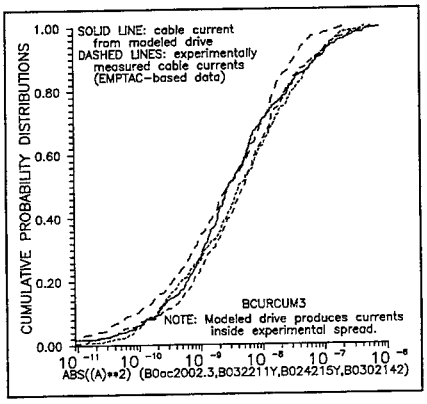

Fig. 3. The model squared cable current distribution (solid line) does not stray outside the bounds provided by an overlay of three squared cable current distributions (various dashed lines) which were obtained under slightly varied measurement conditions.

FORMULAS RELATING POWER-FLUX DISTRIBUTION AND FIELD DISTRIBUTION: NORMAL AND LOG-NORMAL CASES

We shall discuss primarily the mixed normal/log-normal field quadrature distribution here, as this case encompasses the pure normal and pure log-normal cases by implication. Essentially there are three types of quantities for which we require distribution definitions. The first are bipolar phase quadrature field components such as $H_z \sin \phi$ or $H_z \cos \phi$, which we shall generically denote as u or v. The second are phase quadrature field components squared, which we shall generically denote as x or y. Thirdly, we have power fluxes which we shall denote as z, and which are the sum of two squares

$$z = x + y = u^2 + v^2 \tag{2}$$

Conventional wisdom has been that z should have a chi square distribution with two degrees of freedom under ideal conditions. In reality, we find it usually is more nearly log-normal in distribution. The pure log-normal distribution density function $f(z)$ is

$$f(z) = \frac{1}{\sqrt{2\pi}} \frac{\exp\left(-(\ln z - \tau_o)^2/(2\sigma^2)\right)}{z\sigma} \tag{3}$$

and the cumulative probability distribution $F(Z)$ is

$$F(Z) = \int_{-\infty}^{\frac{\ln Z - \tau_o}{\sigma}} \frac{1}{\sqrt{2\pi}} \exp(-w^2/2)\, dw = \Phi\left(\frac{\ln Z - \tau_o}{\sigma}\right) \tag{4}$$

where $\Phi(\ )$ is the cumulative normal distribution function. Thus, if Z is selected to be greater than fraction $F(Z) = p$ of the values, we would have

$$Z(p) = e^{\tau_o + \sigma\Phi^{-1}(p)} \tag{5}$$

where $\Phi^{-1}(\ )$ is the inverse of the cumulative normal distribution function. This formula tends to generate a distribution with an upper tail having unrealistically large values of Z.

This problem is resolved by mandating that, above some cross-over probability P, the distribution density of z shall be chi-square with two degrees of freedom,

$$f_2(z) = \frac{e^{-z/\nu}}{\nu} \tag{6}$$

giving a cumulative probability distribution of

$$F_2(Z) = 1 - e^{-Z/\nu} \tag{7}$$

For $F_2(Z) = p$ above P, we thus have

$$Z(p) = -\nu \ln(1 - p) \tag{8}$$

In general, τ_o and σ will be known and P can be guessed at. Also, (5) and (8) must match at P. This gives us an equation uniquely determining ν

$$\nu = \frac{e^{\tau_o + \sigma\Phi^{-1}(P)}}{-\ln(1 - P)} \tag{9}$$

Figure 4 shows $F(Z)$ and $F_2(Z)$ joined at $P = .9$, with the cumulative distribution of EMPTAC data set B050MBHZ overlaid. For this data set, with $P = .9$ we found (9) to give $\nu = 7.62E\text{-}8$.

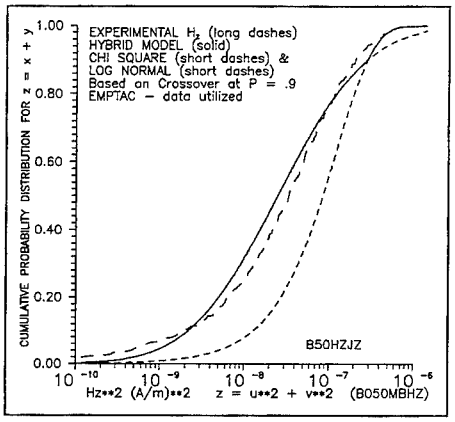

Figure 4. Hybrid log-normal/chi-square distribution (solid line), with measured $|H_z|^2$ from Run B050MBHZ overlaid (line in long dashes). Crossover occurs at $P = .9$.

Distribution of the Squares

In general, the distribution of $x = u^2$ is not very interesting, although we cannot go from the distribution of z to the distribution of u (which is needed) without, in the process, finding $g(x)$, the distribution of x. If z has a distribution $f(z)$, one can show that x and y have a distribution $g(x)$, which, upon being autoconvolved, gives back $f(z)$. In other words, one can obtain $g(x)$ by Fourier transforming $f(z)$, taking the square root of the transform, and inverse transforming the square root.

Although we cannot prove it, numerical tests based on the autoconvolution procedure have convinced us that the distribution of x must be log-normal if z is log normal. Thus, for $p \leq P$ we have

$$g(x) = \frac{1}{\sqrt{2\pi}} \frac{\exp\left(-(\ln x - \tau_o')^2/(2\sigma'^2)\right)}{x\sigma'} \tag{10}$$

and the cumulative probability distribution of x, $G(X)$,

$$G(X) = \Phi\left(\frac{\ln X - \tau_o'}{\sigma'}\right) \tag{11}$$

To a fairly good approximation we have empirically found that (τ_o', σ') are related to (τ_o, σ) by

$$\begin{aligned} \tau_o' &= \tau_o - 1. - 0.5(\sigma - 1.) \\ \sigma'^2 &= -.1 + .2\sigma + 1.8\sigma^2 \end{aligned} \tag{12}$$

For the region $(p > P)$ where z has a chi square distribution, the transform of $f_2(z)$ and the inverse transform of the square root can be taken canonically. This manipulation yields a distribution density for x

$$g_2(x) = \frac{e^{-x/v}}{\sqrt{\pi x v}} \tag{13}$$

and a cumulative distribution function $G_2(X)$ of

$$G_2(X) = 2\,\Phi(\sqrt{2X/v}\,) - 1 \tag{14}$$

at least for p and $G_2(X) \geq \frac{1}{2}$. If X is selected to be greater than $G(X) = p$ of the values, we have, for $p \leq P$

$$X(p) = e^{\tau_o' + \sigma' \Phi^{-1}(p)} \tag{15}$$

and for $p \geq P$

$$X(p) = \frac{\nu}{2}\left((\Phi^{-1}((p+1)/2)\right)^2 \tag{16}$$

If Eqs. (12) were exact, (15) and (16) would meet at $p = P$. In actuality, they will differ slightly

$$R\, e^{\tau_o' + \sigma' \Phi^{-1}(P)} = \frac{\nu}{2}\Phi^{-1}\left((P+1)/2\right) \tag{17}$$

where $R \approx 1$ and $\ln R \approx 0$. This slight mismatch maybe incorporated into the model by replacing τ_o' with $\tau_o' + \ln R$, which is alright as (12) for τ_o' is only an approximate fit anyway.

Figure 5 shows $G(X)$ and $G_2(X)$ joined at $P = .9$.

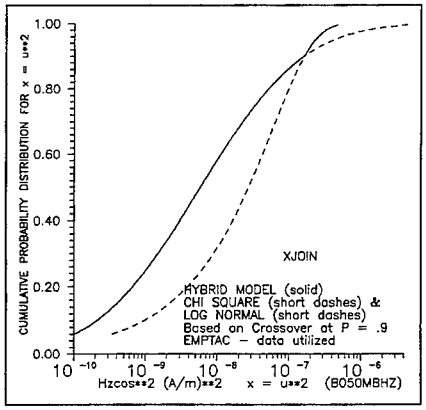

Figure 5. The cumulative probability distribution obtained by joining the log normal, $G(x)$ of (11), and the chi square, $G_2(x)$ of (14), at $P = .9$.

Distribution of the Bipolar Phase Quadrature Components

If $x = u^2$ has a monopolar log-normal distribution density $g(x)$ given by (10), u will have a bipolar log-normal distribution density $s(u)$ given by

$$s(u) = \frac{1}{\sqrt{2\pi}} \frac{\exp\left(-(2 \ln |u| - \tau_o')^2/(2\sigma'^2)\right)}{\sigma' |u|} \tag{18}$$

and a cumulative probability distribution

$$S(U) = \tfrac{1}{2} + \tfrac{1}{2}\Phi\left(\frac{2\ln U - \tau_o'}{\sigma'}\right) \tag{19}$$

at least for $U > 0$ or $S(U) > \tfrac{1}{2}$. Thus, if U is selected to be greater than the fraction $S(U) = p$ of the values, we have, for $p < P'$,

$$U(p) = e^{(\tau_o' + \sigma'\Phi^{-1}(2p - 1))/2} \tag{20}$$

at least for $p = S(U) > \tfrac{1}{2}$ or $U > 0$. We must here note that P', the u crossover probability, introduced just above differs from P, the crossover probability of x and z. If we want x and z to crossover at $P = .90$, u must crossover at $P' = .05$ and .95, as u is bipolar, while x and z were monopolar.

For the regions $p > .95 = P'$ or $p < .05$, where z has a chi square distribution density, u has a normal distribution,

$$s_2(u) = \frac{1}{\sqrt{2\pi}} \frac{e^{-u^2/(2\sigma_g)}}{\sigma_g} \tag{21}$$

or

$$S_2(U) = \Phi(U/\sigma_g) \tag{22}$$

where σ_g is related to ν by

$$\nu = 2\sigma_g^2 \tag{23}$$

If U is selected to be greater than $S_2(U) = p$ of the values, we have for $p \geq P'$ or $p \leq 1 - P'$

$$U(p) = \sigma_g \Phi^{-1}(p) \tag{24}$$

At $p = P'$, (20) and (24) for $U(P')$ might not match perfectly:

$$\rho e^{(\tau_o' + \sigma'\Phi^{-1}(2P' - 1))/2} = \sigma_g \Phi^{-1}(P') \tag{25}$$

where $\rho \approx 1$. This situation permits two varieties of correction: σ_g is related to ν, which (through (9)) is not a very precisely defined quantity, and may be replaced by σ_g/ρ. Alternatively, τ_o', which also is not very precise, may be replaced by $\tau_o' + 2 \ln \rho$.

We do not know if $2 \ln \rho = \ln R$, nor does this seem a very important issue, as both are *ad hoc* corrections to heuristic factors.

Figure 6 shows $S(X)$ and $S_2(X)$ joined at $P' = .95$.

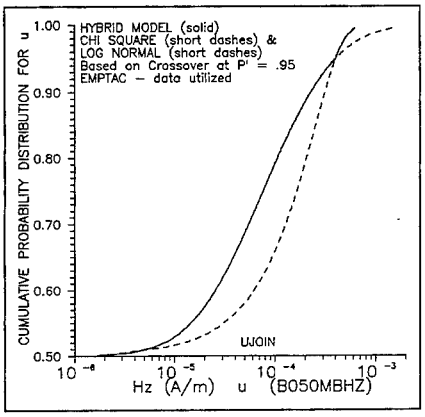

Figure 6. The cumulative probability distribution obtained by joining the log normal, $S(u)$ of (19), and the chi square, $S_2(u)$ of (22), at $P' = .95$.

APPLICATION OF THE HYBRID POWER-FLUX DISTRIBUTION TO CELESTRON 8 SATELLITE TELESCOPE DATA

A hybrid normal/log-normal fit to the cumulative distribution of the magnetic field squared was also attempted for the Celestron 8 satellite telescope data for frequency swept from 8 GHz to 18 GHz. In this case, it turns out that a hybrid fit is better made with crossover at $p = .875$. Figure 7 shows $F(Z)$ and $F_2(Z)$ joined at $P = .875$, with the cumulative distribution of the Celestron 8 data set overlaid. For this data set, with $P = .875$ we found (9) to give $\nu = 2.104$.

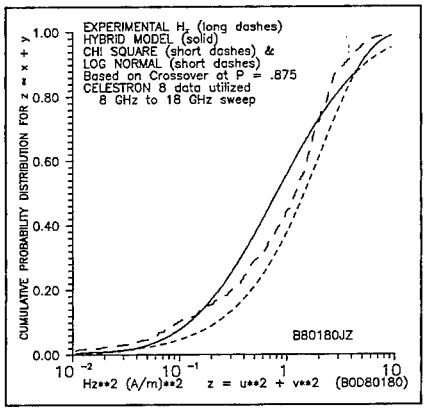

Figure 7. Hybrid log-normal/chi-square distribution (solid line), with measured $|H_z|^2$ from Celestron 8 8 GHz to 18 Ghz sweep overlaid (line in long dashes). Crossover occurs at $P = .875$. This hybrid fit to the data is not so good as the EMPTAC data fit appearing in Fig. 4.

THE LEHMAN DISTRIBUTION

Work has recently come to our attention which deduces a somewhat different overmoded enclosure power-flux distribution that the simple chi square result.[4] This new result shows excellent agreement between theory and observation on the upper tail of the distribution, which is where harmful effects will occur if they occur at all. While we are not sure just why this novel procedure should yield power-flux distributions which agree with the upper tail (as opposed to the midpoint, where most models seem to work best, or, for that matter, as opposed to the lower tail), we are most impressed with the result.

This work concurs that the internal cavity response should incorporate the physics which leads to a power-flux distribution z_1 which is chi square with two degrees of freedom. However, a hypothesis is additionally put forward that the field external to the cavity can come from any of three directions, and thus should result in inward power leakage z_2 being chi square with six degrees of freedom. These assumptions imply the overall internal cavity response should have a power-flux distribution density which is the product of these two variables

$$z = z_1 z_2 \tag{26}$$

In two dimensions, the power flux distribution density thus becomes representable as

$$f_{\chi_2^2}(z_1) f_{\chi_6^2}(z_2)\, dz_1\, dz_2 \tag{27}$$

where this expression gives the probability that z_1 is between z_1 and $z_1 + dz_1$, while z_2 is between z_2 and $z_2 + dz_2$. However, z, z_1, and z_2 are not all independent variables. If (26) holds, the probability that z_1 is between z_1 and $z_1 + dz_1$, while z is between z and $z + dz$ is obtained from the variable transformation

$$\begin{aligned} z_1 &= z_1' \\ z_2 &= z'/z_1' \end{aligned} \tag{28}$$

The two-dimensional distribution density then becomes

$$f_{\chi_2^2}(z_1') f_{\chi_6^2}(z'/z_1') \frac{\partial(z_1, z_2)}{\partial(z_1', z')}\, dz_1'\, dz' \tag{29}$$

where

$$\frac{\partial(z_1, z_2)}{\partial(z_1', z')} = \begin{vmatrix} \partial z_1/\partial z_1' & \partial z_2/\partial z_1' \\ \partial z_1/\partial z' & \partial z_2/\partial z' \end{vmatrix} = \begin{vmatrix} 1 & -1/z_1'^2 \\ 0 & 1/z_1' \end{vmatrix} = 1/z_1' \tag{30}$$

is the Jacobian of the variable transformation. We now wish to find the probability that z is between z and $z + dz$ regardless of z_1'. This 1D probability differential is obtained by summing

all the 2D probability differentials of z_1' and z' over z_1' ; i.e., by integrating (29) over all possible z_1'

$$f(z')dz' = \int_0^\infty f_{\chi_2^2}(z_1')f_{\chi_6^2}(z'/z_1')\ \frac{dz_1'\,dz'}{z_1'} = \int_0^\infty [\lambda e^{-\lambda z_1'}]\,[\lambda^3(z'/z_1')^2 e^{-\gamma z'/z_1'}]\frac{dz_1'\,dz'}{z_1'} \qquad (31)$$
$$= \Lambda^2 z' K_2(2\sqrt{\Lambda z'})\,dz'$$

Here, λ, γ, and Λ are constants related by

$$\Lambda = \gamma\lambda \qquad (32)$$

with Λ related to the mean power-flux density by (1).

Figure 8 illustrates the cumulative probability distribution agreement between the Lehman distribution and EMPTAC data, while Figure 9 illustrates the agreement for the Celestron 8. We do not know, at this time, if the Lehman distribution would apply to the situation where the microwave source is actually internal to the cavity, as in the JAYCOR study.[3] Also, we do not know if the power fluxes external to an open geometry (such as a helicopter) could be characterized simply as a chi square distribution with six degrees of freedom. It seems that this model somehow manages to ignore the "trend" on power-flux data, and give a correct upper-tail representation irrespective of the gross overall shape of the response distribution. This accomplishment is a major keystone in the successful representation of cable-driving fields; previously, we had no real idea how to insert "trend" effects into the model (other than using a log normal representation). The Lehman model, as represented in Figures 8 and 9, provides something that Figures 4 and 7 do not: a smooth, data-derived representation for the upper end of the distribution which does not require case-by-case tweaking.

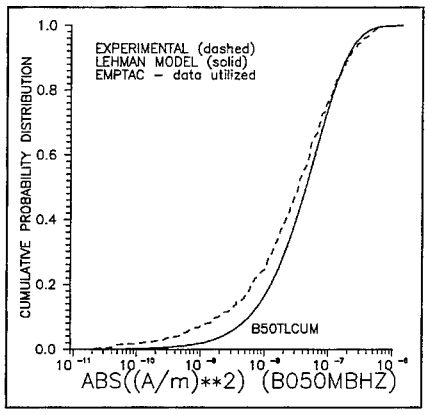

Figure 8. Lehman distribution compared with EMPTAC data. Note the remarkable upper end match. The Lehman distribution is based on Λ = 3.814e+7 $(A/m)^{-2}$.

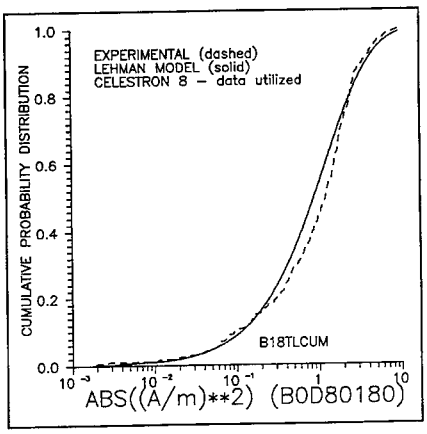

Figure 9. Lehman distribution compared with Celestron 8 data. Note the remarkable upper end match. The Lehman distribution is based on $\Lambda = 1.951\ (A/m)^{-2}$.

We should point out, however, that we have not yet discovered how to back the phase-quadrature field-component distributions out of the Lehman distribution for the power flux. Taking the inverse transform of the square root of the Fourier transform of $f(z)$ in (1) or (31), either numerically or canonically, seems formidable. Also, it may occur that we are unable to guess what function, when autoconvolved, gives back $f(z)$ of (1) or (31).

CONCLUSIONS

EM power flux inside an overmoded cavity can be statistically represented by a log-normal distribution or by a logarithmic convolution of a chi square distribution with two degrees of freedom upon a chi square distribution with six degrees of freedom. Deducing the distribution of electromagnetic fields within the cavity, given the distribution of power flux is not a trivial procedure, however. At present, we can perform the deduction for the log-normal, but not for the convolved chi square model. It is, however, necessary to have the statistical field distribution to model the fields which actually couple to and drive the enclosure cabling. Log-normal modeling of the power-flux distribution leads to a field distribution model which is also log normal. This procedure for deducing the cable-drive field distribution yields predicted cable currents with distributions which lie well within experimental uncertainty and repeatability (i.e., well within a factor of two).

REFERENCES

1. R. Holland & R. St. John, *10th ACES Conference Proceedings*, Vol. I, p. 554-568, 1994.
2. R. Holland & R. St. John, *11th ACES Conference Proceedings*, Vol. I, p. 308-320, 1995.
3. R. Price, H.T. Davis, & E.P. Wenaas, *Phys. Rev. E*, Vol.48, p. 4716-4729, 1993.
4. T. H. Lehman and R. M. Marshall, "Application of Statistical Physics to Derivation of Stress and Strength Distributions," 26 September 1991, unpublished.

Power and Ground Plane Modeling and Decoupling in High Speed Printed Circuit Board and Multichip Modules

Frank Y. Yuan, Cheung-Wei Lam, and Lawrence M. Rubin
Quad Design Technology, Inc.
1385 Del Norte Road
Camarillo, California

I. INTRODUCTION

This paper presents the modeling and analysis of power and ground plane effects in printed circuit board (PCB) and multichip module (MCM) circuits. Ground noises has been a major source to radiation EMI problems as well as a significant factor in signal integrity of high speed digital systems [1-6]. For the sub-nanosecond rise/fall times and over 100 MHz clock rates used in today's digital designs, the signal bandwidth ranges up to 1 to 5 GHz and beyond the first few resonant frequencies of most PCB/MCM power/ground substrates. Simple lumped element models used by digital circuit designers can no longer accurately capture the distributed ground effects. Full-wave rigorous electromagnetic field solutions [7-8], however, become impractical for complex digital circuit simulation due to the extremely high computational requirement. It is also difficult to be integrated with the time-domain circuit type of simulations used in most digital designs as well as to be understood and utilized easily by digital circuit designers.

Recently, an efficient modeling approach is developed by the author which extracts an equivalent circuit model from rigorous integral equation solution for the power/ground plane structures [6]. First, the electromagnetic field problem is analyzed by mixed potential integral equation method along with a boundary element algorithm where scalar potential is explicitly retained. The solution under specified boundary conditions of either fixed port voltages or injected currents gives rise to a frequency domain multiport network representation of the system. To avoid repeated solution at every single frequency and thus reduce the required computational time, a special quasi-static approximation is introduced to simplify the complex frequency dependance of the system, while retaining the important AC characteristics. Through a node reduction and decomposition scheme, an equivalent circuit model of the system is constructed with frequency independent R, L, C circuit elements. The equivalent circuit model gives accurate high frequency characteristics of the system up to certain frequency limit well above most digital signal bandwidth, as demonstrated by examples and comparison with measurements and full-wave solutions. It can be used as a macromodel for the power/ground planes either alone for ground effect simulation, or be combined with an external network such as a signal circuit for system simulation, and can be easily integrated with general purpose circuit simulators such as SPICE and other CAD simulation tools.

As an alternative approach as well as a verification method, a two-dimensional FDTD modeling of power/ground planes is also developed. The 2-D FDTD method is very efficient and simple in implementation. It gives direct time domain results in voltage or current wave forms. In our implementation,

parallel planes are modeled as 2-D structures with TEM wave propagation. This is equivalent to a two dimensional R, L, C mesh circuit. Simple drivers/receivers and R,L,C elements can be attached to any grid points between the planes. Simulation results show that the FDTD method corresponds very well with the equivalent circuit approach.

Simulation results for several typical and practical examples are discussed in comparison with available experimental measurements and well known results. Ground noise figures and the decoupling effect are analyzed by examining transient waveforms across power/ground planes with various source/load conditions, and with or without decoupling capacitors.

II. Integral Equation Modeling and Solution

The general interconnects and power/ground substrates in PCB/MCM are modeled as multi-layered dielectric structures embedded with arbitrarily shaped conductors. The conductor planes and signal traces are connected to each other and to external circuits or power supplies through circuit port, vias or ground pins. External currents or voltages are maintained at those ports on the conductors. The induced charges and currents produce electromagnetic fields which satisfy boundary conditions on the conductor surfaces. Also, the surface charges, surface currents, and the external current flowing into the conductors should satisfy the general continuity relation. This system can thus be characterized by the following set of mixed potential integral equations (MPIE) which completely describes the potentials, current, and charge distributions in the conductor system.

$$Z_s \mathbf{n} \times \boldsymbol{J}_s(\boldsymbol{r}) - \mathbf{n} \times i\omega\mu \int_S d\boldsymbol{r}' \boldsymbol{G}_A(\boldsymbol{r}, \boldsymbol{r}') \bullet \boldsymbol{J}(\boldsymbol{r}') + \mathbf{n} \times \nabla\Phi(\boldsymbol{r}) = 0 \tag{1}$$

$$\nabla \bullet \boldsymbol{J}_s(\boldsymbol{r}) - i\omega q_s(\boldsymbol{r}) - \nabla \bullet \boldsymbol{J}^i(\boldsymbol{r}) = 0 \tag{2}$$

$$\Phi(\boldsymbol{r}) - \frac{1}{\varepsilon} \int_S d\boldsymbol{r}' \boldsymbol{G}_\phi(\boldsymbol{r}, \boldsymbol{r}') q_s(\boldsymbol{r}') = 0 \tag{3}$$

By solving these equations, the voltage and current distributions over the conducting planes can be obtained in relation to the injected currents or fixed port potentials for given excitations. Notice that the external current is considered as localized source in the above formulation. Notice also that the scalar potential is retained as a explicit variable in the above MPIE's, unlike in other mixed potential formulations. If we consider the scalar potential as a close approximation to voltage defined in a static sense, the above formulation enables us to obtain an explicit relation between port voltage and injected current, and thus a multiport network representation or an equivalent circuit for the substrate system.

A boundary element approach or method of moment is applied to solve the integral equations. The total conductor surface, domain S, is divided into subdomains (elements) with quadrilateral shapes. The charge and current on each element are expanded in term of known basis functions. Following point matching method or Galerkin's method, the integral equations become a set of linear equations (in matrix notation) as

$$(\boldsymbol{Z}_s - i\omega\boldsymbol{L})\boldsymbol{I} - \boldsymbol{P}\boldsymbol{V} = 0 \tag{4}$$

$$\boldsymbol{P}^T\boldsymbol{I} - i\omega\boldsymbol{C}\boldsymbol{V} = \boldsymbol{J}^i \tag{5}$$

where $\mathbf{Z}_s$, $\mathbf{L}$, $\mathbf{P}$, and $\mathbf{C}$ are matrices; vector $\mathbf{V}$ represents the potential (voltage) while vector $\mathbf{I}$ represents the surface currents; $\mathbf{J}^i$ vector is the externally injected port currents. Depending on the specified

boundary (terminal) condition, we can solve for either the unknown port voltages with specified port currents, or the unknown port currents with specified port voltages, along with the charge, current and potential over the conductor surface. Solution of these equations enables us to obtain an explicit relation between port voltages and injected currents, and thus a multiport network representation or an equivalent circuit for the system.

III. Quasi-Static Approximation and Equivalent Circuits

The above integral equation/boundary element approach is a rigorous full-wave analysis developed in the frequency domain. This formulation of the system, as represented by the matrix equations, has complex frequency dependence. The resulting multiport network, though convenient for single frequency circuit simulation, would have to be updated for every single frequency in wideband or transient applications. To simplify the frequency dependance, we make the quasi-static approximation for systems satisfying the following relation

$$\frac{h}{\lambda} = hf\sqrt{\varepsilon\mu} \ll 1 \tag{6}$$

where h is the characteristic dimension of the structure and f is the operating frequency. First, the exponential retardation factor are neglected in Green's functions. Second, for good conductors,

$$\mathbf{Z}_s - i\omega\boldsymbol{L} \approx R_s \qquad (\omega \to 0) \tag{7}$$

$$\mathbf{Z}_s - i\omega\boldsymbol{L} \approx -i\omega\boldsymbol{L} \qquad (\omega \gg 0) \tag{8}$$

With this assumption, the surface resistance $\mathbf{Z}_s$ can be considered as the first order low frequency approximation for the total resistance. Solving linear equations (4) and (5) under the quasi-static approximation with specified port voltages, we obtain the system solution, $\mathbf{J}^i=\mathbf{Y}\mathbf{V}^i$, where $\mathbf{J}^i$ and $\mathbf{V}^i$ are the port currents and voltages, respectively, and $\mathbf{Y}$ is an admittance matrix representing the system. Keeping only the first and second order terms in the frequency expansion of the result, the $\mathbf{Y}$ matrix has the following form as

$$\boldsymbol{Y} = \frac{1}{-i\omega}(\boldsymbol{L})^{-1} - i\omega\boldsymbol{C} \tag{9}$$

where $(\boldsymbol{L})^{-1}$ denotes a matrix with elements equal to the inverse of the corresponding elements of $\mathbf{L}$, not the inverse matrix of $\mathbf{L}$.

From the admittance matrix, an equivalent circuit representing the system can be constructed. In fact, the admittance matrix is the same $\mathbf{Y}$ matrix in a nodal formulation of the circuit in frequency domain, and can be used directly for frequency domain solutions. The equivalent circuit consists of branches between every pair of ports. Each branch has an inductance L in series with a resistance R, and then in parallel with a capacitance C. The branch admittance between nodes m and n is given by

$$Y_{mn} = \frac{1}{R_{mn} - i\omega L_{mn}} - i\omega C_{mn} \tag{10}$$

It should be noticed that the quasi-static approximation and therefore the resulting equivalent circuits are based on the coupled MPIE's. Therefore the effects of displacement current are not neglected completely as in quasi-magnetostatic based inductance or capacitance solvers. It is also important to

point out that in extracting the equivalent circuits, additional surface elements can be selected as internal nodes in addition to the physical ports. This leads to larger equivalent circuits with more internal loops, and therefore gives more complex frequency behavior and higher accuracy.

Since the equivalent circuit captures the wideband frequency behavior and distributed characteristics, it should correctly predict the wave effects such as propagation delay, resonance, and signal reflection on the power/ground plane structure. Numerical examples show that it indeed captures those effects correctly. However, it is fundamentally limited by the retardation effect, and does not include losses due to radiation effects.

The equivalent circuits are utilized to simulate transient response of complex interconnect and plane structures. External circuits such as driver/receiver or IC die models can be combined with the equivalent circuits for system signal simulations. An efficient circuit simulator specifically for the equivalent circuit is developed in our simulation program which provides both time-domain and frequency domain capability. For time-domain transient solution, a modified nodal formulation (MNA) of the equivalent circuit eliminates the unnecessary internal inductance nodes and therefore greatly reduces the rank of the linear system. Combined with uniform time step for the linear circuit portion, this approach gives us very efficient simulation time and thus enables us to do what-if type of analysis for realistic circuit boards and designs [9]. Frequency domain simulations are useful for gaining insight of high frequency characteristics of the complex systems. Also, in practice, experimental measurements and characterization of high-speed/high-frequency system are mostly made in frequency domain in terms of S-parameters. It is also useful for verification of the simulation code's accuracy and limitation in comparison with experimental measurements and other benchmark results.

IV. 2-D FDTD Modeling and Simulation

Power and ground plane structures with large parallelism can be modeled very well as planar circuits. The concept of a planar circuit was first introduced by Okoshi [10] as a circuit having one dimension very small in comparison with the wavelength and an arbitrary shape in two other dimensions. The 2-D FDTD method, which has been used successfully to analyze different planar structures [11], is adopted here to analyze parallel power and ground plane structures.

Separation d between power and ground planes is typically much smaller than a wavelength. This allows us to neglect tangential E, normal H and the variation of the remaining field components in the normal direction. The voltage $V = E_n d$ between planes and the surface currents $\bar{J} = \hat{n} \times \bar{H}$ are then governed by the following 2-D partial differential equations:

$$\nabla V = -L_S \frac{\partial}{\partial t} \bar{J} - R_S \bar{J} \tag{11}$$

$$\nabla \bullet \bar{J} = -C_S \frac{\partial}{\partial t} V - J_S(V) \tag{12}$$

where $L_S = \mu_0 d$, $C_S = \varepsilon_0 \varepsilon_r / d$, R_S is sheet resistivity, and $J_S(V)$ is used to model lump source and load elements. In the 2-D FDTD method, these equations are solved numerically using a leapfrog center-difference scheme [11]. At nodes where a lump element is present, (12) is solved as described in [12]. Plane boundary conditions are implemented by simply setting J_n zero.

V. EXAMPLES AND VERIFICATION

As the first example, a simple parallel plane structure as shown in Figure 1 is analyzed. In our simulation, the planes were discretized into 414 facets and the vias structures were simply modeled as a pair of nodes. A 14-node and a 42-node equivalent circuit were extracted from the field solution, and the latter was used in frequency domain calculation of S-parameters. Figure 2 shows the comparison of simulated and measured results. The measured S21 was given by K. Lee et al in [1], and used in Figure 2. It is evident that the agreement is quite good up to about 5 GHz, and the simulation captured the essential characteristics of the system. Towards higher frequency, however, the simulated result shifted away from the measurement in a systematic fashion. This behavior is within our expectation due to the limit of quasi-static approximation. But for most current commercial digital applications, as we pointed out before, 5 Ghz is a sufficiently high estimate of the signal source bandwidth while the computational requirement is practical. A full-wave simulation, though possible under the current framework, would be too costly and unnecessary.

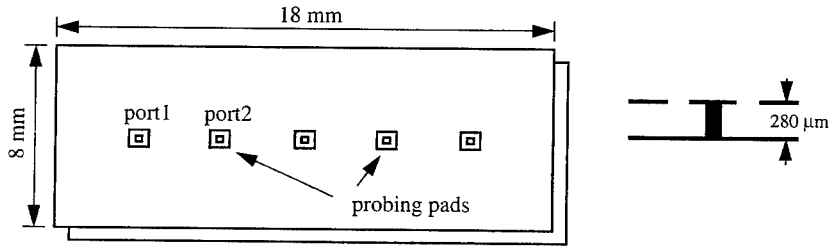

Figure 1. Test plane structure measured by HP Lab. The planes are made with 16 mΩ/sq. tungsten. The dielectric is alumina with ε of 9.6.

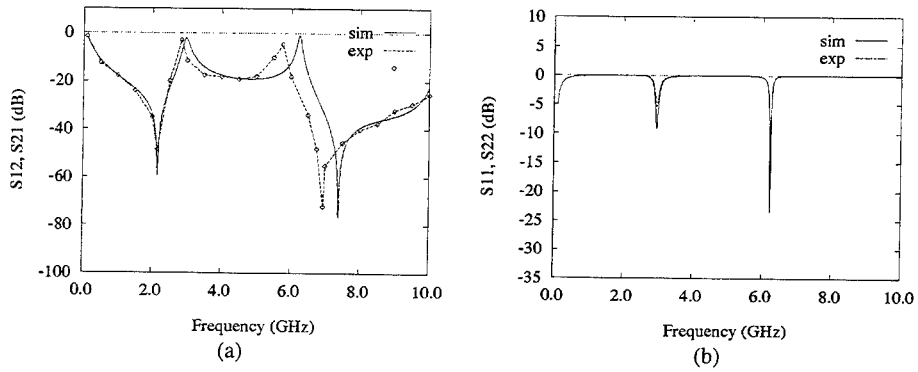

Figure 2. Comparison of simulated and measured S-parameters on the test plane structure, (a) S12 and (b) S11.

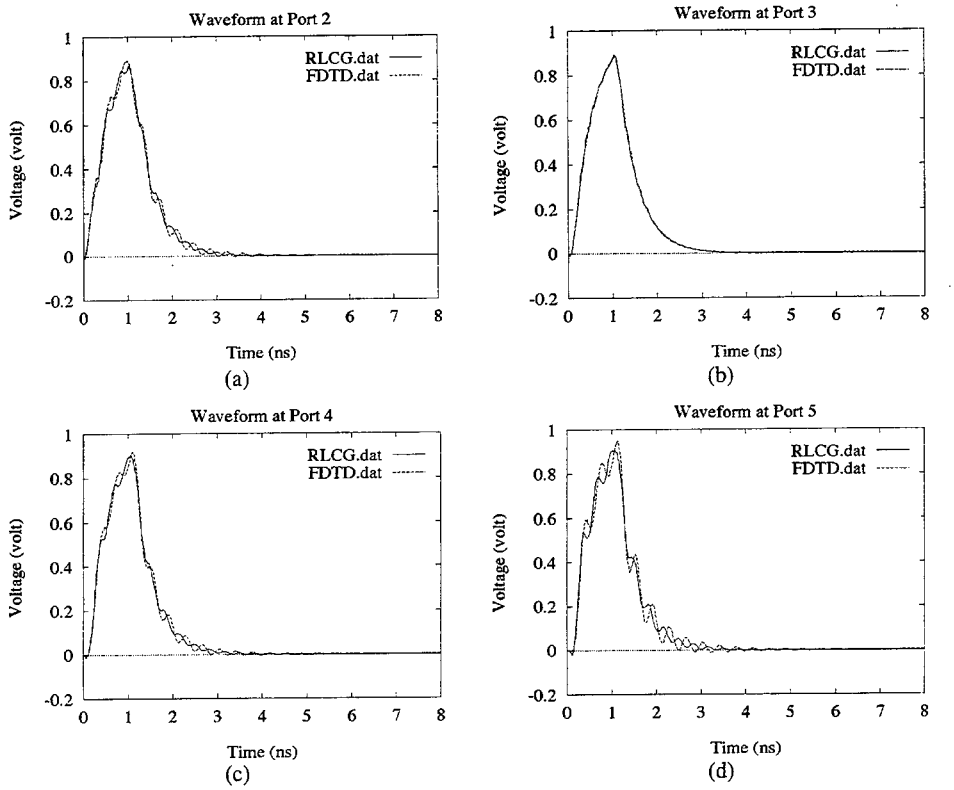

Figure 3. Comparison of transient waveforms on the test planes by FDTD and by equivalent circuit simulations. (a) waveform at Port 2, (b) waveform at Port 3, (c) waveform at Port 4, and (d) waveform at Port 5.

To further study the transient characteristic of the system, and to see the effect of high frequency limit on high speed digital signal, time domain simulations using both equivalent RLC circuit and 2-D FDTD are carried out on this test structure. A pulse signal of 5 volt magnitude, 0.2 ns rise/fall time, and 1.0 ns duration is applied at Port 1. All five ports are terminated with 50 ohm load. Transient waveforms are calculated. In the FDTD simulation, a grid size of 1 mm by 1 mm and a time step of 10 ps are used. Figure 3(a), (b), (c), and (d) show the voltage waveforms at Port 2, Port 3, Port 4, and Port 5, respectively, where solid lines are the results obtained by equivalent RLC circuit while dashed lines are FDTD results. Good agreements again are evident and demonstrate the validity of our approaches.

The second example analyzes the power/ground noises (ground bounce) and the effect of decoupling capacitors in reducing those noises. Figure 4 shows a realistic power/ground substrate in PCB board. The size of the power/ground planes is 10 by 10 inch, with a thickness of 10 mil and dielectric

constant of 4.5. An active device is connected to the power supply planes at Port 1. When the device switches, it draws a transient current from the DC power supply, and thus induces transient ground noises across the DC power/ground planes. When many active devices switch simultaneously, large transient noises fluctuate DC supply significantly and cause device malfunction. The most common practice in digital design to solve those simultaneous switching noise (SSN) or ground bounce problems is using decoupling capacitors to decouple the power and ground planes. However, due largely to the lack of true distributed, accurate electromagnetic model of power/ground structures, effective uses of decoupling capacitors is still mostly based on experiences or try and error instead of rigorous simulation. In this example we apply the equivalent circuit model to simulate those effects.

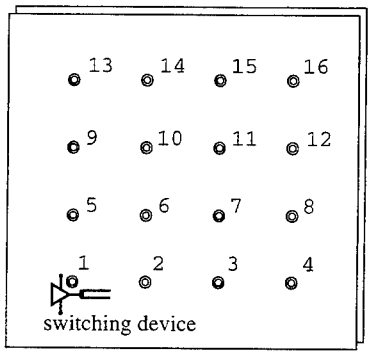

Figure 4. Parallel power and ground planes with switching device at Port 1.

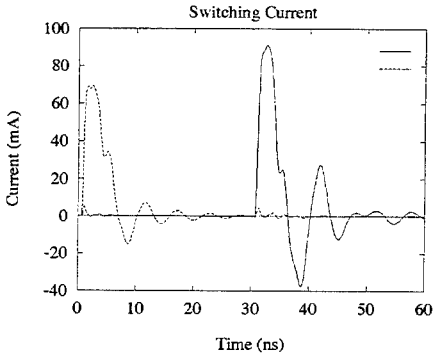

Figure 5. Switching current drawn from power supply by the active device.

The above power/ground planes are modeled by a 32-node equivalent circuit. Figure 5 shows the switching current drawn from the power supply for a real device. As a current source to the power/ground circuit, it has a 50 ohm internal resistance, and is applied at Port 1. Figure 6 show the noise waveforms at various locations across the planes when the planes are open loaded (no loads). We see more than 15 mV noise level due to one switching device. Devices and interconnects such as strip lines or microstrip lines on PCB are usually terminated by matching loads. To see the effect of those resistive loads, a 50 ohm resistance is placed at each of the 16 ports. Figure 7 shows the noise waveforms with the resistive loads. It is clear that resistive terminations have little effect on the ground noise, as shown by the simulation results, since the resistance values (~50 ohm) are in most situation much higher than the plane impedance. To see the effects of decoupling capacitors, a 10 pF capacitance is placed at each the ports. Figure 8 shows that the ground noise level is reduced by more than 60% due to the de-caps. When 100 pF decoupling capacitors are used at all the ports, the ground noise level is reduced to less than 10% of that without de-caps, as shown by Figure 9. It is necessary to point out that the decoupling capacitors used in the above simulation are ideal capacitances. In real applications, decoupling capacitors are frequency dependent devices and lose their decoupling capability significantly towards high frequency region due to inductive effects.

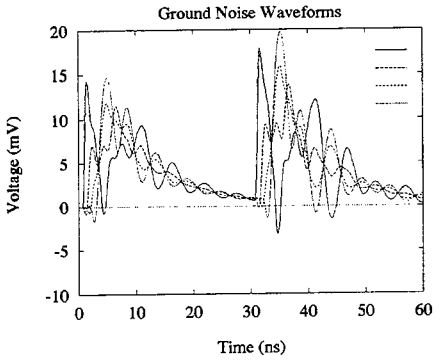

Figure 6. Ground noise without loads.

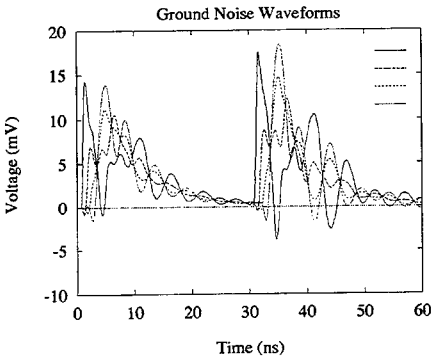

Figure 7. Ground noise with resistive loads.

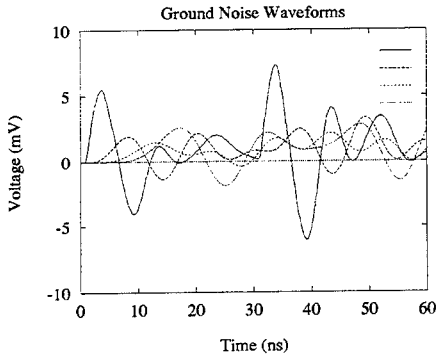

Figure 8. Ground noise with 10 pf de-caps.

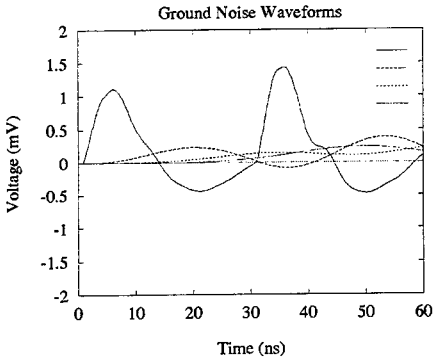

Figure 9. Ground noise with 100 pf de-caps.

VI. Conclusion

In this paper, power and ground plane effects in high speed digital circuits are analyzed using integral equation/equivalent circuit method as well as 2-D FDTD method. The simulation results of both approaches correlate very well with each other, and compare very well with measured results. In particular, ground noises due to active device switching are analyzed. The effectiveness of decoupling capacitors in reducing ground noises are examined. The equivalent circuit model from electromagnetic solution provides a useful and understandable presentation of complex power/ground structures to digital circuit designers in practical design process. It can be easily integrated with other digital simulators or CAD tools, and combined with signal networks and device models, for accurate packaging and system level design simulation.

REFERENCES

[1] K. Lee and A. Barker, "A Comparison of Power Supply Planes in Thick and Thin MCM's," *IEEE 3rd Topical Meeting on Electrical Performance of Electronic Packaging*, pp. 3-6, Monterey, CA, Nov. 1994.

[2] R. Mittra and S. Chebolu, "Electromagnetic Modeling of Simultaneous Switching Noise in Power and Ground Planes in Electronic Packages", *IEEE 3rd Topical Meeting on Electrical Performance of Electronic Packaging*, pp. 207-210, Monterey, CA, Nov. 1994.

[3] J. Fang, Y. Liu, Y. Chen, Z. Wu, and A. Agrawal, "Modeling of Power/Ground Plane Noise in High Speed Digital Electronics Packaging," *IEEE 2nd Topical Meeting on Electrical Performance of Electronic Packaging*, pp. 206-208, Monterey, CA, Oct. 1993.

[4] R. Senthinathan, S. Nimmagadda, J. Prince, and A. Cangellaris, "Modeling and Simulation of Coupled Transmission Line Interconnects Over a Noisy Reference Plane," *IEEE Trans. Comp. Hybrids, Manuf. Technol.*, vol. CHMT-16, pp 705-713, 1993.

[5] W. Becher, B. McCredie, G. Wilkins, A. Iqbal, "Power Distribution Modeling of High Performance First Level Computer Packages," *IEEE 2nd Topical Meeting on Electrical Performance of Electronic Packaging*, pp. 203-205, Monterey, CA, Oct. 1993.

[6] F. Y. Yuan, T. Postel, and L. Rubin, "Analysis and Modeling of PowerDistribution Networks and Plane Structures in Multichip Modules and PCB's," *IEEE Electromagnetic Compatibility Symposium Proceedings*, pp. 447-452, Atlanta, GA, Aug. 1995.

[7] *Numerical Techniques for Microwave and Millimeter-Wave Passive Structures*, edited by T. Itoh, New York, John Wiley & Sons, 1989.

[8] *Analysis and Design of Planar Microwave Components*, edited by K. Gupta and M. Abouzahra, New York, IEEE Press, 1994.

[9] J. Vlach and K. Singhal, *Computer Methods for Circuit Analysis and Design*, Van Nostrand Reinhold, New York, 1994.

[10] T. Okoshi and T. Miyoshi, "The planar circuit - An approach to microwave integrated circuitry," *IEEE Trans. Microwave Theory Tech.*, vol. MTT-20, pp. 245-252, Apr. 1972.

[11] W. Gwarek, "Analysis of an arbitrarily-shaped planar circuit - A time-domain approach," IEEE Trans. Microwave Theory Tech., vol. MTT-33, pp. 1067-1072, Oct. 1985.

[12] M. Piket-May, "FD-TD modeling of digital signal propagation in 3-D circuits with passive and active loads," *IEEE Trans. Microwave Theory Tech.*, vol. MTT-42, pp. 1514-1523, Aug. 1994.

SESSION 17:

ARRAYS

Chair: L. Epp

SYNTHESIS OF PHASED ARRAY APERTURE DISTRIBUTIONS

Ross A. Speciale

Redondo Beach, California

ABSTRACT

A conceptually fundamental new method of electronic beam steering, that is eminently suited for application to large, high-directivity, low-sidelobe phased arrays is here described, and analytically evaluated. Most remarkably, the new method requires a number of beam-steering controls that is much smaller than the very large number of radiating array elements, thus making order-of-magnitude cost reductions possible. A non-symmetric, linear beam-forming network is used to connect a very large number of radiating array elements to a much smaller number of amplitude-, and phase-controlled microwave sources (in transmission), or of receiver front-ends (in reception). The used linear beam-forming network is designed to be simultaneously impedance-matched to the large set of array elements, on one side, and to the much smaller set of sources (or receivers), on the other, thus totally eliminating the notorious array-blindness phenomenon. Further, the network transfer-response is specified, by design, so that each of the sources simultaneously feeds all the array elements, and conversely each of the array elements is simultaneously fed by all the sources, in transmission. Similarly, each of the array elements simultaneously excites all the receiver front-end, and each of the receivers is simultaneously excited by all the array elements, in reception. Practically relevant aperture distributions, known to correspond to a carefully selected set of specified far-field patterns, are synthesized as linear combinations of the various mutually-complementary, component wave-field patterns, generated by the relatively few controlled sources, on the array aperture. Electronic beam steering is then obtained by appropriately selecting the relative amplitudes and relative phases of the sources in transmission, or of the receivers in reception, as required to match the required complex values of the linear combination weights. An extensive set of formal expressions is here given, that states the conditions for the applicability of the new electronic beam-steering method, and identifies its largely irrelevant limitations.

1 - SUMMARY OF PREVIOUS FUNDAMENTAL RESULTS.

Recently reported, fundamental analytic results have already established a rigorous theoretical basis for performing an unusually-advanced design of phased array beam-forming networks [1] . The reported new results apply to very general, linear, electrically-large, and non-necessarily reciprocal beam-forming networks, used to connect a large number N of array elements, to a much smaller number n of amplitude-, and phase-controlled sources, in transmission, or of receiver front-ends, in reception (Figures 1 and 2). Such non-symmetric beam-forming networks, that are eminently suited for large, high-directivity, low-sidelobe, electronically-steered phased arrays, can be simultaneously impedance-matched, by design, to a large set of N array elements on one side, and to a much smaller set of n sources, or receivers on the other, simultaneously accounting for the proximity-coupling between the array elements, and for any internal cross-coupling between the sources, or between the receivers.

The attained, simultaneous impedance match is totally independent from the amplitude, and phase settings of the sources, in transmission, and from the direction of the incident aperture illumination, in reception, thus completely eliminating the notoriously adverse *'array blindness'* phenomenon. Further, the wave-transfer responses of the considered beam-forming networks, to and from the N array elements, can be specified, by design, so that all the required, practical aperture distributions of the array, those

distributions that are known to correspond to any given set of desired radiation patterns, can be synthesized by appropriately selecting the relative-amplitude, and the relative-phase settings of the n sources, in transmission, and of the n receivers, in reception. The new, advanced beam-forming network design method, made possible by the recently reported fundamental results, provides thus a significantly less expensive, and more reliable alternative to the use of the notoriously unaffordable active aperture phased arrays, that require outrageously large numbers of low-efficiency, semiconductor T/R modules, distributed across the whole array aperture, at geometrically-constrained, and hardly-serviceable locations. The following summary of the most fundamental previous results is included, mainly for the reader's convenience, and as a starting point of the ensuing, much expanded discussion of aperture distribution synthesis.

1.1 - THE NON-SYMMETRICALLY PARTITIONED IMPEDANCE MATRIX.

A non-symmetrical partitioning of the $(n+N)$ x $(n+N)$ impedance matrix $Z_{(n+N)}$ of the completely general, linear beam-forming network shown in Figures 1 and 2, has been recognized as a rather obvious mathematical expedient, consistent with the physical separation of the $n+N$ ports in an n-port interface-1, and an N-port interface-2. The chosen block-structure of the impedance matrix $Z_{(n+N)}$ is then :

$$Z_{(n+N)} = \left| \begin{array}{c|c} Z_1 & Z_2 \\ \hline Z_3 & Z_4 \end{array} \right| \qquad (1)$$

The selected matrix partitioning generates the four impedance-matrix blocks Z_1 (n x n), Z_2 (n x N), Z_3 (N x n), and Z_4 (N x N), where (in agreement with Figures 1 and 2) it is assumed that $n \leq N$, and that the impedance matrix $Z_{(n+N)}$ is non-necessarily symmetric.

1.2 - THE TWO IMPEDANCE MATRIX TRANSFORMATIONS.

A first previous fundamental result is given by the two matrix transforms :

$$Z_{in1} = Z_1 - Z_2 \cdot (Z_4 + Z_{L2})^{-1} \cdot Z_3 \qquad (2)$$

$$Z_{in2} = Z_4 - Z_3 \cdot (Z_1 + Z_{L1})^{-1} \cdot Z_2 \qquad (3)$$

The first transform expresses the n x n input-impedance matrix Z_{in1}, observable at the n ports of

interface-1 , with an N-port load-network L_2 , characterized by the N x N impedance matrix Z_{L2} , connected to the N ports of interface-2, while the second transform expresses the N x N input-impedance matrix Z_{in2} , observable at the N ports of interface-2, with an n-port load-network L_1 , characterized by the n x n impedance matrix Z_{L1} , connected to the n ports of interface-1 . The two impedance-matrix transforms (2) and (3) hold for any integer values of n , and N , including $n > N$, and the scalar case of $n = N = 1$ that describes impedance transformations through a simple two-port network.

1.3 - THE BILATERAL IMPEDANCE-MATCH CONDITION.

A second, most fundamental previous result defines the necessary and sufficient conditions for attaining a *simultaneous*, multiport impedance match at both beam-forming network interfaces, so that an input voltage-wave vector a_i incident upon interface-1 (in transmission) only generates an outgoing voltage-wave vector b_j at interface-2 , with the outgoing interface-1 voltage-wave vector b_i being identically zero, while similarly an input voltage-wave vector a_j incident upon interface-2 (in reception) only generates an outgoing voltage-wave vector b_i at interface-1 , with the outgoing interface-2 voltage-wave vector b_j being identically zero. Obviously, both the input-interface *reflections*, and the *cross-talk* between its ports are totally suppressed, under the given impedance-match conditions. Clearly, with such simultaneous, bilateral impedance match, a *very specific* beam-forming network $(n+N)$ x $(n+N)$ scattering matrix S exists that, when non-symmetrically partitioned as the corresponding impedance matrix $Z_{(n+N)}$, has an identically-zero n x n leading block S_1 , and an identically-zero N x N trailing block S_4 , while the blocks S_2 (n x N) , and S_3 (N x n) are non-zero. Indeed, a major previous fundamental result states that :

$$S = (Z - Z_o) \cdot (Z + Z_o)^{-1} = \left|\begin{array}{c|c} 0 & S_2 \\ \hline S_3 & 0 \end{array}\right| \qquad (4)$$

if, *and only if*, the wave-normalizing impedance matrix Z_o has the structure :

$$Z_o = \left|\begin{array}{c|c} Z_{I1} & 0 \\ \hline 0 & Z_{I2} \end{array}\right| \qquad (5)$$

where the leading n x n block Z_{I1} , and the trailing N x N block Z_{I2} a) are the only non-zero blocks of the

matrix Z_e , b) are non-necessarily diagonal or symmetric, c) are expressed by :

$$Z_{I1} = \left(I_n - Z_2 \cdot Z_4^{-1} \cdot Z_3 \cdot Z_1^{-1} \right)^{1/2} \cdot Z_1 = \left(I_n - P_n \right)^{1/2} \cdot Z_1 \qquad (6)$$

$$Z_{I2} = \left(I_N - Z_3 \cdot Z_1^{-1} \cdot Z_2 \cdot Z_4^{-1} \right)^{1/2} \cdot Z_4 = \left(I_N - P_N \right)^{1/2} \cdot Z_4 \qquad (7)$$

and d) represent the *'image-impedance matrices'* of the $(n+N)$-port beam-forming network (a *conceptual extension* of the well-known classical scalar concept).

1.4 - THE TRANSFORMATION PROPERTIES OF THE IMAGE-IMPEDANCE MATRICES.

The third, previous fundamental result shows the unique transformation properties of the two image-impedance matrices Z_{I1} , and Z_{I2} , regarded as the impedance matrices Z_{L1} , and Z_{L2} of two very specific, multiport load-networks, that are *'totally matched'* to the given beam-forming network at its two interfaces. Indeed, by substituting Z_{I2} for Z_{L2} in (2), and Z_{I1} for Z_{L1} in (3), we obtain :

$$Z_{I1} = Z_1 - Z_2 \cdot \left(Z_4 + Z_{I2} \right)^{-1} \cdot Z_3 \qquad (8)$$

$$Z_{I2} = Z_4 - Z_3 \cdot \left(Z_1 + Z_{I1} \right)^{-1} \cdot Z_2 \qquad (9)$$

Clearly, the two image-impedance matrices Z_{I1} , and Z_{I2} , representing totally matched multiport load-networks, exhibit the unique characteristic of transforming into one another, through the given $(n+N)$-port beam-forming network.

1.5 - EXPRESSIONS OF THE IMAGE-MATCHED RESPONSES S_2 AND S_3 .

The fourth, previous fundamental result defines the *forward*, and *backward* voltage-wave transfer responses of any given $(n+N)$-port beam-forming network, under simultaneous bilateral impedance match. The two voltage-wave transfer responses S_2 , and S_3 are expressed by the matrix functions :

$$S_2 = Z_2 \cdot Z_4^{-1} \cdot \left[I_N + \left(I_N - Z_3 \cdot Z_1^{-1} \cdot Z_2 \cdot Z_4^{-1} \right)^{1/2} \right]^{-1} = M_n \cdot \left[I_N + \left(I_N - P_N \right)^{1/2} \right]^{-1} \qquad (10)$$

$$S_3 = Z_3 \cdot Z_1^{-1} \cdot \left[I_n + \left(I_n - Z_2 \cdot Z_4^{-1} \cdot Z_3 \cdot Z_1^{-1} \right)^{1/2} \right]^{-1} = M_N \cdot \left[I_n + \left(I_n - P_n \right)^{1/2} \right]^{-1} \qquad (11)$$

and independently map the incident voltage-wave vectors a_i , and a_j to the corresponding output voltage-wave vectors b_j (in transmission), and b_i (in reception) :

$$b_i = S_2 \cdot a_j \qquad (12) \qquad\qquad b_j = S_3 \cdot a_i \qquad (13)$$

1.6 - DESIGN OF BEAM-FORMING NETWORKS WITH PRESCRIBED IMPEDANCE-MATCH, AND VOLTAGE-WAVE TRANSFER RESPONSES.

The fifth, previous fundamental result establishes a rigorous theoretical basis for performing the design of a linear $(n+N)$-port beam-forming network, that is required to be simultaneously, and bilaterally impedance-matched to a given set of N proximity-coupled array elements, regarded as a load-network L_2 characterized by the impedance-matrix $Z_{L2} = Z_{II}$, and to a given set of n sources (in transmission), or of receivers (in reception), regarded as a load-network L_1 characterized by the impedance matrix $Z_{LI} = Z_{II}$, while at the same time exhibiting the two prescribed voltage-wave transfer-responses S_2, and S_3, under simultaneous, bilateral impedance match conditions.

The rigorous design basis is established by the following matrix functions, expressing the four blocks Z_i $(i = 1, 2, ..., 4)$ of the beam-forming network impedance matrix $Z_{(n+N)}$:

$$Z_1 = \left(I_n - S_2 \cdot S_3 \right)^{-1} \cdot \left(I_n + S_2 \cdot S_3 \right) \cdot Z_{II} \qquad (14)$$

$$Z_2 = 2 \left(I_n - S_2 \cdot S_3 \right)^{-1} \cdot S_2 \cdot Z_{I2} \qquad (15)$$

$$Z_3 = 2 \left(I_N - S_3 \cdot S_2 \right)^{-1} \cdot S_3 \cdot Z_{II} \qquad (16)$$

$$Z_4 = \left(I_N - S_3 \cdot S_2 \right)^{-1} \cdot \left(I_N + S_3 \cdot S_2 \right) \cdot Z_{I2} \qquad (17)$$

1.7 - THE KEY ROLE OF THE AUXILIARY MATRIX PRODUCTS.

The four matrix products M_n, M_N, P_n, and P_N, appearing in the expressions (6), (7), (10), and (11), play a remarkable key role in establishing the functional relations between the four impedance-matrix blocks Z_i $(i = 1, 2, .., 4)$ and the *'image matrices'* Z_{II}, Z_{I2}, S_2, and S_3.

All four matrix products have the *physical* dimensions of *pure numbers*, and different orders, the orders being $n \times N$ for M_n, $N \times n$ for M_N, $n \times n$ for P_n, and $N \times N$ for P_N, and are defined by :

$$M_n = Z_2 \cdot Z_4^{-1} \qquad (18) \qquad\qquad M_N = Z_3 \cdot Z_1^{-1} \qquad (19)$$

$$P_n = M_n \cdot M_N = M_{Pn} \cdot \Lambda_{Pn} \cdot M_{Pn}^{-1} \qquad (20)$$

$$P_N = M_N \cdot M_n = M_{PN} \cdot \Lambda_{PN} \cdot M_{PN}^{-1} \qquad (21)$$

Most remarkably, the matrix product P_n is generally of full-rank n (therefore *non-singular*), save for pathological situations, but the rank of the matrix product P_N is always equal to n , so that the matrix P_N is always very much singular, having at least $N - n$ zero eigenvalues in its spectral matrix Λ_{PN} .

The n non-zero eigenvalues of the matrix P_N are *equal* to those of the matrix P_n , while the corresponding eigenvectors are the columns of the matrix product $M_N \cdot M_{Pn}$, as proved by :

$$P_N \cdot (M_N \cdot M_{Pn}) = M_N \cdot (M_n \cdot M_N) \cdot M_{Pn} = M_N \cdot P_n \cdot M_{Pn} = (M_N \cdot M_{Pn}) \cdot \Lambda_{Pn} \qquad (21')$$

The full relevance of these results to the design of non-symmetric beam-forming networks becomes obvious in the following Section 2.4 .

2 - SUMMARY OF MAJOR NEW RESULTS.

The use of a non-symmetric beam-forming network, connecting a large number N of array elements to a much smaller number n of sources (or receivers), provides a significantly less expensive alternative to the use of the notoriously unaffordable active aperture arrays, that require outrageously large numbers of semiconductor *T/R* modules, physically embedded at geometrically-constrained, hardly-serviceable locations. An overwhelmingly vast collection of new, fundamental results has been obtained, by analyzing the two idealized, cascaded connections of the $(n+N)$-port beam-forming networks A , and B shown in Figures 3, and 4. The new analytic results quantitatively identify the natural transmission wave-modes of any $(n+N)$-port beam-forming network, and establish a rigorous basis for the determination of the required minimum number n of amplitude-, and phase-controlled sources (or receivers), as function of the specified beam-steering performance.

2.1 - THE TWO IMPEDANCE MATRICES Z_C AND Z_D .

The beam-forming networks A , and B in Figures 3, and 4 are mutually identical, save for network B being *'flipped'* by 180° left-to-right, thus exchanging the relative locations of its two interfaces. The resulting 'Type-C' (Fig. 3) , and 'Type-D' (Fig. 4) cascaded connections are both symmetric, and are characterized by the $2n$ x $2n$ impedance matrix Z_C , and by the $2N$ x $2N$ impedance matrix Z_D , respectively, with the four n x n blocks of Z_C expressed by :

$$Z_{1C} = Z_{4C} = \frac{1}{2} (2 I_n - P_n) \cdot Z_1 \qquad (22)$$

$$Z_{2C} = Z_{3C} = \frac{1}{2} P_n \cdot Z_1 \qquad (23)$$

while the four N x N blocks of Z_D are expressed by :

$$Z_{1D} = Z_{4D} = \frac{1}{2} (2 I_N - P_N) \cdot Z_4 \qquad (24)$$

$$Z_{2D} = Z_{3D} = \frac{1}{2} P_N \cdot Z_4 \qquad (25)$$

2.2 - THE IMAGE-IMPEDANCE MATRICES Z_{IC} AND Z_{ID} .

The beam-forming networks A and B are mutually impedance-matched at the common interface in both the Type-C, and the Type-D connections, so that as a consequence the two (input *and* output) image-impedance matrices are, respectively :

$$Z_{IC} = Z_{I1} = \left(I_n - P_n \right)^{1/2} \cdot Z_1 \qquad (26)$$

$$Z_{ID} = Z_{I2} = \left(I_N - P_N \right)^{1/2} \cdot Z_4 \qquad (27)$$

2.3 - THE SCATTERING MATRICES S_{TC} AND S_{TD} .

The auto-normalized scattering matrices S_{TC} , and S_{TD} of the Type-C, and Type-D connections are of orders $2n$ x $2n$, and $2N$ x $2N$, respectively, and have both identically-zero leading, and trailing blocks.

The two non-zero, n x n blocks of the matrix S_{TC} are expressed by :

$$S_{2C} = S_{3C} = S_C = S_2 \cdot S_3 = M_{Pn} \cdot \Lambda_{SC} \cdot M_{Pn}^{-1} \qquad (28)$$

while the two non-zero, N x N blocks of the matrix S_{TD} are expressed by :

$$S_{2D} = S_{3D} = S_D = S_3 \cdot S_2 = M_{PN} \cdot \Lambda_{SD} \cdot M_{PN}^{-1} \qquad (29)$$

Quite remarkably, the modal matrix of the block S_C is the M_{Pn} modal matrix of the matrix product P_n , while the modal matrix of the block S_D is the M_{PN} modal matrix of the matrix product P_N . The corresponding diagonal spectral matrices Λ_{SC} , and Λ_{SD} are expressed respectively by :

$$\Lambda_{SC} = \left[I_n - \left(I_n - \Lambda_{Pn} \right)^{1/2} \right] \cdot \left[I_n + \left(I_n - \Lambda_{Pn} \right)^{1/2} \right]^{-1} = Diag\left[e^{-\gamma_{ICi}} \right] \qquad (30)$$

$$\Lambda_{SD} = \left[I_N - \left(I_N - \Lambda_{PN} \right)^{1/2} \right] \cdot \left[I_N + \left(I_N - \Lambda_{PN} \right)^{1/2} \right]^{-1} = Diag\left[e^{-\gamma_{IDi}} \right] \qquad (31)$$

The n columns of the modal matrix M_{Pn} identify the n *'natural transmission modes'* of the Type-C connection. These n modes are obviously linearly independent, and provide thus a basis for the expansion

of any arbitrary excitation, as a linear combination of natural modes. The natural logarithms of the n λ_{SCi} eigenvalues in the Λ_{SC} spectral matrix are expressed by :

$$-\gamma_{ICi} = \alpha_{ICi} - j\,\varphi_{ICi} = \cosh^{-1}\left(\frac{2}{\lambda_{Pni}} - 1\right) = 2\cosh^{-1}\left(\frac{1}{\sqrt{\lambda_{Pni}}}\right) \qquad (32)$$

and are the corresponding single-mode propagation-constants through the Type-C connection. All the n natural modes of the Type-C connection are generally propagating, save for the pathological case of P_n being singular. It is indeed easy to see that $\lambda_{SCi} = 0$, if $\lambda_{Pni} = 0$. The same discussion applies to the n λ_{SDi} non-zero eigenvalues in the Λ_{SD} spectral matrix, while the $N - n$ λ_{SDk} , corresponding to the identically-zero λ_{PNk} eigenvalues, identify the set of *'natural cut-off modes'* of the Type-D connection (more about this in the following Section 2.4).

2.4 - SPECTRAL ANALYSIS OF THE AUTO-NORMALIZED SCATTERING MATRIX S .

The above-reported new results lead to a very fundamental, *symbolic* spectral analysis of the block-traceless $(n+N)$ x $(n+N)$ auto-normalized scattering matrix S of a non-symmetric beam-forming network, defined by the expressions (4), (10), and (11) of Sections 1.3 , and 1.5 . This diagonalization of the matrix S is given by :

$$S = M_S \cdot \Lambda_S \cdot M_S^{-1} \qquad (33) \qquad\qquad S \cdot M_S = M_S \cdot \Lambda_S \qquad (33')$$

where the modal matrix M_S , and its inverse M_S^{-1} are expressed by :

$$M_S = \left|\begin{array}{c|c} M_{Pn} & -P_n^{-1/2} \cdot M_n \cdot M_{PN} \\ \hline M_N \cdot M_{Pn} \cdot \Lambda_{Pn}^{-1/2} & M_{PN} \end{array}\right| \qquad (34)$$

$$M_S^{-1} = \frac{1}{2}\left|\begin{array}{c|c} M_{Pn}^{-1} & M_{Pn}^{-1} \cdot P_n^{-1/2} \cdot M_n \\ \hline M_{PN}^{-1} \cdot M_N \cdot P_n^{-1/2} & M_{PN}^{-1} \end{array}\right| \qquad (35)$$

while the corresponding spectral matrix Λ_S is given by :

$$\Lambda_S = \left| \begin{array}{c|c} \Lambda_{SC}^{1/2} & 0 \\ \hline 0 & -\Lambda_{SD}^{1/2} \end{array} \right| \qquad (36)$$

The expression (33') can be expanded, using (34) and (36), and can be split into the four equivalent transforms :

$$S_2 \cdot \left(M_N \cdot M_{Pn} \cdot \Lambda_{Pn}^{-1/2} \right) = M_{Pn} \cdot \Lambda_{SC}^{1/2} \qquad (37)$$

$$S_2 \cdot M_{PN} = \left(P_n^{-1/2} \cdot M_n \cdot M_{PN} \right) \cdot \Lambda_{SD}^{1/2} \qquad (38)$$

$$S_3 \cdot M_{Pn} = \left(M_N \cdot M_{Pn} \cdot \Lambda_{Pn}^{-1/2} \right) \cdot \Lambda_{SC}^{1/2} \qquad (39)$$

$$S_3 \cdot \left(P_n^{-1/2} \cdot M_n \cdot M_{PN} \right) = M_{PN} \cdot \Lambda_{SD}^{1/2} \qquad (40)$$

Most remarkably, the block $\Lambda_{S4} = -\Lambda_{SD}^{1/2}$ includes $N - n$ identically-zero eigenvalues, that correspond to the $N - n$ identically-zero eigenvalues of the spectral matrix Λ_{PN} of the matrix-product P_N , while the remaining n eigenvalues are *equal* to those in block $\Lambda_{S1} = \Lambda_{SC}^{1/2}$, save for a *sign change* . The $2n$ non-zero eigenvalues in the spectral matrix Λ_S , and the corresponding eigenvectors, identify the two sets of n *'forward'*, and n *'backward'* , *'natural transmission modes'* of any given non-symmetric beam-forming network, while the $N - n$ eigenvectors, that correspond to the zero-eigenvalues in block Λ_{S4} , identify its *'natural cut-off modes'* . These are the $N - n$ interface-2 a_j voltage-wave vectors, for which the corresponding *'received'* interface-1 $b_i = S_2 \cdot a_j$ vectors are identically zero. The so-identified a_j vectors constitute the *'null-space'* of the $n \times N$ matrix-block S_2 , and form the columns of its rank $N - n$ *'complete right annihilator'* matrix S_{20} [2 , 3] . The $(n+N)$-port beam-forming network performs, under each of these excitations, as a *'multiport hybrid'* , with the n interface-1 ports being all simultaneously *'totally decoupled'* , or (in the terminology of directional couplers) *'vestigial'* .

2.5 - THE TWO RECTANGULAR ABCD-MATRICES K_F AND K_B .

Two rectangular ABCD-matrices, that linearly relate the interface-1 (V_i , I_i) , and the interface-2 (V_j , I_j) bi-vectors, have been defined, and proved to be fully equivalent to the Z-matrix $Z_{(n+N)}$ of an

$(n+N)$-port beam-forming network. The $2n$ x $2N$ *'forward'* ABCD-matrix K_F is defined by :

$$\begin{vmatrix} V_i \\ - - \\ I_i \end{vmatrix} = K_F \cdot \begin{vmatrix} V_j \\ - - - \\ -I_j \end{vmatrix} = \left| \begin{array}{c|c} A & B \\ \hline C & D \end{array} \right| \cdot \begin{vmatrix} V_j \\ - - - \\ -I_j \end{vmatrix} \tag{41}$$

while the $2N$ x $2n$ *'backward'* ABCD-matrix K_B is similarly defined by :

$$\begin{vmatrix} V_j \\ - - - \\ I_j \end{vmatrix} = K_B \cdot \begin{vmatrix} V_i \\ - - - \\ -I_i \end{vmatrix} = \left| \begin{array}{c|c} \alpha & \beta \\ \hline \gamma & \delta \end{array} \right| \cdot \begin{vmatrix} V_i \\ - - - \\ -I_i \end{vmatrix} \tag{42}$$

Two mutually-equivalent expressions of the four n x N blocks A , B , C , D of K_F , and of the four N x n blocks α , β , γ , δ of K_B have been obtained, by rather convoluted, indirect procedures :

$$A = \frac{1}{2}\left(I_n + S_C^{-1}\right) \cdot S_2 = P_n^{-1} \cdot M_n \tag{43}$$

$$B = -\frac{1}{2}\left(I_n - S_C^{-1}\right) \cdot S_2 \cdot Z_{I2} = \left(I_n - P_n\right) \cdot P_n^{-1} \cdot M_n \cdot Z_4 \tag{44}$$

$$C = -\frac{1}{2} Z_{II}^{-1} \cdot \left(I_n - S_C^{-1}\right) \cdot S_2 = Z_1^{-1} \cdot P_n^{-1} \cdot M_n \tag{45}$$

$$D = \frac{1}{2} Z_{II}^{-1} \cdot \left(I_n + S_C^{-1}\right) \cdot S_2 \cdot Z_{I2} = Z_1^{-1} \cdot P_n^{-1} \cdot M_n \cdot Z_4 \tag{46}$$

$$\alpha = \frac{1}{2} S_3 \cdot \left(I_n + S_C^{-1}\right) = M_N \cdot P_n^{-1} \tag{47}$$

$$\beta = -\frac{1}{2} S_3 \cdot \left(I_n - S_C^{-1}\right) \cdot Z_{II} = M_N \cdot \left(I_n - P_n\right) \cdot P_n^{-1} \cdot Z_1 \qquad (48)$$

$$\gamma = -\frac{1}{2} Z_{I2}^{-1} \cdot S_3 \cdot \left(I_n - S_C^{-1}\right) = Z_4^{-1} \cdot M_N \cdot P_n^{-1} \qquad (49)$$

$$\delta = \frac{1}{2} Z_{I2}^{-1} \cdot S_3 \cdot \left(I_n + S_C^{-1}\right) \cdot Z_{II} = Z_4^{-1} \cdot M_N \cdot P_n^{-1} \cdot Z_1 \qquad (50)$$

The given *second* form of each of the eight ABCD-matrix blocks proves the matrices K_F , and K_B to be *rational* functions of the blocks Z_i of the Z-matrix $Z_{(n+N)}$. Further both the K_F , and K_B rectangular ABCD-matrices have been proved to be rigorously consistent with the impedance-matrix transforms (2), (3), (8), and (9) , and to correctly represent the $2n$ x $2n$ ABCD-matrix K_C of the Type-C connection, and the $2N$ x $2N$ ABCD-matrix K_D of the Type-D connection, with the two matrix products :

$$K_C = K_F \cdot K_B = \left| \begin{array}{c|c} \left(2 I_n - P_n\right) \cdot P_n^{-1} & 2 \left(I_n - P_n\right) \cdot P_n^{-1} \cdot Z_1 \\ \hline 2 Z_1^{-1} \cdot P_n^{-1} & Z_1^{-1} \cdot \left(2 I_n - P_n\right) \cdot P_n^{-1} \cdot Z_1 \end{array} \right| \qquad (51)$$

$$K_D = K_B \cdot K_F = \left| \begin{array}{c|c} M_N \cdot \left(2 I_n - P_n\right) \cdot P_n^{-2} \cdot M_n & 2 M_N \cdot \left(I_n - P_n\right) \cdot P_n^{-2} \cdot M_n \cdot Z_4 \\ \hline 2 Z_4^{-1} \cdot M_N \cdot P_n^{-2} \cdot M_n & Z_4^{-1} \cdot M_N \cdot \left(2 I_n - P_n\right) \cdot P_n^{-2} \cdot M_n \cdot Z_4 \end{array} \right| \qquad (52)$$

Finally, if $n < N$, as it is here assumed to be, the $2n$ x $2N$ ABCD-matrix K_F has a $2n$ x $2\,(N - n)$ complete right annihilator matrix K_{F0} with $2\,(N - n)$ columns, that represent interface-2 voltage/current excitation bi-vectors that simultaneously generate *zero* interface-1 voltages, and currents.

2.6 - THE RECTANGULAR T-MATRICES T_F AND T_B .

Two rectangular, auto-normalized T-matrices, that linearly relate the interface-1 (b_i , a_i), and the interface-2 (a_j , b_j) voltage-wave bi-vectors, have been defined, and proved to be fully equivalent to the auto-normalized scattering matrix S of an $(n+N)$-port beam-forming network. The $2n$ x $2N$ *'forward'* T-matrix T_F is defined and expressed by :

$$\left| \begin{array}{c} b_i \\ \hline a_i \end{array} \right| = T_F \cdot \left| \begin{array}{c} a_j \\ \hline b_j \end{array} \right| = \left| \begin{array}{c|c} S_2 & 0 \\ \hline 0 & S_C^{-1} \cdot S_2 \end{array} \right| \cdot \left| \begin{array}{c} a_j \\ \hline b_j \end{array} \right| \qquad (53)$$

while the $2N$ x $2n$ *'backward'* T-matrix T_B is similarly defined and expressed by :

$$\begin{vmatrix} b_j \\ - - \\ a_j \end{vmatrix} = T_B \cdot \begin{vmatrix} a_i \\ - - \\ b_i \end{vmatrix} = \left|\begin{array}{c|c} S_2 & 0 \\ \hline 0 & S_3 \cdot S_C^{-1} \end{array}\right| \cdot \begin{vmatrix} a_i \\ - - \\ b_i \end{vmatrix} \qquad (54)$$

The given auto-normalized T-matrices rigorously represent the $2n$ x $2n$ auto-normalized T-matrix T_C of the Type-C connection, and the $2N$ x $2N$ auto-normalized T-matrix T_D of the Type-D connection, with the two matrix products :

$$\begin{vmatrix} b_i \\ a_i \end{vmatrix} = T_C \cdot \begin{vmatrix} a_k \\ b_k \end{vmatrix} = T_F \cdot T_B \cdot \begin{vmatrix} a_k \\ b_k \end{vmatrix} = \begin{vmatrix} S_C & 0 \\ 0 & S_C^{-1} \end{vmatrix} \cdot \begin{vmatrix} a_k \\ b_k \end{vmatrix} \qquad (55)$$

$$\begin{vmatrix} b_k \\ - - \\ a_k \end{vmatrix} = T_D \cdot \begin{vmatrix} a_j \\ - - \\ b_j \end{vmatrix} = T_B \cdot T_F \cdot \begin{vmatrix} a_j \\ - - \\ b_j \end{vmatrix} = \left|\begin{array}{c|c} S_D & 0 \\ \hline 0 & S_3 \cdot S_C^{-2} \cdot S_2 \end{array}\right| \cdot \begin{vmatrix} a_j \\ - - \\ b_j \end{vmatrix} = \left|\begin{array}{c|c} S_D & 0 \\ \hline 0 & S_D^S \end{array}\right| \cdot \begin{vmatrix} a_j \\ - - \\ b_j \end{vmatrix} \qquad (56)$$

Quite remarkably, the three-fold matrix product :

$$S_D^S = S_3 \cdot S_C^{-2} \cdot S_2 \qquad (57)$$

is a *'semi-inverse'* [2] of the matrix-block S_D , defined by the expressions (29) , and (31) , such that :

$$S_D^S \cdot S_D \cdot S_D^S = S_D^S \qquad (58) \qquad\qquad S_D \cdot S_D^S \cdot S_D = S_D \qquad (59)$$

3 - CONCLUSIONS : A rigorous analysis of two idealized, cascaded connections of non-symmetric beam-forming networks leads to the identification, and formal definition of the set of linearly independent, natural transmission modes. These are represented by a vector-basis spanning the space of all phased array aperture distributions that can be *exactly* synthesized, while many more can be adequately approximated by *least squares* solutions. The given results prove that electronic beam steering can be performed with a number of electronic controls *much smaller* than the number of array elements.

[1] R. A. Speciale,'Advanced Design of Phased Array Beam-Forming Networks,' Proc. of ACES 96.
[2] J. S. Frame,'Matrix Functions and Applications,' IEEE Spectrum, March-July, 1964.
[3] S. Wolfram,"Mathematica,' pp. 660-662, and 832.

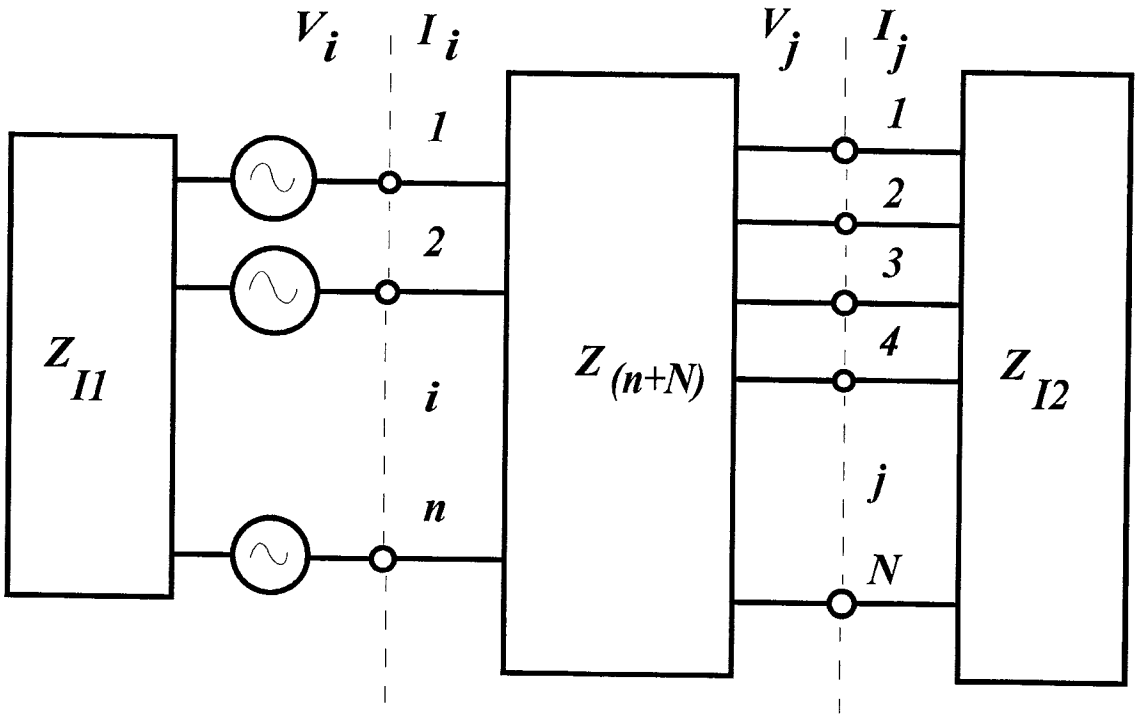

Figure 1 - Unconditional, Bilateral Image-Impedance Match: Forward-Wave, n-Phase Excitation, with Arbitrary Wave Amplitudes and Phases.

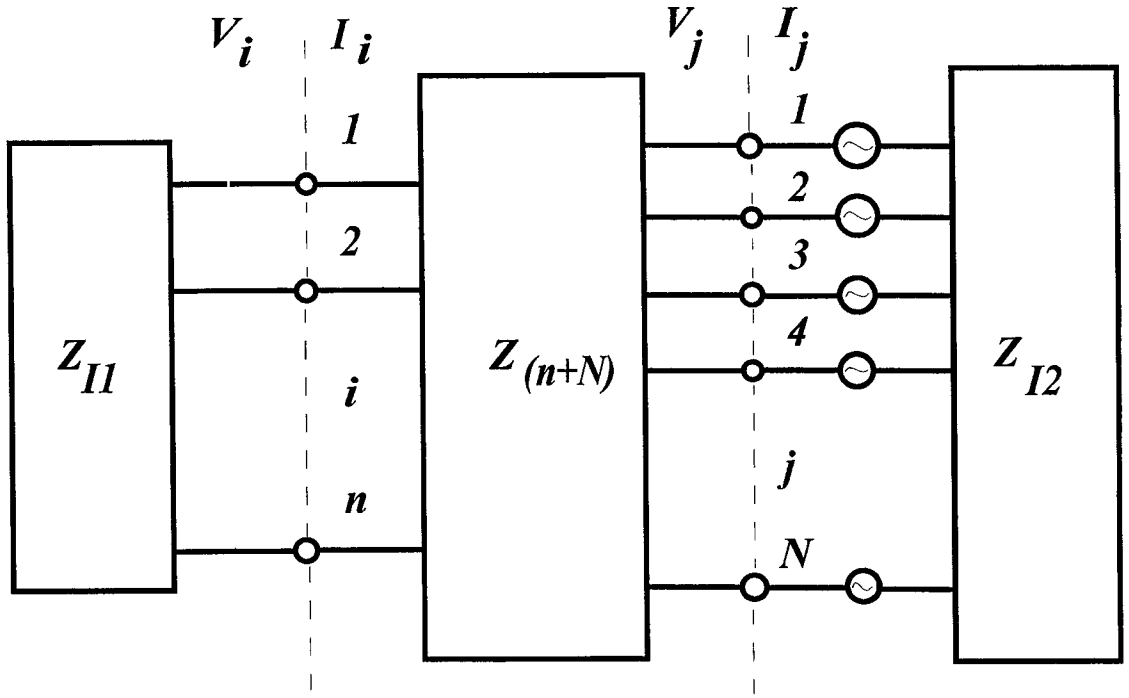

Figure 2 - Unconditional, Bilateral Image-Impedance Match: Backward-Wave, N-Phase Excitation, with Arbitrary Wave Amplitudes and Phases.

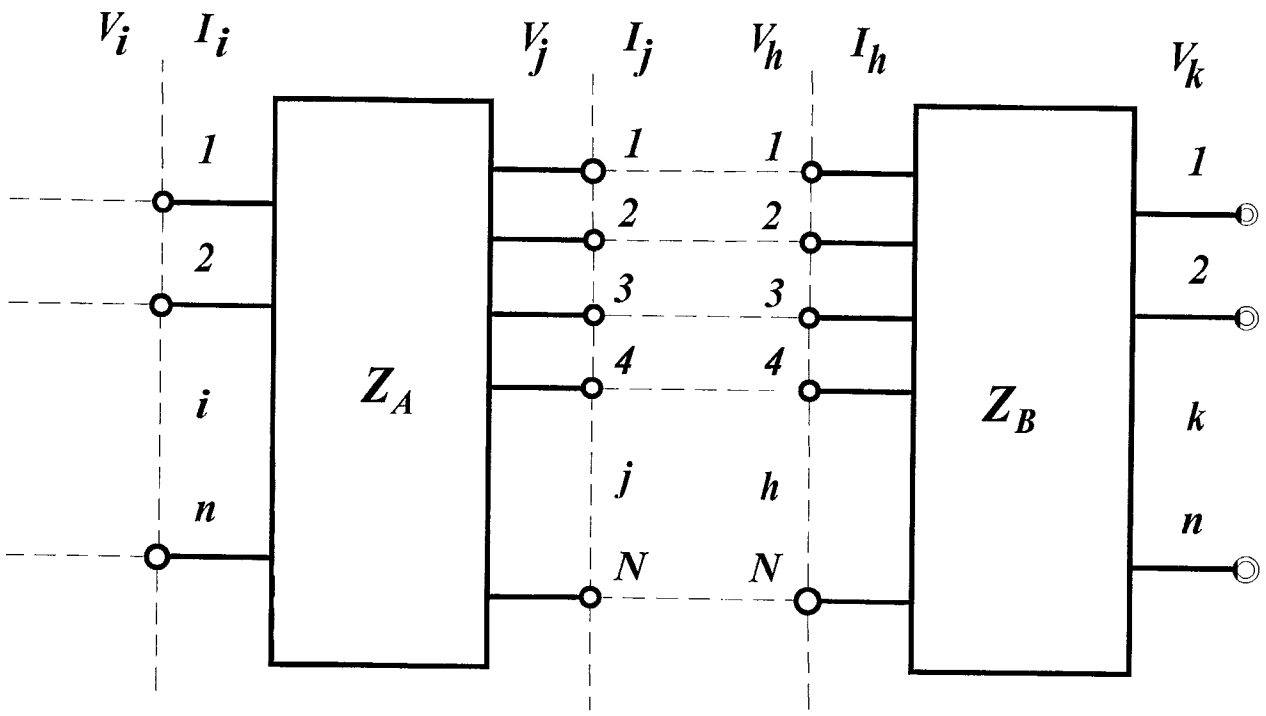

Figure 3 - Type-C Cascaded Connection of Two Impedance-Matched Enantiomorphic (n+N)-Port Beam-Forming Networks A and B.

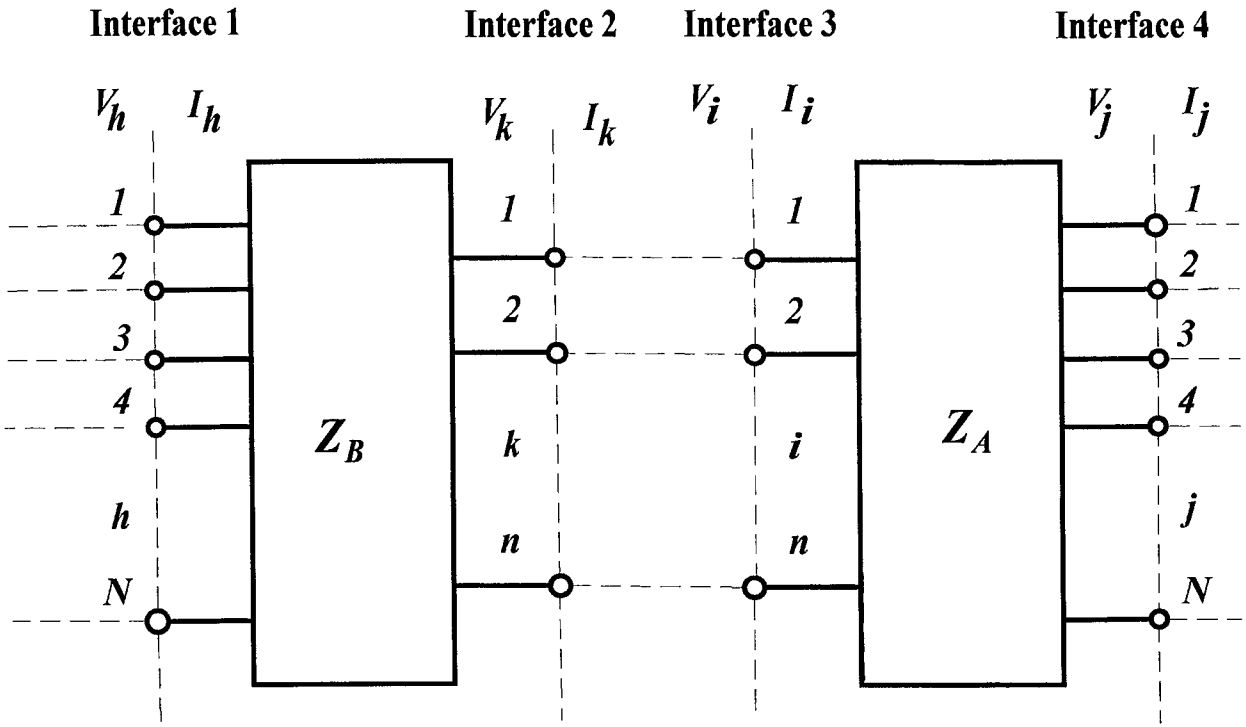

Figure 4 - Type-D Cascaded Connection of Two Impedance-Matched Enantiomorphic (n+N)-Port Beam-Forming Networks A and B.

NEW RESULTS IN THE SYNTHESIS OF APERTURE-FIELD DISTRIBUTIONS FOR ULTRA-HIGH GAIN PHASED ARRAYS.

Ross A. Speciale

Redondo Beach, California

Renewed analytical and numerical studies of rather unusual aperture-field distributions for ultra-high-gain phased arrays have generated interesting new results, and have provided a deeper insight, and understanding of the underlaying radiation process. The analyzed aperture-distributions are planar, and are synthesized as carefully-weighted linear combinations of *TE* and *TM* cylindrical wave-modes of equal azimuthal order ' *m* ' . The used *TE* and *TM* cylindrical modes are mathematically defined as linear combinations of W. W. Hansen's *M* and *N* basis vector-fields, using only Bessel functions of the first kind to express the radial dependence of the five *TE* , and of the five *TM* field-components . The computed analytical expression of the radial component S^*_R of the complex Poynting Vector show that the radial energy-flow density of the combined *TE* and *TM* aperture-fields becomes identically zero, *everywhere* in the half-space above the $Z = 0$ plane of the aperture, if the two mode-types are linearly combined with *equal weights*. At the same time, however, the axial component S^*_Z of the complex Poynting Vector of the combined *TE* and *TM* fields is non-zero, and oriented along the positive Z-axis, in the direction of the desired ultra-high gain beam. It appears then that the linear combination of *TE* and *TM* cylindrical wave-modes, with equal order *m* and weights, results in *total cancellation* of the radial energy-flow, *everywhere* in the $Z > 0$ radiation half-space, at all radial, azimuthal, and axial positions. Present analysis efforts are being directed towards the determination of an optimum, finite aperture-truncation radius, and of an optimum radial *'filtering'* (or *'windowing'*). As no rigorous procedure is as yet known for determining the optimum combination of truncation radius and radial filter evolution, a rather heuristic approach is used. Analytical integration of the truncated and filtered aperture-field distributions is being attempted, by expanding the used truncation filter in terms of Bessel functions of the first kind. Closed-form integration of the radiated far-field of the truncated aperture, in cylindrical coordinates, appears possible.

The three components of the total electric field, in cylindrical coordinates, are expressed by :

$$E_R = E_R^{TE} + E_R^{TM} = -\,i\,e^{im\varphi}\,\frac{a}{R}\left[\left(1+\beta\frac{K_Z}{K}\right) m\,J_m(K_R R) - \beta\frac{K_Z}{K}\,(K_R R)\;J_{m+1}(K_R R)\right] e^{iK_Z z} \qquad (1)$$

$$E_\varphi = E_\varphi^{TE} + E_\varphi^{TM} = e^{im\varphi}\,\frac{a}{R}\left[\left(1+\beta\frac{K_Z}{K}\right) m\,J_m(K_R R) - (K_R R)\,J_{m+1}(K_R R)\right] e^{iK_Z z} \qquad (2)$$

$$E_Z = E_Z^{TM} = -\,e^{im\varphi}\,\frac{a}{R}\,\beta\frac{K_R}{K}\,(K_R R)\;J_m(K_R R)\,e^{iK_Z z} \qquad (3)$$

while the three components of the complex Poynting Vector, in cylindrical coordinates, are given by :

$$S^*_Z = \frac{1}{2\eta}\left(\frac{a}{R}\right)^2 \{ 2\left(1 + \beta\,\frac{K_Z}{K}\right)\left(\beta + \frac{K_Z}{K}\right) m\, J_m(K_R R)\,[\, m\, J_m(K_R R) - (K_R R)\, J_{m+1}(K_R R)\,] \tag{4}$$

$$+ (1 + \beta^2)\,\frac{K_Z}{K}\,(K_R R)^2\, J^2_{m+1}(K_R R)\,\}$$

$$S^*_\varphi = -\frac{1}{2\eta}\left(\frac{a}{R}\right)^2 \frac{K_R}{K}\,(K_R R)\,\{\left[\, 1 + \beta\left(\beta + 2\,\frac{K_Z}{K}\right)\right] m\, J^2_m(K_R R) \tag{5}$$

$$- 2\,\beta\,\frac{K_Z}{K}\,(K_R R)\, J_m(K_R R)\, J_{m+1}(K_R R)\,\}$$

$$S^*_R = -(1 - \beta^2)\,\frac{1}{2\eta}\left(\frac{a}{R}\right)^2 \frac{K_R}{K}\,(K_R R)\,[\, m\, J_m(K_R R) - (K_R R)\, J_{m+1}(K_R R)\,]\, J_m(K_R R) \tag{6}$$

The quantity a is an arbitrary amplitude-scaling factor for all the aperture fields, while the parameter $\beta = b / a$ is the arbitrary ratio of the amplitude factor b of the *TM* mode field-components to the amplitude a of the *TE* mode components. As the expression (6) clearly shows, the radial component S^*_R of the complex Poynting Vector, that expresses the radial energy-flow density, becomes identically zero, everywhere in the $Z > 0$ half-space, for $\beta = \pm 1$, i. e. when the *TE* , and *TM* field components have equal amplitude factors and phases. In all the given expressions the normalized radial wave-number K_R / K , is related to the axial wave-number by :

$$\frac{K_R}{K} = \pm\sqrt{1 - \left(\frac{K_Z}{K}\right)^2} = \pm\sqrt{1 - \cos^2\gamma} = \sin\gamma \tag{7}$$

where γ is the angle between the propagation-vector K and the Z-axis.

The results of preliminary computations, with $m = \beta = a = 1$, show that the electric-field components E_R , E_φ , and E_Z (Figure 1) have a decaying oscillatory radial dependence, while the axial component S^*_Z of the complex Poynting Vector is sharply peaked at the center of the circular aperture (Figure 2) . The azimuthal component S^*_φ of the complex Poynting Vector is zero a the center of the aperture, and has a mostly non-decaying oscillatory radial dependence. The axial ratio $\rho = E_\varphi / E_R$ is exactly equal to 1 , on axis (at the center of the aperture), thus representing pure circular polarization, and evolves through many poles and zeros with increasing radius.

[1] J. A. Stratton, Electromagnetic Theory, Sec. 6.10, p. 371, Eq. (55).

[2] Speciale R. A. , and Wacker P. F. , "Ultra High Gain Antenna Arrays," 6th Annual Review of Progress in Applied Computational Electromagnetics, Naval Postgraduate School, Monterey, California, March 19 - 22 , 1990 , pp. 241 - 252.

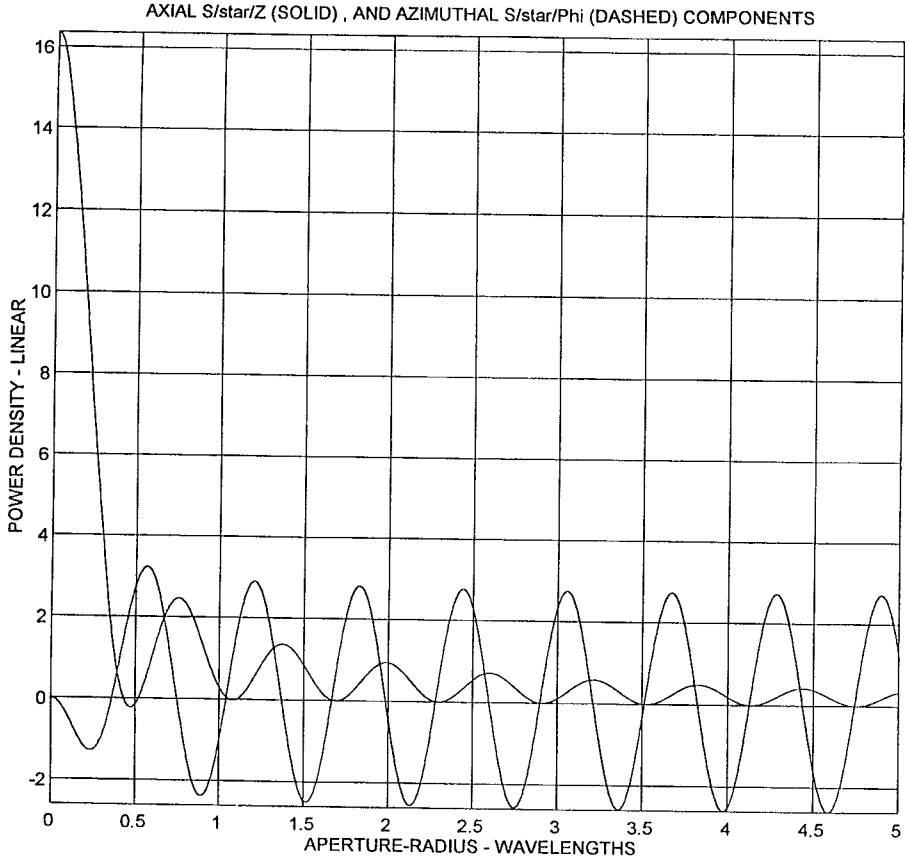

Figure 2 - Axial (Solid) , and Azimuthal (Dashed) Components of the Complex Poynting Vector , for m = 1 , Beta = 1 , and Kz/K = 0.5774 .

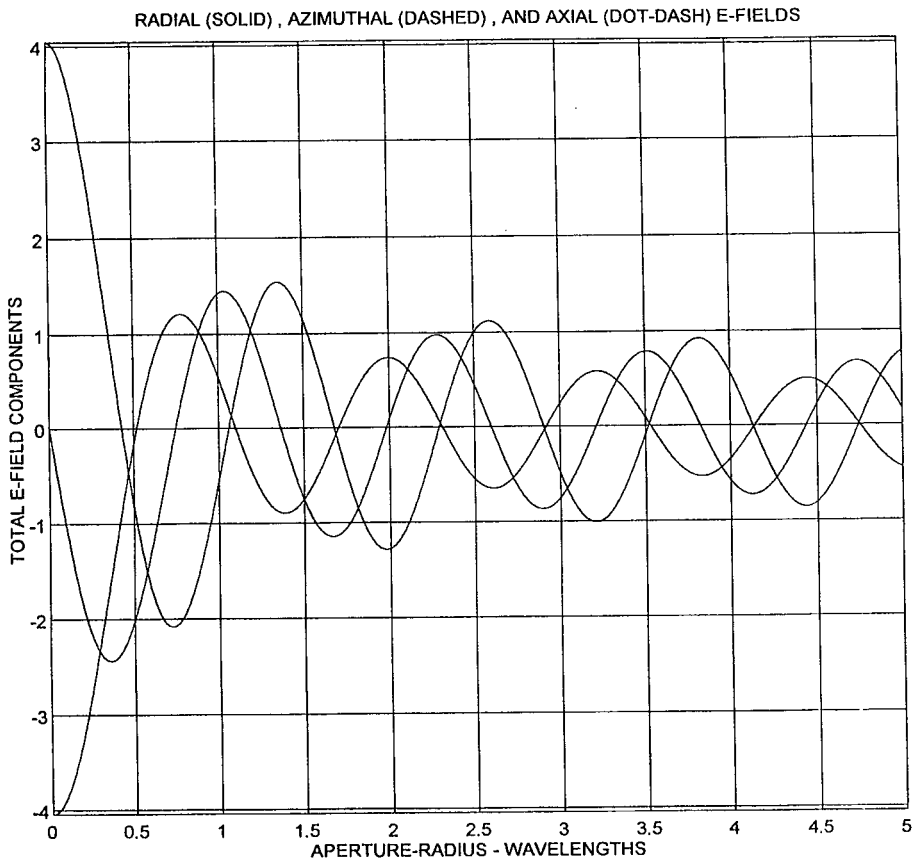

Figure 1 - Radial (Solid) , Azimuthal (Dashed) , and Axial (Dot-Dash) Components of the Total Electric Field , for m = 1 , Beta = 1 , and Kz/K = 0.5774 .

ADVANCED DESIGN OF PHASED ARRAY BEAM-FORMING NETWORKS

Ross A. Speciale

Redondo Beach, California

ABSTRACT

Recent, very general, and fundamental results, in the theory of electrically large microwave networks, lead to new, advanced designs of high-efficiency beam-forming networks, for high-directivity, electronically-steered phased arrays.

On the basis of the rigorous, new results, the beam-forming networks of electronically-steered phased arrays can be simultaneously impedance-matched to any given set of radiating elements on one side, and to any given set of mutually-coherent, phase- and amplitude-controlled microwave sources on the other. Further, the impedance-match attained in transmission, also holds in reception, as long as the used set of mutually-coherent receivers has the same internal impedances as the used set of sources.

The attained impedance-match simultaneously accounts for both the electromagnetic proximity coupling between all the radiating array elements, and for any given internal cross-coupling of the set of sources, in transmission, or of the set of receivers, in reception.

The resulting impedance-match is totally independent from the amplitude, and phase settings of the sources, in transmission, and from the direction of the incoming beam, in reception, completely suppressing the notorious array-blindness effect, for all beam directions. Further, beam-forming networks can be designed with, besides prescribed impedance match, also prescribed transmission responses, in both the transmission and reception modes, and with a number of beam-steering control components, much smaller than the number of array elements.

1 - WAVE SCATTERING AND IMPEDANCE NORMALIZATION.

It is generally known that a one-port load, with impedance Z_L , connected at the end of a single transmission line, with wave-impedance Z_o , generates a reflected wave b , that is related to the incident wave a by the (single-mode) reflection coefficient :

$$\Gamma = \frac{b}{a} = \frac{Z_L - Z_o}{Z_L + Z_o} \qquad (1)$$

The given expression of the reflection coefficient Γ is consistent with the definitions of the incident, and reflected voltage-waves :

$$a = \frac{1}{2}\left(V + Z_o I \right) \qquad (2) \qquad\qquad b = \frac{1}{2}\left(V - Z_o I \right) \qquad (3)$$

The scalar wave-impedance Z_o of the used transmission line is clearly an essential quantity, in the definitions of the incident and reflected waves a , and b , and of the reflection coefficient Γ , and it is quite obvious that the same one-port load with impedance Z_L , would generate a totally different reflection Γ^*, if it were connected at the end of a transmission line with a different wave-impedance Z_o^* [1] :

$$\Gamma^* = \frac{b^*}{a^*} = \frac{Z_L - Z_o^*}{Z_L + Z_o^*} = \Gamma - \frac{1 - \Gamma^2}{1 - \gamma\,\Gamma}\,\gamma \qquad (4)$$

where the lower-case symbol γ stands for :

$$\gamma = \frac{Z_o^* - Z_o}{Z_o^* + Z_o} \qquad (5)$$

The wave-impedance Z_o (or Z_o^*) of the used transmission line is said to establish a basis for the *normalization* of the waves a , and b , and of the reflection coefficient Γ (or Γ^*).

Similarly, an n-port load-network N, characterized by a (non-necessarily diagonal) n x n impedance matrix Z_L , connected to the ends of n transmission lines, each with wave-impedance Z_{oi} ($i = 1, 2, \ldots, n$), generates n outgoing waves b_i , that are related to the corresponding ingoing waves a_i by the (single-mode) scattering matrix :

$$S = \left(Z_L - Z_o \right) \cdot \left(Z_L + Z_o \right)^{-1} \qquad (6)$$

so that :

$$b_i = S \cdot a_i \qquad (7)$$

The given expression of the scattering matrix S is consistent with the definitions of the *ingoing* , and *outgoing* voltage-waves a_i , and b_i :

$$a_i = \frac{1}{2}\left(V_i + Z_0\, I_i \right) \qquad (8) \qquad\qquad b_i = \frac{1}{2}\left(V_i - Z_0\, I_i \right) \qquad (9)$$

If the used n transmission lines with wave-impedances Z_{oi} are *not* electromagnetically *coupled* to one another, the n x n wave-normalization matrix Z_o is *diagonal* :

$$Z_o = Diag\left(z_{o1}, z_{o2}, \ldots, z_{on} \right) \qquad (10)$$

The selected values of the n wave-impedances Z_{oi} , of the used transmission lines, must be consistent with the intended, ultimate application of the n-port load-network, for the scattering matrix S to faithfully

represent the actual scattering response, in the intended system environment.

Most frequently, however, the scattering matrix S is only used as an experimentally accessible representation of the network scattering response, in an appropriate *reference* environment, and then the values of the n wave-impedances Z_{oi} are all set equal to the nominal, scalar wave-impedance z_o of the used measurement system, as defined by at least one physical calibration standard [2-4].

In this reference case, the normalizing impedance matrix Z_o in expressions (6)-(10) becomes a *scalar* matrix :

$$Z_o = Diag\left(z_o , z_o , \ldots , z_o \right) \qquad \textbf{(10')}$$

It is quite obvious, however, that an n-port load-network N, characterized by a *non-diagonal* impedance-matrix Z_L (including many non-zero cross-coupling elements $Z_L(i,j)$, with $i \neq j$), can never appear to be matched ($S = 0$) to a set of n uncoupled transmission lines, or any other network similarly characterized by an n x n *diagonal* impedance matrix.

This is definitely true, in particular, if the considered n-port load-network N is physically composed of the set of n radiating elements of a phased array, as defined at the n circuit-ports, where very specific sets of mutually-coherent, amplitude- and phase-controlled array-excitation signals are injected, to generate the various, desired radiated beams in transmission.

The impedance-mismatch between the set of n array elements, and the beam-forming network of any given electronically-steered phased array, the steering-dependent impedance-mismatch that is due to the electromagnetic proximity coupling between the necessarily closely-spaced array elements, is notoriously known to introduce a quite unacceptable, total array blindness, for selected angular beam-pointing directions, besides obviously adversely affecting the array efficiency in all beam-pointing directions.

Physically realizable conditions for attaining impedance match between the beam-forming network and the set of radiating elements on one side, and between the beam-forming network and the set of mutually-coherent sources, on the other, can only be formulated by introducing the rather unconventional concept of a *non-diagonal* normalizing impedance matrix Z_o, such as the '*characteristic-impedance matrix*' of a set of mutually-coupled transmission lines.

2 - CONDITIONS FOR SIMULTANEOUS, BILATERAL IMPEDANCE-MATCH.

We are considering here a linear, *non-necessarily reciprocal* beam-forming network, shown in figures 1 and 2, that has n ports on its left-side interface-1, connected to a set of n mutually-coherent microwave sources, in transmission, or to a set of n mutually-coherent receivers, in reception, while the N ports on the right-side interface-2 are connected to the N radiating elements of an electronically-steered phased array. The considered, linear beam-forming network is characterized by its $(n + N)$ x $(n + N)$ impedance matrix $Z_{(n+N)}$, that for $n \leq N$ can be asymmetrically partitioned in the four matrix blocks Z_i :

$$Z_{(n+N)} = \left| \begin{array}{c|c} Z_1 & Z_2 \\ \hline Z_3 & Z_4 \end{array} \right| \qquad \textbf{(11)}$$

where Z_1 is n x n , Z_2 is n x N , Z_3 is N x n , and Z_4 is N x N .

At the same time, the set of amplitude- and phase-controlled sources (in transmission), or of receivers (in reception), connected to the n ports of the left-side interface-1, is characterized by the n x n , non-diagonal, internal impedance matrix Z_{I1} , while the set of N radiating array elements, connected to the right-side interface-2, is characterized by the N x N , non-diagonal internal impedance matrix Z_{I2} , that includes all the numerous non-zero cross-terms due to the mutual electromagnetic proximity couplings between elements.

Using the non-diagonal impedance matrices Z_{I1} , and Z_{I2} as the normalizing impedance matrices for the interface-1 , and interface-2 respectively, we define the total normalizing matrix Z_o in the block-matrix form :

$$Z_o = \left| \begin{array}{c|c} Z_{I1} & 0 \\ \hline 0 & Z_{I2} \end{array} \right| \qquad (12)$$

This very specific new definition of the normalizing impedance matrix Z_o leads to a re-definition of the ingoing, and outgoing voltage-wave vectors a_i , and b_i of interface-1 , and a_j , and b_j of interface-2 , that are now expressed by the vector-matrix relations :

$$\left| \begin{array}{c} a_i \\ \hline a_j \end{array} \right| = \frac{1}{2} \left[\left| \begin{array}{c} V_i \\ \hline V_j \end{array} \right| + \left| \begin{array}{c|c} Z_{I1} & 0 \\ \hline 0 & Z_{I2} \end{array} \right| \cdot \left| \begin{array}{c} I_i \\ \hline I_j \end{array} \right| \right] \qquad (13)$$

$$\left| \begin{array}{c} b_i \\ \hline b_j \end{array} \right| = \frac{1}{2} \left[\left| \begin{array}{c} V_i \\ \hline V_j \end{array} \right| - \left| \begin{array}{c|c} Z_{I1} & 0 \\ \hline 0 & Z_{I2} \end{array} \right| \cdot \left| \begin{array}{c} I_i \\ \hline I_j \end{array} \right| \right] \qquad (14)$$

that can be expanded, and split in the four equivalent expressions :

$$a_i = \frac{1}{2}\left(V_i + Z_{II} \cdot I_i \right) \qquad (15) \qquad b_i = \frac{1}{2}\left(V_i - Z_{II} \cdot I_i \right) \qquad (16)$$

$$a_j = \frac{1}{2}\left(V_j + Z_{I2} \cdot I_j \right) \qquad (17) \qquad b_j = \frac{1}{2}\left(V_j - Z_{I2} \cdot I_j \right) \qquad (18)$$

The voltage-waves a_i , and b_i would physically exist and propagate (in mutually opposite directions) along a set of n coupled transmission lines, with characteristic impedance matrix [5,6] $Z_{o1} = Z_{II}$, if one such set of coupled lines would be inserted, at the physical location of interface-1 , between the beam-forming network and the set of sources (in transmission), or the set of receivers (in reception).

Similarly, the voltage-waves a_j , and b_j would physically exist and propagate along a second set of N coupled transmission lines, with characteristic impedance matrix $Z_{o2} = Z_{I2}$, if one such set of coupled lines would be inserted, at the physical location of interface-2, between the beam-forming network and the set of the radiating array elements.

In both cases, the voltage-waves a_i , b_i would represent the mutually-orthogonal fundamental wave-modes (the *'normal modes'* !) of the first set of n coupled lines, while the voltage-waves a_j , b_j would similarly represent the orthogonal modes of the second set of N lines.

A clear understanding of the given physical interpretation of the voltage-wave re-definitions (13)-(18) is obviously crucial to the determination of *simultaneous*, multiport impedance-match conditions for both network interfaces.

The desired conditions for simultaneous impedance match at both beam-forming network interfaces are expressed by the very specific block-traceless scattering matrix S , defined as :

$$S = \left| \begin{array}{c|c} 0 & S_2 \\ \hline S_3 & 0 \end{array} \right| \qquad (19)$$

that is consistent with the voltage-wave vector relations:

$$b_i = S_2 \cdot a_j \qquad (20) \qquad\qquad b_j = S_3 \cdot a_i \qquad (21)$$

It is then quite expedient to rewrite the expression (6) as:

$$S \cdot \left(Z_L + Z_o \right) = Z_L - Z_o \qquad (6')$$

which, by substituting $Z_L = Z_{(n+N)}$, Z_o from (12), and S from (19), becomes:

$$\left|\begin{array}{c|c} 0 & S_2 \\ \hline S_3 & 0 \end{array}\right| \cdot \left|\begin{array}{c|c} Z_1 + Z_{I1} & Z_2 \\ \hline Z_3 & Z_4 + Z_{I2} \end{array}\right| = \left|\begin{array}{c|c} Z_1 - Z_{I1} & Z_2 \\ \hline Z_3 & Z_4 - Z_{I2} \end{array}\right| \qquad (22)$$

The $(n + N)$ x $(n + N)$ matrix expression (22) can be expanded, and split in the four equivalent expressions:

$$S_2 \cdot Z_3 = Z_1 - Z_{I1} \qquad (23) \qquad\qquad S_2 \cdot \left(Z_4 + Z_{I2} \right) = Z_2 \qquad (24)$$

$$S_3 \cdot \left(Z_1 + Z_{I1} \right) = Z_3 \qquad (25) \qquad\qquad S_3 \cdot Z_2 = Z_4 - Z_{I2} \qquad (26)$$

that, by eliminating the blocks S_2, and S_3, lead to the two simultaneous impedance-match conditions :

$$Z_{I1} = Z_1 - S_2 \cdot Z_3 = Z_1 - Z_2 \cdot \left(Z_4 + Z_{I2} \right)^{-1} \cdot Z_3 \qquad (27)$$

$$Z_{I2} = Z_4 - S_3 \cdot Z_2 = Z_4 - Z_3 \cdot \left(Z_1 + Z_{I1} \right)^{-1} \cdot Z_2 \qquad (28)$$

The two non-linear matrix expressions (27), and (28), together with :

$$S_2 = Z_2 \cdot \left(Z_4 + Z_{I2} \right)^{-1} \qquad (24')$$

$$S_3 = Z_3 \cdot \left(Z_1 + Z_{II} \right)^{-1} \qquad (25')$$

clearly relate the four blocks Z_i ($i = 1, 2, \ldots, 4$) of the $(n + N)$ x $(n + N)$ impedance matrix Z_{n+N}, of the beam-forming network N, to the internal impedance matrices Z_{II}, of the set of sources (or of receivers), and Z_{I2}, of the set of radiating array elements, and to the two rectangular blocks S_2 (n x N) and S_3 (N x n) of the uniquely specific scattering matrix S, that is normalized to the (non-diagonal) matrices Z_{II}, at interface-1, and Z_{I2}, at interface-2.

Explicit, closed-form matrix expressions of the four matrix-blocks Z_i, as functions of the four matrix-blocks Z_{II}, Z_{I2}, S_2, and S_3 are given in the following Section 4.

It is, however, conceptually very instructive to first establish the physical significance of the expressions (27), and (28), that clearly establish simultaneous conditions for attaining a bilateral impedance match between the beam-forming network N, the set of sources (or of receivers), connected at interface-1, and the set of array elements, connected at interface-2.

3 - PHYSICAL INTERPRETATION OF THE IMPEDANCE-MATCHING CONDITIONS.

It is fairly easy to prove that the impedance-transformation properties of the beam-forming network N of figures 1, and 2, are rigorously represented by the two matrix transforms :

$$Z_{in1} = Z_1 - Z_2 \cdot \left(Z_4 + Z_{L2} \right)^{-1} \cdot Z_3 \qquad (29)$$

$$Z_{in2} = Z_4 - Z_3 \cdot \left(Z_1 + Z_{L1} \right)^{-1} \cdot Z_2 \qquad (30)$$

where the n x n matrix Z_{L1}, and the N x N matrix Z_{L2} are here assumed to characterize a totally arbitrary n-port load-network L_1, and a totally arbitrary N-port load-network L_2, connected in turn to the left-side interface-1, and respectively to the right-side interface-2, of the beam-forming network N.

Similarly, the n x n matrix Z_{in1} on the left-side of (29), represents the transformed impedance matrix, seen at the left-side *'input'* interface-1, with the N-port load-network L_2 (with impedance matrix Z_{L2}) connected at the right-side *'output'* interface-2, and the N x N matrix Z_{in2}, on the left-side of (30), represents the transformed impedance matrix, seen at the right-side *'input'* interface-2, with the n-port load-network L_1 (with impedance matrix Z_{L1}) connected at the left-side *'output'* interface-1.

The physical significance of the simultaneous impedance-match conditions (27) and (28) becomes then obvious, by recognizing the formal analogy between those expressions, and the impedance-transformation mappings (29), and (30).

Clearly, the simultaneous impedance-match conditions (27), and (28) state that the internal impedance matrix Z_{I2}, of the set of radiating array elements must electrically transform, through the beam-forming network N (from interface-2 to interface-1) to an *'input'* impedance matrix Z_{in1} *equal* to the internal impedance matrix Z_{II} of the set of sources (or of receivers), while at the same time the internal impedance matrix Z_{II} of the set of sources (or of receivers) must electrically transform (from interface-1 to interface-2) to an *'input'* impedance matrix Z_{in2} *equal* to the internal impedance matrix Z_{I2} of the set of radiating array elements.

The simultaneous impedance-match conditions (27), and (28) obviously provide a far-reaching, fundamental generalization of the classical concepts of *scalar* image impedances of *two-port* networks, to the domain of linear, electrically-large, *multiport* microwave networks.

4 - CLOSED-FORM EXPRESSIONS OF THE FOUR BLOCKS Z_i OF THE MATRIX $Z_{(n+N)}$.

It is fairly easy to solve the set of four, simultaneous matrix equations (23)-(26) (Appendix 2 of the original, unpublished monograph is available from the author), for the four blocks Z_i ($i = 1, 2, \ldots, 4$) of the impedance matrix $Z_{(n+N)}$ of the $(n + N)$-port beam-forming network :

$$Z_1 = \left(I_n - S_2 \cdot S_3 \right)^{-1} \cdot \left(I_n + S_2 \cdot S_3 \right) \cdot Z_{11} \tag{31}$$

$$Z_2 = 2 \left(I_n - S_2 \cdot S_3 \right)^{-1} \cdot S_2 \cdot Z_{12} \tag{32}$$

$$Z_3 = 2 \left(I_N - S_3 \cdot S_2 \right)^{-1} \cdot S_3 \cdot Z_{11} \tag{33}$$

$$Z_4 = \left(I_N - S_3 \cdot S_2 \right)^{-1} \cdot \left(I_N + S_3 \cdot S_2 \right) \cdot Z_{12} \tag{34}$$

The closed-form matrix expressions (31)-(34) clearly provide a fundamentally rigorous basis for the design of an $(n + N)$-port beam-forming network N, that is simultaneously matched to a given set of sources (or of receivers), characterized by an internal impedance matrix Z_{11} , and connected to the left-side interface-1, and at the same time to a given set of radiating array elements, characterized by an internal impedance matrix Z_{12} , connected to the right-side interface-2 (figures 1 and 2).

The matrix expressions (31)-(34) also clearly provide the possibility of specifying, besides the bilateral impedance match, both the forward-wave-transmission matrix-block S_3 of the beam-forming network N, as defined by the expression (21), and the backward-wave-transmission matrix-block S_2 , as defined by the expression (20) .

The matrix-block S_3 clearly maps the *'input'* voltage-wave vector a_i , generated by the set of mutually-coherent, amplitude- and phase-controlled sources (in transmission), to the *'output'* voltage-wave vector b_j , that directly excites the set of radiating array elements, thus generating any of the required, very specific, and practically significant aperture distributions. Obviously, only the few, carefully-selected aperture-distributions, that result in radiated beams of specified directivity, sidelobe level, and pointing direction need to be considered as practically significant.

Similarly, the matrix S_2 clearly maps the *'input'* voltage-wave vector a_j , generated by the set of array elements (in reception), under the various space-wave excitations due to beams incident upon the array aperture from any of the specified pointing directions, to the *'output'* voltage-wave vector b_i , that directly drives the set of receivers connected to interface-1 .

The quantitative specification of the forward-, and backward wave-transmission blocks S_3 , and S_2 clearly fully determines, in conjunction with the specified impedance matrices Z_{11} , and Z_{12} , all four blocks Z_i ($i = 1, 2, \ldots, 4$) of the impedance matrix Z_{n+N} of the beam-forming network N, thus

establishing a rigorous basis for the choice of a most appropriate network topology, and for a quantitative network synthesis and design.

It is clear that, in both the transmission and the reception modes, the aperture distributions corresponding to given, specified beam characteristics (directivity, sidelobe level, and pointing direction) are fully determined, and known, in the form of *K*-space spectra, so that the corresponding voltage-wave vectors b_j (in transmission), and a_j (in reception) can easily be determined by way of inverse Fourier transforms.

A substantial measure of freedom can, however, be exercised in selecting the corresponding interface-1 voltage-wave vector a_i (in transmission), and b_i (in reception). Indeed, each of the mutually-coherent sources, in transmission, and each of the receivers, in reception, can easily be phase-controlled through a full 360^o range, while the only limitation to the corresponding amplitude control is a practical limit on the extent of the amplitude-control dynamic-range.

Practical limitations on the amplitude-control dynamic-range of the sources depend on source-efficiency considerations, while in the case of receivers non-linearity at the upper end of the range, and unacceptable signal-to-noise ratio at the lower end of the range are of primary concern.

Finally, it is very interesting to observe that, in principle, the fundamental beam-forming network design expressions (31)-(34) appear to provide valid solutions even for networks with an interface-1 number of ports n substantially smaller than the number N of radiating array elements. This rather fundamental observation clearly opens the possibility of very substantial, and advantageous reductions in the required total number of very expensive, and highly critical beam-steering control components (such as digital phase-shifters, and gain-controlled amplifiers), as compared to the notoriously unaffordable active-aperture phased array designs.

5 - CLOSED-FORM EXPRESSIONS OF THE IMAGE-IMPEDANCE MATRICES.

Closed-Form expressions of the two image-impedance matrices Z_{II} , and Z_{I2} , of any given beam-forming network N, as functions of the matrix blocks Z_i ($i = 1, 2, \ldots, 4$) of the impedance matrix $Z_{(n+N)}$ can be found by solving the two, simultaneous matrix-Riccati equations (27), and (28) :

$$Z_{II} = \left(I_n - Z_2 \cdot Z_4^{-1} \cdot Z_3 \cdot Z_1^{-1} \right)^{1/2} \cdot Z_1 \qquad (35)$$

$$Z_{I2} = \left(I_N - Z_3 \cdot Z_1^{-1} \cdot Z_2 \cdot Z_4^{-1} \right)^{1/2} \cdot Z_4 \qquad (36)$$

The required solution procedure is rather convoluted, but straightforward. The expressions (35), and (36) provide a way to determine which internal-impedance matrices the set of sources (or of receivers), and the set of radiating array elements should have, to be bilaterally matched to some given beam-forming network N.

The expressions (35), and (36) are (not surprisingly) irrational functions of the impedance-matrix blocks Z_i , and it is easy to verify that these expressions reduce to the well-known definitions of the scalar image-impedances of a simple two-port network for $n = N = 1$.

It is of fundamental interest to notice that, for a theoretical, totally lossless beam-forming network, with purely imaginary impedance matrix Z_{n+N} , the eigenvalues of the image-impedance matrices Z_{II} , and Z_{I2} are either purely real (resistive), within any given passband, or purely imaginary (reactive), within any given stop-band. The eigenvalues of the two image impedance matrices Z_{II} , and Z_{I2} express the

common values of impedance of different sets of (n or N) one-port loads, that separately match the beam-forming network N , under a finite number of very specific excitation patterns a_i , and a_j.

It is also interesting to observe that an infinite number of different beam-forming networks may all share the same image-impedance matrices Z_{II} , and Z_{II} while all differing in the forward-, and backward transmission properties, as specified by the scattering-matrix blocks S_2 , and S_3 .

6 - CLOSED-FORM EXPRESSIONS OF THE TRANSMISSION MATRICES S_2 , AND S_3 .

Closed-form expressions of the forward-, and backward-wave-transmission matrices S_3 , and S_2 can be obtained from the expressions (24'), and (25'), in the forms :

$$S_3 = Z_3 \cdot Z_1^{-1} \cdot \left[I_n + \left(I_n - Z_2 \cdot Z_4^{-1} \cdot Z_3 \cdot Z_1^{-1} \right)^{1/2} \right]^{-1} \tag{37}$$

$$S_2 = Z_2 \cdot Z_4^{-1} \cdot \left[I_N + \left(I_N - Z_3 \cdot Z_1^{-1} \cdot Z_2 \cdot Z_4^{-1} \right)^{1/2} \right]^{-1} \tag{38}$$

The expressions (37), and (38) provide the solution to the problem of determining the array-excitation voltage-wave vector b_j , that corresponds to any given amplitude-, and phase-setting of the n sources connected to interface-1, and similarly to the problem of determining the voltage-wave vector b_i , reaching the set of n receivers connected to interface-1, that corresponds to any given array-aperture space-wave excitation, as represented by the voltage-wave vector a_j generated, at interface-2, by the set of receiving array elements.

The expressions (37), and (38) hold, under the obvious assumption of the considered beam-forming network actually being impedance-matched on both sides, in transmission as well as in reception, as specified by the expressions (31)-(34) , or (35), and (36).

7 - CONCLUSIONS.

The formulated, fundamental generalizations of the classical concepts of scalar image impedance, and of scalar image transfer-function, originally restricted to the theory of simple two-port networks, to the broader domain of electrically-large, linear, multiport microwave networks, provide a rigorous basis for the synthesis, and the engineering design of advanced, high-efficiency beam-forming networks for high-directivity, low-sidelobe, electronically-steered phased arrays.

High beam-forming-network efficiency, and total elimination of the notorious 'array-blindness' phenomenon, are attained by enforcing newly-formulated conditions for simultaneous, bilateral impedance match, between the beam-forming network and the set of array radiating elements on one side, and between the beam-forming network and the set of mutually-coherent, amplitude-, and phase-controlled microwave sources (or receivers).

The attained impedance match rigorously accounts for both the mutual, electromagnetic proximity-coupling between any two array elements, and for any given, internal cross-coupling of the set of microwave sources.

Further, the attained impedance match is totally independent from the specific amplitude, and phase settings of the array-excitation sources, in transmission, and from the selected beam-steering direction, in both transmission, and reception.

The newly-formulated analytical results are rigorously valid even for highly non-symmetric beam-forming networks, with vastly different numbers of ports on the two interfaces connecting to the set of array elements on one side, and to the set of microwave sources, on the other.

The new analytical results are also rigorously valid for *non-reciprocal* networks, such as beam-forming networks including non-reciprocal ferrite phase shifters, and active amplifiers, as long as such devices can be considered linear, at least below an acceptable maximum power level.

The fundamental generality of the new analytic results introduces thus the possibility of designing high-efficiency beam-forming networks, that include substantially smaller numbers of the very expensive beam-steering controls, as compared to the notoriously unaffordable active-aperture designs.

8 - REFERENCES.

[1] Speciale R. A. , "Derivation of the Generalized Scattering Parameter Renormalization Transform," 1980 IEEE-ISCAS International Symposium on Circuits and Systems Digest of Technical Papers, Houston, Texas, April 28-30, 1980, pp. 166-169, IEEE Cat. No. 80CH1564-4.

[2] Franzen N. R. , Speciale R. A. ,"A New Procedure for System Calibration and Error Removal in Automated S-Parameter Measurements," Proceeding of the 1975 5th European Microwave Conference, Hamburg, Germany, September 1-4, 1975, Microwave Exhibitions and Publishers, Sevenoaks, Kent, UK.

[3] Speciale R. A. , "Super-TSD. A Generalization of the TSD Network Analyzer Calibration Procedure, Covering n-Port Measurements with Leakage," 1977 IEEE-MTT-S International Symposium on Microwave Theory and Techniques Digest of Technical Papers, San Diego, California, June 21-23, 1977, pp. 114-117, IEEE Cat. No. 77CH1219-5 MTT.

[4] Speciale R. A. , "Generalization of the TSD Network Analyzer Calibration Procedure, covering n-Port Measurements with Leakage," IEEE Trans. on Microwave Theory and Techniques, Vol. MTT-25, No. 12, pp. 1100-1115, December 1977.

[5] Speciale R. A. ,"The Normal Wave-Modes of Uniform, Non-Homogeneous, Lossy Sets of Coupled Transmission Lines," Unpublished Research Report, 1981.

[6] Speciale R. A. , "The Auto-Normalized Waves and Scattering Matrices of Linear 2n-Port Networks," Unpublished Research Report, 1981.

[7] US Patent No. 5,347,287 - Awarded September 13, 1994 in the Author's name ; [7a] US Patent Pending - Submitted September 12, 1994 in the Author's name.

[8] Speciale R. A. , "Computer-Simulation of Isotropic, Two-Dimensional Guided-Wave Propagation," published in the Proceedings of the 1995 11th Annual Review of Progress in Applied Computational Electromagnetics, Naval Postgraduate School, Monterey, California, March 20 - 24, 1995 , pp 639 - 647.

[9] Speciale R. A. , "Wave-Field Patterns on Electrically Large Networks," published in the Proceedings of the 1995 11th Annual Review of Progress in Applied Computational Electromagnetics, Naval Postgraduate School, Monterey, California, March 20 - 24, 1995 , pp. 656 - 663.

[10] Speciale R. A. , "Symmetry Analysis of Large Two-Dimensional Clusters of Coupled Cavity Resonators," 9th Annual Review of Progress in Applied Computational Electromagnetics, Naval Postgraduate School, Monterey, California, March 22 - 26, 1993, pp. 281 - 288.

[11] Speciale R. A. , "Sectored Cylindrical Cavity Resonators," 8th Annual Review of Progress in Applied Computational Electromagnetics, Naval Postgraduate School, Monterey, California, March 16 - 20, 1992, pp. 274 - 281.

[12] Speciale R. A. , and Wacker P. F. , "Ultra High Gain Antenna Arrays," 6th Annual Review of Progress in Applied Computational Electromagnetics, Naval Postgraduate School, Monterey, California, March 19 - 22, 1990, pp. 241 - 252.

[13] Speciale R. A. , "Wave Propagation on Infinite, Two-Dimensional Structures," 5th Annual Review of Progress in Applied Computational Electromagnetics, Naval Postgraduate School, Monterey, California, March 20 - 24, 1989, pages 200 - 244.

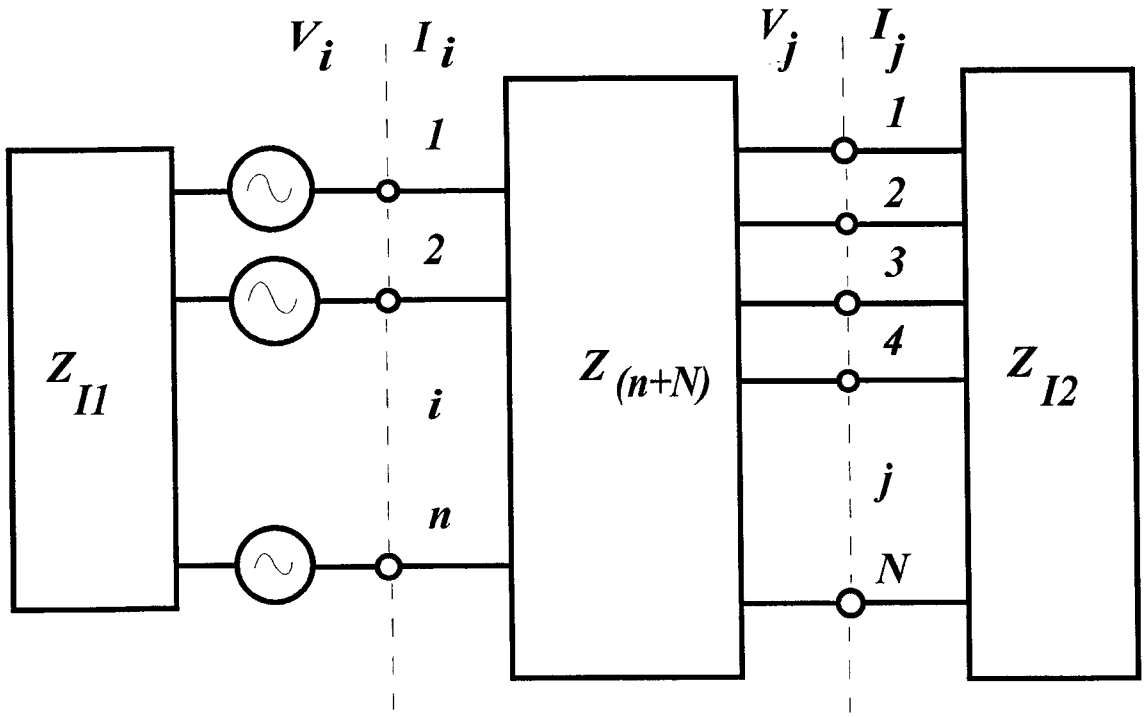

Figure 1 - Unconditional, Bilateral Image-Impedance Match: Forward-Wave, n-Phase Excitation, with Arbitrary Wave Amplitudes and Phases.

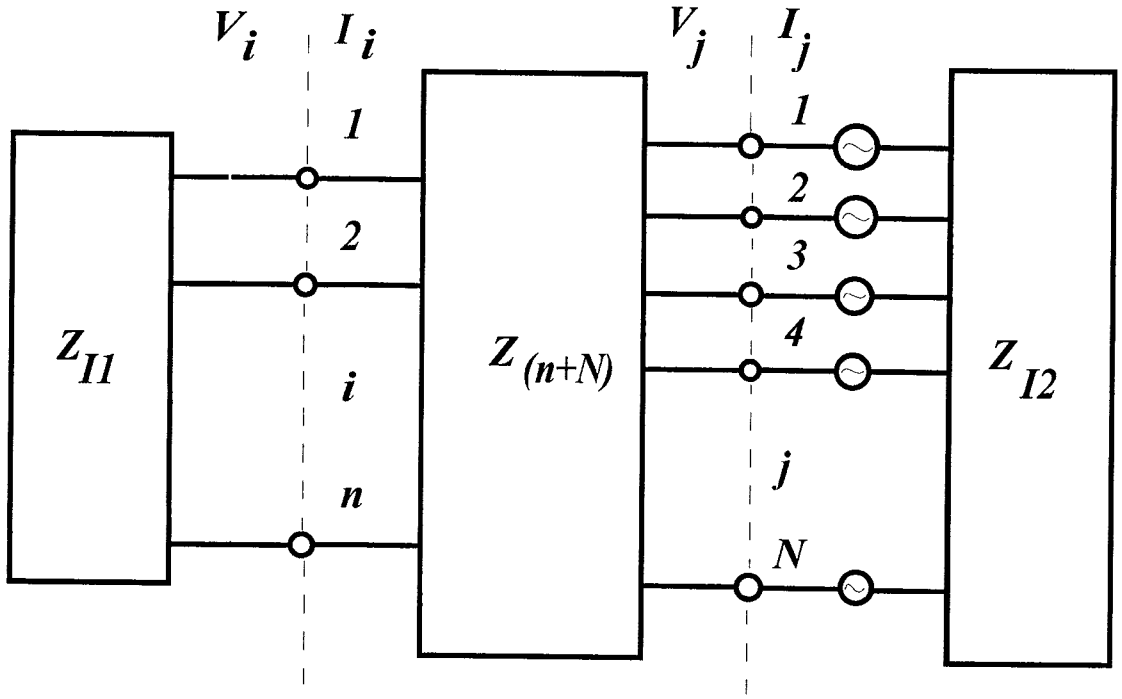

Figure 2 - Unconditional, Bilateral Image-Impedance Match: Backward-Wave, N-Phase Excitation, with Arbitrary Wave Amplitudes and Phases.

SESSION 18:

FINITE ELEMENTS

Chair: J. Jin

Adaptive Mesh Refinement Concepts for Electromagnetics

Zhong Chen and Robert Lee
lee@ee.eng.ohio-state.edu
ElectroScience Laboratory
Department of Electrical Engineering
The Ohio State University
1320 Kinnear Road
Columbus, OH 43212

I. Introduction

Adaptive mesh refinement (AMR) methods have been widely used for the finite element method (FEM) within many engineering disciplines [1, 2, 3, 4]. However, with the exception of the static case [5, 6], AMR methods are seldom applied to time-varying electromagnetics. One of the reasons is that the FEM codes in electromagnetics have only recently reached a mature enough level to consider the use of AMR. A second reason is that the traditional mesh refinement techniques are not well suited for electromagnetic problems. The traditional AMR methods are based on the assumption that the error is local, which means that the error within a given element is caused by the meshing of the region bounded by that element. Thus, once an estimate of the error is made for the solution, one can refine the regions where the errors occur to obtain a better solution. Unfortunately, numerical dispersion error is global, which means that the error in a given element is due to error in other elements, possibly far from the given element. Even if we can properly predict the error in an element, we do not know where the error comes from.

In this paper, we present a traditional approach to a posteriori error estimation. Next, we discuss in more detail the relationship between the error and the discretization. Finally, we propose some ideas to consider for doing AMR for electromagnetics.

II. Traditional Approaches to A Posteriori Error Prediction

Let us assume that FEM is used to solve for the fields in a three-dimensional region Ω. The differential equation for the region Ω is

$$\nabla \times \left(\frac{1}{j\omega\mu} \nabla \times \vec{E} \right) + j\omega\epsilon^* \vec{E} = 0 \qquad (x, y, z) \in \Omega \tag{1}$$

where the exp($j\omega t$) time harmonic variation has been suppressed and $\epsilon^* = \epsilon - j\sigma/\omega$. We can apply FEM to each of the elements in the mesh separately and the sum up the contributions for each element. The variation expression for the sum of elements is

$$\sum_m \int\int\int_{\Omega_m} \frac{1}{j\omega\mu} \left(\nabla \times \vec{E}\right) \cdot \left(\nabla \times \vec{\phi}_i\right) + j\omega\epsilon^* \vec{E} \cdot \vec{\phi}_i + \; dv$$
$$= \sum_m \int\int_{\partial\Omega_m} (\hat{n} \times \vec{H}) \cdot \vec{\phi}_i \, dS \tag{2}$$

where $Omega_m$ is the volume in element m and $\partial\Omega_m$ is the surface enclosing that element. The continuity of tangential $\vec{E}$ and normal $\vec{D}$ is enforced directly at the nodes. Assuming that there are no surface currents or charges at the inter-element boundaries, the surface integral in (2) vanishes everywhere except at the boundary of the mesh.

Because a polynomial approximation is used to represent the fields within each element, the solution contains some error. Let us denote the finite element approximation for the electric field to be $\tilde{E}$. Since the numerical solution is not correct, we can write that $tildeE$ satisfies,

$$\nabla \times \left(\frac{1}{j\omega\mu} \nabla \times \tilde{E}\right) + j\omega\epsilon^* \tilde{E} = \vec{r}_m \qquad (x, y, z) \in \Omega_m \tag{3}$$

where $\vec{r}_m$ is the residual due to the error in the FEM solution. This residual is one of two sources of error in the solution. The other source of error is caused by the discontinuity in the tangential magnetic field at inter-element boundaries. In (2), we assume that the tangential magnetic field is continuous in an integral sense and set the surface integral to zero at inter-element boundaries. In reality, the numerical solution for the tangential magnetic field, which can be obtained numerically from the electric field, is discontinuous. We can define the error $vece$ to be

$$\vec{e} = \vec{E} - \tilde{E} \tag{4}$$

The variational expression for the error is

$$\int\int\int_{\Omega} \frac{1}{j\omega\mu} (\nabla \times \vec{e}) \cdot \left(\nabla \times \vec{\phi}_i\right) + j\omega\epsilon^* \vec{e} \cdot \vec{\phi}_i + \frac{1}{j\omega\mu\epsilon^*} \nabla \cdot (\epsilon^* \vec{e})(\nabla \cdot \vec{\phi}_i)$$
$$- (\vec{r} \cdot \vec{\phi}_i) \, dv = \sum_{m,k} \int\int_{\partial\Omega_{mk}} \vec{\rho}_{mk} \cdot \vec{\phi}_i \, dS \tag{5}$$

where $\partial\Omega_{mk}$ is the surface joining elements m and k and $\vec{\rho}_{mk}$ represents the discontinuity of the tangential magnetic field. The terms, $\vec{r}$ and $\vec{\rho}_{mk}$, are known a posteriori from the original FEM solution for the electric fields. Thus, we can solve for the error by applying FEM to (5). The same shape functions that are used to approximate the fields in (2) can also be used to approximate the error in (5). However, it has been found [2] that the dominant term in the error is associated with the polynomials which are one order higher than those used to approximate the fields. Therefore, a higher order shape function is used to approximate the error. Because of the higher order approximation, a direct solution of (5) is not efficient for estimating the error in the FEM solution.

In order to make the error calculation efficient, the error in each element must be decoupled from the other elements. To accomplish this decoupling, we must remove the constraint that the

fields be continuous at the nodes. In addition, the variable $\vec{\rho}_{mk}$ must be decomposed into two independent terms, $\vec{\rho}_m$ and $\vec{\rho}_k$, where the first term is associated with the mth element and the second is associated with the kth element. The resulting equation for the error in element Ω_m is

$$\iiint_{\Omega_m} \frac{1}{j\omega\mu}(\nabla \times \vec{e}) \cdot \left(\nabla \times \vec{\phi}_i\right) + j\omega\epsilon^* \vec{e} \cdot \vec{\phi}_i - (\vec{r}_m \cdot \vec{\phi}_i)\, dv = \iint_{\partial\Omega_m} \vec{\rho}_m \cdot \vec{\phi}_i \, dS \tag{6}$$

Since the elements are decoupled, the error in each element is found by solving an $N_e \times N_e$ matrix equation (from (6)) where N_e is the number of unknowns associated with the element. The manner in which we divide $\vec{\rho}_{mk}$ into $\vec{\rho}_m$ and $\vec{\rho}_k$ is important in determining how accurately the error is approximated. Unfortunately, there does not seem to be a way to split $\vec{\rho}_{mk}$ such that the accuracy of the error is optimized. In our case, we choose a simple splitting scheme proposed by Ohtsubo and Kitamura [4] where the division is based on the relative sizes of neighboring elements.

This scheme has been implemented in [7], and the results are somewhat mixed. Sometimes the error is accurately predicted, and other times it is not. This has also been noted by other researchers doing a posteriori error prediction for time varying electromagnetic fields [8]. We discuss the causes of this in the next section.

III. Relationship Between Error and Discretization

Discretization error is produced by the incorrect modeling of the field variation within the computation domain. The field variation is due to two factors for time-harmonic waves. One is the sinusoidal variation of the field due to the frequency of the wave. In finite element methods, a polynomial variation is assumed for the field; therefore, an error is expected in modeling the sinusoidal variation, with more error as the frequency increases. The error causes the wave to be dispersive. This error is commonly called numerical dispersion error [9], and its effect is global, which means that the element size in one region may strongly affect the accuracy of the solution far away. The second cause of field variation is geometrical discontinuities. For example, the fields vary rapidly near perfectly conducting sharp corners and edges as well as material discontinuities. Some field components even approach infinity at perfectly conducting corners and edges. It is important to choose the discretization to properly model the field behavior near these geometrical features. Let us call this error geometric-based error. Geometric-based errors are local, which means that the error within a given element is caused the by meshing of the region around that element.

The problems with using a posterior error estimators such as the one presented in the previous section is due to the fact that both local and global errors are present. The a posteriori error estimators can accurately predict local errors such as the case with electrostatics, but it cannot predict global errors very well.

Even if we can develop an a posteriori method to predict both the local and global errors, it is not clear that it would be useful in AMR methods. As we stated in the introduction, AMR

methods assume that the error in a given element can be reduced by refining the grid near the region where the error is present. For global errors this cannot work. Consider the one-dimensional problem of a plane wave propagating in free space in the $+zdirection$. Assuming the electric field to be x polarized, the solution is

$$E_x = e^{-jkz} \tag{7}$$

assuming an $\exp(j\omega t)$ time convention. However, if we were to solve this problem using FEM with linear elements, we would obtain an approximate solution due to the discretization of the field. An analysis [9] can be performed based on the assumption that the mesh is uniform and the computation domain is infinite, which in effect removes the boundary condition from consideration. The numerical solution is

$$E_x = e^{-j\hat{k}z} \tag{8}$$

where $\hat{k}$ is given by

$$\frac{\hat{k}}{k} = \frac{1}{kh} \arccos\left[\frac{1-(kh)^2/3}{1+(kh)^2/6}\right] \tag{9}$$

with h being the grid spacing. It is clear that the numerical solution is dispersive because $\hat{k}$ is not a linear function of frequency.

The numerical dispersion error is a phase error $(k-\hat{k})z$ which increases as a function of z. One way to view this is that the wave accumulates error as it propagates along the z direction. Thus, the rightmost (largest in z) element has the greatest error. If we accurately predict the error in the numerical solution and apply the AMR method, we would end up refining the rightmost elements of the grid without recognizing the the error is due to all the elements equally. In this case AMR methods fail.

IV. Development of Adaptive Mesh Refinement Methods for Electromagnetics

In order to use AMR, we must somehow minimize numerical dispersion error or decouple it from geometric-based discretization error. For an optimal solution, we should do both. Since numerical dispersion error is a cumulative error, it is convenient to choose an initial mesh distribution which is uniform. The relationship between mesh density and numerical dispersion has been the subject of numerous studies. Thus, the mesh density can be chosen to obtain an acceptable level of numerical dispersion error. Once the numerical dispersion error is minimized, the AMR methods can be applied to reduce geometric-based errors.

At each level of refinement, the associated matrix equation must be solved. For three-dimensional geometries, iterative matrix solvers are used. The computation costs are expensive because many iterations are required for the matrix solution to converge. One way to reduce the computation costs is to find an analogous problem to solve which has the same geometric-based errors, but is less expensive to solve. Let us consider the two-dimensional problem of a

TM_z polarized plane wave incident on a square perfectly conducting infinite cylinder with sides of length 0.5λ. The small cylinder size is chosen so that there is not much numerical dispersion error. An analogous problem for this case would be the electrostatic problem of a perfectly conducting square cylinder in a constant field. Both these problems have the same geometric-based errors, i.e., both numerical solutions have the most errors at the corners of the grid. In Figure 1, we plot $|E_z^{ref} - E_z|$ all the way around the cylinder at a distance $\lambda/20$ from the cylinder for the time-varying problem. The electric field E_z is generated from a uniform grid with a grid spacing of $\lambda/20$. A first order absorbing boundary condition is used to truncate the grid. To determine how much error is in our solution, a reference electric field solution E_z^{ref} is generated from a finely discretized mesh (spacing of $\lambda/80$). As we expect the errors are greater at the corners of the cylinder. To demonstrate that the error is local as well as geometric-based, we use a non-uniform mesh with the finer mesh near the corners to try to remove the error there. We observe in Figure 1 that the error at the corners is reduced.

For the static problem, we plot the difference of the potential $V_{ref} - V$ with the same grids as the time varying case in Figure 2. Again, we use an approximate outer boundary condition for electrostatics. The reference solution is obtained from a grid whose spacing is four times as fine as the solution associated with V. The error behaves the same way as the time-varying case for both the uniform and non-uniform grid. If a relationship can be found between the level of errors in the time-varying and electrostatic problems, then we can use the electrostatic solution to perform the mesh refinement. The advantages of performing the refinement on the electrostatic problem is that the iterative solver converges much faster for this problem. Once the desired mesh is obtained, then a final solution can be obtained for the time-varying case.

V. Conclusions

At this point, much of the research needs to still be done on AMR for electromagnetics. The discussion here provides some important concepts which must be kept in mind when developing AMR methods.

VI. References

[1] D. W. Kelly, J. P. De S. R. Gago, and O. C. Zienkiewicz, "A posteriori error analysis and adaptive processes in the finite element method: part I—error analysis," *Int. J. Num. Methods Eng.*, Vol. 19,pp. 1593-1619,1983.

[2] D. W. Kelly, "The self-equilibration of residuals and complementary a posteriori error estimates in the finite element method," *Int. J. Num. Methods Eng.*, Vol. 20,pp. 1491-1506,1984.

[3] O. C. Zienkiewicz and J. Z. Zhu, "A simple error estimator and adaptive procedure for practical engineering analysis," *Int. J. Num. Methods Eng.*, Vol. 24,pp. 337-357,1987.

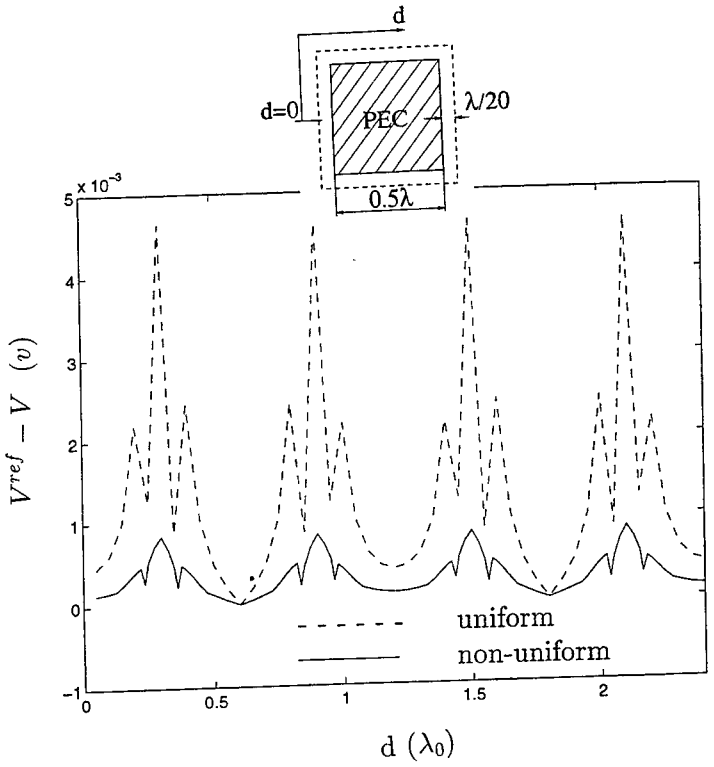

Figure 2: Plot of $V^{ref} - V$ as a function of position (denoted by d) around a perfectly conducting square cylinder. The same mesh is used as in the time-varying case.

[4] H. Ohtsubo and M. Kitamura, "Element by element a posteriori error estimation and improvement of stress solutions for two-dimensional elastic problems," *Int. J. Num. Methods Eng.*, Vol. 29,pp. 223-244,1990.

[5] P. Fernandes, P. Girdinio, P. Molfino, and M. Repetto, "Local error estimates for adaptive mesh refinement," *IEEE Trans. Magnetics*, Vol. 24, pp. 299-302, January 1988.

[6] P. Fernandes, P. Girdinio, G. Molinari, M. Repetto, "Local error estimation procedures as refinement indicators in adaptive meshing," *IEEE Trans. Magnetics*, Vol. 27, pp. 4189-4192, September 1991.

[7] U. Pekel and R. Lee, "An a posteriori error reduction scheme for the three dimensional finite element solution of Maxwell's equations," *IEEE Trans. Microwave Theory and Techniques*, MTT-43, pp. 421-427, February 1995.

[8] F. J. C. Meyer and D. B. Davidson, "Error estimates and adaptive procedures for the 2D finite element/boundary element method in electromagnetics," Progress in Electromagnetic Research Symposium, Seattle, WA, July, 1995.

[9] R. Lee and A. C. Cangellaris, "A study of discretization error in the finite element approximation of wave solutions," *IEEE Trans. Antennas and Propagat.*, AP-40, pp. 542-549, May 1992.

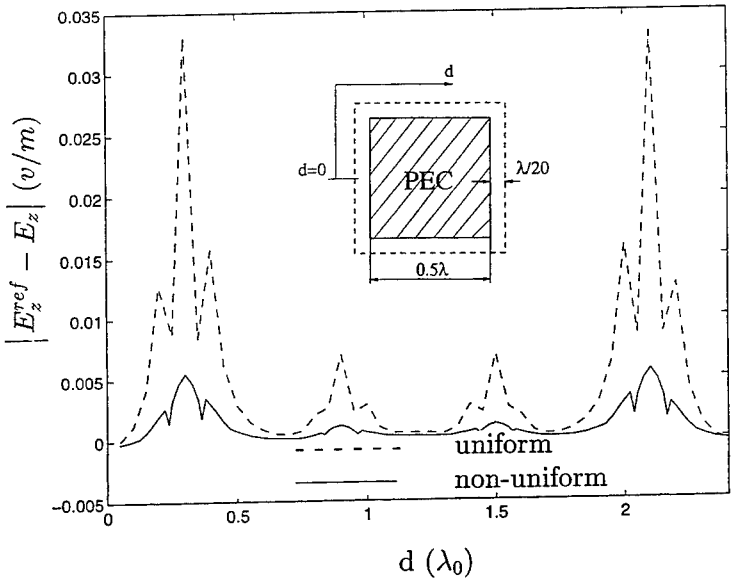

Figure 1: Plot of $|E_z^{ref} - E_z|$ as a function of position (denoted by d) a distance $\lambda/20$ from a perfectly conducting square cylinder.

ANALYSIS OF COMPLETE BASIS SETS OF DIVERGENCELESS VECTOR EXPANSION FUNCTIONS FOR FINITE ELEMENT PROBLEMS

Michael J. Walker
Department of Electrical Engineering
HQ USAFA/DFEE
2354 Fairchild Dr., Suite 2F6
USAF Academy, CO 80840-6236
email: walker@shelter.usafa.af.mil
719/472-4213 (work)
fax: 719/472-3756

Abstract.

When edge-based, vector functions are developed from linear polynomials and the enforcement of Nedelec's constraints, the resulting set of vectors is also divergenceless. This has led to some confusion as to which feature is responsible for how well these functions work as finite element approximation expansions, the constraints or zero divergence. The set of vectors form a complete basis with respect to Nedelec's constraints, but an incomplete basis of divergenceless vectors, providing an opportunity for comparing the two features. Complete basis sets of divergenceless expansion functions for both 2D and 3D, linear and quadratic finite element problems are developed. They are used as vector expansion functions for approximating the electric and magnetic field in a finite element analysis of cavity resonance. Similar analysis is performed using sets of vector expansions constrained by Nedelec's criteria and the results are compared. The severity of the problems encountered with the divergenceless expansions supports the conclusion that Nedelec's criteria are the key to developing good vector expansion functions. A basic understanding of barycentric coordinate notation used in finite element calculations is assumed.

Introduction.

When the finite element method is used to solve the weak form of the reduced Helmholtz wave equation, the resulting eigenvalue problem contains solutions which do not conform to Maxwell's divergence equations. These spurious solutions should be the eigenvectors corresponding to an eigenvalue of zero. Actually, their non-zero eigenvalues are on the same order as the desired true solutions. Thus, spurious solutions increase computational effort, because they must be separated from the set of true solutions [1]. They also waste some of a limited number of eigenvalues.

In an attempt to suppress the spurious modes, zero divergence was enforced on the vector expansion functions themselves. The "standard" set of edge-based vector functions was the result. These functions did not suppress the spurious modes, but did appear to calculate them accurately enough to make the eigenvalues very nearly zero and thus easy to separate with a single calculation.

Current research in electromagnetic finite element techniques has switched from advocating vector expansion functions with zero divergence to vector functions which satisfy the Nedelec constraints for the purpose of dealing with spurious solutions. Since any vector field can be expressed as the gradient of a potential, the Nedelec constraints require the potential to be approximated with the same

polynomial order as the field [2]. It is thought to be the Nedelec-constraints which allow the spurious modes to be so accurately calculated and then separated [2]. Because the linear, Nedelec-constrained expansions resulted in the same "standard" set of divergenceless vectors, there has been some confusion as to which feature is responsible. Although complete with respect to Nedelec's constraints, this is not a complete basis of divergenceless vector functions.

Problem Formulation.

The inner product of the curl-curl form of the reduced wave equation and a testing function can be put into the "weak" form below by removing one of the derivatives from the electric field using Green's Theorem.

$$\left\langle L(\overline{E}), \overline{W} \right\rangle = \iiint \left[(\nabla \times \overline{E}) \cdot (\nabla \times \overline{W}^*) - \omega^2 \mu \varepsilon \overline{E} \cdot \overline{W}^* \right] d\overline{x} + \oint\!\!\!\oint_S \left(\hat{n} \times (\nabla \times \overline{E}) \right) \cdot \overline{W}^* ds = 0$$

By assuming the walls of the cavity problem to be perfect conductors, the surface integral component is removed by the boundary conditions, and the equation can be put into eigenvalue form with $k^2 = \omega^2 \mu \varepsilon$ as the eigenvalue.

$$\iiint (\nabla \times \overline{E}) \cdot (\nabla \times \overline{W}^*) \, d\overline{x} = k^2 \iiint \overline{E} \cdot \overline{W}^* \, d\overline{x}$$

If the field and testing function are modeled as a finite sum of weighted vector expansions defined over triangular or tetrahedral elements, as below, the eigenvalue equation takes the following form.

$$\overline{E} = \sum_i c_i \overline{\Psi}_i \qquad \overline{W} = \sum_j d_j \overline{\Psi}_j$$

$$\sum_{i,j} c_i d_j^* \iiint (\nabla \times \overline{\Psi}_i) \cdot (\nabla \times \overline{\Psi}_j^*) \, d\overline{x} = k^2 \sum_{i,j} c_i d_j^* \iiint \overline{\Psi}_i \cdot \overline{\Psi}_j^* \, d\overline{x}$$

Choosing the same expansions for the field and testing function sets i=j. After differentiating with respect to each of the testing function's weighting factors, the resulting system of equations can be put into matrix form. Also, because the vectors are real functions, the complex conjugate operators can be ignored. The final form of the eigenvalue equation is given below.

$$[B]^{-1}[A][c] = k^2[c] \tag{1}$$

where

$$A_{ji} = \iiint (\nabla \times \overline{\Psi}_i) \cdot (\nabla \times \overline{\Psi}_j) \, d\overline{x} \tag{2}$$

and

$$B_{ji} = \iiint \overline{\Psi}_i \cdot \overline{\Psi}_j \, d\overline{x} \tag{3}$$

Nedelec-Constrained Expansion Sets.

The "standard" set of linear expansions conforming to Nedelec's constraints is given by

$$\bar{\varphi}_{ij} = w_{ij}\left(L_i \nabla L_j - L_j \nabla L_i\right)$$

where $ij = [12,13,23]$ for 2D and $ij = [12,13,14,23,24,34]$ for 3D problems. L_i is the barycentric variable associated with node i, ∇L_i is the gradient of L_i, and w_{ij} is the edge length between nodes i and j. In addition to conforming to Nedelec's constraints, the linear expansions are also divergenceless. This set of vectors has also been called zero-order expansions because the component tangent to each element edge is always a constant; it is unity along one edge and zero on all the others [3].

When a second order polynomial is used to develop a set of Nedelec constrained expansions, the resulting vectors are very similar. Two expansions are defined per edge with their tangent component varying linearly along that edge, and zero on all others.

$$\bar{\varphi}_{ij1} = w_{ij} L_i \nabla L_j \qquad \text{and} \qquad \bar{\varphi}_{ij2} = w_{ij} L_j \nabla L_i$$

Two independent expansions are also defined for each triangular face. These expansions are defined such that they have identically zero tangential edge components along all element edges.

$$\bar{\varphi}_{ijk1} = L_i\left(L_j \nabla L_k - L_k \nabla L_j\right) \quad \text{and} \quad \bar{\varphi}_{ijk2} = L_j\left(L_i \nabla L_k - L_k \nabla L_i\right)$$

The net result is eight expansions defined per triangular (2D) element or twenty expansions per tetrahedron (3D). Simple inspection shows that conforming to Nedelec's constraints is not the same as enforcing zero divergence on the expansions.

Complete Divergenceless Expansion Sets.

An arbitrary linear vector in 2D and 3D has 6 and 12 degrees of freedom, respectively, as in the equations below.

$$\bar{F} = (A + Bx + Cy)\hat{x} + (D + Ex + Gy)\hat{y}$$

$$\bar{F} = \left(A + Bx + Cy + Dx^2 + Exy + Gy^2\right)\hat{x} + \left(H + Ix + Jy + Kx^2 + Lxy + My^2\right)\hat{y}$$

A quadratic vector has 12 and 30 degrees of freedom. The zero divergence requirement eliminates one degree of freedom from each linear case and 3 and 4 degrees of freedom from the quadratic cases. Thus, the size of the basis sets of divergenceless vector expansions must be 5 and 11 or 9 and 26, respectively, in order to be a complete basis. For example, in the linear, 2D case, the following set of five independent vectors are all divergenceless.

$$\{\hat{x}, \hat{y}, y\hat{x}, x\hat{y}, x\hat{x} - y\hat{y}\}$$

Five linear, 2D divergenceless vectors were developed by evaluating the tangential component of an arbitrary vector at five different points on a triangular element. Setting one value to unity and the rest to zero, in turn, produced five independent vectors. When the non-zero value was the component tangent to an edge, evaluated at the edge midpoint, the resulting expansion is called an "edge" expansion. When the non-zero value was the component tangent to one of the two dimensional directions, evaluated at the center of the triangular element face, it is called a "face" expansion. The five expansions are summarized with the two equations below, where D=2 is the dimension.

EDGE: $$\overline{\psi}_{ijk} = \frac{Dw_{kj}}{Z}\left[\left(X_{ij} - X_{ii}\right)\Sigma + Z\left(L_i - L_j\right)\nabla L_i\right] \qquad ijk=[\,231,\ 321,\ 312\,] \qquad (4)$$

FACE: $$\overline{\psi}_i = \frac{(D+1)w_{li}}{Z}\left[DX_{ii}\Sigma + Z\left(1 - DL_i\right)\nabla L_i\right] \qquad i=[\,2,\ 3\,] \qquad (5)$$

where $$\Sigma = \sum_{m=1}^{D} L_m \nabla L_m \qquad Z = \nabla\cdot\Sigma = \sum_{m=1}^{D} X_{mm} \qquad X_{ij} = \nabla L_i \cdot \nabla L_j$$

The linear, 3D divergenceless vector expansions are developed in a similar manner. However, to get eleven independent vectors, eleven evaluation points were used. Three points result from the three vector components at the tetrahedron center while the last eight are from the two tangential components at the center of each of the four triangular faces. The resulting expressions are three dimensional extensions of the linear expansions already derived. When D=3, Equation (1) becomes a 3D "face" expansion with ijk = [241, 341, 231, 431, 321, 421, 312, 412], and Equation (2) becomes a 3D "interior" expansion with i = [2, 3, 4].

Quadratic divergenceless expansions were also developed. In 2D, the nine expansions were defined by evaluating the tangential edge components at the two endpoints and the midpoint of each edge. Equation (6) is the expression for the vectors with non-zero values at the nodes, while Equation (7) is the expressions with non-zero values at the midpoints.

$$\overline{\psi}_{ij} = w_{ij}\left[L_j\left(A\left(L_j - 1\right) + BL_i\right)\nabla L_i + L_i\left(A + CL_i + DL_j\right)\nabla L_j\right] \qquad (6)$$

where $$A = \frac{X_{ii}}{2X_{ik}} - \frac{3X_{ij}}{2X_{jk}} \qquad B = -\frac{X_{ij}}{X_{ik}} \qquad C = \frac{X_{ij}}{2X_{ik}} - \frac{3X_{jj}}{2X_{jk}} \qquad D = \frac{3X_{ij}}{X_{jk}}$$

and $$X_{ij} = \nabla L_i \cdot \nabla L_j$$

for $$ij = [\,12,\ 21,\ 13,\ 31,\ 23,\ 32\,]$$

$$\overline{\psi}_{ij} = w_{ij}\left[L_j\left(E\left(L_j - 1\right) + FL_i\right)\nabla L_i + L_i\left(E(1-L_i) + GL_j\right)\nabla L_j\right] \tag{7}$$

where $E = \dfrac{2\left(X_{ii}X_{jj} - X_{ij}^2\right)}{X_{ik}X_{jk}}$ $F = \dfrac{4X_{ij}}{X_{ik}}$ $G = -\dfrac{4X_{ij}}{X_{jk}}$

and ij = [12, 13, 23]

In 3D, the three point evaluation of each edge tangential component and two tangential evaluations at the center of each triangular face provide the 26 necessary equations to define a complete set of divergenceless vectors.

Results.

The divergenceless sets of vectors were used as the finite element expansions for calculating the resonant frequencies of circular cavities using the matrix development above. The eigenvalues of $[B]^{-1}[A]$ represent the square of the wavenumbers associated with the resonant frequencies of the cavity. Two finite element models of the cavity were used, a simple 13 node, 12 element model and a denser 31 node, 42 element model. Both are shown in Figure 1. Tables 1 and 2 compare the wavenumbers calculated using linear and quadratic divergenceless expansions and linear Nedelec expansions with the exact solutions for TM and TE fields, respectively.

Several problems were discovered when working with the complete sets of divergenceless vectors. The 2D, linear "face" expansions and 3D, linear "interior" expansions have zero curl. This means that any term of matrix $[A]$ referencing one of these expansions is always zero. If D is the dimension of the problem and N the number of elements, then the matrix $[A]$ would have DN columns and rows identically zero. This means $[B]^{-1}[A]$ would also have DN columns identically zero. Thus, for every i'th column of zeroes, a solution exists with an eigenvalue of zero and an eigenvector with a value of unity in the ith term and zeroes everywhere else. Therefore, the linear divergenceless sets are inherently creating at least DN spurious solutions. Of the remaining solutions, additional spurious solutions also appeared comparable to the number produced by the Nedelec constrained expansion sets. Tables 1 and 2 list the total number of unknowns, the number of natural zeroes (spurious solutions), and the number of zeroes due to zero curl. All zero solutions are "wasted" eigenvalues because they could have been used calculating real solutions instead of spurious ones. The use of linear divergenceless vectors in these examples is guaranteed to waste at least half of the eigenvalues before the first calculation is ever made.

Additionally, the Nedelec sets provide tangential field continuity along the entire edge and face, whereas the "edge" and "face" terms of the linear divergenceless sets only enforce continuity at discrete points. This weakening of the tangential boundary condition results in the significant loss of solution accuracy also visible in the results in Tables 1 and 2. Continuity was not a problem with the quadratic expansions because they are identically zero everywhere across opposite edges and faces. Their accuracy is on the same order as the linear Nedelec solutions, but it took three times as many unknowns and significantly more complicated calculations to achieve this improvement.

The divergenceless quadratic vectors have serious problems of their own. If the finite element contains any total right angles, that is two edges perpendicular in 2D or three edges all mutually perpendicular in 3D, the expansions become undefined. The result is a non-unique set of solutions to the expansion equations (6) and (7). This was not a factor in the two circular cavity models, but as a potential expansion for any finite element problem, it needs to be addressed. While this may appear to be avoidable with careful geometry discretization, some other difficulties arise. Even if the right angles are exactly avoided, the resulting element shapes may have to become very distorted to do so. On the other hand, some geometries may have angles which approach, but aren't exactly, right angles. In either case, expansion terms will be created with extremely varying magnitudes and this will result in various computational difficulties when trying to manipulate the resulting matrices.

Conclusions.

Two important features of finite element approximation functions were analyzed by comparing the accuracy of the solutions they provided to a simple 2D resonant cavity problem. A complete basis set of vectors conforming to Nedelec's constraints were compared with complete basis sets of divergenceless vectors with the intent of identifying which feature was responsible for isolating the spurious solutions so they could easily be removed from the true solutions. Although both sets provided this capability, the linear divergenceless expansions produced DN additional spurious solutions. They also enforced a weakened version of the tangential continuity requirement, leading to less accurate true solutions. The quadratic expansions had only the same accuracy of true solutions, using three times the unknowns, and produced similar numbers of spurious solutions. Therefore, the use of Nedelec-constrained vectors is recommended over complete sets of divergenceless vectors due to their superior performance.

References.

[1] "Cavity Resonances: FEM Analysis Using the Vector Helmholtz Equation," *Electromagnetic Analysis Using the Finite Element Method-Education Extension Short Course*, Georgia Institute of Technology, Oct 1990.

[2] Peterson A. F., "Vector Finite Element Formulation for Scattering from Two-Dimensional Heterogeneous Bodies," *IEEE Transactions on Antennas and Propagation*, Vol. 42, No. 3, pp. 357-365, Mar 1994.

[3] Peterson, A. F., 'Edge-Based Tangential Vector Expansion Functions for the Numerical Solution of the 2D Vector Wave Equation," *Electromagnetic Analysis Using the Finite Element Method-Education Extension Short Course*, Georgia Institute of Technology, Oct 1990.

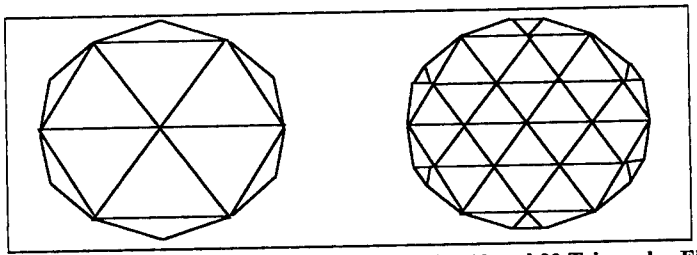

Figure 1. Finite Element Model of Circular Cavity with 12 and 32 Triangular Elements.

TYPE	EXACT	NEDELEC (LINEAR)		ZERO DIVERGENCE (LINEAR)		ZERO DIVERGENCE (QUADRATIC)	
NODES		13	31	13	31	13	31
TRIANGLES		12	42	12	42	12	42
UNKNOWNS		24	72	48	156	72	216
NATURAL ZEROES		12	30	12	30	37	97
ZERO-CURL ZEROES				24	84		
SOLUTIONS	2.405	2.6766	2.4512	1.9692	2.8011	2.4141	2.4060
	3.832	3.5789	3.8685	3.1171	4.2970	4.0511	3.8433
	3.832	3.5789	3.8685	3.4350	4.4849	4.0511	3.8433
	5.136	5.3534	5.0816	4.8784	5.6988	5.3904	5.2203
	5.136	5.3534	5.0816	5.1959	5.8017	5.3904	5.2203
	5.520	6.3450	5.4053	5.7953	6.1414	5.6610	5.6266
	6.380	9.2978	5.8635	14.8092	6.9113	5.6610	5.7115
	6.380	9.2998	6.3161	14.8488	7.0784	6.2488	5.7115
	7.016	9.2998	6.3161	14.8812	7.3084	6.9966	5.7570
	7.016	9.3074	6.4189	15.4506	7.4252	6.9966	5.7570
	7.588	9.3074	7.1323	15.4730	8.0467	7.3583	5.7576
	7.588	9.3163	7.1323	20.4980	8.2065	9.0757	5.8008

Table 1. Two Dimensional Circular Cavity Resonant Wavenumbers - TM Polarization.

TYPE	EXACT	NEDELEC (LINEAR)		ZERO DIVERGENCE (LINEAR)		ZERO DIVERGENCE (QUADRATIC)	
NODES		13	31	13	31	13	31
TRIANGLES		12	42	12	42	12	42
UNKNOWNS		12	54	36	138	36	162
NATURAL ZEROES		1	13	1	13	7	49
ZERO-CURL ZEROES				24	84		
SOLUTIONS	1.841	1.8594	1.8575	2.3238	2.3999	1.7681	0.4081
	1.841	1.8594	1.8575	2.4539	2.5381	1.7681	1.8318
	3.054	3.3010	3.1013	4.0947	4.1115	1.8080	1.8318
	3.054	3.3010	3.1013	4.1154	4.1444	2.7868	2.6839
	3.832	3.7966	3.8222	4.7852	4.9286	2.7868	2.6839
	4.201	6.1903	4.2754	8.3119	5.5331	3.8928	2.6947
	4.201	6.3569	4.2817	8.4511	5.8787	4.4983	2.7869
	5.318	6.3569	5.2672	8.5721	6.5818	4.4983	2.7869
	5.318	6.9524	5.2672	8.7199	6.7411	4.5202	2.8010
	5.331	6.9524	5.3925	8.8904	7.1386	4.9536	3.1072
	5.331	7.4763	5.3925	9.6215	7.1876	5.3427	3.1072

Table 2. Two Dimensional Circular Cavity Resonant Wavenumbers - TE Polarization.

Multi−Mode S−Parameter Computation Using Finite Elements and Perfectly Matched Absorbers

Gary C. Lizalek, Jeffrey J. Ruehl, and John R. Brauer
The MacNeal−Schwendler Corporation
4300 West Brown Deer Road
Milwaukee, WI 53223 USA
Email: john.brauer@macsch.com, phone 414/357−0333, fax 357−0347

Abstract—**Multi−mode scattering [S] parameters of waveguide structures are computed using multiple types of edge−based finite elements. The modes are excited by the fields of special "waveguide" 2D+ finite elements. The excited modes propagate through a model made of 3D edge finite elements, and are terminated with perfectly matched absorber finite elements. Typical computations are shown to agree closely with measurements or theory.**

INTRODUCTION

Scattering [S] parameters are important in characterizing the behavior of microwave circuits, such as waveguide and microstrip filters and junctions. Also, as computer clock speeds increase, S−parameters are increasingly being measured on digital circuits.

Finite elements have been used for many years to analyze microwaves, but S−parameter computation presents special challenges. Microwave circuits often contain several modes, so "generalized" S−parameters often need to be computed. The modal fields must be computed as functions of frequency for use in exciting the ports of the circuit. The 3D microwave circuit must be modeled with edge finite elements so that S−parameters can be computed accurately for devices with sharp conducting corners [1]. Finally, for the microwave engineer to be able to observe wave propagation and reflection, "reflectionless" terminations are needed at the ports.

This paper describes a new method of computing S−parameters using multiple types of edge finite elements. 2D+ elements are used to model port cross sections to determine the modal fields for port excitation and modal decomposition. Hexahedral, pentahedral, and tetrahedral edge finite elements are used to model the 3D microwave circuit. Port terminations of low reflection are obtained using perfectly matched absorbers. S−parameter equations are derived, and typical results are shown.

ELEMENTS FOR PORT CROSS SECTIONS

The modal fields at port cross sections are computed using new 2D+ "waveguide" finite elements [2]. Quadrilateral and triangular elements are of first or second order.

To compute the modal fields and propagation constants, we choose the transverse components of the magnetic vector potential $\vec{A}$ and the electric scalar potential ϕ (volts). The electric field is then:

$$\vec{E} \equiv -j\omega\vec{A}_t - \nabla\phi \qquad (1)$$

We transform the potentials as follows, where c_0 is the speed of light in vacuum:

$$\vec{A}'_\tau \equiv j\vec{A}_\tau \quad , \qquad \phi' \equiv \frac{\phi}{c_0} \tag{2}$$

Substituting (2) in (1), and denoting transverse components by τ and the complex propagation constant in the longitudinal z direction by $\gamma = \alpha + j\,\beta$:

$$\vec{E} = -\omega\vec{A}'_\tau - c_0\nabla_\tau\phi' + \gamma c_0\phi'\,\hat{z} \tag{3}$$

$$\vec{E}_\tau = -\omega\vec{A}'_\tau - c_0\nabla_\tau\phi' \quad , \qquad E_z = \gamma c_0\phi' \tag{4}$$

Using Faraday's Law, Ampere's Law, and the Galerkin method results in the matrix equation:

$$[K]\begin{Bmatrix}\vec{A}'_\tau \\ \phi'\end{Bmatrix} = \gamma^2\,[M]\begin{Bmatrix}\vec{A}'_\tau \\ \phi'\end{Bmatrix} \tag{5}$$

where [K] and [M] are symmetric indefinite matrices. The eigenvectors of (5) define the modal fields. The matrices of (5) have been derived for first order and second order quadrilateral and triangular finite elements for the case of real eigenvalues γ^2. Thus we obtain both propagating modes where $\gamma = j\,\beta$ and evanescent modes where $\gamma = \alpha$. Good results have been obtained for lossless waveguide and microstrip ports [2]. Lossy ports have both their β and α computed by means of perturbational techniques, provided that $\beta >> \alpha$.

3D HEXA, PENTA, AND TETRA EDGE ELEMENTS

The 3D microwave circuit is modeled using hexahedral, pentahedral, and tetrahedral edge finite elements [3]. Because a hexahedron must be replaced by at least five tetrahedrons, isoparametric edge hexahedrons and isoparametric edge pentahedrons have greater accuracy with far fewer unknowns than do the edge tetrahedrons, and are therefore used as much as possible.

The 3D elements have only the three components of the magnetic vector potential $\overline{A}$ expressed through edge vector unknowns. First order element unknowns are $\overline{A}$ values along all element edges. Second order element unknowns include additional $\overline{A}$ edge and face normal projections. Unlike nodal elements, the edge elements have no (nonzero) spurious eigenvalues and are able to accurately model interior conducting corners such as commonly used in waveguides and microstrips.

PERFECTLY MATCHED ABSORBERS AT PORTS

Ports are terminated using the new perfectly matched absorber method [4] for FEA, denoted here as PMA to differentiate it from Berenger's perfectly matched layer method for FDTD. The advantage of PMA over other methods such as ABCs is that any number of modes can be terminated at very low reflection.

The PMA is automatically created with layers that increase in thickness with layer number beyond the port. The complex anisotropic material properties are automatically chosen to obtain matching to inhomogeneous materials modeled both with first order edge finite elements

or with second order edge finite elements. The PMA elements may be either hexahedrons or pentahedrons.

S–PARAMETER COMPUTATION METHOD

The general representation for electric and magnetic fields in a microwave circuit is:

$$\vec{E}(x,y,z,t) = E_\tau(x,y)e^{-\gamma z}e^{+j\omega t}\,\hat{\tau} + E_z(x,y)e^{-\gamma z}e^{+j\omega t}\,\hat{z} \quad (6)$$

$$\vec{H}(x,y,z,t) = H_\tau(x,y)e^{-\gamma z}e^{+j\omega t}\,\hat{\tau} + H_z(x,y)e^{-\gamma z}e^{+j\omega t}\,\hat{z} \quad (7)$$

where τ indicates components transverse to the plane of a port and z indicates the longitudinal (normal) component.

In order to compute S–parameters, the transverse components must be known. The transverse fields can be expressed in terms of forward c^+ and backward c^- travelling waves without loss of generality (where the sign of c^- waves is different for E and H fields so that power flows in the proper directions):

$$(\vec{E})_\tau = c^+\,\vec{e}(x,y)\,e^{-\gamma z} + c^-\,\vec{e}(x,y)\,e^{+\gamma z} \quad (8)$$

$$(\vec{H})_\tau = c^+\,\vec{h}(x,y)\,e^{-\gamma z} - c^-\,\vec{h}(x,y)\,e^{+\gamma z} \quad (9)$$

$$(\vec{E})_\tau = (\,c^+\,e^{-\gamma z} + c^-\,e^{+\gamma z}\,)\,\vec{e}(x,y) \quad (10)$$

$$(\vec{H})_\tau = (\,c^+\,e^{-\gamma z} - c^-\,e^{+\gamma z}\,)\,\vec{h}(x,y) \quad (11)$$

Note that the transverse components can be represented by a complex amplitude and the real transverse eigenvector modal fields $\vec{e}$ and $\vec{h}$ computed using (5). In general, both transverse and longitudinal components can exist. For a specific time and at a specific location these two components become pure imaginary and pure real respectively. This applies to both the electric field and magnetic field of a mode. In the general case these components maintain this orthogonality over time and distance. Since the transverse component is the only component of interest, its modal vector field can be represented by a pure real vector field without loss of generality or phase information. Hence (10) and (11) can be rewritten as:

$$E_\tau\,\vec{e}\,(x,y) = (\,a\,e^{-\gamma z} + b\,e^{+\gamma z}\,)\,\vec{e}\,(x,y) \quad (12)$$

$$H_\tau\,\vec{h}\,(x,y) = (\,a\,e^{-\gamma z} - b\,e^{+\gamma z}\,)\,\vec{h}\,(x,y) \quad (13)$$

where a is an incoming port wave and b is an outgoing port wave.

The modal vector field amplitudes must be normalized, in which case (12) and (13) can be shown to yield the familiar S–parameter power flow equation [5]:

$$\frac{1}{2}\,(\,aa^* - bb^*\,) = P \quad (14)$$

To allow for multiple modes, the total fields are expressed as the sum of modal fields $\vec{e}_m$ times their modal participation factors:

$$\vec{E}_{total} = \sum_{m=1}^{N} \left(E_{\tau_m} \vec{e}_m \right) \tag{15}$$

where the modes are orthogonal, i. e.,

$$\text{For } m \neq n: \iint_{S_n} \left(\vec{e}_m \cdot \vec{e}_n \right) ds \; = 0 \tag{16}$$

Thus:

$$E_{\tau_n}\Big|_{S_n} = \frac{\iint_{S_n} \left(\vec{E} \cdot \vec{e}_n \right) ds}{\iint_{S_n} \left(\vec{e}_n \cdot \vec{e}_n \right) ds} = \left(a_n \, e^{-\gamma z} + b_n \, e^{+\gamma z} \right) \tag{17}$$

$$H_{\tau_n}\Big|_{S_n} = \frac{\iint_{S_n} \left(\vec{H} \cdot \vec{h}_n \right) ds}{\iint_{S_n} \left(\vec{h}_n \cdot \vec{h}_n \right) ds} = \left(a_n \, e^{-\gamma z} - b_n \, e^{+\gamma z} \right) \tag{18}$$

Hence the incoming and outgoing port waves are:

$$a = (E_\tau + H_\tau)/2 \;, \qquad b = (E_\tau - H_\tau)/2 \tag{19}$$

Subscripts can be put on a and b, where the first subscript represents the port number and the second the excited port number.

With a and b known, the [S] matrix can be derived, here based on a two−port circuit for clarity and simplicity. This derivation is valid and has been implemented in general for any number of ports.

Assuming a two−port, two evaluations will be required. One has its excitation at port one and the other has its excitation at port two. For an N−port, this pattern continues until all N ports have been excited individually for each mode of interest, thereby generating multiple matrix equations. The S−parameter matrix equations for the two−port are:

$$\begin{bmatrix} b_{11} \\ b_{21} \end{bmatrix} = \begin{bmatrix} S_{11} & S_{12} \\ S_{12} & S_{22} \end{bmatrix} \begin{bmatrix} a_{11} \\ a_{21} \end{bmatrix} \tag{20}$$

$$\begin{bmatrix} b_{12} \\ b_{22} \end{bmatrix} = \begin{bmatrix} S_{11} & S_{12} \\ S_{12} & S_{22} \end{bmatrix} \begin{bmatrix} a_{12} \\ a_{22} \end{bmatrix} \tag{21}$$

Combining them gives:

$$\begin{bmatrix} S_{11} & S_{12} \\ S_{12} & S_{22} \end{bmatrix} \begin{bmatrix} a_{11} & a_{12} \\ a_{21} & a_{22} \end{bmatrix} = \begin{bmatrix} b_{11} & b_{12} \\ b_{21} & b_{22} \end{bmatrix} \tag{22}$$

Hence we obtain the expression for the S−parameters:

$$\begin{bmatrix} S_{11} & S_{12} \\ S_{12} & S_{22} \end{bmatrix} = \begin{bmatrix} b_{11} & b_{12} \\ b_{21} & b_{22} \end{bmatrix} \begin{bmatrix} a_{11} & a_{12} \\ a_{21} & a_{22} \end{bmatrix}^{-1} \tag{23}$$

A similar relation applies to a multi−mode N−port circuit.

Since the a's and b's can be calculated for each case separately, (23) shows that a matrix inversion and multiplication are the only additional computations required to determine all of the S−parameters for any N−port circuit. Sequential application of the port field excitations [6] can be accomplished using only one finite element matrix decomposition with multiple forward and backward substitutions for each frequency.

EXAMPLES

The above equations and multiple types of finite elements are used to compute multi−mode S−parameters in a new software package MicroWaveLab^{TM}[7]. The microwave circuits to be analyzed are modeled with 3D edge elements, along with PMA elements and 2D+ waveguide finite elements at all of its port cross sections.

The S−parameters are to be computed first for the three−stub waveguide filter of Fig. 1. This is a two−port air−filled device with perfectly conducting metal walls.

Fig. 2 shows the finite element model developed for the filter. Due to symmetry of the geometry and of the TE10 waveguide excitation to be analyzed, only one half of the filter need be modeled. The 3D finite elements are all isoparametric second order edge hexahedrons.

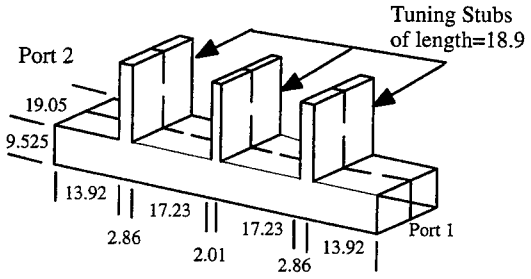

Fig. 1. Geometry of three−stub filter to be analyzed. Dimensions are in mm.

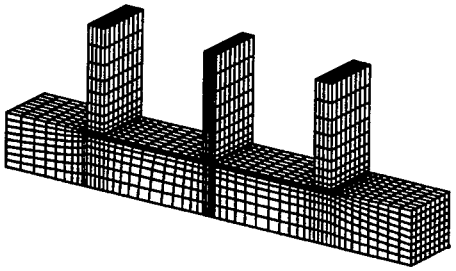

Fig. 2. Hexahedral mesh for one−half model of filter of Fig. 1. Note the mesh biasing toward the stub junctions.

The computed magnitude of S11 versus frequency is graphed in Fig. 3. Note that the notches in the computed filter response agree closely with the measured S11. The computed propagating fields are shown in Fig. 4.

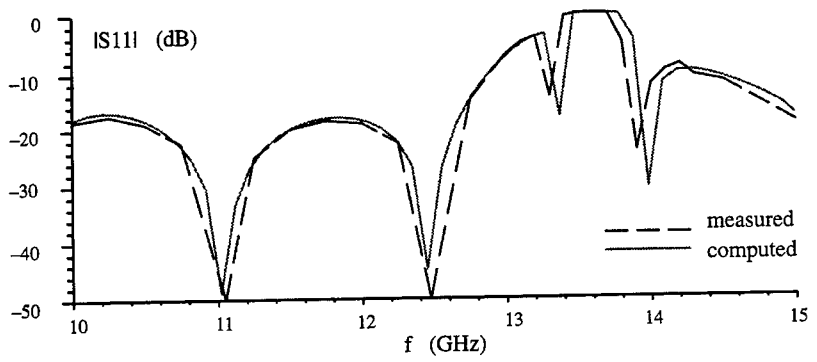

Fig. 3. S11 of filter of Fig. 1 from 10 to 15 GHz.

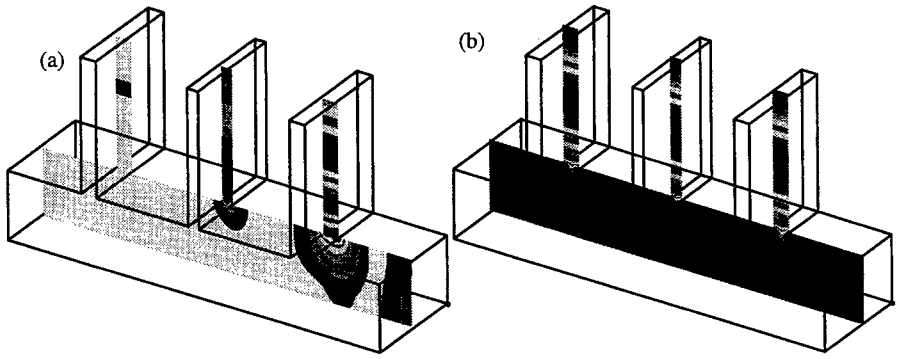

Fig. 4. E field magnitude in filter of Fig. 1 with power input at port 1.
a). at 13.5 GHz (band stop), b). at 11.0 GHz (band pass).

The second example shows different modes at different ports and is the cylindrical-to-rectangular air-filled waveguide transition shown in Fig. 5. It is modelled with 3D finite elements that are second order edge tetrahedrons. Three PMA layers of total thickness 0.41 mm are used on each port. Fig. 5 shows both the real and imaginary contours of electric field, which are seen to be displaced from each other, indicating that a traveling wave propagates with small reflections. The reflection by the PMA is more than 40 db down.

Fig. 6 graphs the computed S21 vs. frequency, where port 1 is the cylindrical waveguide operated in its vertically polarized TE11 mode and port 2 is the rectangular waveguide operated in its TE10 mode. The transmission loss is less than −0.015 db over the frequency range, showing that almost all of the energy input at port 1 reaches port 2.

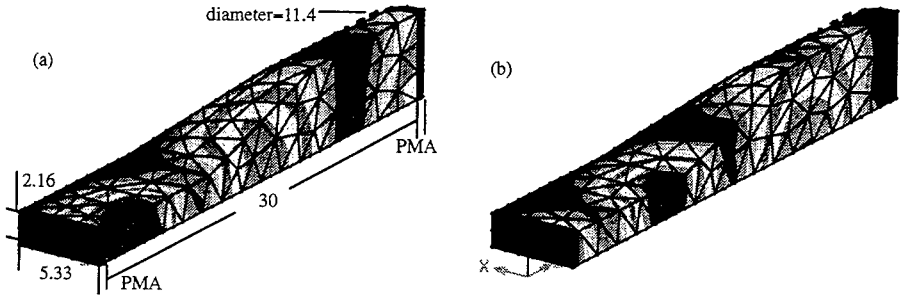

Fig. 5. Geometry and mesh for 1/4 model of cylindrical to rectangular waveguide transition, dimensions in mm. a). Contours of real E at 18.6 GHz, b). Imaginary E.

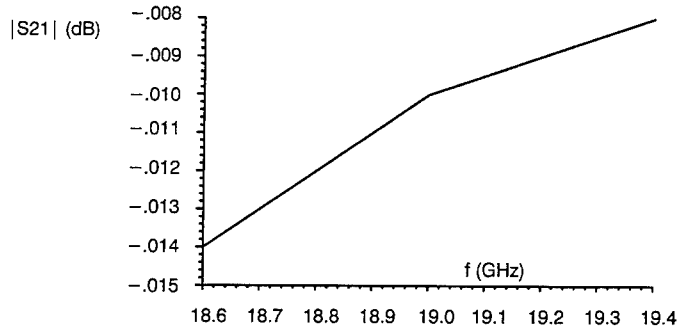

Fig. 6. Computed S21 of transition of Fig. 5.

The final example shows different modes at the same port. Fig. 7 shows an overmoded air–filled cylindrical waveguide of radius 12.7 mm operated at 15 GHz. Table 1 shows that the propagation constants computed using (5) agree closely with theoretical values [5]. The computed modes include a degenerate duo for the fundamental TE11 mode and and a degenerate trio for TE01 and TM11 modes, as shown in Fig. 7.

TABLE 1. Propagation constants (1/m) of cylindrical waveguide of Fig. 7.

Mode	TE11	TM01	TE21	TE01	TM11
Theoretical	278.96	250.94	202.49	88.25	88.25
Computed	278.96, 278.96	250.95	202.48, 202.48	88.32	88.31, 88.30

CONCLUSION

A new method has been derived for computing S–parameters of microwave circuits using a variety of edge finite elements. The method allows multiple modes at multiple ports of arbitrary geometry. The computed S11 of a stub filter shows good agreement with measurements. The computed S21 for a cylindrical to rectangular mode transition is reasonable. Also, multiple mode degeneracies in an overmoded cylindrical waveguide are accurately analyzed.

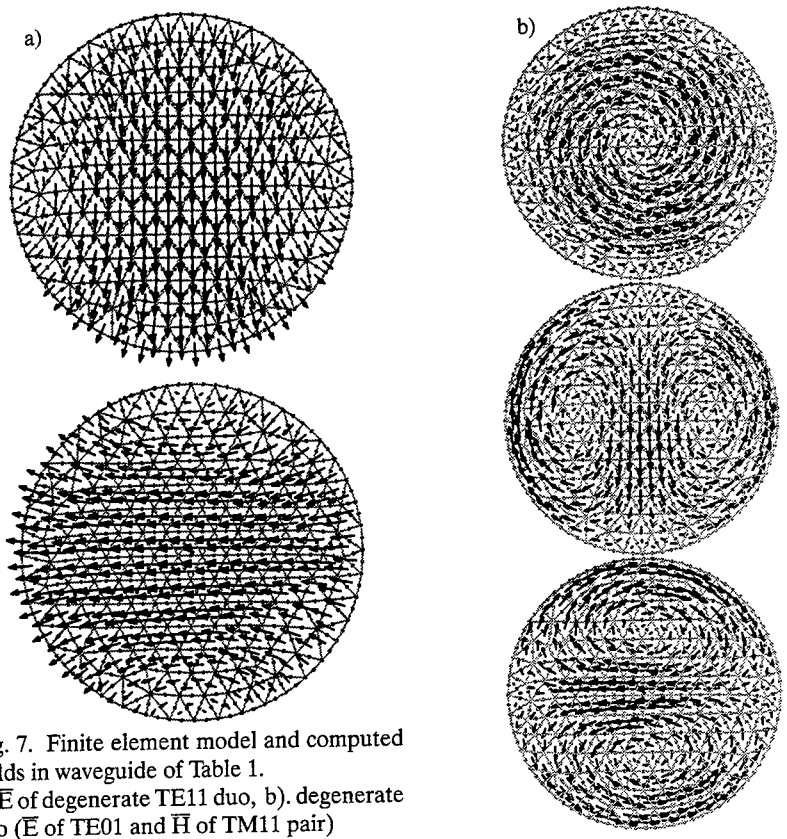

Fig. 7. Finite element model and computed fields in waveguide of Table 1.
a) $\overline{E}$ of degenerate TE11 duo, b). degenerate trio ($\overline{E}$ of TE01 and $\overline{H}$ of TM11 pair)

REFERENCES

[1] I. Bardi, O. Biro, R. Dyczij–Edlinger, K. Preis, and K. R. Richter, "On the treatment of sharp corners in the FEM analysis of high frequency problems," *IEEE Trans. Magnetics*, v. 30, Sept. 1994, pp. 3108–3111.

[2] Jin–Fa Lee, Gary Lizalek, and John Brauer, "Finite element analysis of waveguides using edge–based magnetic vector potential and nodal–based electric scalar potential," *Proc. Applied Computational Electromagnetics Society Symposium*, Monterey, CA, March 1995, pp. 1054–1061.

[3] J. F. DeFord and P. Saladin, "Analysis of waveguide components using H_0–curl hexahedral edge elements in MSC/EMAS," *Digest of IEEE Microwave Theory & Techniques Symposium*, Orlando, FL, May 1995, pp. 1207–1210.

[4] David M. Kingsland, Zachary S. Sacks, and Jin–Fa Lee, "Perfectly matched anisotropic absorbers for finite element applications in electromagnetics," *Proc. ACES Symposium*, Monterey, CA, March 1995, pp. 490–497.

[5] S. Ramo, J. Whinnery, and T. Van Duzer, *Fields and Waves in Communication Electronics*, New York: Wiley & Sons, 1965, p. 603 and p. 431.

[6] John R. Brauer and Franz Hirtenfelder, "Surface integrals on 3D and 2D finite element models for skin effect excitations and open boundaries," *IEEE Trans. Magnetics*, v. 28, March 1992, pp. 1659–1662.

[7] MicroWaveLab is a proprietary product of the MacNeal–Schwendler Corporation, 815 Colorado Boulevard, Los Angeles, CA 90041 USA.

Characterization of MIMICS Using A Parallelized 3D FEM Code [1]

Jong-Gwan Yook and Linda P. B. Katehi
Radiation Laboratory
Department of Electrical Engineering and Computer Science
The University of Michigan, Ann Arbor, MI 48109-2122, U. S. A.
Tel: 313-764-0502, Fax: 313-747-2122, Email: yookjong@engin.umich.edu

Abstract

In this paper, two different types of parallelization schemes for the 3D-FEM based on distributed memory machine are presented and the performance of each scheme is closely examined. According to our study, the *task parallelization* strategy provides an almost linearly scalable FEM code. The parallelized version of the code renders an efficient and fast computation of the circuit parameters. Also, using the parallelized 3D-FEM code, microwave hermetic transition structures for a microwave package are characterized. With the modeling flexibility of the 3D-FEM, the performance of the transitions including the parasitic resonances is clearly understood and, based on this results, design guidelines for improved transitions may be derived.

1 Introduction

The three dimensional finite element method (3D-FEM) is a well established technique which has been extensively applied for the characterization of the 2D and 3D circuits which contain complicated dielectric and metallic configurations [1, 2]. For the analysis of 3D circuit discontinuities the 3D FEM is proved to be very accurate, computationally inexpensive and highly parallelizable. With the above observation, in this paper, a parallelized version of the edge-based vector FEM is developed and applied for the characterization of transitions for microwave and millimeter-wave packages.

In general, packages for low frequency integrated circuits (ICs) have been designed without consideration of the high frequency effects and have revealed satisfactory performance. However, for microwave and millimeter-wave ICs the package should be designed and manufactured very carefully considering all spurious effects [3]-[6]. In this paper, transitions developed for an MMIC package operating in 18 to 40 GHz frequency range are fully characterized and even further several ways of improving the overall performance are presented.

Furthermore, using the fact that the FEM is a frequency domain technique the 3D FEM Fortran code can be parallelized very effectively utilizing the strategy of *task parallelization* and

[1]This work has been supported by NASA Lewis Research Center and the Army Research Office.

the performance of the parallel code optimized on a distributed memory parallel computer (IBM SP2) will be discussed. This type of parallelization leads to nearly linear performance improvement as we increase the number of CPUs. In contrast to the task parallelization, parallelization of the linear equation solver, bi-conjugate gradient method (BiCG), is also implemented and its performance is compared to that of the task parallelization.

2 Parallelization strategies

2.1 Approach 1 : Parallelization of the Linear Equation Solver : [A][x] = [b]

From the observation that the most time consumed by the FEM code is for the solution of the linear equation, our effort is first focused on the effective parallelization of the iterative equation solver. The bi-conjugate gradient method with diagonal preconditioner implemented in our FEM code requires one matrix-vector multiplication in every iteration. The FEM matrix [**A**] is computed once in the whole course of iterations but the unknown coefficient vector [**x**] has to be renewed in every iteration. Also, to maximize the usage of the storage space and to minimize the number of floating point operations in the conjugate gradient type solver, only non-zero matrix entries and its integer coordinates are stored.

For a parallel matrix-vector multiplication we broadcast the main FEM matrix in the beginning of the BiCG iteration. Since the matrix [**A**] is fixed during the iterations, it is only needed to be broadcasted once. But in every iteration we need to broadcast a vector [**x**] which will be multiplied by the matrix [**A**] and will collect the results from the nodes after the multiplications are performed. The following shows an example of broadcasting the matrix [**A**] using message passing paradigm.

```
CALL MP_BCAST(A,MessageLength,Source,AllGroup)
```

When the size of the matrix or message is too large to handle, we can broadcast small part of the message separately as shown below:

```
IF (TaskID.EQ.0) THEN ← master node
  DO I = 1,NumOfTask-1
     Destination = I
     Ntype = I
     CALL MP_SEND(A,MessageLength,Destination,Ntype,MessageID)
  ENDDO
ELSEIF(TaskID.NE.0) THEN ← slave nodes
  Source= 0
  CALL MP_BRECV(A,MessageLength,Source,TaskID,MessageID)
ENDIF
```

Note that to ensure the synchronism between the *source* (master node) and *destination* (slave nodes), we have used block receive subroutine (MP_BRECV). After we broadcast the [**A**], the

vector [x] is also broadcasted in a similar way in every iteration. Now, each small portion of the matrix-vector multiplication is carried out in each node simultaneously and the final results are gathered to form the resulting vector. In the following an example of the parallel pseudo-Fortran code for matrix-vector multiplication is shown:

```
N = INT(MatrixSize/NumberOfTask)
Nstart = TaskID*N + 1
Nstop = Nstart + N - 1
DO I = Nstart,Nstop ← matrix-vector multiplication at each node
   VI = Ã · x̃
ENDDO
CALL MP_GATHER(VI,V,BlockLength,Destination,AllGroup)
```

where $\tilde{\mathbf{A}}$ and $\tilde{\mathbf{x}}$ are part of the original matrix or vector assigned to each CPU. In the above example, we could utilized the sparsity of the matrix and as a result we have indirect index scheme which would cause inefficient memory/cache access.

2.2 Approach 2 : Parallelization of the Tasks

Since the 3D-FEM in our study is a frequency domain technique, the set of Maxwell's curl equations at a certain frequency point under given boundary conditions are independent on those of the other frequency point. As a result, the set of linear equations at each different frequency points can be formed and solved independently and simultaneously to obtain the complete spectrum of the scattering parameters over a range of frequency region for a given problem. For example, to compute the frequency response of the microwave circuits transitions and package over a wide frequency spectrum we need to solve the problem at many different frequency points. Due to the nature of the problem, the computational tasks corresponding to different frequency points can be distributed equally to each different CPU and performed solution process at the same time. This type of parallelization scheme is often called *embarrassingly parallelized* version of the FEM code, since it only requires minimum parallelization skill but can provide perfect parallelization. This approach is equivalent to using many separate computers in a fast network without requiring any communication between them. This would be considered as not real parallelization in a strict sense, but it can be beneficial to the users of the parallel computers and provides a truly scalable parallelization strategy.

2.3 Performance analysis

To find out the most effective parallelization strategy, we implemented the above two approaches and assessed performance improvement in terms of the total amount of time required to solve a given problem. First, with the *approach 1* we tested two different problem size (M=38109 and 76709, M is the matrix size). As shown in Fig. 1, for the smaller problem size increasing the number of CPUs does not guarantee faster execution time. However, for the larger problem size as we increase the number of CPUs the total execution time decreased and increased again

slightly as we further increased the number of CPUs. This phenomenon can be explained by considering that heavy communication overhead due to the message passing causes performance degradation and finally compensates the advantage of using many CPUs. For larger problems, the advantage of using many CPUs exceeds the disadvantage of communication overhead up to a certain number of CPUs. The optimum number of CPUs and problem size are dependent on the capacity of the communication link and the performance of the switch.

3 Applications

In this section, we will present several numerical examples including hermetic transitions for 18 to 40 GHz packages. All of the computations are performed by using the parallelized FEM code utilizing the *task parallelization* with the observation that the approach 2 is superior to the first.

3.1 Hermetic wall transition

In this section, the effect of the hermetic wall on top of the microstrip-thru-CPW transition with extended vias is investigated. The hermetic wall is formed by a ceramic material bonded on top of a metal plate which forms the upper part of the wall. Figure 3 shows the geometrical details of the hermetic transition structure with extended via holes. The height of the ceramic is equal to the substrate thickness while its relative dielectric constant is chosen to be $\epsilon_{r2} = 2.3$ in contrast to the 12.5 of the substrate. In Figure 4, the magnitude of the scattering parameters obtained using the FEM and FDTD are compared. After placing the hermetic wall on top of the CPW section, the overall return loss has increased by 2 to 3 dB while its overall frequency dependency has remained unchanged. In the whole frequency region considered here from 10 to 25 GHz, the return loss is less than -5 dB. However, in the low end of this frequency region, up to 13 GHz, the return loss is less than -10 dB. The effect of the hermetic wall is small as it is expected from the field distribution in the CPW structure. A typical problem size (M), number of iterations for convergence (Iter), and convergence time (T) are given as follows:

$$\mathrm{M} \simeq 92000, \mathrm{Iter} \simeq 6000, \mathrm{T} \simeq 1600 \text{ sec.}$$

3.2 Hermetic bead transition

As another type of hermetic transition, hermetic bead could be used for effective packaging element. In this section, we investigated the effect of the rectangular and circular hermetic bead transitions. The radius of the circular ring is chosen as H_1 so that the circular ring fits into the square hole. As shown in the Figure 5 the performance of circular ring is very similar to the square one except at the lower frequency region. The degraded performance of the circular ring is mainly due to the effect of the conductor placed closer than the square one. A typical problem size (M), number of iterations for convergence (Iter), and convergence time (T) are given as follows:

$$\mathrm{M} \simeq 81000, \mathrm{Iter} \simeq 3100, \mathrm{T} \simeq 600 \text{ sec.}$$

4 Conclusion

In this paper, we have investigated two different types of parallelization schemes and found that the second approach (*task parallelization*) renders linearly scalable 3D-FEM code. Using the above scheme, several different types of packaging elements are carefully characterized and compared well with other full-wave technique, such as the FDTD technique.

Acknowledgment

The authors would like to thank the Maui High Performance Computing Center (MHPCC) and also the University of Michigan Center for Parallel Computing (CPC), which is partially funded by NSF grant CDA-92-14296 and the Ford Motor Company, for the use of their computational facilities.

References

[1] J. Yook, N. Dib, and L. Katehi, "Characterization of High Frequency Interconnects Using Finite Difference Time Domain and Finite Element Methods," *IEEE Trans. Microwave Theory Tech.*, vol. 42, No. 9, pp. 1727-1736, Sep. 1994.

[2] J. Yook, N. Dib, E. Yasan and L. Katehi, "A Study of Hermetic Transitions for Microwave Packages," *IEEE MTT-S International Microwave Symposium*, pp. 1579-1582, May 1995.

[3] Linda P. B. Katehi, "The Role of EM Modeling in Integrated Packaging," pp.982-985, *1992 IEEE AP-S Digest*, July 1992.

[4] H. J. Kuno and T. A. Midford, "The Evolution of MMIC Packaging," pp.1005-1008, *1992 IEEE AP-S Digest*, July 1992.

[5] D. W. Griffin and A. J. Parfitt, "Electromagnetic Design Aspects of Packages for Phased Array Modules That May Incorporate Monolithic Antenna Elements," pp. 986-989, *1992 IEEE AP-S Digest*, July 1992.

[6] Bernhard A. Ziegner, "High Performance MMIC Hermetic Packaging," *Microwave Journal*, pp. 133-139, Nov. 1986.

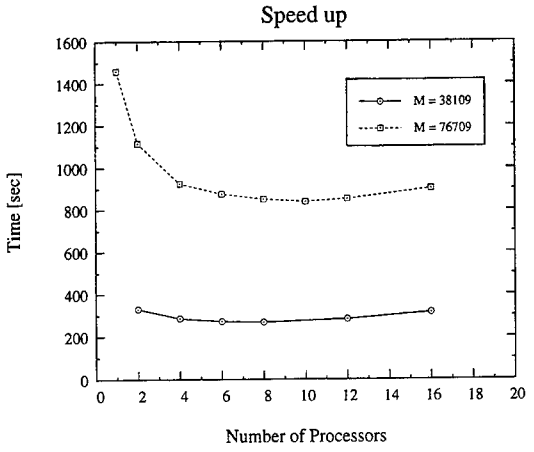

Figure 1: Number of processors vs. execution time for two different size problems. The M is the number of unknowns which is equivalent to the matrix size to be solved.

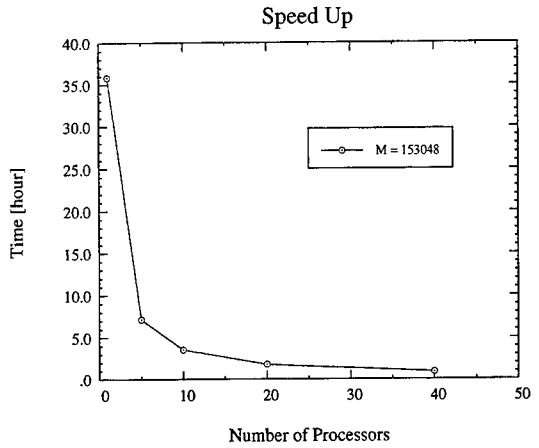

Figure 2: Number of processors vs. execution time with the approach 2. The M is the number of unknowns which is equivalent to the matrix size to be solved.

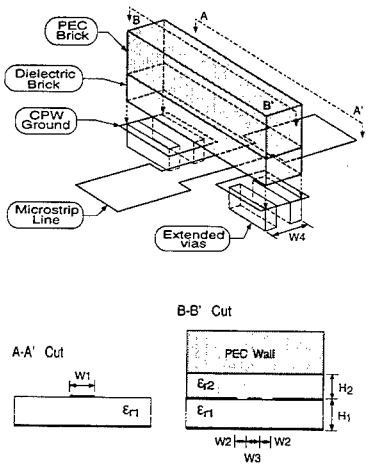

Figure 3: Geometry of the microstrip-thru-CPW transition with hermetic wall on top of the extended PEC via grounding case. The width of the hermetic wall is 1.6 mm. $W_1 = 0.48$ mm, $W_2 = 0.14$ mm, $W_3 = 0.2$ mm, $W_4 = 1.6$ mm, $H_1 = H_2 = 0.635$ mm, $\epsilon_{r1} = 12.5$, and $\epsilon_{r2} = 2.3$.

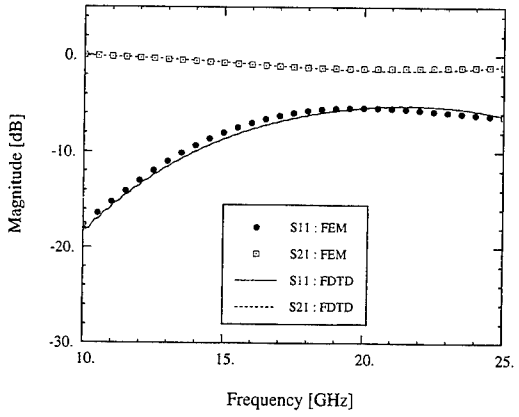

Figure 4: Comparison of the scattering parameters for the transition with hermetic wall on top and extended PEC via under the circuit plane.

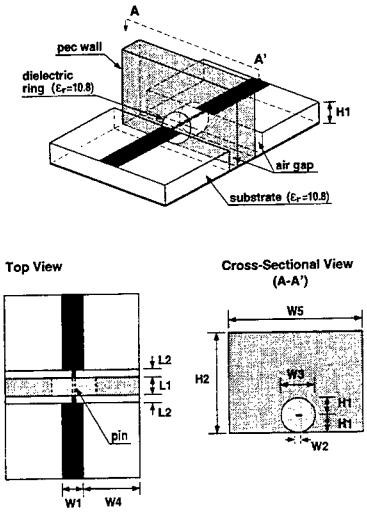

Figure 5: Geometry of the hermetic bead transition. $W_1 = 0.55$ mm, $W_2 = 0.21$ mm, $W_3 = 1.27$ mm, $W_4 = 2.225$ mm, $W_5 = 5.0$ mm, $H_1 = 0.635$ mm, $H_2 = 4.0$ mm, $L_1 = 1.50$ mm, $L_2 = 0.40$ mm, and $\epsilon_r = 10.8$.

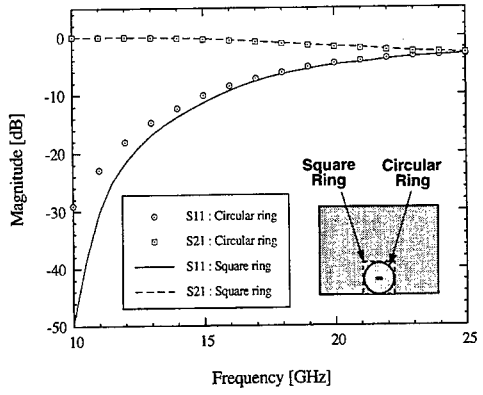

Figure 6: Comparison of the scattering parameters of the hermetic bead transition with square and circular dielectric ring of radius equals H_1.

Combined PML and ABC for Finite Element Analysis of Scattering Problems

J. M. Jin and W. C. Chew
Center for Computational Electromagnetics
Department of Electrical and Computer Engineering
University of Illinois at Urbana-Champaign
Urbana, Illinois 61801-2991
E-mail: jjin@uxh.cso.uiuc.edu

ABSTRACT

A perfectly matched layer (PML) is combined with an absorbing boundary condition (ABC) for mesh truncation in the finite element solution of electromagnetic scattering problems. It is shown that the combined PML and ABC has less undesired reflection than the PML or ABC alone.

I. INTRODUCTION

When solving open-region scattering problems using the finite element method (FEM), the infinite region exterior to the scatterer must be truncated with an artificial boundary to limit the number of unknowns. Consequently, a boundary condition must be introduced at this artificial boundary for a unique finite element solution. Such a boundary condition should make the boundary appear as transparent as possible to the scattered field, or in other words, it should minimize the reflection of the scattered field incident upon the boundary. An ideal boundary condition is one that possesses zero reflection for all angles of incidence. However, except for those derived from the boundary integral representation or the eigenfunction expansion of the scattered field, this ideal condition is unrealizable and its approximation is often sought.

One such approximation is the so-called absorbing boundary conditions (ABCs), which are usually derived from differential wave equations [1-3]. The ABCs are applied at the artificial boundary directly and, as a result, their use does not introduce additional unknowns. However, they do not yield zero reflection for all angles of incidence and thus are not exact. To minimize the solution error, they are often applied at some distance away from the scatterer, resulting in an extended discretization region. However, the ABCs have two advantages in that (i) they do not increase the condition number of the FEM matrix and (ii) they can have a perfect absorption at some prescribed angles of incidence.

Another approximation is to use fictitious absorbers, a good example of which is Berenger's perfectly matched layers (PML) [4-7]. Since the PML involves several parameters, it can be designed to outperform the first- and second-order ABCs. However, compared to the ABCs, the PML has several disadvantages when applied to FEM. First, it enlarges the discretization region since its volume requires numerical discretization as well. Second, it increases the condition number of the FEM matrix, and hence the number of iterations when an iterative solver is employed. The PML usually performs best at and close to the normal incidence. Although this performance range can also be extended to

large angles of incidence by either increasing the PML thickness or the maximum loss tangent, doing so will either increase the discretization region or the matrix condition number.

In this paper, we combine the PML and ABC to fully exploit their advantages and suppress the disadvantages. We show that the combined PML and ABC can extend its best performance to large angles of incidence without increasing its thickness and loss tangent. This allows us to keep the number of unknowns to a minimum while improving the condition number of the FEM matrix.

II. FORMULATION

The PML as a material absorbing boundary was recently introduced by Berenger for truncating the mesh in the numerical solution of the partial differential equations for wave scattering [4]. Various researchers have sought a different interpretation of this material absorbing boundary and extended it to three dimensions [5-7]. In particular, Chew and Weedon have interpreted the perfectly matched layers as coordinate stretching in frequency domain [5], whereas Sacks *et al.* have interpreted them as fictitious anisotropic materials possessing zero reflection at their interface [7]. By introducing a loss tangent in a PML, the wave propagating in the PML will be attenuated in the direction normal to the interface. As such, the PML, when backed by a perfectly electrical conductor (PEC), can be used as the absorbing boundary for numerical solution of wave scattering.

Unfortunately, when a PML is backed with a PEC surface, its reflection coefficient is no longer zero for all angles of incidence. Since an obliquely incident plane wave has a much longer effective wavelength in the direction normal to the interface, it will experience less attenuation than the normally incident waves. As a result, the reflection coefficient of a PEC-backed PML increases with the angle of incidence and reaches 1 at the grazing incidence. Although the reflection within a certain range of incidence angle can be reduced by increasing the PML thickness and loss tangent [8], a large thickness will increase the volume of discretization and a large loss tangent will increase the condition number of the FEM matrix, making the FEM solution less efficient and more problematic.

On the other hand, a PEC surface is not the only choice for terminating a PML; one can choose other surfaces as well, such as impedance surfaces or mathematical surfaces described by absorbing boundary conditions. As predicted in [9], such a termination should improve the absorption of the fictitious absorbers. In particular, when the first- and second-order ABCs are employed, the FEM matrix will retain its original sparsity and symmetry. However, we must realize that traditional ABCs are designed to have a zero reflection at the normal incidence and this reflection increases with the angle of incidence in much the same manner as the PEC-backed PML. Therefore, a combination of the PML with such ABCs will not improve its performance significantly. A better choice is to use the ABCs whose angle of perfect absorption can be controlled by some parameters.

In the following, we combine the PML with ABC and investigate the improvement of their performance for the FEM solution of wave scattering in frequency domain. The use of the combined PML and ABC for wave scattering is illustrated in Fig. 1. The scattered electric field satisfies the vector wave equation [5]

$$\nabla_e \times \left\{ [\mu_r]^{-1} \cdot (\nabla_e \times \mathbf{E}^{sc}) \right\} - k_0^2 [\varepsilon_r] \cdot \mathbf{E}^{sc} = \mathbf{F}^{inc} \tag{1}$$

where ε_r and μ_r denote the permittivity and permeability, and $\mathbf{F}^{\text{inc}} = 0$ within the PML and outside the PML,

$$\mathbf{F}^{\text{inc}} = \nabla \times \left\{ [\mu_r]^{-1} \cdot (\nabla \times \mathbf{E}^{\text{inc}}) \right\} - k_0^2 [\varepsilon_r] \cdot \mathbf{E}^{\text{inc}} \tag{2}$$

Also in (1),

$$\nabla_e = \hat{x} \frac{1}{\sqrt{e_x}} \frac{\partial}{\partial x} \frac{1}{\sqrt{e_x}} + \hat{y} \frac{1}{\sqrt{e_y}} \frac{\partial}{\partial y} \frac{1}{\sqrt{e_y}} + \hat{z} \frac{1}{\sqrt{e_z}} \frac{\partial}{\partial z} \frac{1}{\sqrt{e_z}} \tag{3}$$

in which $e_x = e_y = e_z = 1$ outside the PML, and

$e_x = s_x, \quad e_y = e_z = 1$ for the PML normal to the x axis

$e_y = s_y, \quad e_x = e_z = 1$ for the PML normal to the y axis

$e_z = s_z, \quad e_x = e_y = 1$ for the PML normal to the z axis

In the above, s_x, s_y, and s_z are complex numbers. For two-dimensional problems (assuming E-polarization and no variation along the z axis), (1) is reduced to

$$\frac{1}{\sqrt{s_x}} \frac{\partial}{\partial x} \left(\frac{1}{s_x \mu_r} \frac{\partial}{\partial x} \frac{E_z^{\text{sc}}}{\sqrt{s_x}} \right) + \frac{\partial}{\partial y} \left(\frac{1}{\mu_r} \frac{\partial E_z^{\text{sc}}}{\partial y} \right) + k_0^2 \varepsilon_r E_z^{\text{sc}} = F_z^{\text{inc}} \tag{4}$$

for the PML normal to the x axis. A similar equation can be obtained for the PML normal to the y axis. The ABC can be written uniformly as

$$\hat{n} \times \left[s_n^{-1} (\nabla_e \times \mathbf{E}^{\text{sc}}) \right] + P(\mathbf{E}^{\text{sc}}) = 0 \tag{5}$$

where P denotes an operator. In particular, for the first-order ABC, it is given by

$$P(\mathbf{E}^{\text{sc}}) = jk_0 \cos\theta_a \hat{n} \times (\hat{n} \times \mathbf{E}^{\text{sc}}) \tag{6}$$

where θ_a denotes the angle of perfect absorption. For the second-order ABC, it is given by

$$P(\mathbf{E}^{\text{sc}}) = jk_0 p_0 \hat{n} \times (\hat{n} \times \mathbf{E}^{\text{sc}}) + \frac{p_2}{jk_0} \left\{ \nabla \times [\hat{n} \cdot (\nabla \times \mathbf{E}^{\text{sc}}) \hat{n}] + \nabla_t (\nabla \cdot \mathbf{E}_t^{\text{sc}}) \right\} \tag{7}$$

where p_0 and p_2 are parameters controlling two angles of perfect absorption. For two-dimensional problems, (5)-(7) reduce to

$$\frac{1}{s_n} \frac{\partial E_z^{sc}}{\partial n} = -jk_0 \cos\theta_a E_z^{sc} \tag{8}$$

for the first-order ABC, and

$$\frac{1}{s_n}\frac{\partial E_z^{sc}}{\partial n} = -jk_0 p_0 E_z^{sc} - \frac{p_2}{jk_0}\frac{\partial^2 E_z^{sc}}{\partial t^2} \tag{9}$$

for the second order ABC.

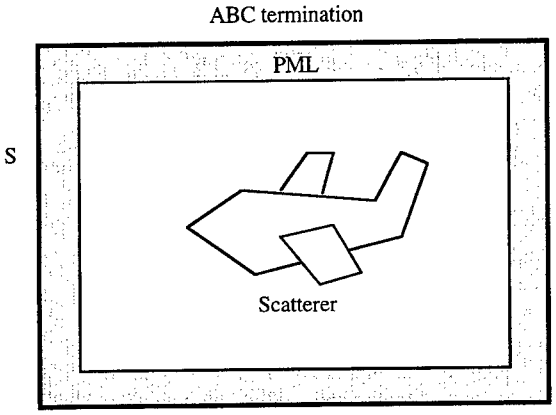

Figure 1. Illustration of the use of combined PML and ABC for truncating the computa-tional domain in wave scattering.

The boundary-value problem described above can be solved by seeking the stationary point of the functional [10]

$$\begin{aligned} F(\mathbf{E}^{sc}) = \tfrac{1}{2}\iiint_V \left\{(\nabla_e \times \mathbf{E}^{sc})\cdot[\mu_r]^{-1}\cdot(\nabla_e \times \mathbf{E}^{sc}) - k_0^2 \mathbf{E}^{sc}\cdot[\varepsilon_r]\cdot\mathbf{E}^{sc}\right\} dV \\ - \iiint_V \mathbf{E}^{sc}\cdot\mathbf{F}^{inc}\, dV - \tfrac{1}{2}\oiint_S \mathbf{E}^{sc}\cdot P(\mathbf{E}^{sc})\, dS \end{aligned} \tag{10}$$

This variational problem can be discretized and solved using the FEM [11].

III. NUMERICAL VERIFICATION

To evaluate the performance of the combined PML and ABC, we have written one-, two-, and three-dimensional FEM programs for some special problems. In all examples that follow, we let

$$s_x = s_y = s_z = 1 - j\delta_{\max}(l/L)^2 \tag{11}$$

where $\delta_{\max}$ denotes the maximum loss tangent (LTMAX), l is the distance from the air/PML interface, and L is the thickness of the PML.

First, we calculated the reflection coefficient of an ABC-backed PML using one-dimensional FEM and compared with those obtained with the PEC-backed PML and ABC. Representative results are given in Figs. 2 to 5, where for the first-order ABC we let $\theta_a = 60$ degrees and for the second-order ABC we choose $p_0 = 1.03597$ and $p_2 = -0.76537$ so that perfect absorption occurs at $\theta = 22.5$ and 67.5 degrees, respectively [3]. As can be seen, the reflection coefficient of the combined PML and ABC is reduced significantly over a wide range of incidence angle.

Then we applied the combined PML and ABC to a parallel-plate waveguide, whose two plates are 1 cm apart. Both ends of the waveguide are terminated with the combined PML and ABC and the first higher-order mode, whose cutoff frequency is 15 GHz, is launched at the center of the waveguide. The reflection coefficient obtained using the two-dimensional FEM is shown in Figs. 6 and 7, from which we can see that the combined PML and ABC is superior to the PEC-backed PML near the cutoff. At the cutoff, the wave is incident on the PML at grazing and hence there is a total reflection. Note that the results in Figs. 6 and 7 are consistent with those in Figs. 2 and 4.

Finally, we applied the combined PML and ABC to a rectangular waveguide whose cross-section is $2\text{ cm} \times 0.5\text{ cm}$. Again, we terminated both ends of the waveguide with the ABC-backed PML and launched the TE_{10} mode (whose cutoff frequency is 7.5 GHz) at the center. The reflection coefficient obtained using the three-dimensional FEM is given in Fig. 8 and again the ABC-backed PML outperforms the PEC-backed PML near the cutoff.

In passing, we note that although the PML has the drawback of total reflection at the cutoff for waveguide problems, this drawback does not exist for open-region scattering problems since the PML is always placed at some distance away from the scatterer. Since the ABC-backed PML has a much smaller reflection than the PEC-backed PML near the grazing incidence, it can be placed closer to the scatterer, resulting in a smaller computational domain.

IV. CONCLUSION

In this paper we combined the PML with ABC for truncating meshes in the FEM solution of partial differential equation for wave scattering. We showed that the combined PML and ABC has a significantly better performance than the PEC-backed PML or ABC alone.

Although the PML has achieved great success in time domain analysis, its usefulness in frequency domain remains unclear. When we performed computations for three-

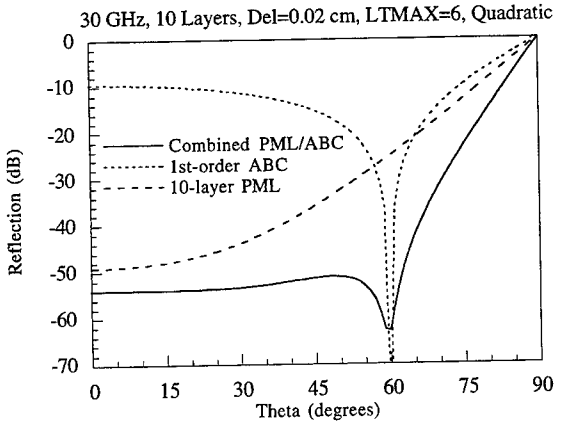

Figure 2. Comparison of reflection coefficient of a 10-layer PML, first-order ABC, and their combination.

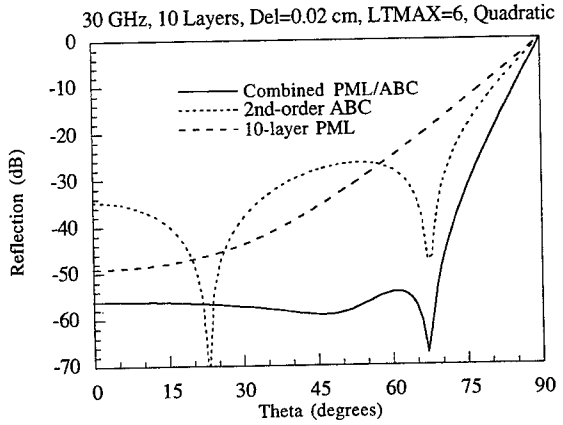

Figure 3. Comparison of reflection coefficient of a 10-layer PML, second-order ABC, and their combination.

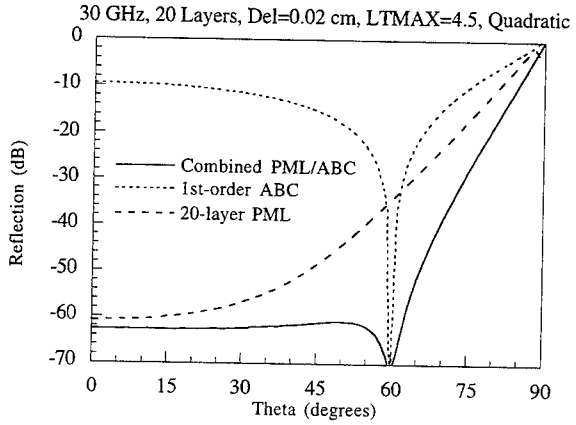

Figure 4. Comparison of reflection coefficient of a 20-layer PML, first-order ABC, and their combination.

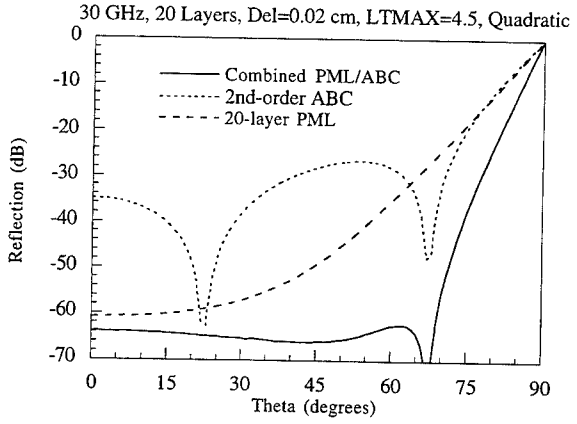

Figure 5. Comparison of reflection coefficient of a 20-layer PML, second-order ABC, and their combination.

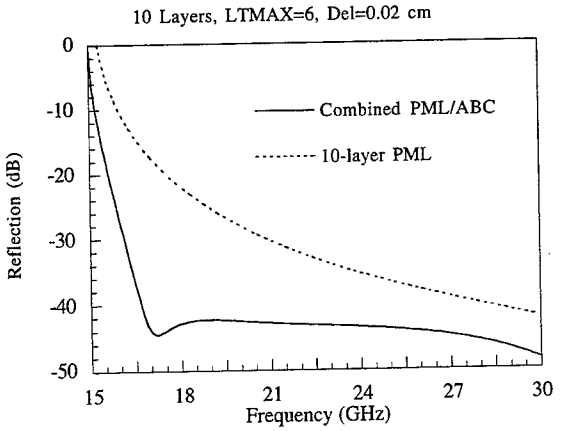

Figure 6. Reflection coefficient of a parallel-plate waveguide terminated with a 10-layer PML and a PML combined with the first-order ABC.

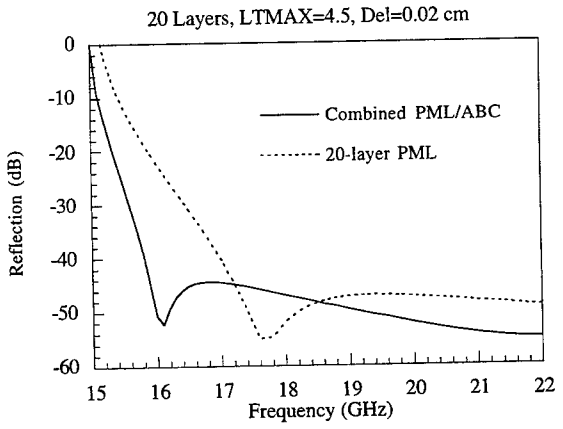

Figure 7. Reflection coefficient of a parallel-plate waveguide terminated with a 20-layer PML and a PML combined with the first-order ABC.

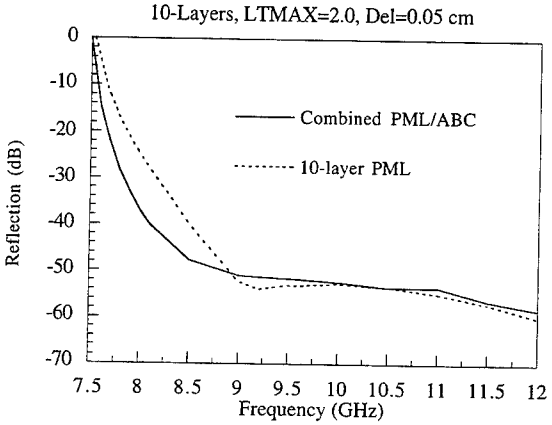

Figure 8. Reflection coefficient of a rectangular waveguide terminated with a 10-layer PML and a PML combined with the first-order ABC.

dimensional problems using an iterative method, we observed that the inclusion of a PML increases substantially the matrix condition number and thus the iteration number for convergence. Therefore, unless a better PML is developed, the use of PML in three dimensions is limited since it requires the use of a direct method for solving the FEM matrix equation.

ACKNOWLEDGMENT

This work was supported by the National Science Foundation under grants NSF ECE 94-57735 and 93-02145, and the Office of Naval Research under grants N00014-95-1-0848 and N00014-95-1-0872.

REFERENCES

[1] B. Engquist and A. Majda, "Absorbing boundary conditions for the numerical simulation of waves," *Math. Comput.*, vol. 31, pp. 629-651, July 1977.

[2] A. Bayliss, M. Gunzburger, and E. Turkel, "boundary conditions for the numerical solution of elliptic equations in exterior regions," *SIAM J. Appl. Math.*, vol. 42, pp. 430-451, Apr. 1982.

[3] T. G. Moore, J. G. Blaschak, A. Taflove, and G. A. Kriegsmann, "Theory and application of radiation boundary operators," *IEEE Trans. Antennas Propagat.*, vol. AP-36, pp. 1797-1812, Dec. 1988.

[4] J.-P. Berenger, "A perfectly matched layer for the absorption of electromagnetic waves," *J. Computational Phys.*, vol. 114, pp. 185-200, 1994.

[5] W. C. Chew and W. H. Weedon, "A 3D perfectly matched medium from modified Maxwell's equations with stretched coordinates," *Microwave Opt. Tech. Lett.*, vol. 7, pp. 599-604, 1994.

[6] D. S. Katz, E. T. Thiele, and A. Taflove," Validation and extension to three dimensions of the Berenger PML absorbing boundary condition for FD-TD meshes," *IEEE Microwave Guided Wave Lett.*, vol. 4, pp. 268-270, 1994.

[7] Z. S. Sacks, D. M. Kingsland, R. Lee, and J.-F. Lee, "A perfectly matched anisotropic absorber for use as an absorbing boundary condition," *IEEE Trans. Antennas Propagat.*, vol. AP-43, pp. 1460-1463, Dec. 1995.

[8] W. C. Chew and J. M. Jin, "Perfectly matched layers in the discretized space: An analysis and optimization," *Electromagnetics*, to appear.

[9] J. M. Jin, J. L. Volakis, and V. V. Liepa, ``A fictitious absorber for truncating finite element meshes in scattering," *Proc. Inst. Elec. Eng., part H*, vol. 139, no. 5, pp. 472-476, Oct. 1992.

[10] J. M. Jin and W. C. Chew, "Variational formulation of electromagnetic boundary-value problems involving anisotropic media," *Microwave Opt. Tech. Lett.*, vol. 7, pp. 348-351, 1994.

[11] J. M. Jin, *The Finite Element Method in Electromagnetics*. New York: John Wiley & Sons, 1993.

Modelling Microstrip Patches Using the Finite Element Method

D.B.Davidson, D.H.Malan, C.B.Wilsen

Department of Electrical and Electronic Engineering
University of Stellenbosch, Stellenbosch 7600, South Africa
e-mail: davidson@firga.sun.ac.za

Abstract

A combined Finite Element / Moment Method formulation for the analysis of scattering and radiation from cavity-backed microstrip antennas is reviewed. Edge-based elements are used to discretise the functional. A variety of problems encountered during implementation are discussed, and results computed compared to published and measured data for two representative problems.

1 Introduction

Microstrip antennas are widely used nowadays since they are lightweight, conformal, and relatively easy and cheap to fabricate. Indeed, the only major problem of standard designs that on occasions inhibits their use is their inherently narrow bandwidth. In the microwave regime, where their limited bandwidth (typically only a few percent) is acceptable, they are probably the antenna of first choice for many applications, especially aerospace.

There are several approaches to modelling these antennas: early work used cavity and transmission line models, and subsequent work with the Method of Moments (MoM) and the Sommerfeld potentials achieved good results. Recently, the Finite Element Method (FEM) has emerged as a powerful tool for microstrip antenna analysis. It offers a number of advantages. As implemented in this paper, the actual model is of a patch residing in a cavity, which is often a better model of a flush-mounted antenna than the infinite dielectric required by the Sommerfeld MoM formulations. Furthermore, inhomogeneous substrate and superstrate regions can be handled with ease; published work on reducing the radar cross section of microstrip antennas indicates that this can be done via lossy partial coatings or shorting pins, which can be incorporated very easily within a FEM mesh.

2 Formulation

The formulation used here is that originally published by Jin and Volakis [1], and with extensions in [2, §9.3–9.4]. We shall briefly summarize the formulation, retaining the original notation. (Other researchers intending to implement this formulation should note that there are some errors in the published work; details are available from Jin or the present authors). For a source-free cavity, the electric field inside the cavity is governed by:

$$\nabla \times \left(\frac{1}{\mu_r} \nabla \times \mathbf{E} \right) - k_0^2 \varepsilon_r \mathbf{E} \; = \; 0 \tag{1}$$

Any solution to this equation must satisfy two different boundary conditions. On the cavity wall, the electric field vanishes, therefore:

$$\hat{n} \times \mathbf{E} = 0 \tag{2}$$

At the aperture (cavity opening), the fields in the region above it need to be linked with those directly below. An appropriate boundary condition is [2, pp.311–320]:

$$\hat{z} \times [\frac{1}{\mu_r} \nabla \times \mathbf{E}(\mathbf{r})]_{z=0-} = 2k_0^2 \hat{z} \times \int\int_{S_a} [\hat{z} \times \mathbf{E}(\mathbf{r}')] \cdot \overline{\overline{G}}_0(\mathbf{r}, \mathbf{r}') dS' - 2jk_0 Z_0 \hat{z} \times \mathbf{H}^{inc}(\mathbf{r}) \tag{3}$$

S_a is the aperture of the cavity; see Figure 1 for the geometry. There are a variety of approaches for terminating the FEM mesh; recently, attention has focused on various absorbing boundary conditions, in particular on adapting Berenger's Perfectly Matched Load [3] (derived for the Finite Difference Time Domain Method) to the FEM (see, for example, [4]). However, for these cavity-backed structures, the FEM/MoM hybridization remains most attractive since the mesh termination is done right at the aperture of the cavity, and the FEM mesh is thus only required in the cavity. Using a sparse (not banded) iterative matrix solver, the rather wide matrix bandwidth that results is not a major drawback. Hence we confine this paper to the FEM/MoM scheme.

Since plane wave illumination is assumed, the excitation field can be written in terms of the incident magnetic field $\mathbf{H}^{inc}$ only. The source and observation point coordinates are indicated by primed and unprimed variables, respectively. (In equation (3) both source and observation points lie on the cavity aperture.)

$\overline{\overline{G}}_0$ is the free space dyadic Green's function defined as:

$$\overline{\overline{G}}_0(\mathbf{r}, \mathbf{r}') = \left(\bar{\bar{\mathbf{I}}} - \frac{1}{k_0^2} \nabla \nabla' \right) G_0(\mathbf{r}, \mathbf{r}') \tag{4}$$

with

$$G_0(\mathbf{r}, \mathbf{r}') = \frac{e^{-jk_0|\mathbf{r}-\mathbf{r}'|}}{4\pi|\mathbf{r}-\mathbf{r}'|} \tag{5}$$

and

$$\bar{\bar{\mathbf{I}}} = \hat{x}\hat{x} + \hat{y}\hat{y} + \hat{z}\hat{z} \tag{6}$$

It can be shown [2, pp.267–277, pp.311–320] that an equivalent variational problem for equation (1) and boundary conditions (2) and (3) is:

$$\begin{aligned} \delta F(\mathbf{E}) &= 0 \\ \hat{n} \times \mathbf{E} &= 0 \quad \text{at cavity wall} \end{aligned} \tag{7}$$

where

$$\begin{aligned} F(\mathbf{E}) = & \frac{1}{2} \int\int\int_V \left[\frac{1}{\mu_r} (\nabla \times \mathbf{E}) \cdot (\nabla \times \mathbf{E}) - k_0^2 \epsilon_r \mathbf{E} \cdot \mathbf{E} \right] dV \\ & - k_0^2 \int\int_{S_a} [\hat{z} \times \mathbf{E}(\mathbf{r})] \cdot \left\{ \int\int_{S_a} [\hat{z} \times \mathbf{E}(\mathbf{r}')] G_0(\mathbf{r}, \mathbf{r}') dS' \right\} dS \\ & + \int\int_{S_a} \{\nabla \cdot [\hat{z} \times \mathbf{E}(\mathbf{r})]\} \left\{ \int\int_{S_a} G_0(\mathbf{r}, \mathbf{r}') \nabla' \cdot [\hat{z} \times \mathbf{E}(\mathbf{r}')] dS' \right\} dS \\ & + 2jk_0 Z_0 \int\int_{S_a} [\hat{z} \times \mathbf{E}(\mathbf{r})] \cdot \mathbf{H}^{inc}(\mathbf{r}) dS \end{aligned} \tag{8}$$

In deriving (8), the second term of (3) has been manipulated to reduce the order of the singularities that have to be integrated by two [2, pp.311–320]. Solving the above variational problem (finding a suitable stationary point) will yield a solution to (1) subject to the two boundary conditions.

When a source is present in the cavity, the formulation is modified by the addition of further terms which include the volume electric and/or magnetic currents (see [2, §9.4] for details).

3 Discretisation

The cavity to be analyzed is rectangular in shape. It was therefore decided to use first order brick elements for the discretisation. Edge-based elements were chosen above nodal-based elements because they provide a

divergence-free solution within the element, avoiding the possibility of spurious modes [5]. They also give a more natural treatment of the electric field at material interfaces, allowing for a jump in the normal component of the field at the interface [6]. (The original explanation of the suppression of spurious modes was that the elements are divergence free. This is true *within* the element. However, the basis functions — at least the "first" order ones used here — are discontinuous at their edges. More sophisticated analyses have recently been published, relating to the improved approximation of the zero-frequency eigenmodes possible with edge-based elements [7].)

In a brick element edge-based formulation, there are twelve unknowns associated with each element, namely the tangential electric field along each edge of the brick. The field at any point inside the brick is computed by linearly interpolating between these tangential edge fields. Inside the brick the field can thus be written as [2, pp.249–250]:

$$\mathbf{E}^e = \sum_{i=1}^{12} \mathbf{N}_i^e E_i^e \tag{9}$$

where

$$\mathbf{N}_i^e = N_{xi}^e \hat{x}, \qquad \mathbf{N}_{i+4}^e = N_{yi}^e \hat{y}, \qquad \mathbf{N}_{i+8}^e = N_{zi}^e \hat{z} \tag{10}$$

In the above, E_i^e is the tangential electric field at each edge. $\mathbf{N}_i^e$ is the appropriate vector interpolation function, consisting of an interpolation function and a unit vector. As an example, the vector interpolation function corresponding to the x-directed edge with the lowest y and z coordinates is given — assuming that the aperture lies in the x-y plane. ($\mathbf{N}_1^e$ in equation (9)).

$$\mathbf{N}_1^e = \frac{1}{l_y^e l_z^e}(y_c^e + \frac{l_y^e}{2} - y)(z_c^e + \frac{l_z^e}{2} - z)\hat{x} \tag{11}$$

y_c^e,z_c^e are the y and z coordinates of the centre of the element, and l_y^e,l_z^e are the lengths of the element in the y and z directions.

Clearly, the above function is x-directed, and varies linearly from one to zero in the y and z directions through the body of the element. Also note that the interpolation function is divergence free (within the element). Similar interpolation functions can be constructed for each of the other eleven edges.

Representing the electric field throughout the cavity as a sum of the fields in all the elements, and substituting this into (8), we obtain [2, pp.311–320]:

$$F = \frac{1}{2}\sum_{e=1}^{M}\{E^e\}^T[K^e]\{E^e\} + \frac{1}{2}\sum_{s=1}^{M_s}\sum_{t=1}^{M_s}\{E^s\}^T[P^{st}]\{E^t\} - \sum_{s=1}^{M_s}\{E^s\}^T\{b^s\} \tag{12}$$

M is the total number of elements in the cavity, while M_s is the number of elements touching the aperture of the cavity. { } denotes a vector, { }^{T} denotes a vector transposed, and [ ] denotes a square matrix. E^e is a vector which, for each element, consists of the twelve unknown edge-fields. E^s is a four element vector, consisting of the edges that touch the aperture for those elements having one face that lies in the plane of the aperture.

The elemental submatrices and vector are given by:

$$[K^e] = \int\int\int_{V^e}\left[\frac{1}{\mu_r^e}\{\nabla\times\mathbf{N}^e\}\cdot\{\nabla\times\mathbf{N}^e\}^T - k_0^2\epsilon_r^e\{\mathbf{N}^e\}\cdot\{\mathbf{N}^e\}^T\right]dV \tag{13}$$

$$[P^{st}] = 2\int\int_{S^s}\{\nabla\cdot\mathbf{S}^s\}\left\{\int\int_{S^t}\{\nabla'\cdot\mathbf{S}^t\}^T G_0 dS'\right\}dS - 2k_0^2\int\int_{S^s}\{\mathbf{S}^s\}\cdot\left\{\int\int_{S^t}\{\mathbf{S}^t\}^T G_0 dS'\right\}dS \tag{14}$$

$$\{b^s\} = -2jk_0Z_0\int\int_{S^s}\{\mathbf{S}^s\}\cdot\mathbf{H}^{inc}dS \tag{15}$$

V^e denotes the volume of an element. S^s and S^t are the areas (of the faces of a pair of elements) coinciding with the aperture. $[P^{st}]$ has to be evaluated for every possible combination of such pairs.

N^e is a twelve element vector of interpolation functions, while S^s is a four element vector of interpolation functions. S^s is a subset of N^e, and consists of those interpolation functions corresponding to the four edges lying in the aperture plane, for an element touching the aperture.

Introducing a global connected numbering system, which uses the same edge-number for edges shared between adjacent elements, the above equation can be written as [2, pp.311–320]:

$$F = \frac{1}{2}\{E\}^T[K]\{E\} + \frac{1}{2}\{E\}^T[P]\{E\} - \{E\}^T\{b\} \tag{16}$$

To minimize this, the derivative is taken separately with respect to each unknown (edge-field), and the resultant expression set equal to zero. This produces a system of equations of the form:

$$[A]\{E\} = \{b\} \tag{17}$$

In the above, $[A]$ is a square matrix which can be assembled from the elemental submatrices as follows: The elemental submatrix $[K^e]$ is computed for each element in turn. Using the global numbers of the edges, the entries from each elemental matrix are simply added at the right places in the $[A]$ matrix until all the elements have been handled. The elemental $[P^{st}]$ submatrix is computed for each possible pair combination of aperture touching elements, and the entries also added to the $[A]$ matrix using the global numbering system.

The elemental $\{b\}$ vector for every element touching the aperture is computed, and similarly added to the global $\{b\}$ vector.

All that remains is to impose the boundary condition of equation (2) at any perfectly conducting surfaces. This is done by setting the edges that lie along these surfaces (eg. along the cavity walls) to zero. Practically, this means removing every row and column in the system of equations (17) that corresponds to an edge lying on a perfect conductor. Solving the resulting reduced system of equations yields the electric fields inside the cavity.

To find the scattered field in the half space above the cavity the following equation can be integrated over the aperture of the cavity [8, p.30]:

$$\mathbf{H}^{sc}(\mathbf{r}) = \frac{jk_0}{Z_0}\int\int_{S_a}[\hat{z}\times\mathbf{E}(\mathbf{r}')]\cdot\overline{\overline{G}}_0(\mathbf{r},\mathbf{r}'ds' \tag{18}$$

The RCS can then be found from:

$$\sigma = \lim_{r\to\infty} 4\pi r^2 \frac{|\mathbf{H}^{sc}(\mathbf{r})|^2}{|\mathbf{H}^{inc}(\mathbf{r})|^2} \tag{19}$$

4 Computer implementation

Although the formulation is readily available, a computer code implementing this was not. The above formulation was programmed (by the second author) using FORTRAN77. Initial development was done on a 486DX2 66MHz PC, but later memory and speed requirements necessitated a move to a variety of workstations, including a SPARCServer 1000, HP720 and an IBM RS6000. (Problems were encountered porting the code, especially with the SPARCServer — the problems were eventually traced to subtle compiler differences). A number of problems emerged during the implementation. Details may be found in [8, Chapter 4]; the following discussion highlights the most significant aspects.

A problem was encountered when trying to evaluate equation (14) for the case when the two integration surfaces coincide with one another, which required more attention than the literature had indicated. In this situation, the Green's function becomes singular. Several possible approaches exist: firstly, the singularity can simply be ignored by choosing two sets of non-coincidental integration points for the two surface integrals; another possibility, suggested in [2, pp.311–320], is to subtract the singularity, and integrate it analytically. The result is then added again after the remaining nonsingular part has been integrated numerically. A third approach is to convert the coordinate system to polar coordinates, in which case the singularity vanishes, and standard numerical integration techniques can be employed. After experimenting with all three, the last approach was adopted as it seemed to give the fastest convergence to acceptable accuracy.

A Romberg driver routine using trapezoidal integration was used throughout to speed up the numerical integration. Substantial symmetry and repetition also exists which was exploited. Even so, setting up the $[A]$ matrix requires a non-trivial amount of time, although a full investigation into the sensitivity of the final results on this integration accuracy has not been performed and the integration residual could possibly be relaxed.

The $[A]$ matrix generated by the above discretisation is very sparse — less then ten percent populated. Because the section of the matrix corresponding to edges lying in the plane of the aperture is full, the matrix is unfortunately not particularly narrow band. The most efficient storage method is therefore to store only the non-zero entries and their indices, which was the approach adopted. Searching the index matrix when the structure became large proved surprisingly time-consuming, and a scheme using "bins" to store the non-zero entry index information was implemented [8]. A method of conserving both execution time and memory is to impose the boundary condition of equation (2) before the $[A]$ matrix and $\{b\}$ vector are set up. This means that any rows and columns that are eventually zeroed do not have their entries computed.

An attractive feature of the above formulation is that the incident wave only influences the $\{b\}$ vector. Once the $[A]$ matrix has been assembled for a particular structure at a particular frequency, it can be re-used every time a new incident wave is specified. Setting up a $\{b\}$ vector for a new incident wave typically takes only a few seconds.

The code presently has the capability to use Gaussian elimination, conjugate gradient or bi-conjugate gradient iteration to solve the resulting system of linear equations. The first is most appropriate for small problems with multiple right hand sides (such as a monostatic RCS calculation). The iterative schemes become very attractive for large problems, and we have found the bi-conjugate gradient method to converge at least four times faster than the conjugate gradient method [8, Chapter 4]. This is probably due to the particular conjugate gradient algorithm implemented — for a general complex-valued matrix — which by using both the matrix and its Hermitian transpose, effectively squares the condition number of the matrix. The well-known drawback of the iterative solvers is that the problem must be re-solved for each new right hand side.

5 Results

The input impedance, radiation patterns and radar cross section (RCS) of a cavity-backed microstrip structure can be found once the electric field in the cavity has been solved using the hybrid FEM/MoM. These parameters have been computed using our code for a number of different configurations, and compared with both published and measured results. Details are available in [8, Chapter 5]; two representative results are shown here.

To demonstrate the ability of our code to handle lossy materials, a cavity filled with two separate layers was analyzed. The top layer consists of dielectric material with $\epsilon_r = 2 - 2j$, while the bottom layer is free space, as illustrated in Figure 1. Results for this structure are given in Figure 2 and compared to the results of other workers.

In order to confirm the ability of the code to handle more complex structures, and also to provide data that can be experimentally verified, a patch antenna was designed, built, and measured in our anechoic chamber. The structure is illustrated in Figure 3 and results are given in Table 1. There is a shift in resonant frequency which is not unusual with numerical models of resonant structures; the results shown correspond to a mesh size (in the horizontal plane) of about 17 elements per wavelength in the dielectric and we have not yet performed further convergence checks, which could reduce this discrepancy. The radiation patterns in the principal planes have also been measured and computed, and are available in [8, §5.4]. Satisfactory agreement was found, except close to grazing incidence, which might be expected since the formulation assumes an infinite ground plane, whereas the measured structure had a substantial but finite ground.

One of the major strengths of the FEM is that the electric and magnetic fields within the cavity are readily available. The real (in phase with the driving current) cavity fields for the patch in the stepped cavity with an air superstrate are shown in Figure 4, demonstrating the expected modal distribution. Note that because the substrate and superstrate are actually very thin, the graph has been scaled by a factor of ten in the vertical direction.

At the symposium, radiation and scattering results will be presented for other microstrip structures, including some novel ones incorporating lossy superstrates that illustrate the power of the FEM as a modelling tool for this class of problems.

Run times are obviously highly computer dependent. The problem shown in Figure 1, using an $8 \times 6 \times 14$ discretization, running on the IBM RS6000 workstation with the highest possible level of optimisation, required around 51 minutes to set up the $[A]$ matrix, around 30 seconds per RCS look-angle, and about 1.9 MBytes of RAM (using double precision throughout). (We have benchmarked the RS6000 at around 14.7 MFLOP/s on a 300×300 LU decomposition using LINPACK routine `dgefa` with maximum optimisation). The problem in Figure 3, with a $12 \times 12 \times 6$ mesh, required about 2 hours and 30 minutes to set up the matrix, 16 MBytes of

Air superstrate

	Impedance (ohms)	Resonant Frequency (GHz)
Computed	$49.29 + 9.86i$	2.911
Measured	$50.24 + 8.73i$	3.005

Taconic superstrate $\epsilon_r = 2.2$

	Impedance (ohms)	Resonant Frequency (GHz)
Computed	$46.74 + 9.01i$	2.845
Measured	$46.39 + 8.64i$	2.955

Table 1: Comparison of our code with measured impedance data for the stepped cavity of Figure 3. The feed point (a coaxial probe) is offset from the centre by 5.37 mm and 5.00 mm in the x and y directions, and the patch was recessed into the cavity to allow various superstrates to be fitted above it.

RAM and around 20 minutes to compute the impedance. Some guidelines on the scaling with problem size of both run time and memory requirements may be found in [8, Chapter 4].

6 Conclusion

A combined FEM/MoM formulation suitable for analyzing cavity-backed patch antennas has been reviewed. We have implemented the formulation and confirmed the accuracy and power of the method. Several points of interest encountered in the computer implementation have been discussed. RCS results for a partially filled cavity have been presented, and impedance results for a stepped cavity with both substrate and superstrates presented and compared to measured data for a cavity-backed patch designed specifically to the validate the code. Results for the fields *inside* the cavity have also been shown. Some guidelines on execution times and memory requirements have been given.

Acknowledgements

The manufacturing ingenuity of Messrs. T.Coates and W.Croukamp of the Centre of Electronic Services of the University is gratefully acknowledged. The work reported in this paper is based on Mr. Malan's M.Eng. thesis [8].

References

[1] J. Jin and J. L. Volakis, "A hybrid Finite Element method for scattering and radiation by microstrip patch antennas and arrays residing in a cavity," *IEEE Trans. Antennas Propagat.*, vol. 39, pp. 1598–1604, November 1991.

[2] J. M. Jin, *The Finite Element Method in Electromagnetics*. New York: John Wiley & Sons, Inc, first ed., 1993.

[3] J.-P. Berenger, "A perfectly matched layer for the absorption of electromagnetic waves," *Journal of Computational Physics*, vol. 114, pp. 185–200, October 1994.

[4] Ü. Pekel, "Mesh truncation in the finite-element frequency-domain method with a perfectly matched layer (PML) applied in conjunction with analytic and numerical absorbing boundary conditions," *Microwave and Optical Technology Letters*, vol. 9, pp. 176–180, July 1995.

[5] X. Yuan, "Three-dimensional electromagnetic scattering from inhomogeneous objects by the hybrid moment and finite element method," *IEEE Trans. Microwave Theory Tech.*, vol. 38, pp. 1053–1058, Aug. 1990.

[6] G. Mur, "The finite element modeling of three-dimensional electromagnetic fields using edge and nodal elements," *IEEE Trans. Antennas Propagat.*, vol. 41, pp. 948–953, Jul. 1993.

[7] J. P. Webb, "Edge elements and what they can do for you," *IEEE Trans. Magn.*, vol. 29, pp. 1460–1465, March 1993.

[8] D. H. Malan, "Hybrid finite element and moment method modelling of microstrip patches," Master's thesis, Dept. Electrical & Electronic Engineering, University of Stellenbosch, December 1995.

[9] C. J. Reddy, M. D. Deshpande, C. R. Cockrell, and F. B. Beck, "Electromagnetic scattering analysis of a three dimensional cavity backed aperture in an infinite ground plane using a combined FEM/MoM approach.," tech. rep., NASA-Langley Research Center, Oct. 1994.

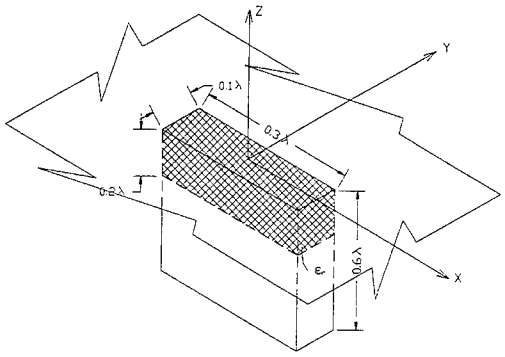

Figure 1: Cavity with lossy layer; $\epsilon_r = 2 - 2j$

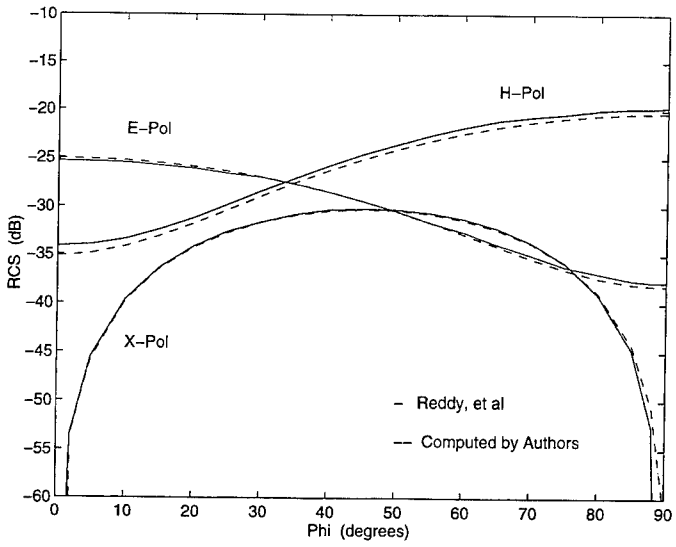

Figure 2: Comparison of our code with computed RCS results [9, Fig 7(b), p.29] for the structure in Figure 1. Azimuthal scan with $\theta = 40°$.

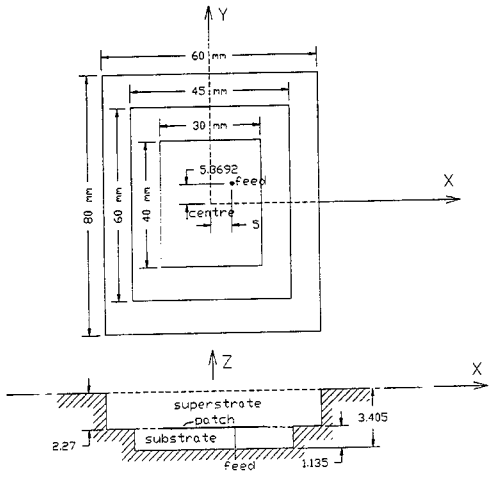

Figure 3: Microstrip patch in stepped cavity, substrate $\epsilon_r = 2.48$

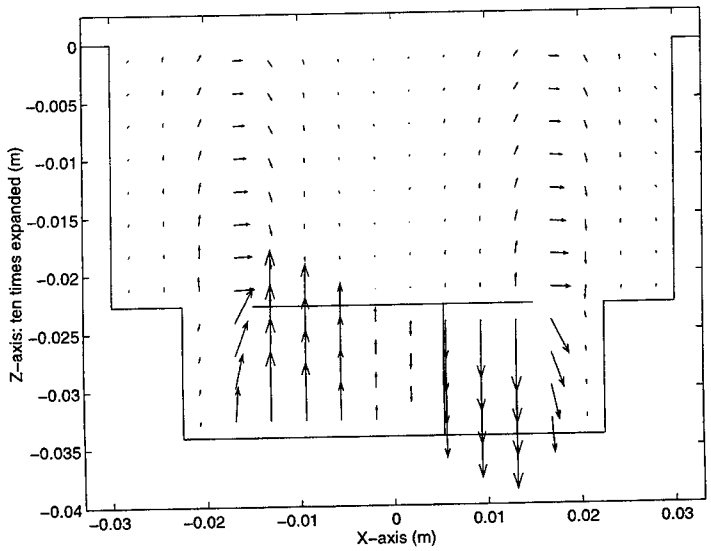

Figure 4: Real electric field inside the stepped cavity (with air superstrate): x-z plane, $y = 0$

$\mathcal{H}_1(curl)$ Tangential Vector Finite Element Method With Additional Constraint Equation

Pavel Bretchko Sergey V. Polstyanko
Jin-Fa Lee *Member*, **IEEE**
Department of Electrical and Computer Engineering, Worcester Polytechnic Institute,
Worcester, MA 01609, USA

Abstract

This paper presents a formulation for modeling waveguiding structures uniform in wave propagation direction with arbitrary shape in the transverse plane containing materials characterized by arbitrary permittivity and permeability tensors. The formulation leads to a quadratic eigenvalue problem of dimension N. To reduce appearance of spurious modes and consequently to avoid excessive computational time constraint equation is introduced. In general case it is a generalized eigenvalue equation of the first order. The proposed method has been validated by analyzing different waveguiding structures. Computed solutions show good agreements with previously published results.

1 Introduction

Recent technological advances enable the integration of different materials into composite microwave and millimeter wave integrated circuits which involve ferrite materials as substrates and superstrates. Moreover, dielectric waveguides which employ anisotropic materials play an important role as fundamental components of optoelectronic and microwave devices. Consequently, numerous efforts have been devoted to the analysis of different transmission lines involving materials characterized by $[\epsilon]$ and/or $[\mu]$ tensors [1]-[5]. Most of such cases involve complex transversal shapes. Because of this, they do not have analytical solutions and require development of computational methods for modeling structures with nonreciprocal effects.

The Tangential Vector Finite Element Method (TVFEM) [8] is now a well-established numerical technique for the analysis of great variety of electromagnetic problems. In this paper this approach is modified by adding a constraint equation that allows to increase convergence of the iterative process of solving generalized eigenvalue problem that is a result of formulation. To demonstrate validity of this method, numerical results for different structures are presented and compared with published data.

2 Formulation

We consider a three dimensional anisotropic waveguide uniform in the z direction with an arbitrary cross section Ω in the xy plane and assume that the boundary of the Ω consists of either perfect electric conductor (PEC) or perfect magnetic conductor (PMC). The time harmonic form, with $e^{j\omega t}$ assumed, of the Maxwell's equations reads:

$$\begin{aligned} \nabla \times \vec{E} &= -j\omega\mu_0[\mu]\vec{H} \\ \nabla \times \vec{H} &= j\omega\epsilon_0[\epsilon]\vec{E} \\ \nabla \cdot [\mu]\vec{H} &= 0 \\ \nabla \cdot [\epsilon]\vec{E} &= 0 \end{aligned} \tag{1}$$

where $[\epsilon]$ and $[\mu]$ are the relative permittivity and permeability respectively:

$$[\epsilon] = \begin{bmatrix} \epsilon_{xx} & \epsilon_{xy} & \epsilon_{xz} \\ \epsilon_{yx} & \epsilon_{yy} & \epsilon_{yz} \\ \epsilon_{zx} & \epsilon_{zy} & \epsilon_{zz} \end{bmatrix} \quad [\mu] = \begin{bmatrix} \mu_{xx} & \mu_{xy} & \mu_{xz} \\ \mu_{yx} & \mu_{yy} & \mu_{yz} \\ \mu_{zx} & \mu_{zy} & \mu_{zz} \end{bmatrix} \tag{2}$$

Note that in the current formulation, we assume both $[\epsilon]$ and $[\mu]$ being complex, nonsymmetric tensors. To solve Maxwell's equations, we convert the first-order differential equations involving two field quantities into second order differential equations involving scalar and vector potentials defined as

$$\begin{aligned} \vec{B} &= \nabla \times \vec{A} \\ \vec{E} &= -j\omega\vec{A} - c\nabla\varphi \end{aligned} \tag{3}$$

However the vector potential $\vec{A}$ defined by (3) is not unique unless a gauge condition is imposed. Instead of using the conventional Coulomb or Lorenz gauge we choose $A_z = 0$. This condition will greatly simplify the computations. By using equations (1)-(3) and the gauge condition, Maxwell's equations become

$$\nabla \times [\nu]\nabla \times \vec{A}_\tau - k_0^2[\epsilon]\vec{A}_\tau + jk_0[\epsilon]\nabla\varphi = 0 \tag{4}$$

$$-jk_0\nabla \cdot [\epsilon]\vec{A}_\tau - \nabla \cdot [\epsilon]\nabla\varphi = 0 \tag{5}$$

where $k_0 = \omega^2\epsilon_0\mu_0$ is the free-space wavenumber and $[\nu] = [\mu]^{-1}$ denotes the inverse matrix of $[\mu]$. Taking into account that $\nabla = \nabla_\tau - \gamma\hat{z}$, where $\nabla_\tau = \hat{x}\partial/\partial x + \hat{y}\partial/\partial y$, equations (4)-(5) can be rewritten as

$$\begin{aligned} \nabla_\tau \times \nu_{zz}\nabla_\tau \times \vec{A}_\tau - \gamma\nabla_\tau \times [\nu]_m\hat{z} \times \vec{A}_\tau - \gamma\hat{z} \times [\nu]_n\nabla_\tau \times \vec{A}_\tau + \gamma^2\hat{z} \times [\nu]_\tau\hat{z} \times \vec{A}_\tau - \\ -k_0^2[\epsilon]_\tau\vec{A}_\tau + jk_0[\epsilon]_\tau\nabla_\tau\varphi - jk_0\gamma[\epsilon]_n\varphi = 0 \end{aligned} \tag{6}$$

$$\begin{aligned} \nabla_\tau \times [\nu]_\tau\nabla_\tau \times \vec{A}_\tau + \nabla_\tau \times [\nu]_n\nabla_\tau \times \vec{A}_\tau + \nabla_\tau \times [\nu]_m\nabla_\tau \times \vec{A}_\tau - \gamma\nabla_\tau \times [\nu]_\tau\hat{z} \times \vec{A}_\tau - \\ -k_0^2[\epsilon]_m\vec{A}_\tau + jk_0[\epsilon]_m\nabla_\tau\varphi - jk_0\gamma\epsilon_{zz}\varphi = 0 \end{aligned} \tag{7}$$

$$-jk_0\nabla_\tau \cdot [\epsilon]_\tau\vec{A}_\tau + jk_0\gamma[\epsilon]_m\vec{A}_\tau - \nabla_\tau \cdot [\epsilon]_\tau\nabla_\tau\varphi + \gamma[\epsilon]_m\nabla_\tau\varphi + \gamma\nabla_\tau \cdot [\epsilon]_n\varphi - \gamma^2\epsilon_{zz}\varphi = 0 \tag{8}$$

where

$$\begin{aligned} [\epsilon]_\tau &= \begin{bmatrix} \epsilon_{xx} & \epsilon_{xy} \\ \epsilon_{yx} & \epsilon_{yy} \end{bmatrix} \quad [\epsilon]_n = \begin{bmatrix} \epsilon_{xz} \\ \epsilon_{yz} \end{bmatrix} \quad [\epsilon]_m = \begin{bmatrix} \epsilon_{zx} & \epsilon_{zy} \end{bmatrix} \\ [\nu]_\tau &= \begin{bmatrix} \nu_{xx} & \nu_{xy} \\ \nu_{yx} & \nu_{yy} \end{bmatrix} \quad [\nu]_n = \begin{bmatrix} \nu_{xz} \\ \nu_{yz} \end{bmatrix} \quad [\nu]_m = \begin{bmatrix} \nu_{zx} & \nu_{zy} \end{bmatrix} \end{aligned} \tag{9}$$

Equations (6) and (7) represent transversal τ and longitudinal z components of the equation (4). Since equation (5) can be derived from (4) by taking divergence of (4) and than dividing it by $-jk_0$, only two of equations (6) and (8) are independent.

As it was stated earlier we consider only PEC and PMC boundary conditions. In $\vec{A}$, φ formulation this conditions could be written as following:
on PEC s

$$\begin{cases} \hat{n} \times \vec{A}_\tau = 0 \\ \varphi = 0 \end{cases} \tag{10}$$

on PMC s

$$\begin{cases} \hat{n} \times ([\nu]\nabla \times \vec{A}_\tau) = 0 \\ \{[\epsilon](jk_0\vec{A}_\tau + \nabla\varphi)\} \cdot \hat{n} = 0 \end{cases} \tag{11}$$

where $\hat{n}$ is a unit vector in the same plane of Ω, normal to the boundary and directed outwards.

3 Galerkin's Procedure

Equations (6),(8) and boundary conditions (10),(11) describe a well defined boundary value problem (BVP) and are ready for the application of the finite element method. Galerkin's weighted residual approach [7] has been used to construct our finite element formulation and leads to non-symmetric matrices only if either $[\epsilon]$ or $[\mu]$ is nonsymmetric. Application of the Galerkin's method for the current (BVP) results in the following bilinear form

$$\begin{aligned} B(\vec{v},\vec{a}) &= \int_\Omega \{(\nabla_\tau \times \vec{v}_\tau)\cdot\nu_{zz}(\nabla_\tau\times\vec{a}_\tau) - k_0^2\vec{v}_\tau[\epsilon]_\tau\vec{a}_\tau + \nabla_\tau v_z\cdot[\epsilon]_\tau\nabla_\tau a_z \\ &+ jk_0\vec{v}_\tau\cdot[\epsilon]_\tau\nabla_\tau a_z + jk_0\nabla_\tau v_z\cdot[\epsilon]_\tau\vec{a}_\tau\}d\Omega \\ &+ \gamma\int_\Omega\{(\hat{z}\times\vec{v}_\tau)\cdot[\nu]_n(\nabla_\tau\times\vec{a}_\tau) - (\nabla_\tau\times\vec{v}_\tau)\cdot[\nu]_m(\hat{z}\times\vec{a}_\tau) \\ &- jk_0\vec{v}_\tau\cdot[\epsilon]_n a_z + jk_0 v_z[\epsilon]_m\vec{a}_\tau + v_z[\epsilon]_m\nabla_\tau a_z - \nabla_\tau v_z\cdot[\epsilon]_n a_z\}d\Omega \\ &- \gamma^2\int_\Omega\{\vec{v}_\tau\cdot[\nu]_\tau\vec{a}_\tau + \epsilon_{zz}v_z a_z\}d\Omega \end{aligned} \tag{12}$$

where $\vec{v},\vec{a}$ are the testing and trial fields, respectively. To form the bilinear form, we have employed the Green's theorems and set both the testing and trial spaces be the same. Moreover, to facilitate our discussion, we have employed a vector notation for the potentials as

$$\vec{a} = \begin{bmatrix} \vec{a}_\tau \\ a_z \end{bmatrix} = \begin{bmatrix} \vec{A}_\tau \\ \varphi \end{bmatrix} \tag{13}$$

In the Galerkin's process, we need to find a complex number γ and a vector function $\vec{a}\in\Lambda^h$, such that $B(\vec{v},\vec{a})=0$ for every $\vec{v}$ in the finite dimensional space Λ^h, where Λ^h is our trial function space for $\vec{v}$ and $\vec{a}$. In our approach we have chosen the $\mathcal{H}^1(curl)$ TVFEM basis functions [8] (shown in Fig.1).

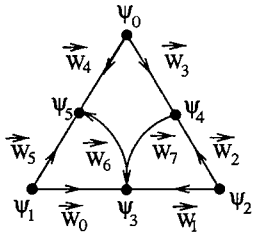

$$\vec{W}_0=\xi_1\nabla\xi_2 \qquad \vec{W}_2=\xi_2\nabla\xi_0 \qquad \vec{W}_4=\xi_0\nabla\xi_1$$
$$\vec{W}_1=\xi_2\nabla\xi_1 \qquad \vec{W}_3=\xi_0\nabla\xi_2 \qquad \vec{W}_5=\xi_1\nabla\xi_0$$
$$\vec{W}_6=4\xi_1(\xi_2\nabla\xi_0-\xi_0\nabla\xi_2) \qquad \vec{W}_7=4\xi_2(\xi_0\nabla\xi_1-\xi_1\nabla\xi_0)$$

$$\Psi_0=\xi_0(2\xi_0-1) \qquad \Psi_3=4\xi_1\xi_2$$
$$\Psi_1=\xi_1(2\xi_1-1) \qquad \Psi_4=4\xi_0\xi_2$$
$$\Psi_2=\xi_2(2\xi_2-1) \qquad \Psi_5=4\xi_1\xi_0$$

Figure 1: Basis functions for the $\mathcal{H}^1(curl)$ TVFEM

In this case each trial function $\vec{a}\in\Lambda^h$ can now be written as [5]

$$\vec{a}_\tau=\sum_{i=0}^{7}a_{\tau i}\vec{W}_i \qquad a_z=\sum_{i=0}^{5}a_{zi}\psi_i \tag{14}$$

where $\vec{W}_i$ and ψ_i are basis functions for vector and scalar potentials, respectively, and ξ_i is the Lagrangian interpolation polynomial, or simplex coordinates at node i [7].

4 Generalized Eigenmatrix Equation

Finally, a generalized eigenmatrix equation can be obtained by setting $B(\vec{v},\vec{a})=0$ for every $\vec{v}\in\Lambda^h$. The result is

$$\sum_{\Omega_e}\left(\begin{bmatrix}[A]_e & [D]_e\\ [F]_e & [H]_e\end{bmatrix}+\gamma\begin{bmatrix}[B]_e & [E]_e\\ [G]_e & [K]_e\end{bmatrix}+\gamma^2\begin{bmatrix}[C]_e & 0\\ 0 & [L]_e\end{bmatrix}\right)\begin{bmatrix}\underline{a}_\tau\\ \underline{a}_z\end{bmatrix}=0 \tag{15}$$

where $\sum_{\Omega_e}$ means the summation over the contributions from each element and $[\underline{a}_\tau,\underline{a}_z]^T$ are the corresponding coefficient vector for the finite element solution of $\vec{a}$. The element matrices in equation (15) are given by

$$\begin{aligned}
([A]_e)_{pq} &= \int_{\Omega_e}\{(\nabla\times\vec{W}_p)\cdot\nu_{zz}(\nabla\times\vec{W}_q)-k_0^2\vec{W}_p[\epsilon]_\tau\vec{W}_q\}d\Omega\\
([B]_e)_{pq} &= \int_{\Omega_e}\{(\hat{z}\times\vec{W}_p)\cdot[\nu]_n(\nabla\times\vec{W}_q)-(\nabla\times\vec{W}_p)\cdot[\nu]_m(\hat{z}\times\vec{W}_q)\}d\Omega\\
([C]_e)_{pq} &= \int_{\Omega_e}\{-\vec{W}_p\cdot[\nu]_\tau\vec{W}_q\}d\Omega\\
([D]_e)_{pq} &= jk_0\int_{\Omega_e}\{\vec{W}_p\cdot[\epsilon]_\tau\psi_q\}d\Omega\\
([E]_e)_{pq} &= -jk_0\int_{\Omega_e}\{\vec{W}_p\cdot[\epsilon]_n\psi_q\}d\Omega\\
([F]_e)_{pq} &= jk_0\int_{\Omega_e}\{\nabla_\tau\psi_p\cdot[\epsilon]_\tau\vec{W}_q\}d\Omega\\
([G]_e)_{pq} &= jk_0\int_{\Omega_e}\{\psi_p[\epsilon]_m\vec{W}_q\}d\Omega\\
([H]_e)_{pq} &= \int_{\Omega_e}\{\nabla_\tau\psi_p\cdot[\epsilon]_\tau\nabla_\tau\psi_q\}d\Omega\\
([K]_e)_{pq} &= \int_{\Omega_e}\{\psi_p[\epsilon]_m\nabla_\tau\psi_q-\nabla_\tau\psi_p\cdot[\epsilon]_n\psi_q\}d\Omega\\
([L]_e)_{pq} &= \int_{\Omega_e}\{-\epsilon_{zz}\psi_p\psi_q\}d\Omega
\end{aligned} \tag{16}$$

Equation (15) could be rewritten in more compact form:

$$[\mathcal{A}]\tilde{a}+\gamma[\mathcal{B}]\tilde{a}+\gamma^2[\mathcal{C}]\tilde{a}=0 \tag{17}$$

where $\tilde{a}=[\underline{a}_\tau\,\underline{a}_z]^T$ and

$$[\mathcal{A}]=\sum_{\Omega_e}\begin{bmatrix}[A]_e & [D]_e\\ [F]_e & [H]_e\end{bmatrix}\quad[\mathcal{B}]=\sum_{\Omega_e}\begin{bmatrix}[B]_e & [E]_e\\ [G]_e & [K]_e\end{bmatrix}\quad[\mathcal{C}]=\sum_{\Omega_e}\begin{bmatrix}[C]_e & 0\\ 0 & [L]_e\end{bmatrix} \tag{18}$$

5 Constraint Equations

Solving matrix equation (17) results in the set of eigenpairs $<\gamma_i,\vec{a}_i>$. But in addition to the set of physical solutions, for which $\gamma\neq 0$, we also get a set of solutions corresponding to $\gamma=0$. These nonphysical solutions form a vector function space Δ, where

$$\Delta=\left\{\begin{bmatrix}\vec{v}_\tau\\ v_z\end{bmatrix}:\vec{v}_\tau=\frac{j}{k_0}\nabla_\tau v_z\right\} \tag{19}$$

One can verify that any vector $\vec{v} \in \Delta$ will be a possible solution of equations (6)-(8) for $\gamma = 0$ and thus it is a valid nontrivial solution of the matrix equation (17). Physically these solutions correspond to the electric field $\vec{E} = 0$. From (19) it can be seen that the number of these nonphysical solutions will be equal to the number of free nodes in our discretization. The occurrence of these additional solutions in the iterative process will slow down the convergence of the desired eigenpairs in the Lanczos algorithm. Thus the elimination of these nonphysical solutions becomes an important task to solve. Based on equations (12),(19) one can deduce that for all physical solutions $\vec{a}$ with $\gamma \neq 0$ and for any $\vec{v} \in \Delta$ the following orthogonality relation holds

$$\int_\Omega \left\{ \frac{j}{k_0} \nabla_\tau \cdot (\hat{z} \times [\nu]_n \nabla_\tau \times \vec{A}_\tau) + j k_0 [\epsilon]_m \vec{A}_\tau + [\epsilon]_m \nabla_\tau \varphi \right\} d\Omega - \\ -\gamma \int_\Omega \left\{ \frac{j}{k_0} \nabla_\tau \cdot (\hat{z} \times [\nu]_\tau \hat{z} \times \vec{A}_\tau) + \epsilon_{zz} \varphi \right\} d\Omega = 0 \tag{20}$$

After employing Galerkin's procedure, equation (20) can transforms to the following form

$$\int_\Omega \left\{ -\frac{j}{k_0} \nabla_\tau v_z \cdot (\hat{z} \times [\nu]_n \nabla_\tau \times \vec{a}_\tau) + j k_0 v_z [\epsilon]_m \vec{a}_\tau + v_z [\epsilon]_m \nabla_\tau a_z \right\} d\Omega - \\ -\gamma \int_\Omega \left\{ -\frac{j}{k_0} \nabla_\tau v_z \cdot (\hat{z} \times [\nu]_\tau \hat{z} \times \vec{a}_\tau) + \epsilon_{zz} v_z a_z \right\} d\Omega = 0 \tag{21}$$

The corresponding matrix equation is

$$\sum_{\Omega_e} \left(\begin{bmatrix} [\tilde{A}]_e & [\tilde{B}]_e \end{bmatrix} + \gamma \begin{bmatrix} [\tilde{C}]_e & [\tilde{D}]_e \end{bmatrix} \right) \begin{bmatrix} \underline{a}_\tau \\ \underline{a}_z \end{bmatrix} = 0 \tag{22}$$

where

$$\begin{aligned} ([\tilde{A}]_e)_{pq} &= \int_{\Omega_e} \{ -\frac{j}{k_0} \nabla_\tau \varphi_p \cdot (\hat{z} \times [\nu]_n \nabla_\tau \times \vec{W}_q) + j k_0 \varphi_p [\epsilon]_m \vec{W}_q \} d\Omega \\ ([\tilde{B}]_e)_{pq} &= \int_{\Omega_e} \{ \varphi_p [\epsilon]_m \nabla_\tau \varphi_q \} d\Omega \\ ([\tilde{C}]_e)_{pq} &= \int_{\Omega_e} \{ \frac{j}{k_0} \nabla_\tau \varphi_p \cdot (\hat{z} \times [\nu]_\tau \hat{z} \times \vec{W}_q) \} d\Omega \\ ([\tilde{D}]_e)_{pq} &= \int_{\Omega_e} \{ -\epsilon_{zz} \psi_p \psi_q \} d\Omega \end{aligned} \tag{23}$$

In general case condition (22) must be applied during iterative process of solving generalized eigenvalue problem of the second order (18). The problem reduces tremendously when permeability and permittivity tensors of materials in waveguide have 2-by-2-by-1 form

$$[\epsilon] = \begin{bmatrix} \epsilon_{xx} & \epsilon_{xy} & 0 \\ \epsilon_{yx} & \epsilon_{yy} & 0 \\ 0 & 0 & \epsilon_{zz} \end{bmatrix} \quad [\mu] = \begin{bmatrix} \mu_{xx} & \mu_{xy} & 0 \\ \mu_{yx} & \mu_{yy} & 0 \\ 0 & 0 & \mu_{zz} \end{bmatrix} \tag{24}$$

In this case matrices $[\mathcal{B}]$ in equation (18) and $[\tilde{A}]_e$, $[\tilde{B}]_e$ in (22) are equal zero. The resulting equation can be written as follows

$$[\mathcal{A}]\tilde{a} + \gamma^2 [\mathcal{C}]\tilde{a} = 0 \tag{25}$$

with corresponding constraint condition

$$a_z = -[\tilde{C}]_e^{-1} [\tilde{D}]_e a_\tau \tag{26}$$

The eigenvalue problem (25) can be solved easily as described in [5]. The equation (26) can be used as a set of additional constraints to restrict the solution space to physical modes. In the first step of the Lanczos algorithm, the initial vector is constructed in such a way that it satisfies equation (26). Theoretically, this choice is sufficient to ensure that our solution becomes orthogonal to the subspace of nonphysical solutions. But due to the rounding error in our solution technique, we need to impose condition (26) on each iteration step of the Lanczos algorithm.

6 Numerical Results

In this section the proposed method is validated with some examples. The comparison of results obtained numerically with previously published data is also provided where possible.

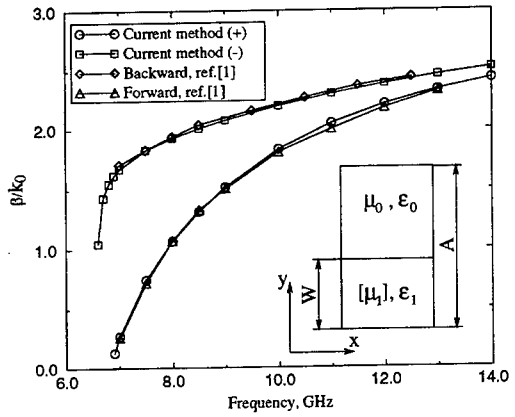

Figure 2: Normalized propagation constant of the TE_{01} mode of a rectangular waveguide loaded with a ferrite slab. $A = 22.86mm$, $A/W = 3$, $\epsilon_r = 9$, $4\pi M_s = 2000G$, and $H_0 = 200Oe$

The first example is a rectangular waveguide partially filled with ferrite material with external magnetic field in the $-\hat{x}$ direction (see Fig.2). In this case permeability tensor has the following form:

$$[\mu] = \begin{bmatrix} 1 & 0 & 0 \\ 0 & \mu & jk \\ 0 & -jk & \mu \end{bmatrix} \tag{27}$$

where μ and k depend on the operating frequency ω, the applied dc magnetic field H_0, and the magnetization of the ferrite M_s. Namely, $\mu = 1 + \omega_0\omega_m/(\omega_0{}^2 - \omega^2)$, $k = -\omega\omega_m/(\omega_0{}^2 - \omega^2)$, $\omega_m = (4\pi M_s g)/\mu_0$, $\omega_0 = gH_s$, where g is the electron gyromagnetic ratio.

The results for mode TE_{01} for structure with dimensions $A = 22.86mm$, $A/W = 3$, and $\epsilon_r = 9$, $4\pi M_s = 2000G$, and $H_0 = 200Oe$ have been obtained numerically and compared with results from [1] for forward and backward propagation (See Fig.2). As evidenced from the figure, good agreements are observed.

The example field distribution for above structure is shown in Fig. 3. It is evident from the picture that for forward direction the region with highest magnitude of electric and magnetic field shifts toward the bottom of the structure. On the contrary, for backward direction it shifts up, and higher energy is concentrated near the top of the ferrite slab. This behavior will be vice verse for the case with external magnetic field directed in $+\hat{x}$ direction.

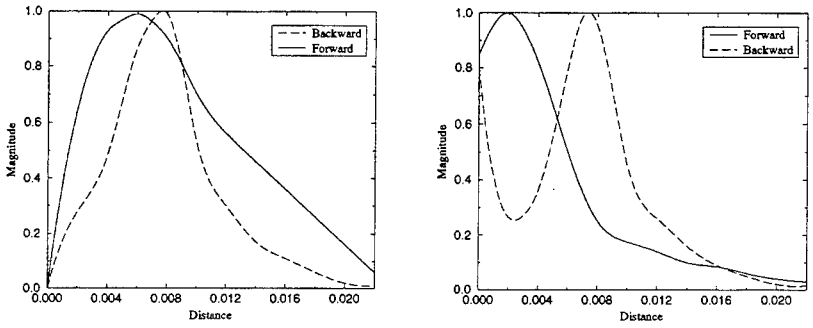

a b

Figure 3: Distribution of the normalized magnitude of the electric (a) and magnetic (b) fields in rectangular waveguide for forward and backward directions versus the distance along the y-axis for the operating frequency $f = 8GHz$

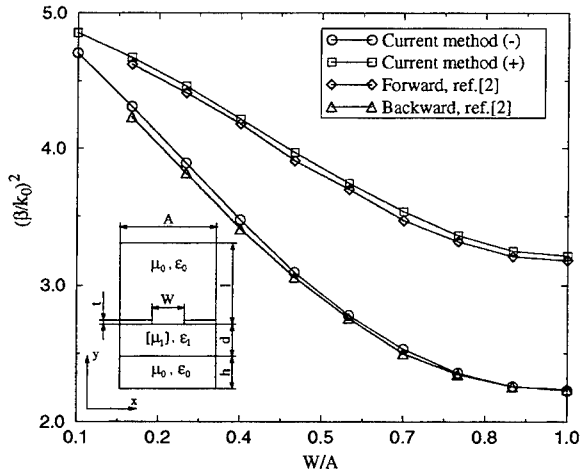

Figure 4: Normalized propagation constant versus slot width for the finline with single-layered ferrite, $A = 3mm$, $h = 1mm$, $d = 1mm$, $l = 3mm$, $t = 70\mu m$, $f = 20GHz$, $\epsilon_1 = 12.5$, $4\pi M_s = 5000G$, and $H_0 = 500Oe$

Figure 4 displays normalized propagation constant versus slot width for the structure with dimensions $A = 3mm$, $h = 1mm$, $d = 1mm$, $l = 3mm$, $t = 70\mu m$. Operating frequency is $20GHz$, magnetization $4\pi M_s = 5000G$, magnetic field $H_0 = 500Oe$, ferrite material has relative permittivity $\epsilon_1 = 12.5$

In the table bellow comparison of the number of iterations for discussed above structures is made. From the table it is obvious that with employing constraint equation the iterative process converges faster than

without it.

Structure	Number of iterations		Number of unknowns
	with constr.	without constr.	
rectangular waveguide	18	15	2217
finline	13	9	3741

Although for relatively simple structure that are used as an example total gain is only several iterations, for other more complicated structures with more unknowns savage in computational time could be significant.

7 Conclusion

In this paper $\mathcal{H}^1(curl)$ TVFEM is modified by imposing additional constraint equations. This allows to avoid appearance of nonphysical solutions and consequently increase convergence of method. This approach can be used for modeling waveguiding structures uniform in wave propagation direction with arbitrary shape in transverse plane containing materials characterized by arbitrary permittivity and permeability tensors. To show the validity of the present method, computations have been carried out for some examples.

References

[1] J. Pereda, L. Vielva, et. al., "FDTD Analysis of Magnetized Ferrites: An Approach Based on the Rotated Richtmyer Difference Scheme", *IEEE Microwave and Guided Wave Letters*, Vol. 3, no. 9, Sept. 1993.

[2] T. Kitazawa, "Analysis of Shielded Striplines and Finlines with Finite Metalization Thickness Containing Magnetized Ferrites", *IEEE Trans. Microwave Theory Tech.*, Vol. 39, no. 1, pp. 70-74, Jan. 1991.

[3] K. Hayata, K. Miura and M. Koshiba, " Full Vectorial Finite Element Formalism for Lossy Anisotropic Waveguides. "*IEEE Trans. Microwave Theory Tech.*, Vol. 37, pp.875-883, No.5,May 1989.

[4] L. Valor and J. Zapata, "Efficient Finite Element Analysis of Waveguides with Lossy Inhomogeneous Anisotropic Materials Characterized by Arbitrary Permittivity and Permeability Tensors", *IEEE Trans. Microwave Theory Tech.*, Vol. 43, No. 10, pp.2452-2459, October 1995

[5] S. Polstyanko, J.-F. Lee, "H^1(curl) Tangential Vector Finite Element Method for Modeling Anisotropic Optical Fibers", to appear in Journal of Lightwave Technology, November 1995.

[6] Jin-Fa Lee, " Finite Element Analysis of Lossy Dielectric Waveguides. " *IEEE Trans. Microwave Theory Tech.*, Vol. 42, pp.1025-1031, No.6,June 1994.

[7] J. Jin, *The Finite Element Method in Electromagnetics* . John Wiley & Sons, INC., New York, 1993

[8] J. Lee, D. Sun, Z. Cendes, " Full-Wave Analysis of Dielectric Waveguides Using Tangential Vector Finite Elements. " *IEEE Trans. Microwave Theory Tech.*, Vol.39, pp 1262-1271,No 8, Aug. 1991.

Extension of Higher–Order 3–D Vector Finite Elements to Curved Cells and Open-Region Problems

J. Scott Savage and Andrew F. Peterson
School of Electrical and Computer Engineering
Georgia Institute of Technology
Atlanta, GA 30332

I. Introduction

In a previous paper, the finite element implementation of higher–order vector basis functions on regular tetrahedra was presented [1]. Two sets of vector functions were introduced. The first set consisted of low–order functions with constant tangential, linear normal (CT/LN) components on the tetrahedral cell boundaries. The second set included higher–order functions, with linear tangential, quadratic normal (LT/QN) components on the cell boundaries. An implementation of both sets indicates that higher order basis functions allow for more accurate solutions of three-dimensional problems, while retaining the benefit of allowing no spurious modes. Thus, accurate results are possible with relatively coarse finite element meshes. However, coarse meshes can present geometry modeling errors which eliminate the advantages of using higher–order elements.

This paper extends the use of these vector basis functions to curved tetrahedra to allow accurate modeling of more generic geometries. The details of implementing vector functions on curved cells will be presented, including a discussion of numerical integration on triangles and tetrahedra. Results for cavity resonators with curved boundaries demonstrate that the advantages of using higher–order basis functions on geometries with curved boundaries can be retained.

Also, the implementation of a local radiation boundary condition (RBC) with higher–order vector basis functions will be discussed. Error trends will be presented for both a first and a second order RBC. An RBC will extend the application of these finite elements to open region problems including scattering analysis.

II. Higher–Order Vector Basis Functions

The basis functions used in this paper were first proposed by Nedelec [2]. The basis functions impose only tangential field continuity across cell boundaries, and therefore do not allow spurious modes. They are also mixed order elements in that they represent normal field components more accurately than tangential components. The lowest order vector basis functions have a constant tangential component and a linear normal component on tetrahedra boundaries (CT/LN). The higher–order basis functions in this paper have a linear tangential component and a quadratic normal component on tetrahedra boundaries (LT/QN). These basis functions are summarized in Table 1, where they are written in terms of simplex coordinates.

Table 1 3-D Vector Basis Functions on Tetrahedra	
(CT/LN) 6 Functions per Cell	(LT/QN) 20 Functions per Cell
<u>6 Edge Based</u> for all $i < j$, $L_i \nabla L_j - L_j \nabla L_i$	<u>12 Edge Based</u> for all $i \neq j$, $L_i \nabla L_j$ <u>8 Face Based</u> for all $i < j < k$, $L_i L_j \nabla L_k - L_i L_k \nabla L_j$ $L_i L_j \nabla L_k - L_j L_k \nabla L_i$

Element matrices for the basis functions of Table 1 were derived analytically and presented in [1]. The basis functions were tested by computing the wavenumbers of a rectangular cavity resonator of dimension $1 \times 0.5 \times 0.75$ meters. Six unstructured tetrahedral meshes of varying density were used to determine the convergence rates of the two basis function sets. An average error for each basis set on each mesh was computed by averaging the error in the lowest eight wavenumbers computed. Fig. 1 shows the error convergence of both basis sets as a function of the average mesh edge length. An exponential curve fit through the data indicates that the CT/LN basis functions offer $O(h^2)$ convergence, while LT/QN basis functions offer $O(h^4)$ convergence, where h is the average edge length. Fig. 2 shows the average error of both basis functions as a function of the matrix size. This figure demonstrates that higher–order basis functions are more efficient than low–order basis functions.

The greater efficiency of higher–order basis functions allows more accurate solutions to a given problem using less–dense meshes. However, when using straight, or linear, tetrahedra, coarse meshes can lead to geometry modeling errors which may reduce the advantages of using higher–order elements. To demonstrate this problem, a cylindrical cavity was discretized using linear tetrahedra. The meshes were scaled so that the total mesh volume matched the volume of the cylinder. The cylinder had unit radius and height. The analytical fundamental wavenumber is 2.40483. CT/LN basis functions were used on a dense 589 cell mesh with 533 unknowns. The first CT/LN wavenumber is 2.37160, an error of 1.38%. LT/QN basis functions were used on a coarse 175 cell mesh with 896 unknowns. The first LT/QN wavenumber is 2.42523, an error of 0.85%. Although the LT/QN analysis did give a more accurate prediction, the solution improvement is unsatisfactory considering the number of unknowns. The loss of efficiency in the solutions is a result of geometry modeling errors. Therefore, the finite element procedure of this paper was extended to curved or quadratic tetrahedra.

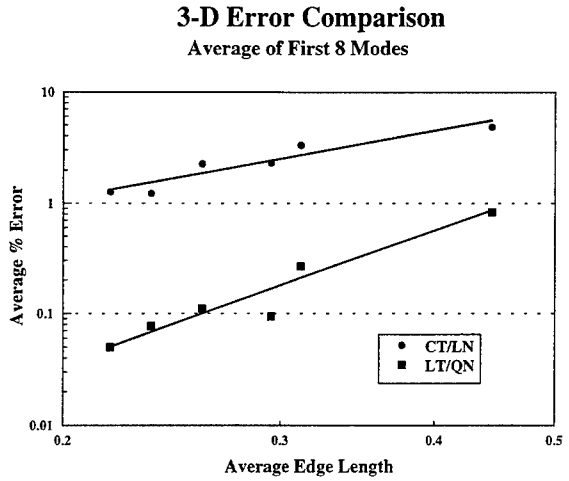

Fig. 1. An error comparison between CT/LN and LT/QN basis functions. The exponential behavior of the CT/LN curve is $O(h^2)$, while the convergence rate of the LT/QN curve is $O(h^4)$.

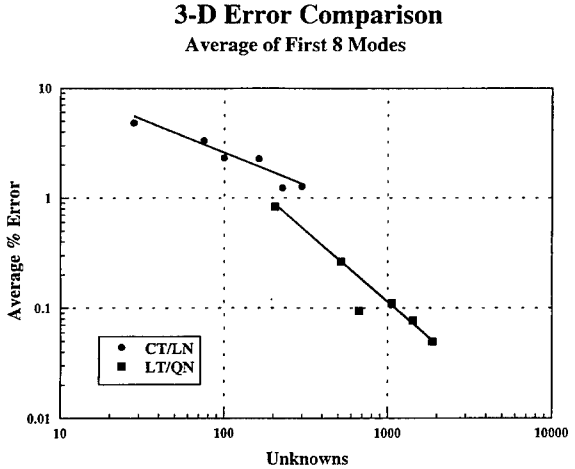

Fig. 2. An error comparison between CT/LN and LT/QN basis functions. This figure indicates that LT/QN basis functions provide more efficient solutions for a rectangular cavity.

III. Extension to Curved Cells

The extension of vector basis functions on tetrahedra to curved cells involves mapping a quadratic (curved) tetrahedra to a linear (straight) tetrahedra [3]. A quadratic tetrahedra is defined by 10 nodes, one on each of the 4 vertices and one on each of the 6 edge midpoints. The transformation is facilitated by the use of the Jacobian matrix. The Jacobian is defined by

$$\mathbf{J}=\begin{bmatrix} \frac{\partial x}{\partial L_1} & \frac{\partial y}{\partial L_1} & \frac{\partial z}{\partial L_1} \\ \frac{\partial x}{\partial L_2} & \frac{\partial y}{\partial L_2} & \frac{\partial z}{\partial L_2} \\ \frac{\partial x}{\partial L_3} & \frac{\partial y}{\partial L_3} & \frac{\partial z}{\partial L_3} \end{bmatrix} \tag{1}$$

where L_i is the *i-th* simplex coordinate. The Jacobian is a function of position within a quadratic tetrahedra and the coordinates of the 10 defining nodes [3]. Vectors can be written in a local coordinate system which is related to the cartesian coordinate system by

$$\begin{bmatrix} V_x \\ V_y \\ V_z \end{bmatrix} = \mathbf{J}^{\mathbf{T}} \begin{bmatrix} V_{L_1} \\ V_{L_2} \\ V_{L_3} \end{bmatrix} \tag{2}$$

The basis functions can be transformed to the local coordinate system by observing that

$$\nabla L_i = \hat{L}_i \tag{3}$$

for i=1, 2, 3. For example, consider the first LT/QN basis function,

$$\overline{\mathbf{B}}_1 = L_1 \nabla L_2 = \begin{bmatrix} 0 & L_1 & 0 \end{bmatrix}^{\mathbf{T}} \tag{4}$$

Also, the curl of any basis function can be transformed to local coordinates. Continuing the example, let $\overline{\mathbf{C}}_i = \nabla \times \overline{\mathbf{B}}_i$, so

$$\overline{\mathbf{C}}_1 = \nabla \times \overline{\mathbf{B}}_1 = \nabla L_1 \times \nabla L_2 = \nabla L_3 = \begin{bmatrix} 0 & 0 & 1 \end{bmatrix}^{\mathbf{T}} \tag{5}$$

The element matrices are then transformed as follows

$$\int_x \int_y \int_z \nabla \times \overline{\mathbf{B}}_i \cdot \nabla \times \overline{\mathbf{B}}_j dz dy dx = \int_{L_1} \int_{L_2} \int_{L_3} \frac{1}{|\mathbf{J}|} \overline{\mathbf{C}}_i^{\mathbf{T}} \mathbf{J} \mathbf{J}^{\mathbf{T}} \overline{\mathbf{C}}_j dL_3 dL_2 dL_1 \tag{6}$$

$$\int_x \int_y \int_z \overline{\mathbf{B}}_i \cdot \overline{\mathbf{B}}_j dz dy dx = \int_{L_1} \int_{L_2} \int_{L_3} \overline{\mathbf{B}}_i^{\mathbf{T}} \mathbf{J}^{-\mathbf{T}} \mathbf{J}^{-1} \overline{\mathbf{B}}_j |\mathbf{J}| dL_3 dL_2 dL_1 \tag{7}$$

The integrands on the right hand side of (6) and (7) can easily be computed with knowledge of the simplex coordinate location and the defining 10 node locations. The integrals are over the tetrahedron defined by the cartesian coordinates (0,0,0), (1,0,0), (0,1,0), (0,0,1). Generally, this integration must be implemented numerically. In this paper, numerical integration was performed using Gaussian quadrature rules developed by Keast [4].

While it may seem that using numerical integration for the construction of each element matrix might greatly reduce the efficiency of the FEM algorithm, the overall solution time is only slightly increased. This is due to the fact that filling the global matrix requires much less time than solving the matrix equation, and using quadratic tetrahedra does not add any additional unknowns to the problem.

In fact, using numerical integration actually simplifies the implementation of the FEM algorithm. Therefore, quadratic tetrahedra retain the benefits of higher–order elements implemented on curved geometries.

Returning to the example at the end of the last section, the two cylindrical cavity meshes were altered by converting the tetrahedra on the curved boundary to quadratic tetrahedra. The resulting meshes more closely represent the actual cylindrical boundary. Table 2 summarizes the results of each of the cases. The quadratic mesh has little effect on the CT/LN results. This is because a relatively dense mesh was used, and the difference between the linear and quadratic meshes is quite small. The quadratic mesh greatly improves the LT/QN results on a coarse mesh, however. The error in the linear mesh is 0.85% while the error in the quadratic mesh is 0.018%. Clearly, the quadratic tetrahedra much more closely represent the cylindrical waveguide than the linear tetrahedra in a coarse mesh.

Table 2
Cylindrical Cavity, k=2.40483

	CT/LN	LT/QN
Linear	2.37160	2.42523
Quadratic	2.36441	2.40527

IV. Extension to Open Regions

The weak form of the vector Helmholtz equation over a spherical region, Γ, is

$$\iiint_{\Gamma} \frac{1}{\mu_r} \nabla \times \overline{\mathbf{T}} \cdot \nabla \times \overline{\mathbf{E}}^{tot} - k^2 \varepsilon_r \overline{\mathbf{T}} \cdot \overline{\mathbf{E}}^{tot} = -\iint_{\partial\Gamma} \overline{\mathbf{T}} \cdot \hat{r} \times \nabla \times \overline{\mathbf{E}}^{tot} \tag{8}$$

where $\partial\Gamma$ is the spherical boundary. The surface integral of (8) requires careful consideration in a finite element implementation. In scattering analysis, if the scatterer is completely enclosed by the spherical boundary, $\partial\Gamma$, then the surface integral can be expressed as the sum

$$\iint_{\partial\Gamma} \overline{\mathbf{T}} \cdot \hat{r} \times \nabla \times \overline{\mathbf{E}}^{tot} = \iint_{\partial\Gamma} \overline{\mathbf{T}} \cdot \hat{r} \times \nabla \times \overline{\mathbf{E}}^{inc} + \iint_{\partial\Gamma} \overline{\mathbf{T}} \cdot \hat{r} \times \nabla \times \overline{\mathbf{E}}^{s} \tag{9}$$

where $\overline{\mathbf{E}}^{inc}$ is the known incident field and $\overline{\mathbf{E}}^{s}$ is the scattered field. A local RBC is an approximation of the scattered field term of (9). In this paper, the standard first order and an alternative second order RBC were chosen [5]. The alternative second order RBC was chosen since it preserves the symmetry of the global finite element matrix. The first order RBC is

$$\iint_{\partial\Gamma} \overline{\mathbf{T}} \cdot \hat{r} \times \nabla \times \overline{\mathbf{E}}^{s} = jk \iint_{\partial\Gamma} \overline{\mathbf{T}} \cdot \overline{\mathbf{E}}^{tot}_{tan} \tag{10}$$

and the symmetric second order RBC is

$$\begin{aligned} \iint_{\partial\Gamma} \overline{\mathbf{T}} \cdot \hat{r} \times \nabla \times \overline{\mathbf{E}}^{s} = {} & jk \iint_{\partial\Gamma} \overline{\mathbf{T}} \cdot \overline{\mathbf{E}}^{s}_{tan} \\ & + \beta(r) \iint_{\partial\Gamma} (\hat{r} \cdot \nabla \times \overline{\mathbf{T}})(\hat{r} \cdot \nabla \times \overline{\mathbf{E}}^{s}) \\ & - \beta(r) \iint_{\partial\Gamma} (\nabla \cdot \overline{\mathbf{T}}_{tan})(\nabla \cdot \overline{\mathbf{E}}^{s}_{tan}) \end{aligned} \tag{11}$$

where

$$\beta(r)=\frac{1}{2jk+\frac{2}{r}} \tag{12}$$

The first two terms on the right hand side of (11) are identical to the element matrices in a 2–D FEM analysis and are easily computed. The third term of (11) involves the surface divergence of the basis functions on the spherical boundary. Unfortunately, the surface divergence of Nedelec's curl–conforming basis functions is not finite along tetrahedra edges on the boundary. Therefore, the singular behavior of the surface divergence of each basis function is approximated by "smearing" the singularity over a finite domain. This is a 3–D analog to the 2–D procedure of [6].

To determine the accuracy of the RBC, a single test function on a spherical mesh boundary was chosen and the integrals of (10) and (11) were computed using samples of outward propagating spherical harmonics. In one example, the radius of the boundary was chosen as 5 wavelengths, the first harmonic was used to represent the scattered field, and sampled CT/LN basis functions were used to represent the scattered field. The error in (10) and (11) was computed as a function of the size of the cells on which the test function lay. Figs. 3 and 4 show the accuracy of the RBC's as a function of the length of the edge on which the test function lies. Both error trends converge to theoretical results predicted in [5].

V. Conclusion

This paper has extended the use of higher–order, 3–D, curl–conforming vector basis functions to quadratic tetrahedral cells and to open region problems. These extensions to basic basis function theory are necessary for efficient finite element modeling of complex three–dimensional electromagnetic problems.

VI. References

[1] J. S. Savage and A. F. Peterson, "Higher–order vector finite elements for tetrahedral cells," *IEEE Trans. Microwave Theory Tech.*, (accepted for publication in 1996).

[2] J. C. Nedelec, "Mixed finite elements in R^3," *Num. Math.*, vol. 35, pp. 315–341, 1980.

[3] P. P. Silvester and R. L. Ferrari, *Finite Elements for Electrical Engineers*. Cambridge, UK, Cambridge University Press, 1983.

[4] P. Keast, "Moderate–degree tetrahedral quadrature formulas," *Computer Meth. Appl. Mechanics Eng.*, pp. 339–348, 1986.

[5] A. F. Peterson, "Accuracy of 3–D radiation boundary conditions for use with the vector Helmholtz equation," *IEEE Trans. Antennas Prop.*, vol. AP-40, pp. 351–355, 1992.

[6] A. F. Peterson, "Vector finite element formulation for scattering from two–dimensional heterogeneous bodies," *IEEE Trans. Antennas Prop.*, vol. AP-43, pp. 357–365, 1994.

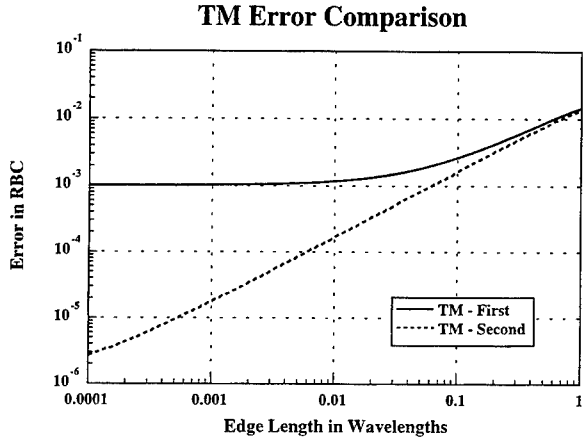

Fig. 3. An error comparison between the first and second order vector RBC. Transverse magnetic components of the first spherical harmonic were used to represent the scattered field.

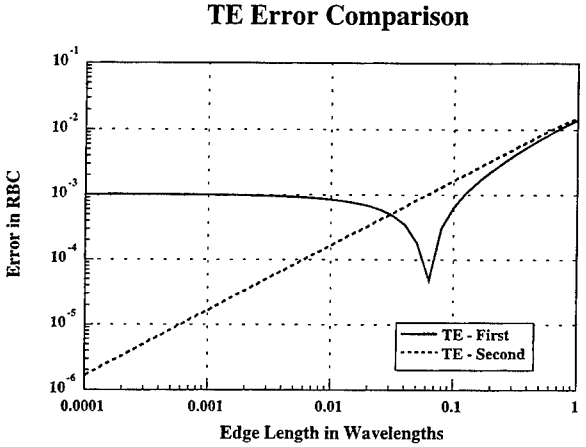

Fig. 4. An error comparison between the first and second order vector RBC. Transverse electric components of the first spherical harmonic were used to represent the scattered field.

The Hybrid FEM/BEM Solution for EM Scattering from Arbitrary Cavity with Lossy and Anisotropic Material

Jin Xu, Yilong Lu, and Jeffrey S. Fu
School of Electrical and Electronic Engineering
Nanyang Technological University
Singapore 639798

Abstract— **In this paper, a hybrid finite element method (FEM) and boundary element method (BEM) formulation is presented for solution of electromagnetic (EM) scattering from 3-dimensional cavity of arbitrary shape and filled with arbitrary inhomogeneous, anisotropy, and lossy materials. This formulation is useful to study scattering characteristics of anisotropic materials for possible design of better radar absorbing materials and structures, which are not shared by isotropic materials, in radar cross section reduction (RCSR) and other applications. Numerical examples are given to validate the formulation and to compare the scattering effects.**

I. INTRODUCTION

Modelling electromagnetic scattering from cavity-backed aperture in a ground plane has long been an interesting topic of computational electromagnetics. It would also be interesting to study scattering from anisotropic material which might be utilized to achieve extraordinary radiation and scattering characteristics not shared by isotropic materials in radar cross section reduction (RCSR) and other applications. The plane-wave scattering problems of microstrip patch antenna in an isotropic thin infinite substrate was treated in [1]. The scattering problem for a rectangular microstrip patch on a uniaxial thin infinite substrate was later reported in [2]. The scattering and resonance due to a uniaxial anisotropy in thick substrates were presented in [3].

In the past, the radiation and scattering problems with anisotropic materials have mainly been treated by the method of moment (MoM). Using MoM requires the knowledge of the Green's function of a cavity. Its application is therefore restricted to some regular shapes such as rectangular or cylindrical cavities. MoM is also not suitable to inhomogeneous problems. Moreover, applying MoM results in dense matrix equations. To solve dense matrix equation of order N requires CPU time proportion to $O(N^3)$ and memory proportional to $O(N^2)$, making MoM not suitable to large complex problems.

In this paper, a hybrid finite element method (FEM) and boundary element method (BEM) formulation is derived to solve electromagnetic scattering from 3-dimensional cavity of arbitrary shape and filled in with arbitrary inhomogeneous, anisotropy, and lossy materials.

Hybrid FEM/BEM approach has the advantages of both FEM and BEM [4]. The proposed approach employs the FEM for the interior fields within the cavity, whereas the BEM for the exterior fields outside the cavity. A complete system of equations can be obtained by coupling of the interior and exterior fields on the aperture of cavity according to the fields

continuity conditions. The resulting equations are then solved for the solution of interior and surface fields.

We have calibrated the accuracy of the computational scheme by comparing the results with examples by other methods. We have also applied this approach to simple rectangular cavities with lossy and anisotropic materials to show the effects of anisotropic materials on backscattering.

II. Formulation

The geometry of a cavity recessed in a ground plane is shown in Fig.1. The cavity is filled with material of inhomogeneous,lossy and anisotropic dielectric material. The dielectric material is assumed with (complex) scalar permeability μ and a (complex) tensor permittivity $\bar{\bar{\epsilon}}$:

$$\mu = \mu' - j\mu'' = \mu_0\mu_r, \tag{1}$$

$$\bar{\bar{\epsilon}} = \bar{\bar{\epsilon}}' - j\bar{\bar{\epsilon}}'' = \epsilon_0\bar{\bar{\epsilon}}_r = \epsilon_0 \begin{bmatrix} \epsilon_{xx} & \epsilon_{xy} & \epsilon_{xz} \\ \epsilon_{yx} & \epsilon_{yy} & \epsilon_{yz} \\ \epsilon_{zx} & \epsilon_{zy} & \epsilon_{zz} \end{bmatrix}. \tag{2}$$

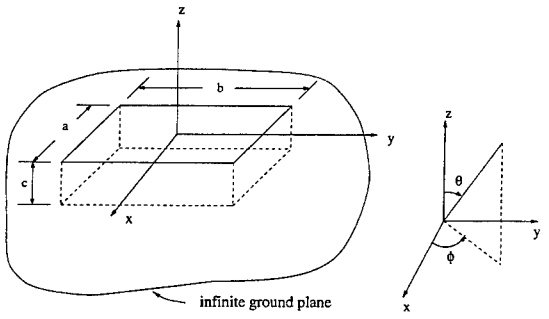

Fig. 1. Geometry of a cavity in a ground plane.

Assuming a harmonic time dependence of the form $\exp(j\omega t)$, from Maxwell's equations, the electric field vector wave equation (3) in source-free anisotropic medium is

$$\nabla \times \left(\mu_r^{-1} \cdot \nabla \times \mathbf{E}\right) - k_0^2 \bar{\bar{\epsilon}}_r \cdot \mathbf{E} = 0. \tag{3}$$

Applying the generalized variational principle

$$\mathcal{F}(\phi) = \frac{1}{2}\langle \mathcal{L}\phi, \phi \rangle - \frac{1}{2}\langle \mathcal{L}\phi, \kappa \rangle + \frac{1}{2}\langle \phi, \mathcal{L}\kappa \rangle - \langle \phi, f \rangle \tag{4}$$

where κ is any function that satisfies the same boundary condition as ϕ, the functional for electric fields inside the cavity can be obtained:

$$\mathcal{F}(\mathbf{E}) = \frac{1}{2}\int\int\int_V [\nabla \times (\mu_r^{-1}\nabla \times \mathbf{E}) - k_0^2 \bar{\bar{\epsilon}} \cdot \mathbf{E}] \cdot \mathbf{E} dV - jk_0 Z_0 \int\int_S \mathbf{E} \cdot \mathbf{n} \times \mathbf{H}^{inc}(r), \tag{5}$$

where V denotes the volume occupied by the cavity, S the area of the cavity aperture, $\mathbf{n}$ the unit vector normal to the aperture surface and pointing away from the cavity, $\mathbf{H}^{inc}(r)$ the incident field.

On the interface between the cavity and free space, the boundary relationship between the tangential electric and magnetic fields is given by

$$\hat{a}_z \times [\nabla \times \mathbf{E}(r)]_{z=0+} = -2jk_0 Z_0 \mathbf{H}^{inc}(r) - 2k_0^2 \hat{a}_z \times \int\int_{s_a} [\hat{a}_z \times \mathbf{E}(r')] \cdot \overline{\overline{G}}_0(r, r') dS'. \quad (6)$$

For the solution of electric field $\mathbf{E}$, the variation is

$$\delta \mathcal{F}(\mathbf{E}) = 0. \quad (7)$$

Applying 3-D finite element method to the volume integral and boundary element to the surface integral in (5), the cavity volume V can be discretized into a number of such finite volumes as tetrahedra, and the aperture surface S can be discretized into such associated finite area as triangles. In each element, the electric field components can be expressed, in general, in terms of basis (shape) functions N_j^e and nodal values E_{pj}^e as

$$E_p = \sum_{j=1}^{n} N_j^e(x, y, z) E_{pj}^e, \qquad p = x, y, z. \quad (8)$$

Applying Rayleigh-Ritz procedure to extremize the hybrid FEM/BEM formulation, we can obtain the matrix equation

$$\begin{bmatrix} K_{xx} + Q_{xx} & K_{xy} + Q_{xy} & K_{xz} \\ K_{yx} + Q_{yx} & K_{yy} + Q_{yy} & K_{yz} \\ K_{zx} & K_{zy} & K_{zz} \end{bmatrix} \begin{bmatrix} E_x \\ E_y \\ E_z \end{bmatrix} = \begin{bmatrix} B_x \\ B_y \\ B_z \end{bmatrix}, \quad (9)$$

where the matrix elements are given by

$$[Q_{xx}^e] = 2k_0^2 \int\int_{s^e} \{N^e\} [\int\int_{s^e} \{N^e\}^T G_0 dS'] dS - 2 \int\int_{s^e} \frac{\partial \{N^e\}}{\partial y} [\int\int_{s^e} \frac{\partial \{N^e\}^T}{\partial y} G_0 dS'] dS, \quad (10)$$

$$[Q_{xy}^e] = 2 \int\int_{s^e} \frac{\partial \{N^e\}}{\partial y} [\int\int_{s^e} \frac{\partial \{N^e\}^T}{\partial x} G_0 dS'] dS, \quad (11)$$

$$[Q_{yx}^e] = 2 \int\int_{s^e} \frac{\partial \{N^e\}}{\partial x} [\int\int_{s^e} \frac{\partial \{N^e\}^T}{\partial y} G_0 dS'] dS, \quad (12)$$

$$[Q_{yy}^e] = 2k_0^2 \int\int_{s^e} \{N^e\} [\int\int_{s^e} \{N^e\}^T G_0 dS'] dS - 2 \int\int_{s^e} \frac{\partial \{N^e\}}{\partial x} [\int\int_{s^e} \frac{\partial \{N^e\}^T}{\partial x} G_0 dS'] dS, \quad (13)$$

$$[K^e_{xx}] = \int\int\int_{V^e} \{\nu(\frac{\partial\{N^e\}}{\partial y}\frac{\partial\{N^e\}^T}{\partial y} + \frac{\partial\{N^e\}}{\partial z}\frac{\partial\{N^e\}^T}{\partial z}) - k_0^2\epsilon_{xx}\{N^e\}\{N^e\}^T\}dV, \quad (14)$$

$$[K^e_{yy}] = \int\int\int_{V^e} \{\nu(\frac{\partial\{N^e\}}{\partial z}\frac{\partial\{N^e\}^T}{\partial z} + \frac{\partial\{N^e\}}{\partial x}\frac{\partial\{N^e\}^T}{\partial x}) - k_0^2\epsilon_{yy}\{N^e\}\{N^e\}^T\}dV, \quad (15)$$

$$[K^e_{zz}] = \int\int\int_{V^e} \{\nu(\frac{\partial\{N^e\}}{\partial x}\frac{\partial\{N^e\}^T}{\partial x} + \frac{\partial\{N^e\}}{\partial y}\frac{\partial\{N^e\}^T}{\partial y}) - k_0^2\epsilon_{zz}\{N^e\}\{N^e\}^T\}dV, \quad (16)$$

$$[K^e_{pq}] = -\int\int\int_{V^e} (\nu\frac{\partial\{N^e\}}{\partial q}\frac{\partial\{N^e\}^T}{\partial p} + \frac{1}{2}k_0^2\epsilon_{pq}\{N^e\}\{N^e\}^T)dV, \quad p,q = x,y,z, \quad p \neq q. \quad (17)$$

The nodal fields can then be solved after imposing necessary boundary conditions. Once the fields on the cavity surface have been found, the far zone scattering field can be computed from [5]

$$\mathbf{E}^s = \frac{e^{-jk_0r}}{r}[\hat{\theta}^i A_\theta + \hat{\phi}^i A_\phi], \quad (18)$$

where

$$\begin{bmatrix} A_\theta \\ A_\phi \end{bmatrix} = \frac{jk_0}{2\pi}\int\int_S \begin{bmatrix} E^a_x\cos\phi^i + E^a_y\sin\phi^i \\ (-E^a_x\sin\phi^i + E^a_y\cos\phi^i)\cos\theta^i \end{bmatrix} e^{jk_0\sin\theta^i(x\cos\phi^i + y\sin\phi^i)}dxdy, \quad (19)$$

and E^a_x and E^a_y are the x and y components of the outgoing field on the aperture S. The Radar Cross Section (RCS) σ can be found by:

$$\sigma = \lim_{r\to\infty} 4\pi r^2\frac{|H^s(r)|^2}{|H^i(r)|^2}. \quad (20)$$

III. Numerical Experiment

In all cases, the incident plane wave given by

$$\mathbf{E}^i = [-\hat{\phi}^i I_\perp + \hat{\theta}^i I_\parallel]e^{j\vec{k}^i_0\cdot\vec{r}}, \quad (21)$$

where $\vec{k}^i = k_0(\hat{x}\sin\theta^i\cos\phi^i + \hat{y}\sin\theta^i\sin\phi^i + \hat{z}\cos\phi^i)$, $I_\perp$ denotes the amplitude of the vertical polarization, and $I_\parallel$ is the amplitude of the horizontal polarization.

To verify the formulation and the associated computer program, we first calibrate the accuracy of the method to some isotropic examples. Fig. 2 shows the RCS curves of a $0.4\lambda\times0.4\lambda\times0.25\lambda$ cavity filled the material of $\epsilon_r = 2-0.5j$ and $\mu_r = 1.2-0.1j$. The curves show good agreement between the computational results and the MoM solutions [6].

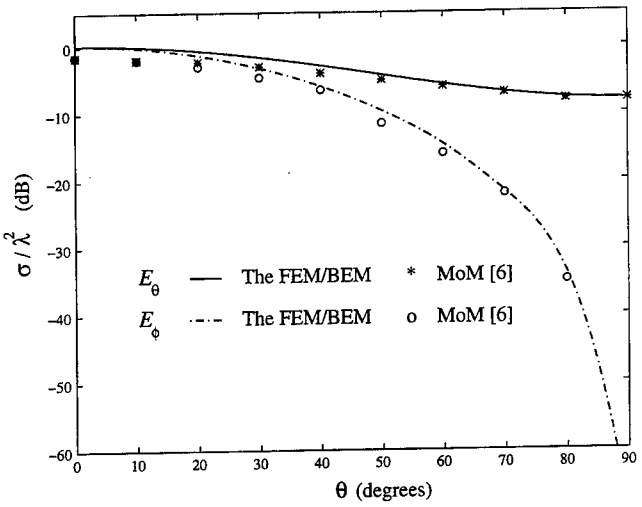

Fig. 2. Backscattering RCS pattern for a cavity versus incident angle. $\epsilon_r = 2 - 0.5j$, $\mu_r = 1.2 - 0.1j$, $a = 0.4\lambda$, $b = 0.4\lambda$, $c = 0.25\lambda$, $\phi^i = 0°$.

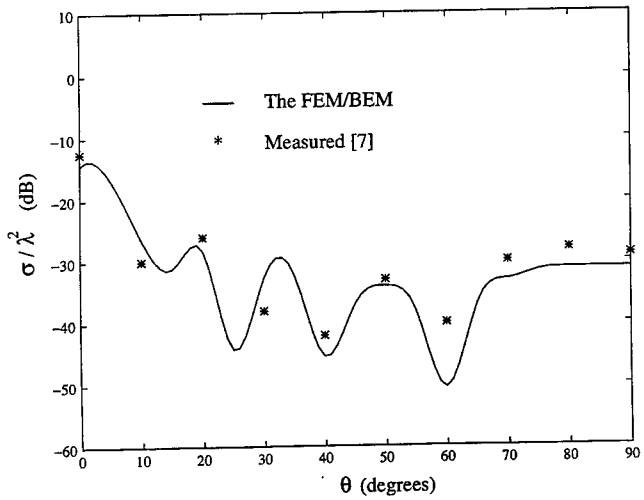

Fig. 3. Comparison of the computed and measured backscattering RCS of a cavity. $a = 2.89$ inch, $b = 2.10$ inch, $c = 0.057$ inch, $f = 9.2$ GHz, θ-polarized, $\epsilon_r = 4$, $\mu_r = 1$.

Fig. 3 displays the backscattering RCS of a cavity at 9.2 GHz. The cavity is filled in with of material $\epsilon_r = 4$, $\mu_r = 1$. Even with relatively small mesh size, good agreement between the computational results and the measured data [7] is observed.

Figs. 4 and 5 show some experiment of RCS curves with different materials, including isotropic and anisotropic materials. For the experiments, the cavity size remains same as $a = 1.0\lambda$, $b = 0.25\lambda$, $c = 0.25\lambda$. The parameters of materials are shown in the captions of Figs. 4 and 5. In Fig. 4, the anisotropic material is lossy and is charactered by three sets of materials. The incident plane wave is θ-polarized, and the incident direction is from $\phi^i = 90°$. The RCS corresponding to the 3 anisotropic material are about 7 dB, 10 dB, and 12dB, respectively. In Fig. 5, the anisotropic material is still lossy and charactered by two different parameters. The incident plane wave is ϕ-polarized, and from the direction $\phi^i = 0°$.

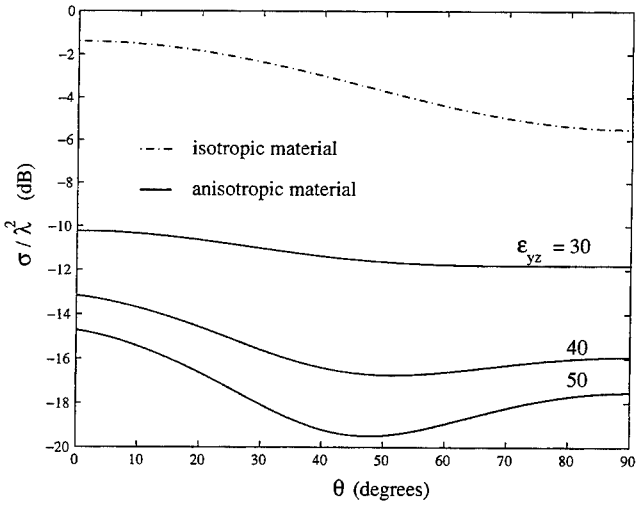

Fig. 4. Comparison of backscattering RCS in a cavity filled with the isotropic material and the anisotropic materials, respectively. θ-polarized on the plane $\phi = 90°$. Isotropic case: $\epsilon_r = 7.0 - 1.5j$, $\mu_r = 1.8 - 0.1j$; Anisotropic case: $\epsilon_{xx} = \epsilon_{yy} = \epsilon_{zz} = 7.0 - 1.5j$, $\epsilon_{xy} = \epsilon_{yx} = \epsilon_{xz} = \epsilon_{zx} = 0$.

Fig. 6 shows two dispersion curves of backscattering RCS from 2.5 to 6 GHz in a cavity filled with the isotropic material and the anisotropic material, respectively. The cavity is of size 7.32 cm×5.20 cm×0.158 cm. The incident plane wave is θ-polarized and the incident angle is (θ^i, ϕ^i)=(45°, 20°). Comparing with the isotropic case, 10 to 25 dB reduction can be obtained for the anisotropic case.

Figs. 4 to 6 show that greater reduction of RCS are possible using proper anisotropic material compared with using only isotropic materials. Using anisotropic material, there is more freedom in designing better radar absorbing materials and structures.

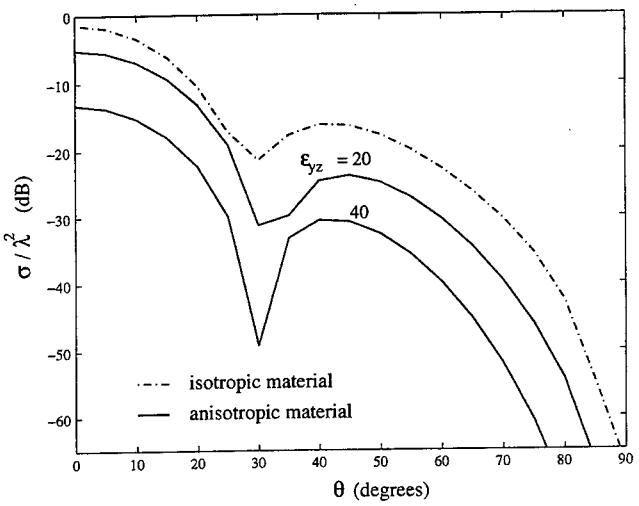

Fig. 5. Comparison of backscattering RCS in a cavity filled with the isotropic material and the anisotropic materials, respectively. $\phi - polarized$, $\phi^i = 0°$. Isotropic case: $\epsilon_r = 7.0 - 1.5j$, $\mu_r = 1.8 - 0.1j$; Anisotropic case: $\epsilon_{xx} = \epsilon_{yy} = \epsilon_{zz} = 7.0 - 1.5j$, $\epsilon_{xy} = \epsilon_{yx} = \epsilon_{xz} = \epsilon_{zx} = 0$.

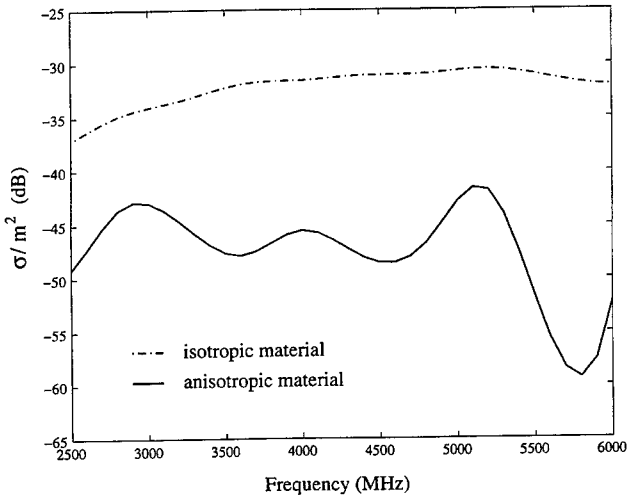

Fig. 6. Comparison of backscattering RCS against frequency in a cavity filled with the isotropic material and the anisotropic materials, respectively. θ-polarized, $\phi^i = 45°$, $\theta = 20°$. Isotropic material: $\epsilon_r = 2.17 - 0.0033j$, $\mu_r = 1$; Anisotropic material: $\epsilon_{xx} = \epsilon_{yy} = \epsilon_{zz} = 2.17 - 0.0033j$, $\epsilon_{xy} = \epsilon_{yx} = 0$, $\epsilon_{xz} = \epsilon_{zx} = \epsilon_{yz} = \epsilon_{zy} = 100$.

IV. Conclusions

The hybrid FEM/BEM approach for 3-D scattering from a cavity of arbitrary shape and filled in with arbitrary inhomogeneous, anisotropic, and lossy material is formulated and implemented. Hybrid FEM/BEM approach has the advantages of both FEM and BEM.

The proposed approach employs the FEM for the interior fields within the cavity, whereas the BEM for the exterior fields outside of the cavity. A complete system of equations can be obtained by coupling of the interior and exterior fields on the surface of cavity aperture according to the fields continuity conditions. The resulting equations are then solved for the solution of interior and surface fields.

This formulation is useful to study scattering characteristics of anisotropic materials for possible design of radar absorbing materials and structures, which are not shared by isotropic materials, in radar cross section reduction (RCSR) and other applications.

References

[1] E.H. Newman and D. Forri, "Scattering from a microstrip patch," *IEEE Transactions on Antennas and Propagation*, vol. AP-35, no. 3, 1987.

[2] D.M. Pozar, "Radiation and scattering from a microtrip patch on a uniaxial substrate," *IEEE Transactions on Antennas and Propagation*, vol. AP-35, no. 6, pp. 613–621, 1987.

[3] K.-L. Wong and J. Row, "Radar cross section and resonance of a rectangular microstrip patch anatennas in a uniaxilly anisotropic substrate-superstrate geometry," *IEEE Transactions on Antennas and Propagation*, vol. AP-35, no. 6, pp. 613–621, 1987.

[4] J.-M. Jin and J.L. Volakis, "A finite element-boundary integral formulation for scattering by three-dimensional cavity-backed aperture," *IEEE Transactions on Antennas and Propagation*, vol. 39, no. 1, pp. 97–104, 1991.

[5] H. Ling, R.-C. Chou, and S.-W. Lee, "Shooting and bouncing rays: Calculating the rcs of an arbitrarily shaped cavity," *IEEE Transactions on Antennas and Propagation*, vol. 37, no. 2, pp. 194–204, 1989.

[6] K. Barkeshli and J.L. Volakis, "Electromagnetic scattering from an aperture formed by a rectangular cavity recessed in a ground plane," *Journal of Electromagnetic Waves and Applications*, vol. 5, no. 7, pp. 715–733, 1991.

[7] J.-M. Jin and J.L. Volakis,"A Hybrid finite element Method for for scattering and Radiation by Microstrip Patch Antennas and Arrays Residing in a cavity," *IEEE Transactions on Antennas and Propagation*, vol. 39, no. 11, pp. 1598–1604, 1991.

SESSION 19:

FUTURE FIELDS FOR FDTD ANALYSIS

Chairs: D. Katz and M. Piket-May

FDTD Analysis of a Dielectric Leaky-Wave Antenna Using PML

Min Chen, Bijan Houshmand*, and Tatsuo Itoh

Department of Electrical Engineering
University of California, Los Angeles
Los Angeles, CA 90095, USA

*Jet Propulsion Laboratory
Oak Grove Drive
Pasadena, CA 91109

ABSTRACT

The Finite Difference Time Domain (FDTD) method associated with the Perfectly Matched Layer (PML) technique is applied to analyze a dielectric leaky-wave antenna comprising metal strips etched on a rectangular dielectric rod. The radiation pattern of the leaky-wave antenna can be predicted by using FDTD. Good agreement between FDTD and measurement results is shown. Other absorbing boundary conditions (ABC's) such as first order Mur and super-absorbing first order Mur are used for comparison. It is shown that by using PML, the absorbing boundaries can be placed much closer to the dielectric rod.

INTRODUCTION

Open dielectric leaky-wave structures have been found useful as frequency-scannable antennas especially for millimeter-wave frequency range [1]. One such class of dielectric waveguides is that with metal strips periodically residing on the top of a rectangular dielectric rod [2], as shown in Fig. 1. Several theoretical works have discussed this type of structure. Most of them analyzed the structures using approximate models to simplify the three-dimensional problem to a two-dimensional one. Using the effective dielectric constant (EDC) method, a spectral domain approach [3] and a transverse equivalent network technique [4] were employed to analyze this periodic structure. Another method, using a space-domain approach based on a waveguide model to confine the dielectric rod by two side walls, was proposed [5].

Being versatile, FDTD can be used to characterize this kind of dielectric leaky-wave structures rigorously. However, the major drawback of the FDTD method is that it requires a large amount of computational time and storage. The absorbing boundary condition (ABC) used to truncate the computational domain of FDTD may provide a solution to this problem. A perfect ABC should be able to allow the outgoing wave passing through without causing reflections. Consequently, the computational domain can be small as possible by placing absorbing boundaries near to the open structure considered.

A novel ABC, the so-called "Perfectly Matched Layer (PML)", which was recently proposed by Berenger [6,7] has been claimed to be more effective than any other type of ABC's in use.

Applications of PML for several different structures have been investigated recently. However, up to date application of PML to a 3-D dielectric waveguide structure, especially a highly directive leaky-wave antenna has not been discussed.

In this paper, it is demonstrated that the radiation characteristics of a dielectric leaky-wave antenna can be determined by FDTD. The comparison of the performance of PML ABC with those of the first order Mur and super-absorbing first order Mur is also discussed. The FDTD results presented in this paper are validated by experimental data.

METHOD

The conventional FDTD algorithm is applied to analyze the dielectric leaky-wave structure in Fig. 1. A y-polarized electric field is assumed for the dielectric waveguide. Because of cut-off frequency in the dielectric waveguide, a modulated Gaussian pulse is used for excitation. The dominant mode E^y_{11} for the dielectric waveguide is excited by imposing the proper field distribution on the transverse cross section of the waveguide. The space steps are chosen such that the maximum step size is less than 1/10 of the smallest wavelength of interest and the structural dimensions can be modeled accurately. A convergence study was conducted by iteratively reducing the space steps by one half until no significant change in computed results was observed. Once the space steps are selected, the time step can be chosen by satisfying the Courant stability criterion. In addition, calculation of the radiation pattern is done by a frequency domain transformation. First, transformation of the near field from time domain to frequency domain is made followed by a spatial Fourier transformation to obtain the far field.

The ABC used to terminate the computational domain plays an important role for FDTD simulation of open structures. The recent Berenger PML ABC can absorb propagation wave effectively by using nonphysical lossy media adjacent to the outer grid boundaries backed by perfectly conducting walls. Based on the splitting of the field components into two sub-components, the electric loss σ and magnetic loss σ^* for a PML medium are specified by satisfying the PML impedance matching condition:

$$\frac{\sigma}{\varepsilon} = \frac{\sigma^*}{\mu},$$

where ε and μ ($=\mu_o$) are the PML permittivity and permeability.

Care must be taken while applying PML technique for the dielectric waveguide structures [8]. As shown in Fig. 2 the dielectric rod must extend to the PML region to ensure the same field distribution. The averaging of the tangential permittivities is assumed at the dielectric-air interfaces. To have the same decay for the different dielectric materials inside the PML region, the electric losses corresponding to the different materials are assigned by imposing

$$\frac{\sigma_1}{\sigma_2} = \frac{\varepsilon_1}{\varepsilon_2}.$$

Besides, the losses in the PML region are assumed to increase quadratically with depth and the PML region is 6-layer thick.

RESULTS

For the periodically metal-strip-loaded dielectric waveguide with the parameters shown in Fig. 1, it can be shown that the structure exhibits fast-wave propagation and is suitable for use as a leaky-wave antenna. Fig. 3 shows the computed and measured radiation pattern of the leaky-wave antenna. Good agreement can be observed in the mainbeam region. The computed and measured mainbeam angles are -18.18° and -17.85° respectively. The computed and measured 3 dB beamwidths are 3° and 3.4° respectively. However, a lower second mainbeam occurs in the sidelobe region for the measurement. This is believed to be attributable to the radiation from the waveguide launcher which was not modeled in the FDTD simulation.

In addition to the application of the PML ABC, the first order Mur ABC and the super-absorbing first order Mur ABC are also used for comparison. In the first case, the absorbing boundaries for the side walls are placed 20 grid cells ($\approx \lambda_o$) away from the dielectric waveguide. The computed radiation patterns corresponding to the three different ABC's are shown in Fig. 4(a). Only slight discrepancy can be seen in the sidelobe region. Next, the absorbing boundaries are placed much closer to the dielectric waveguide. A distant of 5 grid cells ($< 0.5\lambda_o$) is used. Fig. 4(b) shows the resultant radiation patterns. The computed radiation patterns obtained by using first order Mur ABC and super-absorbing first order Mur ABC show discrepancies as compared to previous case. In contrast, the pattern corresponding to PML preserves accurately the shape in the mainbeam region.

CONCLUSION

In this paper, the capability of FDTD in the characterization of a dielectric leaky-wave antenna has been demonstrated. Good agreement between theoretical and experimental results was shown, indicating validity of the FDTD algorithm in simulation of the antenna pattern of such structure. Because of the superior performance of PML ABC, it can be placed closely to the dielectric waveguide from the side walls without significantly effecting the accuracy of the calculated results.

ACKNOWLEDGMENT

This work was supported by the Army Research Office under contract # DAAH04-93-G-0068.

REFERENCE

[1] T. Itoh, "Application of gratings in a dielectric waveguide for leaky-wave antennas and band-reject filters," *IEEE Trans. Microwave Theory Tech.*, vol. MTT-25, pp. 1134-1138, Dec. 1977.

[2] K. L. Klohn, R. E. Horn, H. Jacobs, and E. Freibergs, "Silicon waveguide frequency scanning linear array antenna," *IEEE Trans. Microwave Theory Tech.*, vol. MTT-26, pp. 764-773, 1978.

[3] R. Mittra and R. Kastner, "A spectral domain approach for computing the radiation characteristics of leaky-wave antenna for millimeter-waves," *IEEE Trans. Antennas Propagat.*, vol. AP-29, pp. 652-654, July 1981.

[4] M. Guglielmi, Z. M. Lu, J. Encinar, S. T. Peng and A. A. Oliner, "Metal-strip-loaded rectangular dielectric rod leaky-wave antennas : experimental verification of a new simple theory," in 1990 AP-S Int. Symp. Dig., pp. 1922-1925.

[5] M. Ghomi, B. Lejay, J. L. Amalric, and H. Baudrand, "Radiation characteristics of uniform and nonuniform dielectric leaky-wave antennas," *IEEE Trans. Antennas Propagat.*, vol. AP-41, pp. 1177-1186, Sep. 1993.

[6] J.-P. Berenger, "A perfectly matched layer for the absorption of electromagnetic waves" *J. Comp. Phys..*, vol. 114, no.2, pp. 185-200, Oct. 1994.

[7] D. Katz, E. Thiele, and A. Teflove, "Validation and extension to three dimensions of the Berenger PML absorbing boundary condition for FDTD meshes," *IEEE Microwave and Guided Wave Lett.*, vol. 4, no. 8. pp. 268-270, Aug. 1994.

[8] A. Bahr, A. Lauer and I. Wolff, "Application of the PML Absorbing Boundary Condition to the FDTD Analysis of Microwave Circuits," *IEEE MTT-S Int. Microwave Symp. Dig.*, pp. 27-30, May 1995.

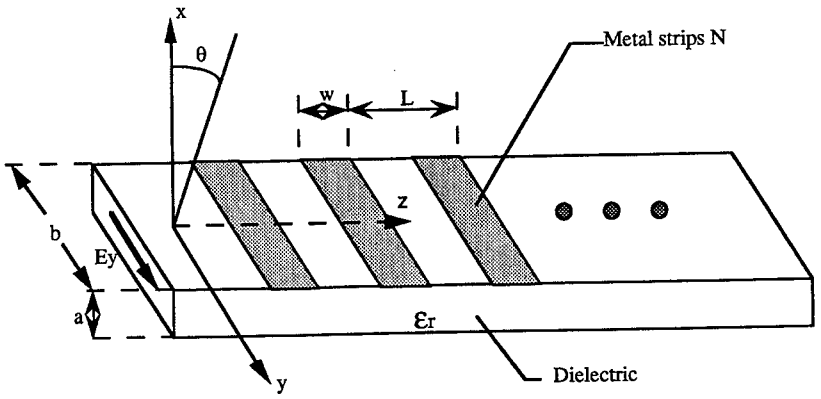

Fig. 1 A metal-strip-loaded leaky-wave antenna with the following parameters:
a = 1.5748mm, b=3 mm, L = 2.5 mm, w =0.5L, ε_r = 2.33, N =29, Freq. = 80 GHz.

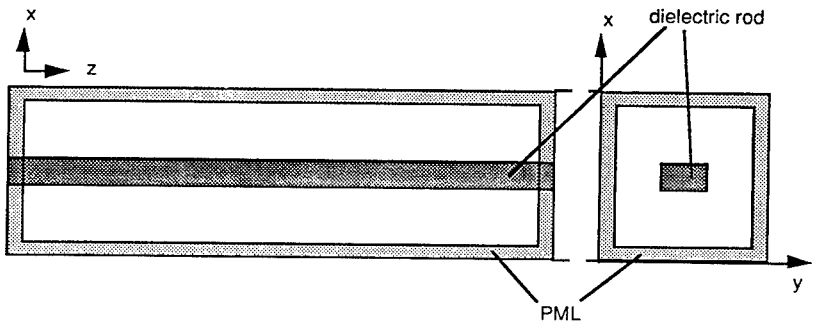

Fig. 2 FDTD simulation setup.

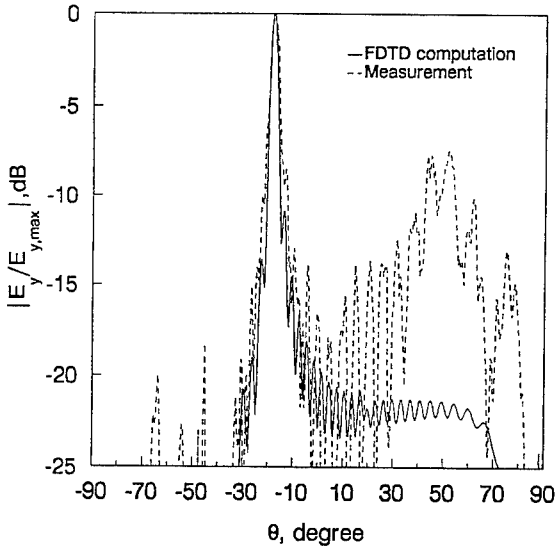

Fig. 3 Computed and measured radiation patterns of the leaky-wave antenna in the x-z plane.

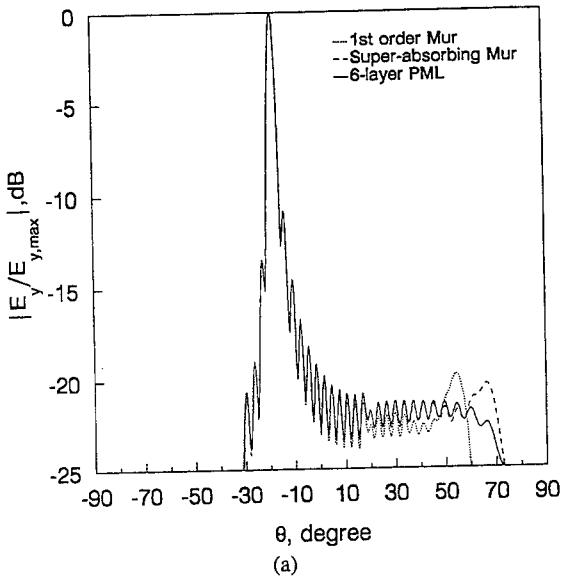

(a)

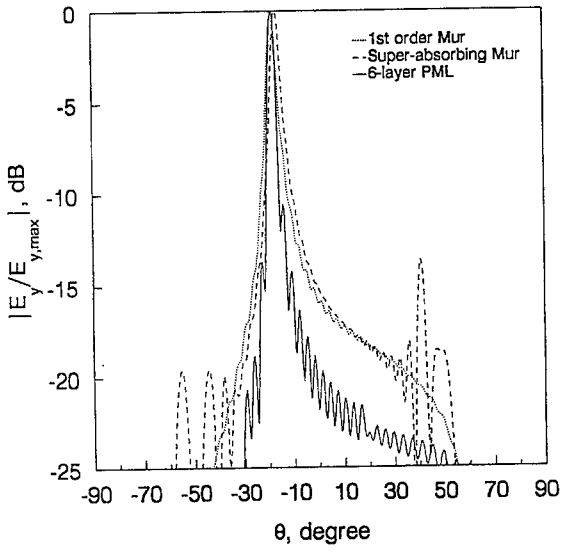

(b)

Fig. 4 Comparison of computed radiation patterns corresponding to various ABC's for the abosrbing boundaries: (a) 20 grid cells (b) 5 grid cells away from the four sides of the dielectric waveguide.

FDTD ANALYSIS IN CYLINDRICAL COORDINATES OF A TEM PYRAMIDAL HORN ANTENNA

D. Menditto, P. Tognolatti - Electrical Eng. Dept., University of L' Aquila, Italy
F. Bardati - DISP, "Tor Vergata" University of Rome, Italy

I- Introduction

Multi-frequency radiometry is the spectral measurement of the electromagnetic field spontaneously irradiated by a lossy body in the microwave frequency range. The spectrum of the radiation detected by a radiometer is dependent on the local temperature distribution inside the body. It is this dependency that allows multi-frequency radiometry to be used as a tool for thermal measurements. In fact, information about interior temperature is contained in radiometric data measured externally to the body and can be extracted through a temperature retrieval [1].

A major source of system errors or even impracticability of microwave radiometry for body temperature measurement is the antenna used to receive thermal radiation. The antenna may be of either non-contacting (elliptical reflector, microwave lens) or contacting type, usually a truncated waveguide filled with high-permittivity low-loss material to give a good impedance matching between the antenna and the body. Antenna losses are additional sources of thermal noise. Other drawbacks to contacting antennas exist, namely the disturbance due to the effect of the antenna heat capacity on the temperature pattern to be measured and the tissue structure deformation due to the pressure exercised by the antenna on the skin surface. The main problem in the design of a non-contacting radiometric antenna is the mismatch at the skin-air interface. A way to overcome partially the problem is to receive vertically-polarized thermal radiation at the pseudo-Brewster angle [2]. This can be accomplished by a broad-band antenna at either focus of an elliptical reflector.

We are interested in a TEM pyramidal horn antenna as a possible device to receive thermal radiation. Basically, a TEM horn (Fig. 1) consists of two almost triangular plates belonging to planes at angle β(flare angle). The plates are fed through a parallel-plate waveguide supporting only the TEM mode. Typical applications of these antennas are for short-pulse radars such as those used in ground-penetrating systems and for electromagnetic compatibility measurements. For radiometric applications, almost perfectly conducting plates are preferred. Kanda [3] investigated theoretically and experimentally the receiving and transmitting transient responses of the TEM horn. In his analysis it is assumed that the horn flare angle and the plate widths are chosen in such a way that the plates guides only the TEM mode by maintaining a constant characteristic impedance. The far-field is computed from the spherical wave that is assumed to exist at the horn open end (antenna aperture). For far-field evaluation, the TEM horn antenna is approximated by a V-shaped dipole operating in the end-fire mode and radiation is computed so as for travelling-wave antennas [4]. The optimum characteristic impedance variation between the horn feed point and the open end is formulated as the solution of a first-order Riccati equation. A near-optimum solution due to Hecken [5] has been adopted. In [6] the reflection of the waveform impinging on the TEM horn open end is analysed in terms of high-order even TM-modes. Theoretical results are compared to observations and the optimum taper function between the feed point and the open end is investigated so as to minimise the internal reflected waveform.

In the aforementioned papers it is shown that possible ways to reduce reflections from the antenna open end are plate shaping and addition of resistive pads and loading. However, having in mind radiometric applications, resistive materials are unpractical since they provide additional noise to the receiver. The design of a TEM horn antenna will take advantage from a numerical method that is able to solve Maxwell's equations inside a volume including the antenna with appropriate boundary conditions on the conducting plates. Let S' be either plate. The second plate, S'', is generated by rotating S' of the angle β around the z-axis, that is the straight line where the planes of the plates

have intersection. We consider the class of boundary-value problems that are defined by an electric-wall boundary-condition on S' and S''. In this paper a 3-D Finite-Difference Time-Domain (FDTD) method is developped in cylindrical coordinates r,φ,z to cope with the geometry of TEM horn antennas with flat plates. In fact, being performed on planes, stair-case approximations of plate boundaries are more accurate than they would be in the case of a rectangular frame (parallel-piped Yee cell). Recently, Yee's original, rectilinear, orthogonal mesh has been used for the FDTD analysis of some broadband antennas such as resistive monopole [7], conical [8], bow-tie [9], TEM horn antennas [10].

In the next Section, some of the issues that are encountered when the standard FDTD method is adapted to a cylindrical frame will be considered. The method will be tested on a simple structure for which the electromagnetic field can be obtained analytically. In Section III, the method will be applied to a TEM horn antenna and preliminary results will be given. Because of large computer time, we explored a new method to speed up computations. The method is based on multiple time step for temporal iteration and will be accounted for, together with some results, in Section IV.

II- FDTD in the cylindrical coordinate system

The cuts of the elemental cell obtained with coordinate surfaces of the cylindrical system r,φ,z are shown in Fig. 2. The location and orientation of each electromagnetic field component belonging to the cell are also shown. The spatial finite increments along coordinate lines are Δr, $r\Delta\varphi$, and Δz, respectively, and the time step is Δt. The approximation of the derivatives in Maxwell's curl equations by central differences gives the FDTD scheme in cylindrical coordinates reported in the Appendix. The computation domain, Ω, is defined as

$$\Omega = \{r,\varphi,z | r_{min} \le r \le r_0; -\varphi_0 \le \varphi \le \varphi_0; 0 \le z \le z_0\}.$$

In cylindrical coordinates a cell volume is a function of r, because the arc length $r\Delta\varphi$. Therefore the usual constraint of a spatial increment not larger than $0.05\lambda - 0.1\lambda$ (λ is the smallest wavelength corresponding to electromagnetic propagation in Ω) will be enforced at the upper bond of r. On the contrary, Courant stability condition for time step will be enforced for $r = r_{min}$.

The cylindrical FDTD has been tested on a domain for which analytical time-harmonic solutions are known. If the boundaries $r = r_{min}, r = r_0, \varphi = \pm\varphi_0$ are perfect conductors and the structure is filled with a homogeneous lossless dielectric, we obtain an ideal waveguide having sectoral cross-section [11]. We assume that only one mode propagates in the sectoral waveguide, i.e., a TE_{pq} mode for given p,q. Let Z_{pq} be the modal impedance, real in the absence of losses. If the waveguide is terminated at $z = 0, z = z_0$ by walls having Z_{pq} as surface impedance no reflections will occur. Only the TE_{pq} will propagate in the structure, provided the field source has been designed in such a way to excite that mode alone. If $\underline{E}_t, \underline{H}_t$ are TE_{pq} transverse fields at $\bar{z}$, $0 < \bar{z} < z_0$, then the currents $\underline{J}, \underline{M}$, given by $\underline{J} = \hat{z} \times \underline{H}$, $\underline{M} = -\hat{z} \times \underline{E}$, will radiate a null field for $z < \bar{z}$ and the selected mode for $\bar{z} < z$. In the test case, the time-excitation was $sin(2\pi ft)1(t)$, where f is frequency and $1(t)$ the step function. Time-harmonic response was recovered after the transient response was extinguished at a set of points of Ω. To evaluate the time-harmonic response field amplitude, a common procedure is that of evaluating the swing of the transient response, then FDTD iterations are stopped when swing variation, corresponding to subsequent time periods, is lower than a threshold. Alternatively, the DFT of the transient response can be performed. Field values at given points are stored during FDTD time-evolution and are transformed after each time-period $1/f$ according to the following equation ($A(\underline{r},t)$ is a component of $\underline{E}$ or $\underline{H}$):

$$\dot{A}(\underline{r}) = \frac{2}{N_{step}} \sum_{n=0}^{N_{step}-1} A(\underline{r}, n\Delta t) e^{-j2\pi fn\Delta t}$$

In the above equation, N_{step} is the number of time-steps in one period, $N_{step} = 1/(f\Delta t)$, $\dot{A}$ is a complex number the modulus of which is the magnitude of the field component for time-harmonic analysis at frequency f, and $j = \sqrt{-1}$.

As a test case, the mode TE_{11} has been considered, for which the transverse eigenvalue, β_r, is the first zero of

$$J'_m(\beta_r r_0)Y'_m(\beta_r r_{min}) - J'_m(\beta_r r_{min})Y'_m(\beta_r r_0) = 0$$

where J'_m, Y'_m are the first derivatives of Bessel functions of first and second kind, respectively, and order m, and

$$m = p\pi/(2\varphi_0), \qquad p = 1 \ .$$

As an example, results for E_r at point $\underline{r}_P \in \Omega$ are reported in Figs. 3-5. They have been obtained by means of cylindrical FDTD when it is used alone or together with DFT. The analytical solution is also shown. The relative error between the numerical and analytical solutions is small (a few %). As expected, it decreases when DFT is used. It is interesting the comparison between the numerical solution, when E_r is plotted as a function of z, and the analytical one (a unitary step at $z = \bar{z}$). A non-null field for $z < \bar{z}$ as well as a ripple for $\bar{z} < z$ can be appreciated from the diagrams. They are due to reflections and spurious mode excitation. Indeed, the ratio E_r / H_φ, which equals Z_{11} over the waveguide cross-section for the analytical solution, depends on the point where the ratio is evaluated for the numerical solution. However, the relative difference is less than 3.5% in our computations (as large as 14% if DFT is not used).

III - The TEM pyramidal horn

The cylindrical FDTD algorithm has been used for field computations in the case of a TEM horn antenna. The plate geometry (Fig. 6) is trapezoidal and is cut out from an isosceles triangle with apex at $(r_{apex}, 0, 0)$ and angle α. r_a and r_b are distances from z-axis of the trapezoid smaller and larger basis, respectively. The field source is a voltage, V_g, across the plate apices. In our model this results in an electric field E_φ related to V_g by

$$V_g(t) = -r_a \int_{-\beta/2}^{\beta/2} E_\varphi(r_a, \varphi, 0, t)\, d\varphi \ .$$

The gap between the plates at the source points is $r_a\beta$ (Fig. 7). We assumed

$$E_\varphi(r_a, \varphi, 0, t) = -V_g(t)/(r_a\beta) \ .$$

The computation domain has been chosen in such a way to take symmetries into account. Because of symmetries, the electric field is perpendicular to the plane $\varphi = 0$, therefore this plane can be considered an electric wall. Moreover, the electric field lies on the plane $z = 0$ that can be considered a magnetic wall. In our model, therefore, the computation domain is the following cylinder

$$\Omega_H = \{r, \varphi, z | r_{min} \le r \le r_0; 0 \le \varphi \le \varphi_0; 0 \le z \le z_0\}$$

In conclusion, the boundary of Ω_H, $\partial\Omega_H$, is composed by two surfaces, where total reflection occurs, and four surfaces through which there is radiation. We use Mur first-order

absorbing boundary conditions [12] on these surfaces. According to [9], the voltage has been assumed a Gaussian impulse

$$V_g(t) = V_0 \frac{t}{\tau_p} e^{\frac{1}{2}} e^{-\frac{t^2}{2\tau_p^2}} \quad ,$$

where $\tau_p = 0.065\,\tau_a$, τ_a being the time required by the electromagnetic field to propagate through the antenna from the apex to the aperture $r = r_b$.

Time-dependent results are shown in Fig. 8. A grey scale is used, where black is for maximum. The impulse propagates within the antenna, reaches the horn front end where a partial reflection takes place, and then propagates in the space surrounding the antenna. It is interesting to observe that the impulse propagates without appreciable reflections beyond $\partial\Omega_H$.

IV- The multiple time-step method

In cylindrical FDTD, the time step, evaluated according to Courant condition, is unnecessarily small for cells at $r > r_{min}$. This leads to an inefficient use of computer resources. A way to counteract this problem is to subdivide Ω into N annular subdomains Ω_ℓ as

$$\Omega_\ell = \{r, \varphi, z | r_{\ell-1} \geq r \geq r_\ell\} \quad , \quad \ell = 1,\ldots,\mathrm{N}, \quad r_N = r_{min}$$

The Courant stability condition can be written for each subdomain as

$$u\Delta t_\ell \leq \frac{1}{\sqrt{\frac{1}{\Delta r^2} + \frac{1}{(r_\ell \Delta\phi)^2} + \frac{1}{\Delta z^2}}}$$

where, for simplicity, we assume that u is the maximum phase velocity in Ω. If the time-step is given according to the above equation, we expect a better use of computer resources. However, a problem to face is the continuity of the solution at the boundary between adjacent subdomains. Let us consider the interface between Ω_ℓ and $\Omega_{\ell+1}$. If the following equation holds

$$(2s+1)\Delta t_{\ell+1} = \Delta t_\ell \quad ,$$

with s integer, the required field continuity can be easily satisfied. We will consider the case $s = 1$, i.e. $3\Delta t_{\ell+1} = \Delta t_\ell$.

Figs. 9 and 10 are of help to understand how field components are computed from field "time history". Boxes are used for time-space samples of E and H components, as they are processed by the FDTD algorithm. Circles are for E-field, squares are for H-field. Segments between boxes serve as symbols of difference operators between the corresponding field components. An empty box is for a field component to be evaluated, a black box is for a field component that has already been obtained by means of the FDTD algorithm. Only field behaviour with r and t are considered explicitly. Fig. 9 shows the usual scheme by which the field at $t = (n+1)\Delta t$ is computed from the values at $t = (n+1/2)\Delta t$ and $t = n\Delta t$, in the case of single time-step.

Fig. 10 refers to the case of time steps according to the rule $3\Delta t_{\ell+1} = \Delta t_\ell$. Assume that $r = \bar{r}$ is the boundary between subdomains with different time-steps. For $r < \bar{r}$ the time step is Δt, while for $r > \bar{r}$ the time step is $3\Delta t$. Assume now that H_1 is to be computed at $t = (n+1/2)\Delta t$ (Fig. 10 (a)). From the scheme it results that E_3 must be known to perform this computation. However E_3 (grey box) cannot be achieved by the finite-difference scheme. Instead E_3 can be obtained by means of extrapolation of previous values of the E-field, e.g., from E_1 and E_2. At $t = (n+1)\Delta t$ (Fig. 10 (b)), the electric field is to be computed only for $r \leq \bar{r}$. At $\bar{r}$ the value, E_4, is obtained from E_3, H_1 and H_2 by means of difference operators. It should be noticed that, in this example of multiple time step, one third of computations along the line $r = \bar{r}$ is not performed according to the finite difference algorithm. We expect, therefore, some loss of accuracy.

The multiple time-step technique has been tested on the sectoral domain already introduced in Section II for the single-step method. The domain has been divided into two subdomains at $r = \bar{r}$. Numerical results (Figs. 11-13) have been compared to the analytical solution as well as to the results obtained by the single-step technique, when the lower time-step has been retained for the whole domain. The differences between the numerical and analytical solutions are small, while a lower accuracy can be appreciated in the comparison with the single-step results. However, computer time has been reduced by about 35%.

V- Conclusions

We have considered the cylindrical FDTD as a tool for the electromagnetic analysis of a class of broad-band antennas including common TEM horn antennas. The algorithm has been tested on a domain obtained from a sectoral waveguide. Preliminary results have been obtained for the geometry obtained by revolution of an almost triangular plate. In a cylindrical frame, the time step selected according to Courant stability condition at points near the z-axis may result excessively small for field evaluation at points that are far from the axis. To speed up computations, therefore, the multiple-step technique has been worked out and experimented.

References

[1] F. Bardati, V. J. Brown, and P. Tognolatti, "Two-dimensional temperature retrieval in biological structures by multi-frequency microwave radiometry: A Sobolev-space solution", ACES J. Special Issue on Bioelectromagnetic Computation, Vol. 7, pp. 110-120, 1992.

[2] F. Bardati, and D. Solimini, "Radiometric sensing of biological layered media", Radio Sci. Vol. 18, pp. 1393-1401, 1983.

[3] M. Kanda, "Transients in a resistevely loaded linear antenna compared with those in a conical antenna and a TEM horn", IEEE Trans. Antennas Propagat., vol. AP-28, pp.. 132-136, 1980.

[4] E. A. Theodoru, M. R. Gorman, P. R. Rigg, and F. N. Kong, "Broadband pulse-optimised antenna", IEE Proc., Vol. 128, Pt. H, pp. 124-130, 1981.

[5] R. P. Hecken, "A near-optimum matching section without discontinuities", IEEE Trans. Microwave Theory Tech., Vol. MTT-20, pp. 734-739, 1972.

[6] S. Evans and F. N. Kong, "TEM horn antenna: input reflection characteristics in transmission", IEE Proc., Vol. 130, Pt. H, pp. 403-409, 1983.

[7] J. G. Maloney, and G. S. Smith, "A study of transient radiation from the Wu-King resistive monopole-FDTD analysis and experimental measurements", IEEE Trans. Antennas Propagat., Vol. 41, pp. 668-676, 1993.

[8] J. G. Maloney, and G. S. Smith, "Optimisation of a conical antenna for pulse radiation: An efficient design using resistive loading", IEEE Trans. Antennas Propagat., Vol. 41, pp. 940-947, 1993.

[9] K. L. Shlager, G. S. Smith, and J. G. Maloney, "Optimization of bow-tie antennas for pulse radiation", IEEE Trans. Antennas Propagat., Vol. 42, pp. 975-982, 1994.
[10] K. L. Shlager, G. S. Smith, and J. G. Maloney, "Accurate analysis of metallic TEM horn antennas for pulse radiation using the FDTD method", IEEE AP-S Symp. Dig., pp. 1786-1789, June 1994.
[11] C. A. Balanis, *Advanced Engineering Electromagnetics*, Wiley, New York, NY, 1989, p. 539.
[12] G. Mur, "Absorbing boundary conditions for the finite-difference approximation of the time-domain electromagnetic-field equations", IEEE Trans. EM Comp., Vol. EMC-23, pp. 377-382, 1981.
[13] K. S. Kunz, and R. J. Luebbers, *The Finite Dfference Time Domain Method for Electromagnetics*, CRC Press, Boca Raton, FL, 1993.

Appendix

Let $\underline{r} \equiv (r,\varphi,z)$ be a point of Ω. We adopt the following rule for scalars $f(\underline{r}),g(\underline{r},t)$ defined in Ω: $f(i,j,k) = f(i\Delta r + r_{min}, j\Delta\varphi, k\Delta z)$, $g^n(i,j,k) = g(i\Delta r + r_{min}, j\Delta\varphi, k\Delta z, n\Delta t)$. With reference to the elemental cell of Fig. 2 for field component locations, the finite-difference time-domain approximations of Maxwell's curl equations in the presence of electric and magnetic current sources, $\underline{J}(r,\varphi,z,t)$ and $\underline{M}(r,\varphi,z,t)$, are:

$$H_r^{n+1}(i,j+\tfrac{1}{2},k+\tfrac{1}{2}) = H_r^n(i,j+\tfrac{1}{2},k+\tfrac{1}{2}) + \frac{\Delta t}{\mu(i,j+\frac{1}{2},k+\frac{1}{2})}\Big[\frac{E_\varphi^{n+\frac{1}{2}}(i,j+\frac{1}{2},k+1) - E_\varphi^{n+\frac{1}{2}}(i,j+\frac{1}{2},k)}{\Delta z} - \frac{1}{\tau(i)\Delta r}\frac{E_z^{n+\frac{1}{2}}(i,j+1,k+\frac{1}{2}) - E_z^{n+\frac{1}{2}}(i,j,k+\frac{1}{2})}{\Delta\varphi}\Big] - \frac{\Delta t}{\mu(i,j+\frac{1}{2},k+\frac{1}{2})} M_r^{n+\frac{1}{2}}(i,j+\tfrac{1}{2},k+\tfrac{1}{2}) \tag{A1}$$

$$H_\varphi^{n+1}(i+\tfrac{1}{2},j,k+\tfrac{1}{2}) = H_\varphi^n(i+\tfrac{1}{2},j,k+\tfrac{1}{2}) + \frac{\Delta t}{\mu(i+\frac{1}{2},j,k+\frac{1}{2})}\Big[\frac{E_z^{n+\frac{1}{2}}(i+1,j,k+\frac{1}{2}) - E_z^{n+\frac{1}{2}}(i,j,k+\frac{1}{2})}{\Delta r} - \frac{E_r^{n+\frac{1}{2}}(i+\frac{1}{2},j,k+1) - E_r^{n+\frac{1}{2}}(i+\frac{1}{2},j,k)}{\Delta z}\Big] - \frac{\Delta t}{\mu(i+\frac{1}{2},j,k+\frac{1}{2})} M_\varphi^{n+\frac{1}{2}}(i+\tfrac{1}{2},j,k+\tfrac{1}{2}) \tag{A2}$$

$$H_z^{n+1}(i+\tfrac{1}{2},j+\tfrac{1}{2},k) = H_z^n(i+\tfrac{1}{2},j+\tfrac{1}{2},k) + \frac{\Delta t}{\mu(i+\frac{1}{2},j+\frac{1}{2},k)[\tau(i)+\frac{1}{2}]\Delta r}\Big\{\frac{E_r^{n+\frac{1}{2}}(i+\frac{1}{2},j+1,k) - E_r^{n+\frac{1}{2}}(i+\frac{1}{2},j,k)}{\Delta\varphi} - [\tau(i)+1]E_\varphi^{n+\frac{1}{2}}(i+1,j+\tfrac{1}{2},k) + \tau(i)E_\varphi^{n+\frac{1}{2}}(i,j+\tfrac{1}{2},k)\Big\} - \frac{\Delta t}{\mu(i+\frac{1}{2},j+\frac{1}{2},k)} M_z^{n+\frac{1}{2}}(i+\tfrac{1}{2},j+\tfrac{1}{2},k) \tag{A3}$$

$$E_r^{n+\frac{1}{2}}(i+\tfrac{1}{2},j,k)=E_r^{n-\frac{1}{2}}(i+\tfrac{1}{2},j,k)-\frac{\Delta t}{\varepsilon(i+\frac{1}{2},j,k)}[\frac{H_\varphi^n(i+\frac{1}{2},j,k+\frac{1}{2})-H_\varphi^n(i+\frac{1}{2},j,k-\frac{1}{2})}{\Delta z}$$
$$-\frac{H_z^n(i+\frac{1}{2},j+\frac{1}{2},k)-H_z^n(i+\frac{1}{2},j-\frac{1}{2},k)}{[\tau(i)+\frac{1}{2}]\Delta r\Delta\varphi}]-\frac{\Delta t}{\varepsilon(i+\frac{1}{2},j,k)}J_r^n(i+\tfrac{1}{2},j,k) \qquad \text{(A4)}$$
$$-\frac{\Delta t\sigma(i+\frac{1}{2},j,k)}{\varepsilon(i+\frac{1}{2},j,k)}E_r^{n-\frac{1}{2}}(i+\tfrac{1}{2},j,k)$$

$$E_\varphi^{n+\frac{1}{2}}(i,j+\tfrac{1}{2},k)=E_\varphi^{n-\frac{1}{2}}(i,j+\tfrac{1}{2},k)-\frac{\Delta t}{\varepsilon(i,j+\frac{1}{2},k)}[\frac{H_z^n(i+\frac{1}{2},j+\frac{1}{2},k)-H_z^n(i-\frac{1}{2},j+\frac{1}{2},k)}{\Delta r}$$
$$-\frac{H_r^n(i,j+\frac{1}{2},k+\frac{1}{2})-H_r^n(i,j+\frac{1}{2},k-\frac{1}{2})}{\Delta z}]-\frac{\Delta t}{\varepsilon(i,j+\frac{1}{2},k)}J_\varphi^n(i,j+\tfrac{1}{2},k) \qquad \text{(A5)}$$
$$-\frac{\Delta t\sigma(i,j+\frac{1}{2},k)}{\varepsilon(i,j+\frac{1}{2},k)}E_\varphi^{n-\frac{1}{2}}(i,j+\tfrac{1}{2},k)$$

$$E_z^{n+\frac{1}{2}}(i,j,k+\tfrac{1}{2})=E_z^{n-\frac{1}{2}}(i,j,k+\tfrac{1}{2})-\frac{\Delta t}{\varepsilon(i,j,k+\frac{1}{2})\ \tau(i)\Delta r}\{\frac{H_r^n(i,j+\frac{1}{2},k+\frac{1}{2})-H_r^n(i,j-\frac{1}{2},k+\frac{1}{2})}{\Delta\varphi}$$
$$-[\tau(i)+\tfrac{1}{2}]H_\varphi^n(i+\tfrac{1}{2},j,k+\tfrac{1}{2})+[\tau(i)-\tfrac{1}{2}]H_\varphi^n(i-\tfrac{1}{2},j,k+\tfrac{1}{2})\} \qquad \text{(A6)}$$
$$-\frac{\Delta t}{\varepsilon(i,j,k+\frac{1}{2})}J_z^n(i,j,k+\tfrac{1}{2})-\frac{\Delta t\ \ \sigma(i,j,k+\frac{1}{2})}{\varepsilon(i,j,k+\frac{1}{2})}E_z^{n-\frac{1}{2}}(i,j,k+\tfrac{1}{2})$$

In the above equations, i,j,k are integers. μ,ε,σ are permeability, permittivity and conductivity, respectively, and are time-independent, i.e., the material filling Ω is, generally, inhomogeneous and dispersionless. The distance, r, of a point from the z-axis is $\tau(i)\Delta r$ where $\tau(i)=r_{min}/\Delta r+i$.

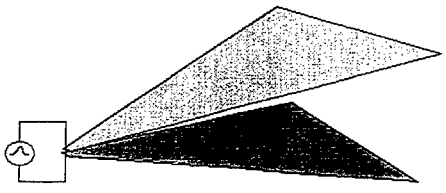

Fig. 1 - TEM pyramidal horn view.

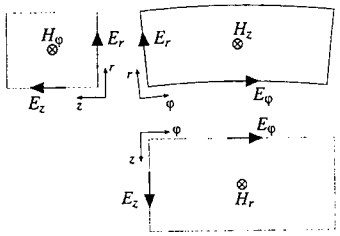

Fig. 2 - Cuts of the elemental cell with coordinate surfaces of the cylindrical system.

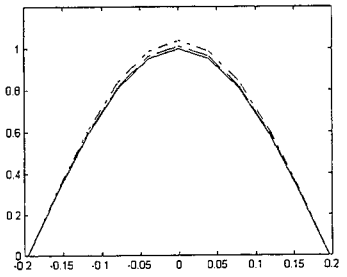

Fig. 3 - $E_r(r_P,\varphi,z_P)$ vs. φ, $r_P=(r_0-r_{min})/2, z_P=z_0/2$. (r_P,φ,z_P) a point of the sectoral domain. Solid line: analytical solution; dotted/dashed line: FDTD alone; dashed line: FDTD+DFT. E_r normalized to $E_r(r_P,0,z_P)$. $r_{min}=0.08$, $r_0=0.1$, $\varphi_0=\pi/16$, $z_0=0.08$. Excitation at plane $\bar{z}=0.25z_0$. Lengths in meter. Frequency f=5 GHz.

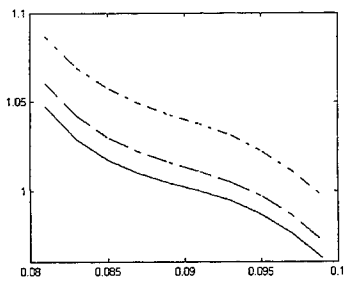

Fig. 4 - $E_r(r,0,z_P)$ vs. r, z_P and other data as in Fig. 3.

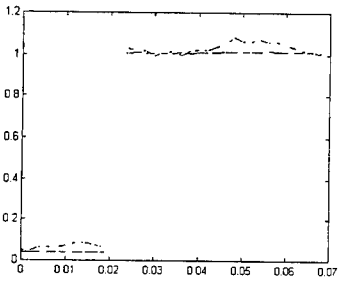

Fig. 5 - $E_r(r_P,0,z)$ vs. z, r_P and other data as in Fig. 3.

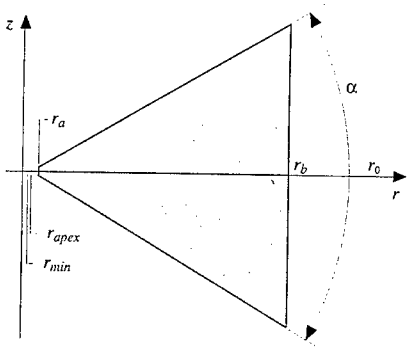

Fig. 6 - Geometry of TEM horn (r,z-plane cut). $r_{min}=0.05$, $r_0=0.275, \alpha=60°$. $r_{apex}=0.0825$, $r_a=0.0875$, $r_b=0.2375$. Lengths in meter.

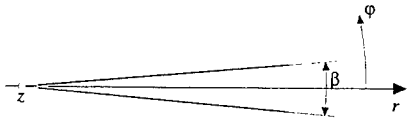

Fig. 7 - Geometry of TEM horn (r,φ-plane cut). $\beta=10$.

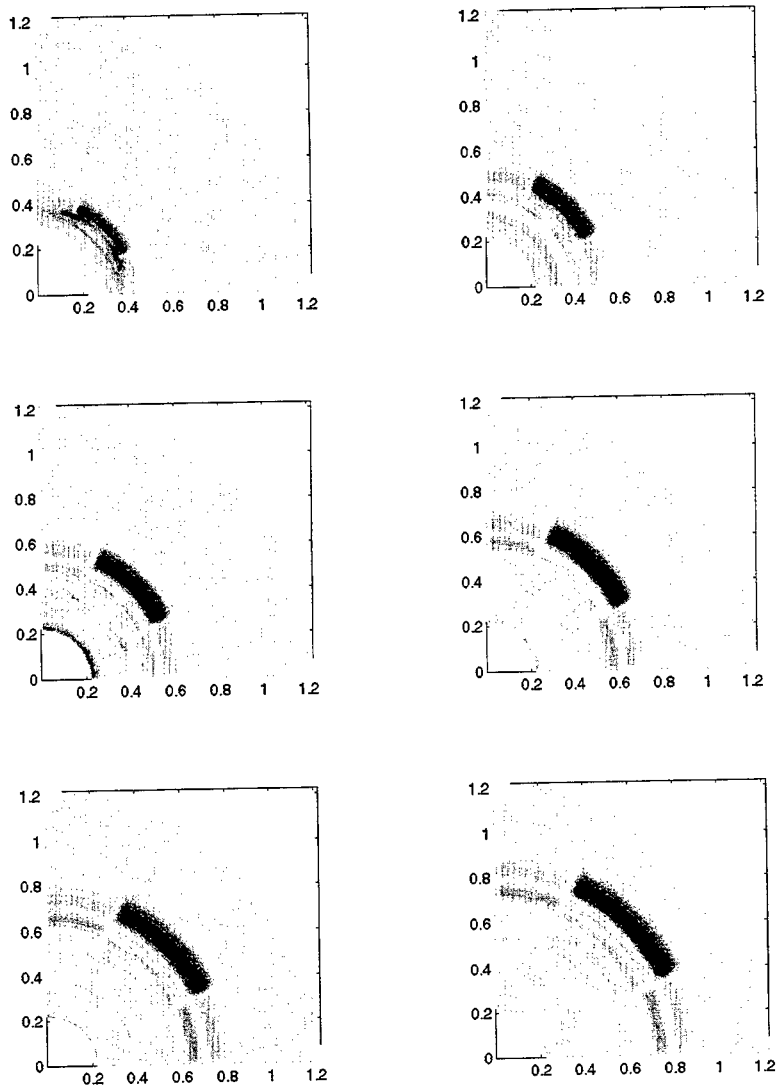

Fig. 8 a - Magnitude of the electric field in a region including the TEM horn antenna. Field on the $z = 0$ plane of symmetry (magnetic wall). $\Delta r = 0.0025m$, $\Delta t = 7.2 \cdot 10^{-13} s$. Diagrams at $t = n' \Delta\tau$, $n' = 1,\ldots,6$, $\Delta\tau = 100\,\Delta t$. $V_0 = 1V$.

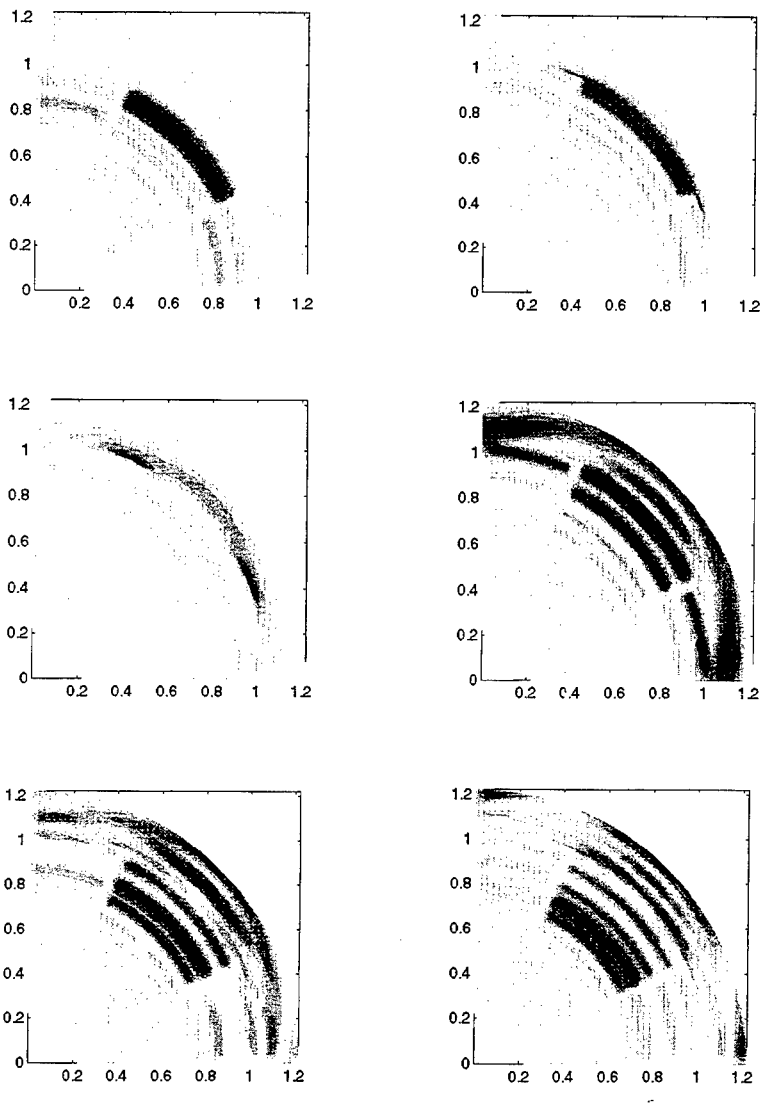

Fig. 8 b - As Fig. 8 a, for $n' = 7,\ldots,12$.

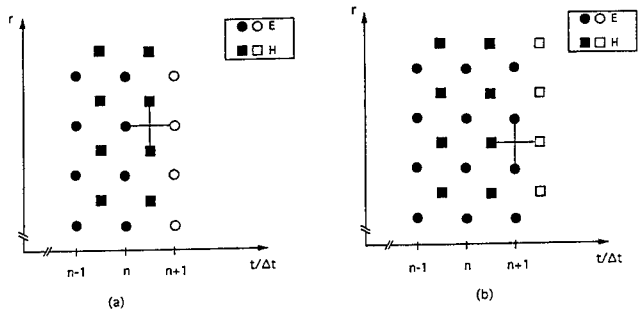

Fig. 9 - Scheme for single time-step FDTD algorithm. Segments are for difference operator between field components symbolized by boxes.

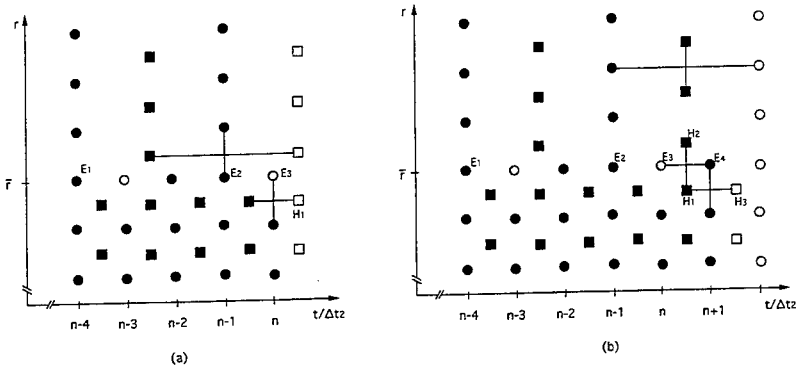

Fig. 10 - Scheme for multiple time-step algorithm. The case of two subdomains and time steps given by $3\Delta t_2 = \Delta t_1$.

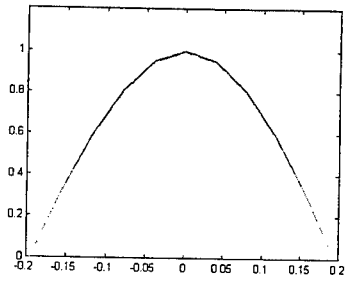

Fig. 11 - $E_r(r_P, \varphi, z_P)$ vs. φ for structure and other data as in Fig. 3. Multiple time-step technique for two subdomains separated by the surface $r = \bar{r}$, $\bar{r} = 0.088$ m.

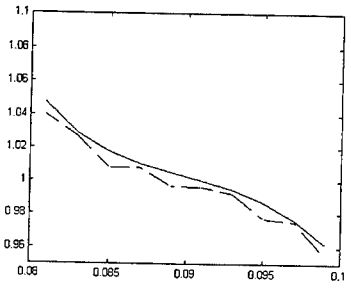

Fig. 12 - As Fig. 4 and multiple time-step technique.

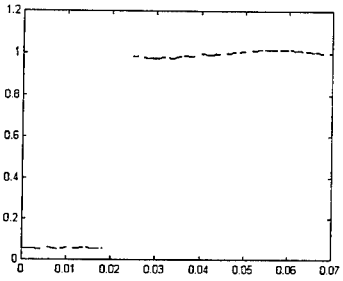

Fig. 13 - As. Fig. 5 and multiple time-step technique.

A Modified FDTD (2,4) Scheme for Modeling Electrically Large Structures With High Phase Accuracy

Mohammed F. Hadi
Kuwait University

Melinda Piket-May
Eric T. Thiele
University of Colorado at Boulder

The modified FDTD (2,4) scheme (M24 scheme) [1, 2] is a high-order FDTD scheme that exhibits extremely low phase errors in its field solutions compared to the conventional Yee scheme. Unlike other higher-order FDTD schemes proposed in the past the M24 scheme is capable of combining with the conventional Yee scheme [3] to produce a stable hybrid algorithm. This unique ability allows the M24 scheme to utilize virtually all the available FDTD tools that have been developed over the past three decades. Of particular importance, the seamless hybriding of the two schemes facilitates the successful modeling of conducting surfaces and absorbing boundary conditions. Two problems that have posed formidable obstacles to previously proposed high-order schemes.

This paper serves to validate the M24 scheme presented in [1] by using it to solve the problem of plane wave propagation through a building. The results of this experiment will demonstrate the huge savings in computer resources that can be realized by using the M24 scheme in modeling electrically large structures.

In the remainder of this paper the standard Yee scheme will be referred to as the S22 scheme, the standard (2,4) scheme as the S24 scheme and the standard (4,4) scheme as the S44 scheme [4]. The space and time steps are given by h and Δt, the resolution factor or number of FDTD cells per wavelength is given by R, and the physical and numerical wave numbers are given by γ_i and $\tilde{\gamma}_i$.

1 The Modified (2,4) FDTD Scheme

The M24 updating equations for the TM Maxwell's equations can be derived using

$$\left[\epsilon \frac{\partial E_z}{\partial t}\right]_{\text{FDTD}} = K_1 \left[\epsilon \frac{\partial E_z}{\partial t}\right]_{C_2} + K_2 \left[\epsilon \frac{\partial E_z}{\partial t}\right]_{C_3} + (1 - K_1 - K_2) \left[\epsilon \frac{\partial E_z}{\partial t}\right]_{C_1} \quad (1)$$

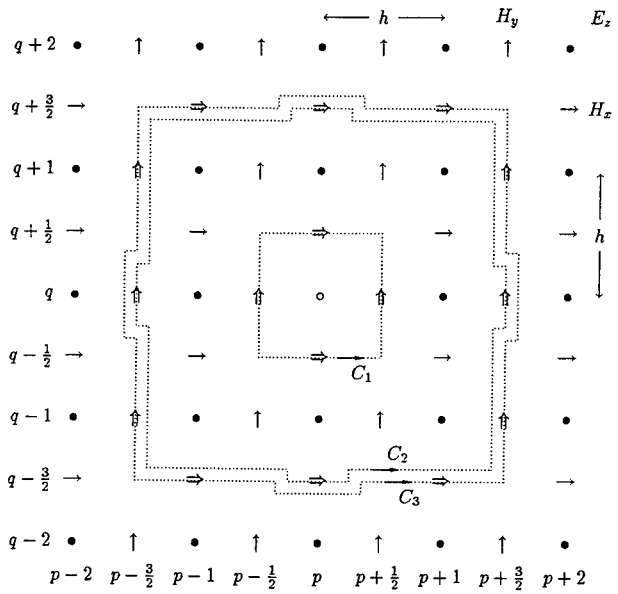

Figure 1: The three concentric loops used by the M24 Scheme

where C_1, C_2 and C_3 are the modified Ampere's loops illustrated in Figure 1:

$$\begin{aligned}
\epsilon \frac{\partial E_z}{\partial t} &= \frac{K_1}{3h}\left(H_x|_{i,j-\frac{3}{2}} - H_x|_{i,j+\frac{3}{2}} + H_y|_{i+\frac{3}{2},j} - H_y|_{i-\frac{3}{2},j}\right) \\
&\quad + \frac{K_2}{6h}\left(\begin{array}{c} H_x|_{i-1,j-\frac{3}{2}} + H_x|_{i+1,j-\frac{3}{2}} - H_x|_{i-1,j+\frac{3}{2}} - H_x|_{i+1,j+\frac{3}{2}} \\ +H_y|_{i+\frac{3}{2},j-1} + H_y|_{i+\frac{3}{2},j+1} - H_y|_{i-\frac{3}{2},j-1} - H_y|_{i-\frac{3}{2},j+1} \end{array}\right) \\
&\quad + \frac{1-K_1-K_2}{h}\left(H_x|_{i,j-\frac{1}{2}} - H_x|_{i,j+\frac{1}{2}} + H_y|_{i+\frac{1}{2},j} - H_y|_{i-\frac{1}{2},j}\right) \qquad (2) \\
-\mu \frac{\partial H_x}{\partial t} &= \frac{K_1}{3h}\left(E_z|_{i,j+\frac{3}{2}} - E_z|_{i,j-\frac{3}{2}}\right) + \frac{1-K_1}{h}\left(E_z|_{i,j+\frac{1}{2}} - E_z|_{i,j-\frac{1}{2}}\right) \qquad (3) \\
\mu \frac{\partial H_y}{\partial t} &= \frac{K_1}{3h}\left(E_z|_{i+\frac{3}{2},j} - E_z|_{i-\frac{3}{2},j}\right) + \frac{1-K_1}{h}\left(E_z|_{i+\frac{1}{2},j} - E_z|_{i-\frac{1}{2},j}\right) \qquad (4)
\end{aligned}$$

The corresponding dispersion relation and stability criterion are given by

$$\left(\frac{3h}{c\Delta t}\right)^2 \sin^2\left(\frac{\omega\Delta t}{2}\right) =$$
$$\left[K_1 \sin\left(\frac{3\tilde{\gamma}_{i,x}h}{2}\right) + 3(1-K_1)\sin\left(\frac{\tilde{\gamma}_{i,x}h}{2}\right)\right]$$
$$\left\{\sin\left(\frac{3\tilde{\gamma}_{i,x}h}{2}\right)[K_1 + K_2\cos(\tilde{\gamma}_{i,y}h)] + 3(1-K_1-K_2)\sin\left(\frac{\tilde{\gamma}_{i,x}h}{2}\right)\right\}$$
$$+\left[K_1 \sin\left(\frac{3\tilde{\gamma}_{i,y}h}{2}\right) + 3(1-K_1)\sin\left(\frac{\tilde{\gamma}_{i,y}h}{2}\right)\right]$$
$$\left\{\sin\left(\frac{3\tilde{\gamma}_{i,y}h}{2}\right)[K_1 + K_2\cos(\tilde{\gamma}_{i,x}h)] + 3(1-K_1-K_2)\sin\left(\frac{\tilde{\gamma}_{i,y}h}{2}\right)\right\} \quad (5)$$

and

$$\Delta t = \frac{3h}{c\nu\sqrt{2(3-4K_1)(3-4K_1-2K_2)}} \quad (6)$$

where $K_1 < 0$, $K_2 < \frac{3}{2} - 2K_1$ and $\nu \geq 1$.

To find the optimum values for K_1 and K_2, (5) is solved for $\tilde{\gamma}_i$ as a function of K_1 and K_2 at all propagation angles, then the results are plugged into the global dispersion error

$$\Phi_{\gamma_i} = \frac{1}{2\pi}\int_0^{2\pi}\left(\frac{\gamma_i - \tilde{\gamma}_i(\phi)}{\gamma_i}\right)^2 d\phi \quad (7)$$

where ϕ is the propagation direction. This error is in turn minimized in terms of K_1 and K_2 using an optimization routine to find their optimum values.

Figure 2 shows the minimum resolution factors needed to keep the total accumulated phase error under 5° for maximum propagation paths up to $D_{\max} = 1000\lambda_o$. This figure shows that the M24 scheme is capable of modeling structures up to $1000\lambda_o \times 1000\lambda_o$ with as little as $R = 6$ while maintaining reasonable phase accuracy. In contrast, the S22 scheme requires at least $R \simeq 200$ to achieve the same phase accuracy.

2 Plane Wave Propagation Through an Electrically Large Building Model

The one major obstacle that stands between the higher-order schemes and practical use is their inability to model material discontinuities caused by perfect conductors and absorbing boundary conditions. A straightforward approach for the M24 scheme to handle these situations is to use it in a hybrid algorithm along with the S22 scheme where the S22 cells are used as buffers between the M24 and the troublesome regions. These buffers can be as thin as one Yee cell—as long as the M24 cells do not intrude inside the conductor or the outer absorbing regions.

In this example a convergence test is performed to demonstrate the advantage of using the M24 scheme over the S22 scheme in modeling electrically large and complex structures. The

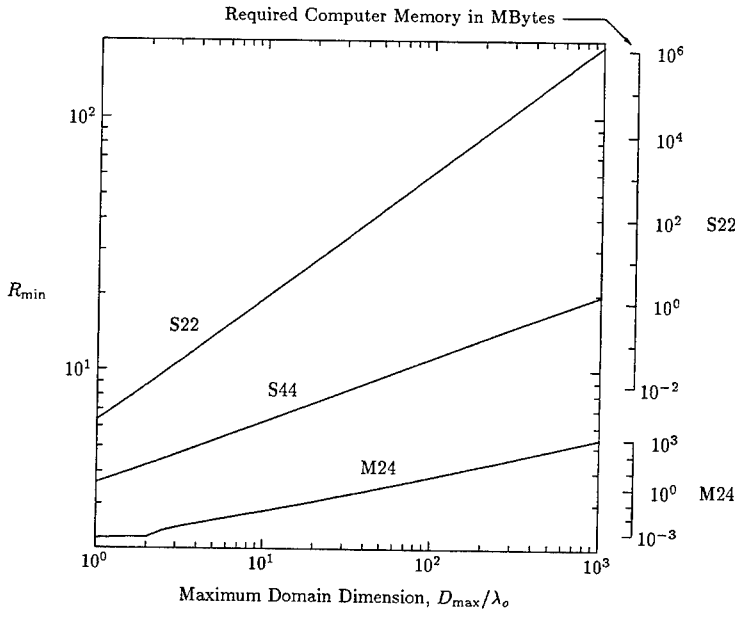

Figure 2: Minimum resolution factors and computer memory requirements for the S22, S44 and M24 schemes that will keep the total phase error under 5°. Computer memory values are based on 4 bytes per real number and square computational domains that are $D_{max} \times D_{max}$ large.

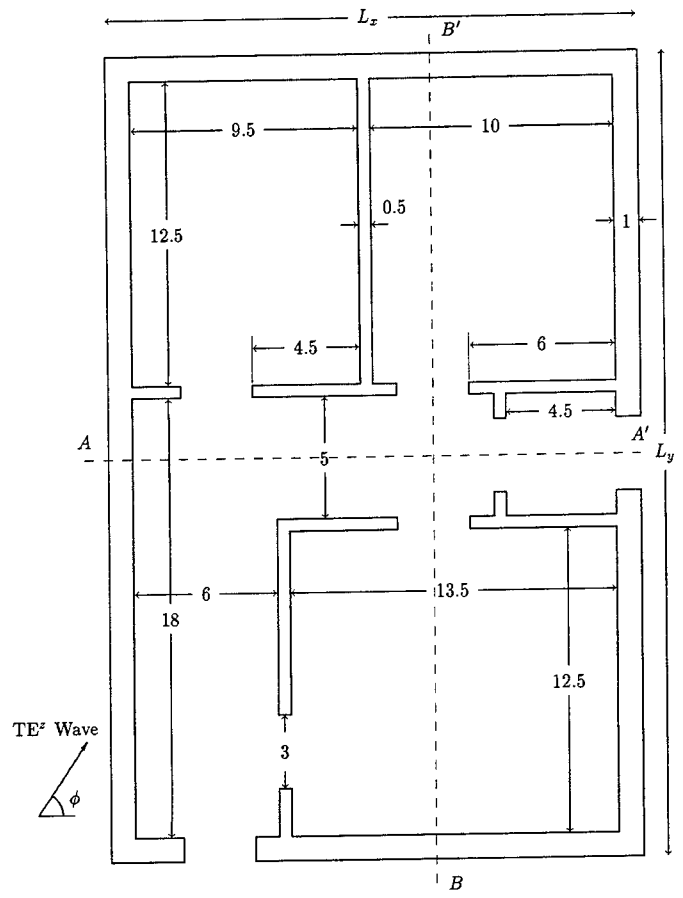

Figure 3: A small building in the path of a plane wave. Unit length is the free space wavelength at 900 MHz or 33.3 cm ($L_x = 22\lambda_o$, $L_y = 33\lambda_o$, $\epsilon_r = 2.4$, $\sigma = 0$)

Table 1: Computer costs of the different runs based on a single Cray C-90 processor

Algorithm and Resolution	Executable Size	CPU Time
S22 at $R = 100$	1.5 GBytes	5.5 hours
Hybrid M24/S22 at $R = 10$	29 MBytes	72 seconds

problem modeled is that of plane wave propagation through the simplified two-dimensional building model detailed in Figure 3. The outer dimensions of the building are $L_x = 22\lambda_o$ and $L_y = 33\lambda_o$ at $f = 900$ MHz. The walls are made of concrete with a dielectric constant $\epsilon_r = 2.4$ [5] and conductivity $\sigma \simeq 0$. Due to the relatively large size of the model, special attention must be paid when simulating the plane wave source and absorbing boundary conditions (ABCs). These special requirements are detailed in [2]. The incident plane wave is injected in the computational domain using the total field/scattered field formulation [6] and the ABCs chosen are those introduced by Berenger [7], dubbed the PMLs.

The building model was simulated using both the S22 and hybrid M24/S22 algorithms on a Cray C-90 machine. In the hybrid algorithm the S22 contribution was limited to the PMLs and a $\lambda_o/2$-thick buffer between the PMLs and the rest of the computational domain. Figure 5 shows a comparison of the collected H_z magnitudes from the two algorithms. Since an exact solution was not available, an S22 run at $R = 100$ was used as a benchmark for comparison's sake. This figure is only a sampling of the simulation results that are presented in [2].

Table 1 demonstrates the clear advantage of incorporating the M24 scheme in the building model in terms of computer costs. This table lists the computer costs of the different FDTD runs that produced Figure 5. By using the M24 scheme in the building model the required memory was reduced by a factor of 54:1 and the simulation times by a factor of 274:1 while maintaining the reliability of the field solutions to a large degree. The "executable Size" column in Table 1 includes all the initialization arrays used to construct the FDTD updating coefficients as well as double precision for all real numbers. Removing the coefficient construction process to a separate program and opting for single precision format will reduce both listed sizes by approximately 68%.

Although at $R = 10$ the hybrid M24/S22 results are much better than the S22 results, the fit between them and the reference data is not perfect. This is due to the relatively low efficiency of the M24 scheme in dealing with dielectric interfaces. In this area the M24 scheme is only as good as the S22 scheme. Once this problem is solved, the full potential of the M24 scheme would be realized and a better fit with the reference data would be possible with resolution factors as low as $R = 5$. Work is already in progress on a possible technique that, if successful, could eliminate this dielectric transition problem or at least reduce its severity.

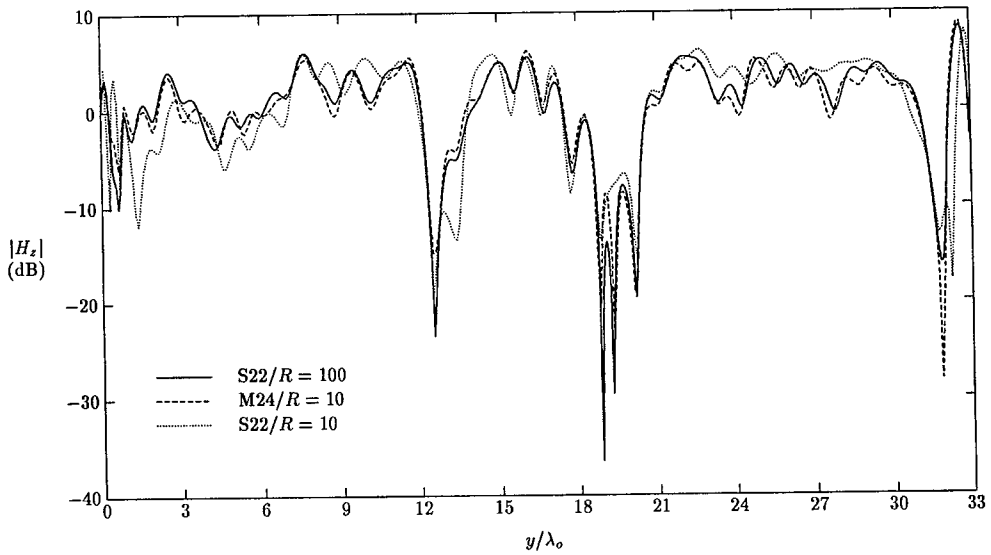

Figure 5: Comparing data from the S22 and hybrid M24/S22 algorithms along B-B' at $R = 10$ and $\phi = 0$

3 Conclusion

The FDTD method has long suffered from the excessive phase errors accumulated in its field solutions. It has been shown in [1, 2] and in this paper that the M24 scheme has effectively solved this problem. This accomplishment was made possible by incorporating two tuning parameters, (K_1, K_2), in the FDTD updating equations. When tuned properly, these parameters help reduce the phase errors in the FDTD calculations for $R \geq 5$ well below the noise floor caused by the available FDTD tools today (source conditions, ABCs, ...etc). Given the high speed computers available today, It is now possible to model structures that are thousands of wavelengths large with exceptionally low phase errors.

Work is still needed in improving the various FDTD tools for the M24 scheme to realize its full potential. While those tools are quiet adequate for the conventional FDTD scheme, they quickly show their flaws once they are used with the highly accurate M24 scheme. For example, at $R = 10$ the overall noise floor of the FDTD algorithm is a relatively high -30 dB due to the total field/scattered field source conditions. Another example is the need to enlarge the computational domain to twice the size of the relatively small $(22\lambda_o \times 33\lambda_o)$ building due to ABC limitations. At its less than optimal present state, however, the M24 scheme still represents a major step forward for the FDTD method in modeling electrically large structures.

References

[1] M. F. Hadi and M. Piket-May, "Using the Integral Forms of Maxwell's Equations to Modify and Improve the FDTD (2,4) Scheme," *11th Annual Review of Progress in Applied Computational Electromagnetics,* pp. 767–774, March, 1995.

[2] M. F. Hadi, *A Modified FDTD (2,4) Scheme for Modeling Electrically Large Stuctures with High Phase Accuracy,* Ph.D. Dissertation, ECEN Dept., University of Colorado, Boulder, CO, 1996.

[3] K. S. Yee, "Numerical Solution of Initial Boundary Value Problems Involving Maxwell's Equations in Isotropic Media," *IEEE Trans. Antennas Propagat.,* vol. 14, pp. 302–306, 1966.

[4] J. Fang, *Time Domain Finite Difference Computations for Maxwell's Equations,* Ph.D. Dissertation, EECS Dept., University of California, Berkeley, CA, 1989.

[5] A. R. Von Hippel, *Dielectric Materials and Applications,* New York, NY: John Wiley, 1954.

[6] D. E. Merewether, R. Fisher, and F. W. Smith, "On Implementing a Numeric Huygen's Source Scheme in a Finite Difference Program to Illuminate Scattering Bodies," *IEEE Trans. Nuclear Science,* vol. 27, pp. 1829–1833, 1980.

[7] J-P. Berenger, "A Perfectly Matched Layer for the Absorption of Electromagnetic Waves," *J. Computat. Phys.,* vol. 114, pp. 185–200, 1994.

Application of the FDTD Method to Three-Dimensional Propagation in a Magnetized Ferrite

Joseph Schuster and Raymond Luebbers
Department of Electrical Engineering
The Pennsylvania State University

Abstract. This paper extends the FDTD method to include frequency-dependent anisotropic magnetized ferrites with an arbitrary direction of the biasing magnetic field. The recursive convolution method is used to update the magnetic fields inside the ferrite. The additional storage of a maximum of three complex numbers per cell is required. This reduces to two when the biasing field is aligned with one of the coordinate axes. Both scattered and total field formulations are developed.

1. Introduction

The Finite Difference Time Domain (FDTD) method has become increasingly popular for application to a wide range of electromagnetic scattering and radiation problems. In the standard Yee FDTD algorithm [1], the constitutive parameters ϵ, μ and σ are assumed to be constant with respect to frequency for all media located in the computational space; therefore, modifications to the Yee algorithm are required to allow for modeling of propagation in dispersive media. In [2] and [3] it was demonstrated that, because of the exponential nature of the time domain susceptibility functions of Debye and Lorentz materials, the convolution relating the time domain electric field and the electric flux density can be performed efficiently using recursion. Their approach has therefore come to be known as the *recursive convolution* (RC) method.

The FDTD method was applied to propagation in dispersive, gyrotropic media in [4] and [5] using the RC method. This was done for one-dimensional propagation along the direction of the applied static magnetic field using a total field formulation. The four convolutions in the update equations require the storage of four complex numbers per cell. The RC approach was also applied in [6] to lossless ferrites for a two dimensional problem with the biasing field parallel to the z axis. This approach requires four convolutions per magnetic field component. Propagation in magnetized ferrites has also been analyzed with the FDTD method using the Maxwell curl equations and the equation of motion of the magnetization vector [7,8]. Results in these papers were also limited to situations where the biasing field was aligned with one of the coordinate axes.

In this paper an approach for including anisotropic frequency-dependent magnetized ferrites in FDTD calculations is developed with the RC approach used to include the frequency dependence of the ferrite. This formulation allows for an arbitrary direction of the biasing field and can be used in either total and scattered field forms. This approach was specifically developed to be compatible with an existing FDTD code using the Yee cell spatial discretization, but it is also compatible with other discretization schemes. Consideration is given to reduce the number of variables added to the FDTD calculation for storing the convolution history of the anisotropic ferrite. Some example results in

Section 4 illustrate the accuracy by comparisons with single-frequency calculations.

2. Susceptibility Tensor

Using the notation of [9], the permeability tensor for a fully saturated magnetized ferrite with the biasing field parallel to the z axis is

$$\tilde{\mu} = \mu_0 (\tilde{I} + \tilde{\chi}) = \mu_0 \begin{pmatrix} 1+\chi_{11} & \chi_{12} & 0 \\ \chi_{21} & 1+\chi_{22} & 0 \\ 0 & 0 & 1 \end{pmatrix}, \tag{1}$$

where

$$\chi_{11}(\omega) = \chi_{22}(\omega) = \frac{(\omega_0 + j\omega\alpha)\omega_m}{(\omega_0 + j\omega\alpha)^2 - \omega^2}, \tag{2}$$

$$\chi_{12}(\omega) = -\chi_{21}(\omega) = \frac{j\omega\omega_m}{(\omega_0 + j\omega\alpha)^2 - \omega^2}, \tag{3}$$

and $\tilde{I}$ is the identity matrix. In (2) and (3), $\omega_0 = \gamma H_0$, where H_0 is the magnitude of the static magnetic field and γ is the gyromagnetic ratio ($\gamma = 1.76 \times 10^7$ *radians*/sec ·*oersted* in cgs units); $\omega_m = \gamma 4\pi M_s$, where M_s is the saturation magnetization; and α is the damping factor.

The non-zero elements of the time domain susceptibility tensor are the inverse Fourier transforms of (2) and (3). Each of these elements is a real-valued function, but as shown in [5], the non-zero elements of the time-domain susceptibility tensor can be expressed as the real parts of the complex-valued functions

$$\hat{\chi}_{11}(t) = \hat{\chi}_{22}(t) = \frac{\omega_m}{1+\alpha^2}(\alpha - j)\exp\left[-\frac{\omega_0}{1+\alpha^2}(\alpha - j)t\right] \tag{4}$$

and

$$\hat{\chi}_{12}(t) = -\hat{\chi}_{21}(t) = \frac{\omega_m}{1+\alpha^2}(1 + j\alpha)\exp\left[-\frac{\omega_0}{1+\alpha^2}(\alpha - j)t\right], \tag{5}$$

where $t \geq 0$ and the carat "^" indicates a complex-valued quantity. Note that both (4) and (5) contain

the exponential term required by the RC method and that the exponentials are the same. For an arbitrarily directed static biasing magnetic field, the susceptibility tensor is given by

$$\tilde{\chi}' = R\tilde{\chi}R^{-1} = \begin{pmatrix} \chi'_{11} & \chi'_{12} & \chi'_{13} \\ \chi'_{21} & \chi'_{22} & \chi'_{23} \\ \chi'_{31} & \chi'_{32} & \chi'_{33} \end{pmatrix} \tag{6}$$

where R is the operator for the rotation from the unprimed reference frame in which $\boldsymbol{H}_0 = H_0\hat{\boldsymbol{z}}$, to the primed reference frame where $\boldsymbol{H}'_0 = H_0\sin\theta\cos\phi\,\hat{x}' + H_0\sin\theta\sin\phi\,\hat{y}' + H_0\cos\theta\,\hat{z}'$.

3. FDTD Formulation for Magnetized Ferrite

In the frequency domain $\boldsymbol{B}(\omega) = \tilde{\mu}(\omega)\boldsymbol{H}(\omega)$, but in the time domain the components of $\boldsymbol{H}(t)$ and $\boldsymbol{B}(t)$ are related by the convolution

$$B_i(t) = \mu_0 H_i(t) + \mu_0 \int_0^t \chi'_{ij}(\tau) H_j(t-\tau)\,d\tau\,, \tag{7}$$

where the subscript indices denote Cartesian vector components and the convention of an implied summation over all repeated indices is understood. All fields are in the primed frame, but for simplicity the primes have been dropped. In terms of the temporally discretized fields $B_i(t)$ at $t = n\Delta t$ is given by

$$B_i^n = \mu_0 H_i^n + \mu_0 \sum_{m=0}^{n-1} H_j^{n-m} \int_{m\Delta t}^{(m+1)\Delta t} \chi'_{ij}(\tau)\,d\tau \tag{8}$$

and $B_i(t)$ at $t = (n+1)\Delta t$ is given by

$$B_i^{n+1} = \mu_0 H_i^{n+1} + \mu_0 \sum_{m=0}^{n} H_j^{n-m+1} \int_{m\Delta t}^{(m+1)\Delta t} \chi'_{ij}(\tau)\,d\tau \tag{9}$$

Subtracting (8) from (9) and using the finite difference approximation $\dfrac{B_i^{n+1} - B_i^n}{\Delta t} = (\nabla \times \boldsymbol{E})_i$ for the Maxwell-Faraday curl equation gives

$$-\Delta t(\nabla \times \boldsymbol{E})_i = \mu_0\left(\delta_{ij} + (\chi'_0)_{ij}\right)H_j^{n+1} - \mu_0 H_i^n + \mu_0 \sum_{m=0}^{n-1} (\Delta\chi'_m)_{ij} H_j^{n-m}\,, \tag{10}$$

where

$$\tilde{\chi}'_m = \int_{m\Delta t}^{(m-1)\Delta t} \tilde{\chi}(\tau)\, d\tau, \quad \Delta\tilde{\chi}'_m = \tilde{\chi}'_m - \tilde{\chi}'_{m-1} \tag{11}$$

and δ_{ij} is the symbol for the Kronecker delta defined by $\delta_{ij} = 1$ *for* $i=j$, and $\delta_{ij} = 0$ *for* $i \neq j$.

The elements of $\tilde{\chi}'_m$ can be easily calculated by first evaluating (11) using the susceptibility tensor in (4) and (5) for the H_0-$H_0\hat{z}$ reference frame, and then applying the transformation of (6). In the unprimed frame the non-zero elements of $\tilde{\chi}_0$ given in [5] are

$$(\chi_0)_{11} = (\chi_0)_{22} = \frac{\omega_m}{\omega_0} Re\left\{1 - \exp\left[-\frac{\omega_0}{1+\alpha^2}(\alpha - j)\Delta t\right]\right\} \tag{12}$$

and

$$(\chi_0)_{12} = -(\chi_0)_{21} = \frac{\omega_m}{\omega_0} Re\left\{j\left(1 - \exp\left[-\frac{\omega_0}{1+\alpha^2}(\alpha - j)\Delta t\right]\right)\right\} \tag{13}$$

When the complex-valued expressions in (4) and (5) are used in evaluating (11), it can be shown that

$$\Delta\hat{\chi}_{m-1} = \Delta\hat{\chi}_m \exp\left[-\frac{\omega_0}{1+\alpha^2}(\alpha - j)\Delta t\right], \tag{14}$$

where (14) holds in the primed frame as well. Evaluating $\Delta\hat{\chi}_0$ in the unprimed frame gives

$$(\Delta\hat{\chi}_0)_{11} = (\Delta\hat{\chi}_0)_{22} = \frac{\omega_m}{\omega_0}\left[1 - \exp\left(-\frac{\omega_0}{1+\alpha^2}(\alpha - j)\Delta t\right)\right]^2 \tag{15}$$

and

$$(\Delta\hat{\chi}_0)_{12} = -(\Delta\hat{\chi}_0)_{21} = -j\frac{\omega_m}{\omega_0}\left[1 - \exp\left(-\frac{\omega_0}{1+\alpha^2}(\alpha - j)\Delta t\right)\right]^2 \tag{16}$$

The summation in (10) represents the convolution of $\tilde{\chi}(\tau)$ with the magnetic field up to time step n, and can be written as the real part of the complex vector

$$\hat{\Psi}_i^n = \sum_{m=0}^{n-1} (\Delta \hat{\chi}_m)_{ij} H_j^{n-m}, \tag{17}$$

where on the Yee grid [1] the components of $\hat{\Psi}$ are co-located with the corresponding components of $\boldsymbol{H}$. Equation (10) can then be written as

$$\left(\delta_{ij} + (\chi_0')_{ij}\right) H_j^{n+1} = H_i^n + Re\{\hat{\Psi}_i^n\} - \frac{\Delta t}{\mu_0}\left(\nabla \times \boldsymbol{E}^{n+1/2}\right)_i . \tag{18}$$

Equation (18) represents a set of three linear equations which can be solved simultaneously, yielding the finite difference equation

$$H_i^{n+1} = \xi_{ij}' \left\{ H_j^n + Re\{\hat{\Psi}_j^n\} - \frac{\Delta t}{\mu_0}\left(\nabla \times \boldsymbol{E}^{n+1/2}\right)_j \right\} \tag{19}$$

for H_i^{n+1}, where $\tilde{\xi}' = \left(\tilde{I} + \tilde{\chi}_0'\right)^{-1}$. Because of the relation in (14) between $\Delta\hat{\chi}_m'$ and $\Delta\hat{\chi}_{m-1}'$, the components of $\hat{\Psi}$ can be updated recursively at each time step using

$$\hat{\Psi}_i^n = \left(\Delta\hat{\chi}_0'\right)_{ij} H_j^n + \hat{\Psi}_i^{n-1} \exp\left(-\frac{\omega_0}{1+\alpha^2}(\alpha - j)\Delta t \right). \tag{20}$$

If the fields are spatially discretized using the three-dimensional Yee grid, then co-located components transverse to the component being updated must be obtained by averaging the four nearest neighbors. For example, in the update equation for $H_x^n(I, J+1/2, K+1/2)$, the y component of $\boldsymbol{H}^n$ in (19) and (20) would be given by

$$\begin{aligned} H_y^n = \frac{1}{4}\Big[& H_y^n(I+1/2, J, K+1/2) + H_y^n(I-1/2, J, K+1/2) + \\ & H_y^n(I+1/2, J, K-1/2) + H_y^n(I-1/2, J, K-1/2) \Big] \end{aligned} \tag{21}$$

with the analogous equations for the y components of $\hat{\Psi}$ and $\nabla \times \boldsymbol{E}$. At a ferrite - perfect conductor interface some of these fields may lie inside the conductor. Since the tangential magnetic field is discontinuous at the surface of a perfect conductor, only the tangential magnetic fields which are outside the conductor should be averaged. This also holds for the components of $\hat{\Psi}$ and $\nabla \times \boldsymbol{E}$ co-located with these fields.

The scattered field formulation follows from making the substitutions $B_i(t) = B_i^{inc}(t) + B_i^{sct}(t)$ and $H_i(t) = H_i^{inc}(t) + H_i^{sct}(t)$ in (9), and recognizing that $B_i^{inc}(t) = \mu_0 H_i^{inc}(t)$ is always satisfied. Equation (9) then becomes

$$B_i^{sct}(t) = \mu_0 H_i^{sct}(t) + \mu_0 \int_0^t \chi'_{ij}(\tau) \left(H_j^{inc}(t-\tau) + H_j^{sct}(t-\tau) \right) d\tau , \qquad (22)$$

where $H_i^{inc}(t)$ is an analytically specified incident field. The relative simplicity of this equation is due in part to $\chi'_{ij}(\tau)$ being zero in free space. To convert the integral in (22) to a summation as in (10), the incident field will also be considered to be piecewise constant over each time step. With this approximation the finite difference equation for $H_i^{sct,n-1}(t)$ is found to be

$$H_i^{sct,n-1} = \xi'_{ij} \left\{ H_j^{sct,n} + Re\{\hat{\Psi}_j^n\} - \frac{\Delta t}{\mu_0} (\nabla \times E^{n-1/2})_j \right\} + \zeta'_{ij} H_j^{inc}((n-1)\Delta t), \qquad (23)$$

where $\tilde{\xi}$ is given above and $\tilde{\zeta} = \tilde{\xi}\tilde{\chi}'_0$. The scattered field complex accumulator $\hat{\Psi}$ is updated recursively at each time step using

$$\hat{\Psi}_i^n = \left(\Delta\chi'_0 \right)_{ij} \left\{ H_j^{sct,n} + H_j^{inc}(n\Delta t) \right\} + \hat{\Psi}_i^{n-1} \exp\left(-\frac{\omega_0}{1+\alpha^2} (\alpha - j)\Delta t \right). \qquad (24)$$

For both the total and scattered field formulations, the additional memory requirements are the three components of a complex accumulator $\hat{\Psi}$. This reduces to two when the static magnetic is parallel to one of the coordinate axes. Thus with this formulation there is only one accumulator for each magnetic field component despite the anisotropic nature of the ferrite material and arbitrary orientation of the static biasing magnetic field.

4. Results Obtained for Anisotropic Dispersive Magnetized Ferrites

The accuracy of the above formulation will be demonstrated by calculating scattering from an anisotropic frequency-dependent ferrite sphere with a uniform internal static biasing field. Comparisons will be made with a frequency-independent FDTD code, and by changing the direction of the static magnetic field so as to change the anisotropic susceptibility tensor.

Fig. 1 shows the frequency dependence of the real and imaginary parts of the diagonal and off-diagonal elements of the ferrite permeability tensor with $\omega_0 = 2\pi \times 20\,GHz$, $\omega_m = 2\pi \times 10\,GHz$, $\alpha = 0.1$ and the static magnetic field is in the z direction. In Fig. 2 the co-polarized and cross-polarized backscatter from a magnetized ferrite sphere composed of this material with a permittivity of ϵ_0 was calculated using (23) and (24), and compared to results from an FDTD code for magnetized ferrites that does not include the frequency dependence of the ferrite constant constitutive parameters [10,11]. The calculation parameters for both FDTD calculations are: cubical 0.75 mm cells, sphere radius 1.5 cm, 2000 time steps (although the single-frequency code converged in about 1000 time steps), Gaussian pulsed plane wave incidence. For the single frequency FDTD code the time step was at the Courant limit. For the dispersive code the time step was reduced to 1/2 of the Courant limit time step in order to maintain stability. For the single frequency results the constitutive parameters of the ferrite were

changed for each frequency. The dispersive results were obtained from a single FDTD calculation using (23) and application of fast Fourier transformation to the transient backscattered fields. For both calculations the internal biasing field is assumed to be uniform inside the sphere and parallel to the z-axis. It is clear that the FDTD calculations based on (23) agree very well with results obtained using the single frequency FDTD code.

To demonstrate that the frequency dependence of the ferrite material is significant, Fig. 3 shows the cross-polarized backscatter vs frequency calculated using constant constitutive parameters evaluated at 2.25 GHz and 9.75 GHz. For these calculations the transient backscatter was calculated using the FDTD code that does not include the frequency-dependence of the magnetized ferrite. The results differ greatly from those in Fig. 2 and it is clear that the frequency dependence of the magnetized ferrite is important in determining results over a wide frequency band, and that a single-frequency approximation to the constitutive parameters is not useful for transient calculations.

The cross-polarized backscatter is relatively large due to the Faraday rotation of the polarization within the sphere. Fig. 4 shows the variation in this component of the backscatter for different incident plane wave directions (θ_{inc} and ϕ_{inc}) and polarizations (p_θ and p_ϕ) with the applied magnetic field along the z-axis. Calculations are made with the frequency-dependent FDTD code described in this paper. As expected this component of the backscatter decreases as the angle between the incidence direction and the static magnetic field increases, although incident field polarization and shape of the scatterer also play a part.

In Fig. 5 incident plane wave direction and polarization are changed in the same was as in Fig. 4. However the direction of the biasing magnetic field inside the sphere is changed so as to keep the same relative orientation with respect to the incident field as in Fig. 2. Since the spherical geometry is invariant under rotations the results should be the same. The agreement between these curves for the cross-polarized backscatter indicates the accuracy of the results produced by the formulation in this paper when the anisotropic tensor is modified as the biasing field is changed.

References

1. Yee, K. S. "Numerical solution of initial boundary value problems involving Maxwell's equations in isotropic media," *IEEE Trans. Antennas Propagat.*, vol. AP-14, pp. 302-307, May 1966.
2. R. J. Luebbers and F. P. Hunsberger, "FDTD for *N*th-order dispersive media," *IEEE Trans. Antennas Propagat.*, vol. AP-40, pp. 1297-1301, November 1992.
3. R. J. Luebbers, F. P. Hunsberger, K. S. Kunz, R. B. Standler and M. Schneider, "A frequency-dependent finite-difference time-domain formulation for dispersive materials," *IEEE Trans. Electromagn. Compat.*, vol. EMC-32, pp. 222-227, August 1990.
4. F. P. Hunsberger, R. Luebbers and K. S. Kunz, "Finite-difference time-domain analysis of Gyrotropic media - I: Magnetized plasma," *IEEE Trans. Antennas Propagat.*, vol. 40, pp. 1489-1495, Dec. 1992.
5. F. P. Hunsberger, "Extension of the Finite-difference time-domain method to gyrotropic media," Ph. D. Thesis, Pennsylvania State University, 1991.
6. C. Melon, Ph. Leveque, T. Monediere, A. Reineix and F. Jecko, "Frequency dependent Finite-Difference Time-Domain [$(FD)^2TD$] formulation applied to ferrite material," *Microwave Opt. Technol. Lett.*, vol. 7, no. 12, pp. 577-579, Aug. 1994.
7. A. Reineix, T. Monediere and F. Jecko, "Ferrite analysis using the finite-difference time-domain (FDTD) method," *Microwave Opt. Technol. Lett.*, vol. 5, no. 13, pp. 685-686, Dec. 1992.

8. J. A. Pereda, L. A. Vielva, M. A. Solano, A. Vegas, and A. Prieto, "FDTD analysis of magnetized ferrites: application to the calculation of ferrite-loaded waveguides," *IEEE Trans. Microwave Theory Tech.*, vol. 43, pp. 350-357, Feb. 1995.
9. D. M. Pozar, Microwave Engineering, Reading, Mass: Addison-Wesley, 1990, ch. 10.
10. J. Schneider and S. Hudson, "The Finite-Difference Time-Domain method applied to anisotropic materials," *IEEE Trans. Antennas Propagat.*, vol. AP-41, pp. 994-999, 1993.
11. J. Schuster and R. Luebbers, "Application of FDTD to anisotropic materials," *IEEE AP-S International Symposium Digest* Vol 3., pp 1422-1425, June 1994.

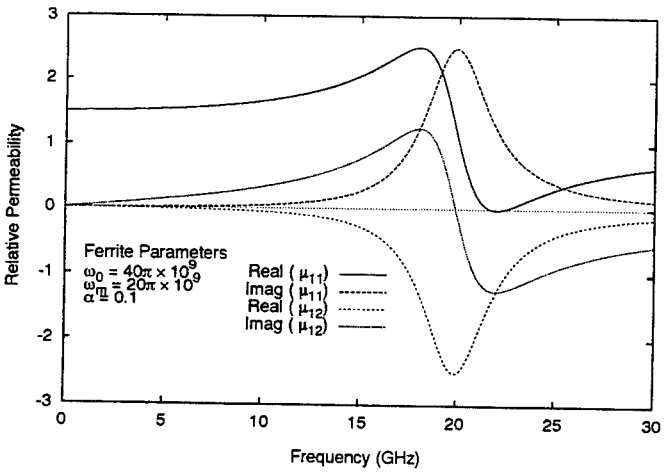

Figure 1: Relative complex permeability *vs.* frequency for a magnetized ferrite with the static magnetic field parallel to the z axis.

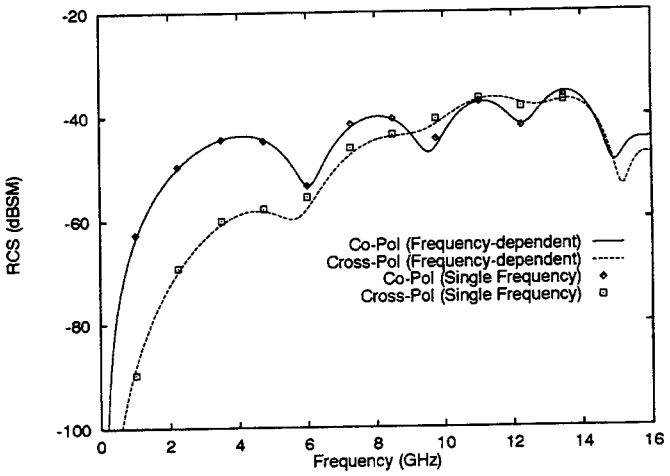

Figure 2: Backscatter *vs.* frequency for an anisotropic magnetized ferrite sphere calculated using the frequency-dependent FDTD formulation of this paper compared at specific frequencies with results from previous FDTD formulations valid at a single frequency.

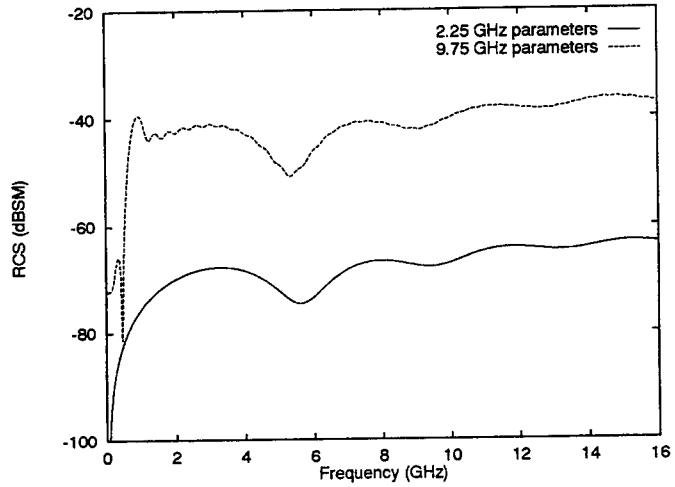

Figure 3: Cross-polarized backscatter *vs.* frequency for anisotropic magnetized ferrite sphere calculated using single frequency FDTD code with parameters of 2.25 and 9.75 GHz. Comparison with Fig. 2 shows effect of frequency dependence on scattering results.

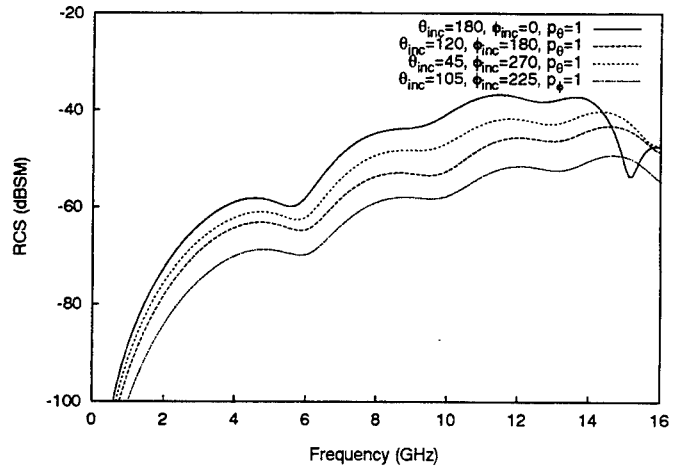

Figure 4: Cross-polarized backscatter *vs.* frequency for anisotropic magnetized ferrite sphere for different pulsed plane wave incidence angles and polarizations with the static magnetic field aligned with the z axis.

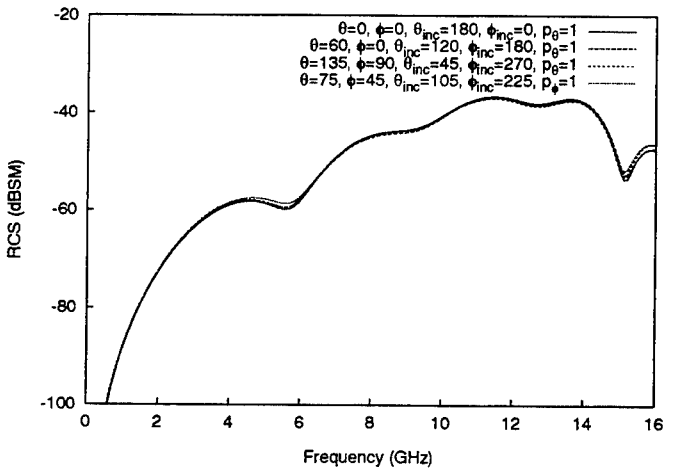

Figure 5: Cross-polarized backscatter *vs.* frequency for anisotropic magnetized ferrite sphere for different pulsed plane wave incidence angles and polarizations with the static magnetic field alignment rotated along with the incidence angle

Symmetry-Aided FDTD Analysis of Finite Phased Arrays

David Crouch
Advanced Electromagnetic Technologies Center
Hughes Electronics Corporation
Rancho Cucamonga, CA 91729

Abstract

Reductions of the memory and run-time required for finite-difference time-domain (FDTD) analysis of finite phased array are realized through the use of symmetry for arrays having one or more planes of symmetry. The principle of linear superposition is used to calculate the fields radiated by the array for an excitation having an arbitrary amplitude and phase or time-delay distribution from the fields radiated by the individually-excited array elements. Rather than simulating the entire array and calculating the radiation from each element in the presence of all of the other elements, however, we take advantage of the symmetry of the array in order to reduce the size of the problem. The array's symmetry planes are replaced with different combinations of electric and magnetic walls, eliminating that part of the array opposite the boundary from the computational grid. The resulting field patterns are not single-element patterns, but are nonetheless a complete set for describing the radiated fields for an arbitrary excitation of the array. Results are shown for a two-by-two array of wire dipoles and are compared with results calculated with the conventional FDTD method and with the method of moments.

1. Introduction

The finite-difference time-domain (FDTD) method is frequently applied to the analysis of individual antennas, but is seldom applied to the analysis of finite phased arrays due to large memory and run-time requirements. Using one of the largest FDTD antenna models constructed to date, Thiele and Taflove [1] studied a finite linear phased array of Vivaldi quad-elements, simulating the entire array for each set of amplitude and phase distributions. The use of superposition in the FDTD analysis of finite phase arrays was validated by Reuter [2], who calculated the near fields of an eight-element phased-array of monopoles by carrying out eight FDTD runs, each with a different element excited, and using the principle of linear superposition to calculate the near fields for an arbitrary distribution of amplitudes and phases. With or without the use of superposition, however, conventional FDTD analyses of large arrays of simple elements or even of small arrays of complex elements require large amounts of computer memory and CPU time. It is therefore of interest to explore any means of reducing the computational resources required for the FDTD analysis of finite phased arrays.

Symmetry is often used in FDTD analysis to reduce the size of the computational grid. Consider, for example, a rectangular waveguide excited in its TE_{10} mode. This particular mode is symmetric about planes bisecting both the narrow and wide dimensions of the guide, labeled AA' and BB', respectively, in Figure 1. As long as no obstructions capable of breaking the symmetry are introduced, one can replace plane AA' with a magnetic wall and plane BB' with an electric wall and directly calculate the fields in one quadrant only of the waveguide, thereby realizing a factor of four reduction in the memory and run-time requirements.

The same principle can be applied in the analysis of phased arrays possessing one or more planes of symmetry. Figure 2 illustrates a two-element array having a single plane of symmetry between the elements, labeled AA'. Notice that AA'

must be a plane of symmetry with respect to the excitation as well as with respect to the array itself. A symmetry plane will be called a plane of positive mirror symmetry if the tangential component of the electric field and the normal component of the magnetic field are continuous with zero normal derivative while the normal component of the electric field and the tangential component of the magnetic field are zero. A symmetry plane will be called a plane of negative mirror symmetry if the tangential component of the electric field and the normal component of the magnetic field are zero while the normal component of the electric field and the tangential component of the magnetic field are continuous with zero normal derivative.

If the excitations of the two elements are represented by $V_1(t)$ and $V_2(t)$, respectively, then if $V_2(t) = -V_1(t)$, AA' is a plane of negative mirror symmetry; by replacing AA' with an electric wall and simulating one half of the array only, one can calculate the fields radiated by the two-element array when the elements are oppositely excited. If the two elements are identically excited, $V_2(t) = V_1(t)$ and AA' is a plane of positive mirror symmetry; by replacing AA' with a magnetic wall and again simulating one half of the array only, one can calculate the fields radiated by the two-element array when the elements are identically excited. The fields radiated by the array when excited with an arbitrary set of amplitudes and phases can then be calculated by invoking the principle of linear superposition. By adding the fields calculated with AA' replaced with an electric wall to those calculated with AA' replaced with a magnetic wall, one obtains the single-element field pattern radiated when element 1 only is excited. Similarly, by subtracting the two field patterns, one obtains the single-element pattern radiated when element 2 only is excited. Finally, the pattern for an arbitrary excitation of the array can be calculated via superposition after applying the set of amplitudes and phases of interest to the single-element patterns. As only one half of the array need be accounted for in the computational grid, its size is reduced by a factor of two, which in turn reduces the memory and run-time requirements by the same factor.

2. Theory

Consider a two-by-two planar array of radiating elements like that shown in Figure 3. This array has two planes of symmetry, labeled AA' and BB'. If the excitations of elements 2 and 3 are such that the electric field lines in quadrants 2 and 3 are positive mirror images of those of elements 1 and 4, respectively, then the plane AA' can be replaced with a magnetic wall. If the electric field lines are negative mirror images, however, then the plane AA' can be replaced with an electric wall. The same considerations apply to plane BB'; if the excitations of elements 3 and 4 are positive mirror images of those of elements 2 and 1, respectively, then the plane can be replaced with a magnetic wall, and if they are negative images, BB' can be replaced with an electric wall.

There are then four possible combinations of boundary conditions with which the symmetry planes can be replaced. We will denote the field pattern produced by the array when both AA' and BB' are replaced with magnetic walls by $\Phi(+,+)$, since both planes AA' and BB' are planes of positive mirror symmetry. If the magnetic wall at plane BB' is then replaced with an electric wall, the electric and magnetic fields in quadrants 3 and 4 change sign relative to those in quadrants 2 and 1, respectively; we denote the resulting field pattern by $\Phi(+,-)$, since plane BB' becomes a plane of negative mirror symmetry. Replacing the magnetic wall at AA' with an electric wall changes the signs of the fields in quadrants 2 and 3, and the resulting field pattern is represented by $\Phi(-,-)$. Finally, replacing the electric wall at BB' with a magnetic wall again changes the signs of the fields in quadrants 3 and 4, producing the field pattern $\Phi(-,+)$. The combinations of electric and magnetic wall boundary conditions and the resulting field patterns are illustrated in Fig. 4 and summarized in Table 1.

AA' Boundary Condition	BB' Boundary Condition	Resulting Field Pattern
Magnetic Wall	Magnetic Wall	$\Phi(+,+)$
Magnetic Wall	Electric Wall	$\Phi(+,-)$
Electric Wall	Electric Wall	$\Phi(-,-)$
Electric Wall	Magnetic Wall	$\Phi(-,+)$

Table 1.

The set of excitations described above is a complete set for describing radiation from the array, just as is the single-element set obtained by simulating the entire array and exciting each element individually in the presence of all the other elements. One set can easily be obtained from the other;

$$\Phi_1 = \frac{1}{4}\left[\Phi(+,+) + \Phi(+,-) + \Phi(-,-) + \Phi(-,+)\right],$$

$$\Phi_2 = \frac{1}{4}\left[\Phi(+,+) + \Phi(+,-) - \Phi(-,-) - \Phi(-,+)\right],$$

$$\Phi_3 = \frac{1}{4}\left[-\Phi(+,+) + \Phi(+,-) - \Phi(-,-) + \Phi(-,+)\right],$$

$$\Phi_4 = \frac{1}{4}\left[-\Phi(+,+) + \Phi(+,-) + \Phi(-,-) - \Phi(-,+)\right],$$

where $\Phi_{1\text{-}4}$ are the single-element field patterns radiated when elements 1-4 are excited individually in the presence of all the other elements. Any time- or frequency-domain pattern can now be constructed using time or phase delayed versions of $\Phi_{1\text{-}4}$. In the time domain, we have

$$\Phi_{Total}(t) = A_1\Phi_1(t) + A_2\Phi_2(t-\tau_2) + A_3\Phi_3(t-\tau_3) + A_4\Phi_3(t-\tau_4),$$

where $A_{1\text{-}4}$ and $\tau_{1\text{-}4}$ are an arbitrary set of amplitudes and time delays, respectively. In the frequency domain we obtain

$$\phi_{Total}(\omega) = A_1\phi_1(\omega) + A_2\phi_2(\omega)e^{i\omega\tau_2} + A_3\phi_3(\omega)e^{i\omega\tau_3} + A_4\phi_4(\omega)e^{i\omega\tau_4},$$

where $\phi_n(\omega)$ is the Fourier transform of $\Phi_n(t)$. These same principles can be applied to the analysis of larger arrays.

3. Results

The principles described in the previous section will be demonstrated by applying them to a two-by-two array of wire dipoles. The geometry is that shown in Figure 3, with the wire elements aligned vertically, parallel to the symmetry plane AA'. Each wire element is 29.5 cm. in length and 0.005 cm. in radius; the width of the array is 20 cm, and the height measured from feed to feed is 50 cm. Electric and magnetic walls replace the symmetry planes AA' and BB' as discussed in the previous section. Because the array has front-to-back symmetry, the plane of the array is also a symmetry plane and is replaced with a magnetic wall, which in combination with the other symmetry planes reduces the size of the computational grid by a factor of eight compared to that required by conventional FDTD using the same cell size.

A uniform Cartesian grid of size 30 x 60 x 30 is used, with $\Delta x = \Delta y = \Delta z = 1.0$ cm and $\Delta t = 17.33$ ps. A thin-wire sub-cell model [3] is used to model the wire antenna. The free-space boundaries are terminated with second-order Liao boundary conditions [4]; with the above grid dimensions, the Liao boundaries are 20 and 21 cells away from the array in the horizontal and vertical directions, respectively. The array is excited with the time derivative of a Gaussian pulse;

$$V(t) = -\sqrt{2e}\,\frac{t-5t_p}{t_p}\exp\left[-\left(t-5t_p\right)^2/t_p^2\right],$$

where $t_p = 150$ ps and the pulse is normalized to 1 volt at its peak.

Four FDTD runs were carried out to calculate the symmetric field patterns $\Phi(+,+)$, $\Phi(+,-)$, $\Phi(-,+)$, and $\Phi(-,-)$; for each run, a frequency-domain near-to-far field transformation was performed to calculate the E- and H-plane gain at 0.5, 1.0, and 1.5 GHz. The results were then compared to those calculated using the method-of-moments (MoM) code NEC-2 [5]. Due to the fact that the FDTD thin-wire approximation does not accurately calculate the fields near the end of a thin wire, the physical end of a wire was assumed to lie beyond the last cell in which the thin-wire approximation was used [6]. Excellent agreement between the two calculations was obtained when that length was taken to be 3/4 of a cell, which is used in the results presented below. The single-element field pattern obtained by exciting element 1 only, Φ_1, was then synthesized through linear superposition of the four symmetric field patterns. The results are shown in Figures 4, 5, and 6 at 0.5, 1.0, and 1.5 GHz, respectively. One sees that there is excellent agreement between the FDTD- and MoM-calculated field patterns.

In order to validate the use of symmetry and to gauge the memory and run-time savings, the array was also simulated using a conventional FDTD code that uses symmetry only in the plane of the array. In order to maintain the same grid resolution as the symmetry-based code, the grid was expanded to 60 x 120 x 30. The results were nearly identical for the two calculations; the real and imaginary parts of E_θ in the far field agree to three or four decimal places. Both sets of calculations were carried out on a PC equipped with a 90 MHz Pentium CPU and 56 megabytes of memory. The conventional FDTD code requires 28.4 megabytes of memory and 12310 seconds of CPU time for a single run, while the symmetry-based code requires only 6.9 megabytes and 2957 seconds of CPU time for a single run. In either case, four FDTD runs are required to calculate all four single-element field patterns, to which any desired set of amplitudes and phases can be applied; without symmetry, 49240 seconds of CPU are required for such a calculation, while only 11828 seconds are required when symmetry is used, yielding a memory and run-time ratio of 4:1, as expected.

4. Conclusions

The computational resources - memory and CPU time - required for FDTD simulations of finite phased arrays can be reduced if the array of interest possesses one or more planes of symmetry. Each plane of symmetry can be replaced by an electric or a magnetic wall, eliminating that part of the structure on the opposite side of the wall from the computational grid and reducing the memory and run-time requirements by a factor of two. For a planar array having two planes of symmetry, a factor of four reduction in memory and run-time requirements is obtained. This technique can also be applied to three-dimensional arrays having one or more planes of symmetry. The FDTD analysis of a three-dimensional array having three planes of symmetry can be carried out with one-eighth the computational resources required for a conventional FDTD analysis.

5. References

[1] E. Thiele and A. Taflove,"FD-TD Analysis of Vivaldi Flared Horn Antennas and Arrays," *IEEE Trans. Antennas Propagat.*, vol. AP-42, no. 5, pp. 633-641, May 1994.

[2] C.E. Reuter, *FD-TD Modeling of the Sigma-60 Deep Hyperthermia Applicator*, Ph.D Dissertation, Northwestern University, Evanston, IL., 1994.

[3] K.S. Kunz and R.J. Luebbers, *The Finite Difference Time Domain Method for Electromagnetics*. Boca Raton, FL: CRC Press, 1993.

[4] Z. P. Liao, H. L. Wong, B. -P. Yang, and Y. -F. Yuan, "A transmitting boundary for transient wave analysis," Sci. Sin., Ser. A, vol. 27, no. 10, pp. 1063-1076, 1984.

[5] G.J. Burke and A.J. Poggio, "Numerical Electromagnetics Code (NEC) - Method of Moments," NOSC Tech. Document 116, vol. 2, 1981.

[6] J.J. Boonzaaier, *The Electromagnetic Radiation and Scattering by Thin Wires - A Finite-Difference Time-Domain Approach*, Ph.D. Dissertation, University of Pretoria, Pretoria, South Africa, 1994.

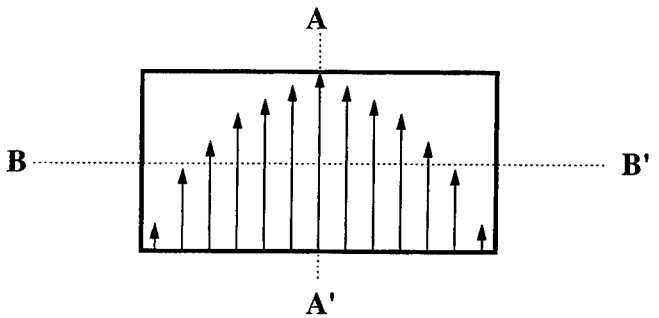

Figure 1. Illustration of use of symmetry in the calculation of fields within a waveguide excited in the TE_{10} mode. The vertical symmetry plane AA' can be replaced by a magnetic wall, and the horizontal symmetry plane BB' can be replaced by an electric wall.

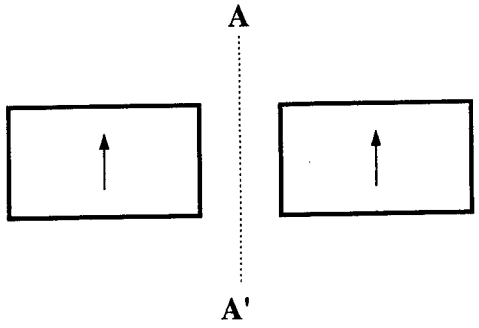

Figure 2. Symmetry plane of a two-element phased-array antenna. If the two elements are symmetric about AA' and are either identically or oppositely excited, the plane AA' can be replaced by a magnetic or an electric wall, respectively.

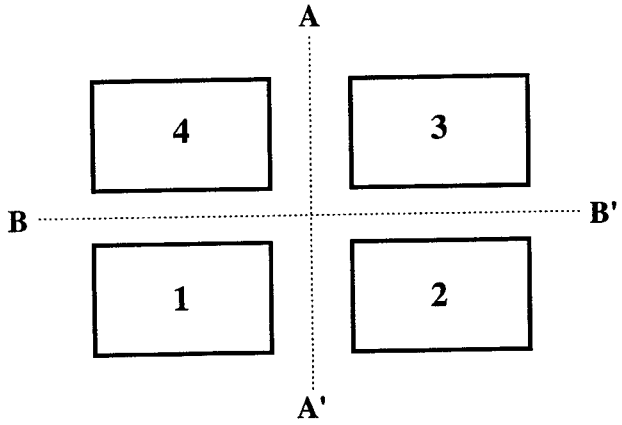

Figure 3. Symmetry planes of a 2x2 phased array. If the array elements themselves are symmetric with respect to the planes AA' and BB', then the symmetry planes can be replaced by one of four possible combinations of electric and magnetic walls, depending on the excitations of the individual elements. For example, if all elements are excited in phase, the AA' can be replaced by a magnetic wall, and BB' by an electric wall.

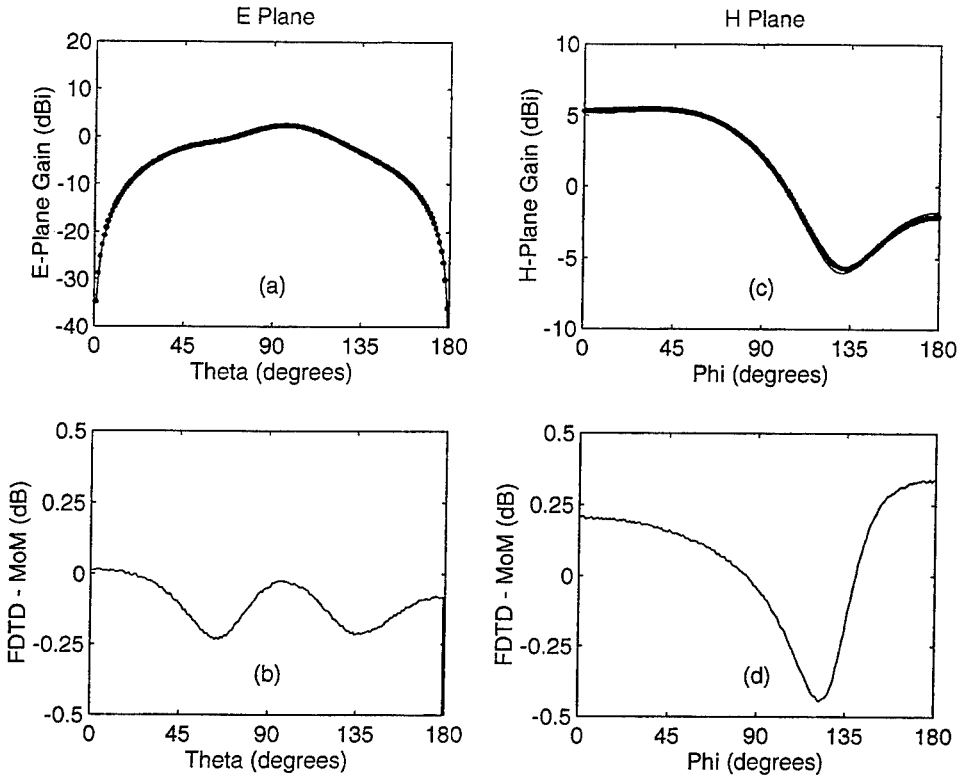

Figure 4. E- and H-plane gain patterns for 2x2 phased array at 0.5 GHz obtained by linear superposition of the symmetric field patterns. At this frequency, the 1 cm. cell size corresponds to a resolution of 60 cells/wavelength. The solid lines in (a) and (b) are the results of a symmetry-aided FDTD calculation, and the dotted lines are the method-of-moments results (NEC-2). (a) E-Plane gain. (b) Difference between symmetry-aided FDTD and method-of-moments calculations for E-Plane gain. (c) H-Plane gain. (d) Difference between symmetry-aided FDTD and MoM calculations for H-Plane gain.

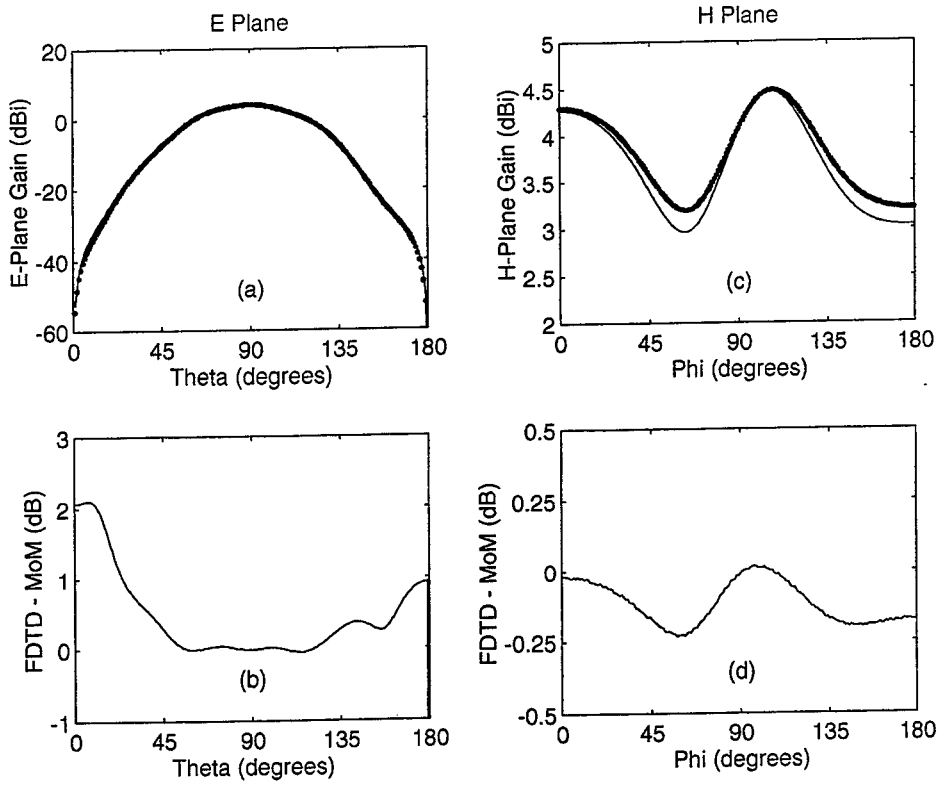

Figure 5. E- and H-plane gain patterns for 2x2 phased array at 1.0 GHz obtained by linear superposition of the symmetric field patterns. At this frequency, the 1 cm. cell size corresponds to a resolution of 30 cells/wavelength. The solid lines in (a) and (b) are the results of a symmetry-aided FDTD calculation, and the dotted lines are the method-of-moments results (NEC-2). (a) E-Plane gain. (b) Difference between symmetry-aided FDTD and method-of-moments calculations for E-Plane gain. (c) H-Plane gain. (d) Difference between symmetry-aided FDTD and MoM calculations for H-Plane gain.

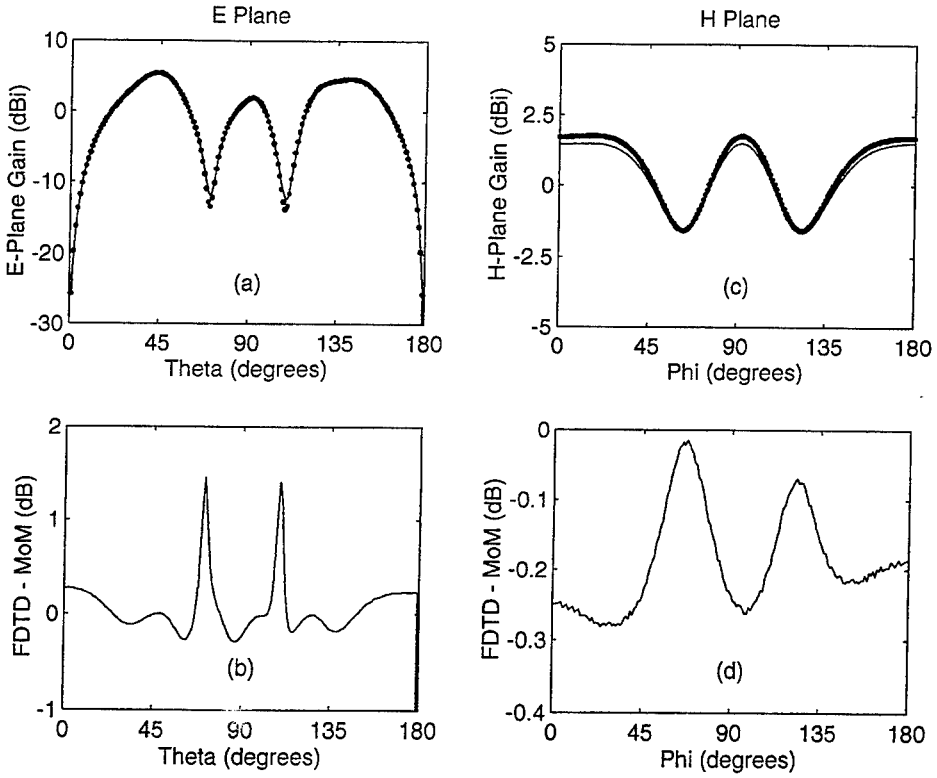

Figure 6. E- and H-plane gain patterns for 2x2 phased array at 1.5 GHz obtained by linear superposition of symmetric field patterns. At this frequency, the 1 cm. cell size corresponds to a resolution of 20 cells/wavelength. The solid lines in (a) and (b) are the results of a symmetry-aided FDTD calculation, and the dotted lines are the method-of-moments results (NEC-2). (a) E-Plane gain. (b) Difference between symmetry-aided FDTD and method-of-moments calculations for E-Plane gain. (c) H-Plane gain. (d) Difference between symmetry-aided FDTD and MoM calculations for H-Plane gain.

Conformal FVTD with a Rectangular Grid for PEC Scattering Objects

K. S. Yee and J. S. Chen
Lockheed Palo Alto Research Labortory

Abstract -- In this paper we describe a "conformal" FVTD with a rectangular grid. It is called conformal because the boundary condition on the scatterer is fully used to prescribe the boundary condition at the boundary nodes of the computational volume. The computational volume is a union of FDTD cubes and the inner boundary is no more than one FDTD cube away from the scattering surface. Numerical examples demonstrate that this new technique to approximate boundary condition is more accurate than the classical FDTD with very little extra calculations. The algorithm itself is as simple as the original FDTD.

I. INTRODUCTION

Conformal numerical computations in time domain has occupied the attention of many researchers [1-28] since the demonstration of the FDTD can be used for a wide varieties of applications. Among other difficulties, current progress in 3-D conformal calculations seems to be impeded by non availability of good quality three dimensional grids, the search of which is under intensive investigation by many researchers. For PEC boundary condition we have recently discovered a conformal technique, making use of the original stair casing grid for the FDTD. The algorithm we use is FVTD (finite volume time domain) instead of FDTD. The interpolation and extrapolation used in this paper has some similarity with the extrapolation of the FDTD electric field components used in [6, 7, 17], but our bookkeeping is much simpler. We essentially interpolate or extrapolate along the surface normal whereas the extrapolation used in [6, 7] are along the direction of the edges of the FDTD cubes.

II. THE GRID

The whole space is divided into FDTD cubes (Figure 1a). We define:

An FDTD cube is an **interior cube** if its center is inside the bounding surface of the scatterer (Figure 1b)

An FDTD cube is a **boundary cube** if it intersects the scattering surface (Figure 1c).

The union of the interior cubes and the boundary cubes form a volume and the boundary of this volume is to be the interior boundary of our computational volume (Figure 1d). The outer boundary of the computational volume can be rectangular or it does not have to be. The nodes (vertices) of the interior boundary will be **boundary nodes** (vertices) and we describe how to assign the electric vector **E** in them in the boundary condition simulation. Note that

the boundary nodes are exterior of the scattering surface and the maximum distance from the scattering surface is $\sqrt{3}\Delta x$ away from the surface.

III. THE ALGORITHM

The grid constructed in section II is used for computation. We assign the three rectangular components of the electric field at the vertices of the FDTD cubes and assign the three components of the magnetic field at the centers of the FDTD cubes. More specifically, we call the FDTD cubes **electric cubes**; and we call the cubes formed by connecting the centers of the FDTD cubes **magnetic cubes**. Thus, at the vertices of the electric cubes we assign the electric vector **E** and at the vertices of the magnetic cubes we assign the magnetic vector **H**. The electric vector and the magnetic vector are updated in time by leapfrogging. The algorithm starts with the volume surface integral form of the Maxwell's equations:

$$-\int_V \dot{\vec{B}}\,dv = \int_{\partial V} \hat{n}\times\vec{E}\,da \qquad (1a)$$

$$\int_V \dot{\vec{D}}\,dv = \int_{\partial V} \hat{n}\times\vec{H}\,da \qquad (1b)$$

The discretized equations corresponding to (1a)-(1b) are

$$\frac{1}{\Delta t}\int_V \left(\vec{B}^{n+1/2}-\vec{B}^{n-1/2}\right)dv = -\int_{\partial V} \hat{n}\times\vec{E}^{n}\,da \qquad (2a)$$

$$\frac{1}{\Delta t}\int_V \left(\vec{D}^{n+1}-\vec{D}^{n}\right)dv = \int_{\partial V} \hat{n}\times\vec{H}^{n+1/2}\,da \qquad (2b)$$

where in equation (2a) we take the volume to be an electric cube and in (2b) we take the volume to be a magnetic cube. The discretized equations (2a) and (2b) are very similar to the FDTD equations in terms of simplicity and accuracy. The difference is in the convenience of simulating "conformal" boundary condition. **With FDTD stair casing and for PEC boundary condition we assign the total electric field on the boundary edge to be zero** (Figure 2a). **For our conformal FVTD we will not assign the electric field along a boundary edge to be zero.** Instead, we make use of the scattering surface and interpolate or extrapolate for the electric vector at the boundary electric vertices (Figure 2b). More details will be given in the next section on the boundary condition simulation. In our simulation we always choose the computation volume to be a union of electric cubes. This means that the

inner boundary vertices and the outer boundary vertices are electric vertices. The magnetic vertices in our computational volume are always interior vertices.

IV. THE PEC BOUNDARY CONDITION SIMULATION

We call the inner boundary electric vertices of the computation volume to be **boundary vertices**. The assignment of the electric vector at these boundary vertices can be distinguished into three categories.

i. The boundary vertex is cloest to the smooth points of the scattering surface where two continuous surface tangential directions are given for the neighboring surface points.

ii The boundary vertex is closest to a smooth edge point where only one direction of the surface tangent is known.

iii. The boundary vertex is closest to a conical surface point where no tangential direction is known.

We will elaborate in more details as we proceed. Our rational for the following approximation is that whenever there a sharp edge, we round the edge with a small-radius cylindrical surface and whenever there a sharp tip we also round it with a small-radius spherical surface.

For a boundary vertex not on the scattering surface, we assume that our surface is such that it is closest to a smooth surface point, an edge point, or a conical point. If this condition is not met, other approximation will have to be made.

a. Approximation near a smooth surface point (Figure 3)

When a boundary vertex (node) is closest to a smooth surface point an approximate surface normal can be assigned to this boundary node (point **p**). If we approximate the surface locally by its tangent plane we can also find the "foot" of the surface normal through a boundary vertex. At the foot of the normal (point **1**)through this boundary vertex we know two components, $\mathbf{E} - \mathbf{n}(\mathbf{n} \cdot \mathbf{E})$, of the electric field. The extension of the normal through this boundary vertex will intersect an interior FDTD face (a FDTD face is an **interior face** if all the vertices of the face are interior nodes of the computational volume) At the point of intersection (point **2**) the electric vector can be interpolated. Making use of the tangential (to the scattering surface) components at this point and that at the "foot" of the normal we can interpolate for the tangential components of the electric field at this boundary node. The "normal" component can be extrapolated. This way we will have the electric field **E** at a boundary vertex approximately . The mathematical steps are:

i. The electric vector **E** at the point **2** can be interpolated from the electric vectors located at the four vertices of the face where the point **2** lies.

ii. The vector **E - n (n•E)** (tangential componenets) at the point **1** is known; and the same vector at the point 2 is now also known. The vector **E(p) - n (n•E(p))** at the point **p** can be interpolated.

iii. Extrapolate to set **n•E(p) = n•E(2).**

iv. Approximate **E(p) = [E(p) - n (n•E(p))] + n (n•E(p))**

Potential trouble in term of instability can be expected because of the interpolation and/or the extrapolation. The accuracy, while not expected to be as good as the conformal overlapping grids, is nevertheless more accurate than the stair casing FDTD where the scattering object boundary is approximated by rectilinear boundary.

b. Approximation near a smooth edge point.

If the boundary vertex is closest to a smooth boundary edge, we can connect this node with a boundary edge point. Let $\hat{n}$ be the unit vector along the line joining the boundary node and the boundary edge point and let $\hat{t}$ be the unit tangent along the boundary edge at the boundary edge point and let $\hat{u} = \hat{t} \times \hat{n}$ be another direction. We assume that the edge is rounded that now $\hat{u}$ is another surface tangential direction on the surface. For a PEC body we take the tangential components along $\hat{u}$ and $\hat{t}$ to be known and carry out the interpolation and extrapolation as in **case a.**

c. Approximation near a conical point

When the boundary vertex is closest to a conical point we connect the line between the boundary vertex and the conical point. Let $\hat{n}$ be the unit vector along this line. We assume now that the tangent plane to the surface is normal to this unit vector $\hat{n}$. The two components of the electric vector normal to $\hat{n}$ are now assigned and the interpolation and extrapolation are carried out as in **case a** again.

Alterntives to procedure **b** and **c** would be:

b' With reference to Figure 3 we now suppose that point **1** is a smooth edge point. In this case only the tangential component of the electric field along the edge is known at the point **1.** We interpolate for this component at the point **p** with data at the points **1** and **2.** For the two components orthogonal to the edge, we simply extrapolate the data from point **2** to point **p.**

c' Again with reference to Figure 3, we now suppose that point **1** is a conical point. In this case no tangential component of the electric field at the point **1** is known. We simply extrapolate the electric vector **E** from point **2** to point **p.**

V. NUMERICAL EXAMPLES

We have performed the RCS calculations (see Figures 4-7) with our method discussed in this paper for a PEC sphere, an ellipsoid of revolution, a small cone-sphere, and a flat plat triangle-circle. The incident field is a plane Gaussian linearly polarized wave. At 150 MHz the spatial discretization length, Δx, is 1/20 of the wavelength. The results show that the interpolation-extrapolation near the boundary with just the rectangular grid is not as accurate as our FDTD/FVTD conformal technique. Nevertheless, it is an improvement over the stair casing FDTD.

VII CONCLUSION

By means of interpolation and extrapolation near the boundary, we can make use of only a rectangular grid and the exact boundary condition for PEC smooth scatterers. The amount of extra calculation over the stair casing FDTD is minimal; but the accuracy is not as good as the conformal FDTD/FVTD hybrid.

REFERENCES

1. R. Holland, "Finite-difference solutions of Maxwell's equations in generalized non orthogonal coordinates", *IEEE Trans. Nuc. Sci.*, vol. NS-30, pp.4589-4591, 1983.
2. Fusco, M. A."FDTD Algorithm in Curvilinear Coordinates," *IEEE Trans. Antennas and Propagation*, vol.-38 pp. 76-89, Jan. 1991
3. Fusco, M. A., M. V. Smith, and L. W. Gordon, "A three-Dimensional FDTD Algorithm in Curvilinear Coordinates," *IEEE Trans. Antennas and Propagation*, vol-39 pp. 1463-1472, Oct.1991
4. Kane S. Yee, "Numerical Solution to Maxwell's Equations with Non-orthogonal Grids", *Proc. of 1st Review of Numerical Electromagnetic Codes*, March 19-21,1985. Also Lawrence Livermore Technical Report UCRL-93268, April 1987.
5. Weiland, T, "On the numerical solution of Maxwell's equations and applications in the field of accelerator physics. *Particle Accelerators*, 15:pp.245-292, 1984
6. Jurgens, T. G., A. Taflove, and K. R. Umashankar, and T. G. Moore, " Finite difference time domain modeling of curved surfaces," *IEEE Trans. AntennasPropagation*, vol. 40, April 1992.
7. Jurgens, T. G., and A. Taflove, " Three-Dimensional Contour FDTD Modeling of Scattering from Single and Multiple Bodies," *IEEE Tran. AntennasPropag.* vol. 41, No. 12 ,pp.1703-1708.
8. Madsen, N. K. and R. W. Ziolkowski, " Numerical solution of Maxwell's equations using irregular nonorthogonal grid," *Wave Motion*, vol.10, pp. 583-596, March 1988.
9. N. K. Madsen and R. W. Ziolkowski, " A Three-dimensional Modified Finite Volume Technique for Maxwell's Equations", *Electromagnetics*, vol. 10, nos.1-2,pp.147-161, Jan. 1990.
10. K. N. Madsen, "Divergence Preserving Discrete Surface Integral Methods for Maxwell's Curl Equations Using Non-Orthogonal Unstructured Grids", Lawrence Livermore National Laboratory UCRL JC-109787, Feb. 1992.

11. Kane S. Yee, J. S. Chen, and A. H. Chang, "Conformal Finite Difference Time Domain (FDTD) with Overlapping Grids", *IEEE Trans on Ant. and Propagation*, vol. 40, No. 9, pp.1068-1075, Sept., 1992.
12. Kane S. Yee and J. S. Chen, "Conformal Hybrid Finite Difference Time Domain and Finite Volume Time Domain ", *IEEE. Trans. Antennas Propag.* vol. 42. No. 10, Oct. 1994.
13. Chen, J. S., J. V. Prodan, and K. S. Yee "An FDTD/FVTD 2D-algorithm to solve Maxwell's equations, " *ACES 1995 Conference Proceeding*.
14. Riley, D. and C. D. Turner, "Finite-Volume Hybrid-Grid (FVHG) Techique for the Solution of the Transin: Maxwell's Equations," *ACES Newsletter*, July 1994.
15. Liu, Y., "Fourier Analysis of Numerical Algorithms for the Maxwell Equations," Proc. of the 31st Aerospace Sciences Meeting and Exhibit, AIAA-94-0233, January 11-14 1994 / Reno , NV.
16 Liu, Y., " A Generalized Finite-Volume Algorithm for Solving the Maxwell Equations on Arbitrary Grids," *Conference Proceeding vol. I, 10th Annual Review of Progress in Applied Computational Electromagnetics*, March21-26, 1994.
17 Fang, Jiayuan and Jishi Ren, "A Locally Conformal Finite-Difference Time-Domain Algorithm of Modeling Arbitrary Shape Planar Metal Strips," *IEEE Transactions on Microwave Theory and Techniques*, Vol. 41, No. 5, May 1993.
18. Chan, C. H., H. Sangani, K. S. Yee, and J. T. Elson, "A Finite-Difference Time-Domain Method Using Whitney Elements, " *Microwave and Optical Technology Letters*, Vol. 7, No. 14, Oct. 1994 pp. 673-676.
19. Cangellaris, A. C.,. C. C. Lin, and K. K. Mei, "Point -matched time domain finite-element methods ", presented at Nat. Radio Sci. Meeting at Boston, MA, June 1984.
20. Cangellaris, A. C.,. C. C. Lin, and K. K. Mei, "Point -Matched Time Domain Finite-Element Methods for Electromagnetic Radiation and Scattering " *IEEE Trans, Antennas Propagation*, Vol. AP-35, pp. 1160-1173, Oct. 1987.
21. Mur, G. and A. T. de Hoop, " A finite element method for computing three-dimensional electromagnetic fields in inhomogeneous media," *IEEE Trans. on Magnetics*, vol. MAG-21, pp.2188-2191, November 1985.
22. Mur, G. "A mixed finite element method for computing three-dimensional time-domain electromagnetic fields in strongly inhomogeneous media," IEEE Trans. on magnetics, vol. 26, no. 2 March 1990.
23. Mur, G. , "The finite-element modeling of three-dimensional time-domain electromagnetic fields in strongly inhomogeneous media," *IEEE Trans. on magnetics*, vol. 28, no. 2 March 1992.
24. Lee, J. F. , "Solving Maxwell's equations by finite element time domain methods," to be submitted.
25. K. Mahadevan, R. Mittra and P. M. Vaidya, "Use of Whitney's edge and face elements for efficient finite element time domain solution of Maxwell's equations," *Journal of Electromagnetic Waves and Applications*, vol. 8, no. 9/10, pp. 1173-1191, September 1994.
26. K. Mahadevan and R. Mittra, "Radar cross section computation of inhomogeneous scatterers using edge-based finite element method in frequency and time domains," *Radio Science*, vol. 28, no. 6, pp. 1181-1193, November-December 1993.
27. Shankar, V., M. V. Mohammadian, and W. F. Hall, "A time-domain differential solver for electromagnetic scattering problems," *IEEE Proc.*, vol. 77, pp.709-721, May 1989.
28. Shankar, V., M. V. Mohammadian, and W. F. Hall, "A time-domain finite-volume treatment for the Maxwell's equations," *electromagnetics.*, vol. 10, pp.127-145, Jan. 1990.

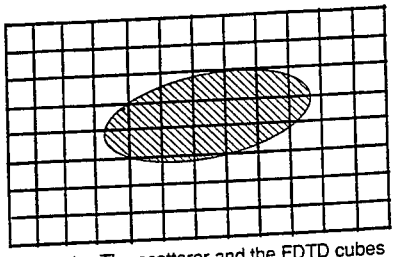

Figure 1a The scatterer and the FDTD cubes

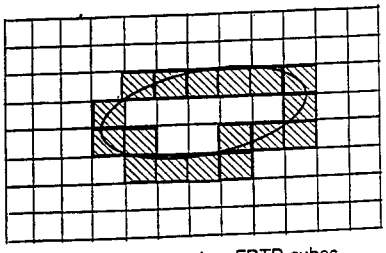

Figure 1c The boundary FDTD cubes

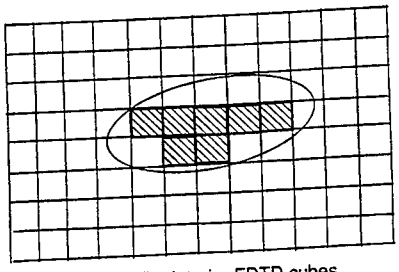

Figure 1b The interior FDTD cubes

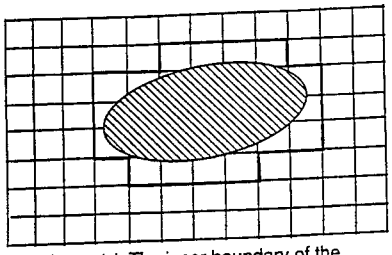

Figure 1d The inner boundary of the computational volume

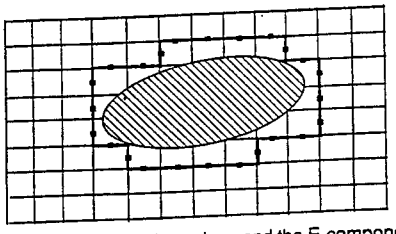

Figure 2a The inner boundary and the E-component locations of the FDTD computational volume

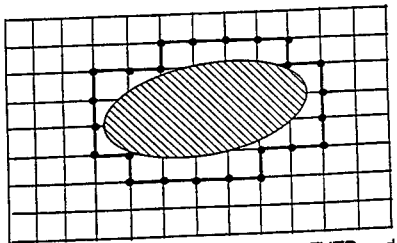

Figure 2b The inner boundary of the FVTD and its electric field **E** locations

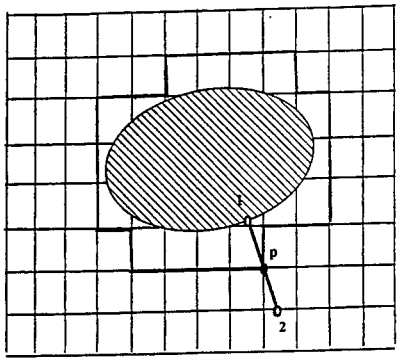

Figure 3 Interpolation for the electric vector **E** at a point p closest to a smooth surface point **1**. Point **1** is the 'foot' of the surface normal; tangential components at **p** are interpolated from data at points **1** and **2**; the normal component at **p** is obtained by extrapolation from point **2**

Fig 4 RCS from a PEC sphere , Radius= 1m

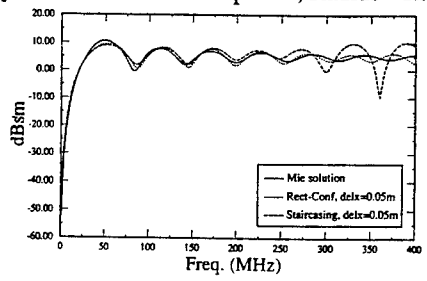

Fig. 5 RCS from a PEC Ellipsoid

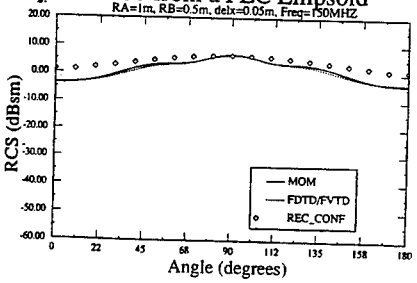

Fig. 6 RCS for Cone-Sphere

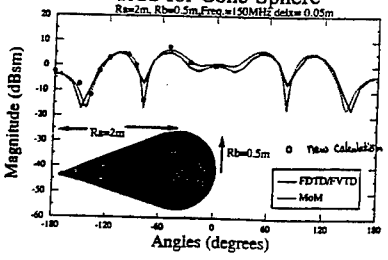

Fig. 7 RCS from EMCC target #1

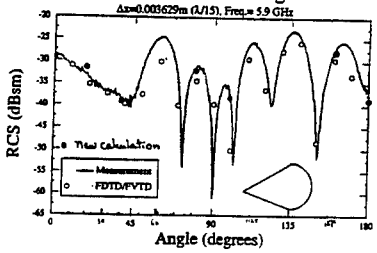

Application of Recent Advances in FDTD Modeling to the Problem of Acoustic Propagation in Shallow Water

John B. Schneider and Frank D. Hastings
School of Electrical Engineering and Computer Science
Washington State University
Pullman, WA 99164-2752, U.S.A.
schneidj@eecs.wsu.edu and fhasting@eecs.wsu.edu

Chris J. Railton
Centre for Communications Research
Faculty of Engineering
University of Bristol
Bristol, BS8 1TR, U.K.
chris@comms-research.bristol.ac.uk

1 Introduction

Over the past 30 years, the Yee finite-difference time-domain (FDTD) algorithm has been used with great success to solve a multitude of electromagnetics problems. FDTD modeling has been applied to problems ranging from dosimetry calculations to the analysis and design of circuit inter-connects. The success that the FDTD algorithm has enjoyed can be attributed both to the elegance of the original algorithm *and* to the contributions made by the numerous researchers who have enhanced the technique.

Approximately 11 years ago, Jean Virieux published two papers that outlined a staggered-grid finite-difference scheme for the study of time-domain acoustic propagation [1, 2]. Virieux's papers appeared in the acoustics literature, and, despite the fact that in certain cases his algorithm is indistinguishable from Yee's, it appears that he was unaware of the work that had already been done in the electromagnetics community. Virieux's work has served as the foundation for several subsequent publications and is often cited in the acoustics literature.

Fortunately, recent publications indicate that the acoustics and electromagnetics communities are becoming more aware of the other's problems and the "tools" available to solve them. For example, at the 1995 ACES Symposium Maloney and Cummings discussed many of the similarities between acoustic and electromagnetic FDTD modeling [3]. Furthermore, they showed how the Berenger PML ABC could be used in acoustics problems. Another example is the work by Botteldooren who cites several papers in the electromagnetics literature as part of his presentation of a "quasi-Cartesian" acoustics FDTD technique [4].

In this paper, the ultimate goal is accurate modeling of acoustic propagation in shallow water. Although this is an acoustics problem, recent advances in FDTD modeling that have been presented in the electromagnetics literature can be used to improve the accuracy and lessen the computational burden needed to solve this problem. As was shown in [3], the Berenger absorbing boundary condition (ABC) can be used without modification if the material does not support elastic waves (water is such a material). However, as shown here (Sec. 3), even when the material is elastic (such as a penetrable solid bottom), the Berenger ABC can be used in a modified form to obtain an elastic ABC that is superior to those which have been previously used.

As discussed in Sec. 4, the recently proposed modified conformal path finite-difference time-domain (CPFDTD) algorithm can also be applied to this problem. The CPFDTD algorithm attempts to eliminate staircasing errors by distorting the grid only in the vicinity of material boundaries. The modified algorithm used here differs from the original CPFDTD algorithm in the way that neighboring nodes are borrowed (a.k.a., the "nearest neighbor approximation") and, hence, does not suffer the stability problems of the original algorithm.

(This proceedings paper concentrates on presenting some of the ways in which electromagnetic FDTD modeling is applicable to acoustic modeling. Simulations of acoustic propagation in a shallow water environment will be presented at the Symposium.)

2 Governing Equations

Some similarities between FDTD implementations of Maxwell's equations and the acoustic equations are discussed in [3] and [5]. These discussions are restricted to materials, such as liquids and gases, that only support compressional waves. Compressional waves (sometimes called longitudinal, pressure, or P waves) give rise to compression or rarefaction of the material in the direction of propagation. However, in general, solids can also support shear waves (S waves) where the particle displacement is transverse to the direction of propagation. A three-dimensional (3D) "elastic" FDTD scheme can be constructed to model the propagation of both pressure and shear waves [6]. Here, for brevity, we will restrict consideration to two dimensions. In two dimensions, the fields can be separated into two independent sets that are somewhat analogous to the TE and TM cases in electromagnetics. One set, known as SH, supports the propagation of a shear wave whose orientation is perpendicular to the two-dimensional (2D) plane. The other set, known as P-SV, can support both a pressure wave and a shear wave (where the shear orientation is parallel to the 2D plane).

SH Equations

$$\begin{aligned}
\rho\frac{\partial v_y}{\partial t} &= \frac{\partial \tau_{xy}}{\partial x}+\frac{\partial \tau_{zy}}{\partial z}\\
\frac{\partial \tau_{xy}}{\partial t} &= \mu\frac{\partial v_y}{\partial x}\\
\frac{\partial \tau_{zy}}{\partial t} &= \mu\frac{\partial v_y}{\partial z}
\end{aligned}$$

P-SV Equations

$$\begin{aligned}
\rho\frac{\partial v_x}{\partial t} &= \frac{\partial \tau_{xx}}{\partial x}+\frac{\partial \tau_{xz}}{\partial z}\\
\rho\frac{\partial v_z}{\partial t} &= \frac{\partial \tau_{xz}}{\partial x}+\frac{\partial \tau_{zz}}{\partial z}\\
\frac{\partial \tau_{xx}}{\partial t} &= (\lambda+2\mu)\frac{\partial v_x}{\partial x}+\lambda\frac{\partial v_z}{\partial z}\\
\frac{\partial \tau_{zz}}{\partial t} &= \lambda\frac{\partial v_x}{\partial x}+(\lambda+2\mu)\frac{\partial v_z}{\partial z}\\
\frac{\partial \tau_{xz}}{\partial t} &= \mu\left(\frac{\partial v_x}{\partial z}+\frac{\partial v_z}{\partial x}\right)
\end{aligned}$$

Despite the potential for confusion, we have retained the usual elastic notation where λ and μ are the Lamé coefficients (these are related to the compressibility and rigidity of the material and μ is often referred to as the modulus of rigidity), ρ is the density, v is the velocity, and τ is the stress (force per unit area). Suitable unit cells for these two sets of equations are shown in Fig. 1 where the velocities and stresses are offset temporally by a half time step.

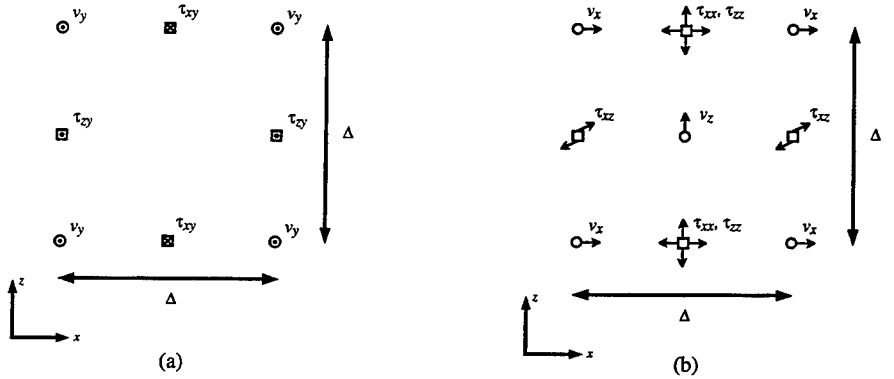

Figure 1: Unit cells showing the location of field evaluation points. (a) SH grid. (b) P-SV grid.

Even though two stress components, τ_{xx} and τ_{zz}, are spatially and temporally collocated, developing the code for these sets of equations should be straightforward for anyone experienced in writing electromagnetic FDTD code.

Furthermore, if the rigidity of a material is zero (i.e., $\mu = 0$ as is the case for liquids and gases), shear waves are not supported and the P-SV equations collapse to a form that is completely analogous to the TM case. In this case, τ_{xx} and τ_{zz} are equal and can be treated as a single scalar quantity. Thus, the stresses can be equated with the negative of the pressure which is itself analogous to the electric field. The velocities are analogous to the magnetic field (albeit with a change of sign and a change in the associated "direction" of the field, e.g., an x-directed velocity would be equated with a z-directed magnetic field).

Two boundaries that are common in acoustic modeling are hard and soft boundaries. At a hard boundary the normal component of velocity is zero, while at a soft boundary (often called a free or pressure-release boundary) the pressure is zero. A typical soft boundary is the air-sea interface as "seen" from within the water. A hard boundary is often assumed when a very rigid material abuts a fluid (for example a rocky ocean bottom would appear hard as seen from the water). A soft boundary can be treated in the same way a PEC is treated in TM electromagnetic simulations. A hard boundary can be thought of either as a perfect magnetic conductor in a TM simulation *or* as a PEC in a TE simulation (where now the magnetic field is analogous to pressure and the electric field components are analogous to the components of velocity). These facts permit borrowing of the techniques developed in the electromagnetics literature to minimize the impact of a staircase approximation to a material interface.

3 Elastic Perfectly Matched Layer ABC

Absorbing boundary conditions (ABCs) are enforced at the edges of a computational domain to absorb outgoing waves and thereby model an unbounded region. A number of ABCs have been introduced for use in FDTD modeling of elastic wave propagation (see [7] for references). However, these methods generally only perform well within restricted ranges of incident angles and frequencies. The Perfectly Matched Layer (PML) ABC [8] has been used extensively in electromagnetic FDTD modeling and has been shown to provide excellent absorption over a wide range of angles and frequencies. Although the stress-velocity equations are not suitable for direct application of this ABC, it is possible to obtain a suitable form using an approach introduced by Randall [6]. In this method, velocities are transformed to potentials that, for the 2D case, satisfy two scalar wave equations. The PML then consists of two independent overlapping grids that propagate potentials.

Figure 2 shows the geometry of a 2D, finite-difference grid with a PML. In the interior the P-SV formulation is used, while in the PML the shear and compressional waves are handled separately using potentials. The velocity-potential conversions take place in a one grid-cell wide overlap region. Square grid cells of area Δ^2 are assumed. Velocity is related to potential by [6]

$$\vec{v} = (\frac{\partial \Phi}{\partial x} - \frac{\partial \Psi}{\partial z})\hat{x} + (\frac{\partial \Phi}{\partial z} + \frac{\partial \Psi}{\partial x})\hat{z} \tag{1}$$

where Φ is the compressional potential and Ψ is the y-component of the shear potential. Potentials are computed using

$$\frac{\partial^2 \Phi}{\partial t^2} = c_p^2(\frac{\partial v_x}{\partial x} + \frac{\partial v_z}{\partial z}) \tag{2}$$

$$\frac{\partial^2 \Psi}{\partial t^2} = c_s^2(\frac{\partial v_x}{\partial z} - \frac{\partial v_z}{\partial x}) \tag{3}$$

where $c_p = \sqrt{(\lambda + 2\mu)/\rho}$ is the P-wave velocity, $c_s = \sqrt{\mu/\rho}$ is the S-wave velocity. In the overlap region, the potentials are computed using (2) and (3) while the velocities are computed using (1). The reader is referred to [6] for the finite-difference forms of these equations.

The potentials satisfy the following scalar wave equations

$$\frac{\partial^2 \Phi}{\partial t^2} = c_p^2 \nabla^2 \Phi \tag{4}$$

$$\frac{\partial^2 \Psi}{\partial t^2} = c_s^2 \nabla^2 \Psi \tag{5}$$

To simulate these equations using a standard leap-frog scheme, each is rewritten as a set of three coupled equations

$$\frac{\partial \Phi}{\partial t} = (\lambda+2\mu)\left(\frac{\partial A_x}{\partial x}+\frac{\partial A_z}{\partial z}\right) \quad (6) \qquad \rho\frac{\partial A_x}{\partial t} = \frac{\partial \Phi}{\partial x} \quad (8) \qquad \rho\frac{\partial A_z}{\partial t} = \frac{\partial \Phi}{\partial z} \quad (10)$$

$$\frac{\partial \Psi}{\partial t} = \mu\left(\frac{\partial B_x}{\partial x}+\frac{\partial B_z}{\partial z}\right) \quad (7) \qquad \rho\frac{\partial B_z}{\partial t} = \frac{\partial \Psi}{\partial x} \quad (9) \qquad \rho\frac{\partial B_z}{\partial t} = \frac{\partial \Psi}{\partial z} \quad (11)$$

Equations (6), (8), and (10) can be decoupled to obtain (4), while (7), (9), and (11) can be used to obtain (5). The fictitious fields $\vec{A}$ and $\vec{B}$ are introduced as part of a field-dividing process.

Equations (10) and (11) propagate energy without loss. To simulate an unbounded medium the fields must be attenuated. Thus, following Berenger [8], we modify the lossless equations by dividing the potentials and adding loss terms to get

$$\begin{aligned} \frac{\partial \Phi_x}{\partial t}+(\lambda+2\mu)q_{px}\Phi_x &= (\lambda+2\mu)\frac{\partial A_x}{\partial x} \\ \rho\frac{\partial A_x}{\partial t}+q^*_{px}A_x &= \frac{\partial(\Phi_x+\Phi_z)}{\partial x} \\ \frac{\partial \Psi_z}{\partial t}+\mu q_{sz}\Psi_z &= \mu\frac{\partial B_z}{\partial x} \\ \rho\frac{\partial B_z}{\partial t}+q^*_{sz}B_z &= \frac{\partial(\Psi_x+\Psi_z)}{\partial x} \end{aligned} \qquad \begin{aligned} \frac{\partial \Phi_z}{\partial t}+(\lambda+2\mu)q_{pz}\Phi_z &= (\lambda+2\mu)\frac{\partial A_z}{\partial z} \\ \rho\frac{\partial A_z}{\partial t}+q^*_{pz}A_z &= \frac{\partial(\Phi_x+\Phi_z)}{\partial z} \\ \frac{\partial \Psi_z}{\partial t}+\mu q_{sz}\Psi_z &= \mu\frac{\partial B_z}{\partial z} \\ \rho\frac{\partial B_z}{\partial t}+q^*_{sz}B_z &= \frac{\partial(\Psi_x+\Psi_z)}{\partial z} \end{aligned}$$

The potentials are divided such that $\Phi = \Phi_x + \Phi_z$ and $\Psi = \Psi_x + \Psi_z$. The q_{ij} and q^*_{ij} terms ($i = p$, s and $j = x$, z) control loss and vary with depth in the PML [7]. As shown in Fig. 2, some loss terms are set to zero within the edge portions (as opposed to corner) of the PML. Terms q_{ix} are zero for the top and bottom PML, while terms q_{iz} are zero for the left and right PML. This dictates that exponential decay occurs only in the direction perpendicular to the edge of the PML. In the corners, losses are nonzero in both directions, and the variation of loss with depth corresponds to that in the appropriate neighboring PML edge region. The reader is referred to [8] for the finite difference implementation of these equations.

To examine the angular performance of the ABC at a single frequency, reflection coefficients are estimated using numerical simulation. Figure 3 shows the test geometry, consisting of two distinct computational domains, Ω_1 and Ω_2, which are used to evaluate the ABC. Grid Ω_1 is terminated by a PML on the top edge, and grid Ω_2 is made large enough so that reflections from its boundaries do not interfere with the test. A source is placed one S-wave wavelength below the PML region in Ω_1 and at the corresponding location in Ω_2. The source is constructed such that either a pure P-wave or a pure S-wave can be introduced ("pure" indicating that the other component is absent). Waves radiating away from the source in Ω_1 will intersect the lower edge of the overlap region with an incident angle θ_i. For this example, we use 16 grid spaces per S-wave wavelength, and, for stability, we use $c_p\delta t/\Delta = 0.707$ where δt is one time step and Δ is one spatial step. The compressional and shear wave speeds are $c_p = 5710$ m/s and $c_s = 2930$ m/s, respectively, which are typical of basalt (commonly used to model the ocean bottom).

The reflection coefficients are defined as follows

$$R_{pp} = \frac{\Phi_{\Omega_1}-\Phi_{\Omega_2}}{\Phi_{\Omega_2}} \qquad R_{ps} = \frac{\Psi_{\Omega_1}}{\Phi_{\Omega_2}} \qquad R_{ss} = \frac{\Psi_{\Omega_1}-\Psi_{\Omega_2}}{\Psi_{\Omega_2}} \qquad R_{sp} = \frac{\Phi_{\Omega_1}}{\Psi_{\Omega_2}}$$

where the subscript indicates the grid from which the potential is taken. In this way, R_{pp} and R_{ps} measure the reflected P and S waves due to an incident P wave, and R_{ss} and R_{sp} measure the reflected S and P waves due to an incident S wave. (On both grids the potentials are computed along a line one grid space below the PML.)

Figure 4 shows R_{pp} and R_{ss} as a function of θ_i for a PML depth of 16 grid spaces. Differences between the two factors are due to variation in the PML depth and source location relative to the S- and P-wave wavelengths. For both factors, reflections remain below 0.1% over the range $0° \le \theta_i \le 80°$. Although not shown here, R_{ps} and R_{sp} were found to be below -200 dB over all angles, indicating that this type of reflection is negligible.

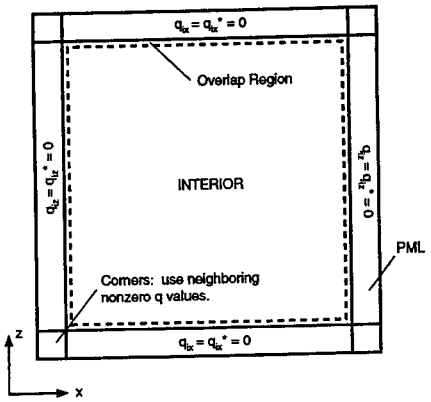

Figure 2: Computational grid with PML absorbing boundary. Interior fields are computed with velocity-stress formulation, and PML fields are computed using potentials. In the overlap region the waves are transferred back and forth between velocities and potentials.

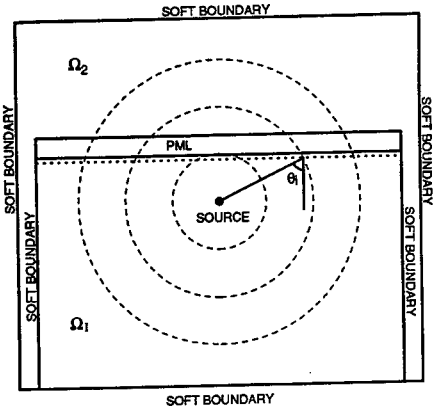

Figure 3: Geometry for computing reflection coefficients. Domain Ω_1 is terminated on the upper edge with a PML. The dimensions are such that reflections are caused only by the ABC for the duration of the simulation. Domain Ω_2 is large enough so that no reflections occur.

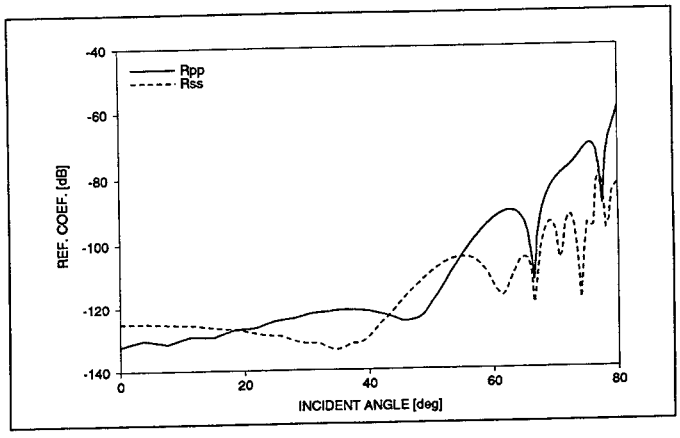

Figure 4: Reflection factors R_{pp} and R_{ss} for PML depth $\delta = 16\Delta$.

(It should be noted that as currently formulated, this ABC can only be used along a homogeneous portion of the computational domain. For example, it could be used to "underlie" a basalt bottom in order to make it appear semi-infinite. However, it could not be used at the basalt-water interface where surface waves may contain coupled shear and compressional components.)

4 Modified Contour Path FDTD for Hard and Soft Boundaries

As mentioned previously, hard and soft boundaries appear commonly in acoustics problems and, provided the surrounding medium does not support shear waves, can be treated in the same way that perfectly conducting surfaces are handled in electromagnetic FDTD code. However, this fact may not be obvious from a direct inspection of the linear acoustics equations. These equations for a fluid or gas are typically written as

$$\frac{\partial \vec{v}}{\partial t} = -\frac{1}{\rho}\nabla p \qquad (12) \qquad\qquad \frac{\partial p}{\partial t} = -\rho c^2 \nabla \cdot \vec{v} \qquad (13)$$

where c is the speed of sound (since there is no shear wave present, the subscript p has been dropped), p is the pressure (the negative of the stress), v and ρ are still the velocity and density, respectively. Equation (12) is merely Newton's law of motion while (13) comes from the underlying continuity equation (i.e., conservation of mass). Integrating these yields

$$\int_V \frac{\partial p}{\partial t}\, dv = -\int_V \rho c^2 \nabla \cdot \vec{v}\, dv = -\oint_S \rho c^2 \vec{v} \cdot d\vec{s} \qquad (14) \qquad\qquad \int_V \frac{\partial \vec{v}}{\partial t}\, dv = -\int_V \frac{1}{\rho}\nabla p\, dv = -\oint_S \frac{1}{\rho} p\, d\vec{s} \qquad (15)$$

The usual integral representation of Maxwell's equations contains line and surface integrals that suggest a reinterpretation of the FDTD grid—not only can a node represent the field found at a point, it can also be thought of as the flux through a face or the field along a line. Once this "dual" interpretation of nodes is recognized, the integral equations provide a convenient way to construct update equations for a distorted grid. In undistorted regions the update equations are the same whether obtained using a differential or an integral approach. The CPFDTD algorithm uses this fact and distorts the grid only in the vicinity of an interface [9]. It thus maintains the simplicity of the usual FDTD scheme in the majority of the computational domain and yet it can provide greater accuracy since, unlike the standard approach, it has the ability to "conform" to an interface. Fortunately, it is possible to apply the same conformal scheme to acoustics problems where (14) is used to obtain the update equations for pressures in the vicinity of a hard boundary and (15) is used to obtain the update equations for velocities in the vicinity of a soft boundary.

Unfortunately, as originally proposed, the CPFDTD algorithm uses a non-reciprocal "nearest neighbor approximation" that can lead to unstable behavior. Recently, a modification was presented that corrects this instability by making the nearest neighbor approximation reciprocal [10]. The primary objective in introducing this modification was to guarantee stable results—in fact, the modified CPFDTD scheme can be used to analyze resonant structures that consistently produced unstable results using the original scheme. However, even when the original CPFDTD scheme produces stable results, the modified scheme can still provide greater accuracy. (The reader is referred to [10] and [11] for details concerning the two- and three-dimensional forms of the modified CPFDTD scheme).

To illustrate the improved accuracy provided by the modified CPFDTD scheme, consider a wedge illuminated by a line source which is located exactly along the line that bisects the wedge. Figure 5 shows a portion of this wedge together with the source (the wedge is assumed to extend infinitely far to the right). Since the problem is symmetric about the bisecting line, the fields found along two lines that are offset from, but parallel to, the two faces of the wedge should be identical. Figure 5 identifies two such lines, the "measurement lines," that originate at the source. If the wedge is oriented as shown in Fig. 5, the horizontal (or bottom) face will exactly align with the computational grid while the tilted face will not. Because of this misalignment, an FDTD simulation of this problem will not produce symmetric fields and the amount of asymmetry provides a measure of the error associated with modeling the tilted face (numeric dispersion along the different measurement lines notwithstanding).

Figure 6 shows the amount of asymmetry produced when the standard FDTD scheme (i.e., a staircase approximation of the tilted face), and the original and modified forms of the CPFDTD scheme are used to model a wedge whose edges form an angle of 3.814° with the bisecting line. The asymmetry was calculated by taking the absolute value of the difference between the pressures found along the two measurement lines. The line source was a pressure node being driven by a delayed Ricker wavelet and the discretization was such that 20 points per

wavelength were used at the frequency corresponding to the centroid of the wavelet's spectral energy. (A Ricker wavelet is a broadbanded, finite-duration pulse that is often used in the acoustics community to model an "explosive" source. See [12] for an example.) The source was approximately 15 cell widths (15Δ) from the tip of the wedge. The measurement was taken 500 time steps after the start of the simulation. The computational domain was large enough so that no spurious boundary reflections were present at the time the measurement was taken. Measurements along Line #2 were taken directly from the pressure nodes and bivariate interpolation was used to obtain the pressures at the corresponding locations along Line #1.

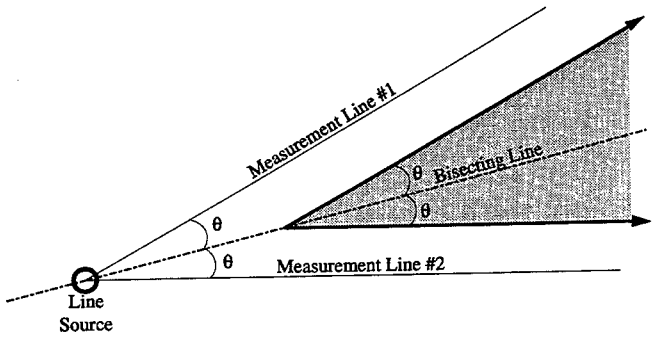

Figure 5: Wedge test geometry. The wedge is acoustically hard. The bottom measurement line and the bottom face of the wedge are aligned with the grid.

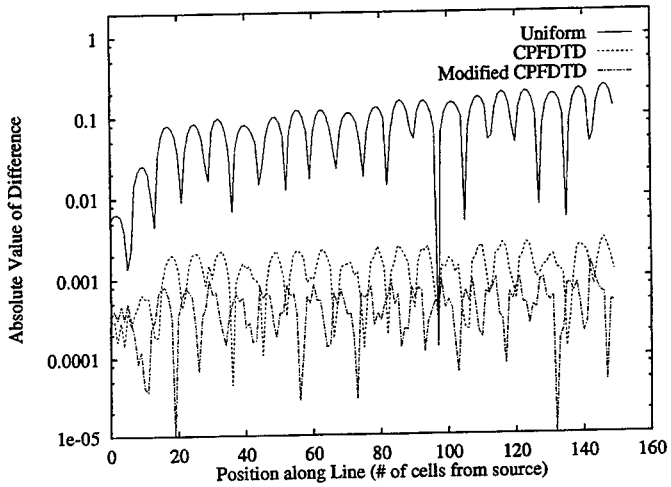

Figure 6: Absolute value of the difference of the fields found along two measurement lines as obtained using uniform FDTD, CPFDTD, and the modified CPFDTD techniques. Results are for a hard wedge with $\theta = 3.814°$.

Figure 6 clearly shows that the amount of asymmetry is reduced significantly by using either one of the contour path techniques, with the original CPFDTD technique reducing the difference by approximately 40 dB. An additional

reduction in asymmetry (of approximately 7 dB) is realized by using the modified CPFDTD technique. The results shown here are consistent with those found using various wedge angles.

It is worth noting that using the CPFDTD scheme at a soft boundary does not require the nearest neighbor approximation; hence, it is stable and does not require modification.

5 Conclusions

Many of the enhancements that have found their way into electromagnetic FDTD modeling are also applicable, at least indirectly, to acoustic FDTD modeling. The incorporation of these enhancements into acoustic modeling has the potential to significantly impact problems ranging from ultrasonic medical imaging to underwater mine detection.

Acknowlegements: J.B.S. and F.D.H. thank the Office of Naval Research, Code 321OA, for supporting this work.

References

[1] J. Virieux, "*SH*-wave propagation in heterogeneous media: Velocity-stress finite difference method," *Geophysics*, vol. 49, no. 11, pp. 1933–1942, 1984.

[2] J. Virieux, "*P-SV* wave propagation in heterogeneous media: Velocity-stress finite difference method," *Geophysics*, vol. 51, no. 4, pp. 889–901, 1986.

[3] J. G. Maloney and K. E. Cummings, "Adaptation of FDTD techniques to acoustic modeling," in *11th Annual Review of Progress in Applied Computational Electromagnetics*, vol. 2, (Monterey, CA), pp. 724–731, Mar. 1995.

[4] D. Botteldooren, "Acoustical finite-difference time-domain simulation in a quasi-Cartesian grid," *J. Acous. Soc. Am.*, vol. 95, no. 5, pp. 2313–2319, 1994.

[5] K. S. Kunz and R. J. Luebbers, *The Finite Difference Time Domain Method for Electromagnetics.* Boca Raton, FL: CRC Press, 1993.

[6] C. J. Randall, "Absorbing boundary condition for the elastic wave equation: Velocity-stress formulation," *Geophysics*, vol. 54, no. 9, pp. 1141–1152, 1989.

[7] F. D. Hastings, J. B. Schneider, and S. L. Broschat, "Application of the perfectly matched layer (PML) absorbing boundary condition to elastic wave propagation," to appear in *J. Acoust. Soc. Am.*, 1996.

[8] J.-P. Berenger, "A perfectly matched layer for the absorption of electromagnetics waves," *J. Comput. Phys.*, vol. 114, no. 1, pp. 185–200, 1994.

[9] T. G. Jurgens, A. Taflove, K. Umashankar, and T. G. Moore, "Finite-difference time-domain modeling of curved surfaces," *IEEE Trans. Antennas Propagat.*, vol. 40, no. 4, pp. 357–366, 1992.

[10] C. J. Railton, I. J. Craddock, and J. B. Schneider, "An improved locally distorted CPFDTD algorithm with provable stability," *Electron. Lett.*, vol. 31, no. 18, pp. 1585–1586, 1995.

[11] C. J. Railton and I. J. Craddock, "Analysis of general 3-D PEC structures using improved CPFDTD algorithm," *Electron. Lett.*, vol. 31, no. 20, pp. 1553–1554, 1995.

[12] C. Peng and M. N. Toksöz, "An optimal absorbing boundary condition for finite difference modeling of acoustic and elastic wave propagation," *J. Acoust. Soc. Am.*, vol. 95, no. 2, pp. 733–745, 1994.

FDTD Analysis of Small Loop Antennas for Partial Exposure of Rat Head at 837 MHz

K.W. Chan, J.A. McDougall, C.K. Chou
City of Hope National Medical Center, Duarte, CA 91010-3000

Introduction

The effects of low-level electromagnetic exposures at cellular telephone frequencies are being investigated. Rats have been selected to receive microwave energy in one side of the head. Existing cellular phone antennas are inappropriate for exposing rats because of the difference in shape and size of rat and human heads. An antenna must be developed to produce the required energy distribution in the rat head, mostly on one side of the brain similar to that of humans operating cellular phones. This will enable biologists to investigate any effect that may occur from low-level electromagnetic exposures of rats.

It has been decided that these will be long-term exposure studies at multiple sites involving hundreds of animals. The problem of keeping the animals in a free habitat and being able to deliver electromagnetic energy to their heads repeatedly with precision is difficult. There is also the controversy of possible changes in experimental end-points due to stress resulting from restraining the animals. The issue of restraining the animals during exposures remains to be decided by the biologists. At 837 MHz, conflicts with existing communication channels are minimized while the studies are still within the frequencies of interest. The goal of this project is to develop antennas suitable for partial exposure of the head of an average size rat. The FDTD method has been used to simulate exposure conditions produced by different antenna designs and to evaluate energy absorption in the rat head. Initially an ellipsoid was used to represent a rat in both the experimental and numerical models to determine the basic design requirements. After the appropriate antennas are identified, the ellipsoid will be replaced with CT based rat models to determine the energy distribution inside the rat head. The ellipsoid model has allowed the preliminary antenna design and evaluation to be carried out while the CT based rat model is being developed.

Ellipsoid Model

An ellipsoid was initially used in FDTD models to determine the feasibility of using certain types of antennas to satisfy the requirements of these exposure studies. The models were simulated at 1 mm resolution because of the small size of the antennas. The dimensions of this ellipsoid was chosen based on the size of an average rat. It was 20 cm long and had a center diameter of 5.6 cm. The model was composed of brain equivalent tissue covered at one end with a 45 mm long, 2 mm thick cone shaped shell consisting of bone material. The dielectric properties of the tissues and other materials at 837 MHz are listed in Table 1. The antennas were positioned in the FDTD models at approximately 35 mm from the tip of the cone shaped shell and 2 - 10 mm from its surface as shown in Figure 1. To minimize staircasing errors, the antenna was aligned with the FDTD grid and the

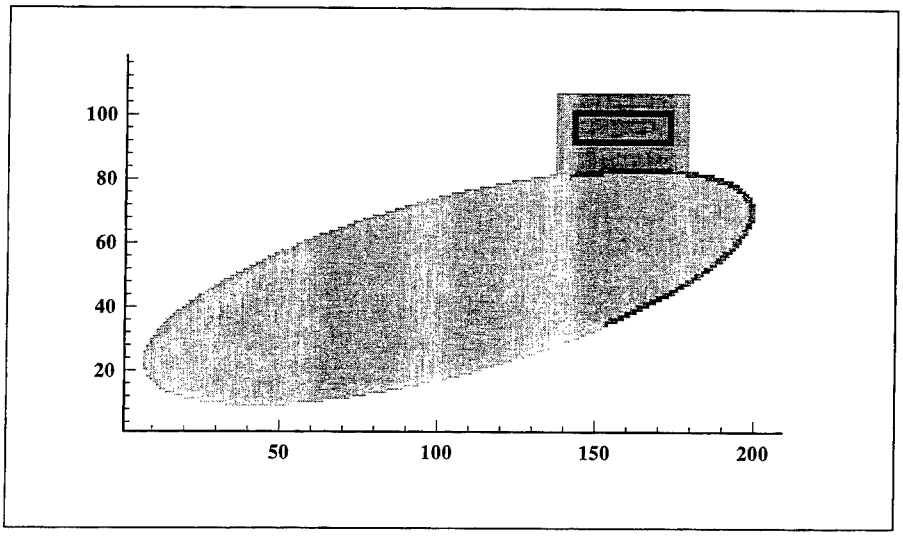

Figure 1 The configuration of a loop on a printed circuit board (PCB) located at one end of a 20 cm long, 5.6 cm diameter ellipsoid with a 2 mm thick cone shaped shell.

ellipsoid was tilted approximately 15° from its horizontal position to keep the antenna tangent to the surface of the cone shell. This also minimized the amount of staircasing at the surface of the ellipsoid where the field intensity was highest. The antenna position around the circumference of the ellipsoid, as compared to a rat, is not unique because of rotational symmetry around the ellipsoid. This model was used to simulate the partial head exposure of a rat.

Table 1. Properties of tissue and circuit board materials used in the FDTD models

837 MHz	Copper	Brain	Skull	PCB
σ(S/m)	5.9×10^7	0.86	0.33	0.0
ϵ	1.0	43.0	21.0	1 - 16
ρ(kg/m^3)	N/A	1000	1500	N/A

Preliminary Assessments

A few simple models of short dipoles and small loops located in close proximity to the ellipsoid have been simulated to evaluate the effectiveness of these antennas for near field exposures. It is found that short dipoles are very inefficient for producing adequate energy deposition in high dielectric tissues. The high electric fields near the ends of the dipole also produce power absorption patterns that

are inappropriate for the exposure studies. When small loops are properly aligned with the ellipsoid as shown in Figure 1, they provide more desirable energy distributions than the dipoles. The energy is coupled into the ellipsoid mainly through the magnetic fields of the loop. The undesirable electric fields seen with dipoles are also reduced because loops have voltage minimums located closest to the ellipsoid.

After selecting the small loop as the antenna for the exposure studies, the detail requirements must be determined before prototype devices can be developed. A peak specific absorption rate (SAR) of about 10 W/kg in on side of the rat brain is required. The estimated target volume is approximately 10 x 10 x 25 mm^3 enclosed by the half-power deposition boundaries. Since hundreds of animals will be involved in these studies, it has been decided that the loops should be driven individually by cellular phones. This will eliminate potential cabling problems associated with using a common power source. The output impedance of typical cellular phones is 50Ω with a maximum power output of 0.6 W. In order to produce 10 W/kg of SAR, the source and loop impedances should be matched to provide optimal power transfer. It is also necessary to minimize the loop area to maintain high magnetic field strengths for coupling energy into the tissue. But the impedance of a small loop is typically very low and higher loop impedance requires longer loop length which results in larger loop area. A compromise is necessary.

As indicated in literature, the radiation patterns produced by rectangular and circular loops are similar [1]. To better conform to the FDTD grids and to minimize staircasing errors, the rectangular loop was used for all simulations. A number of loops with various aspect ratios and dimensions were modeled to determine the optimal length and width of a loop required to provide adequate coverage of the intended exposure target volume. The sides of the loop that are parallel to the tissue must be longer than 25 mm, and the other two sides are adjusted to optimize power deposition in the ellipsoid. The results indicate that a rectangular loop of approximately 30 mm x 10 mm will satisfy the exposure requirements. The impedance of this loop is about 10 - 15 Ω, depending on its distance from the ellipsoid. This problem of impedance variations due to loop movements or placement errors during exposure of live rats has led to the development of loops on printed circuit boards (PCB) to minimize impedance and SAR changes.

Loop Antenna Development

If the rat is put in a plastic restraining tube during exposure, it is still very difficult to prevent the animal from moving or rotating its head for long durations without enduring extreme stress. The idea of putting the loop on PCB is to embed it in a small styrofoam helmet, light enough to be mounted on a rat head. With a less stressful restraining system and some animal training, this loop and helmet configuration will have less impact on normal behavior of a rat. Loop placement should be repeatable from day to day for long term exposure studies and small errors in positioning should produce insignificant changes in energy distributions in the tissue. A 31 mm x 10 mm rectangular loop was implemented on PCB to investigate the effects of loop positioning at the rat head. The circuit board has a 5 mm margin around three sides of the loop and an appropriate spacing on the fourth side to maintain a fixed separation between the ellipsoid and the loop. The circuit board has a thickness of 1 mm and a dielectric constant of 4.5 simulating fiberglass epoxy materials. The results indicate only slight increases in impedances with the loop on a PCB. Simulations with 2 mm thick PCB also show little improvement.

In order better understand the impedance characteristics of loops on PCB, the simulations were repeated with dielectric constants of the board material varied from 1 to 16. The thickness of the board was maintained at 2 mm while the spacing between the loop and ellipsoid was kept at 4 mm. An impedance curve is obtained indicating very steep changes in impedance as the dielectric constant of the circuit board material was varied. This impedance curve is similar to those found in the literature for loops in free space with sharp peaks at $\lambda/2$ and return to low impedances at λ. The computed SAR indicates that it is possible to produce 10 W/kg of peak SAR with 0.6 W of maximum input power. But some impedance matching may be required to optimize power transfer from the source to the loop.

The idea of choosing an appropriate dielectric constant for the PCB material to match the real part of the loop impedance and compensating the loop inductance with appropriate capacitance is appealing. But the 50Ω impedance point is located along the lower slope of a sharp peak, similar to those in Figure 2. Its influence on impedance and SAR variations due to placement errors must be determined. Besides, the exact spacing between the loop and the rat head may vary because of movement. There is also the uncertainty of parameter changes when dealing with an actual rat. After some literature search on loading loops with dielectric materials [2], several board thickness were simulated to determine if this can provide an additional degree of freedom for implementing the loop.

The possibility of varying the circuit board thickness to gain extra design freedom was accomplished by putting identical loops on both sides of the board. In order to maintain a single loop configuration and to avoid loop connection problems, the loops were shorted at the four corners and on either side of the driving point. The problem of mutual coupling between the loops was also reduced with this double-sided single loop configuration. The technique provided a mechanism to vary loop impedance with circuit board thickness instead of its dielectric property.

Intermediate Results

A series of simulations for 2 or 4 mm thick boards and dielectric constants of 1 - 16 were modeled with this double-sided single loop configuration. The loops were located at either 4 mm or 7 mm from the surface of the ellipsoid where the spacing was maintained by the circuit board. The 4 curves in Figures 2 - 4 indicate the impedance and SAR characteristics due to loop placement and board thickness changes as a function of the dielectric constant of the board.

The impedance curves are separated into two groups associated with the thickness of the PCB. The curves for the 4 mm thick boards are shifted to the left of the 2 mm boards, and the real part of the impedance has a steeper transition towards the $\lambda/2$ peak. As the spacing between the loop and the ellipsoid is widened from 4 mm to 7 mm, there is a decrease in loop impedance. The normalized peak SAR produced in the ellipsoid with one watt of loop input power is shown in Figure 4.

The loops on 2 mm thick boards produced much higher SAR than the 4 mm boards. For loop spacings of 4 and 7 mm from the ellipsoid, the curves in Figure 4 cross each other at dielectric constants of 7.6 and 5.4 for the 2 and 4 mm thick boards respectively. Before the curves cross, the SAR in the ellipsoid is lower for the 7 mm spacing. But after the crossing, the 7 mm spacing loops produce increasingly higher SAR than the 4 mm configurations as dielectric constant is increased. The difference in SAR for the loops at 4 and 7 mm from the ellipsoid is much less before the curves cross

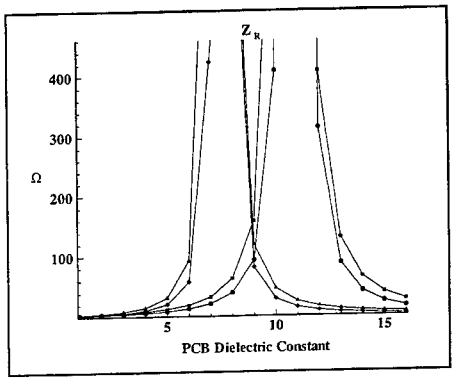

Figure 2 Real part of loop impedance.

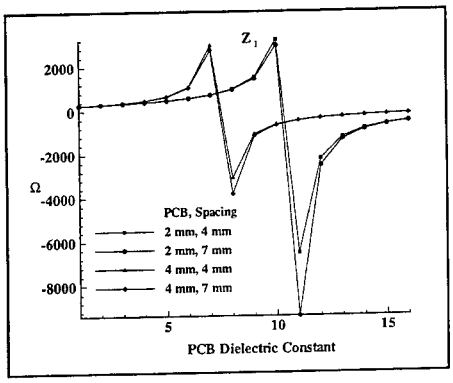

Figure 3 Imaginary part of loop impedance.

each other and widens after the crossing. To minimize SAR changes due to loop spacing variations, the dielectric constant of the board must be less than that indicated by the crossing points of the curves for the particular board thickness. At the crossing point there is practically no change in SAR for 4 and 7 mm spacings. This can be explained by the raw data for SAR and input power. The relationship with the board dielectric constant is linear with SAR, but non-linear with the loop input power. These cause the curves to cross as SAR is normalized by the input power.

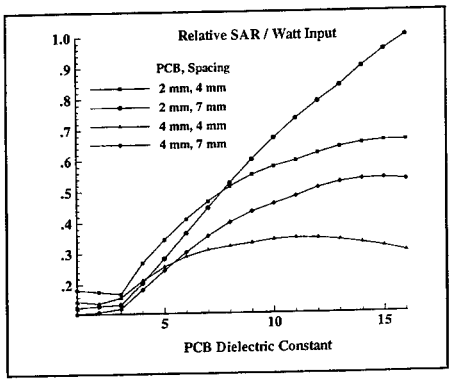

Figure 4 Relative Peak SAR in the ellipsoid normalized to one watt of loop input power.

SAR variations due to loop movement and placement errors can be minimized by selecting circuit board parameters indicated by the crossing points of the appropriate curves. However, if the input power to the loop is unstable, SAR fluctuations are still possible. A mismatch between the source and loop impedance because of variations in loop positioning can cause the input power to fluctuate. Therefore impedance matching becomes another issue that must be addressed to maintain the stability of power absorption in the rat head.

It has been decided that impedance matching will be limited to simple methods with non-bulky devices because of physical and experimental limitations. It is important to maintain a light weight loop and helmet configuration, and to reduce the possibility of perturbing the field distributions because of nearby objects. Assuming that 4 - 7 mm is the anticipated range of loop spacing, the real part of the loop impedance can vary from 35 Ω to 55 Ω and the imaginary part is about 700 Ω for both 2 and 4 mm thick boards. The inductive reactance of the loop can be compensated with a small

chip capacitor at the driving point to form a parallel resonance circuit. A high circuit Q can cause sharp changes in power transfer due to small variations in reactive inductance of the loop, therefore a low to moderate Q is desired. It may also be advantageous or necessary to select circuit boards with higher losses to lower the circuit Q. The input power change due to variations in the real part of the loop impedance is estimated to be about 3%. The SAR in the ellipsoid is expected to have similar variations, which is acceptable by the requirements of the exposure studies. However, if this condition is not adequate, impedance matching between the loop and source should be optimized with the parameters of the most likely configurations to minimize SAR changes.

The electric field distribution around the loop and in the ellipsoid is shown in Figure 5 which indicates a current maximum and a voltage minimum on the side of the loop closest to the ellipsoid. This condition is similar to that reported by Balzano [3], where SAR induced by cellular phones in a human head is mostly due to current along the antenna and the effects of electric fields are less significant. The length of the distribution can be modified by the loop length, and the width of the pattern can be modified to a limited extent by varying the separations between the loops with circuit board thickness. The depth of the pattern is mainly controlled by tissue attenuation where only the peak SAR is controllable through adjustments of input power to the loop. The spacing between the loop and the ellipsoid can cause changes in power requirement, but it has little effect on the distribution patterns because of the much larger ellipsoid located in the near field of a small loop.

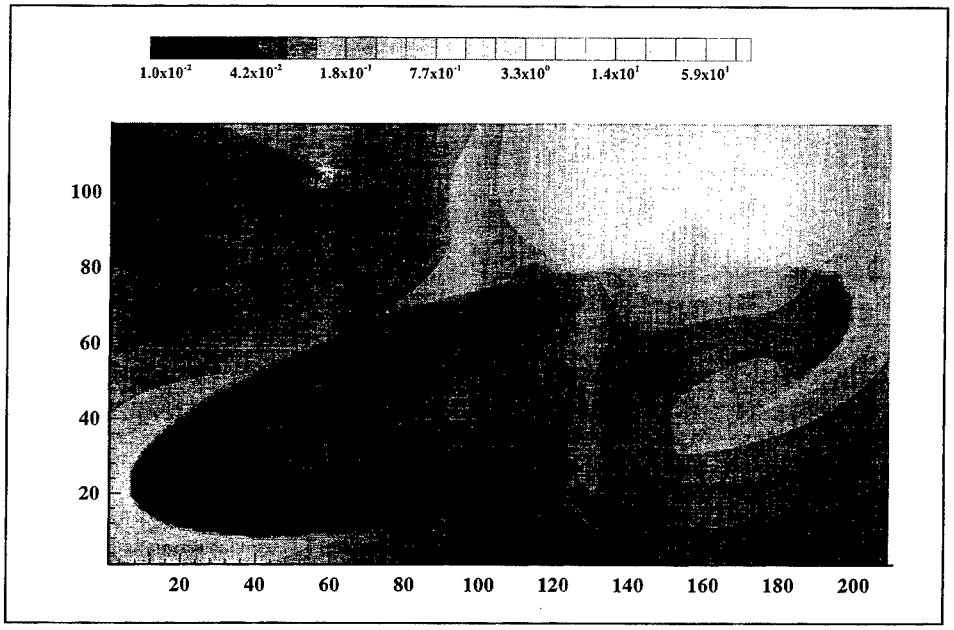

Figure 5 Relative electric field distributions of a 31 x 10 mm loop on 2 mm thick PCB of dielectric constant 8, at 7 mm from the ellipsoid.

Conclusion

There are two main concerns in maintaining the stability of SAR within the target volume of a rat head. The changes in SAR due to loop movement and spacing errors as a results of impedance changes are resolved by putting the loops on circuit boards to control the spacing and by selecting circuit board parameters indicated by the crossing points of the SAR curves. The other concern is impedance changes resulted from loop spacing errors causing fluctuations in power transfer from the source to the loop. The inductive reactance is compensated with appropriate capacitors to form a resonance circuit. The resistive part of the impedance can introduce about 3% of SAR changes which is acceptable for the present application and extensive matching is not required.

The results obtained so far for the analysis of small loops in close proximity to an ellipsoid tissue model is only the first step in developing antennas for the described exposure studies. We have to verify these findings experimentally with ellipsoid models and then repeat the numerical simulations with actual rat models obtained from CT images. Finally the design must be tested on rats before implementing the actual exposure studies on hundreds of animals.

Acknowledgement

This project was sponsored by the Wireless Technology Research, Limited Liability Company.

Reference

[1] G. S. Smith, "Loop Antennas" in "Antenna Engineering Handbook", 2nd Edition, edited by Johnson and Jasik, McGraw Hill, Chapter 5, 1984.

[2] J. P. Cassey and R. Bansal, "Square Loop Antenna with a Dielectric Core", Journal of Applied Physics, 63(6):1820-1823, 15 March 1988.

[3] Q. Balzano, O. Garay and T. Manning, "Electromagnetic Energy Exposure of the Users of Portable Cellular Telephones", IEEE Transactions on Vehicular Technology, 44(3):390-403, August 1995.

Scattering From Complex Geometries Using a Parallel FVTD Algorithm

Vineet Ahuja and Lyle N. Long

Department of Aerospace Engineering
The Pennsylvania State University
University Park, PA

1 Abstract

A 3-D explicit finite volume algorithm has been developed to simulate scattering from complex geometries on parallel computers using structured body conformal curvilinear grids. Most simulations with realistic 3-D geometries require a large number of grid points for adequate spatial resolution making them suitable to parallel computation. The simulations have been carried out using a multi-block/zonal approach in the message passing paradigm on the SP-2. Each zone is placed on a separate processor and inter-processor communication is carried out using the Message Passing Library (MPL). Integration of the Maxwell's equations is performed using the four stage Runge-Kutta time integration method on a dual grid. This method of integrating on a staggered grid seems to give enhanced dissipative and dispersive characteristics. Results obtained in the past, have shown extremely good comparisons for scattering from the sphere and the ogive with the exact solution and standard FDTD type algorithms. Comparisons for non-axisymmetric targets like the NASA almond with experimental data has also been found to be extremely good. Scattering from complex 3-D bodies like a trapezoidal wing and an engine inlet has also been investigated.

2 Introduction

Scattering problems in electromagnetics have been numerically modelled since the conception of Yee's leapfrog algorithm [1] in 1966. However, the production of staircasing errors [2] coupled with the difficulty in predicting the radar return for low RCS geometries encouraged the development of various finite difference [3] [4], finite volume [5] [6], and finite element algorithms [7]. The complexity in the shapes of the scatterers being modelled has lead to a transition from the use of Cartesian grids. Body-fitted structured grid algorithms are being used because they utilise curvilinear orthogonal grids that map the surface of the body exactly by a transformation between the physical and the computational domain. However, in the last few years, unstructured grid methodology has become very popular mainly due to the relative ease with which unstructured grids can be generated around complex configurations [8], [9]. Unstructured grid solvers are replacing structured solvers for steady state aerodynamic problems [10] [11], particularly those that need to solve the Euler equations. Since Maxwell's equations can be readily put in the form of the Euler equations unstructured grids seemed to be promising in CEM too. Unstructured grid solvers have been found to be very expensive and have been plagued with problems of numerical accuracy. Over the years, there has also been a tremendous boost in the computational resources available, both in terms of speed and memory. The onset of parallel computing has made a huge impact on the choice of the algorithm and the type of mesh to be considered. In the present paper, we make use of a Runge-Kutta based scheme on a dual structured grid that has multi-block capability. The algorithm is easily parallelized and is especially suited to message passing since the dual grid requires that only half the total variables be communicated between processors.

3 Numerical Model

Maxwell's equations can be written in the integral form as

$$\int\int_V \int \frac{\partial \mathbf{B}}{\partial t} dV = -\int\int_S \mathbf{n} \times \mathbf{E} \quad dS \tag{1}$$

$$\int\int_V \int \frac{\partial \mathbf{D}}{\partial t} dV = \int\int_S \mathbf{n} \times \mathbf{H} \quad dS \tag{2}$$

The above equations are solved only for the scattered fields as the analytical solution of the incident field is known. A dual grid approach is taken with the electric and magnetic field components being solved on separate grids. Time integration is carried out using the four-stage Runge-Kutta time marching method.

$$\mathbf{Q}_i^m = \mathbf{Q}_i^n - \gamma_m \Delta t \mathbf{R}_i^{m-1} \qquad m = 1, 2, 3, 4$$

$$\mathbf{Q}_i^{n+1} = \mathbf{Q}_i^{m=4}$$

The time step is denoted by n and each stage of the Runge-Kutta method by m, where the coefficients are $\gamma_m = \frac{1}{4}, \frac{1}{3}, \frac{1}{2}, 1$ respectively.

$$\mathbf{Q_1} = \begin{bmatrix} H_x \\ H_y \\ H_z \end{bmatrix} \qquad \mathbf{Q_2} = \begin{bmatrix} E_x \\ E_y \\ E_z \end{bmatrix} \tag{3}$$

The residuals $\mathbf{R_i}$ are defined as

$$\mathbf{R_1} = \frac{1}{\Delta V} (\Delta \mathbf{F} + \Delta \mathbf{G} + \Delta \mathbf{K}) \tag{4}$$

$$\mathbf{R_2} = \frac{1}{\Delta V_d} (\Delta \mathbf{L} + \Delta \mathbf{M} + \Delta \mathbf{N}) \tag{5}$$

where

$$\Delta \mathbf{F} = \frac{1}{\mu} \left(\mathbf{S}^{\xi}_{i+1,j+1/2,k+1/2} \times \mathbf{E}^{\xi}_{i+1,j+1/2,k+1/2} - \mathbf{S}^{\xi}_{i,j+1/2,k+1/2} \times \mathbf{E}^{\xi}_{i,j+1/2,k+1/2} \right)$$

$$\Delta \mathbf{G} = \frac{1}{\mu} \left(\mathbf{S}^{\eta}_{i+1/2,j+1,k+1/2} \times \mathbf{E}^{\eta}_{i+1/2,j+1,k+1/2} - \mathbf{S}^{\eta}_{i+1/2,j,k+1/2} \times \mathbf{E}^{\eta}_{i+1/2,j,k+1/2} \right)$$

$$\Delta \mathbf{K} = \frac{1}{\mu} \left(\mathbf{S}^{\zeta}_{i+1/2,j+1/2,k+1} \times \mathbf{E}^{\zeta}_{i+1/2,j+1/2,k+1} - \mathbf{S}^{\zeta}_{i+1/2,j+1/2,k} \times \mathbf{E}^{\zeta}_{i+1/2,j+1/2,k} \right)$$

In the above expressions $\mathbf{S}^{\xi}, \mathbf{S}^{\eta}, \mathbf{S}^{\zeta}$ represent the projected surface areas of constant ξ, η, ζ faces respectively. It should be noted that the electric field points used in the evaluation of the above fluxes lie in the center of the cell faces and are not computed directly from the integration process. Instead they are extrapolated from the electric field points comprising the corners of the cell faces.

Most central differencing algorithms require the addition of some sort of explicit artificial dissipation to damp out the spurious numerical high frequency waves. However, for a spatially staggered scheme the dissipation characteristics with a four stage Runge-Kutta method are quite different. This has been analysed with the help of a one-dimensional system of hyperbolic equations in [12]. The low wavenumber components propagate without being damped. However, the high frequency components are damped due to the grid induced dissipation caused by the staggering of the spatial derivatives. It should be pointed out that the above analysis is for a one-dimensional case on a uniformly spaced mesh with perfect staggering. In reality, however, body-fitted grids are usually clustered and may have imperfections like skewed cells or cells with high aspect ratios. Also, the staggering used in the algorithm is not completely perfect in three dimensions. All the above reasons contribute in the production of spurious diffusion [13] for the high wavenumber components that are not completely damped by the grid induced dissipation. Hence the need for explicitly adding artificial dissipation. When required, fourth order dissipation [14] is added

$$D\mathbf{Q} = D_{\xi}\mathbf{Q} + D_{\eta}\mathbf{Q} + D_{\zeta}\mathbf{Q} \tag{6}$$

where $D_\xi \mathbf{Q}$, $D_\eta \mathbf{Q}$, and $D_\zeta \mathbf{Q}$ are the fourth order dissipation operators in the ξ, η and ζ directions respectively and can be explicitly written as

$$D_\xi \mathbf{Q} = d_{i+\frac{1}{2},j,k} - d_{i-\frac{1}{2},j,k} \qquad D_\eta \mathbf{Q} = d_{i,j+\frac{1}{2},k} - d_{i,j-\frac{1}{2},k} \qquad D_\zeta \mathbf{Q} = d_{i,j,k+\frac{1}{2}} - d_{i,j,k-\frac{1}{2}}$$

where the above $d_{i\pm\frac{1}{2},j,k}$ can be represented as

$$d_{i+\frac{1}{2},j,k} = \frac{(\Delta V_d)_{i-\frac{1}{2},j,k}}{\Delta t} \Omega \left(\mathbf{Q}_{i+2,j,k} - 3\mathbf{Q}_{i+1,j,k} + 3\mathbf{Q}_{i-1,j,k} - \mathbf{Q}_{i-2,j,k} \right)$$

The coefficient Ω is a constant whose value is $\frac{1}{256}$
Hence inserting the expressions for artificial dissipation in equation 5 and rewriting it

$$\mathbf{R_2} = \frac{1}{\Delta V_d} \left(\Delta \mathbf{L} + \Delta \mathbf{M} + \Delta \mathbf{N} - D\mathbf{Q} \right) \tag{7}$$

Boundary conditions have to be defined only for the E-field components since the H-field components are offset by half a cell from the boundaries. At the surface of the scatterers the PEC boundary condition has been used and at the outer boundary the Liao boundary condition has been utilized [15], [16].

The farzone scattered fields are calculated in accordance with the derivation of retarded potentials from scattered surface currents in [17].

$$\mathbf{w}\left[t - (\vec{r} \cdot \hat{r})/c\right] = \left(\frac{1}{4\pi c}\right) \frac{\partial}{\partial t} \left\{ \int_s \mathbf{j}_s(t)\, ds \right\} \qquad \mathbf{u}\left[t - (\vec{r} \cdot \hat{r})/c\right] = \left(\frac{1}{4\pi c}\right) \frac{\partial}{\partial t} \left\{ \int_s \mathbf{m}_s(t)\, ds \right\}$$

Adaptation of this technique for computing the far-field transformation on curvilinear dual grids has been discussed in [16].

4 Parallelization Issues and Performance

The computer that was used for the message passing algorithm is the IBM 9076 Scalable Power parallel system (SP-2) which is a tightly clustered group of RISC system/6000 processors. Efficiency in message passing is provided by a low latency high bandwith switch. "Latency" is the startup time that is required at the time of communication between processors, or in other words, it is the time taken to send a message in the limit as the message size goes to zero. "Bandwidth" refers to the message size that is passed per unit time. Communication time is roughly equal to the sum total of the time taken for startup and the actual time required to transfer data. The efficiency of a message passing algorithm is gauged by its ability to minimize the communication-to-computation ratio and to balance the workload effectively by partitioning the data structure evenly. Domain decomposition techniques are best suited for structured data problems where partitioning of the computational domain can be easily done.

4.1 Implementation in MPL

Since the grid for the algorithm discussed in the previous section consists of the E-field grid and the H-field dual grid, a Processor Domain (PD) for our purposes is a combination of the two. Message passing is carried out between two adjacent processor domains (PD's) by creating pseudo boundaries or shadow blocks between them. As is evident from figure 1 the interior cell values (E-fields in this case) are passed from one processor over to its neighbouring processor and they constitute the pseudo boundary conditions for the neighbouring processor and vice versa. Parallelization of the algorithm was performed on the SP-2 using the Message Passing Library (MPL). MPL uses the Single Program Multiple Data (SPMD) model wherein the same program resides on all processors and is executed by each one of the processors. However, each processor has its identifier processor number and this permits MPL to have processor based conditional statements. The reason for using a SPMD model is that in a distributed memory system, memory and address space is local to each processor and the only way data can be shared among processors is by passing messages. Each processor has it's own processor domain to work with. Each processor domain is either bounded by pseudo boundaries or a combination of physical and pseudo boundaries. A pre-determined processor (with processor ID=0) acts as the control processor and carries out the pre-processing tasks involved in setting up the parallel environment and all parameters required for message passing. It reads

in the grid and distributes it to the various processors depending upon the type of domain decomposition. Each processor then generates its own dual grid from the information it has about its own grid. The grid and the constructed dual grid together constitute the processor domain of the processor. The processor then computes the volumes and surface areas of the cells that are located in its processor domain. It also calculates the time step required for computation on its own processor domain. This information about the minimum time step on each processor domain is then communicated to the processor with $ID = 0$. The processor with $ID = 0$ in turn determines the minimum time step for the entire computational domain and broadcasts it to all the processors.

Message passing between processors is carried out by issuing explicit MPL calls. For example

$$CALL\ \ MP_BSEND(qeast, jmax \times kmax \times 3 \times r4size, taskid + 1, msgid)$$

will send the array "qeast" of size $(jmax \times kmax \times 3 \times r4size)$ to the processor with a processor identification number equal to (taskid+1). Similarly, the call

$$CALL\ \ MP_BRECV(qeast, jmax \times kmax \times 3 \times r4size, taskid - 1, msgid, nbytes)$$

will receive the array "qeast" of size$(jmax \times kmax \times 3 \times r4size)$ from the processor with a processor identification number equal to (taskid-1).

Since the whole simulation is a time dependent process, all processors are forced to be synchronized after each Runge-Kutta stage with the MPL call:

$$CALL\ MP_SYNC(allgrp)$$

which blocks all execution on all processors until all processors have made the corresponding call.

4.2 Message Passing Performance

Performance of a parallel algorithm is gauged on the basis of how well an algorithm scales with the increase in the number of processors and its communication to computation ratio. The lower the communication to computation ratio, the higher is the efficiency of the program. The test case of scattering from the NASA almond for a grid size of 225720 grid points was run for 10,000 iterations. The entire computational domain was spread over 7 processors. A first run was made of the code with the far zone integration and the artificial dissipation switched off. The communication time listed includes time to perform inter-processor communication and latency time including latency time for synchronisation after each time step.

$$\frac{average\ communication\ \&wait\ time}{average\ computational\ time} = 0.0650$$

Next the performance of the code was evaluated after switching on artificial dissipation. Fourth order artificial dissipation requires that additional message passing be performed since the fourth order derivative stencils require that an additional field point be communicated from adjacent domains on either side. In comparison to the previous efficiency ratio, it is seen that there is a 5.8 percent increase in the computational time required whereas the communication requirement has increased by 10.2 percent. The relative increase in the amount of communicat ion over the computations has lead to a slight deterioration in the efficiency ratio.

$$\frac{average\ communication\ \&wait\ time}{average\ computational\ time} = 0.06775$$

Lastly, the computer code's performance with the near to far field transformation was analysed. In this case, the time taken for message passing showed a five-fold increase over the communication time needed with the far zone transformation switched off. This increase can be attributed to the message passing involved in passing and summing up the potential arrays over all the processors that have a part of the far zone integration surface defined in their respective processor domains.

$$\frac{average\ communication\&wait\ time}{average\ computational\ time} = 0.2708$$

Table 1: Performance of Codes in μsecs/node/timestep

Algorithm	Computer	μsecs/node/timestep
Serial		
FDTD	RS/6000	14.0
FVTD	RS/6000	94.0
Message Passing		
FVTD	SP-2 (4-node)	12.76
FVTD	SP-2 (16-node)	3.99

4.3 Performance Results

In this section the performance of the FVTD algorithm will be compared against the FDTD algorithm [4] in terms of the computational time required.

Table 1 shows the time taken per grid point per iteration for both the FVTD and FDTD codes. In the serial mode the FDTD algorithm is 6.7 times faster than the FVTD algorithm. This is attributed to the fact that the FDTD is run on Cartesian grids whereas the FVTD algorithm is used on curvilinear grids and the additional cost of the transformation from the physical to the computational grid is incurred while computing the numerical fluxes. Also, the FVTD algorithm has a four-stage time integration process which is a further overhead. The numbers in Table 1 can be misleading chiefly because of two reasons: Firstly, the FVTD algorithm requires fewer cells per wavelength than the FDTD algorithm [12]. Secondly, the curvilinear nature of the FVTD grid requires far less cells in the computational domain than is required by the stair-stepped Cartesian grid needed for the FDTD algorithm. Table 2 shows the number of grid points required by the two algorithms to adequately resolve the scattering wave patterns for an ogive shaped target [15].

Table 2: Grid Point Comparison for the Ogive

Algorithm	Grid Dimensions	Total Grid Points
FDTD	$400 \times 100 \times 100$	4 Million
FVTD	$200 \times 31 \times 32$	198,400

Here, it can be clearly seen that approximately 20 times more grid cells are required by the FDTD algorithm over the FVTD algorithm. This shows that even though the FDTD algorithm is much faster than the FVTD algorithm , it may not be that attractive in the overall scheme of things.

5 Results

One of the most important EMCC benchmark targets is the NASA almond. It is important partly, because of the nature of its geometry and, because it remains one of the more difficult bodies for which to procure an accurate RCS. Looking at it from a cross-sectional view, it resembles a circular-arc airfoil. However, it has a finite thickness that is rapidly varying in the spanwise direction. This makes it rather difficult to grid using a standard grid generator. The almond is 9.936 inches long and it's geometrical specifications are defined in [18]. A sinusoidal clustering of grid points was used along the rotational direction. The clustering was necessary to avoid getting high aspect ratio cells. Since an O-H type grid was desired, an axis of symmetry was added to the almond that extended from the leading and trailing edges of the almond to the outer boundaries at both ends (figure 2). Along each equiangular curve of surface points a standard grid generator, HYPGEN [19], was used to create a planar grid. All the planar grids were then combined to obtain a fully three-dimensional grid (figure 3). Two grids were employed for all the cases run for the almond. One of the grids has 198 x 20 x 57 grid points and the other consists of 198 x 45 x 57 grid points. One-dimensional domain decomposition was employed in all cases along the longest

dimension. The computational domain was spread across 7 processors equally on the IBM SP-2. The far zone integration surface was defined six cells away from the surface of the almond. Due to the nature of the grid used for this test case, odd-even decoupling was observed. It was suppressed by adding fourth order artificial dissipation, as previously discussed in Section 3. Scattering from the almond was investigated for all angles of incidence from 0 degrees to a 180 degrees at intervals of 15 degrees at a frequency of 1.19 GHz.

The monostatic RCS computed was compared to experimental results obtained for Vertical/Vertical polarization by Woo et al [18]. For experimental measurements the metallic almond target was made out of aluminium. The experimental results have been plotted by sweeping through the rotational ϕ direction at 5 degree intervals. A comparison of the FVTD and experimental results is compared in figure 4. Each FVTD point in figure 4 represents a complete FVTD run for the angle of incidence represented by ϕ on the abcissa scale. The FVTD computational results are in very good agreement with the experimental observations and are mostly within a 2 db agreement margin at all angles except those at 45 degrees and 135 degrees where the algorithm seems to underpredict and overpredict the measured RCS respectively.

The steady state or time harmonic scattered E_z field solution for nose on incidence at 3Ghz is shown in figure 5 for both planes parallel and perpendicular to the direction of polarization.

5.1 Scattering from a trapezoidal wing

One of the main contributors to aircraft RCS is the scattering from the leading edge of wings [20]. The radar returns from wings are important for normal and near-normal incidence. In order to gain some qualitative insight into the scattering from wings a perfectly conducting wing was chosen as the next target for investigation. The wing used in this case is the trapezoidal Lockheed Wing-C [22] with camber and twist. The purpose of this test case was three-fold. Firstly to demonstrate the ability of the algorithm to tackle realistic three-dimensional configurations. Secondly, to evaluate the robustness of the dual grid based algorithm in working with different types of grids, in particular a C-H based grid system with a split line extending from the trailing edge of the wing to the outer boundary. Lastly, to get a qualitative perspective into the mechanism of scattering at normal incidence for the wing.

The grid pertaining to a single zone of the wing is depicted in figure 6. Ghost points pertaining to the magnetic field were introduced to solve for the electric field points that lie on the split line between the trailing edge and the outer boundary. The grid consisted of a 109 x 42 x 146 grid points. It was generated using PACMAPS, which is part of the TEAM (Three-Dimensional Euler/Navier-Stokes Aerodynamic Method) [21]. Since the grid is designed to simulate steady state aerodynamic problems it has some limitations that restrict its feasibility for time dependent electromagnetic problems. The grid cells at the pinch that is introduced to close the grid at the wing tip are extremely small, thereby making the time step extremely small. This makes evaluation of RCS at realistic frequencies a very time consuming process requiring hundreds of thousands of time steps. However, the grid can still be used to obtain qualitative scattered field patterns.

Domain decomposition is performed along the largest dimension. A wideband Gaussian pulse is incident on the leading edge of the wing. The incident field is linearly polarized along the z-direction and the direction of propagation is one of forward incidence to the wing. Figure 7 shows the scattered field along various cross-sections of a part of the wing. Electric field continuity is maintained along the split line, thereby showing that the dual grid did not create any unnecessary problems in treating grid configurations of this type. Figure 8 depicts the intensity of the H_y field component of the magnetic field along the various cross-sections of the dual grid of a section of the wing. Both figures are indicative of the fact that the primary scattering effects take place normal to the planform of the wing as scattered field patterns do not show a significant difference along the different planes in the spanwise direction. Next a sinusoidal excitation was used with exactly the same polarization and incidence as the Gaussian excitation. The scattered field E_z and H_y patterns are shown in figures 9 and 10.

5.2 Scattering from an engine inlet

Since the wing, fuselage and engine are important parts of any aircraft configuration the last test case pertains to an aircraft engine. In this case an engine inlet was used as the scatterer. The center body, and the engine cowl are treated as perfectly conducting. The fan section was also treated as a closed PEC boundary. This seems to be a reasonable approximation when using wavelengths that are large compared to the inner annulus height. Figure 11 depicts a planar slice of the grid [23] that was used in this case. It consists of 242 x 40 x 65 grid points. Since

one dimension is considerably larger than the other two dimensions, one-dimensional domain decomposition was utilized along the primary direction for parallelization purposes. As is evident outside the cowl this grid is rather coarse. This grid has been used in the solution of aeroacoustics and aerodynamic type problems. However, there are certain limitations when the grid is used to solve for electromagnetic fields. Low frequency excitations would lead to the formations of creeping waves, that would not be captured as the grid does not completely enclose the engine. High frequency excitation, on the other hand would be difficult to resolve as one moves away from the inlet and the center body. A sinusoidal excitation of 500 Mhz was used in this case. Compared to the diameter of the inlet cowl and the grid used, this excitation is to be high frequency. The incident wave travels along the axial direction of the engine and is linearly polarized along the transverse direction. Figure 12 shows the scattered E_z field pattern along a planar slice of the grid. The scattered field pattern is clearly seen close to the center body and around the inlet. Beyond that the grid is very course and the disturbance appears to be damped. There appear to be strong interference effects from within the cavity between the center body and the shroud, and within the cavity between the center body and the shroud, and currents seem to oscillate back and forth between the center body and the fan.

6 Conclusions and Future Work

A time domain algorithm has been presented to solve Maxwell's equations over generic body conformal grids for three dimensional geometries. The dual nature of Maxwell's equations are well exploited in that the algorithm uses a dual mesh. The staggered nature of the algorithm gives it better dispersion and dissipation characteristics. With a second order staggered scheme resolution normally provided by fourth order non-staggered schemes can be obtained. In most cases, the dissipation provided by the grid staggering precludes the need to explicitly add any artificial dissipation. The message passing approach provided more control and flexibility in distributing data over the computational resource and load balancing. The far field transformation too, was better suited to a message passing environment. The dual nature of the grid aided in parallelization, since only one of the fields had to be communicated between processors. Comparisons of results obtained for scattering from the almond are in good agreement with experimental observations. Simulations for the engine inlet and the wing demonstrate the capability of handling complex configurations.

References

[1] Yee, K.S., "Numerical Solution of Initial Boundary Value Problems Involving Maxwell's Equations in Isotropic Media", *IEEE Transactions on Antennas and Propagation* Vol. AP-14, No. 3, May 1966.

[2] Holland, R., "Pitfalls of staircase Meshing", *IEEE Transactions in Electromagnetic Compatibility* Vol. 38 No. 12, 1993.

[3] Goorjian, P.M., "Algorithm Development for Maxwell's Equations for Computational Electromagnetism", AIAA Paper 90-0251, Reno, Nevada, Jan 1990.

[4] Kunz, K.S., and Luebbers, L.J., "The Finite-difference Time Domain Method for Electromagnetics", CRC Press, 1993.

[5] Shankar, V., "A Gigaflop Performance Algorithm for Solving Maxwell's Equations of Electromagnetics", AIAA Paper 91-1578, Honolulu, June 1991.

[6] Noack, R.W. and Anderson, D.A., "Time Domain Solutions of Maxwell's Equations Using a Finite Volume Formulation", AIAA Paper 92-0451, Reno, Nevada, Jan 1992.

[7] Madsen, N.K., and Ziolkowski, R.W., "A Three-Dimensional Modified Finite Volume Technique for Maxwell's Equations", *Electromagnetics* Vol 10, pp 147-161, 1990.

[8] Shostko, A., "Three Dimensional Parallel Unstructured Grid Generation", AIAA Paper 94-0418, Reno, Nevada, Jan 1994.

[9] Lohner, R., and Parikh, P., "Three Dimensional Grid Generation by the Advancing Front Method", *Int Journal of Numerical Methods in Fluids* No. 8, 1988.

[10] Weinberg, Z. and Long L.N., "A Massively Parallel Solution of the Three Dimensional Navier-Stokes Equations on Unstructured Adaptive Grids", AIAA Paper 94-0760, Reno, Nevada, Jan 1994.

[11] Barth, T.J., and Jespersen, D.C., "The Design and Application of Upwind Schemes on Unstructured Meshes", AIAA Paper 89-0366, Reno, Nevada, Jan 1989.

[12] Ahuja, V., "A Finite Volume Time Domain Method For Maxwell's Equations on Parallel Computers", PHD Dissertation, The Pennsylvania State University, 1995.

[13] Vichnevetsky, R., "Wave Propagation Analysis of Difference Schemes For Hyperbolic Equations: A Review", *International Journal For Numerical Methods in Fluids*, Vol 7, 1987.

[14] Jameson, A., Schmidt, W., and Turkel, E., "Numerical Solutions of the Euler Equations by Finite Volume Methods Using Runge-Kutta Time-Stepping Schemes", AIAA Paper 81-1259, Palo Alto, California, June 1981.

[15] Ahuja, V., and Long, L.N., "A FVTD Algorithm for Maxwell's Equations on Massively Parallel Machines", ACES, Monterey, California, March 1995.

[16] Ahuja, V., and Long, L.N., "A Message Passing Finite Volume Algorithm for Maxwell's Equations on Parallel Machines", AIAA Paper 95-1967, San Diego, California, June 1995.

[17] Luebbers, R.J., Kunz, K.S., Schneider, M. and Hunsberger, F., "A Finite-Difference Time-Domain Near Zone to Far Zone Transformation", *IEEE Transactions on Antennas and Propagation*, Vol 39, No. 4, April 1991.

[18] Woo, A.C., Wang, H.T.G., and Schuh, M.J., "Benchmark Radar Targets for the Validation of Computational Electromagnetics Programs", *IEEE Antennas and Propagation Magazine* Vol 35, No. 1, 1993

[19] Chan, W.M., "User Guide for Hypgen - Version 1.3", 1993.

[20] Fuhs, A.E., "Radar Cross Section Lectures", American Institute of Aeronautics and Astronautics, 1988.

[21] Raj, P., Sikora, J.S., and Olling, C.R., "Three-dimensional Euler/Navier-Stokes Aerodynamic Method", Technical Report AFWAL-TR-87-307, 1989.

[22] Long, L. N., Khan, M. M. S., and Sharp, H. T., "Massively Parallel Three-Dimensional Euler/Navier-Stokes Method", *AIAA Journal* Vol 29, No. 5, 1991.

[23] Ozyoruk, Y., and Long, L. N., "A new efficient algorithm for computational aeroacoustics on parallel computers", *Journal of Computational Physics*, to appear, 1996.

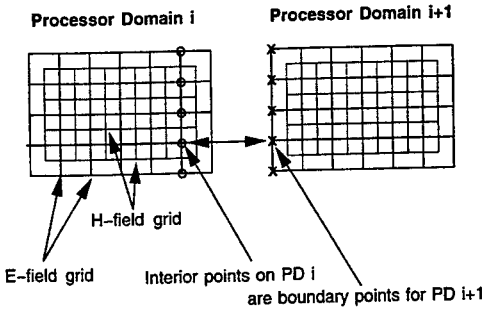

Figure 1 Processor Domain Decomposition.

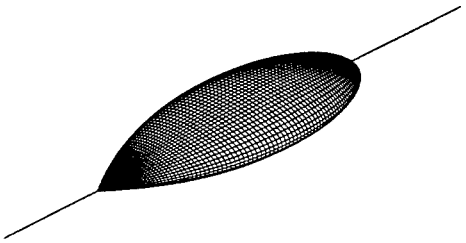

Figure 2 Surface grid for the NASA almond.

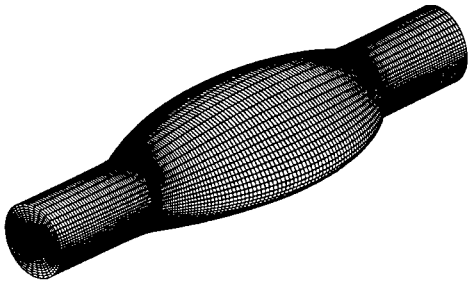

Figure 3 Outer grid for the NASA almond.

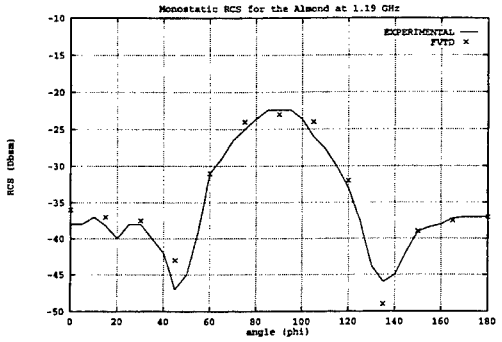

Figure 4 RCS for the NASA almond - VV Polarization.

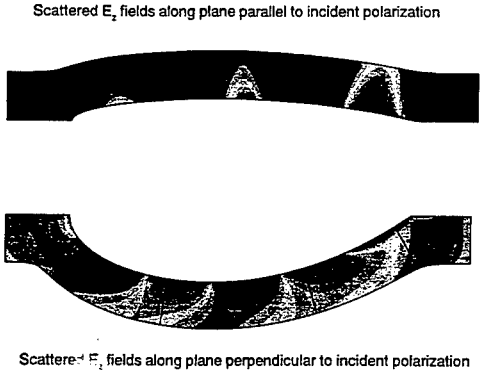

Figure 5 Scattered E_z fields for the almond at 3 GHz.

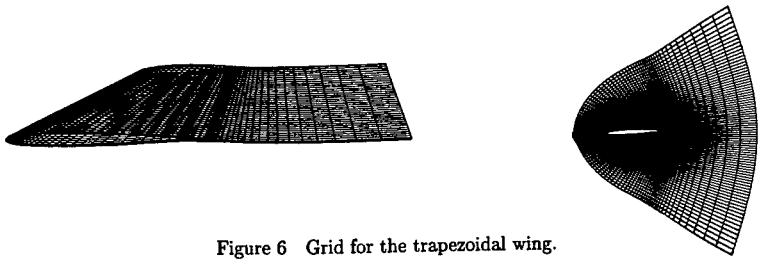

Figure 6 Grid for the trapezoidal wing.

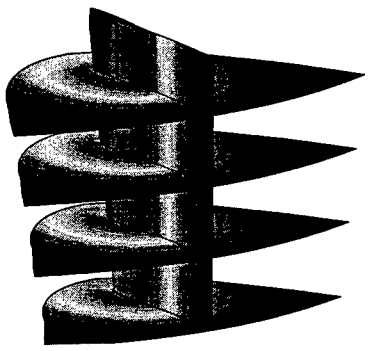

Figure 7 Scattered E_z fields for the trapezoidal wing.

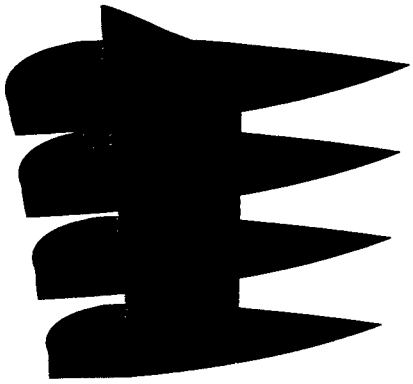

Figure 8 Scattered H_y fields for the trapezoidal wing.

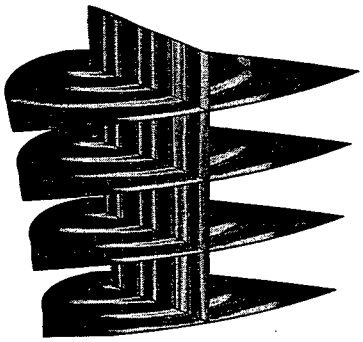

Figure 9 Scattered E_z fields for the trapezoidal wing.

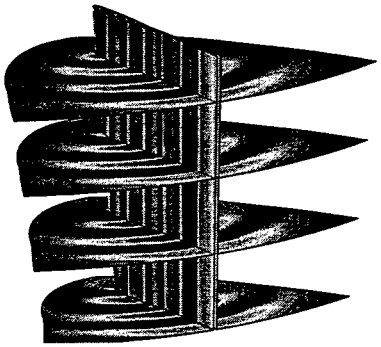

Figure 10 Scattered H_y fields for the trapezoidal wing.

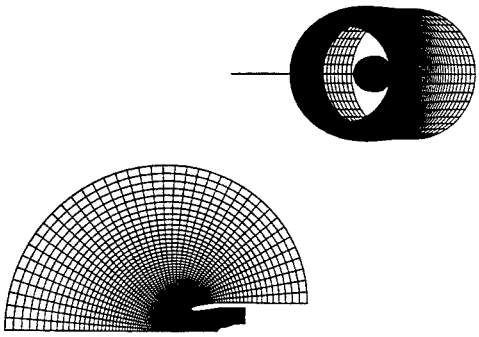

Figure 11 Grid for the Engine Inlet.

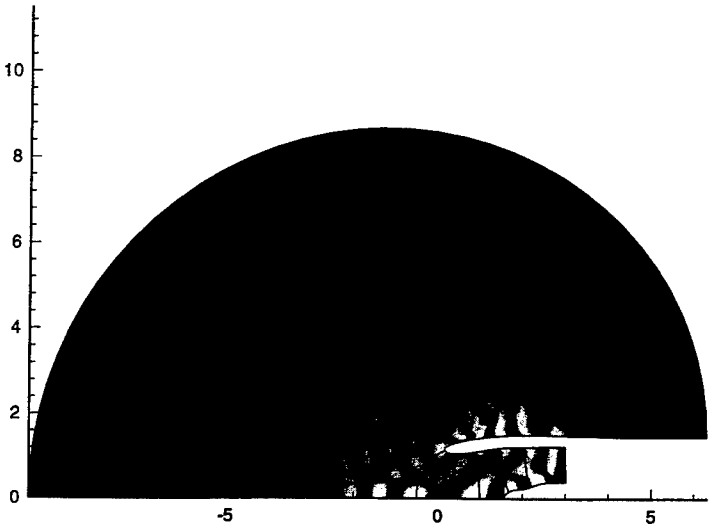

Figure 12 Scattered E_z fields for a planar slice of the inlet.

FDTD Simulation of High Frequency Devices by Using Locally Refined Meshes

P.Thoma and T.Weiland

Technische Hochschule Darmstadt, FB 18, FG TEMF,
Schloßgartenstr. 8, D-64289 Darmstadt, Germany

Abstract

The Finite Difference Time Domain method (FDTD) has become a valuable tool for analyzing practical high frequency devices. However, complex structures often require large computer resources for the simulations especially when an automatic structure optimization is performed. In many cases locally refined meshes can help to reduce the computational cost to acceptable sizes. In this paper a subgridding extension is presented where special care is taken on the stability of the numerical algorithm. The accuracy and dispersion of the method are studied by regarding simple test examples before the practical applicability is demonstrated by computing the scattering parameters of a microstrip structure.

1. Introduction

The simulation of high frequency devices by using the Finite Difference Time Domain (FDTD) method has become of increasing importance during the last decade [1,4,5]. The major advantage of this method in comparison to many other popular ones is the enormous flexibility combined with a large numerical efficiency. However, the application of plain FDTD methods shows some restrictions arising from limited computer resources. To circumvent these problems many researchers have successfully introduced special features into the basic algorithm in order to make the method more applicable to realistic problems (e.g. thin wire models, incorporation of static field solutions, narrow slot models, lumped circuit element models, etc.) [4-9].

Many practical structures, especially those containing small important details, still require large amounts of mesh cells for accurate discretizations. In many cases the number of cells can be reduced by introducing a sequence of locally refined meshes into the base mesh. Some so called subgridding schemes have already been presented in the past, but among our knowledge none of these schemes actually keeps all the important properties of the FDTD method namely stability and convergence (e.g. [10]). In this paper we will present a consistent subgridding extension where convergence and stability can be proven for the discrete system.

The basis of our formulation is the integral form of the discretized Maxwells equations which is given by the Finite Integration (FI) method [2,3]. In time domain both FDTD and FI methods finally lead to the same algorithm although they use different derivations of the fundamental equations.

Based on the integral formulation, we start with pointing out the important properties of the FI method. These properties manifest in the existence of *curl* and *source* matrices in grid and dual grid which fulfill a set of important relations. Focusing on these properties we then derive a consistent subgridding scheme which is fully "compatible" with FDTD. Due to this systematic approach, the method can also be applied to a special FI based Finite Difference Frequency Domain method.

After proposing the method for FDTD we study numerical dispersion and stability by regarding some simple test examples. Finally we show the application of the scheme to a practical microstrip scattering parameter problem by performing a computation involving several subgrids.

2. The Method

The Finite Integration Technique (FIT) transforms Maxwells equations and the corresponding material relations into discrete matrix equations from an integral oriented point of view. The electric voltage and the magnetic flux are both allocated on a grid; the electric flux and magnetic voltage are allocated on a dual grid. The correspondence between both grids is given by the discrete material relations. In time domain the method finally yields the following system of equations [2,3]:

$$C\,e = -\partial b/\partial t \tag{1}$$
$$\tilde{C}\,h = \partial d/\partial t + j \tag{2}$$
$$\tilde{S}\,d = q \tag{3}$$
$$S\,b = 0 \tag{4}$$
$$d = D_\epsilon\,e \tag{5}$$
$$b = D_\mu\,h \tag{6}$$

where e, d and h, b represent electric and magnetic voltage and flux values in grid and dual grid, respectively. The diagonal matrices D_ϵ and D_μ contain averaged material properties and mesh dimensions. The so called *curl* and *source* matrices are describing the topology of grid (S, C) and dual grid $(\tilde{S}, \tilde{C})$.

It can be shown that for the curl and source matrices the following properties hold:

$$S\,C = 0 \tag{7}$$
$$\tilde{S}\,\tilde{C} = 0 \tag{8}$$
$$C = \tilde{C}^T \quad . \tag{9}$$

These properties are essential for stability (thus energy conservation) and divergence conservation of the discrete system.

When introducing subgrids into the base computation mesh, the common set of equations can be applied inside each grid. Modifications are necessary at the transition planes of mesh and submesh. Fig.(1) shows the coupling scheme between the field components in base mesh to the components in submesh and vice versa.

The relation $C = \tilde{C}^T$ implies that the coupling factor of a magnetic voltage to an electric flux component must be equal to the coupling factor between the corresponding electric voltage and magnetic flux. It can be shown that for this scheme modified source matrices exist which fulfill $SC = 0$ and $\tilde{S}\tilde{C} = 0$.

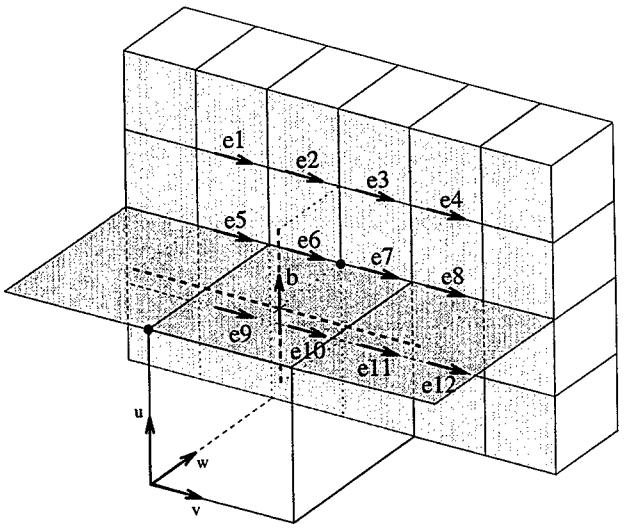

Figure 1: The picture shows the coupling between a base mesh magnetic flux component and submesh electric voltage components at the transition plane. We use linear interpolation of the tangential magnetic voltage in base mesh to the tangential electric flux at submesh boundary. It is essential to use the same coupling coefficients for e, b and h, d, respectively.

The transversal termination of the transition plane between mesh and submesh requires a shift of the dual mesh nodes in submesh next to the transition plane onto their neighbouring mesh nodes inside submesh. Perfect conducting materials crossing the transition plane also require a modification of the coupling scheme. It can be shown that for all these modifications the scheme is still consistent.

The time integration can be performed by using a modified leap frog scheme [1]. Two time steps are performed inside the submesh during one field updating cycle in base mesh. The time step width is limited by the well known Courant criteria. Due to the modification of the dual mesh at the termination of the transition plane, the time step width has to be reduced once by a factor of two when subgrids are present. The updating scheme becomes recursive when subgrids contain subgrids again.

3. EXAMPLES

The numerical dispersion of the FDTD method due to the finite discretization step width causes reflections at the transition of different mesh step sizes. In practical computations the reflections can be reduced to sufficiently low values when using about twenty mesh steps per wavelength. In the following investigations we will study the reflections by regarding two test structures which have been discretized by using quite coarse meshes with about fifteen steps per wavelength.

The first test structure consist of a rectangular waveguide being fed at one port with the fundamental H_{10} mode at a frequency of f=6 GHz. The waveguide cross section dimensions are 0.9in x 0.4in. The input reflection is calculated by using a high performance open boundary operator [12].

The second test example is derived from the first one by adding a conductor along the axis of the waveguide. This waveguide is fed by a 3.3 GHz TEM mode at one port for which the input reflection is computed.

For each of the test structures three computations are performed by using 1) an uniform mesh, 2) a graded mesh with ratio 1:2, 3) a submesh inside the base mesh. Fig.(2) shows the test structures and the different discretizations. The results for the input reflection are compared in the following table:

Mode	uniform mesh	graded mesh (1:2)	submesh
H_{10}	-122 dB	-37 dB	-34 dB
TEM	-107 dB	-37 dB	-27 dB

The reflections for the H_{10} mode are in the same order of magnitude when using non-uniform meshes and submeshes, respectively. The reflections at the mesh to submesh transition are larger for the TEM mode than for the H_{10} mode. This effect is caused by the dependence of the transversal mode pattern (and thus wave impedance) on the transversal discretization step width around the edges of the inner conductor. Reducing these reflections by using a edge correction model is currently under development [9].

The numerical stability of the algorithm is tested by performing about 100,000 time steps for a loss free resonator structure. The resonator is derived from the second test structure by terminating the waveguide at the ports with perfect conducting planes. The fields are excited by a dipole stimulation using a very short gaussian pulse. Fig. (3) shows the time signal of an electric field component inside the resonator. A violation of the energy conservation would cause an increase or decrease of the electric field amplitude versus time.

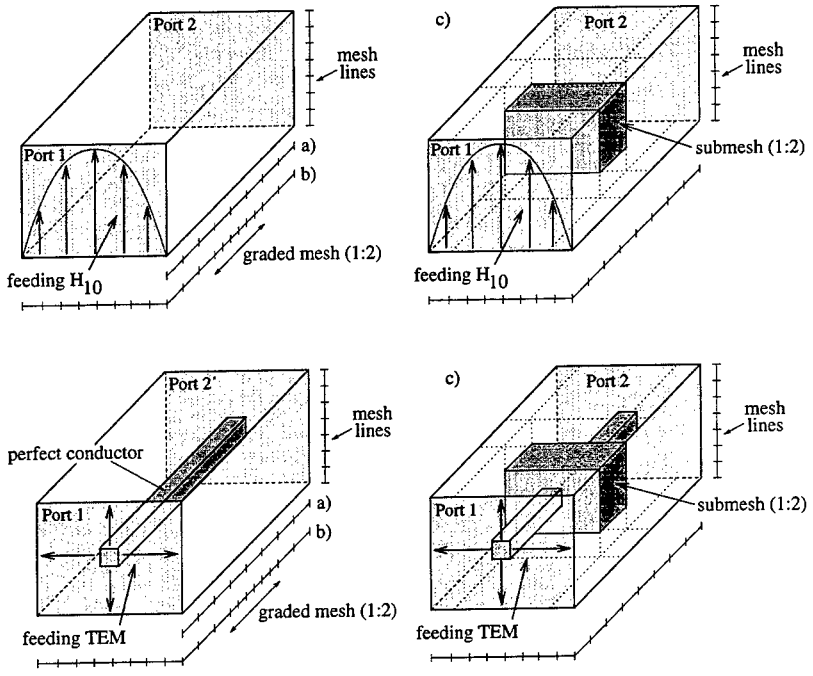

Figure 2: *This picture shows the two test structures used for investigating numerical reflections of the method. For each structure three computations have been performed by using different discretizations.*

The next example is given by a practical microstrip phase shifter, see Fig.(4) [13]. There are two important areas which require fine discretizations in this structure:

1) The small widths of the stubs require a fine discretization to properly resolve the field variations around the edges.

2) The transition of strip lines with different widths causes heavy field variations due to the behavior of the surface current.

For this filter the scattering parameters have been computed and the phase of the transition coefficient has been compared with measurement. Three different discretizations have been studied: 1) a non uniform base mesh, 2) an additional subgrid around the stubs, 3) additional subgrids around the stripline transitions. The discretizations are shown in Fig.(5). The results for the phase of the

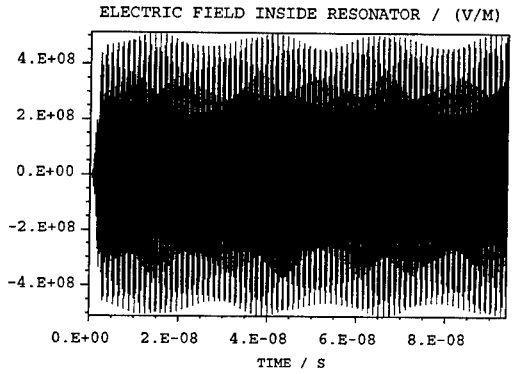

Figure 3: *The numerical stability is investigated by calculating the resonant fields in a loss free resonant structure. This plot shows a component of the electric field versus time for about 100,000 time steps. No unstable high frequency oscillations arise.*

Figure 4: *The microstrip phase shifter consists of a stripline transition with two stubs. One stub is open ended, the other one is terminated by a via interconnect structure. The scattering parameters are computed and the phase of the transition coefficient is compared with measurement.*

transition coefficient are compared in Tab.(1). It turns out that a very good agreement between measurement and simulation can be achieved by encapsulating all important structure details in subgrids. The computation time increases from about 15 minutes on a SUN-SPARCSTATION 20 without subgrids to 40 minutes with subgrid 1 up to 60 minutes with all subgrids.

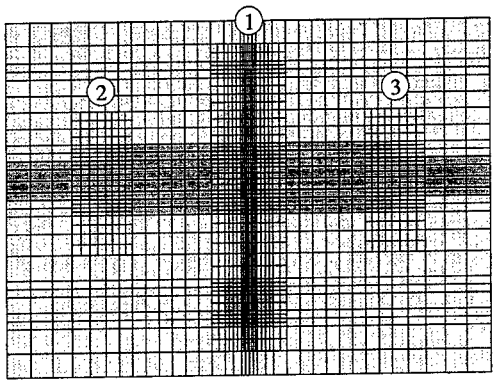

Figure 5: *The filter structure has been discretized by using up to three subgrids inside the base mesh. Important areas in this structure are the stubs and the transitions of strip lines with different widths.*

Frequency / GHz	base mesh	subgrid 1	subgrid 1-3	measured
6	-64.33	-65.34	-63.82	-63.54
9	-127.09	-127.248	-125.57	-124.28
12	-184.17	-183.86	-181.48	-179.76
15	-241.55	-239.79	-237.49	-237.29
18	-312.79	-305.39	-301.35	-301.22

Table 1: *The table shows a comparison of the transmission coefficient phase in degrees obtained for different discretizations and measurement [13]. The agreement between simulation and measurement becomes better when important structure details are encapsulated in subgrids.*

4. Conclusions

In this paper a consistent subgridding extension for the FDTD method has been presented. It has been shown that numerical reflections at the transition planes between mesh and submesh are in the same order of magnitude as those which arise from using non uniform grids. The practical application of the proposed scheme has been demonstrated by calculating the scattering parameters for a typical microstrip structure. The computed results for the phase of the transmission coefficient are in very good agreement with measurement.

REFERENCES

[1] K.S. Yee: *Numerical solution of initial boundary value problems involving Maxwell's Equations in isotropic media.* IEEE Transactions on antennas and propagation, vol. 17, 1966, p 585-589.

[2] T. Weiland: *A Discretization Method for the Solution of Maxwells Equations for Six-Component Fields.* Electronics and Communication (AEÜ), vol. 31, 1977, pp 116.

[3] T. Weiland: *On the unique numerical solution of Maxwellian eigenvalue problems in three dimensions.* Particle accelerators, vol. 17, 1985, p 227-242.

[4] K.S. Kunz, R.J. Luebbers: *The Finite Difference Time Domain method for electromagnetics.* CRC Press, 1992, p 194-201.

[5] A. Taflove: *Computational Electrodynamics: The Finite Difference Time Domain Method*, Artech House, 1995.

[6] A. Taflove, K.R. Umashankar, B. Beker, F. Harfoush, K.S. Yee: *Detailed FD-TD Analysis of Electromagnetic Fields Penetrating Narrow Slots and Lapped Joints in Thick Conducting Screens.* IEEE Transactions on Antennas and Propagation, 1988, p 247-257.

[7] J.G. Maloney, G.S. Smith: *The Efficient Modeling of Thin Material Sheets in the Finite-Difference Time-Domain (FDTD) Method.* IEEE Transactions on Antennas and Propagation, vol. 40, 1990, p 323-330.

[8] C. Railton: *The Simple Rigorous and Effective Treatment of Thin Wires and Slots in the FDTD Method.* 24th European Microwave Conference, 1994, p 1541-1546.

[9] D.B. Shorthouse, C.J. Railton: *The Incorporation of Static Field Solutions Into the Finite Difference Time Domain Algorithm*, IEEE MTT, 1992, p 986-994.

[10] S.S. Zivanovic, K.S. Yee: *A subgridding method for the Time Domain Finite Difference method to solve Maxwells Equations.* MTT, 1991, p 471-479.

[11] P. Thoma, T. Weiland: *A consistent subgridding scheme for the Finite Difference Time Domain method*, International Journal of Numerical Modelling, accepted for publication.

[12] M. Dohlus, P. Thoma, T. Weiland: *Broadband simulation of open waveguide boundaries within large frequency ranges*, IEEE MTT, submitted for publication

[13] *Microwave Engineering Europe*, Miller Freeman Technical Ltd., November 1994, p 11-21.

SESSION 20:

NUMERICAL ERROR ANALYSIS AND CONTROL II

Chair: J. Volakis

A WWW-Based Data Base for Code Validation

C.W. Trueman
Electromagnetic Compatibility Laboratory
Concordia University
Montreal, Quebec, Canada

S.R. Mishra
David Florida Laboratory
Canadian Space Agency
Ottawa, Ontario, Canada

Abstract- Code validation compares computed results against reference data, such as measurements, to demonstrate the degree of agreement obtainable for a given problem with a particular computational electromagnetics code. By solving many problems we can explore and document the code's strengths and limitations. The result is "modeling guidelines" for constructing input geometries which the code can solve accurately, and specifying restrictions on input geometry to avoid cases that the code cannot solve reliably. Such guidelines advise the user on how to wield the code effectively and on what pitfalls to avoid. The user of a computational electromagnetics code may want to review the code-validation studies supporting the code, both to assess the code's accuracy and to learn how to construct good input geometries. However, those studies may not be readily available in the manuals or in the literature.

The David Florida Laboratory RCS Data Base is at present an extensive collection of measured RCS data available on the world-wide web for code-validation purposes. The purpose of this paper is to extend the data base by adding computations done with various computer codes, for comparison with the measured data. Code developers and those using computational electromagnetics codes are invited to contribute computations to the data base. The data base can serve as a library of code-validation problems solved with a given code. Further if one problem is solved with several codes, their accuracy can be compared readily. The data base may thus become a rich source of information about the capabilities of the various computer codes available today.

Introduction

Code validation is the testing of a computational electromagnetics(CEM) computer code to assess the accuracy to which the code solves reference problems which have reliably-known solutions[1,2]. When a new CEM code is written or an existing code is modified for better performance, the developer solves reference problems to demonstrate the accuracy of the new code and compares it with other methods in computational electromagnetics. The code developer builds a modest "experience base" of problems solved with the new code, and in doing so inevitably formulates rules, called "modeling guidelines" for using the code effectively. The developer publishes a "user's guide" which states the modeling guidelines, and gives input data and results for simple problems, to serve as a tutorial in using the code[3,4]. In addition the developer may publish one or more papers describing how the code performs for more complex problems. The code is then released into the community.

To solve a new problem with the CEM code, the user must construct a discretization of the geometry, called a "computer model" or simply a "model". For example, in surface patch modeling[3] a continuously-curved surface must be replaced by planar triangular patches leading to a faceted

discretization. A new user of a CEM code must learn to construct good discretizations. This often starts with "running" the sample problems in the "user's guide", as a confidence check both that the code is implemented correctly on the user's hardware, and that the user understands the details of supplying input geometry data to the code. The next step the user takes often consists of carrying out his own "code validation" for the CEM code. This consists of solving some problems of special interest in his area of application, for which he has reliable reference data. This is the user's first exercise in constructing discretizations for problems not in the user's guide. The user judges the accuracy of the CEM code in comparison his reference results, either measured or computed by other methods. Now the user is ready to try to wield the code as a tool to solve new problems.

A community of users who carry out code validation for a CEM code for their own purposes greatly expands the "experience base" of validation problems that have been solved with code. But this "experience base" is not collected in a single location and so is not readily accessible because it is distributed among many individuals. Some of these applications are published as conference papers or journal articles, and then contribute to the published experience base, available to all. The aggregate of everyone's experiences testing a given code, that is, the community's experience base, is always much larger than the published experience base.

The purpose of this paper is to introduce a means of sharing code validation studies freely by taking advantage of the world-wide web(WWW). At the David Florida Laboratory of the Canadian Space Agency, a series of measurements were carried out for the purpose of code validation[5]. In order to make this extensive collection of measured RCS data available to the community, the "DFL Code-Validation RCS Data Base"[6] was set up to permit users on the web to browse through a list of the available results and to copy those of interest to them. This paper extends the DFL RCS Data Base to become a hub for the posting and exchange of code validation results, both measured and computed. This paper describes the various purposes of the DFL RCS Data Base, and how it can serve various needs of the user community. We will review the purposes of "code validation" and the nature of the certification it bestows on a CEM code. The paper will describe how the DFL RCS Data Base might improve the community's confidence in the available CEM methods.

The Purposes of Code Validation

All methods in CEM make simplifying assumptions in their formulation, and none satisfy their boundary conditions exactly. Hence none provide an exact solution to a given problem. Though some methods can display the error incurred in satisfying the boundary conditions point-by-point on the surface, this is not easily correlated with the error in, for example, the radar cross-section. Few methods provide an estimate of the overall accuracy expected of the results. The user must be able to assess the accuracy of the approximate solution that the code generates for the problem at hand. The first purpose of code validation is to document the code's accuracy by comparing results for specific problems with measured or other reference data to display the degree of agreement. This "certifies" the code's accuracy for the classes of problem for which it has been tested.

All CEM codes require that the actual geometry be simplified to obtain a "model" of the geometry which the code is capable of solving. The model determines how the code will enforce the boundary conditions. Finite-difference or finite-element methods subdivide three-dimensional space into elements and assign material types to the elements; changes in material type from element to

element determine the location of the surfaces of the object hence determine where the boundary conditions will be enforced. Moment methods usually determine current flow or equivalent current flow on the surfaces of the object; hence the surface is directly subdivided into elements. All discretizations are limited in bandwidth, specified as rules governing the element size compared to the wavelength.

Few codes can solve any arbitrary collection of elements that the user might assemble. Knowing the assumptions, both mathematical and numerical, that were made in formulating the code suggests possible limitations. The code developer must explore and document geometrical limitations on the model, required to ensure the validity of assumptions , approximations, and simplifications made in formulating the code. The second purpose of code validation is to convey this information to the user, in the form of "modeling guidelines" to aid in the construction of discretizations for solution by the code. These must include guidelines for good practice in building a model that does not infringe on the code's limitations, and specific rules for identifying constructions that do violate these limitations and so may not be solved accurately by the code.

Modeling Guidelines

Modeling guidelines are the result of solving a variety of problems with the code to explore the code's limitations. A given discretization might be solved over a considerable bandwidth, seeking the frequency limitations of the code. A geometry might be discretized in various ways and the results compared, to identify the best practice in assembling a model. Modeling guidelines have two purposes, namely to identify good practices in constructing discretizations, and to identify bad discretizations that the code cannot solve accurately. Modeling guidelines should provide "rules-of-thumb" for the user to follow in subdividing the geometry into elements leading to a model that does not infringe on the code's limitations. Conversely, modeling guidelines must explicitly identify constructions of elements which do infringe on the code's shortcomings and which are not expected to be accurately solved. When a code's modeling guidelines ignore limitations, the naive user may be misled into believing that the code can solve any geometry at all.

Modeling guidelines that identify specific constructions of elements that the CEM code cannot solve accurately can be built into an "integrity checker" program. An "integrity checker" first looks for gross errors in a model, such as duplicated elements, or elements that cross or overlap in ways not intended by the code developers. Then the integrity checker sorts through the model, and systematically verifies that the discretization complies with the "modeling guideline" limitations. For example, in wire-grid modeling using the "Numerical Electromagnetics Code"(NEC)[4], the modeling guidelines identify a variety of limitations. For example: the length of "segments" must be at least twice the wire radius; the ratio of the lengths of segments making up wire junctions must not greater than five; the ratio of the radii of segments at wire junctions should be less than ten; and so forth. These have been built into program CHECK[7] which identifies all transgressions of the modeling guidelines and allows the user to repair them before proceeding to run the NEC code to solve the problem. Systematic integrity checking improves the quality of the results obtained with the NEC code and would be useful for all CEM codes.

For an inexperienced user, clearly-written, informative modeling guidelines greatly increase the usefulness of a CEM code, providing rules for the construction of a good model, and spelling out the

limitations to help avoid building a bad model. Modeling guidelines are akin to "necessary" conditions that must be satisfied by the input geometry if it is to be correctly solved by the CEM code. However, modeling guidelines are not "sufficient" conditions that guarantee that the CEM code will solve the problem to a preset accuracy.

Reference Data for Code Validation

The Mie series[8] is an exact solution to the problem of scattering from a perfectly-conducting sphere or dielectric sphere and is frequently used generate reference data fort testing scattering codes. But few other geometries in three-dimensional radiation or scattering have a mathematically-exact solution. Approximate analytic solutions, such as those of King and Harrison for dipole antennas and crossed wires[9], are sometimes used to generate reference data for comparison with numerical computations, but when there is disagreement there is doubt about which solution is the correct one. Computed data obtained from a very different computational method is sometimes used as reference data for code validation. Most often measured data is used.

Measured data can never be regarded as "exact". The physical limitations of the measurement setup lead to measurement error. "Measurement validation"[2] is usually necessary to ensure that the data from the available measurement setup is sufficiently accurate to be useful for code validation. For example, RCS measurements for a standard target such as a metal cube might be compared with measurements done at other facilities. Good correspondence lends us confidence in the measured data from the same setup for other, similar targets. Another source of "measurement validation" data is computations. Agreement between measured data and results computed with a well-established CEM code lends considerable confidence to the measurement setup. An awareness that the measured data is not the "exact" solution is essential in assessing code validation comparisons.

Model Validation

Given a new problem in radiation or scattering, the engineer selects a suitable computational method, discretizes the geometry according to the modeling guidelines and restrictions, and computes the desired results. The engineer must assess the degree of confidence that can be placed in those results. Is the computed RCS accurate to within 3 dB or 1 dB? Is the resonant frequency accurate to one percent or one-tenth of one percent? CEM codes do not inherently provide a guarantee of the accuracy of a computation.

Recall that the first objective of code validation is to assess the accuracy of the code in solving standard geometries. The first axiom of "code validation" is that the accuracy attained in solving a new problem will be comparable to that for similar problems solved in the past. Thus our engineer should be able to consult the code validation results supporting the code, looking for a similar problem previously solved. But such code-validation studies are not often published comprehensively.

If no published code-validation comparison for a similar problem can be found, then "model validation" may be required to assess the accuracy of the computations. Also, because the accuracy of results with most CEM codes is dependent upon the details of the discretization, the sponsor may wish to carry out "model validation" to increase confidence in the accuracy of the results. A measurement

program is set up, in which a suitable physical model is built and measured data are acquired, and compared with the computations. Often, both the details of the discretization and the details of the measurement procedure can be adjusted to iron out shortcomings. Good agreement between computations and measurements greatly increases the confidence that can be placed in both. Once model validation is done for, say, an aircraft with certain HF wire antennas, then the computer model can be used with confidence for other configurations of wire antennas, without further model validation. If another, similar aircraft must be studied, we would expect a similar discretization to obtain comparable accuracy, and so model validation might not be required for the new aircraft type.

Model validation is in fact further code validation carried out independently by the user community, and broadens the experience base for that CEM code. Regrettably, such applications are rarely published, either because the results are proprietary or classified, or because they are thought to be of no interest to the community. More and better-documented case studies add to the confidence that can be placed in a given CEM code.

Traceable Code Validation

Ideally, we should be able to examine the evidence supporting the claim that a given CEM code is a useful tool. We might consider that comparisons of the results obtained with the code with exact mathematical results to be the best evidence, and with measured results to be almost as good. These are "primary standards". Comparing computed results with those obtained by from another CEM code is a "secondary standard" because we are relying on the accuracy of that code, presumably established against primary standards in the past. In practice it is difficult to obtain comprehensive code-validation information for any CEM code. Hence the need of users to do their own "code validation" and "model-validation" studies, to establish for their own purposes the accuracy that can be expected of a given CEM code. It is especially frustrating to try to obtain the numerical values of measured data that has been published in a code-validation study, only to be told that the data is no longer available, because it has be lost when some individual left the organization, or is written on a tape for a computer no longer operational.

The DFL RCS Data Base

The DFL RCS Data Base[6] is intended to streamline the process of establishing confidence in a given CEM code. The data base contains measured RCS data for a great many targets, from very simple strips and rods, to much more complex objects such as simplified aircraft and ship geometries. Users can download the numerical values of the measured data as needed. Code-developers thus have ready access to a library of measured RCS data for various targets for use in establishing the accuracy of a new code and in testing its limitations. Code users wishing to establish confidence in a given CEM code can obtain measured data for comparison with their own discretizations and computations using that code.

Further, users and developers are invited to contribute their computations and measurements to the data base. The intention is that a user wishing to examine the evidence supporting the accuracy of a certain CEM code can look into the DFL RCS Data Base and find computations with that code

compared with measurements for various targets, including the details of the discretization. This may save new users of a given CEM code the expense of extensive code-validation studies of their own, as such studies are readily available on the DFL RCS Data Base. Further, a new user can examine the details of the discretizations available on the data base to learn to build his own models effectively.

Another objective is to allow a user to compare the performance of various codes to choose the one most suitable for a given application. Thus, if a given target has been solved using a number of different CEM codes, the user can examine the RCS predicted by the various codes in relation to one another and to the measured RCS. If such comparisons are available for a variety of targets, the user has quick access to a comprehensive comparison of the performance of the various computational techniques available for that problem.

Those developing a CEM code may wish to use the DFL RCS Data Base to demonstrate their code's performance relative to other codes. By contributing data to the DFL RCS Data Base computed with their code for various problems, the capabilities of the code are exhibited, relative to other methods. Potential users shopping for a code can evaluate various codes one against the other.

Data Required for Each Problem

The DFL RCS Data Base[6] consists of a collection of target geometries, and the RCS for each as a function of frequency, for one, several or many angles of incidence. The RCS has been measured for most targets in a 6 by 6 by 6 m anechoic chamber by the method described in Ref. [5]. For each target a description of the geometry is given in sufficient detail to allow the user to construct a discretization for computation. RCS data for one or a few angles of incidence is given in an "rplot" file. RCS data for many angles of incidence is given in the form of a "table" file. A detailed description of these file formats is available on the database itself. The RCS data base provides graphing programs which can be downloaded to be executed on a PC computer . Program RPLOT is used to compare the measured and computed RCS as a function of frequency for a single angle of incidence. Program CPLOT is used to display the RCS as a color contour map as a function of frequency and incidence angle, in a rectangular-axis format. Program POLPLOT displays RCS as a polar-format color contour map, with the radial axis proportional to the frequency and the angle axis corresponding to the angle of incidence[10]. The polar format reveals intriguing patterns related to scattering centers such as edges and tips[11].

Contributing to the Data Base

A contribution to the DFL RCS Data Base has four parts: identification, problem, method and data. The contributor must identify himself or herself, with name, title, organization, and email address. The problem being addressed must be clearly identified, either as one already on the data base or as a new problem. The method used for solving the problem must be fully described. For computations, the contributor must identify which CEM technique and code was used, including references to the code's manuals, if available, and to the literature. The discretization of the target should be included in the submission so that users can examine it to learn how to create models for that code. Information about the computer resources that are required should include the disc space needed, the memory requirements, and the running time on a specific processor. Or, measured data can be submitted to the data base, including a description of the measurement facility and the instrumentation and methods

used. The target RCS must be supplied over the required frequency range in either "rplot" format for individual angles of incidence, or "table" format if many incidence angles have been computed to permit plotting a contour map. Detailed instructions for submission can be found on the data base itself. The user may not actually submit data to the DFL site, but instead might submit a pointer to his own computer on the web site where the data can be found as required by other users.

Users are invited to post new problems to the data base. It is our intention to expand the data base to include other catagories of problems than radar cross-section, and so new problems are not restricted to RCS computations. The problem geometry must be described in detail, including a drawing if required for clarity. Measured data is desirable if the problem is to be used as a reference for code validation, although computations alone can be posted as an invitation to others to solve the geometry with their code and compare with the results already posted.

Contributors to the DFL RCS Data Base are asked to agree to permit users to publish their data in comparison to other data for code validation purposes. Users of data from the DFL RCS Data Base are asked to acknowledge in their publications both the data base and the originator of data.

Conclusion

Although the community has a great deal of experience with certain techniques and computer codes in computational electromagnetics, specific comparisons between computed results and measurements for code validation are not readily available. Code manuals give few such comparisons and the user must search the literature for more. Most such comparisons are not published. The user wishing to assess the accuracy of a CEM code often carries out his own code-validation study. The DFL RCS Data Base is intended to make measured data for code validation readily available to all. Further, users are invited to contribute computations to the data base. Then at one central site, the user will find comparisons of measured results with computations by various CEM methods, and also comparisons for a given CEM method for various targets.

Those developing a new computational method may wish to post their results to the data base to arouse the community's interest, showing both the types of problem that the code can solve, and the accuracy of the results compared to other codes. For commercially-available codes there may be an advantage in displaying the code's capabilities in an open forum. Code users can search the data base to examine the community's experience base with a given CEM code, to discover its capabilities and limitations, and can look for problems similar to the one at hand to find suitable solution methods and assess the accuracy likely to be achieved.

If the community shows an interest in contributing to the DFL RCS Data Base, then in time the data base will provide a useful forum for comparing the relative performance of various computer codes for standard problems. The user looking for a code to solve a given problem can examine results obtained with various codes to identify that most suitable. The user looking for validation studies for a given code will find various problems solved with that code, and can assess the accuracy of that code, and perhaps compare his own computations for his discretization with those posted on the data base. The data base can thus serve as a valuable exchange for information about methods in computational electromagnetics. The DFL RCS Data Base can be found on the world wide web, at http://lucas.incen.doc.ca/rcs.html.

References

1. Applied Computational Electromagnetics Society Journal, Special Issue on Electromagnetics Computer Code Validation, 1989.
2. C.W. Trueman and S.R. Mishra, "Numerical Computation and Measurement: Building an Experience Base for Code Validation", invited paper, Latsis Symposium 1995 on Computational Electromagnetics, Zurich, Switzerland, Sept. 19-21, 1995.
3. D.R Wilton and S-U. Hwu, "Junction Code User's Manual-Electromagnetic Scattering and Radiation by Arbitrary Configurations of Conducting Bodies and Wires", Technical Report No. 87-18, Applied Electromagnetics Laboratory, Dept. of Electrical Engineering, University of Houston, May 30, 1989.
4. G.J. Burke and A.J. Poggio, "Numerical Electromagnetics Code - Method of Moments, Part III: User's Guide," Technical Document 116, Naval Electronic Systems Command(ELEX 3041), July, 1977.

5 S.R. Mishra, C.L. Larose and C.W. Trueman, "Precision Radar Cross-Section Measurements for Computer Code Validation", IEEE Trans. on Instrumentation and Measurement, Vol. 42, No. 2, pp. 179-185, April 19936. C.A. Balanis, "Advanced Engineering Electromagnetics", Wiley, New York, 1989.

6. S.R. Mishra, C.L. Larose, M. Flynn and C.W. Trueman, "A Database Program for Organization, Presentation and Distribution of Measured Antenna and RCS Pattern Data", 16th Meeting and Symposium, Antenna Measurement Techniques Association, Long Beach, California, Oct. 3-7, 1994.
7. C.W. Trueman and S.J. Kubina, "Verifying Wire-Grid Model Integrity with Program CHECK," Applied Computational Electromagnetics Society Journal, Vol. 5, No. 2, Winter, 1990, pp. 17-42.7. R.W.P. King and C.W. Harrison, "Antennas and Waves: A Modern Approach", The M.I.T. Press, Cambridge, Mass., 1969
8. C.A. Balanis, "Advanced Engineering Electromagnetics", Wiley, New York, 1989.
9. R.W.P. King and C.W. Harrison, "Antennas and Waves: A Modern Approach", The M.I.T. Press, Cambridge, Mass., 1969

10 C. L. Larose, S. R. Mishra, and C. W. Trueman, "Graphics for Visualizing RCS as a Function of Frequency and Angle," IEEE Antennas and Propagation Magazine, vol. 36, pp. 7-13, June 1994

11. C.L. Larose, S.R. Mishra, and C.W. Trueman, "Target Geometry Revealed from Polar Format RCS Contour Maps", submitted for consideration for publication in the ACES Journal.

Code Scaling

Michael J. Schuh and Alex C. Woo
NASA Ames Research Center
Mail Stop 237-2
Moffett Field, CA 94035-1000

Abstract

The order of an electromagnetics algorithm or code is defined by the rate at which the CPU time, $C_{cpu} = O(f^{\alpha})$, and memory, $C_m = O(f^{\beta})$, requirements grow with frequency. Knowledge of this information helps in the prediction of computer run times and memory requirements for problems of interest. This paper presents a methodology for determining the computational and memory orders of a code. These results are presented for a finite-volume time domain (FVTD) code and a methods-of-moment (MoM) code. Computer resource requirements are plotted for computer runs that calculate the bistatic radar cross section (RCS) for spheres of different electrical sizes within a set error level from the Mie-series solution. These plots are used to calculate the computational and memory orders of the codes.

Introduction

An important characteristic of an electromagnetics code is the rate at which the computational and memory requirements grow with the size of the electrical problem. Codes have often been characterized in terms of how the resources scale with the number of unknowns. Although this information is useful for comparing certain codes, the number of unknowns does not have a consistent meaning among various algorithms. Therefore, a scaling of resources based on frequency is more physically meaningful. The frequency or target size can be represented in many ways. We have chosen to use the ratio of the sphere radius and the wavelength.

This paper presents a method to determine the scaling of resources required to run different codes and shows the results of the application of this method to two electromagnetic codes. It describes some alternative scaling methods, but does not present an exhaustive study of all possible methods. The codes were only evaluated in the range for which computer resources were available. It can be argued that the results would have been different had the investigated range of the solutions, the computer codes representing the algorithms, or the computers been changed.

It is not our intent to compare different algorithms or codes. Neither of the codes presented here was completely optimized for the machine on which it was run, and the codes were run on different machines.

Description

Target selection

An ideal target is characterized by a known solution, and is easily modeled. It is important to have an indisputable reference solution in accuracy comparisons. We selected a perfectly electrically conducting (PEC) sphere as our reference for this paper because (1) it has an exact series solution and (2) meshes and grids can be easily generated for it.

Accuracy Criteria

In order to maintain consistent quality of solutions across a range of target sizes, we required each solution to meet a defined accuracy criterion. Without this criterion, scaling orders are often skewed. For example, if the

small-target solutions are highly accurate and the large-target solutions have poor accuracy, the order of the algorithm would appear to be less than if the same accuracy was present in the solutions for all target sizes. For this study, the accuracy criterion used was 1 dB root-mean-square (RMS) for bistatic angles from 0° to 180° in increments of 0.1°. The RMS error is calculated as follows:

$$\text{ERROR}_{\text{RMS}} = \frac{1}{n}\left\{\sum_{i=1}^{n}(\text{RCS}_{exact}(i) - \text{RCS}_{code}(i))^2\right\}^{\frac{1}{2}}$$

where the radar cross section (RCS) is in dB. We believe that this method, of the several we tried, yielded results that are most likely to satisfy engineering requirements.

As an example of the RMS error criteria, the series solution and calculated bistatic RCS solution for a 5-λ-radius sphere is shown in Figure 1 for HH polarization. The calculated solution has an RMS error of 0.97 dB. The computed solution was generated by ARCCEM, a NASA Ames finite-volume time domain (FVTD) code based on the Rockwell Science Center algorithm [1,2] and implemented on a Thinking Machines Corporation CM-5 massively parallel computer.

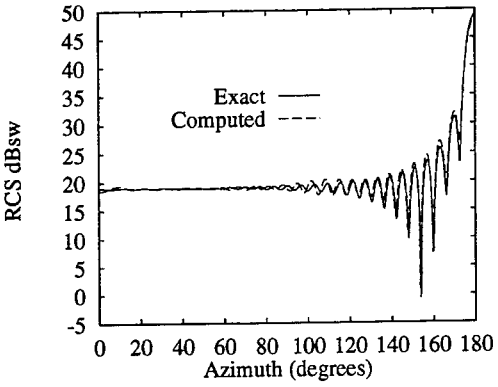

Figure 1. *Series solution versus calculated solution for HH sphere; radius/wavelength = 5; ka = 31.4.*

The difference between the ARCCEM solution and the exact series solution (or error) has a maximum value of 8 dB at an azimuthal angle of 154° due to a 0.25° angular shift of the null location. One of the error characterization methods that was ruled out was the use of the maximum deviation as the criterion. Many solutions *looked* good but had high maximum errors resulting from slight angular shifts near null locations. Most engineering environments have requirements that are satisfied by the RMS error over the maximum error criterion. In related work, Hamilton et al. [3] used a measure of error to show that higher-order methods such as their fast multipole method (FMM) are capable of providing accurate solutions at lower cost than that for a flat-patch method-of-moment (MoM) code.

Scaling Results

The central processing unit (CPU) and memory scaling of electromagnetic codes has been a topic of much debate. In this section, scaling results from an FVTD code and an MoM code are presented. They show some interesting and surprising results.

ARCCEM FVTD Scaling Results

The ARCCEM FVTD code was used to calculate results within 1.0 dB RMS of the Mie-series solution for spheres with radius/wavelength ratios from 1 to 10 on the CM-5 massively parallel computer. Error data for the FVTD code were obtained by selecting a particular sphere size and then searching by trial and error to find the most cost effective grid with respect to memory and CPU requirements.

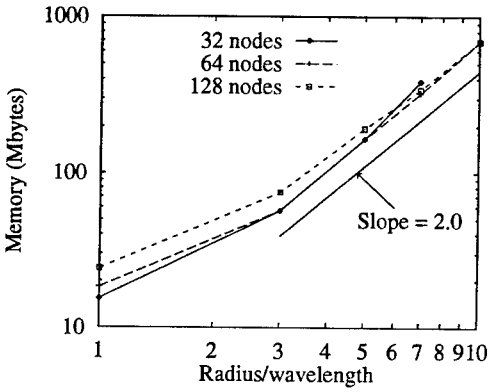

Figure 2. *Memory use for ARCCEM code on HH sphere with 1-dB RMS accuracy.*

Figure 2 shows the memory use on a log-log plot for 32-, 64-, and 128-node runs. The CM-5 can be run only in configurations with 2^n nodes. The NASA Ames machine is configured to support runs with 32, 64, and 128 nodes. As expected, the memory required to run the different sizes of spheres is only a weak function of the number of nodes and a strong function of the sphere size. For each sphere size, the same grid was used on all three machine configurations. The required memory varied with the number of nodes because of how the computer distributed the variables across the nodes. For example, an array of length 160 might require 5 memory locations on each of 32 nodes, 3 memory locations on each of 64 nodes, and 2 memory locations on each of 128 nodes. This allocation results in a 100% efficient utilization of the memory on 32 nodes, 83% on 64 nodes, and 63% on 128 nodes. The CM-5 software tries to distribute the variables to provide optimum balance between memory use, computational efficiency, and communication costs. The memory utilization for the 128 node case started at 35% for the 1-λ sphere and increased to 99% for the 10-λ sphere.

It has been argued that the memory requirement for FVTD codes should scale with target size at an order of 2 to 3 or more. For example, an order of 2 is predicted if the number of grid points varies with the surface area and the number of grid points to the outer boundary remains constant. Similarly, an order of 3 is predicted if the number of grid points to the outer boundary also scales with the problem size. In addition, the order would be greater than 3 if the grid point density per wavelength increased with problem size as a result of dissipation and dispersive phase errors.

The order of the memory requirement varies from 1.0 to 2.0 for the case shown in Figure 2. The grid requirements for a 1-λ-radius sphere are driven by the need to resolve the sphere surface more than by the need to resolve the electromagnetic wave. The results show that grid density on the surface of the sphere in grid points per wavelength decreases from 10.8 to 8.5 as the sphere size increases from 1 λ to 3 λ in radius. The density then slowly increases from 8.5 to 10.0 as the size of the sphere increases from 3 λ to 10 λ. The number of grid points from the sphere surface to the outer boundary is six for each run. The slopes of the memory-use lines in

Figure 2 would be higher if not for the increases in the fraction of the allocated memory used as the electrical sphere size increases. The decrease in the surface grid density relative to λ from the 1-λ sphere to the 3-λ sphere is responsible for the change in slope of the lines at the 3-λ sphere in Figure 2. These results show that for the larger target sizes, the memory requirement is a strong function of the surface area and the grid density required to define the field waves.

It has been debated that the CPU requirements for FVTD codes should scale with the target size at an order of between 2 and 4. A value of 2 is predicted if the grid scales with the surface area alone and a value of 3 is predicted if in addition the grid scales with the frequency between the surface and the outer boundary. If the code must be run for a longer period of time to allow fields to propagate along the full length of the target, then the order will be increased from 2 to 3 or from 3 to 4. If the grid-points-per-wavelength density must be increased as the target size increases, then the order may be even higher. Each of these mechanisms may play a role in determining the scaling.

Figure 3 shows that the required CPU resources grow with frequency to the power of 2.3 for the larger spheres. The slope from the 1-λ-sphere case to the 3-λ-sphere case is 0.5 and increases to 2.3 for the larger spheres. This change is due to sphere geometry resolution requirements and to increases in computational efficiency. There is additional work associated with the 1-λ sphere as a result of the grid density required to define the sphere and the inefficient memory use. As bigger sphere cases are run, the gridding is governed by the grid density required to define the incident field wavelength. Thus, for the 3-λ sphere there are approximately 8.5 grid points per λ and for the 10-λ sphere there are approximately 10 grid points per λ.

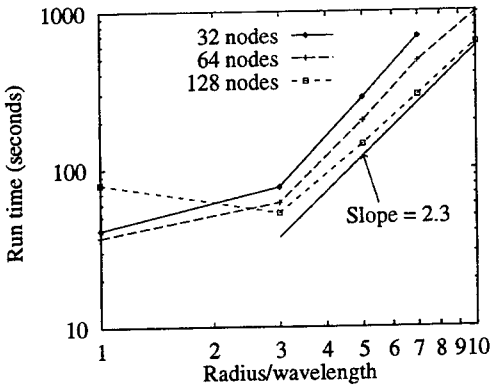

Figure 3. *CPU run times for ARCCEM code on HH sphere with 1-dB RMS accuracy.*

The 128-node, 1-λ-sphere run time was higher than expected because the CM-5 spent 49 seconds of the 80-second run writing the RCS contour data to the parallel-disk input/output (I/O) system. Analysis of the timing data shows that the longer I/O times correlate with a low fraction of allocated memory used. The 128-node, 1-λ-sphere case has a very poor fraction of allocated memory used. In short, the 1-λ-sphere case is so small that the CM-5 has trouble running it efficiently. This should not be considered a defect of the machine or of the FVTD code.

On the CM-5, there is insufficient work to keep all the CPUs loaded for the small sphere. As the sphere size increases, the work per CPU increases for a fixed machine size. As the sphere size increases from 1 λ to 10 λ, the computational rate for each CPU increases from 68 to 1409 points per second for the 128 node cases.

Increases in computation rate, as the sphere size increases, cause the slopes of the lines in Figure 3 to be lower.

Another way to measure the run time of a time domain code is to look at the distance the incident sine wave radiation is propagated in terms of wavelengths. The results show that the code run time, in terms of wavelengths, varies linearly with the size of the sphere. Thus, in the end, for ARCCEM, $C_{cpu} = O(f^{2.3})$ and $C_m = O(f^{2.0})$, because the grid scales with the surface area and the density required to define λ, the run time scales with the target's electrical size, and the computational efficiency increases as the computer becomes more fully loaded with increasing problem size.

ParaMoM Scaling Results

The ParaMoM code [4-6] was used to calculate results within 1.0-dB RMS error of the Mie-series solution for spheres with radius/wavelength ratios from 0.8 to 3.1 on 32 nodes of a Intel Paragon massively parallel computer. ParaMoM is an advanced MoM code that uses higher-order surface patches to obtain more accuracy with fewer unknowns. The workstation version of ParaMoM includes a grid generator. The ParaMoM grid generator was used with an IGES (initial graphics exchange specification) surface definition of a 1-m-radius sphere and different maximum grid edge lengths as inputs to generate the various grids that were used in this study.

ParaMoM was run with each grid at multiple frequencies until the lowest frequency was identified at which the results failed to satisfy a 1-dB RMS error level. The minimum sphere size at which a 1-dB RMS error criterion is exceeded is controlled by resonant sphere sizes. For this reason, a maximum sphere size is also defined. It is defined as the largest sphere size that satisfied the 1-dB RMS error criterion while ignoring the resonant solution spikes. For example, Figure 4 shows that for the 0.17-m-grid case the minimum-sphere-size solution is the 0.99-λ radius sphere and the maximum-sphere-size solution is the 1.9-λ-radius sphere. ParaMoM was run with the electric field integral equation (EFIE) formulation for all cases. A limited series of tests showed that even with the resonant solution spikes, the EFIE formulation was more cost effective than the magnetic (MFIE) or combined (CFIE) field integral formulations.

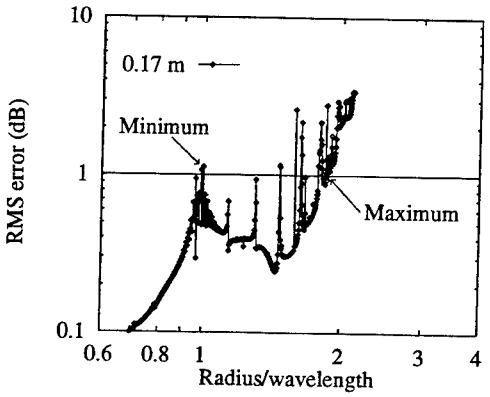

Figure 4. *Minimum and maximum sphere size solutions for 0.17-m grid on a sphere.*

The maximum-sphere-size data set is more representative of the scaling that would be found with geometries that have fewer resonant sizes. Figure 5 shows the grid edge lengths used versus the electrical sphere size for both the minimum- and maximum-sphere-size solutions for a 1-m-radius sphere.

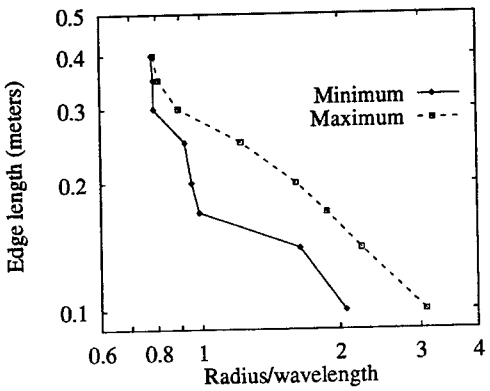

Figure 5. *Grid edge lengths required to satisfy 1-dB RMS error criterion for ParaMoM code on HH 1-m-radius sphere.*

Figure 6 shows that the memory use has a slope of 4.0 at the higher frequencies for the maximum sphere-size case. The slope of 4.0 was obtained from a least squares regression of the last five data points. ParaMoM's memory usage is $N * (N + RHS) * 8$ where N is the number of unknowns, RHS is the number of right-hand sides, and 8 is the number of bytes required to store a complex number. Since only one surface current solution is required to calculate the bistatic RCS, $RHS = 1$. For a constant number of unknowns per wavelength, N grows in proportion to the sphere area. Since the area grows with the square of the sphere size, the theoretical slope should be 4, which agrees with the measured value in Figure 6. A slope greater than 4 would show that the ParaMoM code requires more nodes per wavelength at higher frequencies than at lower frequencies. A value less than 4 would show the reverse trend. The results show that the nodes per wavelength is almost constant at 3.2 for the last 5 points of the maximum-sphere-size data set.

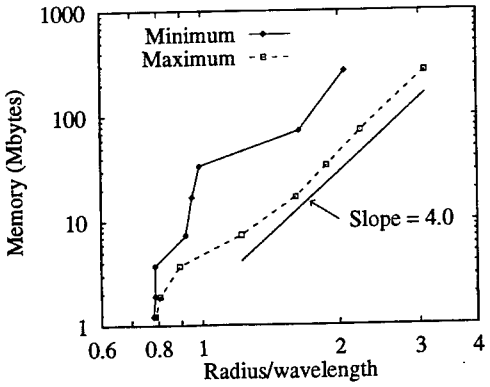

Figure 6. *Memory use for ParaMoM code on HH sphere with 1-dB RMS accuracy.*

ParaMoM has two code sections that consume a vast majority of the computer time: the dense matrix fill and matrix LU factor sections. CPU times for these sections and the total run time are shown in Figure 7 for the

maximum-sphere-size solutions. Only the LU decomposition was optimized on this machine. The matrix fill, even though lower order than the matrix LU factor, took the largest fraction of the total run time. Had the matrix fill been optimized, it would most likely have taken a much smaller fraction of the total run time but maintained the same scaling.

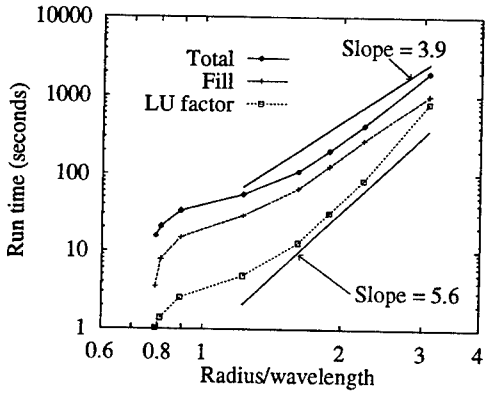

Figure 7. *CPU times as a function of maximum sphere size for ParaMoM on HH sphere with 1-dB RMS accuracy.*

The matrix fill section is an N^2 operation and the matrix LU factor is an N^3 operation. Theoretically, the two should scale as the 4th and 6th power of the sphere size, respectively. The total run time should scale at some intermediate value depending on the amount of time that is spent in each section. Again, a least squares regression is used to determine line slopes. The total run time scales as the sphere size to the power of 3.9 for the last five points of the maximum-sphere-size solution. The matrix fill and LU factor lines have slopes of 3.9 and 5.6, respectively, for the last five points of the maximum-sphere-size case. These values are lower than the theoretical slopes because as the problem size grows, the computer runs more efficiently.

In the end, using the maximum-sphere-size data set for ParaMoM, $C_{cpu} = O(f^{3.9})$ and $C_m = O(f^{4.0})$. ParaMoM has these slopes because the grid scales with the surface area, and the grid density required to define λ is nearly constant with sphere size. It is also apparent that the N^3 matrix LU factor operation with $O(f^6)$ computational requirements will eventually overwhelm the N^2 operations and the C_{cpu} order will approach and possibly exceed a value of 6 depending on the grid density requirements.

Conclusion

The quality of the grid used in a computation directly influences the run time and solution accuracy. For many codes, it is easy to generate a quick grid, run the code, and get an answer. It is much more difficult to get an accurate answer with a grid that uses the least amount of memory and CPU time. The optimization effort required to determine the ideal grid adds significantly to the time required to generate the order of a code.

It is also important to understand the influence of the computer used in the calculations. The TMC CM-5's performance had a large impact on the ARCCEM scaling results. This is underscored by the fact that the 1-λ-radius sphere was so small that the CM-5 computational rate for for the 10-λ-radius sphere was 20 times that of the 1-λ-radius sphere. Likewise, the Paragon performance reduced C_{cpu} by reducing the N^3 operation to $N^{2.8}$.

We explicitly avoided using scaling that is based on the number of unknowns and instead used scaling based on target size. This allows the direct comparison of the scaling of different algorithms and avoids the challenge of understanding how unknowns are used in different algorithms.

We have not addressed the issue of the number of runs required of each code to fill a frequency and monostatic RCS matrix. The bistatic case is optimal for both the FVTD code and the MoM code in that only one run is required. However, for a matrix of solutions, the FVTD code will require separate runs for multiple incident fields and frequencies. The number of frequency runs can be reduced by using a pulse rather than a cosine wave as an incident field, and the number of runs required to fill a view angle matrix can be significantly reduced by using the monostatic/bistatic approximation [7]. The MoM code will have to be run at multiple frequencies and will have a small additional cost for the multiple look angles. It is easy to see that a run matrix could be defined that would favor one approach over another; the skewing of results to favor one run code or algorithm over another by the selection of a specific run matrix has been avoided entirely by comparing bistatic results.

We encourage others to benchmark their codes using the procedure outlined in this paper. We encourage the presentation of both the scaling figures and supporting information describing why the code ran with the measured scaling. This information will help a project manager best determine which code will be most cost effective in filling his run matrix.

Acknowledgments

Computer resources for this effort were provided by the NASA Ames Numerical Aerodynamic Simulation Systems Division. These results would not have been possible without these resources.

References

1) V. Shankar, W. F. Hall, and A. H. Mohammadian, "A CFD-based finite-volume procedure for computational electromagnetics - interdisciplinary applications of CFD methods," in Proc. AIAA 9th Computational Fluid Dynamics Conference, Buffalo, 13-15 June 1989.

2) V. Shankar, W. F. Hall, and A. H. Mohammadian, "A time domain differential solver for electromagnetic scattering problems," Proceedings of the IEEE, Vol. 77, No. 5, May 1989, pp. 709-721.

3) L. Hamilton, J. Ottusch, M. Stalzer, R. S. Turley, J. Visher, S. Wandzura, "FastScat^{TM} Benchmark Data," HAVE FORUM Meeting, Colorado Springs, CO, 20 October 1994.

4) D. L. Wilkes and C. C. Cha, "Method of Moments Solution with Parametric Curved Triangular Patches," IEEE Antennas and Propagation International Symposium Digest, 1991, pp. 1512-1515.

5) "Syracuse Research Corporation, Parametric Method of Moments (ParaMoM) RCS Prediction Package User's Manual," Version 1.0, SRC Technical Report TD 92-1321, October 1992.

6) Xianneng Shen, G. E. Mortensen, C. C. Cha, G. Cheng, and G. C. Fox, "Parallelization of the Parametric Patch Moment Method Code," ACES Conference, March 20-25, 1995, pp. 702-709.

7) M. J. Schuh, A. C. Woo, and M. P. Simon, "The Monostatic/Bistatic Approximation," IEEE Antennas and Propagation Magazine, Vol. 36, No. 4, August 1994, pp. 76-78.

An Overview of Numerical Dispersion Error in PDE Methods for Electromagnetics

Robert Lee

lee@ee.eng.ohio-state.edu
ElectroScience Laboratory
Department of Electrical Engineering
The Ohio State University
1320 Kinnear Road
Columbus, OH 43212

I. Introduction

In partial differential equation (PDE) methods, the choice of discretization is usually the most critical consideration for the accuracy and efficiency of the method. Too coarse a discretization can produce substantial errors in the solution, while too fine a discretization can be computationally expensive. The optimal discretization is the coarsest one in which we meet the desired error criteria. Thus, it is important to understand discretization error as thoroughly as possible.

Discretization error is produced by the incorrect modeling of the field variation within the computation domain. The field variation is due to two factors for time-harmonic waves. One is the sinusoidal variation of the field due to the frequency of the wave. In finite difference and finite element methods, a polynomial variation is assumed for the field; therefore, an error is expected in modeling the sinusoidal variation, with more error as the frequency increases. As we show later in this paper, the error causes the wave to be dispersive. This error is commonly called numerical dispersion error. There has been a great deal of literature on finding the dispersion relation for various finite elements and finite difference schemes. Although the numerical dispersion error was recognized as a source of error, people did not realize that this error grows with the size of the computation domain and is therefore dominant for electrically large geometries. Bayliss et al. [1] are the first to demonstrate the relationship between the dispersion analysis and the growth of the error as a function of computation domain size for wave problems. Since then, much work has been done to analyze this growth in both the frequency and the time domain [2-9].

The second cause of field variation is geometrical discontinuities. For example, the fields vary rapidly near perfectly conducting sharp corners and edges as well as material discontinuities. Some field components even approach infinity at perfectly conducting corners and edges. It is important to choose the discretization to properly model the field behavior near these geometrical

features; however, the purpose of this paper is to address the numerical dispersion error. To this end, we plan to analyze the finite element method (FEM) in the frequency domain and the finite difference time domain (FDTD) method for numerical dispersion error in computation domains composed of free space. We show the reduction of numerical dispersion error through the use of higher order elements. We also demonstrate the effect of numerical dispersion on the accuracy of absorbing boundary conditions (ABC's).

II. One-Dimensional Analysis of Numerical Dispersion

Let us consider the problem of a $+z$-propagating plane wave in free space where the electric field is polarized in the x direction. In performing the numerical dispersion analysis, the grid is assumed to be uniform. Also, the grid is assumed to be infinite, so that the boundary conditions do not enter into the analysis. In the following sections a plane wave propagating in free space is modeled with FEM in the frequency domain and FDTD in order to determine the numerical dispersion error.

A. *Finite elements frequency domain*

The plane wave satisfies the one-dimensional Helmholtz equation,

$$\left(\frac{d^2}{dz^2} + k^2\right) E_x(z) = 0 \tag{1}$$

where k is the wave number given by $k = \omega\sqrt{\mu\epsilon}$ (in this case it is the free space wave number). The solution to this trivial problem is

$$E_x = e^{-jkz} \tag{2}$$

assuming an $\exp(j\omega t)$ time convention. However, if we were to solve this problem using FEM with linear elements, we would obtain an approximate solution due to the discretization of the field. An analysis [4] can be performed based on the assumption that the mesh is uniform and the computation domain is infinite, which in effect removes the boundary condition from consideration. The numerical solution is

$$E_x = e^{-j\hat{k}z} \tag{3}$$

where $\hat{k}$ is given by

$$\frac{\hat{k}}{k} = \frac{1}{kh} \arccos\left[\frac{1-(kh)^2/3}{1+(kh)^2/6}\right] \tag{4}$$

with h being the grid spacing. It is clear that the numerical solution is dispersive because $\hat{k}$ is not a linear function of frequency. The error in the numerical solution is a phase error $(k-\hat{k})z$

which increases as a function of z. In the table below, we present the amount of phase error in the plane wave solution for various grid spacings after the wave has traveled one wavelength

h/λ	$\hat{k}/k$	Phase Error per λ (°)
1/10	0.9845	5.58
1/15	0.9928	2.59
1/20	0.9959	1.48
1/25	0.9974	0.94

The wave accumulates error as it propagates through the grid. For a uniform grid, the solution at the largest value of z has the largest error, and its error is due equally to all the elements in the grid.

B. Finite difference time domain

To study numerical dispersion in the time domain, we first study the solution for a time-harmonic solution. The FDTD solution for the electric field of a time-harmonic plane wave is

$$E_x = e^{j(\omega t - \hat{k}z)} \tag{5}$$

where the numerical wave number $\hat{k}$ is not only a function of the grid spacing h but also a function of the time step Δt. It is given by [2]

$$\frac{\hat{k}}{k} = \frac{2}{kh} \arcsin\left[\frac{h}{c\Delta t} \sin\left(\frac{\omega \Delta t}{2}\right)\right] \tag{6}$$

where c is the speed of light. Let us define the variable p to be $p = c\Delta t/h$. Then the FDTD method is numerically stable for $p \leq 1$ and unstable otherwise. A table is given below for sample grid spacings and values of p.

h/λ	p	$\hat{k}/k$	Phase Error per λ (°)
1/10	0.25	1.0161	5.81
1/20	0.25	1.0039	1.40
1/10	0.50	1.0129	4.64
1/20	0.50	1.0031	1.12
1/10	0.75	1.0075	2.70
1/20	0.75	1.0018	0.65
Any	1.00	1.0000	0.00

Unlike the frequency domain case, $\hat{k}$ is always greater that k. Also, it is interesting to note that as p increases, the solution becomes more accurate. In fact, for $p = 1$ the wave is dispersionless since the errors due to the spatial discretization exactly cancels the error due to the time discretization.

Usually the FDTD excitation is not time-harmonic. Instead, the time behavior is usually a pulse such as one in a Gaussian form. The effect of numerical dispersion is to cause distortions in the pulse shape as the wave propagates.

III. Use of Higher Order Formulations

It is obvious that the use of higher order elements for FEM or the use of higher order difference schemes in FDTD can reduce the numerical dispersion error. What is more important is whether going to a higher order formulation is more computationally efficient than reducing the grid spacing. In the following sections, we present the equations associated with the numerical wave number for the quadratic elements in FEM and compare its computation costs to the linear elements. Also, we compare the computation costs of the traditional FDTD method and an FDTD scheme which is fourth order accurate in space and second order accurate in time.

A. Higher order elements in FEM in the frequency domain

A standard dispersion analysis of the one-dimensional Helmholtz equation in (1) with quadratic elements produces the following equation,

$$\frac{\hat{k}}{k} = \frac{1}{kh}\cos^{-1}\left[\sqrt{\frac{2(kh)^4 - 11(kh)^2 + 15}{(kh)^4 + 4(kh)^2 + 15}}\right] \tag{7}$$

A simple study of the expression under the radical reveals that for frequencies below cutoff ($kh \leq \pi$) the numerical solution does not exhibit artificial damping, except for a cutoff region given by $\sqrt{2.5} \leq kh \leq \sqrt{3}$.

The phase error per wavelength for various grid spacings is shown below:

h/λ	$\hat{k}/k$	Phase Error per λ (°)
1/10	0.9984	0.57
1/15	0.9997	0.12
1/20	0.9999	0.03
1/25	0.99996	0.016

Comparing the table above to the results for the first order element, we observe the the quadratic elements produce a solution with considerably smaller phase errors for a given grid spacing. The above table provides a good approximation for the phase errors in two and three dimensional problems. In [4], it is demonstrated by numerical examples on two-dimensional geometries that the quadratic elements are much more computationally efficient than linear elements for a given accuracy. The comparisons are based on the use of a banded matrix solver. Let us consider the case for an iterative solver such as the conjugate gradient method. The major computation cost is the matrix-vector multiply. For a two dimensional problem with linear

quadrilateral elements, each row contains approximately 9 nonzero terms, while for quadrilateral elements with quadratic variations, the average number of nonzero terms per row is 19. Thus, the matrix-vector multiply contains $9N$ multiplications for linear elements and $19N$ multiplications for quadratic elements where N is the number of nodes in the grid.

To determine which element is more computationally expensive for an electrically large geometry, let us consider a 10λ by 10λ region of space. If we specify that the largest phase error allowable is 5°, then we should choose a grid spacing such that there is only 0.5° of phase error per wavelength. For linear elements, this requires a grid spacing of approximately $\lambda/35$, while for quadratic elements, the spacing is approximately $\lambda/11$. Thus, the numbers of nodes in the grid with linear and quadratic elements are 123,201 and 12,321, respectively. For this geometry, the quadratic elements are clearly more efficient (234099 multiplications per matrix-vector multiply versus 1,108809 multiplications for the linear element). It is expected that the quadratic elements will perform even better for larger geometries and not quite as well for smaller geometries.

For three-dimensional geometries with nodal elements, the contrasts are even greater. For a cube region with 10λ on a side and 3 unknowns per node, the matrix vector multiply requires $81N$ multiplications for linear elements and $244N$ for quadrilateral elements. The numbers of nodes in a grid composed of linear and quadratic elements are 43 million and 1.37 million, respectively. Compared to the two-dimensional case, we see that the quadratic elements are even more efficient relative to the linear elements (334 million multiplications to 3.5 billion multiplications).

IV. Higher order FDTD schemes

The use of higher order accuracy FDTD schemes have been proposed [2] to reduce numerical dispersion. We expect that the numerical dispersion should be reduced by a higher order accurate finite difference method, but again, the critical question is whether the gain in accuracy overcomes the added computation costs associated with the higher order scheme. Such an analysis [5] has been done comparing the regular FDTD method which is second order accurate in space and time to a higher order FDTD method which is fourth order accurate in space but second order accurate in time.

In [5], it is shown that the number of floating point operations N_{22} for the regular FDTD method is

$$N_{22} = 6(4^m)N_o N_t \left(\frac{d}{\lambda}\right)^{1.6m} \tag{8}$$

where N_o is the number of floating point operations associated with one of the unknowns per time step in the regular FDTD method, N_t is the number of time steps required for the regular FDTD method, and m is the dimension of the problem. The length d represents the characteristic dimension of the domain.

For the FDTD scheme which is fourth order accurate in space and second order accurate in time, the number of floating point operations N_{24} is

$$N_{24} = 6(2.5^{m+1})N_o N_t \left(\frac{d}{\lambda}\right)^{1.6m} \tag{9}$$

From (8) and (9), we see that $N_{22} \approx N_{24}$ for two dimensional problems, so there does not seem to be any advantages in terms of numerical dispersion to using the higher order scheme in this case. In three dimensions, $N_{22} \approx 1.6N_{24}$. Although there seems to be an advantage in three dimensions, one must be careful because a higher order method cannot be applied at material interfaces, which may possibly limit the usefulness of the higher order schemes.

The gains which can be achieved with even higher order methods such as one which is fourth order accurate (or higher) in space and time has not been fully evaluated at this point and may provide potential improvements in accuracy and efficiency.

V. Coupling Between Numerical Dispersion Error and the Outer Boundary Condition

If we run a numerical simulation, there are both phase and magnitude errors, which are caused by the presence of boundary conditions. To demonstrate the interaction of numerical dispersion with different boundary conditions, let us consider the one-dimensional case where the computation domain is finite with two different boundary conditions. We assume that the computation domain is discretized into uniform segments and is between $z = 0$ and $z = a$. The first boundary condition is Dirichlet with

$$E_x(0) = 1, \qquad E_x(a) = e^{-jka} \tag{10}$$

The numerical solution $\hat{E}_x$ can be derived analytically and is given by

$$\hat{E}_x(z) = e^{-j\hat{k}z} + \left(e^{-jka} - e^{-j\hat{k}a}\right)\left(\frac{\sin \hat{k}z}{\sin \hat{k}a}\right) \tag{11}$$

In (11), the equation has been written in a form to decouple the error due to numerical dispersion from the error due to the interaction of the boundary condition with the numerical dispersion. The first term is the numerical solution in the absence of a boundary condition, and the second term represents the effect of the boundary condition. By studying the second term, it is clear that this term causes both magnitude and phase errors which generally increase as the electrical size of the computation domain grows. For electrically large geometries, the error caused by the second term in (11) becomes the dominant contribution to the overall error.

On the other hand, we can consider a boundary condition which does not interact strongly with the numerical dispersion. One example of such is a mixed combination of Dirichlet and generalized Neumann boundary conditions. Mathematically, we set

$$E_x(0) = 1, \qquad \left(\frac{d}{dz} + jk\right) E_x(a) = 0 \tag{12}$$

The analytically derived numerical solution is given by

$$\hat{E}_x(z) = e^{-j\hat{k}z} + j\frac{\left[(\hat{k}/k) - 1\right] e^{-j\hat{k}a}}{(\hat{k}/k)\cos\hat{k}a + j\sin\hat{k}a}\sin kz \tag{13}$$

Let us consider the second term in (13), which represents the interaction between the numerical dispersion and the boundary condition. We can assume that $.95 < \hat{k}/k < 1$ for common choices of grid densities. Since $\hat{k}/k$ is close to one, the magnitude of the denominator in the second term is almost constant with respect to $\hat{k}a$, and also the numerator is small; therefore, the numerical error is relatively insensitive to the size of the computation domain.

The differences between the two boundary conditions illustrate the point that one must consider the effect of the interaction between numerical dispersion and the boundary condition in choosing the optimal boundary condition. We must not only look at the accuracy and efficiency but also the sensitivity of the boundary condition to numerical dispersion. One must also be careful in drawing conclusions based on numerical results for electrically small geometries. One boundary condition may be better than another a low frequencies, but worse at a higher frequency. A more detailed discussion, including a two-dimensional analysis is given in [10]

VI. Conclusions

This papers is intended to provide an overview of the effect of numerical dispersion error on the overall solution. We demonstrate that this type of error is the same, whether we are considering the frequency or the time domain. We show that it is desirable to use higher order elements or differencing schemes to reduce the numerical dispersion. The coupling between the errors in absorbing boundary conditions and the numerical dispersion error is often ignored. We show that this error may be dominant for many simulations. Finally, we wish to emphasize that with a better understanding of numerical dispersion, we can develop methods to minimize this error. One such approach is given in [11], where an element has been developed which produces almost no numerical dispersion.

VII. References

[1] A. Bayliss, C. I. Goldstein, and E. Turkel, "On Accuracy conditions for the numerical computation of caves," *Journal of Computational Physics*, Vol. 59, pp.396-404, 1985.

[2] J. Fang, "Time Domain Finite Difference Computations for Maxwell's Equations," Ph.D. Dissertation, Dept. EECS, University of California, Berkeley, 1989.

[3] A. F. Peterson and R. J. Baca, "Error in the Finite Element Discretization of the Scalar Helmholtz Equation Over Electrically Large Regions," *IEEE Microwave and Guided Wave Letters*, Vol. 1, pp. 219-222, August 1991.

[4] R. Lee and A. C. Cangellaris, "A study of discretization error in the finite element approximation of wave solutions," *IEEE Trans. Antennas and Propagat.*, AP-40, pp. 542-549, May 1992.

[5] A. C. Cangellaris and R. Lee, "On the accuracy of numerical wave simulations based on finite methods," *J. of Electromagnetic Waves and Applications*, vol. 6,no. 12, pp. 1635-1653, 1992.

[6] S. L Ray, "Numerical dispersion and stability characteristics of time-domain methods on nonorthogonal meshes," *IEEE Trans. Antennas and Propagat.*, AP-41, pp. 233-235, February 1993.

[7] P. G. Petropoulos, "Stability and phase error analysis of FDTD in dispersive dielectrics," *IEEE Trans. Antennas and Propagat.*, AP-42, pp. 62-69, January 1994.

[8] P. G. Petropolous, "Phase error control for FDTD methods of second and fourth order accuracy," *IEEE Trans. Antennas and Propagat.*, AP-42, pp. 859-862, June 1994.

[9] G. Warren and W. R. Scott, "An investigation of numerical dispersion in the vector finite element method using quadilateral elements," *IEEE Trans. Antennas and Propagat.*, AP-42, pp. 1502-1508, November 1994.

[10] R. Lee, Z. Chen, J. Jevtic, and J. F. Lee, "Important considerations in the evaluation of absorbing boundary conditions," submitted to *Electromagnetics*.

[11] J. Jevtic and R. Lee, "Solenoidal edge elements," submitted to *Radio Science*.

Non-rigorous CEM Error Estimates and Their Limitations

Andrew F. Peterson
School of Electrical & Computer Engineering
Georgia Institute of Technology
Atlanta, GA 30332-0250
peterson@ee.gatech.edu

1. Introduction

Although numerical solution procedures for dynamic electromagnetic field problems are well-established, systematic techniques for estimating the error associated with the numerical results they produce are not. This paper explores some simple procedures for estimating the discretization error levels in MoM and FEM results. Primarily, we review predictable trends in the behavior of discretization error and discuss ways of extrapolating approximate error levels from numerical results. Preliminary results were presented in [1]; this presentation will extend these examples and discuss some of the limitations of the extrapolation procedure.

2. Classification of Various Sources of Error

Assuming that the computer code under consideration is performing correctly (i.e., no "bugs"), there remain a number of independent sources of error associated with a particular MoM or FEM result. These can be grouped according to the following designations:

- Approximations used to simplify the mathematical formulation prior to discretization (examples include the thin-wire kernel used in wire antenna modeling, local RBCs used in FEM modeling, etc.)
- Geometrical and material approximations (the infinite conductivity assumption often used with conducting structures, the assumption of a uniform and/or lossless permittivity, the use of flat facets to represent a curved surface, etc.)
- Discretization errors (the use of a finite number of basis functions, basis functions that do not incorporate edge singularities, etc.)
- Numerical errors (finite precision arithmetic, limited precision for special function calculations, accuracy of numerical quadrature rules, etc.).

In practice, any of these errors may dominate in a particular situation. In the following, we focus only on estimating the discretization error. Generally, the user would like an estimate of the error as a

function of the number of basis and testing functions or the density of functions per wavelength, since that is the primary user-controlled input once a code is created.

3. *Predictable trends associated with polynomial interpolation error*

If a linear combination of the basis functions used in a discretization can exactly represent the solution, the method-of-moments process will adjust the coefficients to produce the exact solution. If the basis functions can not exactly represent the solution, even the best possible choice of coefficients leaves some residual error, known as *interpolation error*. Interpolation error is the difference between the true result and the approximation provided by the basis functions, assuming that the best possible coefficients are found for the basis functions. [This definition of interpolation error excludes additional error arising from suboptimal coefficients for the basis functions, as might be expected in a typical MoM or FEM procedure, and thus should be a lower bound on the overall discretization error. However, it should lead to the correct error trend as the cell size vanishes.] If the basis functions are piecewise polynomials that are complete to polynomial order p, the interpolation error associated with the representation is relatively easy to characterize [2]. The following example illustrates the analysis.

Consider the quadratic function

$$f(x) = a + b\,x + c\,x^2 \tag{1}$$

Suppose f(x) is approximated on the interval ($-\Delta/2 < x < \Delta/2$) using two piecewise-linear interpolation functions (subsectional triangle functions), i.e.,

$$f(x) \cong f_{ap}(x) = f(-\Delta/2)\,B_1(x) + f(\Delta/2)\,B_2(x) \tag{2}$$

where B_1 and B_2 are defined throughout the interval by

$$B_1(x) = \frac{1}{2} - \frac{x}{\Delta} \tag{3}$$

$$B_2(x) = \frac{1}{2} + \frac{x}{\Delta} \tag{4}$$

By direct substitution, the function f_{ap} can be expressed in the form

$$f_{ap}(x) = a + b\,x + c\,(\Delta/2)^2 \tag{5}$$

The piecewise-linear approximation captures the correct constant and linear dependence, but obviously can not represent the quadratic term. In this case, the error between f and f_{ap} reaches a maximum at x=0 and has the peak value

$$|\,\text{error}\,| = \frac{c\,\Delta^2}{4} \tag{6}$$

As the interval size shrinks to zero, the peak error decreases as $O(\Delta^2)$. In other words, a 50% decrease in Δ causes a 75% decrease in the error. The same result holds if f(x) is an arbitrary polynomial and a piecewise-linear basis is employed.

This result is easily generalized to other polynomial orders, with the result that a representation of polynomial degree p results in an interpolation error of order Δ^{p+1} as $\Delta \to 0$ [2]. In a situation where variable-sized cells are employed, the error estimate is valid as long as Δ corresponds to the largest cell in the discretization. A similar behavior is obtained for polynomial representations in two or three dimensions.

4. Trends obtained from plane-wave dispersion analysis

An alternate way of investigating the error trends associated with a particular representation is to consider the distortion that a plane wave solution undergoes as it propagates across the computational domain. Consider the one-dimensional scalar Helmholtz equation

$$\frac{d^2E_z}{dx^2} + k^2 E_z(x) = 0 \tag{7}$$

and the use of piecewise-linear basis and testing functions. In addition, we assume that the mesh is uniform and large in extent, and ignore boundaries. Under these conditions, the m-th finite element equation can be written

$$2E_m - E_{m-1} - E_{m+1} - k^2\Delta^2\left(\frac{2}{3}E_m + \frac{1}{6}E_{m-1} + \frac{1}{6}E_{m+1}\right) = 0 \tag{8}$$

where Δ is the cell size and E_{m-1}, E_m, and E_{m+1} are the basis function coefficients for $E_z(x)$ at $x_m-\Delta$, x_m, and $x_m+\Delta$, respectively.

Equation (7) has a traveling wave solution $E_z(x) = E_0 e^{\pm jkx}$, while (8) has the solution

$$E_z(x_m) = E_0 e^{\pm j\beta x_m} \tag{9}$$

where

$$\beta = \frac{1}{\Delta}\cos^{-1}\left\{\frac{1 - \frac{(k\Delta)^2}{3}}{1 + \frac{(k\Delta)^2}{6}}\right\} \tag{10}$$

Consequently, Equations (9) and (10) are the numerical solutions that would be obtained for waves on an infinite, uniform mesh.

The phase error ($k\Delta - \beta\Delta$) across a single cell is easily tabulated as a function of Δ from Equation (10), and is summarized in Table 1. It is easily discerned that the error decreases as $O(\Delta^2)$ as $\Delta \rightarrow 0$, in agreement with the theoretical interpolation error associated with piecewise-linear basis functions.

Table 1

Predicted phase error per wavelength as a function of cell size Δ for linear basis functions, from Equation (10), and the total solution error per wavelength.

Δ	phase error per λ	% error per λ
0.2 λ	20.103°	34.9 %
0.1	5.670	9.9
0.05	1.464	2.6
0.025	0.369	0.64
0.0125	0.0925	0.16
0.00625	0.0226	0.04

A number of authors have carried out dispersion analyses for scalar and vector volumetric representations in one, two, and three dimensions [3-5]. Dispersion analysis is somewhat less general than the polynomial interpolation analysis of the previous section, since it usually requires a uniform mesh and a uniform plane wave excitation. In some cases, the dispersion analysis predicts a different behavior (an error decreasing at a greater power of Δ as $\Delta \rightarrow 0$) than that predicted by interpolation analysis. For example, Warren has shown that mixed-order edge elements of the curl-conforming Nedelec variety (which are only complete to order p–1) produce a plane-wave error that appears to behave as $O(\Delta^{p+1})$ as $\Delta \rightarrow 0$, like scalar representations that are complete to polynomial degree p [5]. In other situations, the error at special locations within the mesh may behave as $O(\Delta^{2p})$ as $\Delta \rightarrow 0$ [4-6]. This behavior is known as *superconvergence*. Although neither interpolation analysis nor dispersion analysis is likely to predict the correct error behavior for every numerical result, the $O(\Delta^{p+1})$ trends are observed in many actual electromagnetic simulations [1].

5. *Error level estimation from successive results*

Knowledge of error trends can be used to provide simple error estimates from two successive results, as previously described [1]. Suppose that two results are obtained using a different cell sizes, and it is known that the error behaves as as $O(\Delta^{p+1})$ as $\Delta \rightarrow 0$. If we denote the result obtained with N cells (each of dimension Δ_N) as R_N, for small enough cells we have

$$R_M \cong R_{exact} + K(\Delta_M)^{p+1} \tag{11}$$

$$R_N \cong R_{exact} + K(\Delta_N)^{p+1} \tag{12}$$

where "K" and "R_{exact}" represent unknown quantities, and $\Delta_N < \Delta_M$. By treating (11) and (12) as equalities and solving the linear equations simultaneously, we obtain an error estimate

$$Error_N \cong K(\Delta_N)^{p+1} \tag{13}$$

as well as an improved estimate R_{exact} of the exact result. Examples of this procedure for MoM and FEM calculations are presented in [1].

This error estimate is not useful in practice unless discretization error is the dominant error associated with the results. Unfortunately, in practice there are often approximations incorporated into electromagnetic modeling codes that dominate the error at some point, such as the so-called "thin-wire" kernel often used in wire antenna modeling (where the source currents are replaced by a filament on the axis of the wire) or the use of a local RBC within FEM codes [1]. In these cases, an error estimate such as (13) may still be a valid indication of the discretization accuracy, but not of the overall accuracy of the numerical result. In any event, the validity of the error estimation process is enhanced if the underlying formulation on which the computer code is based avoids approximations that do not improve as $\Delta \rightarrow 0$.

A more difficult issue is the treatment of a corner or edge where the unknown quantity is known to be singular; if the basis functions do not incorporate the proper singularity the results may appear to converge (to the wrong solution) or in some cases may diverge as the number of basis functions is increased.

6. An alternate approach: Error estimation using residual computations

A procedure sometimes employed for adaptive grid refinement algorithms in FEM codes is to compute the residual of the equation being solved on a finer grid than the solution. This provides a relative error estimate that may suggest which region of the mesh supports the most error. By means of defining a suitable error measure or norm, such a calculation can be used to quantitatively measure the error. If "calibrated" with known solutions, such an error calculation could provide useful insight into the overall accuracy of a particular numerical result. This approach is independent of trends in the error and represents an alternate means of estimating error levels.

Qualitative calculations of this sort were illustrated for wire antenna problems two decades ago [7], and were investigated (also more than a decade ago) by the present author in the context of volume integral equation formulations for dielectric scatterers [8]. However, they apparently have never been used for quantitative error estimation. One reason may be that relatively few problems can be found that are suitable for calibrating these error levels. It is hoped that benchmark problem libraries continue to proliferate so that suitable standard solutions are available.

7. *Conclusions*

In many electromagnetic field modeling situations, predictable trends in the behavior of discretization error can be used to provide simple estimates of the overall error levels. These estimates are not mathematically rigorous bounds, and will occasionally be incorrect, but they represent an improvement over the present practice of reporting no error estimates with numerical results. The primary cost of the process is the need to solve a problem twice at different discretization densities. The primary conceptual drawback to the approach is that it will not correctly estimate errors other than the discretization errors, and might therefore systematically underestimate the actual error levels present if poorly-understood approximations built into the code are actually the limiting factors.

Even without a belief that the procedure will provide valid error estimates, however, one should have difficulty objecting to the premise that it is good computational engineering to solve a problem twice with different cell densities and compare the results. Of course, once the problem is solved twice, the error estimates can be obtained with minimal effort.

Although the ideas expressed in this paper are hardly new, they have not been adapted to any significant degree in computational electromagnetics. It is hoped that the users of electromagnetic modeling software request features such as these in codes of the future, developers provide them, and the research community continues to explore these ideas. The rationale for including error estimates with numerical results is clear; the means for obtaining accurate overall error estimates remains elusive.

8. *References*

[1] A. F. Peterson, "A simple approach for estimating error bars to accompany moment-method and finite-element-method results," *IEEE Antennas and Propagation Magazine*, vol. 35, pp. 61-62, December 1993.

[2] G. Strang and G. J. Fix, *An Analysis of the Finite Element Method.* Englewood Cliffs: Prentice-Hall, 1973.

[3] R. Lee and A. C. Cangellaris, "A study of discretization error in the finite element approximation of wave solutions," *IEEE Trans. Antennas Propagat.*, vol. 40, pp. 542-549, May 1992.

[4] W. R. Scott, Jr., "Errors due to spatial discretization and numerical precision in the finite element method," *IEEE Trans. Antennas Propagat.*, vol. 42, pp. 1565-1570, November 1994.

[5] G. S. Warren, *The analysis of numerical dispersion in the finite element method using nodal and vector elements*. Ph.D. Dissertation, Georgia Institute of Technology, Atlanta, Georgia, 1995.

[6] D. S. Burnett, *Finite Element Analysis*. Reading: Addison-Wesley, 1987.

[7] E. K. Miller and Deadrick, "Some computational aspects of thin-wire modeling," in *Numerical and Asymptotic Techniques in Electromagnetics*, ed. R. Mittra. New York: Springer-Verlag, 1975.

[8] A. F. Peterson, "Numerical difficulties and software validation needs associated with EFIE formulations for dielectric scatterers," *Proceedings of the Fourth Annual Review of Progress in Applied Computational Electromagnetics*, Monterey, CA, March 1988.

Comparisons of Staggered and Non-staggered Schemes for Maxwell's Equations *

David Gottlieb † Baolin Yang ‡

January 4, 1996

Abstract

We present here a comparison of the efficiency of staggered vs. non-staggered methods for the numerical solution of the one dimensional Maxwell's equations.

The total work needed to achieve a certain accuracy for different schemes is estimated by considering the stability condition and phase error of staggered and non-staggered schemes. Our conclusion is that staggered grid methods are much better than non-staggered schemes for low order accuracy schemes, but their advantage decreases as the order of accuracy increases. In particular, fourth order compact schemes are almost equivalent.

We also introduce spectral staggered grid methods and demonstrate that there is no advantage in using staggered grid spectral methods. Numerical results verifying our claims are presented.

1 Introduction

We consider, in this paper, the numerical solution of the fundamental time dependent Maxwell's curl equations. The standard scheme in FD-TD methods is the Yee scheme [2]. This scheme is second order accurate scheme both in space and time and the unknowns E and H are given in a staggered set of grid points. It had been argued that the staggering is one of the most important features of this scheme. Recently, Petropoulos [4] gave a convincing evidence for the superiority of fourth order schemes over second order schemes. It has been also suggested (see [2]) that it may be necessary to convert second-order accurate FD-TD algorithms to those having fourth-order accuracy. The same type of analysis indicates that spectral methods might be of value as a possible alternative to finite differences for the solution of the Maxwell's equations. In fact, since polynomial spectral methods require only π points to resolve a wave, one can minimize the amount of total work needed for computations.

This note is addressing the question whether staggering is also necessary for high accuracy schemes as fourth order methods and spectral methods. In particular we consider second order schemes (staggered and non-staggered), fourth order explicit schemes (staggered and non-staggered), fourth order compact schemes (S and NS) as well as spectral polynomial methods (S and NS). All of those schemes were applied to the one dimensional Maxwell's equations.

*Research was supported by Air Force Grant AFOSR-95-0074.

To answer the above question we define the concept of the total work $W(e)$ needed to achieve a given accuracy e for the phase of a wave solution for the Maxwell's equation. Basically we look at the number of points N required to achieve a certain accuracy in the phase and the time step Δt, allowable by the scheme. The work W then is defined as

$$W = \frac{N}{\Delta t}. \tag{1}$$

We then compute the work required for the various schemes.
The results can be summarized as follows

- For second order schemes the staggered scheme requires *half* of the work of the non-staggered scheme. This explains the success of the Yee scheme.
- The fourth order staggered explicit schemes is more efficient than the non-staggered. However the improvement is not that dramatic in fact we can expect an improvement of about 36%.
- The staggered and non-staggered compact schemes are equivalent.
- The compact fourth order schemes are preferable to the explicit schemes.
- Within spectral polynomial schemes there is no difference between staggered and non staggered schemes.

It seems that the attractiveness of the staggered grid method diminish as the order of accuracy increases.

The main advantage of non-staggered grids, in our opinion, is the imposition of boundary conditions. In the staggered grid approximation one can impose the boundary conditions only on the variables that are defined on the boundary points. Thus boundary conditions in terms of *characteristic* variables are not easily implemented. It is our opinion that characteristic boundary conditions are important in the numerical solutions of the Maxwell's equations, especially for increased order of accuracy.

The paper is organized in the following way: In Section 2 we present the equations and the finite difference schemes considered. We also introduce the comparison methods used in this paper. In Section 3 we analyze the results of the comparisons. In Section 4 we construct a version of Spectral method for non-staggered scheme and finally Section 5 contains the numerical confirmation of the theory.

2 The Equations and Schemes

Consider the free space 1-D Maxwell's equations:

$$\begin{cases} \dfrac{\partial E}{\partial t} = -\dfrac{1}{\epsilon}\dfrac{\partial H}{\partial x} \\ \dfrac{\partial H}{\partial t} = -\dfrac{1}{\mu}\dfrac{\partial E}{\partial x} \end{cases} \tag{2}$$

where E is the electric field vector and H is the magnetic field vector. ϵ is the permitivity, and μ is the permeability.

Denote the speed of the wave by

$$c = \frac{1}{\sqrt{\epsilon\mu}} \tag{3}$$

and assume the initial condition

$$\begin{cases} E(x,0) = e^{2\pi i\omega x} \\ H(x,0) = \sqrt{\frac{\epsilon}{\mu}} e^{2\pi i\omega x} \end{cases}, \tag{4}$$

The solution of the system is then given by

$$\begin{cases} E(x,t) = e^{2\pi i\omega(x-ct)} \\ H(x,t) = \sqrt{\frac{\epsilon}{\mu}} e^{2\pi i\omega(x-ct)} \end{cases} \tag{5}$$

We discretize now (5) in space by several different finite difference approximations:
Consider the differencing and averaging operators, respectively,

$$\delta_x q_i = q_{i+\frac{1}{2}} - q_{i-\frac{1}{2}},\ \mu_x q_i = \frac{1}{2}(q_{i+\frac{1}{2}} + q_{i-\frac{1}{2}}) \tag{6}$$

Then the second order difference operators for the staggered and non-staggered second order schemes are given by:

I. *Second-order Staggered:*

$$\frac{du}{dx}|_i = \frac{1}{\Delta x}\delta_x u|_i + O(\Delta x^2) \tag{7}$$

II. *Second-order Non-staggered:*

$$\frac{du}{dx}|_i = \frac{1}{\Delta x}\delta_x \mu_x u|_i + O(\Delta x^2) \tag{8}$$

The fourth order explicit schemes are given by;

III. *Fourth-order Explicit Staggered:*

$$\frac{du}{dx}|_i = \frac{1}{\Delta x}\delta_x (I - \frac{1}{24}\delta_x^2) u|_i + O(\Delta x^4) \tag{9}$$

IV . *Fourth-order Explicit Non-staggered:*

$$\frac{du}{dx}|_i = \frac{1}{\Delta x}\delta_x \mu_x (I - \frac{1}{6}\delta_x^2) u|_i + O(\Delta x^4) \tag{10}$$

And finally the fourth order compact schemes are given by

V . *Fourth-order Compact Staggered:*

$$(I + \frac{1}{24}\delta_x^2)\frac{du}{dx}|_i = \frac{1}{\Delta x}\delta_x u|_i + O(\Delta x^4) \tag{11}$$

VI . *Fourth-order Compact Non-staggered:*

$$(I + \frac{1}{6}\delta_x^2)\frac{du}{dx}|_i = \frac{1}{\Delta x}\delta_x \mu_x u|_i + O(\Delta x^4) \tag{12}$$

Our analysis is based on the following considerations: 1. The total amount of work is proportional to the number of grid points N and the number of time steps $n \sim (\Delta t)^{-1}$. 2. The number of operations needed per time step is the same for staggered and non-staggered schemes. We therefore define

Definition 1: The total Work to achieve an accuracy e for the phase is defined as

$$W(e) \;=\; \frac{N(e)}{\Delta t} \tag{13}$$

Thus the work depends on two factors. First the time step Δt is restricted by the stability condition of the scheme. Secondly the number of grid points should be enough to resolve the different wave scales of the problem.

We first consider the CFL condition for the schemes **I** - **VI**. We assume that the discretization in time is the same for the various schemes. i.e second order for second order schemes, and fourth order for the fourth order schemes. Clearly the time step is inversely proportional to the maximum of the magnitude of the *symbol* $F(z)$ where $z = sin(k\frac{\Delta x}{2})$ can range between -1 and 1. We list the symbols and there maximum in the following:

$$F_{\mathrm{I}} \;=\; 2zi \tag{14}$$

$$F_{\mathrm{II}} \;=\; 2z\sqrt{1-z^2}i \tag{15}$$

$$F_{\mathrm{III}} \;=\; 2z(1+\frac{1}{6}z^2)i \tag{16}$$

$$F_{\mathrm{IV}} \;=\; 2z\sqrt{1-z^2}(1+\frac{2}{3}z^2)i \tag{17}$$

$$F_{\mathrm{V}} \;=\; \frac{2z}{(1-\frac{1}{6}z^2)}i \tag{18}$$

$$F_{\mathrm{VI}} \;=\; \frac{2z\sqrt{1-z^2}}{1-\frac{2}{3}z^2}i \tag{19}$$

If we denote now the number of points by $N \sim (\Delta x)^{-1}$ we get the following estimation for the allowable time steps:

$$c\Delta t_{\mathrm{I}} N_I \;\sim\; .5 \tag{20}$$

$$c\Delta t_{\mathrm{II}} N_{II} \sim 1. \tag{21}$$
$$c\Delta t_{\mathrm{III}} N_{III} \sim .4286 \tag{22}$$
$$c\Delta t_{\mathrm{IV}} N_{IV} \sim .7287 \tag{23}$$
$$c\Delta t_{\mathrm{V}} N_{V} \sim .4167 \tag{24}$$
$$c\Delta t_{\mathrm{VI}} N_{VI} \sim .5774 \tag{25}$$

It is clear that non-staggered methods allow larger time steps than the staggered methods, however this will be compensated by the better accuracy of the staggered scheme. This allows coarser grids and therefore smaller number of grid points to achieve the same accuracy.

We consider now the number of points required for a certain limit on the *phase error*. Assume the following solutions for the finite difference equations

$$\begin{cases} E(x,t) = e^{2\pi i\omega(x-\tilde{c}(\omega)t)} \\ \\ H(x,t) = \sqrt{\frac{\epsilon}{\mu}} e^{2\pi i\omega(x-\tilde{c}(\omega)t)} \end{cases} \tag{26}$$

The Phase Error is defined by

$$e(\omega,t) = |2\pi i\omega t(c-\tilde{c}(\omega))| \tag{27}$$

See [8].

We also define $j = \omega ct$ to be the number of periods in time and $p = \frac{1}{\omega\Delta x}$ to be the number of grid points per wave length. We get the following formulae for the phase errors

$$e_{\mathrm{I}}(p,j) = 2\pi j[1 - \frac{sin(\frac{\pi}{p})}{\frac{\pi}{p}}] \tag{28}$$
$$e_{\mathrm{II}} = 2\pi j[1 - \frac{sin(\frac{2\pi}{p})}{\frac{2\pi}{p}}] \tag{29}$$
$$e_{\mathrm{III}} = 2\pi j[1 - \frac{27sin(\frac{\pi}{p}) - sin(\frac{3\pi}{p})}{\frac{24\pi}{p}}] \tag{30}$$
$$e_{\mathrm{IV}} = 2\pi j[1 - \frac{8sin(\frac{2\pi}{p}) - sin(\frac{4\pi}{p})}{\frac{12\pi}{p}}] \tag{31}$$
$$e_{\mathrm{V}} = 2\pi j[1 - \frac{sin(\frac{\pi}{p})}{\frac{\pi}{p}(1 - \frac{1}{6}sin^2(\frac{\pi}{p}))}] \tag{32}$$
$$e_{\mathrm{VI}} = 2\pi j[1 - \frac{sin(\frac{2\pi}{p})}{\frac{2\pi}{p}(1 - \frac{2}{3}sin^2(\frac{\pi}{p}))}] \tag{33}$$

If we replace the $sin(\cdot)$ by its power series and retain only the terms of the lowest order, we get the leading order estimates for the phase error. Now to attain the same level of error, we know approximately how many grid points we need per wave length (N_{ppw}).

$$N_{\mathrm{I}} = 2\pi(\frac{2}{6})^{\frac{1}{2}}(\frac{\pi j}{e})^{\frac{1}{2}} \tag{34}$$

$$N_{\mathrm{II}} = 2\pi(\frac{8}{6})^{\frac{1}{2}}(\frac{\pi j}{e})^{\frac{1}{2}} \quad (35)$$

$$N_{\mathrm{III}} = 2\pi(\frac{3}{320})^{\frac{1}{4}}(\frac{\pi j}{e})^{\frac{1}{4}} \quad (36)$$

$$N_{\mathrm{IV}} = 2\pi(\frac{1}{15})^{\frac{1}{4}}(\frac{\pi j}{e})^{\frac{1}{4}} \quad (37)$$

$$N_{\mathrm{V}} = 2\pi(\frac{17}{2880})^{\frac{1}{4}}(\frac{\pi j}{e})^{\frac{1}{4}} \quad (38)$$

$$N_{\mathrm{VI}} = 2\pi(\frac{1}{90})^{\frac{1}{4}}(\frac{\pi j}{e})^{\frac{1}{4}} \quad (39)$$

Non-staggered schemes have a larger time step limit. But staggered schemes need less number of grid points per wave length. In order to determine which method is better, the most appropriate way is to look at the total Work.

3 Comparisons

To this end, we are able to give the total Work ($W(e)$ see (13)) for different schemes to attain the same level of **phase error**:

$$W_{\mathrm{I}} \sim 82.68(\frac{j}{e}) \quad (40)$$

$$W_{\mathrm{II}} \sim 165.37(\frac{j}{e}) \quad (41)$$

$$W_{\mathrm{III}} \sim 15.81(\frac{j}{e})^{\frac{1}{2}} \quad (42)$$

$$W_{\mathrm{IV}} \sim 24.79(\frac{j}{e})^{\frac{1}{2}} \quad (43)$$

$$W_{\mathrm{V}} \sim 12.90(\frac{j}{e})^{\frac{1}{2}} \quad (44)$$

$$W_{\mathrm{VI}} \sim 12.77(\frac{j}{e})^{\frac{1}{2}} \quad (45)$$

An immediate observation is that if $\frac{j}{e}$ is large then the fourth order schemes are always superior. Thus, if long time integration is needed or high accuracy is required then fourth order are better. The aim of this paper though is to compare staggered and non-staggered schemes. To see this, we give the factors between the total Work in the following:

$$\frac{W_{\mathrm{II}}}{W_{\mathrm{I}}} = 2 \quad (46)$$

$$\frac{W_{\mathrm{IV}}}{W_{\mathrm{III}}} = 1.5682 \quad (47)$$

$$\frac{W_{\mathrm{VI}}}{W_{\mathrm{V}}} = 0.9901\ . \quad (48)$$

Note that in the case of second order schemes the improvement is dramatic. For fourth order explicit schemes the staggered scheme is still better, but the improvement is less than that in

the second order case. It is interesting to notice that the non-staggered compact fourth order scheme is even faster than the staggered one. In the next section we will show that the there is no improvement for spectral methods. Thus staggered mesh methods lose the superiority when the order of accuracy increases.

Remark 3.1 *We haven't considered discretization error in time in our analysis. However, numerical experiments of fourth order schemes with fourth order Runge-Kutta scheme in time show that the factors in (46)-(48) still hold approximately when we consider the computation work needed for non-staggered and staggered schemes to attain* **the same level of accuracy**.

4 Staggered Chebyshev Collocation Method

For staggered Chebyshev collocation method, we impose boundary condition on H:

$$\begin{cases} H(1,t) = h_1(t) \\ H(-1,t) = h_{-1}(t) \end{cases} \tag{49}$$

Consider the staggered mesh:

$$Gauss - Lobatto\ points:\ x_i = cos(i\pi/N), i = 0, \ldots, N$$

for the discretization of H(x,t) and

$$Gauss\ points:\ y_j = cos((j + \frac{1}{2})\pi/N), j = 0, \ldots, N-1$$

for the discretization of E(x,t).

Then the Chebyshev collocation method for the staggered mesh is given by:

$$\frac{\partial E_{N-1}(y_j,t)}{\partial t} = -\frac{1}{\epsilon}\frac{\partial H_N(x,t)}{\partial x}|_{x=y_j}, \qquad j = 0, \ldots, N-1 \tag{50}$$

and

$$\frac{\partial H_N(x_i,t)}{\partial t} = -\frac{1}{\mu}\frac{\partial E_{N-1}(x,t)}{\partial x}|_{x=x_i}, \qquad i = 1, \ldots, N-1$$

$$H_N(1,t) = h_1(t) \tag{51}$$

$$H_N(-1,t) = h_{-1}(t)$$

where $E_{N-1}(x,t)$ is the approximating Chebyshev polynomial of degree $N-1$ and $H_N(x,t)$ is the approximating Chebyshev polynomial of degree N. Numerical computations of staggered Chebyshev collocation method don't show any advantage of staggered method over non-staggered method.

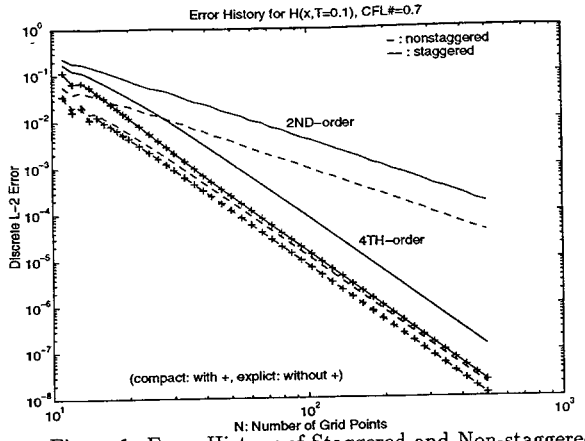

Figure 1: Error History of Staggered and Non-staggered Schemes

5 Examples

Example 1 *In this experiment, we use leap-frog scheme in time for second order schemes and fourth order Runge-Kutta method in time for the fourth order schemes. The time step is chosen according to the conditions in section 2 with the same scaling. We plot their error history for different number of grid points, see figure 1.*

Example 2 *In this experiment, we verifies the ratios of the $N'_{ppw}s$ needed for staggered and non-staggered schemes. Leap-frog scheme is used in time for second order schemes and fourth order Runge-Kutta scheme is used in time for fourth order schemes. We choose the* **time steps** *according to the conditions in section 2 and we got the N needed for staggered and non-staggered schemes to attain the same level of accuracy.*

The factors between $N'_{ppw}s$ and the factors between work of staggered and non-staggered schemes in section 2 and 3 are verified here. See table (1)-(3). Note that the scale we took for estimated Work is the same in the same table. So the ratios of Work do reflect the relative efficiency of staggered and non-staggered schemes.

Example 3 *The error history of staggered and non-staggered Chebyshev methods is compared. For the comparison to be meaningful, we fix H in boundary treatment in both methods. See figure (2). There is no gain in accuracy for non-staggered method. We also experimented with the largest time step we can choose for the two methods and no difference was observed.*

Table 1: Number of Grid Points Needed for Second Order Schemes to Attain the Same Level of Error

error	8e-5	4e-5	2e-5	1e-5
Non-staggered$(N \cdot Work)$	394 · 77618	592 · 175232	793 · 314425	996 · 496008
Staggered $(N \cdot Work)$	197 · 38809	296 · 87616	397 · 157609	498 · 248004
ratio	2. · 2.	2. · 2.	2. · 2.	2. · 2.

Table 2: Number of Grid Points Needed for Fourth Order Non-compact Schemes to Attain the Same Level of Error ($CFL \approx 0.9$)

error	8e-6	4e-6	2e-6	1e-6
Non-staggered$(N \cdot Work)$	183 · 45957	217 · 64621	259 · 92056	308 · 130183
Staggered$(N \cdot Work)$	112 · 29267	133 · 41272	158 · 58245	188 · 82464
ratio	1.634 · 1.570	1.632 · 1.566	1.639 · 1.581	1.638 · 1.579

Table 3: Number of Grid Points Needed for Fourth Order Compact Schemes to Attain the Same Level of Error ($CFL \approx 0.7$)

error	8e-6	4e-6	2e-6	1e-6
Non-staggered $(N \cdot Work)$	116 · 23304	138 · 32982	164 · 46581	195 · 65856
Staggered $(N \cdot Work)$	99 · 23521	117 · 32851	139 · 46367	166 · 66129
ratio	1.172 · 0.991	1.180 · 1.004	1.180 · 1.005	1.175 · 0.996

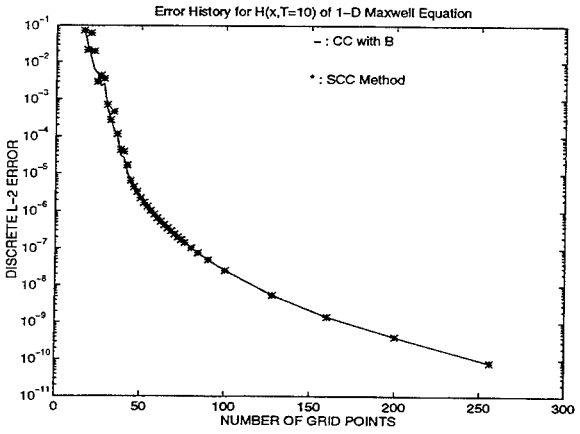

Figure 2: Error History: Staggered and Non Staggered Chebyshev Method (B: fixing H for boundary treatment)

References

[1] D. GOTTLIEB AND S. ORSZAG, *Numerical Analysis of Spectral Methods: Theory and Applications*, SIAM, Philadelphia, 1977.

[2] A. TAFLOVE, *Computational Electrodynamics: The Finite-Difference Time-Domain Method*, Artech House, Boston · London, 1995.

[3] J.P. BERENGER, *A perfectly matched layer for the absorption of electromagnetic waves*, AJ. Comput. Phys. **114**, pp. 186-200, 1994.

[4] P. G. PETROPOULOS, *Phase Error Control For FD-TD Methods of Second and Fourth Order Accuracy*, IEEE Trans. Antennas and Propagation, vol. 42, No. 6, 1994

[5] , D. FUNARO AND D. GOTTLIEB *A new method of imposing boundary conditions in pseudospectral approximations of hyperbolic equations*, Math. Comp. **57**, pp. 599-613, 1998

[6] , D. FUNARO AND D. GOTTLIEB *Convergence Results for pseudospectral approximations of hyperbolic systems by a penalty-type boundary treatment*, Math. Comp. **57**, pp. 585-596, (1991).

[7] , W.S.DON AND D. GOTTLIEB *The Chebyshev-Legendre Method: implementing Legendre Methods on Chebyshev points*, SIAM J. Numer. Anal. **31**, pp. 1519-1534, 1998

[8] H. KREISS AND J. OLIGER *Methods for the Approximate Solution of Time Dependent Problem*, Garp Publication Series No. 10, 1973

[9] D.A. KOPRIVA AND J.H. KOLIAS *A conservative staggered-grid Chebyshev Multidomain method for compressible flows* ICASE Report No. 95-18, 1995

MINIMIZING THE NUMBER OF FREQUENCY SAMPLES NEEDED TO REPRESENT A TRANSFER FUNCTION USING ADAPTIVE SAMPLING

E. K. Miller
3225 Calle Celestial, Santa Fe, NM 87501-9613
505-820-7371, emiller@esa.lanl.gov

0.0 ABSTRACT

One of the most commonly encountered problems in wave-equation applications such as arise in acoustics and electromagnetics is that of estimating transfer functions from discrete frequency samples of a first-principles, or generating model (GM) such as NEC, FERM, E-PATCH, etc. This problem has been approached in a mostly *ad hoc* way wherein the GM samples are spaced uniformly and closely enough such that linear interpolation yields a reasonably smooth graphical representation of the continuous response. Often, additional sampling between the original ones is done subsequently to improve the result, a process that may be repeated several times until an apparently satisfactory outcome is obtained. This approach will usually result in substantial oversampling, with a concomitant increase in the associated cost, while offering no assurance that important details of the true GM transfer function have not been missed. At the same time, there is no quantitative measure of how much the linearly interpolated estimate might differ from the actual response between the sampled values. The procedure described here uses model-based parameter estimation with rational-function, overlapping fitting models (FMs) to automatically determine where the GM needs to be sampled to reduce the mismatch between the FM and GM below a specified value.

1.0 A SUMMARY OF THE BASIC IDEA

As demonstrated elsewhere [Miller (1995), (1996)], hereafter referred to as RI and RII respectively, a rational function, as a generalization of a pole series, is a good choice for approximating an electromagnetic frequency response. The possibility of exploiting that idea to automate sampling of a first-principles, or generating model (GM) subject to a specified estimation error was also considered; a detailed description of one approach is given here. The basic idea is to use a series of rational-function fitting models (FMs), $M_i(n_i,d_i)$, of index number i and numerator and denominator polynomial orders n_i and d_i respectively, i = 1, . . ., N, where some of the GM samples for each M_i are shared by FMs M_{i-1} and M_{i+1}, etc. A small number of GM samples are computed across the bandwidth of interest to begin the process with a different subset of these samples assigned to each of the initial, low-order FMs employed. A sequence of more closely spaced FM estimates is then generated from each FM. In the frequency range where two (or more) FMs overlap, the differences between their estimates are computed. The minimum match in digits, E_i, is then determined for each FM. If any of these is less than a specified estimation error, EE, a new GM sample is computed at the frequency where $ME_1 \equiv \min[E_1,E_2,\ldots,E_N]$ occurs. The FMs that contain the new GM sample are then increased by one in order (alternating between increasing n and d as new GM samples are added). In order to avoid ill-conditioning, when the order of one or more of the affected FMs reaches some specified maximum value, it may be split into two lower-order, overlapping, new FMs. New E_i's are computed over the bandwidth spanned by the FMs thus affected and ME_2 is determined. This process continues with ME_3, ME_4, etc. until all E_i's exceed EE. A final GM sample density of about 3 per resonance can be achieved without initial knowledge of where these resonances are located for an EE of 10^{-2}.

2.0 RATIONALE' FOR USING A RATIONAL-FUNCTION FITTING MODEL

The above-described procedure is known as model-based parameter estimation (MBPE). In contemplating using MBPE for electromagnetic (EM) or any other phenomena, the first issue to consider is what FMs might be appropriate. Unless a FM is physically based, MBPE is basically a curve-fitting procedure. While curve fitting can be a useful tool, MBPE is potentially much more powerful when the problem physics are explicitly involved in the process and might therefore be described as "smart" curve fitting. As discussed in RI and RII, exponential and pole series occur in numerous ways in EM, and thus provide obvious choices for FMs. Furthermore, the two most frequently used domains for formulating and solving EM problems, and for many other physical phenomena as well, are the time domain (TD) and frequency domain (FD), for which generic descriptions are given by exponential and pole series respectively, which together form a Laplace-transform pair. As mentioned in RI, the same transform relationship exists between other observable pairs that are also described by exponential and pole series (see Table I of RI). Thus, we use the terms "waveform domain" (WD) and "spectral domain" (SD) respectively, for phenomena that are described by exponential series and pole series, as a generalization of their more specific and familiar TD and FD forms. While a pole series does not fully describe an electromagnetic transfer function, it can be a good approximation to that response and provide a concise way to represent it. For purposes of the present discussion, which is to reduce the number of samples of EM observables that are needed in the first place, the FM does not have to be exact so long as it leads to an acceptably accurate and parsimonious representation.

The generic WD and SD FMs can be expressed as

$$f(x) = f_p(x) + f_{np}(x) = \Sigma R_\alpha \exp(s_\alpha x) + f_{np}(x),\ \alpha = 1, \ldots, P \qquad (1)$$

and

$$F(X) = F_p(X) + F_{np}(X) = \Sigma R_\alpha/(X - s_\alpha) + F_{np}(X),\ \alpha = 1, \ldots, P \qquad (2)$$

where "x" represents the WD independent variable and "X" is its SD, or transformed, counterpart. For the time-frequency transform pair, x would be the time variable t and X would be the complex frequency s, in general, but for most purposes would be limited to the radian frequency $j\omega$. The exponential or pole series contributions are designated respectively by $f_p(x)$ and $F_p(X)$, and represent what we might call the "resonant" response, with the non-pole part denoted by $f_{np}(x)$ and $F_{np}(X)$. The FM parameters, the complex resonances (or poles), "s_α," and the modal amplitudes (or residues), "R_α," (or their polynomial counterparts) are quantified by fitting samples of the relevant observable to the desired model, $f_p(x)$ or $F_p(X)$. The various FMs and their estimated parameters provide a mathematically-concise and physically insightful way to characterize electromagnetic and other wave-equation phenomena. Subsequent attention is here limited to the spectral domain.

3.0 SAMPLING IN THE SPECTRAL DOMAIN

Spectral-domain function sampling begins with the FM given by Eq. (2) and assumes the availability of samples denoted by

$$F_i = F(X_i) = \Sigma R_\alpha/(X_i - s_\alpha) + F_{np}(X_i),\ \alpha = 1, \ldots, P \qquad (3)$$

where, in contrast to waveform sampling, there is no requirement that the samples X_i be uniformly spaced (RI). However, also in contrast to waveform sampling where the FM can be a purely exponential series at late times, spectral sampling can not avoid the presence of the generally unknown non-pole term. The possibility of using variable numerator and denominator polynomials orders provides a way to approximate the effect of the non-pole term by simply increasing the order of the numerator polynomial. For example, an increase of one in the numerator order has the effect of representing F_{np} by a constant, which, when absorbed into the rational function results in equal numerator and denominator

orders. If F_{np} is represented by a constant and a term linear in X, this has the effect of making the numerator order one greater than the denominator. Thus, by varying the relative orders of the polynomials which comprise the FM, various approximations of the non-pole, SD contribution are included.

Therefore, in general we use a SD FM given by

$$F(X) = N(X)/D(X) \tag{4a}$$

where the numerator and denominator polynomials N(X) and D(X) are given by

$$N(X) = N_0 + N_1X + N_2X^2 + \cdots + N_nX^n \text{ and } D(X) = D_0 + D_1X + D_2X^2 + \cdots + D_dX^d. \tag{4b}$$

The coefficients of the SD FM can be obtained from sampled values of the response, or from function sampling. How this is done is easy to see by rewriting Eq. (4) as

$$F_iD_i = N_i,\ i = 0, \ldots, D - 1 \tag{5a}$$

with $F_i = F(X_i)$ the function samples and (5b)

$$D_i = D_0 + D_1X_i + D_2(X_i)^2 + \cdots + D_d(X_i)^d,\ N_i = N_0 + N_1X_i + N_2(X_i)^2 + \cdots + N_n(X_i)^n. \tag{5c}$$

There are d + n + 2 unknown coefficients in the set of homogeneous equations given by (5a), requiring a constraint or additional condition to make the sampled equations solvable. As discussed in RI, there is no unique choice for this constraint, but if we set $D_d = 1$, then the following equations result:

$$F_0D_0 + X_0F_0D_1 + \ldots + F_0(X_0)^{d-1}D_{d-1} - N_0 - X_0N_1 - \ldots - (X_0)^nN_n = -(X_0)^dF_0$$
$$F_1D_0 + X_1F_1D_1 + \ldots + F_1(X_1)^{d-1}D_{d-1} - N_0 - X_1N_1 - \ldots - (X_1)^nN_n = -(X_1)^dF_1$$
$$\vdots$$
$$F_{d-1}D_0 + X_{d-1}F_{d-1}D_1 + \ldots + F_{d-1}(X_{d-1})^{d-1}D_{d-1} - N_0 - X_{d-1}N_1 - \ldots - (X_{d-1})^nN_n = -(X_{d-1})^dF_{d-1} \tag{6}$$

where $D \geq n + d + 1$ is required for a solution. Note that the matrix coefficients are comprised of a product of a data sample and the the frequency at which the sample is taken raised to a power. The exponentiation of the sampling frequencies suggests that large dynamic numerical ranges in the matrix coefficients may result if d and n are very large. One way to avoid this is to scale the frequency, so that, for example, if the sampling range is centered at 1 GHz, a scaling of 10^9 in the frequencies leads to nominal scaled values near unity. It is also possible to center the SD model about a frequency in the interval of interest so that terms like $(X_s - X_{ref})^n$ result. Combing scaling and translation similarly produces terms like $[(X_s - X_{ref})/X_{ref}]^n$.

An over-sampled system, i.e., one where $D > n + d + 1$, can be handled in various ways, one of which is to employ a pseudo inverse for the solution, but which has the disadvantage of approximately squaring the condition number. Another approach would be to employ overlapping windows of different data sets to compare performance of their respective, lower-order FMs.

Besides quantifying the FM using function sampling, derivatives of the response can also be used, as can various combinations of function and derivative sampling. One result using derivatives is that the samples can then be spaced more widely in frequency than using function sampling alone. A more important consideration is that in some circumstances a derivative sample can be obtained for a computation operation count that is of order $1/X_s$ of the first function sample alone. If a derivative provides in-

formation concerning the response from it is obtained that is equivalent to that provided by a function sample, an obvious computation advantage is achieved. Using derivative sampling in the context of a frequency-domain integral equation is discussed more fully in RII. Thus, a given FM, whether an exponential series or a pole series, can be quantified by a variety of data and also by using various approaches. Although determining the time or frequency derivatives of some response may not be an obvious observable in computational electromagnetics (CEM) and such derivatives are unlikely to be measurable, they can be obtained from computation.

4.0 ADAPTING AND OPTIMIZING SAMPLING OF THE FPM

A major advantage of MBPE, and a prime motivating factor for its use, is its potential for minimizing the operation count needed for computing various EM (and other wave-equation phenomena) responses. This is especially the case concerning the time-frequency domain transform pair, where there is more flexibility with respect to sample placement and model order in frequency than in time. As noted in RI in connection with waveform sampling, it's necessary that a polynomial representation of the sampled data be developed, which leads to a need for uniform sample spacing. Actually, this requirement is not inconsistent with how most time-domain computations are performed, where equal time steps are most-often used throughout the time interval for which the model is run. However, it also means that if subsequent evaluation of the time response shows that it was undersampled, it's not very practical to add new samples to the original result; instead, the model computation must be entirely repeated with a new time step. This is not the case for all WD models, however, as is demonstrated by sampling the far fields of a source distribution (model 4 in Table I of RI), where new observation angles can be added to an existing set without repeating any previous computation. This advantage is always true in the FD, where adding one, or several, new function or derivative samples to an existing set can be done while fully retaining the benefit of whatever samples have already been obtained.

Ideally, the goal of minimizing the operation count required to obtain an EM transfer function would involve choosing sample locations and derivative orders (if used) such that the new information provided by each new sample is the maximum that can be provided over the range of interest relative to the cost of obtaining that sample. If this goal were to be realized for each of the samples ultimately needed for computing the FM parameters while satisfying a specified error criterion, then the overall cost should be a minimum for the chosen error measure. This idea is illustrated conceptually in Fig. 1 below.

There seems to be no obvious or unique approach for achieving this goal, since n and d, the number of samples D and the frequency range they span, are all free parameters in developing a FM. This means that some computer experimentation will usually be required to determine suitable numerical values for them. A few of the several sampling strategies that seem worth considering are discussed immediately below, followed by a discussion of possible error measures.

4.1 Adaptive Sampling Strategies

Adaptive sampling strategies form a basis for much numerical analysis. Three possibilities that might be applicable to transfer-function representation are listed below.

1) A strategy similar to one found useful for adaptive numerical quadrature based on Romberg's method (RM) [Miller (1970)] might be adapted to the spectral-estimation problem. It involves choosing a starting subinterval over which five successive uniformly spaced samples of an integrand are developed upon which RM is applied to the three trapezoidal-rule quadrature values that are obtained (samples 1 and 5, 1,3 and 5, and all five samples). An error estimate provided by the RM shows whether new samples are required in either half of the original subinterval. If this is the case, new samples are added where indicated half way between the original ones and the process is successively repeated. On the other hand, if the initial error is smaller than specified, the process is repeated while doubling the subinterval size. This kind of adaption handles sharply peaked integrands, yielding maximum-to-minimum sample spacings of 10^6, but it may not be as well-suited to spectral estimation since for many EM appli-

cations, the resonances are relatively uniformly spaced.

2) The first two samples could be taken at the endpoints of the variable range with additional samples subsequently developed by evenly subdividing this range into subintervals until the error criterion has been satisfied over all subintervals that are thus formed.

3) If an error measure is available as a continuous function of the independent variable over the range of interest, then placing a new sample wherever that measure is a maximum seems to be an obvious choice as a way to achieve the greatest amount of additional information from a single additional sample. This approach is used for the procedure implemented here.

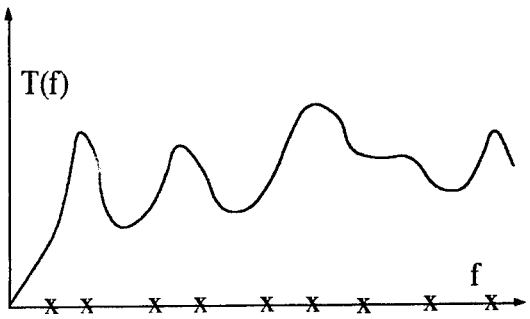

Figure 1. Conceptual diagram to illustrate optimal placement of frequency samples in developing a fitting-model representation of a transfer function T(f). Since there is no computational penalty in doing so, we can expect that the samples would generally be non-uniformly spaced as a means of maximizing the information provided by each.

4 Estimation of Error or Uncertainty

An adaptive process can be only as effective as the error measure used for estimating the degree to which the FM (or its equivalent) differs from the GM (or whatever process whose results the FM is to approximate). This observation is a general one that applies to all manner of numerical processes having the goal to minimize the number of accurate samples that are needed as a means of reducing the cost of developing a sampled representation of some process over a specified range of independent variable(s). For an SD application, it appears desirable to use lower-order FM's over subintervals of the spectral range to be covered to avoid possible ill-conditioning. It then follows that two or more FM's will be needed to span the spectral range of interest, leading to the situation illustrated in Fig. 2. By using overlapping FM's which share common data, their differences, or mismatch errors, can then be used to estimate FM uncertainty as a function of frequency. The minimum match (maximum error), $\Delta MM_{i,j}(f) \equiv \max\{[|M_i(f) - M_j(f)|]/[|M_i(f)| + |M_j(f)|]\}$ is then computed for each pair of overlapping models as a function of frequency. Subsequent sample placement and type would then be chosen to maximize the information acquired from each sample by adding each new sample at the frequency where the minimum match, ME_i, for all FMs occurs. Sampling of the GM would be concluded when the specified error criterion is satisfied. Also note that, alternatively, an exact error measure results from comparing a FM result with a GM sample $G(f_k)$, using the measure $\Delta GM_{i,k} \equiv [|G(f_i) - M_k(f_i)|]/[|G(f_i) + M_k(f_i)|]$. However, doing this potentially would require more GM samples with a consequent increased computer time, while providing, in addition, only a pointwise error measure in f. Thus, $\Delta MM_{i,j}(f)$ requires less computation and yields a global , but approximate, error measure while $\Delta GM_{i,k}$ requires more computation and yields a pointwise, but exact, error measure.

There at least three kinds of errors that the FM might produce relative to GM results:

1) Non-physical results, e.g., negative conductance or resistance;
2) Amplitude shifts in transfer functions; and
3) Resonance shifts between transfer functions;

with the latter two occurring either between two (or more) FM's or between a FM and the GM result, and for which different sampling decisions might be made. For non-physical errors, an additional GM sample at the peak in negative conductance would seem most appropriate. For baseline-shift errors, an additional sample could be placed at the location of the maximum error if it exceeds the specified error criterion. For resonance-shift errors, an additional sample could be put between the response peaks, again if the shift exceeds the specified error criterion.

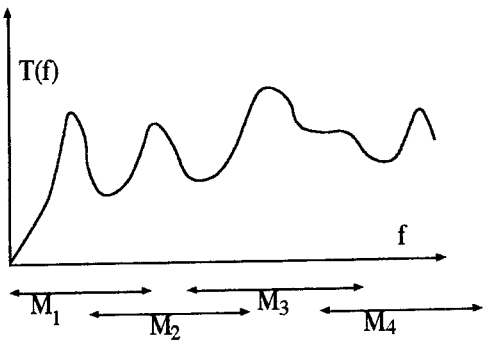

Figure 2. The possibility of developing a FM-representation of a transfer function over a wide frequency interval by employing a number of subinterval, lower-order Fitting Models, M_i, is illustrated here. Each FM represents the response over a frequency interval $F_i = F_{i,u} - F_{i,l}$ where the adjacent FM's share some frequency samples and the difference between them, $\Delta MM_{i,j}(f) = [\,|M_i(f) - M_j(f)|/[|M_i(f)| + |M_j(f)|]$ provides a normalized, mutual-error estimate between FM's i and j. By evaluating $\Delta MM_{i,j}(f)$ as a function of frequency, new samples, either function or derivative, can be placed where $\Delta MM_{i,j}(f)$ exhibits values that exceed a specified amount and where, therefore, the corresponding FM results are most uncertain.

To summarize, for a FM having numerator and denominator polynomials of order n and d, respectively, n + d + 1 samples of the GM are needed, which can range, on the one hand, from using n + d + 1 different frequencies to, on the other hand, using one function sample and n + d derivatives at a single frequency. The "best" approach would be that which minimizes the GM operation count required to achieve some specified accuracy or uncertainty in the transfer function being estimated, using an appropriate mix of function and derivative samples. By varying the n and d parameters of the rational-function FM, the effects of non-pole contributions and poles that lie outside the frequency interval of interest can be approximated, although it's worth considering other approaches to this problem.

4.3 Adaptive Sampling of a Simulated Transfer Function

A pole series provides a good test for an adaptive sampling strategy because many actual EM transfer functions exhibit a marked resonance structure and its properties are controllable. A 20-pole series having poles at $s_i = -\sqrt{i}/20 + j*i$, i = 1,2,...,20 was used as a GM. The initial GM samples were placed at 0.5 intervals from s = j*3.5 to = j*11, numbered from 1 to 16. Six FMs were employed which spanned GM sample numbers 1-6, 1-8, 5-10, 7-12, 9-16 and 11-16, respectively. Thus, four of the six FMs (1,3,4,6) were initially of order 6, using n = 3 and d = 2, while two (2 and 5) were of order 8, using n = 3 and d = 4. The latter two FMs are arranged to include the endpoints so that there are a minimum of two overlapping FMs across the entire frequency range of interest. The estimation error, EE, was set at 10^{-2}, or, when measured in digits, EE = 2. Some results for applying the adaptive procedure outlined above are shown in Figs. 3-5.

The real part of the final fitting model is shown in Fig. 3, on which are also indicated the original and additional GM samples, whose values in order of sampling, are 6.2, 7.2, 9.2, 5.3, 8.2, 9.35, 4.15, 6.25, 5.05, 1.05, 8.3, 7.05, 4.2, and 10.95. It's also of interest to observe the behavior of the minimum-match values for each of the FMs, E_i, as the process of model modification continues, a result that is shown in Fig. 4. Also shown is ME_i, the minimum-match value for all six FMs, as a function of

model iteration number. An E_i can remain constant for several iterations if none of the added GM samples is contained in its frequency span and its E_i is unchanged as well. Although this behavior is not guaranteed, ME_i can be see in this example to exhibit a monotonic increase. Finally, it's significant to note, as demonstrated by Fig. 5, that the FM-FM and FM-GM mismatch errors are well-correlated, with the former being generally somewhat greater than the latter, for the individual GM samples [part (a)] and where the frequency averages of these quantities are plotted for each model iteration [part (b)]. This result indicates that the FM mismatch is a reliable indicator of the error between the FMs and the GM they are intended to approximate.

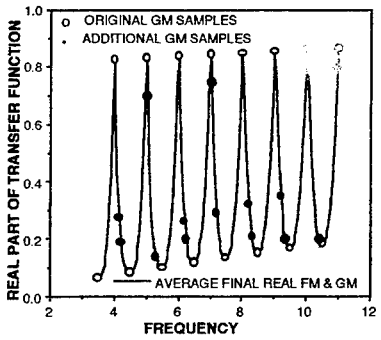

Figure 3. Result obtained from adaptive sampling of the pole-series GM described in the text. The original 16 samples of the real part of the GM are indicated by the o's and the additional 14 samples needed to obtain a 0.01 normalized match between overlapping FMs across the 3.5 to 11 frequency range are shown as •. The final FM, obtained from averaging the individual FMs in their regions of overlap, is shown by the solid line. The final FM-GM match is also better than 0.01 (see Fig. 5 for further discussion).

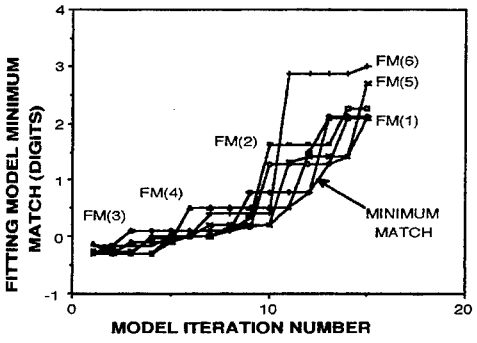

Figure 4. An illustration of how the FM parameter ME_k can vary with model iteration number k. The E_i curve for each FM is indicated by FM(i), where the initial set of FMs is number 1 on the horizontal axis. For this particular case, ME increases monotonically, from less than 0 for the first several models (indicating that the normalized errors are greater than unity) to the two-digit specified estimation error at k = 15.

A result for the same GM as above, but with an added pole at $s = -j/\sqrt{20} + j*7.5$ using 16 initial GM samples spaced at 0.5 intervals beginning at 3.75 is shown in Fig. 6, again using an EE of 0.01. An additional 16 GM samples were required for this example, 2 more than previously because of the added pole. Although the locations of the initial GM samples are shifted relative to the poles in this case compared with the previous example, and there is an added pole in the frequency range covered by the FMs, the final performance is comparably good, indicating the robustness of the adpative-sampling approach.

6.0 CONCLUDING DISCUSSION

This discussion has illustrated adaptive sampling of a pole-based transfer function like those that arise in EM frequency response using model-based parameter estimation (MBPE). A useful fitting model (FM) for this purpose, the "model-based" part of MBPE, is a rational function which serves as a generalization of a pole series that characterizes the resonance behavior of EM observables. The "parameter-estimation" part of MBPE is the process of obtaining numerical values for the coefficients of the FM by matching them to sampled values of the EM observable of interest.

A FM provides a reduced-order representation of the results obtained from a first-principles, or generating model (GM) based directly on Maxwell's equations or from experimental measurements. It offers the possibility of reducing the sampling required of the GM when using it to develop a response such as a broadband transfer function. This is particularly the case where the response contains details that might be missed if the GM samples are too-widely space. Adaptive sampling of the GM is made possible by using several, low-order, overlapping FMs that share initial GM samples chosen to cover a given frequency range. The FM results are compared at other frequencies within their shared bandwidths and new GM samples are added wherever the FM differences exceed a specified level. A final set of FMs is thus developed for the GM samples that provides a continuous representation over a given frequency range while meeting a desired-accuracy, or uncertainty, specification. Such adaptive sampling can not only greatly reduce the number of GM samples that would otherwise normally be used but also ensures that fine details of the response are not missed.

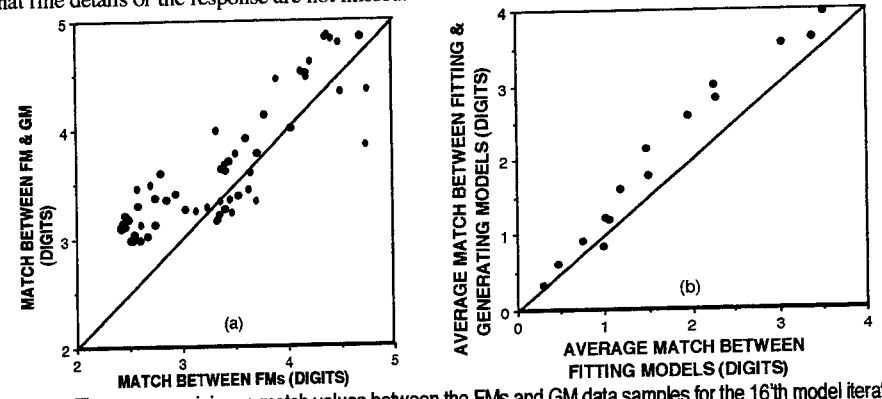

Figure 5. The average minimum-match values between the FMs and GM data samples for the 16'th model iteration of the above example (a) and the frequency-averaged values of these quantities for each of the 16 FM sets (b). In both cases the FM-FM minimum match is seen to be generally less than the FM-GM value, showing that the former is a conservative error estimate of the accuracy achieved by the FMs.

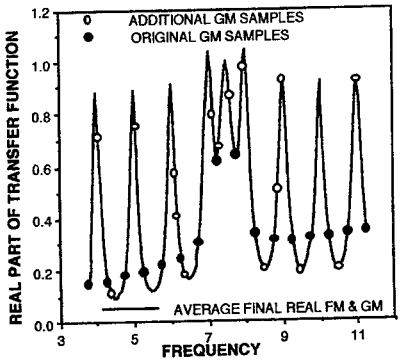

Figure 6. Results for the real component of the 20-pole GM used above but with an added pole at s = -j/√20 +j*7.5 and using initial GM samples shifted by 0.25 in frequency. Shown is the average final FM for a 0.01 specified estimation error as obtained at the 16'th additional GM sample.

REFERENCES

Miller, E. K. (1970), "A Variable Interval Width Quadrature Technique Based on Romberg's Method", Journal of Computational Physics, 5, pp. 265-279.

Miller, E. K. (1995), "Model-Based Parameter Estimation in Electromagnetics: I--Background and Theoretical Development," Applied Computational Electromagnetics Society Newsletter, **10** (3), Nov.

Miller, E. K. (1996), "Model-Based Parameter Estimation in Electromagnetics: II--Applications to EM Observables," Applied Computational Electromagnetics Society Newsletter, submitted for publication.

SESSION 21:

MODELING TOOLS FOR VISUALIZATION: PRE- AND POST-PROCESSING

Chair: J. Karty

Matlab NEC Toolbox: the Cross Platform GUI Pre- and Post-processing Tool for NEC Applications

Yilong Lu

School of Electrical and Electronic Engineering
Nanyang Technological University
Singapore 639798

I. Introduction

The Numerical Electromagnetics Code (NEC) [1] has been widely used for realistic modeling of the electromagnetic response of wire antennas and other metal structures. NEC itself is not user friendly and requires extensive knowledge, experience, and time to be used correctly and effectively. Without a proper tool, it is very tedious and error prone process to establish a proper NEC geometry model and input file required by NEC execution, especially for large and complex problems. Although there are some NEC tools available, such as IGUANA, WIREGRID, EZNEC, EAM:NEC, NEC-WIN, most of them are for PCs and their geometry inputs are still not efficient and they are only convenient to use for small or medium size problems. For large problems, the NEC computations have to be run on a workstation or a supercomputer, it is therefore highly desirable to have a set of user friendly and efficient NEC pre- and post-processing tools available for multi-platform including workstations and PCs (mainly for pre-processing).

The lack of cross platform user friendly pre- and post-processors for NEC application motivates us to develop a NEC Toolbox that could be portable to different platforms. It has been found that Matlab [2] is a very powerful computing tool as well as an environment able to handle complex computations and graphics as well as graphical user interface (GUI). Matlab is available for most platforms, including PCs, workstations, and supercomputers. To develop the NEC pre- and post-processing toolbox using Matlab allows portability across different platforms. Another major reason for selecting Matlab as the developing software is that it is an engineer oriented software, numerous tools and functions have been built in the software, hence time would not be wasted in developing auxiliary functions which are readily available. Moreover, Matlab m-file and script programming allow creation, modification, and assembly from parts for complex structures by only simple script programming. Matlab's ASCII m-file and script file structure allows user to add other customized functions to the Toolbox very easily.

This Matlab NEC Toolbox contains both pre- and post-processing tools. The preprocessing tools have the features of *text editing*, *graphical editing*, *script creation*, *automatic conversion*, and a number of library component m-files. The post-processing

tools including three modules *freplot, patplot* and *necplot*, allowing user to view, save, and print more than 23 different plots from NEC output files. All plots from the toolbox can be easily saved in many different formats, including PostScript, for future use or for printing.

II. Pre-Processing Modules

The preprocessing tools have the features of *text editing, graphical editing, script creation, automatic conversion*, and a number of utility and library component m-files.

A. NEC Card Editor

The GUI NEC Card Editor enables users to create a new NEC input data file or alternatively, to edit an existing NEC input data file. The user can also invoke the Graphical Editor which shall be capable of converting geometry input into geometry data cards. During card entry, the template shall automatically recommend default values for applicable data fields, provide guidance for correct data entry and carry out comprehensive error checking before accepting the user's input. The on-line help on all cards is also implemented so users do not need additional user guide.

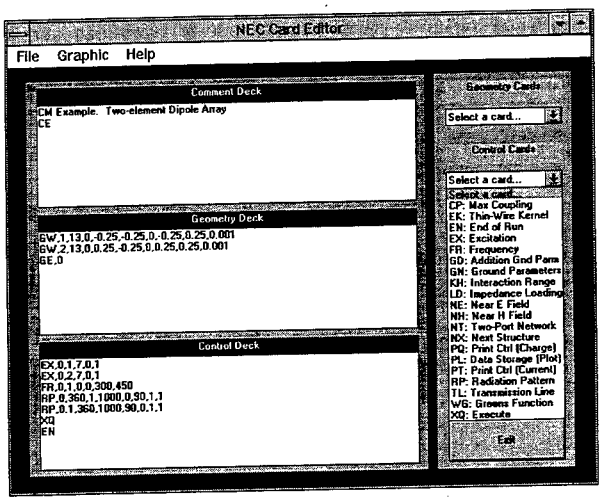

Fig. 1. An NEC Card Editor window with **Control Cards** selection activated.

The Deck frame consists of three editable text boxes which are the **Comment Deck**, the **Geometry Deck** and the **Control Deck** respectively, as shown in Fig. 1. The console frame on the right contains two popup menu and two command pushbuttons. The popup menu labeled as **Geometry Cards** is for selecting a geometry data cardtype while the **Control Cards** menu is for selecting a program control cardtype. The

Graphic popup menu or pushbutton is for invoking the Graphic Editor. Select a program control cardtype from the **Control Cards** popup menu is also illustrated in Fig. 1. A template for the selected cardtype is shown in Fig. 2. And the on-line help of a card is illustrated in Fig. 3.

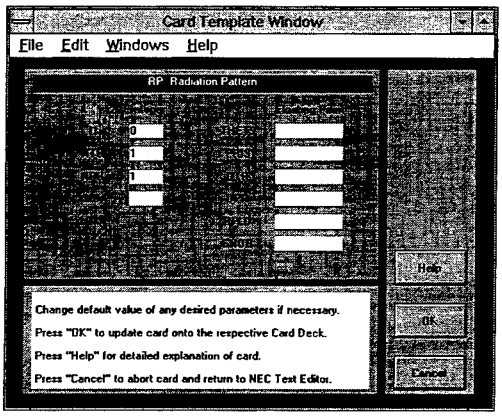

Fig. 2. A Card Template Window making data entry easier.

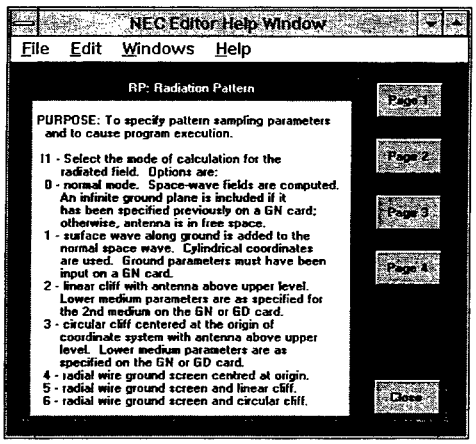

Fig. 3. A NEC Editor Help Window displaying information for data entry.

B. Graphic Editor

Users can also invoke the GUI Graphic Editor to create, view, and edit a 3-D representation of an antenna structure for conversion to a standard NEC Geometry data

format. Using this graphical editor, one can create a desired structure by inputting and transforming (scaling, rotation, translation), assembling (adding and deleting) library components. The graphical editor also allows input of structure files in 3DV format (a popular 3-dimensional wire-grid modeling format).

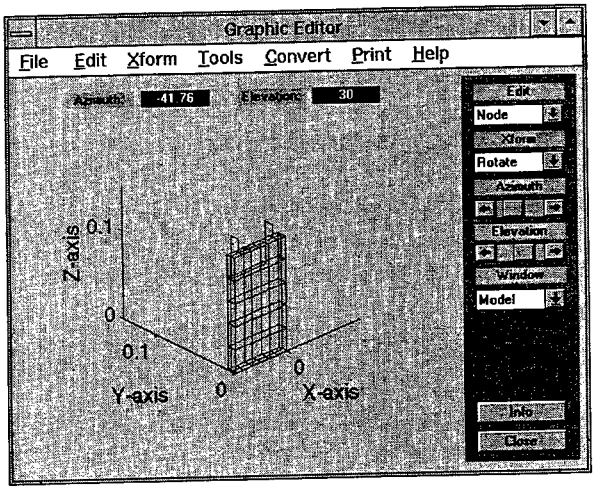

Fig. 4. A Graphic Editor window.

The graphic editor provides editing utilities for line model, patch model, and line-patch mixed model, as shown in Figs. 4 and 5. User can locate, a node or a line or a patch to perform various editing functions.

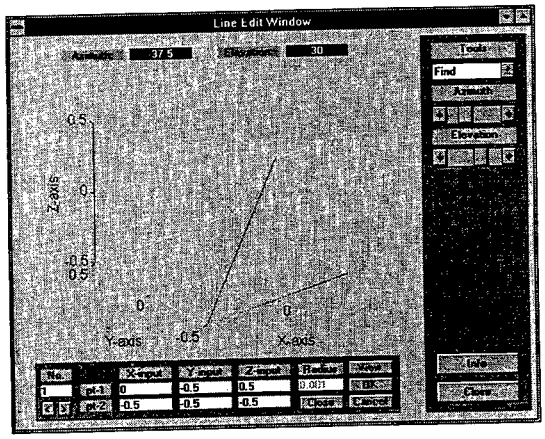

Fig. 5. A Line Edit Window with **Find** option activated.

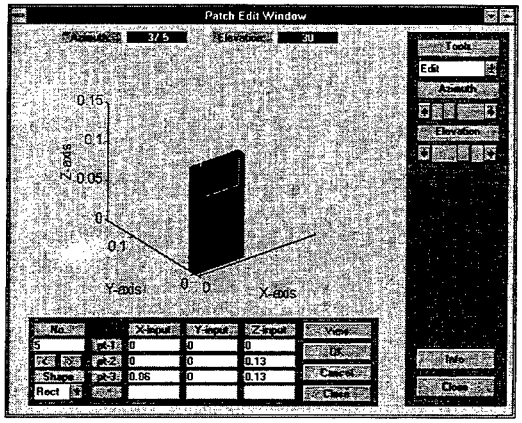

Fig. 6. A Patch Edit Window with **Edit** option activated.

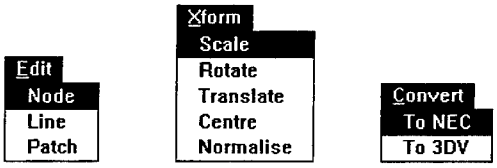

(a) edit (b) transform (c) convert

Fig. 7. Some of the options of the graphic editor.

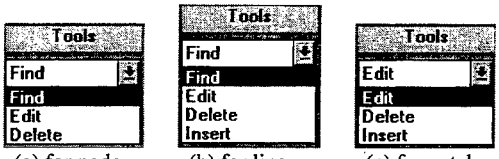

(a) for node (b) for line (c) for patch

Fig. 8. Options for node, line, and patch editing.

C. Script Programming Creation

Creation of a wireframe model or NEC input file can be easily and efficiently done by simple *Script Programming* making use of the utility functions and library component m-files as well as plenty of Matlab mathematics functions. These utilities with matrix representation of variables in Matlab allow creation of such basic components as a line, a circle, a ellipse, a helix, a rectangular plane, a polygon with desired topology and segment size be done with one line coding from the least necessary information. Complex model can be created by assembling simpler components in script

programming. Any structure coded in script can be considered as a library component which can be easily modified or transformed for other uses.

III. Post-Processing Modules

The post-processing tools including **freplot**, **patplot**, and **necplot** for plotting 9 different frequency related curves, 9 various radiation patterns either in polar or x-y plot, and wire frame model, segment model and 3 color current intensity distributions. All plots from the toolbox can be easily saved in all the formats Matlab allows, including color PostScript, for future use or for printing.

A. Freplot

The GUI frequency related plotting tool **freplot** allows user to view, save, and print nine different curves (Smithchart, VSWR, |Z|, R, X, |Y|, G, B, and Power) by just pressing buttons from the **freplot** window as shown in Fig. 9. The VSWR, |Z|, R, X, |Y|, G, B, and Power curves are in x-y plot.

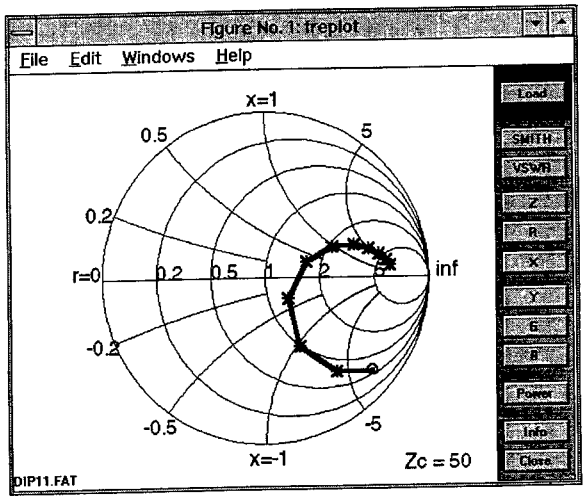

Fig. 9. A **freplot** window with **SMITH** option activated.

B. Patplot

The GUI radiation pattern plotting tool **patplot** allows user to view, save, and print, either in poplar or x-y plot, nine different types of radiation patterns (Vertical-Gain, Horizontal-Gain, Total-Gain, magnitude{E_θ}, phase{E_θ}, magnitude{E_ϕ}, and phase{E_ϕ}) by just pressing buttons from the **patplot** window as shown in Figs. 10 and 11. Automatic scaling is done to make the scaling is always best suitable to a curve.

The information of curve type, pattern cutting plane, frequency, and maximum value of a curve are also displayed.

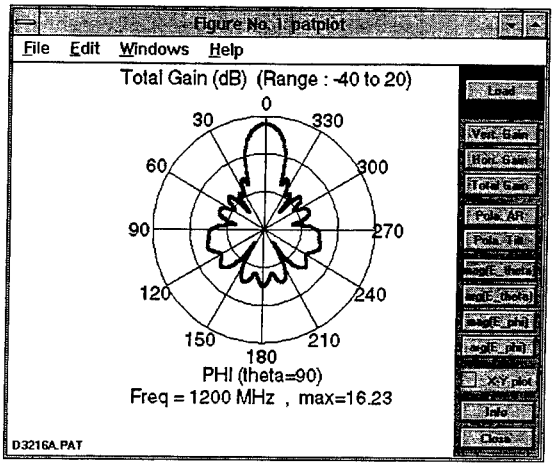

Fig. 9 A **patplot** window with **Total Gain** activated and **X-Y plot** disabled.

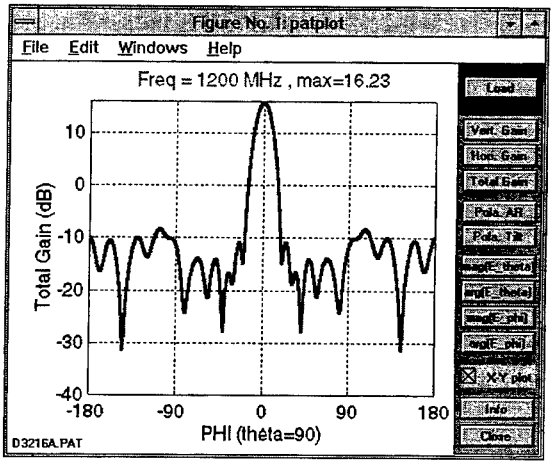

Fig. 10. A **patplot** window with **Total Gain** activated and **X-Y plot** enabled.

C. Necplot

The GUI wire structure model and current Intensity Distribution Plotting Tool **necplot** allows user to view, save, and print 5 different types of the wire structure mode (wire

frame model, segment model, color Real{I}, Imag{I}, and magnitude{I} intensity distribution models with color bar indicating the intensity-color mapping. User can also change viewing angle by dragging the "Azimuth" or "Elevation" sliders using mouse or set the viewing angle values after pressing the "View Angle" button. Fig. 11 shows the necplot window with button "Abs(I)" is activated.

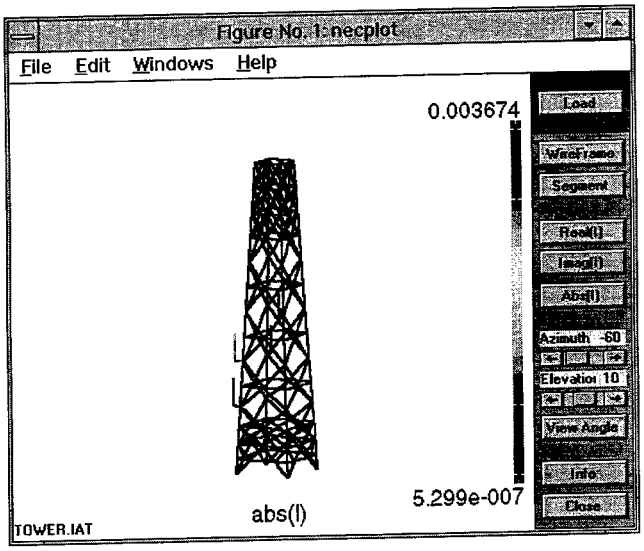

Fig. 11. A **necplot** window with **Abs(I)** option activated.

IV. Conclusion

A Matlab NEC Toolbox has been developed for pre- and post-processing of NEC applications. Matlab is widely available able to handle complex computations and graphics with GUI on a variety of major platforms, including PCs, Macintosh, workstations, and supercomputers. This Matlab NEC toolbox is portable across different platforms. Moreover, Matlab m-file and script programming allow creation, modification, and assembly from parts for complex structures by only simple script programming. Matlab's ASCII m-file and script file structure allows user to add other functions to the Toolbox very easily.

References

[1] J. Burke and A. J. Poggio, *Numerical Electromagnetics Code (NEC) - Method of Moment*, Lawrence Livermore Laboratory, Jan. 1981.

[2] *MATLAB Reference Guide,* Natick, MA: The Mathworks, Inc, 1992.

COMPUTATION AND GRAPHIC VISUALIZATION OF PLANE-WAVE K-SPACE SPECTRA AND FAR-FIELD PATTERNS WITH MATLAB 4.0

Ross A. Speciale

Redondo Beach, California

A very simple and highly practical computation procedure has been recently developed, coded, tested, validated, and intensively used to generate, and graphically visualize the plane-wave *k*-space spectra of given aperture-field distributions, and the corresponding far-field patterns. The complex, planar input aperture-field distributions to be processed can be either defined analytically or read-in as files of numerical data. The new, highly-efficient procedure has been developed and coded using the very concise, and powerful high-level programming language of MATLAB 4.0 . The MATLAB 4.0 numerical computation and graphic visualization system, that runs on both IBM-type PC's under Windows 3.1, and on many different work-stations under UNIX, is eminently suited to rapid prototyping, development, and debugging of even rather sophisticated algorithms of applied computational electromagnetics.

The developed MATLAB 4.0 codes accept both analytical and numerical definitions of the input planar aperture-field distributions, represented by complex, square matrices with typical dimensions in the range between 64 x 64 up to 512 x 512. Rectangular, circular, elliptic, and any other arbitrary aperture shape can be evaluated by *'truncating'* the given field-distributions at the aperture perimeter (setting it to *zero* beyond it). Any arbitrary type of amplitude and phase taper can be represented and processed, enabling thus comparative evaluations in terms of directivity, side-lobe level and structure, and in terms of the evolution of the far-field pattern under electronic beam steering. Beam steering is simulated by introducing an appropriate phase-slope, in the desired beam-steering direction, prior to computing the *k*-space spectrum and the far-field pattern. The plane-wave *k*-space spectra are computed using the MATLAB 4.0 built-in *2D FFT* function, that includes essentially unlimited zero-padding capability, thus providing increased *k*-space, and far-field angular resolutions.

The input amplitude and phase distributions, the *k*-space spectra, and the far-field patterns are visualized in great detail, and in color, in a vast variety of *2D*, and *3D* graphic presentation formats, including *3D* isometric projections of the amplitudes of the plane-wave components (expressed in dB) of the *k*-space spectra, *2D* azimuth and elevation cuts through the far-field patterns, and *2D* contour displays of the main beam and side-lobe cross-sections. A vast collection of processing-time bench-marks has been obtained on different PC models and on various work-stations.

Two MATLAB 4.0 *'scripts'* have been coded, to test the computation and visualization procedure. The *hsn.m* script defines the radial dependence of the aperture-field amplitude-distribution as a Hansen's *'One Parameter Distribution for Circular Apertures'* [1] , with the *'edge taper'* , and with the corresponding first-sidelobe dB-level controlled by the well-known parameter *H* (for Hansen !) .

This radial dependence, normalized to unity at the circular aperture center, is expressed by :

$$A = g(p) = I_0\left(H\sqrt{\pi^2 - p^2}\right) / I_0(H\pi) \qquad (1)$$

where the variable p is defined as a linear function of the normalized radius r/R :

$$p = 2\pi\frac{r}{R} \qquad (2)$$

Similarly, the *shx.m* script uses a *'Separable Hansen'* amplitude distribution, defined on a square aperture, computed as the product of mutually-identical X-axis, and Y-axis amplitude tapers, equal to the radial amplitude taper in (1) , and expressed by :

$$A = g(p_x, p_y) = I_0\left(H\sqrt{\pi^2 - p_x^2}\right) \cdot I_0\left(H\sqrt{\pi^2 - p_y^2}\right) / I_0^2(H\pi) \qquad (3)$$

where the variables p_x , and p_y are linear functions of the normalized X , and Y coordinates:

$$p_x = 2\pi\frac{x}{L} \qquad (4) \qquad\qquad p_y = 2\pi\frac{y}{L} \qquad (5)$$

In both the *hsn.m* , and the *shx.m* scripts the given amplitude distributions are combined with the *'phase-taper'* , required for the beam-steering angles $\varphi = 0°, \pm 45°, \pm 90°$, and $0° \le \theta \le 70°$, by performing an element-by-element matrix multiplication of the amplitude-distribution matrix A , by a *'phase-rotation'* matrix-exponential $E = e^{jPH}$, where the total-phase matrix PH is expressed by :

$$PH = \pi \sin\theta \left[(46 - x)\cos\varphi + (46 - y)\sin\varphi \right] \qquad (6)$$

The aperture coordinates x , and y are here measured in lattice-units from position (1,1) , and the MATLAB-unique element-by-element matrix product is coded as " $AC = A .* E$ " .

The real matrices A , and PH , and the complex matrices E , and AC are all of size 91 x 91 in both *hsn.m* , and *shx.m* , but the rows and columns of these matrices, located outside the central 61 x 61 regions are set to zero, and so are the elements of the matrix A in *hsn.m* , that are located beyond the maximum aperture radius of 30 lattice units from the central *A(46,46)* element.

The k-space spectrum is computed by using the built-in MATLAB 4.0 *2D FFT* function [3], after zero padding the complex matrix AC from size 91 x 91 to 512 x 512 , to increase both the k-space, and the far-field angular resolution. The k-space spectrum, and the θ-plane cuts through the far-field patterns are computed assuming the lattice unit to be exactly equal to $\lambda/2$, so that the spectrum just exactly covers the *'visible space'* , and all the grating lobes are out of it. Further, the given aperture distributions are assumed to have single polarization, and to be continuous, singularity-free functions of position.

Figures 1-6 show typical examples of the generated graphic displays, unfortunately without the very appealing, high-quality color-effects.

REFERENCES.

[1] R. C. Hansen,'Planar Arrays,' Chapter 10, Section 10.1.6 of 'The Handbook of Antenna Design' , Vol. 2 , A. W. Rudge et al. Editors, Peter Peregrinus, Ltd. . London, UK, 183, pp. 156-161.

[2] R. C. Hansen,'A one-parameter Circular Aperture Distribution with Narrow Beamwidth and Low Sidelobes,' IEEE Trans. AP-24, 1976, pp. 477-480.

[3] The MATLAB Reference Guide, The Math Works, Inc. , 1992, pp. 182-185.

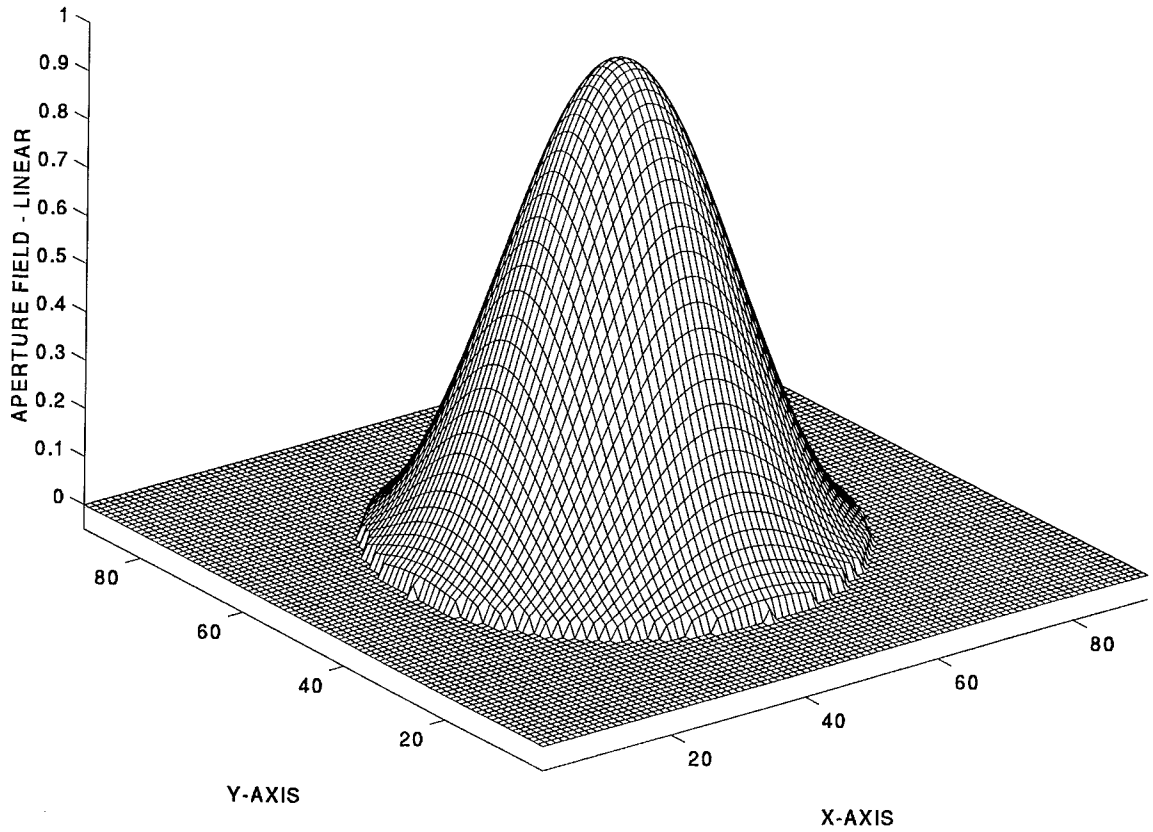

Figure 1 - Hansen's Aperture Distribution For Circular Apertures : Parameter H = 1.7254 , Relative Sidelobe Level = - 40 dB.

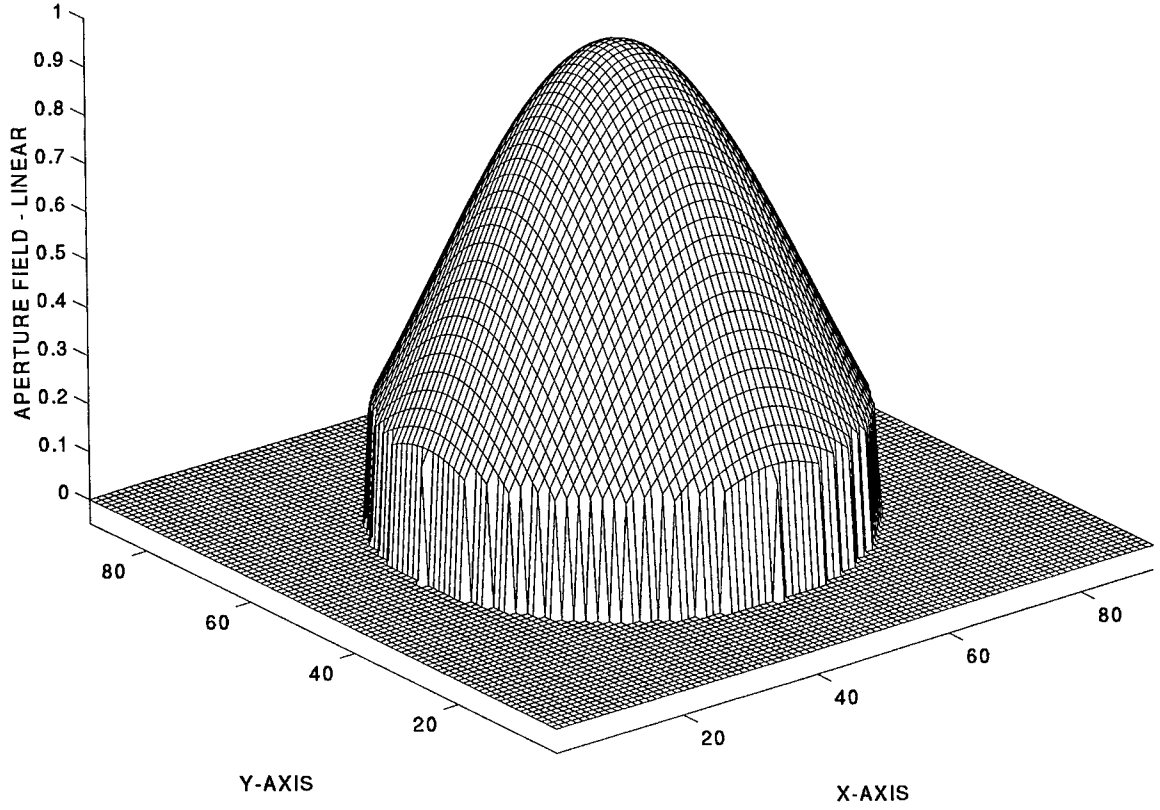

Figure 2 - Hansen's Aperture Distribution For Circular Apertures : Parameter H = 0.8899 , Relative Sidelobe Level = - 25 dB.

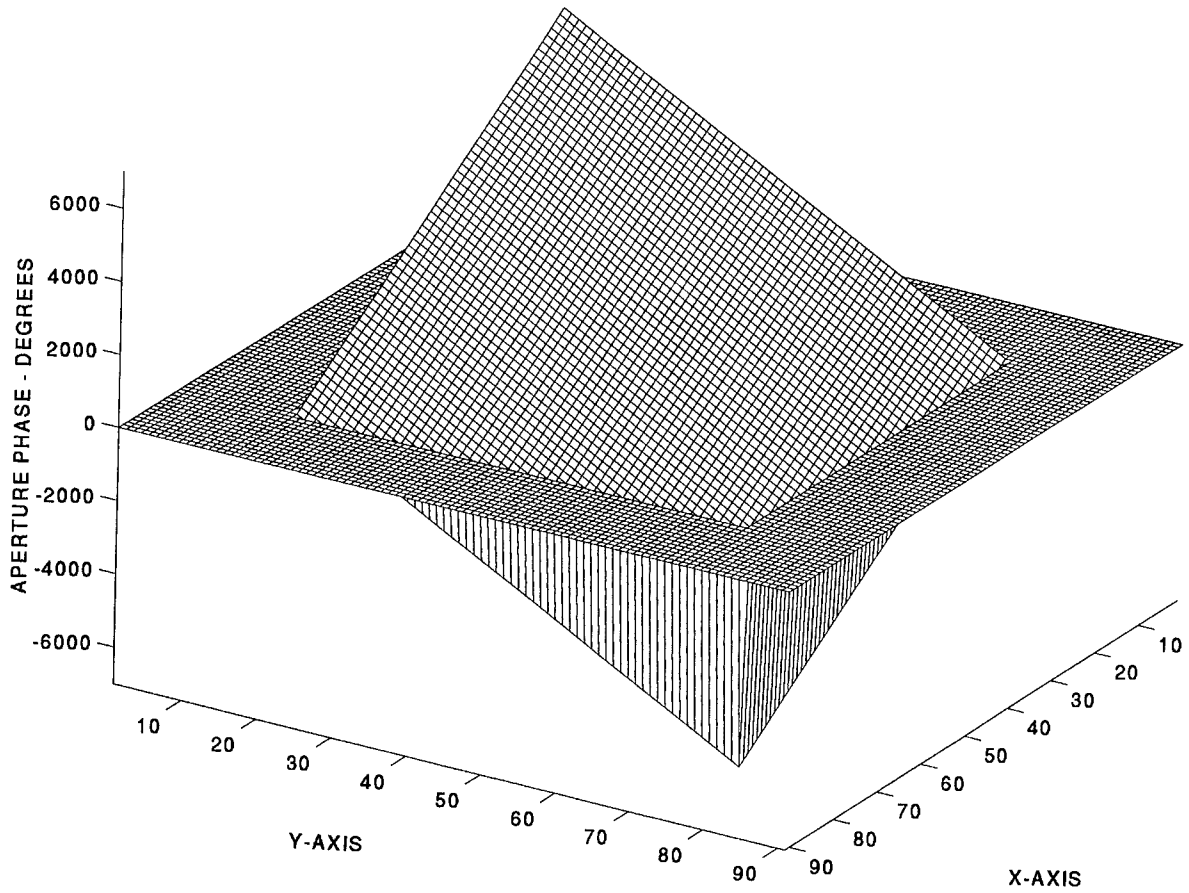

Figure 3 - Total linear Phase Tilt in the Theta-Plane :
Angle Phi = 45 Degrees , Angle Theta = - 60 Degrees.

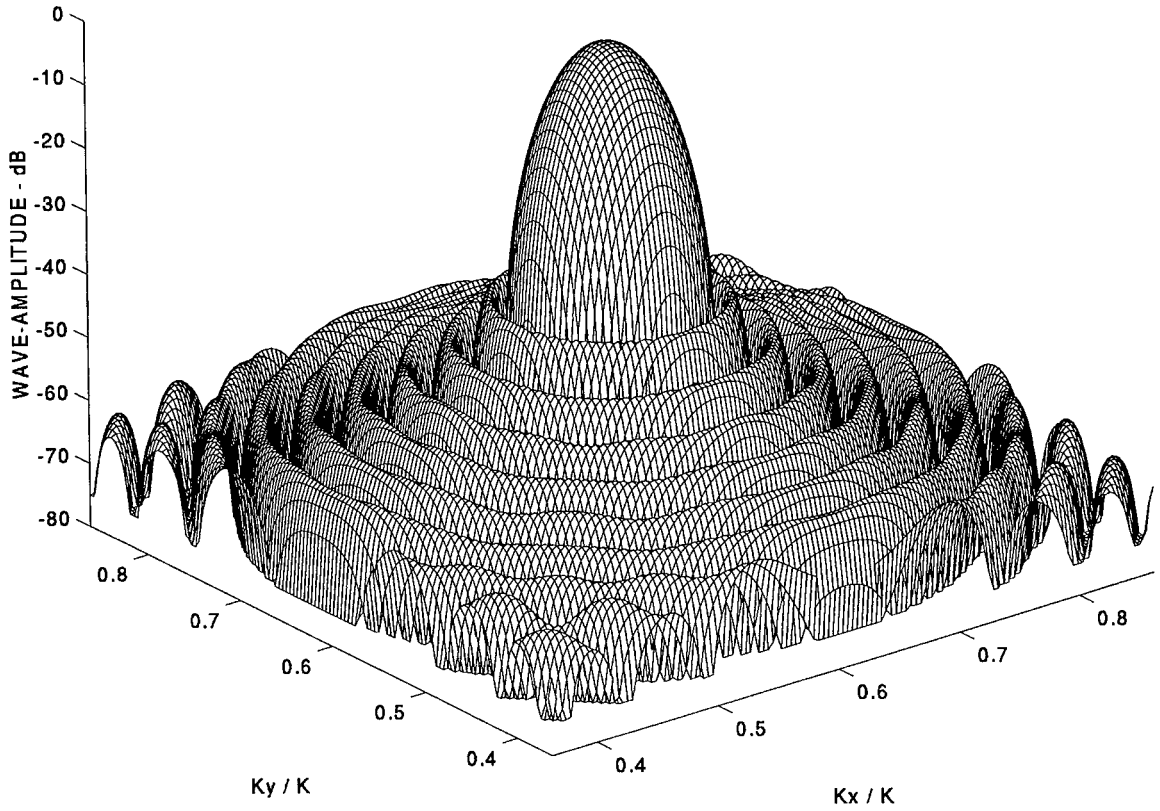

Figure 4 - Plane-Wave Spectrum of the Hansen's Distribution. Zoomed Detail of the Beam Region. SLL = - 40 dB.

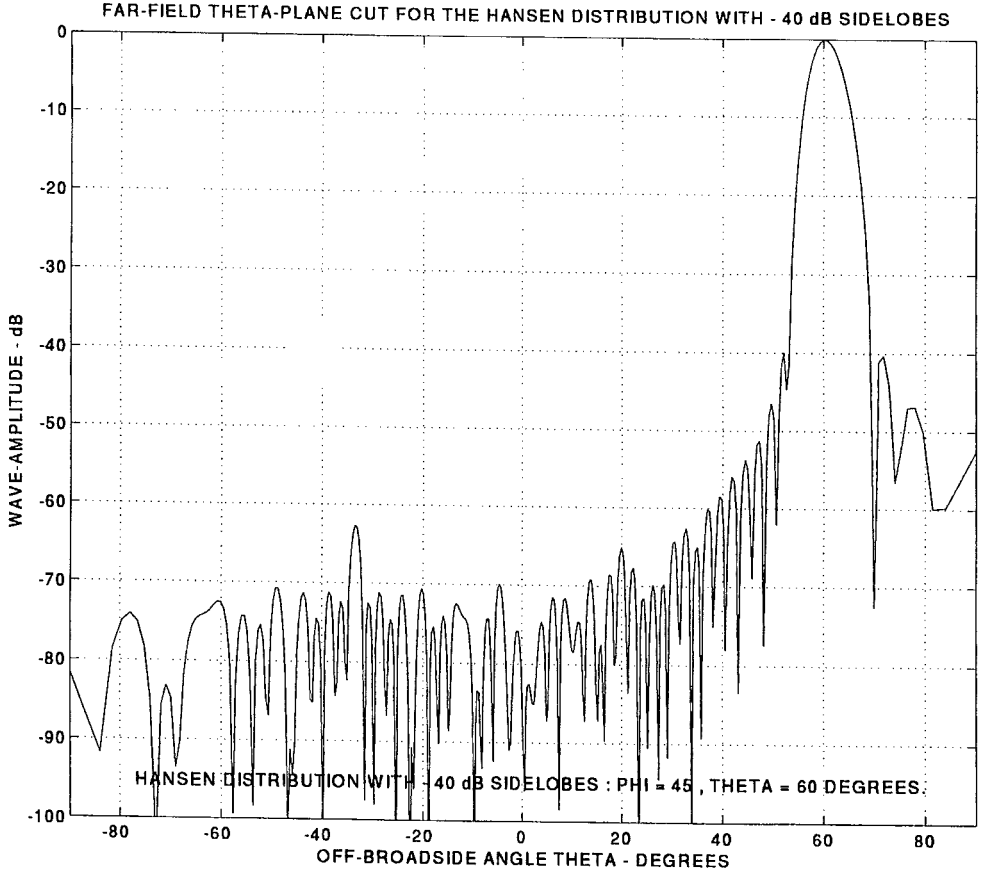

Figure 5 - Far-Field Theta-Plane Cut for the Hansen's Distribution. Parameter H = 1.7254 . Relative Sidelobe Level = - 40 dB.

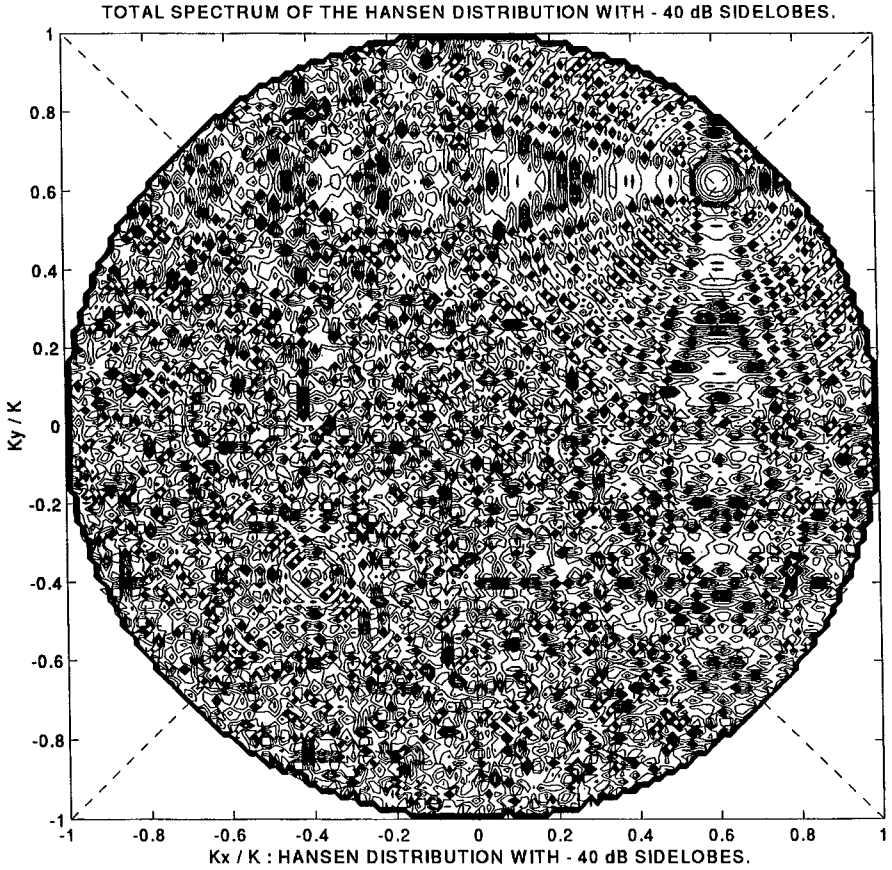

Figure 6 - Contour Plot of the K-Space Spectrum of the Hansen's Distribution. Angle Phi = 45 Degrees . Angle Theta = 60 Degrees. SLL = - 40 dB.

THE INTELLIGENT COMPUTATIONAL ELECTROMAGNETICS EXPERT SYSTEM (ICEMES)

Andrew L.S. Drozd[1]
Timothy W. Blocher[2]
Victor K.C. Choo[3]
Kenneth R. Siarkiewicz[2]

1.0 INTRODUCTI

This paper reviews the results of research and development to establish a prototype Artificial Intelligence/Expert System (AI/ES) based pre-processor capability for Computational Electromagnetics (CEM) codes. The AI/ES-enhanced pre-processor capability, called the Intelligent Computational Electromagnetics Expert System (ICEMES), makes use of a commercially-available AI/ES tool and an existing government-developed CEM code. Specifically, the present version was designed using Gensym Corporation's G2 Real Time Expert System and built for the US Air Force's General Electromagnetic Model for the Analysis of Complex Systems (GEMACS) program.

The initial capability is intended to alleviate usage difficulties associated with individual CEM codes applied to complex system electromagnetics modeling, simulation, and analyses. It combines advanced knowledge/rule-base modeling and simulation technologies with conventional CEM software codes and user support utilities to provide a new, powerful, intelligence-driven pre-processor system. The intelligent pre-processor concept is aimed at: (a) significantly enhancing the analyst's efficiency in the development of complex system geometry models where burdensome modeling tasks are assigned to the intelligent engine; (b) facilitating the automatic selection of the most appropriate physics formalisms and solution techniques within the constraints of select CEM tools, methods, and algorithms applied to electromagnetics problem-solving (i.e., CEM modeling optimization and validation); and (c) assisting the analyst in implementing effective CEM assessment methodologies for the development of valid simulation models.

Inherent in the overall concept and approach is the demonstrated ability of the ICEMES to read and convert available Computer-Aided Design/Manufacturing/Engineering (CAD/CAM/CAE) data for the automatic generation of corresponding CEM geometry models. In particular, the AI/ES-enhanced pre-processor would generate these models within the restriction and modeling constraints of the GEMACS code, and would also create relevant command stream inputs in accordance with the code's required syntaxes and formats. The CAD/CAM/CAE data types of interest include facet and IGES. Such are provided in CAD and CEM analysis programs such as ACAD, AutoCAD, ProEngineer, BRL-CAD, CADRA, SDRC I-DEAS, and Apatch. Considerations are also given to mathematical library functions for B-splines, NURBS, interpolations, smoothing, etc. available from a number of sources including Netlib, IMSL, and DT_NURBS.

Demonstrations have focused on generating a complete complex system structure model (e.g., an aircraft comprised of hybrid, canonical geometry elements such as GTD cylinders and plates, and MoM mesh structures), and on CEM-to-CEM conversions (e.g., MoM-to-GTD or vice versa) for select portions of the geometry. Although fundamental geometry modeling knowledge for GEMACS is presently embedded within ICEMES' knowledge-base (KB), its architecture and rule-base structure is sufficiently flexible and modular to accommodate the inclusion of other CEM knowledge, formalisms/codes, and software support functions. The latter includes but, is not limited to input/output data managers, network communications, and visualization tools.

[1]ANDRO Consulting Services, P.O. Box 543, Rome, NY 13442-0543
[2]Rome Laboratory/ERST, 525 Brooks Road, Rome, NY 13441-4505
[3]Kaman Sciences Corporation, 258 Genesee Street, Utica, NY 13502

The results of the ICEMES development and demonstration discussed in this paper are based on Phase I research performed by the authors under US Air Force Contract No. F30602-95-C-0198, sponsored under the DoD Small Business Innovation Research (SBIR) Program, Topic AF-055 entitled, "AI/ES Pre-processor for CEM".

1.1 Objectives

The objectives of the Phase I effort focused on defining the general software design of an AI/ES pre-processor, developing a preliminary rule base, and demonstrating its functionality using a select CEM tool. This involved:

- Adapting a commercial AI/ES tool for the CEM-based pre-processor.
- Developing a flexible, modular architecture to encompass various government and university CEM formalisms/codes.
- Implementing knowledge to automatically generate optimized (valid) CEM structure models (and associated command streams) from system architectural files, that are consistent with the CEM tool modeling constraints, input syntaxes and formats.
- Establishing and demonstrating a capability to validate user-generated CEM models.
- Automatically having the expert system determine the most appropriate physics/solution technique(s) and define the most accurate/efficient simulation approach, for a user-defined analysis scenario.
- Providing an interactive front-end to aid novice as well as CEM experts.

2.0 BACKGROUND

In the present context CEM modeling, simulation, and analyses are necessitated by the government's mission requiring the assured life-cycle performance, desired operability, and long-term survivability of military systems in electromagnetically-rich environments, both intentional as well as unintentional. Whereas CEM computer codes are used as one means of assessing such performance early on in the life-cycle of systems, such codes may present certain usage difficulties to the novice or non-CEM analyst, and may require a significant degree of user proficiency or knowledge of CEM assessment methodologies. These factors can make CEM modeling, simulation, and analysis daunting tasks.

As it continues to mature, ICEMES is expected to resolve many of these potential drawbacks. It will consist of advanced knowledge/rule-based simulation technologies "wrapped around" conventional CEM engineering wisdom and experience, proven assessment methodologies, and certain code-specific constraints that collectively represent core CEM knowledge. The environment for capturing this collective knowledge is the expert system's Knowledge Base (KB).

In the evolution of ICEMES, a wealth of knowledge related to various CEM codes (e.g., GEMACS, NEC-MOM, NEC-BSC, CARLOS-3D, and others), formalisms, and modeling tasks will be embodied within the KB structure. The CEM formalisms of interest include but, are not limited to: Method of Moments (MoM), Geometrical Theory of Diffraction (GTD), Uniform Theory of Diffraction (UTD), Shooting and Bouncing Rays/Physical Theory of Diffraction/Physical Optics (SBR/PTD/PO), Finite Element Analysis/Modeling (FEA/M), and hybrids thereof. The modeling methodology and step-by-step tasks within ICEMES' knowledge/rule base are driven by: (a) general knowledge, usually associated with CEM theory, experience, and assessment practice; and (b) specific knowledge, that pertains to the modeling restrictions, constraints and guidelines associated with individual codes and their inherent physics formalisms.

To facilitate access to this knowledge in order to automatically generate complex system CEM structure models, the system must incorporate or provide the following: (a) Graphical User Interfaces (GUIs) that include a Modeling Assistant and Help Functions; (b) a 3-D Interactive Geometry Modeler (IGM) or visualization capability which allows the operator to display the models, institute modifications, and dynamically translate any such changes to the expert system; and (c) links to external data files including CAD and CEM model libraries, CEM Data Dictionaries, Relational DataBase Management System (RDBMS), and flat/text files.

On a broader level, the ICEMES capability could be considered a potential component of other, more general computational environments and systems that support Concurrent Engineering and Integrated Product Team thrusts. This aspect is further discussed later.

The availability of a mature ICEMES capability is expected to effectively address the government's needs with regard to assuring desired electromagnetic properties (i.e., compatible performance, operation, and functionality) of advanced system procurements and existing assets. It is also expected to similarly benefit the commercial/private sector and a variety of civilian applications which include but, are not limited to: commercial aircraft and satellite designs, consumer electronics, wireless telecommunications systems, Intelligent Transportation System (ITS) communications items, medical equipment, power utility systems, and automobile design/manufacturing.

3.0 WHY ARTIFICIAL INTELLIGENCE AND EXPERT SYSTEMS FOR CEM?

There are several important reasons for selecting AI/ES/KB technologies for the CEM pre-processor concept design. To begin, the fusion of software is facilitated with the use of an expert system. Depending upon the specific expert system, a "common" simulation environment can be provided that readily permits the integration of various CEM codes, physics/solution methods, and processing algorithms. This environment employs rule-based and procedural techniques for knowledge incorporation, for establishing relationships among components or "objects" of the KB, and for defining inherited properties which can be used to share information and data among various objects of the KB environment. Such information and data associated with objects and any of their "clones" (implying a parent-child relationship) are characterized as attributes consisting of: parameters, variables, constants, formulas, boundary constraints, and other descriptors. In this way, like characteristics of various codes, algorithms, or solution methods can be identified and "linked" to provide a vehicle for item-to-item or object-to-object communications and data sharing.

For certain expert systems, programming and entity description, modification, and manipulation are based on an object-oriented structure and approach. This helps to facilitate problem definition and rapid prototyping of the KB, which in turn, expedites the development of a mature simulation capability. G2 is an example of this type of expert system.

G2 also performs automated rule-based logic inferencing and deductive reasoning using a combination of backward chaining, forward chaining, and dynamic code/KB/rule modification or reconfiguration. In essence, the system has the ability to "learn" based on what it "observes", and to optimize certain aspects of the rule base and its functionality. This becomes important when establishing the design of a system that can be used by a novice, a non-CEM analyst, or a CEM expert. For example, the expert system can learn about its user(s) and develop corresponding user profiles.

Expert systems like G2 make use of procedures which like subroutines in FORTRAN or PASCAL contain and execute a series of rules for a specific purpose. Special functions can also be developed using tailored procedures in conjunction with external control rules.

Another very important aspect of most expert systems is their ability to accommodate or contain both general and specific knowledge for a given domain application. In this way generic, common, or universal aspects of a problem can be assigned to all objects and items of the KB, as appropriate; also, specific rules or knowledge including tailored attributes can be selectively defined for certain objects or items. For CEM, general knowledge expressed as rules, procedures, and object attributes may refer to CEM theory, practical experience, or conventional practice. Specific knowledge, on the other hand, expressed similarly, may refer to certain aspects of codes and their unique formalisms.

Expert systems therefore provide an environment to perform automated inferencing, reasoning, and decision-making; in this case, to assist the analyst in implementing effective CEM simulation/assessment methodologies, and step-by-step modeling procedures for generating "optimized" CEM models using the most appropriate physics/solution methods.

While this concept has been demonstrated to be advantageous for CEM pre-processing applications, its utility can be extended to establish an effective means of performing intelligent post-processing of computed CEM results. This topic will be the subject of future papers as the technology and developments progress for the present application.

3.1 Definitions

The following keywords and definitions are applicable to AI/ES/KB technologies and applications. These are provided to assist the reader in understanding certain key AI/ES/KB concepts and how these apply to the present topic.

- Artificial Intelligence (AI) - Captured "human" knowledge or intelligence manifested as computer hardware or software systems that perform reasoning/inferencing and decision making.
- Expert System (ES) - A computer program application of AI that emulates the behavior of a human expert in a well-bounded domain of knowledge (a vehicle for captured knowledge consisting of dialog structure, inference engine, and knowledge/rule base).
- Knowledge Engineering - Development of a (concept-oriented) rule-based ES for a domain task.
- Knowledge Base (KB) - A set of facts (captured knowledge) and rules-of-thumb (heuristics) on the domain task.
- Knowledge Encoding - Implementing domain knowledge using an ES applications development/modeling environment or "shell".
- Knowledge Representation - Hierarchical rules (IF-THEN-ELSE), procedures (collections of rules), functions, relations, and object-classes with associated attributes (parameters, variables, constants, etc.).
- Domain Knowledge/Domain Expert - Knowledge derived from a general "source" and/or from human expertise/experience, respectively.

4.0 PROTOTYPE SYSTEM

An Architecture design has been developed establishing a flexible framework to accommodate the inclusion of new features and functions as the ICEMES continues to evolve. At the heart of the architecture is the expert system which functions as a Data Server in addition to a reasoning engine in the present concept. The ES Data Server stores and routes commands and data to each of its linked components. While the Data Server can be an entirely separate software program, its functionality and purpose has presently been incorporated as part of the expert system, as a separate knowledge base.

The ICEMES design based on the Expert System Server configuration consists of a series of interlinked KBs, with a main or master KB performing certain overhead functions. Separate KBs are used to incorporate the knowledge and interfaces required for each specific formalism or process, and respective software package (e.g., GEMACS, NEC, geometry modelers, etc.) that are integrated within it. Since each of these KBs share the same basic structure, they can easily be duplicated and updated to accommodate new analysis capabilities, including individual CEM formalisms and unique CEM code modeling constraints. Using this approach, the end-user is not required to have all of the modules or analysis programs in order to operate the system. The knowledge is incorporated into the KBs via objects, rules, procedures, and relations.

The layered elements of the architecture consist of:

- GUI Plug-in Layer (User Control Panel)
- Core AI/ES Server/Module (Control Kernel)
- AI/ES Modeling Environment
- N-Partitioned KB Sets to Accommodate Individual CEM Formalisms
- Data Translation and Storage Environment
- Intermodule Communications Interfaces
- External CAD Files (CAD Engine Interface), System Files and Storage Files for CEM Models
- Geometry Modeler
- CEM Data Dictionary Interface
- External CEM Codes, Display Programs and Data Files.

In the future, the expert system will function as a separate component in order to enhance modularity, portability, maintenance, and future expansion. The modified concept is illustrated in Figure 1. The modularized design offers several advantages over the server layout. In particular, it allows the many system functions that do not require the expert system to be performed by more traditional C or FORTRAN programs. These functions include: user interfaces, on-line help systems, object storage, data translation, and software interfacing. This allows the expert system to focus on tasks and functions that require the use of its inference engine. The modified approach will also limit the number of direct links between the expert system and external programs. These interfaces may, for some expert systems, become a bottle neck thereby slowing system performance.

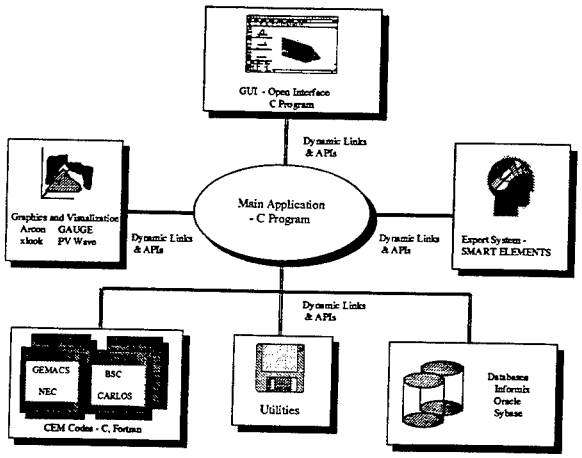

Figure 1. ICEMES Configuration

Further, each module will now be a separate program, including the expert system. The ICEMES' primary application module serves as the main controller for the entire system. The main application is typically coded in C and C++. The flexibility and portability of C/C++ enables the main application to communicate with the GUIs, Expert System Module, the Graphics Module as well as virtually any other C, FORTRAN or PASCAL programs. The main program performs a number of house-keeping functions such as identifying authorized users, loading user profiles, storing data, and calling the various modules. This application also performs many of the normal simulation functions that do not require the expert system's reasoning/inferencing capability.

This modified approach allows the individual modules to be maintained and upgraded independently of each other. In addition, the linking process does not fix the design to operate with a single version of any one of the components. The use of Application Program Interfaces (APIs) also simplifies the incorporation of additional tools as the system grows.

4.1 ICEMES KB Structure

A block diagram of the ICEMES Core Structure Hierarchy is illustrated in Figure 2. This diagram provides details on the individual nature of the internal KB partitions and their purpose. The block diagram emphasizes the partitioning of knowledge first as a function of the CEM formalism (i.e., "general" knowledge) then by individual CEM codes and their peculiar modeling constraints (i.e., "specific" knowledge). This approach supports modularity, portability, and expansion to include other formalisms and code constraints.

4.2 User Modeling Scenario

The User Modeling Scenario (UMS) is a methodology or roadmap which describes the general procedures involved in a typical ICEMES model development session. The methodology, with the GUI as its infrastructure, is illustrated in Figure 3. The current methodology is based on the feasibility demonstration for GEMACS, however, the approach is generally applicable to other CEM formalisms and codes. The figure implies that a fairly comprehensive query-response system exists and a significant degree of user interaction is possible (depending on the analyst's CEM domain expertise).

The analyst has the option of using a standard set of pull-down menus, tool bars, or an automated Assistant to navigate through the system during a modeling session. The Assistant consists of menus that lead the operator through

each step of the modeling task, and provides recommendations along the way regarding the use of various modeling parameters as requested by the user or as determined by ICEMES.

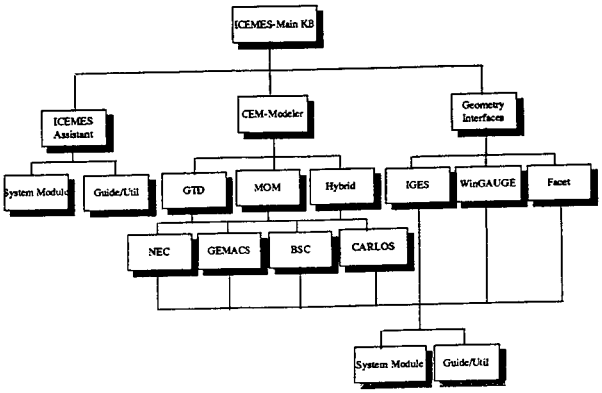

Figure 2. ICEMES KB Construction

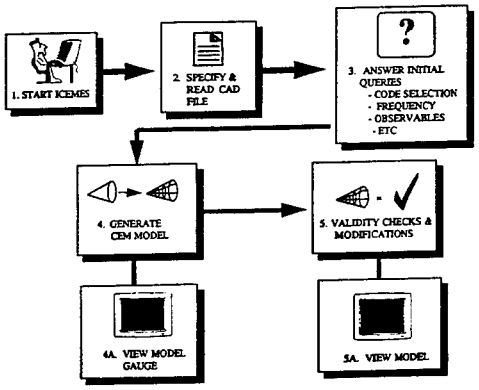

Figure 3. ICEMES Operations Flow

Also, ICEMES exhibits three levels of user interaction capability for error detection and validation. These include automatic, interactive, and none (or No Corrections mode).

In the automatic mode, the ICEMES will implement corrections and use the methods that it logically determines to be best for generating optimum CEM geometry models; in this mode, the CEM model is generated without querying the user to any significant degree. The user has the option of changing the CEM model once it is generated by the ICEMES.

In the interactive mode, the ICEMES identifies problem areas and recommends possible solutions in the process of model development. The ICEMES flashes messages describing any errors that are detected as well as suggesting methods to fix the problem. The user has the option of ignoring the problem, fixing the problem, or exiting the validation mode.

The user must acknowledge the queries before the program proceeds to the next step in the modeling task. Alternatively, ICEMES posts warning messages in a scroll bar such that the user can view all issued messages at once rather than having to continually respond to a series of system prompts.

Finally, in the no corrections mode ICEMES performs a straight-forward conversion between the CAD and CEM models without checking for possible errors or performing any type of optimization or validation.

5.0 ICEMES FUNCTIONAL FLOW

For a given modeling task, ICEMES is designed to perform the following functions, in order: parse CAD files; generate the CEM structure model; validate or optimize it for the specified electromagnetic conditions; support graphical viewing of the model for user inspection and verification; and output a final data set that is compatible with the CEM code (GEMACS) for subsequent processing and analysis.

Regarding CAD file parsing, the present version of ICEMES accepts IGES and facet-based CAD inputs. In the future, the list of file types and formats will expand to include various CEM as well as CAD model data.

ICEMES converts input data, whether CAD geometry or CEM, into a set of generic CEM objects in order to maximize the applicability of its inherent knowledge. This is illustrated in Figure 4. Generic objects are intended to represent the basic building blocks that can be combined to form complex CEM geometries. The generic CEM objects considered in the Phase I design include points, wires, plates, and cylinders. The generic CEM components permit the analyst to perform a number of data manipulations prior to selecting the analysis code or formalism type. This approach also provides a convenient method of sharing input data sets among CEM codes.

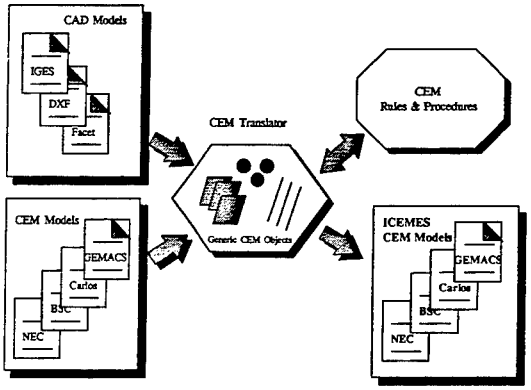

Figure 4. Generic CEM Object Definition

The ICEMES model validation and correction measures eventually act upon the generic CEM objects. Thus, any size adjustments, position changes, connectivity modifications, etc. are applied directly to the generic CEM model components. Ultimately, the ICEMES will enable the operator to also incorporate the changes into the CAD geometry.

Other validations that are performed during the model generation and optimization process include: finite-element resizing (plate sizing), connectivity checking (MoM wire segments-to-GTD objects and GTD plates-to-GTD cylinder), incomplete definitions, and MoM element sizing and connection angles. Each of these validations is based upon assessing the relevant electromagnetic conditions and "physical" parameters defined for the given problem, such as: frequency, object dimensions, relative location of source(s) with respect to the system geometry, specified observables (e.g., field points, wire currents, patch current densities, etc.), and any specified accuracy constraints.

The CEM model is displayed using the WinGAUGE or XGAUGE visualization tools. Both of these programs were exclusively developed to display and manipulate GEMACS input geometry models as well as certain GEMACS computed outputs. ICEMES makes use of these codes by first writing a GEMACS-compatible data file from the generic CEM data model, then issuing a command to launch the display program(s). After viewing the CEM model, the user has the option of modifying it and re-assessing impacts or tradeoffs with ICEMES.

Once the geometry complies with the basic CEM rules, it passes through a "filter" for the application code selected. This filter converts the generic parameters into a specific format required by the CEM code.

6.0 SAMPLE PROBLEM DEMONSTRATIONS

Several test cases were developed to demonstrate ICEMES' initial capabilities, particularly, its ability to: read in simplified CAD-based aircraft geometries; convert CAD data into a valid CEM model; detect anomalies and recommend modifications; automatically update the CEM model; and generate a GEMACS/GAUGE-compatible input data set.

A series of demonstrations was performed to show ICEMES' ability to detect and correct for anomalous conditions such as: ill-defined geometries based on disconnected or misaligned objects (as defined in the CAD data or by the user in the CEM model); and mounting MoM wire segments too close to a GTD object (i.e., cylinder or plate) edge and its diffraction center(s). It was also demonstrated with these test cases that depending upon the frequency and the location of the source, certain portions of the structure model are subject to CEM-to-CEM conversion (e.g., GTD-to-MoM or vice versa). Other test cases focused on demonstrating ICEMES' ability to detect non-planar conditions for faceted wing structures or plate entities, and to represent these accordingly in the GEMACS model. Related conversions involved the automatic creation of a single, large GTD plate sized to the frequency of interest, from a multi-faceted wing structure.

Each of the cases successfully demonstrated ICEMES' ability to effectively address the above types of validations for GEMACS. The details and results of the sample problem validations will be the subject of a future paper.

7.0 CONCLUSIONS/FUTURE DIRECTIONS

The ICEMES capability is considered an innovative, significant step forward in the successful adaptation and integration of next-generation software technologies with existing CEM codes. The prototype system developed in Phase I was successfully demonstrated to meet each of the technical objectives directed at the development of an intelligent pre-processor to support the GEMACS structure model task. The next stage in ICEMES' development will focus on expanding its architecture to encompass additional CEM formalisms, codes and associated data formats, and algorithms. Several candidate codes and formalisms were briefly mentioned in this paper. Other ancillary features and capabilities will also be adapted to ICEMES' architecture and functionality. These will include: database management systems, CEM model libraries, data dictionaries to provide required CEM model parameters and defaults, interactive geometry modeling and visualization tools, and tailored graphical user interfaces (GUIs).

Since ICEMES' architectural design emphasizes a stand-alone capability which is "loosely coupled" to the individual CEM tools, databases, and other software functions, its applicability is not necessarily restricted to CEM. Due to its inherent modularity and ability to communicate with other codes and applications, ICEMES has the potential to be integrated with other simulation architectures and computational environments, such as: the Air Force's Integrated Computational Environment/Research and Engineering Framework (ICE/REF)[4] which stresses Concurrent Engineering applications, the use of common-type data, and a "global" modeling/simulation environment; the Air Force's Electromagnetic Modeling and Simulation Environment for Systems (EMSES), a subset of ICE; and the joint Air Force/Navy Microwave and Millimeter-Wave Advanced Computational Environment (MMACE). The ICEMES concept design is generally in conformance with architectural and functional features of ICE/REF, EMSES, and MMACE that include "code wrappers", Applications Program Interface (API) routines, CAD file data extraction, library structures generated via database managers, and the CEM Data Dictionary.

[4]K.R. Siarkiewicz, B. Hantman, et. al., "Computational Electromagnetics Using the Research and Engineering Framework as a Backbone", Applied Computational Electromagnetics Society Newsletter, Vol. 10, No. 3, November 1995.

NECSHELL - A New Graphical User Interface for the NEC Code.

M. Y. Mikhailov*, V. O. Lomtev* and A. A. Efanov**

* Aerospace Monitoring Center, Krylova St. 19, Lvov, 290044, Ukraine
FAX: (007)-(0322)-74-12-17
E-mail: MMY%AMC.LVIV.UA@RELAY.USSR.EU.NET
LOMTEV%AMC.LVIV.UA@RELAY.USSR.EU.NET
** Dept. of Electrical Engineering, National University of Singapore
10 Kent Ridge Crescent, Singapore 0511
FAX: (+65) 777-3117
E-mail: EFANOV@EESERVER.EE.NUS.SG
EFANOV@SIGMA.ICMP.LVIV.UA

ABSTRACT - The new graphical user interface NECSHELL has been developed for the NEC81 Numerical Electromagnetic Code (PC-version of the NEC-2 code). The program works on IBM PC under Microsoft Windows 3.1 operating system.

INTRODUCTION

The NECSHELL is a graphical user interface for user-friendly input and output for the NEC81 Numerical Electromagnetic Code. The program has been designed for "intuitive" user interaction with easy-to-learn procedures, thus allowing a user to rapidly provide usable results in a "learn as you go" environment.

The NECSHELL makes it possible to perform the following functions:
- to prepare an input deck for the NEC81 program (pre-processor);
- to run NEC81 executable module;
- to visualize the output data (post-processor).

The main system requirements are as follows: 80386 or later processor, math co-processor, 4 MB RAM, 3 MB of hard disk space, VGA monitor. The software has been written in Microsoft Visual C/C++. The NEC81 source code has been compiled using Microsoft FORTRAN PowerStation compiler ver. 1.0.

PRE-PROCESSOR FUNCTIONS

The NECSHELL pre-processor functions are as follows:
- creation of a new input deck;
- reading of an existing input deck in the "standard" and "free" NEC input data formats;
- visualization of an antenna described in the input deck with several functions (rotation, scaling, etc.);
- modification of the input deck;

- print out the antenna image.

A user can create a new NEC input deck or can open an existing NEC input deck file. The deck must contain a description of a single antenna only. However, it is possible to open several NEC input decks simultaneously in different windows.

During the reading of an existing NEC input deck file the NECSHELL program checks a format validity of all the cards and gives proper warning messages if any errors have been found. A correct order of the cards in a deck is also checked.

A NEC input deck could be opened as a Deck window or as a simple text window. The typical view of the NECSHELL pre-processor windows is shown in Fig. 1, where there are two independent Deck windows with the HELIX.NEC and the CORNER2.NEC input data sets, and two text windows with the DIPOLE.NEC input data set and the HELIX.OUT output data set.

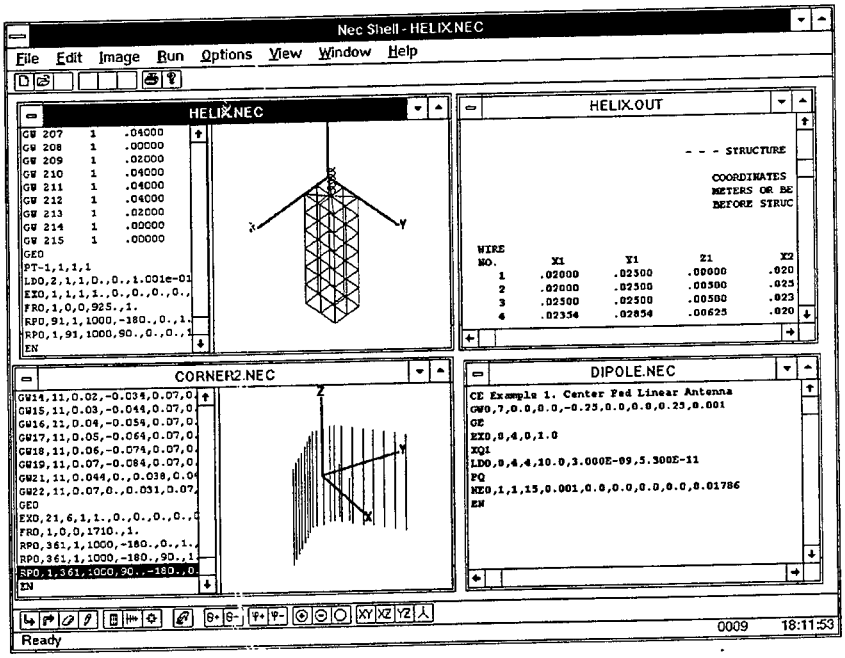

Figure 1. NECSHELL pre-processor windows.

There is a tool bar at the bottom of the main NECSHELL window with the 6 functional groups of the buttons. The first group (4 buttons) is used for an editing of an opened input NEC deck. The second group (next 3 buttons) makes it possible to jump immediately to a first comment card, first geometry card or a first control card, respectively. The next button ("a hand pressing a key" icon) starts the NEC81 executable. The next group (4 buttons marked as Θ+, Θ-, φ+, φ-) is used for an antenna image rotation. The next group (3 buttons marked as +, -, and an empty circle) makes it possible to zoom in/out an image. The last group (4 buttons) is used for a quick change of an antenna image orientation. All the tool bar functions are also available from the main menu.

A Deck window is divided into two parts by a vertical splitter line. The ASCII deck presentation appears in the left part of the window, and the graphical presentation (3-dimensional view of an antenna) appears in the right part. The current position of the splitter line could be easily changed by its clicking-and-drugging.

An antenna image can be rotated and zoomed. These functions could be performed from the main menu as well as by clicking a proper button from the tool bar. An antenna image orientation is specified by the Θ and φ angles. Actually, they specify a position of the observer's point of view on the antenna.

Using the "Image Parameters" dialog box (Fig.2) accessible from the main menu it is possible to specify any desired Θ and φ angles, their increments, zoom factor and the coordinate axes presentation options.

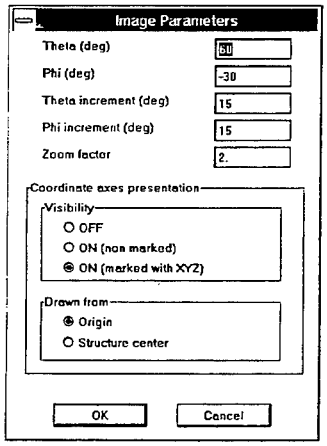

Figure 2. Image Parameters dialog box.

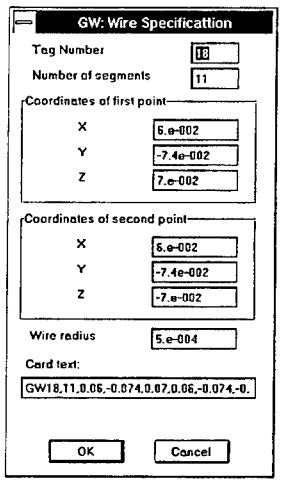

Figure 3. GW-card dialog box.

An opened NEC input deck can be edited. It is possible to modify any existing card, to delete it, or to insert a new card.

Any card could be chosen by a mouse or by a keyboard from the left part of the Deck window, or just by a clicking at the desired element of the antenna image from the right part. The currently chosen card is highlighted. A corresponding element of an antenna image is shown in red color.

Every currently chosen card could be modified. To activate the modification it is necessary just to double-click at the card. Then a proper dialog box is opening. Most of the cards have their own customized dialog boxes. As an example, the GW-card dialog box is shown in Fig. 3. Every dialog box has several data fields, and the text field at the bottom part of the dialog box where it is possible to enter the whole card string as a text. The program checks a validity of an input data (where possible), and if the entered data is not correct, a proper error message will be displayed.

It is possible to remove an existing card from a deck and to insert a new card into the deck. These operations could be made in the several alternative ways (from the main menu, from the tool bar or by pressing a proper "hot" key).

If an insert operation has been requested, the proper Insert Card dialog box is opening (Fig. 4), where the names of the available new cards are listed. The contents of the list is dependent on the previous choice of the current card:
- the comments cards are available only, if the current card is a comment card;
- the geometry cards are available only (Fig. 4a), if the current card is a geometry card;
- the control cards are available only (Fig. 4b), if the current card is a control card.

A user can choose a desired card and click "OK" button. Then a proper dialog box for this card will be opened.

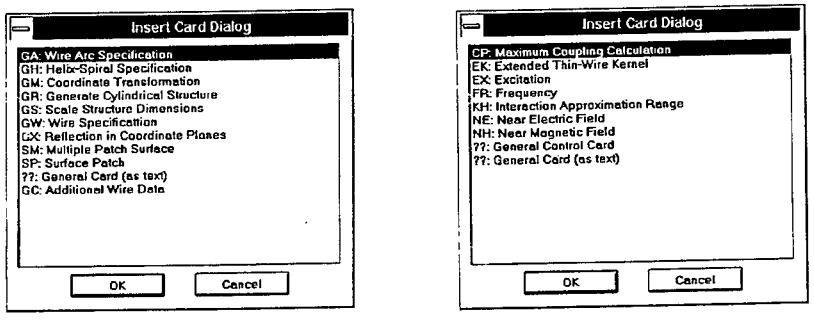

a) b)

Figure 4. Insert Card dialog box.

Any window could be printed out from the main menu. The print preview option is also available. It is possible to assign a desired font for every window.

An electromagnetic analysis could be run for an opened input NEC deck. The NECSHELL program runs the NEC81 executable module in the DOS window. The DOS session is running in the background mode. This makes it possible to continue the work with the NECSHELL during the run. It is possible to start several NEC81 runs simultaneously.

There is an option accessible from the main menu, which specifies a behavior of the DOS NEC-run window on the completion the NEC81 run. A user can choose an auto-close option (which is the most convenient one), or a manual close. The manual close is very useful, if the NEC81 executable module prints error messages.

POST-PROCESSOR FUNCTIONS

The NECSHELL post-processor capabilities are under construction at the moment of a submission of the present report (January, 1996).

The NECSHELL post-processor functions are as follows:
- reading of a standard ASCII NEC output file;
- visualization of any far-zone radiation patterns asrectangular and polar plots, contour maps and 3D surfaces;
- visualization of the current distributions along any wires (as rectangular plots) and for the whole structure (using pseudo-colors on a 3D view of an antenna image);
- visualization of the frequency characteristics (input impedances/admittances only) as rectangular plots;
- spreadsheet presentation of any tabular data available from an output NEC file;
- print out any available plots.

A NEC output file could be opened as a simple text window (Fig. 1) or as a special NEC Output window. The typical view of the NECSHELL post-processor windows is shown in Fig. 5, where the NEC Output window is opened for the HELIX.OUT data set.

An Output window is divided into two parts by a vertical splitter line. The structure of the output NEC file is displayed in the left part of the window as the subdirectory-tree structure. A user can go up and down on this structure by clicking any desired item. The right part of the window immediately shows an output data sub-set for the chosen active item.

The output data sub-sets could be shown as text or as the graphical plots for the radiation patterns and for the current distributions. The SAMPLE1.OUT, SAMPLE2.OUT and SAMPLE3.OUT windows (Fig. 5) show the typical presentations of the calculated radiation patterns. The current position of the splitter line could be easily changed by its clicking-and-drugging. There is a Graphic parameters dialog box, accessible from the main menu where it is possible to enter all the necessary settings for the plots.

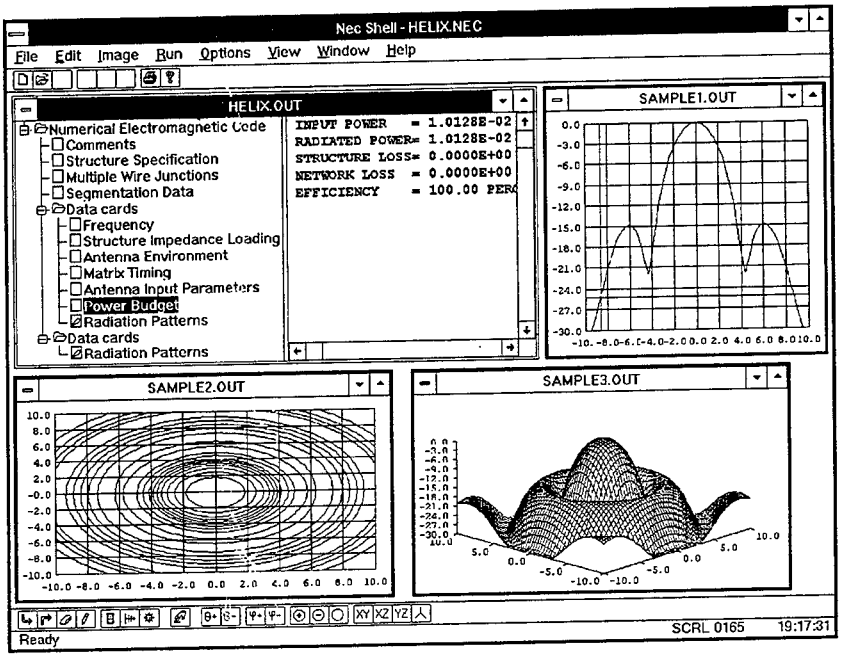

Figure 5. NECSHELL post-processor windows.

ACKNOWLEDGMENTS

This project has been supported by the Nedrud Data Systems, Inc., 220 Versailles Drive, Melbourne Beach, FL 32951-3434, Tel/FAX: (407) 984-1405, E-mail: 75124.1657@compuserve.com.
The authors would like to thank Professor Richard W. Adler for helpful discussions.

SESSION 22:

FINITE ELEMENT ANALYSIS

Chair: J. Brauer

FINITE ELEMENT SCATTERING AND RADIATION ANALYSIS USING PRISMATIC MESHES AND ARTIFICIAL ABSORBERS FOR CONFORMAL DOMAIN TRUNCATION

M. Casciato, M. Nurnberger, T. Özdemir and J. Volakis
Radiation Laboratory
Department of Electrical Engineering and Computer Science
1301 Beal Ave.
University of Michigan
Ann Arbor, MI 48109-2122

1 Introduction

A substantial portion of the effort involved in any finite element (FEM) analysis is devoted to mesh generation. Unstructured tetrahedral meshes are a popular choice because of their superb geometrical fidelity and fail-safe nature. However, tetrahedral mesh generation is very demanding in terms of CPU time and requires high level user expertise. Partly structured meshes, on the other hand, are easy to generate and applicable to a wide range of geometries such as smooth scatterers and conformal antennas. In this paper, we employ prismatic meshes to model microstrip antennas for resonance behavior analysis and non-canonical three dimensional objects for scattering analysis. These meshes are structured in the third dimension and this leads to substantial simplification in mesh generation.

Another important task involved in the FEM implementation is the termination of the mesh. The most accurate approach is the use of a Green's function to relate the tangential electric and magnetic fields over the boundary. Unfortunately, for large targets the Green's function approach requires storage of a large matrix which is partially full. Therefore, it is useful to find a termination scheme which preserves the sparsity of the finite element matrix without comprimising accuracy. One such technique is the use of an absorbing boundary condition (ABC) at a surface close to the scatterer or radiator, and a review of available ABCs has been given by Senior and Volakis [1]. However, ABCs are limited in their ability to conform to the surface of the scatterer and they may also require *a priori* knowledge of the wave's properties. Also in an FEM solution, they generally reduce the rate of convergence. Another way of terminating the mesh is to use a metal-backed layer of isotropic or anisotropic absorbing material [2]-[5], and such layers are often referred to as artificial absorbers since their material parameters may be physically unrealizable. In this paper, we employ an isotropic absorber for terminating the mesh. The efficiency of this absorber has already been demonstrated in [3].

In the sections to follow, we explore the details of the prismatic mesh generation and the artificial absorber termination scheme, and provide numerical data on antenna and scattering analysis.

2 Prismatic mesh and artificial absorber termination

The prismatic mesh generation starts with the tessellation of the antenna or the scatterer surface using a triangular grid. The volume mesh is then grown along the surface normal by repeating the same surface grid at successive layers. The building block of the resulting mesh is the distorted triangular prism and for our analysis Whitney-1 type edge-based vector shape functions are employed [6]. The accuracy of these shape functions has been extensively verified in [7]. If desired, prismatic elements can be easily subdivided into tetrahedrals for use in codes which have not been converted to recognize the prismatic elements and the almond results presented in the next section have been obtained through this procedure.

The simplicity of the prismatic mesh generation stems from the fact that the unstructured mesh (grid) is only needed over the surface and that an unstructured surface mesh is much easier to generate than an unstructured volume mesh. Having generated the surface grid, the prismatic mesh can be grown using a variety of available packages. Figure 1 shows a sample view of the graphical user interface (GUI) of the mesh generator PRISM [8]. The mesh generator PRISM grows the volume mesh by specifying the number of layers, thickness per layer, and the order of the numbering of the surface triangle nodes (for defining surface normal). Figure 2 shows the volume mesh generated for a sphere with the inner spherical surface exposed.

For scattering analysis, the entire scatterer surface must be modeled but for antenna analysis the mesh needs to be defined only over the aperture and its vicinity. The antenna resonance behavior is predominantly dictated by its near field configuration and thus it suffices to only model the immediate neighborhood of the antenna (see Figure 5c). The volume mesh is still grown along the surface normal but care must be taken when terminating the substrate/superstrate layers (see Figure 3). The artificial absorber used to terminate the mesh is a metal-backed lossy dielectric layer whose material parameters are chosen to match wave impedances on both sides of the air-absorber or substrate/superstrate-absorber interface. This guarantees zero reflection from the interface at normal incidence and once the wave is inside the absorbing layer, it undergoes attenuation so that its energy is greatly reduced by the time it re-exits the layer. This way, while the metallic boundary on the back of the layer enables us to terminate the mesh, its lossy dielectric lining absorbs the incoming electromagnetic energy and thereby simulates a transparent boundary. To assess the performance of this termination technique, we take a look at the planar absorbing layer shown in Figure 4a. Its E and H polarized planewave reflection coefficients are plotted with dashed lines in Figure 4b for both real ($\sin\phi \leq 1$) and imaginary ($\sin\phi > 1$) incidence angles ϕ with $\phi = 0$ corresponding to normal incidence [9]. A substantially better performance can be obtained however by using a uniaxial anisotropic absorber as shown in the same figure with solid line [4]. Particularly noticeable is the improvement for angles away from normal and for complex incidence angles. The latter are significant for illumination due to sources in the near zone. That is, the absorber's performance for complex angles of incidence determines how close the absorber can be placed to the scattering surface.

An important feature of the artificial absorber termination is that it can be applied conformally, and this minimizes the computational domain and hence the problem size. In the next section, we present results for antenna and scattering analysis using the isotropic absorber

for truncating the mesh. At the conference, we will also present results obtained by using the anisotropic absorber.

3 Numerical Results

To illustrate the applicability of the proposed technique, two examples are considered, one dealing with antenna analysis and the other with scattering by a non-canonical structure. For simplicity both cases employed a simple version of a homogeneous artificial absorber consisting of three layers each $0.05\lambda_o$ thick with constitutive parameters $\epsilon_r = \mu_r$=1-j2.7 (see Figure 3).

Of particular interest in antenna analysis is the computation of the resonant frequency which is a rather sensitive quantity and its accurate computation provides a good test of the proposed method. Figure 5 shows the results for a sectoral patch antenna mounted on the conical surface illustrated in the figure. The patch resides on a substrate having $\epsilon_r = 2.32$ and a thickness $h = 0.114cm$. Its dimensions are given in Figure 5a and on the basis of the approximate cavity model it resonates at $3.2GHz$. From the computed input impedance plot, it is seen that the resonance frequency predicted by the FEM code is $3.115GHz$ (for θ=35°), which is within 3 percent of the cavity model. The plot shows that the resonance frequency drops with the cone angle θ. The FEM computations were carried out using prismatic edge elements [7]. A total of 2358 prisms were used for this analysis resulting in 3790 degrees of freedom.

As a scattering example we consider the radar cross section of the 9.936 inch long NASA metallic almond [10]. Our finite element code FEMATS [11] was used to model the almond illuminated with a plane wave at a frequency 1.19GHz. This code employs edge-based tetrahedral elements and the mesh was again terminated using the aforementioned 3-layer homogeneous artificial absorber. For ease of mesh generation, a structured prismatic mesh was first generated conformal to the almond's surface and consisted of nine 0.05λ layers with the outer three layers occupied by the artificial absorber. Figure 6a shows the mesh with the inner almond surface exposed. The structured prismatic mesh was then turned into a tetrahedral mesh (by dividing each prism into five tetrahedra) resulting in a total of 46,878 edges. Figure 6b displays the radar cross section (RCS) computations compared with measured data for both polarizations of incidence [10]. The patterns are taken in the plane most parallel to the flat side of the almond (non-symmetric plane), with zero degrees corresponding to incidence tip-on. As seen, the calculations are in good agreement with the measured data except at near 90 degrees for HH polarization. However, other reference calculations based on a moment method code are in agreement with the FEMATS data, suggesting that the discrepancy may be due to minor alignment errors in the measurement.

4 Conclusion

In this paper we investigated the application of prismatic elements to FEM analysis along with artificial absorbers for mesh truncation. The ease of generating the prismatic volume mesh combined with the accuracy and conformal applicability of the artificial absorber termination

scheme provides us with an efficient analysis tool for antenna and scattering applications. As was seen in the above examples (the patch antenna and the NASA almond), results were in good agreement with the reference data. Uniaxial anisotropic absorber promises even more accurate results and results based on mesh truncation using this new absorber will be also presented at the conference.

References

[1] T.B.A. Senior and J.L. Volakis, *Approximate Boundary Conditions in Electromagnetics.* Stevenage, UK, IEE Press, 1995.

[2] C. Rappaport and L. Bahrmasel,"An absorbing boundary condition based on anechoic absorbers for EM scattering computation," *J. Electromagn. Waves Appl.* **6**, pp. 1621-1634, 1992.

[3] T. Özdemir and J.L. Volakis, "A comparative study of an absorbing boundary condition and an artificial absorber for truncating finite element meshes," *Radio Sci.* **29**, pp. 1255-1263, 1994.

[4] Z.S. Sacks, D.M. Kingsland, R. Lee and J.F. Lee, "A perfectly matched anisotropic absorber for use as an absorbing boundary condition," to appear in *IEEE Trans. Antennas Propagat.*

[5] J.P. Berenger, "A perfectly matched layer for the absorption of electromagnetic waves," *J. Comp. Phys.* **114**, pp. 185-200, 1994.

[6] Bossavit, A.,"Whitney forms: a class of finite elements for three-dimensional computations in electromagnetism," *IEE Proc. Part A*, Vol. 135, No. 8, November 1988.

[7] T. Özdemir and J. L. Volakis, "Triangular prisms for edge-based vector finite element analysis," IEEE AP-S Int. Symp. Digest, Vol. 1, pp. 48-51, Newport Beach, California, June 19-24, 1994.

[8] S. Pandya, *Personal Communication*, NASA Ames Research Center.

[9] S. R. Legault, T. B. A. Senior and J. L. Volakis, "Design of Planar Absorbing Layers for Domain Truncation in FEM Applications", *submitted to Journal of Electromagnetic Waves.*

[10] A. Woo, H.T.G. Wang, M. J. Schuh and M. J. Saunders, "Benchmark radar targets for the validation of computational electromagnetics programs," *IEEE Antennas and Propagat. Magazine*, **35**, pp. 84–89, Feb. 1993.

[11] A. Chatterjee and J.L. Volakis, "Conformal absorbing boundary conditions for 3D problems: Derivation and applications," *IEEE Trans. Antennas and Propagat.*, **43**, pp. 860-866, Sept. 1995.

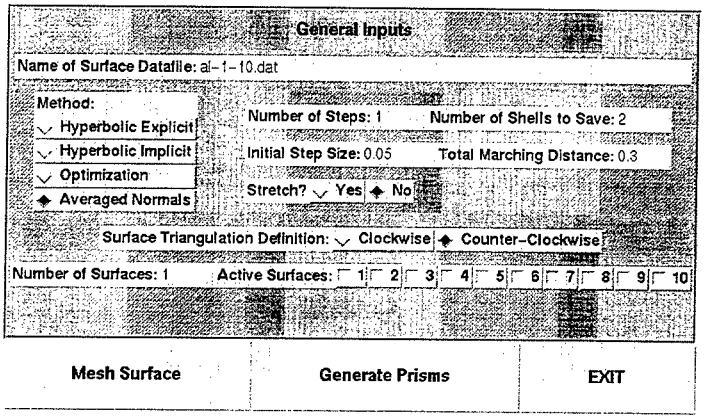

Figure 1: Graphical User Interface of PRISM

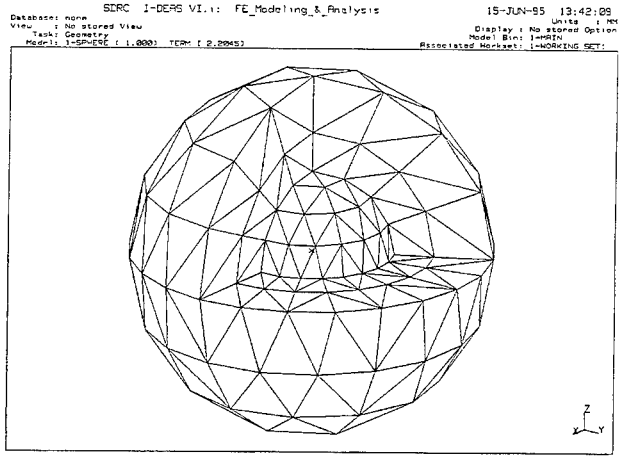

Figure 2: Prismatic mesh grown from the surface of a sphere using PRISM (innner spherical surface is exposed)

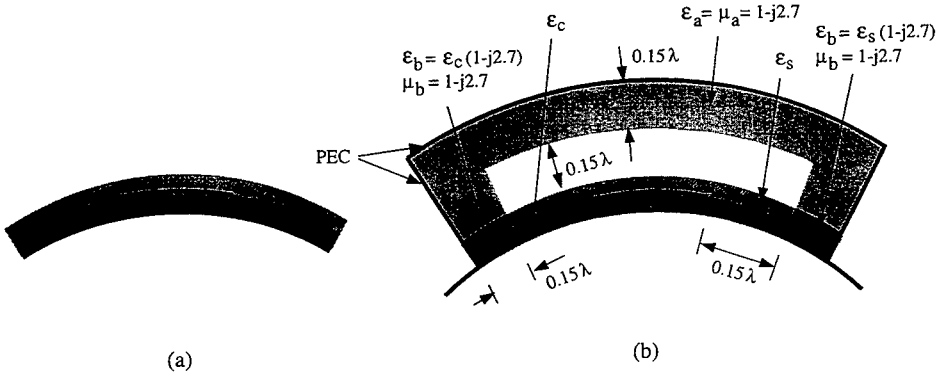

Figure 3: Illustration of the finite element mesh truncation using an artificial absorber

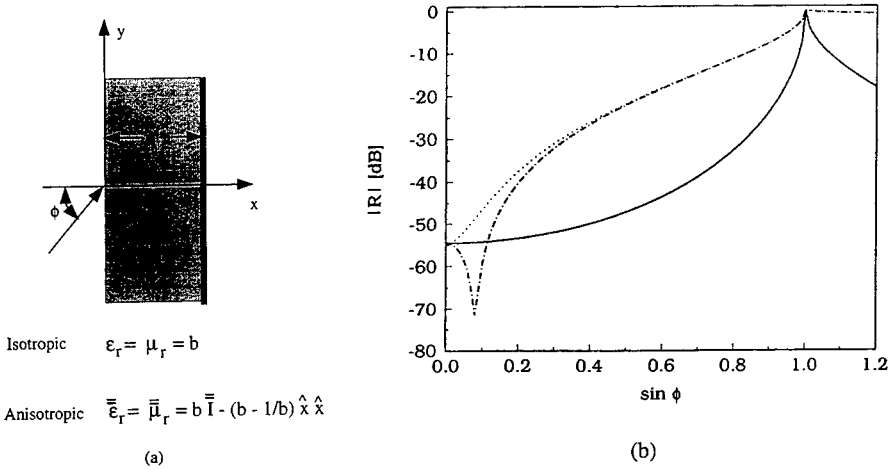

Figure 4: Artificial Absorber. (a) Geometry and (b) Plane wave reflection coefficient vs angle of incidence for t=0.25 wavelengths and b=1-j2.

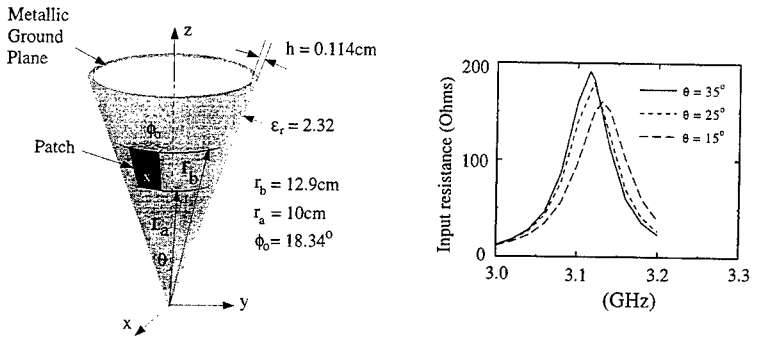

(a) (b)

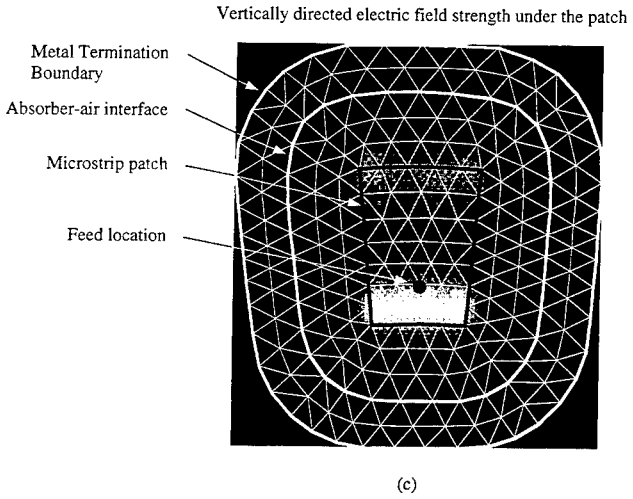

(c)

Figure 5: Microstrip sectoral patch on cone. (a) Configuration, (b) patch input resistance as a function of frequency for different cone angles and (c) vertical electric field strength inside the substrate with the surface mesh superimposed

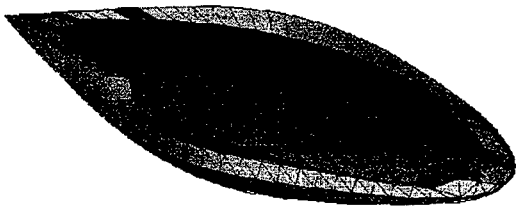

(a)

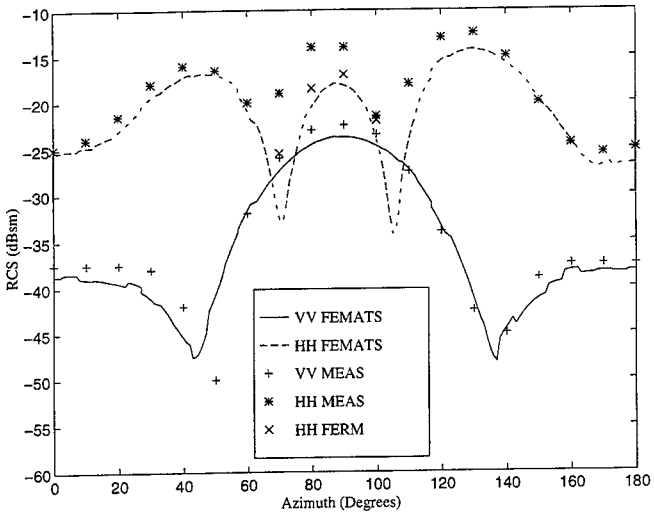

(b)

Figure 6: NASA metallic almond. (a) Surface and volume prismatic conformal mesh and (b) backscatter RCS pattern calculations and measurements at 1.19GHz.

Application of Fast Multipole Method to Finite Element–Boundary Integral Solution of Scattering Problems

Ninglong Lu and Jian-Ming Jin
Electromagnetics Laboratory
Department of Electrical and Computer Engineering
University of Illinois at Urbana-Champaign
Urbana, Illinois 61801-2991
E-mail: jjin@uxh.cso.uiuc.edu

ABSTRACT

The finite element–boundary integral method is a powerful technique for dealing with scattering and radiation problems involving complex geometries and inhomogeneous media. The capability of the technique is limited mainly by the full matrix generated by the discretization of the boundary integrals involving the Green's function. In this paper, this limitation is lifted using the fast multipole method, which evaluates the boundary integrals at a reduced complexity. The resulting new technique is applied to the problem of electromagnetic scattering by cavity-backed apertures and microstrip antennas. Numerical results are presented to demonstrate its validity and capability.

I. INTRODUCTION

The finite element and boundary integral methods represent two powerful numerical techniques for solving boundary-value problems in electromagnetics. However, these two methods differ from each other with respect to their advantages and disadvantages. For example, the finite element method is especially suitable for dealing with complex inhomogeneous media because of its relatively simple formulation, and is efficient for large problems because it yields a sparse and banded matrix. However, this method is not well suited for solving open-region problems because it does not incorporate radiation conditions into its formulation. On the other hand, because of the use of Green's function, the boundary integral method automatically incorporates the radiation conditions into its formulation and, thus, is very efficient in dealing with open-region problems. However, since the Green's function is usually unavailable for complex inhomogeneous media, the method is only applicable to problems involving homogeneous media.

To eliminate the disadvantages of the finite element and boundary integral methods, while retaining their advantages, a hybrid technique has been developed for solving open-region electromagnetic problems. This technique divides an open-region problem into interior and exterior problems and employs the finite element method to deal with the interior problem. The exterior problem is formulated using the boundary integral method, which, when coupled with the interior fields, provides an efficient solution to the original problem. This technique, often referred to as the finite element–boundary integral (FE–BI) method or the finite element–moment method (FE–MM), has been applied to a variety of electromagnetic problems with remarkable success.

Although the FE–BI method is remarkably more powerful than the finite element and boundary integral methods alone, it still has a bottleneck, which is the full matrix generated by the boundary integral formulation. This bottleneck effect becomes obvious if we consider a general three-dimensional volumetric problem whose linear dimension is L. The total number of discrete unknowns is proportional to L^3, and the total number of surface unknowns is proportional to L^2. Therefore, the memory requirement and computing time per iteration (assuming that an iterative solver is used) for the finite element matrix are proportional to L^3, whereas those for the boundary integral matrix are proportional to L^4, thus limiting the capability of the FE–BI method. In our previous work, this problem was circumvented by using structured elements (brick elements) and an iterative solver. With brick elements, the boundary integrals can be cast into the form of a discrete Fourier transform, which can be evaluated efficiently using the fast Fourier transform (FFT). This, however, limits the applicability of the method to certain geometries and results in a staircase approximation for curved boundaries. To model general geometries accurately, unstructured meshes must be used, which, however, will prohibit the use of the FFT.

In this work, we develop a scheme to efficiently evaluate the boundary integrals using the recently developed fast multipole method (FMM). Since the application of the FMM does not depend on the choice of the elements, we can use more general elements, such as tetrahedral and triangular prisms, to model arbitrary geometries more accurately. The low operation count of the FMM (proportional to L^3), coupled to the sparseness of the FEM matrix, results in a more efficient method for our problems. In this paper, we describe this general method by applying it to the problem of scattering by cavity-backed apertures and microstrip antennas in a ground plane.

II. FORMULATION

Consider the problem of electromagnetic scattering by a cavity-backed aperture in a ground plane. As shown in [1], the electric field inside the cavity and at the aperture can be calculated by seeking the stationary point of the functional given by

$$\begin{aligned} F(\mathbf{E}) = \frac{1}{2}\iiint_V \left[\frac{1}{\mu_r}(\nabla\times\mathbf{E})\cdot(\nabla\times\mathbf{E}) - k_0^2\varepsilon_r\mathbf{E}\cdot\mathbf{E}\right]dV \\ + \iint_S \nabla\cdot\mathbf{M}(\mathbf{r})\left[\iint_S G_0(\mathbf{r},\mathbf{r}')\nabla'\cdot\mathbf{M}(\mathbf{r}')\,dS'\right]dS \\ - k_0^2\iint_S \mathbf{M}(\mathbf{r})\cdot\left[\iint_S G_0(\mathbf{r},\mathbf{r}')\mathbf{M}(\mathbf{r}')\,dS'\right]dS \\ - 2jk_0Z_0\iint_S \mathbf{M}(\mathbf{r})\cdot\mathbf{H}^{\text{inc}}(\mathbf{r})\,dS \end{aligned} \tag{1}$$

where V denotes the volume of the cavity and S denotes the aperture of the cavity. Also, $\mathbf{H}^{\text{inc}}(\mathbf{r})$ denotes the incident magnetic field, $\mathbf{M} = \mathbf{E}\times\hat{n}$ is the equivalent magnetic current over the aperture, and $G_0(\mathbf{r},\mathbf{r}')$ denotes the free-space Green's function.

The functional in (1) can be discretized by first subdividing the volume of the cavity into small elements and then representing the field as

$$\mathbf{E} = \sum_{i=1}^{N} E_i \mathbf{N}_i \tag{2}$$

where $\mathbf{N}_i$ denotes the vector basis function, E_i denotes the expansion coefficient, and N denotes the total number of expansion terms. At the cavity's aperture, the magnetic current can be expanded as

$$\mathbf{M} = \mathbf{E} \times \hat{n} = \sum_{i=1}^{N_s} E_i^a \mathbf{S}_i \tag{3}$$

where $\mathbf{S}_i$ is the vector basis function, E_i^a is the expansion coefficient, and N_s is the total number of expansion terms. Note that the numbering of coefficients in (3) is different from that in (2) and a superscript "a" is used to emphasize this difference.

Substituting (2) and (3) into (1), we obtain the discretized functional

$$F = \frac{1}{2}\sum_{i=1}^{N}\sum_{j=1}^{N} E_i K_{ij} E_j + \frac{1}{2}\sum_{i=1}^{N_s}\sum_{j=1}^{N_s} E_i^a P_{ij}^a E_j^a - \sum_{i=1}^{N_s} E_i^a b_i^a \tag{4}$$

where

$$K_{ij} = \iiint_V \left[\frac{1}{\mu_r} (\nabla \times \mathbf{N}_i) \cdot (\nabla \times \mathbf{N}_j) - k_0^2 \varepsilon_r \mathbf{N}_i \cdot \mathbf{N}_j \right] dV \tag{5}$$

$$\begin{aligned} P_{ij}^a = {} & 2 \iint_S (\nabla \cdot \mathbf{S}_i) \left[\iint_S (\nabla' \cdot \mathbf{S}_j) G_0(\mathbf{r}, \mathbf{r}') dS' \right] dS \\ & - 2k_0^2 \iint_S \mathbf{S}_i \cdot \left[\iint_S \mathbf{S}_j G_0(\mathbf{r}, \mathbf{r}') dS' \right] dS \end{aligned} \tag{6}$$

$$b_i^a = 2jk_0 Z_0 \iint_S \mathbf{S}_i \cdot \mathbf{H}^{\text{inc}}(\mathbf{r}) dS \tag{7}$$

Taking the partial derivative of F in (4) with respect to each E_i and setting the resultant expression to zero, we obtain a set of linear algebraic equations (a matrix equation), which can be solved using either a direct method or iterative method.

When an iterative solver is employed to solve the resultant matrix equation, we have to compute a matrix-vector multiplication in each iteration. For this problem, the matrix-vector multiplication consists of two parts. One is contributed by the finite element discretization and is given by

$$\sum_{j=1}^{N} K_{ij} E_j \tag{8}$$

Since $[K]$ is a sparse matrix whose sparsity is independent of N, the operation count for calculating (8) is proportional to $O(N)$. The other part is contributed by the boundary integral and is given by

$$\sum_{j=1}^{N_s} P_{ij}^a E_j^a \tag{9}$$

Since $[P^a]$ is a full matrix, the operation count for calculating (9) is proportional to $O(N_s^2)$. Therefore, this calculation is very time consuming, especially for shallow cavities with a large aperture. In the following, we describe a procedure for evaluating (9) efficiently using the fast multipole method (FMM).

The FMM, as originally developed in [2]-[6], is designed to speed up the matrix-vector multiplication required in iterative solvers. To describe the FMM, we start with the addition theorem [7]

$$\frac{e^{-jk_0|\mathbf{r}+\mathbf{d}|}}{|\mathbf{r}+\mathbf{d}|} = -jk_0 \sum_{l=0}^{\infty} (-1)^l (2l+1) j_l(k_0 d) h_l^{(2)}(k_0 r) P_l(\hat{d}\cdot\hat{r}) \tag{10}$$

where j_l is a spherical Bessel function of the first kind, $h_l^{(2)}$ is a spherical Hankel function of the second kind, P_l is a Legendre polynomial, and $d < r$. Employing the elementary identity [8]

$$4\pi(-j)^l j_l(k_0 d) P_l(\hat{d}\cdot\hat{r}) = \oint\!\!\oint e^{-j\mathbf{k}\cdot\mathbf{d}} P_l(\hat{k}\cdot\hat{r}) d^2\hat{k} \tag{11}$$

where the integral is over a unit sphere, we obtain

$$\frac{e^{-jk_0|\mathbf{r}+\mathbf{d}|}}{|\mathbf{r}+\mathbf{d}|} = -\frac{jk_0}{4\pi} \oint\!\!\oint e^{-j\mathbf{k}\cdot\mathbf{d}} \sum_{l=0}^{\infty} (-j)^l (2l+1) h_l^{(2)}(k_0 r) P_l(\hat{k}\cdot\hat{r}) d^2\hat{k} \tag{12}$$

Truncating the infinite summation and denoting

$$T_L(\hat{k}\cdot\hat{r}) = \sum_{l=0}^{L} (-j)^l (2l+1) h_l^{(2)}(k_0 r) P_l(\hat{k}\cdot\hat{r}) \tag{13}$$

Equation (12) can be approximated as

$$\frac{e^{-jk_0|\mathbf{r}+\mathbf{d}|}}{|\mathbf{r}+\mathbf{d}|} \approx -\frac{jk_0}{4\pi} \oint\!\!\oint e^{-j\mathbf{k}\cdot\mathbf{d}} T_L(\hat{k}\cdot\hat{r}) d^2\hat{k} \tag{14}$$

To use the FMM, we first divide the area of the cavity's aperture into several groups denoted by G_m $(m = 1,2,\ldots,M)$. Now, let $\mathbf{r}_i$ be the field point in a group G_m centered at $\mathbf{r}_m$, and $\mathbf{r}_j$ be the field point in another group $G_{m'}$ centered at $\mathbf{r}_{m'}$. It is not difficult to see

$$\begin{aligned}\mathbf{r}_i - \mathbf{r}_j &= (\mathbf{r}_i - \mathbf{r}_m) + (\mathbf{r}_m - \mathbf{r}_{m'}) - (\mathbf{r}_j - \mathbf{r}_{m'}) \\ &= \mathbf{r}_{im} + \mathbf{r}_{mm'} - \mathbf{r}_{jm'}\end{aligned} \tag{15}$$

Substituting this into (14), we have

$$\frac{e^{-jk_0|\mathbf{r}_i - \mathbf{r}_j|}}{|\mathbf{r}_i - \mathbf{r}_j|} \approx -\frac{jk_0}{4\pi}\iint e^{-j\mathbf{k}\cdot(\mathbf{r}_{im} - \mathbf{r}_{jm'})} T_L(\hat{k}\cdot\hat{r}_{mm'})\, d^2\hat{k} \tag{16}$$

When this is substituted into (6), we obtain

$$\begin{aligned}P_{ij}^a = \frac{jk_0}{8\pi^2}\Big[k_0^2 \iint \mathbf{U}_{mi}(\hat{k})\cdot T_L(\hat{k}\cdot\hat{r}_{mm'})\mathbf{U}_{m'j}^*(\hat{k})\, d^2\hat{k} \\ -\iint V_{mi}(\hat{k}) T_L(\hat{k}\cdot\hat{r}_{mm'}) V_{m'j}^*(\hat{k})\, d^2\hat{k}\Big]\end{aligned} \tag{17}$$

where

$$\mathbf{U}_{mi}(\hat{k}) = \iint_S e^{-j\mathbf{k}\cdot\mathbf{r}_{im}}\mathbf{S}_i(\mathbf{r}_{im})\, dS \tag{18}$$

$$V_{mi}(\hat{k}) = \iint_S e^{-j\mathbf{k}\cdot\mathbf{r}_{im}}\nabla\cdot\mathbf{S}_i(\mathbf{r}_{im})\, dS \tag{19}$$

Using (17), we can rewrite the matrix-vector multiplication as

$$\begin{aligned}\sum_{j=1}^{N_s} P_{ij}^a E_j^a = \sum_{m'\in B_m}\sum_{j\in G_{m'}} P_{ij}^a E_j^a + \frac{jk_0}{8\pi^2}\Bigg[k_0^2 \iint \mathbf{U}_{mi}(\hat{k})\cdot \sum_{m'\in B_m} T_L(\hat{k}\cdot\hat{r}_{mm'}) \sum_{j\in G_{m'}} \mathbf{U}_{m'j}^*(\hat{k})\, d^2\hat{k} \\ -\iint V_{mi}(\hat{k}) \sum_{m'\notin B_m} T_L(\hat{k}\cdot\hat{r}_{mm'}) \sum_{j\in G_{m'}} V_{m'j}^*(\hat{k})\, d^2\hat{k}\Bigg] \qquad i\in G_m\end{aligned} \tag{20}$$

where B_m denotes the neighboring groups of group G_m including G_m itself. Therefore, the first term in (20) is the contribution from nearby groups (including the self-group) and is calculated directly. The second term is the far interaction to be calculated by the FMM.

Obviously, in the FMM, the addition theorem is used to translate the scattered field of different elements within a group into a single center. The field scattered by all the other group centers is first received by the group center and then redistributed to the elements within the group. It has been proven [6] that the operation count for calculating (20) is proportional to $O(N_s^{1.5})$. This complexity can be reduced further using a multilevel FMM [9]. For example, in the two-level FMM implemented in this work, the aperture of the cavity is divided into two sets of groups with different group sizes. When the observation

and integration points are far apart, the FMM is performed on larger groups, and when those points are not very far apart, the FMM is performed on smaller groups. As a result, the complexity is reduced to $O(N_s^{1.33})$.

III. NUMERICAL RESULTS

Based on the formulation described above, a computer program was written to examine the validity and capability of the proposed technique. In this program, triangular prisms were used to discretize the volume of the cavity; consequently, the aperture of the cavity was divided into triangular patches. The divergenceless edge-based basis functions were developed and used to discretize the electric field. The FEM matrix was stored in a compact two-dimensional array $A(N,K)$, where K denotes the maximum number of nonzero elements in a row of the array; typically, $K < 30$. For the implementation of the FMM, the number of groups was chosen to be $M \sim \sqrt{N_s}$ and the infinite summation in (13) is truncated at $L = k_0 D + \ln(\pi + k_0 D)$, where D is the maximum diameter of a group. The biconjugate gradient method was employed to solve the system of equations.

One of examples considered is the scattering by a 16.256λ long, 0.2λ wide, and 0.85λ deep rectangular crack in a ground plane. The bistatic radar cross section (RCS) in the plane parallel to the longer dimension of the crack is shown in Fig. 1 for the incidence angle $\theta = 20°$. The incident electric field is ϕ polarized (horizontally polarized). The result obtained using the triangular prism elements is compared to that obtained using the brick elements and the agreement is good.

The performance of the two-level FMM is shown in Fig. 2, from which we see that the computational complexity is very close to $O(N_s^{1.33})$. The problem for this case is a cavity-backed square aperture with one layer of elements.

IV. CONCLUSION

A new technique was described in which the fast multipole method (FMM) is employed to evaluate efficiently the boundary integrals in the finite element–boundary integral (FE–BI) solution of three-dimensional scattering problems. As was shown numerically, this technique has a computational complexity of $O(N_s^{1.5})$ with a one-level scheme and $O(N_s^{1.33})$ with a two-level scheme. The technique was validated by numerical results for scattering by cavity-backed apertures and microstrip antennas on a ground plane.

ACKNOWLEDGMENT

Helpful discussions with Dr. J. M. Song and Prof. W. C. Chew are greatly appreciated. This work was supported by the National Science Foundation under the grant ECS-9457735 and by the Office of Naval Research under the grant N00014-95-1-0848.

This paper is an abbreviated version of a paper to be published in *IEEE. Trans. Antennas Propagat.*

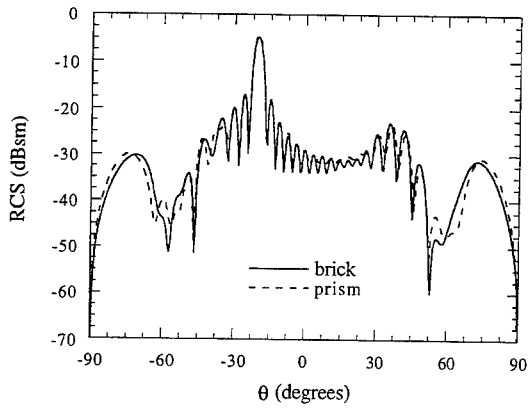

Figure 1. Bistatic RCS of a 16.256λ long, 0.2λ wide, and 0.85λ deep rectangular crack in a ground plane in the plane parallel to the longer dimension of the crack for the incidence angle $\theta = 20°$. The incident electric field is ϕ-polarized.

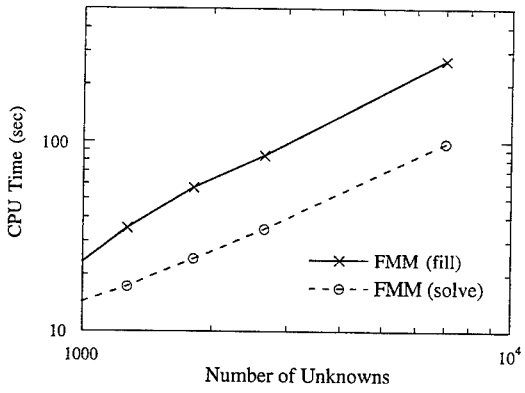

Figure 2. CPU time versus the number of unknowns for the multilevel FMM. The computational complexity is very close to $O(N_s^{1.33})$.

REFERENCES

[1] J. M. Jin, *The Finite Element Method in Electromagnetics*. New York: Wiley, 1993.

[2] V. Rokhlin, "Rapid solution of integral equations of scattering theory in two dimensions," *J. Comput. Phys.*, vol. 86, pp. 414-439, Feb. 1990.

[3] N. Engheta, W. D. Murphy, V. Rokhlin, and M. S. Vassiliou, "The fast multipole method (FMM) for electromagnetic scattering problems, " *IEEE. Trans. Antennas Propagat.*, vol. AP-40, pp. 634-641, June 1992.

[4] C.C. Lu and W. C. Chew, "A fast algorithm for solving hybrid integral equation," *IEE Proc. Pt. H*, vol. 140, pp. 455-460, Dec. 1993.

[5] R. Coifman, V. Rokhlin, and S. Wandzura, "The fast multipole method for the wave equation: a pedestrian prescription," *IEEE. Trans. Antennas Propagat. Magazine*, vol. 35, pp. 7-12, June 1993.

[6] J. M. Song and W. C. Chew, "Fast multipole method solution using parametric geometry," *Microwave Optical Tech. Lett.*, vol. 7, pp. 760-765, Nov. 1994.

[7] M. Abromowitz and I. A. Stegun, Eds. *Handbook of Mathematical Functions*. New York: Dover, 1972.

[8] J. A. Stratton, *Electromagnetic Theory*. New York: McGraw-Hill, 1941.

[9] J. M. Song and W. C. Chew, "Fast multipole method solution of combined field integral equation," *Proceedings of 11th Annual Review of Progress in Applied Computational Electromagnetics*, vol. 1, pp. 629-636, Mar. 20-25, 1995.

Use of Perfectly-Matched Absorber Boundaries in Finite Element Analysis of Patch Antennas

J. F. DeFord and G. C. Lizalek
MacNeal-Schwendler Corporation
Milwaukee, WI 53223

Introduction

Efficient and effective radiation boundary conditions are critical to the accurate computation of antenna near-fields in finite-element analysis. Recently, a new method of terminating outgoing radiation on a finite-element mesh was developed by P. Simon and K. McInturff [1], and independently by Kingsland, et al. [2]. This method, dubbed as the perfectly-matched absorber (PMA) approach, is similar in spirit to the perfectly-matched layer introduced by Berenger [3], but avoids the use of non-Maxwellian media. A PMA is a layer composed of an orthotropic material that has the following properties:

$$\epsilon_r = \begin{bmatrix} \epsilon_1 & 0 & 0 \\ 0 & \epsilon_1 & 0 \\ 0 & 0 & \epsilon_2 \end{bmatrix}, \quad \mu_r = \begin{bmatrix} \mu_1 & 0 & 0 \\ 0 & \mu_1 & 0 \\ 0 & 0 & \mu_2 \end{bmatrix}, \tag{1}$$

where $\epsilon_1/\epsilon_i = \mu_1/\mu_i = \epsilon_i/\epsilon_2 = \mu_i/\mu_2 \equiv \kappa$, with ϵ_i and μ_i the permittivity and permeability of the media abutting the PMA, respectively. The constant $\kappa = \kappa' - j\kappa''$ determines the propagation constant β_z (z is the direction normal to the PMA surface) in the PMA layer, i.e.,

$$\beta_z = k\kappa \cos\theta_i \tag{2}$$

where $k = \omega\sqrt{\epsilon_i \mu_i}$ is the propagation constant in the media abutting the PMA, and θ_i is the incident angle of the plane wave, as measured from the surface normal. A PMA will damp both TE (to z) and TM polarized plane waves equally, and theoretically is perfectly matched at the PMA surface when the layer is infinitely thick. In practice, of course, the layer has a finite thickness and is terminated in some fashion, which leads to a finite reflection. In the subsequent discussion we will assume the PMA is terminated by a perfect electric conductor, which yields an overall reflection coefficient Γ for the layer that is dependent on the layer thickness and is given by

$$\Gamma = e^{-j2\beta_z w}, \tag{3}$$

where w is the layer thickness. Examination of Eqns. (2) and (3) reveals that when $\kappa'' > 0$ a PMA will yield minimal $|\Gamma|$ for normally incident radiation, with the thickness necessary to produce a given $|\Gamma|$ increasing as the incident angle increases, or the frequency decreases.

Note also that $k_0 \cos\theta_i \equiv k_z$ is the z component of the propagation vector for the incident plane wave. For evanescent incident fields, that is, when k_z is imaginary, the roles of κ' and κ'' are reversed. Thus, for evanescent fields, the rate of attenuation in the PMA is determined by the real part of κ, which is an important constraint in choosing the PMA material properties for application to general purpose analysis.

Construction of PMA in Practical Analysis Problems

We can use Eqns. (2) and (3) to determine the overall thickness of the PMA based on our frequency range of operation, and the spread in incident angles we expect to see in the radiated fields. However, there are several practical complexities that must be considered when using PMA with patch antennas, and also in more general applications:

- *Effect of material inhomogeneities at PMA boundary.* When a material boundary intersects the PMA, such as happens when analyzing a patch antenna on a dielectric substrate covering an infinite ground plane, we will (without further justification) simply modify the material properties in the PMA adjacent to the dielectric region as indicated in Eqn. (1).
- *PMA material properties at corners and edges, since surface normal becomes ill-defined.* There are several methods for dealing with this problem, but we will avoid it altogether by using a portion of a sphere for PMA boundary for the example discussed herein.
- *Optimization of performance when both propagating and evanescent modes are present.* This issue is alluded to above, and imposes the requirement that $\kappa' = \kappa''$.
- *PMA meshing requirements.* The remainder of the discussion will focus on this issue.

PMA meshing considerations are listed below:

(i) Spectrum of incident angles, or equivalently, the frequency range.

(ii) Maximum allowable reflection coefficient.

(iii) Minimum number of element layers for desired performance.

In practice, the reflection coefficient produced by the PMA is a function not only of the overall thickness of the PMA, but also of the depth of the individual element layers that make up the mesh in the PMA. This is because a minimum field sampling density must be maintained in order to obtain accurate results with finite elements. The required sampling density is a function of the nature of the basis functions and the variation of the fields, but as a rule of thumb there should be at least 5 elements per wavelength for 2nd-order (mid-noded) elements in propagating fields, and approximately 1 element per 1/e distance in evanescent fields. If the PMA mesh layers are thicker than these bounds, then numerical errors begin to dominate the performance, and $|\Gamma|$ will rise above what is predicted by Eqn. (3).

In the following discussion we assume only propagating modes are present (the analysis for evanescent modes is similar). The 1/e distance in the PMA will be smallest for normal incidence and highest frequency, and therefore the thickness for each layer Δ_i must each obey the constraint

$$n_e \Delta_i \kappa'' \leq \min\left(\frac{1}{k\cos\theta_i}\right). \tag{4}$$

where n_e is the number of elements per 1/e distance. However, the thickness t of the PMA is determined by the required performance at large incident angles/low frequencies, i.e.,

$$t = \frac{\ln|\Gamma_0|}{-2\kappa''}\max\left(\frac{1}{k\cos\theta_i}\right). \tag{5}$$

Therefore if we require that all elements in the PMA have a thickness that satisfies Eqn. (4) (applying the equality), and we want a reflection coefficient of $|\Gamma_0|$ at largest incident angle and lowest frequency, then the mesh will be uniform in the z direction, and the number of element layers is given by

$$N_{uniform} = \frac{n_e B \ln|\Gamma_0|}{-2} \quad , \tag{6}$$

where B is the effective operating bandwidth of the PMA given by

$$B = \left[\frac{\max(k\cos\theta_i)}{\min(k\cos\theta_i)}\right] . \tag{7}$$

For example, if we use $n_e = 1$ (mid-noded elements), the desired $|\Gamma_0|$ is –50dB, a frequency range of 10% is needed, and the expected spectrum of incident angles of +– 30°, then $N_{uniform} = 4$. These same requirements but for a frequency range of an octave yields $N_{uniform} = 7$, and a factor of 10 in frequency yields $N_{uniform} = 33$. Conversely, a substantial spread in incident angles, which is more often the problem in patch antenna analysis, will also drive up the layer count. The linear relationship between the bandwidth of $k\cos\theta_i$ is the cause of the problem.

To avoid the inefficiencies of the uniform mesh, we have relaxed the constraint imposed by Eqn. (4) at the back (or terminated end) of the PMA. The rationale for this approach is that for values of $k\cos\theta_i$ near the maximum of the design range the fields will be damped out in the layers nearest the surface of the PMA, whereas for minimal $k\cos\theta_i$ the full PMA thickness is needed. The layers at the back of the PMA can have a larger thickness because the fields are only significant in these layers for relatively small values of $k\cos\theta_i$. We have implemented in the commercial finite-element analysis software product MicroWaveLab™ a PMA meshing scheme that takes advantage of the observation noted above with an element layer thickness given by

$$\Delta_i = \Delta_0 r(r+1)^{i-1} \quad i = 1, 2, \ldots , \tag{8}$$

where r is a constant, and Δ_0 is the width of the first layer (index 0). Each succeeding element layer has a thickness that is a fixed multiple r of the total preceeding mesh thickness. Δ_0 is chosen to satisfy Eqn. (4), and the number of layers is determined using the relation

$$N_{graded} = \frac{\ln\left[\frac{n_e B \ln|\Gamma_0|}{-2}\right]}{\ln(r+1)} + 1 = \frac{\ln(N_{uniform})}{\ln(r+1)} + 1 \ . \tag{9}$$

Thus for large bandwidth problems, where the bandwidth may come from either a spread in k or in incident angles, the graded mesh yields a number of layers that grows only as the logarithm of the uniform case.

The best value of r will generally depend on n_e. Via numerical experimentation in a waveguide terminated with 2 layers of H_1-curl elements, we achieved minimal reflection coefficients around –55dB when $r = 2$, and this is the value that is used for the numerical results presented herein. As a comparison with the uniform mesh, for the case listed above that yielded $N_{uniform} = 33$,

the equivalent PMA using the graded scheme has $N_{graded} = 5$. This meshing technique yields a relatively large bandwidth PMA with minimal element count. For most situations, only 3 layers are needed, which gives good performance over a total bandwidth of $B \approx 2.9$ when $r = 2$, $n_e = 1$, and $\Gamma_0 = -60$dB.

Patch Antenna Example

The geometry for the patch antenna we investigate is shown in Fig. 1. This patch has been analyzed in detail J. T. Aberle [4], providing both method-of-moments (MoM) solutions and measurement data. The mesh we used for this geometry is shown in Fig. 2. The PMA is not shown, as it is automatically generated within the MicroWaveLab™ solver. The mesh in the model as shown is composed of tetrahedra. The PMA mesh is extruded from the outer spherical surface, and thus is composed of prism elements with a radial size variation given by Eqn. (8). There are a total of three layers of elements in the PMA. The first layer thickness, Δ_0, is chosen to be the average size (height) of all tetrahedra touching the PMA boundary. $\kappa'' = \kappa'$ is chosen using Eqn. (4), with $\Gamma_0 = -60$dB and $n_e = 1$, and $\max(k\cos\theta_i) = 2\pi f_{\max}\sqrt{\epsilon_r}/c_0$, where ϵ_r is the dielectric constant in the material adjacent to the PMA.

Results for the fundamental mode on this patch are shown in Fig. 3. For the relatively coarse mesh used in this example, the results are quite good, with the computed resonance of 2.41 GHz within 2% of the measured value. The problem was run on an HP9000/735-125, taking approximately 20 min. per frequency, and requiring 18MB RAM and 270MB of disk.

Conclusion

We have presented a method of meshing the PMA layer that achieves high bandwidth performance with minimal element count. The proposed meshing scheme uses an element layer thickness that increases geometrically within the PMA. Results are included for a circular patch that show good agreement with MoM and measured data.

References

[1] P. Simon and K. McInturff, private communication, Sept., 1994.

[2] D. M. Kingsland, Z. S. Sacks, and J. F. Lee, "Perfectly matched anisotropic absorbers for finite element applications in electromagnetics," ACES Conference Proceedings, March 20–25, 1995, pp. 490–497.

[3] J. P. Berenger, "A perfectly matched layer for the absorption of electromagnetic waves," J. Comp. Phys., Vol. 114, 1994, pp. 185–200.

[4] J. T. Aberle, *Analysis of Probe-Fed Circular Microstrip Antennas*, Ph.D. Dissertation, University of Massachusetts, Electrical and Computer Engineering Dept. (1989).

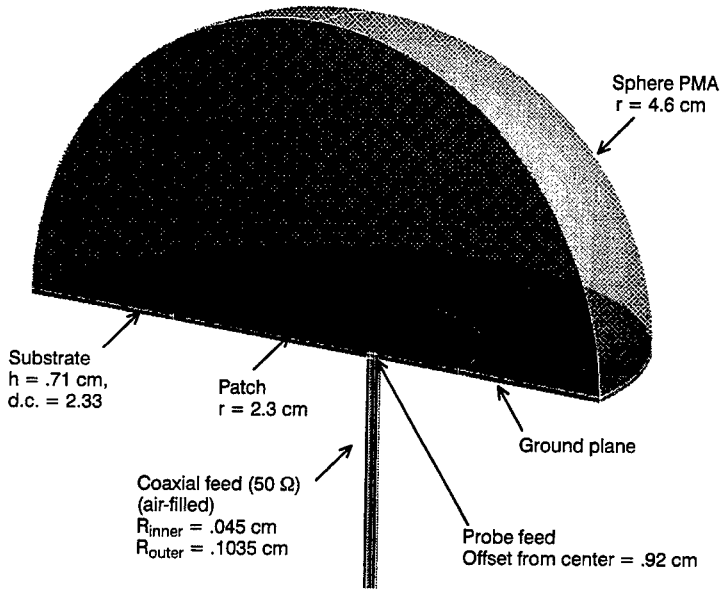

Figure 1: Circular patch problem geometry.

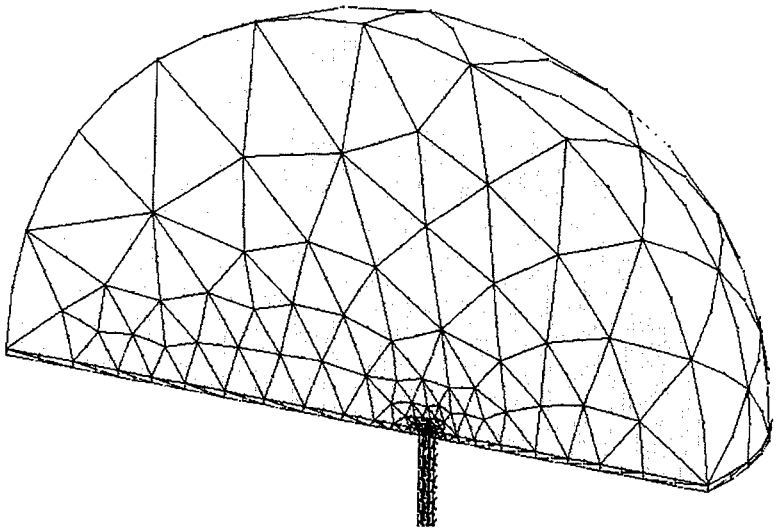

Figure 2: Mesh of circular patch. Some of mesh in coax is not shown. Visible mesh is composed entirely of tetrahedra, and the PMA (not shown) is composed of prisms.

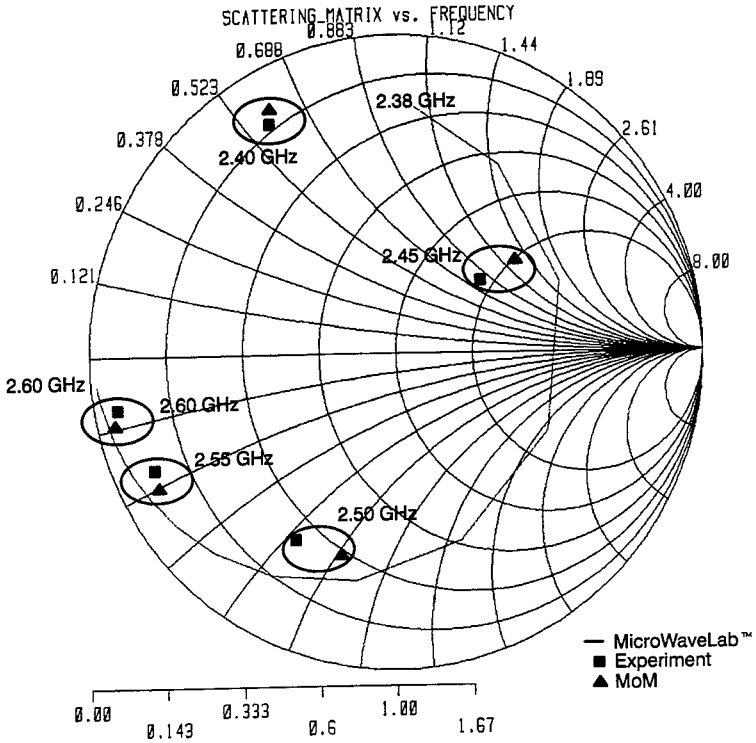

Figure 3: Smith chart of results for fine mesh. Length of coax has been de-embedded. Experimental and MoM data taken from Ref. [4].

A New Permanent-Magnet Synchronous Motor Design Configuration and Finite Element Analysis

Q. K. Zhang[1], N. Ida[1], Y. R. Qiu[2], Z. R. Jiang[3]

1. Department of Electrical Engineering, The University of Akron, Akron, OH 44325 USA
2. Department of Electrical Engineering, Xi'an Jiaotong University, Xi'an, Shaanxi 710049, P.R. CHINA
3. Northwest Polytechnique University, Xi'an, Shaanxi 710068, P.R. CHINA

Abstract: **This paper describes a configuration of a high-field permanent-magnet synchronous machine which may save expensive permanent-magnet materials. The airgap field was investigated and the steady state stator core loss was calculated by means of finite element analysis. Tests were made to verify the analyses.**

I. INTRODUCTION

Permanent-magnet AC machines are becoming increasingly significant for drive systems. There are many applications for which permanent-magnet machines have definite advantages over other machines. The simple replacement of an induction-machine rotor by one of the field-enhancing permanent-magnet designs will produce a machine which has a higher efficiency than that of the induction motor since its steady state operation is at synchronous speed thereby eliminating all steady state rotor conductor losses, and since the existence of the permanent magnets reduces the requirement of armature magnetizing current therefore eliminating associated stator copper loss [3]. However, such permanent-magnet machines generally have higher cost because they use expensive rare earth permanent-magnet materials. In addition, such a machine will produce a rotor field which is seriously distorted, and therefore will cause more stator core losses than induction motors.

This paper describes a configuration of a high-field machine which uses a combination of two different types of permanent-magnet materials in the design of its rotor. This machine will have lower cost compared to those currently used [1] because one of the two types of permanent-magnet materials has much lower market price than the commonly used rare earth materials. Finite element method was employed to analyze the magnetic field in the permanent-magnet machines. The stator back EMFs were calculated based on FFT analysis for airgap flux densities at no load. The steady state stator core losses considering both eddy and hysteresis effects were calculated at rated load. Experiments were made to compare with the computed results.

II. DESIGN CONSIDERATION

The configuration of the new design is shown in Fig. 1. The rectangular magnets are made from rare earth materials (e.g. Neodymium iron boron) which has high level of magnetic energy. The arc magnets consist of common magnetic materials such as iron oxide which have inferior magnetic properties. The amount of rare earth materials may be reduced due to the use of iron oxide which has much lower market price, thus the total cost of the permanent magnets will be decreased while airgap field distributions are maintained. The relative dimensions of the two types of magnets are not unique. An optimal combination of dimensions and distributions between the two may be obtained. The rotor cage winding is designed for self-starting use. The design of parameters of rotor cage windings not only affects the start performance of motors but also determines if motors can be pulled in synchronous operation.

III. ANALYSIS OF AIR-GAP FIELD

A 2-D finite element program was developed by the authors to analyze the steady-state performance of the machine. The representation of the permanent magnets made use of an equivalent surface current model. The nonlinearity of the laminated core was taken into account. Computations were made for the new model machines of the configurations shown in Fig. 1 (model 1) and a model machine (model 2) of a similar configuration described in [1]. The models are

obtained by the replacement of an induction-motor rotor by the two field-enhancing permanent-magnet configurations. The main data of the model machines are listed in table 1. Fig. 2 shows the computed airgap flux density wave for the model shown in Fig. 1 at no load. It is seen that the flux distribution is far from a desired sine wave, that is, it contains a series of high order harmonics other than the fundamental.

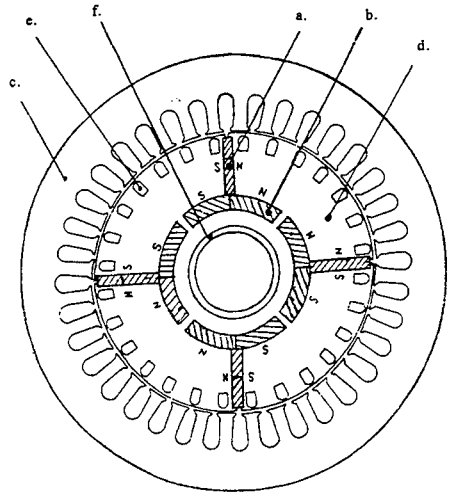

a. magnet NdFeB
b. magnet Fe_2O_3
c. stator lamination
d. rotor lamination
e. rotor cage bar
f. nonmagnetic material

Fig.1 Configuration of the PM synchronous machine

Table 2 shows the amplitudes of the fundamental, 3rd, and 5th order components of the airgap flux density for model 1 and model 2, respectively. These results were obtained from FFT analysis for the corresponding radial airgap flux density waves.

It may be seen that the new design produces a fundamental airgap flux density very close to that of the earlier design model 2[1], while the ratios of its 3rd and 5th harmonics to the fundamental are still acceptable.

Tests were made for model 2 to verify the analysis. One of the tests is on the phase back EMF which is induced in the stator windings due to the rotor magnetic fields. The phase back EMF considering the harmonic fields was calculated from

$$E_{ph} = \sqrt{\sum_{v=1}^{N_v} E_{phv}^2} \tag{1}$$

where:

N_v is the number of the harmonics

E_{phv} is the magnitude of the vth harmonic phase back EMF.

According to the winding theory of AC electric machines, E_{phv} is given by

$$E_{phv} = \frac{\sqrt{2}}{\pi} \omega N_{ph} k_{\omega v} l_e \tau_p B_{rv} \tag{2}$$

Where:

ω is the electrical angle speed of the rotor

N_{ph} is the number of series turns per phase
$k_{\omega v}$ is the harmonic winding factors
l_e is the effective axial stator length
τ_p is the pole pitch at midgap
B_{rv} is the magnitude of the vth radial airgap flux density harmonics. B_{rv} was obtained from FFT analysis for the airgap flux density distribution wave shown in Fig. 2.

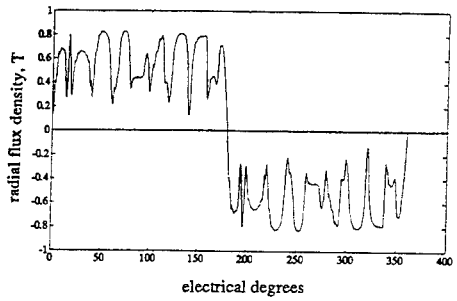

Fig.2 Airgap flux density distribution at no load

Table 1. Data of the model machines

number of phases	3	rated voltage	380 V (line-line
number of poles	4	rated power	15 kw
speed	1500 rpm	airgap length	0.5 mm
rotor diameter	189 mm	stator core length	165 mm
rotor magnets	Neodymium iron boron, iron oxide.		

Table 2. Radial airgap flux density harmonics

	B_{r1} (Gauss)	B_{r3} (Gauss)	B_{r5} (Gauss)
Model 1 (Fig.1)	7408	2789	1014
Model 2	7759	2721	1023

For the model of the configuration similar to that described in [1] (model 2), the measured phase back EMF is 239 V, the computed value from (1) and (2) is 234 V. This very good consistency between the two values verifies that the program developed for the analysis is correct. For the model shown in Fig. 1 (model 1) the computed phase back EMF from (1) and (2) is 225 V, the computed fundamental back EMF from (2) is 223 V.

The back EMF is an important design consideration. For a given stator supply voltage, the value of the back EMF determines whether a machine runs at leading or lagging power factor. The rated imposed supply voltage for the model machine is 220 V (phase value), so the machine will run at leading power factor. Fig. 3 shows the computed flux distribution for the model shown in Fig. 1 at no load. It may be seen that the flux due to high-energy magnets composes the main part of the airgap flux, as expected.

IV. CALCULATION OF STATOR CORE LOSS

The distorted rotor magnet field contains high order harmonics. The airgap harmonic fields penetrate into the stator

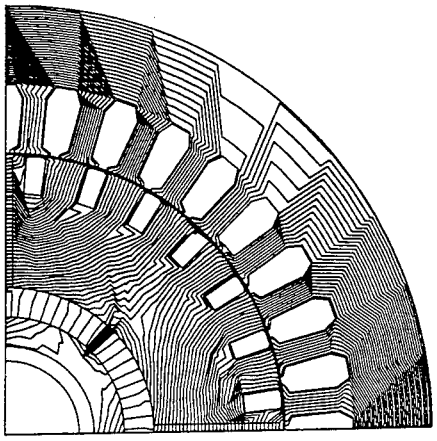

Fig.3 Flux distribution in one pole at no load

core thereby causing an increase of stator core losses including eddy and hysteresis losses. A very important design consideration is evaluation of the stator core losses caused by the distorted airgap fields. The quantitative calculation of the stator core losses requires detailed knowledge of the distribution of the fields in all parts of the stator core. In this paper, a 2-D finite element method was used to obtain the flux density distribution within one pole over a complete cycle of the stator current thus determining the stator core losses at rated load.

Steady state operation condition was assumed, and the harmonic currents in the stator windings were neglected. Thus, the rotor was considered to rotate at constant synchronous speed while the stator currents vary sinusoidally with a fundamental frequency of ω radians/second. The field distribution at several time instants in the complete fundamental current cycle is obtained by simultaneous rotation of the rotor grid and phase shift of the stator currents [3]. The stator grid was generated by repeating the finite element pattern over each phase zone so that each element in one phase zone will have the same shape and area as the element in the corresponding position in the other two phase zones.

Starting with a fixed rotor rotation position for which time instant $\omega t=0$ was assumed and an initial phase angle of one of three stator phase currents equals to θ_0 which was determined by the shaft load, one finite element solution in one pole was obtained for the particular rotor position and the instantaneous stator currents. Another finite element solution was obtained for the rotor position which was reached by rotating rotor $\pi/15$ electrical degrees from the previous position and for the stator currents at $\omega t=\pi/15$. Following this procedure, five finite element solutions were obtained for the time instants at $\omega t_i=(i-1)\pi/15$ (i=1,2,...5) and five equally spaced rotor rotation positions over zero to $\pi/3$ electrical degrees.

According to the symmetry of the three stator windings and currents, and the assumption of steady state operation, the field solutions corresponding to $\omega t=\pi/3+(i-1)\pi/15$ and $\omega t=2\pi/3+(i-1)\pi/15$ (i=1, ...5) can be obtained by shifting the field solutions at $\omega t=(i-1)\pi/15$ (i=1, ...5) among the phase zones.

In each stator core element the radial and circumferential flux density was obtained at the fifteen time instants $\omega t=(i-1)\pi/3+(j-1)\pi/15$ (i=1, ...3, j=1, ...5) in a half cycle. The fifteen symmetry counterparts in another half cycle can be easily obtained by simply taking opposite signs to those in the first half cycle. Fig. 4-6 show the radial and circumferential flux density waveforms in three different stator core elements. These waveforms were plotted using the thirty values above.

The element flux density time waveforms were approximately expressed as the sum of the fundamental and the high order harmonics as follows (for element k):

$$B_{rk}(t) = \sum_{v=1}^{N_v} B_{rkv} \cos(v\omega t + \theta_{rkv}) \tag{3}$$

$$B_{ck}(t) = \sum_{v=1}^{N_v} B_{ckv} \cos(v\omega t + \theta_{ckv}) \tag{4}$$

where:

N_v is the number of the harmonics

B_{rkv} and B_{ckv} are the magnitudes of the vth radial and circumferential flux density components in element k, respectively.

θ_{rkv} and θ_{ckv} are the initial phase angles of them, respectively. They were determined by the FFT analysis for the kth element's flux density waveforms similar to those shown in Fig. 4-6.

The kth element's flux density vector in the finite element solution plane is given by

$$\mathbf{B}_k(t) = B_{rk}(t)\mathbf{r}^0 + B_{ck}(t)\boldsymbol{\phi}^0 = \sum_{v=1}^{N_v} \mathbf{B}_{kv}(t) \tag{5}$$

where

$$\mathbf{B}_{kv}(t) = B_{rkv}\cos(v\omega t + \theta_{rkv})\mathbf{r}^0 + B_{ckv}\cos(v\omega t + \theta_{ckv})\boldsymbol{\phi}^0 \tag{6}$$

and the $\mathbf{r}^0$ and $\boldsymbol{\phi}^0$ are the unit vectors along the radial and circumferential directions, respectively.

The distorted rotation field in the solution plane given by (5) was decomposed into two translational components by projecting $\mathbf{B}_k(t)$ onto the major and minor axis associated with the ellipse determined by $\mathbf{B}_{k1}(t)$, the kth element's fundamental flux density vector. Fig. 7 shows the major and minor translational flux density waveforms associated with a stator tooth element.

The total core loss for element k was calculated as the sum of the loss associated with the two translational fields [3], [4]. The core loss associated with the major and minor axis element translational flux density was calculated using the expressions derived in [4], except that the eddy current loss factor and hysteresis loss factor for a fundamental component flux density used the data for the lamination material used in the model machines, and for standard frequency of 50Hz.

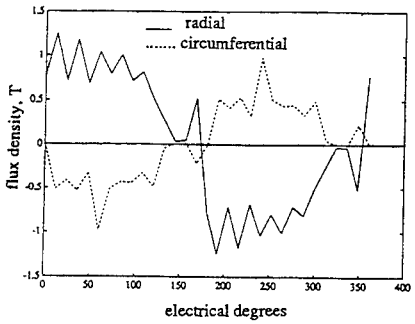

Fig.4 Flux density distribution in a stator tooth tip at rated load

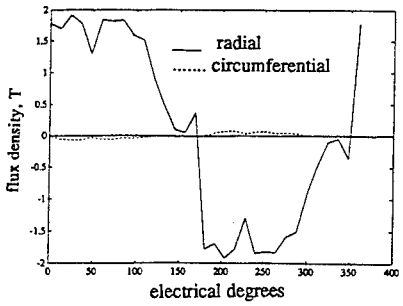

Fig.5 Flux density distribution in a stator tooth stem at rated load

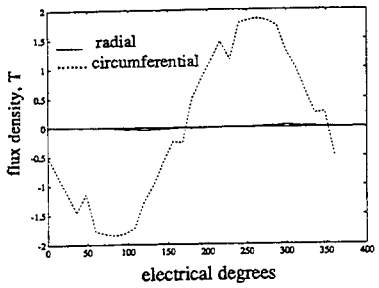

Fig.6 Flux density distribution in the stator yoke at rated load

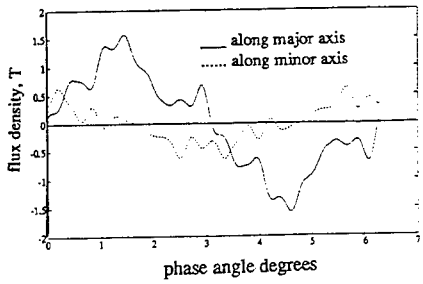

Fig.7 Translational flux density waveforms

The total stator core loss was obtained by adding the computed core loss in all stator elements. Table 3 lists the stator core losses calculated for the two model machines at rated load using this method. Experiments were made with the model machine (model 2). The measured stator core loss at rated load is also listed in Table 3. Good consistency is shown between the calculated and measured stator core losses. This shows that the calculation is effective and practical.

Table 3.

	Model 2	Model 1	Induction motor
Calculated (W)	424	413	—
Measured (W)	457	—	285

From the computed results the stator core losses of the two configurations differ very little. This may be attributed to their similar field distributions. Table 3 also lists the stator core loss of the prototype induction motor from which the two permanent-magnet synchronous machines were made. It seems that the induction motor has much lower stator core loss than the two synchronous motors, but the efficiency of the former is only about 88% while the efficiency of the latter may reach (92-93)%. This is because the field-enhancing permanent-magnet synchronous motors eliminate all steady state rotor conductor losses and some stator copper loss, as mentioned earlier.

V. CONCLUSION

A permanent-magnet synchronous machine configuration capable of saving expensive permanent-magnet materials has been developed with the aid of computer software and is shown to be an important design from the point of view that it can provide the required airgap field distribution and produces an acceptable stator core loss comparable to the earlier developed configurations.

REFERENCES

[1] F.A. Fouad, T.W. Nehl and N.A. Demerdash," Magnetic Field Modeling of Permanent-Magnet Type Electronically Operated Synchronous Machines Using Finite Elements ", IEEE Trans. PAS, vol. 100, Sept. 1981, pp 4125-4135.

[2] K.J. Binns and T.M. Wong, "Analysis and Performance of a High-Field Permanent-Magnet Synchronous Machine" IEE Proceedings, Vol. 131, B, 6, November 1984, pp.252-258.

[3] R. Schiferl and T.A. Lipo, "Core Loss in Buried Magnet Permanent Magnet Synchronous Motors", IEEE Transactions on Energy Conversion, Vol. 4, No. 2, June 1989, pp. 279-284.

[4] J.D. Lavers, P.P. Biringer and H. Hollitscher, "A Simple Method of Estimating the Minor Loop Hysteresis Loss in Thin Laminations", IEEE Transactions on Magnetics, Vol. 14, No. 5, September 1978, pp. 386-388.

[5] J.D. Lavers, P.P. Biringer and H. Hollitscher, "Estimation of Core Losses When the Flux Waveform Contains the Fundamental plus a Single Odd Harmonic Components", IEEE Transactions on Magnetics, Vol. 13, No. 5, September 1977, pp. 1128-1130.

Investigation of ABC Behavior in Axisymmetric Electrostatic Finite Element Analysis

A. Konrad and Lin Han
Department of Electrical and Computer Engineering, University of Toronto
Toronto, Ontario, CANADA M5S 3G4

Abstract—**Procedures using first and second order asymptotic boundary conditions (ABC-s) on circular and arbitrary boundaries are presented. Both exact and approximate ABC-s for arbitrary boundaries are derived. Different formulations of ABC are applied to the finite element solution of unbounded axisymmetric electrostatic problems. Results for circular and elliptic boundaries are obtained and compared with analytical solutions.**

I. Introduction

There are numerous procedures for solving open boundary problems by the finite element method (FEM). Absorbing and asymptotic boundary conditions are the most efficient methods and perhaps better choice for open boundary problems than other techniques. This is due to the fact that they preserve the sparsity of the finite element coefficient matrix, and do not introduce other numerical calculations except the line (surface for 3D) integration on the boundaries having absorbing or asymptotic boundary conditions.

Asymptotic and absorbing boundary conditions are derived based on cylindrical or spherical harmonic expansions, and need a circular (2D) or spherical (3D) truncated boundary. Only by using this kind of boundary, can asymptotic and absorbing boundary conditions be imposed on the system of equations produced by FEM. When solving problems with large aspect ratios, it would be useful to be able to impose ABC on an arbitrary boundary because this can save computer memory and make it easier to generate a finite element mesh.

In this paper, exact and approximate formulations for first and second order ABC-s on circular and arbitrary boundaries are presented. The behavior of these ABC-s are investigated by solving some axisymmetric electrostatic problems with truncated circular and elliptic boundaries.

II. Theory And Formulations

A. ABC on a Circular Truncated Boundary

In the spherical coordinate system (r,θ,ϕ), the m-th order operator for ABC is given by [1]

$$B_m = \prod_{n=1}^{m} \left(\frac{\partial}{\partial r} + \frac{2n-1}{r}\right) = O\left(\frac{1}{r^{2m+1}}\right) \tag{1}$$

For axisymmetric problems in the cylindrical coordinate system (ρ, ϕ, z), the potential Φ is independent of the angle ϕ. The first and second order ABC-s are obtained by substituting m=1, 2 into (1) [2], [3]

$$\frac{\partial \Phi}{\partial r} + \frac{\Phi}{r} = 0 \tag{2}$$

$$\frac{\partial \Phi}{\partial r} + \frac{\Phi}{r} - \frac{\cot\theta \partial \Phi}{2r \partial \theta} - \frac{1}{2r}\frac{\partial^2 \Phi}{\partial \theta^2} = 0 \tag{3}$$

where r denotes

$$r = \sqrt{\rho^2 + z^2} \tag{4}$$

B. ABC on an Arbitrary Truncated Boundary

If the positive directions of θ, n and r for an arbitrary boundary are as shown in Fig. 1, then using vector algebra we can express the normal and tangential derivatives of Φ as follows:

$$\frac{\partial \Phi}{\partial n} = \frac{\partial \Phi}{\partial r}\cos\alpha - \frac{1}{r}\frac{\partial \Phi}{\partial \theta}\sin\alpha \tag{5}$$

$$\pm\frac{\partial \Phi}{\partial t} = \frac{\partial \Phi}{\partial r}\sin\alpha + \frac{1}{r}\frac{\partial \Phi}{\partial \theta}\cos\alpha \tag{6}$$

where the $\pm$ corresponds to two cases. Case 1: the positive direction of t is as shown in Fig. 1; Case 2: the positive direction of t is the opposite of that shown in Fig. 1. After eliminating the second term in (5) and (6), we have

$$\frac{1}{\sin\alpha}\frac{\partial \Phi}{\partial n} \pm \frac{1}{\cos\alpha}\frac{\partial \Phi}{\partial t} = \frac{\partial \Phi}{\partial r}(\tan\alpha + \cot\alpha) \tag{7}$$

Considering the ABC-s given by (2) and (3), we obtain expressions for the first and second order ABC-s on the arbitrary boundary as (8) and (9), respectively.

$$\frac{\partial \Phi}{\partial n} + \frac{1}{r\cos\alpha}\Phi \pm \tan\alpha\frac{\partial \Phi}{\partial t} = 0 \tag{8}$$

$$\frac{\partial \Phi}{\partial n} + \frac{1}{\cos\alpha}\left(\frac{\Phi}{r} - \frac{\cot\theta}{2r}\frac{\partial \Phi}{\partial \theta} - \frac{1}{2r}\frac{\partial^2 \Phi}{\partial \theta^2}\right) \pm \tan\alpha\frac{\partial \Phi}{\partial t} = 0 \tag{9}$$

The sign of the third term in (8) and (9) depends on the assumed positive direction of t.

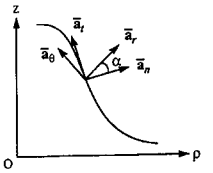

Fig. 1. Arbitrary boundary type 1

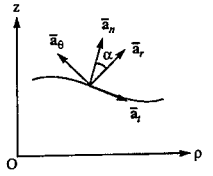

Fig. 2. Arbitrary boundary type 2

If the positive directions of θ, n and r for an arbitrary boundary are as shown in Fig. 2, then using a similar derivation as above, we obtain again (8) and (9) as the ABC-s on the arbitrary boundary. As before, the sign of the third term in (8) and (9) corresponds to two cases. Case 1: the positive direction of t is as shown in Fig. 2; Case 2: the positive direction of t is the opposite of that shown in Fig. 2.

C. Approximate ABC Formulation

In the local orthogonal coordinate system $(\bar{a}_r, \bar{a}_\theta)$ shown in Fig. 1, we can write the gradient of Φ as

$$grad\Phi = \frac{\partial \Phi}{\partial r}\bar{a}_r + \frac{1}{r}\frac{\partial \Phi}{\partial \theta}\bar{a}_\theta \tag{10}$$

If r is sufficiently large, then the second term in (10) can be neglected and we have

$$grad\Phi \equiv \frac{\partial \Phi}{\partial r}\bar{a}_r \tag{11}$$

In any local orthogonal coordinate system such as $(\bar{a}_n, \bar{a}_t)$ shown in Fig. 1, the gradient of Φ can be expressed as

$$grad\Phi = \frac{\partial \Phi}{\partial n}\bar{a}_n + \frac{\partial \Phi}{\partial t}\bar{a}_t \tag{12}$$

Then, from (11) and (12) we have

$$\frac{\partial \Phi}{\partial r}\bar{a}_r \cong \frac{\partial \Phi}{\partial n}\bar{a}_n + \frac{\partial \Phi}{\partial t}\bar{a}_t \tag{13}$$

which yields

$$\frac{\partial \Phi}{\partial n} \cong \frac{\partial \Phi}{\partial r}\bar{a}_r \bullet \bar{a}_n \tag{14}$$

From (14), we can see that the normal derivative of Φ on the arbitrary boundary is the projection of $\partial\Phi/\partial r$ along the normal direction to the boundary (Figs.1 and 2). By using (2) and (3), we obtain the first and second order approximate ABC-s on the arbitrary boundary as (15) and (16), respectively:

$$\frac{\partial \Phi}{\partial n} \cong -\frac{\Phi}{r}\cos\alpha \tag{15}$$

$$\frac{\partial \Phi}{\partial n} \cong \left(-\frac{\Phi}{r} + \frac{\cot\theta\,\partial\Phi}{2r\,\partial\theta} + \frac{1}{2r}\frac{\partial^2\Phi}{\partial\theta^2}\right)\cos\alpha \tag{16}$$

In the next section, the FEM implementation of the above ABC-s will be presented.

III. Variational FEM Implementation

A. General Neumann Boundary Condition

For 2D axisymmetric Laplace's equation problems, the functional corresponding to the general Neumann boundary condition is given by [4]

$$F_2(\Phi) = \int_L \varepsilon\left(\frac{1}{2}f_1\Phi^2 - f_2\Phi\right)\rho\,dl \tag{17}$$

where ε is the permittivity of the material and L is the boundary with the general Neumann boundary condition. The latter can be described as follows

$$\frac{\partial \Phi}{\partial n} + f_1\Phi = f_2 \tag{18}$$

where f_1 and f_2 are coefficients which may be constant, a function of position, or an operator of Φ. If f_1 is an operator of Φ and is *self-adjoint*, the functional corresponding to (18) is given by

$$F_2(\Phi) = \int_L \varepsilon\left(\frac{1}{2}\Phi f_1\Phi - f_2\Phi\right)\rho\,dl \tag{19}$$

From (2) to (16), we can see that all ABC-s include an operator of Φ. It can be shown that the operators appearing in (8) and (9) are not self-adjoint because the operator $\frac{\partial}{\partial t}$ is not self-adjoint. Consequently, results obtained with (8) and (9) are not satisfactory. This will be shown in the next section.

B. Asymptotic Boundary Condition

It is clear from (2), that when we choose a *circular* (2D) boundary, we can use (17) directly because (2) can be interpreted as a general Neumann boundary condition. As for (3), we can interpret it with $f_2 = 0$, then use (19). The functionals corresponding to the first and second order ABC-s on circular boundaries are given by (20) and (21):

$$F_2(\Phi) = \frac{1}{2}\int_L \varepsilon\{\Phi^2\}\frac{\rho}{r}dl \tag{20}$$

$$F_2(\Phi) = \frac{1}{2}\int_L \varepsilon\{\Phi^2 + \frac{1}{2}(\frac{\partial\Phi}{\partial\theta})^2\}\frac{\rho}{r}dl \tag{21}$$

By discretization, we obtain an expression for the unknown Φ in a finite element, say element e, in following form

$$\tilde{\Phi}^e = \sum_{j=1}^{n} N_j^e \Phi_j^e = [N^e]^T[\Phi^e] = [\Phi^e]^T[N^e] \tag{22}$$

where n is the number of nodes in the element, Φ_j^e is the value of Φ at node j of element e, and N_j^e is an interpolation function of element e. The superscript T denotes transpose. Substituting (22) into (20) and (21), then differentiating the resulting functional, we obtain

$$\frac{\partial F_2^e}{\partial \tilde{\Phi}^e} = \int_{L^e} \varepsilon\{[N^e][N^e]^T\}\frac{\rho}{r}dl\,[\Phi^e] \tag{23}$$

$$\frac{\partial F_2^e}{\partial \tilde{\Phi}^e} = \int_{L^e} \varepsilon\{[N^e][N^e]^T + \frac{1}{2}\left[\frac{\partial N^e}{\partial\theta}\right]\left[\frac{\partial N^e}{\partial\theta}\right]^T\}\frac{\rho}{r}dl\,[\Phi^e] \tag{24}$$

where, F_2^e is the functional for element e, and L^e denotes the edges of element e with ABC. From (23) and (24), we obtain the local coefficient matrix associated with the first and the second order ABC-s for element e as (25) and (26), respectively:

$$[K_{ABC}^e] = \int_{L^e} \varepsilon\{[N^e][N^e]^T\}\frac{\rho}{r}dl \tag{25}$$

$$[K_{ABC}^e] = \int_{L^e} \varepsilon\{[N^e][N^e]^T + \frac{1}{2}\left[\frac{\partial N^e}{\partial\theta}\right]\left[\frac{\partial N^e}{\partial\theta}\right]^T\}\frac{\rho}{r}dl \tag{26}$$

$[K_{ABC}^e]$ is the contribution to the global finite element coefficient matrix by element e due to an ABC on one or more of its edges.

Using a similar procedure, we can obtain the local coefficient matrices associated with the exact arbitrary ABC-s (8) and (9) as (27) and (28), respectively, and the approximate arbitrary ABC-s (15) and (16) as (29) and (30), respectively:

$$[K_{ABC}^e] = \int_{L^e} \varepsilon\{\frac{1}{r\cos\alpha}[N^e][N^e]^T \pm \frac{\tan\alpha}{2}([N^e]\left[\frac{\partial N^e}{\partial t}\right]^T + \left[\frac{\partial N^e}{\partial t}\right][N^e]^T)\}\rho dl \tag{27}$$

$$[K_{ABC}^e] = \int_{L^e} \varepsilon\{\frac{1}{r\cos\alpha}\left([N^e][N^e]^T + \frac{1}{2}\left[\frac{\partial N^e}{\partial\theta}\right]\left[\frac{\partial N^e}{\partial\theta}\right]^T\right) \pm \frac{\tan\alpha}{2}[N^e]\left[\frac{\partial N^e}{\partial t}\right]^T + \left[\frac{\partial N^e}{\partial t}\right][N^e]^T\}\rho dl \tag{28}$$

$$[K_{ABC}^e] = \int_{L^e} \varepsilon\{[N^e][N^e]^T\}\cos\alpha\frac{\rho}{r}dl \tag{29}$$

$$[K_{ABC}^e] = \int_{L^e} \varepsilon\{[N^e][N^e]^T + \frac{1}{2}\left[\frac{\partial N^e}{\partial\theta}\right]\left[\frac{\partial N^e}{\partial\theta}\right]^T\}\frac{\rho}{r}dl \tag{30}$$

It should be noted that the derivation of (27) and (28) is based on the assumption that (8) and (9) can be used in the form of (19).

IV. RESULTS

In order to test the above formulations, we use them to solve the following problems having ABC-s on circular and elliptic boundaries.

A. Half Sphere Above Ground

The half sphere's potential is V_0=1V, its radius is R_0=0.5m. The analytical solution of the potential along the z-axis is given by [3]:

$$\Phi(z) = V_0 - \frac{(z^2 - R_0^2)}{z\sqrt{z^2 + R_0^2}} \tag{31}$$

A small gap (0.01m) with a homogeneous Neumann boundary condition separates the ground (z=0) from the sphere.

(1) Solution with ABC for Circular Boundary

When we choose the circular truncated boundary (r=1.0m) and use (25) and (26), the equipotential lines are as shown in Fig. 3. The potential distributions along the z-axis compared with the analytical solution are shown in Fig. 4. Both results in Fig. 3 and Fig. 4 are computed using first order elements. The total number of nodes and elements are 121 and 100, respectively. Table 1 shows the error for different orders of element and ABC.

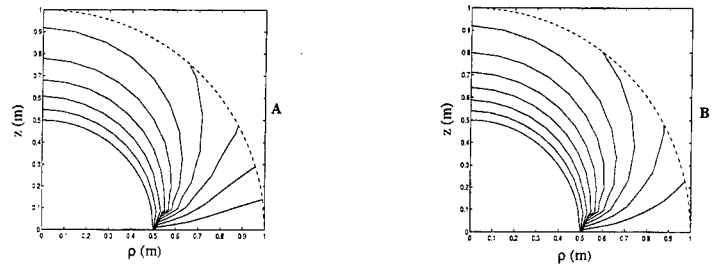

Fig. 3. Equipotential lines, 1st order ABC (A), 2nd order ABC (B)

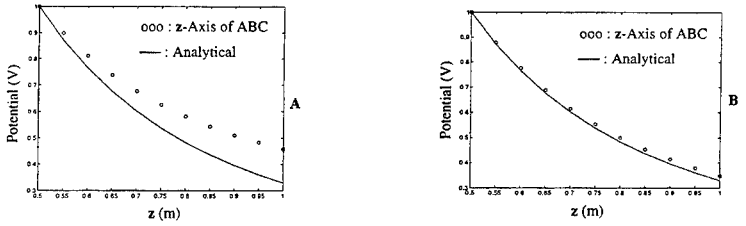

Fig. 4. Potential along the z axis, 1st order ABC (A), 2nd order ABC (B)

(2) Solution with Exact ABC for Arbitrary Boundary

For different order ABC-s, the equipotential lines are shown in Fig. 5. The potential distributions along the z-axis compared with the analytical solution are shown in Fig. 6. Table 2 shows the error corresponding to different orders of ABC.

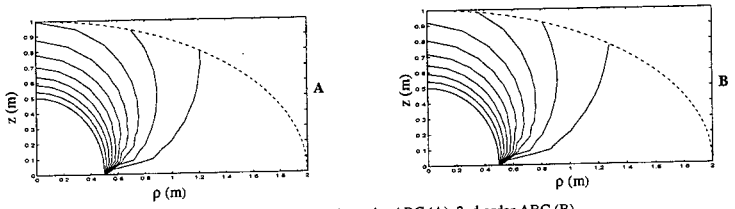

Fig. 5. Equipotential lines, 1st order ABC (A), 2nd order ABC (B)

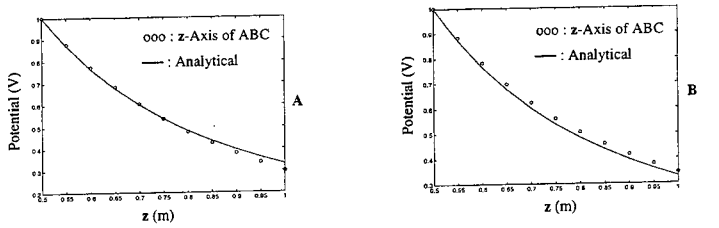

Fig. 6. Potential along the z axis, 1st order ABC (A), 2nd order ABC (B)

Circular Boundary (R=1.0)	Average Error (%)	Maximum Error (%)
1st Order Element and 1st Order ABC (121 Nodes, 100 Elements)	17.68	39.2
1st Order Element and 2nd Order ABC (121 Nodes, 100 Elements)	2.85	5.61
2nd Order Element and 1st Order ABC (441 Nodes, 100 Elements)	15.4	30.6
2nd Order Element and 2nd Order ABC (441 Nodes, 100 Elements)	0.88	2.34

Table 1: Error for the different orders of element and ABC

Elliptic Boundary (Rx=2.0, Ry=1.0)	Average Error (%)	Maximum Error (%)
1st Order Element and 1st Order ABC (121 Nodes, 100 Elements)	2.44	9.68
1st Order Element and 2nd Order ABC (121 Nodes, 100 Elements)	3.56	5.14

Table 2: Error for the different orders of element and ABC

(3) Solution with Approximate ABC for Arbitrary Boundary

For different order ABC-s, the equipotential lines are shown in Fig. 7. The potential distributions along the z-axis compared with the analytical solution are shown in Fig. 8. Table 3 shows the error corresponding to different orders of ABC.

Elliptic Boundary (Rx=2.0, Ry=1.0)	Average Error (%)	Maximum Error (%)
1st Order Element and 1st Order ABC (121 Nodes, 100 Elements)	13.57	31.67
1st Order Element and 2nd Order ABC (121 Nodes, 100 Elements)	2.44	9.68

Table 3: Error for the different orders of element and ABC

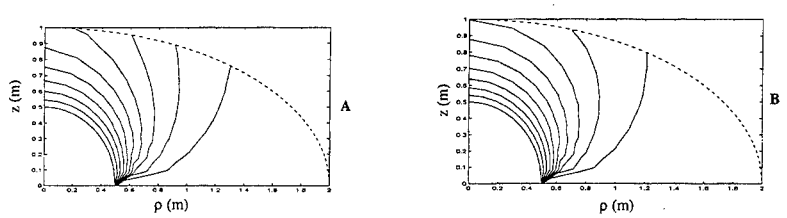

Fig. 7. Equipotential lines, 1st order ABC (A), 2nd order ABC (B)

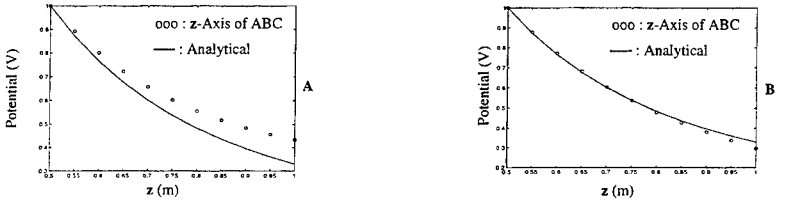

Fig. 8. Potential along the z axis, 1st order ABC (A), 2nd order ABC (B)

B. Insulator With Large Aspect Ratio

The meshes for circular and non-circular boundaries are shown in Fig. 9. The comparison of equipotential lines of ABC and Dirichlet boundary condition are shown in Fig. 10. The result with Dirichlet boundary condition is obtained by choosing a truncated circular Dirichlet boundary at R=59.984m. The results with ABC are obtained by using (26) and (28). From Fig. 10, we can see that for this kind of problem with large aspect ratio, using arbitrary boundary with ABC can save computer memory, although its accuracy is not as good as the circular boundary with ABC, the result near the object is still almost the same as the result with a Dirichlet boundary condition very far away.

CONCLUSIONS

We can draw the following conclusions from the numerical results:

A. The 2nd order ABC on a circular boundary combined with 2nd order elements will yield very satisfactory results compared with analytic solutions and it is the recommended procedure to treat open boundary problems.

B. ABC on an arbitrary boundary is less accurate compared with ABC on a circular boundary but its near field accuracy is still satisfactory; It saves more computer memory than the circular boundary with ABC and is more flexible for the generation of FEM mesh.

C. When the arbitrary boundary is far enough, the simpler approximate ABC may be used without significant loss of accuracy compared with the exact ABC.

REFERENCES

[1] A. Khebir, *Asymptotic and Absorbing Boundary Conditions for Finite Element Analysis of Digital Circuit and Scattering Problems*, Ph. D. Thesis, University of Illinois at Urbana-Champaign, 1990.

[2] J-F. Lee and R. Mittra, "Mesh truncation in the finite element analysis for static and magnetic fields," *The MSC 1991 World Users's Conference*, March 1991, E/EAD Paper# 66. †

[3] J. R. Brauer, S. M. Schaefer and R. Mittra, "Simulation of static open boundary problems in MSC/EMAS," *The MSC 1991 World Users's Conference*, March 1991, E/EAD Paper# 69. †

[4] Jianming Jin, *The Finite Element Method In Electromagnetics*, New York: Wiley, 1993, Ch. 4.

†: Technical paper published by The MacNeal-Schwendler Corporation, 9076 North Deerbrook Trail, Milwaukee, Wisconsin 53223-243

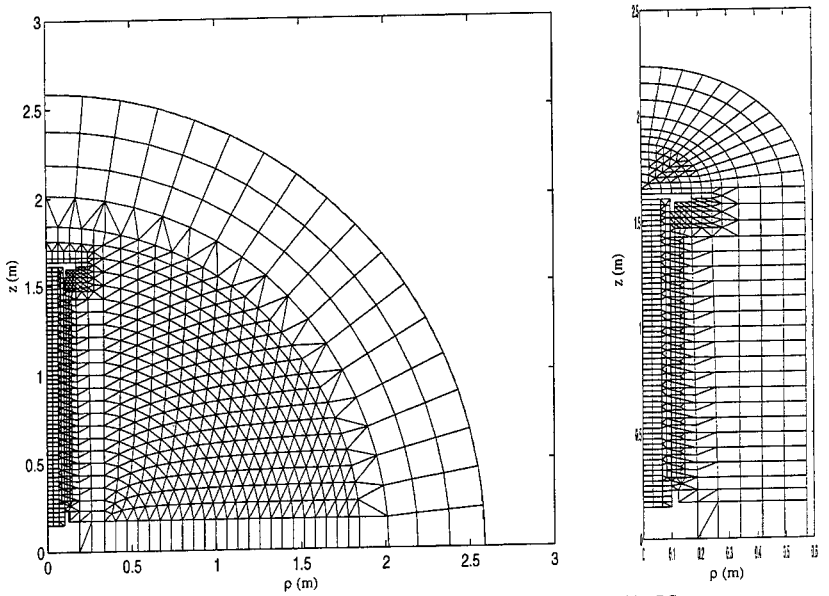

Fig. 9. Two Meshes of the Insulator Model for FEM Analysis with ABC

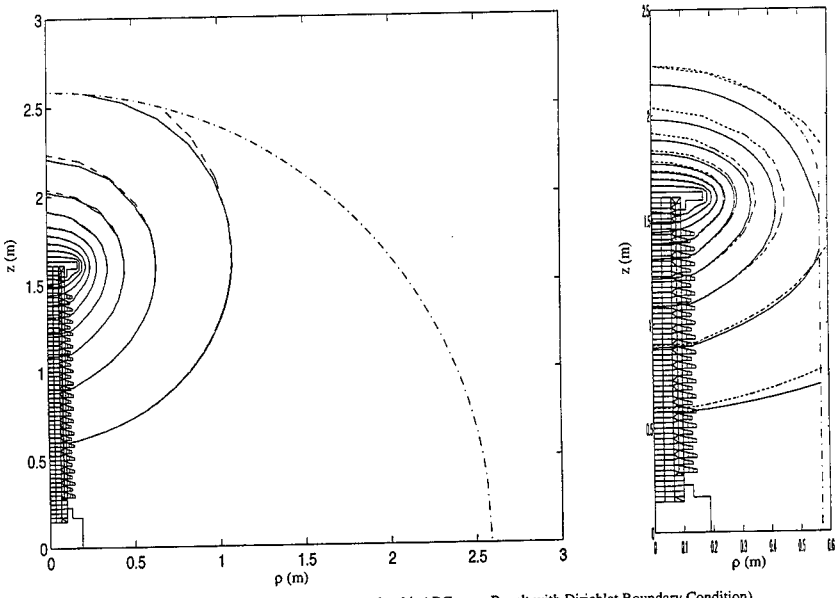

Fig. 10.Equipotential lines (⟵ : Result with ABC; - - -: Result with Dirichlet Boundary Condition)

AN EFFICIENT SCHEME FOR FINITE ELEMENT ANALYSIS IN THE FREQUENCY DOMAIN

M. Kuzuoglu and R. Mittra*
Electromagnetic Communication Laboratory
University of Illinois at Urbana-Champaign
1406 W. Green St., Urbana, IL 61801

J. Brauer and G. Lizalek
The MacNeal Schwendler Corporation
4300 West Brown Deer Road
Milwaukee, WI 53223

I. Introduction

It is well known that an FEM formulation of electromagnetic boundary value problems over a closed spatial domain, yields a matrix equation of the form

$$\left[A_0 + A_1\omega + A_2\omega^2\right]x = f \tag{1}$$

where the $n \times n$ matrices A_0, A_1 and A_2 have complex entries (n is the number of unknowns), ω is the angular frequency, x is the $n \times 1$ vector whose entries represent the unknown field components at particular nodes and f is the $n \times 1$ excitation vector. Equation (1) is typically solved for the unknown vector x, by using a matrix solver that takes advantage of the sparsity of the three matrices appearing in (1).

Typically, it is desirable to obtain the unknown vector $x(\omega)$ over a band of frequencies, i.e., for ω in a certain interval $I = [\omega_l, \omega_h]$, where ω_l and ω_h are the lowest and highest frequencies in the interval of interest. The most straightforward way to deal with this problem is to define a set of frequencies $\{\omega_i\}_{i=1}^{N}$ such that $\omega_l \le \omega_1 < \cdots < \omega_N \le \omega_h$, and solve (1) at these frequencies to yield $x(\omega_i)$, $i = 1,2,\ldots,N$. The value of $x(\omega)$ at any arbitrary frequency $\omega \in I$ can be determined by using a suitable interpolation method, such as piecewise linear, piecewise quadratic or spline approximations. However, the interpolation technique requires that (1) should be solved N times, and this can be quite time-consuming owing to the fact that N has to be chosen sufficiently large to reduce the approximation error. In the next section, an alternative method based on a power series expansion will be presented and it will be shown how the solution vector $x(\omega)$ can be derived over the desired frequency band by solving (1) at a relatively small number of frequencies, viz., ω_i, $i = 1,2,\ldots,M$, where M is much smaller than N.

II. Power Series Representation of the Solution of the FEM Equation

Consider an arbitrary frequency ω_0 in $I = [\omega_l, \omega_h]$. Let the solution vector $x(\omega)$ be expressed in terms of a power series expansion about ω_0 as follows:

* Supported by the Turkish Scientific and Technical Research Council as a NATO B2 Scholar

$$x(\omega) = x_0 + x_1(\omega - \omega_0) + x_2(\omega - \omega_0)^2 + \cdots \tag{2}$$

The radius of convergence of this series is finite, and is determined by the singularities of $x(s)$ in the complex frequency plane $s = \sigma + j\omega$. For instance, if the closest singularity to $j\omega_0$ is $s^* = \sigma^* + j\omega^*$, then the radius of convergence of the series is $R = |s^* - j\omega_0|$. It is not possible, in general, to locate *a priori* the singularities of $x(s)$ for a particular problem and, hence, it is quite difficult to determine the radius of convergence of the power series in (2) for an arbitrary value of ω. Nonetheless, as we show below, it is possible to derive an upper bound for the range $u = |\omega - \omega_0|$ such that (2) is convergent.

Let the system matrix in (1) be denoted by $A(\omega)$ given by

$$A(\omega) = A_0 + A_1\omega + A_2\omega^2 \tag{3}$$

and let $A(\omega)$ be also expressed in the form

$$A(\omega) = \overline{A}_0 + \overline{A}_1(\omega - \omega_0) + \overline{A}_2(\omega - \omega_0)^2 \tag{4}$$

Here, once again, $\overline{A}_0$, $\overline{A}_1$ and $\overline{A}_2$ are $n \times n$ complex matrices, which can be derived by equating (3) and (4) to get

$$\overline{A}_0 = A_0 + A_1\omega_0 + A_2\omega_0^2 \tag{5}$$

$$\overline{A}_1 = A_1 + 2A_2\omega_0. \tag{6}$$

$$\overline{A}_2 = A_2 \tag{7}$$

It is important to note that the new matrices $\overline{A}_0$, $\overline{A}_1$ and $\overline{A}_2$ are obtained via simple matrix additions and scalar multiplications of the original ones.

Equation (1) can now be replaced by

$$[\overline{A}_0 + \overline{A}_1(\omega - \omega_0) + \overline{A}_2(\omega - \omega_0)^2]x = f \tag{8}$$

To analyze the conditions for the existence of a convergent power series representation of the solution of equation (8), we first multiply both sides by $\overline{A}_0^{-1}$ to yield

$$[I + \overline{A}_0^{-1}\overline{A}_1(\omega - \omega_0) + \overline{A}_0^{-1}\overline{A}_2(\omega - \omega_0)^2]x = \overline{A}_0^{-1}f \tag{9a}$$

$$\tilde{A}(\omega)x = \tilde{A}_0^{-1}f \tag{9b}$$

A power series representation of x in terms of the powers of $(\omega - \omega_0)$ can now be obtained by considering the power series expansion of the inverse of the matrix $\tilde{A}(\omega)$. given in (9b). At this point, we observe that for any matrix A we can write [1]

$$(I+A)^{-1} = \sum_{j=1}^{\infty} (-1)^j A^j \qquad \text{provided that} \qquad \sigma(A) < 1 \tag{10}$$

where $\sigma(A)$ represents the spectral radius of the matrix A, defined as $\sigma(A) = \max_i |\lambda_i|$, λ_i denoting the i*th* eigenvalue of A. Using this result, we deduce that

$$\tilde{A}^{-1}(\omega) = \sum_{j=1}^{\infty} (-1)^j [\overline{A}_0^{-1}\overline{A}_1(\omega-\omega_0) + \overline{A}_0^{-1}\overline{A}_2(\omega-\omega_0)^2]^j \tag{11}$$

provided that

$$\sigma\{\overline{A}_0^{-1}\overline{A}_1(\omega-\omega_0) + \overline{A}_0^{-1}\overline{A}_2(\omega-\omega_0)^2\} < 1 \tag{12}$$

For an arbitrary matrix A, $\sigma(A) \le \|A\|$, where $\|.\|$ denotes any matrix norm. Hence, if $\|A\| < c$, where c is an arbitrary constant, then $\sigma(A)$ is automatically less than c. Therefore, (13) can be replaced by the inequality

$$\left\|\overline{A}_0^{-1}\overline{A}_1(\omega-\omega_0) + \overline{A}_0^{-1}\overline{A}_2(\omega-\omega_0)^2\right\| < 1 \tag{13}$$

Using the triangle inequality and letting $u = |\omega - \omega_0|$, we can write

$$\left\|\overline{A}_0^{-1}\overline{A}_1(\omega-\omega_0) + \overline{A}_0^{-1}\overline{A}_2(\omega-\omega_0)^2\right\| \le \left\|\overline{A}_0^{-1}\right\|\left\|\overline{A}_1\right\|u + \left\|\overline{A}_0^{-1}\right\|\left\|\overline{A}_2\right\|u^2 < 1 \tag{14}$$

This, in turn, leads us to the inequality

$$\left\|\overline{A}_2\right\|u^2 + \left\|\overline{A}_1\right\|u - \frac{1}{\left\|\overline{A}_0^{-1}\right\|} < 0 \tag{15}$$

where we should recognize that $u > 0$.

The quadratic function $\tilde{f}(u) = \left\|\overline{A}_2\right\|u^2 + \left\|\overline{A}_1\right\|u - \frac{1}{\left\|\overline{A}_0^{-1}\right\|}$ has the roots:

$$u_{1,2} = \frac{-\left\|\overline{A}_1\right\| \pm \sqrt{\left\|\overline{A}_1\right\|^2 + 4\dfrac{\left\|\overline{A}_2\right\|}{\left\|\overline{A}_0^{-1}\right\|}}}{2\left\|\overline{A}_2\right\|} \tag{16}$$

It is clear that one of the roots is strictly positive, provided that both $\left\|\overline{A}_0^{-1}\right\|$ and $\left\|\overline{A}_2\right\|$ are different from zero. If $u \in (0, u^*)$, where $u^* = \dfrac{-\left\|\overline{A}_1\right\| + \sqrt{\left\|\overline{A}_1\right\|^2 + 4\dfrac{\left\|\overline{A}_2\right\|}{\left\|\overline{A}_0^{-1}\right\|}}}{2\left\|\overline{A}_2\right\|}$, the conditions $u > 0$ and $\tilde{f}(u) < 0$ are both

satisfied and the power series (11) is convergent. For any $u \in (0,u^*)$, we can evaluate the coefficients in the power series of $x(\omega)$ by following the procedure given below. We begin with the expression

$$\begin{aligned} x(\omega) &= x_0 + x_1(\omega-\omega_0) + x_2(\omega-\omega_0)^2 + \cdots \\ &= [I - \overline{A}_0^{-1}\overline{A}_1(\omega-\omega_0) - \overline{A}_0^{-1}\overline{A}_2(\omega-\omega_0)^2 + \left(\overline{A}_0^{-1}\overline{A}_1\right)^2(\omega-\omega_0)^2 \\ &+ \overline{A}_0^{-1}\overline{A}_1\overline{A}_0^{-1}\overline{A}_2(\omega-\omega_0)^3 + \overline{A}_0^{-1}\overline{A}_2\overline{A}_0^{-1}\overline{A}_1(\omega-\omega_0)^3 \\ &+ \left(\overline{A}_0^{-1}\overline{A}_2\right)^2(\omega-\omega_0)^4 + \cdots]\overline{A}_0^{-1}[f_0 + f_1(\omega-\omega_0) + f_2(\omega-\omega_0)^2 + \cdots] \end{aligned} \tag{17}$$

where $f_0 + f_1(\omega-\omega_0) + f_2(\omega-\omega_0)^2 + \cdots$ denotes the power series expansion of the excitation vector f at $\omega = \omega_0$. Next, we equate both sides of (17), term by term, to obtain the following expressions of first three coefficients of $x(\omega)$:

$$x_0 = \overline{A}_0^{-1} f_0 \tag{18}$$

$$x_1 = \overline{A}_0^{-1} f_1 - \overline{A}_0^{-1}\overline{A}_1\overline{A}_0^{-1} f_0 = \overline{A}_0^{-1} f_1 - \overline{A}_0^{-1}\overline{A}_1 x_0 \tag{19}$$

$$\begin{aligned} x_2 &= \overline{A}_0^{-1} f_2 - \overline{A}_0^{-1}\overline{A}_1\left[\overline{A}_0^{-1} f_1 - \overline{A}_0^{-1}\overline{A}_1 x_0\right] - \overline{A}_0^{-1}\overline{A}_2 x_0 \\ &= \overline{A}_0^{-1} f_2 - \overline{A}_0^{-1}\overline{A}_1 x_1 - \overline{A}_0^{-1}\overline{A}_2 x_0 \end{aligned} \tag{20}$$

The higher order coefficients can be evaluated in a similar manner. It is important to note that only a single inverse, viz., $\overline{A}_0^{-1}$, is needed in the iteration procedure, and if an LU decomposition of $\overline{A}_0$ has already been carried out, successive applications of $\overline{A}_0^{-1}$ would be little time-consuming. In addition, the LU decomposition also enables us to estimate the condition number of $\overline{A}_0$, defined by $\kappa(\overline{A}_0) = \left\|\overline{A}_0\right\|\left\|\overline{A}_0^{-1}\right\|$ (see appendix A) and, obviously, this equality may be used to estimate the norm of $\overline{A}_0^{-1}$.

Finally, let us discuss how this power series representation can be used to approximate $x(\omega)$ in a given interval $I = [\omega_l, \omega_h]$. The procedure can be outlined as follows:

Step 0: Choose an arbitrary ω_0 in the interval $I = [\omega_l, \omega_h]$ and form the matrices $\overline{A}_0$, $\overline{A}_1$ and $\overline{A}_2$ (equations 5-7). It is important to notice that these matrices depend on ω_0. Choose any matrix norm $\|\cdot\|$ and find the interval for $u = |\omega - \omega_0|$ as $(0,u^*)$ where $u^* = \dfrac{-\left\|\overline{A}_1\right\| + \sqrt{\left\|\overline{A}_1\right\|^2 + 4\dfrac{\left\|\overline{A}_2\right\|}{\left\|\overline{A}_0^{-1}\right\|}}}{2\left\|\overline{A}_2\right\|}$. $x(\omega)$ can be determined from its power series expansion (17) for any ω satisfying $|\omega - \omega_0| < u^*$.

Step 1: For any $\omega_i \in I$, $i \geq 0$, find the corresponding u_i^* as explained in step 0. The power series for $x(\omega)$ in powers of $(\omega - \omega_i)$ converges for ω satisfying $|\omega - \omega_i| < u_i^*$.

Step 2: Check whether $\bigcup_i (\omega_i - u_i^*, \omega_i + u_i^*)$ covers the set $I = [\omega_l, \omega_h]$. If the answer is positive, then let $M = i$ (maximum number of points ω_i in the interval) and refrain from choosing additional points. Otherwise, choose the next point ω_{i+1} and go to step 1.

The important consideration in choosing ω_i's is that we aim to cover $I = [\omega_l, \omega_h]$ with the smallest possible number of intervals centered about ω_i's. Of course, the magnitudes of u_i^*'s play an important role in this procedure. However, it is clear that this analysis, which yields estimates for the radius of convergence of the power series expansion, provides us a tool for choosing centers of expansion of x in the frequency range of interest.

III. Numerical Results

To test the validity of the theory presented in this paper, the following example is considered

$$\frac{d^2x(z)}{dz^2} + k^2 x(z) = f(z) \tag{21}$$

$$x(0) = 0 \qquad x'(\pi) = 0 \tag{22}$$

It is clear that $x(z)$ satisfies the one-dimensional Helmholtz equation over the interval $[0, \pi]$ with the boundary conditions given in (22). The wavenumber k is defined as $k = \omega/c$ where c is the speed of light in vacuum. This boundary value problem can be solved by the finite element method by a uniform mesh discretization with nodes at $z_i = ih, \quad i = 0,1,\ldots,N$ where $h = \pi/N$, employing the usual piecewise linear shape functions. The singularities of this problem lie on the $j\omega$ axis at $\omega_n = \pm\frac{2n+1}{2}c, \quad n = 0,1,2,\ldots$

The matrix $A(\omega)$ given by (3) is obtained as $A(\omega) = A_0 + A_2\omega^2$ where [2]

$$A_0 = \frac{-1}{h}\begin{bmatrix} 2 & -1 & 0 & \cdots & \cdots & 0 \\ -1 & 2 & -1 & \cdots & \cdots & 0 \\ 0 & -1 & 2 & -1 & \cdots & 0 \\ \vdots & & \ddots & \ddots & \ddots & \vdots \\ 0 & 0 & \cdots & -1 & 2 & -1 \\ 0 & 0 & \cdots & 0 & -1 & 1 \end{bmatrix}$$

and

$$A_2 = \frac{h}{6c^2}\begin{bmatrix} 4 & 1 & 0 & \cdots & \cdots & 0 \\ 1 & 4 & 1 & \cdots & \cdots & 0 \\ 0 & 1 & 4 & 1 & \cdots & 0 \\ \vdots & & \ddots & \ddots & \ddots & \vdots \\ 0 & 0 & \cdots & 1 & 4 & 1 \\ 0 & 0 & \cdots & 0 & 1 & 2 \end{bmatrix}$$

Let ω_0 be an arbitrary frequency in the interval $I=(0.5c,1.5c)$, and $A(\omega)$ can also be expressed as $A(\omega)=\overline{A}_0+\overline{A}_1(\omega-\omega_0)+\overline{A}_2(\omega-\omega_0)^2$ where $\overline{A}_0=A_0+A_2\omega_0^2$, $\overline{A}_1=2A_2\omega_0$ and $\overline{A}_2=A_2$. After some manipulations, u^* is obtained as

$$u^*=-\omega_0+\omega_0\left[1+\frac{1}{\omega_0^2\|\overline{A}_0^{-1}\|\|A_2\|}\right]^{\frac{1}{2}} \tag{23}$$

The table given below demonstrates the values of u^*, $[\omega_0-u^*,\omega_0+u^*]$ and $\|\overline{A}_0^{-1}\|$ for different values of ω_0 with $N=80$.

ω_0	u^*	$[\omega_0-u^*,\omega_0+u^*]$	$\|\overline{A}_0^{-1}\|$
3e8	0.67e8	[2.33e8,3.67e8]	50.9
2.5e8	0.52e8	[1.98e8,3.02e8]	79.4
2e8	0.31e8	[1.69e8,2.31e8]	173.2
1.75e8	0.17e8	[1.58e8,1.92e8]	367.2
1.6e8	0.07e8	[1.53e8,1.67e8]	955.6
1.55e8	0.04e8	[1.51e8,1.59e8]	1937.5
1.52e8	0.015e8	[1.505e8,1.535e8]	4866.6

It is clear that as ω_0 tends to $0.5c$, the matrix $\overline{A}_0$ almost becomes singular and the radius of convergence of the power series becomes gradually smaller.

Next, we are going to discuss the rate of convergence of the power series expansion, and derive some *a priori* bounds for the norms of differences of any arbitrary iterate and the unknown exact solution.

The iteration formula which yields the coefficients of the power series expansion of $x(\omega)$ can be written

$$x_k=\overline{A}_0^{-1}\left[f_k-\overline{A}_1x_{k-1}-\overline{A}_2x_{k-2}\right] \tag{24}$$

Let $x^{(k)}=x_0+x_1(\omega-\omega_0)+\cdots+x_k(\omega-\omega_0)^k$, and let x be the exact solution of (9a). Then we have (for details, see appendix B):

$$\begin{aligned}\|x^{(k)}-x\|\le\|\overline{A}_0^{-1}\|\left[\|\overline{A}_1\|\|x^{(k-1)}-x\||\omega-\omega_0|+\|\overline{A}_2\|\|x^{(k-2)}-x\||\omega-\omega_0|^2\right]\\ +\|\overline{A}_0^{-1}\|\|f-\{f_0+f_1(\omega-\omega_0)+\cdots+f_k(\omega-\omega_0)^k\}\|\end{aligned} \tag{25}$$

The above equation is helpful for estimating, *a priori*, the convergence of the iterates. We will now illustrate its usage for the example characterized by (21) and (22), with $N=200$ and $\omega_0=3e8$. In the following tables, we present the results for the upper bounds of $\|x^{(k)}-x\|$, i.e., the norm of the difference between an iterate and the exact solution for different iteration numbers k. These results are helpful for estimating the order of error in the solution before initiating the computations.

(i) $\omega = 2.9e8$

k	1	2	3	4	5
$\|x^{(k)} - x\|$	4.69e-2	6.95e-3	1.03e-3	1.53e-4	2.27e-5

(ii) $\omega = 2.8e8$

k	1	2	3	4	5
$\|x^{(k)} - x\|$	0.227	6.74e-2	1.99e-2	5.93e-3	1.76e-3

(iii) $\omega = 2.7e8$

k	1	2	3	4	5
$\|x^{(k)} - x\|$	0.648	0.288	0.128	5.71e-3	2.54e-3

(iv) $\omega = 2.5e8$

k	1	2	3	4	5
$\|x^{(k)} - x\|$	[illegible]	2.86	2.12	1.57	1.16

IV. Conclusions and Future Work

The solution to the FEM matrix equation (1) can be derived in an interval $I = [\omega_l, \omega_h]$ of ω, either by directly solving (1) at a set of frequencies and then interpolating for the intermediate values, or by choosing a set of frequencies around which $x(\omega)$ can be obtained by means of a power series expansion. Typically, the series approach is computationally more efficient than the direct interpolation scheme, because the former requires the LU decomposition of a large matrix at a relatively small number of frequencies. Issues pertaining to the rate of convergence of the series expansion and the estimation of the number of operations needed in each iteration step are currently being investigated. Additional numerical experiments that test and validate the theory presented in this paper for more general problems will be carried out in the future. Techniques related to increasing the frequency interval via rational function approximation [3], will also be extended to this case.

Appendix A

In this appendix we show how we can estimate the condition number $\kappa_\infty(A)$ of a matrix A, with respect to the infinity norm, which is defined as [4]

$$\kappa_\infty(A) = \|A\|_\infty \left\|A^{-1}\right\|_\infty$$

It is relatively straightforward to compute $\|A\|_\infty$, however, we need to calculate A^{-1} to determine the other factor, which is obviously difficult. Nevertheless it is possible to estimate the condition number $\kappa_\infty(A)$ in a manner described below. We begin with the equation

$$Ay = d \quad \Rightarrow \quad \left\|A^{-1}\right\|_\infty \geq \frac{\|y\|_\infty}{\|d\|_\infty}$$

The idea behind the estimator is to choose d such that the norm of the solution y is large and then set

$$\kappa_\infty(A) = \|A\|_\infty \frac{\|y\|_\infty}{\|d\|_\infty}$$

Consider, for instance, the case when $A = T$ is upper triangular. The relation between d and y is completely specified by the "back-substitution" formula

$$\begin{aligned} & p_i := 0 \quad (i = 1,2,\ldots n) \\ & For \quad k = n, n-1, \ldots 1 \\ & \qquad y_k := (d_k - p_k)/t_{kk} \\ & \qquad p_i := p_i + t_{ik} y_k \qquad (i = 1,2,\ldots k-1) \end{aligned} \tag{A.1}$$

Normally, this algorithm is used to solve a *given* triangular system $Ty = d$. However, we are free to choose the r.h.s. vector d, subject to the constraint that y is large relative to d. One way to encourage the growth in y is to choose d_k from the set $\{-1,+1\}$ depending upon whether $(1-p_k)/t_{kk}$ or $(-1-p_k)/t_{kk}$ is larger in magnitude. Since d is a vector in the form $d = (\pm 1,\ldots,\pm 1)^T$, we obtain the estimator $\kappa_\infty(T) = \|T\|_\infty \|y\|_\infty$.

We can now use these ideas to estimate the condition number of a square nonsingular matrix A whose $PA = LU$ decomposition is known, by proceeding as follows

(i) Apply the lower triangular version of algorithm (A.1) to U^T to obtain a solution of $U^T y = d$ that has alarge norm.

(ii) Solve the triangular systems

$$\begin{aligned} L^T r &= y \\ Lw &= \mathrm{Pr} \\ Uz &= w \end{aligned}$$

(iii) $\kappa_\infty(A) = \|A\|_\infty \frac{\|z\|_\infty}{\|r\|_\infty}$.

The important point here is that if A is ill-conditioned, and $PA = LU$, then the matrix. U is also ill-conditioned, whereas the matrix L tends to be fairly well-conditioned. Thus it is more advantageous to apply algorithm (A.1) to U rather than to L.

Appendix B

In this appendix we provide the error estimates of the higher order approximations of the solution x, generated by the power series representation.We begin by writing (9a) in the form

$$x = -[\bar{A}_0^{-1}\bar{A}_1(\omega - \omega_0) + \bar{A}_0^{-1}\bar{A}_2(\omega - \omega_0)^2]x + \bar{A}_0^{-1} f \tag{B.1}$$

The solution of this equation is

$$x = [I + \bar{A}_0^{-1}\bar{A}_1(\omega - \omega_0) + \bar{A}_0^{-1}\bar{A}_2(\omega - \omega_0)^2]^{-1}\bar{A}_0^{-1} f \tag{B.2}$$

which implies that

$$\|x\| \le \frac{1}{1 - \left(\|\bar{A}_0^{-1}\|\left\{\|\bar{A}_1\||\omega - \omega_0| + \|\bar{A}_2\||\omega - \omega_0|^2\right\}\right)}\|\bar{A}_0^{-1}\|\|f\| \tag{B.3}$$

Now, consider

$$x - x_0 = -[\bar{A}_0^{-1}\bar{A}_1(\omega - \omega_0) + \bar{A}_0^{-1}\bar{A}_2(\omega - \omega_0)^2]x + \bar{A}_0^{-1}(f - f_0)$$

Using the triangle inequality and (B.3), we obtain

$$\|x - x_0\| = \frac{\|\bar{A}_0^{-1}\|\left\{\|\bar{A}_1\||\omega - \omega_0| + \|\bar{A}_2\||\omega - \omega_0|^2\right\}}{1 - \|\bar{A}_0^{-1}\|\left\{\|\bar{A}_1\||\omega - \omega_0| + \|\bar{A}_2\||\omega - \omega_0|^2\right\}}\|f\| + \|\bar{A}_0^{-1}\|\|f - f_0\| \tag{B.4}$$

Let $x^{(1)} = x_0 + x_1(\omega - \omega_0)$ where $x_1 = \bar{A}_0^{-1} f_1 - \bar{A}_0^{-1}\bar{A}_2 x_0$. Then

$$\begin{aligned} x - x^{(1)} = {} & \bar{A}_0^{-1}\bar{A}_1(\omega - \omega_0)(x - x_0) - \bar{A}_0^{-1}\bar{A}_2(\omega - \omega_0)^2 x \\ & + \bar{A}_0^{-1}(f - f_0 - f_1(\omega - \omega_0)) \end{aligned}$$

which implies that

$$\begin{aligned} \|x^{(1)} - x\| \le {} & \|\bar{A}_0^{-1}\|\left[\|\bar{A}_1\|\|x_0 - x\||\omega - \omega_0| + \|\bar{A}_2\|\|x\||\omega - \omega_0|^2\right] \\ & + \|\bar{A}_0^{-1}\|\|f - \{f_0 + f_1(\omega - \omega_0)\}\| \end{aligned} \tag{B.5}$$

Similarly for $x^{(2)} = x_0 + x_1(\omega - \omega_0) + x_2(\omega - \omega_0)^2$, we derive the result

$$\begin{aligned} \|x^{(2)} - x\| \le {} & \|\bar{A}_0^{-1}\|\left[\|\bar{A}_1\|\|x^{(1)} - x\||\omega - \omega_0| + \|\bar{A}_2\|\|x_0 - x\||\omega - \omega_0|^2\right] \\ & + \|\bar{A}_0^{-1}\|\|f - \{f_0 + f_1(\omega - \omega_0) + f_2(\omega - \omega_0)^2\}\| \end{aligned} \tag{B.6}$$

Finally, for $k \ge 2$, this result can be generalized to yield

$$\begin{aligned} \|x^{(k)} - x\| \le {} & \|\bar{A}_0^{-1}\|\left[\|\bar{A}_1\|\|x^{(k-1)} - x\||\omega - \omega_0| + \|\bar{A}_2\|\|x^{(k-2)} - x\||\omega - \omega_0|^2\right] \\ & + \|\bar{A}_0^{-1}\|\|f - \{f_0 + f_1(\omega - \omega_0) + \cdots + f_k(\omega - \omega_0)^k\}\| \end{aligned} \tag{B.7}$$

which serves to provide us the desired estimate for the k*th* order approximation to the desired solution.

References

[1] K. E. Atkinson, "An Introduction to Numerical Analysis", 2nd ed., New York: Wiley, 1989.

[2] W. G. Strang and G. J. Fix, "An Analysis of the Finite Element Method", Englewood Cliffs, N. J., Prentice-Hall, 1973.

[3] E. Chiprout and M. S. Nakhla, "Asymptotic Waveform Evaluation and Moment Matching for Interconnect Analysis", Kluwer Academic Publishers, 1994.

[4] G. H. Golub and C. F. van Loan, "Matrix Computations", The Johs Hopkins University Press, Baltimore, Maryland, 1983.

Finite Element Modeling of Head Coils for High-Frequency Magnetic Resonance Imaging Applications†

J. G. Harrison, Department. of Physics, University of Alabama at Birmingham,
J. T. Vaughan, NMR Center, Massachussetts General Hospital

I. Introduction

Very high-resolution magnetic resonance imaging which exceeds current state-of-the-art capabilities in other medical imaging modalities such as PET and CAT is now possible with magnets operating at 4.1 T. A National Resource Facility for imaging at 4.1 T has been established at the University of Alabama at Birmingham where clinical and computational studies have been ongoing for the last five years. One part of the research effort has been to use computational modeling to address three principal issues: 1) surface and head coil design, 2) safety issues related to RF power deposition in tissues, and 3) modeling the effect of electrical and chemical changes in the area to be imaged on the resulting MR image. In this paper we will summarize our results in the first two of those areas and defer remarks about the third area, which is still in its very early stages, to the conclusion.

The organization of this paper is as follows. We will begin with some background information regarding the safety issues addressed in our work. Then we will outline the finite-element modeling of the RF and thermal components of our problem and discuss the hardware and software tools employed in our lab. Representative results for our modeling will also be presented and discussed. Finally, we will outline some our plans for improving our modeling efforts and discuss some of the exciting new areas in MRI which may also point to new areas of research using our modeling tools.

One further remark in regard to organization. In order to provide a more informative view of some of the figures in this paper, we have placed color gif files on the world wide web that can be viewed with a web browser. Simply point your browser to ftp://ftp.phy.uab.edu/pub/aces_12. The file names will correspond to the figures as numbered in this paper.

II. Safety Issues in Imaging at 4.1 T

A. Magnetic Resonance Imaging

The basic relationships in magnetic resonance (MR) work will be introduced here strictly for purposes of establishing notation; there are a number of very good monographs on MR and MRI that may be consulted for a more thorough introduction to the field. We may use a proton (hydrogen) as our prototype nucleus and recall that the Zeeman splitting resulting from the interaction of the proton's nuclear magnetic moment ($\vec{\mu}$) with an applied field $\vec{\mathbf{B}}$ may be writ-

ten as

$$U = -\vec{\mu} \bullet (\vec{B}_0 + \vec{B}_1) \qquad (1)$$

where we have split $\vec{B}$ into a static part B_0 associated with the 4.1 T magnet in our case and a time-varying part B_1 associated with the head coil. The energy splitting, ΔE, is related to the RF field frequency for resonant absorption as

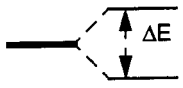

$$\nu = \frac{\Delta E}{h} \qquad (2)$$

where h is Planck's constant. For protons, this resonant frequency is about 174.5 MHz for a B_0 of 4.1 T. One of the reasons for interest in operating at 4.1 T as opposed to the more common clinical value 1.5 T is a scaling law which predicts better signal-to-noise ratios for imaging at higher B fields. The associated RF wavelengths are also shorter leading to better resolution. Preliminary work at 6.0 T is underway at several labs and a few proposals for operating at 15 T have been made in the past.

B. Energy Deposition and Local Heating

Although clinical precautions are always taken in regard to MRI, we should note some aspects of operating at higher fields and higher RF frequencies that prompted the safety studies that we are engaged in. First, the wavelengths involved are given by $\lambda = \frac{c}{\nu\sqrt{\varepsilon}}$ where ε is the (relative) permittivity of the tissue. For muscle at these frequencies, ε has a value of about 60 resulting in a wavelength of about 22 cm, comparable to some anatomical dimensions. This suggests the possibility of structural resonances which could lead to otherwise unexpected nonlocal deposition of RF energy. Anecdotal reports of such effects have been found in work at considerably higher frequencies in hyperthermia treatment for cancer. Given the extensive use of MRI in brain and heart imaging, the possibility of nonlocal heating in the vicinity of sensitive anatomical structures can not be overlooked. While specific absorption rate (SAR) safety standards have been in place for a number of years, they are global standards based on whole-body or large-structure dosing. Local heating might well exceed such global standards on a small scale. Ideally we would like to develop conservative, yet useful local standards based on computer modeling of local-heating at these frequencies and assuming an effective cw heating mode. By using a cw standard we take a more conservative approach in light of the fact that the usual mode of operation is pulsed. Finally, we should note that the dielectric materials we are dealing with here (tissues) are quite lossy and thus another mode of energy deposition is via dielectric losses. Since displacement currents increase with increasing frequency, we expect larger contributions to that heating mechanism with higher B fields (i.e. higher RF frequencies).

III. Finite Element Modeling of RF and Thermal Problems

In the course of our work in this area we have employed two software packages to address the problems of RF energy deposition in tissues and the resultant heat-flow problem. In our

initial efforts we high-symmetry models which allowed us to reduce the full three-dimensional problem to effective two-dimensional ones. We have since expanded to full three-dimensional capability allowing for more detailed and realistic models of cranial and thoracic regions.

A. Finite-element modeling of RF problem

For this type of problem we, of course, can no longer rely on Biot-Savart type of treatment of the fields since eddy currents and displacement currents are a key part of the problem. In order to incorporate a full Maxwell-equation treatment of the problem we have a number of options as to how to proceed. Because of the longer-term goal of dealing with low-symmetry structures with considerable substructure, we chose to use a finite-element approach to the problem as being the most adaptive to a progressively more involved problem definition. To that end, we first employed the Mawell® suite of programs which we were able to run on a relatively modest platform consisting of a Gateway 386/33 pc with 8 Mb of memory and 80 Mb of disk space. In this package the problem reduces to solving the Maxwell-Ampere equation in terms of the vector potential, $\vec{\mathbf{A}}$:

$$\nabla\times\left(\frac{1}{\mu}\nabla\times\vec{\mathbf{A}}\right) = -(\sigma + i\varepsilon\omega)\,(i\omega\vec{\mathbf{A}} + \nabla\Phi) \qquad (3)$$

Using the geometric modeling module we constructed 2-d systems as well as 3-d problems with axial symmetry. One such system was a composite cylinder made up of layers of fat and muscle and a single-loop coil positioned near the surface to simulate a simple model of a surface coil. The loop current was adjusted to correspond to power levels of 3 and 6 watts. Typical models employed about 4000 finite elements.

For more complex systems we employ the MSC/EMAS® suite of programs together with MSC/Aries® to construct 3-d models. One such system is illustrated in Fig. 2 as an 8-element head coil with a simple two-layer cylindrical load with dielectric parameters appropriate to fat and brain. The system was "tuned" by adjusting the grounded capacitors on each element to achieve resonance at 174.5 MHz with a total power of 3 watts. Typical models employed about 25000 elements. The platform needed for this work was thus much bigger and consisted of an HP 735 workstation with 208 Mb memory and 2 Gb of disk space.

For both types of problems one of the most troublesome part of the problem definition was that of finding acceptable dielectric parameters. The most useful compendium of dielectric permittivity and electrical conductivity values for muscle, fat, and brain was that of Duck[3] but there still remains a lack of experimental values for more specific tissue types and other frequencies. Table I contains the values we used in both the 2-d and 3-d work. More extensive discussion of work on these models may be found in Ref. 1 and 2.

B. Finite element modeling of steady-state heating.

In order to deal with this part of the problem we employed a standard approximation in

dealing with passive heating of vascularized tissue known as the bioheat equation[4]:

$$\nabla \bullet (-\mathbf{K_T} \nabla \mathbf{T}) + \beta (\mathbf{T} - \mathbf{T_b}) = \mathbf{P} \qquad (4)$$

where $\beta = \frac{R \rho \rho_b c_b}{K_b}$,

R = blood perfusion rate
ρ, ρ_b = tissue and blood density, respectively
T_b = blood temperature
c_b = specific heat of blood
ρ, ρ_b = tissue and blood thermal conductivity, respectively

and $P = \frac{1}{2\sigma}\int |\mathbf{J}|^2 d^3r$ is the power density associated with the eddy currents.

With the Maxwell suite, we used the Electrostatic Solver module (Poisson's Equation) to solve equation (4) iteratively. Fig 1 summarizes the thermal heating results for our simple mutiple-layer cylinder. In spite of the obvious crudeness of that model, we found surprisingly good agreement with the experiments on porcine tissue[5]. For the full 3-d problems we used the the Heat Flow module in the MSC/Nastran® suite of programs. As yet we have not incorporated the bioheat term in this latter work.

IV. **Conclusion**

We have been able to apply finite element modeling techniques to the RF heating problem and have found reasonably good agreement with experiments Our current efforts are focussed on construction of more realistic and detailed model of the head. To that end we are using the wealth of digitized data available through the National Library of Medicine's "Visible Human" project to constructed digitlzed slices for use in the MSC/Aries module for model construction.

Some the most exciting applications of the high-resolution images from MRI include a variety of "functional imaging" projects in which one tries to correlate changes in images (related to electrochemical changes) resulting from selected stimuli. These may give greater insight into the process of learning, neurological problems associated with epilepsy, Parkinson's disease and even attention-deficit disorder. The third part of research efforts will be to try to model the correlation between image and electrochemical change. With such a tool one can carry out computer simulations of drug effects and side effects. The potential in that area is obviously very exciting.

† Work supported by HHS Biotechnology Resource Grant #1-41 RR07723-01

® Maxwell is a registered trademark of Ansoft Corporation
® MSC/EMAS and MSC/Aries are trademarks of the MacNeal-Schwendler Corporation
® MSC/Nastran is a proprietary version of NASTRAN® maintained by the MacNeal-Schwendler Corporation
® NASTRAN is a registered trademark of NASA.

References

1. J.H. McDuffie, J. G. Harrison, G. M. Pohost, and J. T. Vaughan, "3D Numerical Modeling of High Frequency Volume Coils for Climical NMR", Proc. Soc. Magn. Reson., 185, 1995.

2. J. T. Vaughan, H. P. Hetherington, J. G. Harrison, J. O. Otu, J. W. Pan, and G. M. Pohost, "High frequency volume coils for clinical nuclear magnetic resonance imaging and spectroscopy", Magn. Res. Med. 32, 206-218 (1994).

3. F. Duck, Physical Properties of Tissue, (Academic Press, San Diego, 1990).

4. I. A. Brezovich, J. H. Young, and M- T. Wang, "Temperature Distributions in Hyperthermia by Electromagnetic Induction", Medical Physics, 10, 57 (1983).

5. J. T. Vaughan, J. Harrison, H. P. Hetherington, W. T. Evanochko, and G. M. Pohost, "Radiofrequency Surface Coil Heating Measurements in Porcine Muscle", Proc. Soc. Magn. Res. in Med. , 4026, 1992.

6. National Library of Medicin (US) Board of Regents "Electronic Imaging: Report of the Board of Regents", USD HHS, Public Health Sevice, NIH. NIH pub 90-2197.

Table I. Dielectric and Bioheat Parameters for Tissues

fat	skin	muscle	freq.
$\varepsilon = 12$ $\sigma = 0.06$	$\varepsilon = 60$ $\sigma = 0.33$	$\varepsilon = 83$ $\sigma = 0.9$	71 MHz
$\varepsilon = 6$ $\sigma = 0.1$	$\varepsilon = 50$ $\sigma = 0.53$	$\varepsilon = 57$ $\sigma = 1.0$	175 MHz
$\beta = 2.3 \times 10^3$	$\beta = 7.6 \times 10^3$	$\beta = 1.9 \times 10^3$	$W/m^3/°C$

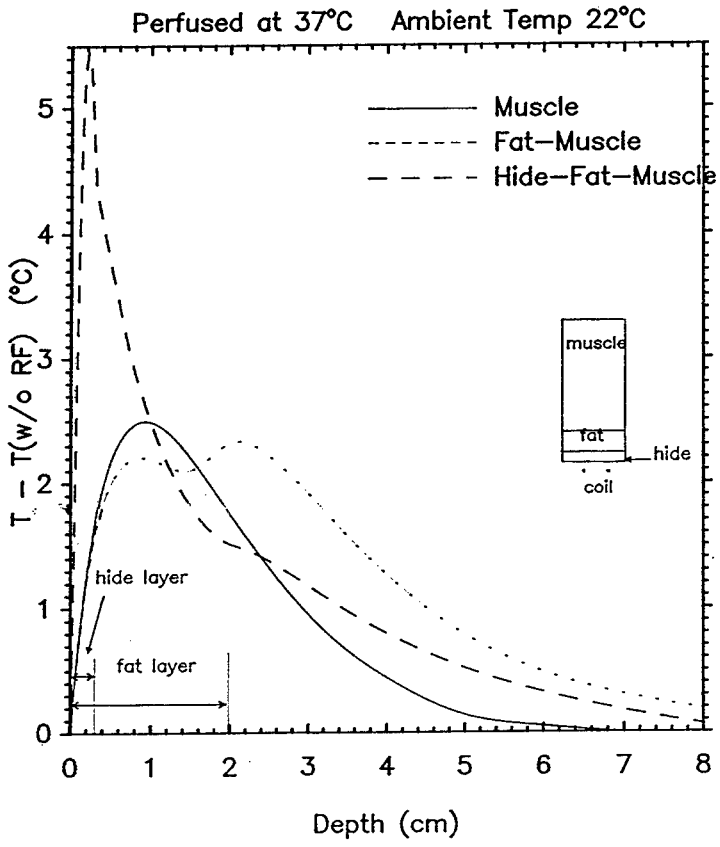

Fig. 1 Temperature Elevation for Cylinder Model

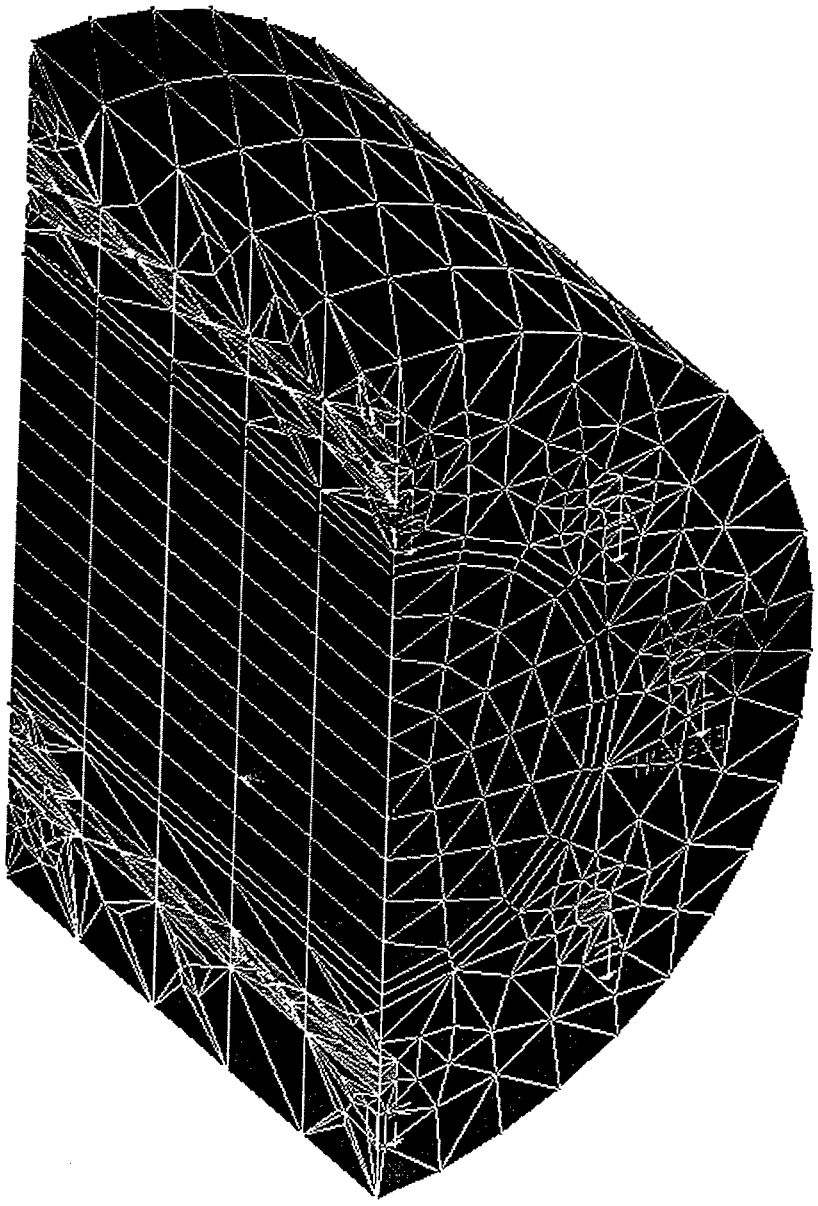

Figure 2. 8-element Head Coil Model

$\mathcal{H}_1(curl)$ TVFEM in Conjunction with PML for Modeling 3D Waveguide Discontinuities.

Sergey G. Perepelitsa, Romanus Dyczij-Edlinger, Jin-Fa Lee Member, **IEEE**
Department of Electrical and Computer Engineering, Worcester Polytechnic Institute.

Higher order vector finite element methods offer the possibility of using a coarse grid to obtain accurate solutions of Maxwell's equations while at the same time, retaining the geometric flexibility of finite element methods. As early as 1980, Nedelec introduced a family of mixed finite elements in R^3 [1] that is unisolvent as well as conforming in $\mathcal{H}(curl)$. In this paper we discuss the application of the $\mathcal{H}_1(curl)$ TVFEM [2] for the analysis of waveguide discontinuities. This is a higher order scheme which is incomplete to second-order for the vector field $\vec{E}$, but is complete to first-order in the range of the *curl* operator, i.e. the magnetic field $\vec{H}$. The discussion in this paper is based on the $\vec{E}$-field formulation, however, a straightforward modification can be made for the $\vec{H}$-field formulation. For a general anisotropic medium, the bilinear form obtained from applying Galerkin method is

$$B(\vec{W},\vec{E}) = \int_\Omega \{(\vec{\nabla}\times\vec{W})\cdot([\mu_r]^{-1}\vec{\nabla}\times\vec{E}) - k_0^2\vec{W}\cdot[\epsilon_r]\vec{E}\}\, d\Omega - \int_\Gamma \{\vec{W}\times([\mu_r]^{-1}\vec{\nabla}\times\vec{E})\}\, ds$$

Where $\vec{W}$ and $\vec{E}$ are expanded using the $\mathcal{H}_1(curl)$ vector finite elements. The newly developed frequency domain PLM [3] has been also incorporated into the current formulation for truncating waveguide ports. The resulting matrix equation is solved using bi-conjugate gradient method with diagonal preconditioner. The field distribution and S-parameters are obtained from the results of the computed total electric field. Various examples have been studied and corresponding results are presented as verification of the method.

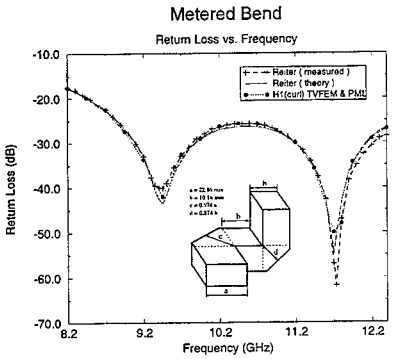

Figure 1:
Metered Bend: S_{11}-parameter vs. freq.

References

[1] J.C. Nedelec, "Mixed Finite Elements in R^3", Num.Math., vol. 35, pp. 315, 1980
[2] J-F.Lee, "Tangential Vector Finite Elements and Their Application to Solving Electromagnetic Scattering Problems", ACES newsletter, vol. 10, no.1, pp.52, 1995
[3] Z.S. Sacks, D.M. Kingsland, R. Lee, J.F. Lee, "A Perfectly Matched Anisotropic Absorber for Use as an Absorbing Boundary Condition", Submitted to *IEEE Trans Antenna Prop.*

SESSION 23:

METHOD OF MOMENTS APPLICATIONS

Chair: A. Peterson

GLOBAL FOURIER-SERIES BASIS FUNCTIONS FOR EM SCATTERING

M. H. Smith,
Georgia Tech Research Institute,
Georgia Institute of Technology

A. F. Peterson,
School of Electrical and Computer Engineering,
Georgia Institute of Technology

Abstract -- Previous results reported for global Fourier/FFT basis functions applied to integral equation formulations of EM scattering problems have indicated significant efficiencies to be obtained over the use of conventional finite-domain basis functions. Some limitations were also reported, however. These included slow convergence in the region of discontinuous derivatives (edges) in the TE formulation, and the inability to extract actual current values from the product of current times a Jacobian at points where the Jacobian is zero. In the present work, formulations for global Fourier-series basis functions are developed for TM and TE electric field, and TE magnetic field, integral equations. Rather than relying solely on FFT approximations of integrands, these formulations combine Fourier representation of integrands with analytical integrals to handle singularities. Also included is a second-order correction, accounting for surface curvature, to the usual approximation of the self-term in the TE magnetic field case. Solutions are obtained directly for surface currents. 2D results for circular and square cylinders are compared with exact and conventional moment-method results. Good accuracy is obtained with a 4:1 reduction in the number of unknowns from the conventional moment-method formulations. The extension of global basis functions to 3D surfaces is discussed.

I. INTRODUCTION

In this paper we present a formulation for the calculation of electromagnetic scattering by integral equations using global Fourier-series basis functions. This is developed in some detail for the 2-D problem of scattering from infinite conducting cylinders of arbitrary cross section. Basis functions and the approach for describing the problem geometry are descibed in Section II. In Sections III, IV and V, the Transverse Magnetic Electric-Field Integral Equation (TM EFIE), Transverse Electric Magnetic-Field Integral Equation (TE MFIE) and the Transverse Electric Electric-Field Integral Equation (TE EFIE) formulations are treated. Global Basis Function (GBF) results for circular cylinders are compared with exact solutions, and with results obtained with finite-domain Pulse Basis Function (PBF) integral equations. GBF results for cylinders with square cross section are compared with reference results in Section VI. The extension of this GBF approach to 3-D closed surface problems is currently being investigated. A brief outline of our approach is presented in Section VII.

II. DESCRIPTION OF GEOMETRY AND BASIS FUNCTIONS

In the same manner as is discussed in James' 1994 paper [1], a 2-D contour in the X-Y plane is mapped onto a unit circle, parameterized by θ. Discrete points, spaced non-uniformly on the contour, are assigned to points spaced uniformly in θ around the circle. Points on the contour are spaced more closely in regions of high curvature and near edges. The distribution of points on a segment bounded by two edges can be described with a cosine function, to obtain smooth functions in the θ domain. For a segment between l_1 and l_2, let α be sampled evenly on $[0,\pi)$ and define the sample points on the segment by

$$l = \frac{l_2+l_1}{2} - \frac{l_2-l_1}{2}\cos(\alpha) \ .$$

For a total of N points around the complete contour, the corresponding points in the theta domain are $\theta_n = 2\pi n/N$, n = 0,1,...,N-1.

We next describe x and y in terms of Fourier series. The coefficients for the Fourier series can be obtained via FFTs if the FFT coefficients are rotated to associate the n = 0 FFT term with zero frequency. For an even number of points N, an extra coefficient must be generated by dividing the n = N/2 term by 2, and replicating it so that it winds up at the maximum positive and negative frequencies. The results are Fourier exponential series which yield real results for any value of theta. Spatial derivatives can then be computed by appropriately modifying the Fourier coefficients. We have series of the form,

$$x(\theta) = \sum_{m=-M}^{M} \xi_m \exp(jm\theta)$$

and

$$\frac{dx}{d\theta} = \sum_{m=-M}^{M} jm\xi_m \exp(jm\theta) \ .$$

The Jacobian is

$$\frac{dl}{d\theta} = \sqrt{\left(\frac{dx}{d\theta}\right)^2 + \left(\frac{dy}{d\theta}\right)^2} \ .$$

The basis functions are interpolation functions, each of them unit value at one sample point and zero at all other sample points. They are

$$b_n = \frac{1}{N}\left[\frac{\sin\left((N-1)\frac{\theta-\theta_n}{2}\right)}{\sin\left(\frac{\theta-\theta_n}{2}\right)}\right] + \cos\left[N\frac{\theta-\theta_n}{2}\right], \ N \text{ even}$$

and

$$b_n = \frac{1}{N}\left[\frac{\sin\left(N\frac{\theta-\theta_n}{2}\right)}{\sin\left(\frac{\theta-\theta_n}{2}\right)}\right], \ N \text{ odd} \ .$$

II. TM EFIE FORMULATION

We wish to solve

$$E_z^{inc}(\theta) = jk\eta \int_0^{2\pi} J_z(\theta') G(\theta,\theta') \frac{dl}{d\theta'} d\theta' ,$$

where

$$G = \frac{1}{4j} H_0^{(2)}(kR(\theta,\theta'))$$

and $R(\theta,\theta')$ is the distance between the two points on the original contour corresponding to θ and θ'. From the series expansion given in [2],

$$H_0^{(2)}(z) \to 1 - j\frac{2}{\pi}\left[\ln\left(\frac{z}{2}\right) + \gamma\right], \quad z \to 0 ,$$

where $\gamma = 0.57721567$ (Euler's constant). Since $R \to dl/d\theta \, |\theta-\theta'|$ as $\theta \to \theta'$,

$$H_0^{(2)}(kR) \to 1 - j\frac{2}{\pi}\left[\ln\frac{|\theta-\theta'|}{2} + \ln\left(k\frac{dl}{d\theta}\right) + \gamma\right], \quad \theta \to \theta' .$$

We define

$$\frac{d}{d\theta}\left[j\frac{2}{\pi}\sin(\Delta\theta)\ln\left(\sin\frac{|\Delta\theta|}{2}\right)\right] \equiv S(\Delta\theta) ,$$

obtaining

$$S(\Delta\theta) = j\frac{2}{\pi}\left[\cos(\Delta\theta)\ln\left(\sin\frac{|\Delta\theta|}{2}\right) + \frac{\sin(\Delta\theta)\cos\frac{\Delta\theta}{2}}{\sin\frac{\Delta\theta}{2}}\right] .$$

$S(\Delta\theta)$ is a periodic function with a singularity at $\Delta\theta = 0$, and obviously has an anti-derivative. At $\theta' = \theta$ we have the finite limit

$$H_0^{(2)}(kR) + S(\theta-\theta') \to 1 - j\frac{2}{\pi}\left[\ln\left(k\frac{dl}{d\theta}\right) + \gamma - 1\right], \quad \theta' \to \theta .$$

Hence the singularity in the integral can be removed by replacing $H_0^{(2)}(kR)$ with $H_0^{(2)}(kR) - S(\Delta\theta)$, leaving a quantity which can be integrated numerically (by simply summing its values at all sample points and dividing by 2π). This leaves an integral with $S(\Delta\theta)$ in the integrand. This remaining integral can be integrated by parts, since $S(\Delta\theta)$ has an exact anti-derivative, and derivatives of all other terms can be calculated.

To get a quick feel for the accuracy of the resulting method, we consider a perfectly conducting circular cylinder, with a circumference of 1 λ_0, centered at the origin. For an incident plane wave travelling in the $\phi = 0$ direction, the magnitude of the current at $\phi = \pi$ can be calculated exactly to be .006237 [3]. Table 1 compares results for GBF with results for PBF [3] for different numbers of unknowns.

Table 1. Comparison of GBF and PBF results for TM EFIE

Number of Unknowns	Magnitude of Current, GBF	Magnitude of Current, PBF
16	.006232	.006302
32	.006236	.006271
64	.006237	.006254

III. TE MFIE FORMULATION

For the TE MFIE case we wish to solve

$$H_z^{inc} = -J_T - \left[\frac{\delta A_y}{\delta x} - \frac{\delta A_x}{\delta y}\right]_{S^+} ,$$

where J_T indicates tangential current, and S^+ indicates evaluation at an infinitesimal distance ϵ outside the contour. The vector potential $\mathbf{A}$ is given by

$$A(\theta) = \int_0^{2\pi} \hat{T}(\theta')\, J_T(\theta')\, G(\theta,\theta')\, \frac{dl}{d\theta'}\, d\theta' ,$$

where T-hat is a unit tangent vector. The quantity in brackets (curl $\mathbf{A}$) is then

$$\left[\frac{\delta A_y}{\delta x} - \frac{\delta A_x}{\delta y}\right] = -\frac{k}{4j}\int_0^{2\pi} J_T(\theta')\, H_1^{(2)}(kR)\left[T_y(\theta')\,\frac{\delta R}{\delta x} - T_x(\theta')\,\frac{\delta R}{\delta y}\right]\frac{dl}{d\theta'}\, d\theta .$$

It can be shown [3] that the contribution to (curl $\mathbf{A}$) of the current right at the point of singularity reduces to 1/2 J_T. This can be accomplished by projecting the problem in the vicinity of the singularity onto normal and tangential coordinates, using $H_1^{(2)}(Z) \rightarrow j2/\pi Z$ [2], and letting the observation point be distance ϵ outside the contour. The integrand so obtained submits to a simple trig substitution, after which the limit may be taken as ϵ approaches zero. This value of 1/2 J_T is often used by itself for the diagonal terms of the MFIE matrix. However, it is possible to obtain a correction to this by considering the limit of the integrand as $\theta' \rightarrow \theta$ with $\epsilon \equiv 0$, thus picking up the contribution of of all points up to the singularity. Writing Taylor series approximations of the form

$$x(\theta') = x(\theta) + \frac{dx}{d\theta}(\theta'-\theta) + \frac{1}{2!}\frac{d^2x}{d\theta^2}(\theta'-\theta)^2$$

and

$$R = \frac{dl}{d\theta}|\theta'-\theta| + \frac{1}{2!}\frac{d^2l}{d\theta^2}|\theta'-\theta|^2 ,$$

we find that the integrand has limit at $\theta = \theta'$ of

$$L = -\frac{\frac{dy}{d\theta}\frac{d^2x}{d\theta^2} - \frac{dx}{d\theta}\frac{d^2y}{d\theta^2}}{4\pi\left(\frac{dl}{d\theta}\right)^2} .$$

This is proportional to curvature at the observation point. The diagonal terms of the matrix then become -1/2 - 2πL/N.

For H_z of unit magnitude traveling in the $\phi = 0$ direction, the current at $\phi = \pi$ can be calculated exactly to be 1.7071 [3]. A 10 - cell PBF model using quadrature integration for the off-diagonal terms yields 1.749 [3]. An 8 - unknown GBF formulation yields 1.7098, and 16 unknowns yield 1.7074. With 32 unknowns, but no curvature correction, the result is 1.7436, as opposed to 1.7071 when curvature correction is restored.

IV. TE EFIE FORMULATION

For the TE EFIE problem, we must consider the complete expression for $\boldsymbol{E}$ as a function of vector potential $\boldsymbol{A}$. If $\boldsymbol{H} \equiv \nabla \times \boldsymbol{A}$, then

$$E = \frac{\nabla\nabla\cdot A + k^2 A}{j\omega\epsilon} .$$

The principal differences between the TE EFIE problem and the TM EFIE problem are that we must account for the divergence of $\boldsymbol{A}$, which was zero for the TM problem, and we must account for the vector direction of J_T. From the usual development of the wave equation for $\boldsymbol{A}$ using the Lorentz gauge, it can be seen that

$$\nabla\cdot A = \int (\nabla\cdot J)\, G(r, r')\, dV .$$

From the derivatives of the basis functions, the divergence of J_T is known, and $\nabla\cdot\boldsymbol{A}$ can be calculated in the same manner as E_z was in the TM EFIE problem. Once $\nabla\cdot\boldsymbol{A}$ is known at all the sample points around the contour, its gradient can be calculated using the derivatives of the underlying basis functions. The tangential component of $\boldsymbol{A}$ is found from

$$A_T(\theta) = \int_0^{2\pi} \hat{T}(\theta)\cdot\hat{T}(\theta')\, J_T(\theta')\, G(\theta,\theta')\, \frac{dl}{d\theta'}\, d\theta' .$$

We find for this integrand that a sampling problem exists when it is evaluated only at the original sample points (assuming one basis function per sample point). Using the Fourier series definitions of the various quantities of interest, it is a simple matter to increase the density of sample points for the integration. Otherwise, the development of this case follows naturally from the previous two cases.

To absolutely guarantee that no undersampling occurs, it would be necessary to increase the sampling density by a factor of four. Experience shows that factors from 1.2 to 2.0 suffice. Table 2 shows results for different combinations of number of basis functions and up-sampling ratio. The problem is the same as that for Section III; the exact answer is 1.7071.

Table 2. Results for GBF TE EFIE; Compare to 1.7071

Number of Basis Functions	Up-Sampling Ratios		
	1.2	1.5	2.0
8	1.6877	1.6962	1.7022
16		1.7060	1.7066
32	1.7068	1.7069	1.7070

V. Results for Square Cross Section Cylinder

Scattering was calculated for the problem of a plane wave, with unit magnetic field, incident on a square cylinder with sides 11 λ_0 wide. The angle of incidence was at a 45° angle to one of the sides. It was found that the TM EFIE formulation was improved by using the same up-sampling scheme as was necessary for the TE EFIE formulation. Figures 1-3 show calculated current density as a function of azimuth angle, with 0° corresponding to the direction towards the plane wave source. The reference data were generated with a combined-field integral equation model with 640 unknowns [4]. The agreement of the TM EFIE GBF and TE EFIE GBF formulations with the reference data was good. The agreement of the TE MFIE GBF formulation with the reference data was excellent.

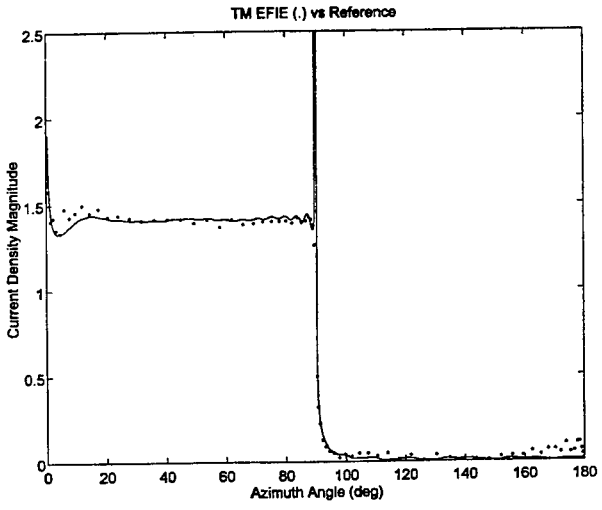

Figure 1. Comparison to Reference Data of TM EFIE GBF Results Generated with 160 Unknowns and an Up-Sampling Ratio of 1.8.

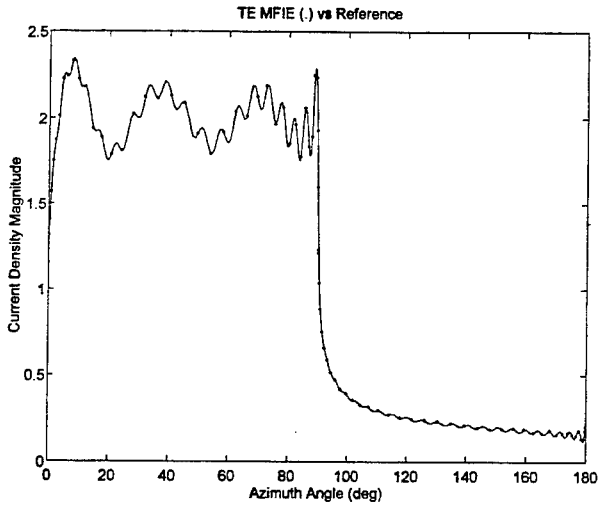

Figure 2. Comparison to Reference Data of TE MFIE GBF Results Generated with 160 Unknowns and No Up-Sampling.

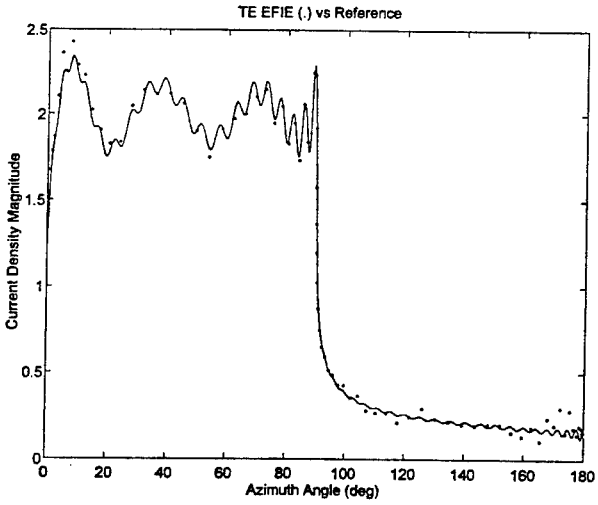

Figure 3. Comparison to Reference Data of TE EFIE GBF Results Generated with 160 Unknowns and Up-Sampling Ratio of 1.8.

VI. Extension to Three Dimensional Surfaces

We are currently investigating the extension of a similar GBF approach to three dimensional surfaces. This involves the mapping of the surface onto a sphere. Scalar interpolation functions have been designed to cover uniformly spaced constant-θ contours, each having an arbitrary number of points uniformly spaced in ϕ. These basis functions have been designed to preserve continuous derivatives at the poles of the sphere. Vector basis functions have been formulated by creating continuous, closed-loop vector fields, and weighting them with the scalar interpolation functions. A curvature correction for the TE MFIE diagonal matrix elements has been derived in a manner similar to that discussed in Section III. We are experimenting with an alternative method of handling singularities, that of performing coordinate transformations to place the pole of a new sphere at each observation point, allowing the $\sin(\theta)$ term in the integration over the new sphere to kill off the singularity. It is expected that results will be available in time for the presentation of this work.

REFERENCES

[1] R. M. James, "On The Use of Fourier Series/FFT's as Global Basis Functions in the Solution of Boundary Integral Equations for EM Scattering," IEEE Trans. Antennas Propagat, vol. 42, no. 9, pp. 1309-1316, Sept. 1994.

[2] M. Abramowitz and I. E. Stegun, Eds., *Handbook of Mathematical Functions*, Washington, D.C., U.S. Government Printing Office, 1972, Sect. 9.

[3] Peterson, Ray and Mittra, *Computational Methods for EM Scattering*, IEEE Press, in preparation.

[4] K. R. Aberegg and A. F. Peterson, "Application of the Integral Equation - Asymptotic Phase Method to Two-Dimensional Scattering," IEEE Trans. Antennas Propagat, vol. 43, no. 5, pp. 534-537, May 1995.

A NUMERICALLY STABLE METHOD OF MOMENTS TIME DOMAIN MODEL

L.B. Gravelle+ and J.-P. Estienne*
+Scientific Research & Modeling, Ottawa, Ontario, Canada.
*MATRA MARCONI Space, Toulouse, France.

Abstract - **An implicit time domain model for the analysis of wires and conducting surfaces is presented. The model is based on the method of moments numerical technique using Lagrange second order time domain basis functions which plays an important role on the road to stability. With this type of formulation, the method of moments can finally be utilized for the analysis of fast transients directly in the time domain for structures including wires and surfaces. The model's stability and accuracy are presented for a complex systems including conducting surfaces, transmission lines and non-linear loads.**

1. INTRODUCTION

The aim of this paper is to present a numerically stable technique able to calculate transient currents and fields associated with wire and surface structures including junctions between wires and surfaces. This numerical technique will be able to analyze the electromagnetic response of three-dimensional objects to an impinging field and/or to a conducted source (voltage or current source). It is very well suited to the analysis of antennas, circuits as well as field penetration/coupling onto various structures (satellites, air planes, equipment, ...).

The formulation is an integro-differential equation technique for time domain analysis of thin wire/surface structures. Through the use of the method of moments (MOM), the integral equation, defining the time-dependent current distribution on a wire/surface structures, is reduced to a system of equations to be solved simultaneously for each time steps as an initial valued problem.

The first development in this area is due to Miller and Burke in the 70's. They developed a transient scattering model [1] solving directly in time, via the MOM, the scattering of thin wire structure. This was the first time that the E.F.I.E. (Electric Field Integral Equation) was solved using the MOM in the time domain. The scatterer was defined as a collection of interconnected wires. Kirchoff's law was not strictly applied at multiple wire-node junction locations, since the current was expanded at the center of each segment as second order Legendre polynomial in both time and space. Except for an extension of the Miller model to surfaces [2] (continuity of currents on the edges wasn't forced), there was no significant progress during the next two decades.

Recently, with the new capabilities of the modern digital computers, advances in electromagnetic computational methods have been made possible. Rao [3] presented an equivalent solver for surfaces only, which uses edge functions and first order expansion in time. The algorithm is of first order accuracy in time with edge functions, leading to an iterative explicit algorithm, a marching-on-in-time solution. Unfortunately, instabilities appear very early . For this reason, it is not applicable to large structures such as satellites. Furthermore, the addition of wire is not reported.

In the following section the theory behind the model will be presented. We will start with a general overview of the field equations. Then we present the boundary conditions followed by the critical selection of the basis function. These theories will lead us to the E.F.I.E. formulations on which the MOM shall be applied.

2. THE THEORY BEHIND THE MODEL

The type of formulation used is based on the E.F.I.E. for which three-dimensional objects may be represented by electrically small elements where the current information is concentrated in one plane. Within wire structures, the total current on the wire is concentrated at its center, therefore when applying the tangential electric field boundary condition on the surface of the wire, no singularities occur at the field evaluation points. For the case of surface structures, the total inside and outside surface currents are concentrated on an infinitely thin surface, therefore eliminating instability that would be induced by the very small discretisation of the metal thickness.

2.1. THE GENERAL FIELD EQUATION

Starting with Maxwell's equations, we first derive Faraday's equation. In Faraday's equation, the electric field E is expressed in terms of the scalar potential ϕ and the magnetic vector potential **A** as follows:

$$\vec{E}(\vec{r},t) = -\nabla\phi - \frac{\partial \vec{A}(\vec{r},t)}{\partial t} \tag{1}$$

where the magnetic vector potential, A, is defined via the current distribution vector, **J**:

$$\vec{A}(\vec{r},t) = \frac{\mu}{4\pi}\int_V \frac{\vec{J}(\vec{r}',\tau)}{R}\,dv' \tag{2a}$$

and the scalar potential, ϕ, via the charge density scalar, ρ:

$$\phi(\vec{r},t) = \frac{1}{4\pi\varepsilon}\int_V \frac{\rho(\vec{r}',\tau)}{R}\,dv' \tag{2b}$$

In equation (2) μ and ε are respectively the permeability and permittivity of the surrounding medium, V represent the integration volume, R (=|**r**-**r**'|) is the distance between the observation point **r** and the source point **r**' and τ (=t-R/c) is the retarded time. By introducing some basic assumptions with respect to wires:

- The radial component of the current is uniform
- The currents are localized on the external surface of the wire (skin effect)

and surface:

- The internal and external surface currents are concentrated on a mathematically thin surface,

the volume integrals may be reduced to contour integrals for wires and surface integrals for patches. Thus Faraday's equation may then be re-written as an integro-differential equation, referred to in the literature as E.F.I.E.:

- Wires

$$\vec{E}(\vec{r},t) = -\frac{1}{4\pi\varepsilon}\vec{\nabla}_c\int_{C(r')}\frac{\lambda(\vec{r}',\tau)}{2\pi a\cdot R}\,ds' - \frac{\mu}{4\pi}\frac{\partial}{\partial t}\int_{C(r')}\frac{\vec{I}(\vec{r}',\tau)}{2\pi a\cdot R}\,ds' \tag{3a}$$

- Patches

$$\vec{E}(\vec{r},t) = -\frac{1}{4\pi\varepsilon}\vec{\nabla}_s\int_{S(r')}\frac{\rho(\vec{r}',\tau)}{R}\,ds' - \frac{\mu}{4\pi}\frac{\partial}{\partial t}\int_{S(r')}\frac{\vec{J}(\vec{r}',\tau)}{R}\,ds' \tag{3b}$$

where a is the radius of the wire.

Equation (3) presents an important disadvantage, there are two unknowns (**I** & λ for wires and **J** & ρ for patches) to solve which, in computer terms, translates into twice the memory requirements and a fourfold increase in CPU time. We may get rid of one unknown through the use of the equation of continuity:

$$\vec{\nabla}_c \cdot \vec{I}(\vec{r},t) = -\frac{\partial \lambda(\vec{r},t)}{\partial t} \tag{4}$$

At this point we introduce a new quantity, ψ, which is the time derivative of the scalar potential ϕ:

- Wires

$$\psi(\vec{r},t) \equiv \frac{\partial \phi(\vec{r},t)}{\partial t} = -\frac{1}{4\pi\varepsilon}\int_{C(r')} \frac{\vec{\nabla}'_c \cdot \vec{I}(\vec{r}',\tau)}{2\pi a \cdot R}\, ds' \tag{5a}$$

- Patches

$$\psi(\vec{r},t) \equiv \frac{\partial \phi(\vec{r},t)}{\partial t} = -\frac{1}{4\pi\varepsilon}\int_{v} \frac{\vec{\nabla}'_s \cdot \vec{J}(\vec{r}',\tau)}{R}\, dv' \tag{5b}$$

By taking the time derivative of equation (3) and introducing equation (5) we derive the following basic equations for the models:

- Wires

$$\frac{\partial \vec{E}(\vec{r},t)}{\partial t} = +\frac{1}{4\pi\varepsilon}\vec{\nabla}_c \int_{C(r')} \frac{\vec{\nabla}'_c \cdot \vec{I}(\vec{r}',\tau)}{2\pi a \cdot R}\, ds' - \frac{\mu}{4\pi}\frac{\partial^2}{\partial t^2}\int_{C(r')} \frac{\vec{I}(\vec{r}',\tau)}{2\pi a \cdot R}\, ds' \tag{6a}$$

- Patches

$$\frac{\partial \vec{E}(\vec{r},t)}{\partial t} = \frac{1}{4\pi\varepsilon}\vec{\nabla}_s \int_{S(r')} \frac{\vec{\nabla}'_s \cdot \vec{J}(\vec{r}',\tau)}{R}\, ds' - \frac{\mu}{4\pi}\frac{\partial^2}{\partial t^2}\int_{S(r')} \frac{\vec{J}(\vec{r}',\tau)}{R}\, ds' \tag{6b}$$

2.2. *The Boundary Conditions*

Applying the boundary conditions characterizing the problem at hand we are able to derive the appropriate formulation. For this application we know that the total tangential electric fields on the surface of a perfectly conducting metal is zero,

$$\left.\begin{aligned} \vec{E}^T_{//} &= \vec{E}^I_{//} + \vec{E}^S_{//} \\ \frac{\partial}{\partial t}\vec{E}^T_{//} &= \frac{\partial}{\partial t}\vec{E}^I_{//} + \frac{\partial}{\partial t}\vec{E}^S_{//} \end{aligned}\right\} = 0 \tag{7}$$

where T denotes the total electric fields, I the incident fields and S the scattered fields. Distributed and lumped equivalent electric components may also be introduced by imposing the total tangential electric fields on the surface to

$$\begin{aligned} \vec{E}^T_{//} &= Z(t)\cdot\vec{J}_{//} \\ \frac{\partial}{\partial t}\vec{E}^T_{//} &= \frac{\partial}{\partial t}\left\{Z(t)\cdot\vec{J}_{//}\right\} \end{aligned} \tag{8}$$

in which Z(t) represents the electrical condition imposed on the surface of the object (and/or at the node of a wire segment).

Substituting the boundary condition for perfectly conducting surface, equation (7), into the electric field integral equation (6) we obtain, by projecting the electric field onto the surface, the following integro-differential equation in the time domain:

- Wires

$$\frac{\partial \vec{E}^I_{//}(\vec{r},t)}{\partial t} = -\frac{1}{4\pi\varepsilon}\vec{\nabla}_c\int_{C(r')}\frac{\vec{\nabla}'_c\cdot\vec{I}_{//}(\vec{r}',\tau)}{2\pi a\cdot R}ds' + \frac{\mu}{4\pi}\frac{\partial^2}{\partial t^2}\int_{C(r')}\frac{\vec{I}_{//}(\vec{r}',\tau)}{2\pi a\cdot R}ds' \qquad (9a)$$

- Patches

$$\frac{\partial \vec{E}^I_{//}(\vec{r},t)}{\partial t} = -\frac{1}{4\pi\varepsilon}\vec{\nabla}_s\int_{S(r')}\frac{\vec{\nabla}'_s\cdot\vec{J}_{//}(\vec{r}',\tau)}{R}ds' + \frac{\mu}{4\pi}\frac{\partial^2}{\partial t^2}\int_{S(r')}\frac{\vec{J}_{//}(\vec{r}',\tau)}{R}ds' \qquad (9b)$$

where $\mathbf{I}_{//}(\mathbf{r}',\tau)$ & $\mathbf{J}_{//}(\mathbf{r}',\tau)$ are the current at the source point r' and at retarded time τ.

2.3. *THE BASIS FUNCTIONS*

The definition of an appropriate basis function is the most important part of the model development. The function must be able to follow the wire current variations as closely as possible while remaining as simple as possible. A complex function will lead to an non-derivable formulation or a formulation involving complex, time consuming numerical integration.

The temporal approximation should be of the second order since their is a double time derivative of the unknown (a first order function is possible but lead to less accurate results, finite difference would be required). As for the spatial approximation, a first order function shall limit the complexity of the formulation while still representing the wire current fairly accurately.

In order to follow the wire current variations, the object is discretised into sub-sections. Within each sub-section the current is approximated by the chosen basis function leading to a system of equations. This system of equations is defined by the inter-relationship of each sub-section unknown current.

The unknown wire current is approximated on each segments/patches by a function (the basis function), it is defined as follows:

$$\vec{J}(\vec{r}',t') = \sum_{i=1}^{N_e+N_w}\sum_{j=1}^{N_T}\vec{J}_{i,j}\left(\vec{r}'-\vec{r}_i, t'-t_j\right)\cdot U\left(\vec{r}'-\vec{r}_i\right)\cdot V\left(t'-t_j\right) \qquad (10)$$

where N_e, N_w & N_T are respectively the number of edges, wire nodes and time steps. This summation allows us to have a general expression defining all the currents on the objects. The functions U and V are pulse functions defined below,

$$U\left(\vec{r}'-\vec{r}_i\right) = U\left(\vec{r}''_i\right) = \begin{cases} 1 & ;\ \vec{r}' \in \left(S_i^{\pm}, T_i^{\pm}\right) \\ 0 & ;\ \vec{r}' \notin \left(S_i^{\pm}, T_i^{\pm}\right) \end{cases} \qquad (11)$$

$$V\left(t'-t_j\right) = V\left(t''_j\right) = \begin{cases} 1 & ;\ \left|t'-t_j\right| \le \delta_j/2 \\ 0 & ;\ \left|t'-t_j\right| > \delta_j/2 \end{cases} \qquad (12)$$

The unknown wire/surface currents are approximated on each segments/patches by the following basis function:

$$\vec{J}_{i,j}\left(\vec{r}_i^{\,"}, t_j^{"}\right) = \begin{cases} \left(\sum_{s=-}^{+} \sum_{m=n}^{n+2} B_j^m\left(t_j^{"}\right) \cdot \vec{\Lambda}_i^s\left(\vec{r}_i^{\,"}\right) \right) \cdot J_{i,j+m} & ; \text{ if } \vec{r}' \in \left(S_i^{\pm}, T_i^{\pm}\right) \\ 0 & ; \text{ if } \vec{r}' \notin \left(S_i^{\pm}, T_i^{\pm}\right) \end{cases} \tag{13}$$

where $S_i^{\pm}$ and $T_i^{\pm}$ refer respectively to the segments and patches (the ± sign refers to a convention determining the segment/patch connected to node/edge i), $\Lambda_i^s(r_i^{"})$ is the spatial basis function for both segments and patches as defined in the report by Hwu and Wilton [4], s takes on the + or - sign convention and the temporal basis function, B_j^m, the second order Lagrange polynomial:

$$B_j^m\left(t_j^{"}\right) = \prod_{\substack{q=n \\ q \neq m}}^{n+2} \frac{t_j^{"} + t_j - t_{j+q}}{t_{j+m} - t_{j+q}} \tag{14}$$

The variable n in the previous summation is chosen in such a way as to force the temporal interpolation into the past and present time. Interpolation into the future would cause erroneous results because of the causal nature of the phenomena, it is not allowed. Thus,

$$\text{for } \vec{r}' \in \left(S_i^{\pm}, T_i^{\pm}\right) \;\; \& \;\; t_j^{"} \leq \delta_j / 2 \text{ we have } \quad n = \begin{cases} -2 & \text{if } \dfrac{\left|\vec{r}' - \vec{r}\right|}{c \cdot \delta} \leq 0.5 \\ -1 & \text{if } \dfrac{\left|\vec{r}' - \vec{r}\right|}{c \cdot \delta} > 0.5 \end{cases}.$$

The spatial basis function, $\Lambda_i^s(r_i^{"})$, is defined as follows:

- Wires

$$\vec{\Lambda}_i^{\pm}\left(\vec{r}_i^{\,"}\right) = \alpha_i^{\pm} \frac{\vec{\rho}_i^{"\pm}\left(\vec{r}_i^{\,"}\right)}{2\pi a_i^{\pm} \cdot h_i^{\pm}} \tag{15a}$$

  we include the radius in the wire spatial basis function since the radius may be varying between segments.

- Patches

$$\vec{\Lambda}_i^{\pm}\left(\vec{r}_i^{\,"}\right) = \alpha_i^{\pm} \frac{\vec{\rho}_i^{"\pm}\left(\vec{r}_i^{\,"}\right)}{h_i^{\pm}} \tag{15b}$$

in which $\alpha_i^{\pm} = \begin{cases} +1 & \text{if } \left|\vec{r}' - \vec{r}_i\right| \in S_i^{+} \\ -1 & \text{if } \left|\vec{r}' - \vec{r}_i\right| \in S_i^{-} \end{cases}$.

The vector representation of the spatial basis function is shown in figure 1.

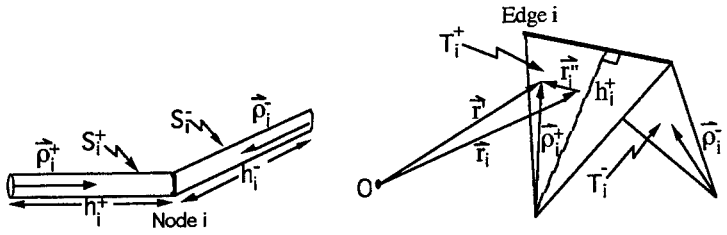

Figure 1. Vector representation of the spatial basis functions.

2.4. APPLYING THE MOM TECHNIQUE

The technique of moments enables us to solve an integro-differential system by transforming the problem into a linear system. The linear system is obtained by applying the boundary conditions coupled with a testing procedure. The weighting functions chosen for the present application are Dirac functions for the temporal content and a Galerkin type for the spatial content:

- spatial weighting functions => basis functions
- Temporal weighting functions => Dirac functions

The weighting functions are defined on an observation node, u, common to the observation segments S_u^+ & S_u^- :

$$\vec{g}_{u,v}^{\pm} = \vec{\Lambda}_u^{\pm}\left(\vec{r}_u''\right)\cdot\delta\left(t - t_v\right) \tag{16}$$

where

- Wires

$$\vec{\Lambda}_u^{\pm}\left(\vec{r}_u''\right) = \begin{cases} \alpha_u^{\pm}\dfrac{\vec{\rho}_u''^{\pm}\left(\vec{r}_u''\right)}{2\pi a_u^{\pm}\cdot h_u^{\pm}} & \text{if} \quad \left|\vec{r}_{obs} - \vec{r}_u\right| \in S_u^{\pm} \\ 0 & \text{if} \quad \left|\vec{r}_{obs} - \vec{r}_u\right| \notin S_u^{\pm} \end{cases} \tag{17a}$$

- Patches

$$\vec{\Lambda}_u^{\pm}\left(\vec{r}_u''\right) = \begin{cases} \alpha_u^{\pm}\dfrac{\vec{\rho}_u''^{\pm}\left(\vec{r}_u''\right)}{h_u^{\pm}} & \text{if} \quad \left|\vec{r}_{obs} - \vec{r}_u\right| \in T_u^{\pm} \\ 0 & \text{if} \quad \left|\vec{r}_{obs} - \vec{r}_u\right| \notin T_u^{\pm} \end{cases} \tag{17b}$$

and $\delta\left(t - t_v\right) = \begin{cases} 1 & \text{if} \quad t = t_v \\ 0 & \text{if} \quad t \neq t_v \end{cases}$.

The testing procedure consist of taking the inner product of the E.F.I.E. with the weighting functions:

$$\left\langle \frac{\partial}{\partial t}\vec{E}^I, \vec{g}\right\rangle = -\left\langle \frac{\partial}{\partial t}\phi, \vec{\nabla}\cdot\vec{g}\right\rangle + \left\langle \frac{\partial^2\vec{A}}{\partial t^2}, \vec{g}\right\rangle \tag{18}$$

where the inner product is defined as

$$\langle \vec{f}, \vec{g} \rangle \equiv \iint_s \vec{f} \cdot \vec{g}\, ds \qquad (19)$$

$\vec{f}$ being the E.F.I.E. operator.

The final system of equations is obtained by separating the wire current contributions previously calculated ($t < t_v$) from the unknown node/edge currents at time t_v. This will result in an iterative numerical solution of a matrix Z multiplying the unknown vector **J** of which the product equals the source vector (impinging fields, current and/or voltage sources and the radiated wire/patch current contributions).

3. NUMERICAL RESULTS

The case studies presented in this section aim to present the good correlation between this model and available data in the literature, the stability of the simulations as well as the possibility of analyzing complex structures including wire-to surface junctions, non-linear components and time-delayed controlled sources. Analyzed are illuminated dipole antennas and surface plate, the radiation from an electrostatic discharge and two transmission lines over a finite ground plane with non-linear elements.

3.1. ILLUMINATED DIPOLE ANTENNA

As a first analysis, we present the current calculated at the center of a 1 meter dipole antenna illuminated by an electric field impinging at a 45 degree angle to the antenna. The source is a gaussian type defined as $E_I(t) = A*\exp(-\alpha^2*(t_c-t)^2)$ with A=2340V/m, α=3.63E09 and t_c=2.5ns. The time signature of the dipole's center current has the same form as found in the literature [5], the level vary slightly due to the fact that the field strength and the dipole wire radius were not made available.

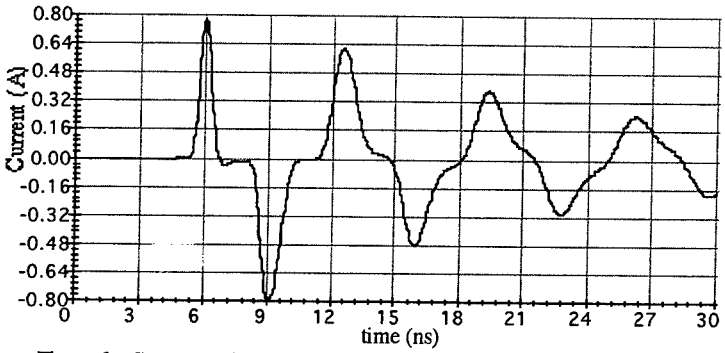

Figure 2. Current at the center of a gaussian illuminated 1m dipole antenna.

3.1. *ILLUMINATED SURFACE PLATE*

Next we present the current calculated at the edge of a 2 meter by 2 meter conducting plate. The plate is illuminated by an electric field impinging at a 90 degree angle to the plate with a gaussian time signature centered at 80ns and an α constant of 5.0E07. In previous time-domain MOM models, [3] & [6], high instabilities where encountered early in the analysis ([6] remedies the problem with the use of FIR filters). The results from our model shows a very stable analysis partially due to the temporal basis function.

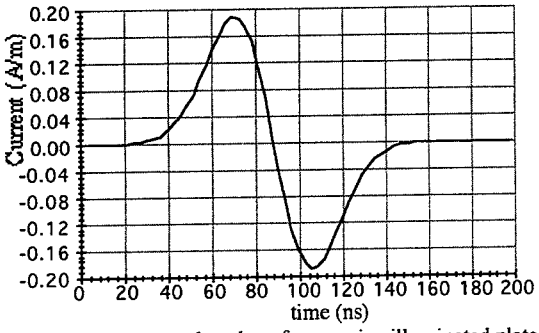

Figure 3. Current at the edge of a gaussian illuminated plate.

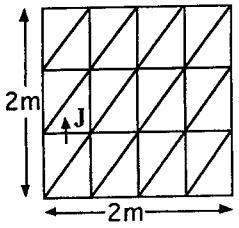

Figure 4. The geometry of the plate.

3.3. *ESD RADIATED FIELD*

From available ESD current measurements the radiated electric field were calculated assuming a dipole as the current carrier and thus the radiator. The current signature, see the inset graph in Figure 6, was defined with the use of an ESD and a rounded step functions, it's peak amplitude is 11 A with a 1ns rise time. The electric field was calculated at 1.5m away in broadband. Shown in Figure 5 are the result of the measurements and the dipole model presented by Ma [7], and in Figure 6 the result of the MOM model. The difference between the experiment and the models is due to simplicity of the chosen dipole radiator, nevertheless the results between the experiment and the MOM model are very similar.

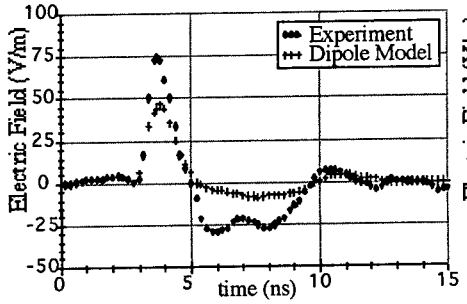

Figure 5. ESD radiated field measurements and model from Ma.

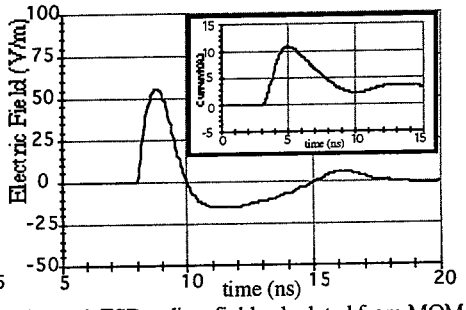

Figure 6. ESD radiate field calculated from MOM, on the inset graph the ESD current time signature.

3.4. *Transmission Lines over Finite Ground Plane*

A validation of the model for a complex system is presented in figures 7 through 9. The system analyzed consist of a 10x4cm plate discretised into triangular patches onto which is connected two transmission lines represented by wires of 1mm diameter and 2cm long. The transmission lines are coupled by induction as well as through a voltage controlled voltage source with a time delay, $V_L(t) = 10000*R_S*I_S(t-160ns)$; the source resistance, R_S, is set to $1m\Omega$; the load resistance, R_L, is set to 100Ω; the voltage source is a pulse with a rise and fall time of 10ns and a pulse width of 30ns centered at 35ns; and the non-linear inductance is a step function starting at 20nH with a fall time of 30ns centered at 100ns (the intrinsic inductance of the transmission lines is also 20nH). The stability of the time domain method of moment model is well demonstrated by the analysis of this system.

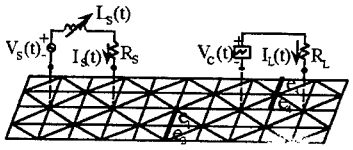

Figure 7. Transmission line structure.

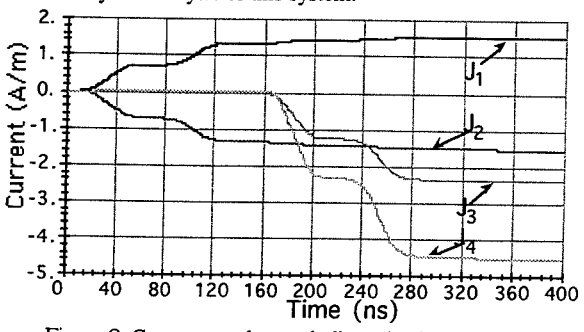

Figure 8. Currents on the patch discretized ground plane.

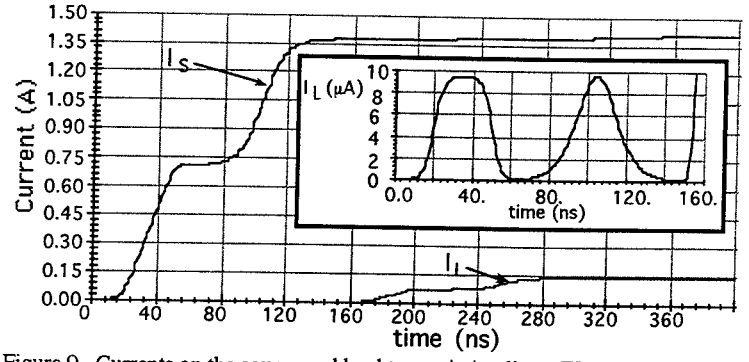

Figure 9. Currents on the source and load transmission lines (TLs), on the inset graph is shown the induced current on the load TL due to the current of the source TL.

4. CONCLUSION

In the above discussion, a new numerical time domain boundary integral method is presented. The method is implicit and demonstrates very stable results. We demonstrated its utility with a survey of various applications. Basic examples were chosen to validate the MOM model. They also demonstrated the accuracy, convergence and stability properties of the method. A complex structure was analyzed to present the versatility of the model.

This type of formulation is very well suited for the analysis of antennas for which their response to transient electromagnetic excitation are still not well understood. Moreover with this method, the analysis of antennas or circuits loaded with discrete elements (linear or time-dependent) is readily obtained. Previous method solving such time-domain problems were analyzed via a frequency domain type of formulation along with the inverse Fourier transform. This yields a tedious and time consuming simulation for non-harmonic excitations or elements. The direct technique offers greater efficiency than transformation techniques (FFT and FFT^{-1}), the ability to treat non-linearities, the convenience of wide broad-band information from a single calculation and the resonnances of complex objects.

As opposed to other methods, finite difference and finite elements, for which the total region needs to be discretised, the method of moments is a numerical technique that is well adapted to three-dimensional geometries.

REFERENCES

[1] Miller, E.K., A.J. Poggio and G.J. Burke, "An integro-differential equation technique for the time domain - Analysis of thin wire structures," *Journal of computational physics*, no. 12, pp.24-18 , 1973.

[2] Beneguel,Y., "Etude de la forme temporelle se l'équation intégrale du champ électrique. Application aux antennes," *Annales des télécommunications*, Mai-juin, 1983.

[3] Rao, S.M. and D.R. Wilton, "Transient scattering by conducting surfaces of arbitrary shape," *IEEE Trans. on Antennas Propagation*, vol. AP-39, no. 1, Jan.1991.

[4] Hwu, S.-U. and D.R. Wilton, Electromagnetic Scattering and Radiation by Arbitrary Configurations of Conducting Bodies and Wires, Technical Report Number 87-17, Department of Electrical Engineering, University of Houston, Texas, May 1988.

[5] Landt, J.A., E.K. Miller and F.J. Deadrick, Time-Domain Computer Models of Thin-Wire Antennas and Scatterers, Technical Report Number UCRL-74848, Lawrence Livermore Laboratory, Livermorek, CA, Nov. 1973.

[6] Sadigh, A. and E. Arvas, "Treating the instabilities in marching-on-in-time method from a different perspective," *IEEE Trans. on Antennas Propagation*, vol. AP-41, no. 12, pp. 1695-1702 , Dec.1993.

[7] Ma, M.T., "How high is the level of electromagnetic fields radiated by an ESD?," in *Proc. 8th Int. EMC Symp.* (Zurich, Switzerland), pp. 361-365, March 1989.

Method of Moments Analysis of the Celestron-8 Telescope

R. R. DeLyser, P. Ensaf
University of Denver
Denver, Colorado

P. McDaniel
Phillips Laboratory/WSA
Kirtland AFB, New Mexico

Background

This paper describes numerical analyses on a Celestron-8 telescope (Figure 1) in order to determine its susceptibility to high power microwaves. Beginning with analysis at low frequencies, the initial approach was to model the telescope's outer most shell as an open ended cylinder. Even though there is an aperture for the eyepiece, it is sufficiently small at low frequencies to ignore. We modeled the resulting open ended cylinder using Mathematica [1], and analyzed that model using CARLOS-3D [2] (Code for Analysis of Radiators on Lossy Surfaces) over a frequency range of 0.7 GHz - 3.0 GHz. We then proceeded to create a model which included the interior geometry of the telescope which consisted of two interior cylinders and the aperture for the eyepiece. The interior cylinders (Figure 1) are at the center of the large aperture, where a convex reflecting mirror resides (the short plastic cylinder) and at the eyepiece (the long metal cylinder). The two reflecting mirrors are not shown in Figure 1. The CARLOS-3D model (Figure 2) was analyzed over a frequency range of 0.5 GHz to 3.0 GHz. Each of the models, the open cylinder and that shown in Figure 2, were discretized with triangular cells, each having sides no longer than 1/10 of a wavelength (λ) in length corresponding to a frequency of 1.0 GHz. The models are illuminated at incidence angles θ and ϕ (see Figure 2) both equaling 45°.

Also of interest was the verification and validation of the results using different discretization techniques. We therefore discretized the model in Figure 2 for cell side lengths of $\lambda/5$ at 1.0 GHz. We analyzed this model for a frequency range of 0.5 GHz -3.0 GHz and compared the results for Quality Factor (Q), total energy, and exiting power for the $\lambda/5$ discretized model to those of $\lambda/10$ model. We noticed pronounced differences in the results over this frequency range. These results, other problems encountered while using CARLOS-3D, and methods for rectification of these problems are discussed in the following.

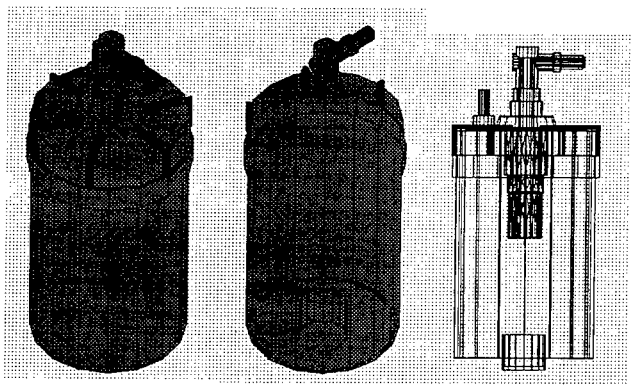

Figure 1. The Celestron-8 telescope.

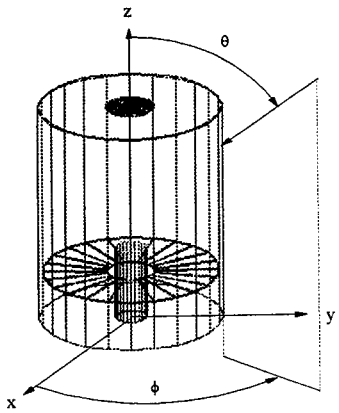

Figure 2. The CARLOS-3D model for the telescope.

Preliminary Observations

The interior of the model of figure 2 was divided into cubes of side length 1.5 cm (λ/10 at 2.0 GHz). A total of 3717 grid points were created. These grid points are the locations of the field points calculated by CARLOS-3D. Using the fundamental equations describing the electric and magnetic energies along with power exiting the cavity, we calculated Q [3, 4] for the cavity given by

$$Q = \omega \frac{U}{P} \tag{1}$$

where ω is the operating angular frequency, U is the total energy in the cavity and P is the power exiting the cavity. In order to investigate mesh sizes, we discretized the model of Figure 2 to λ/5 and λ/10 at 1.0 GHz and analyzed that model over frequency range of 0.5 GHz up to 3.0 GHz. Figure 3 shows that the results for these models are profoundly different.

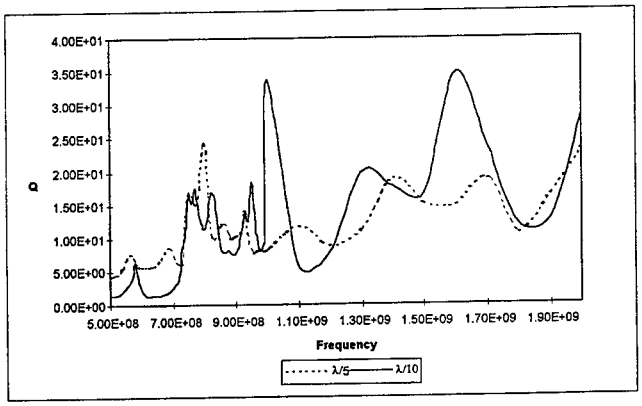

Figure 3. Telescope model quality factors, θ polarization, λ/5 and λ/10 models.

These discrepancies led us to further investigate meshes using only the open cylinder model with two different discretization schemes, λ/10 and λ/18 at 1.0 GHz. We analyzed these models for a frequency range of 0.1 GHz to 2.0 GHz. Again the results were very different. At this point it was clear that we had to investigate fully the problems with CARLOS-3D that lead to different results for different meshes. This final report addresses five areas of study: (1) the field calculations in CARLOS-3D, (2) non-uniform meshing schemes, (3) the matrix solution in CARLOS-3D and how it might be improved using iterative refinement and improved Gaussian Quadrature, (4) High Frequency Structure Simulator (HFSS) models and results, and (5) testing results.

Field Calculation Method and Results

We first approached the meshing problem by comparing the field quantities for the open cylinder models (λ/10 and λ/18). Doing this, we realized that there were large differences in field values near the cylinder walls compared to those field values more towards the center of the cylinder. During conversations with the creators of CARLOS-3D, we discovered that even though the currents throughout each cell are known, CARLOS-3D calculates near fields using values of currents at the centroid of each triangular cell. In this scenario, each current source will now act similar to an infinitesimal dipole. Therefore, the field quantities are calculated using [5]

$$E_z(x,y,z) \propto \sum_{n=1}^{N} \frac{e^{-jkr_n}}{kr_n{}^3} \cos(\theta) J_n \qquad (2)$$

where k is the propagation constant, J_n is the n_{th} surface current, and r_n is the distance from the n_{th} surface current to the field point. This model differs significantly from one that can be used with takes advantage of the current distributions that are known. In that case the distance r from the field point varies according to where the current is calculated on the surface. The distance r is a very critical quantity since for small r, the inverse cubic variation will have a large effect on the field calculations. Figures 4, 5 and 6 show the percent difference between the λ/10 and λ/18 models in the electric field quantities along the x-axis at the end cap, the center, and at the aperture. It is evident in Figures 4, 5 and 6 that the biggest differences are close to the cavity boundary. This error is caused by the crude approximation used to calculate the near fields. A more suitable approach would be to use a solution technique which considers the changes in r along with changes in the current density. This solution is given by [6]

$$\mathbf{E}^s(\mathbf{r}) = -j\omega\mu \int_{\partial V_s} \mathbf{J}_s(\mathbf{r}')g(r,r')ds + \nabla \int_{\partial V_s} \frac{1}{j\omega\varepsilon} \nabla'\cdot\mathbf{J}_s(\mathbf{r}')g(r,r')ds' \qquad (3)$$

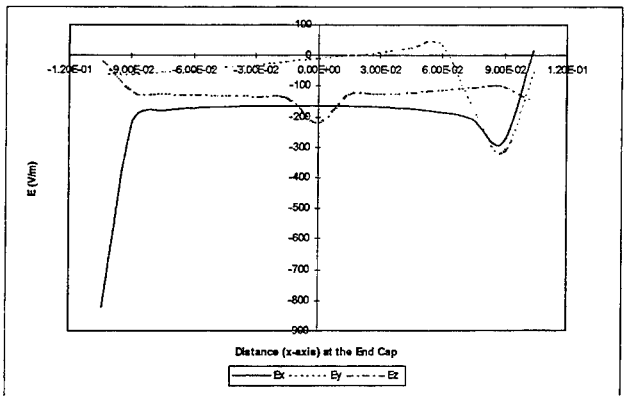

Figure 4. Percent difference in the electric field quantities for both models, end cap.

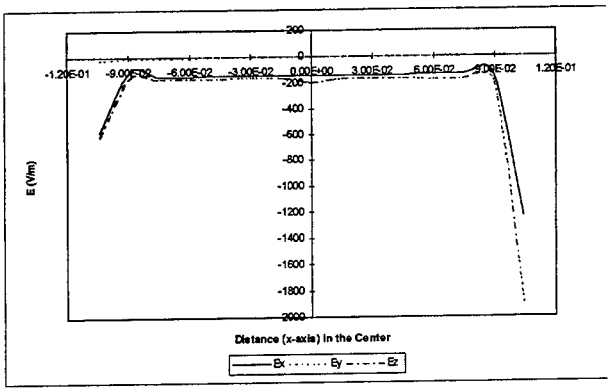

Figure 5. Percent difference in the electric field quantities for both models, center.

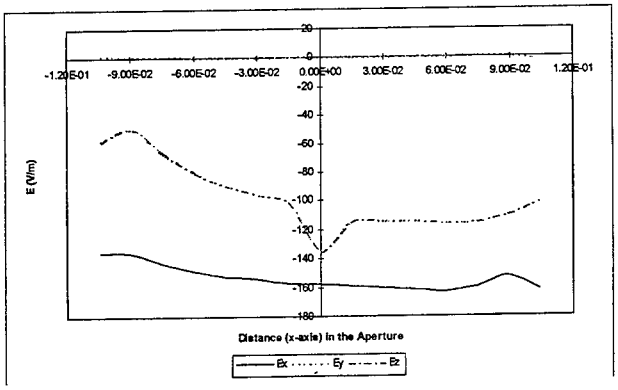

Figure 6. Percent difference in the electric field quantities for both models, at the aperture.

where $g(r,r')$ is the free space Green's Function, ω is the angular operating frequency, ε and μ are the permittivity and permeability of free space, respectively. The functional dependence of $\mathbf{J}_s(\mathbf{r})$ is determined by the basis functions which are linear.

Meshing Methods And Results

In the neighborhood of a conducting edge, electric and magnetic field components behave in a particular manner dependent on the wedge angle ϕ_o [7]. The electric field is given by

$$E \propto \rho^{\nu} \sin(\nu\phi) \qquad J_z \propto \rho^{\nu-1} \tag{5}$$

where

$$\nu = \frac{\pi}{\phi_o} \tag{6}$$

At the open edge of the open cylinder, $\phi_o=2\pi$, and at the end cap $\phi_o=3\pi/2$. For our geometry then, at the top edge $J_\phi \propto \rho^{-1/2}$ and at the bottom edge $J_\phi \propto \rho^{-2/3}$. A program was written to vary the width of the triangular cells to accurately model the edge currents. A constant current was maintained through each cell edge corresponding to its distance from the edge. In this way the cell widths can be determined. Figure 7 shows some results for this meshing scheme.

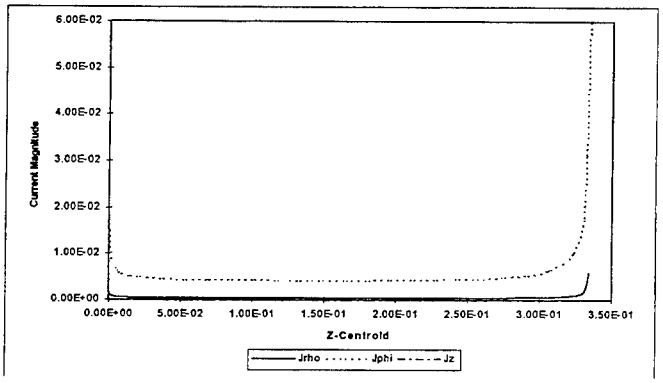

Figure 7. Surface currents using a non-uniform meshing scheme: $\lambda/18$ model, incidence angle is $\theta = 90°$, $\phi = 0°$, ϕ polarization, f = 500 MHz.

At this point, we decided to do another frequency sweep for the $\lambda/10$ and $\lambda/18$ models. The results for Q were still very different. The results for power exiting the cavity and energy for the θ polarization (results are similar for the ϕ polarization) are given in Figures 8 and 9. The energy calculations for the two meshes are much better, but the differences in the power calculations are pronounced. We can see now that the major contributors to different Qs for different meshes are the power differences in the aperture. Graphs of the differences of the power calculations over the aperture for the case of Figures 8 and 9 for the ϕ polarization are shown in Figure 10. These differences can be explained by the fact that our power calculations are at 177 points in the aperture and are vector calculations giving positive and negative

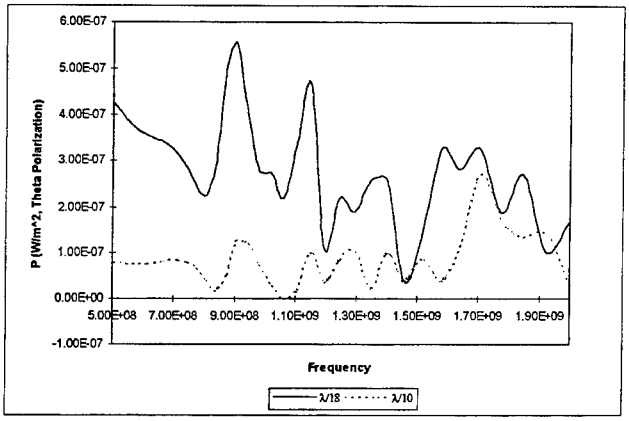

Figure 8. Power for the non-uniform meshes.

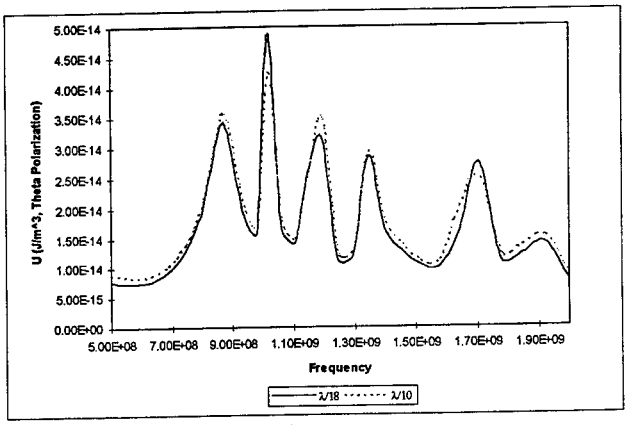

Figure 9. Energy for the non-uniform meshes.

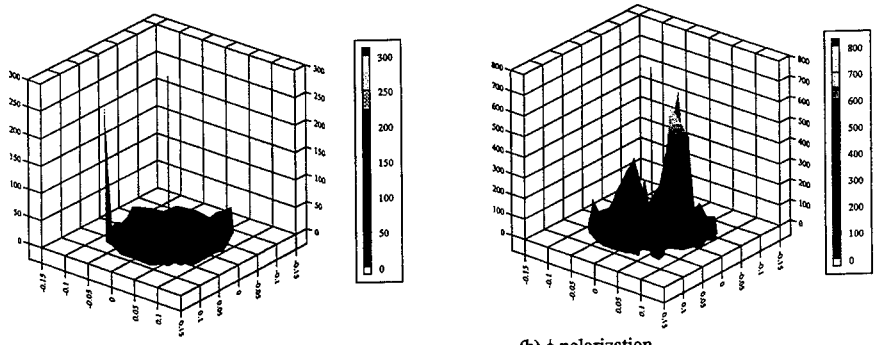

(a) θ polarization. (b) ϕ polarization.

Figure 10. % difference in aperture power magnitude for the non-uniform meshes.

results which are summed over the area of the aperture. This process is inherently prone to more error than the energy calculations which are calculations of field magnitudes (all positive values) over 3717 points that represent the volume of the cavity

High matrix condition number and numerical Integration of the matrix elements

Other numerical difficulties resulting from using CARLOS-3D, may be due to the large condition number of the impedance matrix for large models and the accuracy of the matrix elements. A standard iterative refinement technique was implemented to overcome the high matrix condition number for the large λ/18 model, but no significant changes in the results occurred. However, at higher frequencies or for the full telescope model, this could be a factor. The integrals of the matrix elements are calculated using Gaussian Quadrature. The option exists in CARLOS-3D to change namelist variables to improve the Gaussian Quadrature integrations. Figures 11 - 16 present the percent differences in currents on the cylinder (the primary calculation for this MOM code) for iterative refinement versus iterative refinement and improved Gaussian Quadrature. Note that the differences are greater for currents near the rectangular edge at the end cap.

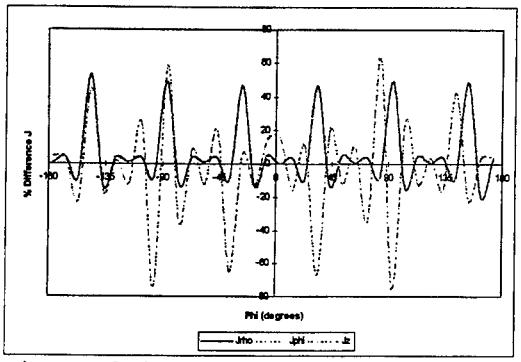

Figure 11. Percent difference in currents for the cylinder side at the end cap for the λ/18 mesh, f = 500 MHz, θ = 90° and ϕ = 0°.

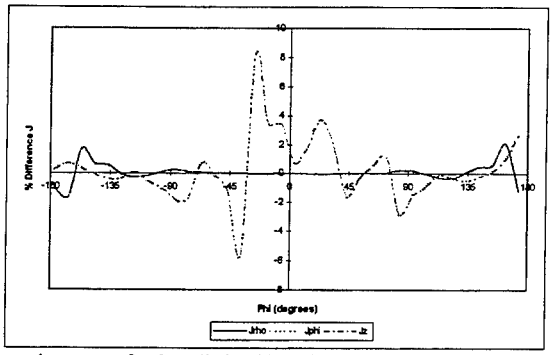

Figure 12. Percent difference in currents for the cylinder side at the center for the λ/18 mesh, f = 500 MHz, θ = 90° and ϕ = 0°.

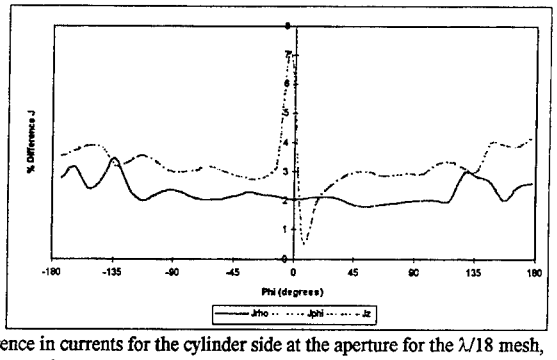

Figure 13. Percent difference in currents for the cylinder side at the aperture for the λ/18 mesh, f = 500 MHz, θ = 90° and ϕ = 0°.

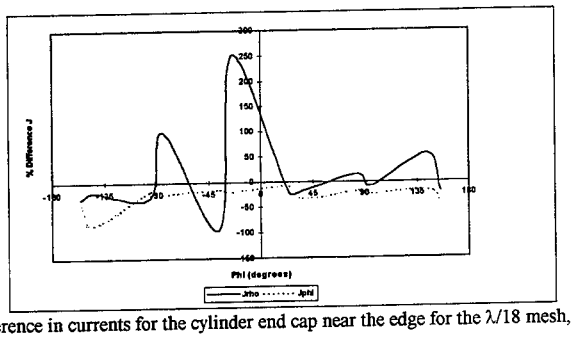

Figure 14. Percent difference in currents for the cylinder end cap near the edge for the λ/18 mesh, f = 500 MHz, θ = 90° and ϕ = 0°.

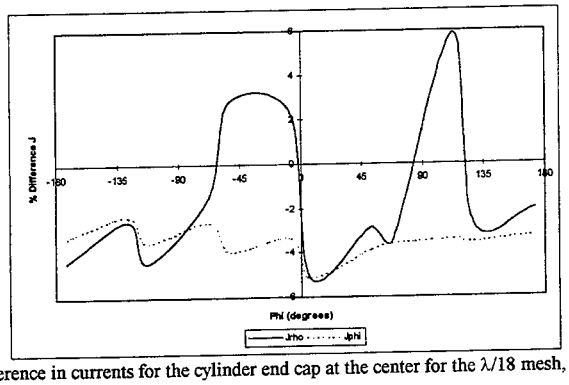

Figure 15. Percent difference in currents for the cylinder end cap at the center for the λ/18 mesh, f = 500 MHz, θ = 90° and ϕ = 0°.

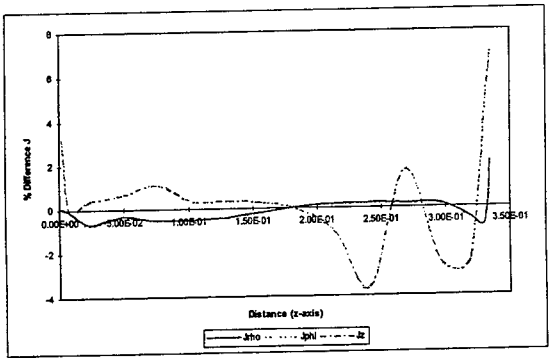

Figure 16. Percent difference in currents for the cylinder side along the z axis at ϕ = 3° for the λ/18 mesh, f = 500 MHz, θ = 90° and ϕ = 0°

CARLOS-3D field results

Figures 17 shows the electric field distribution for the open-ended cylindrical cavity at operating frequencies of 1.8 GHz and 1.35 GHz as given by CARLOS-3D. These frequencies are near the resonance frequencies (1.36 GHz and 1.822 GHz) for the TE_{211} and TE_{311} modes for a closed cylindrical cavity of the dimensions of our open cavity. It is evident that the results obtained from CARLOS-3D show these modes and agree with results from the High Frequency Structure Simulator (HFSS)[8]. The HFSS results have proven to be accurate as compared with the physical testing. This indicates that CARLOS-3D is functioning properly but does not provide the accuracy which is required for calculation of Q. However, implementing the accurate procedure outlined above for calculating the near fields will most likely provide the desired results.

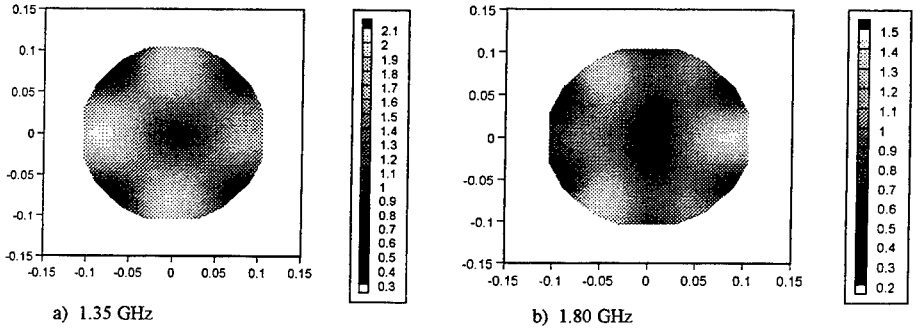

a) 1.35 GHz b) 1.80 GHz

Figure 17. Magnitude of the Electric Field, ϕ=0°, θ=180°, z=16.4 cm

Conclusions

We implemented the method of iterative refinement in order restore full machine precision and to lower the condition number of the impedance matrix generated by MOM but did not make noticeable improvements in the near field calculations. However, all the methods in this report were applied to an empty open-ended cylindrical cavity. Therefore, we may or may not see different responses to the method of iterative refinement related to changes in the internal geometry. Certainly the trend is for higher condition numbers and larger meshes. A full up model of this telescope may result in improvement of the solution using iterative refinement. Improved Gaussian Quadrature did make substantial differences in the results. However, in many situations one does not have the luxury to invest large amount of time to search for suitable quadrature values. Therefore, an adaptive method is necessary in order to avoid comprehensive analysis trying to find the appropriate order of the Gaussian Quadrature.

Non-uniform meshing schemes made substantial improvements in the energy calculations. However, the same improvement was not noticed for the power calculation. The crude approximation for calculating the near fields severely affects the result of these calculations and until the appropriate formulation for calculating the near fields, to include the variations of current over individual triangular cells and of distance to the field point is implemented in CARLOS-3D, adequate accuracy of near fields can not be obtained. CARLOS-3D calculations for this paper were done for an empty open-ended cylindrical cavity. This was done solely to understand the effect of the formulations implemented in CARLOS-3D along with avoiding computationally intensive problem. Once the necessary modifications of CARLOS-3D have been made, the true model of the telescope will be implemented and analyzed.

Acknowledgments

This work was funded by Phillips Laboratory/WSTS and the Air Force Office of Scientific Research.

References

[1] Wolfram, S., Mathematica, Addison-Wesley, 1991.
[2] J.M. Putnam, L.N. Madgyesi-Mitschang and M.B Gedera, CARLOS-3D™ Three Dimensional Method Of Moments Code, McDonnell Douglas Aerospace-East, December 1992.
[3] R. R. DeLyser and P. Ensaf, "Analysis to Determine the Quality Factor of a Complex Cavity," Final Report for the Summer Faculty Research Program at the Phillips Laboratory, Sponsored by the Air Force Office of Scientific Research, September, 1994.
[4] R. R. DeLyser, "An Analysis Approach to Determine Quality Factors of Large , Complex Cavities," Final Report for the Summer Faculty Research Program at the Phillips Laboratory, Sponsored by the Air Force Office of Scientific Research, September, 1993.
[5] Balanis, C.A., Antenna Theory, John Wiley & Sons, New York, pp. 100-109, 1989.
[6] Johnson J.H. Wang, Generalized Moment Method In Electromagnetics, John Wiley & Sons, New York, pp. 74-75, 1991.
[7] Ishimaru, Akira, Electromagnetic Wave Propagation, Radiation, and Scattering, Prentice Hall, New Jersey, pp. 578-580, 1991.
[8] R. R. DeLyser, H. Pohle, "Finite Element Method Analysis of the Celestron-8 Telescope", these proceedings.

SESSION 24:

FDTD ANALYSIS AND APPLICATIONS

Chair: A. Elsherbeni

Dynamic Analysis of V Transmission Lines

Omar M. Ramahi[+], *Atef Z. Elsherbeni*[*], *and Charles E. Smith*[*]

+Digital Equipment Corporation
PKO3-1/R11
129 Parker St.
Maynard, MA 01754, U. S. A.
ramahi@poboxa.enet.dec.com

**Department of Electrical Engineering*
The University of Mississippi
University, MS 38655, U. S. A.
atef@sphinx.ee.olemiss.edu

I. INTRODUCTION

Several new shapes of transmission lines structures have been introduced recently [xx-xx]. These new configuration are proposed to give further flexibility to the design of transmission media that can give characteristics that are otherwise difficult to obtain using traditional microstrip and other structures. Amongst these new configuration is the V transmission line, shown in Fig.1. The V line line is characterized by the angle α, the width of the signal line, and the thickness and composition of the dielectric substrate. These geometrical parameters can give added degrees of freedom to design transmission lines that meet specific requirements. For instance by varying the angle α, the characteristic impedance of the line can be affected while maintaining a fixed substrate thickness. Also, the closer proximity of the ground plane to the signal conductor reduces the electromagnetic coupling and thus crosstalk between adjacent lines. It is also speculated that the V line have additional advantage from an EMC/EMI perspective since it has the potetial of lower radiation.

These new transmission lines configurations, and especially the V line, have thus far been analyzed through the use of conformal mapping techniques which are based on pure-TEM propagation and zero dispersion, or on the use of graphical approximation [1,2]. However under the assumption of pure-TEM or even quasi-static propagation, the dispersive nature of these structures and other propagation features can be overlooked In this work, we employ the Finite Difference Time Domain (FDTD) method to analyze the V line. The strength of the FDTD method is: first, it can comfortably model the intricate irregular geometries involved such as bends; second, it gives a full-wave analysis which the quasi-static study cannot achieve; and third, it gives the response of the transmission line to a very wide band of frequencies in one single computer run.

II. FDTD FORMULATION

The FDTD method has been successfully applied to the analysis of microstrip transmission line structures and has proven a reliable and robust technique for these problems. (There are many excellent papers on the use of FDTD in transmission line structures; see [3,4] for example.) When adapting the FDTD method to the study of the V line, careful considerations have to be given to its non-rectangular geometry. For this, we employ two techniques: The first uses the classical staircase approximation to the slanted metallic sections of the ground plane, and the second employs a recently introduced simple formulation which uses a more accurate polygonal approximation [5].

Let us consider a V line having a cross section in the x-y plane and propagation in the z-direction. Using the polygonal approximation in [5], the H_z component is updated in the FDTD scheme according to the formula:

$$\begin{aligned} H_z^{n+\frac{1}{2}}(i+\frac{1}{2},j+\frac{1}{2},k) = \\ H_z^{n-\frac{1}{2}}(i+\frac{1}{2},j+\frac{1}{2},k) \\ +\frac{2\Delta_t}{\Delta_x\Delta_y}(E_x^n(i+\frac{1}{2},j+1,k)\Delta_x \\ +E_y^n(i,j+\frac{1}{2},k)\Delta_y). \end{aligned} \tag{1}$$

What is noticeable is that this new formulation does not involve any extra calculation than the standard FDTD staircase approximation would require, and it can be directly incorporated into an FDTD code. The only limitation is that the cell size needs to be considered in advance to allow for proper fitting of the metallic boundary in its proper physical location. Nevertheless, this is a minor drawback compared to the implementation effort and cost that other techniques require [6,7].

III. NUMERICAL RESULTS

The authors are not aware of any published results showing either measurement on the V line or any results based on numerical or analytical techniques. Therefore, to allow a measure of corroboration, we considered a V line that was analyzed for its quasi-static behavior in the work of Schutt-Aine [1].

The parameters of the line used in this work are:

1. Width of signal line: 3.18mm.
2. Thickness of the signal line is zero (i.e., the tangential fields of the cells adjacent to the line are set to zero.)

3. Height of substrate: 6.10mm.
4. Dielectric constant of substrate: 2.55
5. $\alpha = 60$ degrees.

The dimensions of the FDTD cells were chosen as follows: $\Delta_x = 0.5545mm$, $\Delta_y = \Delta_z = 0.318mm$. The time step is set to $\Delta_t = 0.278$ picosecond. The excitation pulse is Gaussian with a width of $40\Delta_t$, sufficient enough for predicting the frequency response up to 15GHz. The pulse is turned on at $150\Delta_t$ to eliminate any unwanted high frequency errors. The size of the computational domain is (40,42,200). An Absorbing Boundary Condition (ABC) was applied at all the boundaries except for the ground plane. For the excitation of the line, we positioned an x-directed current source 10 cells from one end of the line such that the reflection caused from this end due to the ABC can be considered as an integral part of the incident wave form. This does not pose any hazard since the interest of this analysis is to study the characteristic impedance and effective dielectric constant of the line which require the dominant mode traveling in only one direction along the line.

As explained in [1], from a topological perspective, having part of the ground plane close to the signal conductor can significantly alter the field distribution in the proximity of the line from that of a simple microstrip structure. A series of simulations showed that to observe the dominant mode, the observation point has to be placed at a distance farther than would be required in a microstrip line case, thus, making the analysis of the V line more memory intensive. It is premature to make a definite conclusion here since further effects need to be studied in more detail to reach a more thorough understanding of the full-wave behavior.

Two important characteristics of transmission lines were analyzed in this study: The characteristic impedance of the line and the effective relative permittivity. In Fig. 2, we show the characteristic impedance for the line having the parameters given above. The characteristic impedance was calculated by taking the ratio of the Fourier transforms of the voltage and current We observe a monotonic increase in the impedance that is similar to the behavior observed in microstrip transmission lines. Figure 3 gives the effective relative permittivity which was calculated using the procedure detailed in [3]. As mentioned earlier, presently there is no measured or computed data to compare to, however, the values for the lower end of the spectrum are close to what was obtained by schutt-Aine [1]. Our calculation for the impedance at 1GHz resulted in *71 Ohms* where that obtained in [1] was *76 Ohms*, using measurements, and *78 Ohms* using conformal mapping. We note here that the conformal mapping technique used in [1] did not take into account the ground plane extensions (which are on the same plane as the signal conductor) [8]. For the effective relative permittiviy, however, the FDTD method gave a value of *1.95* at 1GHz which compares very favorably with *1.957*, which was measured in [1]. This gives us an indication of the validity of the FDTD results computed in this work.

Finally, we observe that the staircase approximation has an effect on the FDTD results as the higher end of the spectrum is approached. This is an expected outcome since staircase approximations give an increasing error as the wavelength becomes smaller. For critical applications, it is recommended that the polygonal approximation be used.

While the polygonal approximation has proven its effectiveness, the modification of the FDTD time-marching scheme can lead to instability, and this puts a stricter limit on the time-step allowable to guarantee stability [5]. The experience of these authors is that the time step for the

polygonal approximation scheme needs to be scaled down by at least 30-60% to guarantee stability. However, this is an empirical observation and further work is forthcoming [9].

IV. SUMMARY

In this work, a dynamic analysis of the V transmission line is presented. To the knowledge of the authors, no previous analysis existed. The FDTD method was used in conjunction with a recently introduced formulation to accurately model the curved boundaries introduced by the V line. Numerical results were obtained for the characteristic impedance of the line and its relative effective permittivity. Since no measurements appeared in the literature for the frequencies considered in this work, we compared the behavior over the lower end of the spectrum and found good agreement with quasi-static analysis.

ACKNOWLEDGMENT

This work was supported in part by the Army Research Office under grant number DAAH04-94-G-0355, and Digital Equipment Corporation.

REFERENCES

[1] J. Schutt-Aine, "Static analysis of V transmission lines," *IEEE Trans. Microwave Theory Tech.*, vol. MTT-40, no. 4, pp. 659-663, April 1992.

[2] N. Yuan, C. Ruan and W. Lin, "Analytical analyses of V, elliptic, and circular-shaped microshield transmission lines," *IEEE Trans. Microwave Theory Tech.*, vol. MTT-42, no. 5, pp. 855-859, May 1994.

[3] X. Zhang, J. Fang, K. Mei and Y. Liu, "Calculations of dispersive characteristics of microstrips by the time-domain finite difference method," *IEEE Trans. Microwave Theory Tech.*, vol. MTT-36, no. 2, pp. 263-267, Feb. 1988.

[4] P. Cherry and M. F. Iskander, "FDTD analysis of high frequency electronic interconnection effects," *IEEE Trans. Microwave Theory Tech.*, vol. MTT-43, no. 10, pp. 2445-2451, Oct. 1995.

[5] P. Mezzanotte, L. Roselli, and R. Sorrentino, "A simple way to model curved metal boundaries in FDTD algorithm avoiding staircase approximation," *IEEE Microwave & Guided Wave Lett.* vol. 5, no. 8, pp. 267-269, August 1995.

[6] M. Fusco, "FDTD algorithm in curvilinear coordinates," *IEEE Trans. Antennas Propagat.*, vol. 38, pp. 76-89, Jan. 1990.

[7] J. Fang and J. Ren, "A locally conformed finite-difference time-domain algorithm of modeling arbitrary shape planar metal strips, " *IEEE Trans. Microwave Theory Tech.*, vol. MTT-41, no. 5. pp. 830-838, May 1993.

[8] J. Schutt-Aine, private communications.

[9] C. Railton, "Stable and efficient FDTD algorithms for the analysis of three dimensional structures including curved PEC surfaces and edges," to be presented in the Progress in Electromagnetics Research Symposium, Innsbruck, Austria, July 8-12, 1996.

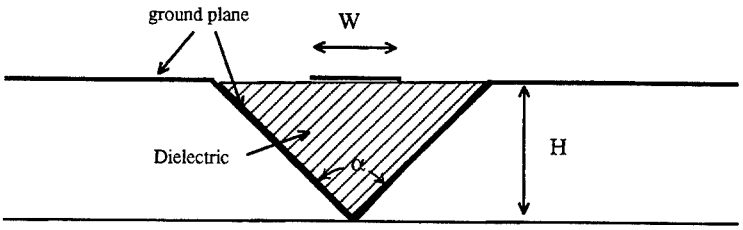

Fig. 1. Cross section of the V line. W: width of signal conductor, H, height substrate, and α is the characteristic angle.

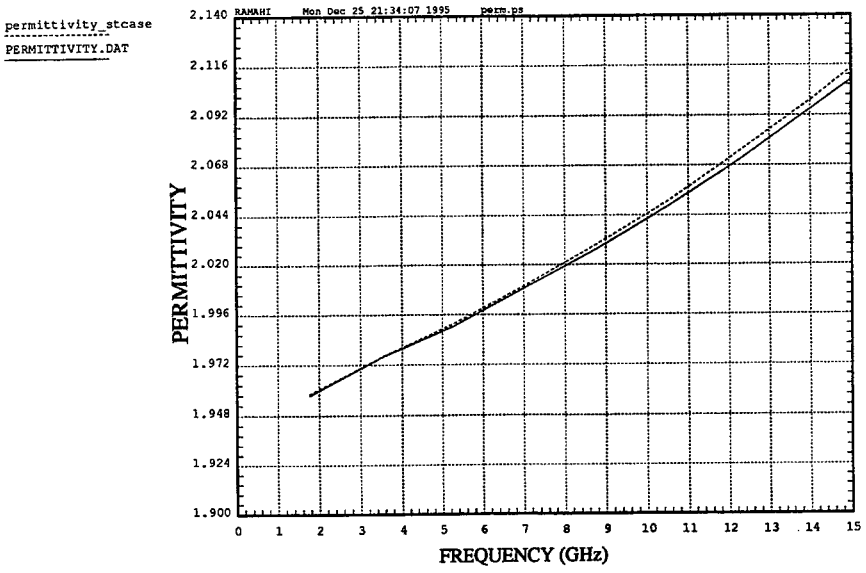

Fig. 2. Calculated values of the effective relative permittivity for the V line.
Solid line: polygonal approximation. Dashed line: staircase approximation.

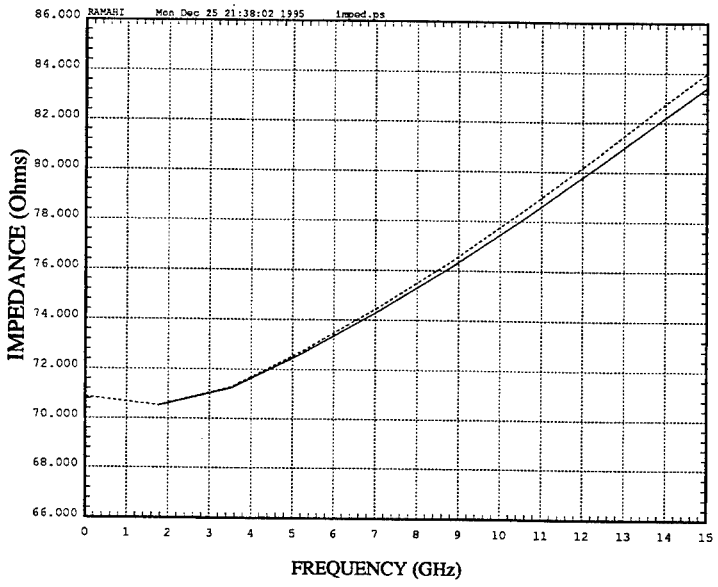

Fig. 3. Calculated values of the characteristic impedance of the V line.
Solid line: polygonal approximation. Dashed line: staircase approximation.

AN ABSORBING BOUNDARY CONDITION FOR THE FDTD METHOD USING DIGITAL FILTER DESIGN TECHNIQUE

Chien-Nan Kuo and Tatsuo Itoh

Department of Electrical Engineering
University of California, Los Angeles
Los Angeles, CA 90095-1595

Abstract

This paper presents the synthesis of an absorbing boundary condition for the Finite-Difference Time-Domain method based on the technique of digital filter design. The field components on the truncated boundary are updated by representing the relationship between the interior field and the boundary field as an infinite impulse response filter. This approach is applied to a highly dispersive rectangular waveguide and a microstrip line. The results are validated by reflection coefficient calculation.

1 Introduction

On the application of using the Finite-Difference Time-Domain (FDTD) method to the analysis of waveguiding structures, the computation domain in the modeling of the structures is truncated to be as small as possible because of the computer memory limitation and computing time reduction. A special algorithm known as the absorbing boundary condition (ABC) on the truncated boundary is required in order to reduce spurious reflection from the boundary. A good ABC implementation can minimize the reflection over a wide frequency range without giving up too much computing cost.

Many ABC realizations have been developed. One popular approach, based on Mur's ABC [1], applies cascaded one-wave equations by recognizing that the fields near the boundary are outgoing in the waveguided direction [2, 3]. Since the wave velocities are matched at certain frequencies only, wideband absorption cannot be easily obtained in highly dispersive structures. A different approach places layers of non-physical absorbers called the perfectly matched layers (PML) on the boundary [4, 5, 6]. This ABC realization can perform well absorption over a wide frequency range in dispersive structures. An extension has been derived to adequately absorb evanescent waves [7]. Another approach utilizes the diakoptic technique which applies time-domain Green's function and takes time convolutions [8, 9, 10]. Usually the numerical cost of time convolutions is significantly larger than that of the wave-equation approach.

An alternative approach realizes the ABC based on the technique of digital filter design by using an allpass digital filter to implement the relationship between the interior

field, which is the input signal, and the boundary field, which is the output signal [11]. This realization provides wideband absorption and requires little computing effort as well as memory burden. In this paper, the filter approach is generalized by using infinite impulse response (IIR) filters for efficient absorption of propagating and evanescent waves. The stability of the ABC is studied by the poles of the filter.

2 Formulation

Consider an ABC boundary where the wave is outgoing in the $+z$ direction. Since field components near the boundary satisfy the one-wave equation, the E-field can be expressed as

$$E(z) = E_o e^{j(\omega t - \gamma(\omega) z)}, \tag{1}$$

where γ, which equals to $\beta - j\alpha$, denotes the complex propagation constant and is frequency dependent. Therefore, the value of the tangential field E_M on the boundary can be updated from the value of the interior field E_{M-1} by

$$E_M = E_{M-1} e^{-j\gamma(\omega)\Delta z}, \tag{2}$$

where the exponential factor indicates the property of wave propagation, including propagating and evanescent waves.

To combine with the FDTD algorithm, Eq. (2) is transformed into a finite difference form by designing a digital system, in which the system function is defined as

$$G(\Omega) = \frac{\sum_{n=0}^{N} b_n e^{-jn\Omega}}{\sum_{n=0}^{N} a_n e^{-jn\Omega}} \equiv e^{-j\Gamma(\Omega)\Delta z}, \tag{3}$$

where Ω is the normalized frequency. With this equation, $\Gamma(\Omega)$ matches $\gamma(\omega)$ over the frequency range in interest, Actually, the digital system is an Nth-order IIR filter, which input signal and output signal are E_{M-1} and E_M, respectively. The implementation is illustrated in Fig. 1. On the entire boundary the same IIR filter is applied to update boundary fields, since the phase of the guided wave follows Eq. (1) not only in a certain grid but also over the entire boundary.

The choice of filter coefficients a_n and b_n involves a procedure of complex curve-fitting. In practical optimization, if $\Gamma(\Omega)$ is not well-matched with $\gamma(\omega)$, the discrepancy causes wave reflection. Consequently, the objective of the filter design is to minimize the reflection coefficient. According to the continuity condition on the boundary, the reflection coefficient R can be derived from the ratio $G(\omega)$ between the total fields E_M and E_{M-1}, which includes the reflected wave, and is expressed as

$$R = \frac{e^{-j(\Gamma-\gamma)\Delta z} - 1}{1 - e^{-j(\Gamma+\gamma)\Delta z}}. \tag{4}$$

3 Results and discussions

The first case is to consider the absorption of the dominant mode in a highly dispersive rectangular waveguide with a second-order IIR filter. The cross-section dimensions of the waveguide are 3 cm × 1.5 cm. To optimize the coefficients of the filter, the structure is pre-simulated by TE_{10}-mode excitation to obtain the complex propagation constant. The E-fields at two neighboring points are recorded, and the ratio leads to the calculation of the normalized attenuation and phase constants as plotted in Fig. 2 (a) and (b). The frequency dispersion can be observed in the curve of the phase constant. Subsequently, the coefficients are optimized as a_1 = -1.4074665, a_2 = 0.40844664, b_0 = -0.35247524, b_1 = 1.2957203, and b_2 = -0.94269684. The optimized curves are also plotted in the same figure. The poles of the filter are at z_1 = 0.99834113 and z_2 = 0.40912533, as shown in Fig. 2(c), which are both inside the unit circle. The solution to optimize the set of coefficients is not unique. The condition is not only to reduce the reflection coefficient but also to obtain poles inside the unit circle for a stable ABC scheme. The numerical calculation of the reflection coefficient based on Eq. (4) is shown in Fig. 2(d), which is validated by the FDTD simulation. With the complex propagating constant known, the performance of the ABC is available in advance.

The second structure is a microstrip line which is an open structure. The width of the microstrip line is 9.6 mil and the thickness of the substrate, which has a dielectric constant of 9.9, is 10 mil. The complex propagation constant is also obtained by a pre-simulation of the dominant-mode excitation. The normalized attenuation and phase constants are plotted in Fig. 3(a) and (b). The coefficients of the optimized second-order IIR filter are a_1 = -1.9805548, a_2 = 0.98423582, b_0 = -0.95873958, b_1 = -1.9185786, and b_2 = 0.96352007. The positions of poles are at z_1 = 0.99027738 + j0.059887608 and z_2 = 0.99027738- j0.059887608, as shown in Fig. 3(c). Since this structure is not highly dispersive, the reflection coefficient can be reduced less than -60 dB over a wide frequency range from 0 to 20 GHz. The reflection coefficients of the numerical theory and FDTD simulation are plotted in Fig. 3(d).

4 Conclusion

An absorbing boundary condition for the FDTD method is realized using the concept of digital filter design to obtain well absorption of probating and evanescent waves over a wide frequency range. Based on the complex propagating constant, this technique is very suitable for waveguiding structures. In the analysis of discontinuity problems, the ABC boundary can be placed near the discontinuity without causing a significant influence to the results, and, therefore, the numerical cost can be greatly reduced.

5 Acknowledgments

This work was supported by Hughes Micro, JSEP contract F49620-92-C-0055, and Army Research Office contract DAAH04-93-G-0068.

References

[1] G. Mur, "Absorbing boundary conditions for the finite-difference approximation of the time-domain electromagnetic-field equation," *IEEE Trans. Electromagentic Compat.*, vol. EMC-23, pp. 377-382, 1981.

[2] R. L. Higdon, "Absorbing boundary conditions for difference approximations to the multi-dimensional wave equation," *Mathematics of Computation,* vol. 47, no. 176, pp. 437-459, Oct. 1986.

[3] J. Fang, "Absorbing boundary conditions applied to model wave propagation in microwave integrated-circuits," *IEEE Trans. Microwave Theory and Tech.*, vol. 42, no. 8, Aug. 1994.

[4] J. Berenger, "A perfectly matched layer for the absorption of electromagnetic waves," *J. Comp. Phys.*, vol. 114, no. 2, pp. 185-200, Oct. 1994.

[5] D. S. Katz, E. T. Thiele, A. Taflove, "Validation and extension to three dimensions of the Berenger PML absorbing boundary condition for FD-TD meshes," *IEEE Miocrwave and Guided Wave Lett.*, vol. 4, no. 8, pp. 268-270, Aug. 1994.

[6] R. Mittra and Ü/ Pekel, "A new look at the perfectly matched layer (PML) concept for the reflectionless absorption of electromagnetic waves," *IEEE Miocrwave and Guided Wave Lett.*, vol. 5, no. 3, pp. 84-86, March 1995.

[7] J. Fang and Z. Wu, "Generalized perfectly matched layer - an extension of Berrenger's perfectly matched layer boundary condition," *IEEE Miocrwave and Guided Wave Lett.*, vol. 5, no. 12, pp. 451-453, Dec. 1995.

[8] T.-W. Huang, B. Houshmand and T. Itoh, "Efficient modes extraction and numerically exact matched sources for a homogeneous waveguide cross-section in a FDTD simulation," *1994 IEEE MTT-S Int. Microwave Symp. Digest,* pp. 31-34, May 23-27, San Diego, CA.

[9] E. Tentzeris, M. Krumpholz, N. Dib and L. Katehi, "A waveguide absorber based on analytic Green's functions," *25th European Microwave Conference Proc.*, pp. 251-254, Sept. 1995.

[10] M. Mrosowski, M. Niedźwiecki, and P. Suchomski, "A fast recursive highly dispersive absorbing boundary condition using time domain diakoptics and Laguerre polynomials," *IEEE Miocrwave and Guided Wave Lett.*, vol. 5, no. 6, pp. 183-185, June. 1995.

[11] Z. Bi, K. Wu and J. Litva, "Designing dispersive boundary condition (DBC) for the FD-TD method using digital filtering theory," *1992 IEEE AP-S Int. Symp. Digest,* pp. 326-329.

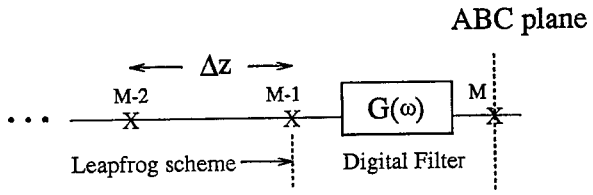

Figure 1: ABC realization by using an IIR filter to update the boundary field.

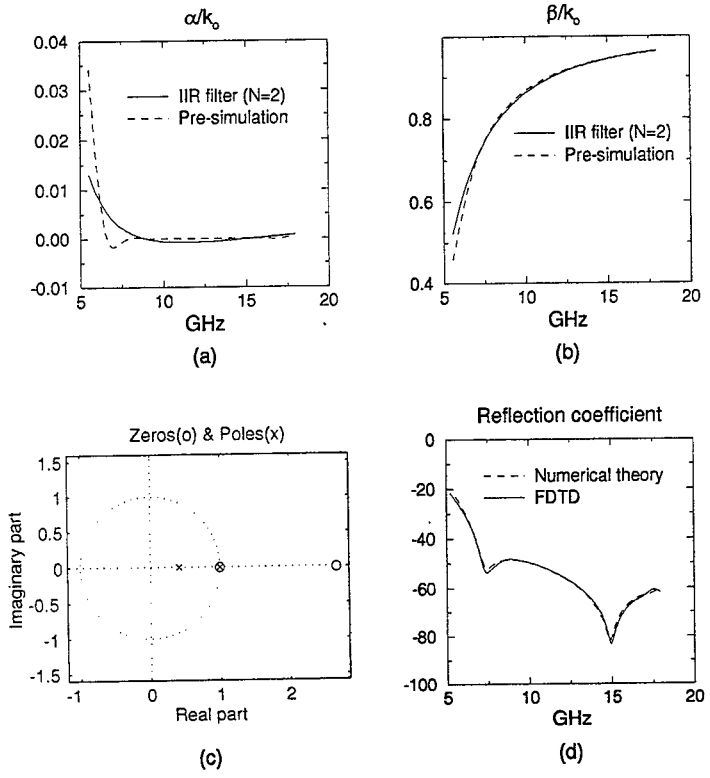

Figure 2: The synthesis of ABC for a rectangular waveguide. (a) The normalized attenuation constant, (b) the phase constant, (c) the poles of the filter, and (d) the reflection coefficient.

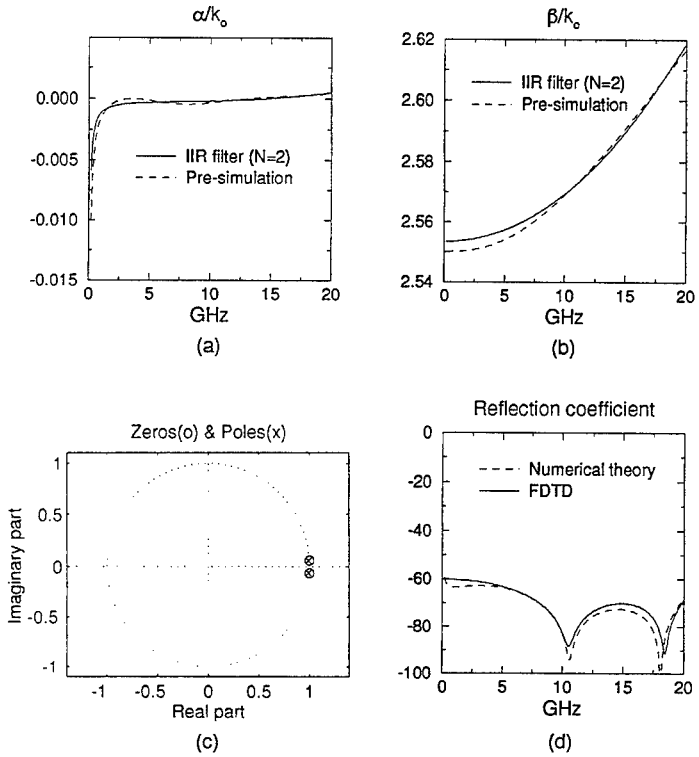

Figure 3: The synthesis of ABC for a microstrip line. (a) The normalized attenuation constant, (b) the phase constant, (c) the poles of the filter, and (d) the reflection coefficient.

Application of the FD-TD Method to the Electromagnetic Modeling of Patch Antenna Arrays

Michael F. Pasik
Sandia National Laboratories
Computational Electromagnetic and Plasma Physics Department
Albuquerque, New Mexico 87185-1186
and Gerardo Aguirre and Andreas C. Cangellaris
Department of Electrical and Computer Engineering
Center for Electronic Packaging Research
University of Arizona
Tucson, AZ 85721

January 10, 1996

Abstract

The FD-TD method and the Berenger Perfectly Matched Layer (PML) absorbing condition are applied to the modeling of a 32-element patch array. Numerical results for the return loss at the array feed are presented and compared to measured results for the purpose of model validation.

1 Introduction

The Finite Difference Time Domain (FDTD) algorithm developed by Yee [1] has found widespread use in electromagnetic analysis. The ability of FDTD to provide in a single run the broadband response of a structure is attractive for microwave/millimeter-wave component analysis, antenna design, and the prediction of radiated emissions from packaged electronic components and systems. The nature of the algorithm makes it ideally suited for implementation on massively parallel computers, facilitating analysis at the system rather than component level. With recent advances in desktop computing, the method has gained popularity for problems traditionally analyzed using frequency domain techniques [2].

However, the method is not without its limitations. One of the fundamental complications in using the method, which is of relevance to this paper, has been the proper truncation of the grid for outgoing waves. One of the more popular techniques used to address this problem has been one-way wave equations (or annihilators), such as the first and second order Mur [3] algorithms. Unfortunately, this approach tends to be narrow band and directional. Another approach has been to introduce absorbing media to cause the decay of the fields. However, reflections from the absorbing material have limited the use of this approach. Recently Berenger proposed the Perfectly Matched Layer (PML) [4] which overcomes this problem by matching the phase velocity and impedance of the absorber to the physical medium.

In this paper we apply the FDTD method with the PML absorbing boundary condition to a 32-element patch antenna array. While integral equations techniques are well-suited for the analysis of such radiators, recent advances in portable electronics call for novel antenna designs which can benefit from the modeling versatility of the FDTD method. More specifically, active antennas are recently being considered for use in smart id cards, miniature GPS receivers, personnel sensors, and highway automation applications. The increased effective length, increased bandwidth, improved noise factor, and reduced mutual coupling in array applications are some of the attributes of active antennas that explain the interest in their use in small form factor transceiver designs [5]. The presence of non-linear devices within the antenna structure necessitates the use of a non-linear electromagnetic solver for the modeling of electromagnetic radiation from the antenna. FDTD has been demonstrated as the method of choice for such modeling [6].

In the next section we discuss the issues relating to the excitation and characterization of the patch antenna array with respect to the FDTD algorithm. Also, we will provide a brief overview of the PML. In Section 3, we provide numerical results for the return loss of the array.

2 Theory

2.1 FDTD

Because the Finite-Difference Time-Domain method is well known [1], [7], we will focus our discussion on the issues specific to the structure under consideration.

2.1.1 Excitation and Characterization Techniques

The feed for the patch array consists of a short section of coaxial line, modeled with a stair step approximation, representing the coaxial feed. The inner conductor of the coaxial line extends to the microstrip line connected to the feed network of the patch array. A port plane is then defined at some chosen reference plane. In the port plane we solve Laplace's equation to find the quasi-TEM transverse electric field distribution. This field is imposed on the boundary as an incident field. Assuming TEM propagation, with an appropriately averaged cell velocity, the incident and reflected fields are separated. A Mur type one-way wave equation is then applied to the reflected field at the port plane.

To compute the return loss for the coaxial line-driven patch antennas, a separate simulation of the uniform section of the coaxial line, defined in the port plane, is performed to determine the incident field waveform (voltage, current, or Poynting flux) in the reference plane and to characterize the coaxial line. The incident waveform from the port simulation is then used to determine the reflected waveform in the simulation of the patch antenna. An FFT of the ratio of the incident and reflected waveforms provides the return loss as a function of frequency. To reduce the computation time, the late time response can be computed efficiently using either Prony's Method [8] or the Matrix Pencil Method [9].

2.2 Berenger PML

The Berenger PML [4] splits the field into sub-components and introduces electric and magnetic conductivities to cause the decay of propagating fields. The values of the PML conductivities are assigned directly at the corresponding field locations on the grid. The conductivities are chosen to satisfy the matching condition

$$\frac{\sigma_i}{\epsilon} = \frac{\sigma_i^*}{\mu} \tag{1}$$

where i indicates the direction (x, y, or z) and σ^* represents magnetic losses, which enforces the continuity of the wave impedance and phase velocity independent of frequency. Alternatively, the PML can be interpreted in terms of stretched coordinates [10]. To reduce the numerical reflections from the PML interface, a gradual spatial variation of the conductivities is used

$$\sigma_i(x_i) = \sigma_{i,max}\left(\frac{x_i}{L}\right)^2 \tag{2}$$

where L is the length of the PML and $\sigma_{i,max}$ is the maximum conductivity value. The PML region is terminated with a PEC. The apparent reflectivity from the PML region is given by [4]

$$R = e^{\frac{-2\langle\sigma_i\rangle L}{\epsilon_0 c}} \tag{3}$$

where $\langle\sigma_i\rangle$ denotes the spatially integrated conductivity value. For the aforementioned parabolic profile it is $\langle\sigma_i\rangle = \sigma_{i,max}/3$.

We have implemented the PML in a code [11] which supports multiple blocks (conformal regions of space with separate meshes) as a new type of block using the PML field update equations. The PML and standard blocks are connected by forcing the losses to be zero over the cells in the connection plane of the PML block, thereby allowing the total field to be decomposed into the partial field components. This configuration reduces the total overhead in the problem by incurring the overhead of the PML only where needed. It should be noted that because of conductor masking [11] the PML absorbing boundary condition results in additional field solve regions which avoid the issues associated with implementing boundary conditions on massively parallel architectures.

3 Numerical Results

In Figure 1 the geometry of a section of a coaxial transmission line-fed microstrip patch array is shown. The entire array consists of 192 patches and is formed by six of the sub-sections shown in Figure 1 aligned side by side and driven in phase. The grounded dielectric substrate is 0.031 inches thick with a dielectric constant of 2.2.

Exploiting the symmetry in Figure 1, we simulated only the lower 16 patches and the associated feed network. A small ten element long stair-step approximation to the coaxial transmission line was used to drive the antenna. A nearly uniform grid with 148 by 103 cells in the plane of the antenna and 10 cells in the transverse direction (4 cells in the substrate) was used. This grid resulted in a coarse discretization of the geometry. The inset-fed patch feed lines and gaps were each modeled as being one cell wide. The serpentine line used to feed clusters of eight patches was separated by only 1-2 cells from itself and adjacent patches in some locations.

PML blocks were located at 3 cells from the edge of feed line on the right side and 5 cells from the edge of the patches on the left side with $\sigma_{i,max} = 10.7$ S. On the lower side a PML block was also placed 5 cells from the edge of the patches with $\sigma_{i,max} = 10.5$ S. A PML block with $\sigma_{i,max} = 20.2$ S was placed 6 cells above the plane of the patches. The PML parameters were based on $m = 2$ and $q \approx 4$. The PML blocks were chosen to be 8 cells thick. Of the 423236 cells in the simulation 55% of them were located in PML blocks.

The total CPU time required on an HP 9000/735 workstation was approximately 11 hours for 17700 time steps. In Figure 2 we show the computed and measured return loss. The measured return loss curve was derived from a VSWR measurement of the first array sub-section with the other five sections left open (no difference was noted from the case of match terminating the other five sections).

The array was designed to work at 17 ± 0.3 GHz with a thin dielectric coating, however the measurements were made without the coating present. The poor agreement is most likely due to the inadequate resolution of the power splitting network. At the time this paper was written further studies were under way to comprehend the reasons for these discrepancies.

4 Acknowledgments

The authors would like to thank M.D. Sena of Sandia National Laboratories, for providing the patch array geometry and measured results presented in Figure 1. This work was supported in part by the United States Department of Energy under Contract DE-AC04-94AL85000.

References

[1] K. S. Yee, "Numerical solution of initial boundary value problems involving Maxwell's equations in isotropic media," *IEEE Trans. Antennas Propagat.*, vol. AP-14, pp. 302-307, May 1966.

[2] D. M. Sheen, S. M. Ali, M. D. Abouzahra, and J.A. Kong, "Application of the Three-Dimensional Finite-Difference Time-Domain Method to the Analysis of Planar Microstrip Circuits," *IEEE Trans. Microwave Theory Tech.*, vol. 38, no. 7, pp. 849-857, July 1990.

[3] G. Mur, "Absorbing Boundary Conditions for the Finite Difference Approximation of the Time-Domain Electromagnetic Field Equations," *IEEE Trans. Electromagnetic Compatibility*, vol. 23, no. 4, pp. 377-382, Nov. 1981.

[4] J.-P. Berenger, "A perfectly matched layer for the absorption of electromagnetic waves," *J. Comp. Physics*, vol. 114, pp. 185-200, 1994.

[5] J. Lin and T. Itoh, "Active Integrated Antennas," *IEEE Trans. Microwave Theory Tech.*, vol. 42, no. 12, pp. 2186-2194, Dec. 1994.

[6] B. Toland, J. Lin, B. Houshmand, and T. Itoh, "FDTD Analysis of an Active Antenna," *IEEE Microwave and Guided Wave Lett.*, vol. 3, no. 11, pp. 423-425, Nov. 1993.

[7] A. Taflove and M. E. Brodwin, "Numerical Solution of Steady-State Electromagnetic Scattering Problems Using the Time-Dependent Maxwell's Equations," *IEEE Trans. Microwave Theory Tech.*, vol. 23, no. 8, Aug. 1975.

[8] W. L. Lo and R. Mittra, "A combination of FD-TD and Prony's methods for analyzing microwave circuits," *IEEE Trans. Microwave Theory Tech.*, vol. 39, no. 12, pp. 2155-2163, Dec. 1991.

[9] T. K. Sakar and O. Pereira, "Using the Matrix Pencil Method to Estimate the Parameters of a Sum of Complex Exponentials", *IEEE Antennas and Propagat. Magazine*, vol. 37, no. 1, Feb. 1995.

[10] W. C. Chew and W. H. Weedon, "A Perfectly Matched Medium from Modified Maxwell's Equations with Stretched Coordinates", *Microwave and Optical Technology Letters*, vol. 7, no. 13, pp. 599-604, Sep. 1994.

[11] D. B. Seidel, M. L. Kiefer, R. S. Coats, T. D. Pointon, J. P. Quintenz, and W. A. Johnson, "The 3-D Electromagnetic, Particle-In-Cell Code, QUICKSILVER," Proceedings of the CP90 Europhysics Conference on Computational Physics, pp. 475-482, 1991.

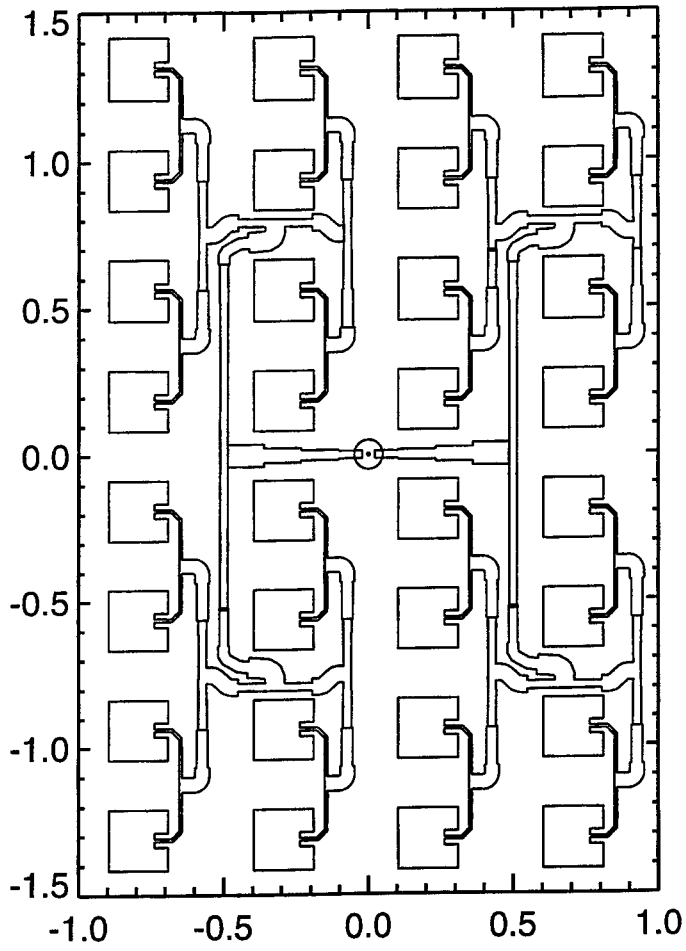

Figure 1: A subsection of a microstrip patch array antenna (in units of inches).

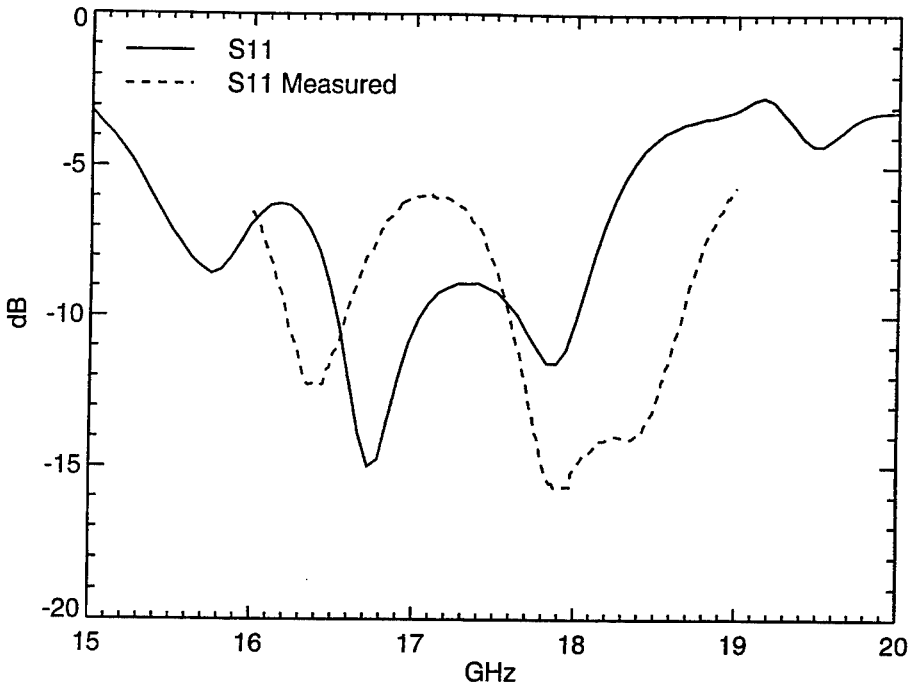

Figure 2: Computed and measured return loss for a subsection of a patch array antenna.

SESSION 25:

MICROWAVE COMPONENTS

Chairs: M. Baginski and M. Ney

PARALLEL COUPLED MICROSTRIP PATCH RESONATORS ON A FERRIMAGNETIC LAYER

José de Ribamar Silva Oliveira* and Adaildo Gomes d'Assunção**
* Federal Center of Technological Education of Maranhão - São Luís - MA - Brazil
** Federal University of Rio Grande do Norte - Natal - RN - Brazil

Abstract

The properties of parallel coupled microstrip patch resonators on ferrite substrates are investigated. A fullwave analysis is used in the spectral domain, by using a combination of the Green's functions technique and the moment method (Galerkin). Curves are presented for the even and odd resonant mose frequencies versus the structural parameters and/or the magnitude of the applied d.c. magnetic field.

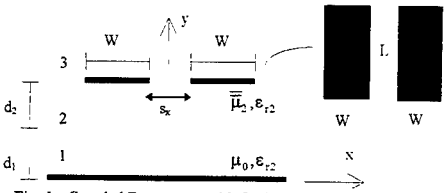

Fig. 1 - Coupled Resonators with ferrimagnetic substrates

Introduction

A growing interest in the development of microstrip devices on ferrimagnetic materials has been observed, lately [1]-[4]. This is particularly due to the fact that the characteristics of these devices can be altered by varying the intensity and/or direction of the applied d.c. magnetic field.

Analyses of microstrip patch resonators and antennas on magnetized layers were presented by several authors [1]-[3]. Nevertheless, these works were performed for a single conducting patch on a single ferrimagnetic layer.

In this work, a fullwave analysis is used to investigate the properties of two parallel coupled microstrip patch resonators on a two layer substrate, where the grounded one is a dielectric material and the other one is ferrite. It is assumed that the ferrimagnetic layer is normally biased [4]-[6].

This analysis is developed in two steps. In the first one, the Green's functions, or impedance matrix, for the structure considered is obtained [7]. In the second one, the Galerkin method is used to obtain the characteristic equations for the even and odd resonant modes, from which the resonant frequencies are determined as functions of the structural parameters and of the magnitude of the applied d.c. magnetic field [8]]-[9].

Curves are presented for the resonant frequency of the even and odd resonant modes as function of the geometry parameters, as well as of the normalized magnitude of the d.c. magnetic field. Results for the particular case of a single microstrip patch resonator on two layers substrate are presented, also. In this case the numerical results were obtained by increasing the conducting patches spacing.

Note that a good agreement was observed when the results of this work were compared to those available in the literature for the particular case of: a) single microstrip patches on single ferrite

substrate [2] and b) coupled microstrip patches on double dielectric layers [10].

Theory

The structure considered is shown in Fig. 1. Region 2 is assumed to be filled with a ferrimagnetic material and regions 1 and 3 are filled with dielectric materials. Particularly, region 3 is air. The externally applied magnetic field is considered to be along the y direction. Then, in the region 2, the permeability tensor is given by [4]-[6].

$$\overline{\overline{\mu}}_2 = \mu_0 \cdot \begin{bmatrix} \mu_r & 0 & -jk_r \\ 0 & 1 & 0 \\ jk_r & 0 & \mu_r \end{bmatrix} \tag{1}$$

with

$$\mu_r = 1 - \frac{(\gamma H_0)(\gamma 4\pi M_S)}{f^2 - (\gamma H_0)^2} \tag{2}$$

$$k_r = \frac{\gamma 4\pi M_S f}{f^2 - (\gamma H_0)^2} \tag{3}$$

where γ is the gyromagnetic ratio, $4\pi M_s$ is the magnetization saturation, H_0 is the magnitude of the external applied magnetic field, f is the operation frequency, and μ_0 is the free space permeability.

The analysis is developed by using a combination of the Hertz vector potentials, to determine the Green's functions for the structure considered, and Galerkin method [4]-[9].

The Hertz vector potentials are assumed to be along the y direction, which is the same for H_0, so that the electric, $\overline{\Pi}_{ei}$ and the magnetic, $\overline{\Pi}_{hi}$ are given, respectively, by

$$\overline{\Pi}_{ei} = \Pi_{ei}\hat{a}_y \qquad (i = 1, 2, 3) \tag{4}$$

$$\overline{\Pi}_{hi} = \Pi_{hi}\hat{a}_y \qquad (i = 1, 2, 3) \tag{5}$$

The Hertz vector potentials, $\overline{\Pi}_{ei}$ and $\overline{\Pi}_{hi}$, in region 2, should satisfy, respectively, the wave equations given by

$$\nabla^2 \overline{\Pi}_{e2} + \omega^2 \varepsilon_{r2}\varepsilon_0\mu_0 \left(\frac{\mu_r^2 - k_r^2}{\mu_r}\right)\overline{\Pi}_{e2} = 0 \tag{6}$$

$$\nabla^2 \overline{\Pi}_{h2} + \omega^2 \varepsilon_{r2}\varepsilon_0\mu_0 \overline{\Pi}_{h2} - \left(\frac{\mu_r - 1}{\mu_r}\right)\frac{\partial^2 \overline{\Pi}_{h2}}{\partial y^2} = 0 \tag{7}$$

From Maxwell's equations, the electric and magnetic field components in the ferrimagnetic layer

(region 2), is obtained as

$$\overline{E}_2 = -j\omega\mu_0\mu_r\nabla\times\overline{\Pi}_{h2} + \omega^2\varepsilon_{r2}\varepsilon_0\mu_0\left(\frac{\mu_r^2 - k_r^2}{\mu_r^2}\right)\overline{\Pi}_{e2} + \frac{1}{\mu_r}\nabla\nabla\cdot\overline{\Pi}_{e2} \tag{8}$$

$$\overline{H}_2 = j\omega\varepsilon_{r2}\varepsilon_0\mu_0\left(\frac{\mu_r^2 - k_r^2}{\mu_r^2}\right)(\overline{\overline{\mu}})^{-1}\nabla\times\overline{\Pi}_{e2} + \omega^2\varepsilon_{r2}\varepsilon_0\mu_0\mu_r\overline{\Pi}_{h2} + \nabla\nabla\cdot\overline{\Pi}_{h2} \tag{9}$$

For regions 1 and 3, equations (6) to (9) are still valid, considering that $\mu_r = 1$ and $k_r = 0$. Then, the wave equations for $\overline{\Pi}_{ei}$ and $\overline{\Pi}_{hi}$ are obtained in the spectral domain, for each dielectric region i (i = 1, 2, 3) in Fig. 1. The Fourier transformation is defined by [2]

$$\tilde{\Psi}(\alpha,\beta) = \int_{-\infty}^{\infty}\int_{-\infty}^{\infty}\Psi(x,z)e^{j(\alpha x+\beta z)}dxdz \tag{10}$$

$$\Psi(x,z) = \frac{1}{(2\pi)^2}\int_{-\infty}^{\infty}\int_{-\infty}^{\infty}\tilde{\Psi}(\alpha,\beta)e^{-j(\alpha x+\beta z)}d\alpha d\beta \tag{11}$$

where $\Psi(x,z)$ is a generic function.

By using (10) and (11), the wave equations for $\tilde{\Pi}_{ej}$ and $\tilde{\Pi}_{hj}$ for dielectric region 1 (j = 1, in Fig. 1) are obtained as

$$\frac{\partial^2\tilde{\Pi}_{e1}}{\partial y^2} - \gamma_1^2\tilde{\Pi}_{e1} = 0 \tag{12}$$

$$\frac{\partial^2\tilde{\Pi}_{h1}}{\partial y^2} - \gamma_1^2\tilde{\Pi}_{h1} = 0 \tag{13}$$

where

$$\gamma_1^2 = \alpha^2 + \beta^2 - \omega^2\mu_0\varepsilon_0\varepsilon_{r1}, \tag{14}$$

for region 3 (in Fig. 1), they are derived as

$$\frac{\partial^2\tilde{\Pi}_{e3}}{\partial y^2} - \gamma_0^2\tilde{\Pi}_{e3} = 0 \tag{15}$$

$$\frac{\partial^2\tilde{\Pi}_{h3}}{\partial y^2} - \gamma_0^2\tilde{\Pi}_{h3} = 0 \tag{16}$$

where

$$\gamma_0^2 = \alpha^2 + \beta^2 - \omega^2 \mu_0 \varepsilon_0, \tag{17}$$

and, for the ferrimagnetic region 2 (Fig. 1) they are given by

$$\frac{\partial^2 \tilde{\Pi}_{e2}}{\partial y^2} - \gamma_{e2}^2 \tilde{\Pi}_{e2} = 0 \tag{18}$$

$$\frac{\partial^2 \tilde{\Pi}_{h2}}{\partial y^2} - \gamma_{h2}^2 \tilde{\Pi}_{h2} = 0 \tag{19}$$

where

$$\gamma_{e2}^2 = \alpha^2 + \beta^2 - \omega^2 \mu_0 \varepsilon_0 \varepsilon_{r2} \left(\frac{\mu_r^2 - k_r^2}{\mu_r} \right) \tag{20}$$

and

$$\gamma_{h2}^2 = \mu_r \left(\alpha^2 + \beta^2 \right) - \omega^2 \mu_0 \mu_r \varepsilon_0 \varepsilon_{r2} \tag{21}$$

Solving the boundary value problem by imposing the boundary conditions, in the Fourier domain, the transformed electric field components at the interface air / ferrimagnetic ($y = d_1 + d_2$ in Fig. 1) are expressed as functions of the transformed surface current density components, as

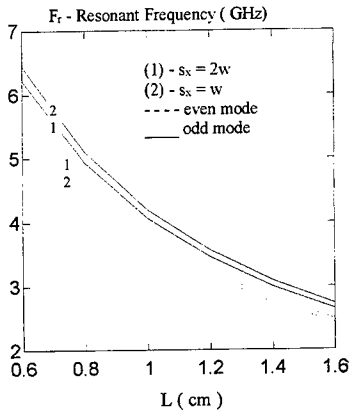

Fig. 2 - Resonant frequency versus patch length - W = 0.2 cm, d_1 = 0.0, d_2=0.127 cm, ε_{r2} = 15.2, H_0 = 5024.0 Oe, γ = 2.8 MHz/Oe, $4\pi M_s$ = 1.200 G.

$$\tilde{E}_x = \tilde{Z}_{xx} \tilde{J}_x + \tilde{Z}_{xz} \tilde{J}_z \tag{22}$$

$$\tilde{E}_z = \tilde{Z}_{zx} \tilde{J}_x + \tilde{Z}_{zz} \tilde{J}_z \tag{23}$$

Using the Galerkin method and Parseval's theorem[2], the determinantal equation is obtained to determine the resonant frequency. In this analysis even and odd resonant modes are considered, allowing the determination of their resonant frequencies.

Results

Fig. 2 shows the numerical results obtained for coupled microstrip resonators on a ferrimagnetic layer, for s_x = w and 2w, where s_x is the distance between the coupled conducting patches.

As expected the results obtained in this work, when s_x increases, approach those for a single microstrip patch. Furthermore, when the magnitude H_0 increases the

resonant frequencies approach those for coupled resonators on a dielectric layer with $\varepsilon_r = 15.2$.

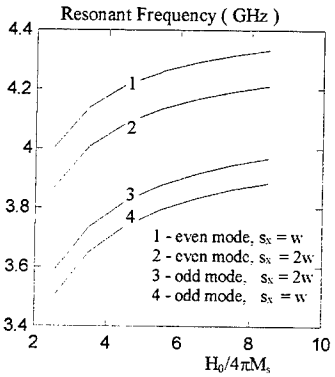

Fig. 3 - Resonant frequency versus $H_0/4\pi M_s$ - w = 0.2 cm, L = 1.0 cm, d_1 = 0.0, d_2 = 0.127 cm, ε_{r2} = 15.2, $4\pi M_s$ = 1200 G, γ = 2,8 MHz/Oe.

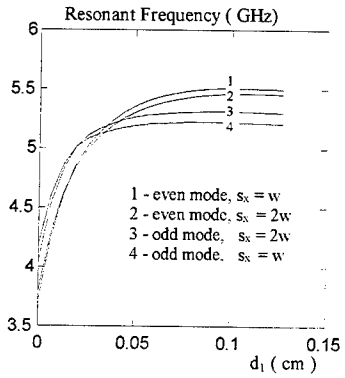

Fig. 4 - Resonant frequency versus d_1 - w = 0.2 cm, L = 1.0 cm, d_2 = 0.127 cm, ε_{r2} = 15.2,$4\pi M_s$ = 1200 G, γ = 2,8 MHz/Oe, H_0 = 5024 Oe

The behavior of the resonant frequencies of two parallel coupled resonators versus the normalized magnitude of the applied d.c. magnetic field is shown in Fig. 3. Note that when $H_0/4\pi M_s$ increases the resonant frequencies approaches those results for the resonant frequency of coupled resonators on a dielectric substrate with $\varepsilon_r = 15.2$, once that in (2) and (3), μ_r and k_r approaches 1 and 0, respectively.

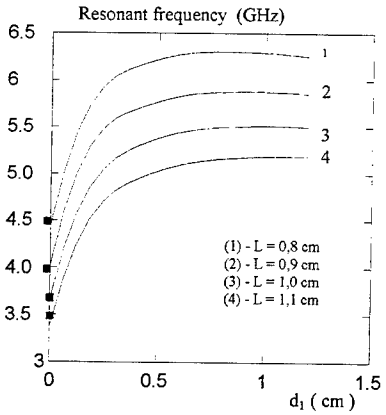

Fig. 5 - Resonant frequency versus d_1 for an isolated patch - w = 0.4 cm, ε_{r1} = 1.0, ε_{r2} = 15.2, d_2 = 0.127 cm, H_0 = 5024.0 Oe, $4\pi M_s$ = 1200 G.
■ - Ref. [2]

Fig. 4 shows the dependence of the resonant frequencies versus the thickness of the grounded layer, d_1, which is air-filled. Observe that for higher values of d_1 the resonant frequencies remain constants.

Results for a single suspended microstrip patch resonator are shown in Fig. 5, which depicts the resonant frequency versus the thickness of the grounded layer. Dielectric region 1 is air-filled. Results are shown for several values of the patch length, L. Note that the results for small values of d_1 approach those for microstrip resonator on a single ferrimagnetic layer, studied in [2].

Conclusion

A fullwave analysis of parallel coupled microstrip resonators on ferrite substrates was performed in the spectral domain. The dyadic Green's functions, for the even and odd resonant modes, for the structure considered were obtained by using Hertz vector potentials. Numerical results were obtained showing the

effect of the externally applied d.c. magnetic field. Agreement with results available in the literature was observed for several particular cases. The technique which is quite general and accurate can be used to investigate other planar structures with other substrates, such as semiconductors and anisotropic dielectric materials.

Acknowledgment

The authors wish to thank the support received from CNPq and CAPES, Brazilian Agencies for Research and Development.

References

[1] - D.M.POZAR, "Radiation and scattering characteristic of microstrip antennas on normally biased ferrite substrates", *IEEE Trans. Antennas Propagat.*, AP-40, n.9, p. 1084-1092, September 1992.

[2] - A.G. D'ASSUNÇÃO e E.J.A. DANTAS, "On the resonant frequency of magnetized rectangular microstrip patch resonators", *IEEE AP-S Antennas Propagation Symp.*, Ann Arbor, MI, p. 1508-1511, June 1993.

[3] - H.-Y. YANG, J.A. CASTANHEDA and G. ALEXOUPOLOS, "The RCS of a microstrip patch on an arbitrarily biased ferrite substrate", *IEEE Trans. Antennas Propagat.*, AP-41, No. 12, pp. 1610-1614, December 1993.

[4] - M. R. M. L. ALBUQUERQUE, "Análise de linhas de microfita e de linhas de lâminas sobre substratos ferrimagnéticos magnetizados", (in Portuguese) Campinas: State University of Campinas, 1993, 168 p.

[5] - R. A. WALDRON, "Ferrites - An Introduction for Microwave Engineers, Van Nostrand, 1961.

[6] - N. G. ALEXÓPOULOS , "Integrated-circuit structures on anisotropic substrates", *IEEE Trans. Microwave Theory Tech.*, v. MTT-33, n. 10, p. 847-881, Oct. 1985.

[7] - R. E. COLLIN, *Field Theory of Guided Waves*, McGraw-Hill Company, 1960.

[8] - R. F. HARRINGTON, *Time-Harmonic Electromagnetic Fields*, McGraw-Hill Company, 1961.

[9] - J. R. JAMES and P. S. HALL, *Handbook of Microstrip Antennas*, Peter Peregrinus Ltd., IEE, London, 1989

[10]-A. K. SHARMA and B. BHAT, " Spectral domain analysis of interacting microstrip resonant structures", *IEEE Trans. Microwaves Theory Tech.*, v. MTT-31, n. 8, pp. 681-687, August, 1983.

FULLWAVE ANALYSIS OF CIRCULAR CYLINDRICAL BACKED SLOTLINES

Laércio Martins de Mendonça and Adaildo Gomes d'Assunção
Federal University of Rio Grande do Norte
Department of Electrical Engineering
CP 1655, 59072-970 Natal, RN, Brazil

ABSTRACT

A fullwave analysis of conductor backed cylindrical slotlines is presented. These structures are suitable for the development of microwave integrated circuits to be mounted on curved surfaces. This analysis is performed in the Fourier domain, by combining Hertz vector potentials and Galerkin method, to determine the propagating modes characteristics. In the analysis, lossless and lossy dielectric regions were considered. Agreement was observed, for several particular cases, with the results available in the literature. This technique can be used to analyze those obtained by coupling two lines or by replacing the dielectric substrate region by a anisotropic one.

INTRODUCTION

The study of circular cylindrical slotted lines (Fig. 1) has been performed by several authors [1]-[5]. Quasi-static and fullwave analyses were used to investigate the transmission line characteristics. In these analyses, which are basically performed for a slotted coaxial cable, small values for r_1, r_2 and $r_2 - r_1$, (Fig. 1) were considered.

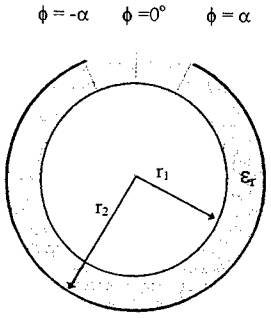

Fig. 1 - Cross sectional view of a slotted coaxial cable.

In this work, the analysis of a conductor backed cylindrical slotline, as shown in Fig. 2, is presented. Note that for this structure large values are assumed for r_2 and r_1, while very small values for $r_2 - r_1$ are considered. Also, note that if r_1, increases the structure of Fig. 2, which is a conductor backed slotline, approaches that of a conductor backed slotline (Fig. 3).

The slotline structures shown in Figs. 2 and 3 are suitable for the development of several (monolithic) microwave integrated circuits [6]-[11], requiring the study of their properties.

The technique that combines Hertz vector potentials and moment method has proven to be accurate and efficient in the analysis of planar transmission lines, in the spectral domain [6]. Thus, it was chosen to investigate the properties of non-planar transmission lines.

Therefore, the main objective of this work is to analyze the structure shown in Fig. 2, in the spectral domain, by using Hertz vector potentials [12] and Galerkin method [13].

In this work, it was observed that the numerical results obtained for the particular cases of a a) circular slotted coaxial cable, and b) (planar) slotline and conductor backed slotline, showed agreement with the results presented in the literature [7]-[11].

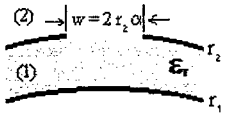

Fig. 2 - Geometry of a conductor backed cylindrical slotline.

THEORY

To analyze the structure shown in Fig. 1, the electric and magnetic fields are expressed as functions of the Hertz vector potentials in each dielectric region i (i=1,2) in Fig. 2. These potentials are considered to be oriented along $\hat{a}_r$, giving

$$\vec{\pi}_e = \pi_e \hat{a}_r \quad (1)$$

$$\vec{\pi}_h = \pi_h \hat{a}_r \quad (2)$$

The non-planar structures considered in this work are assumed to be uniform along z direction and the time dependence is harmonic.

From Maxwell's equations, the electric and magnetic fields are obtained as functions of $\vec{\pi}_e$ and $\vec{\pi}_h$, for dielectric region i (i=1,2), in Fig. 2, as

$$\vec{E} = -j\omega\mu_0 \nabla \times \vec{\pi}_h \quad (3)$$

$$\vec{B} = j\,\omega\,\mu_0\,\varepsilon\,\nabla \times \vec{\pi}_e \quad (4)$$

where ω is the operating frequency ($\omega = 2\pi f$), μ_0 is the free space magnetic permeability and ε is the electric permittivity.

The wave equations for the Hertz potentials are derived as

$$\nabla^2 \pi_e + \omega^2 \mu_0 \varepsilon \pi_e = 0 \quad (5)$$

$$\nabla^2 \pi_h + \omega^2 \mu_0 \varepsilon \pi_h = 0 \quad (6)$$

To solve the boundary value problem in the Fourier domain, the following transformation is used [14]

$$\tilde{\Omega}(r,m) = \int_{-\infty}^{\infty} \Omega(r,\phi)\, \exp(-jm\phi)\, d\phi \quad (7)$$

$$\Omega(r,\phi) = \sum_{m=-\infty}^{m=\infty} \tilde{\Omega}(r,m) \exp(jm\phi) \quad (8)$$

where $\sim$ means the transformed function.

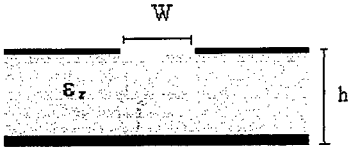

Fig. 3 - Cross section of a conductor backed slotline.

From (8), (5) and (6), the transformed wave equations are obtained as

$$\frac{d^2}{dr^2}\tilde{\pi}_{e,h}(r,m)+\frac{1}{r}\frac{d}{dr}\tilde{\pi}_{e,h}(r,m)-\zeta_i^2\tilde{\pi}_{e,h}(r,m)=0 \tag{9}$$

with

$$\zeta_i^2=\gamma_i^2-(m/r)^2 \tag{10}$$

and

$$\gamma_i^2=k_i^2-\beta^2 \tag{11}$$

where γ_i and k_i are the propagation constant and the wave number, in region i (i=1,2 in Fig. 1), respectively, and β is the line phase constant.

To solve the boundary value problem, in the spectral domain, the surface current density components, at $r = r_2$, are expressed as functions of the electric field components in the slot as

$$\begin{bmatrix}\tilde{J}_\phi\\ \tilde{J}_z\end{bmatrix}=\begin{bmatrix}\tilde{Y}_{\phi\phi} & \tilde{Y}_{\phi z}\\ \tilde{Y}_{z\phi} & \tilde{Y}_{zz}\end{bmatrix}\begin{bmatrix}\tilde{E}_\phi\\ E_z\end{bmatrix} \tag{12}$$

where $\tilde{Y}_{\phi\phi}$, $\tilde{Y}_{\phi z}$, $\tilde{Y}_{z\phi}$ and $\tilde{Y}_{zz}$ are the dyadic Green's function components for the structure considered [10].

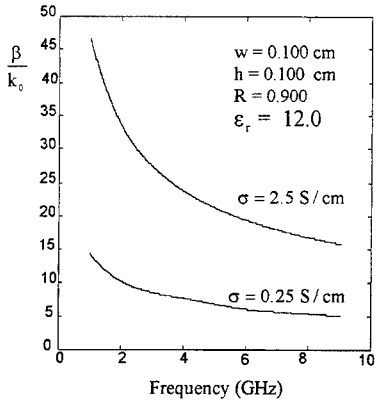

Fig. 4 - Normalized phase constant versus frequency for conductor backed cylindrical slotlines with lossy dielectric. $R = r_1 / r_2$.

By using the moment method [9],[13], the characteristics equation for the propagation constant is determined [10], for the dominant and higher order modes. Therefore, the effective permittivity for the structure considered is obtained.

RESULTS

Numerical results are presented for several cases, including conductor backed cylindrical slotlines and (planar) slotlines .

Fig. 4 shows the frequency dependence for the normalized phase constant of conductor backed cylindrical slotlines with lossy dielectric regions. For this structure (Fig. 2), $R = r_1 / r_2$ and $h = r_2 - r_1$.

Fig. 5 shows the numerical results obtained in this work for a conductor backed cylindrical slotline and those for a (planar) slotline available in the literature [11].

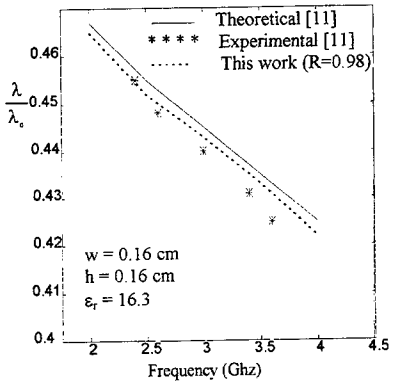

Fig. 5 - Normalized wavelength versus frequency for a conductor backed cylindrical slotline (---), with R=0.98, and a (planar) slotline.

CONCLUSION

The analysis of conductor backed cylindrical slotlines was performed, in the spectral domain, by using a Green's function technique and the moment (Galerkin) method.

Numerical results were presented for the normalized phase constant and wavelength as functions of frequency, for the dominant mode.

For some particular cases, agreement was observed between our results and those presented in the literature. As expected the results obtained for the conductor backed cylindrical slotline structure approach those obtained for the planar structure, when the conducting surface radius, r_1, in Fig. 1, increases.

This technique is quite general and can be used to analyze, for instance, the cases of coupled slotlines and slotlines with anisotropic dielectric regions.

References

[1] P. P. Delogne and A. A. Laloux, "Theory of the slotted coaxial cable," IEEE Trans. Microwave Theory Tech., vol. MTT-28, pp. 1102-1107, Oct. 1980.

[2] J. R. Wait and D. A. Hill, "Propagation along a braided coaxial cable in a circular tunnel," IEEE Trans. Microwave Theory Tech., vol. MTT-23, pp. 401-405, 1975.

[3] D. A. Hill and J. R. Wait, "Calculated transmission loss for a leaky feeder communication system in a circular tunnel," Radio Sci., vol. 11, pp. 315-321, 1976.

[4] J. R. Waitt and D. A. Hill, "Influence of spatial dispersion of the shield transfer impedance of a braided coaxial cable," IEEE Trans. Microwave Theory Tech., vol. MTT-25, pp. 72-74, 1977.

[5] J. R. Waitt, "Electromagnetic theory of the lossely coaxial cable: Part I," IEEE Trans. Microwave Theory Tech., vol. MTT-24, pp. 547-553, 1976.

[6] M. G. R. Maia, A. G. d'Assunção and A. J. Giarola, "Dynamic analysis of microstrip lines and finlines on uniaxial anisotropic substrates," IEEE Trans. Microwave Theory Tech., vol. MTT-35, pp. 881-886, Oct. 1987.

[7] J. Bornemann, "A scattering-type transverse resonance technique for the calculation of (M)MIC transmission line characteristics, " IEEE Trans. Microwave Theory Tech., vol. 39, no.12, Dec. 1991.

[8] N. G. Alexópoulos and A. Nakatani, "Cylindrical substrate microstrip line characteristics," IEEE Trans. Microwave Theory Tech., vol. MTT-35, no. 9, pp. 843-849, Sep.1987

[9] K. C. Gupta, R. Garg and I. J. Bahl, *MICROSTRIP LINES AND SLOTLINES*, Artech House, 1979.

10] L. M. Mendonça, "New procedures to Analyze Non-Planar Transmission Lines" (in Portuguese), Ph.D. dissertation, Federal University of Paraíba, Campina Grande, PB, Brazil, Dec. 1994.

[11] E. Mariani, C. Heinzman, J. Agrios and B. Cohn, "Slot line Characteristics," IEEE Trans. Microwave Theory Tech., vol. MTT-17, no. 12, pp. 1091-1096, Dec.1969 .

[12] R. E. Collin, *FIELD THEORY OF GUIDED WAVES*, McGraw-Hill, NewYork, 1960.

[13] R. F. Harrington, *FIELD COMPUTATION BY MOMENT METHODS*, McMillan Co., New York, 1968.

[14] E. O. Brigmam, *THE FAST FOURIER TRANSFORM*, Prentice Hall, Inc., Englewood Cliffs, 1974.

PROPERTIES OF TAPERED MICROSTRIP LINES ON DIELECTRIC AND MAGNETIZED FERRIMAGNETIC LAYERS

Adaildo Gomes d'Assunção, Francinete de Lima and Maria Rosa M. Lins de Albuquerque
Department of Electrical Engineering
Federal University of Rio Grande do Norte, 59072-970 Natal, RN, Brazil

Abstract

An investigation on the properties of tapered microstrip lines on dielectric and magnetized ferrimagnetic layers is presented. The effects produced on the properties of tapered microstrip transmission lines by variations on their structural parameters, including the properties of the substrates, were investigated. The variations on the substrate properties were obtained for microstrip lines on ferrites, by varying the magnitude of the applied dc magnetic field. For these structures, a linear variation of the conducting strip width was considered, while the substrate thickness was kept constant. The analysis was developed in the spectral domain, by using a combination of the segmentation, Hertz vector potentials, and Galerkin methods. In the analysis, the Hertz vector potentials were assumed to be oriented along the applied d.c. magnetic field. Results are shown for tapered microstrip lines, for the input impedance, reflection coefficient, and VSWR. Agreement was observed with the results available in the literature for tapered lines on dielectric substrates.

Introduction

The interest on microwave devices using microstrip transmission lines on ferrimagnetic layers has increased [1]-[4], lately. Mainly, this is due to the possibility of altering the performance of these devices by changing the properties of their ferrimagnetic substrates, according to the magnitude and direction of the applied d.c. magnetic field [4],[6].

Therefore, the characteristics of microstrip circuits, such as antennas [1],[2] and couplers [4], may be varied by altering the ferrimagnetic layer properties, according to a variation on the intensity or direction of the externally applied d.c. magnetic field.

In this work, the analysis of microstrip line tapers on ferrimagnetic layers is developed. This analysis is performed in the Fourier domain, by considering a simplified model for the tapered line section, and using the Green's function technique and the Galerkin method [1],[4],[6]. The analysis is developed for the dominant mode and it is assumed that a uniform external magnetic field H_o is applied along the microstrip longitudinal direction (direction z, in Fig. 1).

Results were obtained for the input impedance and reflection coefficient for both the taper on ferrites and on isotropic dielectric substrates. It should be mentioned that the results for the taper on isotropic dielectric substrates were obtained as a particular case of the analysis developed for tapers on ferrites. Furthermore, a good agreement was observed, for this particular structure, when the results of this work were compared to those available in the literature.

Theory

The structure considered in this work is shown in Fig. 1. It is a tapered microstrip transmission line section on a magnetized ferrimagnetic layer. Region 1 is ferrite and since that the bias is applied along z direction, the permeability tensor $\tilde{\mu}$ of the ferrimagnetic substrate is given by [1],[3]

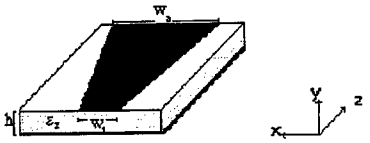

Fig. 1 - Tapered microstrip line section on ferrite.

$$\tilde{\mu} = \begin{bmatrix} \mu & ik & 0 \\ -ik & \mu & 0 \\ 0 & 0 & \mu_0 \end{bmatrix} \tag{1}$$

with μ and k given by

$$\frac{\mu}{\mu_o} = 1 - \frac{\gamma^2 H_o 4\pi M_s}{\omega^2 - (\gamma H_o)^2} \tag{2}$$

$$\frac{k}{\mu_o} = \frac{\gamma 4\pi M_s}{\omega^2 - (\gamma H_o)^2} \tag{3}$$

where $4\pi M_s$ is the saturation magnetization, γ is the gyromagnetic ratio, ω is the operating frequency, and μ_0 is the permeability of free-space.

Furthermore, region 2, in Fig. 1, is air filled and a linear variation of the conducting strip width, W(z), is considered, while the substrate thickness, h, is kept constant.

In the first step of this analysis, the tapered microstrip transmission line section is divided into N subsections, and, in the second step, it is modeled as a cascaded combination of uniform microstrip subsections. Then, to analyze each of these microstrip subsection, the Green's function technique and Galerkin method are used.

To determine the dyadic Green's function for each microstrip subsection, Hertz vector potentials along z direction (Fig. 1) are assumed, so that

$$\bar{\pi}_e = \pi_e z \tag{4}$$

$$\bar{\pi}_h = \pi_h \hat{z} \tag{5}$$

These electric and magnetic Hertz potentials should satisfy the following wave equations

$$\nabla^2 \bar{\pi}_e + \omega^2 \frac{\left(\mu^2 - k^2\right)}{\mu} \varepsilon \bar{\pi}_e = 0 \tag{6}$$

$$\nabla^2\overline{\pi}_h + \omega^2\mu_o\varepsilon\overline{\pi}_h + \frac{(\mu_o-\mu)}{\mu}\frac{\partial^2\overline{\pi}_h}{\partial\eta^2} = 0 \tag{7}$$

From Maxwell's equations, the expressions for the electric, $\overline{E}$, and magnetic, $\overline{H}$, fields are obtained as

$$\overline{E} = -j\omega\mu\nabla\times\overline{\pi}_h + \omega^2\mu_o\left(\frac{\mu^2-k^2}{\mu^2}\right)\varepsilon\overline{\pi}_e + \frac{\mu_o}{\mu}\nabla\nabla.\overline{\pi}_e \tag{8}$$

$$\overline{H} = j\omega\mu_o\frac{(\mu^2-k^2)}{\mu^2}\varepsilon(\overline{\mu})^{-1}\nabla\times\overline{\pi}_e + \omega^2\mu\varepsilon\overline{\pi}_h + \nabla\nabla.\overline{\pi}_h \tag{9}$$

To solve the boundary value problem, the transformation given by [4]

$$\widetilde{\Omega}(\alpha,y) = \int_{-\infty}^{\infty}\Omega(x,y)e^{-jx\alpha}dx \tag{10}$$

$$\Omega(x,y) = \frac{1}{2\pi}\int_{-\infty}^{\infty}\widetilde{\Omega}(\alpha,y)e^{j\alpha x}d\alpha \tag{11}$$

is used, where ~ means the transformed function.

Furthermore, the wave equations for $\overline{\pi}_e$ and $\overline{\pi}_h$, as well as the expressions for the electric and magnetic fields components, were obtained, after some algebraic manipulation, in the Fourier domain.

Then, by imposing the boundary conditions for the structure considered (Fig. 1), the final expressions for π_e and π_h, in the ferrite substrate (region 1) and dielectric layer (region 2), were obtained, from which the transformed electric and magnetic fields expressions were derived.

Therefore, for each uniform microstrip subsection, at y = h (Fig. 1), the transformed electric field components are expressed as functions of the transformed surface current density components, as given by

$$\widetilde{E}_x(\alpha) = \widetilde{Z}_{xx}(\alpha,\beta)\widetilde{J}_x(\alpha) + \widetilde{Z}_{xz}(\alpha,\beta)\widetilde{J}_z(\alpha) \tag{12}$$

$$\widetilde{E}_z(\alpha) = \widetilde{Z}_{zx}(\alpha,\beta)\widetilde{J}_x(\alpha) + \widetilde{Z}_{zz}(\alpha,\beta)\widetilde{J}_z(\alpha) \tag{13}$$

where $\widetilde{Z}_{xx}$, $\widetilde{Z}_{xz}$, $\widetilde{Z}_{zx}$, and $\widetilde{Z}_{zz}$ are the dyadic Green's function components for the microstrip structure considered.

After the determination of the impedance matrix $[\widetilde{Z}]$, Galerkin method and Parseval's theorem are used to derive the determinantal equation for the propagation constant and effective permittivity[4].

To determine the characteristic impedance for each uniform microstrip subsection, a power-current definition is used [4]

$$Z_0 = \frac{2P}{I^2} \tag{14}$$

with

$$P = \frac{1}{2}\mathrm{Re}\iint\left(E_x H_y^* - E_y H_x^*\right)dydx \tag{15}$$

and

$$I = \int_{-w/2}^{w/2} J_z(x)dx \tag{16}$$

Note that this analysis gives numerical results for tapered microstrip lines on dielectric substrates as a particular case, which is obtained by imposing $k = 0$ and $\mu = 1$ in the derived equations.

In order to obtain the vswr and the input impedance and reflection coefficient, the values for the characteristic impedance and effective permittivity are determined for the N microstrip subsections, taking into account that a linear variation was considered for the strip width along the taper (Fig. 1). After that, the transmission line theory is used to determine the taper input parameters from given values for the load impedance (Z_L), input (W_1) and output (W_2) conducting strip width, frequency (f), microstrip substrate height (h), and ferrimagnetic material parameters. Finally, an interactive procedure is used to study the cascaded combination of the uniform microstrip subsections.

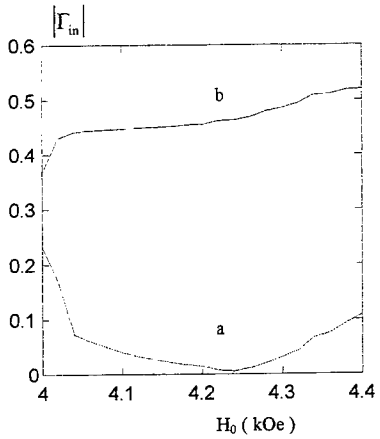

Fig. 3 - Input impedance reflection coefficient versus H_0. $\mathbf{H_0}$ is in z direction.

Therefore, the determination of several parameters of the microstrip taper, or tapered microstrip line, on ferrites and their circuits, such as impedance transformers and antennas, is achieved.

Results

Results for the vswr and input impedance and reflection coefficient are presented for microstrip lines on both ferrimagnetic and dielectric substrates. Fig. 2 shows the results obtained for the vswr as function of the magnitude of the applied d.c. magnetic field, H_o , for different values of the load impedance, Z_L.

In Fig. 3, the results obtained for the magnitude of the input reflection coefficient are shown versus the magnitude of H_o, for the same values of Z_L considered in Fig. 2.

Fig. 4 depicts the results obtained for the input impedance of the tapered microstrip line section on ferrite substrate considered in Fig. 2.

Note, from Figs. 2 to 4, that the variation of H_0 allows to change the properties of microstrip tapers on ferrites, showing a magnetic impedance matching possibility, for instance.

Finally, the numerical results obtained for the particular case ($\mu = 1$ and $k = 0$) of tapers on dielectric substrates are in agreement with the results available in the literature [7].

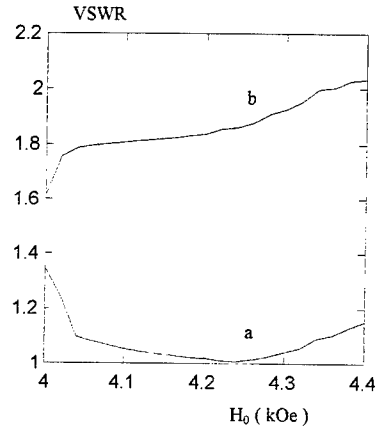

Fig. 2 - VSWR versus H_0. F = 9 GHz, W_1 = 0.1519 cm, W_2 = 0.4807 cm, h = 0.1150 cm, L = 0.15 cm, ε_r = 16.6, $4\pi M_s$ = 2300 G, and γ = 2,86 MHz/Oe. Load impedance, Z_L, values: a) 10 - j1 Ω and b) 15 + j15 Ω. $\mathbf{H_0}$ is in z direction (Fig. 1).

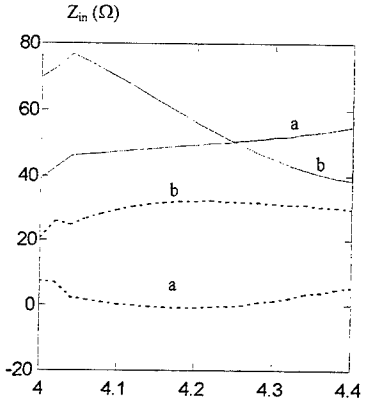

Fig. 4 - Input inpedance versus H_0. Rin (——) and X_{in} (-------). $\mathbf{H_0}$ is in z direction.

Conclusion

The analysis of microstrip tapered lines on ferrites was developed. The variation of the conducting strip width was assumed. A combination of Hertz potentials and Galerkin method was used to analyze the microstrip subsections in a model based on a segmentation of the considered structure. It was observed that the analysis developed in this work is accurate and can be used to investigate others planar structures properties. Also, a magnetic impedance matching possibility for microstrip circuits was observed.

Acknowledgment

This work was partially supported by the Brazilian Research Agency CNPq.

References

[1] A.G. D'ASSUNÇÃO and E.J. DANTAS, "On the resonant frequency of magnetized rectangular microstrip patch resonators", IEEE/AP-S Int. Antennas and Propagation Symp., Ann Arbor, MI, p. 1508-1501, June 1993.

[2] D.M. POZAR, "Radiation and scattering characteristic of microstrip antennas on normally biased ferrite substrates", IEEE Trans. Antennas and Propagation, vol. AP-40, p. 1084-1092, Sept. 1992.

[3] M. GESHIRO and T. ITOH, "Analysis of a coupled slotline on a double layered substrate containing a magnetized ferrite", IEEE Trans. Microwave Theory Tech., vol. MTT-40, p. 765-768, April 1992.

[4] M.R.M.L. ALBUQUERQUE, A.G. D'ASSUNÇÃO and A.J. GIAROLA, "Spextral domain analysis of coupled microstrip lines on magnetized ferrite substrates", Int. Journal of Infrared and Millimeter Waves, vol. 14, p. 1531-1544, 1993.

[5] R. A. PUCEL and D. J. MASSÉ, "Microstrip propagation on magnetic substrates part 1: Design Theory", IEEE Trans. Microwave Theory Tech.; v. MTT-20, p. 309-313, 1972.

[6] M.R.M.L.ALBUQUERQUE, A. G. D'ASSUNÇÃO, M. R. G. MAIA, and A. J. GIAROLA, "Dynamic characteristics of microstrip lines on magnetized ferrite substrates", Proc. 20th European Microwave Conference, Budapest, Hungary, p. 1317 - 1321, 1990.

[7] K.N. SURYANARAYANA RAO, V. MAHADEVAN, and S.P. KOSTA, "Analysis of straight tapered microstrip transmission lines - ASTMIC", IEEE Trans. Microwave Theory Tech., vol. MTT-25, p. 164, Feb. 1977.

Frequency and Time Domain Computations of S-Parameters Using the Finite Integration Technique

R.Schuhmann, M.Clemens, P.Thoma, T.Weiland

Technische Hochschule Darmstadt, FB 18, Schloßgartenstr. 8, 64289 Darmstadt, Germany
Phone:+49(0)6151/164028, Fax:+49(0)6151/164611,
e-mail: dd80@temf00.temf.e-technik.th-darmstadt.de

Abstract

The computation of S-parameters for microwave structures is of increasing importance for many technical applications. It requires the simulation of infinitely long waveguides connected to the port planes by appropriate open waveguide boundary conditions. Within electromagnetic field-computation using the Finite Integration Technique (FIT), a broadband waveguide boundary operator is available, which allows the calculation of S-parameters over a wide frequency range from only one time domain-computation, if the simulated waveguide is homogeneously filled and lossfree.

In this paper we present a new formulation of this operator, which is also applicable to frequency domain calculations using FIT. Starting with the solution of the two dimensional eigenvalue problem given by the waveguide to be simulated, this algorithm yields a large system of equations with a non-symmetric complex system matrix, which can be solved by modern Krylov subspace-type methods.

After giving a short introduction to the method, we derive the open waveguide boundary operator as well as its implementation in time and fequency domain algorithms. Finally we present two realistic examples of microwave structures to demonstrate the applicability of the operator to both approaches.

Introduction

A well-known discretization approach in the computation of electromagnetic fields is the so-called Finite Integration Technique (FIT, cf. [8, 9]). Similar to Finite Difference approaches (cf. [10]), the electric and magnetic fields within FIT are represented as discrete vectors on a grid doublet, consisting of the normal grid G and its dual grid $\tilde{G}$. Starting from Maxwell's equations in their integral form, the analytical operators **curl** and **div** can be transformed in matrix operators C and S (respectively $\tilde{C}$ and $\tilde{S}$ on the dual grid), yielding algebraic equations

$$\begin{aligned} C\mathbf{e} &= -\dot{\mathbf{b}} \\ \tilde{C}\mathbf{h} &= \mathbf{j} + \dot{\mathbf{d}} \\ S\mathbf{b} &= 0 \\ \tilde{S}\mathbf{d} &= q. \end{aligned} \tag{1}$$

In these so-called Maxwell's Grid Equations (MGE's), the vectors **e** and **h** represent the electric and magnetic voltages along grid lines, and **d** and **h** are electric resp. magnetic flux quantities through grid faces. C, $\tilde{C}$, S and $\tilde{S}$ are topological matrices, consisting only of $\{-1, 0, 1\}$.

The electric and magnetic material equations in grid space are

$$\begin{aligned} \mathbf{d} &= D_\epsilon \mathbf{e} \\ \mathbf{j} &= D_\kappa \mathbf{e} \\ \mathbf{b} &= D_\mu \mathbf{h}, \end{aligned} \tag{2}$$

where D_ϵ, D_κ and D_μ are diagonal matrices for cartesian (and some other) grids. For more details see references [1, 8, 9].

The Waveguide Boundary Operator

Derived from evaluated line integrals around grid faces, the discretized **curl**-operator C is a large sparse $3N_P \times 3N_P$ matrix (N_P =number of grid points), connecting only neighbouring components of the discrete field vector **e**. Thus the introduction of any boundary condition only requires the correction of those entries in C refering to the tangential $\vec{E}$-components at the boundary plane.

In the following we consider the waveguide termination shown in Fig.1.

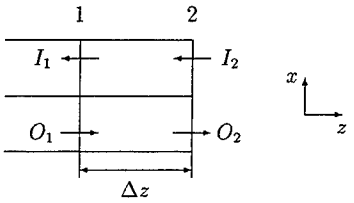

Figure 1: Coefficients of an incoming, respectively, outgoing wave at a waveguide boundary.

To obtain the tangential $\vec{E}$-field at the boundary plane 2, a modal expansion at plane 1 is performed, one grid step in front of the termination.

As a first step, the eigenmodes in the infinitely long waveguide have to be determined. Applying MGE's in frequency domain to the calculation of lossless waveguides with arbitrary shaped cross-sections (cf. [6, 8]) yields an algebraic eigenvalue problem

$$A_{2D} \cdot \mathbf{e}_i - \omega^2 D_1 \mathbf{e}_i = k_{z,i}^2 D_2 \, \mathbf{e}_i, \tag{3}$$

where A_{2D} is the $2N_{2D} \times 2N_{2D}$ sparse system-matrix, $\mathbf{e}_i$ is the discrete ith eigenmode, and $k_{z,i}$ is its propagation constant at a given frequency ω. The magnetic fields of the eigenmodes can be obtained in frequency domain by

$$\mathbf{h}_i = -\frac{1}{j\omega} D_\mu^{-1} C_{2D} \, \mathbf{e}_i. \tag{4}$$

The eigenmodes in a waveguide satisfy the analytical orthogonality relation

$$\int\int_A (\vec{E}_i(x,y) \times H_j^*(x,y)) \cdot dA = \delta_{ij}. \tag{5}$$

Within FIT, one can find an exact discrete analogon of this equation:

$$(\mathbf{e}_i, \mathbf{h}_j) := \mathbf{e}_i \mathbf{K} \mathbf{h}_j = \delta_{ij} \tag{6}$$

with a topological matrix $\mathbf{K}$ (cf. [1]). The tangential field in plane 1 can now be written as a superposition of all these modes

$$\mathbf{e}(x, y, z_1) = \sum_1^\infty a_i \mathbf{e}_i(x, y), \tag{7}$$

expanding the (2-dimensional) vectors $\mathbf{e}_i$ and $\mathbf{h}_j$ to full 3D-length where necessary. The coefficients a_i are given in gridspace by

$$a_i = (\mathbf{e}(z_1), \mathbf{h}_i). \tag{8}$$

Each of these coefficients a_i can be split up into two parts propagating along $\pm z$-direction, named I_1 and O_1 as shown in Fig.1. In frequency domain representation the coefficients of a single mode at planes 1 and 2 satisfy

$$\begin{aligned} I_1 = e^{-jk_z\Delta z} I_2 \quad , \quad O_2 = e^{-jk_z\Delta z} O_1 \\ a_1 = I_1 + O_1 \quad , \quad a_2 = I_2 + O_2 \end{aligned} \tag{9}$$

From this we get the following algorithm to obtain the tangential $\vec{E}$-components at plane 2:

1. Compute (some of) the discrete 2D-eigenmodes (including their propagation constants) of the infinitely long waveguide by solving the eigenvalue problem (3).
2. Perform a modal expansion of the tangential electric field at plane 1, yielding coefficients a_i for a number of modes.
3. For each mode, compute $a_2 = I_2 + O_2$ at plane 2, where I_2, representing a wave coming from outside the structure, is known a priori. From (9) we have
$$a_2 = I_2(1 - e^{-2jk_z\Delta z}) + a_1 e^{-jk_z\Delta z}. \tag{10}$$
4. Compute the tangential electrical field at plane 2 from (7).

The final computation of the desired S-parameters is quite a simple task, since the amplitudes of the outgoing waves O_2 at the boundary plane (respectively their power O_2^2) just have to be normalized to the power of the exciting mode (I_2^2).

Time Domain Implementation

To implement the open waveguide boundary operator in a leap-frog type time-domain scheme (cf. [1]), equations (9) have to be transformed from the frequency domain representation above (with $k_{z,i} = k_{z,i}(\omega)$) into a time domain formulation.

If we restrict the waveguide to be homogeneously filled (and still lossless), the eigenvectors of eq.(3) and thus the transversal electric mode fields are not frequency dependent. The propagation constant $k_{z,i}$ and the frequency ω are then correlated by the discrete dispersion relation

$$\left(\frac{sin(\omega\Delta t/2)}{c\Delta t/2}\right)^2 = \left(\frac{sin(\omega_c\Delta t/2)}{c\Delta t/2}\right)^2 + \left(\frac{sin(k_{z,i}\Delta z/2)}{\Delta z/2}\right)^2, \tag{11}$$

where Δt is the timestep, and ω_c is the cutoff frequency of the mode.

In [2] a one dimensional discrete transmission line model is derived, which allows to simulate this dispersive behaviour of the waveguide over a wide frequency range. The additional reflection caused by this model can be adjusted a priori by means of the length of the transmission line, and can be limited down to the dimensions of numerical noise. Comparisons with monochromatic calculations show the excellent accuracy of the broadband simulation (cf. [2]).

A remarkable feature of this boundary operator is, that the maximum stable timestep for the field computation is not affected by the open waveguide simulation.

Frequency Domain Implementation

Transforming Maxwell's Grid Equations into the frequency domain yields

$$\begin{aligned} C\mathbf{e} &= -j\omega\mathbf{b} && (12)\\ \tilde{C}D_\mu^{-1}\mathbf{b} &= j\omega D_\epsilon\mathbf{e}+\mathbf{j} && (13)\end{aligned}$$

Inserting (12) in (13) we get the so-called *curl-curl-equation* (cf. [4])

$$\tilde{C}D_\mu^{-1}C\mathbf{e}-\omega^2 D_\epsilon\mathbf{e}=-j\omega\mathbf{j}, \qquad (14)$$

corresponding to the analytical form

$$\mathbf{curl}\ \mu^{-1}\mathbf{curl}\ \vec{\mathbf{E}}-\omega^2\epsilon\vec{\mathbf{E}}=-j\omega\vec{\mathbf{J}}. \qquad (15)$$

The system matrix of (14)

$$A_1=\tilde{C}D_\mu^{-1}C-\omega^2 D_\epsilon \qquad (16)$$

is complex symmetric in the general lossy case and real symmetric in the loss-free case having real material coefficients ϵ and μ.

To implement the open waveguide boundary operator, the algorithm above has to be transformed in a matrix-equation conforming to (14). The tangential field at the boundary plane is (considering only one eigenmode)

$$\begin{aligned}\mathbf{e}(z_2) &= a_2\mathbf{e}_i\\ &= \left[I_2(1-e^{-2jk_{z,i}\Delta z})+a_1e^{-jk_{z,i}\Delta z}\right]\mathbf{e}_i\end{aligned}$$

with

$$\begin{aligned}a_1\mathbf{e}_i &= (\mathbf{e}(z_1),\mathbf{h}_i)\,\mathbf{e}_i\\ &= (\mathbf{e}_i\mathbf{h}_i^T\mathbf{K})\,\mathbf{e}(z_1).\end{aligned}$$

Including this formula in the matrix-equation (14), we get a new linear system

$$A_2\mathbf{e}=\mathbf{r}_2, \qquad (17)$$

with the extended system matrix

$$A_2=A_1+\omega^2 D_\epsilon\sum_i(e^{-jk_{z,i}\Delta z}\mathbf{e}_i\mathbf{h}_i^T\mathbf{K}), \qquad (18)$$

where the summation has to be performed over all modes considered in the modal expansion.

The excitation by the incoming wave(s) with coefficients $I_{2,i}$ is included in the right hand side

$$\mathbf{r}_2 = -j\omega\mathbf{j} - \omega^2 D_\epsilon \sum_i I_{2,i}(1 - e^{-2jk_{z,i}\Delta z})\mathbf{e}_i. \tag{19}$$

The new system matrix is

- *complex* due to the propagating term $e^{-jk_{z,i}\Delta z}$ and
- *nonsymmetric* due to the fact, that the modal expansion is performed in plane 1, but its results are applied in plane 2.

To solve (17), some modern Krylov subspace-type algorithms are applied, among which are the BiCG-algorithm of Jacobs [5] and the stabilized approach TFQMR (Transpose-free Quasi-Minimal Residual) by Freund [3], which is closely related to the CGS-solver by Sonneveld [7].

The performance of all these algorithms strongly depends on the spectrum of the system matrix, which makes a preconditioning of the system matrix almost always mandatory to improve the distribution of its eigenvalues in the complex plane.

Applying preconditioning on complex, nonsymmetric matrices is not yet completely understood and still requires a large amount of numerical experience. In our case we apply a memory-efficient SSOR left-preconditioning with the preconditioning matrix

$$M = (\Delta - L)\,\Delta^{-1}\,(\Delta - U), \tag{20}$$

where Δ is the diagonal, L the strictly lower and U the strictly upper part only of the symmetric part A_1 of the system matrix A_2. This seems to be a reasonable approach, since the non-symmetric 'perturbation' of A_1 by the waveguide boundary operator gets smaller, when the number of grid points is increased. This assumption is confirmed by the numerical results shown below.

Examples

In the first example the S-Parameters of a waveguide coupler (cf. Fig.2) are calculated. The structure is discretized with $53 \times 2 \times 128 = 13568$ grid points, yielding a system of 40704 complex linear equations for the frequency domain approach.

In time domain, the infinetly long waveguides at the boundary ports can be simulated in one single broadband computation within a few minutes of CPU time on a SUN Sparc 20. Approximately the same computation time is needed for each frequency domain calculation at a fixed frequency. Thus the time domain approach must be considered to be superior, as long as only the S-Parameters are to be determined.

If also the field patterns in the structure are of interest, in time domain a monochromatic calculation has to be performed, requiring approximately as much computational cost as the frequency domain algorithm.

The results for the reflection coefficient S_{11} at one of the ports is shown in Fig.3.

Fig.4 shows some typical convergence curves for the equation-solver process in the frequency domain calculation. The application of the PSSOR (Partial SSOR)-preconditioning described above significantly reduces the number of iterations needed.

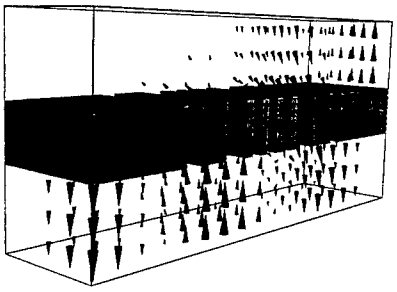

Figure 2: Real part of the electrical field $\mathrm{Re}\{\vec{E}\}$ in a waveguide coupler. Result from frequency domain calculation.

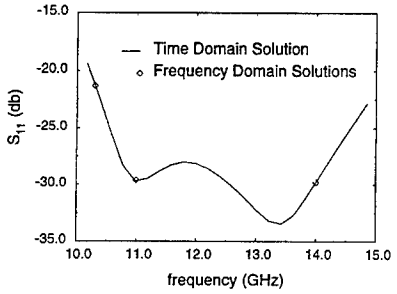

Figure 3: Reflection coefficient S_{11} of the waveguide coupler. The results from the frequency domain computation show excellent agreement with the time domain solution.

The second example shown in Fig.5 is a piece of a chip consisting of two microstrip ports and two thin wires connecting them with resistive blocks on the ground material. The conductivity of the resistive blocks is $\kappa = 13000$ S/m, the substrat has the permittivity $\epsilon_r = 9.0$. The geometrical extensions are about $700\mu m \times 300\mu m$. The structure is discretized with $71 \times 20 \times 85 = 120700$ grid points. The task here was to determine the cross-talk from one wire to the other at a frequency of about 5-20 GHz.

Having inhomogeneous waveguide ports here, their two-dimensional eigenmodes are frequency-dependent, and thus the time domain simulation by the transmission line model is only accurate in a relatively small frequency range. Fig.6 shows the results from several time domain computations optimized for different middle frequencies, versus the results from some frequency domain calculations. Even at the very low cross-talk rates below 50 db, the agreement is very good.

The computation time on a SUN Sparc 20 is about 3-5 hours for one time domain computation, and about 8-12 hours for one frequency domain run. Applying the preconditioned TFQMR-solver in double precision, the storage requirement for the frequency domain computation with 362,100 complex unknowns is about 80 MByte.

Due to the large amount of time steps needed, monochromatic calculations in the time domain are too expensive at frequencies lower than 20 GHz. To obtain field patterns in this frequency

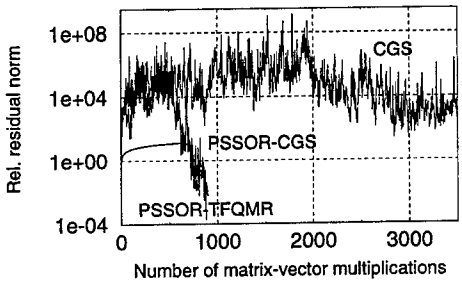

Figure 4: Frequency domain calculation of the waveguide coupler: Convergence curves of PSSOR preconditioned CGS and TFQMR methods versus the CGS method without preconditioning.

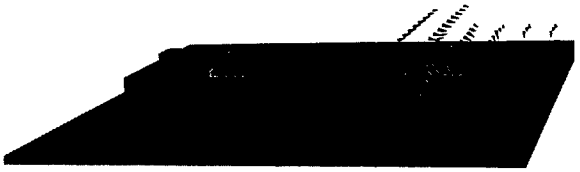

Figure 5: Real part of the magnetic flux density $\mathrm{Re}\{\vec{B}\}$ in a microstrip structure at $f = 5$ GHz. Result from frequency domain calculation.

range, the frequency domain approach proves to be superior here.

Conclusion

In this paper we presented the calculation of S-parameters using an open waveguide boundary operator, which is applicable to both broadband time domain and frequency domain calculations with the Finite Integration Technique (FIT).

In frequency domain, this operator leads to a system of linear equations with a large, sparse, complex and non-symmetric system matrix. To solve this system, modern Krylov subspace-type methods like CGS and TFQMR, combined with a partial SSOR preconditioning, are applied. Two realistic examples with up to 362,100 complex unknowns demonstrate the good performance of these solvers. The agreement with the time domain solutions is excellent.

Applying the time domain algorithm yields the S-parameters within a wide frequency range from a single computation, as long as the waveguide ports are lossless and homogeneously filled.

If one is interested in field patterns at very low frequencies, or if inhomogeneous waveguides have to be simulated, the frequency domain approach becomes competitive due to the large amount of time steps needed for monochromatic time domain calculations.

References

[1] Dohlus, M.: *Ein Beitrag zur numerischen Berechnung elektromagnetischer Felder im Zeitbereich*. Dissertation, TH Darmstadt, 1992, pp. 38-45.

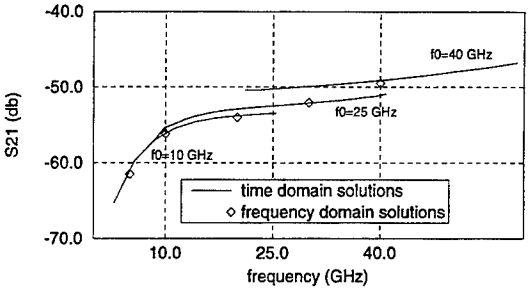

Figure 6: Cross-talk (S-Parameter S_{21}) of the microstrip structure. Three time domain calculations optimized for middle frequencies f_0 = 10 GHz, 25 GHz, 40 GHz versus frequency domain solutions.

[2] Dohlus, M., Thoma, P.: *Broadband Simulation of Open Waveguide Boundaries within Large Frequency Ranges.* IEEE Berlin, 1993.

[3] Freund, R.W.: *A Transpose-Free Quasi-minimal Residual Algorithm for Non-Hermitian Linear Systems.* SIAM Journal on Scientific Computing, vol. 14(2), 1993, pp. 470-482.

[4] Hahne, P.: *Zur numerischen Berechnung zeitharmonischer elektromagnetischer Felder.* Dissertation, TH Darmstadt, 1992.

[5] Jacobs, D.A.H.: *The Exploitation of Sparsity by Iterative Methods*, in: Duff, I.S.: *Sparse Matrices and their Uses.* Springer, 1981, pp. 191-222.

[6] Schmitt, D.: *Zur numerischen Berechnung von Resonatoren und Wellenleitern.* Dissertation, TH Darmstadt, 1995.

[7] Sonneveld, P.: *CGS, a Fast Lanczos-type Solver for Nonsymmetric Linear Systems.* SIAM Journal on Scientific Computing, vol. 10(1), 1989, pp. 36-52.

[8] Weiland, T.: *A Numerical Method for the Solution of the Eigenvalue Problem of Longitudinally Homogeneous Waveguides.* Electronics and Communication (AEÜ), vol. 31, 1977, p. 308.

[9] Weiland, T.: *On the Unique Numerical Solution of Maxwellian Eigenvalue Problems in Three Dimensions.* Particle Accelerators, 1985, vol. 17, pp. 227-242.

[10] Yee, K.S.: *Numerical Solution of Initial Boundary Value Problems Involving Maxwell's Equations in Isotropic Media.* IEEE Transactions on Antennas and Propagation, vol. 17, 1966, pp. 585-589.

Time Domain Analysis of Microwave Structures by MRTD

Michael Krumpholz, Emmanouil Tentzeris, Rob Robertson, Linda P.B. Katehi

Radiation Laboratory, Department of Electrical Engineering and Computer Science
University of Michigan, Ann Arbor, MI 48109-2122

Abstract

The application of the method of moments directly to Maxwell's equations results in new time domain schemes with properties determined by the choice of the basis functions. In particular, expanding the unknown fields in scaling functions results in new multiresolution time domain (MRTD) schemes with highly linear dispersion characteristics. In comparison to Yee's FDTD scheme, these properties allow for a reduction of the mesh size by a factor of five per dimension.

I Introduction

As shown in recent publications on the foundations of the TLM method [1, 2], the method of moments represents a general approach for the discretization of partial differential equations. The application of the method of moments directly to Maxwell's equations yields time domain schemes with properties determined by the choice of the basis functions. While the TLM and FDTD methods are based on the expansion of the unknown fields in subdomain basis functions, multiresolution time domain (MRTD) schemes are derived using scaling and wavelet functions as a complete set of orthonormal basis functions. The dispersion of the MRTD schemes compared to the conventional Yee FDTD scheme shows an excellent capability to approximate the exact solution with negligible error for sampling rates approaching the Nyquist limit [3]. Furthermore, the combination of scaling functions and wavelets leads to a variable mesh grading for regions characterized by strong field variations or field singularities.

For the MRTD schemes presented in this paper, the unknown fields are expanded in pulse functions with respect to time and in a series of Battle–Lemarie scaling functions [4] with respect to space. The Battle–Lemarie scaling functions do not have compact support, thus the MRTD schemes have to be truncated with respect to space. However, this disadvantage is offset by the low–pass and band–pass characteristics in spectral domain, allowing for an apriori estimate of the number of resolution levels necessary for a correct field modeling. Furthermore, for this type of scaling function, the evaluation of the moment method integrals is simplified due to the existence of closed form expressions in spectral domain and simple representations in terms of cubic spline functions in space domain.

We denote the MRTD schemes based on scaling functions only by the S–MRTD scheme. Numerical examples of the S–MRTD scheme are given in this paper for the analysis of transmission lines and resonator structures with dielectric materials.

II Derivation of the S–MRTD scheme

The derivation of the S–MRTD scheme is similar to that of Yee's FDTD scheme which uses the method of moments with pulse functions as expansion and test functions [2]. For the derivation

of S–MRTD, the field components are represented by a series of scaling functions in space and and pulse functions in time. Furthermore, as for Yee's FDTD scheme, the field expansions of the magnetic field components are shifted by half a discretization interval in space and time with respect to the field expansions of the electric field components.

Maxwell's first vector equation,

$$\nabla \times \mathbf{H} = \varepsilon \frac{\partial \mathbf{E}}{\partial t} \quad , \tag{1}$$

for a homogeneous medium with the permittivity ε may be written in the form of three scalar cartesian equations as

$$\frac{\partial H_z}{\partial y} - \frac{\partial H_y}{\partial z} = \varepsilon \frac{\partial E_x}{\partial t} \tag{2}$$

$$\frac{\partial H_x}{\partial z} - \frac{\partial H_z}{\partial x} = \varepsilon \frac{\partial E_y}{\partial t} \tag{3}$$

$$\frac{\partial H_y}{\partial x} - \frac{\partial H_x}{\partial y} = \varepsilon \frac{\partial E_z}{\partial t} \quad . \tag{4}$$

In the same way, the second Maxwell's vector equation for a homogeneous medium with the permeability μ,

$$\nabla \times \mathbf{E} = -\mu \frac{\partial \mathbf{H}}{\partial t} \quad , \tag{5}$$

can be split into three scalar equations similar to eqs. (2), (3) and (4). We consider the discretization of eq. (2) in order to demonstrate the principles of the approach. The other remaining five equations may be discretized in the same way.

The electric and magnetic field components incorporated in eq. (2) are expanded as follows:

$$\begin{aligned}
E_x(\vec{r},t) &= \sum_{k,l,m,n=-\infty}^{+\infty} {}_kE^{\phi x}_{l+1/2,m,n}\; h_k(t)\; \phi_{l+1/2}(x)\; \phi_m(y)\; \phi_n(z) \\
H_y(\vec{r},t) &= \sum_{k,l,m,n=-\infty}^{+\infty} {}_{k+1/2}H^{\phi y}_{l+1/2,m,n+1/2}\; h_{k+1/2}(t)\; \phi_{l+1/2}(x)\; \phi_m(y)\; \phi_{n+1/2}(z) \\
H_z(\vec{r},t) &= \sum_{k,l,m,n=-\infty}^{+\infty} {}_{k+1/2}H^{\phi z}_{l+1/2,m+1/2,n}\; h_{k+1/2}(t)\; \phi_{l+1/2}(x)\; \phi_{m+1/2}(y)\; \phi_n(z) \quad ,
\end{aligned} \tag{6}$$

where ${}_kE^{\phi x}_{l,m,n}$, ${}_kH^{\phi y}_{l,m,n}$ and ${}_kH^{\phi z}_{l,m,n}$ are the coefficients for the field expansions in terms of scaling functions. The indices l, m, n and k are the discrete space and time indices related to the space and time coordinates via $x = l\Delta x$, $y = m\Delta y$, $z = n\Delta z$ and $t = k\Delta t$, where Δx, Δy, Δz and Δt represent the space and time discretization intervals in x–, y–, z– and t–direction. The function $h_m(x)$ is defined as

$$h_m(x) = h(\frac{x}{\Delta x} - m) \tag{7}$$

with the rectangular pulse function

$$h(x) = \begin{cases} 1 & \text{for } |x| < 1/2 \\ 1/2 & \text{for } |x| = 1/2 \\ 0 & \text{for } |x| > 1/2 \end{cases} \quad . \tag{8}$$

The function $\phi_m(x)$ is defined as

$$\phi_m(x) = \phi(\frac{x}{\Delta x} - m) \quad , \tag{9}$$

where $\phi(x)$ represents the cubic spline Battle–Lemarie scaling functions [4].

We insert the field expansions in eq. (2) and sample the equation using pulse functions as test functions in time and scaling functions as test functions in space. For the sampling with respect to time, we need the following integrals [2],

$$\int_{-\infty}^{+\infty} h_m(x)\ h_{m'}(x)\ dx = \delta_{m,m'}\ \Delta x \quad , \tag{10}$$

where $\delta_{m,m'}$ represents the kronecker symbol

$$\delta_{m,m'} = \begin{cases} 1 & \text{for } m = m' \\ 0 & \text{for } m \neq m' \end{cases} \quad , \tag{11}$$

and

$$\int_{-\infty}^{+\infty} h_m(x)\ \frac{\partial h_{m'+1/2}(x)}{\partial x}\ dx = \delta_{m,m'} - \delta_{m,m'+1} \quad . \tag{12}$$

For the sampling with respect to space, we use the orthogonality relation for the scaling functions [4],

$$\int_{-\infty}^{+\infty} \phi_m(x)\ \phi_{m'}(x)\ dx = \delta_{m,m'}\ \Delta x \quad . \tag{13}$$

To calculate the integral corresponding to eq. (12) for scaling functions, we make use of the closed form expression of the scaling function in spectral domain [4]. According to Galerkin's method [5], for complex basis functions, one has to choose the complex conjugant of the basis functions as test functions. We then obtain

$$\int_{-\infty}^{+\infty} \phi_m(x)\ \frac{\partial \phi_{m'+1/2}(x)}{\partial x}\ dx = \frac{1}{\pi} \int_0^{\infty} \left|\tilde{\phi}(\lambda)\right|^2\ \lambda\ \sin\lambda(m' - m + 1/2)\ d\lambda \quad , \tag{14}$$

where $\tilde{\phi}(\lambda)$ is the scaling function in spectral domain given in [4]. This integral may be evaluated numerically resulting in

$$\int_{-\infty}^{+\infty} \phi_m(x)\ \frac{\partial \phi_{m'+1/2}(x)}{\partial x}\ dx = \sum_{i=-\infty}^{+\infty} a(i)\ \delta_{m+i,m'} \quad . \tag{15}$$

The coefficients $a(i)$ for $0 \leq i \leq 8$ are shown in table 1, the coefficients $a(i)$ for $i < 0$ are given by the symmetry relation $a(-1-i) = -a(i)$. The Battle–Lemarie scaling function does not have compact but only exponential decaying support and thus, the coefficients $a(i)$ for $i > 8$ are not zero. However, these coefficients are negligible, since they affect the accuracy of the field computation only for very low values of the wave vector. We therefore use the approximation

$$\int_{-\infty}^{+\infty} \phi_m(x)\ \frac{\partial \phi_{m'+1/2}(x)}{\partial x}\ dx \approx \sum_{i=-9}^{+8} a(i)\ \delta_{m+i,m'} \tag{16}$$

i	$a(i)$
0	1.2918462
1	-0.1560761
2	0.0596391
3	-0.0293099
4	0.0153716
5	-0.0081892
6	0.0043788
7	-0.0023433
8	0.0012542

Table 1: The coefficients $a(i)$.

in order to obtain a MRTD scheme useful for practical applications.

As an example, we consider the sampling of the first term on the left hand side in eq. (2), $\partial H_z/\partial y$, in space and time. We obtain

$$\begin{aligned}
&\iiint\!\!\int \frac{\partial H_z}{\partial y}\ \phi_{l+1/2}(x)\ \phi_m(y)\ \phi_n(z)\ h_{k+1/2}(t)\ dx\ dy\ dz\ dt \\
&\quad = \sum_{k',l',m',n'=-\infty}^{+\infty} {}_{k'+1/2}H^{\phi z}_{l'+1/2,m'+1/2,n'}\ \delta_{l,l'}\ \delta_{n,n'}\ \delta_{k,k'} \left(\sum_{i=-9}^{+8} a(i)\ \delta_{m+i,m'}\right) \Delta x\,\Delta z\,\Delta t \\
&\quad = \left(\sum_{i=-9}^{+8} a(i)\ {}_{k+1/2}H^{\phi z}_{l+1/2,m+i+1/2,n}\right) \Delta x\,\Delta z\,\Delta t \quad . \qquad (17)
\end{aligned}$$

Proceeding in the same way with the two other terms yields a difference equation for a homogeneous medium with the permittivity ε,

$$\begin{aligned}
&\frac{\varepsilon}{\Delta t}\left({}_{k+1}E^{\phi x}_{l+1/2,m,n} - {}_{k}E^{\phi x}_{l+1/2,m,n}\right) \\
&\quad = \frac{1}{\Delta y}\sum_{i=-9}^{+8} a(i)\ {}_{k+1/2}H^{\phi z}_{l+1/2,m+i+1/2,n} - \frac{1}{\Delta z}\sum_{i=-9}^{+8} a(i)\ {}_{k+1/2}H^{\phi y}_{l+1/2,m,n+i+1/2} \ . \qquad (18)
\end{aligned}$$

III Numerical examples

The S-MRTD scheme is applied in the two–dimensional analysis of transmission lines and in the three–dimensional analysis of resonator structures with dielectric materials. Various examples demonstrate the advantages of MRTD over FDTD, in particular, it is shown that the minimum discretization for accurate MRTD results is close to only two points per wavelength representing the Nyquist limit.

The derivation of the two–dimensional(2D) MRTD scheme applied to transmission lines is discussed in detail in [6]. The 2D-MRTD scheme is applied to the analysis of the membrane stripline of Fig. 1 for the first two propagating modes. The analysis for the higher order propagating modes is straightforward. For simplicity in the simulation and without loss of accuracy, we approximate this geometry with the rectangular shielded stripline of Fig. 2. For the analysis

Mode	TEM	Shield TE_{10}
Analytic values	1.4324 GHz	3.4615 GHz
4x2 MRTD	1.4325 GHz	3.4648 GHz
Rel.Error	0.007%	0.095%
4x4 MRTD	1.4325 GHz	3.4641 GHz
Rel.Error	0.007%	0.075%
8x4 MRTD	1.4325 GHz	3.4633 GHz
Rel.Error	0.007%	0.052%
20x10 FDTD	1.4322 GHz	3.4585 GHz
Rel.Error	-0.014%	-0.087%

Table 2: Propagating mode frequencies

using Yee's FDTD scheme, a 20×10 mesh was used resulting in a total number of 200 grid points. When the structure was analyzed with the 2D-MRTD scheme, a 4×2 mesh (8 grid points) was chosen reducing the total number of grid points by a factor of 25. In addition, the execution time for the analysis was reduced by a factor of 4 to 5. The time discretization interval was chosen to be identical for both schemes and equal to the 1/5 of the 2D-MRTD maximum Δt. For the analysis we have chosen $\beta = 30$ and 8,000 time-steps [6].

From Table 2 it can be observed that the calculated frequencies of the two first propagating modes from 2D-MRTD scheme are very close to the theoretical values. The use of non-localized basis functions in the 2D-MRTD scheme causes significant effects. It is impossible to implement localized boundary conditions using the MRTD scheme, so the perfect electric boundary conditions are modelled by use of the image principle in a generic way. This implementation of the image theory is performed automatically for any number of PEC, PMC boundaries.

To calculate the characteristic impedance Z_o for the TEM mode of the stripline, we use the following equation:

$$Z_o = \frac{V}{I} = \frac{\int_{C_v} E_y dy}{\oint_{C_c} H dl} \quad , \tag{19}$$

where the integration paths C_v and C_c are shown in Fig.2. Since both of the schemes used in the analysis are discrete in space-domain, the above integrals are transformed to summations. It can be observed from Table 3 that the accuracy of the calculation of the Z_o by use of the MRTD is much better than that of the Yee's FDTD scheme with a 20x10 mesh (relative error -3.06%). The oscillating values of Z_o within 0.5Ω by use of the MRTD are due to the fact that the very small relative error is not determined by the discretization any more, but by the numerical errors of the MRTD code.

To model anisotropic dielectric material we separate Maxwell's first vector equation in:

$$\nabla \times \mathbf{H} = \frac{\partial \mathbf{D}}{\partial t} \tag{20}$$

and

$$\mathbf{D} = \varepsilon(\vec{r}, t)\, \mathbf{E} \quad , \tag{21}$$

	Z_o (Ω)	Relative error
Analyt. Value [6]	61.03	0.0%
4x2 MRTD	61.17	+0.23%
4x4 MRTD	61.44	+0.67%
8x4 MRTD	61.22	+0.31%
20x10 FDTD	59.16	-3.06%

Table 3: Z_o calculated by 2D-MRTD

Analytical Values (MHz)	27.290	37.136	42.343
FDTD ($10 \times 20 \times 15$)(MHz)	27.250	37.000	42.200
FDTD Relative Error	-0.146%	-0.366%	-0.337%
S-MRTD ($2 \times 6 \times 3$)(MHz)	27.370	37.370	42.420
S-MRTD Relative Error	0.292%	0.599%	0.299%
S-MRTD ($2 \times 5 \times 3$)(MHz)	27.700	38.300	43.970
S-MRTD Relative Error	1.480%	3.040%	3.700%
S-MRTD ($2 \times 4 \times 3$)(MHz)	29.400	41.900	48.600
S-MRTD Relative Error	7.170%	11.360%	12.870%

Table 4: Resonant Frequency data for a cavity one–quarter filled with dielectric material

where $\mathbf{D}$ represents the electric flux vector and $\varepsilon(\vec{r}, t)$ the space– and time–dependent permittivity tensor. These equations can be discretized using scaling and pulse functions in space and time domain as expansion factors in the method of moments [7]. The derivation of the three-dimensional MRTD scheme used to analyze resonant structures with dielectric materials is given in detail in [8]. The structure analyzed is a resonant cavity that is filled one-quarter with a dielectric material(see Fig. 3). The cavity has the dimensions $1m \times 2m \times 1.5m$, and the dielectric material has a relative dielectric constant equal to 64. The MRTD method applied to the structure in Figure 1 at a discretization of $2 \times 6 \times 3$ proved to be the closest approximation to analytic values. This is due to the fact that a discretization of $2 \times 4 \times 3$ is exactly the Nyquist limit for this structure, while a discretization of $2 \times 5 \times 3$ is very close to the Nyquist limit and will generate appreciable errors. The MRTD scheme is compared to analytical values and the Yee's FDTD scheme in Table 4. The time discretization interval $\Delta t = 0.9 \cdot 10^{-10} s$ is identical for both schemes. This time discretization interval was chosen to maximize the linear properties of the MRTD dispersion relation [7]. Both cases were run at 35,000 time steps. For the analysis using Yee's FDTD scheme, a mesh with $\Delta l = 0.1m$ was used resulting in a total number of 3000 grid points. In the $2 \times 6 \times 3$ analysis, a total number of 36 grid points was used, resulting in a factor of 83 memory improvement for MRTD. Additionally a factor of 10 improvement in computation time was found for the MRTD method.

IV Conclusion

The MRTD schemes based on orthonormal wavelet expansions exhibit highly linear dispersion characteristics which result in the capability of providing excellent accuracy for a discretization

close to two points per wavelength and close to the Nyquist sampling limit, respectively. Since the minimum discretization for accurate FDTD results is usually about ten points per wavelength, results for FDTD and MRTD exhibit about the same accuracy using a MRTD mesh with five times less grid points per dimension. For a three–dimensional time analysis, this results in computer savings of one order of magnitude with respect to execution time and two orders of magnitude with respect to memory requirements.

Acknowledgments

This work has been made possible by a scholarship of the NATO science committee through the German Academic Exchange Service and by the U.S. Army Research Office.

References

[1] M. Krumpholz, P. Russer, "Two–Dimensional FDTD and TLM", Int. Journal of Num. Modelling, vol. 7, no. 2, pp. 141-153, February 1993.

[2] M. Krumpholz, C. Huber, P. Russer, "A Field Theoretical Comparison of FDTD and TLM", IEEE Trans. on Microwave Theory and Tech., vol. 43, no. 8, pp. 1935-1950, September 1995.

[3] M. Krumpholz, L.P.B. Katehi, "New Prospects for Time Domain Analysis", IEEE Microwave Guided Wave Letters, vol. 5, no. 11, pp. 382-384, November 1995.

[4] I. Daubechies, "Ten Lectures on Wavelets", Philadelphia, PA: Society for Industrial and Applied Mathematics, 1992.

[5] R.F. Harrington, "Field Computation by Moment Methods", Krieger Publishing Company, Inc., Malabar, Florida, 1982.

[6] E. Tentzeris, M. Krumpholz, L.P.B. Katehi, "Application of MRTD to Printed Transmission Lines", Submitted to the 1996 IEEE Microwave Symposium.

[7] M.Krumpholz, L.P.B.Katehi, "MRTD: New Time Domain Schemes Based on Multiresolution Analysis", To be published in the IEEE Transactions on Microwave Theory and Techniques.

[8] R. Robertson, E. Tentzeris, M. Krumpholz, L.P.B. Katehi, "MRTD Analysis of Dielectric Cavity Structures", Submitted to the 1996 IEEE Microwave Symposium.

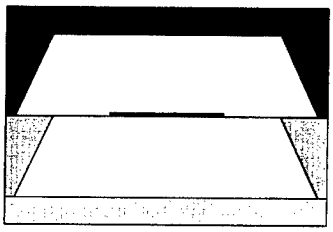

Figure 1: Membrane Stripline.

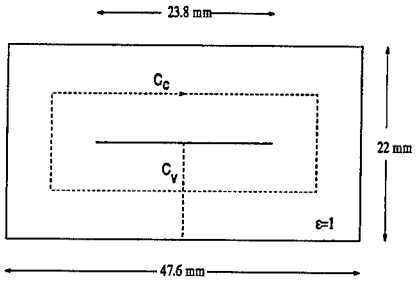

Figure 2: Stripline Geometry.

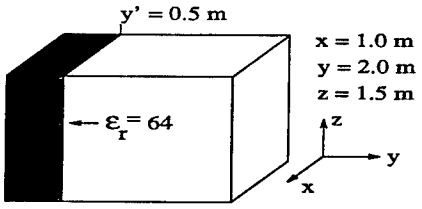

Figure 3: Quarter-Filled Dielectric Resonator

A PARASITE-FREE NON-ORTHOGONAL FINITE-DIFFERENCE FREQUENCY-DOMAIN METHOD FOR THE ANALYSIS OF INHOMOGENEOUS LOSSY WAVEGUIDES

Li Zhao and Andreas C. Cangellaris
Electromagnetics Laboratory, ECE Department
University of Arizona, Tucson, AZ 85721, U.S.A.

Abstract. A non-orthogonal finite-difference approximation of Maxwell's curl equations in the frequency domain is proposed for the dispersive analysis of inhomogeneous, lossy, waveguiding structures. The occurence of spurious modes is avoided by the direct enforcement of Gauss's law in the development of the matrix eigenvalue problem. Perfectly matched layers, constructed using coordinate stretching are used to effect grid truncation for the case of unshielded waveguides. Calculated $\omega - \beta$ diagrams for both shielded and unshielded waveguides are in excellent agreement with published results obtained using analytic or finite element techniques.

1. INTRODUCTION

Over the past several years, a variety of finite element formulations have been presented for the electromagnetic characterization of uniform waveguides with arbitrary cross-sectional geometries. For nodal-based formulations, the occurence of spurious modes is avoided either through the use of penalty terms in the finite element approximation of the vector eigenvalue problem, or by the elimination of the longitudinal component of the field through the use of the relevant differential form of Gauss's law (e.g., [1]). For waveguiding structures that contain metallic regions (e.g., microstrip, coplanar waveguide, etc.), finite element formulations using edge elements are found to be more convenient since they eliminate the need for special treatment of the field singularities occuring at the conducting edges [2].

An alternative to the finite element approximation of such eigenvalue problems is the use of a non-orthogonal finite-difference frequency-domain (FD-FD) technique. The orthogonal FD-FD method has been used with success in the past for the electromagnetic analysis of two- and three-dimensional structures [3]. Its extension to non-orthogonal grids with specific application to the dispersive characterization of lossy waveguides is the theme of this paper.

First, the discretization of Maxwell's equations using the nonorthogonal, finite difference frequency-domain method and the covariant and contravariant components of the fields is discussed. The emphasis is on the specific modifications required to render the formulation free from spurious modes. Next, specific applications of the proposed method to the analysis of shielded and unshielded waveguides are presented to demonstrate the validity of the method.

2. THEORY

The proposed method is based on the numerical discretization of the integral form of Maxwell's curl equations in the frequency domain. The electric field $\mathbf{E}$ and the magnetic field $\mathbf{H}$ are written in terms of their covariant components e_i and h_i, $(i = 1, 2, 3)$, respectively, or their contravariant components e^j and h^j, $(j = 1, 2, 3)$,

$$\mathbf{E} = \sum_{i=1}^{3} e^i \mathbf{a_i} = \sum_{j=1}^{3} e_j \mathbf{a^j} \tag{1a}$$

$$\mathbf{B} = \sum_{i=1}^{3} h^i \mathbf{a_i} = \sum_{j=1}^{3} h_j \mathbf{a^j} \tag{1b}$$

The details of the use of covariant and contravariant and the approximation of Maxwell's equations on non-orthogonal grids can be found in [4]-[5]. On a non-rectangular cell the covariant components of the electric field are placed along the edges, while the contravariant components of the magnetic flux density are placed along the normals at the centers of the edges. The axis of the waveguides is parallel to the z axis, which coincides with the u^3 axis. Since cell edges coincide with material interfaces, the aforementioned placement of the vector fields ensures the continuity of tangential electric field and normal magnetic flux density at material interfaces. In addition, this placement facilitates the enforcement of boundary conditions on conductor surfaces.

Faraday's law is approximated by choosing the surface for the calculation of the magnetic flux to be each of the faces of the grid cell and the contour for the calculation of the circulation of the electric field to be the corresponding bounding contour formed by cell edges. In a dual fashion, Ampère's law is approximated by choosing the surface for the calculation of the electric flux and current flow to be each of the faces of the dual grid cells and the contour for the calculation of the circulation of the magnetic field to be the corresponding bounding contour formed by cell edges.

For propagating modes, the field variation in z is of the form $\exp(-j\gamma z)$, where $\gamma = \beta - j\alpha$ is the complex propagation constant. In view of the fact that $\exp(-j\gamma\Delta z) \sim 1 - j\gamma\Delta z$, $\Delta z \to 0$, and introducing also the normalized covariant and contravariant components of the fields, we obtain the discrete forms of Maxwell's equations as folows

$$j\omega\epsilon_0 \left(\epsilon_r \sqrt{g/g_{11}} E^1\right)_{i+1/2,j} + \left(\sigma \sqrt{g/g_{11}} E^1\right)_{i+1/2,j} =$$

$$h_{3,i+1/2,j+1/2} - h_{3,i+1/2,j-1/2} - j\gamma h_{2,i+1/2,j} \tag{2}$$

$$-j\omega\mu_0 \left(\sqrt{g/g_{11}} H^1\right)_{i,j+1/2} = e_{3,i,j+1} - e_{3,i,j} - j\gamma e_{2,i,j+1/2} \tag{3}$$

$$-j\omega\mu_0 \left(\sqrt{g} H^3\right)_{i+1/2,j+1/2} = e_{2,i+1,j+1/2} - e_{2,i,j+1/2} - e_{1,i+1/2,j+1} + e_{1,i+1/2,j} \tag{4}$$

where ϵ_r is the relative dielectric constant and σ the conductivity.

The development of the eigenvalue equation for the complex propagation constant involves the elimination of either the electric or the magnetic field. The resulting eigenvalue

equation will involve the contravariant components of the selected field quantity. Thus, the covariant components need be transformed to the contravariant ones. For example,

$$e_{1,i+1/2,j} = \left(\sqrt{g}_{11}E^1\right)_{i+1/2,j} +$$

$$\frac{1}{4}\left(\frac{g_{12}}{\sqrt{g_{22}}}\right)_{i+1/2,j}\left(E^2_{i,j+1/2} + E^2_{i+1,j+1/2} + E^2_{i,j-1/2} + E^2_{i+1,j-1/2}\right) \tag{5}$$

Notice that interpolation is necessary since the component $E^2_{i+1/2,j}$ does not actually appear at the point $(i+1/2, j)$.

In order to eliminate spurious modes, the discretized integral form of Gauss's law is used to express the longitudinal component of the electric field in terms of the transverse components. The discrete form of the equation is

$$-j\gamma\left(\sqrt{g}E^3\right)_{i,j} = \left(\sqrt{g/g_{11}}E^1\right)_{i+1/2,j} - \left(\sqrt{g/g_{11}}E^1\right)_{i-1/2,j} +$$

$$\left(\sqrt{g/g_{22}}E^2\right)_{i,j+1/2} - \left(\sqrt{g/g_{22}}E^2\right)_{i,j-1/2} \tag{6}$$

Elimination of the magnetic flux vector from the resulting system of discrete equations yields the following generalized matrix eigenvalue problem

$$[\mathbf{A}]\{\mathbf{E}^{\mathbf{i}}_{\mathbf{t}}\} = (\gamma)^2[\mathbf{B}]\{\mathbf{E}^{\mathbf{i}}_{\mathbf{t}}\} \tag{7}$$

where $\{\mathbf{E}^{\mathbf{i}}_{\mathbf{t}}\}$ is the vector containing the transverse contravariant components of the electric field.

3. NUMERICAL RESULTS

To demonstrate the accuracy of the computer implementation of the proposed formulation a shielded coaxial structure was analyzed first. The center conductor was of circular cross section of radius 0.5 mm. the outer shield is square, 5mm per side. Both inner and outer conductors were assumed to be perfectly conducting. Fig. 1 illustrates the grid used for the discretization. The insulating material was homogeneous and lossy with relative dielectric constant of 4.5 and condictivity 0.05 S/m. Clearly, this structure supports a transverse electromagnetic field mode, for which the phase constant and attenuation constant can be obtained analytically. Figs. 2 and 3 provide a comparison of the analytical results and the numerical results for the phase constant, β, and attenuation constant, α, over a broad frequency range. Very good agreement is observed.

The second example involved a microstrip line on a lossy substrate, analyzed previously in [2] using a finite element formulation. The structure analyzed in [2] was enclosed in a square, perfectly conducting box, 2.5 mm per side. The strip width was 0.25 mm, its thickness was 0.05 mm, and the thickness of the substrate was 0.25 mm. The relative dielectric constant of the substrate was 9.0 and its conductivity 0.05 S/m. The structure modeled using the proposed non-orthogonal, frequency-domain finite-difference (NFDFD)

was enclosed in a rectangular box of width 1.5 mm and height 1.0 mm. Thus, for our simulations the side and top walls of the box were moved closer to the strip by 0.5 mm and 1.5 mm, respectively, compared to the structure studied in [2].

The phase constant and attenuation constant versus frequency for this smaller structure are indicated with the dashed lines in Figs. 4 and 5, respectively. While the differences in the phase constant are slight, differences in the attenuation constant as large as ~ 0.6 dB/m are observed. Notice that for the case of the phase constant the discrepancy between the FEM results for the larger structure and the NFDFD results for the smaller structure is larger at the lower frequencies, as expected. As frequency increases, the fields concentrate in the substrate, and thus the impact of the distance of the shield walls from the strip on the phase constant becomes negligible.

In order to effect an unshielded microstrip geometry, an absorber was introduced over the four cells next to the perfectly conducting walls of the shield used above. The absorber was constructed using coordinate stretching according to the theory presented in [6]. The stretching coefficient was increased quadratically from a value of 1 to a maximum value of 11 over the four absorber cells. The phase constant and attenuation constant calculated for this structure are depicted by the solid lines in Figs. 4 and 5, respectively. As expected, the phase constant is in excellent agreement with that obtained by the FEM analysis for the case of the larger shield. Also, there is now better agreement between the attenuation constants calculated by the two methods. The values obtained by the NFDFD method are $\sim 0.3 dB/m$ larger than those obtained in [2] over the entire frequency range used for the comparison.

4. SUMMARY

In summary, a frequency-domain finite-difference algorithm for the discretization of Maxwell's equations on non-orthogonal grids has been developed for the dispersive analysis of lossy waveguides. Spurious modes are avoided by the direct enforcement of Gauss' law in the development of the discrete eigenvalue problem. The method has been applied to the calulation of the propagation characteristics of coaxial-type and planar waveguides with lossy insulators. Comparisons of the results obtained by the proposed method with results calculated either analytically or by finite element techniques have been used to support the validity of the proposed methodology and its computer implementation.

REFERENCES

[1] W.C. Chew and M.A. Nasir, "A variational analysis of anisotropic, inhomogeneous dielectric waveguides," *IEEE Trans. Microwave Theory Tech.*, vol. 37, pp. 661-668, April 1989.

[2] Jin-Fa Lee, "Finite element analysis of lossy dielectric waveguides," *IEEE Trans. Microwave Theory Tech.*, vol. 42, pp. 1025-1031, 1994.

[3] T. Weiland, "On the numerical solution of Maxwell's equations and applications in the field of accelerator physics," *Particle Accelerators*, vol. 15, pp. 245-292, 1984.

[4] J.A. Stratton, *Electromagnetic Theory*, McGraw-Hill, New York, 1941.

[5] J.-F. Lee, R. Palendech, and R. Mittra, "Modeling three-dimensional discontinuities in waveguides using nonorthogonal FD-TD algorithm," *IEEE Trans. Microwave Theory Tech.*, vol. 40, pp. 346-352, 1992.

[6] M.A. Gribbons, W.P. Pinello, and A.C. Cangellaris, "A stretched coordinate technique for numerical absorption of evanescent and propagating waves in planar waveguiding structures," *Proc. of the 1995 International Microwave Symposium*, vol. 1, pp. 31-34, Orlando, Florida, May 1995.

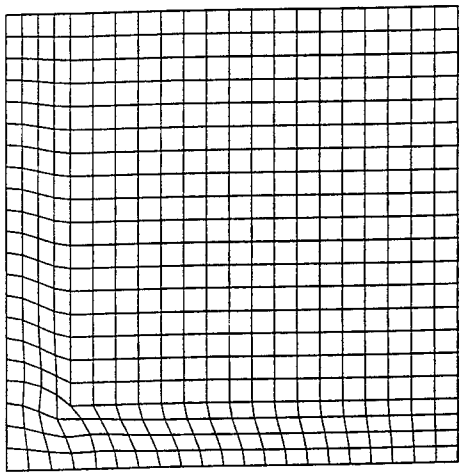

Fig. 1: Grid used for the discretization of the coaxial line.

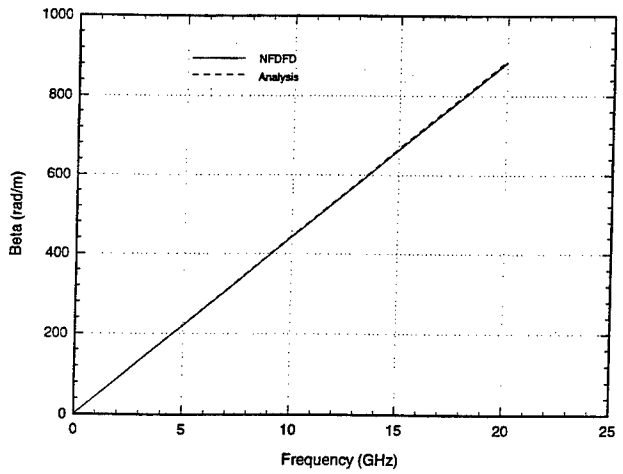

Fig. 2: Phase constant versus frequency for TEM mode propagation in the coaxial, lossy line.

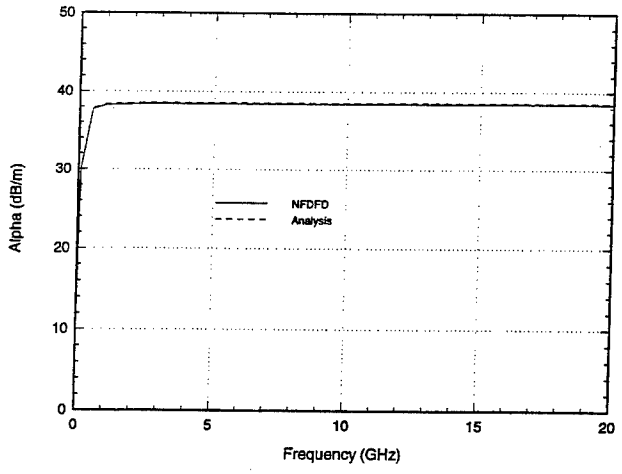

Fig. 3: Attenuation constant versus frequency for TEM mode propagation in the coaxial, lossy line.

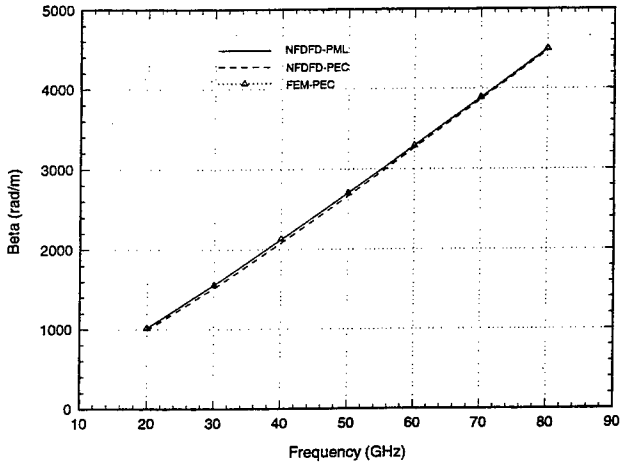

Fig. 4: Phase constant versus frequency for the fundamental mode of the microstrip structure with a lossy substrate.

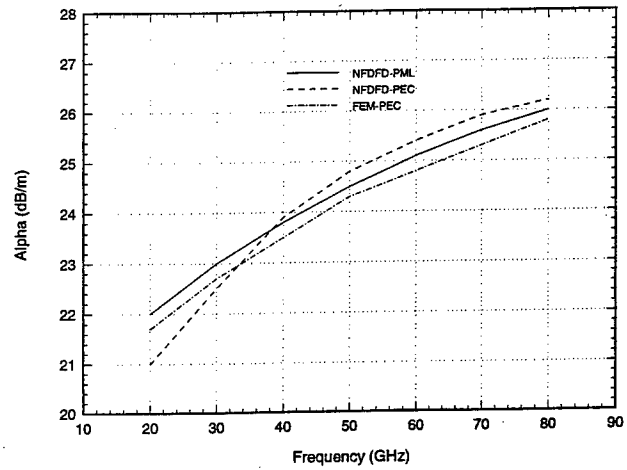

Fig. 5: Attenuation constant versus frequency for the fundamental mode of the microstrip structure with a lossy substrate.

SESSION 26:

BIOMEDICAL ELECTROMAGNETICS

Chairs: A. Morega and R. Gordon

A Spectral Approach to the Cardiography

by

Alexandru M. Morega Daniel Mocanu and Mihaela Morega
Department of Electrical Engineering,
Politehnica University of Bucharest,
ROMANIA

Abstract

The *Impedance Cardiography* (IC) is a well known investigation technique used in monitoring the cardiac cycle and in the evaluation of specific biological parameters such as the cardiac output. The dynamic impedance (an electric signal) that is produced by this procedure helps in interpreting the sources for the changes (e.g. heart malfunction) that might occur with respect to the normal cardiac activity. Although the impedance cardiography is widely used and trusted, it is still a matter of debate how to detect the sources for specific modifications in the impedance diagram. The present work reports preliminary results obtained in using the modal (eigenvalue) analysis related to the boundary element method (applied in modelling the transcutaneous pacing) for the interpretation of the spectral shiftings produced throughout the cardiac cycle. This technique, that we labelled *EigenValue Cardiography* (EVC), when applied in monitoring the cardiac cycle leads to a more detailed output that complement the IC picture of the cardiac activity.

Introduction

The Impedance Cardiography is widely recognised (Wang, X. et al., 1995) as a noninvasive, cost effective, easy to use and capable of long term continuous monitoring medical technique. Kubicek, W.G., (1970, 1993) and Patterson, R.P. (1965, 1985) initially introduced it through the thorax-model by using two sets of circumferential band electrodes. An AC current (100 KHz and 4 mA) is passed through one pair of electrodes while a voltage is picked-up by the second pair of electrodes. The *transfer impedance*, Z, defined by the ratio voltage-to-current, and its first order time derivative, dZ/dt, are quantities of interest used in two main research areas that emerged: (i) the investigation and modelling of physiological mechanisms aimed at interpreting the impedance wave-forms and (ii) the signal processing of the impedance wave-forms. It is worth noting that although, starting with the Minnesota Impedance device [Kubicek, W.G. (1970)], the hardware and software developed for implementing the IC have been continuously refined, their outputs are still focusing the researchers' attention [e.g. Kim, D.W. et al. (1988), Woo, E.J. et al. (1988), Mohamed, O.A et al. (1990), Sepulveda, N.G., et al. (1990)].

A novel technique, conceptually different from the IC, that reveals specific and significant insights of the cardiac cycle - the *EigenValue Cardiography (EVC).* - is introduced in our approach through the transcutaneous pacing modelling. However, the EVC may be seen as a fully stand-alone procedure, complementary to the IC. It is then useful to first briefly introduce the optimal pacing concept and model that led to the EVC idea and then the EVC itself.

The optimal transcutaneous pacing origins of the EVC

The transcutaneous cardiac pacing is a basic procedure used in emergencies (defibrillation, intensive care, etc.). Usually, two electrodes are placed on the thorax and used to apply an electric stimulus. The pacing threshold is reached for current densities that are higher in the chest wall than in the heart wall. Among the factors that significantly contribute to both the success of the intervention and in the reduction of its side-effects (pain, tissues necrosis, etc.) [Webster J.G. (1987)], the electrodes locations play an important role [Geddes L.A. et al. (1984, 1989), Panescu D. et al. (1994)].

Our 2-D analysis [Morega Al.M. et al. (1995)] for a detailed cross-sectional domain through a human torso was based on the boundary element method (BEM), technique recognised to be particularly effective in approaching complex geometries [Brebbia C.A. (1984)]. We considered the steady electrokinetic regime as described by Laplace equation with Dirichlet and Neumann (homogeneous) boundary conditions and proved that the ratio R -- peak current densities chest wall to heart - wall -- reaches the minimum when the positive electrode is positioned under the right scapula and the negative electrode is at the cardiac apex.

Recently, Wang, L. et al. (1995) reported an extended investigation on the optimal pacing. They used several real-life, magneto-resonance images (MRI) that offered the specific anatomic details of a patient, at particular moments of the cardiac cycle. The images were further digitised and used as input to their software tool in order to determine the response to the pacing procedure.

Starting from this experiment, we decided to investigate the behaviour of the eigenvalues of the "stiffness" matrix produced by the BEM. More precisely, the BEM that we used (a steady state approach in the preceding analysis) leads ultimately to an algebraic set of equations, consistent with the element type (constant), quadrature order and type (fourth order, Gauss-Legendre), method of solving the anisotropies, boundary conditions (those imposed by the optimal position for the electrodes) and definition of sub-domains:

$$A\,x = b\,.$$

This system is eventually solved for the solution x (the potential and its normal derivative w.r.t. the interfaces and boundaries of the model [Morega, Al.M. et al., (1995)]. It is possible and reasonable to investigate the eigenvalues spectrum of the stiffness matrix A and, further more, its shifting in response to the modifications of the organs shapes, electric properties, etc. such as for several instants of the cardiac cycle. A time-diagram for each eigenvalue may be produced and, conceivably, used to monitor the cardiac cycle, define quantities of interest, trace their evolution, compare their histories, etc. -- *this is the essence of the EVC.*

In our approach the EVC is intimately related to the BEM. It is essential to recognise and, hence, worth stressing that a *domain* method (such as for instance the Finite Element Method) leads to eigenvalues spectra that are related to *the domain* (organ) rather than to the surfaces - an information whose interpretation does not seem transparent so far. Further more, if in a 2-D context it is a matter of debate whether a boundary method is to be preferred to a domain method, in a 3-D model it seems that there are substantial advantages in using the BEM [Brebbia, C.A., (1984)]. So, besides reducing the problem dimensionality (the order of the algebraic system to be solved), the BEM offers - through its eigenvalues spectra - access to the EVC.

Numerical results

In order to test the EVC effectiveness we used a simplified structure of the torso based on the MRI reported by Wang L. et al. (1995) (fig. 1),

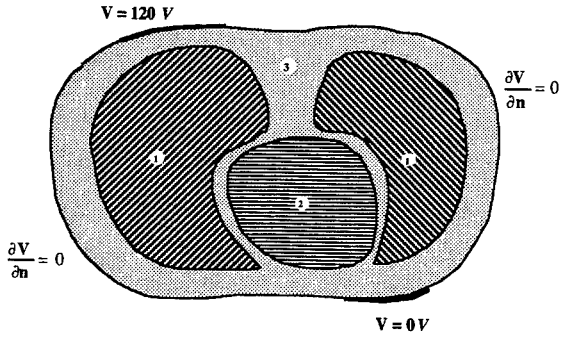

Figure 1. The (simplified) model used in the EVC analysis: **1.** lungs; **2.** heart; **3.** interstitial fluid..

The electric resistivities of these (linear) anatomic media are listed in Table 1,

Table 1. Electrical resistivities of the anatomic media

	Model 1	*Model 2*	*Model 3*	*Model 4*
ρ_{heart} [Ω·cm]	325	500	325	500
ρ_{lung} [Ω·cm]	1,348	1,348	1,325	1,325
ρ_{fluid} [Ω·cm]	150	150	150	150

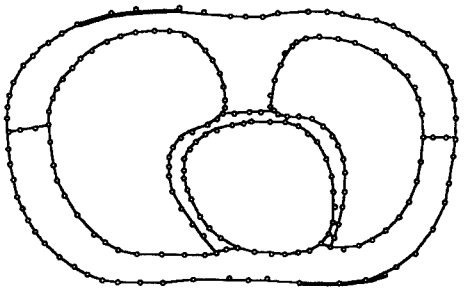

Figure 2. The BEM discretization mesh.

The domain Ω was split in homogeneous sub-domains (fig. 2). Constant elements and the 4-points Gauss-Legendre quadrature [Morega, Al.M. et al., (1992)] were used. The geometry and material properties were input (on a 286 PC compatible) to our home-made code (TURBO PASCAL and BORLAND C) that assembled the BEM matrices and solved this (reduced) problem.

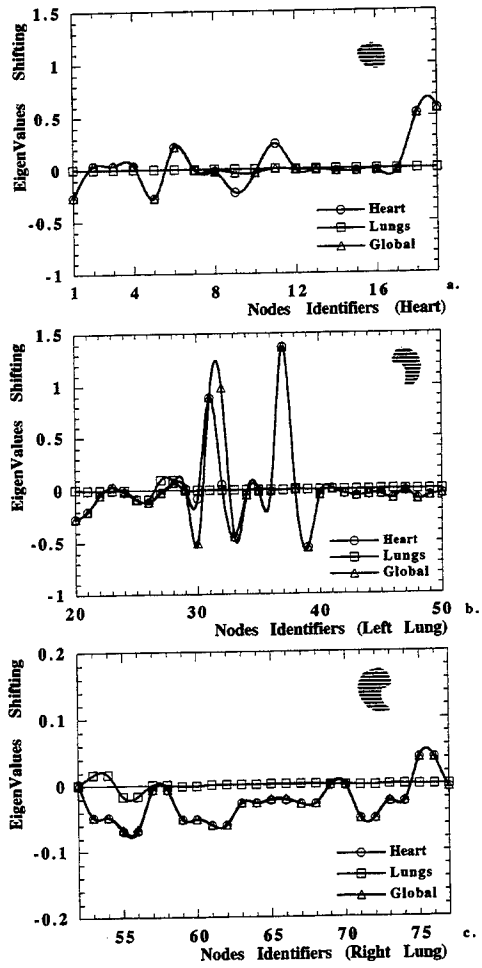

Figure 3. The Eigenvalues displacement w.r.t. the reference state (end-diastole)

The grid-independence for this problem was attained for 212 elements. This phase was hosted by the 286 MS-DOS-machine. The eigenvalues spectra for the stiffness matrix A were independently computed (FORTRAN) on an IBM RISC 6000 workstation.

Four models account for the modifications in shape and electric properties experienced by

lungs and heart between the *end-systole* and *end-diastole* phases of the cardiac cycle. The end-diastole phase (the heart is relaxed and its chambers are filled with blood) is the first model, taken as reference case. In the second model the heart has the shape and electric conductivity corresponding to the end-systolic contraction: the blood being ejected, the volume of the heart is smaller and its electric resistivity is higher. The third model accounts for the right and left lung changes at the end-systolic phase: although filled with blood, their volumes do not change significantly, hence only their electric resistivity is modified (decreased). Model four accounts for the changes in heart *and* lungs simultaneously.

These simple cases evidenced the changes in shapes and (electric) properties of each particular organ through their "modal-signature": for each case we built the stiffness (BEM) matrix A and computed the eigenvalues spectrum [Press W.H. et al. (1989) and SSL-IBM]. In fig. 3 we report the relative changes in the eigenvalues modules experienced by the mesh nodes on the heart surface (fig. 3a) on the left lung surface (fig. 3b) and on the right lung surface (fig. 3c) in the end-systole (fourth) model w.r.t. the end-diastole (first) model.

Conclusions

These preliminary results show that the modal sensitivity of the stiffness matrix (the EVC) may be used to investigate the cardiac cycle. Whereas in the IC it is difficult to identify the sources of changes and their trace in a single quantity, the electric impedance Z [Wang X et al. (1995), Wang L et al. (1995)], the EVC may use (theoretically) as many degrees of freedom (eigenvalues) as needed. Using computational and scanning resources that are currently available, these quantities are obtainable in real time.

At this preliminary stage it is worth noting that some difficulties have to be circumvented. The EVC is sensitive to factors such as the element type (first order, second order, etc.) and mesh adaptiveness in time. Hence, the most appropriate mesh to use for describing successive phases of the cardiac cycle, how to correlate the same patient's EVCardiograms in time to record some meaningful anatomical and physiological modifications, the optimal EVC *number* and *position* of the electrodes (we used the optimal pacing position) are some of the aspects to be addressed by further numerical experiments.

From a practical point of view, the EVC may rely on the MRI - a modern monitoring procedure used recently in the optimal pacing [Wang L. et al. (1995)] - and on a software that may be in fact an appropriate extension of the one used in the BEM pacing optimisation.

References

1. Kubicek, W. G., "Applications of the Minnesota impedance cardiography. Development and evaluation of an impedance cardiographic system to measure cardiac output and other cardiac parameters," University of Minnesota College of Medical Sciences, pp. 1-5, 1970.
2. Patterson, R. P., "Cardiac output determination using impedance plethysmography," M.S. Thesis, University if Minnesota, 1965.
3. Kubicek, W. G., "A bibliography of publications related to impedance cardiography," Minneapolis, MN, 1993.
4. Patterson, R. P., "Sources of thoracic cardiographic electrical impedance signal as determined by a model," Med. Biol. Eng. Comput., vol. 23, pp. 411-417, 1985.
5. Wang, X., Sun, H. H. and Van De Water, J. M., "An advanced signal processing technique for impedance cardiography," IEEE Trans. Biomed. Eng., vol. 42, no. 2, pp. 224-230, 1995.
6. Webster, J. G., "Minimizing cutaneous pain during electrical stimulation, " in *Proc. Ann. Int. Conf.*

IEEE Eng. Med. Biol. Soc., vol. 9, pp. 986 - 987, 1987.
7. Wang, L. and Patterson R. P., "Multiple sources of impedance cardiogram based on 3-D finite difference human thorax models," IEEE Trans. Biomed. Eng., vol. 42, no. 2, pp. 141-148, 1995.
8. Geddes, L. A. and Baker, L. E., *Principles of applied biomedical instrumentation*, 4th ed. New York: Wiley, 1989.
9. Geddes, L. A., Voorhees, W. D., Babbs, C. F., Sisken, R. and DeFord, J., "Precordial pacing windows," Pace, vol. 7, pp. 806 - 812, 1984.
10. Kim, D. W., Baker, L. E., Pearce, J. A. and Kim, W. K., "Origins of the impedance change in impedance cardiography by three-dimensional finite element model," IEEE Trans. Biomed. Eng., vol. 35, pp. 993 - 1000, 1988.
11. Woo, E. J., Hua, P. and Webster, J. G., "A finite element model with node renumbering for adaptive impedance imaging, " Proc. Ann. Int. Conf. IEEE Eng. Med. Biol. Soc., vol. 10, pp. 277 - 278, 1988.
12. Mohamed, O. A., Hagmann, M. J. and Uler, F. G., "Implanted electrodes potential distribution in a man model," Proc. Ann. Int. Conf. IEEE Eng. Med. Biol. Soc., vol. 12, pp. 1496 - 1497, 1990.
13. Sepulveda, N. G., Wikswo, J. P. and Echt, D. S., "Finite element analysis of cardiac defibrillation current distribution," IEEE Trans. Biomed. Eng., vol. 37, pp. 354 - 365, 1990.
14. Panescu, D, Webster, J. G. and Sratbucker, R. A., "Modeling current distributions during transcutaneous cardiac pacing," IEEE trans. Biomed. Eng., vol. BME-41, pp. 549 - 555, 1994.
15. Morega, Al.M., Ciocârlan, B. and Minciunescu, P., "An electrokinetic approach to the transcutaneous optimal pacing efficacy," Rev. Roumaine Sci. Techn. Electrotech. et Energ., submitted, 1995.
16. Brebbia, C. A., *The boundary element method for engineers.* Pentech Press, London, Plymouth, 1984.
17. Morega, Al. M. and Minciunescu, P., "Electrostatic modeling of a cap-rod insulators family," Rev. Roumaine Sci. Techn. Electrotech. et Energ., **37**, 4, pp. 445 - 456, 1992.
18. SSL - IBM Mathematical Library.
19. Press, W. H., Flannery, B. P., Teukolsky, S. A. and Vetterling, W. T., *Numerical Recipes in FORTRAN. The art of scientific computing.* Cambridge Univ. Press, 1989.
20. Mocanu, D., "The electric simulation of the cardiac pacing and monitorization procedures", M.S. Thesis, Polytechnica Univ. of Bucharest, 1995.

Optimal Transcutaneous Pacing

by

Alexandru M. Morega, Bogdan O. Ciocârlan and Mihaela Morega
Department of Electrical Engineering,
Politehnica University of Bucharest,
ROMANIA

Abstract

The transcutaneous pacing is one of the basic medical procedures applied in cardiac emergencies such as fibrillation, cardiac stop, etc. Its application is accompanied by negative side-effects (pains, tissue necrosis, etc.) that need to be reduced if not suppressed and factors such as the electrodes positions, shapes, areas are known to contribute to their reduction.

The present work focusses on the detection of the optimal (electrical) position for the electrodes that minimises the current density in the chest wall (that causes pain) while still preserving the current density in the heart wall above the stimulating threshold.

A cross-sectional (2-D) view through a human torso was considered. Specific boundary conditions (Dirichlet and Neumann) and interface conditions closed the electrokinetic associated problem. We used the boundary element method to find the voltage and current density distributions throughout the computational domain and, further on, to evaluate quantities relevant for the optimal pacing study.

Although the detailed 2-D cross-sectional domain is somewhat remote to the real-life case, it enables an insightful analysis of the process and is relevant in uncovering the (electrical) optimum of the procedure.

Introduction

The transcutaneous cardiac pacing is one of the basic procedures used in medical emergencies (defibrillation, intensive care, etc.). Usually, two electrodes placed on the thorax are used to apply an electric stimulus. Most available pacemakers deliver stimuli with a 20...40 msec duration, currents of order 60...150 mA for applied voltages in the range 100...1000 V and electrode pads with areas of 80...100 cm^2. The pacing threshold is reached for specific values of the current densities, typically higher in the chest wall than in the heart wall and, hence, negative side-effects (such as pain, tissues necrosis, etc.) accompany the pacing. Uniform current density electrodes, high-impedance gels, the duration of the stimulating pulse, the sizes of the electrodes [Bocka, J.J. (1989)] are reported factors that may play a significant role in decreasing the pain. The position of the electrodes is particularly important in further increasing the pacing efficacy [Flack, R.H. et al. (1986)]. Both experimental [Geddes, L.A. et al., (1984, 1989)] and computational efforts [Pilkington, T.C. et al. (1985) Mohamed, O.A. et al., (1990), Sepulveda, N.G. et al., (1990), Fahy, J.B. et al., (1987)] were devoted to finding the optimum placing of the electrodes. 2-D, 3-D finite differences, finite element studies led to the conclusion that the negative (receiving) electrode should be placed on the left lateral chest wall.

Panescu et al. (1994) formulated a detailed 2-D model and used a commercial FEA code [Klein, S.A. et al. (1989)] to solve an electrokinetic problem. They computed the *efficacy index*, R, defined through the ratio between the maximal current density in the chest wall (that causes pain) and the maximal current density in the heart wall (that causes the capture).

Our approach is based on the boundary element method (BEM), technique recognised to be particularly effective in the analysis of complex geometries [Brebbia, C.A. (1984)]. The code which we developed has domain mesh-generation capabilities that enable a fast, accurate processing phase [Morega, Al.M. et al. (19995)]. We consider the steady electrokinetic regime as described by Laplace equation with Dirichlet and Neumann homogeneous boundary conditions and investigated the influence of the electrodes placement upon the ratio R, for electrodes size of 70 cm^2.

The numerical model

The 2-D BEM model for a specific cross-section that passes through the middle of the eight thoracic vertebra, through the fourth costar cartilage at its sternal end and through a series of ribs [Panescu D. et al. (1994), Plonsey, R. (1988)] is shown in fig. 1. The main organs that were considered are: the chest wall (including the fat layer), the thoracic muscles and the dorsals, the sternum and the rib cartilage, the ribs, the backbone, the intercostal muscles, the oesophagus, the lungs, the heart (with atria and ventricles) and the interstitial fluid between the internal organs. The biological tissues are seen as continuous materials and their electrical conductivities are averaged over a volume containing many cells. Each domain is considered linear, time-independent, isotropic and without sources.

The related electrokinetic problem is defined through,

$$div\ \mathbf{J} = 0, \qquad \textit{(steady state form of the electric charge continuity law)}$$

$$\mathbf{J} = \sigma \mathbf{E}, \qquad \textit{(Ohm's law)}$$

$$\mathbf{E} = -\mathbf{grad}\ V, \qquad \textit{(steady state consequence of Faraday's law)}$$

or, consequently, $\Delta V = 0$ (Laplace, scalar problem). Here **J** is the current density, σ is the electric conductivity, **E** is the electric field strength and V is the electrokinetic potential.

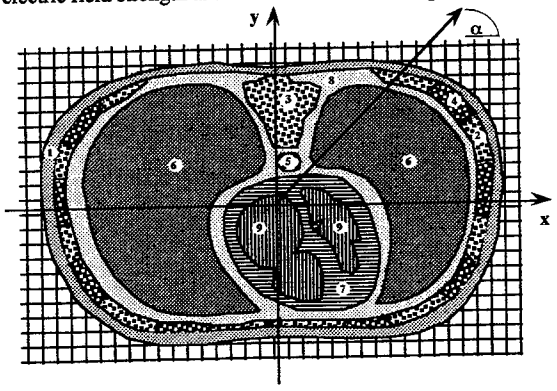

Figure 1. The anatomic model for the optimal pacing study: **1.** thoracic wall (skin, fat, thoracic muscles and dorsals); **2.** ribs; **3.** backbone; **4.** intercostal muscles; **5.** oesophagus; **6.** lungs; **7.** heart; **8.** interstitial fluid; **9.** blood that fills atria and ventricle.

The boundary conditions are (fig. 2): (1) *Dirichlet* (V specified on some parts of the thorax outline, namely at the electrodes level); (2) *Neumann*, homogeneous ($J_n = 0$, or $\partial V/\partial n = 0$ on the rest of the thorax outline) -- no current is emerging throughout the structure, except for the areas covered by the electrodes. On the interfaces between the organs standard conditions ($V_1 = V_2$, $J_{1n} = J_{2n}$, or $\sigma_1 \partial V_1/\partial n = \sigma_2 \partial V_2/\partial n$) were used.

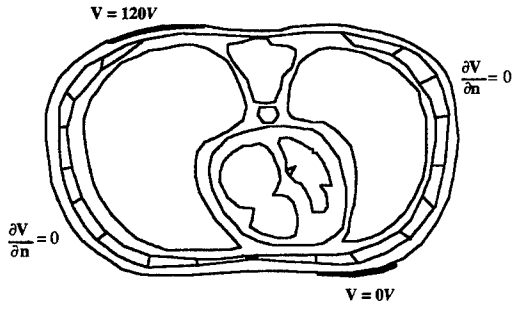

Figure 2. The boundary conditions.

The associated integral equation is:

$$\frac{\alpha_P}{2} u(x,y) = \int_\Gamma \left[G(x,y|x',y') \frac{\partial u(x',y')}{\partial n_\Gamma} - u(x',y') \frac{\partial G(x,y|x',y')}{\partial n_\Gamma} \right] d\Gamma -$$

$$\int_\Omega [G(x,y|x_1,y_1) F(x_1,y_1)] dx_1 dy_1$$

where:

$$\alpha_P = -2\pi \int_\Gamma \frac{\partial G(x,y|x',y')}{\partial n_\Gamma} d\Gamma = \begin{cases} 2\pi, & for\ P(x,y) \in \Omega, \\ \pi, & for\ P(x,y) \in \Gamma, \\ 0, & for\ P(x,y) \in Exterior\ (\Omega) \end{cases}$$

$$G(x,y|x',y') = \frac{1}{2\pi} ln \frac{1}{|r - r'|} = \frac{1}{2\pi} ln \frac{1}{\sqrt{(x-x')^2 + (y-y')^2}}$$

Ω is the domain, Γ is the boundary, $G(x,y|x',y')$ is Green's function in the 2-D problem and $F(x,y|x',y')$ is the interior source term (zero for Laplace equation).

Organ	*Resistivity [Ω·cm]*	
heart wall	500	
lungs	1,100	
ribs and backbone	16,600	
thoracic wall	2,300	
intercostal muscles	1,000	(longitudinal)
	150	(transversal)
oesophagus	2,300	
interstitial fluid	150	
blood	150	

Table I. Electric resistivity for different organs and tissues [after Panescu D. et al. (1994)].

The anisotropy of the intercostal muscles was accounted for through assigning the transverse resistivity for the muscles underneath the electrodes (the current flows perpendicularly to the muscles axis), the longitudinal resistivity for the muscles far apart from the electrodes (the current flows longitudinally) and the average resistivity for the muscles adjacent to the electrodes. Following the different inclusions (organs) the computational domain was divided in homogeneous subdomains (figs. 2, 3) and constant elements[4-points Gauss-Legendre quadrature] [Morega Al.M. et al. (1992)] were used.

The geometry and material properties were input (on a 286 PC compatible) to our home-made code (TURBO PASCAL and BORLAND C) that assembled the BEM matrices. The phase solution was hosted either by the 286 DOS-machine (TURBO PASCAL) for grids of up 300 nodes or by a 4381 IBM MVS-mainframe (FORTRAN) for the basic runs (less than 5 minutes for 832 nodes).

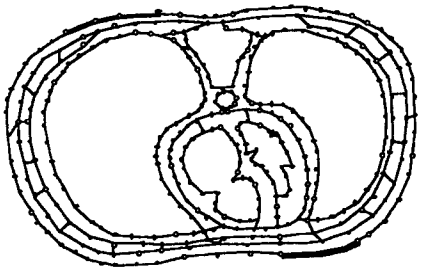

Figure 3. The BEM grid.

The primary unknowns (potential and/or gradient) were solved using either Gauss or LU (Crout version) [Press, W.H. et al. (1980)] -- for up to 300 unknowns -- or the IBM SSL routines for sparse matrices -- for more unknowns. The post-processing phase was then performed on a 286 PC. Other important quantities (electric field strength, current density) were computed thereafter at the interior nodes that were defined by using the automatic mesh-generator. Due to the space constraint we pass over several nontrivial numerical aspects and report here only the principal results.

Figure 5 shows typical spectra of constant voltage lines (left) and current density through out the structure (right) in the case when the electrodes are optimally positioned.

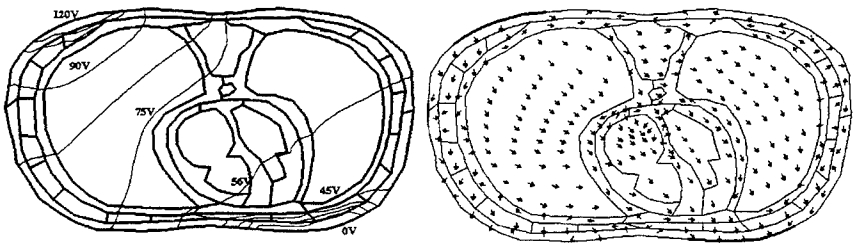

Figure 5. Left: lines of constant voltage; **Right**: current density distribution.

Results

We evaluated the ratio R for different electrodes locations to monitor the pacing efficacy. In the first stage of the analysis (the optimal position) electrodes of 70 cm^2 were considered. The negative electrode (0 V) was centred at the cardiac apex. The positive electrode (120 V) was shifted in the interval 84.24...219.55° until a first minimum, R_{min}, was obtained, then the negative electrode was shifted in the interval -60...60°.

a. The sensitivity of R with respect to the positive electrode position (fig. 6, left)

The negative electrode was centred at the cardiac apex. A first minimum for R (1.01) was found for $\alpha \approx 114°$, i.e. at the right scapula, in the vicinity of the fourth rib. Other positions are almost as good (e.g. $\alpha \approx 158°$). The optimal pacing arrangement for the electrodes is not that sensitive w.r.t. the positive electrode position as it is w.r.t. the negative electrode position. The ratio R is smaller when the electrode is centred on the rib rather than on the intercostal muscle. Further more, the peak current densities registered in the thoracic wall was in the range 8...19 A/cm^2.

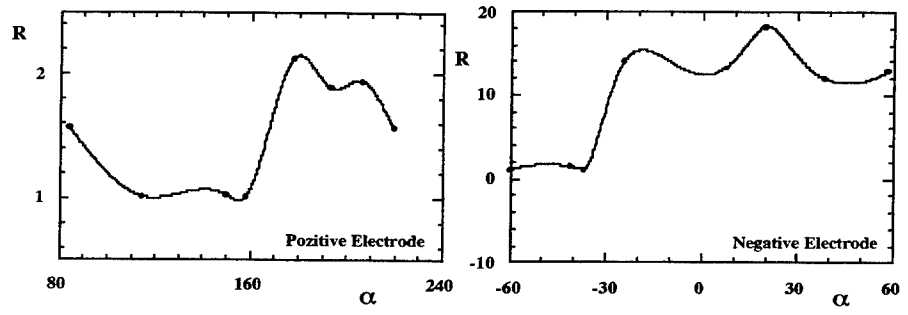

Figure 6. The optimal position (left) for the positive electrodes (the negative electrode is at the heart apex) and (right) for the negative electrode (the positive electrode is at the right scapula)

b. The sensitivity of R with respect to the negative electrode (fig. 6 right)

The positive electrode was kept at a fix location (the previous case) and the negative electrode was shifted around the thorax outline. The (final) minimum value, R_{min} = 1.0178, was found at $\alpha \approx$ 60°, what means at the cardiac apex. The peak current density was in the interval 4...18 A/cm^2.

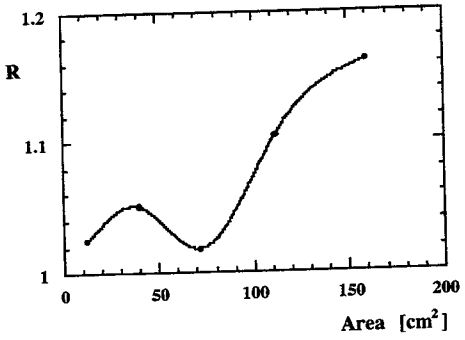

Figure 7. The optimal position for the negative electrode (the positive electrode is at the right scapula)

c. The sensitivity with respect to the electrode size (fig. 7)

Five different electrode sizes (13...160 cm^2) led to the conclusion that R_{min} (1.0178) is obtained for a size of 72 cm^2 (fig. 7), when the optimal position for the electrodes is adopted.

Conclusions

Through our simplified 2-D BEM electrokinetic, linear analysis we found that:

1) the best placement for the electrodes is at $\alpha \approx 114°$, for the positive electrode and at $\alpha \approx 60°$ for the negative electrode. However, other positions may be almost as good.
2) the ratio R is dependent on the negative electrode location rather than on the positive electrode location. It is larger when the electrodes are centred on ribs rather than on intercostal muscles;
3) the peak current density is in the range 4-19 A/cm^2 in the thorax and 2–19 A/cm^2 in the heart;
4) the largest density current value recorded is in the interstitial fluid.
5) the smallest current density value is in the ribs / backbone;
6) the optimal size of the electrodes is 72 cm^2; higher values do not significantly influence R.

References

1. Bocka, J. J., "External transcutaneous pacemakers," Ann. Emergency Med., vol. 18, pp. 45 - 51, 1989.

2. Geddes, L. A. and Baker, L. E., *Principles of applied biomedical instrumentation*, 4th ed. New York: Wiley, 1989.
3. Geddes, L. A., Voorhees, W. D., Babbs, C. F., Sisken, R. and DeFord, J., "Precordial pacing windows," Pace, vol. 7, pp. 806 - 812, 1984.
4. Pilkington, T. C., Morrow, M. N. and Stanley, P. C., "A comparison of finite element and integral equation formulation for the calculation of electrocardiographic potentials," IEEE Trans. Biomed. Eng., vol. BME-32, pp. 166-173, 1985.
5. Mohamed, O. A., Hagmann, M. J. and Uler, F. G., "Implanted electrodes potential distribution in a man model," Proc. Ann. Int. Conf. IEEE Eng. Med. Biol. Soc., vol. 12, pp. 1496 - 1497, 1990.
6. Sepulveda, N. G., Wikswo, J. P. and Echt, D. S., "Finite element analysis of cardiac defibrillation current distribution," IEEE Trans. Biomed. Eng., vol. 37, pp. 354 - 365, 1990.
7. Fahy, j. B., Kim, Y. and Ananthaswamy, A., "Optimal electrode configurations for external cardiac pacing and defibrillation: an inhomogeneous study," IEEE Trans. Biomed. Eng., vol. BME-34, pp. 743 - 748, 1987.
8. Panescu, D, Webster, J. G. and Sratbucker, R. A., "Modeling current distributions during transcutaneous cardiac pacing," IEEE trans. Biomed. Eng., vol. BME-41, pp. 549 - 555, 1994.
9. Klein, S. A., Beckman, W. A. and Myers, G. E., "FEHT A finite element analysis program for heat transfer and electromagnetics," Dept. Mech. Eng., Univ. of Wisconsin, Madison, WI, 1989.
10. Brebbia, C. A., *The boundary element method for engineers*. Pentech Press, London, Plymouth, 1984.
11. Morega, Al. M. and Minciunescu, P., "Electrostatic modeling of a cap-rod insulators family," Rev. Roumaine Sci. Techn. Electrotech. et Energ., **37**, 4, pp. 445 - 456, 1992.
12. Plonsey, R., "Electrocardiography," in Encyclopaedia of medical devices and instrumentation, vol. 2, J. G. Webster, Ed. New York: Wiley, 1988.
13. SSL - IBM Mathematical Library
14. Press, W. H., Flannery, B. P., Teukolsky, S. A. and Vetterling, W. T., *Numerical Recipes in FORTRAN. The art of scientific computing*. Cambridge Univ. Press, 1989.
15. Ciocârlan B, "The electric modeling of the investigation and stimulation techniques used in the cardio-vascular disorders", M.S. Thesis, Polytechnica Univ. of Bucharest, 1995.

VI = Volume I
VII = Volume II

AUTHOR INDEX

Abrams, R. VI-383
Adler. R.W. VI-52
Aguirre, G. VII-1273
Ahuja, V. VII-1072
Anders, R. VI-40, 46
Archambeault B. VII-850
Auclair, P.F. VI-188
Baca, E.A. VI-516
Bader, B. VI-310
Baginski, M.E. VI-334
Bahar, E. VI-205
Balakrishnan, N. VI-448, VII-776
Baranov, V.A. VI-142
Bardati, F. VII-1010
Barnhart, G.A. VII-712
Beggs, J.H. VI-523
Belrose, J.S. VI-2
Benson, T.M. VI-246
Berger, H.S. VII-850
Bindiganavale, S.S. VI-563, 596
Bingle, M. VI-391
Biswas, R. VI-436
Bleszynski, E. VI-580
Bleszynski, M. VI-580
Blocher, S.A. VI-516
Blocher, T.W. VII-696, 1158
Bluck, M.J. VI-196
Boag, A. VII-726
Boley, D. VI-645
Borges, A.R. VI-367
Bowen, T.S. VI-516
Brauer, J. VII-946, 1212
Breakall, J.K. VI-33, 502
Breed, G.A. VI-26
Bretchko, P. VII-980
Bürger, B. VI-653
Burke, G.J. VII-671
Burkholder, R.J. VI-117
Calvetti, D. VI-638
Cangellaris, A. VII-1273, 1311
Casciato, M. VII-1174
Cascio, L. VI-317
Chan, C. VI-436
Chan, K.W. VII-1065
Chen, J.S. VI-221, VII-1049
Chen, M. VII-1004
Chen, S. VI-279
Chen, Z. VII-932
Cherkashin, Y.N. VI-481
Chew, W.C. VII-962
Chizever, H.M. VI-153
Choo, V.K.C. VII-1158
Chou, C.K. VII-1065
Chou, H.T. VI-117
Christopoulos, C. VI-246
Ciocârlan, B. V
Clemens, M. VII-1295
Cloete, J.H. VI-179, 391
Cooper, R.M. VII-687
Crouch, D. VII-1041
Davidson, D.B. VI-179, 391
Davidson, D.B. VII-972
Debicki, M.P. VI-214
DeFord, S.J. VII-1190
de Lima, F. VII-1290
DeLyser, R.R. VI-571, VII-1248
de Menezes, L. VI-294
de Ribamar S. Oliveira, J. VI-367
de-Ribamar S. Oliveira, J. VII-1280
Dodson, S.J. VI-196
Dresel, J. VII-802
Drewniak, J.L. VII-857
Drozd, A.L. VII-1158
Dular, P. VI-456
Dyczij-Edlinger, R. VII-1227
Efanov, A.A. VII-664, 1166
El-Shenawee, M. VI-205
Elsherbeni. A. VII-1260
Ensaf, P. VII-1248
Eremenko, V.A. VI-481
Eremin, Y. VII-758, 763
Esselle, K. VII-826
Estep, D. VI-611
Estienne, J.P. VII-1238
Eswarappa, C VI-302
Evans, J.A. VI-340
Ferguson, R.C. VI-473
Ferreira, J. VI-367
Floyd, Jr., V.M. VI-188
Fourie, A.P.C. VII-802
Fu, J.S. VII-995
Gelosh,D.S. VI-398, 429
Gerace, G.C. VI-188, VII-712
German, F. VI-270
Givati, O..VII-802
Glisson, A.W. VII-784, 842
Gnos, M. VII-769
Goggans, P.M. VI-152
Gomes d' Assunção, VII-1280, 1286, 1290
Goorjian, P.M. VI-533
Gordon, R.K. VI-375, 443
Gothard, G.K. VI-622
Gottlieb, D. VII-1122
Gravelle, L.B..VII-1238
Hadi, M.F. VII-1023
Han, L. VII-1202
Hansen, B. VI-406
Hantman,B. VI-383
Harrison, L.A. VI-375
Harrison, J.G. VII-1220
Hastings,F. VII-1057
Hatfield, J.B. VI-421
Haupt, R.L. VII-742
Henderson, L.W. VI-93
Henderson, J.H. VI-622
Ho, K. VI-436
Hodel, A.S. VI-622
Hoefer, W.J.R. VI-294, 302, 317
Hoffman, A. VI-52
Holland, R. VII-877
Houshmand, B. VII-1004
Hubing, T.H. VII-857
Hutchcraft, W.E. VI-443
Ida, N. VII-1196
Isele, B. VI-287
Itoh, T. VII-1004, 1267
Jakobus, U. VI-101
Jaroszewicz, T. VI-580
Jarriel, Jr., G. VI-334
Jedrzejewski, P. VI-214
Jenn, D.C. VII-832
Jiang, Z.R. VII-1196
Jin, J.M. VII-962, 1182
Junker, G.P. VII-784, 842
Jyonori,Y. VI-492
Kadrovach, B.A. VI-398, 429
Karpenko, A.L. VI-469
Katehi, L.P.B. VII-954, 1303
Kazama, Y. VII-679
Kempfner, E. VII-719
Kishk, A.A. VII-784, 842
Klement, D. VII-719
Knorr, J.B. VII-792, 832
Koltsov, V.V. VI-469
Konrad, A. VII-1202
Kooi, P.S. VII-664
Kopylov, Y.V. VI-142
Kotulski, J.D. VI-228
Krumpholz, M. VI-238, VII-1303
Kubina, S.J. VII-703
Kuo, C-N. VII-1267
Kuzuoglu, M. VII-1212
LaBelle, J. VI-383
Lam, C-W. VII-870, 888
Landstorfer, F.M. VI-101
Larsson, M.G. VI-611
Laskey, K.J. VI-347
Lee, J-F. VI-555, VII-980, 1227
Lee, R. VII-932, 1108
Legros, W. VI-456
Leonard, P.W. VI-354, 421
Leong, M.S. VII-664
Leuchtmann, P. VII-769
Leung, C.Y. VI-196
Linhares, F. VI-367
Lins de Albuquerque, M.R.M. VII-1290
Lizalek, G.C. VII-946, 1190, 1212
Lomtev, V.O. VII-1166
Long, L.N. VII-1072
Longtin, M. VI-347
Lu, N. VII-1182
Lu, Y. VII-734, 995, 1142
Luebbers, R.J. VI-84, VII-1031
Lysiak, K. VI-502,
Madono, K. VII-679
Malan, D. VII-972
Marhefka, R.J. VI-93
Martins de Mendonça, L. VII-1286
McDaniel, P. VII-1248
McDougall, J.A. VII-1065
Mendiitto, D. VII-1010
Michielssen, E. VII-726
Mielewski, J. VI-214
Mikhailov, M.Y. VII-1166
Miller, E.K. VI-588, VII-1132
Misra, P. VII-750
Mishra, S.R. VII-750, 1092
Mittra, R. VI-270, VII-1212
Miyazaki, Y. VI-492
Mocanu, D. VII-1320
Monk, P. VI-619
Mooney, J.E. VI-163

Morega, A.M. VII-1320, 1326
Morega, M. VII-1320, 1326
Morrison, P.J. VI, 347
Mrozowski, M. VI-214, 413, 529
Murphy, R.K. VI-171
Naishadham, K. VII-750
Natsuhara, K. VII-679
Ney, M.M. VI-254, 262
Nicolaides, R. VI-604
Niedźwiecki, M. VI-413
Nott, H.A. VI-326
Nurnberger, M. VII-1174
Okoniewski, M. VI-529
Orlov, N.V. VII-758
Otero, M.F. VI-109
Özdemir, T. VII-1174
Packer, M.J. VI-473
Pasala, K. VI-153
Pasik, M.F. VII-1273
Pathak, P.H. VI-117
Pellerin, T. VII-703
Pena, N. VI-254, 262
Peng, C. VI-645
Perepelitsa, S. VII-1227
Perez, R. VII-861
Peterson, A.F. VII-988, 1116, 1230
Pflug, D.R. VII-696
Piket-May, M. VII-1023
Pocock, M.D. VI-196
Pohle, H. VI-571
Polstyanko, S.V. VI-555, VII-980
Popov, A.V. VI-138, 142,
Popov, V.A. VI-486
Przybyszewski, P. VI-214
Pursel, J.D. VI-152
Putnam, J.M. VI-228
Qiu, Y. VII-1196
Railton, C. VII-1057
Ramahi, O.M. VII-1260
Reichel, L. VI-638
Remacle, J.F. VI-456
Riggs, L.S. VI-163, 334
Riley, D.J..VI-536
Robert, F. VI-456
Robertson, R. VII-1303
Rojas, R.G. VI-109
Romanuk, V.P. VI-486
Ross, D.O. VII-696
Royer, G.M. VI-12
Rozzi, T. VI-317
Rubin, L. VII-888
Ruehl, J. VII-946
Russer, P. VI-238, 287, 310
Sabbagh, H.A. VI-171
Savage, J.S. VII-988
Schmöller, J. VI-287
Schneider, J.B. VII-1057
Schuh, M.J. VII-1100
Schumann, R. VII-1295
Schuster, J.W. VI-84, VII-1031
Seidl, A.A. VI-221
Seregelyi, J.S. VII-818
Sharma, R. VI-448
Shridhar, B.S. VII-776
Siarkiewicz, K.R. VI-383, VII-1158
Sigalas, M. VI-436
Singer, H. VI-653
Skousen, N. VI-406
Smith, C.E. VII-1260
Smith, C.R. VI-163
Smith, M.H. VII-1230
Soukoulis, C. VI-436
Speciale, R. VI-464, 898, 914, 918
Speciale, R. VII-1150
Starke, G. VI-630
Stein, V. VII-719
St. John, R. VII-877
Stuchly, M.A. VI-529
Suchomski, P. VI-413
Suda, T. VII-679
Sullivan, D. VI-406
Sultan, N. VII-703
Sutton, R.W. VI-347
Svigelj, J.A. VI-270
Syed, H.H. VI-76
Tardioli, G. VI-317
Tarplee, M.C. VI-60
Taylor, C.D. VI-523
Tentzeris, E. VII-1303
Terzuoli, Jr., A.J. VI-188, 398, 429
Terzuoli, Jr., A.J. VII-712
Thiele, E.T. VII-1023
Thoma, P. VII-1083, 1295
Tognolatti, P. VII-1010
Trenkic, V. VI-246
Trueman, C.W. VII-703, 1092
Turner, C.D. VI-536
Umé , M. VI-456
Vahldieck, R. VI-279
van Tonder, J. VI-179
Vaughan, J. VII-1220
Velez, J. VI-367
Vinogradov, A.V. VI-142
Volakis, J.L. VI-76, 563, 596, VII-1174
Walles, T.S. VI-398, 429
Walker, M.J. VII-939
Walker, S.P. VI-196
Wang, D-Q VI-604
Warren, D.E. VII-696
Weiland, T. VII-1083, 1295
Weile, D.S. VII-726
Wheless, C.S. VI-68
Wheless, Jr., W.P. VI-68
Williams, R.D. VI-611
Wilsen, C.B. VII-972
Woo, A.C. VII-1100
Woo, L.W. VI-383
Xu, J..VII-995
Yan, K.K. VII-734
Yang, B. VII-1122
Yee, K.S. VII-1049
Yook, J-G VII-954
Younan, N. VI-523
Yousif, H.A. VI-125
Yuan, F. VII-888
Zhang, Q. VI-638
Zhang, Q.K. VII-1196
Zhao, L. VII-1311
Zmyslo, J. VI-502
Zogbi, G. VI-117
Zolotarev, I.P. VI-131, 486
Zook, B. VI-508
Zunoubi, M.R. VI-523